TopFuel

REACTOR FUEL PERFORMANCE 2015

Conference Proceedings Part I

Zurich, Switzerland
13 - 17 September 2015

ENS CONFERENCE

TopFuel 2015 Gold Sponsor

Westinghouse

TopFuel 2015 Silver Sponsor

EDF

organised in cooperation with:

IAEA
International Atomic Energy Agency
Atoms For Peace

AMERICAN NUCLEAR SOCIETY

ATOMIC ENERGY SOCIETY OF JAPAN

CNS

KNS KOREAN NUCLEAR SOCIETY

European Nuclear Society
Avenue des Arts 56
1000 Brussels, Belgium
Phone + 32 2 505 30 54
Fax +32 2 502 39 02
E-mail ens@euronuclear.org
Internet www.euronuclear.org

ISBN 978-92-95064-23-2

Enhanced Accident Tolerant Fuel

TopFuel2015-A0025	PROGRESS ON THE RESEARCH AND DEVELOPMENT OF INNOVATIVE MATERIAL FOR NUCLEAR REACTOR CORE WITH ENHANCED SAFETY	Okonogi, K. (1); Kakiuchi, K. (1); Katayama, Y. (1); Yoshioka, K. (1); Hinoki, T. (2); Hashimoto, N. (3); Kano, F. (1); Matsumiya, H. (1); Takeuchi, Y. (1); Kondo, S. (2); Lee, M. (2); Isobe, S. (3) 1 - Power & Industrial Systems R&D Center, Toshiba Corporation, Japan 2 - Institute of Advanced Energy, Kyoto University, Japan 3 - Faculty of Engineering, Hokkaido University, Japan
TopFuel2015-A0102	LONG-TERM CORROSION BEHAVIOR AND MECHANICAL PROPERTY OF SILICON CARBIDE FOR PWR FUEL CLADDING APPLICATIONS	Kim, W.-J. (1); Kim, D. (1); Lee, H. G. (1); Park, J. Y. (1); Park, J. H. (1) 1 - Korea Atomic Energy Research Institute, Korea, Republic of
TopFuel2015-A0130	SIC/SIC COMPOSITE BEHAVIOR IN LWR CONDITIONS AND UNDER HIGH TEMPERATURE STEAM ENVIRONMENT	Lorrette, C. (1); Sauder, C. (1); Hossepied, C. (1); Billaud, P. (1); Loupias, G. (1); Braun, J. (1); Torres, E. (2); Rebillat, F. (2); Michaux, A. (1); Bischoff, J. (3); Ambard, A. (4) 1 - CEA DEN, DMN, centre de Saclay, France 2 - LCTS, UMR CNRS-UB-CEA-SAFRAN, France 3 - AREVA-NP, France 4 - EDF R&D, MMC Department, France
TopFuel2015-A0145	DEVELOPMENT OF FUELS WITH ENHANCED ACCIDENT TOLERANCE	Bischoff, J. (1); Brachet, J.-C. (2); Lorrette, C. (2); Strumpell, J. (3); Mccoy, K. (3) 1 - AREVA NP, France 2 - CEA-Saclay, DEN-DMN-SRMA, France 3 - AREVA Inc., United States
TopFuel2015-A0157	INNOVATIVE TESTING METHOD FOR JOINTS OF SILICON CARBIDE TUBES	Gentile, M. (1); Abram, T. (1) 1 - The University of Manchester, United Kingdom

PWR Operating Experience

TopFuel2015-A0048	IN-REACTOR PERFORMANCE OF HIPER16(TM) FUEL DESIGN	Jeon, S.-Y. (1); Yoo, J.-S. (1); Kim, H.-J. (1); Choi, K.-S. (1); Kim, J.-I. (1); Jeon, K.-L. (1) 1 - KEPCO Nuclear Fuel , Korea, Republic of
TopFuel2015-A0134	Q12TM ULTRA LOW TIN QUATERNARY ALLOYS FOR STRUCTURAL COMPONENTS IN PWR FUEL ASSEMBLIES	Chabretou, V. (1); Trapp-Pritsching, S. (2) 1 - AREVA NP SAS, France 2 - AREVA GmbH, Germany
TopFuel2015-A0198	POST IRRADIATION EXAMINATIONS OF GAIA LEAD FUEL ASSEMBLIES	Louf, P.-H. (1); Gentet, G. (1); Lippert, H.-J. (2); Mindt, M. (2); Peucker, J. (2); Jasiulevicius, A. (3) 1 - AREVA, AREVA SAS, France 2 - AREVA, AREVA GmbH, Germany 3 - VATTENFALL NUCLEAR FUEL AB, Sweden
TopFuel2015-A0212	PWR FUEL PERFORMANCE AND KEY DEVELOPMENTS IN MATERIAL AND MECHANICAL DESIGN	Halligan, J. (1); Pan, G. (1); Garde, A. (1); Norrell, J. (1) 1 - Westinghouse Electric Co., United States
TopFuel2015-A0214	PERFORMANCE OF M-MDA, RELIABLE CLADDING MATERIAL FOR ADVANCED FUEL	Watanabe, S. (1); Okada, Y. (1); Sato, D. (1); Teshima, H. (1); Kido, T. (2); Shinohara, Y. (2); Kameda, Y. (3) 1 - Mitsubishi Nuclear Fuel Co. Ltd., Japan 2 - Nuclear Development Co. Ltd., Japan 3 - The Kansai Electric Power Co. Inc., Japan
TopFuel2015-A0215	FIRST DNB TESTS AT THE WESTINGHOUSE ADVANCED LOOP TESTER (WALT)	Wang, G. (1); Byers, W. (1); Karoutas, Z. (1); Ray, S. (1); Oelrich, R. (1); Burgos, B. (1) 1 - Westinghouse Electric, United States

Modelling, analysis, methods I

TopFuel2015-A0058	MODELLING CLADDING RESPONSE TO CHANGING CONDITIONS	Tulkki, V. (1); Ikonen, T. (1) 1 - VTT Technical Research Centre of Finland ltd, Finland
TopFuel2015-A0067	THERMODYNAMIC MODELING OF MOLYBDENUM BEHAVIOR IN CHLORIDE MOLTEN SALT	Nichenko, S. (1); Streit, M. (1) 1 - Isotope and Elemental Analysis, Department Nuclear Energy and Safety, Paul Scherrer Institut, Switzerland
TopFuel2015-A0073	EFFECT OF POWER VARIATIONS ACROSS A FUEL BUNDLE AND WITHIN A FUEL ELEMENT ON FUEL CENTERLINE TEMPERATURE IN PHWR BUNDLES IN UNCREPT AND CREPT PRESSURE TUBES	Onder, E. N. (1); Roubtsov, D. (1); Rao, Y. (1); Wilhelm, B. (2) 1 - Canadian Nuclear Laboratories, Canada 2 - University of Guelph, Canada
TopFuel2015-A0075	AREVA'S ARCADIA® CODE SYSTEM – IMPLEMENTATION BENEFITS	Maupin, K. (1); Porsch, D. (2); Kuch, S. (2); Le Bars, F. (3); Opel, S. (2); Simonini, G. (3); Brock, R. (1); Deveney, D. (1); Curca-Tivig, F. (2) 1 - AREVA, AREVA Inc., United States 2 - AREVA, AREVA GmbH, Germany 3 - AREVA, AREVA NP, France
TopFuel2015-A0113	GLOBAL SENSITIVITY ANALYSIS IN FUEL PERFORMANCE MODELLING	Ikonen, T. (1) 1 - VTT Technical Research Centre of Finland, Finland
TopFuel2015-A0136	FEM MODELLING OF THE PWR CONTROL ROD DRAG FORCES IN DEFORMED GUIDE TUBES	Klouzal, J. (1); Dostál, M. (1) 1 - ÚJV Řež, a. s., Czech Republic
TopFuel2015-A0174	A STUDY ON EFFECTS OF CRYSTALLOGRAPHIC TEXTURE ON THE IRRADIATION GROWTH OF ZIRCONIUM ALLOY USING VISCO-PLASTIC SELF CONSISTENT MODELING APPROACH	Liu, W. (1); Tomé, C. (2); Montgomery, R. (3); Stanek, C. (2) 1 - ANATECH Corp., United States 2 - Los Alamos National Laboratory, United States 3 - Pacific Northwest National Laboratory, United States
TopFuel2015-A0190	FUEL ASSEMBLY SEISMIC AND LOCA SAFETY ANALYSIS UNDER END OF LIFE CONDITIONS AND FLOW WATER DAMPING EFFECTS	Lu, R. (1); Marshall, N. (1); Jiang, J. (1); Evans, P. (1) 1 - Westinghouse Electric Company, United States
TopFuel2015-A0201	AREVA SOLUTIONS TO LICENSING CHALLENGES IN PWR & BWR RELOAD AND SAFETY ANALYSIS	Curca-Tivig, F. (1) 1 - AREVA GmbH, Germany
TopFuel2015-A0206	A WESTINGHOUSE LOCAL FUEL DUTY PCI RISK MONITOR AND ANALYSIS TOOL	Boyd, W. (1); Mangham, G. (2) 1 - Westinghouse Electric Company LLC, Nuclear Fuel Methods & Technology, United States 2 - Westinghouse Electric Company LLC, Nuclear Fuel Core Engineering, United States
TopFuel2015-A0230	EFFECTS OF FUEL ROD UNCERTAINTY IN PWR HZP RIA ANALYSIS	Lee, J. (1); Woo, S. (1) 1 - KINS, Korea, Republic of

BWR Operating Experience

TopFuel2015-A0081	GNF FUEL PERFORMANCE 2015 UPDATE	Schneider, R. (1); Dunavant, R. (1); Ledford, K. (1); Fawcett, R. (1); Cantonwine, P. (1) 1 - Global Nuclear Fuel - Americas, United States
TopFuel2015-A0183	MONITORING THE INTEGRITY OF CONTROL ROD WITH AN ONLINE HELIUM LEAK DETECTOR	Ammon, K. (1); Loner, H. (1); Bieli, R. (1); Ledergerber, G. (1) 1 - Kernkraftwerk Leibstadt AG, Switzerland
TopFuel2015-A0187	CORROSION AND HYDROGEN PICKUP IN ZIRCALOY-2 CHANNELS WITH AND WITHOUT PROXIMITY TO CONTROL BLADE	Schrire, D. (1); Karlsson, K. (2); Blomberg, G. (3); Moeckel, A. (4) 1 - Vattenfall Nuclear Fuel, Sweden 2 - Forsmarks Kraftgrupp AB, Sweden 3 - Studsvik, Sweden 4 - Areva, Germany

TopFuel2015-A0188	ATRIUM™ 11 – VALIDATION OF PERFORMANCE AND VALUE FOR BWR OPERATIONS	Cole, S. (1); Graebert, R.-F. (2); Garner, N. (1); Lippert, H.-J. (2); Mollard, P. (3) 1 - AREVA Inc, United States 2 - AREVA GmbH, Germany 3 - AREVA NP, France
TopFuel2015-A0219	WESTINGHOUSE BWR FUEL – EXPERIENCE UPDATE AND EVOLUTION OF HARDWARE AND METHODS DEVELOPMENT	Willman, L. (1); Andersson, S. (1); Hallstadius, L. (1); King, J. (2) 1 - Westinghouse Electric Sweden AB, Sweden 2 - Westinghouse Electric Company LLC, United States
TopFuel2015-A0223	FLAKING OF SHADOW OXIDE ON BWR CLADDING ASSOCIATED WITH PRE-EXISTING SURFACE SCRATCHES	Schrire, D. (1); Ledergerber, G. (2); Karlsson, K. (3); Carling, K. (4) 1 - Vattenfall Nuclear Fuel, Sweden 2 - Kernkraftwerk Leibstadt, Switzerland 3 - Forsmarks Kraftgrupp AB, Sweden 4 - Ringhals AB, Sweden

Advances in designs, materials and manufacturing I

TopFuel2015-A0055	THE CF3: AN ADVANCED FUEL ASSEMBLY DESIGN FOR PWR	Jiao, Y. (1); Ru, J. (1); Guo, X. (1); Xiao, Z. (1); Li, H. (1) 1 - Nuclear Power Institute of China, China
TopFuel2015-A0090	THE MISSION AND ACCOMPLISHMENTS FROM DOE'S FUEL CYCLE RESEARCH AND DEVELOPMENT (FCRD) ADVANCED FUELS CAMPAIGN	Carmack, J. (1); Goldner, F. (2); Braase, L. (1) 1 - Idaho National Laboratory, United States 2 - Department of Energy, United States
TopFuel2015-A0118	TECHNOLOGY READINESS LEVEL (TRL) ASSESSMENT OF ADVANCED NUCLEAR FUELS	Shepherd, D. (1); Rossiter, G. (1); Palmer, I. (1); Marsh, G. (1); Fountain, M. (1); Mathers, D. (1) 1 - National Nuclear Laboratory, United Kingdom
TopFuel2015-A0235	PILOT PROCESS DEVELOPMENT TO CHANGE SURFACE PROPERTIES PROVIDING THE INCREASED STABILITY OF LWR ZIRCONIUM COMPONENTS IN NORMAL OPERATION CONDITIONS AND IN EMERGENCY SITUATIONS	Ivanova, S. V. (1); Glagovskii, E. M. (1); Belugin, I. I. (1); Khazov, I. A. (2); Khomich, M. S. (3); Korogoda, O. P. (3); Khamutovsky, F. N. (3); Pasevich, P. I. (3) 1 - Institute of Industrial Nuclear Technologies of National Research Nuclear University "MEPhI", Russian Federation 2 - FSUE "Krasnaya Zvezda", Russian Federation 3 - "Polishing Technologies" Co., Ltd, Russian Federation
TopFuel2015-A0148	HIGH-RESOLUTION CHARACTERIZATION OF CORROSION AND HYDROGEN PICKUP OF ZR CLADDING ALLOYS	Hu, J. (1); Setiadinata, B. (1); Aarholt , T. (1); Garner, A. (2); Harte, A. (2); Ni, N. (3); Bagot, P. (1); Moore, K. (2); Frankel , P. (2); Lozano-Perez, S. (1); Moody, M. (1); Preuss, M. (2); Grovenor, C. (1) 1 - Department of Materials, University of Oxford, United Kingdom 2 - Materials Performance Centre, School of Materials, The University of Manchester, United Kingdom 3 - Department of Materials, Imperial College London , Royal School of Mines, United Kingdom
TopFuel2015-A0159	TEST REACTOR EVALUATION OF ZIRCONIUM ALLOY NNMCA CORROSION BEHAVIOR	Lutz, D. (1); Lin, Y.-P. (1); Varela, J. (2); Edsinger, K. (3); Kucuk, A. (3); Cantonwine, P. (1) 1 - Global Nuclear Fuel - Americas, United States 2 - GE Hitachi Nuclear Energy, United States 3 - Electric Power Research Institute, United States
TopFuel2015-A0160	TEST REACTOR EVALUATION OF ZIRCONIUM ALLOY SHADOW CORROSION BEHAVIOR	Lutz, D. (1); Lin, Y.-P. (1); Varela, J. (2); Edsinger, K. (3); Kucuk, A. (3); Mcgrath, M. (4); Cantonwine, P. (1) 1 - Global Nuclear Fuel - Americas, United States 2 - GE Hitachi Nuclear Energy, United States 3 - Electric Power Research Institute, United States 4 - Halden Reactor Project, Norway

TopFuel2015-A0191	XANES ANALYSIS OF IRON IN ZIRCALOY-4 OXIDES FORMED AT DIFFERENT TEMPERATURES STUDIED WITH MICROBEAM SYNCHROTRON RADIATION	Ensor, B. (1); Motta, A. (1); Bajaj, R. (2); Seidensticker, J. (2); Cai, Z. (3) 1 - Department of Mechanical and Nuclear Engineering, The Pennsylvania State University, United States 2 - Bettis Atomic Power Laboratory, Bechtel Marine Propulsion Corporation, United States 3 - Advanced Photon Source, Argonne National Laboratory, United States
TopFuel2015-A0216	ADVANTAGES GAINED BY INTRODUCING LOW TIN ZIRLO AS BWR CHANNEL MATERIAL	Andersson, B. (1); Bergmann, U. (1); Dahlbäck, M. (1); Hallstadius, L. (1); Haskins, W. (2); Limbäck, M. (1) 1 - Westinghouse Electric Sweden, Sweden 2 - Westinghouse Electric Company, Western Zirconium Plant, United States
TopFuel2015-A0218	EVOLUTION OF HYDROGEN PICKUP FRACTION WITH OXIDATION RATE ON ZIRCONIUM ALLOYS	Romero, J. (1); Partezana, J. (1); Comstock, R. (1); Hallstadius, L. (2); Motta, A. (3); Couet, A. (4) 1 - Westinghouse Electric Company, United States 2 - Westinghouse Electric Sweden, Sweden 3 - Pennsylvania State University, United States 4 - EDF, France
TopFuel2015-A0012	ELIMINATION OF SOLUBLE BORON IN PWR DESIGNS WITH THE BIGT BURNABLE ABSORBERS	Yahya, M.-S. (1); Yu, H. (1); Kim, Y. (1); Kim, H. H. (2) 1 - Korea Advanced Institute of Science and Technology (KAIST), Korea, Republic of 2 - KEPCO Engineering & Construction Company (KEPCO E&C), Korea, Republic of
TopFuel2015-A0045	RESEARCH ON MANUFACTURING TECHNOLOGY OF LARGE GRAIN SIZE FUEL PELLETS	Wang, P. (1); Xiaoxiang, C. (1) 1 - CNNC Jianzhong Nuclear Fuel CO.,Ltd., China
TopFuel2015-A0109	POSITRON ANNIHILATION SPECTROSCOPY STUDY OF LATTICE DEFECTS IN NON-IRRADIATED DOPED AND UN-DOPED FUELS	Chollet, M. (1); Krsjak, V. (1); Cozzo, C. (1); Bertsch, J. (1) 1 - Paul Scherrer Institut, Switzerland
TopFuel2015-A0117	MODELLING OF POWDER DIE COMPACTION FOR PRESS CYCLE OPTIMIZATION	Bayle, J.-P. (1) 1 - CEA-Marcoule, DEN/DTEC/SDTC/LTAP, France
TopFuel2015-A0245	HIGH TEMPERATURE DECOMPOSITION OF URANIUM-BASED MIXED NITRIDES	Mikhalchik, V. (1); Tenishev, A. (1); Baranov, V. (1); Lunev, A. (1); Shornikov, D. (1) 1 - National Research Nuclear University MEPhI (Moscow Engineering Physics Institute), Russian Federation
TopFuel2015-A0131	CAP1400 FUEL ASSEMBLY SELF-RELIANT DEVELOPMENT PROGRESS IN CHINA	Zhu, L. (1); Ding, J. (1); Gan, F. (1); Zeng, Q. (1); Ding, Y. (1); Zheng, Y. (1); Lu, J. (1); Zhou, Y. (1); Zhou, Q. (1); Liu, J. (1) 1 - Shanghai Nuclear Engineering Research and Design Institute, China
TopFuel2015-A0217	CORROSION BEHAVIOUR OF ALLOY X-750 IN BWR FUEL AT HIGH FLOW RATES	Göransson, K. (1); Gustafsson, C. (2); Lai, H. (3); Tuzi, S. (3); Thuvander, M. (3); Stiller, K. (3); Hallstadius, L. (1); Kucuk, A. (4); Josefsson, B. (5) 1 - Westinghouse Electric Sweden AB, Sweden 2 - Studsvik Nuclear AB, Sweden 3 - Chalmers University of Technology, Sweden 4 - Electric Power Research Institute, United States 5 - Vattenfall Nuclear Fuel AB, Sweden

Multiphysics and thermomechanical modelling I

TopFuel2015-A0083	MODELLING OF FUEL BEHAVIOUR DURING LOSS-OF-COOLANT ACCIDENTS USING THE BISON CODE	Pastore, G. (1); Novascone, S. (1); Williamson, R. (1); Hales, J. (1); Spencer, B. (1); Stafford, S. (1) 1 - Idaho National Laboratory, United States
TopFuel2015-A0104	MODELING OF THE RIM-STRUCTURE THERMAL ANNEALING EXPERIMENTS WITH A NEW FGR MODEL FOR START-3A CODE	Chulkin, D. (1); Shestopalov, A. (1); Kuznetsov, V. (1); Novikov, V. (1) 1 - OJSC «Academician A.A. Botchvar High-Technology Scientific and Research Institute of Inorganic Materials» (OJSC VNIINM), Russian Federation
TopFuel2015-A0110	MULTIPHYSICS SIMULATION OF FAST TRANSIENTS WITH THE FINIX FUEL BEHAVIOUR MODULE	Ikonen, T. (1); Syrjälahti, E. (1); Valtavirta, V. (1); Loukusa, H. (1); Leppänen, J. (1); Tulkki, V. (1) 1 - VTT Technical Research Centre of Finland, Finland
TopFuel2015-A0213	MICRO-MECHANISTIC MODELING OF BLADE WING SWELLING OF THE WESTINGHOUSE BWR CONTROL ROD CR 99	Jinnestrand, M. (1); Seltborg, P. (1); Rebensdorff, B. (1) 1 - Westinghouse Electric Sweden, Sweden
TopFuel2015-A0017	MODELLING OF FISSION GAS RELEASE IN IRRADIATED UO2 UNDER TRANSIENT CONDITIONS	Veshchunov, M. (1); Tarasov, V. (1) 1 - Nuclear Safety Institute (IBRAE), Russian Academy of Sciences, Russian Federation
TopFuel2015-A0020	ASSESSMENT OF STAINLESS STEEL FUEL ROD PERFORMANCE AGAINST LITERATURE AVAILABLE DATA	Giovedi, C. (1); Cherubini, M. (2); Abe, A. (3); D'Auria, F. (4) 1 - UNIVERSITY OF SÃO PAULO, Brazil 2 - NINE, Italy 3 - IPEN/CNEN-SP, Brazil 4 - UNIPI, Italy
TopFuel2015-A0038	MODELING OF AXIAL DISTRIBUTION OF RELEASED FISSION GAS IN KKL BWR FUEL RODS DURING BASE IRRADIATION	Brankov, V. (1); Khvostov, G. (2); Mikityuk, K. (2); Pautz, A. (1); Ledergerber, G. (3); Wiesenack, W. (4); Abolhassani, S. (2); Restani, R. (2) 1 - Swiss Federal Institute of Technology Lausanne, Switzerland 2 - Paul Scherrer Institute, Switzerland 3 - Kernkraftwerk Leibstadt, Switzerland 4 - OECD Halder Reactor Project, Norway
TopFuel2015-A0070	IMPROVING THE ACCURACY OF PCMI SIMULATIONS WITH MORE REALISTIC GEOMETRY AND MATERIAL MODELS	Novascone, S. (1); Perez, D. (1); Hales, J. (1); Williamson, R. (1); Pastore, G. (1); Liu, W. (2); Spencer, B. (1); Gardner, R. (1) 1 - Idaho National Laboratory, United States 2 - Anatech Corp., United States

Enhanced Accident Tolerant Fuel

Screening of Reactor Performance and Safety of Fuel and Cladding Candidates with Enhanced Accident Tolerance

N. R. BROWN[1], M. TODOSOW, L-Y. CHENG, A. CUADRA
Brookhaven National Laboratory
Nuclear Science and Technology Department
PO Box 5000 Upton, NY 11973 USA

ABSTRACT

The United States Department of Energy Advanced Fuels Campaign has recently focused on the development of advanced nuclear fuel and cladding options with the potential for enhanced accident tolerance in light water reactors. Brookhaven National Laboratory has developed and applied an approach to screen the reactor performance and safety characteristics of candidate fuel and cladding concepts. This approach considers potential impacts on nominal operation as well as off-normal and accident conditions. The resultant methodology provides the capability to determine whether a proposed concept has at least equivalent performance and safety characteristics relative to current uranium dioxide (UO_2) fuel and zirconium alloy cladding. The three phases of the methodology are assembly-level screening analyses, three-dimensional core analyses, and transient systems analyses. These analyses inform on the suitability of a proposed fuel-clad system using the best available data. Material properties are assumed based on zero-burnup property data and volumetric weighting of phase fractions for many of the candidate advanced fuels. Uncertainties exist in these assumed properties and other parameters relevant to fuel performance, including swelling, pellet-cladding interaction, gap thickness and equivalent conductance, and fission gas release. This paper features two parts: (1) a review of recent analysis efforts that focuses on lessons learned from screening analyses for advanced fuels and (2) some specific examples of ongoing screening studies related to advanced steel cladding in light water reactors.

1. Introduction and review of lessons learned from recent efforts

Advanced light water reactor (LWR) fuel and cladding materials may offer potential benefits, including enhanced accident tolerance. While materials science considerations are a key driver for research and development (R&D) in advanced LWR fuel and cladding, it is vital to also consider the holistic view of fuel within a nuclear reactor system. Brookhaven National Laboratory (BNL) has developed an approach to screen the reactor performance and safety characteristics of advanced LWR fuel and cladding materials. This approach is important to understand the potential impact of novel materials and to provide information to decision makers.

Over the last several years a number of fuel and cladding materials have been analyzed at BNL from the perspective of LWR nuclear performance and safety characteristics. These analyses have identified potentially promising fuel and cladding options as well as issues that would have to be resolved for specific candidates. The first part of this paper is a review article focused on lessons learned from several years of performing these screening analyses. It is notable that other research laboratories and universities have also performed similar analyses, and this paper also highlights some of those efforts where relevant. The efforts reviewed in this paper focus on fully ceramic microencapsulated fuel [1, 2], ceramic composite fuels [3, 4], and advanced cladding materials [4]. Each of these are examples of candidate fuel or cladding

[1] Present affiliation: Oak Ridge National Laboratory, Oak Ridge, TN 37831 USA, brownnr@ornl.gov

materials being considered that may feature enhanced accident tolerance. The major objective of this paper is to highlight key findings for each of the candidate fuel and cladding materials.

Complete details of the screening methodology applied in each of these analyses are available in the relevant references [1 - 4]. Generally, the analyses are performed for a generic pressurized water reactor (PWR) similar to a Westinghouse AP1000. Some selected analyses in this paper were performed for a generic boiling water reactor (BWR) with lattice arrangements that are similar to GE14. The PWR lattice geometry is a 17 x 17 assembly and the BWR lattice geometry is a 10 x 10 assembly.

In cases where core calculations are employed, a PWR with 3-D geometry similar to the AP1000 is assumed. Thermal and hydraulic feedback is utilized in the core calculations, with a nominal reactor thermal power of 3400 MW. The core calculations in this document assume:

- Nodal neutron diffusion using a hybrid analytical nodal method and nodal expansion method solver
- Reactivity feedback for fuel temperature, moderator temperature, moderator density, boron concentration, and control rods using thermal and hydraulic models appropriate for PWR core analysis
- A 17 x 17 Westinghouse PWR assembly model for the generation of few-group parameters
- A generic cross section for reflector regions representative of a large Westinghouse PWR

Various reactor physics tools have been used in the screening efforts, with commensurate levels of code-to-code comparison to ensure confidence in the results. The lattice calculations reviewed in the document were performed with the Serpent Monte Carlo transport tool or the SCALE (TRITON/NEWT) lattice physics suite. The core calculations were performed using the PARCS nodal simulator with few group parameters from either Serpent or SCALE. Extensive comparison of Serpent and SCALE are detailed in References 1, 2, and 3. The core calculation methodology is detailed in Reference 3. Models used in the screening analyses are appropriate for scoping studies, but are not fully described in this paper.

1.1. Fully ceramic microencapsulated fuel

Dispersion fuels feature reduced heavy metal loading and therefore increased volumetric heat generation in the fuel meat. This paper focuses on the potential application of tri-isotropic carbon (TRISO) fuel in a ceramic or metal matrix within the form factor of an LWR fuel rod. A number of efforts have been devoted to studying fully ceramic microencapsulated (FCM) fuel in LWRs [1, 2, 5 - 13]. High-density uranium nitride (UN with a small admixture of UC) kernels have been identified as potentially promising, because they enable a higher loading of heavy metal than oxide kernels. A representative cartoon of an FCM “fuel pin” is shown in Figure 1. The BNL analysis of FCM fuel was focused on UN fuel kernels, although other kernel types were also considered on a scoping basis. The TRISO particle packing fractions considered were between 0.44 and 0.50. The matrix material considered in the BNL analyses was silicon carbide (SiC) and the cladding material was also SiC.

The primary benefit of FCM fuel is high fission product retention, as the TRISO particles act as a miniature pressure vessel that locally contains the fission products. The potential for oxidation resistance versus zirconium alloy cladding is another significant potential benefit. These fuels also may provide very high specific burnup, in excess of 150 GWd/t (gigawatt days per metric ton of heavy metal).

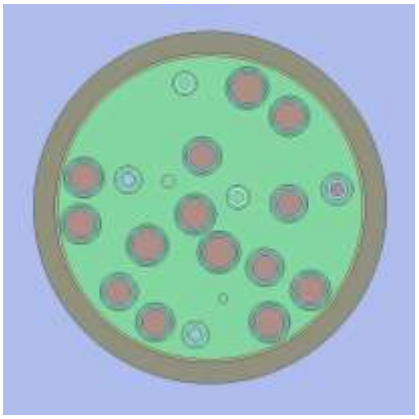

Fig 1. Plot of an FCM pin cell, showing randomly packed fuel particles, surrounding matrix, cladding, and coolant [1]

FCM fuel may be challenging from a fuel management perspective [1]. The high enrichment and reduced self-shielding within the fuel impacts the excess reactivity in fresh fuel, which requires very high burnable absorber loadings. The reactivity swing from beginning-of-life to end-of-life is extreme. One burnable absorber option that appears feasible is admixture of a UB_2 or UB_4 phase in the fuel kernel. This option was first suggested for FCM fuel in Reference 2, but has been explored by a variety of researchers. Admixture of small amounts of a uranium boride phase in the fuel as a burnable absorber is also the subject of a Westinghouse patent [14, 15]. Alternative burnable absorber configurations, such as erbium oxide, have also been considered [7].

Retrofitting of FCM fuel in the form factor of existing LWR assemblies will result in shortened fuel residence time in the core. It is not quite possible to reach 18-month cycles in a 17 x 17 PWR assembly with low-enriched uranium fuel and a realistic particle packing fraction (less than 0.50) [1]. There may be an economic penalty associated with shortened cycles. In addition, multiple studies have identified re-design of the reactor assembly configuration as highly relevant if FCM fuel is to be deployed in LWRs. One particular study focuses on optimization of a PWR assembly design for FCM fuel [11].

Reduced volume of fuel meat implies much higher volumetric heat generation rates in the fuel kernels. One challenge that has been identified is the thermal modeling of an FCM fuel rod, and the difference between the fuel kernel and matrix temperature [2]. Accurate modeling of fast transient events requires best-estimate thermal modeling, including explicit modeling of fuel kernels. Recent work at KAIST has begun to address some of the deficiencies of state-of-the-art reactor systems analysis tools when modeling dispersion fuels in LWRs [12, 13]. Significant additional work is needed in this area, including experiments to validate best-estimate thermal models of FCM fuel configurations.

1.2. Ceramic composite fuels

Ceramic composites have also been proposed as potential advanced LWR fuels. These composite fuels consist of various oxide, nitride, silicide, and boride phases. Relevant examples studied at BNL include UN/U_3Si_2, UN/U_3Si_5, and UO_2/UB_2, among others [3, 4]. Potential advantages of these fuel materials include enhanced thermal conductivity (and other thermal properties) and increased heavy metal density. These fuels are of interest to Westinghouse [15] and Los Alamos National Laboratory [16].

Our analyses for high-density ceramic composites have included consideration of several potential benefits. Because UN, U_3Si_2, and UB_2 phases have a significantly higher heavy metal density than UO_2, there are several options for integrating these fuels into a state-of-the-art LWR. The first option is to increase cycle length, maintain enrichment, and maintain linear power per pin. The second option is to maintain cycle length, maintain enrichment, and

increase linear power per pin. The third option is to maintain cycle length, decrease enrichment, and maintain linear power per pin. Finally, a fourth option is to maintain cycle length, maintain enrichment, maintain linear power per pin, and increase the number of batches in the fuel management scheme. We have considered, to varying degrees of fidelity, each of these potential options [3, 4].

The reactor physics behavior of the high-density composite fuels is typically similar to that of the reference UO_2 fuel. Differences in reactor physics behavior are primarily driven by the differences in self-shielding due to increased ^{238}U density as well as the possible presence of parasitic absorbers (such as ^{14}N) in the fuel. Due to the increased heavy metal density, the neutron spectrum is somewhat harder and the soluble boron reactivity worth is slightly weaker than for UO_2 fuel. Similarly, control rod worth and burnable poison worth is also marginally reduced with a fuel that has a higher heavy metal density than UO_2. In addition, high-density ceramic fuels are more under-moderated, so the moderator temperature coefficient is slightly stronger for these candidate fuels. These are important considerations when considering integration of these potential fuels in an existing LWR. However, a recent study [4] has shown that “drop in” ceramic composite fuels are potentially possible and would enable very similar reactor physics performance when compared to the reference UO_2 fuel.

Significant conclusions also include the fact that a four-batch fuel management scheme with a high-density UN-based composite fuel can closely match the ~18 month cycle length of the reference UO_2 fuel in a three-batch fuel management scheme. Additionally, the reactivity control capability of UB_2 or UB_4 admixture in a ceramic composite fuel can closely match an IFBA coating configuration. Admixture of a boron rich phase as reactivity control offers potentially enhanced flexibility for many advanced PWR fuels, and could even reduce the peak rod gas pressure in UO_2-based fuel pins (compared with IFBA-coating) by distributing the boron throughout an increased number of fuel rods.

2. Advanced steel cladding in LWRs

BNL has initiated independent assessment of how advanced ferritic alloy cladding would impact performance and safety characteristics in a light water reactor. These assessments build upon existing and synergistic ongoing work by BNL, ORNL, and others. This effort supports a DOE-funded effort led by General Electric Global Research (GEGR). One key objective is to develop a detailed report on the feasibility and maturity of the Fe-based cladding concepts. The effort is focused on light water reactors generally, including both PWRs and BWRs. The principle advantage of advanced steel cladding is with respect to oxidation resistance.

2.2. BWR assembly-level studies

One component of the effort has been focused on neutronic screening at the assembly level. A model of a dominant zone BWR lattice, with geometry details from the open literature [17], is shown in Figure 2. This lattice model has been used to initiate scoping calculations to inform on the feasibility of a commercially available alloy, Kanthal APMT, as a cladding and channel box material in BWRs. Kanthal APMT is one example of an iron-chromium-aluminum alloy (FeCrAl). Iron and chromium absorb more neutrons than zirconium, so this effort is aimed at identifying and quantifying the impact of this parasitic absorption.

These studies have been performed in concert with available information in the literature regarding Fe-based (primarily S.S. 304) cladding thicknesses used historically in operating reactors. Assembly-level calculations have been performed with both poisoned (Gd) and un-poisoned assemblies.

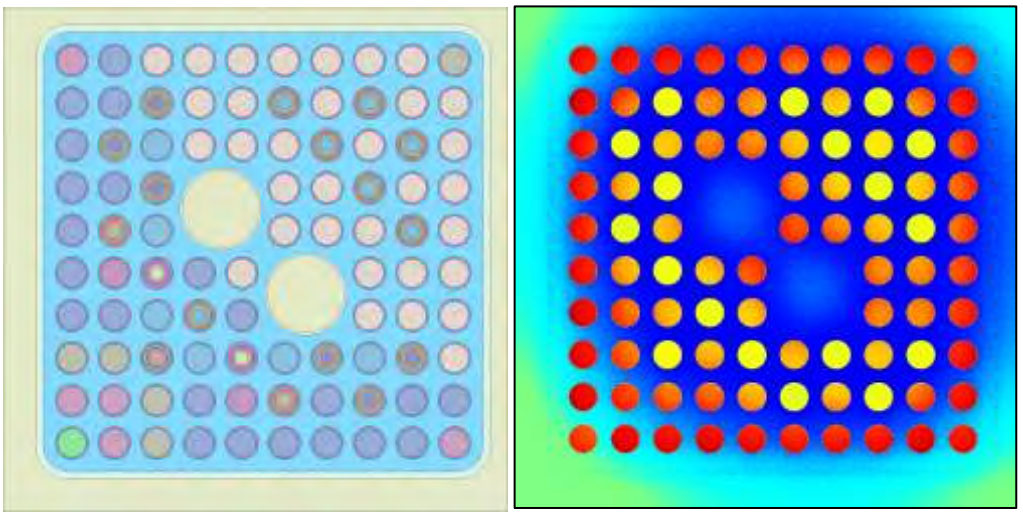

(a) (b)

Fig 2. BWR (a) lattice geometry and (b) thermal neutron flux [blue-green] and power distribution [yellow-red] contours

Figure 3 shows the reactivity deficit of the BWR assembly versus burn-up in gigawatt-day per ton of initial heavy metal (GWd/t). Two cladding and channel box thicknesses are assumed as a fraction of the nominal zirconium alloy thickness: half thickness (0.5) and three-quarters thickness (0.75). These fall within the range of cladding thicknesses used operationally in light water reactors with S.S. 304 cladding, with representative values including 300 μm and 420 μm [18]. Kanthal APMT cladding is anticipated to be thinner than Zirconium alloy due to the enhanced mechanical properties of the cladding. In all cases the hydraulic diameter of the flow channel (clad outer diameter) is maintained and the fuel pellet diameter is increased to maintain a constant gap thickness. In these calculations, the outer dimension of the channel box is reduced.

The poisoned and un-poisoned APMT calculations were compared to poisoned and un-poisoned zirconium alloy clad reference cases. In other words, the reference case for the poisoned assemblies (labeled Gd) was a poisoned zirconium alloy assembly and the reference case for the un-poisoned assemblies was an un-poisoned zirconium alloy assembly. The reactivity deficit is shown as infinite multiplication factor difference. The same radial enrichment assembly layout and fraction of Gd_2O_3 is assumed. This calculation indicates that the hardened neutron spectrum of the poisoned assembly minimizes the initial reactivity deficit, but once the Gd is depleted the assembly level infinite multiplication factor is very similar for both the poisoned and un-poisoned cases. For all of the cases, the reactivity deficit introduced by parasitic absorption in APMT is very significant.

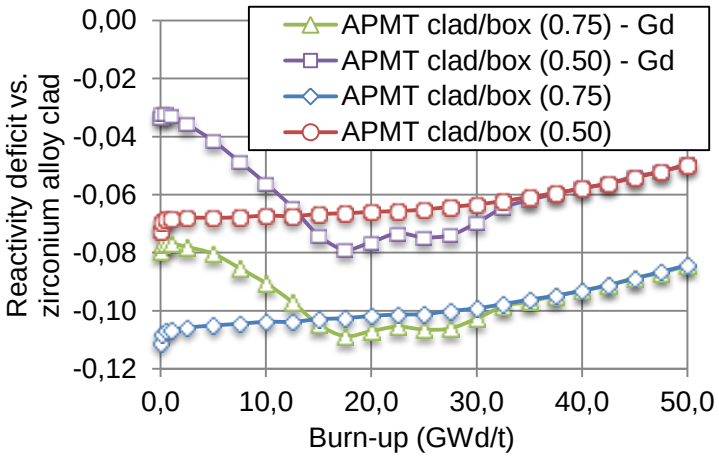

Fig 3. Reactivity deficit versus poisoned (Gd) and un-poisoned zirconium alloy-clad

Replacing the channel box with APMT is expected to be challenging, due to the significant additional parasitic absorption this introduces. This prompted the investigation of an additional case, with half-thickness APMT cladding and a zirconium alloy channel box. It is noted that zirconium alloy may not be the optimal choice as a channel box material. However, the goal of the effort was not to propose maintaining zirconium alloy as the channel box material, but rather to determine the impact of parasitic neutron absorption in the APMT channel box. The impact of the channel box on parasitic absorption is very significant, as shown in Figure 4 (a). Overall, the channel box accounts for more than 50% of the integral reactivity difference for this scoping case. Similarly, the channel box accounts for a significant fraction of the change in thermal (< 1 eV) capture cross section, as shown in Figure 4 (b).

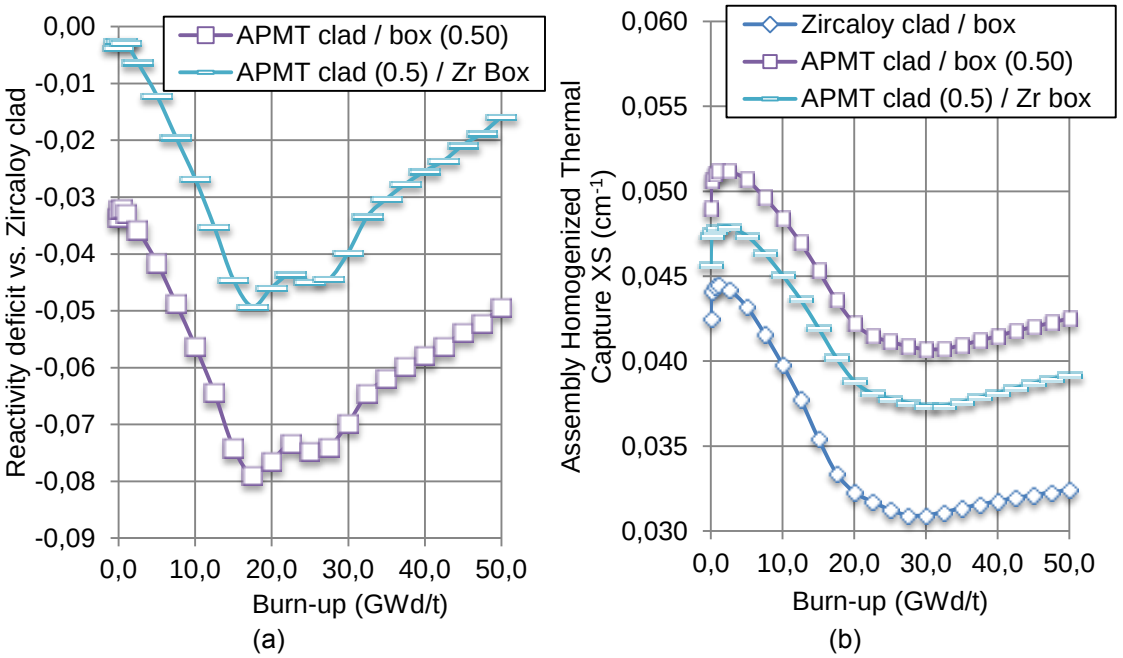

Fig 4. Impact of channel box on reactivity deficit for poisoned (Gd) cases

2.3. Impact of Kanthal APMT on cycle length and natural resource utilization

We investigated the impact of APMT cladding on the natural uranium resource utilization in ton per gigawatt electric-year. This is a measure of how efficiently the natural uranium resources are being used per unit energy generated. This impacts the total uranium cost. Resource utilization was a key metric in the recently completed U.S. DOE-NE Evaluation and Screening of Nuclear Fuel Cycle Options [19]. The natural resource utilization in tons of heavy metal required per gigawatt electric – year (t/GWe-yr) is a function of the discharge burn-up in GWd/t, the uranium enrichment, the tails fraction, and the thermal efficiency.

Calculations of cycle length in effective full power days (EFPD) for a 17 x 17 PWR assembly with 420 µm thick cladding are shown in Figure 5 for compositions approximately ~4.5%, 4.9%, and 5.5%-enriched and corresponding resource utilization calculations in Figure 6. UO_2 with APMT cladding and several different enrichments was compared to UO_2 with zirconium alloy cladding at nominal thickness. It is noted that with 420 µm thick APMT cladding an enrichment of greater than 5% is necessary to match the cycle length obtained with zirconium alloy cladding.

In terms of natural resource utilization, the enrichment of the fuel and the discharge burn-up are competing effects: increased enrichment requires more uranium, but enables higher discharge burn-up and longer cycle lengths. For the specific examples shown in Figure 6, these competing effects cancel and the mass of natural uranium required per unit energy generated is largely independent of enrichment. In all cases, a roughly 20% resource

utilization penalty is incurred with APMT cladding. It is noteworthy that the ~5.5% enriched case would increase enrichment cost and face various other barriers to implementation.

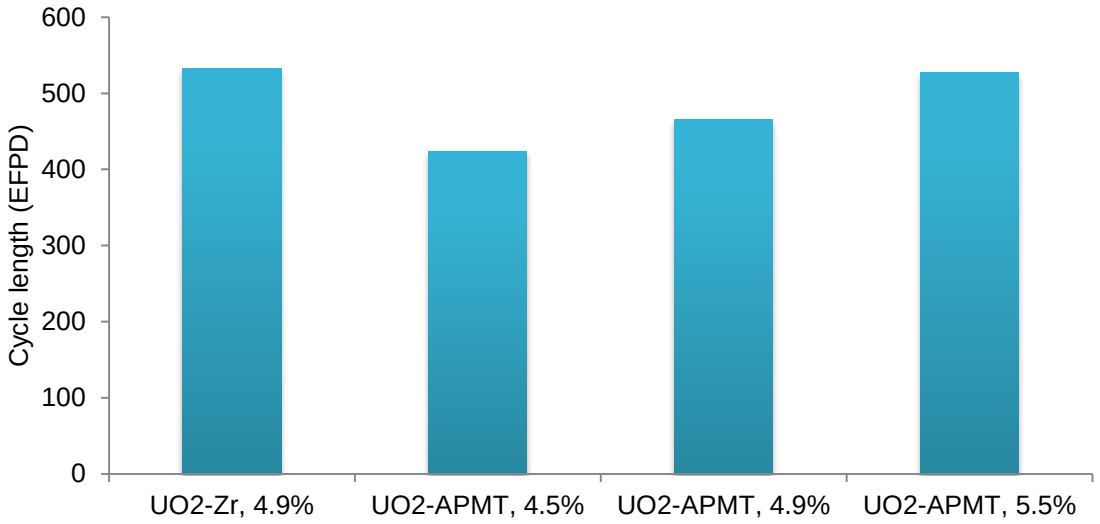

Fig 5. Cycle length in EFPD w/APMT clad at various enrichments

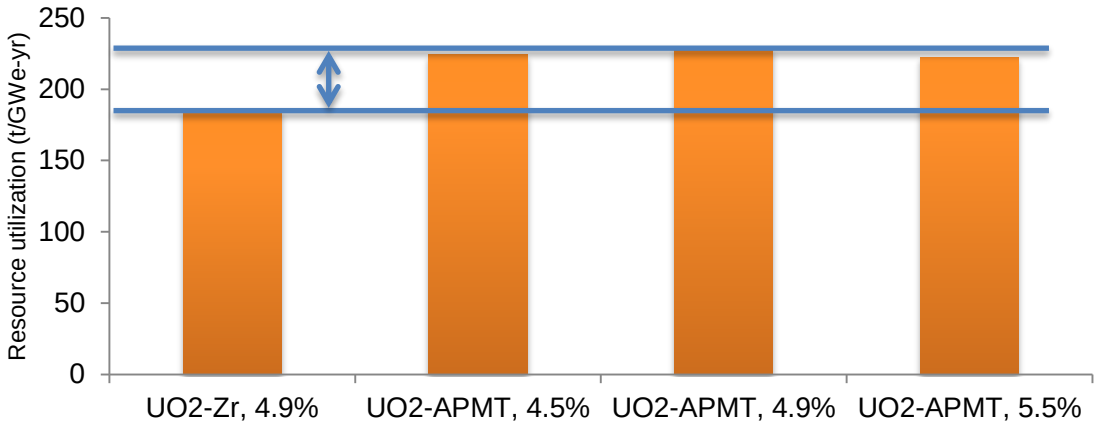

Fig 6. Natural resource required in t/GWe-yr w/APMT clad

2.4. Preliminary core analysis of UO_2 fuel with APMT cladding

We performed preliminary core-level analysis of a PWR with UO2 fuel and APMT cladding. The core model utilized is not described in detail here, but the key parameters show very similar steady state reactor performance of UO_2 fuel with APMT cladding (approximately 5.5%-enriched) and UO_2 fuel with zirconium alloy cladding (approximately 4.9%-enriched). We investigated power peaking, burn-up histories, boron letdown, and reactivity coefficients. Complete results are not detailed in this summary, but included equilibrium cycle calculation with thermal-hydraulic feedback. Radial power peaking and boron concentration within a cycle are shown in Figure 7. It is significant to note that these preliminary scoping calculations assume a fixed fuel-shuffling pattern [3] and that only soluble boron and integral fuel burnable absorbers are used for the reactivity control. Control rods are in an “all rods out” configuration. The important take-aways are not the specific values of the peaking factor or critical boron concentrations, but rather that the values are similar for zirconium alloy and APMT cladding.

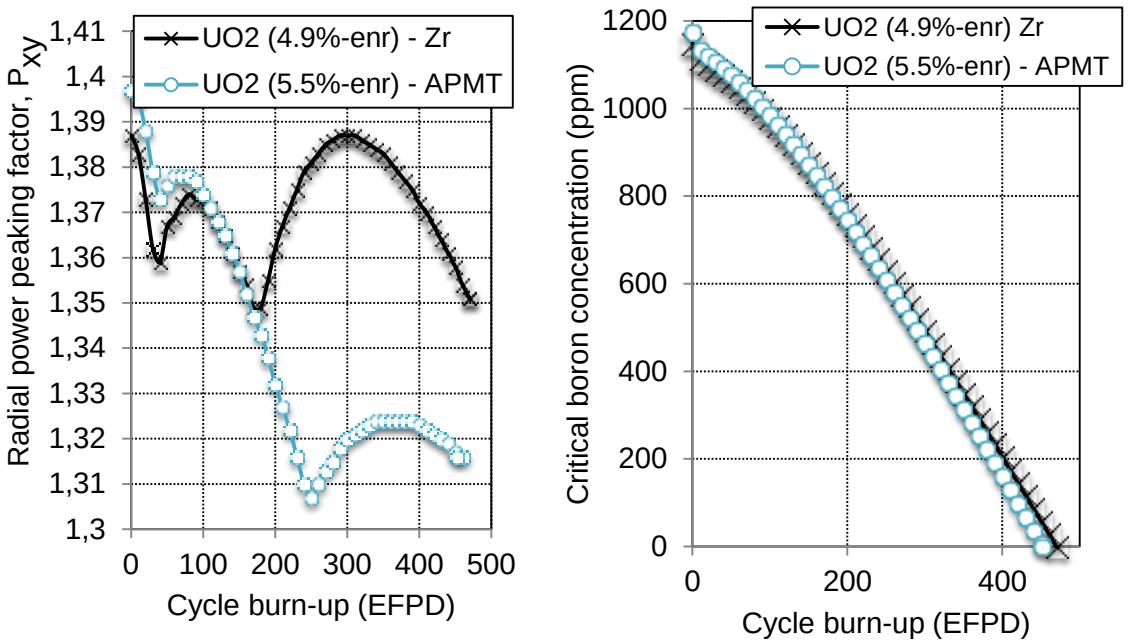

(a) (b)

Fig 7. Preliminary core calculations: (a) radial power peaking and (b) boron concentration

2.5. Large break loss-of-coolant accident analysis

Preliminary systems analyses explored the impact of APMT cladding and modified fuel pellet and cladding dimensions on the progression of a large break loss-of-coolant accident (LB-LOCA). In our calculations, we have assumed that the size of the fuel pellet is increased, which increases the fuel volume, and decreases the volumetric heat generation rate, for a constant power. Our analysis focused on a systems level, thermal hydraulic response using the regulatory-grade TRACE code.

Using the equilibrium axial power distribution from the core calculations as a boundary condition, appropriate thermal properties and fuel rod geometry were integrated into a systems model of a PWR. For this simulation the fuel pellet diameter, cladding thickness, and cladding thermal properties were modified. The behavior of the fuel centerline temperature and peak cladding temperature are shown in Figure 8 and Figure 9, respectively. The cases with APMT cladding assume nominal clad thickness (the same as with zirconium alloy) and half (50%) clad thickness. These cases show the relatively minor impact of changing the cladding material and geometry on the thermal hydraulics of this LB-LOCA.

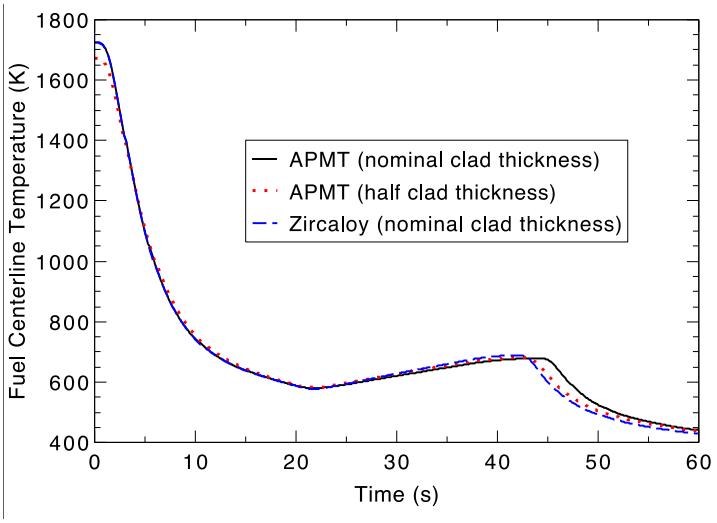

Fig 8. Fuel Centerline Temperature - LBLOCA

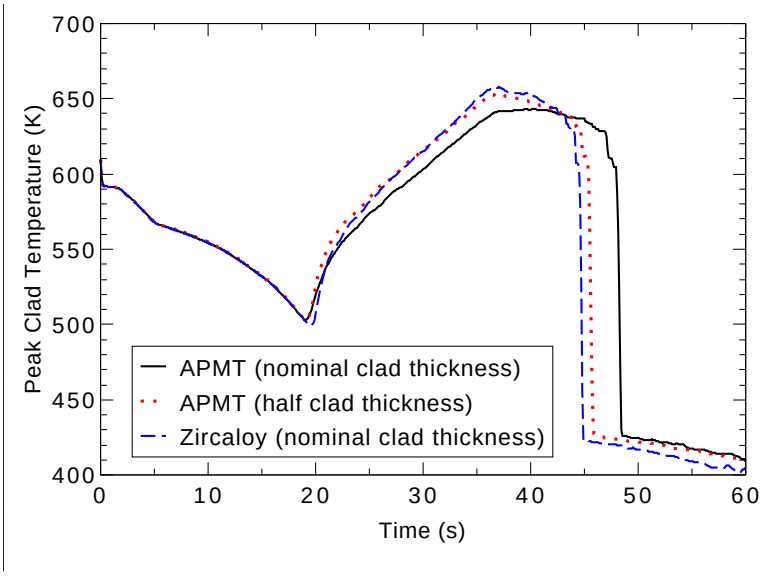

Fig 9. Peak Clad Temperature – LBLOCA

3. Summary

This first part of this paper reviews key lessons learned from recent screening analyses of fully ceramic microencapsulated fuel [1, 2] and ceramic composite fuels [3, 4]. Differences in reactor performance and safety characteristics relative to UO_2 fuel tend to be driven by either reduced heavy metal density (FCM) or increased heavy metal density (ceramic composites). Potential advanced fuels present challenges with respect to reactivity control (changes in control and burnable absorber worth) and typically harden the neutron energy spectrum. Complex fuel geometries (such as FCM) may also challenge the modeling paradigms in state-of-the-art analysis tools. It is notable that typical burn-up limits for UO_2 fuel and zirconium alloy cladding are not expected to be relevant for candidate advanced fuel and cladding materials.

The second part of this paper presents specific examples of ongoing screening studies of advanced steel cladding. These analyses are being performed in support of a DOE-funded GEGR-led effort. The principle advantage of advanced steel cladding is enhanced oxidation resistance. These analyses showed significant reactivity penalties due to parasitic absorption in iron and chromium. Other than parasitic absorption, these analyses show that the reactor performance and safety characteristics of advanced steel cladding are expected to be similar to zirconium alloy cladding.

4. Acknowledgements

This manuscript has been authored by employees of Brookhaven Science Associates LLC under Contract No. DE-SC0012704 and DE-AC02-98CH10886 with the US Department of Energy. The publisher by accepting the manuscript for publication acknowledges that the United States Government retains a non-exclusive, paid-up, irrevocable, world-wide license to publish or reproduce the published form of this manuscript, or allow others to do so, for United States Government purposes.

5. References

[1] N.R. Brown, H. Ludewig, A. Aronson, G. Raitses, M. Todosow, “Neutronic evaluation of a PWR with fully ceramic microencapsulated fuel. Part I: Lattice benchmarking, cycle length, and reactivity coefficients,” *Ann. Nucl. Energy* 62, pp. 538–547 (2013).

[2] N.R. Brown, H. Ludewig, A. Aronson, G. Raitses, M. Todosow, “Neutronic evaluation of a PWR with fully ceramic microencapsulated fuel. Part II: Nodal core calculations and preliminary study of thermal hydraulic feedback,” *Ann. Nucl. Energy* 62, pp. 548–557 (2013).

[3] N.R. Brown, A. Aronson, M. Todosow, R. Brito, K. McClellan, “Neutronic performance of uranium nitride composite fuels in a PWR,” *Nucl. Eng. Des.* 275, pp. 393–407 (2014).

[4] N. R. Brown, M. Todosow, A. Cuadra, “Screening of advanced cladding materials and UN-U3Si5 fuel,” *J. Nucl. Mater.* 462, pp. 26-42 (2015).

[5] K. A. Terrani, L. L. Snead, L.L., J. C. Gehin, “Microencapsulated fuel technology for commercial light water and advanced reactor application,” *J. Nucl. Mater.* 427, 209–224 (2012).

[6] M. Fratoni, K. A. Terrani, “Metal Matrix Microencapsulated (M3) fuel neutronics performance in PWRs,” In: American Nuclear Society Winter Meeting, San Diego, CA (2012).

[7] F. Venneri, W. J. Lee, “Fully ceramic microencapsulated replacement fuel assemblies for light water reactors,” Patent Application US2013/0114781 A1 (2013).

[8] R. S. Sen, M. A. Pope, A. M. Ougouag, K. O. Pasamehmetoglu, “Assessment of possible cycle lengths for fully encapsulated microstructure fueled light water reactor concepts,” Nucl. Eng. Des. 255, pp. 310-320 (2013).

[9] N. M. George, I. Maldonado, K. Terrani, A. Godfrey, J. Gehin, J. Powers, “Neutronics studies of uranium-bearing fully ceramic microencapsulated fuel for pressurized water reactors,” *Nucl. Technol.* 188, pp. 238-251 (2014).

[10] J. J. Powers, A. Worrall, K. A. Terrani, J. C. Gehin, L. L. Snead, “Fully ceramic microencapsulated fuels: characteristics and potential LWR applications,” In: PHYSOR 2014 – The Role of Reactor Physics Toward a Sustainable Future, Kyoto, Japan (2014).

[11] R. A. Shapiro, M. J. Vincenzi, M. Fratoni, “Optimization of fully ceramic micro-encapsulated fuel assembly for PWR,” In: PHYSOR 2014 – The Role of Reactor Physics Toward a Sustainable Future, Kyoto, Japan (2014).

[12] Y. Lee, N. Z. Cho, “Three-dimensional single-channel thermal analysis of fully ceramic microencapsulated fuel via two-temperature homogenized model,” Ann. Nucl. Energy 71, pp. 254-271 (2014).

[13] Y. Lee, N. Z. Cho, “Steady-and transient-state analyses of full ceramic microencapsulated fuel loaded reactor core via two-temperature homogenized thermal-conductivity model,” *Ann. Nucl. Energy* 76, pp. 283-296 (2015).

[14] N. R. Brown, M. Todosow, K. J. McClellan, “Uranium nitride composite fuels in a pressurized water reactor: exploration of multi-batch cycle length and UB4 admixture for reactivity control,” In: PHYSOR 2014 – The Role of Reactor Physics Toward a Sustainable Future, Kyoto, Japan (2014).

[15] E. J. Lahoda, U.S. Patent 7,139,360 B2 (2006).

[16] J. T. White, A. T. Nelson, D. D. Byler, D. J. Safarik, J. T. Dunwoody, K. J. McClellan,

"Thermophysical properties of U3Si5 to 1773 K," *J. Nucl. Mater.* 456, pp. 442-448 (2015).

[17] M. L. Fensin, Optimum Boiling Water Reactor Fuel Design Strategies to Enhance Reactor Shutdown by the Standby Liquid Control System, Masters Thesis, University of Florida (2004).

[18] A. Strasser, J. Santucci, K. Lindquist, W. Yario, G. Stern, L. Goldstein, L. Joseph, An Evaluation of Stainless Steel Cladding for Use in Current Design LWRs, Electric Power Research Institute Report NP-2642 (1982).

[19] R. Wigeland, T. Taiwo, H. Ludewig, M. Todosow, W. Halsey, J. Gehin, R. Jubin, J. Buelt, S. Stockinger, K. Jenni, B. Oakley, "Nuclear Fuel Cycle Evaluation and Screening – Final Report", INL/EXT-14-31465 FCRD-FCO-2014-000106, Idaho National Laboratory Technical Report, October 8 (2014).

REVIEW OF A.A. BOCHVAR INSTITUTE ACTIVITIES IN DEVELOPING POTENTIALLY ACCIDENT TOLERANT FUEL FOR LIGHT WATER REACTORS

A.M. SAVCHENKO, V.B. IVANOV, V.V. NOVIKOV. M.V. SKUPOV, G.V. KULAKOV, V.K. ORLOV, O.I. UFEROV, Y.V. KONOVALOV

Stock Company «A.A. Bochvar High-Technology Research Institute of Inorganic Materials» (SC VNIINM)
123060, Moscow, Russia (VNIINM)

The R&D Program at A.A. Bochvar Institute includes developing advanced fuels for LWRs that for many criteria satisfy accident tolerant fuel (ATF) requirements.

1. ATF cladding development:
- Development of tube type thin-walled clad of SiC-SiC composites.
- Steel cladding for fast reactors and small water cooled reactors. A database of cladding properties and results of in-pile tests of steel cladding is maintained.
- Coated Zr-based alloys claddings.

2. Development of high thermal conductivity fuel to reduce the amount of stored heat:
- An advanced composite fuel,
- Doped UO_2 pelletized fuel (multiphase fuel).
- Nitride and silicide fuel.

3. Combination of methods.

4. Modelling of ATF behaviour, including accident analysis for cold fuel, modelling and calculation of steel clad behaviour in accidents as well as carrying out out-of-pile tests.

5. Fuel cycle with composite fuel and economic aspects of ATF implementation. Since composite fuel possesses improved neutronics characteristics and can improve economics of LWRs, its implementation can compensate for the expense of ATF implementation in reactors. Fuel cycle with multiple recycling of plutonium is alsoconsidered.

1. Introduction

ATF fuel should satisfy two main criteria [1-4]:

1. Tolerant fuel should have similar or better performance in normal operation conditions. “First do no harm”: ATF fuels must first meet steady-state needs and then improve accident conditions.
2. Tolerant fuel should remain stable in accidents at beginning of life (BOL) as well as at end of life (EOL) conditions.

A.A. Bochvar Institute is the Chief Designer of fuel for various types of reactors – LWRs, fast, research and small reactors – icebreakers and Floating Nuclear Power Plants (FNPP) (fig. 1).

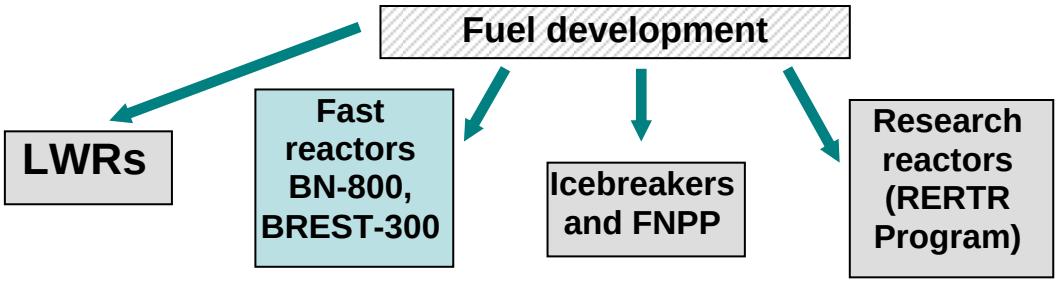

Fig. 1. Scheme of advanced fuel developments at A.A. Bochvar Institute.

Innovation R&D Program in A.A. Bochvar Institute is concentrated mostly on developing novel advanced fuels for various types of reactors, especially for LWRs that for many criteria satisfies accident tolerant fuel (ATF) requirements. Some of the advanced fuel are entirely novel and can be considered for including into international R&D Programs.

2. Main directions on ATF fuel developments

The main activities on ATF in A.A. Bochvar Institute are represented in fig. 2 [5].
It includes cladding and coating development, cold fuel development, combination of methods, modelling, fuel cycle and economic aspects.

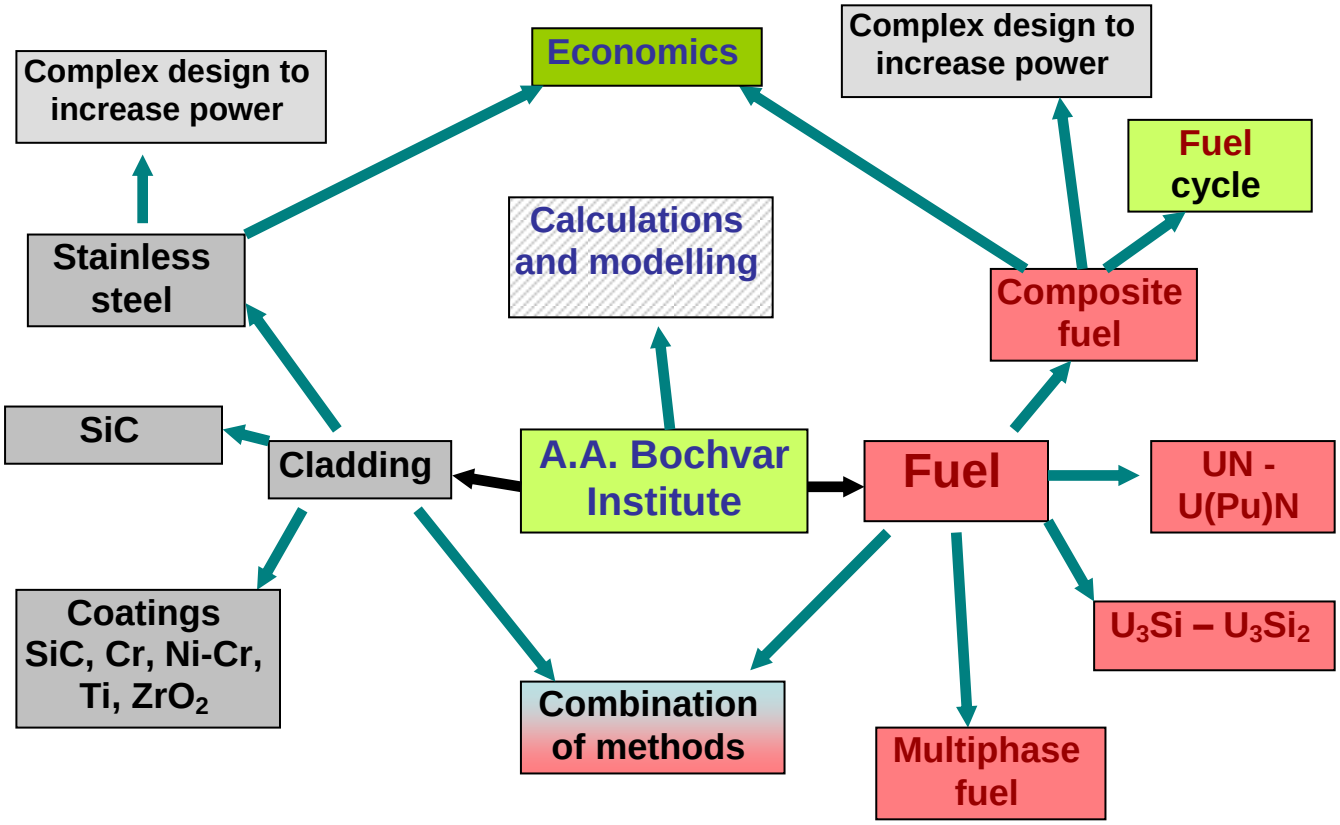

Fig. 2. Main directions on ATF fuel developments in A.A. Bochvar Institute.

3. ATF cladding development

ATF cladding development comprises SiC-SiC composites, stainless steel (ferritic, austenitic, Ni-Cr steels) and coatings on Zr based claddings (ceramic, metallic, multiphase coatings).

3.1. Development of tube type thin-walled clad of SiC-SiC composites

A.A. Bochvar Institute activity on SIC composite is at laboratory-scale level [6]. We developed samples of tube type thin-walled clad of SiC-SiC composites (SiC-SiC fibers and SiC-SiC powder – CVD process (chemical vapour deposition) as well as isostatic pressing and subsequent hard firing. Experimental investigations of properties of SiC-SiC tubes, produced by various methods has been done (fig. 3). Density, porosity, corrosion resistance, mechanical properties (compression and bending strength) up to 600 ^{0}C were studied as well as thermal expansion and structures investigations using metallographic and scanning electronic microscopes.

Fig. 3. SiC/SiC tube appearance and samples produced by various methods

3.2. Steel cladding development

A.A. Bochvar Institute has great experience in fabrication and use of steel cladding either for sodium-cooled fast reactors (SFR), or for small water cooled reactors, particularly FNPP and icebreakers, as well as high-flux SM-2 research reactor (fig. 4) [7].

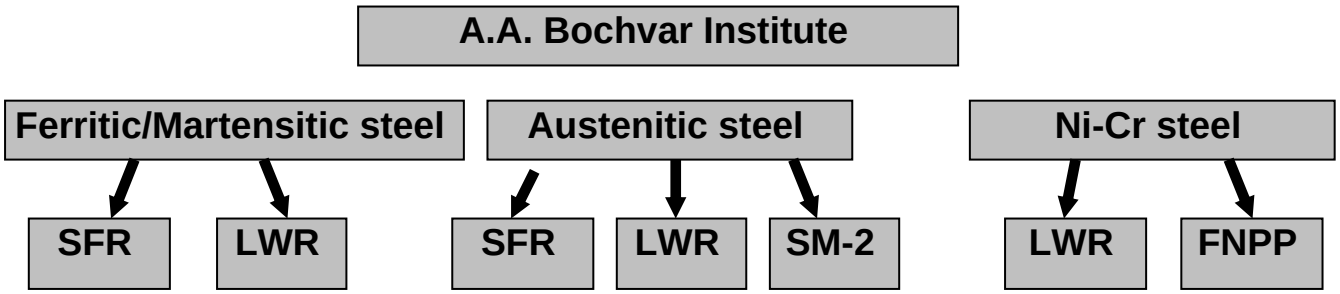

Fig. 4. Main directions on ATF cladding developments in A.A. Bochvar Institute.

Advantages:

- High corrosion resistance in accidents;
- Industrial-scale technology (produced on industrial level at machinery plants);

Drawbacks:

- Neutron capture;
- Stress corrosion cracking (for austenitic steels and radiation induced hardening (for ferritic steels);

Steel claddings with outer diameter from 2 to 30 mm and thickness from 0.1 to 0.7 mm are produced at the industrial scale (fig. 5).

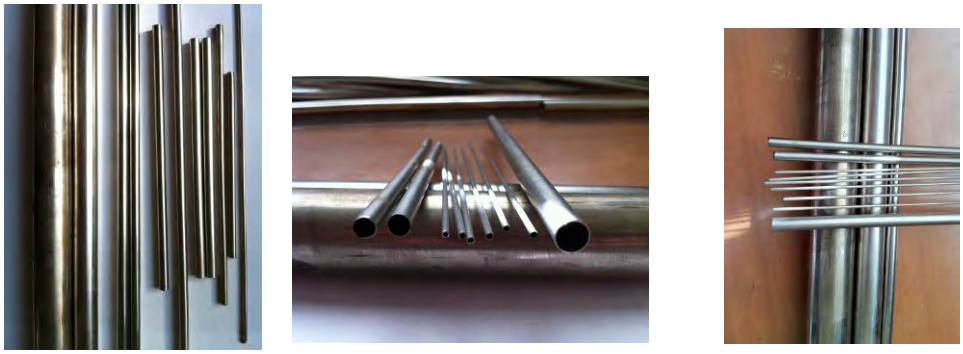

Fig. 5. Steel tube appearance produced at the industrial scale

One of the directions of A.A. Bochvar Institute activity is development and implementation of steel claddings and fuel for water-cooled reactors, operating in severe transients: Bilibinskaya Power Plant, icebreakers, Floating Nuclear Power Plants (FNPP), high flux SM-2 research reactor [8, 9] (fig.6).

Fig. 6. Icebreaker, FNPP, SM-2 reactor

A database has been collected on fuel and claddings properties and in pile tests of fuel clad with steel and calculation programs on its application in icebreakers, FNPP, SM-2 and partly VVER type have been developed.
Steel cladding allows fabricating any complicated shape of cladding, which in turn allows an increase in reactor power. In this case dispersion type fuel should be used, which is developed at A.A. Bochvar Institute.
For steel cladding developed at A.A. Bochvar Institute with dispersion type fuel the following characteristics were achieved in water cooled reactors:
Max burn-up: 1,0 g/cm^3 (under the cladding – entire volume - or 120 MW*d/kgU as recalculated for the standard VVER-1000 fuel rod).
Clad thickness: 0.20 - 0.30 mm

Fuel for SM high flux reactor (100 MW power) (fig. 7)
Steel Cladding Alloy – EI-847.
Clad thickness – 0. 15 mm.
Outer diameter – 5,15 mm.
Max burn-up – 80 at.% or 1,6 g/cm^3 (under the cladding or 200 MW*d/kgU as recalculated for the standard VVER-1000 fuel rod).

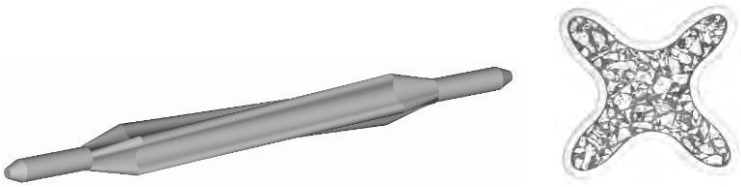

Fig. 7. SM-2 type fuel element

3.3. Protective coatings on Zr based cladding

A.A. Bochvar Institute has unique technologies and facilities for fabrication coated products of various types on an industrial scale level. Coated Zr alloys (fig. 8) will inhibit the high temperature steam oxidation reaction and preserve cladding mechanical properties [10].
We are going to concentrate mostly on ceramic coatings (SiC, ZrN), Cr coatings, Ni-Cr and stainless steel coatings, and Ti-based alloy coatings.

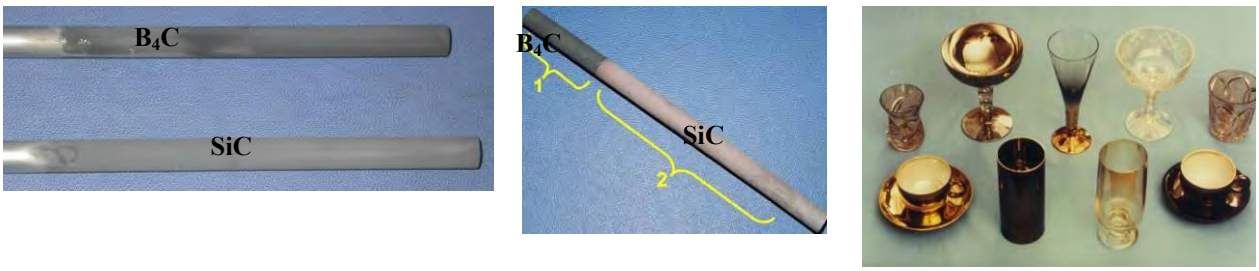

a b c

Fig. 8. Protective coatings (cold spray) on Zr tube and other materials (high speed magnetron spray (a, b– B_4C and SiC; c – Zr)

4. Cold fuel development

One of the ways of developing accident tolerant fuel (ATF) developing is the development of “cold” fuel that allows reducing fuel temperature especially in the first stage of an accident due to a lower amount of stored heat. Fuel themal conductivity higher than 10 W*m/K provides a low operating temperature in the range of 400-600 ^{0}C. The operating fuel temperature can be additionally reduced in case of metallurgical bonding of the fuel with cladding.

In an overview of “International Activities in Accident Tolerant Fuel Development for Light Water Reactors” prepared by INL (USA) in collaboration with IAEA the following main activities on advanced fuel concepts are being considered [1]:
1. Application of higher density fuels (metal, nitride, silicide). The main goal is to increase fuel thermal conductivity and uranium density to compensate for the neutronic inefficiency of some new cladding concepts without increasing enrichment limits.
2. Oxide fuel with additives for higher thermal conductivity and fission product gettering.
3. Microencapsulated fuels – particle fuel dispersed in a ceramic or metallic matrix.
A.A. Bochvar Institute is the Chief Designer of fuel development for LWRs in Russia.
The of cold fuel development at A.A. Bochvar Institute is shown schematically in fig. 9.

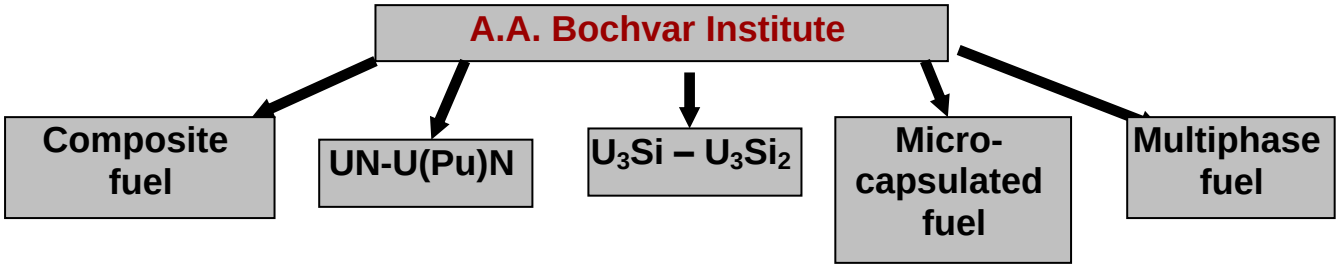

Fig. 9. Scheme of cold fuel developments at A.A. Bochvar Institute.

4.1. Composite fuel

For LWRs advanced composite fuel, based on dispersion type fuel elements (high uranium content metal fuel, including U_3Si, with Zr alloy matrix) is under development now [11-13] (fig. 10). PuO_2 powder can also be added to composite so that in this case the novel fuel becomes an analogue of MOX fuel. The fuel meat retains controllable porosity to accommodate fuel swelling as well as for retention of gaseous fission products. Composite fuel can be considered as ATF due to the following criteria:
- high thermal conductivity,
- metallurgical bonding fuel with cladding that leads to reduced fuel operating temperature as well as improving the performance of fuel elements in severe transients,
- high uranium content within fuel element cladding, that is 25-50 % more than the uranium content of the standard PWR, BWR and VVER-1000 fuel rods, which can allow not only to compensate the worst neutronics characteristics of LWR when using steel claddings, but even for the uranium enrichment of the fuel to be reduced,
- coated (microencapsulated) fuels - fuel particles uniformly distributed in the metallic matrix, which also serves as a getter for oxygen and fission products.

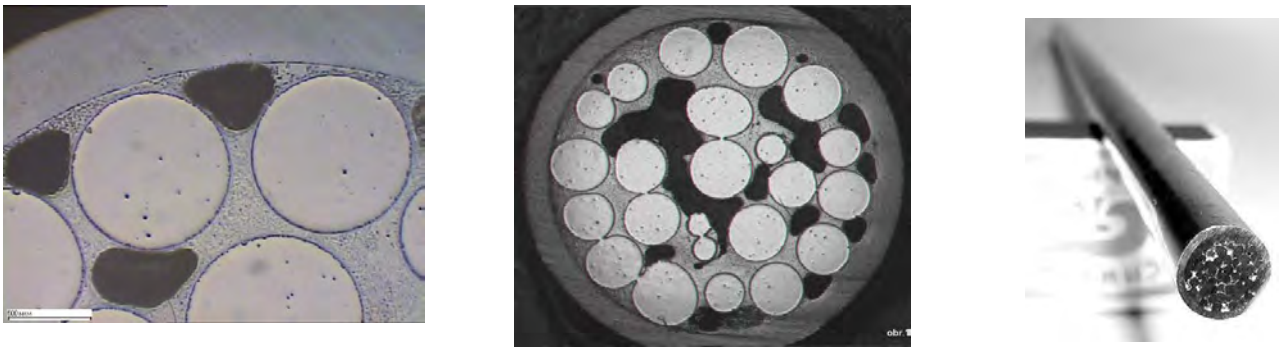

Fig. 10. Structures of composite fuel

Structurally the dispersion fuel meat consists of uniformly distributed higher density fuel granules of U-Mo, U-Nb-Zr or U_3Si alloys that are metallurgically bonded between themselves and to fuel cladding with specially developed Zr-based matrix alloys. A fuel form retains controllable porosity in the range of 14-22% to accommodate fuel swelling.
This type fuel element can be produced by capillary impregnation method [11-13]. Fuel and matrix granules are loaded into the fuel cladding and then heated to the temperature 500 ºC higher than the melting temperature of the matrix alloy. Matrix melts down and under capillary forces moves into gaps between the fuel components to form metallurgical bonds, which promote a high thermal conductivity of a fuel form. As coarse fuel granules compose a skeleton the fuel distribution along the length is uniform (1.01-1.03).
The primary advantages of this novel fuel for application in thermal reactors are high uranium content (25-50% higher in comparison with the standard UO_2 pelletized fuel rod), low temperature of fuel (<500 ºC, i. e. cold fuel), the extension of burn-up (100 MW*d/kgU) and serviceability under transient conditions.
Due to high uranium content and hence intermediate neutron spectrum the main economically significant characteristics for PWR's can be improved:
1. Larger quantities of generated plutonium (~2.5-3 times higher).
2. Increasing of fissionable plutonium isotopes up to 75-78% in spent fuel (harder neutron spectrum).
3. Increasing the breeding ratio up to 0.7-0.8 (by reducing the hydrogen-to-heavy metal ratio).
4. The extension of the operating time will be more than 30% in effective days (up to 500 additional effective days) at 4,95% U^{235} enrichment.
5. Increasing the time between refueling, in other words, increasing the Unit Capacity Factor (UCF). In this case instead of a year or a year and a half fuel cycle at two year cycle becomes feasible.

On the basis of METMET fuel, composite U(Th)-PuO_2 fuel (an analogue of MOX) can be fabricated where depleted uranium alloy and dioxide plutonium powder have initially separate arrangement (it can be also implemented in fast reactors) [12-13].

4.2. Nitride fuel UN – (U,Pu)N

Nitride fuel was developed in A.A. Bochvar Institute for fast reactors with lead coolant (BREST-300) on an industrial scale (fig. 11) [14]. It can be modified for use in LWRs - to increase corrosion resistance in water and to use N15 to reduce neutron activation and capture.

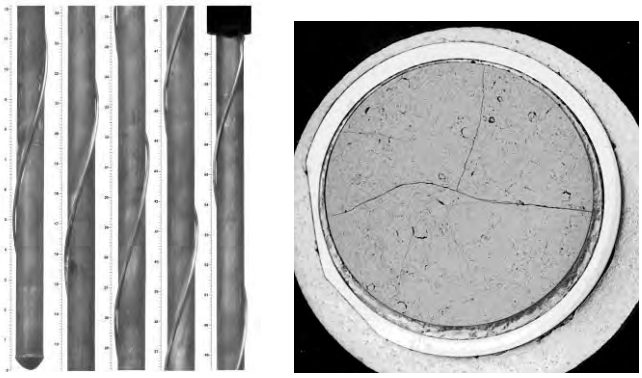

Fig. 11. Mixed nitride fuel after irradiation tests in BOR-60

4.3. Silicide fuel U_3Si – U_3Si_2

A.A. Bochvar Institute developed U_3Si type fuel for RBMK (graphite-moderated boiling water) reactors at laboratory-scale level. Pellets and rods were produced by cast methods followed by U_3Si-phase stabilization annealing. All relevant fuel properties were investigated, including corrosion resistance.

In spite of the generally accepted opinion that fuel is stable only below the melting point – solidus temperature – we assume, that fuel remains stable below the liquidus temperature, that is much higher. This was confirmed experimentally by annealing a RBMK type fuel sample (zirconium clad) at 1150^0C for 30 minutes. The fuel retained its form and dimensions. The inter-diffusion zone was only 30 μm.

Therefore for tolerant fuel we can implement the denser U_3Si instead of U_3Si_2, or the intermediate composition.

Application of cold fuel significantly reduced centerline and average fuel temperature

4.4. Microcapsulated fuel

Particle fuel dispersion in a ceramic or metallic matrix. A.A. Bochvar institute is developing coated particles $(U,Pu)O_2$ for gas reactors [15]. We plan to transfer the technology to UN kernels in future for increased uranium density

4.5. Multiphase metal-ceramic fuel

One more activity on cold fuel deals with modifying by doping the regular uranium dioxide pelletized fuel. A.A. Bochvar institute is developing a concept of γ-U phase fuel alloying that consists of producing an alloy of the two or a multiphase structure, viz., basic γ(U-Mo) and intermetallic or ceramic phases. The intermetallic (ceramic) phase shall have the maximal density of uranium, low molybdenum content, de highly irradiation resistant and precipitate along grain boundaries [16].

Future development is based on the complex compositions containing Mo, Nb, Zr (stabilizing gamma U phase) and O, N, Si, C for forming ceramic and intermetallic high temperature and irradiation resistant phases (tab. 1)

Composition, wt %	Theoretical Density, g/cm^3	Uranium Density, g/cm^3	Difference in heavy metal TD compared to UO_2	Investigated / proposed fuel
UN	14.3	13.5	+40%	Investigated
U_3Si	15.6	14.6	+51%	Investigated
U_3Si_2	12.2	11.32	+17%	Investigated
U-(3-6)Mo	18.1	17.0	+76%	Investigated
U-(2-4)Mo-(0.1-0.6)C	17.6	16.7	+73%	Proposed
U-(3-4)Mo,Nb-(0.3-0.6)N,C,O	17.3	16.3	+69%	Proposed
U-(2-4)Mo-(0.5-0.8)Si,N,C,O	17.0	15.9	+64%	Proposed
UO_2	10,96	9.66		-

Tab 1: Investigated and to be investigated fuel compositions

5. Combination of methods

To improve ATF properties a combination of methods is considered, for example, implementation of relatively brittle SiC claddings with composite fuel can allow an increase in the fuel performance as ductile composite fuel does not stress the cladding at operating temperature, and the fuel porosity will compensate fuel swelling.

Various fuel and cladding materials can be combined together as conceptual designs.

6. Modelling ATF behaviour

Modelling ATF behaviour includes accident analyses for various types of high density cold fuel, modelling and calculation of steel clad behaviour in accidents as well as carrying out all necessary out of-pile tests and measurements [17].

7. Economic aspects

Any proposed fuel system should coincide economically with the current UO_2 - zirconium alloy fuel system. Fuels that require enrichment higher than that of current fuel (about 4.0 to 4.95) are especially likely to cost more because enrichment is a major cost contributor. Increased enrichment could additionally require modification of facilities and fuel handling.

To satisfy these requirements we need:

1. Thin steel claddings - 0.25-0.3 mm instead of 0.58 mm (zirconium alloy).
2. To implement high density fuel (UN, U_3Si, composite fuel)

The second option in most cases can compensate drawbacks in implementation of steel claddings.

The use of novel composite fuel increases the breeding ratio. The higher density fuel reduces the hydrogen-to-heavy metal ratio in the reactor which results in a harder spectrum in which breeding is more effective [13]. Composite fuel refers to the fuel of higher reactivity

8. Fuel cycle

In case of novel composite fuel U(Th)-PuO_2 application we can separate of the newly generated fissile plutonium from burnt fuel without chemical processes with repeated use in PWR or heavy water reactors, which simplifies the closing of the nuclear fuel cycle. Composite fuel crushes and mechanically separates into initial components – fine PuO_2 fraction with fertile plutonium and coarse metallic uranium alloy granules, which contains fissile generated plutonium. Hence in comparison to MOX we can multiply use of generated Pu in spent fuel and instead of partial recycling implement full recycling which drastically reduces the fuel waste (fig. 12) [13].

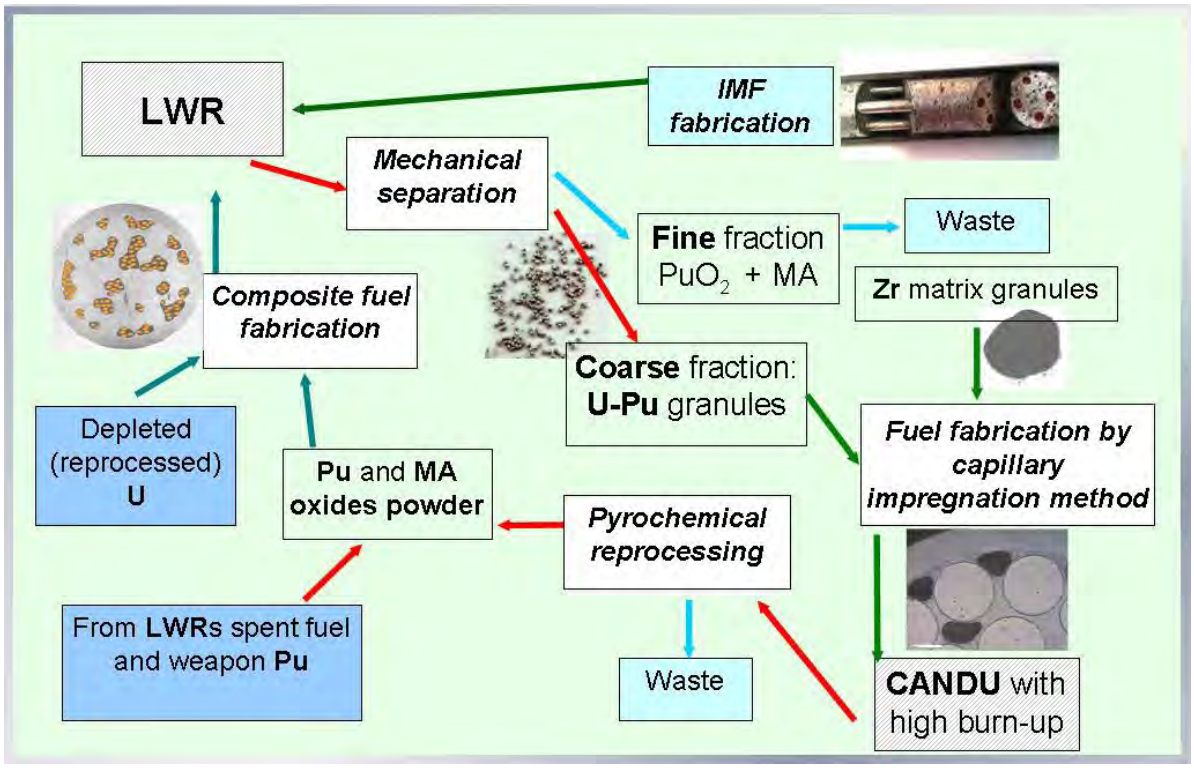

Fig. 12. LWR fuel cycle with composite fuel and multiply recycling of Pu

Thus, using this novel concept based on high density dispersion and composite fuel a closed U-Pu cycle can be implemented in thermal reactors – as the fuel available to these reactors may be increased by ~48% (18% in case of MOX). The remained Pu fissile isotopes can be used from the spent fuel accumulated in thermal reactors.

9. Conclusion

- A.A. Bochvar Institute (VNIINM) is a Chief Designer of the fuel for various types of reactors, particularly LWRs and has a great experience in developing advanced fuels, that for many criteria satisfy ATF requirements. It includes implementation of various types of claddings and clad coatings as well as cold high density fuel.
- Some of the advanced fuel types are entirely novel and can be considered for including into international R&D Programs.
- A.A. Bochvar Institute is willing to conduct developments of ATFin cooperation with IAEA and other Organizations.

References

[1] Shannon M. Bragg-Sitton, Jon Carmack and Frank Goldner, Current Status of the U.S. Department of Energy Accident Tolerant Fuel Development Program, Proceedings of IAEA TM on Proceedings of IAEA TM on Accident tolerant fuel concepts for light water reactors, 13 – 17 October 2014. Oak Ridge National Laboratory, Oak Ridge, TN, USA

[2] Jeremy Bischoff, Patrick Blanpain, John Strumpell, Development of Fuels with Enhanced Accident Tolerance, 13 – 17 October 2014. Oak Ridge National Laboratory, Oak Ridge, USA.

[3] S.J. Zinkle, K.A. Terrani, J.C. Gehin, L.J. Ott, L.L. Snead, Accident tolerant fuels for LWRs: A perspective, Journal of Nuclear Materials 448 (2014) 374-379

[4] Nuclear Fuel Safety Criteria Technical Review, NEA Report No. 7072, second ed., Nuclear Energy Agency, OECD, Paris, 2012

[5] V. Ivanov, V. Novikov, A. Savchenko, A. Vatulin, V. Bezumov, Activity of A.A. Bochvar Institute to Developing Accident Tolerant fuel for Light Water Reactors, Proceedings of IAEA TM on Accident tolerant fuel concepts for light water reactors, 13 – 17 October 2014. Oak Ridge National Laboratory, Oak Ridge, TN, USA

[6] V. N. Bezumov, V. V. Novikov, A. A. Kabanov, R. G. Zakharov, Y. V. Pimenov. "Design Issues Concerning Composite Material Fuel Element Jackets Based on SiC within a Matter of Safety Concept of Water-Cooled Reactor Under Accidents", Proceedings of JR TVEL Conference – Fuel of Novel Generation for Nuclear Reactors, 12-13 November 2014, Moscow, VNIINM

[7] M.V. Leonteva-Smirnova, Structural Materials for Fast Reactors Active Cores, Proceedings of JR TVEL Conference – Fuel of Novel Generation for Nuclear Reactors, 12-13 November 2014, Moscow, VNIINM.

[8] G.V. Kulakov, A.V. Vatulin, S.A. Ershov, Y.V. Konovalov, A.V. Morozov, A.M. Savchenko, V.I. Sorokin, V.V. Fedotov, A.E. Novoselov, V.A. Ovchinnikov, V.Y. Shishin. Development of Dispersion Type Fuel Elements for Floating Nuclear Power Plants (FNPP) and Low Power Reactor Plants (LP RP). Proceedings of 2010 LWR Fuel Performance/TopFuel/WRFPM. Orlando, Florida, USA, September 26-29, 2010, p. 525-531

[9] G.V. Kulakov, A.V. Vatulin, S.A. Ershov, Y.V. Konovalov, A.V. Morozov, A.M. Savchenko, V.I. Sorokin, V.V. Fedotov, A.E. Novoselov, V.A. Ovchinnikov, V.Y. Shishin. The Main Principles Of Irradiated Dispersion Type Fuel "UO2 + Aluminum Alloy" Behavior. Transactions of LWR Fuel Performance Meeting/ Top Fuel 2013, September 15-19, Charlotte, North Carolina, 2013, p. 384-389

[10] V.K. Orlov, V.S. Mitin, V.M. Sergeev, N.N. Krasnobaev, A.V. Mitin, I.I. Akimov. Application of High-Speed Ion-Plasma Magnetron Sputtering for Protective, and Stabilizing Coatings in

Technologies, Journal “Issues of Atomic Science and Engineering. Materials Science and Novel Materials Series”, issue 1 (74), 2013, 184-190
[11] A.M. Savchenko et al. Dispersion type zirconium matrix fuels fabricated by capillary impregnation method, J. Nucl. Mater., 362 (2007) 356-363
[12] A. Savchenko, A. Vatulin, I. Konovalov, A. Morozov, V. Sorokin, S. Maranchak. Fuel of Novel Generation for PWR and as Alternative to MOX Fuel, Journal of Energy Conversion & Management, 51 (2010) 1826-1833
[13] A.M. Savchenko et al. Peculiarities of fuel cycle with advanced composite fuel for thermal reactors, Progress in Nuclear Energy, volume 72, 2014, 119-125
[14] B.D. Rogozkin, N.M. Stepennova, Y.E. Fedorov. Testing Results up to 12% of Heavy Metal Burn-up of Mixed Mononitride Uranium in BOR-60 Reactor, Atomic Energy, 2011, v. 110. issue 6, p. 332-346
[15] S.M. Baranov, E.Y. Vahrushev, I.V. Kalinin, E.V. Klyukin, V.M. Makarov, N.V. Morozov, Z.S. Nikuradze, VNIINM Experimental Facilities for Developments on Microcapsulated Fuel, Proceedings of MAYAT-2014 Conference, 7-9 October 2014, Russia, Zvenigorod
[16] A. Savchenko et al. Novel Trends in Fuel and Matrix Alloying to Reduce Interaction, Proceedings of the Research Reactor Fuel Management (RRFM-2007) Conference, Lyon, France, 11.03-14.03.2007, available through the European Nuclear Society (ENS) website
[17] A.V. Salatov, A.V. Kumachev, M.V. Sypchenko, O.A. Nechaeva, P.V. Fedotov, Pre-test Simulation of MIR-LOCA/72 Experiment with RAPTA-5.2 code, Proceedings of JR TVEL Conference – Fuel of Novel Generation for Nuclear Reactors, 12-13 November 2014, Moscow, VNIINM

ON-GOING STUDIES AT CEA ON CHROMIUM COATED ZIRCONIUM BASED NUCLEAR FUEL CLADDINGS FOR ENHANCED ACCIDENT TOLERANT LWRS FUEL

J.C. Brachet*, M. Le Saux, M. Le Flem, S. Urvoy, E. Rouesne, T. Guilbert, C. Cobac, F. Lahogue, J. Rousselot, M. Tupin, P. Billaud, C. Hossepied
CEA, DEN, DMN, Section for Applied Metallurgy Research
F-91191 Gif-sur-Yvette, France

F. Schuster, F. Lomello,
CEA, DEN, Cross-Functional-Program on Advanced Materials,
F-91191 Gif-sur-Yvette, France

A. Billard, G. Velisa, E. Monsifrot,
IRTES, LERMPS UTBM LRC CEA, site de Montbéliard,
F-90010 Belfort, France

J. Bischoff,
AREVA NP, 10 rue Juliette Récamier,
F-69456 Lyon, Cedex 06, France

A. Ambard
EDF R&D, département MMC, avenue des Renardières,
F-77818 Moret-Sur-Loing, France

* *Corresponding Author, E-mail: jean-christophe.brachet@cea.fr*

ABSTRACT

Chromium coatings aiming to protect the current zirconium alloy nuclear fuel cladding materials from high temperature steam oxidation, especially in accidental conditions, are being developed at CEA in the framework of the French Nuclear Institute in partnership with AREVA and EDF.
The present paper focuses on recent results obtained on chromium-coated cladding on Zircaloy-4 and substrate. A complementary paper is presented by AREVA [1]. Typical as-fabricated microstructures of chromium coatings are illustrated. Preliminary autoclave oxidation tests at 415℃ (steam, 100 bars) have been performed on both uncoated reference materials and on chromium coated Zircaloy-4 based samples, showing very encouraging results for the last generation of Cr coatings fabricated. Additionally, results obtained after High Temperature (HT) oxidation in steam are presented. It is shown that the chromium coatings developed so far may significantly improve the post-HT oxidation clad mechanical properties (i.e. ductility and strength) compared to conventional uncoated materials. As a consequence, the developed chromium coatings provide significant additional margins for loss-of-coolant accident (LOCA) and, to some extent, for beyond LOCA conditions.

1. As-received materials and behavior in nominal conditions

These last years, CEA has studied chromium coatings (thicknesses of a few microns up to ~20µm) on Zircaloy-4 (Zirc-4) substrates, which are able to provide significant additional margins in nominal conditions in light water reactors (LWR) as well as in accidental conditions, such as loss-of-coolant accident (LOCA) [2] [3].

1.1 As-received Cr coating microstructures

Figure 1 illustrates some typical as-received Cr coating microstructures that have been obtained. It can be observed that:

- The first generation of Cr coatings fabricated shows, sometimes, evidences of cracks and porosities located at the Cr grains boundaries and/or at the Chromium - Zircaloy interface, as shown in *Figure 1–(a)*;
- Generally, the Cr grains display a columnar morphology (*Figure 1-(c)*) due to the deposition process used, derived from Physical Vapor Deposition (PVD);
- Last generation of Cr coatings (*Figure 1-(b)*) is characterized by a fully dense microstructure without evidence of defects, as highlighted by high magnification transmission electron microscopy (TEM) examinations on thin foils prepared using the Focus-Ion-Beam (FIB) technique (*Figure 1-(d)*).

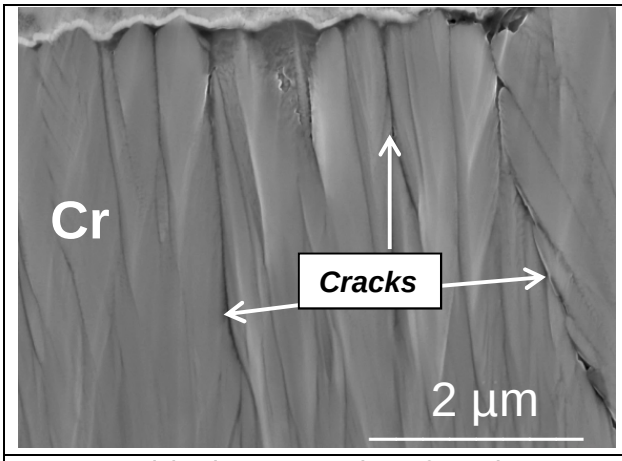

(a) First generation of coating

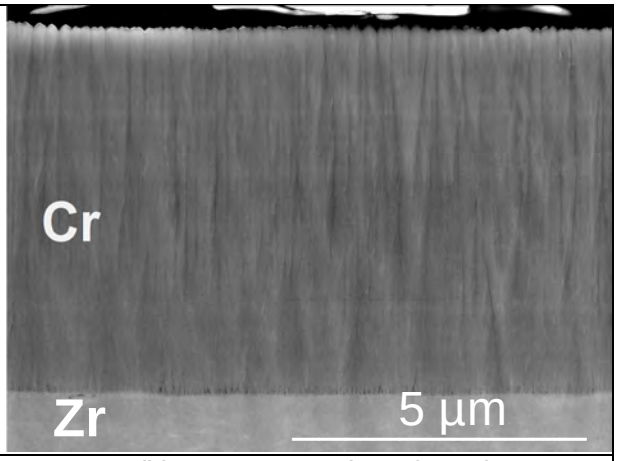

(b) Last generation of coating

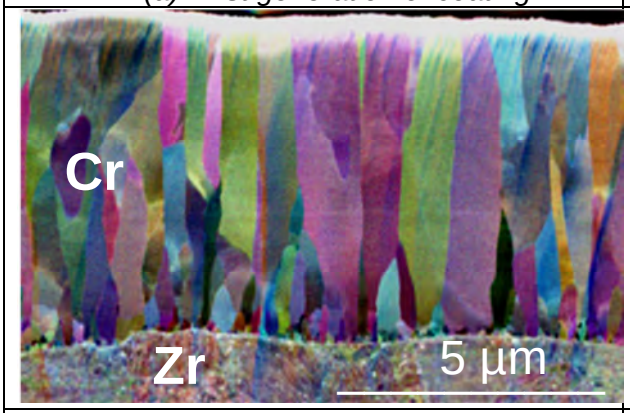

(c) Forward Scattered Detectors Imaging (Field Emission Gun Scanning Electron Microscopy, FEG-SEM)

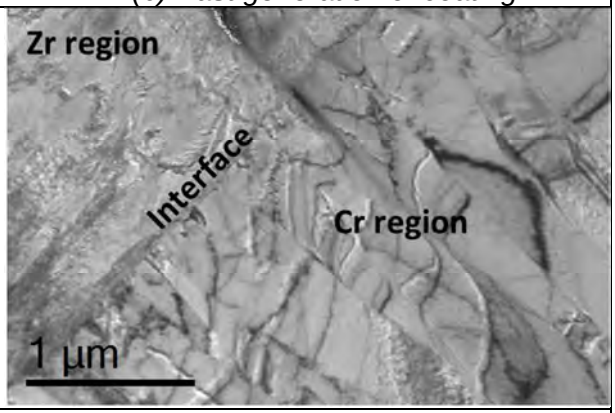

(d) Zircaloy-4/chromium interface as observed by TEM (J. Ribis, B. Arnal, CEA)

Figure 1 – Electron micrographs of some typical as-received Cr coating microstructures

1.2 Behavior upon corrosion in nominal conditions

Some preliminary short tests have been performed on the first generation of coated samples at 360℃ in autoclave with a representative pressur ized water reactor (PWR) primary water environment. The results showed a significant reduction of the oxidation kinetics when compared to reference uncoated materials [2][3]. On-going autoclave tests at 415℃ under steam (100 bars) have confirmed these first results for longer oxidation times. As shown in *Figure 2*, the weight gain of the last generation of Cr-coated samples is much lower than the uncoated reference materials. A weight gain lower than 0,05mg/cm² has been measured on last generation of Cr-coated Zircaloy-4 sample after 200 days at 415℃, corresponding to an outer Cr oxide thickness lower than 250 nm. This weight gain is at least 50 times lower than the weight gain obtained on uncoated reference materials corresponding to more than 15µm thick zirconia outer layer.

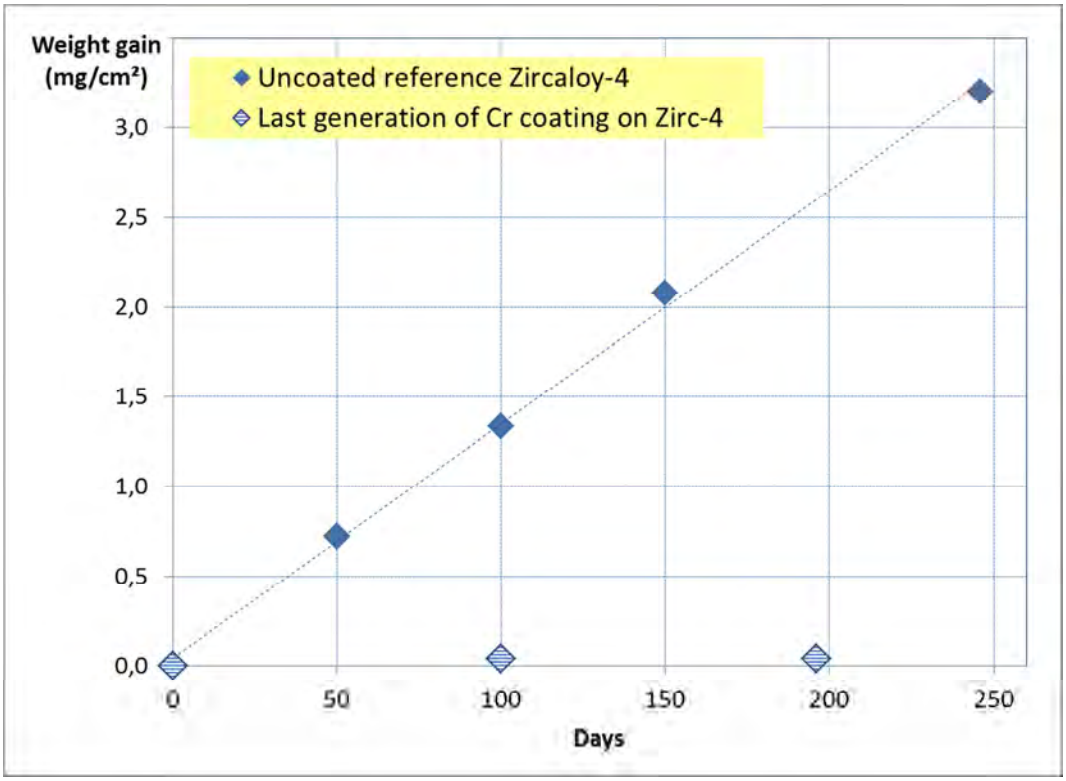

(a)

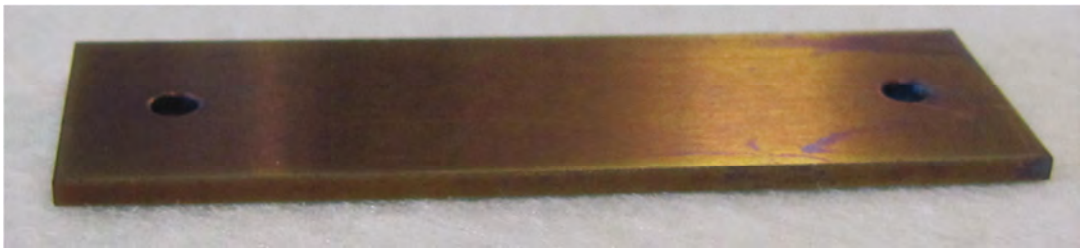

(b)

Figure 2 – Weight gain of uncoated and Cr-coated materials after autoclave tests at 415℃, under 100 bars steam environment (Fig. 2-a), and visual aspect of last generation of Cr-coated sample after 100 days of autoclave testing (Fig. 2-b)

2. Behavior upon High-Temperature oxidation

2.1 High Temperature behavior in steam for typical DBA-LOCA temperature range

Cr-coated Zircaloy-4 sheets samples and clad segments have been tested in the 1000-1200℃ temperature range (typical of design basis accident (DBA) LOCA conditions) under steam, and then water quenched down to Room Temperature (RT) thanks to CEA "DEZIROX" [4] facility. As an example, *Figure 3* shows the weight gain evolution as a function of the steam oxidation time at 1200℃ and some associated optical micrographs of typical Post-Quenching (PQ) microstructures of uncoated and coated materials. It is obvious from these results that coated materials display a much slower HT steam oxidation kinetics, up to at least 1500 s at 1200℃, thus preventing the prior-β_{Zr} substrate from oxygen diffusion and the formation of thick brittle outer ZrO_2 and $\alpha_{Zr}(O)$ layers. Furthermore, for longer oxidation time, i.e., after one side oxidation for 6000 s at 1200℃, it has been shown that the Cr-coated clad segment is able to survive to the final water quenching down to RT while uncoated reference cladding samples broke into numerous (brittle) fragments [1][3].

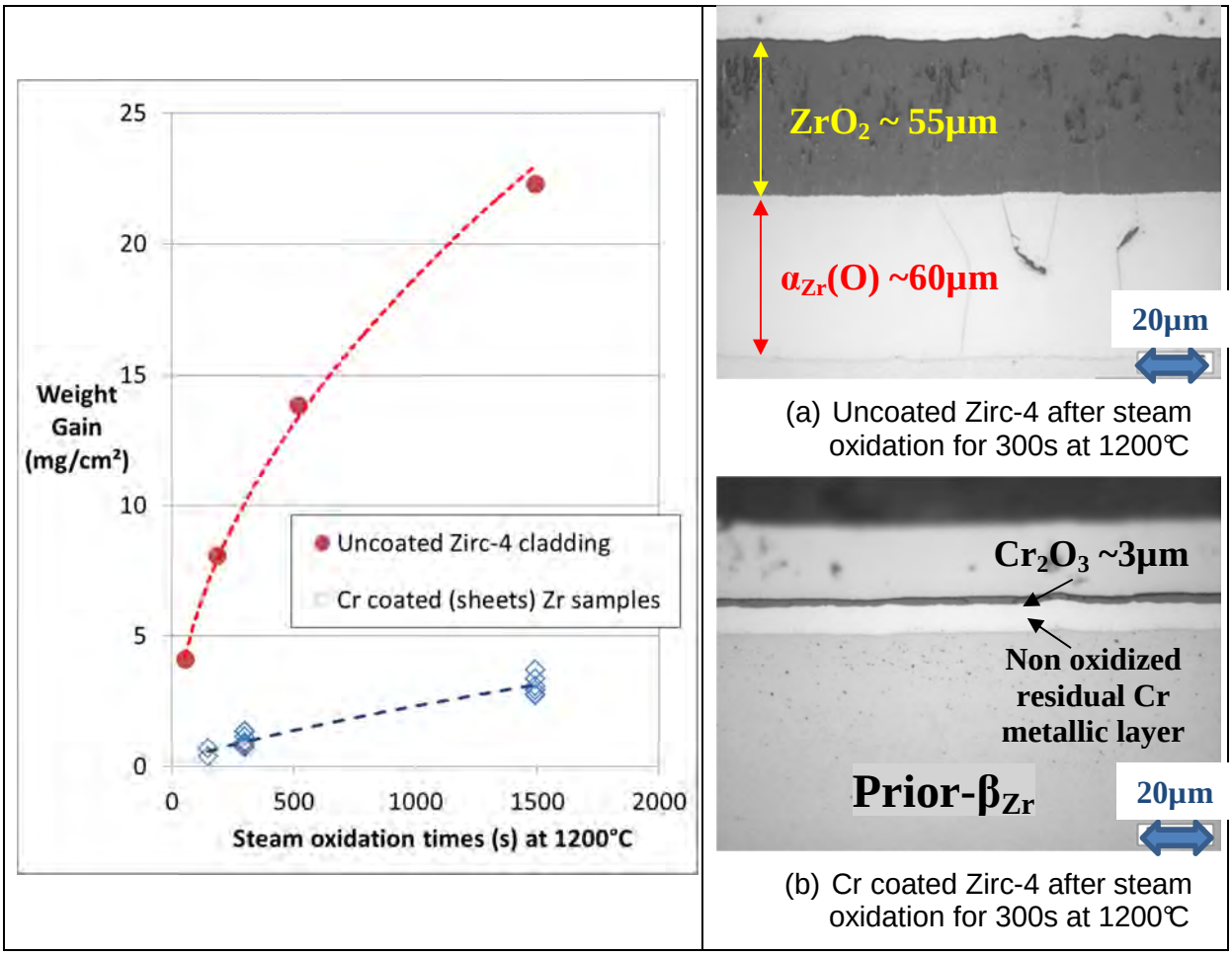

(a) Uncoated Zirc-4 after steam oxidation for 300s at 1200℃

(b) Cr coated Zirc-4 after steam oxidation for 300s at 1200℃

Figure 3 – Comparison between the respective HT steam oxidation behaviors at 1200℃ of uncoated vs. Cr coated Zircaloy-4 samples

Due to their much slower oxidation kinetics, Cr-coated materials exhibit significantly higher PQ residual strength and ductility, as already partially reported in [2] and [3]. For example, Cr-coated clad segments show only a very limited decrease of their residual strength and ductility after steam oxidation for 15000 s at 1000℃ while, due to a high hydrogen pick-up, uncoated reference cladding shows negligible residual strength and ductility in these "post-breakaway" oxidation conditions (*Figure 4*).

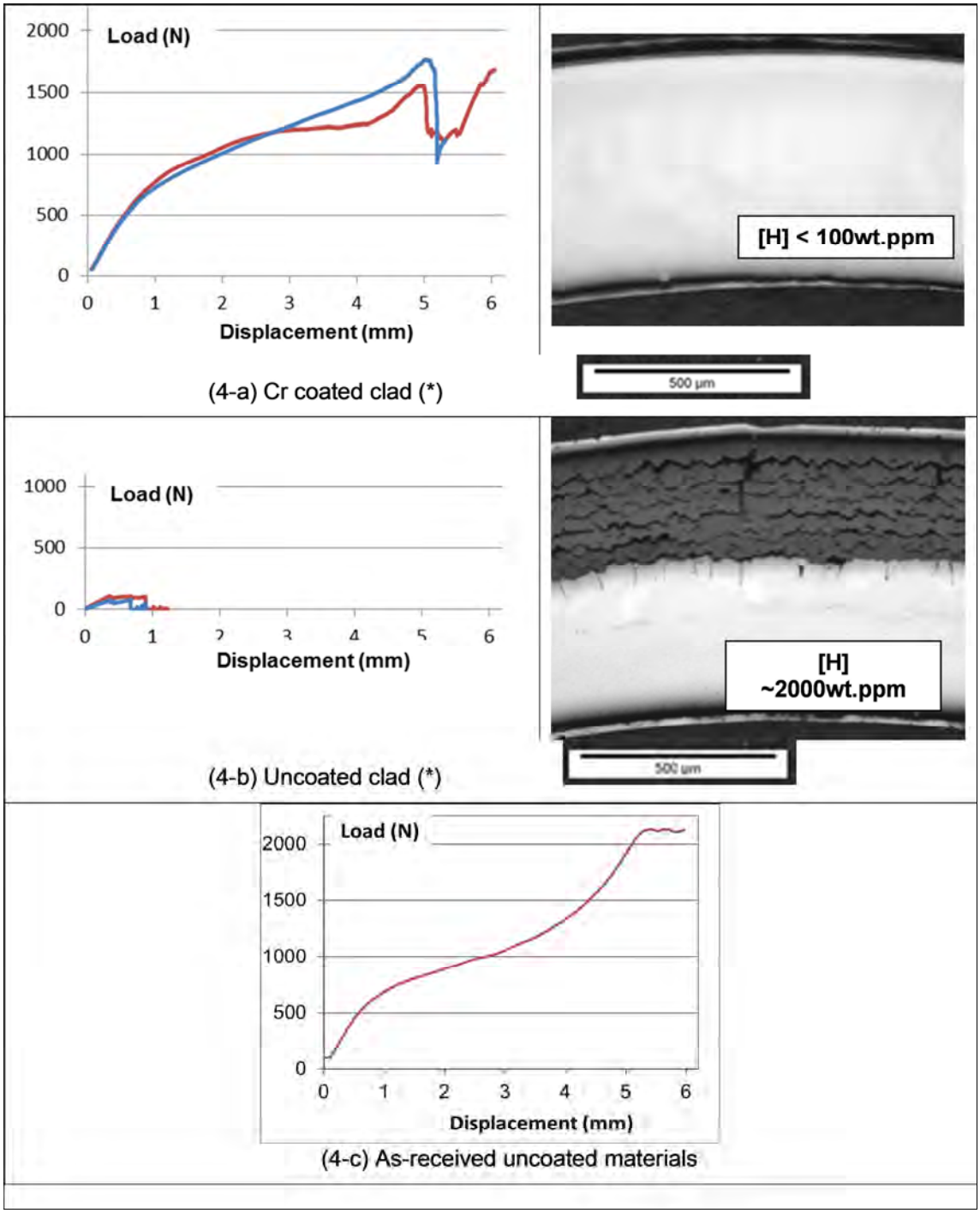

Figure 4 – PQ Ring Compression Test (RCT) behavior at 135℃ and optical micrographs of Cr coated (Fig. 4-a) and uncoated (Fig. 4-b) clads after oxidation for 15000s at 1000℃, and comparison with the as-received uncoated materials RCT behavior (Fig. 4-c)

(*) red and blue curves correspond to two tests performed in the same conditions, thus showing reproducible PQ RCT behaviors for same metallurgical conditions of the tested clads

2.2 Impact of pre-existing Cr coating defects

One issue is the potential negative impact of a pre-existing defect (i.e., as-received crack) within the Cr coating on subsequent oxidation. To give some insights into this point, some preliminary observations that were performed on the first generation of Cr coatings, showing some local defects/cracks in the as-received conditions (before any oxidation experiments), are reported here. *Figure 5* shows the effect of a pre-existing crack on the subsequent oxidation both in nominal and HT steam oxidation conditions. These observations show that a pre-existing crack has only a limited and very localized impact on the overall oxidation of the coated sample. Moreover, there is no experimental evidence here of any local spallation of the Cr coating or of an acceleration of the Zr substrate oxidation.

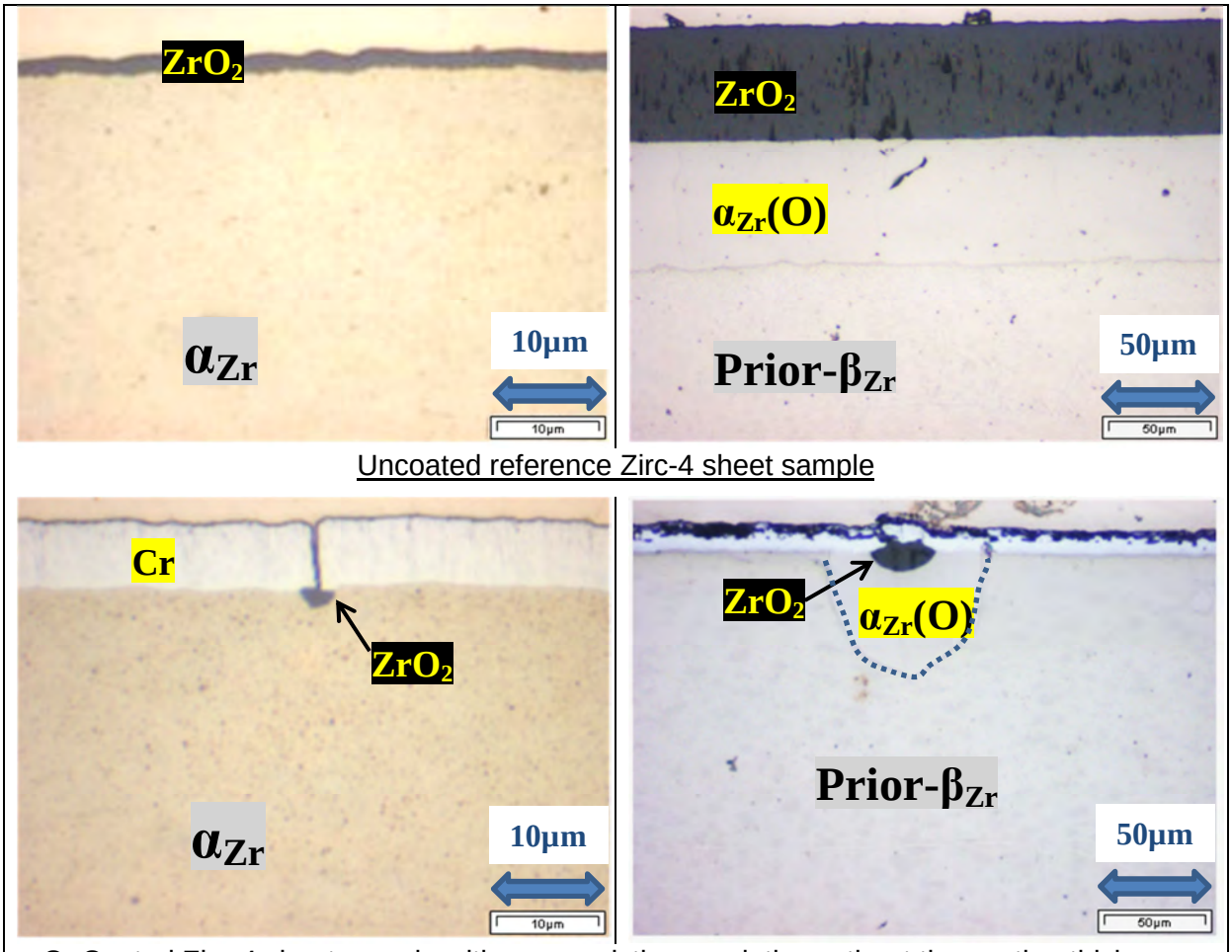

Figure 5 – Optical micrographs of uncoated and Cr coated Zircaloy-4 sheets samples for the 1st generation of Cr coating with some initial (as-received) local defects/cracks:
- after autoclave corrosion test in PWR primary water environment (left)
- and then after re-oxidation at high temperature in steam (right)

2.3 High Temperature behavior in steam for beyond DBA-LOCA temperature range

Thermo-Gravimetric-Analysis (TGA) tests have been performed up to 1300℃ in a helium-oxygen environment on coated and non-coated samples.

Figure 6 shows the post-oxidation appearance of uncoated and coated Zirc-4 samples after HT oxidation for 5600 s at 1300℃ in a helium-oxyge n environment and slow cooling down to RT. This figure shows that, in spite of the slow cooling applied, the uncoated materials is significantly damaged for the severe oxidation conditions experimented here, showing macroscopic cracking, while the integrity of the coated sample is preserved. This last sample is characterized by a significant residual inner prior-β_{Zr} layer (with some α_{Zr}(O) incursions), indicating much lower oxygen diffusion into the metallic substrate than for the uncoated sample (this last one showing thick outer zirconia layers and full transformation of the initial prior-β_{Zr} layer into a brittle α_{Zr}(O) layer). Thus, integrity of the coated sample in these beyond LOCA conditions is maintained due to the existence of a significant residual inner prior-β_{Zr} layer.

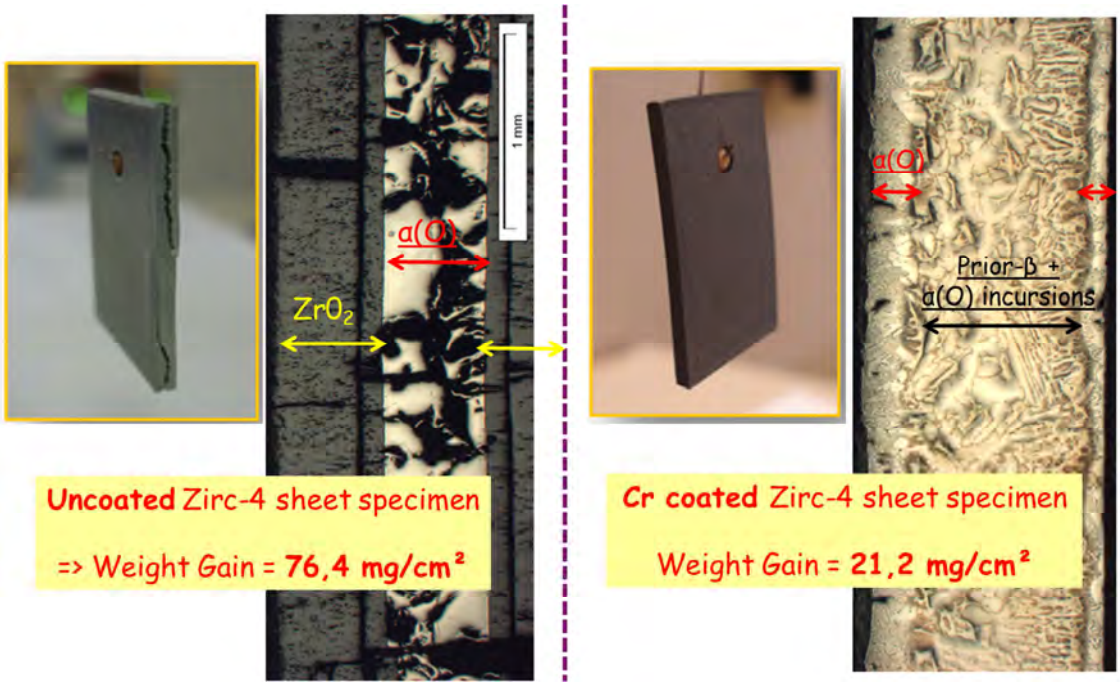

Figure 6 – Post-oxidation appearance of uncoated and 15-20 µm thick Cr coated Zirc-4 samples after HT oxidation for 5600 s at 1300℃ in a helium-oxygen environment and application of a final slow cooling down to RT (TGA experiments)

3. Conclusions and further work

The last generation of Cr coatings developed at CEA in partnership with AREVA and EDF exhibits good behavior in nominal and accidental conditions, by:

- reducing drastically the nuclear fuel clad corrosion in nominal conditions (out-of-pile autoclave tests);
- increasing the HT steam oxidation resistance in DBA-LOCA and, to some extent, for beyond DBA-LOCA conditions;
- then enhancing the post-quench ductility and the resistance to quench (by delaying brittle ZrO_2 and $\alpha_{Zr}(O)$ layers formation);
- decreasing drastically the hydrogen pick-up during steam oxidation at 1000℃, when compared to uncoated materials for “post-breakaway” conditions for these last ones.

There are still some important issues to assess concerning the Cr-coated clad behavior in other relevant nominal and accidental *scenarii*, especially under neutron irradiation. For that, on-going ions irradiation experiments are performed at the CEA JANNUS-Saclay triple beam accelerators facility and it is planned next year to irradiate some Cr-coated nuclear fuel segments fueled with UO_2 pellets in a representative PWR environment in the Halden reactor.

References:

[1] J. Bischoff et al., “Development of fuels with enhanced accident tolerance”, proceedings of TopFuel-2015 WRFP Meeting, Zurich, Switzerland, (Sept. 13-17, 2015)

[2] I. Idarraga et al., “Assessment at CEA of coated nuclear fuel cladding for LWRs with increased margins in LOCA and beyond LOCA conditions”, proceeding of 2013 LWR Fuel Performance Meeting/TopFuel, Charlotte, USA, (Sept. 15-19, 2013)

[3] J.C. Brachet et al., “CEA studies on advanced nuclear fuel claddings for enhanced Accident Tolerant LWRs Fuel”, proceedings of the 8th Int. Symposium “Fontevraud-8” on “Contribution of Materials Investigations and Operating Experience to LWRs’ Safety, Performance and Reliability”, Avignon, France, (Sept. 14-18, 2014)

[4] M. Le Saux et al., « Influence of Pre-Transient Oxide on LOCA High Temperature Steam Oxidation and Post-Quench Mechanical Properties of Zircaloy-4 and M5™ cladding », 2011 WRFP (Topfuel) Meeting, Chengdu, China, (Sept. 11-14, 2011), Paper T3-040

STEAM OXIDATION BEHAVIOR OF PROTECTIVE COATINGS ON LWR MOLYBDENUM CLADDING FOR ENHANCING ACCIDENT TOLERANCE AT HIGH TEMPERATURES

YOUNG-JIN KIM

GE Global Research Center, 1 Research Circle, Schenectady, NY 12309, USA

BO CHENG & PETER CHOU

Electric Power Research Institute, 3420 Hillview Avenue, Palo Alto, California 94304, USA

ABSTRACT

Characteristics of protective coatings (e.g., Zircaloy 2, Zircaloy 4, and FeCrAl coatings) formed by PVD on Mo were analyzed by SEM and TEM before and after the high temperature steam oxidation test. The fine structure and diffusional layer of coatings was observed near the coating/Mo interface as a result of the PVD process and the thickness of diffusional layer was further increased by the oxidation reaction in high temperature steam. In particular, a thin aluminum oxide formed on the outermost layer of FeCrAl coating during steam oxidation provides an excellent protection to the Mo substrate in high temperature steam. Microstructure features such as an interfacial adhesion property with the formation of a thin diffusional layer near the Mo substrate are believed to have a significant effect on coating properties that provides the tolerance of Mo as an ATF under severe accident conditions. It was observed that a thin protective layer (~50μm thickness) of coatings provides the excellent oxidation resistance in 1000^{o}C steam environments. Also, the formation of ZrO_2 on the Zircaloy coating in steam enhances the adherence on the coating/Mo interface and protects Mo against the test environments.

1. Introduction

Zirconium alloys have been used most extensively as fuel assembly materials for water-cooled reactors. Considerable research has been done to ensure that zirconium alloys are corrosion resistant in high temperature water and steam. Zirconium reacts with high temperature water and steam to form ZrO_2 and hydrogen. Oxidation of Zr-based cladding in high temperature steam environment produces a rapid exothermic reaction and accompanies the significant hydrogen production. Thus, under severe accident conditions by the earthquake and tsunami to the Fukushima Daiichi nuclear power plant in 2011, the primary attentions have been given to development of nuclear fuels and claddings that enhance the accident tolerance of LWRs to tolerate loss of active cooling in the core.

EPRI has started accident tolerant fuel (ATF) development program and initiated the conceptual design of an innovative fuel cladding, using Mo or its alloys as an alternate candidate fuel cladding material that may provide several advantages over the current Zr alloys [1-5]. The excellent thermal conductivity and high temperature strength of Mo and its alloys provide attractive features for components in fusion and magnetic devices [6-8]. Mo alloy has been known to possess good tensile and creep strength at temperatures exceeding 1200^{o}C, and some Mo alloys also have adequate ductility at room temperature suitable for fabrication of thin-wall tubes. However, Mo and its alloys react readily with oxygen or other gases at high temperature and oxidized Mo is susceptible to losses from volatile Mo trioxide species, MoO_3, in air and hydroxide, $MoO_2(OH)_2$, in water. As temperature rises, Mo oxides (MoO_2/MoO_3) become a less protective flayer and evaporate so rapidly at elevated temperatures.

Thus, the current proposed Mo cladding for accident tolerant fuel (ATF) includes an external coating of either Zr-alloy or Al-containing stainless steel; both are anticipated to provide good corrosion resistance at light water reactor operation temperatures and form an in-situ oxide of ZrO_2 and Al_2O_3 to protect the Mo alloy in severe loss of coolant environments. The most significant improvements of structural materials including Mo cladding in severe steam oxidation resistance can be achieved by changing the inherent nature of the protective oxide scale or applying a protective coating and its chemistry. Alternate fuel cladding materials,

such as ferritic steels and SiC composites, that provide the oxidation resistance at high temperatures have been also investigated [9, 10].

This paper summarizes the corrosion behavior of Mo under simulated LWR water chemistry conditions and the oxidation resistance of protective coatings and Mo in pure steam at 1000°C or with H_2. The surface morphology and chemistry of coatings analyzed by scanning electron microscope (SEM) and energy dispersive x-ray analysis (EDXA). A focus-ion-beam transmission electron microscope (FIB-TEM) analysis is also conducted for a better understanding of metallurgical interaction of coating elements and Mo substrate at high temperature.

2. Experimental Procedures

2-1. Test Materials

Mo tubes (0.404" OD with ~0.2 mm or 8mil wall thickness) were made of (1) pure Mo formed by powder metallurgy (PM Mo), (2) pure Mo fabricated by low carbon arc cast (LCAC Mo), and (3) Mo containing ~0.3% La_2O_3 (MoLa). In order to enhance the corrosion and oxidation resistance of Mo during normal and accidental conditions, a protective coating was produced on the OD surface of Mo tube by PVD with a bar of Zircaloy 2, Zircaloy 4, or FeCrAl powder (8 wt. % Al + 23 wt. % Cr in Fe balance). Also, the surface morphology and metallurgical interfacial adhesion nature of coatings before and after steam test were analyzed by SEM, EDAX, and FIB-TEM. The conceptual design of proposed Mo cladding with a protective coating has been described [2].

2-2. LWR Water Immersion/High Temperature Oxidation Test

Test system and control of water chemistry condition were described in detail [4]. Immersion tests were performed in simulated BWR water chemistry containing 1.0ppm O_2 (BWR-NWC) or 0.3ppm H_2 (BWR-HWC) at 290°C, and in a simulated PWR water chemistry containing 3.75ppm H_2 at 330°C. A refreshed high purity water loop ensures controlled chemistry and H_2 fugacity during testing. An apparatus and test condition for the steam oxidation test at high temperature was described previously [4].

3. Experimental Results and Discussion

3-1. Microstructure of Coatings

Figures 1 shows the typical SEM image of Zircaloy 2 (~45μm thickness) and FeCrAl (~60μm thickness) coating layer, respectively, formed on Mo tube by the PVD process. Both coatings show no evidence of defects and oxide phases and an excellent interfacial adhesion to the Mo substrate. A similar microstructure of Zircaloy 4 coating was also produced by PVD.

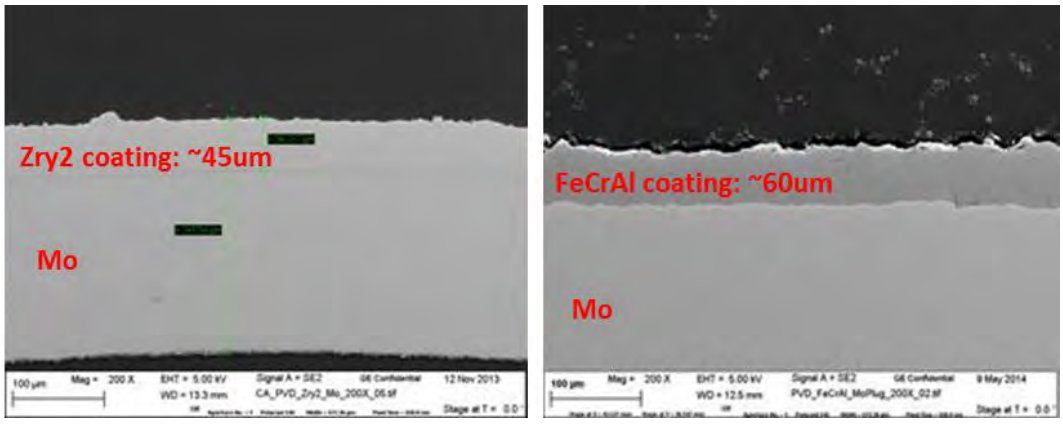

Figure 1: SEM images of Zircaloy 2 and FeCrAl coating on Mo tube by the PVD process

Furthermore, the interfacial characteristic of coating near the Mo substrate was examined by FIB-TEM, since the interfacial adhesion property plays an important role to provide the chemical and metallurgical stability of coating in a given environment. Figures 2 and 3 show the microstructures and elemental profiles of Zircaloy 4 and FeCrAl coating, respectively, near the Mo substrate. It is clearly seen that the diffusion of coating

elements to the Mo substrate was occurred, suggesting that the PVD process produced the interdiffusion layer (~0.3μm thick in the Zircaloy 4 coating and ~0.1μm thickness in the FeCrAl coating). However, more chemical analysis is needed to identify the phases of diffusion layer. From the FIB-TEM result, one can state that the formation of interdiffusion layer at the coating/Mo interface may also be beneficial to provide the metallurgical adhesion of coating to Mo and subsequently contributed to the high corrosion and oxidation resistance.

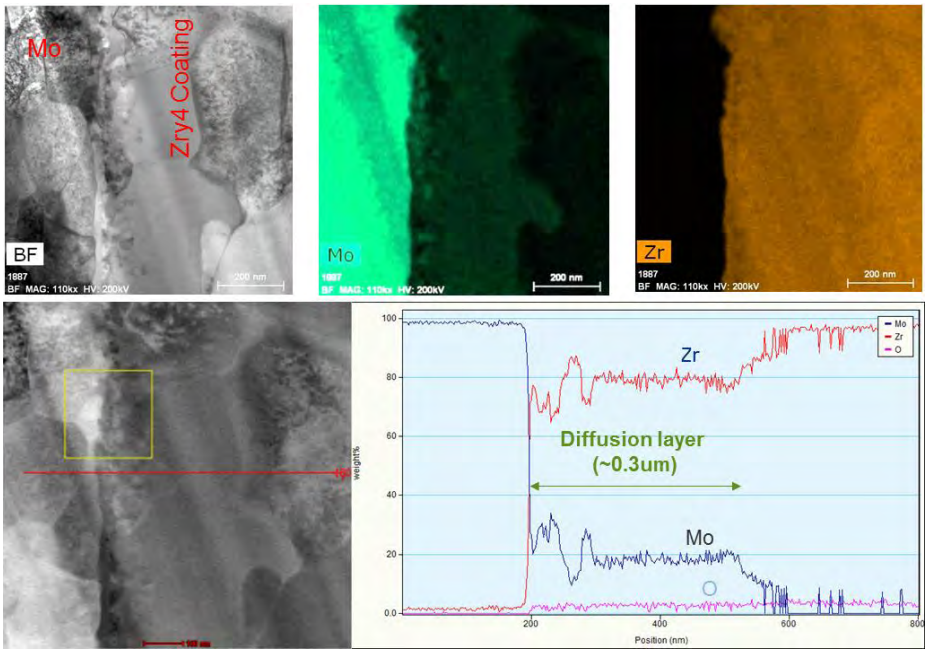

Figure 2: Microstructure and elemental distribution of Zircaloy 4 coating near the Mo substrate

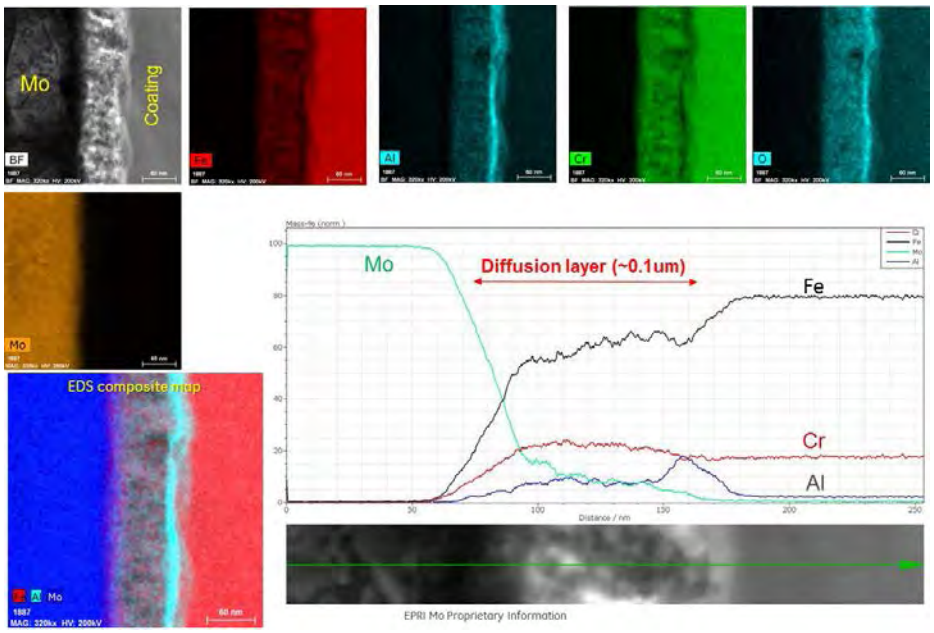

Figure 3: Microstructure and elemental distribution of FeCrAl coating near the Mo substrate

3-2. Corrosion Behavior of Mo and Coatings in LWR

The corrosion rate of PM Mo was measured in a simulated BWR water chemistry containing 1.0ppm O_2 (BWR-NWC) or 0.3ppm H_2 (BWR-HWC) at 290°C and in a simulated PWR primary water chemistry

containing 3.57ppm H_2 at 330°C. Figure 4 shows the weight change of PM Mo specimens under different water chemistry conditions. It is seen that PM Mo specimens are more stable in high temperature water containing hydrogen, while a high susceptibility of pure Mo to corrosion is observed in the presence of oxygen due to the formation of volatile MO_3. The similar corrosion rate of three different Mo specimens (LCAC and MoLa) was also measured under the test water chemistry conditions.

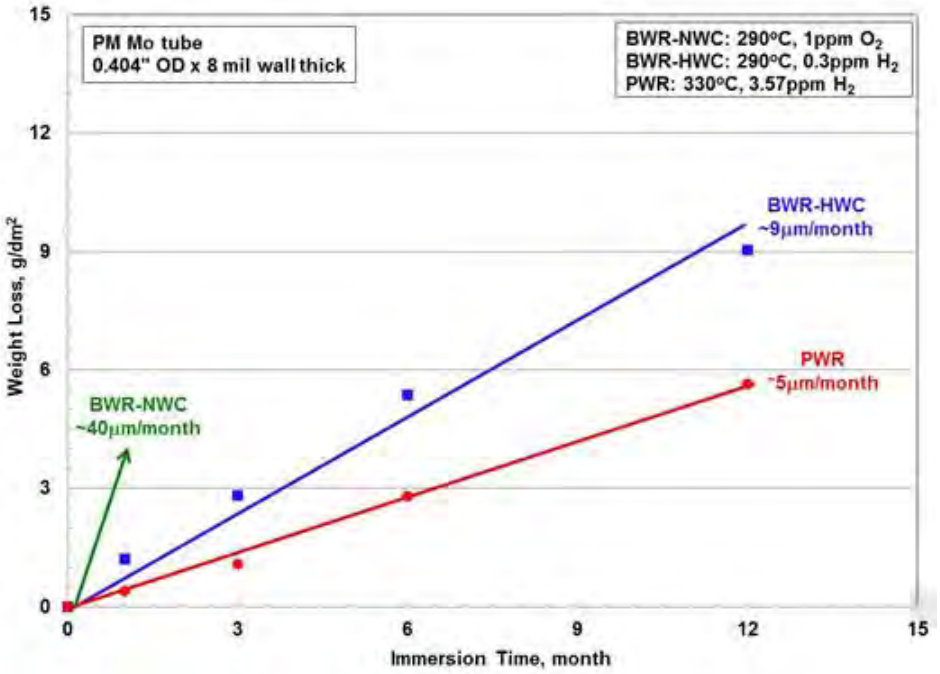

Figure 4: Weight change of Mo as a function of immersion time in simulated BWR and PWR conditions

The corrosion resistance of Zircaloy 2 coating (~45μm thick) and FeCrAl coating (~60μm thick) was also evaluated after immersion for 4 months in 290°C water containing 0.3ppm H_2. As shown in Figure 5, most of Zircaloy 2 coating layer was oxidized to form ZrO_2, although an excellent adhesion of Zircaloy 2 coating on Mo was not degraded, while no loss of FeCrAl coating was observed. A physical separation of FeCrAl coating from the Mo substrate may be caused by the difference in the coefficient of thermal expansion during cooling after testing. The high corrosion of Zircaloy 2 coating may be attributed by an inadequate chemistry of Zircaloy 2 coating that may be lack of alloying elements (e.g., Sn, Ni, Cr and Fe in Zircaloy 2) in the coating layer during PVD process, and more accurate analysis of Zircaloy 2 coating is in progress for a better understanding of corrosion behavior. It is well known that a uniform distribution of fine particles containing such elements in the Zr alloys produces the optimum corrosion resistance in high temperature water.

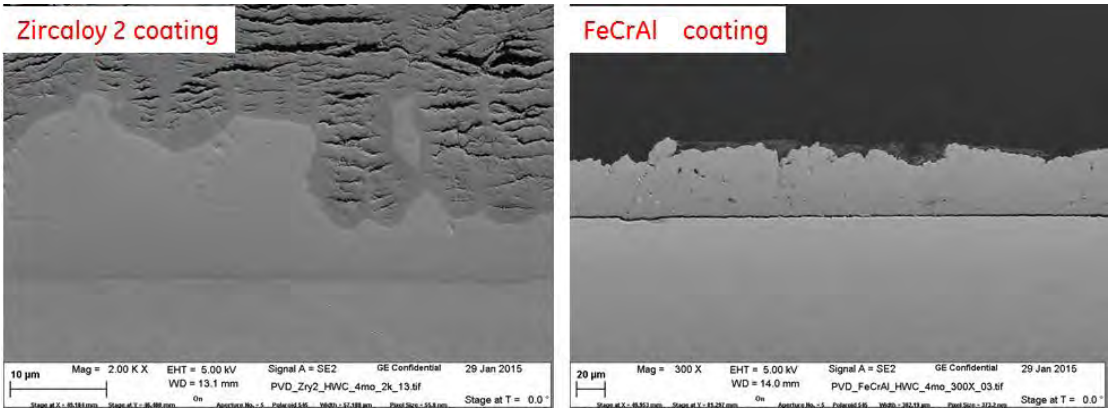

Figure 5: Cross-sectional view of Zircaloy 2 and FeCrAl coating on Mo formed by PVD after immersion for 4 months in 290°C water containing 0.3ppm H_2.

3-3. Oxidation Resistance of Coatings in High Temperature Steam

The oxidation resistance of Zircaloy 2 and FeCrAl coatings was evaluated in 1000^{o}C steam with addition of 10% H_2. After exposure for 4 days, the adhesion and microstructure of interfacial boundary between coating and Mo was analyzed by SEM and EDAX.

The Zircaloy 2 coating was still chemically and physically intact providing the protection to Mo by forming a ZrO2 in steam, confirmed by EDAX, but the complete/physical separation of Zircaloy 2 coating from the Mo substrate was observed (Figure 6). This spallation of Zircaloy 2 coating may be mainly occurred by the difference of thermal expansion coefficient between Zr and Mo during the cooling process after steam test and/or the accelerated crevice attack at the open edges of both ends where no protective coating was presence. The oxidation of Zircaloy 2 coating layer in steam produced the ZrO_2 layer of ~75μm thickness and still provided a oxidation barrier layer to Mo, and thus one can expect that observation of thin Mo wall thickness (from 190μm to 130μm) mainly resulted from the ID dissolution since both OD and ID surfaces were exposed to the test environment.

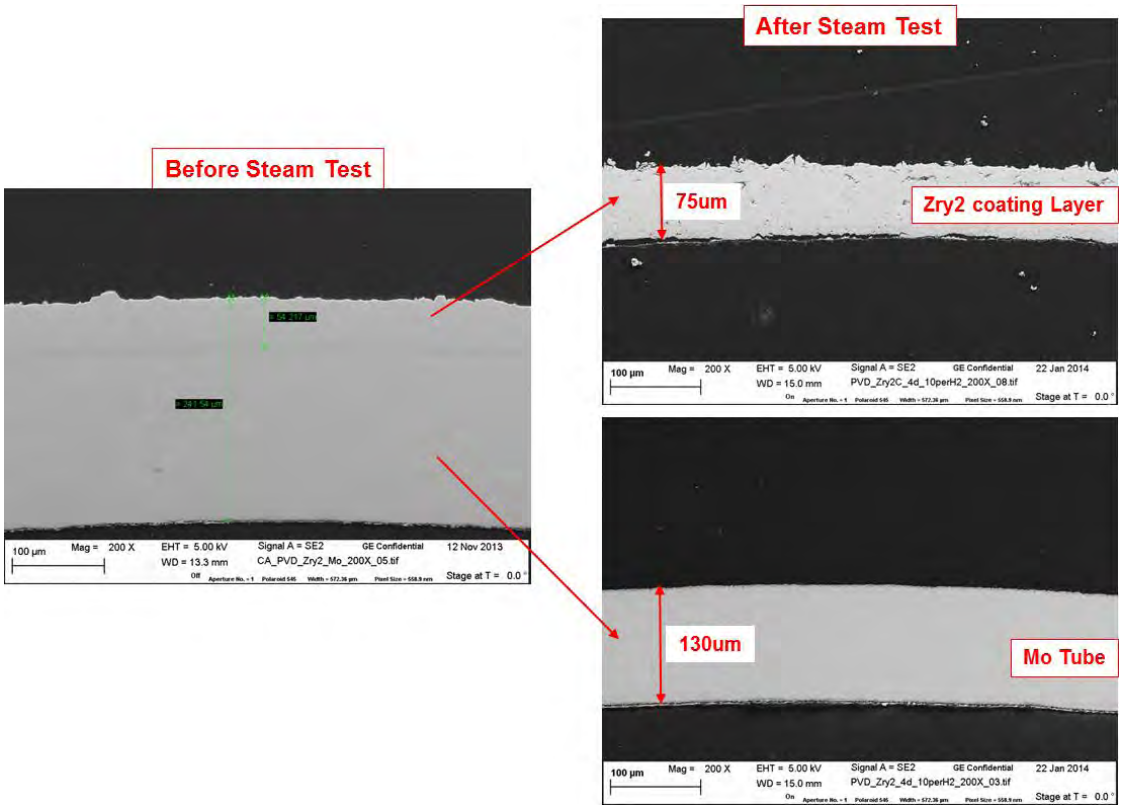

Figure 6: Cross-sectional morphology of Zircaloy 2-coated Mo specimen after steam oxidation test for 4 days in 1000^{o}C steam containing 10% H_2.

The cross-section of FeCrAl-coated Mo specimen was also examined by SEM and EDAX, shown in Figures 7 and 8, respectively [4]. From the cross-sectional image in Figure 7, no significant loss of FeCrAl coating layer were observed and the excellent physical stability was retained under the test conditions. From the EDAX analysis on FeCrAl coating, shown in Figure 8, a thin aluminum oxide formation on the outermost layer of FeCrAl coating during steam oxidation was identified. This indicates the FeCrAl coating to be a promising choice as a protective barrier layer to tolerate the severe accident condition. The formation of alumina scale on various FeCrAl alloys in high temperature steam environments has been also reported in literatures [9, 11, 12]. The oxidation resistance of Al oxide is known to be superior to that of Cr oxide at high temperature (>1000^{o}C) [13, 14] and eventually such a thin alumina layer formed on the outermost surface of FeCrAl coating provides the good oxidation resistance at high temperature.

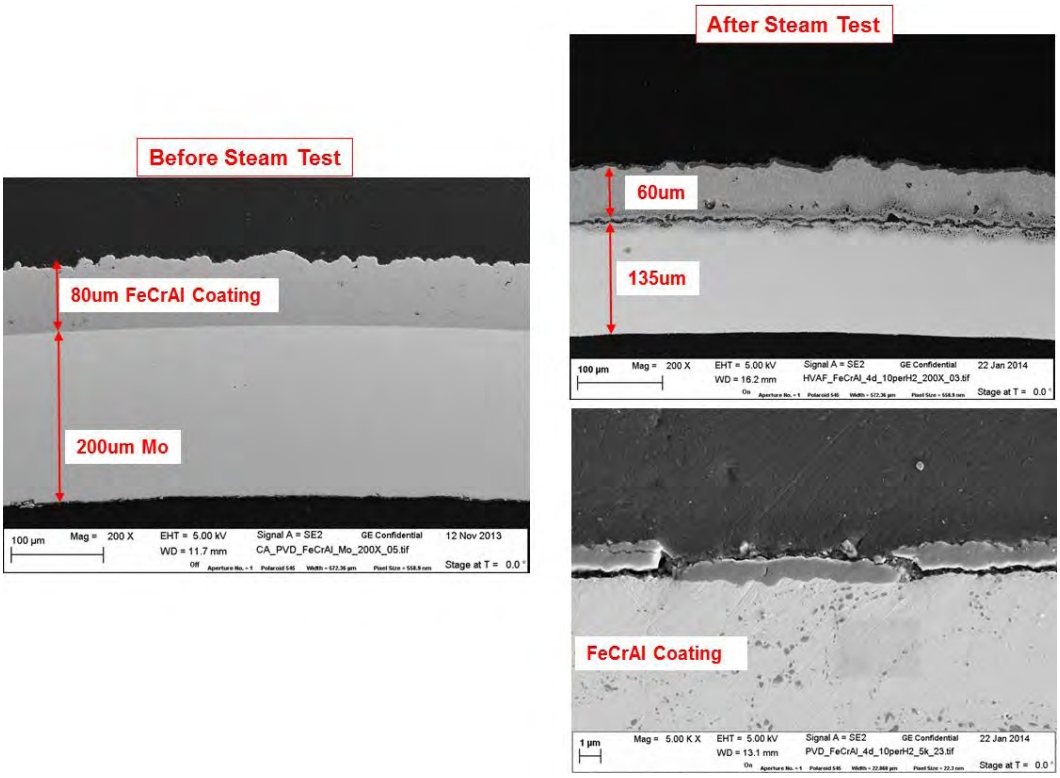

Figure 7: Cross-sectional morphology of FeCrAl-coated Mo specimen after steam oxidation test for 4 days in 1000^{o}C steam containing 10% H_2.

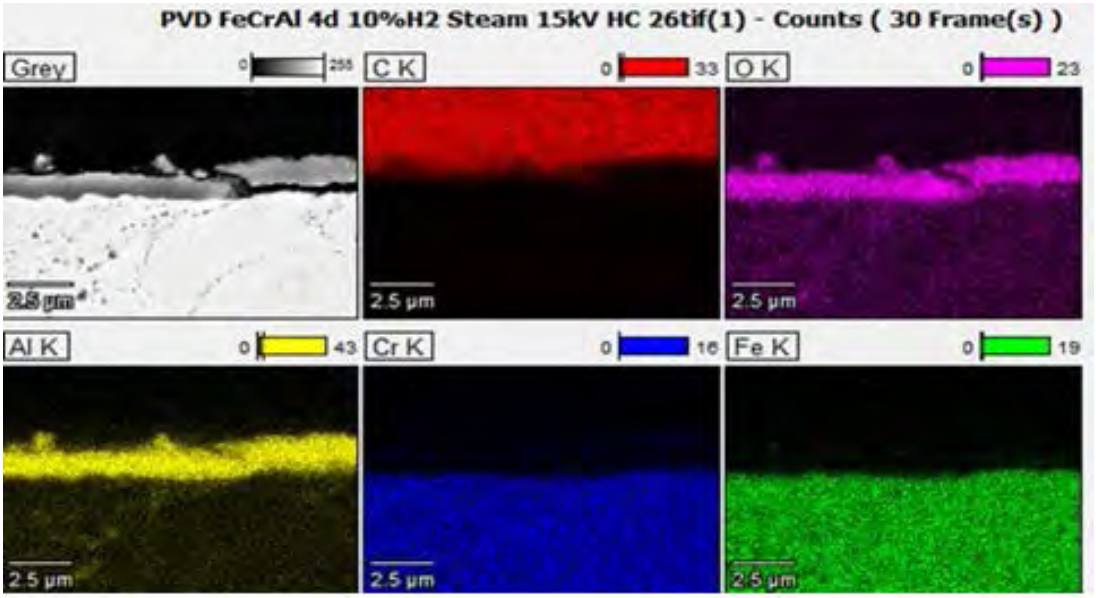

Figure 8: Elemental map of FeCrAl-coated Mo specimen after steam oxidation test for 4 days in 1000^{o}C steam containing 10% H_2.

Because the longevity of steam oxidation resistance of protective coating is an important factor in the successful application of Mo cladding under severe loss of coolant accidents, another effort was devoted to the investigation of the long term steam oxidation resistance of coated Mo specimens. The short-term steam oxidation behavior of protective coatings has been reported in details previously [4]. The surface morphology of Zircaloy 4 and FeCrAl coated Mo specimens after exposure for 7 days in 1000^{o}C steam was

examined by SEM. Some of loss or separation of Zircaloy 4 coating was observed, while such a degradation of FeCrAl coating was not.

In order to examine the possible chemical interaction of protective coatings with the Mo substrate in high temperature steam, the cross-section and elemental analysis of the coating/Mo interface was further conducted. Figure 9 shows the cross-sectional view of Zircaloy 4 coated Mo specimen after testing in 1000 steam for 7 days. It is clearly seen that very low steam oxidation rate of Mo was measured (~25% loss in 7 day exposure) that may result in some loss or delamination of Zircaloy 4 coating in steam. However, an excellent adhesion of thin Zircaloy 4 coating layer (~0.5μm) was still maintained that may provide the sufficient oxidation resistance to the Mo substrate (loss of ~25% thickness of Mo). Elemental analysis of remaining Zircaloy 4 coating layer confirmed the formation of Zr oxide. More steam oxidation evaluation of Zircaloy 2 coating is in progress to understand the effect of Ni on the coating adherence/durability.

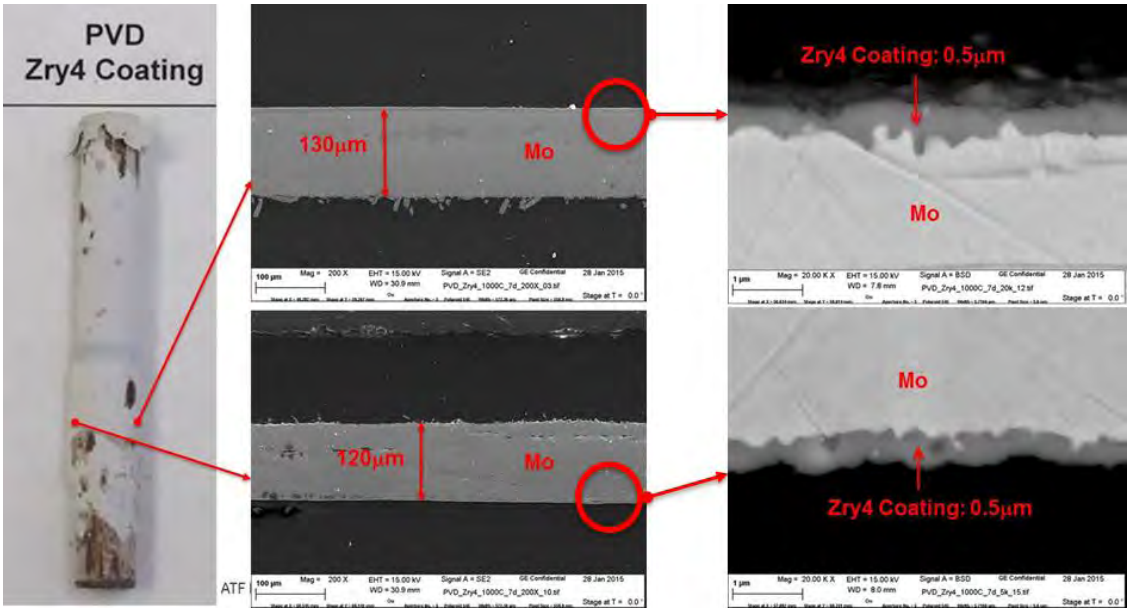

Figure 9. Cross-sectional view of Zircaloy 4 coated Mo tubes after steam oxidation test for 7 days in 1000°C steam.

A similar examination of the morphology and durability of FeCrAl coating was also performed, as shown in Figure 10. The thickness of the Mo tube was ~210μm after a 7 day exposure, indicating almost no loss or dissolution under the test condition. Also, no significant degradation of FeCrAl coating was also observed, except separation of coating at some locations near the inner coating layer, but not at the outmost coating layer. More analysis is in plan to understand these phenomena.

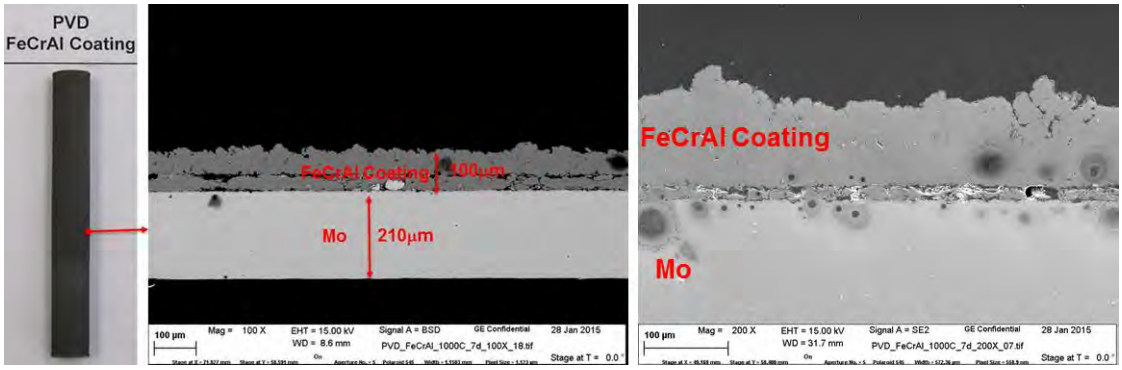

Figure10. Cross-sectional view of FeCrAl coated Mo tubes after steam oxidation test for 7 days in 1000°C steam.

The surface features of FeCrAl coating in Figure 10 was further examined by EDXA near the coating/Mo interface and outermost coating layer, as shown in Figures 11 and 12, respectively. An interesting observation is the extension of interdiffusion layer thickness (~5μm thick in Figure 11), forming the Mo/Fe/Cr phases in the Mo substrate (see Figure 3: ~0.1μm thick diffusion layer in as-coated FeCrAl coating). Al oxide was found along the near coating/Mo boundaries and localized areas in the coating grain boundaries. Al oxide layer (~0.15μm thick) was also formed at the outermost layer of FeCrAl coating. Obviously, the aluminum oxide that forms on the coating surface behaves as an effective barrier that limits the ingress of oxygen or steam into the coating and Mo substrate. It is well described that alumina forming steels are superior to the chromia forming steels and provides the high temperature oxidation protection [13, 14].

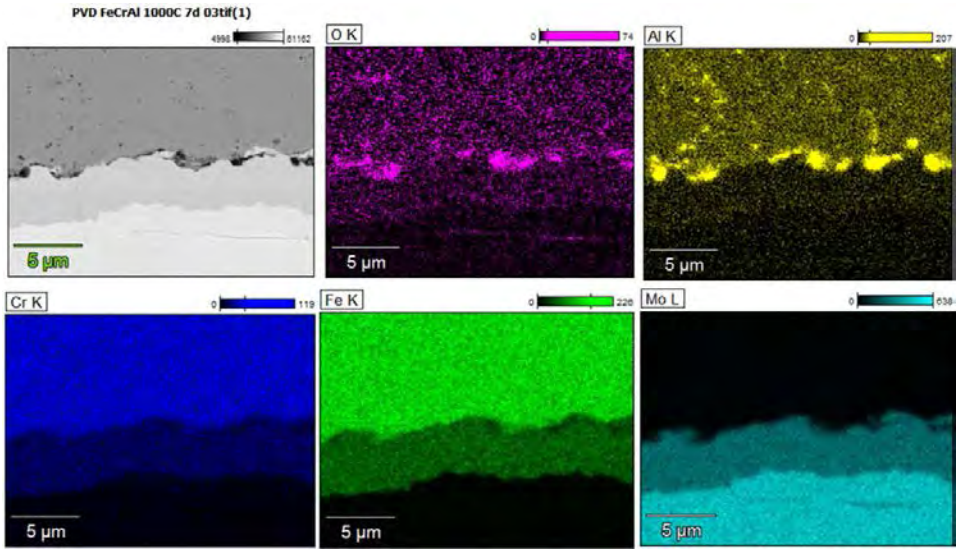

Figure 11: Elemental map of FeCrAl-coated Mo specimen near the coating/Mo interface after steam oxidation test for 7 days in 1000°C steam.

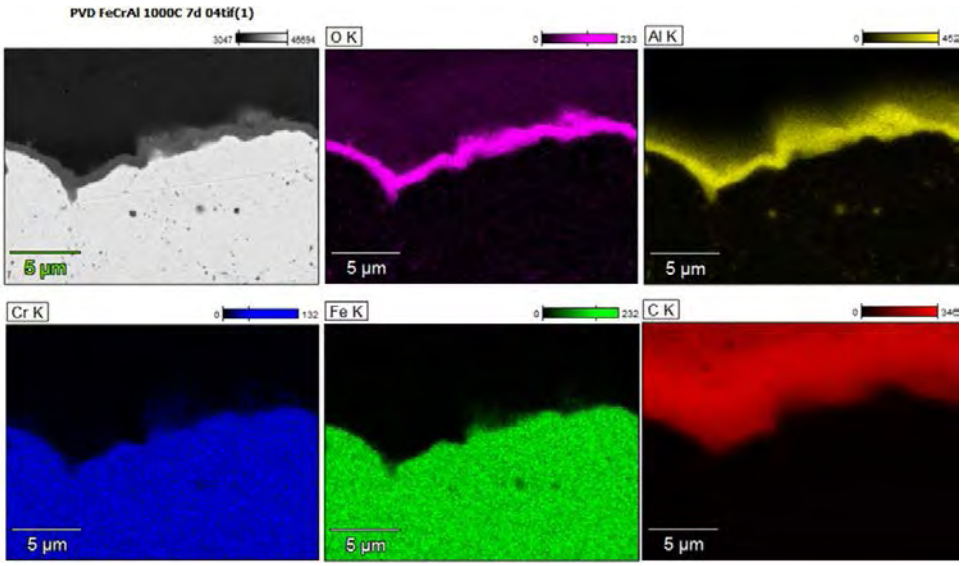

Figure 12: Elemental map of FeCrAl-coated Mo specimen near the outmost coating layer after steam oxidation test for 4 days in 1000°C steam.

In order to understand the excellent oxidation resistance of FeCrAl coating in high temperature steam, the microstructure of coating near the coating/MoLa interfacial layer was further analyzed by FIB-TEM, as shown

in Figure 13. The most straightforward FIB-TEM analysis is that of thin sections prepared from the coating/MoLa interface without damaging the original physical/chemical property. This particular specimen was tested for 3 days in 1000°C steam and the excellent adhesion of FeCrAl coating on MoLa was observed at the coating/MoLa substrate interface (see areas #3 and #4).

Growth of the diffusional layer thickness was observed in area #3 near the MoLa substrate in high temperature steam, suggesting the diffusion of Fe and Cr into MoLa (from ~0.1μm thick to ~4μm thick, see Figures 3 and 13 for comparison). Such an increase in the interdiffussion layer thickness is believed to provide an excellent durability of coating in high temperature steam. Unfortunately, no coating layer was present for analysis in area #2, since the FIB process failed to collect the thin portion of coating segment. Thus, only the microstructure of MoLa was detected and revealed the fine/slightly elongated equiaxed grains, ranging 0.2-2μm that may improve the mechanical strength of MoLa. The fine grains expect to be formed during exposure to high temperature steam. Table I summarizes the chemical composition of areas marked in Figure 13

Figure 13: FIB-TEM analysis of FeCrAl-coated MoLa specimen after steam oxidation test for 3 days in 1000°C steam.

Table 1: Chemical composition of different areas near the FeCrAl coating and MoLa interface after steam oxidation test for 3 days at 1000°C (wt%).

	Fe	Cr	Mo	Al	Si	Ti	Zr	La
Area 1	71.3	22.5	3.9	1.8	0.1	0.04	0.3	---
Area 2	0.3	0.1	98.2	0.1	0.07	---	0.7	0.4
Area 3	34.9	10.6	53.4	0.3	0.2	---	0.6	---
Area 4	1.1	1.3	96.5	0.04	0.1	---	0.8	0.2

From this oxidation study in high temperature steam, a Zircaloy or FeCrAl coating exposed to steam believes to be covered with hydroxyl species due to thermodynamically difficulty for the formation of oxygen species. Thus, water vapor may react more rapidly with coatings than oxygen provided that the formed oxide can grow by transport of hydroxyl ions as well as the diffusion of coating elements (Zr, Fe, Cr, Al). The formation kinetics and rate of Zr oxide (ZrO_2) in the Zircaloy coating and Al oxide (Al_2O_3) in the FeCrAl coating may play a significant role in protecting the Mo substrate.

Several mechanisms have been proposed to understand the high temperature oxidation behavior of alloys in environments that contain water vapor, oxygen or air [16-18]. Transport processes of such elements control the growth of oxide scales or degradation primarily because they determine the rate of oxidation, but also because they affect other properties of the scale as resistance to penetration by aggressive species, stress development, grain growth, creep behavior, etc. In this study, water vapor is considered to enhance the oxidation of coatings and may have an effect on the defect structure and defect-dependent properties of metal/oxide systems. The rate controlling step in oxidation is believed to be the transport of water vapor through the oxide via hydroxyl defects.

4. Conclusion

Environmental resistance of Mo and coatings was investigated in simulated LWR water chemistry and high steam environments. It was observed that a thin protective layer (~50μm thickness) of Zircaloy 2, Zircaloy 4

and FeCrAl coatings provides the excellent oxidation resistance in 1000^{o}C steam environments. In particular, a thin aluminum oxide formed on the outermost layer of FeCrAl coating during steam oxidation believes to play an important role for keeping the mechanical stability/durability of FeCrAl coating and Mo at high temperature. Also, the formation of ZrO_2 on the Zircaloy coating in steam enhances the adherence on the coating/Mo interface and protects Mo against the test environments.

The fine structure and diffusional layer of coatings was observed near the coating/Mo interface as a result of the PVD process and the thickness of diffusional layer was further increased in high temperature steam. Microstructure features such as an interfacial adhesion property with the formation of a thin diffusional layer near the Mo substrate are believed to have a significant effect on coating properties that provides the tolerance of Mo as an ATF under severe accident conditions.

Acknowledgement

Authors express their appreciation to T. Jurewicz for experimental setup and S. Weaver for PVD coating at GEGRC. A. Barbuto and L. Denault are also appreciated for their contribution on sample preparation and SEM analysis. The FIB-TEM analysis was performed by Reza Sharghi-Moshtaghin at GEGRC. This project was performed by EPRI Contract (EP-P46590/C19986).

References

1. B. Cheng “Fuel Behavior in Severe Accidents and Mo Alloy Based on Cladding Design to Improve Accident Tolerance”, Proceeding of 2012TopFuel Meeting, Manchester, UK, September, 2012
2. B. Cheng, Y-J Kim, P. Chou, “Development of Mo Alloy for LWR Fuel Cladding to Enhance Tolerance to Severe Accidents”, Proceeding of 2013TopFuel Meeting, Charlotte, NC, September, 2013
3. Bo Cheng, Peter Chou and Young-Jin Kim, “Enhancing Fuel Resistance to Severe Loss of Coolant Accidents with Molybdenum-alloy Fuel Cladding”, Proceeding of 2014TopFuel Meeting, Sendai, Japan, September, 2014
4. Y-J Kim, Bo Cheng, Peter Chou, “Molybdenum Alloys for Accident Tolerant Fuel Cladding: High Temperature Corrosion and Oxidation Behavior” Proceeding of 2014TopFuel Meeting, Sendai, Japan, September, 2014
5. A.T. Nelson, E.S. Sooby, Y-J Kim, B. Cheng, & S.A. Maloy, J. Nuclear Materials, 448, p.441-447, 2014
6. M. Li, M. Eldrup, T.S. Byun, N. Hashimoto, L.L. Snead, & S.J. Zinkle, “Low Temperature Neutron Irradiation Effects on Microstructure and Tensile Properties of Mo’, J. Nuclear Materials, 376, p. 11-28, 2013
7. K. Abe, T. Takeuchi, & S. Morozumi, J. Nuclear Materials, 99, p. 25-37, 1981
8. B. Pint, K. Terrani, M. Brady, T. Cheng, & J. Keiser, J. Nuclear Materials, 440, p. 420-427, 2013
9. A.M. Russell & K.L. Lee, “Structure-Property Relations in Nonferrous Metals,” John Wiley & Sons, Hoboken, NJ, 2005
10. B.A. Pint, K.A. Terrani, J.R. Keiser, M.P. Brady, Y. Yamamoto, & L.L. Snead, “Material Selection for Fuel Cladding Resistant to Severe Accident Scenarios”, Proceeding of 16th Environmental Degradation of materials in Nuclear Power System-Water Reactors, Ashville, NC, August 11-15, 2013
10. Juan F. Flores, Evan J. Dolley, and Raul B. Rebak, “Environmental and Mechanical Behavior of Ferritic Cr steels in High Temperature Water and Steam”, Proceeding of 16th Environmental Degradation of materials in Nuclear Power System-Water Reactors, Ashville, NC, August 11-15, 2013
11. J. Quadakkers and L. Singheiser, Mater. Sci. Forum, 77, p.369-372, 2001
12. B. A. Pint, R. Peraldi and P. J. Maziasz, Mater. Sci. Forum, 815, p.461-464, 2004
13. A.S. Khanna, “Introduction to High Temperature Oxidation and Corrosion”, ASM International, Materials Park, OH, 2002
14. K. Terrani, S.J. Zinkle, L.L. Snead, J. Nuclear Materials, 44, p.420-434, 2014
16. K. Honda, T. Maruyama, T. Atake and Y. Saito, Oxidation of Metals, 38, p.347, 1992.
17. D. Abriou, J. Jupille, Surface Science Letter, 1-3, L527, p.430, 1999.
18. A. Fry, S. Osgerby, M. Wright, “Oxidation of Alloys in Steam Environments - A Review”, NPL Report MATC(A)90, NPL Materials Center, September 2002.

Feasibility Evaluations of Mo-alloy for Light Water Reactor Fuel Cladding to Enhance Accident Tolerance

Bo Cheng*, Peter Chou* and Young-Jin Kim**

*Electric Power Research Institute (EPRI), Palo Alto, California, U.S.A.
**GE Global Research Center, Schenectady, N.Y., U.S.A.*
Contact: Tel: 1-`650-855-2442; Email: bcheng@epri.com

ABSTRACT

Molybdenum based alloy is selected as a candidate to enhance tolerance of fuel to severe loss of coolant accidents due to its high melting temperature of ~2600°C and ability to maintain sufficient mechanical strength at temperatures exceeding 1200°C. An outer layer of either a Zr-alloy or Al-containing stainless steel is designed to provide corrosion resistance under normal operation and oxidation resistance in steam exceeding 1000°C for 24 hours under severe loss of coolant accidents. Due to its higher neutron absorption cross sections, the Mo-alloy cladding is designed to be less than half the thickness of the current Zr-alloy cladding. A feasibility study has been undertaken to demonstrate (1) fabricability of long, thin wall Mo alloy tubes, (2) formability of a protective outer coating, (3) weldability of Mo tube to endcaps, (4) corrosion resistance in autoclaves with simulated LWR coolant, (5) oxidation resistance to steam at 1000-1500°C, and (6) sufficient axial and diametral strength and ductility. High purity Mo as well as Mo + La_2O_3 ODS alloy have been successfully fabricated into ~ 2 meter long tubes for the feasibility study. Preliminary results are encouraging, and hence rodlets with Mo alloy cladding containing fuel pellets have been under preparation for irradiation at the Advanced Test Reactor (ATR) in Idaho National Laboratory. Additional efforts are underway to enhance the Mo cladding mechanical properties via process optimization. Oxidation tests to temperatures up to 1500°C, and burst and creep tests up to 1000°C are also underway. In addition, some Mo disks in close contact with UO_2 from a previous irradiation program (to >100 GWd/MTU) at the Halden Reactor have been subjected to post irradiation examination to evaluate the chemical compatibility of Mo with irradiated UO_2 and fission products. This paper will provide an update on results from the feasibility study and discuss the attributes of the coated Mo cladding design to meet the challenging requirements for improving fuel tolerance to severe loss of coolant accidents.

Keywords: *Accident tolerant fuel cladding, Mo-alloy cladding, coated Mo tubes*

I. INTRODUCTION

Zr-based alloys have served as the fuel cladding for light water reactors due to unique combination of low neutron cross section, adequate corrosion resistance and mechanical properties. The reliability of Zr-alloy cladding has been steadily improved over the last five decades and has reached an excellent status in recent years. The Fukushima Daiichi accident triggered by the tsunami following an earthquake has illustrated the vulnerability of Zr-alloys to rapid steam oxidation during a severe accident when the reactor core is interrupted for a prolonged period. Without availability of coolant flow into the core to remove the nuclear decay heat, the fuel cladding temperature will rise rapidly. At temperatures exceeding 700-1000°C, depending on the steam pressure, exothermic reaction of Zr with steam will release hydrogen and enthalpy or heat when ZrO_2 is formed. Due to the high packing density of fuel rods in reactor cores, where a typical size core may have ~50,000 fuel rods, the total heat from zirconium oxidation may exceed that of the

nuclear decay heat, if oxidation heat is all released within short during of an hour or so. The excessive oxidation heat may contribute to earlier melting of some reactor core components and subsequently the fuel pellets. The amount of hydrogen generated by zirconium oxidation can be in the order of exceeding 1,000 kg, and, hence, can complicate efforts by plant operators to recover the cooling system to stabilize the plant[1].

For current LWRs, it is most essential to maintain availability of coolant flow into the core under any accident conditions, and the FLEX program initiated by the US NRC is targeted to achieving that objective. Another potential defense is to replace the fuel cladding with another material having substantially higher resistance to steam oxidation, which may provide additional time for plant operators to restore the core cooling systems[2,3]. The U.S. Department of Energy (DOE) launched a multi-year R&D program with funding to the national laboratories and nuclear fuel vendors to develop enhanced accident tolerant fuel (ATF) in 2012[2]. Various international programs have also been launched over the last 3 years[4]. Candidate new cladding materials have included: coated Zr-alloy, SiC-SiC_f composite, Al-containing stainless steel and refractory metal (primarily molybdenum alloy).

EPRI initiated conceptual designs of coated molybdenum alloy cladding by utilizing the high temperature strength (1500°C and beyond) of molybdenum to maintain core geometry for coolability during a design based and beyond the design based loss of coolant accidents, as illustrated in Figure 1[1,3]. Surface coating with Al-containing stainless steel or Zr-alloy is to provide corrosion resistance during normal operation and steam oxidation resistance during loss of coolant accident with a targeted of surviving for hours up to ~1500°C. The inner surface may have a soft liner layer as an option, but its need will be determined following completion of the feasibility study.

Figure 1 Schemetic of Coated Mo-alloy Cladding

This paper outlines the scope of the feasibility study for coated Mo-alloy cladding and shares the results obtained to-date, as well as discusses the challenges ahead for completion of the feasibility study.

II. SCOPE OF FEASIBILITY STUDY AND RESULTS

The feasibility study focuses on the following topics: (1) fabricate Mo-alloy tubes with 0.2-0.25 mm wall thickness and characterize mechanical properties, (2) form surface coating with Al-containing stainless steel or Zr-alloy of ~0.05 mm, (3) weld Mo-alloy tube to endcaps, (4) characterize corrosion resistance of coated and uncoated Mo-alloy tubes in autoclaves with simulated LWR coolants, (5) characterize steam oxidation of coated and uncoated Mo-alloy tubes in steam at 1000-1500°C

Rodlets with coated Mo-alloy cladding containing enriched fuel pellets are also being fabricated for irradiation at the ATR reactor under funding by the US DOE.

The effects of higher neutronic absorption cross sections of Mo on fuel economics and fuel cycle designs were assessed and reported previously[1].

II.1 Fabrication of Thin Wall Mo-Alloy Tubes and Mechanical Properties

Mo-based alloys have been used in high temperature, reducing environments. An extensive test program was undertaken by Bettis and Oak Ridge National Laboratories to evaluate the irradiation properties of various Mo-alloys for potential space reactor fuel material applications[5,6]. Commercial thinwall Mo alloy cladding suitable for LWR applications was not available. Under this ATF program, thinwall Mo-alloy tubes with the outer diameter of 9.4 or 10 mm (0.37 or 0.40 inches) and wall thickness of 0.2-0.25 mm have been fabricated in length of 1.5 meters (5 ft). Tubes have been made of pure Mo, including from low carbon arc cast(LCAC) and power metallurgy (PM) billets, as well as oxide disperse strengthened Mo alloy (Mo-DOS) in which Mo is doped with dispersed La_2O_3. Typical La_2O_3 concentration in weight is ~0.3%, but some tubes with 1% were fabricated. Both LCAC Mo and Mo-ODS were found to retain small residual ductility following irradiation performed by the Bettis/Oak Ridge Program. Excellent tube straightness and uniform wall thickness have been achieved, Figure 2.

Figure 2 Mo-alloy tubes with wall thickness of 0.2 mm and OD of 1.0 cm

Because of its high melting temperature and single phase structure (i.e., absence of phase transition) until melting at ~2600°C, the mechanical strength will be maintained to much higher temperatures than that of common structural alloys including Zr, Fe and Ni based alloys. The Mo-alloy tubes are controlled to have an ultimate tensile strength (UTS) of approximately 450 MPa in stress relieved condition and ~280 MPa in recrystallized condition when tested at 320°C, Table 1. The ductility in uniform elongation ranges from 7 to 14%.

		Stress relieved		Recrystallized	
Test temperature	°C	320	320	320	320
Crosshead Speed	cm/m	0.49	0.49	0.49	0.49
UTS	MPa	441	448	280	283
0.2% yield stress	MPa	373	376	157	158
Uniform elongation	%	7	7	12	14
Fracture elongation	%	11	10	15	16
Reductionof area	%	38	39	64	66

Table 1 Mechanical properties of stress relieved and recrystallized Mo-alloy tubes tested at 320°C

One common issue associated with high strength, thin wall tubes is their propensity to axial split. A test rig with internally pressurized argon gas has been developed to test the diametral properties, including the failure strength and strain and creep rate, of the Mo-alloy tubes at temperatures up to 900°C. Figure 3 illustrates the internally pressurized test results of stress relieved PM Mo tube which ruptured when pressurized to 13.1 MPa (1900 psi) internal pressure at 600°C. The diametral failure strength is calculated as 303 MPa (44 Ksi) and the diametral strain was measured as 1.35%. At 320°C, the tube did not fail when stressed to 303 MPa.

Optimizations of the mechanical properties, particularly the diametral properties, are in progress via two approaches: (1) modification of the tube working and reduction process to alter the texture and (2)

controlling the microstructure of the finished tubes. For microstructure control, tube samples are subjected to heat treatment at >1200°C for pure Mo and >1500°C for Mo-ODS for very short durations (in seconds) using an induction heat treatment facility with an aim to form very fine, equi-axed grain structures, which has been reported to increase both the strength and ductility of molybdenum[7].

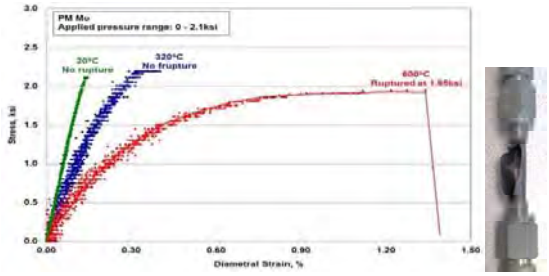

Figure 3 Internally pressurized tubes tested at room temperature, 320, and 600°C, where the sample showed complete ductile rupture at 600°C

II.2 Formation of Surface Protective Coating and Interface Stability

Molybdenum is susceptible to accelerated corrosion and oxidation in oxidizing environments at >~300°C forming volatile MoO_3. Due to the lack of technical basis for alloying Mo to improve its corrosion and oxidation resistance, surface protection via a corrosion resistant outer layer, as depicted in Figure 1, has been pursued for this ATF design. A limited effort of evaluating corrosion resistant Mo alloys, such as Mo-Nb binary alloys, has been explored in parallel.

Fe-Cr-Al alloys with ~20%Cr and ~6%Al has been known to possess excellent corrosion resistance in simulated LWR coolants relying on the formation of a protective Cr_2O_3, as well as excellent oxidation resistance in steam to ~1450°C owing to the formation of a thin Al_2O_3 protective oxide. Zr-alloys can be optimized to possess excellent corrosion resistance in LWRs, and will convert to ZrO_2 rapidly at >1000°C, which is expected to be stable in steam.

This ATF project was designed to first prepare Mo alloy tube samples with an outer protective layer utilizing suitable surface deposition techniques for various testing to demonstrate feasibility of the ATF design. With the consideration cladding length and large tube quantity needed for a fuel reload, it will only be commercially viable if tubes can be fabricated via mechanical co-reduction. Tasks have been implemented to evaluate the feasibility of mechanical co-reduction.

Formation of a corrosion and oxidation resistant outer layer of Al-containing stainless steel or Zr-alloy have been successfully developed using various deposition techniques. Cathode Arc Physical Vapor Deposition or CA-PVD has been found to achieve the deposited layer with (1) excellent thickness uniformity, as shown in Figure 4, (2) excellent adhesion of the coating to the Mo tube, (3) excellent metal density with no visible porosity of the coating.

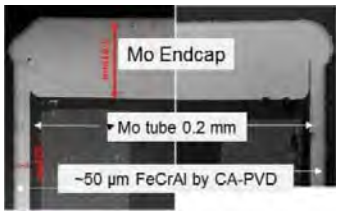

Figure 4 Uniform FeCrAl coating thickness of 50 µm on a welded Mo tube (similar results for Zircaloy coating)

The adhesion of FeCrAl and Zircaloy coating to the Mo tube is due to the formation of a sub-micrometer inter-diffusion zone at the interface during the coating process, as discussed in details in Reference 10.

II.3 Tube to Endcap Welding

Mo tube to endcap welding has been successfully demonstrated via plasma and tungsten welding as well as electron beam (EB) welding. EB welding has been found to produce smaller weld and heat affected zones, as illustrated in Figure 5(a), and has been used to fabricate rodlets for irradiation at the Advanced Test Reactor (ATR) in Idaho National Laboratory (INL).

Resistance projection welding has been demonstrated to fuse Mo tube to endcap at the interface without forming a fusion zone, as shown in Figure 5(b). This technique is preferred for commercial deployment and will required further development.

(a) (b)

Figure 5 Welded samples fabricated by (a) electron beam welding and (b) resistance projection welding

II.4 Corrosion Resistance in Simulated LWR Coolants

The corrosion resistance of pure Mo and Mo-ODS has been characterized in simulated BWR and PWR coolants at 288 and 330°C, respectively, in long term autoclave tests[8,9]. Table 2 summarizes the corrosion data in LWR coolants. It is noted that the corrosion resistance of bare Mo-alloys in simulated BWR environments is excessively high and hence will require protection of the coating of Zr-alloy or Al-containing stainless steel. The corrosion resistance of bare Mo alloy in the simulated PWR water with 3.6 ppm dissolved hydrogen is substantially decreased to ~1 μm per month.

Test Condition	Mo/ML	Zr-coated	FeCrAlcoated
PWR - 330 °C, 3.6 ppm H_2	~1	very low	very low
BWR-HWC - 288°C, 0.3 ppm H_2	~5	very low	very low
BWR-NWC - 288°C, 1 ppm O_2	~50	very low	very low

Table 2 Summary of the corrosion rate (in μm per month) of bare and coated Mo-alloy tubes in simulated LWR coolants

Preliminary results on Mo-alloys containing Nb have been found to significantly reduce the corrosion rate, as shown in Figure 6. Mo-alloy C has an order of magnitude lower corrosion rate (~0.5 μm/mo) than that of the bare, pure Mo tube. The corrosion resistance of Mo alloys is discussed in Reference 9.

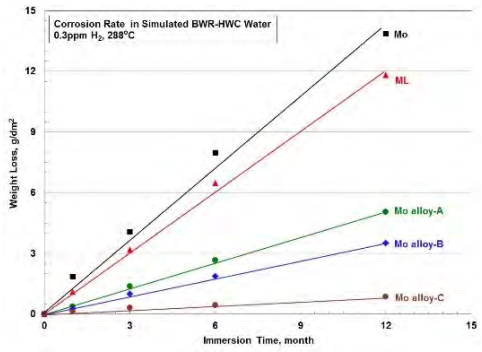

Figure 6 Corrosion resistance of pure and ODS Mo and Nb-containing Mo samples in simulated a BWR-HWC coolant

II.5 Oxidation Resistance in 1000-1500°C Steam

The oxidation resistance of uncoated Mo in oxidizing steam, i.e. steam containing free oxygen, has been known to be poor. In a severe loss of coolant accident, it is anticipated that the reactor core will have excess hydrogen due to corrosion and oxidation of various metallic components in the core.

In pure steam and steam plus 10% hydrogen at 1000°C, uncoated Mo alloy cladding has been found to have reasonable oxidation rate with a thicken loss of ~20-25 µm per day, which is two order of magnitude lower than that of Zr-alloys[9.10].

Coated Mo tubes with both-end welded received full protection from FeCrAl in 1000°C for 7 days, shown in Figure 7. The Zircaloy-4 coated Mo tube showed delamination of the ZrO_2 and suffered some loss in the Mo wall thickness, but the Mo tube remains intact after 7 days.

Figure 7 Mo tubes with both-ends welded to endcaps and coated with either FeCrAl or Zircaloy-4 after testing in 1000°C steam for 7 days

Figure 8 shows cross sections of open-ended Mo tube samples coated with either Zircaloy-2 or FeCrAl after being tested in 1000°C steam for up to 4 days. The Zircaloy-2 coated Mo tube shows the conversion of Zircaloy-2 to a dense ZrO_2 which protects the Mo tube from steam oxidation for up to 4 days. The good integrity of the oxide formed from Zircaloy-2 differs from the flaky oxide formed from Zircaloy-4 as shown in Figure 7. Investigation is underway to verify whether Zircaloy-2 and possibly other Zr-alloys will consistently maintain oxide integrity and provide protection to the Mo cladding.

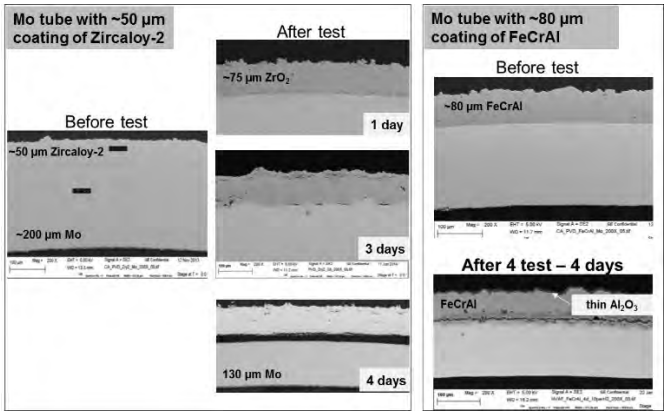

Figure 7 Open-ended Mo-alloy tube samples with coating after oxidation test in 1000C for up to 4 days

An interesting observation of the 1000°C steam tested samples is the formation of an inter-diffusion zone in the FeCrAl coated samples. The thickness was measured to be 2, 4, and 5 µm after 1, 3, and 7 days, respectively. Clearly, the inter-diffusion was not significant enough to impact the cladding integrity at 1000°C for 7 days or much longer.

Tests in steam at 1200-1500°C has been planned to be completed in 2015.

II.6 Irradiation Properties

Previous irradiation tests has shown Mo and its alloys, like other metals and alloys, will suffer from irradiation embrittlement. It is anticipated that improving the diametral mechanical properties through process and microstructure optimization, as discussed above, may lead to better propertied after irradiation.

Four short rodlets with Mo and Mo-ODS cladding and 4% enriched fuel pellets have been under preparation for irradiation in the ATR beginning in 2015. Additional irradiation in ATR and other test reactors have been under preparation to begin in 2016-17, as long as this feasibility test program continues to produce positive results.

III. SUMMARY ON RESULTS TO DATE AND CHALLENGES AHEAD

This feasibility study of coated Mo alloy cladding for accident tolerant fuel has demonstrated excellent corrosion in simulated LWR coolants and great oxidation properties in 1000°C. The thin wall Mo tube has adequate mechanical strength and ductility, though an improvement in the diametral ductility will provide better resistance to pellet-to-cladding mechanical interaction. Fabrication of rodlets for irradiation is underway.

For commercial deployment, it may be necessary to fabricate the coated tubes via mechanical co-reduction, rather than relying on the PVD process, as the later can be prohibitively expensive. A feasibility study on forming metallurgically bonding between the outer coating and the Mo alloy, and then mechanically co-reduction of the bonded tubes have been in progress. It is also necessary to incorporate fabrication process control to achieve optimized mechanical properties.

While the corrosion resistance of the coated cladding may be adequate, it is desirable to improve the corrosion resistance of the Mo tube to ensure full reliability of the cladding in the event of loss of the outer coating. To achieve this feature, Mo alloys, primarily Nb-containing ones are being studied.

ACKNOWLEDGEMENT

The authors gratefully acknowledge the important contributions of Todd Leonhardt (Rhenium Alloys Inc.) for fabrication of thin-wall Mo-alloy tubes; of Stu Malloy and Andy Nelson (LANL) for steam test studies; of Sam Armijo and Peter Ring for evaluation of induction heat treatment and hipping and metal bonding; of Kristine Barret of INL and Richard Howard of ORNL for supporting ATR irradiation of Mo cladded rodlets. The authors thank Jeff Deshon (EPRI) for management support. EPRI Fuel Reliability Program and EPRI Technology Innovation Program provide funding support. Areva has entered collaboration with EPRI on future Mo alloy cladding development. Generous collaborations from the U.S. Department of Energy and the national laboratories are also appreciated.

REFERENCES

1. B. Cheng, P. Chou, and Y-J Kim, "Enhancing Fuel Resistance to Severe Loss of Coolant Accidents with Molybdenum-alloy Fuel Cladding, Paper #100075, WRFPM2014, Sendai, Japan, September 2014
2. S. Bragg Sitten, "Application of MELCOR to ATF concepts for severe accident analysis," presented at EPRI/INL/DOE workshop on Accident Tolerant Fuel, San Antonio, February 2014
3. B. Cheng, "Fuel behavior in severe accidents and Mo-alloy based cladding to improve accident tolerance," TopFuel 2012 paper #A0034, Birmingham, U.K.
4. IAEA Symposium on "Accident Tolerant Fuel Concepts For Light Water Reactors", Oak Ridge National Laboratory, Tennessee, October 13-16, 2014. (Proceedings to be published by IAEA)
5. B. V. Cockeram, R.W. Smith, K.J. Leonard, T.S. Byun, L.L. Snead, J. Nucl. Mater., 382 (2008) 1-23.
6. T. S. Byun, M. Li, B. V. Cockeram, and L. Snead, J. Nucl. Mater., vol. 376, pp. 240-246, 2008.
7. Liu, G. et al., "Nanostructured high-strength molybdenum alloys with unprecedented tensile ductility", *Nature Materials*, **12**, 344-350 (2013)
8. Y-J Kim, B. Cheng, and P. Chou, "Molybdenum Alloys for Accident Tolerant Fuel Cladding: High Temperature Corrosion and Oxidation Behavior", TopFuel2014 Paper #100144, September 14-17, 2014, Sendai, Japan
9. A.T. Nelson, E.S. Sooby, Y-J Kim, B. Cheng, S.A. Maloy, "High temperature oxidation of molybdenum in water vapor environments," J. of Nuclear Materials, 2013
10. Y-J Kim, B. Cheng, and P. Chou, "Steam Oxidation Behavior of Protective Coatings on LWR Mo Cladding for Enhancing Accident Tolerance at High Temperatures",. TopFuel2015 Paper #A0172, September 13-17, Zurich, Switzerland

Westinghouse Accident Tolerant Fuel Program Current Results & Future Plans

S. Ray, P. Xu, E. Lahoda, L. Hallstadius, F. Boylan, and S. Johnson

Westinghouse Electric Company LLC, 5801 Bluff Road, Hopkins SC 29061 USA

Tel. +1- 803-647-3787, E-mail: rays@westinghouse.com

ABSTRACT

In previous Topfuel papers, Westinghouse authors have published the current direction that has been taken regarding Westinghouse's Accident Tolerant Fuel (ATF) program. This paper will discuss the current status, results from initial tests, as well as the future direction of this program. In the cladding area, the basic SiC tubing design being developed by our partner General Atomics was described in some detail in prior papers [7]. Subsequent out of reactor testing of these designs has been performed as well as more detailed analytical model development. The results of this program will be described in a separate paper. This paper will address the current preliminary testing that is being performed on these samples at the Massachusetts Institute of Technology (MIT) test reactor, initial results from these tests, as well as the technical learning from these test results. In the Westinghouse ATF approach, higher density pellets play a significant role in the development of an integrated fuel system. This is because they not only help with improved accident tolerance but also provide significantly improved economics, which is an added incentive for utility adoption. Uranium Silicide and Uranium Nitride/Uranium Silicide pellets that meet the specifications on density have been produced and are being introduced into the ATR for initial irradiation experiments. Over the next two years, the program will culminate in the manufacture of fuel rods that will undergo a six year exposure in the ATR and Halden as a prelude to loading lead test rods in commercial reactors by 2022. The ultimate choice between the various cladding and fuel options will be made on the basis of testing being carried out over the course of the next two years. The major considerations in this choice include: (1) SiC cladding – Demonstrated hermiticity under operating conditions and a realistic path to acceptable manufacturing cost; (2) Cladding coatings – Ability to adhere to the cladding at normal operating conditions and to provide a moderate improvement in accident tolerance; (3) High density pellets – Reasonable swelling rates and steam oxidation rates not significantly inferior to those of UO_2. This paper will describe in detail the test reactor programs that are currently planned over the next two year window, including the design of the test samples, the reactor test conditions, as well as the subsequent post irradiation program. The process for narrowing down the concepts for prototypic test reactor insertion will then be described.

KEYWORDS: *Accident Tolerant Fuel, ATF, SiC, Ceramic Cladding, Coating, U_3Si_2, High Density Fuel*

1. Introduction

The goal of the Westinghouse ATF program is to provide a leap-ahead product in safety and performance margin improvement for current and future LWRs at an economically attractive price to nuclear power providers. Westinghouse is the largest and most experienced fabricator of commercial nuclear fuel in the United States (U.S.) and has been at the forefront of every nuclear fuel innovation since the advent of commercial nuclear power. The Westinghouse ATF program, which began in 2004, advanced significantly during the current first phase (1A) begun in 2012 of this Department of Energy (DOE) program. Phase 1B will culminate in the

manufacture of fuel rods that will undergo a 6 year exposure in the Advanced Test Reactor and the Halden test reactor (Phase 2) as a prelude to loading lead test rods in a commercial reactor in 2022.

During Phase 1A and the continuation in Phase 1B, the Westinghouse team developed the uranium silicide (U_3Si_2) and waterproofed uranium mononitride (UN) fuel options as well as the silicon carbide (SiC) cladding option which will be further enhanced in the next phase of development. New zirconium alloy coating options will also be pursued. In the current phase of the program, the Westinghouse ATF team is further strengthened by addition of several international partners whose work supports the same ATF concepts and is executed in a coherent and integrated manner. This world-class nuclear research and development (R&D) team includes:

- Nuclear companies: Westinghouse and General Atomics (GA)
- Nuclear research universities: Massachusetts Institute of Technology (MIT), Texas A&M University (TAMU), University of Wisconsin (UW), the University of Tennessee (UT), Imperial College in London, and Cambridge University
- National laboratories: Idaho National Laboratory (INL), Los Alamos National Laboratory (LANL), Argonne National Laboratory(ANL), the National Nuclear Laboratory (NNL) in the United Kingdom, OECD Halden Reactor Project (Halden) in Norway, and the Paul Scherrer Institute (PSI) in Switzerland
- Nuclear power operators: Southern Nuclear Operating Company (Southern Nuclear) and Exelon Nuclear
- Specialty expert: Ceramic Tubular Products

This team offers unprecedented experience, knowledge, and ability in progressing new concepts from the R&D of nuclear fuel materials, to in-core experimental evaluation of nuclear fuel materials, to modeling of the behavior and performance of nuclear fuel, and finally to the licensing and manufacture and profitable sale of Generation II and soon Generation III+ commercial LWR nuclear fuel.

In this paper, the current status of the ATF development and future irradiation plan is discussed in detail.

2. ATF Development Progress

In the past year, the Westinghouse ATF team and its partners have been focused on optimization of coatings for zirconium cladding, SiC cladding manufacturing and testing, and high density fuel fabrication for test reactor irradiation. Details in each area are provided below.

2.1. Optimization of Coated Zirconium Cladding

As reported in the Topfuel paper last year, the MAX phase coating made in the first attempt was highly porous. As a result, the oxidation resistance of the coating was not adequate. Significant efforts were made to optimize the cold spray process and increase the coating density to achieve better oxidation resistance.

In order to produce a denser coating, MAX phase powder of smaller particle size was acquired from Sandvik. The particle size now is less than 20 µm as shown in Figure 1. The powders were produced by mechanical attrition and therefore have an irregular-shaped morphology. The elemental energy dispersive spectroscopy (EDS) x-ray mapping of the three main elements: Ti, Al, and C is shown in Figure 1.

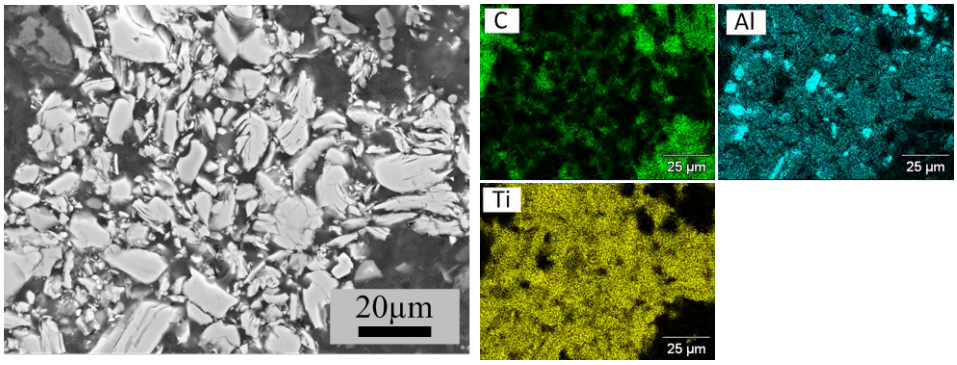

Figure 1. SEM and EDS of Optimized Ti_2AlC powder

A commercial 4000-34 Kintetik cold spray system at the University of Wisconsin was used to deposit these powders using nitrogen propellant gas at a preheat temperature of 600°C and pressure of 35 bar. Deposition was performed on both Zircaloy-4 (referred to hereafter as Zry-4) and ZIRLO®[1] test flat substrates which were surface ground using 320 grit SiC paper and thoroughly cleaned prior to deposition.

Figure 2 shows a cross-sectional scanning electron microscopy (SEM) image of the Ti_2AlC coating on the Zry-4 substrate. Deformation and compaction effects of the powder due to high velocity particle impact are clearly observed in the coatings. The coatings appear homogeneous and coating thickness was about 90 µm. Thinner coatings with a thickness of ~30 µm were also produced in parallel. The porosity level of the coating as determined by ImageJ analysis was about 3%.

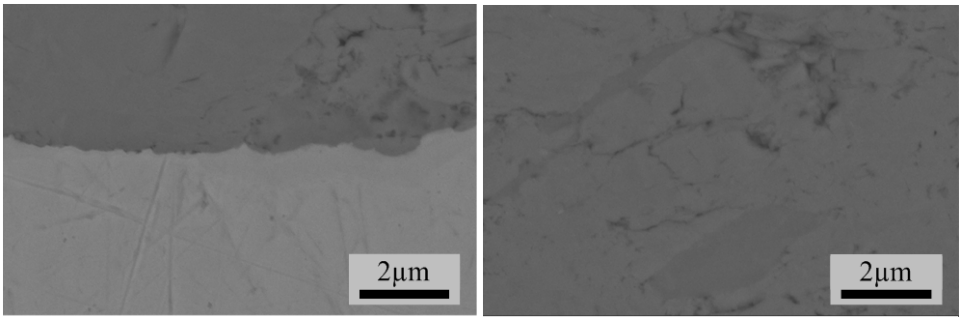

Figure 2. Cross section SEM images showing excellent adhesion of coating to substrate

STOE x-ray diffractometer with CuKα(λ=1.542Å) radiation was used for phase identification in the powders and coatings. Figure 3 shows the X-ray diffraction patterns for the as-received Ti_2AlC powders and the cold sprayed coating. Patterns for the powders and coating are identical in regards to both the position of peaks and relative intensities indicating no oxidation or phase transformation occurred during deposition. However, the commecial Ti_2AlC powder contained a significant amount of secondary phases. The top spectra (a) is that of the the coating while the bottom (b) is for the powder. Patterns were examined for both Ti_2AlC and Ti_3AlC_2, another potential phase that could form during the initial synthesis of this material. The peaks primarily match Ti_2AlC with a few peaks matching Ti_3AlC_2. Formation of $TiAl_2$ and TiC would indicate the MAX-phase was not completely formed and both of these compounds were indexed in the spectra. The region from 2θ=35-45° was expanded to more clearly index the peaks. Very little evidence of TiC was found.

[1] ZIRLO is a trademark or registered trademark of Westinghouse Electric Company LLC, its Affiliates and/or its Subsidiaries in the United States of America and may be registered in other countries throughout the world. All rights reserved. Unauthorized use is strictly prohibited. Other names may be trademarks of their respective owners.

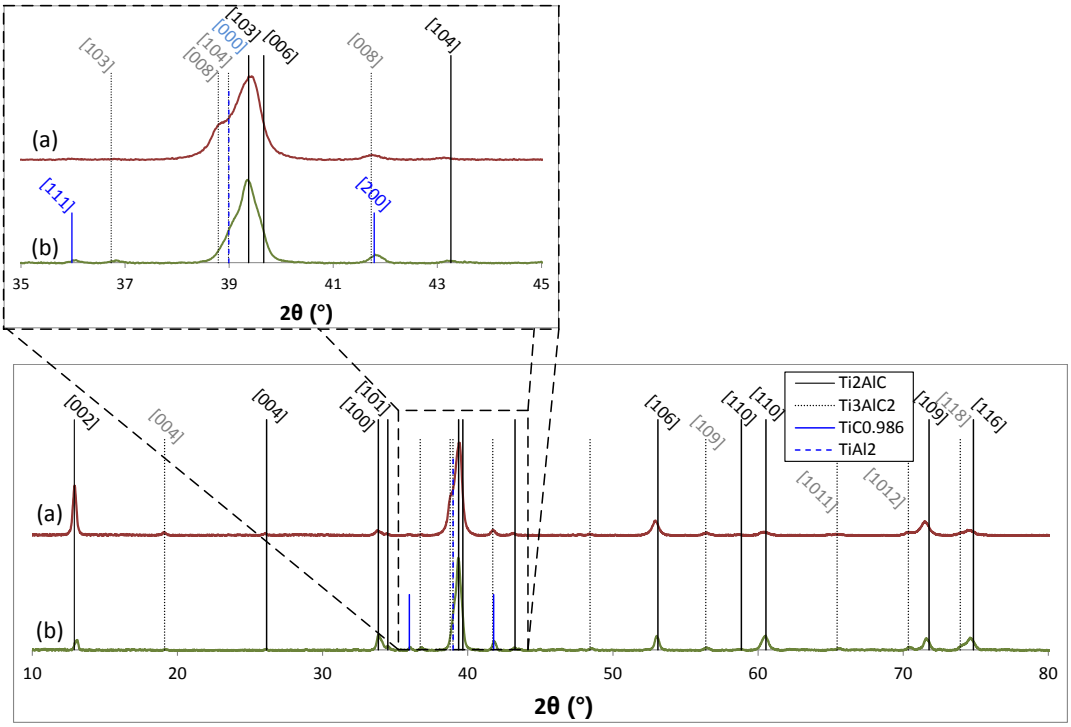

Figure 3. X-ray diffraction showing no phase change after cold spray deposition

Microhardness measurements were performed using Knoop microhardness under a 0.05 kg load. Pin-on-disk wear tests were conducted using a 3 mm diameter ruby (alumina) ball counter-surface using a 0.01 kg applied load and without lubrication. The wear tracks thus created were examined by SEM and their dimensions were measured with a Zygo optical profilometer. Figure 4 shows low load Knoop microhardnesss measurements performed in the cross-sections of the Ti_2AlC coating and Zry-4 using 0.05 kg load. Typical of ceramic materials, the Ti_2AlC coating shows high hardness (~800 HK) compared to the base Zry-4 (~180 HK).

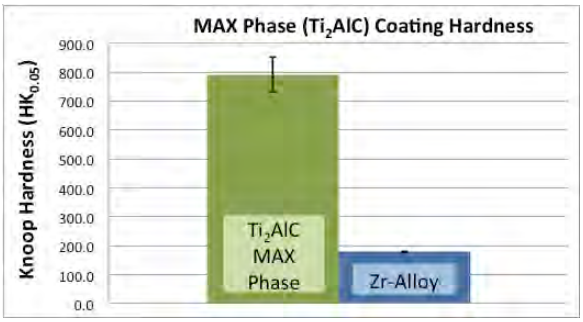

Figure 4. Results of microhardness test performed at 0.05 kg load) of Ti_2AlC coating and Zry-4.

Scratch testing was performed with a Vickers diamond tipped scribe under a constant 50 N load. A pronounced wear track forms on the Zry-4 whereas the wear track on the MAX phase coating is minimal, indicating higher abrasive wear resistance of the MAX phase coating. Figure 5 show corresponding profilometry results of the wear tracks. The wear track depth for the Zry-4 is over 12 µm, but for the MAX phase coating is immeasurable within the profilometer resolution limit.

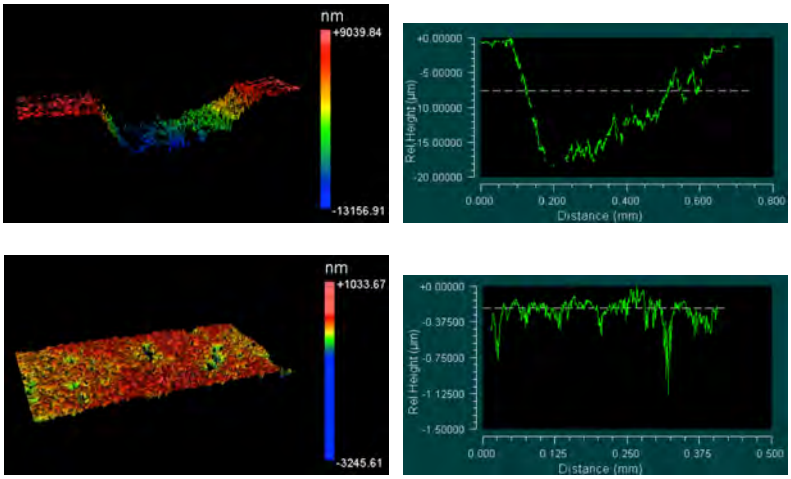

Figure 5. Wear Resistance of the coating

High temperature stability of the coatings was evaluated by subjecting the coated and uncoated Zry-4 samples to an ambient air environment at 700°C for 60 minutes after which the samples were air-cooled and examined for oxidation effects. Figure 6 shows the cross-sectional SEM image and elemental x-ray maps of the MAX phase coated sample, respectively, after the oxidation tests. The coating hinders oxygen diffusion and no oxidation is observed at the interface of the coating and the substrate. Slight oxidation is visible in the top of the coating, but the coating appears to be protective to the underlying Zry-4. An autoclave test is on-going at the Westinghouse Churchill site in 360°C in distilled water. Preliminary evaluation indicates that the coating oxidzied in water but adquately protected Zirconium substrate from oxidation. High temperature LOCA tests will be performed in the near future.

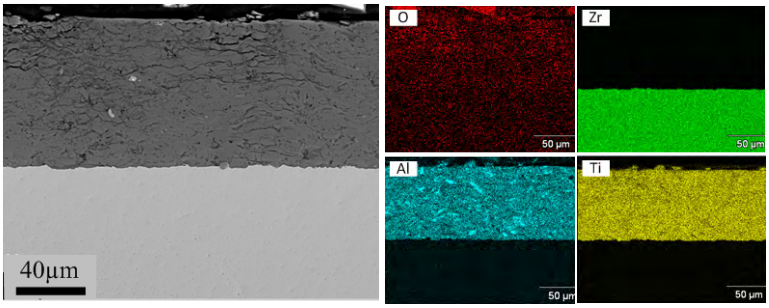

Figure 6. (a) Cross-sectional analysis of MAX phase coating on Zry-4 after oxidation tests at 700 °C for 60 minutes in ambient air and (b) elemental X-ray mapping showing negligible oxidation in the coating and at the coating substrate interface.

The UW team was also successfully coated ZIRLO tubes with Ti_2AlC as shown in Figure 7. The coating appeared to be uniform and to adhere to the tube. The thickness of the coating is ~30µm. Corrosion tests will be performed on these samples in the near future.

Figure 7. Coatings on ZIRLO® tubes.

Coatings are also being developed through the C^3 program at Penn State University (TiAlN) and at Argonne National Laboratory (Pt, Al_2O_3). These samples are undergoing testing in the Westinghouse autoclaves at Churchill at 360**°C.**

2.2 SiC Cladding Development

A detailed status update on SiC cladding fabrication, characterization, and testing will be provided in another Topfuel paper published by our partner, General Atomics. In this paper, we will focus on the two critical issues identified for SiC cladding by the ATF community: dissolution of SiO_2 in LWR coolant and the ability to maintain hemiticity of SiC cladding in operation [4].

It is known that the oxidation rate of SiC at LWR normal operating conditions is low, but dissolution of the oxide product, SiO_2, in coolant could become a major issue due to the high solubility of SiO_2 in water. It was found that the solubility of SiO_2 is highly dependent on the formation and morphology of SiO_2 [5]. Though the solubility of crystalline SiO_2 such as quartz is ~600 ppm in 300°C water, the solubility of amorphous silica can be as high as 1600 ppm. Control of silica along with zeolite forming elements such as aluminum, calcium and magnesium is important for zirconium cladding because precipitation of these species as silicate minerals and the possible incorporation into fuel crud could cause densification of the crud. This could then become a significant barrier to heat transfer, resulting in increased corrosion and hydriding of the fuel elements. EPRI PWR Primary Water Chemistry Guidelines list silica as a diagnostic parameter and the limit varies but in general should be less than 3 ppm. Fuel vendors may have an even lower limit on Si depending on other coolant chemistry and operation conditions [6]. Since the solubility of silica is temperature dependent, the SiO_2 will selectively dissolve from the core and will deposit in the colder parts of the loop in PWRs, and the problem may get more complex in BWRs. The ability to remove silica ions from coolant is limited. Therefore, controlling the oxidation rate of SiC in LWRs is the key. One way to suppress the oxidation rate of SiC is coolant chemistry control. Recent work at ORNL has indicated that the use of H_2 as part of the water chemistry may significantly reduce the corrosion rate of SiC and therefore the formation and dissolution of SiO_2 [18]. In addition, various types of SiC samples are currently being irradiated in the MITR so the oxidation of SiC during irradiation can be evaluated. Testing at BWR conditions is also planned such as a combined proton irradiation and water loop test at BWR conditions.

Loss of hermeticity during normal operation due to microcracking is another major concern for SiC cladding. The SiC ceramic matrix can experience tensile stress which leads to microcracking. One of the triggers for excessive tensile stress is differential swelling. The differential swelling is a phenomenon unique to SiC cladding because the swelling of SiC

saturates at different percentages at different temperatures and thus the degree of swelling differs through the cladding wall due to potentially large temperature gradients. If not designed properly, the differential swelling induced strain and stress could be significant which could cause microcracking in the matrix and subsequently loss of hemiticity. To avoid microcracking at the monolithic SiC layer, a new SiC cladding design was proposed and described in previous Topfuel papers [3, 7]. The new SiC cladding design consists of a monolithic SiC layer on the outside and a CMC layer on the inside. Based on our previous analytical models, the monolithic SiC layer will maintain compressive stress throughout the operation life and thus is not susceptible to microcracking [7]. To validate this concept, a new irradiation experiment is proposed at the High Flux Isotope Reactor (HFIR) at the Oak Ridge National Laboratory (ORNL) where both irradiation and temperature gradient will be simultaneously applied to the SiC cladding designed and fabricated by our ATF program. A preliminary design of the irradiation experiment is shown in Figure 8, and the final design will be presented at the Topfuel conference.

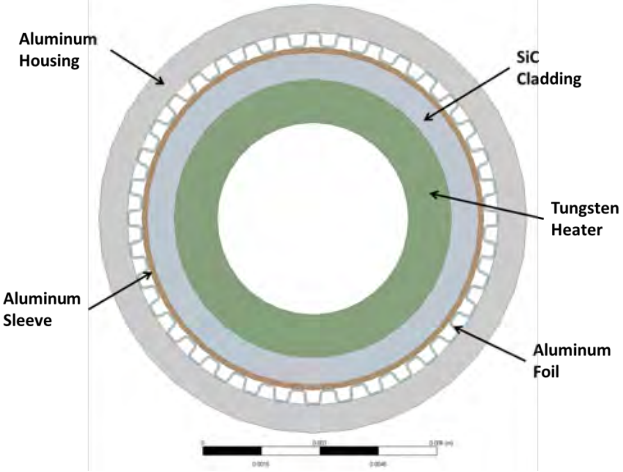

Figure 8. Schematic showing the general design concept for the SiC cladding irradiation

For the capsule design, after input from the community, ORNL has agreed that controlling the temperature of the SiC using a gas gap would introduce too much potential uncertainty in the test. Because the gap would have to be so small (~100um or less), small manufacturing deviations could have led to large temperature uncertainties. The new approach controls the SiC temperature over a much larger spacing, with the temperature change controlled by a micro-folded aluminum foil. This larger spacing makes this approach much less sensitive to manufacturing tolerances and can also accommodate diameter changes in the SiC as it swells without having a large impact on the temperature change. The temperature distribution cross the SiC cladding was calculated using ANSYS and is shown in Figure 9.

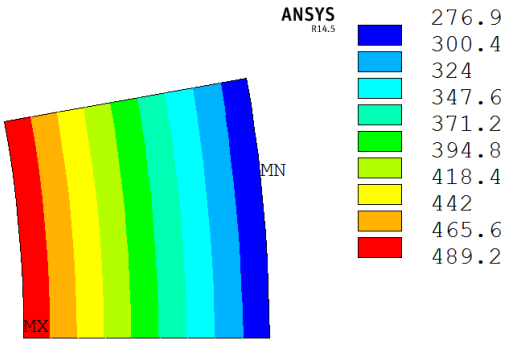

Figure 9. Temperature predication by ORNL (°C) contour plots for the 0.73% linear clad swelling case.

2.3. Development of High Density Fuel Pellets

Work on high density fuel pellet development exploring U_3Si_2 fuel manufacturing options will be described in another Topfuel Paper published by our partner, National Nuclear Laboratory from the UK [19]. A high level overview of the synthesis route is discussed here.

Current experience in the fabrication of U_3Si_2 fuels comes largely from the development of U_3Si_2-Al dispersion fuels for use in test reactors [8]. The initial step in this fabrication route involves induction or arc melting the relevant proportions of elemental U and Si in an inert gas. The resulting U_3Si_2 melt is then crushed and milled to a powder while maintaining an inert environment. For test reactor fuels, the U_3Si_2 dispersoid is typically between 40 and 150µm in size, much larger than the particle size required to form high density compacts suitable for use as LWR fuels. Recent progress in the pelletisation of U_3Si_2 has been made in this program [9,10], although it was found necessary to employ additives and a two-step milling procedure to achieve sufficient size reduction. A binder was also required to aid pressing with the resulting pellets sintered to approximately 95% theoretical density.

Scale-up of this powder metallurgy route is likely to be difficult to achieve economically due to the need to first convert uranium hexafluoride (UF_6) to metallic uranium prior to the melting and communition operations. Consideration is therefore being given to alternative fabrication routes that might permit simpler processing options as shown in Figure 10. A first step in this work has been to carry out a thermodynamic assessment of the potential reactions between UF_6 or UF_4, as likely enriched uranium feed materials, and silicon or silane (SiH_4) gas as potential reactants. Details of this work are reported in a separate Topfuel paper. The results suggest that reactions between UF_6 and Si or SiH_4 to form uranium silicide compounds are favorable (ΔG is negative) over a wide temperature range. The kinetics of the reactions forming different uranium silicide phases are at present unknown, as is the possibility of the formation of a UF_4 via a competing reaction. Reactions of Si with UF_4 are only favoured above approximately 850°C, although in this case no competing reactions are expected.

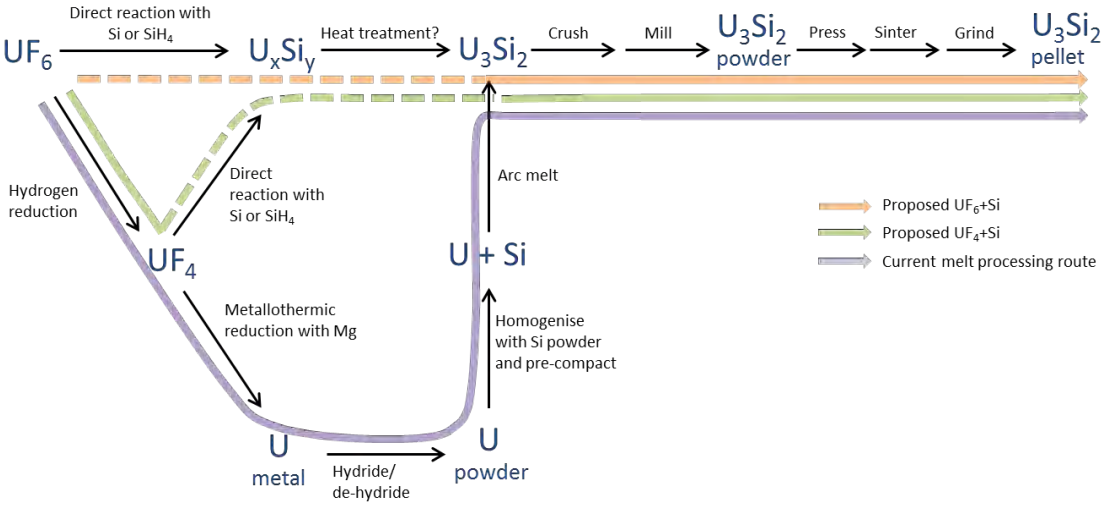

Figure 10. Options for manufacture of U_3Si_2 fuel (dotted lines indicate possible process steps that require further investigation).

The next phase of the work will be to experimentally investigate the kinetics and products of these reactions. This will be carried out using a small scale rig incorporating a removable reaction vessel to evaluate reactions over different temperature ranges and with both Si and Si/H_2 as reactants. The products will be characterized to evaluate the phase purity and compatibility with standard pelleting procedures.

2.4. ATF-1 Irradiation

The ATF-1 irradiation is a series of drop-in style Advanced Test Reactor (ATR) irradiation experiments designed to provide preliminary irradiation performance data on potential accident tolerant fuel concepts under typical LWR conditions [14, 15, 16].

The ATF-1 design consists of a fueled rodlet (fuel plus zirconium cladding) that is encapsulated in a stainless steel capsule. Drop-in tests use the heat generated from fission and gamma heating in the experiment and a temperature control gap between the rodlet and the capsule to maintain temperature. No active control mechanisms exist in drop-in designs. The typical design of an ATF-1 experiment is shown in Figure 11.

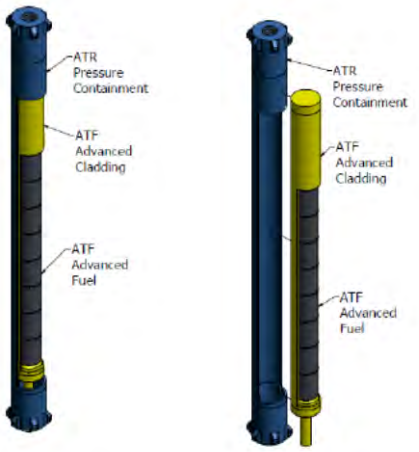

Figure 11. Irradiation test rig at ATR

Machined pellets from this work were incorporated into rodlets and capsules as part of the ATF-1 irradiation experiment. The rodlet component acts similar to cladding under normal LWR irradiation conditions. The ZIRLO® material was used for the tube walls of the rodlet, and Zircaloy-4 was used for the rodlet endcaps. There are 6 rodlets in the Westinghouse U_3Si_2 ATF-1 experiment as shown in the test matrix in **Table 1**. Each rodlet contained a stack of pellets consisting of a depleted U_3Si_2 pellet (0.41% U-235) followed by 12 enriched pellets (5.44% U-235), and then 2 depleted pellets with central holes filled with a melt wire package. The 6 rodlets were designed to operate at a variety of initial power and temperature conditions and remain under irradiation for a variety of burnups. Three of the rodlets are designed to operate at ~275 W/cm (~600°C centerline). Two are designed to operate at ~430 W/cm (`800°C centerline), and one is designed to operate at 461 W/cm (~1000°C centerline). The high temperature rodlet utilizes an Ar/He mix to achieve higher temperatures, and the other rodlets use only He. The desired burnup of the 3 low temperature rodlets is 20, 40, and 70 GWd/tU. For the 2 medium temperature rodlets, burnup is 20 and 70 GWd/tU, and for the high temperature rodlet the desired burnup is 20 GWd/tU. Examination of the melt wire packages after irradiation should help put some bounds on the maximum temperatures experienced by the fuel. After the rodlets were assembled, they were loaded into He filled, stainless steel capsules, and transferred to ATR for irradiation. After irradiation, the capsules will be sent back to the INL Hot Fuels Examination Facility for PIE. The experiments will undergo a variety of examinations including neutron radiography, gamma scanning, fission gas release analysis, optical microscopy, burnup analysis, hardness testing, and density evaluation. Samples from the rodlets will also be examined for thermal properties and by electron microscopy [17].

Rodlet ID Bot End Cap	Initial LHGR (W/cm)	Target Burnup (GWd/tU)	Rodlet Weld/Fill Gas	Predicted Peak Fuel Temperature (°C)
ATF-W01	250	20	100% He	660
ATF-W02	250	40	100% He	660
ATF-W03	250	70	100% He	670
ATF-W04	470	20	100% He	930
ATF-W05	460	70	100% He	960
ATF-W06	500	20	25% He 75% Ar	1260

Table 1. Test Matrix

3. Phase 1b Objectives and Future Plans

The current Westinghouse ATF project has three critical objectives:

1. To provide fuel rods for testing in the Advanced Test Reactor (ATR) at the Idaho National Laboratory and Halden reactor for at least two ATF fuel/cladding options
2. To develop the business and technical detail to justify these choices to the DOE and our utility partners
3. To generate the ATF LTR/LTA project plan on how the project will generate the required technical data needed to convince a utility that the lead test rod (LTR) will operate as intended and to provide the basis for licensing by the Nuclear Regulatory Commission (NRC) for the LTR

Figure 12 presents the flow sheet depicting the responsible parties, quantities, and dates of delivery for these test items to achieve objective 1 in Phase 1B of the program.

The second objective is to develop an “LTR/LTA Project Plan”. As part of the current program, Westinghouse has developed an outline of the programs required between 2016 and the initiation of an LTR program in a commercial reactor(s) in 2022 [11, 12, 13]. Westinghouse will expand the details of the current plan to include a detailed task list with interim milestones, expected time, personnel commitment, and costs to accomplish an LTR/LTA by 2022. Based on the long history of Westinghouse bringing new technologies to market and a long history (11 years) in the ATF area, this task will not pose any significant difficulties.

The third critical objective is to generate sufficient data both experimental and analytical to demonstrate technical, commercial and regulatory feasibility. The Westinghouse team understands that the next stage of testing of prototypical (except for length) ATF rods in a test reactor for 6 years represents a significant commitment for all the members of this task including the DOE, the ATR and Halden test reactors, and the commercial vendors (Westinghouse and GA). It is, therefore, imperative to understand the technical, economic, and licensing issues involved before starting these tests. To support this objective, three papers will be presented by Westinghouse and its partners at this Topfuel conference to discuss technical progress over the past year.

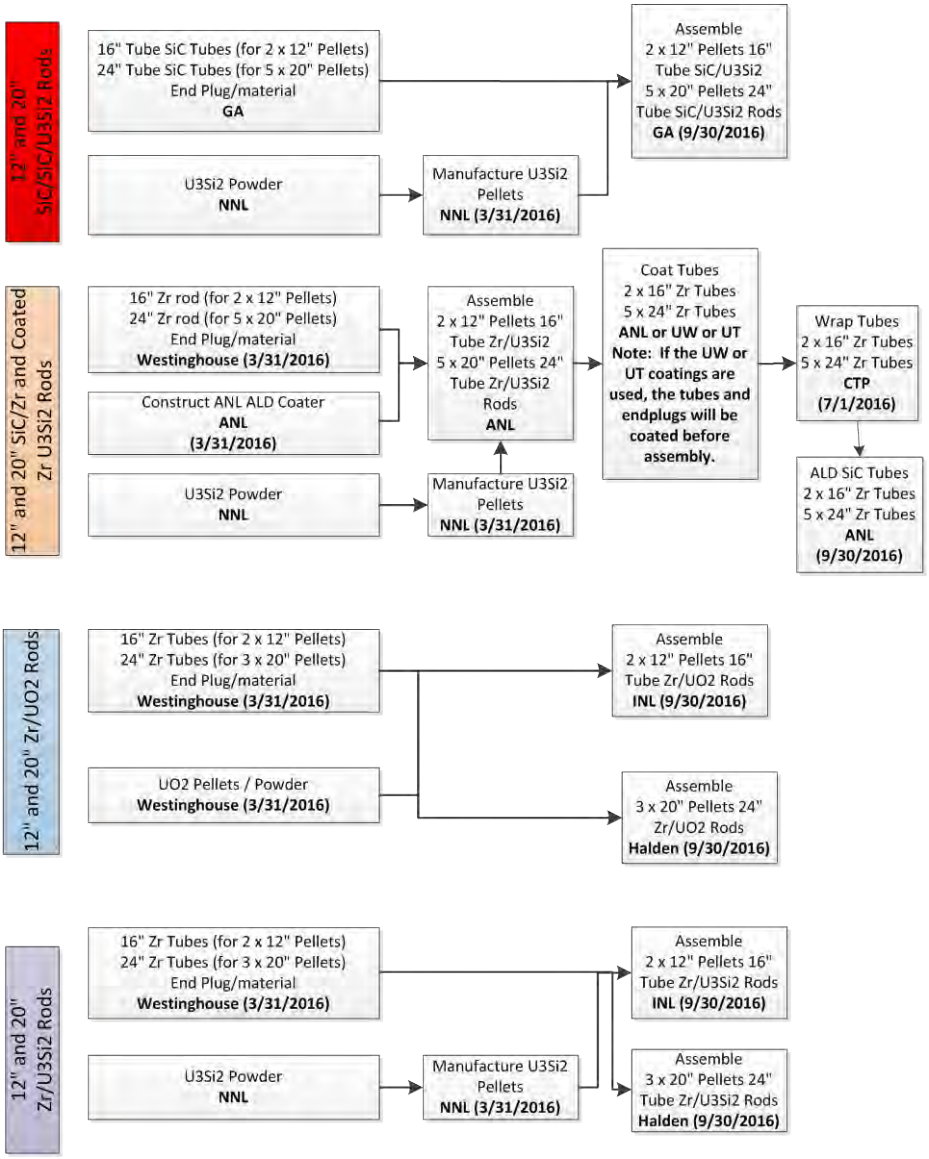

Figure 12. Rodlet irradiation plan

4. Summary

The Westinghouse ATF program has continued making significant progress in three areas: coated cladding, SiC cladding, and high density fuel pellets. The MAX phase coating was optimized and the oxidation resistance was significantly improved. Knowledge gaps and critical issues were identified for SiC cladding in this paper, and critical irradiation tests at MITR and HFIR were planned for 2015 to address these issues. Enriched U_3Si_2 pellets were fabricated and assembled for the ATF-1 irradiation test at ATR, and investigation of commercial manufacturing U_3Si_2 from UF_6 was initiated. The project is on track toward the goal of manufacturing ATF rodlets and being ready for ATR and Halden irradiation by 2016.

5. Acknowledgments

This material is based upon work supported by the Department of Energy under Award Number DE-NE0000566.

This report was prepared as an account of work sponsored by an agency of the United States

Government. Neither the United States Government nor any agency thereof, nor any of their employees, makes any warranty, express or implied, or assumes any legal liability or responsibility for the accuracy, completeness, or usefulness of any information, apparatus, product, or process disclosed, or represents that its use would not infringe privately owned rights. Reference herein to any specific commercial product, process, or service by trade name, trademark, manufacturer, or otherwise does not necessarily constitute or imply its endorsement, recommendation, or favoring by the United States Government or any agency thereof. The views and opinions of authors expressed herein do not necessarily state or reflect those of the United States Government or any agency thereof.

The authors would like to thank the funding agency, the Department of Energy, and the contributing partners in this contract. The authors acknowledge helpful discussion and input from Christian Deck from General Atomics (GA), Kumar Sridharan and Ben Maier from University of Wisconsin (UW), and Dave Goddard from National Nuclear Laboratory in UK.

6. References

1. S. Ray, E. Lahoda and F. Franceschini “Assessment of Different Materials for Meeting the Requirement of Future Fuel Designs”, 2012 LWR Fuel Performance Meeting, Manchester, UK, September 2-6, 2012, Paper A0115, American Nuclear Society (2012).
2. S. Ray, S. Johnson and E. Lahoda “Preliminary Assessment of the Performance of SiC Based Accident Tolerant Fuel in Commercial LWR Systems”, 2013 LWR Fuel Performance Meeting, Charlotte, USA, September 15-19, 2013, Paper #8490, American Nuclear Society (2013).
3. S. Ray, S. Johnson and E. Lahoda “Preliminary Assessment of the Performance of SiC Based Accident Tolerant Fuel in Commercial LWR Systems”, 2014 LWR Fuel Performance Meeting, Sendai, Japan, September 14-17, Paper #100131 (2014).
4. Y. Katoh, K. A. Terrani, and L. Snead “Systematic Technology Evaluation Program for SiC/SiC Composite based Accident-Tolerant LWR Fuel Cladding and Core Structures”, ORNL/TM-2014/210, revision 1.
5. V. Presser, and K. G. Nickel, “1.Silica on Silicon Carbide”, Critical Reviews in Solid State and Materials Sciences, 33[1] (2008)
6. MTLS-06-131, Rev. 4, “Westinghouse Supplement to EPRI PWR Primary Water Chemistry Guidelines Rev. 6”, (2009)
7. C. A. Back, E. Lahoda, R. W. Schleicher, C. P. Deck, H. E. Khalifa, G. M. Jacobsen, J. G. Stone, and O. Gutierrez “SiCf-SiC Composite Fuel Cladding for Light Water Reactors”, 2014 LWR Fuel Performance Meeting, Sendai, Japan, September 14-17, Paper #100159 (2014).
8. S.Nazaré, Low enrichment dispersion fuels for research and test reactors, J. Nucl. Mater, 124, (1984) 14-24.
9. J.M.Harp, P.A.Lessing and R.E.Hoggan, Uranium silicide fabrication for use in LWR Accident Tolerant Fuel, Trans. Am. Nucl. Soc, 110, (2014), 990-3.
10. Jason M. Harp, Paul A. Lessing, Blair H. Park, Jakeob Maupin, “Preliminary Investigation of Candidate Materials for Use in Accident Resistant Fuel”, 2013 LWR Fuel Performance Meeting, Charlotte, USA, September 15-19, 2013, Paper #8306, American Nuclear Society (2013).
11. Edward J. Lahoda, Frank A. Boylan and Peng Xu, “Development of LWR Fuels with Enhanced Accident Tolerance, Task 2 – Description of Research & Development Required to Qualify the Technical Concept,” RT-TR-13-8, http://www.westinghousenuclear.com/docs/RT-TR-13-8_2.pdf, May 31, 2013.
12. Edward J. Lahoda, Frank A. Boylan, Nicole T. Brichacek, Ronald G. Cocherell and Ryan M. Joyce, “Development of LWR Fuels with Enhanced Accident Tolerance Task 3: Licensing Plan for Accident Tolerant Fuel,” RT-TR-13-19, http://www.westinghousenuclear.com/docs/RT-TR-13-19.pdf, September 30, 2013.
13. Frank Boylan, Fausto Franceschini, Steve Johnson, Edward Lahoda, Jeffrey Secker,

Peng Xu, Christina Back, Robert Schleicher, Ronald G. Cocherell and John Williams, “Development of LWR Fuels with Enhanced Accident Tolerance Task 4 – Preliminary Business Plan,” RT-TR-13-20, http://www.westinghousenuclear.com/docs/RT-TR-13-20.pdf, October 2, 2013.
14. S.L. Hayes, K.E. Barrett, “Irradiation Testing of Accident Tolerant Fuels in the ATR (The ATF-1 Test Series),” Idaho National Laboratory Report, PLN-4444 rev. 2, April 2014
15. W.J. Carmack, et al. "Overview of the US DOE accident tolerant fuel development program." Top Fuel 2013, 2013
16. S.M. Bragg-Sitton, “Development of advanced accident-tolerant fuels for commercial LWRs,” Nuclear News, March 2014
17. J.M. Harp, “Post Irradiation Examination Plan for ATF-1 Irradiation Experiments,” Idaho National Laboratory Report, PLN-4751, 2014
18. K. Terrani, Y. Yang, T. Gerczak, Y-J. Kim, R. Rebak, “Hydrothermal Corrosion of SiC-based Materials in LWR Environments”, EPRI ATF Meeting St. Petersburg, Fl, Feb 17, 2015
19. H.R. Foxhall, S.L. Owens, D.T. Goddard, “Thermodynamic Modelling of a Single-stage Production Route for U_3Si_2 Accident Tolerant Fuel”, 2015 Topfuel Meeting, paper A0050.

REACTOR PHYSICS MODELLING OF ACCIDENT TOLERANT FUEL FOR LWRs USING ANSWERS CODES

B.A. LINDLEY
Amec Foster Wheeler
Dorchester – UK

D. KOTLYAR, G.T. PARKS
Department of Engineering, University of Cambridge
Cambridge – UK

J.N. LILLINGTON
Amec Foster Wheeler
Dorchester – UK

B. PETROVIC
Georgia Institute of Technology
Georgia – USA

ABSTRACT

The majority of nuclear reactors operating in the world today and similarly the majority of near-term new build reactors will be LWRs. These currently accommodate traditional Zr clad UO_2/ PuO_2 fuel designs which have an excellent performance record for normal operation and most transients. However, the events at Fukushima culminated in significant hydrogen production and hydrogen explosions, resulting from high temperature Zr/steam interaction following core uncovering for an extended period. These events have resulted in increased emphasis towards developing more accident tolerant fuels (ATFs)-clad systems, particularly for current and near-term build LWRs.

R&D programmes are underway in the US and elsewhere to develop ATFs and the UK is engaging in these international programmes. Candidate advanced fuel materials include uranium nitride (UN) and uranium silicide (U_3Si_2). Candidate cladding materials include advanced stainless steel (FeCrAl) and silicon carbide.

The UK has a long history in industrial fuel manufacture and fabrication for a wide range of reactor systems including LWRs. This is supported by a national infrastructure to perform experimental and theoretical R&D in fuel performance, fuel transient behaviour and reactor physics.

In this paper, an analysis of the Integral Inherently Safe LWR design (I^2S-LWR), a reactor concept developed by an international collaboration led by the Georgia Institute of Technology, within a U.S. DOE Nuclear Energy University Program (NEUP) Integrated Research Project (IRP) is considered. The analysis is performed using the ANSWERS reactor physics code WIMS and the EDF Energy core simulator PANTHER by researchers at the University of Cambridge.

The I^2S-LWR is an advanced 2850 MWt integral PWR with inherent safety features. In order to enhance the safety features, the baseline fuel and cladding materials that were chosen for the I^2S-LWR design are U_3Si_2 and advanced stainless steel respectively. In addition, the I^2S-LWR design adopts an integral configuration and a fully passive emergency decay heat removal system to provide indefinite cooling capability for a class of accidents.

This paper presents the equilibrium cycle core design and reactor physics behaviour of the I^2S-LWR with U_3Si_2 and the advanced steel cladding. The results were obtained using the traditional two-stage approach, in which homogenized macroscopic cross-section sets were generated by WIMS and applied in a full 3D core solution with PANTHER. The results obtained with WIMS/PANTHER were compared against the Monte Carlo Serpent code developed by VTT and previously reported results for the I^2S-LWR. The results were found to be in a good agreement (e.g. < 200 pcm in reactivity) among the compared codes, giving confidence that the WIMS/PANTHER reactor physics package can be reliably used in modelling LWRs with ATFs.

1. Introduction

The majority of nuclear reactors operating in the world today and similarly the majority of near-term new build reactors will be LWRs. These currently accommodate traditional Zr clad UO_2/Pu fuel designs which have an excellent performance record for normal operation and most transients. However, the events at Fukushima culminated in significant hydrogen production and hydrogen explosions, resulting from high temperature Zr/steam interaction following core uncovering for an extended period. These events have resulted in increased emphasis towards developing more accident tolerant fuels (ATFs), particularly for current and near-term build LWRs.

Candidate advanced fuel materials include (among others) uranium nitride (UN) and uranium silicide (U_3Si_2), both of which have higher thermal conductivity than UO_2, leading to improved margins under accident conditions, and also have the benefit of higher heavy metal density leading to the possibility of increased core heavy metal loading [1] [2]. Candidate cladding materials include (among others) advanced stainless steel (FeCrAl), silicon carbide (SiC), and the possibility of adding a coating to Zircaloy clad [3]. Advanced FeCrAl-type steel cladding exhibits exhibits a 2-3 orders of magnitude lower oxidation rate under accident conditions than Zircaloy [4] and is relatively easy to fabricate [5], but has the disadvantage of introducing a large reactivity penalty [4]. SiC cladding has high corrosion resistance in steam, superior to FeCrAl-type steels, can withstand much higher temperatures than Zircaloy and FeCrAl without melting, but is challenging to manufacture and more expensive [5]. R&D programmes are underway in the US and elsewhere to develop ATFs, encompassing fabrication and testing of UN, U_3Si_2, SiC and coated Zr rods [6].

This paper presents the core analysis performed with the ANSWERS reactor physics code suite WIMS/PANTHER [7] [8] for the Integral Inherently Safe Light Water Reactor (I^2S-LWR). The I^2S-LWR concept [9] is a Gen III+ large scale (i.e. 1 GWe) reactor. The design stage is being carried out by a consortium of universities (Michigan, Virginia Tech, Tennessee, Florida Institute of Technology, Idaho, Morehouse College, Brigham Young University, Cambridge, Politecnico di Milano, Zagreb), Idaho National Laboratory, Westinghouse and Southern Nuclear Company. The project is led by the Georgia Institute of Technology.

This innovative PWR includes: an integral primary circuit, a fully passive decay heat removal system aimed at indefinite cooling capability, and the use of new materials. The types of materials that were originally chosen for this design include U_3Si_2 fuel pellets within advanced steel cladding.

The equilibrium cycle core analysis was performed using the WIMS/PANTHER codes and the results were verified in a code-to-code comparison. In the first stage, the 2D results obtained with WIMS [2] were compared against the Monte Carlo code Serpent [10], and a good agreement was observed. In the second stage, the full 3D core results obtained with the WIMS/PANTHER codes were compared with results from the literature for the I^2S-LWR. [11]. This cross-comparison of results provides enhanced confidence in the reliability and accuracy of the results.

2. UK Context for Accident Tolerant Fuel

The UK has a long history in industrial fuel manufacture and fabrication for a wide range of reactor systems including LWRs. This is supported by a national infrastructure to perform experimental and theoretical R&D in fuel performance, fuel transient behaviour and reactor physics.

The UK is seeking to engage with international programmes on ATF research to “strengthen international collaboration opportunities and establish the UK as a centre of expertise for advanced fuel fabrication R&D, and consequently commercial manufacture of such fuels” [14]. Such fuels could be utilized in nuclear new build plants, and also potentially in small modular reactors (SMRs), in which the UK has expressed a strategic interest [15]. The UK Nuclear Industry Research and Advisory Board (NIRAB) recently recommended that the UK perform research on manufacturing advanced cladding materials in order to enable future manufacture of ATF on a commercial scale [16]. Opportunities for ATF use are identified to include Generation III reactors and SMRs.

3. Modelling of Accident Tolerant Fuel with ANSWERS Software

The ANSWERS lattice code WIMS and core simulator PANTHER are used to support the operation of existing PWRs, including in the UK and Belgium [17]. WIMS-PANTHER has recently been validated

for analysis of part-MOX-fuelled PWRs. In academia, WIMS and PANTHER have also been applied to a range of PWR configurations including SMRs [18], seed-blanket-fuelled PWRs [19] [20], PWRs loaded with transuranic fuels [21] [22]. Modelling of ATFs is a natural extension of these capabilities and can largely be performed using existing calculation routes.
Challenges of modeling ATFs include:

- Validation of software for different fuel types. This includes validation of the relevant nuclear data libraries. For stainless steel, an extensive amount of validation has been performed as steel is commonly used in fast and thermal reactors. For other isotopes/ elements, a reasonable amount of experimental data is available, but further validation may be required for use in new applications.
- Modelling of non-standard isotopes. An example is the presence of ^{15}N in UN fuel. The most abundant isotope of nitrogen, ^{14}N, has a large (n,p) cross-section which adversely impacts the neutron economy. It is therefore commonly proposed to increase the ^{15}N content of the nitrogen in the UN fuel through enrichment [1]. While limited experimental data on ^{15}N cross sections is available, it is not usually considered in isolation and hence further experimental validation may be necessary for thermal reactor applications.
- Some candidate ATFs may have the capability to be driven to higher burnups than existing Zircaloy-clad UO_2 fuels. Both stainless steel [4] and SiC [23] are able to withstand higher irradiation than Zircaloy. This leads to the need to validate the reactor physics code for higher enrichments and high burnups, and account for a wider range of actinides.

WIMS10, the most recent release of WIMS, contains nuclear data for high burnup applications, including cross-sections and delayed neutron fraction data for a wider range of isotopes including ^{246}Cm, ^{247}Cm and ^{248}Cm. Use of higher enrichment fuel, being driven to high burnups, leads to increased reactivity swings, which requires use of novel burnable poison arrangements and core loading strategies [24]. PANTHER contains inbuilt multi-objective optimization algorithms which facilitate PWR [25] and VVER [26] core design. These have recently been applied to the non-standard case where PWRs are highly loaded with Pu [27] [28] and have been shown to facilitate low power peaking core design under challenging circumstances.

4. Use of WIMS/PANTHER to model I^{2}S-LWR

4.1. I^{2}S-LWR Core Description

The I^{2}S-LWR core contains 121 assemblies, i.e. as in a Westinghouse 2-loop PWR, with 144-in active fuel height as shown in Fig. 1. The I^{2}S-LWR is designed to achieve 40% higher power rating than a typical 2-loop Westinghouse core (~2850 MWt vs ~2000 MWt). The major modification to achieve this objective was transitioning from a typical 16x16 or 17x17 assembly array to a 19x19 square pitch lattice having approximately the same assembly footprint. The main geometric parameters and fuel design characteristics are shown in Table 1.
The 3-batch I^{2}S-LWR core loading pattern as shown in Fig. 1 is identical to the one adopted by Ref. [11]. There are 40 fresh assemblies per reload out of 121 assemblies. The twice-burnt assemblies are positioned at the outermost peripheral locations to create a low leakage core. The I^{2}S-LWR features 45 reactivity control clusters assemblies with 24 control rods (Ag-In-Cd) in the assembly.
The U_3Si_2 core design includes fresh and burned assemblies as shown in Fig. 1. Fresh assemblies exploit different enrichments (i.e. 4.65, 4.45 and 2.6 $^w/_o$). The active core height of the I^{2}S-LWR fuel axial stack is presented in Fig. 2. In fuel assemblies with integral fuel burnable absorber (IFBA) rods (Fig. 2), only the middle portion (120-in) contains ZrB_2 burnable poison, which is surrounded by 6-in non-IFBA top and bottom layers carrying the same fuel enrichment. Finally, 6-in top and bottom axial blankets are used to create the fuel stack. Lower enrichment (2.6 $^w/_o$) is used in the blankets in order to decrease the axial leakage of neutrons.
The ^{10}B concentration used in the IFBA rods for the I^{2}S-LWR, with U_3Si_2, fuel design, is 2.5 mg/in. Multiple assembly loading patterns are used to flatten the core power distribution. These are depicted in Fig. 3.

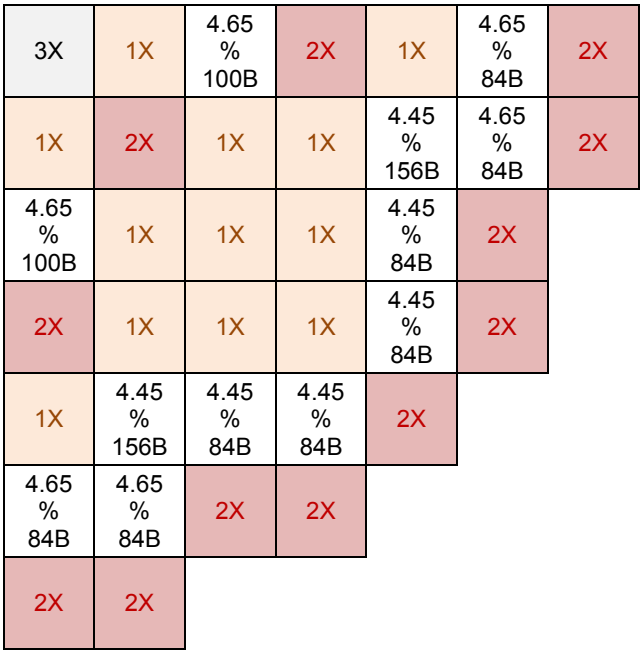

Figure 1 I^2S-LWR equilibrium cycle core loading pattern (bottom right quadrant of the core)

Table 1 Main fuel assembly design parameters

Parameter	**Value**
Lattice type	19×19, square
Cladding material	Advanced SS (FeCrAl)
Fuel rods per assembly	336
Fuel pellet material	U_3Si_2
Fuel rod outer diameter (in)	0.36
Cladding thickness (in)	0.016
Pellet-clad gap width (in)	0.006
Pellet outer diameter (in)	0.316
Pellet inner void diameter (in)	0.1
Fuel pellet dishing (%)	0.3
Fuel density (% of theoretical)	95.5
Fuel rod pitch (in)	0.477

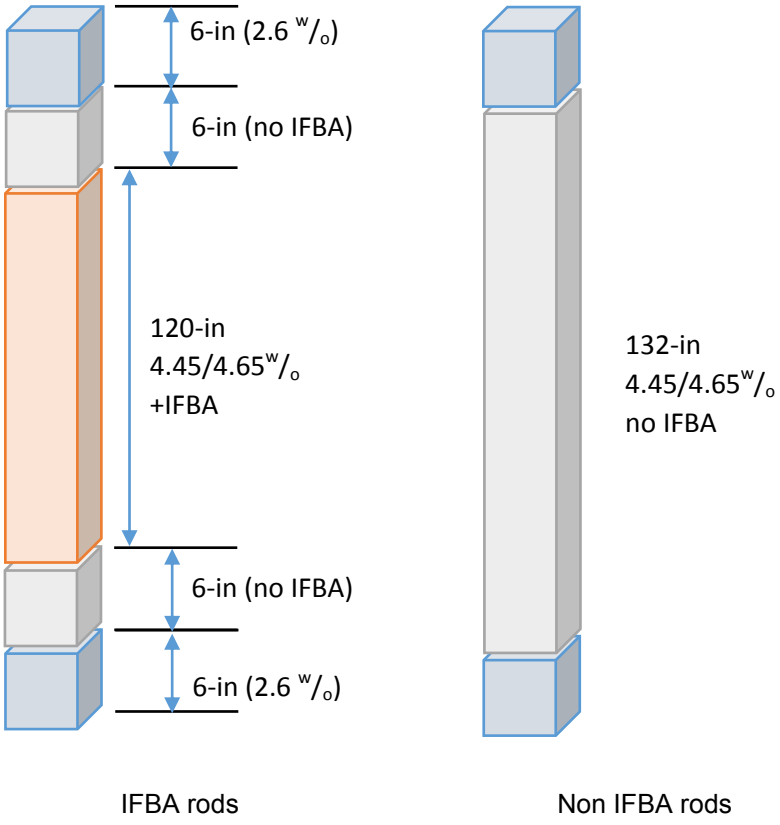

Figure 2 I^{2}S-LWR fuel axial stack

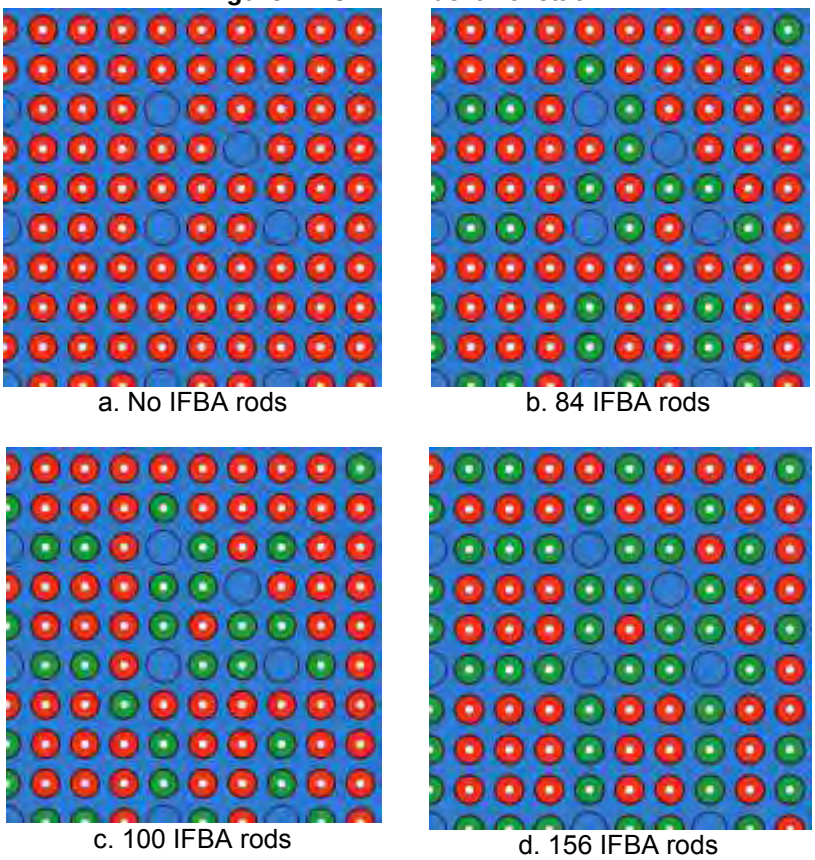

Figure 3 I^{2}S-LWR IFBA loading patterns – the top right quadrant of the assembly is shown; IFBA rods are indicated in green.

4.2. Methods

The current work was divided into the following stages:

1. Verification of the 2D WIMS assembly models against the reference solutions obtained with the Monte Carlo (MC) code Serpent. Serpent is a continuous-energy MC reactor physics code recently developed for reactor physics applications at VTT Technical Research Centre of Finland. Serpent can be used for 2D fuel lattice calculations as well as for 3D full core simulations. JEFF-3.1 cross-section libraries were used for WIMS and Serpent to minimize discrepancies in neutronic parameters (e.g. k_{inf}) that could arise from the use of different nuclear data evaluations.
2. The core physics analysis of the I^2S-LWR core design was performed with the core physics package PANTHER. WIMS10 was used for lattice data generation by employing a 172-group JEFF3.1-based library. WIMS10 utilizes a multicell collision probability method to form 22-group cross-sections, followed by a method-of-characteristics solution to generate data for PANTHER. Results were compared to those reported in Ref. [11], which use deterministic lattice calculates to provide data for a 3D core analysis [12] [13]. PANTHER used the same 3-batch self-generating reloading scheme that was iteratively applied to the U_3Si_2 core design until the main core parameters converged and a 12-month equilibrium cycle was reached.

4.3. Results

4.3.1. WIMS vs. Serpent Comparison

This section presents the single-assembly comparison at fixed temperatures and densities between WIMS and Serpent for different fuel assembly layouts (i.e. different numbers of IFBA rods). Fig. 4 shows criticality curves for the different cases examined. The difference in reactivity, between Serpent and WIMS, for each of the cases is presented in Fig. 5. In addition, Fig. 6 shows the maximum difference in within-assembly power (pin by pin) between Serpent and WIMS. It must be pointed out that the average absolute difference in the assembly power between the codes is much lower (< 0.15%).

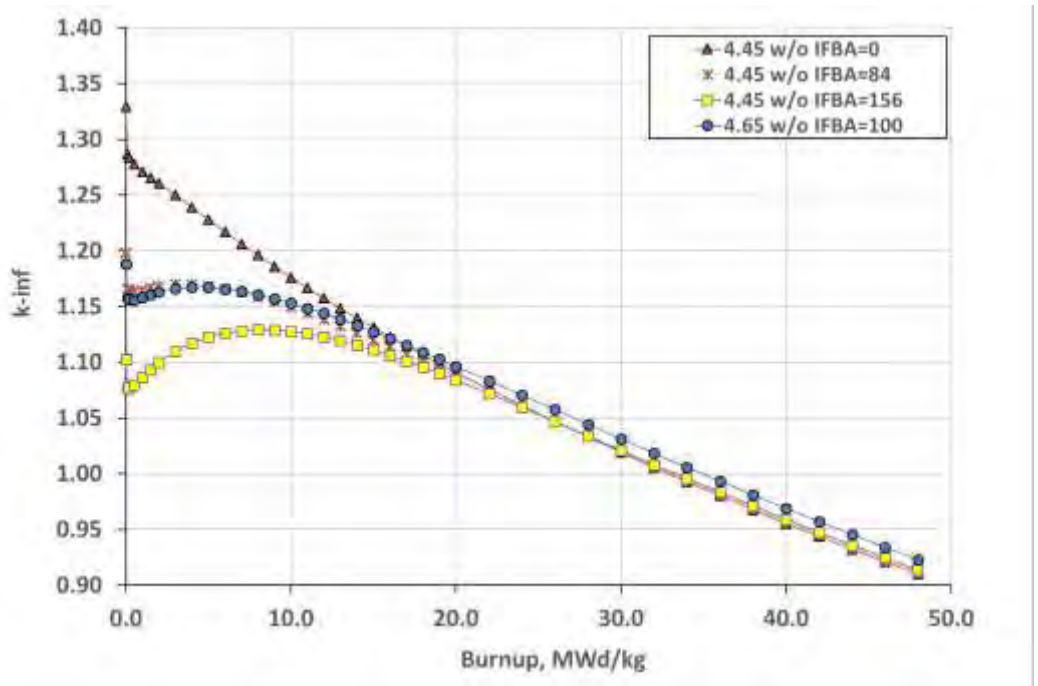

Figure 4 Criticality curves for different IFBA loading patterns (note that k-inf initially increases with burn-up as the burnable poison burns out)

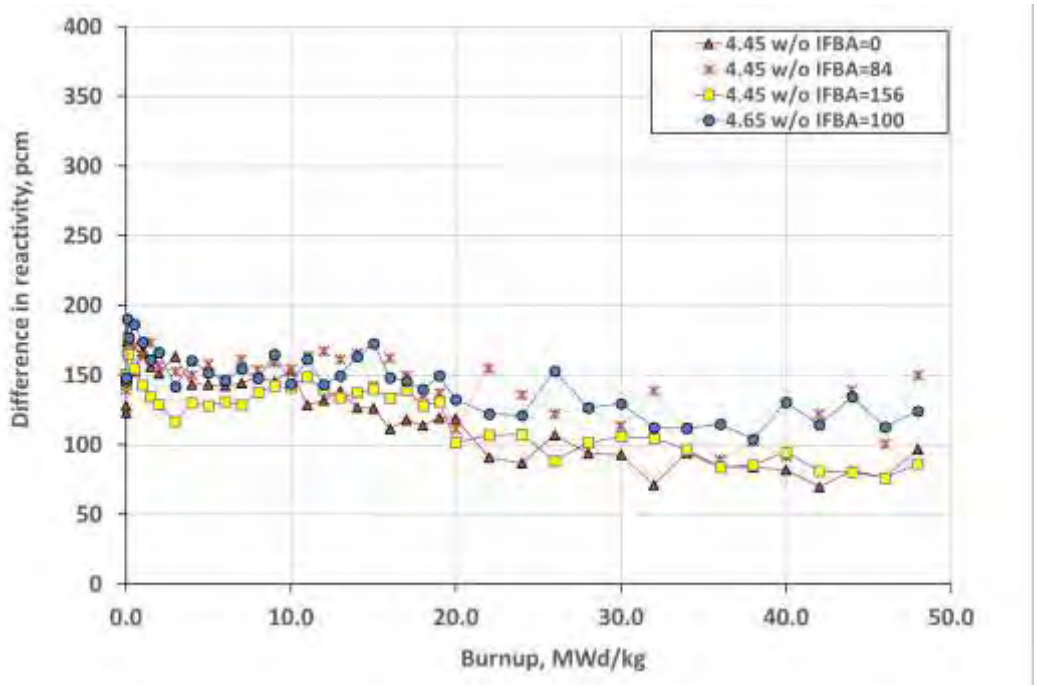

Figure 5 Difference in reactivity (WIMS vs. Serpent) for different IFBA loading patterns

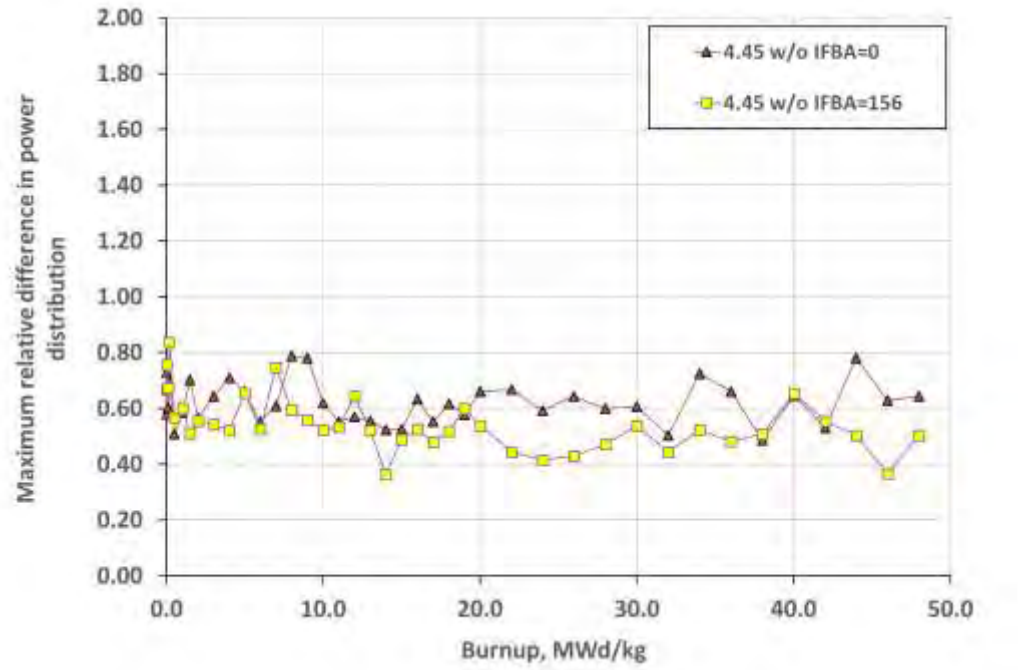

Figure 6 Maximum relative difference (%) in assembly radial power distribution (WIMS vs. Serpent)

4.3.2. Equilibrium Core Analysis

The representative burnup (MWD/t_{HM}) distribution at the beginning of the equilibrium cycle is presented in the octant-core map in Fig. 7. Fig. 8 shows the required boron concentration to maintain criticality over the equilibrium cycle. Power peaking factors and axial offset are reported in Fig. 9. Results are in good agreement with the values reported in Ref. [11] (e.g. assembly burn-ups within around 1%). This cross-comparison of results provides enhanced confidence in the reliability and accuracy of the results.

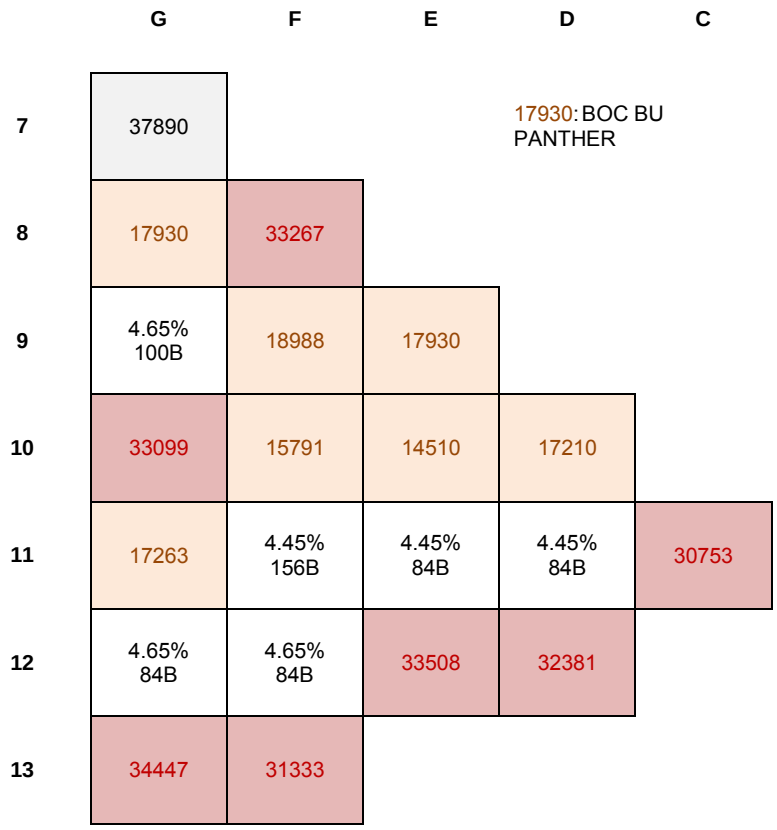

Figure 7 I^{2}S-LWR equilibrium burnup in, PANTHER

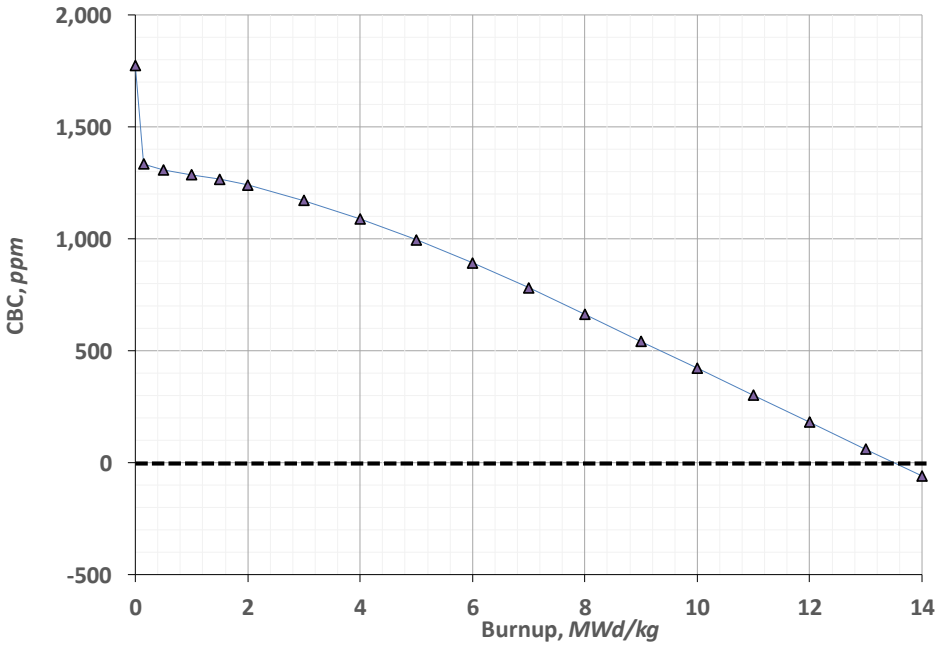

Figure 8 Critical boron concentration (ppm) as a function of burnup in PANTHER

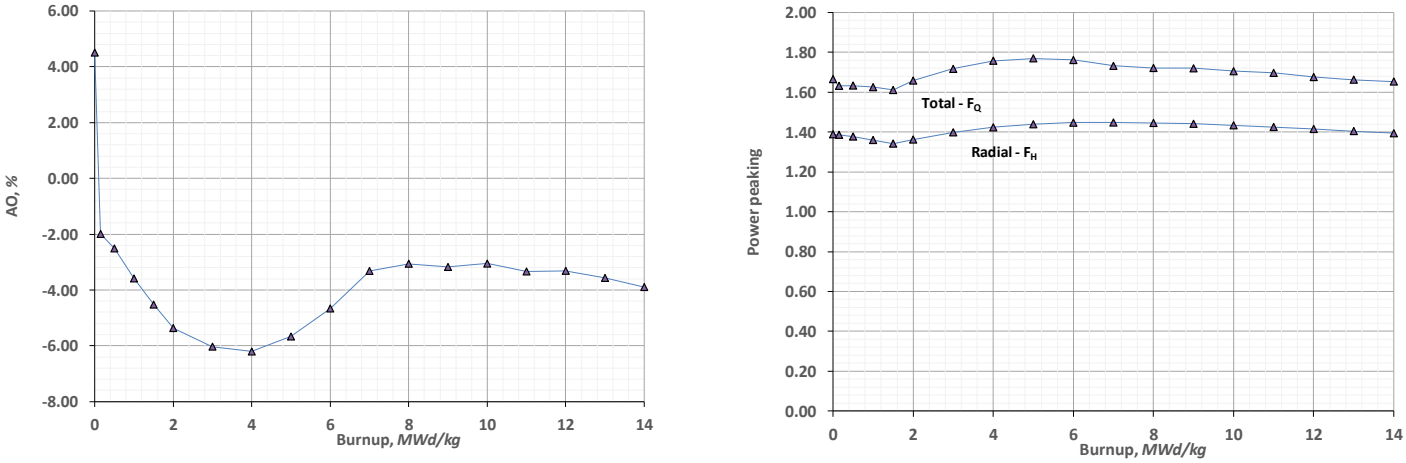

Figure 9 Axial Offset (AO) (left) and radial and total power peaking factors (right) for I^{2}S-LWR calculated using PANTHER

5. Conclusions

The UK has a long history in industrial fuel manufacture and fabrication for a wide range of reactor systems including LWRs. This is supported by a national infrastructure to perform experimental and theoretical R&D in fuel performance, fuel transient behaviour and reactor physics. The ANSWERS lattice code WIMS and core simulator PANTHER are used to support the operation of existing PWRs, including in the UK and Belgium. Modelling of ATFs is a natural extension of these capabilities and can largely be performed using existing calculation routes.Reactor physics modelling of the I^{2}S-LWR equilibrium cycle core was performed with the WIMS-PANTHER codes. The results were compared to reported results for the equilibrium cycle of the I^{2}S-LWR and indicate that there is a reasonable agreement between the codes. One possible source for the observed deviations between the codes is the different cross-section library employed in WIMS to generate lattice parameters. For this study, the JEFF3.1 libraries were used in WIMS, whereas ENDF BVII.0 was used in Ref. [11]. Future work could consider using the ENDF BVII.0 library in WIMS to allow for a more consistent comparison. It may also ultimately be necessary to validate the reactor physics codes against experimental data.

6. Acknowledgement

We are grateful to our colleagues in the ANSWERS team for providing advice and guidance during the preparation of this paper.

7. References

[1] F. Franceschini and E. J. Lahoda, “Advanced Fuel Developments to Improve Fuel Cycle Cost in PWR,” in *GLOBAL 2011*, Makuhari, Japan, Dec. 11-16, 2011.

[2] K. E. Metzger, T. W. Knight and R. L. Williamson, “Model of U3Si2 Fuel System Using Bison Fuel Code,” in *ICAPP2014*, Charlotte, NC, USA, Apr 6-9, 2014.

[3] H. Kim, I. Kim, Y. Koo and J. Park, “Application of Coating Technology on Zirconium-Based Alloy to Decrease High-Temperature Oxidation,” in *17th International Symposium on Zirconium in the Nuclear Industry* , Andhra Pradesh, India, 2013.

[4] A. Abe, C. Giovedi, D. S. Gomes and A. T. Silva, “Revisiting Stainless Steel as PWR Fuel Rod Cladding after Fukushima Daiichi Accident,” *Journal of Energy and Power Engineering,* vol. 8, pp. 973-980, 2014.

[5] E. J. Lahoda and F. Franceschini, “Advanced Fuel Concepts RT-TR-11-12,” Westinghouse Electric Company LLC, Sept 15 2011.

[6] Westinghouse Electric Company LLC, “Enhancing Safety: The Pursuit of Accident Tolerant Fuel,”

[Online]. Available: http://www.westinghousenuclear.com/About/News/Features/View/ArticleId/481/Enhancing-Safety-The-Pursuit-of-Accident-tolerant-Fuel. [Accessed 20 2 2015].

[7] T. Newton et al., “Developments Within WIMS10,” in *PHYSOR2008*, Interlaken, Switzerland, Sep 14-19, 2008.

[8] E. A. Morrison, “PANTHER User Guide E/REP/BBDB/0015/GEN/03 ED/PANTHER/ UG/5.5,” British Energy, 2003.

[9] B. Petrovic, “Integral Inherently Safe Light Water Reactors (I2S-LWR) Concept: Extending SMR Safety Features to Large Power Output,” in *ICAP2014*, Charlotte, NC, USA, Apr 6-9, 2014.

[10] J. Leppanen et al., “The Serpent Monte Carlo code: Status, development and applications in 2013,” *Annals of Nuclear Energy,* p. In Press, 2014.

[11] D. Salazar and F. Franceschini, “I2S-LWR Equilibrium Cycle Core Analysis,” in *PHYSOR2014*, Kyoto, Japan, Sep 29 - Oct 3, 2014.

[12] M. Ouisloumen et al., “PARAGON: The New Westinghouse Assembly Lattice Code,” in *ANS Int. Mtg. on Mathematical Methods for Nuclear Applications*, Salt Lake City, UT, USA, 2001.

[13] L. Mayhue et al., “Qualification of NEXUS/ANC Nuclear Design System for PWR Analyses,” in *PHYSOR2008*, Interlaken, Switzerland, Sep 16-19, 2008.

[14] Department of Energy & Climate Change, “Nuclear R&D - Accident Tolerant Fuel: Grant Notification,” 2014.

[15] Department of Energy and Climate Change, “DECC Science Advisory Group: Horizon Scanning,” October 2013.

[16] Nuclear Innovation and Research Advisory Board, “NIRAB Annual Report 2014”.

[17] J. L. Huttonet al., “Comparison of WIMS/PANTHER Calculations with Measurement on a Range of Operating PWR,” in *PHYSOR 2000*, Pittsburgh, USA, May 2000.

[18] S. Alam, B. A. Lindley and P. G. T, “Feasibility Study of the Design of Homogeneously Mixed Thorium-Uranium,” in *ICAPP2015*, Nice, France, May 3-6, 2015.

[19] C. Harrington, “Reactor Physics Modelling of the Shippingport Light Water Reactor,” MPhil Dissertation, University of Cambridge, 2012.

[20] S. F. Ashley et al., “Fuel cycle modelling of open cycle thorium-fuelled nuclear energy systems,” *Annals of Nuclear Energy,* vol. 69, pp. 314-330, 2014.

[21] T. Fei, E. A. Hoffman, T. K. Kim and T. A. Taiwo, “Performance evaluation of two-stage fuel cycle from SFR to PWR,” in *GLOBAL2013*, Salt Lake City, UT, USA, 2013.

[22] F. Heidet, T. K. Kim and T. A. Taiwo, “Two-Stage Fuel Cycles with Accelerator-Driven Systems,” in *PHYSOR2014*, Kyoto, Japan, Sep 28 - Oct 3, 2014.

[23] L. L. Snead et al., “Handbook of SiC properties for fuel performance modelling,” *Journal of Nuclear Materials,* vol. 371, pp. 329-377, 2007.

[24] Z. Xu, “Design Strategies for Optimizing High Burnup Fuel in Pressurized Water Reactors,” PhD Thesis, Massachusetts Institute of Technology, 2003.

[25] G. T. Parks, “Pressurised water reactor fuel management using PANTHER,” *Nuclear Science and Engineering,* vol. 124, pp. 178-187, 1996.

[26] G. T. Parks and M. P. Knight, “Loading pattern optimization in hexagonal geometry using PANTHER,” in *PHYSOR96*, Mito, Japan, Sep 16-20, 1996.

[27] N. Z. Zainuddin, B. A. Lindley and G. T. Parks, “Towards optimal in-core fuel management of thorium-plutonium-fuelled PWR cores,” in *ICONE 21 21st International Conference on Nuclear Energy*, Chengdu, China, July 29 - Aug 3, 2013.

[28] B. A. Lindley, A. Ahmad, N. Z. Zainuddin, F. Franceschini and G. T. Parks, “Steady-state and transient core feasibility analysis for a thorium-fuelled reduced-moderation PWR performing full transuranic recycle,” *Annals of Nuclear Energy,* vol. 72, pp. 320-337, 2014.

PRELIMINARY EVALUATION OF FeCrAl CLADDING AND U-Si FUEL FOR ACCIDENT TOLERANT FUEL CONCEPTS

J.D. HALES, K.A. GAMBLE
Fuels Modeling and Simulation Department, Idaho National Laboratory
P.O. Box 1544, Idaho Falls, ID 83415, USA

ABSTRACT

Since the accident at the Fukushima Daiichi Nuclear Power Station, enhancing the accident tolerance of light water reactors (LWRs) has become an important research topic. In particular, the community is actively developing enhanced fuels and cladding for LWRs to improve safety in the event of accidents in the reactor or spent fuel pools. Fuels with enhanced accident tolerance are those that, in comparison with the standard UO2-zirconium alloy system, can tolerate loss of active cooling in the reactor core for a considerably longer time period during design-basis and beyond design-basis events while maintaining or improving the fuel performance during normal operations and operational transients. This paper presents early work in developing thermal and mechanical models for two materials that may have promise: U-Si for fuel, and FeCrAl for cladding. These materials would not necessarily be used together in the same fuel system, but individually have promising characteristics. BISON, the finite element-based fuel performance code in development at Idaho National Laboratory, was used to compare results from normal operation conditions with Zr-4/UO2 behaviour. In addition, sensitivity studies are presented for evaluating the relative importance of material parameters such as ductility and thermal conductivity in FeCrAl and U-Si in order to provide guidance on future experiments for these materials.

1. Introduction

In March 2011, a magnitude 9.0 earthquake struck off the coast of Japan. The earthquake and the associated tsunami resulted in tens of thousands of deaths, hundreds of thousands of damaged buildings, and a cost estimated to be in the hundreds of millions of dollars.

One consequence of the tsunami was the flooding of backup power generators at the Fukushima Daiichi Nuclear Power Station. The loss of power to coolant systems led to high temperatures, oxidation of Zr-based alloys, hydrogen production, melted fuel, and hydrogen explosions. As a result, a massive cleanup effort is underway at Fukushima Daiichi. The economic impacts, both those directly related to the cleanup and those affecting the nuclear energy sector generally, are significant.

Following the disaster, efforts to develop nuclear fuels with enhanced accident tolerance were begun by many nations, corporations, and research institutes. In the United States, the Department of Energy's Office of Nuclear Energy accelerated research on this topic as part of its Fuel Cycle Research and Development (FCRD) Advanced Fuels Campaign (AFC). One product of this work is *Light Water Reactor Accident Tolerant Fuel Performance Metrics* [1], a report by AFC that outlines a set of metrics that can be used to guide selection of promising accident tolerant fuel (ATF) concepts. Furthermore, [1] specifies that a down-selection is to occur in the 2016-2017 timeframe, at which time the program will move from a proof-of-

concept stage to a proof-of-principle stage and continue research and development on a small set of concepts.

Given the aggressive development schedule, it is impossible to perform a comprehensive set of experiments to provide material characterization data. Therefore, the AFC plans to utilize computational analysis tools in an effort to understand the proposed materials.

The Nuclear Energy Advanced Modeling and Simulation (NEAMS) program in DOE has for some time been developing computational analysis tools. These include BISON [2-4] and Marmot [5], analysis tools tailored to nuclear fuel at the engineering scale and grain scale, respectively. Recently, NEAMS has introduced what it calls High Impact Problems (HIPs) into its program plan. These HIPs are intended to make a significant advance in a particular area of nuclear power research in a short period of time (3 years or less). NEAMS has chosen an ATF project, which emphasizes utilizing BISON and Marmot to model proposed materials, as its first HIP.

This paper reviews initial work on modelling ATF concepts. The following section reviews BISON and the multiscale materials modelling approach involving Marmot that will be used to investigate novel materials. We then review two promising candidates, FeCrAl for cladding and uranium silicide for fuel, as well as computational studies involving these materials. We conclude with a summary and a review of upcoming work.

2. BISON and Multiscale Materials

BISON is a multidimensional nuclear fuel performance analysis code capable of 1D, 2D, and 3D simulations. It is applicable to engineering scale analysis of LWR fuel, TRISO-coated fuel particles, and metal fuels. Typically, the partial differential equations that BISON solves are the energy and solid mechanics equations for temperature and displacements, respectively. BISON's capabilities include a selection of fuel and cladding thermal and mechanical material models, fission gas release, thermal and mechanical contact, evolving gap conductivity and pressure, axial and radial power scaling, fuel densification and swelling, and other models. Due to the evolution of gap size between fuel and cladding in a light water reactor, solving the energy and mechanics equations in a fully-coupled manner is very important. It is also possible to run BISON coupled with a neutronics code [6].

Many of the material models in BISON are empirical. These models rely on curve-fitting equations to describe material behaviour in regimes spanned by experiments. These models are efficient and have been used with success for many years in many fuel performance codes. However, these models suffer from the serious limitation that they are not applicable beyond the range of the experimental data.

Multiscale modelling is an approach that may be able to extend the useful range of materials models. The approach is to begin with lower length scale models and simulations and then use the knowledge gained to develop new models at higher length scales. The modelling may begin with atomistic simulations that, for example, provide insight into thermal conductivity for a given material. This information can be used at the grain level in a package such as Marmot. Marmot can model grain evolution and other phenomena using input data from the atomistic simulations. The behaviour at the Marmot level may be homogenized for use at the engineering scale (BISON) [7].

Given the desire to place a lead test rod into a commercial reactor in a matter of a few years, it will not be possible to develop empirical models describing the behaviour of the ATF concepts. Multiscale modelling will be used to provide guidance on the material behaviour where experimental data is sparse or non-existent.

3. FeCrAl

One proposed ATF cladding material for light water reactors is based on advanced oxidation-resistant iron alloys with a primarily iron-chromium-aluminum (Fe-Cr-Al) composition with the inclusion of other dopants such as molybdenum, yttrium, titatnium, and carbon. Commercial FeCrAl alloys under consideration for LWR cladding are Kanthal APMT [8], PM2000 [9], and MA956 [10] as investigated by Terrani et al. [11]. According to Terrani et al. [11] oxide dispersion strengthened (ODS) alloys like the commercial ones listed above have increased creep resistance at high temperatures, which is a benefit over Zircaloy during design basis and beyond design basis accidents. Moreover, the oxidation rates of FeCrAl alloys are less than Zircaloy [11,12]. Terrani et al. [11] performed oxidation tests in pure steam at atmospheric pressure, whereas Dryepondt et al. [12] performed oxidation tests at temperatures in the range of 800-1050^{o}C. Additionally, the oxide layer that forms on the cladding prevents hydrogen ingress and hydride formation, which is prevalent in Zircaloy cladding. Thus, the risk of cladding failure due to the precipitation of circumferential hydrides during used fuel disposition is mitigated.

Some of the disadvantages and difficulties of using FeCrAl alloys as a cladding material include their lower melting points than Zircaloy. In addition research of various chromia (Cr_2O_3) forming steels found that the required chromium content for protective barrier formation in steam at 1200 ^{o}C is in excess of 20% [13]. These chromium concentrations would limit the irradiation performance of the alloy [11]. Furthermore, there is limited data on the mechanical properties of FeCrAl alloys and their durability under mechanical stresses and irradiation [12]. For example, the creep data available for MA956 and PM2000 produced by Wasilkowska et al. [14] is limited to a few selected temperatures and is not presented in a manner that is easily implemented into BISON. This lack of data requires multiscale modelling to develop mechanistic material models and sensitivity studies to identify areas where further experiments are required.

To investigate the behaviour of FeCrAl cladding in a fuel performance setting and to identify areas where further research is required, a preliminary model of FeCrAl was added to BISON. The material model allows the selection of three different FeCrAl alloys: Kanthal APMT, PM2000 and MA956. Using the information provided in the datasheets available from the manufacturers of these alloys, the thermophysical properties including specific heat capacity, thermal conductivity, modulus of elasticity, Poisson's ratio, and coefficient of thermal expansion (CTE) are calculated as a function of temperature from the tabulated data. For temperatures between the tabulated points linear interpolation is used. Note that the CTE data is provided as a mean value rather than instantaneous and therefore to obtain the correct thermal strain the method by Niffenegger and Reichlin [15] needs to be employed.

When choosing a potential cladding material for accident tolerant applications, an understanding of the creep behaviour at normal operating and high temperatures as well as under irradiation conditions is of great importance. Of the commercial FeCrAl alloys of interest only MA956 has thermal creep data in a correlated format that allows easy input into BISON. No irradiation creep data exists for any of the FeCrAl alloys. The thermal creep correlation used for MA956 is a Norton law-based creep model proposed by Seiler et al. [16]:

$$\dot{\varepsilon} = \underbrace{A_0 \cdot \exp(\alpha T) \cdot \exp\left(-\frac{Q}{RT}\right)}_{A} \cdot \sigma^n \tag{1}$$

where Q is the activation energy, n is the creep exponent, α is a temperature coefficient, A_0 is the creep coefficient, T is the temperature in Kelvin, R is the ideal gas constant and σ is the effective stress in MPa. The creep behaviour is characterized by three distinct regimes with independent sets of creep parameters. The transition from one regime to the next

occurs at the critical stresses σ_{c1} and $\sigma_{c2,}$ which are calculated by equating equation 1 for two of the regimes. For example the σ_{c1} is defined as

$$\sigma_{c1} = \left(\frac{A_1}{A_2}\right)^{\frac{1}{n_2 - n_1}} \tag{2}$$

where $A_1(A_0, Q, \alpha, R, T)$ and n_1 are parameters in the range $\sigma < \sigma_{c1}$, and $A_2(A_0, Q, \alpha, R, T)$ and n_2 are parameters in the range $\sigma_{c1} < \sigma < \sigma_{c2}$, respectively. Table 1 lists the creep parameters of MA956 for the various stress regimes.

Table 1: Thermal creep parameters for FeCrAl alloy MA956

	A_0 [MPa^{-n}s^{-1}]	**n [-]**	**Q [kJ/mol]**	**α [K^{-1}]**
$\sigma < \sigma_{c1}$	78.978	4.9827	453	0.0
$\sigma_{c1} < \sigma < \sigma_{c2}$	3.466×10^{-124}	41.0	453	0.1
$\sigma > \sigma_{c2}$	8.68×10^{16}	5.2911	486	-0.0122

To demonstrate the behaviour of FeCrAl under light water reactor conditions, the current thermal, mechanical and creep parameters for MA956 were used in a representative 2D axisymmetric example problem. The predicted behaviour was compared to the behaviour of a model using Zircaloy-4 as the cladding material. The geometric dimensions and operational parameters were adapted from Williamson et al. [2] and Metzger et al. [17]. The problem simulates a 10-pellet UO_2 fuel rodlet with cladding. The dimensions of the rodlet are typical of PWR fuel. The pellets had length and diameter of 11.9 mm and 8.2 mm, respectively. The cladding has a thickness of 0.56 mm for both materials for consistency, and a nominal initial radial gap of 80 μm was used. A second-order QUAD8 finite element mesh was used to approximate the geometry using 11 radial and 32 axial elements per pellet as illustrated in Figure 1. The cladding was modelled with 4 elements through the thickness and 326 elements axially.

A simple power history is applied to the fuel. It is assumed the power rises linearly over approximately three hours and then is held constant at 25 kW/m for approximately 3.2 years. A symmetric axial profile is applied the active fuel length of the rodlet such that the maximum power is applied at an axial position of 0.06162 m from the bottom of the fuel stack.

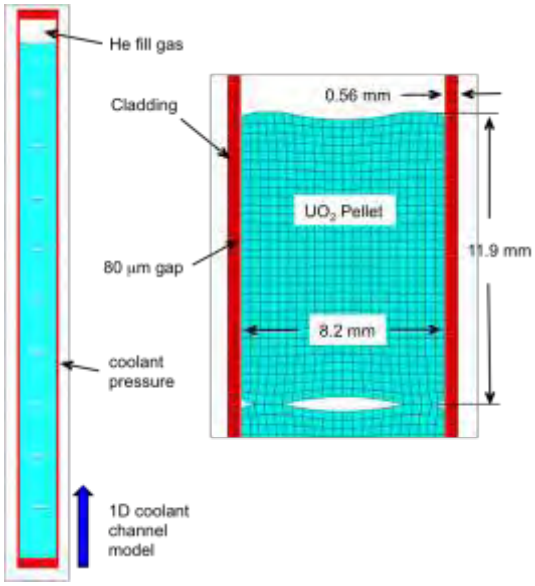

Figure 1: Geometry and mesh for the example problem. Adapted from references [2, 17].

A simple one-dimensional coolant channel model was used to calculate the convective heat transfer coefficient on the outside of the cladding. The operating conditions used are reproduced in Table 2.

Table 2: Operational parameters for the 2D axisymmetric example problem.

Linear average power (W/cm)	250
Fast neutron flux (n/m^{2}s)	7.5x10^{17}
Coolant pressure (MPa)	15.5
Coolant inlet temperature (K)	580
Coolant inlet mass flux (kg/m^2-s)	3800
Rod fill gas	Helium
Fill gas initial pressure (MPa)	2.0
Initial fuel density	95% theoretical
Fuel densification	1% theoretical
Burnup at full densification (MWd/kgU)	5

Comparisons between simulations of the example problem with Zircaloy-4 and MA956 are shown in Figure 2. Fig. 2a presents the comparison of fuel centreline, fuel surface and cladding inner surface temperatures as a function of burnup. It is observed from the beginning of irradiation that the fuel rodlet with MA956 cladding has higher fuel centerline and surface temperatures then the Zircaloy clad rodlet. Significantly less creep is experienced by the MA956 resulting in the fuel-to-clad gap remaining open for a longer duration leading to higher fuel temperatures. The inner cladding surface temperature remains relatively constant for both simulations. The point of fuel-to-clad contact occurs at the points at which the slopes of the curves change (i.e. about 12 MWd/kgU and 38 MWd/kgU for the Zircaloy-4 and MA956 rods respectively).

Since the MA956 rodlet experiences higher fuel temperatures, the fission gas released from the fuel grain boundaries to the plenum region is higher than the Zircaloy-4 rodlet as illustrated in Figure 2b. Subsequently, the larger plenum and gap space within the fuel element due to less creep down of the cladding results in a lower pressure within the plenum. The magnitude of creep experienced by MA956 is very low at normal operating temperatures. However, it is unclear what the effect that irradiation creep would have on the behaviour of MA956 at these temperatures. In Zircaloy-4 it is observed that thermal creep mechanisms are essentially negligible at normal operating temperatures (<600 ^{o}C) where irradiation creep dominates, whereas at high temperatures (e.g. during a LOCA) thermal creep mechanisms are of greatest influence. Therefore, it is important to include irradiation effects of MA956 to see if the creep rate increases during normal operation as with Zircaloy-4.

While the example case above provides the nominal behaviour of MA956 cladding under normal operating conditions and highlights the limited creep experienced, there is still much not known about FeCrAl alloys. Moreover, the dimensions of an accident tolerant fuel rod are not yet set. To gain a preliminary understanding of which mechanical and thermal properties, creep properties, and geometrical dimensions have the greatest influence on important rod properties such as the hoop stress and fuel centreline temperature, a sensitivity analysis was completed using Sandia National Laboratories' Dakota [18] software.

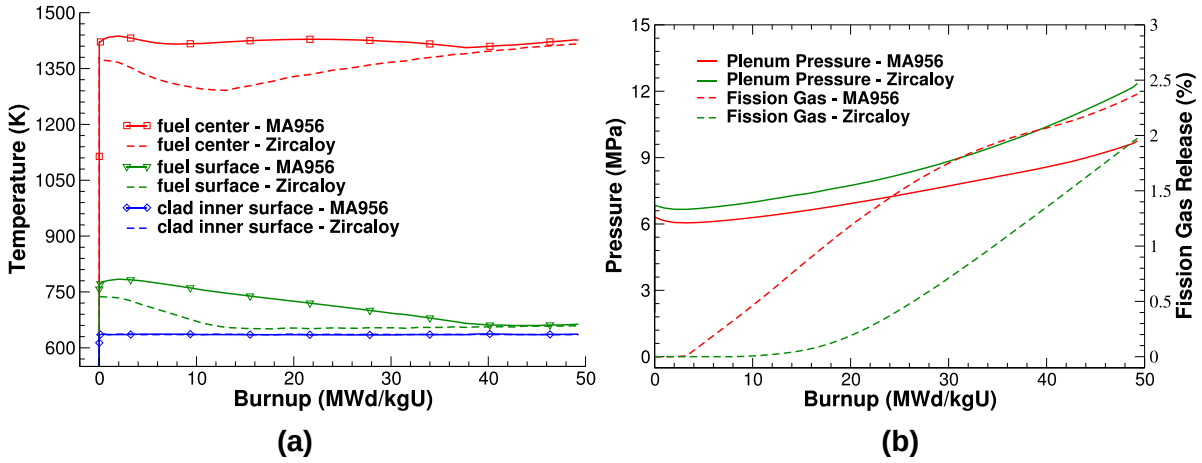

Figure 2: Comparisons between using MA956 or Zircaloy-4 cladding in the example problem for (a) fuel centerline, fuel surface and clad inner surface temperatures, and (b) plenum pressure and fission gas released

Starting with the nominal example problem with MA956 cladding, the Young's modulus, Poisson's ratio, thermal conductivity, radial gap width, and cladding thickness were varied by ± 10% to examine the effects of these parameters on hoop stress on the inner surface of the cladding and the fuel centreline temperature. Since the material properties vary as a function of temperature, a scale factor had to be used to properly vary these parameters. While varying the thermal creep parameters in equation 2 would be of interest, initial investigations indicated that for the example problem investigated here the negligible creep strain experienced does not have an affect on the stress results. Figure 3 shows main effects plots for the two output parameters of interest. The independent parameters (e.g., scale factors and geometry) were given 3 distinct values in a histogram form resulting in 243 simulations in the multidimensional parameter study. The information in a main effects plot is such that a point represents the mean value of the output parameter for all simulations at which the corresponding input parameter had that particular value. For example, the mean clad inner hoop stress is approximately -62.5 MPa for all simulations for which the Young's modulus was scaled by a factor of 0.9.

As expected it is imperative that the dimensions of an accident tolerant fuel rod be determined as the clad thickness and initial gap between the fuel and cladding have a strong influence on the stress state of the clad and the fuel centreline temperature as seen by the large slopes in the main effects plots for these parameters. The final centreline temperature is strongly influenced by the initial gap size. A larger initial gap results in higher temperatures because gap closure takes longer to occur. Similarly, a larger thickness means more material for the heat to pass through causing a slight increase in the centreline temperature. These plots confirm the expected behaviour when certain material parameters are varied. While the datasheets for the FeCrAl alloys provide values for the thermo-physical parameters at certain temperatures, it is uncertain if linearly interpolating between these values is appropriate.

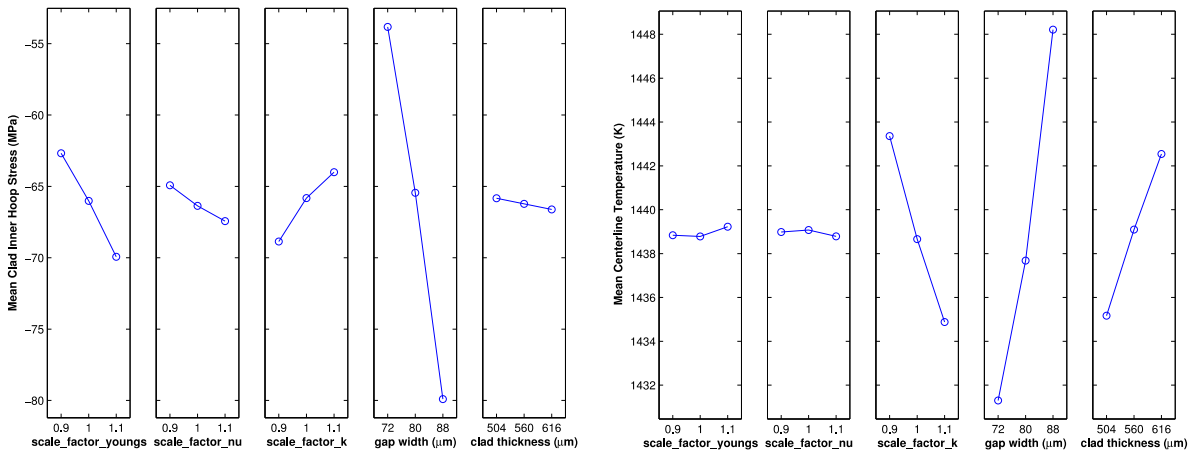

(a) **(b)**

Figure 3: Main effects plots analyzing the sensitivity of MA956 material parameters (a scale factor on Young's modulus and Poisson's ratio, thermal conductivity, gap width, and clad thickness) on the (a) clad inner hoop stress and (b) centerline temperature in the example problem at an axial location of 0.06162 m.

4. U-Si

Uranium silicides are leading candidates for the fuel in accident tolerant fuel rods. U_3Si_2 has a number of advantageous properties compared to UO_2. In particular its higher density and thermal conductivity enable the fuel to operate at much lower temperatures and thermal gradients. This results in lower thermal stresses within the fuel, which should mitigate pellet cracking [17]. Less cracking and lower temperatures should result in much lower fission gas release into the plenum regions than with UO_2 fuel. One disadvantage of uranium silicide is that almost all of the experimental data that is available is for experimental dispersion fuels, not monolithic fuel as would be present in an LWR. This raises the question of whether the data is appropriate for monolithic fuel and can be used in modelling. Furthermore, there is limited data on fission gas mechanisms, creep, and densification behaviour in uranium silicides.

Following a similar investigation as with the FeCrAl cladding, a comparison between two example problems was conducted to investigate the differences between UO_2 and U_3Si_2. In these simulations the cladding was kept as Zircaloy-4 and the fuel properties changed. Material models available in BISON for U_3Si_2 include temperature dependent thermal conductivity and specific heat capacity and burnup dependent volumetric swelling. Fission gas release mechanisms are treated as for UO_2 fuel in the absence of additional information. The details of these models are provided in [17] and are based upon the models of [19-21]. The models for UO_2 include burnup and temperature dependent thermophysical properties, fuel creep, solid and gaseous swelling, densification, relocation, and fission gas release. A similar comparison is presented in Metzger et al.'s paper [17]; however in that case, fuel creep and relocation were turned off for the UO_2 fuel to be consistent with the elastic model used for U_3Si_2. Here we compare the results when using all of the information known about UO_2 to simulate the fuel.

Figure 4a illustrates the fuel centreline, fuel surface, and cladding inner surface temperature histories. The higher thermal conductivity of U_3Si_2 results in a centreline temperature that is approximately 400 K lower than observed for UO_2. Consequently, the lower operating temperatures result in less thermal expansion, and the fuel-to-clad gap remains open longer. As with the FeCrAl simulations, the point of contact occurs when the slope of the fuel surface and centreline curves change. UO_2 has a lower fuel surface temperature because relocation

causes the fuel-clad gap to close more rapidly than in the U_3Si_2 case. Also, larger plenum volume and no fission gas release results in a lower plenum pressure with U_3Si_2 fuel as observed in Figure 4b. While there is no fission gas release in the U_3Si_2 simulation, the plenum pressure constantly increases due to the closing of the fuel-to-clad gap due to thermal expansion, swelling, and cladding creep. As the plenum volume continually decreases the internal pressure must increase, which is observed in Figure 4b. The reason the uranium silicide simulations end at a lower burnup is due to the higher density of uranium in the U_3Si_2 matrix.

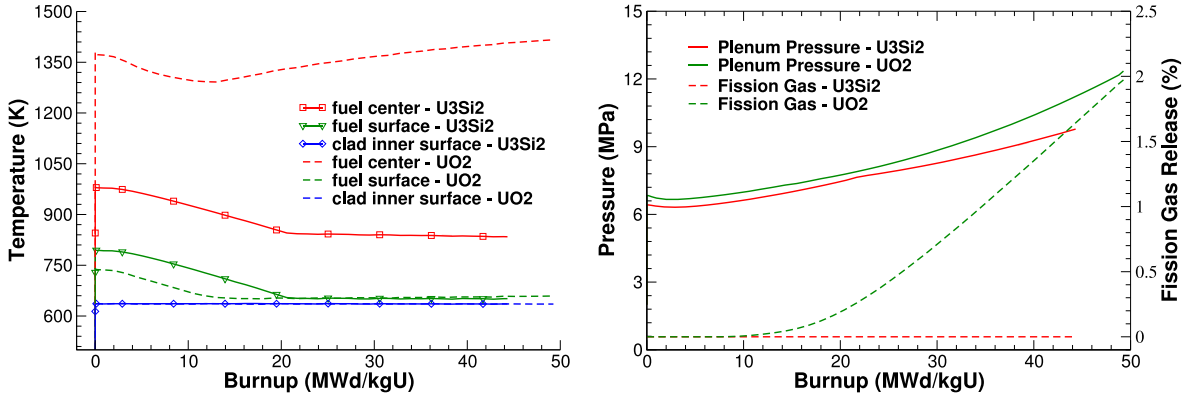

Figure 4: Comparisons between using U_3Si_2 and UO_2 in the example problem (a) fuel centerline, fuel surface, and clad inner surface temperatures, (b) plenum pressure and fission gas release.

Like FeCrAl alloys such as MA956, the mechanical properties and behaviour of U_3Si_2 (e.g., creep) are not well known. Moreover, the optimal dimensions of U_3Si_2 fuel pellets for LWR applications are unclear. Therefore, a sensitivity study was completed using Dakota with the input parameters chosen to be a scale factor on the fuel swelling, the Young's modulus, Poisson's ratio, coefficient of thermal expansion, and the initial pellet radius, where the output quantities of interest are fuel centreline temperature and the hoop stress on the exterior surface of the pellet. The exterior hoop stress is compressive because the sensitivity study takes the last time step of the simulations once contact has already been established.

As expected the Young's modulus and Poisson's ratio have essentially zero effect on the centreline temperature and have a moderate effect on the exterior hoop stress. The input parameters with the most influence on centreline temperature and exterior hoop stress are the swelling factor and pellet radius. The radius of the fuel pellet is significantly correlated with the centreline temperature because the smaller the pellet radius the larger the fuel-to-clad gap. A large gap means reduced heat transfer and subsequently higher fuel temperatures. Contrarily, as the fuel radius is increased, the magnitude of the compressive stress on the exterior of the pellet decreases due to contact occurring prior to creep mechanisms having a strong compressive force on the expanding pellet. Keep in mind that the range of the mean centreline temperature is approximately 4 K. This is because the thermal conductivity of U_3Si_2 increases with temperature and the power history applied in the example case is constant. The parameter with greatest influence on centreline temperature would be the thermal conductivity, but since there is significant data already available it has been left out of the multidimensional parameter study presented here.

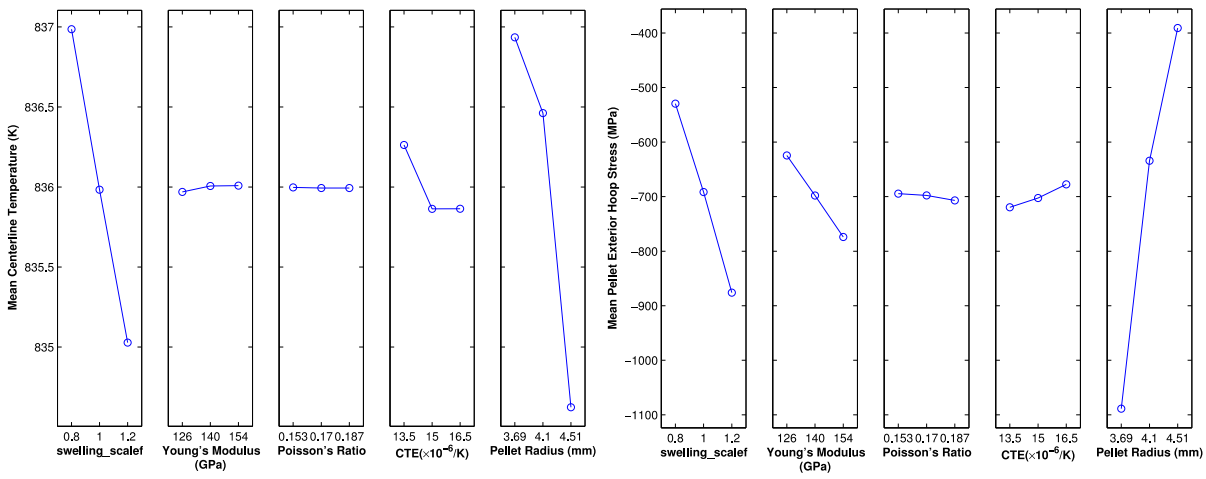

(a) **(b)**

Figure 5: Main effects plots investigating the sensitivity of U_3Si_2 material properties on (a) the fuel centerline temperature and (b) the pellet exterior hoop stress at an axial location of 0.06162 m.

5. Conclusions

FeCrAl and U-Si are leading ATF materials. FeCrAl and U-Si have several advantages over the traditional materials used in LWR fuel rods, Zircaloy and UO_2. FeCrAl alloys experience significantly less creep, have slower oxidation rates, and do not absorb hydrogen from the coolant. U-Si has higher thermal conductivity, higher density, and less expected fission gas release than UO_2. Currently, the main weakness of FeCrAl alloys and U-Si fuels is the lack of experimental data to yield a greater understanding of the behaviour of these materials under normal operating and transient reactor conditions. Therefore we need additional experimental data and/or multiscale modelling to understand the thermophysical properties and irradiation creep behaviour of FeCrAl alloys, as well as the thermophysical properties, creep mechanisms, swelling, densification, and fission gas release pathways of U-Si fuels. Sensitivity analyses were completed to illustrate the capability of investigating the effect of many input variables on the output of interest. We will work with the AFC to refine the geometry of the proposed ATF concepts. Future work will incorporate ongoing experimental data with lower length scale investigations to improve the quality of ATF modelling at the engineering scale.

6. Acknowledgements

The submitted manuscript has been authored by a contractor of the U.S. Government under Contract DE-AC07-05ID14517. Accordingly, the U.S. Government retains a non-exclusive, royalty free license to publish or reproduce the published form of this contribution, or allow others to do so, for U.S. Government purposes.

7. References

[1] S. Bragg-Sitton, B. Merrill, M. Teague, L. Ott, K. Robb, M. Farmer, M. Billone, R. Montgomery, C. Stanek, M. Todosow, and N. Brown, “Advanced fuels campaign: enhanced LWR accident tolerant fuel performance metrics,” INL/EXT-13-29957.

[2] R. L. Williamson, J. D. Hales, S. R. Novascone, M. R. Tonks, D. R. Gaston, C. J. Permann, D. Andrs, and R. C. Martineau, “Multidimensional multiphysics simulation of

nuclear fuel behavior," *J. Nucl. Mater.*, vol. 423, pp. 149–163, 2012. http://dx.doi.org/10.1016/j.jnucmat.2012.01.012.

[3] J. D. Hales, R. L. Williamson, S. R. Novascone, D. M. Perez, B. W. Spencer, and G. Pastore, "Multidimensional multiphysics simulation of TRISO particle fuel," *J. Nucl. Mater.*, vol. 443, pp. 531–543, 2013. http://dx.doi.org/10.1016/j.jnucmat.2013.07.070.

[4] J. D. Hales, S. R. Novascone, B. W. Spencer, R. L. Williamson, G. Pastore, and D. M. Perez, "Verification of the BISON fuel performance code," *Annals of Nuclear Energy*, vol. 71, pp. 81–93, 2014. http://dx.doi.org/10.1016/j.anucene.2014.03.027.

[5] M. R. Tonks, D. Gaston, P. C. Millett, D. Andrs, and P. Talbot, "An object-oriented finite element framework for multiphysics phase field simulations," *Comp. Mat. Sci.*, vol. 51, pp. 20–29, 2012.

[6] J. D. Hales, M. R. Tonks, F. N. Gleicher, B. W. Spencer, S. R. Novascone, R. L. Williamson, G. Pastore, D. M. Perez, "Advanced multiphysics coupling for LWR fuel performance analysis," *Annals of Nuclear Energy*, 2014. http://dx.doi.org/10.1016/j.anucene.2014.11.003.

[7] J. D. Hales, M. R. Tonks, K. Chockalingam, D. M. Perez, S. R. Novascone, B. W. Spencer, and R. L. Williamson, "Asymptotic expansion homogenization for multiscale nuclear fuel analysis," *Comp. Mat. Sci.*, vol. 99, pp. 290–297, 2015. http://dx.doi.org/10.1016/j.commatsci.2014.12.039

[8] Sandvik Kanthal APMT Datasheet, <http://kanthal.com/en/products/material-datasheets/tube/kanthal-apmt/>

[9] Schwarzkopf Plansee PM2000 Datasheet, <http://www.matweb.com/search/datasheet.aspx?matguid=21e9ec9a0de24b47bcf69ab11c375567&ckck=1.>

[10] Special Metals INCOLOY MA956 Datasheet, <http://www.specialmetals.com/documents/Incoloy%20alloy%20MA956.pdf>

[11] K. A. Terrani, S. J. Zinkle, and L. L. Snead, "Advanced oxidation-resistant iron-based alloys for LWR fuel cladding," *J. Nucl. Mater.,* vol. 448, pp. 420-435, 2014. http://dx.doi.org/10.1016/j.jucmat.2013.06.041l

[12] S. Dryepondt, B. A. Pint, and E. Lara-Curzio, "Creep behavior of commercial FeCrAl foils: Beneifical and detrimental effects of oxidation," *Materials Science and Engineering A,* vol. 550, pp. 10-18, 2012.

[13] B. A. Pint, K. A. Terrani, M. P. Brady, T. Cheng, J. R. Keiser, "High temperature oxidation of fuel cladding candidate materials in steam-hydrogen environments," *J. Nucl. Mater.,* vol. 440, pp. 420-427, 2013. http://dx.doi.org/10.1016/j.jnucmat.2013.05.047

[14] A. Wasilkowska, M. Bartsch, U. Messerschmidt, R. Herzog, A. Czyrska-Filemonowicz, "Creep mechanisms of ferritic oxide dispersion strengthened alloys," *J. Materi. Process. Tech.,* vol. 133, pp. 218-224, 2003.

[15] M. Niffenegger and K. Reichlin, "The proper use of thermal expansion coefficients in finite element calculations," *J. Nucl. Eng. Design,* vol. 243, pp 356-359, 2012. http://dx.doi.org/10.1016/j.nucengdes.2011.12.006

[16] P. Sieler, M. Bäker, and J. Rösler, “Variation of creep properties and interfacial roughness in thermal barrier coating systems,” *Advanced Ceramic Coatings and Materials for Extreme Environments,* vol. 32, pp. 129-136, 2011.

[17] K. E. Metzger, T. W. Knight, and R. L. Williamson, “Model of U_3Si_2 Fuel System Using BISON Fuel Code,” *Proc. Of ICAPP 2014,* Charlotte, USA, 2014.

[18] B. M. Adams, L. E. Bauman, W. J. Bohnhoff, K. R. Dalbey, M. S. Ebeida, J. P. Eddy, M. S. Eldred, P. D. Hough, K. T. Hu, J. D. Jakeman, L. P. Swiler, and D. M. Vigil, *"DAKOTA, A Multilevel Parallel Object-Oriented Framework for Design Optimization, Parameter Estimation, Uncertainty Quantification, and Sensitivity Analysis: Version 5.4 User's Manual,"* Sandia Technical Report SAND2010-2183, December 2009. Updated April 2013.

[19] H. Shimizu, “The properties and irradiation behavior of U_3Si_2,” *Technical Report NAA-SR-10621*, Atomics International, 1965.

[20] J. E. Matos and J. L. Snelgrove, “Research reactor core conversion guidebook-Vol 4: Fuels,” (Appendices I-K). *Technical Report IAEA-TECDOC-643*, 1992.

[21] M. R. Finlay, G. L. Hofman and J. L. Snelgrove, “Irradiation behavior of uranium silicide compounds,” *J. Nucl. Mater.,* vol. 325, pp. 118-128, 2004.

LIGHT WATER REACTOR ACCIDENT TOLERANT FUELS IRRADIATION TESTING

J. CARMACK, K. BARRETT, AND H. MACLEAN-CHICHESTER
Idaho National Laboratory
P.O. Box 1624
Idaho Falls, Idaho 83415

ABSTRACT

The purpose of Accident Tolerant Fuels (ATF) experiments is to test novel fuel and cladding concepts designed to replace the current zirconium alloy uranium dioxide (UO_2) fuel system. The objective of this Research and Development (R&D) is to develop novel ATF concepts that will be able to withstand loss of active cooling in the reactor core for a considerably longer time period than the current fuel system while maintaining or improving the fuel performance during normal operations, operational transients, design basis, and beyond design basis events. It was necessary to design, analyze, and fabricate drop-in capsules to meet the requirements for testing under prototypic LWR temperatures in Idaho National Laboratory's Advanced Test Reactor (ATR).

Three industry led teams and one DOE team from Oak Ridge National Laboratory provided fuel rodlet samples for their new concepts for ATR insertion in 2015. As-built projected temperature calculations were performed on the ATF capsules using the BISON fuel performance code. BISON is an application of INL's Multi-physics Object Oriented Simulation Environment (MOOSE), which is a massively parallel finite element based framework used to solve systems of fully coupled nonlinear partial differential equations. Both 2D and 3D models were set up to examine cladding and fuel performance.

1. Introduction

For the U.S. nuclear industry, the safe, reliable and economic operation of the nation's nuclear power reactor fleet has always been a top priority. As a result, continual improvement of the technology, materials, and fuels used has remained central to the industry's success. Decades of research combined with continual operation have produced steady advancements in technology and yielded an extensive base of data, experience, and knowledge on light water reactor (LWR) fuel performance under both normal and accident conditions. Thanks to efforts by governments, private companies, national laboratories, and universities, a variety of different technologies to optimize economic operation have been developed and deployed over time.

One of the missions of the U.S. Department of Energy Office of Nuclear Energy (DOE-NE) is to develop nuclear fuels and claddings with enhanced accident tolerance. Following the Great East Japan Earthquake in 2011, with the resulting tsunami and subsequent damage to the Fukushima Daiichi nuclear power plant complex, enhancing the accident tolerance of LWRs became a topic of serious discussion in the United States. As a result of direction from the U.S. Congress, DOE-NE initiated the Enhanced Accident Tolerant Fuel Development program.

In the Department of Energy, the Fuel Cycle Research and Development Advanced Fuels Campaign has been given the responsibility to conduct research and development on enhanced accident tolerant fuels with the goal of performing a lead fuel assembly or lead fuel rod irradiation in a commercial reactor by 2022. The Advanced Fuels Campaign has defined fuels with enhanced accident tolerance as those that, in comparison with the

standard UO_2-Zircaloy system currently used by the nuclear industry, can tolerate loss of active cooling in the reactor core for a considerably longer time period (depending on the LWR system and accident scenario) while maintaining or improving the fuel performance during normal operations and operational transients, as well as design-basis and beyond design-basis events.

Table 1 shows an overview of the irradiation testing program in 4 phases: 1) **ATF-1** drop-in capsule testing in ATR, **ATF-2** loop testing in ATR, 3) **ATF-3** transient testing of fuel rodlets (from the ATF-2 series) in TREAT, and 4) **ATF-4** transient testing of fuel rods from the commercial power plant irradiated LTR/LTA program in TREAT. Each phase is a series of irradiation experiments conducted with specific objectives. More detail on each of the four phases of the irradiation testing program and their objectives is given in subsequent sections.

Test Series	ATF-1	ATF-H-x	ATF-2	ATF-3	CM-ATF-x	ATF-y
Test Reactor	ATR	Halden	ATR	TREAT	Commercial Power Plant	TREAT
Test Type	Drop-in	Instrumented	Loop	Loop	LTR/LTA	Loop
Test Strategy	Scoping – Many Compositions Nominal conditions	In-pile creep 3-D instrumented BWR condition	Scoping – Focused Compositions PWR Nominal conditions	Focused Compositions Accident conditions	Focused Composition Nominal conditions	Focused Compositions Accident conditions
Fuel	UO_2, U_3Si_2, UN	Selected	Down-selected concepts	Fuel rodlets from ATF-1 and test rods from ATF-2 irradiations	Concepts selected in 2016	Test rods from LTR/LTA irradiations
Cladding	Zr-alloy, coated Mo-L, stainless steels, advanced alloys, SiC	Selected	Selected	Selected	Selected	Selected
Key Features	Fuel-cladding interactions		Fuel-cladding-coolant interactions	Integral testing	Steady State Irradiation	Integral testing
Timeframe	FY14 – FY18+		FY16 – FY22	FY18 – FY25	FY22 – ?	FY – ?

Table 1. Irradiation Testing Program for Accident Tolerant Fuels.

2. Irradiation Tests

This paper lays out an extensive irradiation test program in the Advanced Test Reactor and a test series in the Halden test reactor that will progress from feasibility experiments under normal operating conditions to integral demonstrations under accident conditions to support the LFR/LFA program and eventual qualification of an ATF concept in an operating commercial nuclear power plant. In addition, it is expected that a number of separate effects experiments and irradiations will be conducted in a variety of university test reactors and the High Flux Irradiation Reactor (HFIR).

2.1. ATF-1 Test Series: Drop-in Capsule Testing in ATR

The ATF-1 test series will investigate the performance of a wide variety of proposed ATF concepts under normal LWR operating conditions. Data generated in this test series will be used to assess the feasibility of certain aspects of proposed ATF concepts, as well as provide information to support screening among concepts. The ATF-1 test series will be performed as a series of drop-in capsule tests irradiated in the ATR.

The ATF-1 test series was initiated in February 2015 and will irradiate fuel rodlets that are isolated from the ATR primary coolant by a secondary capsule filled with an inert gas; the cladding of the test rodlets will not be in contact with water coolant during irradiation. Thus, the ATF-1 test series will investigate the irradiation behavior of new fuels (i.e., pellets/compacts) and their interaction with the cladding; however, ATF-1 is not a test series designed to assess the interaction of the cladding with water coolant. The ATF-1 test series will obtain fuel behavior and fuel-cladding interaction data needed to down-select to one or more promising concepts to carry into the next (much more expensive) phase of the irradiation testing program (i.e., ATF-2). It is intended as an early screening evaluation experiment series. This initial complement of test fuels were provided by the Industry led accident tolerant fuel development teams at AREVA, GE, and Westinghouse. Figure 1 provides an overview of each of these activities.

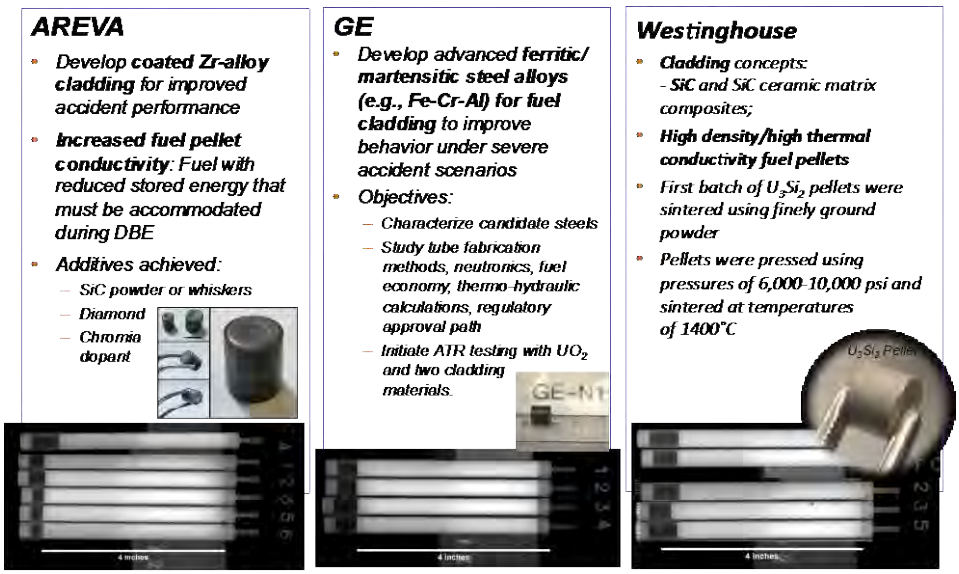

Fig. 1. Summary of Industry Led Accident Tolerant Fuel Development Projects.

Figure 2 provides a schematic of the ATF-1 capsule/rodlet configuration and photographs of the seventeen capsule/rodlets that were loaded into the ATF in February 2015 as the initial compliment of ATF experiments.

Fig. 2. Schematic of ATF-1 Capsule/Rodlet combination and photographs of initial set of ATF-1 samples inserted into ATF-1 experiment.

2.2. ATF-2 Test Series: Loop Testing in ATR

The ATF-2 test series will take the most promising concept(s) from the drop-in capsule test (ATF-1) into loop testing in the ATR. In an ATR loop, experimental ATF rods will be in direct contact with high-pressure water coolant with active chemistry control to mimic the conditions of PWR primary coolant. In addition to continuing the investigation of fuel behavior and fuel-cladding interaction in ATF-1, the ATF-2 experiment series will include cladding-coolant interaction. ATF-2 will be the most prototypic irradiation test possible in the ATR to assess the performance of ATF concepts under normal LWR operating conditions. Figure 3 shows a schematic of the ATF-2 experiment test train. Currently the experiment is being designed to accommodate as many instrumented fuel pins as possible accommodating 16 inch (40.6 cm) and 6 inch (15.2 cm) lengths.

The ATF-2 test series will produce a significant number of irradiated fuel rods. Many of the irradiated fuel rods will be subjected to comprehensive non-destructive as well as destructive postirradiation examination (PIE). However, a substantial portion of these irradiated fuel rods will be only examined non-destructively so that they can be carried over to be prototypic test articles in the next phase of the irradiation testing program (ATF-3). Irradiated fuel rods from this test series could also be used for out-of-pile experiments to simulate loss-of-coolant-accidents (LOCAs).

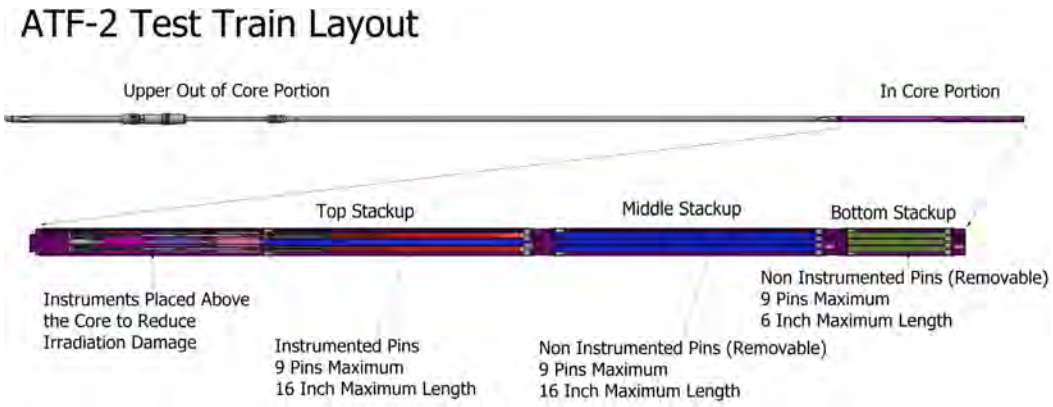

Fig. 3. Schematic of the ATF-2 experiment test train.

2.3. ATF-3 Test Series: Transient Testing of ATF-2 Rods in TREAT

The ATF-3 test series will take the most promising concept(s) from the ATR loop testing phase (ATF-2) into transient testing in TREAT. In TREAT, experimental ATF rods will be subjected to reactivity-initiated accident (RIA) scenarios to investigate their integral performance under this class of accident conditions. It is anticipated that this phase of testing would begin with fresh (unirradiated) fuel rodlets/rods to assess performance under a beginning-of-life (BOL) scenario and progress to the irradiated fuel rodlets/rods of multiple burnup levels obtained from the ATF-1 and ATF-2 test series.

Figure 4 provides a schematic of the conceptual design of an ATF-3 loop experiment and the insertion of the loop in the middle of the TREAT driver core. The loop is self-contained with pump, heat exchanger, and associated flow conditioning components supporting the testing of multiple fuel pins in beyond design basis accident conditions. The ATF-3 experiment series will continue through the design phase over the next few years.

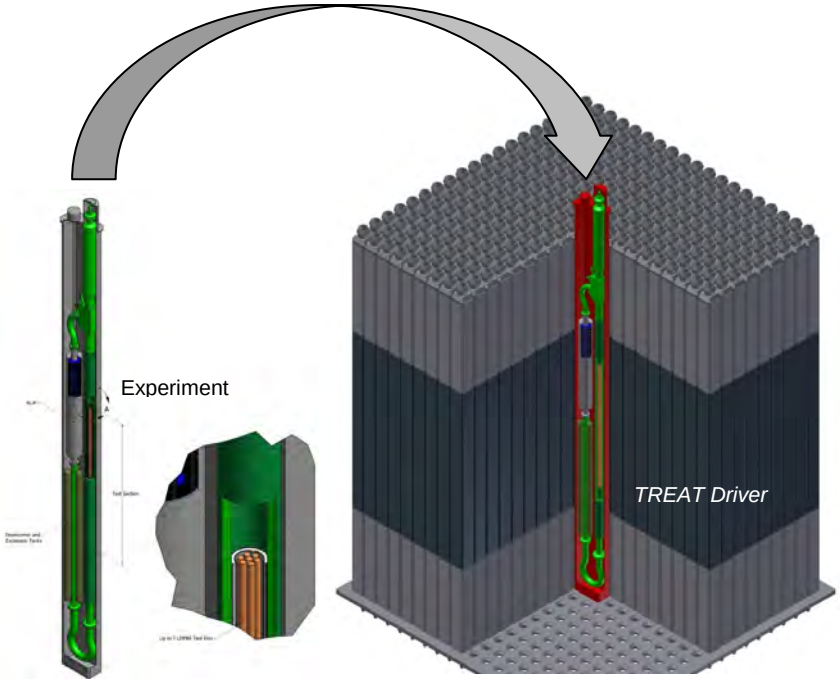

Figure 4. Schematic of Experiment Capsule installed in TREAT Driver Core.

2.4. CM-ATF-x: Lead Fuel Rod or Lead Fuel Assemblies irradiated in commercial nuclear power plant.

The near term goal of the DOE Accident Tolerant Fuel development program is to insert a lead fuel rod or lead fuel assembly into a commercial nuclear power plant by 2022. This lead fuel irradiation will then progress for 1 to 3 years in the commercial nuclear power plant and then will be removed, examined, and subjected to further testing and qualification.

2.5. ATF-4 Test Series: Transient Testing of LTR/LTA Rods in TREAT

The ATF-4 test series assumes that the irradiation of ATF concept(s) in a commercial LWR as part of an LTR/LTA program begins in FY22. The logical final phase of the irradiation test program is to subject a subset of these Lead Test Rods to transient testing in TREAT. Since LTRs will be much longer than can be accommodated in TREAT, either shorter, segmented rods will need to be included in the LTR/LTA program or a sectioning/remanufacturing capability will be needed in the PIE facility in order to prepare appropriate test rods for TREAT. As in the ATF-3 test series, it is anticipated that this phase of testing would begin with fresh (unirradiated) fuel rods, fabricated by the same vendor and process as used for the LTRs, to assess performance under a BOL scenario and progress to irradiated LTR segments of multiple burnup levels.

3. Conclusion

An extensive series of experiments and irradiations are being planned and conducted under the DOE Accident Tolerant Fuel program with the goal of inserting a lead fuel rod or assembly into a commercial power plant by 2022. The ATF irradiations described here are intended to provide the necessary irradiations to generate the data needed to achieve insertion of new fuel technology in a commercial power plant. This is an aggressive goal and the reason behind why a large test series is planned for the ATR and TREAT and additional testing planned for the Halden test reactor.

4. ACKNOWLEDGEMENT

This manuscript has been authored by Battelle Energy Alliance, LLC under Contract No. DE-AC07-05ID14517 with the U.S. Department of Energy. The United States Government retains and the publisher, by accepting the article for publication, acknowledges that the United States Government retains a nonexclusive, paid-up, irrevocable, world-wide license to publish or reproduce the published form of this manuscript, or allow others to do so, for United States Government purposes.

The funding source had no role in the research or writing of this paper, or the decision to submit it for publication.

EVALUATION OF ENHANCED ACCIDENT TOLERANT LWR FUELS

S.M. BRAGG-SITTON, B.J. MERRILL, J. HALES
Idaho National Laboratory
PO Box 1625, Idaho Falls, ID, 83415 – USA

N. BROWN, M. TODOSOW
Brookhaven National Laboratory – USA

K. ROBB
Oak Ridge National Laboratory – USA

ABSTRACT

The U.S. Department of Energy Advanced Fuels Campaign (AFC) is currently funding research and development on a number of fuel technologies for light water reactors (LWRs) that could provide enhanced performance under accident scenarios relative to the current zirconium alloy-uranium dioxide (UO_2) fuel system. The overall mission of the accident tolerant fuel (ATF) research is to develop advanced fuels/cladding with improved performance, reliability and safety characteristics during normal operations and accident conditions, while minimizing waste generation. Evaluating the performance of candidate ATF concepts is a topic of significant discussion among researchers, fuel vendors and utilities to ensure that the developed concepts can meet minimum performance and economic requirements, can be developed within a reasonable time, and can be approved for insertion as a lead fuel rod in a commercial reactor by the 2022 goal established in the U.S. Characterizing the performance enhancements of candidate ATF first requires understanding the performance of the current Zr-UO_2 system under equivalent operations and accident scenarios. Proper evaluation of each concept is dependent on development of data through focused out-of-pile and in-core experiments to support modeling of the fuel and cladding behavior in fuel performance and systems analysis codes; complementary irradiation of ATF concepts will be discussed in a separate paper. This paper will provide an overview of the key evaluation tools and evaluation scenarios currently being considered within the LWR community for ATF. The evaluation toolset includes standard neutronic and thermal-hydraulic analysis for normal operating conditions and transient/accident conditions and analysis of severe accident behavior using modified versions of the MELCOR code for preliminary concept screening. Development of advanced fuel performance analysis using the BISON application based on the Multi-physics Object-Oriented Simulation Environment (MOOSE) at Idaho National Laboratory (INL) has also been initiated. Evaluation scenarios (e.g. accident scenarios) currently being discussed for use across the international ATF development teams are also presented.

1. Introduction

The safe, reliable and economic operation of the nation's nuclear power reactor fleet has always been a top priority for the nuclear industry. Continual improvement of technology, including advanced materials and nuclear fuels, remains central to the industry's success.

1.1 Motivation

The current nuclear power industry is based on mature technology and has an excellent safety and operational record. The current UO_2 – zirconium alloy fuel system meets all

performance and safety requirements while keeping nuclear energy an economically competitive clean-energy alternative for the United States. With the exception of a few extremely rare events, the current fuel system has performed exceptionally well.

The goal of accident tolerant fuel development is to identify alternative fuel system technologies to further enhance the safety, competitiveness, and economics of commercial nuclear power. The development of an enhanced fuel system supports the sustainability of nuclear power, allowing it to continue to generate clean, low-CO_2-emitting electrical power in the United States. Details on the applicable development phases, key ATF attributes, and proposed evaluation metrics are included in previous publications [e.g., 1, 2].

1.2 Constraints

Any new fuel concept proposed for enhanced accident tolerance must be compliant with and evaluated against current design, operational, economic, and safety requirements [2]. The constraints associated with commercial nuclear fuel development and deployment that are applied to ATF designs include:

- *Backward Compatibility*— Compatible with existing fuel handling equipment, fuel rod or assembly geometry, and co-resident fuel in existing LWRs.
- *Operations*— Maintains or extends plant operating cycles, reactor power output, and reactor control.
- *Safety*— Meets or exceeds current fuel system performance under normal, operational transient, design-basis accident (DBA) and beyond design-basis accident (BDBA) conditions.
- *Front end of the nuclear fuel cycle*— Adheres to regulations and policies, for both the fuel fabrication facility and the operating plant, with respect to technical, regulatory, equipment, and fuel performance considerations.
- *Back end of the nuclear fuel cycle*— Cannot degrade the storage (wet and dry) and repository performance of the fuel (assuming a once-through fuel cycle); should consider potential issues associated with a possible future transition to a closed fuel cycle.
- *Economics*— Maintains economic viability with respect to additional costs (e.g., fabrication) and potential cost reductions realized through improved performance (higher burnup for extended cycles and power upgrades) or increased safety margin.

Analysis of proposed fuel and cladding concepts must be conducted using a number of different tools to evaluate potential performance under normal operating conditions, anticipated operational occurrences (AOOs), and DBAs, and prediction of possible behavior under BDBAs. It is also necessary to assess the possible magnitude of enhanced accident tolerance offered by a proposed concept. Analysis tools rely on availability of experimental data to properly model the performance of the candidate materials under each of the modeled scenarios. In many cases, only limited data is available for proposed fuels and cladding materials, or on the interaction between fuel and cladding or cladding and coolant. Hence, some analyses must apply approximations and assumptions early in the development stage before data becomes available. These approximations result in increased uncertainty in the predicted performance until improved data become available.

This paper provides an overview of the set of analysis tools that are currently being employed in screening and evaluation of ATF concepts in the U.S. Department of Energy Advanced Fuels Campaign.

2. Standard Analysis Suite

Design of an advanced fuel system demonstrating enhanced performance and safety relative to the current fuel system first requires understanding the current state-of-the-art fuel system performance under the various system operating regimes. These “regimes” include:

fabrication / manufacturability; normal operations and AOOs; postulated accidents (DBAs); severe accidents (BDBAs); and used fuel storage / transportation / disposition. This paper focuses on analysis over the three operational regimes; it does not address evaluation of fabrication or handling issues (either before or after irradiation).

An assessment of the potential beneficial impact or unintended negative consequences of candidate ATF concepts must address the obvious “fuel-specific” characteristics of the concept, but, perhaps more importantly, the assessment must address how implementation of the concept will affect reactor performance and safety characteristics. This assessment would include neutronics and thermal-hydraulics analyses to ensure that the reactor would operate as intended with the candidate fuel system. Coupled thermal hydraulic-neutronic analysis of candidate ATF concepts is essential in understanding the synergistic impact of the thermal properties and reactivity feedback.

2.1 Standard Screening Analyses for ATF Concepts

Standard evaluation of ATF concepts includes neutronics, thermal-hydraulic analyses, fuel performance, and detailed systems analyses. Each of these analyses is briefly described below. For additional detail on the code set employed in screening analysis for fuel and cladding concepts, see Todosow, et al. [3]. As noted in Bragg-Sitton et al. [2], the analysis fidelity and level of detail depends on the development stage of the modeled concept. During the initial “screening” stage analyses will have limited detail, based on the current state of knowledge for the concept. The level of detail may range from literature reviews and expert judgment through limited experiments and computational analyses. In evaluating the potential performance of an ATF concept, the goal is to have sufficient confidence in the assessment, given a reasonable investment of time and resources, that identified changes relative to the reference fuel system (UO_2-Zr-alloy) are known well enough to proceed with continued development, or to conclude that the concept should be modified or abandoned.

Researchers at Brookhaven National Laboratory (BNL) working within the U.S. DOE Advanced Fuels Campaign have developed and benchmarked a method for screening the reactor performance and safety characteristics of proposed advanced concepts [3]. Key elements in the methodology include: initial screening, three-dimensional core analysis, and transient analysis. Initial screening analysis entails infinite lattice calculations at the fuel assembly level to estimate ATF impact on cycle length/burnup, reactivity and control coefficients, etc. as a function of a selected fuel enrichment. Subsequent 3D core analyses include thermal-hydraulic and temperature feedback, providing a platform for fuel cycle analysis and time-dependent accident analysis. Analysis of selected transients is then conducted to provide an estimate of “coping time” (i.e. time to failure of key components) under the modeled conditions. Screening analyses must indicate a reasonable increase in the coping time for candidate ATF concepts relative to the reference fuel system (e.g. on the order of hours) to be considered “accident tolerant.”

Many light water reactor fuel concepts have been analyzed using the described screening analyses [3]. Some specific examples of the application of screening analyses to date include assessment of inert matrix fuel [4], fully ceramic microencapsulated fuel [5, 6], high-density ceramic composite fuels [7], candidate advanced cladding materials [8], and “drop-in” ceramic composite fuels [8]. These screening analyses provide information on the potential impact of fuel and cladding materials on reactor performance and safety characteristics. In addition, the screening analyses can help identify limitations in state-of-the-art modeling tools that may impact the ability to accurately model all aspects of some concepts. One specific example is identification of the need to implement best-estimate thermal models to accurately model fast transients with fully ceramic microencapsulated fuel [6].

The constraint of “backward compatibility” noted in section 1.2 means that a candidate fuel should be able to replace the current reference fuel without significantly impacting handling

operations, core thermal-hydraulics, emergency systems, etc. This requirement also places reasonable limitations on the possible enrichment of proposed fuels, recognizing that the current limit on fuel enrichment for commercial reactor applications is <5 w/o ^{235}U. Maintaining the backward capability constraint could restrict opportunities for performance optimization, but also reduces issues with licensing the fuel and implementing it in the current LWR fleet. The ability of concepts to adhere to this constraint can be addressed in the initial suite of screening analyses.

Initial Neutronic Screening Analyses: Initial analyses are often performed at the fuel-assembly level (especially for PWRs) using the linear reactivity model (or an appropriate enhancement) [9]. This model is used to estimate the cycle length and discharge burnup as a function of the number of batches in the fuel management scheme, power peaking, etc., and to estimate reactivity and control coefficients relative to the reference UO_2 configuration. Codes selected to conduct these analyses at BNL for candidate ATF include the deterministic TRITON/NEWT code [10] or Monte Carlo codes such as MCNP [11] and Serpent [12]. The Monte Carlo codes provide results that are essentially benchmark quality and are constrained only by the available nuclear data and the geometric detail and statistics employed in the modeling.

Three-Dimensional Core Analyses: Ultimately, core-level analyses are required to assess the potential benefits, as well as any negative aspects, associated with the implementation of a specific concept. The assembly-level lattice analyses described above provide the nuclear data (e.g., neutron cross sections, etc.) for subsequent full-core, three-dimensional analyses that include thermal-hydraulic and temperature feedback. These analyses can be used for fuel cycle analyses and some time-dependent accident analyses. For the ATF concepts both the thermal properties and the reactivity coefficients will change relative to the reference UO_2-Zr alloy system. BNL researchers have selected the PARCS nodal code for this analysis step [13]. Thermal hydraulic analyses can be performed at the assembly or core level for steady-state estimates of the Departure from Nucleate Boiling Ratio (DNBR) or Minimum Critical Power Ratio (MCPR). Codes that can be used for these analyses include VIPRE and COBRA. Coupled thermal-hydraulic – neutronic analysis of candidate ATFs is essential in understanding the synergistic impact of the thermal properties and reactivity feedback.

Transient Analyses: As noted above, ATF concepts must be evaluated over the full spectrum of AOOs, DBAs and BDBAs to estimate potential safety enhancements in addition to evaluating the potential performance enhancements under normal operating conditions. The full spectrum of accidents can be found in Chapter 15 of a standard Safety Analysis Report for the nuclear plant. Thermal hydraulic transients are typically modeled in the TRACE code, but PARCS (standalone) or PARCS-TRACE is used to study reactivity transients where 3-D kinetics effects are important. While this analysis is again limited by the available data on the proposed fuel system, it can provide a preliminary estimate of “coping time.”

One important caveat is that the screening analyses frequently require assumptions for the properties of candidate materials. The best available material properties are used in these analyses, but it is noted that material properties of candidate fuel and cladding materials depend on radiation damage, fraction of cold working, temperature, and other conditions. These dependencies may be unknown or have significant uncertainty for proposed novel candidate fuel or cladding materials, resulting in significant uncertainty in the predicted performance.

2.2 Advanced Fuel Performance Modeling Tools

Detailed measurement of material properties and characteristics is necessary to perform a fuel performance calculation. Behavioral models will include concept-specific material

properties, which must be derived from validated models, experimental data or assumptions. In some cases, the proposed fuel and cladding concept may be similar to the current fuel system, such that existing behavioral models can be applied with limited modification. However, cases in which the concepts deviate significantly from the current system will require development of material-specific behavioral models. The ATF concept development team would be expected to develop such models during the course of fuel and cladding development and testing. If the developed models are sufficient to support fuel performance analysis, then work can proceed using the available analysis tools with the correct behavioral models inserted.

The U.S. DOE Nuclear Energy Advanced Modeling and Simulation (NEAMS) program is developing an advanced modeling and simulation toolset for application in a wide array of problems. Several NEAMS tools function within the Multi-physics Object-Oriented Simulation Environment (MOOSE) [14] framework. MOOSE provides a high-level interface to sophisticated nonlinear solver technology, and it provides the framework upon which other analysis tools are created. The associated fuel performance code, BISON, is a finite element-based code applicable to a wide variety of fuel forms. It solves the fully-coupled equations of thermomechanics and species diffusion, for either 1D spherical, 2D axisymmetric or 3D geometries. MARMOT is a lower-length-scale code that interacts with BISON to predict the effect of radiation damage on microstructure evolution, including void nucleation and growth, bubble growth, grain boundary migration, and gas diffusion and segregation. In addition, MARMOT calculates the effect of the microstructure evolution on various bulk material properties, including thermal conductivity and porosity.

In the absence of specific data on the properties and behaviors of many of the candidate fuel and cladding materials, specific fuel performance modeling within BISON is limited. Hence, a preliminary sensitivity study was conducted at INL to identify trends and to determine the overall impact of the variation of multiple thermophysical parameters on fuel performance [15]. Using a simplified loss of coolant accident scenario, the impact of thermal conductivity, specific heat capacity, Young's Modulus and thermal expansion coefficient on the maximum creep strain, peak cladding temperature, maximum principle stress and maximum von Mises stress was calculated. Note that although creep is the primary nonlinear deformation mechanism for most cladding materials, this parameter does not lend itself to a simple parametric study. A specific creep model must be adopted in future studies of specific ATF candidates. This simplified study was essentially a proof-of-concept in using BISON to investigate ATF performance under a postulated accident condition. Despite the simplified approach to the program, the work points to a few key conclusions. Under LOCA conditions, it was found that creep strain is most sensitive to thermal conductivity and specific heat. Hence, new cladding materials with low thermal conductivity and low specific heat will have the least creep strain.

A recently initiated three-year research task under NEAMS is focused on expanding the existing BISON/MARMOT fuel performance modeling and simulation capability to enable evaluation of leading ATF concepts. Efforts will be made to expand the NEAMS fuel performance code BISON to perform a representative assessment of accident tolerance for selected concepts. Concept-specific material and behavioral models are expected to require experimental data generated by R&D activities under AFC, and it will also rely on lower-length-scale models developed under the NEAMS program (i.e. MARMOT).

3. Analysis of Severe Accident Behavior

Scoping simulations performed using a severe accident analysis code can be applied to investigate the influence of advanced materials on BDBA progression and to identify any existing code limitations. MELCOR is a systems-level severe accident analysis code that is being developed and maintained at Sandia National Laboratories in New Mexico (SNL/NM) for the Nuclear Regulatory Commission to support licensing activities. MELCOR includes the

major phenomena of the system thermal hydraulics, fuel heat-up, cladding oxidation, radionuclide release and transport, fuel melting and relocation, etc.

MELCOR is designed for current LWR core material configurations. As such, the code contains material property definitions for UO_2, Zircaloy, ZrO_2, steel, steel oxide and Inconel for the fuel, cladding, spacer grids, support plates and channel boxes. However, an effort to extend the MELCOR capability to include candidate accident tolerant cladding materials was undertaken beginning in fiscal year (FY) 2012. To date, INL researchers have added properties and behaviors for silicon carbide (SiC) and FeCrAl to the MELCOR reactor core oxidation and material properties routines [16]. These code versions also decouple material composition assignments, such that changes can be made to the composition of one component (e.g. the cladding) without affecting other core structures. These alternate materials may be selected as the sole cladding material or as a coating (or sleeve) on a standard metallic cladding (e.g. SiC sleeve over metallic cladding, such as a Zr-alloy; FeCrAl coating on Zr-alloy). Modifications to include additional fuel materials (beyond UO_2) have not yet been addressed.

Scoping evaluations for candidate materials can be performed using the revised MELCOR models if sufficient data is known from characterization activities. The manner in which a candidate cladding material oxidizes will determine which code version should be used (e.g. SiC or FeCrAl versions). The FeCrAl version of the code should be selected for candidate cladding materials that demonstrate parabolic oxidation behavior (similar to FeCrAl and other metals); in this case, the FeCrAl properties could be overwritten by the user to assess performance of an alternate candidate material. For materials that exhibit both parabolic oxidation and linear volatilization, similar to SiC, the SiC version should be employed, with material-specific properties entered as appropriate. Key material properties and behaviors necessary for MELCOR simulation include:

- Properties of the base material (e.g. SiC) and its oxide (e.g. SiO_2), as a function of temperature and irradiation
  - Melting temperature of the base material, oxide and any eutectics that may form
  - Thermal conductivity
  - Specific heat
  - Density
  - Emissivity
- Oxidation reactions, including oxidation rate, heat of reaction, reaction products, etc.
- Arrhenius relationship for parabolic oxidation rate behavior

In the absence of specific property and behavior data or significant uncertainty in the available data for selected materials, MELCOR can be employed to perform parametric studies. Key parameters, such as the oxidation rate or the material thermal conductivity, can be varied over a reasonable range to determine the overall impact on behaviors of interest, such as peak cladding temperature. In this manner the properties that most impact the accident performance of the fuel system can be identified.

The INL-modified version of MELCOR has been applied in the analysis of a pressurized water reactor accident (specifically Three Mile Island Unit 2 [TMI-2] and the associated loss of coolant accident sequence) to determine potential safety enhancements that could be realized with SiC or FeCrAl cladding materials [16]. Analysis of the impact of FeCrAl replacement of all zirconium alloy components in a boiling water reactor (specifically, Peach Bottom) station blackout scenario (as occurred at Fukushima Daiichi) has been conducted by Oak Ridge National Laboratory (ORNL) [17].

3.1 PWR Severe Accident Analysis

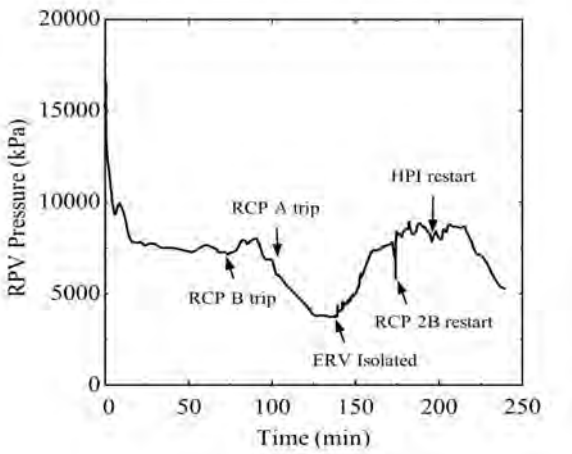

Figure 1. RPV pressure during the TMI-2 loss of coolant accident.

The reactor pressure vessel (RPV) pressure during the TMI-2 accident sequence is shown in Fig. 1; times at which reactor coolant system (RCS) pumps were tripped and restarted are shown. The INL-generated SiC code version substitutes the properties of CVD SiC for Zircaloy in MELCOR's reactor core oxidation (oxidation in air and steam) and material property routines (properties such as thermal conductivity, specific heat, density, emissivity, and heat of formation). See Merrill and Bragg-Sitton [18] for additional detail. The SiC version of MELCOR was benchmarked against available experimental data [e.g., 19] to ensure that present SiC oxidation theory in air and steam were correctly implemented in the code. The FeCrAl code version was also verified against available data to ensure that the code returns oxidation rates that match the adopted oxidation correlations [20]. Benchmarking of the FeCrAl version has not yet been completed.

As an example of the results that can be derived from MELCOR analysis, Fig. 2(a) shows the peak cladding temperature as a function of time during this accident sequence for both Zr-alloy and SiC cladding. The MELCOR-predicted cladding temperature is below the melting temperature of the silica protective scale that forms on the outer surface of SiC (~1873 K) and is well below the decomposition temperature of SiC (~3150 K), such that core geometry would be expected to be maintained. Fig. 2(b) shows results for FeCrAl cladding. In this case the predicted cladding temperature is estimated to be very close to the assumed failure criteria (FeCrAl melt temperature) and also approaches the assumed melting temperature of the FeCrAl oxide (1870 K). Data on the specific melting temperature of FeCrAl oxide is necessary to attain higher confidence in the potential that the FeCrAl cladding would remain intact in this scenario. Additional output information useful in evaluating potential safety enhancements include heat input due to cladding oxidation and total combustible gas production (e.g. H_2, CO, etc., depending on the cladding material selected). Note that the MELCOR analyses are only used for scoping evaluations early in the development of an ATF concept and are not intended to support down-select decisions.

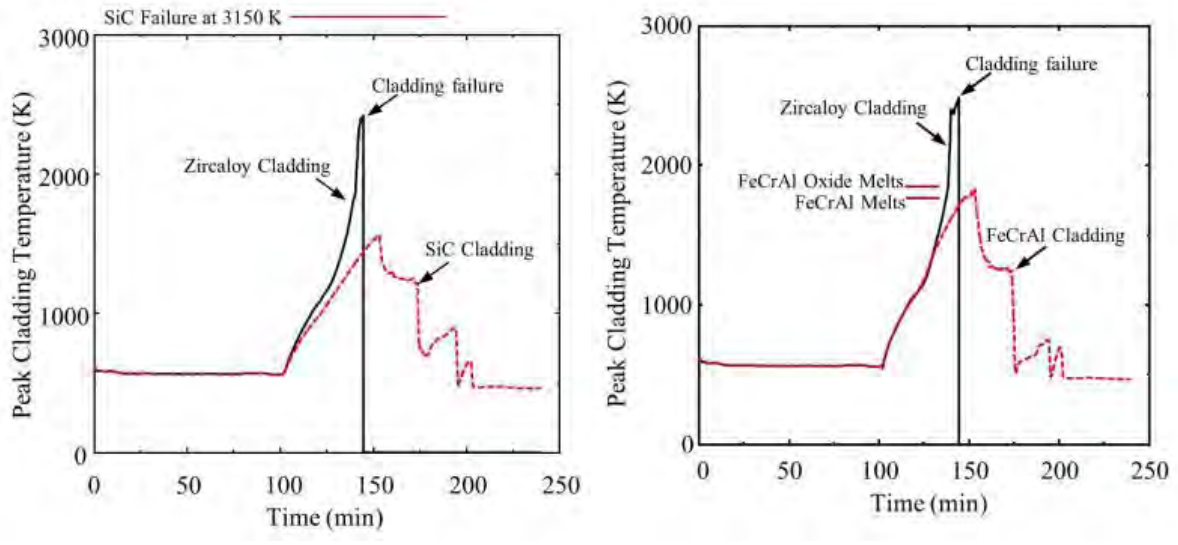

(a) (b)

Figure 2. MELCOR-calculated peak cladding temperature for Zircaloy, SiC and FeCrAl cladding during a TMI-2 event sequence.

3.2 BWR Severe Accident Analysis

MELCOR analyses have also been conducted for a baseline BWR case, namely the Peach Bottom plant (GE BWR4/Mark I) [21]. In this case several station blackout scenarios were modeled in which the loss of all AC power occurs at the time of scram, and DC power is lost at a specified time. This scenario is similar to what occurred at the Fukushima Daiichi plant in Japan. In this example, FeCrAl cladding material was modeled using the most recent material properties available including appropriate oxidation kinetics. Although additional material properties are still required (e.g. production of eutectics), the MELCOR evaluation has been useful in estimating the additional time to the onset of cladding melt and radionuclide release offered by FeCrAl cladding relative to Zircaloy. Other data tracked include the mass of combustible gases (H_2) produced and the cumulative energy release due to material oxidation in the core.

4. Evaluation Scenarios Under Consideration

As noted in section 3, preliminary INL and ORNL analysis of severe accident conditions modeled the TMI-2 and Fukushima accident scenarios. Selection of appropriate “illustrative scenarios” that can be employed across the international community is currently under discussion within the Nuclear Energy Agency (NEA) Expert Group on Accident Tolerant Fuels. This group is conducting work under three task forces: (1) Systems Assessment, (2) Cladding and Core Materials, and (3) Fuel Concepts. Scope for the Systems Assessment task force includes definition of evaluation metrics for ATF, technology readiness level (TRL) definition, definition of illustrative scenarios for ATF evaluation, parametric studies, and selection of system codes. Task forces 2 and 3 focus on compiling data on ATF materials currently under development.

Several countries are actively developing and testing ATF materials. In many cases, similar materials are being investigated in multiple countries. It is of interest to the international nuclear community to have these independent teams adopt common TRL definitions, adopt similar evaluation metrics, and apply similar evaluation scenarios. March 2015 discussions among the Systems Assessment task force members identified two simplified scenarios that can be applied by ATF development teams for LWR plants (PWR, BWR and VVER):

- *Station Blackout:* This scenario is postulated to occur with high system pressure and allowed to continue to the point of RPV failure.
- *Large-break LOCA:* This scenario provides a low-pressure condition in which coolant is lost while there is high decay heat in the reactor.

The proposed scenarios are intended to provide bounding cases for fuel performance. It is expected that each country or development team will utilize fuel performance and system analysis codes that are accepted within the associated organization to conduct these evaluations. All ATF evaluations under the selected accident conditions should be allowed to progress to the point of core failure in the analysis. This allows one to estimate the potential increase in coping time that might be offered by candidate ATF concepts and to assess potential outcomes should failure occur (e.g. if the fuel fails, how does it fail?). Pressure is a very significant parameter in the accident progression, as reflected in the selection of both a high-pressure and low-pressure scenario. Following completion of bounding analyses, researchers should perform parametric studies for these illustrative scenarios to develop a better understanding of the impact of additional variables. Such parametric studies could include variation of the point in the operating cycle that the accident occurs (how much burnup has been accumulated in the fuel?) and the time after reactor scram that core cooling is lost.

These illustrative scenarios will be documented in a future report issued by the NEA Expert Group.

5. Conclusions

Analysis of ATF concepts entails preliminary screening analysis, development of behavioral models to support fuel performance modeling and detailed system analysis. Existing tools can often be applied but may require significant assumptions due to limited data availability for the candidate materials. As more data becomes available material-specific behavioral models can be developed and employed in detailed analyses intended to predict the potential performance enhancements offered by an ATF concept over the reference fuel system (UO_2-Zr-alloy).

6. Acknowledgements

This manuscript has been authored by Battelle Energy Alliance, LLC under Contract No. DE-AC07-05ID14517 with the U.S. Department of Energy. The United States Government retains and the publisher, by accepting the article for publication, acknowledges that the United States Government retains a nonexclusive, paid-up, irrevocable, world-wide license to publish or reproduce the published form of this manuscript, or allow others to do so, for United States Government purposes.

7. References

[1] S. M. Bragg-Sitton, “Metrics for the Evaluation of Light Water Reactor Accident Tolerant Fuel,” in proceedings of the 2014 Water Reactor Fuel Performance Meeting, Sendai, Japan, paper 100143 (2014).

[2] S. M. Bragg-Sitton, et al. *Advanced Fuels Campaign: Enhanced LWR Accident Tolerant Fuel Performance Metrics*, February 2014, INL/EXT-13-29957, FCRD-FUEL-2013-000264 (2014).

[3] M. Todosow, N. Brown, A. Cuadra, L.-Y. Cheng, *Plan for Analyses to be Performed and the Methodology to be Used,* Brookhaven National Laboratory, FCRD-FUEL-2015-000174 (2015).

[4] W. J. Carmack, M. Todosow, M. Meyer, K. Pasamehmetoglu, “Inert matrix fuel neutronic, thermal-hydraulic, and transient behavior in a light water reactor,” *Journal of Nuclear Materials*, 352, pp. 276–284 (2006).

[5] N. R. Brown, H. Ludewig, A. Aronson, G. Raitses, M. Todosow, “Neutronic evaluation of a PWR with fully ceramic microencapsulated fuel. Part I: Lattice benchmarking, cycle length, and reactivity coefficients,” *Annals of Nuclear Energy*, 62, pp. 538–547 (2013).

[6] N. R. Brown, H. Ludewig, A. Aronson, G. Raitses, M. Todosow, “Neutronic evaluation of a PWR with fully ceramic microencapsulated fuel. Part II: Nodal core calculations and preliminary study of thermal hydraulic feedback,” *Annals of Nuclear Energy*, 62, pp. 548–557 (2013).

[7] N. R. Brown, A. Aronson, M. Todosow, R. Brito, K. McClellan, “Neutronic performance of uranium nitride composite fuels in a PWR,” *Nuclear Engineering and Design*, 275, pp. 393–407 (2014).

[8] N. R. Brown, M. Todosow, A. Cuadra, “Screening of advanced cladding materials and UN-U3Si5 fuel,” *Journal of Nuclear Materials*, 462, pp. 26-42 (2015).

[9] M. J. Driscoll, T. J. Downar, E. E. Pilat, “The Linear Reactivity Model for Nuclear Fuel

Management", American Nuclear Society, La Grange Park, Illinois (1990).

[10] Oak Ridge National Laboratory, *SCALE: A Comprehensive Modeling and Simulation Suite for Nuclear Safety Analysis and Design*, ORNL/TM-2005/39 (2011).

[11] Los Alamos National Laboratory, *MCNP-A General Monte Carlo N-Particle Transport Code*, Version 5, LA-UR-03-1987 (2005).

[12] J. Leppänen, M. Pusa, T. Viitanen, V. Valtavirta, T. Kaltiaisenaho, "The Serpent Monte Carlo code: Status, development and applications in 2013," *Annals of Nuclear Energy*, doi:10.1016/j.anucene.2014.08.024 (2014).

[13] T. J. Downar, Y. Xu, V. Seker, N. Hudson, *PARCS v3.0 U.S. NRC Core Neutronics Simulator Theory Manual*, University of Michigan Technical Report, (2012).

[14] D. Gaston, C. Newman, G. Hansen, D. Lebrun-Grandie, "MOOSE: A parallel computational framework for coupled systems of nonlinear equations," *Nuclear Engineering and Design*, 239(10), pp. 1768-1778 (2009).

[15] C. Smith, H. Chichester, J. Johns, M. Teague, M. Tonks, R. Youngblood, *Accident Tolerant Fuel Analysis*, Idaho National Laboratory, INL/EXT-14-33200 (2014).

[16] B. J. Merrill, S. M. Bragg-Sitton, P. W. Humrickhouse, *Status Report on Advanced Cladding Modeling Work to Assess Cladding Performance Under Accident Conditions*, Idaho National Laboratory, INL/EXT-13-30206 Rev. 1 (2014).

[17] L. J. Ott, K. R. Robb, D. Wang, "Preliminary assessment of accident-tolerant fuels on LWR performance during normal operation and under DB and BDB accident conditions," *Journal of Nuclear Materials*, 448(1–3), pp.520–533 (2014).

[18] B. J. Merrill and S. M. Bragg-Sitton, "SiC Modifications to MELCOR for Severe Accident Analysis Applications," in proceedings of the LWR Fuel Performance Meeting, Top Fuel 2013, Charlotte, NC, September 15-19, 2013, paper 8546.

[19] K. A. Terrani, B. A. Pint, C. M. Parish, et al, "Silicon Carbide Oxidation in Steam up to 2 MPa," *J. Amer. Cer. Soc.*, 97(8), pp. 2331-2352 (2014).

[20] B. A. Pint, K. A. Unocic, K. A. Terrani, "Effect of steam on high temperature oxidation behaviour of alumina-forming alloys," *Materials at High Temperatures*, 32(1-2), pp. 28-35 (2015).

[21] K. R. Robb, "Predicted System Response to Station Blackout Severe Accident in a Boiling Water Reactor Employing FeCrAl Cladding", poster presentation, NuMat 2014, Clearwater Beach, FL, Oct. 27 (2014).

TopFuel2015-A0025

NNO-2015-000013／PSNN-2015-0728

PROGRESS ON THE RESEARCH AND DEVELOPMENT OF INNOVATIVE MATERIAL FOR NUCLEAR REACTOR CORE WITH ENHANCED SAFETY

KAZUNARI OKONOGI, KAZUO KAKIUCHI
Isogo Nuclear Engineering Center, Toshiba Corporation
8, Shinsugita-cho, Isogo-ku, Yokohama 235-8523, Japan

YOSHINORI KATAYAMA, FUMIHISA KANO, KENICHI YOSHIOKA
HIROSHI MATSUMIYA, YUTAKA TAKEUCHI
Power & Industrial Systems R&D Center, Toshiba Corporation
8, Shinsugita-cho, Isogo-ku, Yokohama 235-8523, Japan

TATSUYA HINOKI, SOSUKE KONDO, MOONHEE LEE
Institute of Advanced Energy, Kyoto University
Gokasho, Uji, Kyoto 611-0011, Japan

NAOYUKI HASHIMOTO, SHIGEHITO ISOBE
Faculty of Engineering, Hokkaido University
N-13, W-8, Kita-ku, Sapporo 060-8628, Japan

Based on the lessons learned from the Fukushima Daiichi severe accident, accident-tolerant-fuel (ATF) development has been conducted by many institutions in the world. In Japan, Toshiba, Kyoto University and Hokkaido University formed a joint research team that has been pursuing the development of ATF with SiC material, financially supported by the Japanese government, via the Ministry of Education, Culture, Sports, Science and Technology of Japan (MEXT), since November 2012, with development to be completed in March 2016. This paper reports the interim results of the comprehensive study on SiC application to light water reactor core material in Japan. To date, the study has revealed that SiC material has significantly greater tolerance than Zircaloy of severe accident conditions and has identified items to be studied and resolved, such as corrosion resistance, irradiation effect and SiC material properties with a view to practical core and fuel design for commercial utilization.

1. Introduction

In the accident at Fukushima Daiichi nuclear power plant, oxidation of zirconium with high-temperature steam resulted in generation of plenty of reaction heat and hydrogen that caused core melting and explosions in the facility. In order to prevent such a severe accident, defense in depth to ensure the safety of the nuclear power plants in Japan is being discussed. Accident-tolerant-fuel (ATF), which is innovative technology is one of the concepts for enhancing the safety. Toshiba identified silicon carbide (SiC) ceramic as the most promising material for ATF, since SiC has less active characteristics in the presence of high-temperature H_2O, and is expected to be tolerant of severe accident conditions. Moreover, SiC has a smaller neutron absorption cross-section, which is advantageous feature in terms of neutron economy.

Several studies have already started with the aim of developing ATF. The idea of the ATF developments and some results of the studies have been presented at international conferences [1-9] and on US national laboratories' websites [10-13]. Toshiba has been

leading research and development projects to apply SiC composite to LWR cladding and BWR channel box. After 3.11, with the support of the Japanese government, a comprehensive and fundamental study on SiC commenced in 2011 in order to assess the applicability of SiC to LWR as ATF and is currently proceeding. The scoping study consists of the method of SiC monolithic and composite fabrication, SiC material property test, analysis of thermo-mechanical behavior of fuel rod, neutronics, and transient behavior of BWR core with SiC cladding and channel box.

This paper describes the progress of SiC material development, including the fabrication process, corrosion experiments, irradiation test by ion and electron beam, and analytical approach.

2. SiC sample fabrication

SiC material properties depends on the composition and the fabrication process. We fabricated plate samples of monolithic SiC with different processes, namely, chemical vapor deposition (CVD), liquid-phase sintering and reaction sintering, in order to screen the fabrication processes for SiC composite matrix. The details of liquid phase sintered (LPS) SiC samples are listed in Table 1. Those samples contain Al_2O_3 and Y_2O_3 additives to help solidification of SiC powder in the sintering process. The elemental powders were mechanically mixed at room temperature by ball mill or spike mill. The mixture of powders was hot pressed to liquid phase sintered SiC plate, at 1850°C with 20 MPa in argon atmosphere. All the samples subjected to the tests were prepared by Kyoto University.

Table 1: Details of raw materials of LPS SiC

Sample Index	Mechanical Alloying process	Composition of additives		
		Al_2O_3 [%]	Y_2O_3 [%]	Total [%]
LPS6	Ball mill	2.4	3.6	6
LPS12	Ball mill	4.8	7.2	12
SM_LPS3	Spike mill	1.2	1.8	3
SM_LPS6	Spike mill	2.4	3.6	6

3. SiC Property Test

3.1 Corrosion behavior under the simulated severe accident conditions

In order to confirm SiC's tolerance of severe accident conditions, the above-mentioned fabrication methods were compared by exposing SiC composite fabricated by those methods to high-temperature steam. The samples of CVD SiC and LPS SiC were exposed to 100% H_2O steam atmosphere at 1200°C and 1400°C for exposure time of 72 h. Zry-2 sample was also tested as a reference. Figure 1 shows the visual appearance of the samples after the corrosion test. CVD and LPS samples of SiC maintained their original shape and appeared to be somewhat shiny. On the other hand, Zry-2 sample was observed to be swollen and completely white as a result of full oxidation. From the metallography of cross-section of SiC sample, the oxidation penetrated the surface layer only to a depth of ~5 μm in the case of CVD. Figure 2 shows the weight gain of SiC samples vs steam temperature. The corrosion rate of SiC was confirmed to be less than 1/1000 of Zry-2, which means SiC has significant tolerance of severe accident conditions.

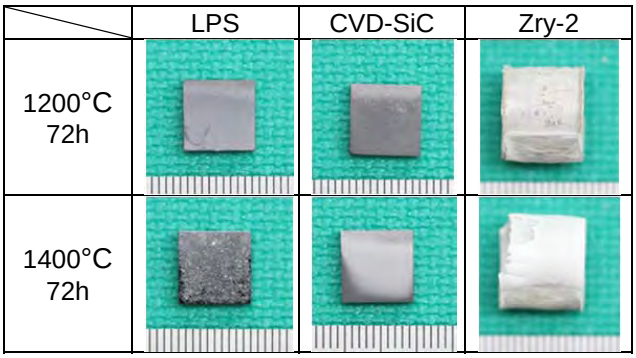

Figure 1. Visual appearance after corrosion test.

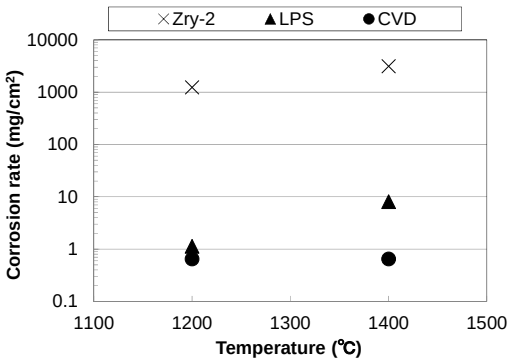

Figure 2. Corrosion rate as a function of the temperature.

3.2 Corrosion behavior under simulated normal operating conditions

The corrosion tests under simulated normal operation conditions were also performed for CVD SiC and LPS SiC samples in an autoclave. Three temperature points, 290°C/320°C/360°C, were selected to cover the current LWR coolant condition. Test samples were exposed for 168 hr with the dissolved oxygen concentration of 8 ppm. The system pressure was maintained at 20 MPa for all water temperature conditions.

The corrosion rate of water temperature dependence of for each sample is shown in Figure 3. This indicates, despite variations, that higher water temperature may accelerate corrosion of SiC. Figure 4 shows the effect of additive material concentration on the corrosion at the water temperature of 360°C. Apparently, the corrosion rate of LPS tends to significantly depend on the additive content relative to CVD. From the metallography study [2], it is presumed that the dissolution of the additive element along the grain boundary caused the corrosion rate to increase.

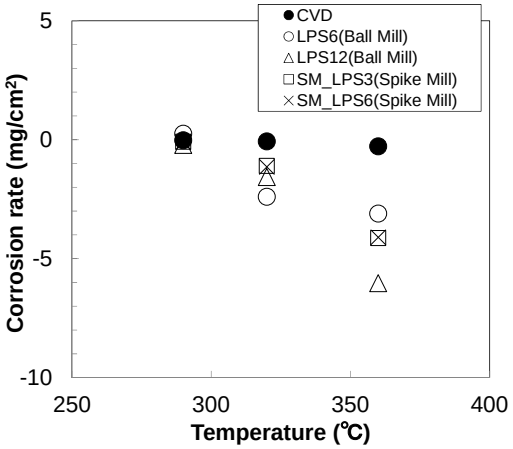

Figure 3. Corrosion rate vs water temperature (for 168 hr).

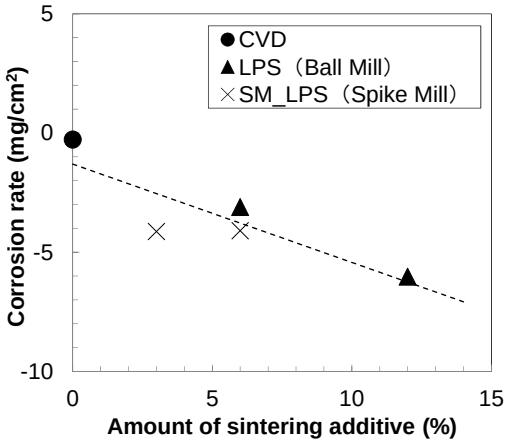

Figure 4. Corrosion rate vs Sintering additives (at 360°C, 168 hr).

3.3 Ion irradiation effect and corrosion test

Prior to the irradiation test in the test reactor, we studied the effect of the irradiation on SiC properties for high-purity sample of CVD SiC by utilizing ion accelerator. Samples were irradiated with 5.1 MeV Si ions up to a maximum of 2.5 DPA in the DuET facility of Kyoto University. The penetration depth is estimated to be approximately 2.5 μm from the surface of the sample. The two points of environment temperature, at 400°C/800°C, were selected. Figure 5 shows the swelling as a function of DPA. The swelling of the irradiated samples was insignificant, less than 40 nm, for both temperature conditions and tends to saturate with increasing DPA. After irradiation, the corrosion behavior under the simulated normal operation was examined. Figure 6 shows the surface observation after the ion irradiation and the corrosion test (at 320°C, 168 hr). It is observed that the corrosion was more significant at the irradiated area of the sample than at the un-irradiated area. The difference in thickness was about 3 μm.

From the above–mentioned results, the ion irradiation effect on the swelling of SiC is insignificant but may increase the corrosion rate under hot water condition.

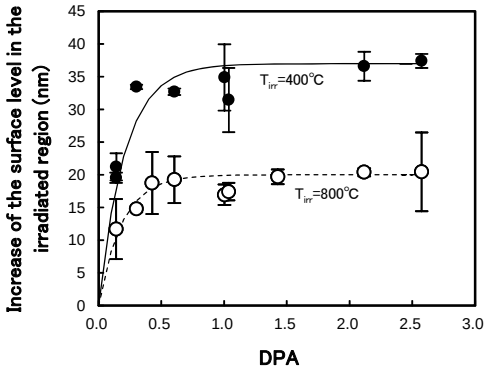

Figure 5. DPA dependence of swelling.

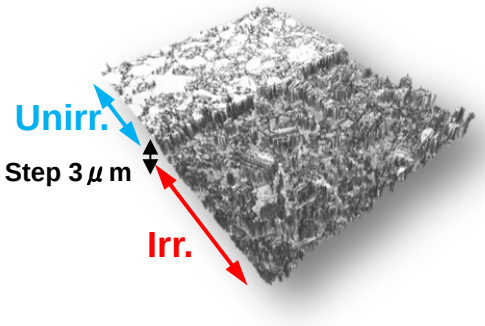

Figure 6. Irradiation Effect on hydrothermal corrosion of SiC.

3.4 Electron beam irradiation test with atmosphere control

In addition, the electron beam irradiation test was conducted by utilizing a transmission electron microscope in Hokkaido University, that enables *in-situ* observation of the influence of irradiation defects on the oxidation process. In the first step prior to the oxidation atmosphere test, we obtained fundamental data for the irradiation effect through the electron beam irradiations. in oxidation atmosphere. Figure 7 shows the number density of defect cluster after electron irradiation at 300-700°C estimated from TEM micrographs. To date, no significant defects have been detected above 400°C.

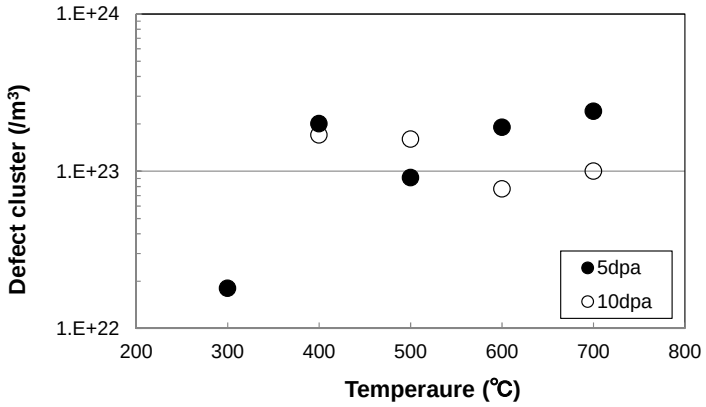

Figure 7. Dependence on the irradiation temperature of number density of defect cluster.

3.5 The effect on the structure of SiC composite material

We are developing an SiC composite, which consists of SiC fibers and SiC matrix, parallel to monolithic SiC. The first trial composite fabricated consisted of carbon-coated fibers bound by LPS SiC matrix. The corrosion test of this composite under simulated severe accident conditions showed significant deformation, as reported in[14]. The result of high-temperature steam exposure is shown in Figure 8. The composite did not keep the shape at 1200°C.

We judged that the surface friction force between fiber and matrix would influence the mechanical behavior. In the second step, we adopted bare SiC fiber instead of carbon-coated fiber in order to reduce the adhesion force between fiber and matrix. The aim is to allow the residual porous in the matrix to keep pseudo elasticity. Figure 9 shows the bending test result. No significant deterioration of the samples was observed for either test condition, exposure in the air at 800°C and 1100°C. In the next phase of this work, we intend to perform the corrosion tests for the composite in order to investigate the behavior under hot steam and water condition.

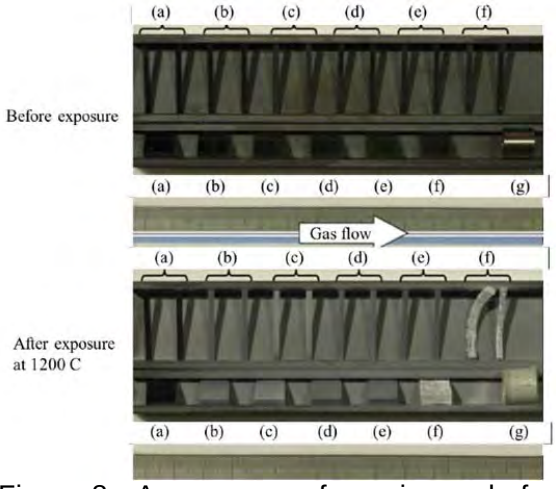

Figure 8 Appearance of specimens before and after 1200 °C steam exposure. ((a) CVD SiC, (b)-(e) LPS SiC, (f) SiC composite, (g)Zry-2)

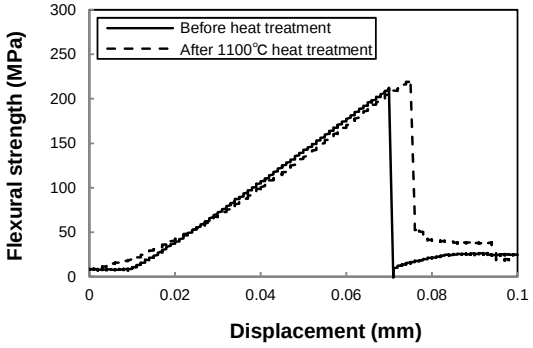

Figure 9. Bending test result of porous SiC composite before and after heat treatment.

4. Criticality test for SiC

From the standpoint of the core nuclear design, the equivalent accuracy in neutronics is required to the SiC fuel relative to the conventional fuel. The criticality experiment was conducted using Toshiba Nuclear Critical Assembly (NCA) for different core configurations in order to confirm the reactivity characteristics of SiC. As shown in Figure 10, special test rods, namely, solid SiC bars, aluminum bars or “air rods,” were inserted in the square UO_2 rod lattice of the test region to vary the neutron spectrum. Figure 11 shows the comparison of SiC reactivity worth for each configuration between the experiment and Monte Carlo analysis by *MCNP* with two sets of cross-section library (*ENDF/B-VII.1* and *JENDL-4.0*) as a parameter. It indicates that the analysis tends to slightly overestimate the reactivity for harder neutron spectrum core configuration relative to well- moderated configuration. We performed sensitivity analysis for cases-1 and 2 to clarify the reason for the tendency. From the analysis, absorption cross-section of 28Si(N,γ) and the scattering cross-section of C and Si were the main cause of the reactivity difference between the test data and the Monte Carlo calculation. Commercial utilization of SiC fuel material would necessarily involve a re-evaluation of the cross-section library of SiC and C [15].

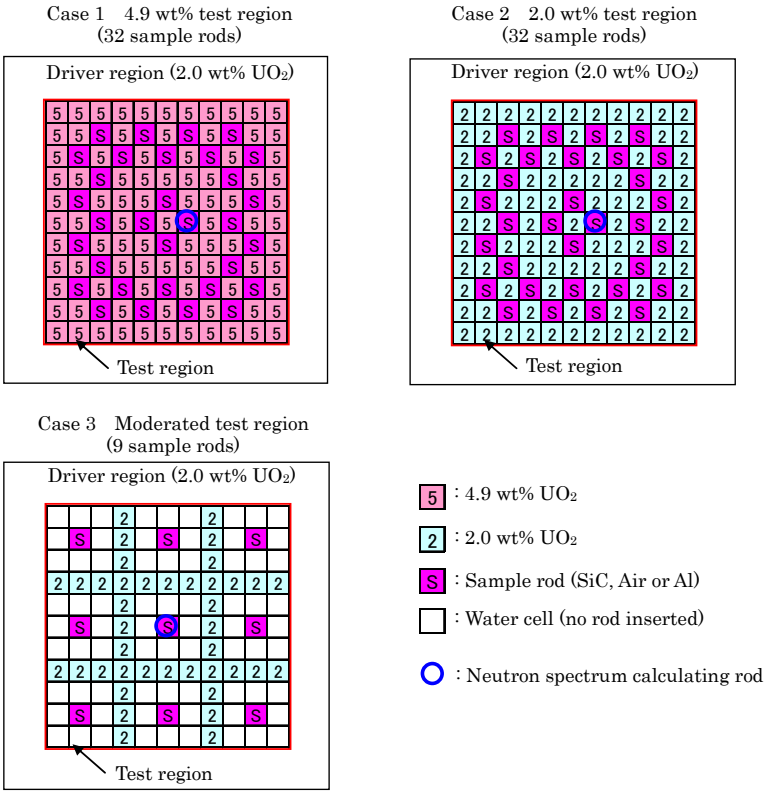

Figure 10. NCA core configurations for SiC reactivity worth measurement.

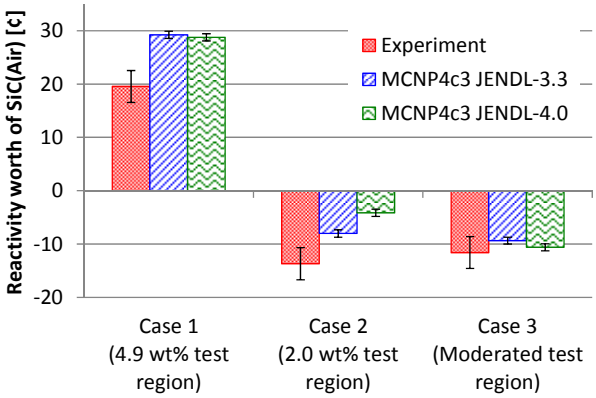

Figure 11. The reactivity worth of SiC (Air). The error bars with experimental values are estimated to be 3 ¢ and those with calculation values are statistical error (1σ).

5. Development of Joint Technology

In the fabrication process of SiC cladding for fuel rods, it is essential to develop the joint technology of cladding pipe and end plug to seal the fuel rod containing uranium pellet. Considering the changes in material properties during irradiation in a reactor, such as thermal expansion and elongation, the cladding and end-piece should be made of same material.

We selected the spark plasma sintering method that enabled the joining of SiC and SiC without any filler material. The test apparatus for joining was developed and the preliminary joining test is being performed as shown in Figure 12. Currently, we are studying the effect of joining parameters, such as plasma temperature and the pressing force, to optimize the joint process.

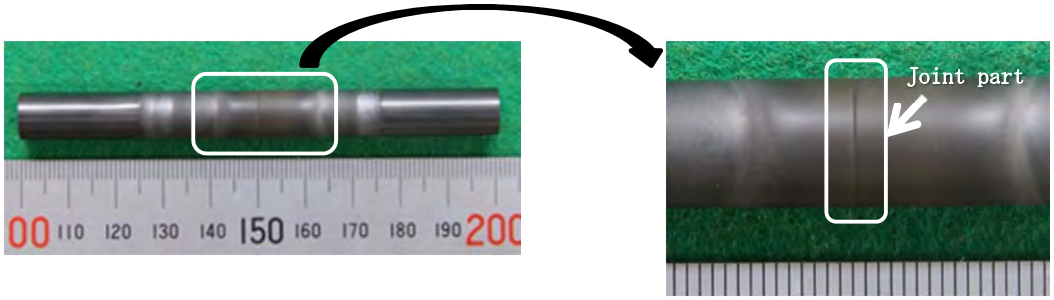

Figure 12. Preliminary joining test results

6. Analytical Study

6.1 Thermo-mechanical behavior in normal operating conditions

We have attempted an analytical study of the behavior of the fuel rod with SiC cladding toward burnup by using a fuel performance analysis code, *FEMAXI-6* [16], developed by JAEA. In order to reflect the SiC characteristics in *FEMAXI* code, we developed a model for evaluating the thermal mechanical properties of SiC, including corrosion of cladding, based on our experiments and references [17-19]. For example, the corrosion characteristics were

assumed to be proportional to exp(-E/RT), whose “T” indicates the temperature of the cladding and “E/R” is constant. This model was incorporated into *FEMAXI* with other SiC properties. Figure 13 shows the cladding hoop stress and corrosion depth history vs burnup up to 75GWd/tU, regarded as a typical performance of the SiC cladding behavior. The corrosion increased almost linearly towards burnup and reached a depth of about 30μm at EOL. These performances imply that SiC cladding does not have a fatal property in terms of the application to LWR fuel. The fuel rod mechanical analysis is to be continued, reflecting the latest test property data of various types of SiC.

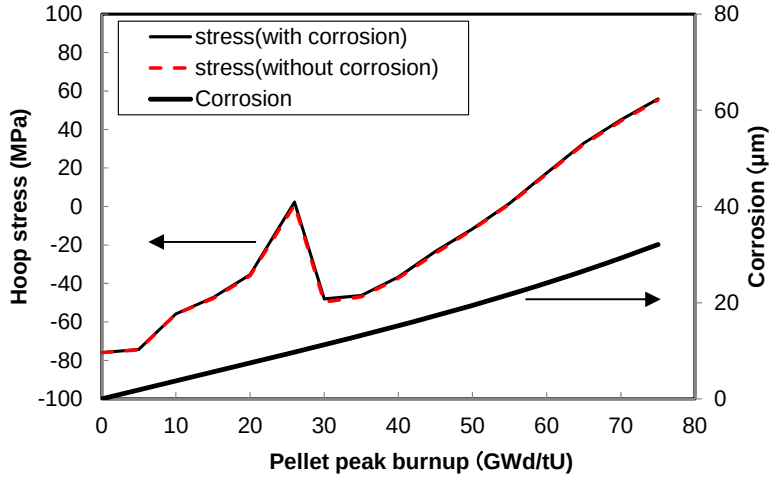

Figure 13. Cladding hoop stress and corrosion depth vs pellet peak burnup.

6.2 Heat-up analyses of SiC in severe accident conditions

It is expected that the metal-water reaction of SiC cladding will progress more mildly than that of Zry tube. Accordingly, the heat and hydrogen generation by the reaction may decrease in the case of accidents in which the core becomes uncovered.

In order to confirm the above-mentioned expectation quantitatively, we carried out the fuel heat-up analysis using the best-estimate safety analysis code under the severe accident conditions. We developed the model of the metal-water reaction of SiC proposed by ORNL, shown in Figure 14 [20], and incorporated it into the fuel rod heat transfer model of the best-estimate safety analysis code. The Zry-water reaction model is the coupled model of the Cathcart and Baker-Just models. Geometrically modeling the typical fuel assembly of BWR, we implemented the severe accident simulation for the uncovered fuel condition by withdrawing water from the bottom of the assembly. Figure 15 shows the oxidation mass response for each cladding material, assuming the successful depressurizing operation during the accident, and then the progress of the fuel heat-up, shifting to the low-pressure condition. It can be seen that the amount of the oxidation mass of SiC is suppressed to within one percent of that of the Zry cladding fuel. As the fuel temperature is attributable mainly to the decay heat, SiC fuel rises much more slowly than Zry fuel and did not reach the melting temperature of the fuel pellet. The hydrogen generation mass was only one sixtieth of that of Zry cladding fuel.

From this analysis, compared with Zry, SiC cladding has significantly greater tolerance of severe accident conditions.

$$\frac{dx}{dt} = \frac{\alpha^2 k_p}{2\rho^2 x} - \frac{k_l}{\rho}$$

$$k_p = p \cdot exp\left(a_p + \frac{E_p}{RT}\right)$$

$$k_l = v^{0.5} p^{1.5} \cdot exp\left(a_l + \frac{E_l}{RT}\right)$$

x: oxide thickness *T:* temperature *p* pressure
v: vapor-phase rate ρ*:* film density of oxidation $\alpha = 3.006$
R: gas constant $a_p/a_l/E_p/E_l$: fretting constant

Figure14. Equation in metal-water reaction of SiC proposed by ORNL.

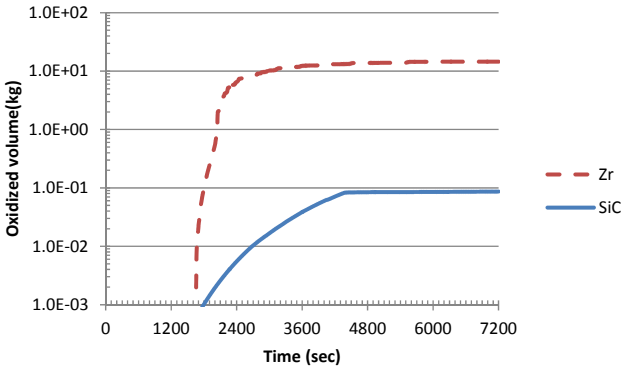

Figure 15. Oxidation mass response during the severe accident after the success of depressurization.

7. Summary and conclusion

A comprehensive feasibility study on silicon carbide for the application to LWR fuel is currently being performed. To date, the results of experiments and simulation analysis have revealed that, compared with conventional Zry, the application of SiC offers significant advantages in severe accident conditions. Therefore, SiC is considered to be the most promising candidate for accident-tolerant fuel to enhance the safety of LWR. On the other hand, with regard to SiC characteristics, corrosion behavior strongly depends on the fabrication process and the environment, and more detailed study is essential to clarify the mechanism under various fabrication and environmental conditions. The effect of neutron irradiation on SiC characteristics in the test reactor is important too.

With regard to future work, we will continue the study on the fabrication process for SiC composite design in order to optimize the SiC characteristics and manufacturability for cladding tube and channel box. In addition, we also intend to enhance the analytical approach for core/fuel design and safety analysis technology.

8. Acknowledgments

This paper includes the results of “Research and Development of Innovative Technologies for Nuclear Reactor Core Material with Enhanced Safety” entrusted to Toshiba by the Ministry of Education, Culture, Sports, Science and Technology of Japan (MEXT).

9. References

1. S. RAY, E. LAHODA and Peng Xu, “Progress on the Westinghouse Accident Tolerant Fuel Program”, Proc. WRFPM 2014, September 14-17, 2014, Sendai, Japan.
2. Y. Kawaharada, F. Kano, Y. Tsuchiya, K. Kakiuchi , K. Okonogi, S. Higuchi, T. Hinoki, N. Hashimoto and S.Ohnuki, “Research and Development of Innovative Technologies for Nuclear Reactor Core Material with Enhanced Safety”, Proc. WRFPM 2014, September 14-17, 2014, Sendai, Japan.

3. S. Kondo, M. Lee, T. Hinoki, Y. Tsuchiya, Y. Kawaharada, F. Kano, “Irradiation damage effect on corrosion rates of SiC in hot water”, Proc. WRFPM 2014, September 14-17, 2014, Sendai, Japan.
4. K. Kitano, Y. Ban, S. Sakurai, F. Inoue, M. Uchihashi, and M. Ukai, “Analysis of the Behavior of BWR Fuel and Core with SiC Cladding and Channel Box”, Proceedings of ICAPP 2014, Charlotte, USA, April 6-9 (2014).
5. B. CHENG, “Fuel behavior in severe accidents and Mo-alloy based cladding design to improve accident tolerant”, Transaction of Top Fuel 2012, Manchester, UK, September 2–6 (2012).
6. S. RAY, E. LAHODA and F. FRANCESCHINI, “Assessment of different materials for meeting the requirements of future LWR fuel designs”, Transaction of Top Fuel 2012, Manchester, UK, September 2–6 (2012).
7. K.A. TERRANI, G. W. CHINTHAKA SILVA, J.R. KEISER, M.P. BRADY, T. CHENG, B.A. PINT and L.L. SNEAD, “High temperature oxidation of Silicon carbide and advanced iron-based alloys in steam-hydrogen environments”, Transaction of Top Fuel 2012, Manchester, UK, September 2–6 (2012).
8. K. YUEH et al., “Silicon carbide composite for BWR channel application”, Transaction of Top Fuel 2012, Manchester, UK, September 2–6 (2012).
9. E. LAHODA and S.C. Johnson, “Challenges in the Development of Silicon Carbide Advanced Fuel Cladding for Light Water Reactor Application”, Proceeding of 2011 Water Reactor Fuel Performance Meeting, Chengdu, China, September 11-14 (2011).
10. I. J. ROOYEN, Pre-Irradiation Testing and Analysis to Support the LWRS Hybrid SiC-CMC-Zircaloy-4 Unfueled Rodlet Irradiation, INL/EXT-12-27189 Revision 1, Idaho National Laboratory, January (2013).
11. Y. Katoh, K. A. TERRANI, and L. L. SNEAD, “Systematic Technology Evaluation Program for SiC/SiC Composite-based Accident-Tolerant LWR Fuel Cladding and Core Structures”, ORNL/TM-2014/210, Oak Ridge National Laboratory, May (2014).
12. S. M. BRAGG-SITTON, Advanced Fuels Campaign Light Water Reactor Accident Tolerant Fuel Performance Metrics, Fuel Cycle Research & Development, INL/EXT-13-29957, Idaho National Laboratory, February (2014).
13. L. J. Ott, K.R. Robb, and D. Wang, “Preliminary assessment of accident-tolerant fuels on LWR performance during normal operation and under DB and BDB accident conditions”, Journal of Nuclear Materials 448 (2014) 520-533, Oak Ridge National Laboratory.
14. T. Hinoki et al., “EFFECT OF CONSTITUENTS OF SILICON CARBIDE COMPOSITES ON OXIDATION BEHAVIOR” IAEA Technical Meeting on Accident Tolerant Fuel Concepts for LWR (In progress)
15. H. Matsumiya et al., “Reactivity measurements of SiC for accident-tolerant fuel,” Progress in Nuclear Energy, DOI: 10.1016/j.pnucene.2014.07.030
16. M. SUZUKI and H. SAITOU, Light Water Reactor Fuel Analysis Code FEMAXI-6 (Ver. 1) -Detailed Structure and User’s Manual-, JAEA-Data/Code 2005-003, Japan Atomic Energy Agency, Japan (2006).
17. L.L. Snead et al.,”Handbook of SiC properties for fuel performance modeling,” J. Nucl. Mater., 371(2007)329.
18. Y. Katoh et al., “Property tailorability for advanced CVI silicon carbide composites for fusion,” Fusion Eng. Des., 81(2006)937.
19. M. Ben-Belgacem et al., “Thermo-mechanical analysis of LWR SiC/SiC composit cladding,” J. Nucl. Mater., 447(2014)125.
20. K. Terrani, et al., “Silicon Carbide Oxidation in Steam up to 2 MPa”, J. Am. Ceram. Soc.（2014）

LONG-TERM CORROSION BEHAVIOR AND MECHANICAL PROPERTY OF SILICON CARBIDE FOR PWR FUEL CLADDING APPLICATIONS

W.-J. KIM, D. KIM, H.G. LEE, J.Y. PARK
Nuclear Materials Development Division, Korea Atomic Energy Research Institute
989-111 Daedeok-daero, Yuseong-gu, Daejeon 305-353 – Republic of Korea

J.H. Park
LWR Fuel Technology Division, Korea Atomic Energy Research Institute
989-111 Daedeok-daero, Yuseong-gu, Daejeon 305-353 – Republic of Korea

ABSTRACT

Recently, there are growing efforts on applying the SiC_f/SiC composites to pressurized water reactor (PWR) fuel cladding because of their potential accident tolerance properties such as an excellent high-temperature mechanical strength and a superior oxidation resistance against high-temperature steam under severe accident conditions. In this study, we evaluated a long-term corrosion behavior of CVD SiC ceramics up to 210 days under PWR-simulating water conditions with and without the control of dissolved hydrogen. In the corrosion test of CVD SiC in 360°C water, the dissolved hydrogen dramatically reduced the corrosion rate of SiC compared with the water condition without the dissolved hydrogen. It was revealed that the dissolution of the surface oxide of SiC primarily contributed to the weight loss at the initial stage of corrosion. Further weight loss hardly occurred because the dissolved hydrogen effectively retarded the formation of surface oxide layer. We also evaluated the hoop strength and fracture behavior of the SiC composite tubes with a triplex structure. The highest fiber volume fraction was obtained using Tyranno SA3-0.8k with the dense winding patterns such as bamboo-like mosaic pattern, which resulted in the high hoop strength compared to other fibers of Tyranno SA3-1.6k and Hi-Nicalon Type S.

1. Introduction

Silicon carbide (SiC) ceramics and composites have attractive properties regarding nuclear applications, including the excellent high temperature properties, irradiation tolerance, inherent low activation and other superior physical/chemical properties [1]. Therefore, they have been considered for use as reactor core materials in various types of advanced nuclear reactors [2-5]. In recent years, there have also been efforts on applying the SiC_f/SiC composites to the pressurized water reactor (PWR) fuel cladding and guide tubes as well as channel boxes for fuel assembly of the boiling water reactor (BWR) [6,7].

SiC ceramics show an outstanding oxidation resistance and a low hydrogen liberation rate in hot steam compared with the current Zr alloys, which promise larger safety margins under severe accident conditions [8]. Moreover, its high temperature strength and stability under high neutron doses also provide high burn-up capability [9]. In spite of the potential benefits of the SiC composite cladding, there are a lot of technical issues such as the fabrication of thin-walled long tubes, the hermetic joining of end-cap seals, capability of fission products retention, and corrosion under the normal operating condition of PWRs [1,7,10,11].

In this study, we investigated the effect of water chemistry on the corrosion behavior of CVD SiC, analogous to the outermost environmental barrier coating of the triplex composite tube, under simulated PWR primary water condition. The corrosion data were compared with and without the control of dissolved hydrogen. In addition, the SiC triplex tubes which consisted of a monolith SiC inner layer, a SiC_f/SiC composite intermediate layer and a monolith SiC outer layer were fabricated by the chemical vapor processes such as CVD and CVI. Influences of filament winding methods, type of SiC fibers on hoop stress of the triplex

tubes were investigated. The damage process during the hoop tests were examined via microstructure observation.

2. Experimental Procedure

2.1 Evaluation of corrosion behavior of CVD SiC

Commercial CVD β-SiC (99.9995%, Morgan Technical Ceramics, Hudson, NH) was used for the corrosion tests. Plate specimens with a dimension of 10 x 10 x 3 mm^3 were machined and mechanically ground using a diamond disk. Corrosion tests were carried out for up to 210 days using a simulated PWR water loop in which water was deoxygenated and pressurized at 360°C under 20 MPa. To simulate the PWR primary water chemistry, the dissolved oxygen and the dissolved hydrogen were maintained to be below 5 ppb and at approximately 2.7 ppm (35 $cm^3/kg \cdot H_2O$), respectively. Deionized water was treated at pH 6.4 with 2.2 ppm LiOH and 1200 ppm H_3BO_3, as listed in Table 1. Our previous experiments [12] performed without the control of dissolved hydrogen had a minor difference in pressure and pH from the water condition in this study as shown in the Table 1. The weight change after each test duration was averaged from three specimens measured using an electronic balance with an accuracy of 0.01 mg.

Table 1. Corrosion test conditions of CVD β-SiC

	Temp. (°C)	Pressure (MPa)	DO (ppb)	DH (ppm)	pH at RT	$LiOH/H_3BO_3$ (ppm)
PWR-simulating loop (without DH control)	360	18.5	< 5	-	6.8	2.2/650
PWR-simulating loop (with DH control)	360	20	< 5	~ 2.7	6.3 – 6.5	2.2/1200

The surface microstructure before and after the corrosion test was analyzed using a scanning electron microscope (SEM). The surface roughness was measured using an atomic force microscope (AFM). Any phase formation on the surface after the corrosion test was characterized using a glancing-angle X-ray diffractometry (GAXRD). The chemical composition of the surface was analyzed using an X-ray photoelectron spectroscopy (XPS) to identify any chemistry change on the surface of the corroded specimens.

2.2 Fabrication and mechanical property of SiC composite tubes

A monolith SiC inner layer was uniformly deposited with a thickness of about 320 μm by a chemical vapor deposition method using methyltricholorosilane (MTS, CH_3SiCl_3) onto the high purity graphite rods with 8.5 mm in diameter and a length of 100 mm. Then the SiC fibers were applied to a SiC-coated cylindrical mandrel by a filament winding method. SiC fiber bundles (tows) consisting of 0.5 to 1.6k filaments were provided on a spool under a little tension which was generated only by the friction of the fiber supplying system. Helical layers of 1 – 2 fly covered the mandrel. The commercial generation III SiC fibers such as Tyranno SA3 and Hi-Nicalon Type S were used in this study. For the fabrication of a composite layer, we varied the fiber winding patterns and angles as well as the type of fibers. A detailed description of the fiber winding method can be found in our previous report [13].

After the filament winding, pyrolytic carbon (PyC) was deposited as an interphase of the SiC_f/SiC composite onto SiC fibers by dehydrogenation of CH_4 using a CVD method. For the infiltration of SiC matrix phase, the isothermal CVI was processed at 1000°C at the low pressure of 3.3 kPa to reduce density gradient to the radial direction of the tubular specimens. Finally a SiC outer layer was deposited by a CVI method with the same conditions to the matrix infiltration in sequent. The SiC outer layer exhibited a thickness around 40 μm.

After removal of graphite mandrel, the polyurethane plug with 8.45 mm in diameter and a length of 22 mm was inserted into the tubular specimen. Hoop stress of the tubular specimens with dimension of a length of 30 mm, an inner diameter of 8.5 mm, and an outer diameter of 9.6 – 10.1 mm was measured by compressing the polyurethane plug using screw driven universal testing machine (Instron 4465, load cell capacity = 5 kN). Axial pressure was applied with loading rate of 0.01 mm/s to the cylindrical polyurethane plug. Radial displacement measurements were made by attaching four displacement transducers (Kyowa, Co. Ltd) to the central section of the outer tube surface. Hoop stress of tubular SiC composite specimens, σ_θ, was calculated by the following equation [14],

$$\sigma_\theta = \frac{r_i^2 P}{r_o^2 - r_i^2}\left(1 + \frac{r_o^2}{r_i^2}\right)$$

where P is the internal pressure, r_i and r_o are the inner and outer radii of the tubular specimens, respectively. Contact stress was typically 50 to 100 N which was determined at the increasing point of radial displacement.

3. Results and Discussion

3.1 Corrosion behavior of CVD SiC in PWR-simulating water

Fig. 1 shows the weight change of the CVD SiC specimens after corrosion tests in 360°C deoxygenated water with the dissolved hydrogen content of 2.7 ppm. The corrosion data of CVD SiC obtained without the control of dissolved hydrogen are also included for the purpose of comparison. According to our previous results [12], the corrosion rate was much higher in the static autoclave containing several ppm of dissolved oxygen than in the loop test, in which the dissolved oxygen content was maintained less than 5 ppb. However, there was also a considerable amount of corrosion occurred even in the loop test without controlling the dissolved hydrogen as indicated in Fig. 1. On the other hand, the weight loss was dramatically reduced, less than 0.03 mg/cm^2 after 210 days of corrosion test, in the PWR-simulating water loop test with the control of dissolved hydrogen. The corrosion rates calculated by a least square fitting method were 9.4 x 10^{-5} and 3.5 x 10^{-2} mg/cm^2·day for the corrosion tests with and without the control of dissolved hydrogen, respectively. The corrosion rate decreased by about four hundred times by the injection of hydrogen in the PWR water.

Fig. 1. Corrosion behavior of the CVD SiC specimens in the 360°C PWR-simulating water loops with and without controlling the dissolved hydrogen.

Fig. 2 shows the SEM micrographs for the surfaces of the CVD SiC specimens before and

after the corrosion tests in the simulated PWR water environment with the control of dissolved hydrogen. Although the specimens have rather rough surfaces because we have not applied a fine polishing for the preparation of test specimens, the surface microstructures are hardly changed after corrosion tests for up to 210 days. Compared with the previous corrosion test results [12,15-18], it is clear that the dissolution of SiC is extremely limited. A preferential corrosion at grain boundaries or a pitting corrosion is hardly observed because of the extremely low corrosion rate with the control of dissolved hydrogen.

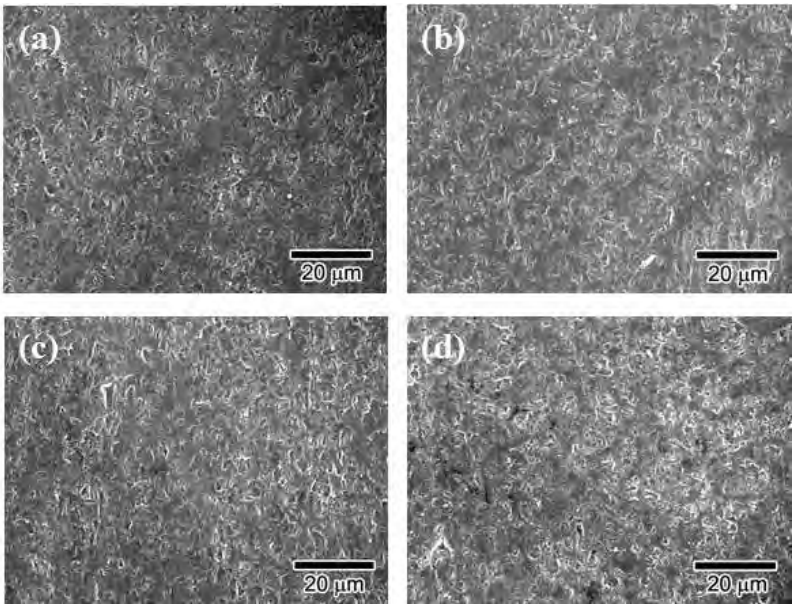

Fig. 2. SEM micrographs of the CVD SiC specimens before (a) and after the corrosion tests for 7 (b), 30 (c), and 210 (d) days in the PWR-simulating water with controlling the dissolved hydrogen.

Figs. 3 and 4 display the AFM surface morphology and roughness of CVD SiC specimens, respectively, before and after corrosion tests. In general, the corrosion of SiC or the formation of SiO_2 causes an increase in surface roughness because of the local corrosion such as pitting or grain boundary attacks and the inhomogeneous growth of SiO_2 [3,19]. However, we cannot observe any meaningful change in surface morphology and roughness after the corrosion tests from the AFM results in Figs. 3 and 4, supporting the absence of a preferential corrosion at grain boundaries or a pitting corrosion.

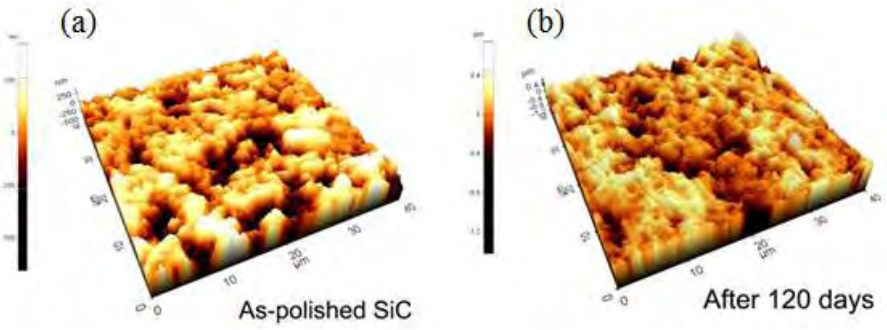

Fig. 3. AFM surface morphologies of the as-polished (a) and the corroded CVD SiC specimens after the corrosion test for 120 days (b).

Fig. 4. Changes in the surface roughness determined by AFM analyses as a function of the corrosion time.

Any phase change of the surface of the corroded specimens was analyzed using glancing-angle X-ray diffraction. Fig. 5 shows the XRD results of CVD SiC before and after the corrosion tests in the PWR-simulating water with the control of dissolved hydrogen. The as-polished SiC specimen generally contains native oxide consisting of amorphous SiO_2 and SiO_xC_y on the surface as will be shown in the XPS analysis. However, only β-SiC was detected in the as-polished specimen despite the low incident angle of the X-ray beam because the thickness of the native oxide was very thin. In addition, no other phase except for the β-SiC was detected in the XRD patterns of the corroded specimens irrespective of the corrosion time.

Fig. 5. Glancing-angle XRD patterns of the CVD SiC specimens before and after the corrosion tests in the PWR-simulating water with controlling the dissolved hydrogen.

Fig. 6 shows the chemical states on the surface of CVD SiC determined by XPS analysis before and after corrosion tests. The Si $2p_{1/2,3/2}$ peak of the as-polished specimen can be distinguished by three peaks, which are attributed to the very thin native oxide and the SiC bulk beneath the oxide layer, as shown in Fig. 6(a). The native oxide Si $2p_{1/2,3/2}$ peaks consist of Si-O bonds originating from SiO_2 and SiO_xC_y peaks located at 103.2 and 102.2 eV, respectively. The Si-C peak from the SiC bulk is located at 100.5 eV. After corrosion test for 7 days, the Si $2p_{1/2,3/2}$ peaks correspond to the native oxide completely disappeared, and only a peak for the Si-C bond remained, as shown in Fig. 6(b). The XPS spectra did not show any change with the further increase of corrosion time.

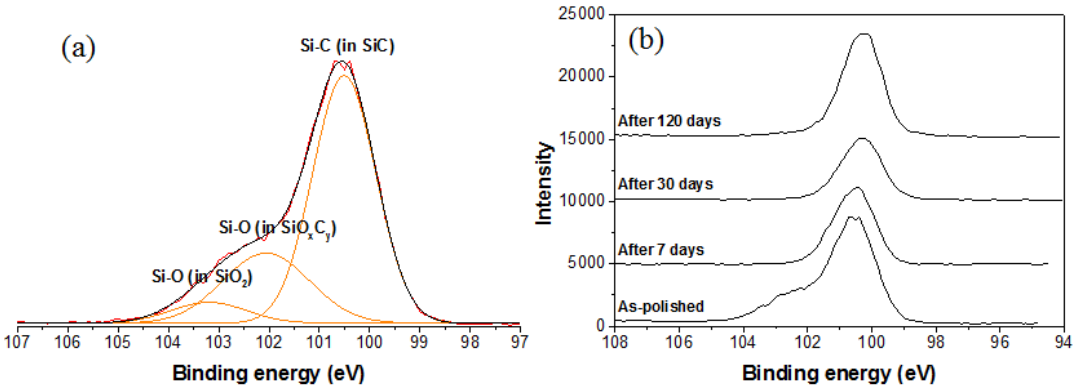

Fig. 6. XPS analysis results of the as-polished (a) and the corroded (b) CVD SiC specimens.

Based on the XPS and weight measurement results in this study, the hydrogen injection is not very effective in preventing the oxide layer from dissolution into the water. On the other hand, the dissolved hydrogen is believed to effectively retard the formation of the oxide or hydroxide layer and thereby significantly reduce the corrosion rate of CVD SiC in the PWR-simulating water.

3.2 Mechanical property of SiC composite tubes

Fig. 7(a) shows the applied load-axial displacement curves of the SiC triplex tubes. Load gradually increases until the polyurethane plug contacts with the tubular specimen at the initial stage, and it steeply increased after the contact. Especially some load drops are observed before failure of the tube which might be caused by the formation of crack in the inner monolithic SiC layer. The stress-radial displacement curve displays an initial almost linear up to almost a half of the curve, as shown in Fig. 7(b). The onset of non-linearity could be associated with matrix cracking and manifests itself in degradation in tube stiffness after a significant load drop and an increase in radial displacement.

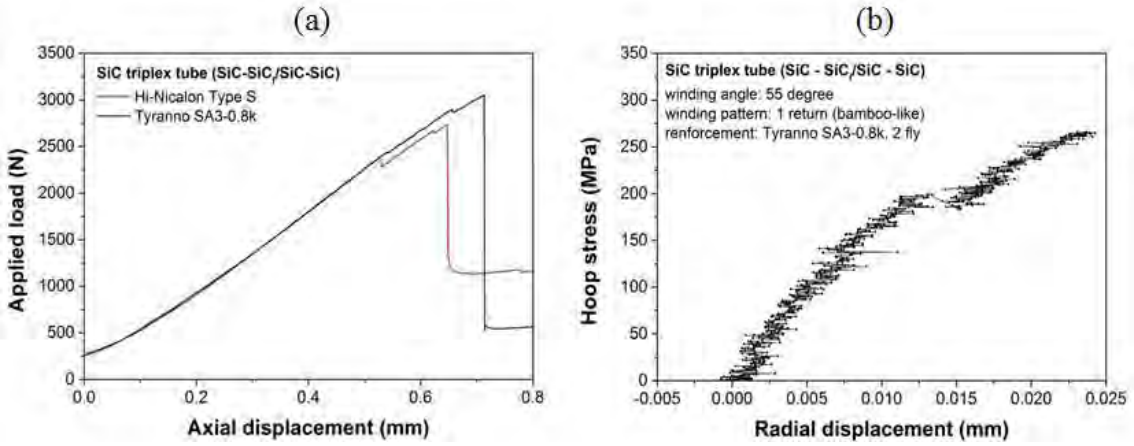

Fig. 7. Typical load-axial displacement (a) and hoop stress-radial displacement curves (b) of the SiC triplex tubes.

Fig. 8 shows the microstructure of the triplex tube interrupted just after a first load drop during the hoop test. Failure of the SiC inner layer has been taken place, as shown in Fig. 8(a). However, the crack from the inner layer does not propagated immediately into the composite layer. In the SiC triplex tube, PyC with about 200 nm in thickness exists between the SiC inner and composite layers, which was formed during the deposition of PyC interphase on SiC fibers. When the crack propagates from inner layer to composite layer, the PyC interphase become the preferred site for crack propagation. It indicates that the

existence of a thin PyC layer play a role of an obstacle of crack propagation. In the SiC_f/SiC composite layer, a significant delamination and detachment of the SiC fiber bundles does not take place but a number of intrabundle microcracks are observed primarily at the matrix/fiber interface to the circumferential direction. The microcracks with several tens of micrometers are occasionally observed through the thickness of the composite layer, as shown in Fig. 8(b). The load drop could be caused by fracture of a SiC inner layer. The quasi-ductile composite layer might suddenly expand after the cracking in a SiC inner layer.

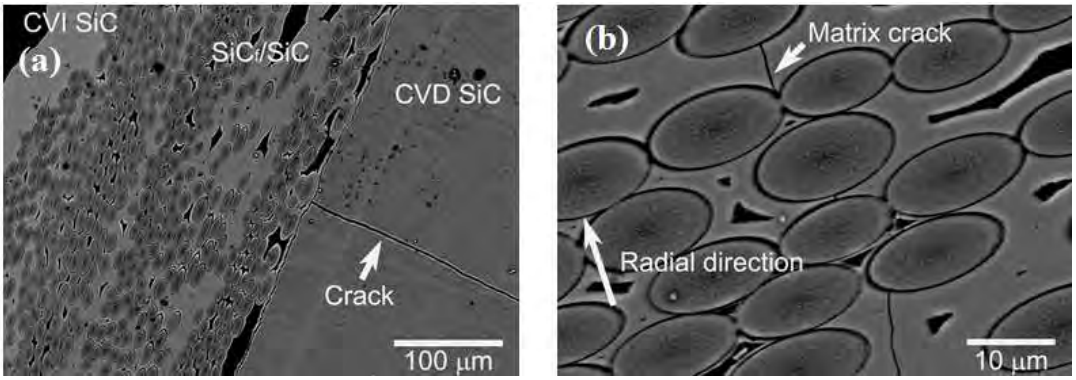

Fig. 8. Microstructure of the SiC triplex tube after a first load drop: (a) a crack in the SiC inner layer and (b) a matrix crack in the SiC_f/SiC composite layer.

Fig. 9 shows the hoop stresses of the SiC triplex tubes as a function of the fiber volume fraction in the triplex tubes, in which each data point corresponds to one test. Although the SiC triplex tubes have a thick monolith layer, the fiber volume fraction still has a significant effect on the hoop stress. The fiber volume fraction of each tube is in the range of 18 to 25%. The hoop stress of the triplex tube tends to be proportional to the fiber volume fraction regardless of both the reinforcement fiber and fly number. The highest fiber volume fraction was obtained when the Tyranno SA3-0.8k fiber was used so that the Tyranno SA3-0.8k reinforced triplex tube exhibited the highest hoop stress [13].

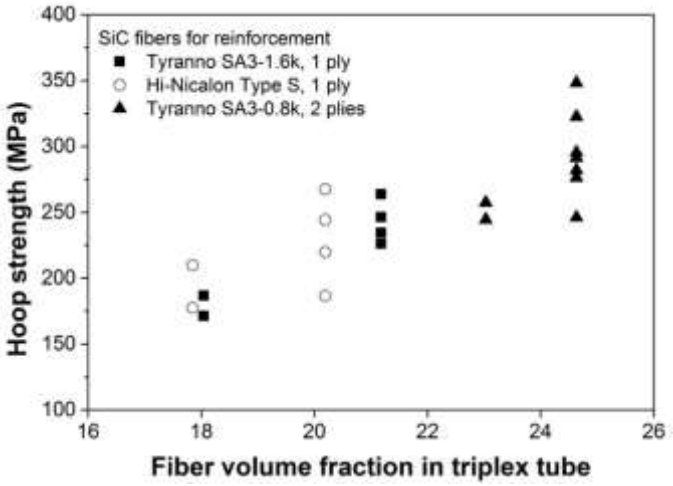

Fig. 9. Hoop stresses of the SiC triplex tubes as a function of the fiber volume fraction.

4. Conclusions

Long-term corrosion behavior of CVD SiC was investigated under simulated PWR primary water conditions. The dissolved hydrogen of about 2.7 ppm dramatically reduced the corrosion rate of SiC at 360°C under 20 MPa. The corrosion weight loss of CVD SiC under the dissolved hydrogen-controlled condition was extremely small compared with the

condition without controlling the dissolved hydrogen. The oxide layer on the SiC specimen was readily dissolved and the SiC bare surface was exposed at the initial stage of the corrosion test. After the dissolution of the oxide layer, however, further corrosion occurred in a very sluggish way. This indicates that the dissolved hydrogen significantly increases the corrosion resistance of the CVD SiC by retarding the formation of the surface oxide layer.

The hoop stresses of the SiC triplex tubes tended to be proportional to the fiber volume fraction of the composite layer. The Tyranno SA3-0.8k reinforced SiC triplex tube exhibited the highest hoop strength because the highest fiber volume fraction was achieved by a filament winding method. Quasi-ductile fracture occurred for the triplex composite tubes. Crack initiated in the SiC inner layer which resulted in the load drop and a sudden increase in radial displacement in the stress-displacement curve. Matrix cracking along the fiber-matrix interface led to a decrease in the slope of the stress-radial displacement curve.

Acknowledgments

This work was supported by the National Research Foundation of Korea (NRF) grant funded by the Korea government (MSIP) (No. 2015M2A8A4001841).

References

[1] Y. Katoh, L.L. Snead, I. Szlufarska, W.J. Weber, Radiation Effects in SiC for Nuclear Structural Applications, Curr. Opin. Solid State Mater. Sci., 16, 143, 2012.
[2] H. Nabielek, W. Kühnlein, W. Schenk, W. Heit, A. Christ, and H. Ragoss, Development of Advanced HTR Fuel Elements, Nucl. Eng. Des., 121, 199, 1990.
[3] D. Kim, W.-J. Kim, J.Y. Park, Compatibility of CVD SiC and SiC_f/SiC Composites with High Temperature Helium Simulating Very High Temperature Gas-Cooled Reactor Coolant Chemistry, Oxid. Met., 80, 389, 2013.
[4] L.L. Snead, T. Nozawa, M. Ferraris, Y. Katoh, R. Shinavski, M. Sawan, Silicon Carbide Composites as Fusion Power Reactor Structural Materials, J. Nucl. Mater., 417, 330, 2011.
[5] L. Chaffron and J. -L. Seran, "Innovative SiC_f/SiC Composite Materials for Fast Reactor," Nuclear Fuels and Structural Materials for the Next Generation Nuclear Reactors, San Diego, USA, June 13-17, 2010.
[6] K. Yueh, D. Carpenter, and H. Feinroth, Clad in Clay, Nucl. Eng. Intern., 55, 14, 2010.
[7] W.-J. Kim, D. Kim, J.Y. Park, Fabrication and Material Issues for the Application of SiC Composites to LWR Fuel Cladding, Nucl. Eng. Technol., 45, 565, 2013.
[8] K.A. Terrani, B.A. Pint, C.M. Parish, C.M. Silva, L.L. Snead, Y. Katoh, Silicon Carbide Oxidation in Steam up to 2 MPa, J. Am. Ceram. Soc., 97, 2331, 2014.
[9] G. Youinou, R.S. Sen, Enhanced Accident Tolerant Fuels for LWRs – A Preliminary System Analysis, INL/EXT-13-30211, Idaho National Laboratory, 2013.
[10] S.J. Zinkle, K.A. Terrani, J.C. Gehin, L.J. Ott, L.L. Snead, Accident tolerant fuels for LWRs: a perspective, J. Nucl. Mater., 448, 374, 2014.
[11] K. Barrett, S. Bragg-Sitton, D. Galicki, Advanced LWR Nuclear Fuel Cladding System Development Trade-off Study, INL/EXT-12-27090, Idaho National Laboratory, ID, 2012.
[12] J.-Y. Park, I.-H. Kim, Y.-I. Jung, H.-G. Kim, D.-J. Park, W.-J. Kim, Long-term corrosion behavior of CVD SiC in 360°C water and 400°C, J. Nucl. Mater., 433, 603, 2013.
[13] D. Kim, H.G. Lee, J.Y. Park, W.-J. Kim, Fabrication and measurement of hoop strength of SiC triplex tube for nuclear fuel cladding applications, J. Nucl. Mater., 458, 29, 2015.
[14] O.M. Jadaan, D.L. Shelleman, J.C. Conway Jr., J.J. Mecholsky Jr., R.E. Tressler, Prediction of the strength of ceramic tubular components: Part I-analysis, J. Test. Eval., 19, 181, 1991.
[15] H. Hirayama, T. Kawakubo, A. Goto, Corrosion behavior of silicon carbide in 290°C water, J. Am. Ceram. Soc., 72, 2049, 1989.
[16] W.-J. Kim, H.S. Hwang, J.Y. Park, W.-S. Ryu, Corrosion behaviors of sintered and chemically vapor deposited silicon carbide ceramics in water at 360°C, J. Mater. Sci.

Lett., 22, 581, 2003.
[17] L. Tan, T.R. Allen, E.Barringer, Effect of microstructure on the corrosion of CVD-SiC exposed to supercritical water, J. Nucl. Mater., 394, 95, 2009.
[18] E. Barringer, Z. Faiztompkins, H. Feinroth, T. Allen, M. Lance, H. Meyer, L. Walker, E. Lara-Curzio, Corrosion of CVD silicon carbide in 500°C supercritical water, J. Am. Ceram. Soc., 90, 315, 2007.
[19] C.H. Henager, Jr., A.L. Shemer-Kiohrn, S.G. Pitman, D.J. Senor, K.J. Geelhood, C.L. Painter, Pitting corrosion in CVD SiC at 300°C in deoxygenated high-purity water, J. Nucl. Mater., 378, 9, 2008.

SiC/SiC COMPOSITE BEHAVIOR IN LWR CONDITIONS AND UNDER HIGH TEMPERATURE STEAM ENVIRONMENT

C. LORRETTE*, C. SAUDER, P. BILLAUD, C. HOSSEPIED,
G. LOUPIAS, J. BRAUN, A. MICHAUX
CEA, DEN, DMN, Section for Applied Metallurgy Research
F-91191 Gif-sur-Yvette, France

E. TORRES, F. REBILLAT
LCTS, UMR CNRS-UB-CEA-SAFRAN, 3 allée de la Boétie
F-33 600 Pessac, France

J. BISCHOFF
AREVA NP, 10 rue Juliette Récamier,
F-69456 Lyon, France

A. AMBARD
EDF R&D, MMC Department, av des Renardières,
F-77 818 Moret-sur-Loing, France

* *Corresponding Author, E-mail: christophe.lorrette@cea.fr*

ABSTRACT

Tubular nuclear-grade SiC/SiC composites produced by CEA were investigated in the present work as cladding material to enhance the accident tolerance of Light Water Reactors (LWRs). A first part reports a preliminary assessment of the behavior of SiC/SiC composite tubes in simulated relevant LWR conditions related with the manufacturing parameters. The dependence of the corrosion rate on the chemical composition of water is also investigated for a better understanding of the hydrothermal SiC corrosion mechanisms. Additionally, the ability of SiC/SiC composite tubes to preserve their geometry and maintain coolability under high temperature steam environment is examined. Oxidation tests are performed to confirm the favorable behavior and to evaluate the oxidation kinetics of the composite exposed to high-temperature steam (up to 1400°C) under pressure and under dynamic gas flow conditions.

1. Introduction

The growing interest for continuous SiC fiber reinforced SiC matrix composites (SiC_f/SiC) as structural material for nuclear applications has resulted in significant improvements over the past decade. Primarily driven by the functional specifications of the fuel cladding element for fast breeder reactors, an important R&D program has led the French Alternative Energies and Atomic Energy Commission (CEA) to propose several innovations to overcome some critical technological issues [1]. Following the event at Fukushima in 2011, these innovative materials are now being seriously considered to enhance the accident tolerance of Light Water Reactors (LWRs). This development is being performed within the French Nuclear Institute in partnership with AREVA and EDF.

Due to their benefits over the conventional zirconium alloys such as low oxidation rates up to about 1600°C and presumably significant reduction in hydrogen generation, the application of SiC/SiC claddings to LWRs would provide favorable perspectives in emergency situation. The “sandwich” cladding design that includes a metal liner in between two layers of composite appears as a robust and technically viable concept [2,3].

The current development phase focuses on assessing the behavior under conditions representative of LWRs. Among the first technical attributes to be investigated is the resistance to corrosion, and other interactions with the coolant in LWR nominal operating conditions. Regarding this issue, the relative attractiveness and benefits of a SiC-based cladding remain to be demonstrated experimentally. Similarly, given the nature of LWR accidents, the study must also be extended to the high temperature steam behavior assessment. These two aspects constitute one of the major directions for current researches at CEA.

This paper addresses preliminary results quantifying and discussing the performance of tubular nuclear grade SiC/SiC composite materials in both normal and accident conditions.

2. Materials and experimental details

Specimens evaluated in this study included SiC/SiC composite tubes without metallic liner of 60 mm lengths. Hi-Nicalon^{TM} type S reinforcements were used for their high purity and near stoichiometric composition (ratio Si/C~1) that confer stability under neutron irradiation. The tubular fibrous preforms were obtained either by an only-braiding process using a multi-path machine or by the association of both filament winding and 2D braiding processes to produce multilayered architectures. They were chemically vapor-infiltrated with a single pyrocarbon (PyC) interphase thickness of less than 100 nm. Outer diameter of tubes was about 10 mm with 0.85 to 0.90 mm wall thickness. To investigate the effect of oxidation on damaged composites, some specimens were intentionally pre-damaged under uniaxial tensile loading at different level of interest (0.05 %, 0.1 %, 0.3 % and 0.5 %) to generate a permanent controlled micro-cracks network in the matrix, thus facilitating the ingress of oxidizing species. These micro-cracks are however invisible on a macroscopic scale whatever the pre-damage level.

Two autoclaves were used to evaluate the oxidation in LWR nominal operating conditions for 3500 h (5 months). One contained distilled water (DW), the second contained LWR like water composition with Lithium, LiOH (2 ppm) and Boron, H_3BO_3 (1000 ppm). Constant temperature and pressure were respectively measured to be 360°C and 180 bar.

As for the accidental simulated experiments, double-sided oxidation exposures were conducted for 4 to 110 hours in steam and air or O_2 mixtures (given in Table 1) with various oxygen contents. Details of the high-pressure and high temperature experimental set-up are described elsewhere [4]. The investigated temperatures were 1200°C and 1400°C and the total pressure was 1 or 10 bar. The linear gas velocity was constant and set to 5 cm/s for all the experiments in the cold furnace zone.

Table 1 – Conditions applied to specimens exposed under high temperature steam

Conditions		Temperature (°C)	Pressure (bar)				Pressure ratio (%)		
			Total	*Water*	*Gas in addition*		P_{H2O}/P_T	P_{O2}/P_T	P_{O2}/P_{H2O}
HP	A	1200	10	0.5	Air	9.5	0,05 (5)	0,19 (19)	3,8
P_{atm}	B	1200	1	0.5	O_2	0.5	0,5 (50)	0,5 (50)	1
	C	1200	1	0.5	Air	0.5	0,5 (50)	0,1 (10)	0,2
	D	1400	1	0.5	Air	0.5	0,5 (50)	0,1 (10)	0,2

For both sets of experiments, specimen weight was measured before and after exposure using microbalance with ± 0.05 mg/cm^2 accuracy. Uniaxial tensile tests were performed at room temperature to evaluate the residual mechanical behavior. Additional characterizations included analyses of composition surface by X-ray photoelectron spectroscopy (XPS) and microstructural post-exposure observations on polished cross-sections by scanning electron microscopy (SEM).

3 Results

3.1 Oxidation in representative nominal LWR conditions

Normal operating conditions for LWRs (temperature and pressure) are related to the hydrothermal oxidation regime of silicon carbide [5]. Under these conditions in water-containing environment, pure silicon carbide materials would be expected to form a protective silica SiO_2 layer due to the thermodynamic driving force. But besides incurring oxidative reactions with water, solution of the oxidation product in the coolant must also be considered to be part of the process.

- **Weigh change and chemical composition analysis of waters**

The results of experiments are compiled in tables 2 and 3. With the exception of one slightly pre-damaged tube, a weight loss is observed for all the tested SiC-based samples. The reference and the low pre-damaged SiC/SiC materials (up to 0.05 % strain) reveal a limited weight change while significant weight loss is mainly observed for SiC/SiC pre-damaged materials above 0.05 % strain, without being related to the level of pre-damage. This means that water infiltrates through the larger crack openings (resulting from highly pre-damaged composites) and oxidizes the SiC materials from the inside and not just on the surface, thus increasing the corrosion rate.

The appearance of samples stays unchanged before and after exposure. No influence of the water chemistry on weight change is evidenced. If the presence of a significant content of Al in solution after 5 months exposure is clearly due to the sample holder made of alumina, Cr, Fe and Ni elements in very low quantities comes from the stainless steel autoclave. By contrast, the presence of Si in solution with a concentration corresponding to water solubility limit of silica at 25°C (0.12 – 0.14 $g.l^{-1}$) suggests a release from the SiC-based samples.

Table 2 – Weight evolutions of high purity CVD β-SiC and CVI-SiC/SiC tubular composites.

	Distilled water			**LWRs water**		
	initial weight (g)	*after oxidation (g)*	*relative change (%)*	*initial weight (g)*	*after oxidation (g)*	*relative change (%)*
SiC/SiC_{REF}	4.2937	4.2912	**- 0.06**	4.2494	4.2472	**- 0.05**
$SiC/SiC_{0.05\%}$	4.6114	4.6142	**+ 0.06**	4.4845	4.7853	**+ 0.02**
$SiC/SiC_{0.10\%}$	4.8429	4.8075	**- 0.73**	4.8059	4.7624	**- 0.91**
$SiC/SiC_{0.15\%}$	4.7344	4.6873	**- 0.99**	4.7553	4.7181	**- 0.78**
$SiC/SiC_{0.30\%}$	4.9728	4.9442	**- 0.58**	4.8866	4.8647	**- 0.45**
$SiC/SiC_{0.50\%}$	5.0001	4.972	**- 0.56**	5.0783	5.0534	**- 0.49**

Table 3 – Chemical composition analysis (and pH) of waters before and after exposure.

Elements	**Distilled water**		**LWRs water**	
	initial	*after 5 months*	*initial*	*after 5 months*
Al	< 0.50	8200	96	4500
Si	< 0.05	84	< 0.05	68
B	8.4	13	1010	970
Li	$< 10^{-3}$	0.86	1.95	0.51
Cr	< 0.03	1.2	< 0.03	30
Fe	< 0.1	13	< 0.1	18
Ni	< 0.05	8	0.22	45
pH	7.0	8.3	7.5	7.9

Compositions are expressed in ppb

- **Post-exposure mechanical tensile behavior**

Residual tensile tests were carried out on the SiC/SiC tubular specimens according to the procedure detailed in [6]. No significant degradation of mechanical behavior is observed after long-term exposure in environments either representative of LWRs or distilled water. The monotonic post-exposure stress-strain curves for the investigated conditions, shown in figure 1a with a comparison to the reference behavior, are characteristic of the expected damageable behavior with a low fiber-matrix bonding. This is the consequence of low interfacial shear strength due to the presence of pyrocarbon interphase, which does not seem to have been affected. The intentional pre-damage of specimens at different strain levels (0.05 to 0.5 %) to allow access of oxidizing species to the bulk material also exhibit a proper post-exposure mechanical behavior that consolidates this assumption (see figure 1b). The fiber-matrix load transfer remains efficient to provide ability to accommodate the deformation for the silicon carbide ceramic composites.

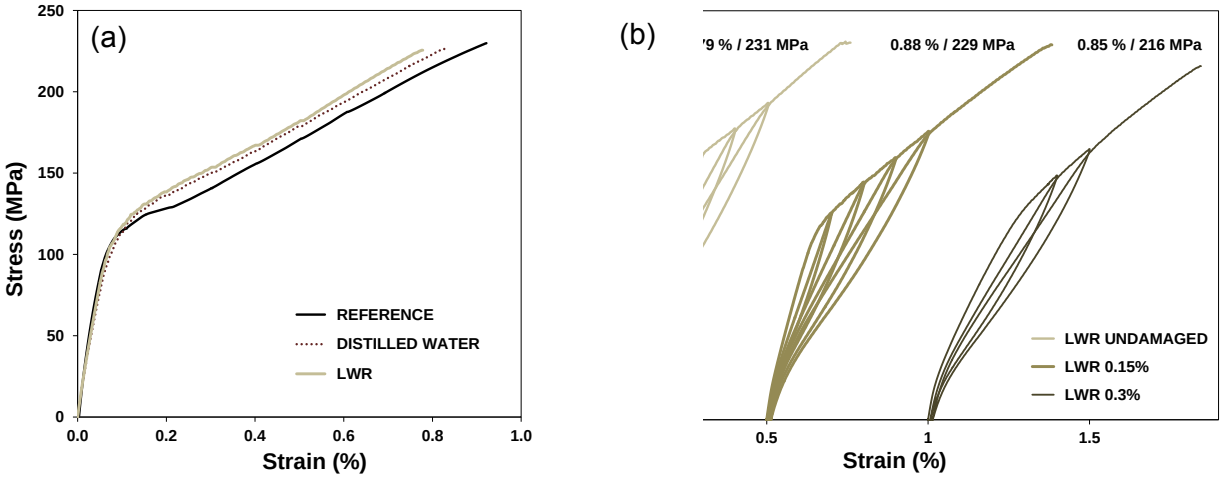

comparison of with the reference curve (monotonic),

(b) Unloading-reloading sequences to confirm the non-sensitivity of mechanical behavior on both as-received and pre-damaged specimens after long-term exposure in LWR environment – Values correspond to strain/stress at failure.

- **Discussion and mechanism**

Regarding these first results, the long-term exposure in autoclave of pure silicon carbide under environments characteristic of normal operating LWR conditions leads to a weight loss. Besides the possible active oxidation such as described by reaction (1), it could be assumed that material recession mainly results from the dissolution of the silica oxide formed initially on the surface and likely to form silicic acid in the aqueous state. Depending on the activity of the solid phases in presence and the water-to-SiC ratio, the sequence of thermodynamically consistent reactions (2) (3) (4) are thought to be possible [7-8]. In both cases, material is being consumed.

$$SiC_{(s)} + 4H_2O_{(l)} \longrightarrow Si(OH)_{4(aq)} + CH_{4(g)} \quad (1)$$

$$\begin{cases} SiC_{(s)} + 2H_2O_{(l)} \longrightarrow SiO_{2(S)} + CH_{4(g)} & (2) \\ SiC_{(s)} + 3H_2O_{(l)} \longrightarrow SiO_{2(S)} + CO_{(g)} + 3H_{2(g)} & (3) \\ SiO_{2(S)} + 2H_2O_{(l)} \longrightarrow Si(OH)_{4(aq)} & (4) \end{cases}$$

As reported by different authors, no evidence of protective silica layer was observed on silicon carbide nuclear grade material tested in similar conditions [5,9]. This result was confirmed in the present study by XPS analysis showing exposed surfaces free of silica scale.

As soon as the silica oxide would form on the surface, it dissolves in the water. However, since solubility of silica depends on temperature, the silica dissolution could raise an issue in case of fuel cladding application as the possible silica particles would be transported through the coolant and then deposited in the colder parts of the power loop or pumps. In the meantime, the SiC-based cladding would undergo continuous thickness loss.

3.2 Oxidation in high temperature steam

The reference oxidation studies of SiC materials in high temperature steam environment have been carried out for needs related to aircraft turbine engine applications [10-11]. Under conditions such as combustion environments (high temperature, high pressure) containing oxygen with water vapor, it is well-established that the SiC oxidation reaction, which is temperature dependent, follows a paralinear oxidation kinetics. Material recession is governed by a two-step process of silica scale formation on the surface of SiC by any or all of the reactions (1) (2) (3) followed by volatilization of this generated oxide.

$$SiC_{(S)} + \frac{3}{2}O_{2(g)} \longrightarrow SiO_{2(S)} + CO_{(g)} \quad (1)$$

$$SiC_{(S)} + 2O_{2(g)} \longrightarrow SiO_{2(S)} + CO_{2(g)} \quad (2)$$

$$SiC_{(S)} + 3H_2O_{(g)} \longrightarrow SiO_{2(S)} + 3H_{2(g)} + CO_{(g)} \quad (3)$$

Water vapor is found to be the primary oxidant specie. It is directly involved in the volatilization of the silica scale to form volatile hydroxides or oxohydroxides that ultimately results in mass loss after relative long-term exposure. Some possible reactions (4) (5) (6) are the following:

$$SiO_{2(S)} + 2H_2O_{(g)} \longrightarrow Si(OH)_{4(g)} \quad (4)$$

$$2SiO_{2(S)} + 3H_2O_{(g)} \longrightarrow Si_2O(OH)_{6(g)} \quad (5)$$

$$2SiO_{2(S)} + 3H_2O_{(g)} \longrightarrow Si_2(OH)_{6(g)} + \frac{1}{2}O_2 \quad (6)$$

By relying on this mechanism, a time series of specimens was performed to determine the oxidation reaction parameters. Figure 2 shows the results for CVI-SiC/SiC tubular composites exposed under various high temperature steam environments, as described in Table 1. The data points report the average and standard deviation of 3 weight change measurements, normalized to the exposed surface area of composites that was obtained by X-ray tomography.

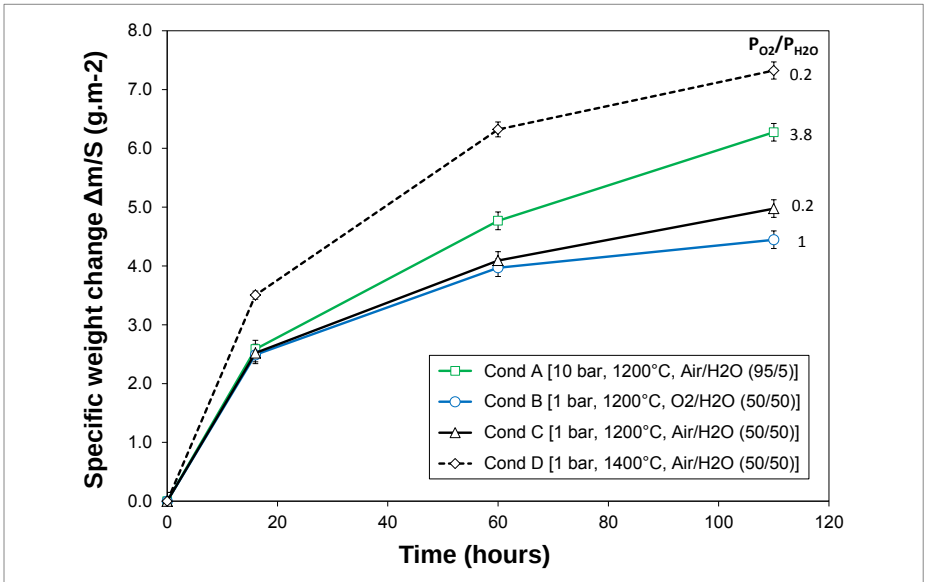

Fig. 2: Specific weight change as a function of time during steam exposure at high temperature (1200 and 1400°C) for CVI-SiC/SiC composite tubes.

For all the investigated conditions, the weight change corresponds to a relatively low gain (between 0.82 and 1.32%) indicating a limited corrosion effect after exposure during 110h at 1200 or 1400°C. As expected and evidenced by metallographic examinations of specimens showing the presence of silica on surface, this reflects a global behavior resulting from the simultaneous oxidation of the composites, mainly the matrix, to form a protective oxide layer and its volatilization. The various curve progressions demonstrate the rate dependence to the partial pressures of oxygen and water, and to the temperature.

- **Analytical approach and determination of the kinetic constants**

This mixed regime is partly explained by the higher solubility of water in the silica relative to oxygen. As a consequence, the oxidation rate (k_p) is affected by the volatilization rate (k_l) and the overall kinetics can be described in terms of measured weight changes by a paralinear kinetics as follows [11]:

$$t = \frac{\alpha^2 k_p}{2k_l^2}\left[-\frac{2k_l\frac{\Delta m_{ox}}{S}}{\alpha k_p} - \ln\left(1-\frac{2k_l\frac{\Delta m_{ox}}{S}}{\alpha k_p}\right)\right] \quad \text{with} \quad \alpha = \frac{M_{SiO2}}{M_{SiO2}-M_{SiC}}$$

where t is the oxidation time (in hour), $\Delta m_{ox}/S$ is the surface weight gain due to growth of the silica scale and M_i is the molecular weight of the species shown in subscript.

The total observed weight change $\Delta m_{exp}/S$ is then given by the sum of the two contributions $\Delta m_{ox}/S$ and $\Delta m_{vol}/S$ that represents the surface weight loss due to oxide volatilization. After a relative long time when the limiting oxide scale thickness is achieved, the weight change can also simply be expressed by the following expression introducing a recession rate (k_r).

$$\frac{\Delta m_{vol}}{S} = -k_r t = -\frac{M_{SiC}}{M_{SiO2}} k_l t$$

The oxidation constants were determined by interpolation from experimental silica thicknesses measured on specimen. For each conditions at 1200°C, a couple of rates (k_p,k_l) was identified and reported in Table 4, as well as the recession rate (k_r).

Table 4 – Identification of the paralinear rate constants for different conditions at 1200°C.

Conditions	Paralinear rate constants		
	k_p ($\mu m^2_{SiO2}.cm^{-4}.h^{-1}$)	k_l ($\mu m_{SiO2}.cm^{-2}.h^{-1}$)	k_r ($\mu m_{SiC}.cm^{-2}.h^{-1}$)
A [10 bar, 1200°C, Air/H_2O (95/5)]	0.178	6×10^{-7}	2.88×10^{-7}
B [1 bar, 1200°C, O_2/H_2O (50/50)]	0.171	1.12×10^{-2}	5.37×10^{-3}
C [1 bar, 1200°C, Air/H_2O (50/50)]	0.143	1.12×10^{-2}	5.37×10^{-3}

- **Residual mechanical tensile behavior**

Because both the integrity and the geometry of specimens were fully retained after oxidation, tensile tests up to failure may have been carried out to determine the residual mechanical behavior at room temperature. Results are presented in figure 3. To assess the influence of oxidation, the reference mechanical tensile behavior of an unexposed material without unloading-reloading cycles is reported. Table 5 summarizes the measured residual mechanical properties for each condition.

Table 5 – Residual mechanical properties at room temperature of specimens after oxidation.

Condition	Tensile test	E (GPa)	Strain to failure (%)	Tensile strength (MPa)
Unexposed(*)	Monotone	280 ± 10	0.66 ± 0,03	456 ± 18
A	Cycled	260	0.66	417
B	Cycled	259	0.63	413
C	Cycled	254	0.69	455
D	Cycled	256	0.65	390

(*) Three specimen tested

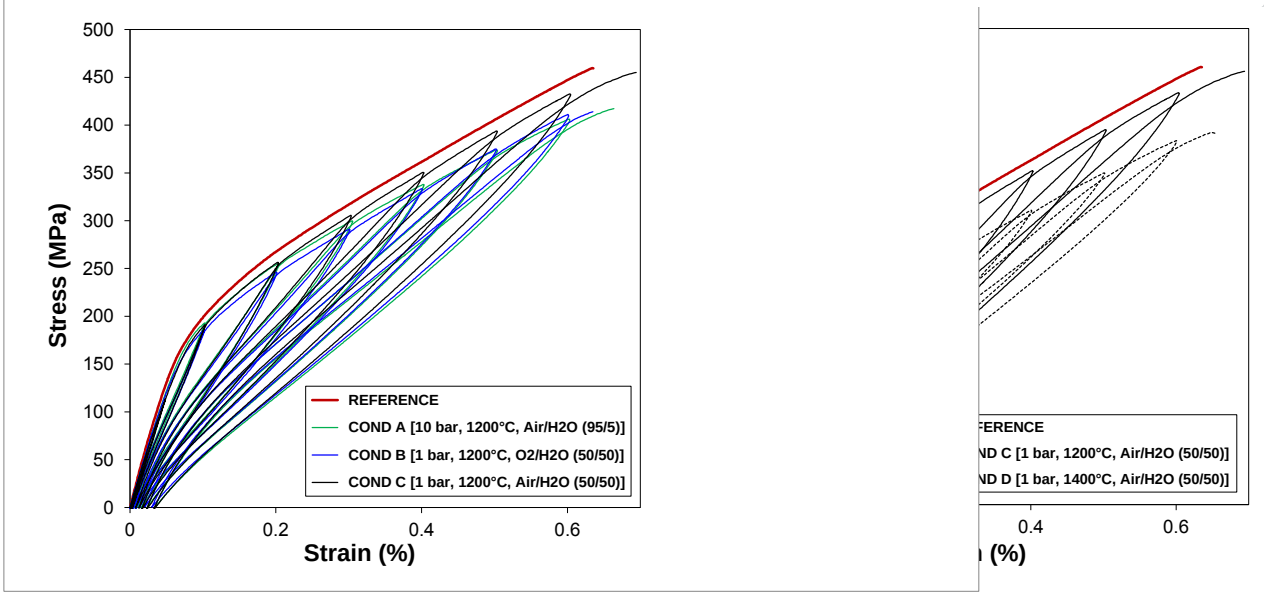

Fig. 3: Residual tensile stress-strain curves of specimens after oxidation, Comparison to the reference behavior without oxidation (monotonic).

Once again, specimens retain a similar “non-linear elastic damageable” mechanical behavior (without plateau) for all the investigated environments. This is a typical behavior for a CVI-SiC/SiC composite material with a pyrocarbon interphase that is characterized by a progressive damage, usually caused by matrix micro-cracking and interfacial debonding until failure. Specimen treated at 1200°C and 1400°C in the different steam environments lead to a very good retention of the strain to failure. A slight decrease of the tensile strength (lower than 10 and 15%) compared to the reference behavior of the non-oxidized material is observed. Moduli of elasticity (E) undergo a decrease of the same order.

The tightening of the hysteresis loops, as well as the low residual strain after unloading for specimen exposed at 1400°C would indicate a higher fiber-matrix load transfer due to oxidation, thus a strong interfacial shear stress.

- **Discussion and mechanism**

At 1200°C, the oxidation conditions investigated did not cause a significant reduction of the residual mechanical properties. All the tested specimens preserve a characteristic damageable mechanical behavior very close to the reference. The fracture surfaces are similar and exhibit wide non-brittle areas characterized by non-oxidized fiber pull out with lengths higher than a hundred micrometers (fig.4a). If no significant difference was observed at low magnification between fibers located at the heart or close to the edges of the composite (fig.4b), the polished cross-section observations at higher magnification reveal some oxidized areas on the surface but without degradation of the fiber reinforcements. This is attributed to the formation of silica from the consumption of the silicon carbide matrix, which ensures a protective function against oxidation (fig.4c). The presence of pyrocarbon at the fiber/matrix interfaces is evidenced using EDS facility (fig.4d).

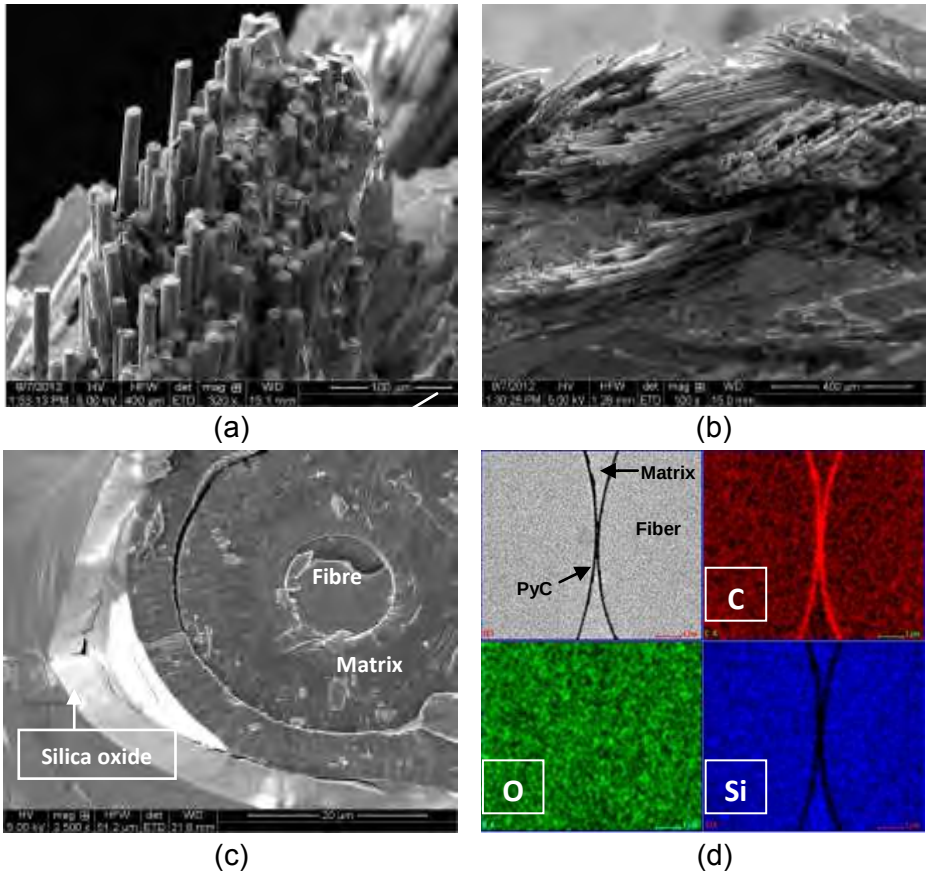

Fig. 4: Post-exposure analysis of specimen
after 110h in condition C [1 bar, 1200°C, Air/H2O (50/50)]

At higher temperature (1400°C), the same investigations on post-mortem specimens reveal fractures surfaces with a slightly more degraded appearance. The presence of well-marked cracks, preferentially located near the matrix layer on the external surface (seal-coat) emphasizes a greater sensitivity to damage in this condition. This result is consistent with the weakening of the residual mechanical properties measured on specimens oxidized at 1400°C compared to the lower investigated temperatures. Here, the oxidation kinetics of the matrix seems to be sufficiently rapid to produce an efficient protective oxide layer but also causes local penetrations of oxide at surface cracks (whether these were pre-existing or appeared during thermal cycles). As a consequence, the presence of oxidized areas in contact with the fibers may be possible which would induce a mechanical anchorage that locally reinforces both the fiber-matrix bonding and the load transfer.

A schematic representation of the assumed oxidation process is depicted in Fig. 4.

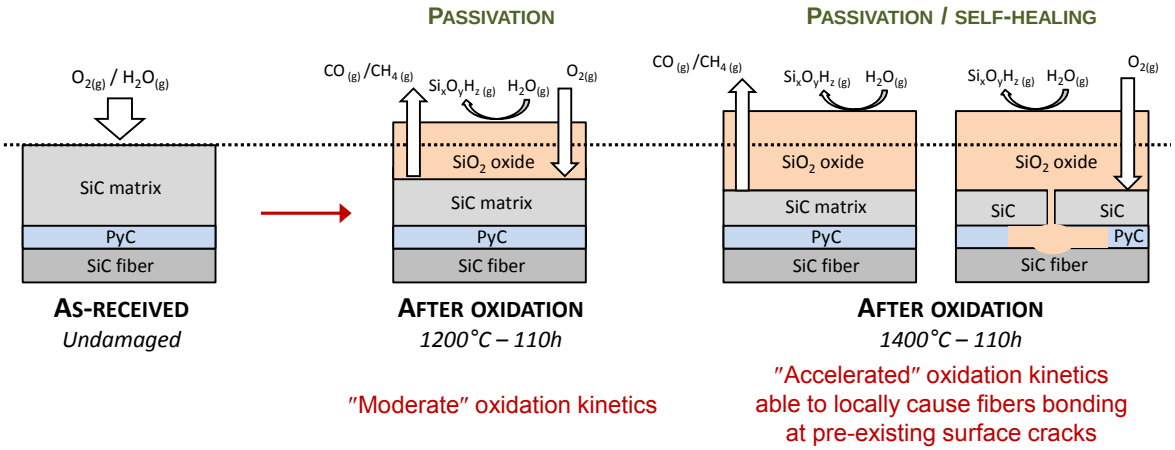

Fig. 4: Proposed oxidation process of CVI-SiC/SiC composite materials
under high temperature steam environment.

Conclusion

First experiments were conducted on nuclear-grade tubular SiC/SiC composite produced at CEA to assess their ability to survive in representative LWR normal operating conditions. The key findings of this work highlight an excellent retention of the mechanical behavior after 5 months exposure to LWR water. In qualitative agreement with other recent studies, a material recession was observed but stays limited to a low weight loss in a closed system (autoclave).

In a second part, the low sensitivity of SiC/SiC composites under the high temperature steam conditions was confirmed. Once again, no signification degradation of the mechanical properties of CVI-HNI SiC/SiC specimen is observed after relatively long exposure times (beyond 100 h at 1200°C).

These preliminary results are positive but significant studies and developments are still necessary to close the technology gap. Qualification for nuclear application requires substantial irradiation testing, additional characterization and the definition of design rules applicable to such an innovative material. Consequently, the use of a SiC-based fuel cladding shows promise for the highest temperature accident conditions but remains a long term perspective.

4 References

[1] M. ZABIEGO, C. SAUDER, P. DAVID, C. GUENEAU, L.BRIOTTET, JJ. INGREMEAU, A. RAVENET, C. LORRETTE, L. CHAFFRON, P. GUEDENEY, M. LE FLEM, JL. SERAN, Overview of CEA's R&D on GFR fuel element design: from challenges to solutions, IAEA - FR13 conference, Paris, France (2013).

[2] M. ZABIEGO, C. SAUDER, C. LORRETTE, P. GUEDENEY, Improved multilayer tube made from ceramic-matrix composite material, the resulting nuclear fuel cladding and associated production method, CEA patent, WO2013017621 A1, (2013).

[3] J.C. BRACHET, C. LORRETTE, A. MICHAUX, C. SAUDER, I. IDARRAGA-TRUJILLO, M. LE SAUX, M. LE FLEM, F. SCHUSTER, A. BILLARD, E. MONSIFROT, E. TORRES, F. REBILLAT, J. BISCHOFF, A.AMBARD, CEA studies on avanced nuclear fuel claddings for enhanced Accident Tolenrant LWRs Fuel (LOCA and beyond LOCA conditions), Fontrevraud 8 - SFEN conference, Avignon, France (2014).

[4] L. QUEMARD, F. REBILLAT, A. GUETTE, H. TAWIL, Development of an original design of high temperature-high pressure furnace, proceedings of High Temperature Ceramic Matrix Composites 5 (HTCMC5), ed. The Am. Ceram. Soc., Westerville, Ohio, USA, 543-548, (2005).

[5] K. TERRANI, Y. YANG, T. GERCZAK, Y. KATOH, L. SNEAD, Y.J. KIM, R.REBAK, Hydrothermal corrosion of SiC-based materials in LWR environments, ICACC 39th, Daytona Beach, Floride, USA (2015).

[6] E. ROHMER, E. MARTIN, C. LORRETTE, Mechanical properties of SiC/SiC braided tubes for fuel cladding, J. Nucl. Mater., 453 16-21, (2014).

[7] V. PRESSER, K.G. NICKEL, Silica on silicon carbide, Critical reviews in Solid State and Materials Sciences, 33 1-99, (2008).

[8] C.H. HENAGER, A.L. SCHEMER-KOHRN, S.G. PITMAN, D.J. SENOR, K.J. GEELHOOD, C.L. PAINTER, Pitting corrosion in CVD SiC at 300°C in desoxygenated hight-purity water, J. Nucl. Mater., 378 9-16, (2008).

[9] W.J. KIM, H.S. HWANG, J.Y. PARK, W.S.RYU, Corrosion behaviors of sintered and chemically vapor deposited silicon carbide ceramics in water at 360°C, J. Mater. Sci. Lett., 22 581-584, (2003).

[10] E. OPILA, R. HANN, Paralinear oxidation of CVD SiC in water vapor, J. Am. Ceram. Soc., 80 [1] 197-205, (1997)

[11] E. OPILA, J.L. SMIALEK, R.C. ROBINSON, D.S. FOX, N.S. JACOBSON, SiC recession caused by SiO2 scale volatility under combustion conditions: II, Thermodynamics and gaseous-diffusion model, J. Am. Ceram. Soc., 82 [7] 1826-1834, (1999)

DEVELOPMENT OF FUELS WITH ENHANCED ACCIDENT TOLERANCE

J. BISCHOFF
AREVA NP
10 rue Juliette Récamier, 69456 Lyon - FRANCE

K. McCOY, J. STRUMPELL
AREVA Inc.
3315 Old Forest Road, Lynchburg VA 24501– USA

J-C. BRACHET, C. LORRETTE
CEA, DEN, DMN, Section for Applied Metallurgy Research
F-91191 Gif-sur-Yvette, FRANCE

ABSTRACT

AREVA is strongly committed to improving fuel behaviour and performance, and especially to increasing fuel safety. Consequently, AREVA is developing some innovative fuel concepts, which include three potential cladding solutions and one fuel meat/pellet concept, through two main collaborative projects consisting of:

- the U.S. Department of Energy (DOE-NE) Enhanced Accident Tolerant Fuels (EATF) program, in partnership with Duke Energy, Dominion Resources, Tennessee Valley Authority (TVA), University of Florida (UF), University of Wisconsin (UW), Savannah River National Laboratory (SRNL) and the Electric Power Research Institute (EPRI)
- the French tri-partite R&D with the CEA, and EDF within the French Nuclear Institute.

Additionally these developments are complemented by experiments performed at the AREVA Technical and Research Centres and by additional assessments of the different potential solutions.

The concepts investigated by AREVA within the DOE project consist of: UO_2 pellets containing additives to increase the thermal conductivity, MAX-phase coatings on zirconium alloys, and, in association with EPRI, the development of molybdenum-based cladding. Additionally, two cladding solutions are being developed within the French Nuclear Institute in partnership with the CEA and EDF: a chromium coating on zirconium alloys as a shorter-term solution, and a SiC/SiC composite sandwich cladding containing a metal liner as a longer-term solution. Consequently, three cladding options are considered ranging from evolutionary concepts (coatings on zirconium alloys) to a breakthrough concept (such as the SiC/SiC sandwich cladding) with gradually increased potential performance in accidental conditions, which is correlated with increasing deployment time.

1. Introduction

For the past 50 years, the nuclear fuel rod concept for Light Water Reactors (LWRs) of UO_2 pellets enclosed in zirconium cladding has been used and optimized to improve its reliability and performance. During the Fukushima Daiichi accident in 2011 the fuel rods underwent the degradation stages of a severe accident, including the rapid oxidation of zirconium, which led on the one hand to the production of large quantities of hydrogen, and on the other hand to additional heat production [1]. As a consequence, the nuclear community decided to find and develop innovative fuel concepts that would exhibit enhanced resistance to accidental conditions, and particularly against exothermic cladding oxidation in high temperature steam typical of Loss of Coolant Accident (LOCA) and Beyond Design Basis Accident (BDBA) conditions.

AREVA is actively participating in the development of some innovative fuel concepts, which include three potential cladding solutions and one fuel meat/pellet concept. These developments are performed through two main collaborative projects consisting of:

- the U.S. Department of Energy (DOE) program on Enhanced Accident Tolerant Fuels (EATF), in partnership with Duke Energy, Dominion Resources, Tennessee Valley Authority (TVA), University of Florida (UF), University of Wisconsin (UW), Savannah River National Laboratory (SRNL) and the Electric Power Research Institute (EPRI) [2],
- the tri-partite R&D with the CEA, and EDF within the French Nuclear Institute.

Additionally these developments are complemented by experiments performed at the AREVA Technical and Research Centres. Finally, AREVA is involved in the various international collaboration programs on Accident Tolerant Fuels (ATF), mainly the OECD-NEA expert group and the IAEA Coordinated Research Project. Figure 1 summarizes schematically the various ATF programs in which AREVA actively participates

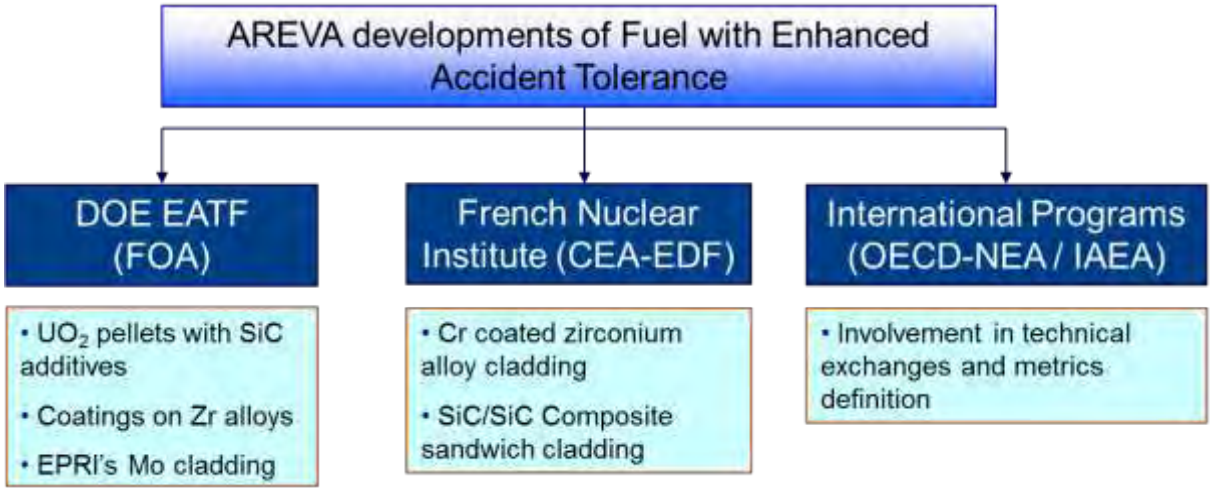

Fig. 1: Schematic describing the various ATF programs in which AREVA actively participates to develop fuels with enhanced accident tolerance.

2. General description of the concepts investigated by AREVA

As part of the DOE Enhanced Accident Tolerant Fuel program, AREVA is developing the following concepts:

- for the cladding:
  - MAX phase coatings on zirconium alloys with Savannah River National Laboratory and the University of Wisconsin,
  - Molybdenum (Mo) cladding (with EPRI)
- for the fuel meat/pellet: adding SiC and diamond to UO_2 pellets to increase the pellet thermal conductivity (with the University of Florida)

As part of the French Nuclear R&D Institute with CEA and EDF, AREVA is developing two potential cladding concepts:

- Chromium coatings on zirconium alloys
- SiC sandwich cladding containing two layers of SiC/SiC composite surrounding a thin metallic layer

Overall, AREVA focuses primarily on new cladding developments with three main cladding concepts being investigated: coatings on zirconium alloys, EPRI's Mo cladding, and CEA's SiC sandwich cladding. Each concept exhibits a different range of potential performance during accident conditions, and various deployment times. The objective is to develop

solutions ranging from evolutionary concepts (for example coatings on zirconium alloys) to revolutionary concepts (such as the SiC/SiC composite sandwich cladding) with gradually increased potential performance in accident conditions, which is itself correlated with a gradual increase in deployment time. Figure 2 schematically describes this evolution of performance with implementation time.

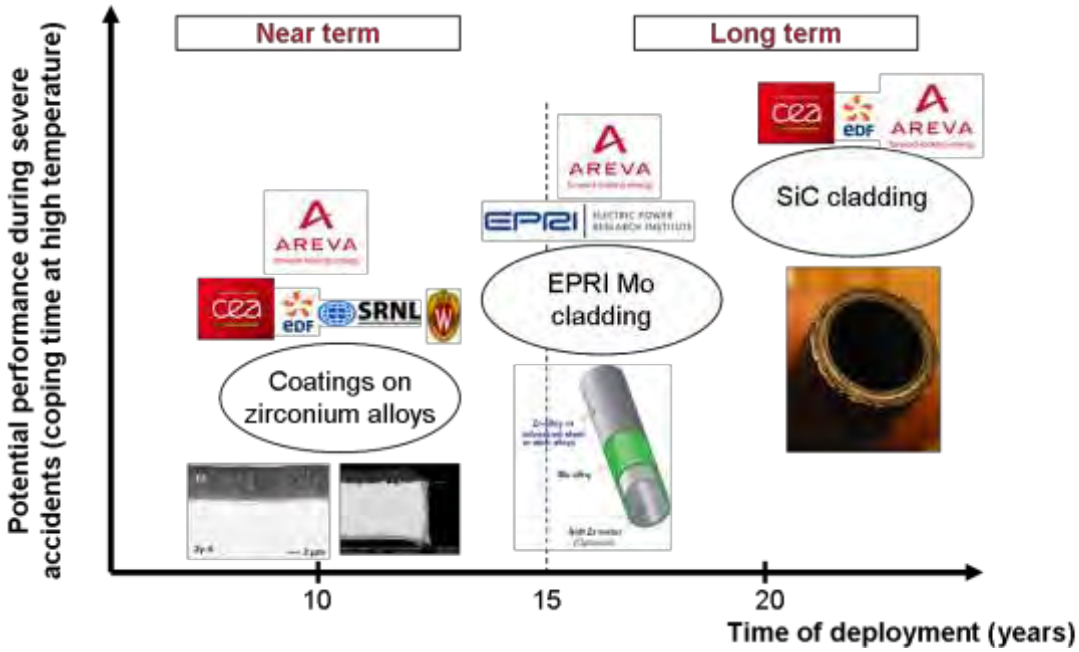

Fig. 2: Potential performance as a function of development time for the various cladding concepts investigated by AREVA.

Benefit of EATF concepts:

The goal of these developments is to increase the “grace time” which corresponds to the additional time given by these solutions to the operators before the core melt during a severe accident. For example, the cladding concepts developed by AREVA aim at reducing/eliminating the high temperature oxidation of zirconium, which currently leads to both large amount of heat and hydrogen production (the oxidation reaction is exothermic) during severe accidents. With a standard zirconium concept, once the core is uncovered rapid oxidation of the zirconium occurs and the core could melt within the order of minutes. With EATF concepts the goal is to reach a “grace time” at least in the order of hours.

The three cladding concepts and the fuel pellet concept developed by AREVA will each have their effect on the “grace time” but, to date, no precise quantification of the additional “grace time” procured by these concepts exists. This is the objective of Task Force 1 of the international collaboration taking place within the OECD-NEA Expert Group on Enhanced Accident Tolerant Fuels. In this Task Force, several standardized severe accident scenarios will be used to assess the benefits of the different EATF concepts developed worldwide and to obtain a more precise quantification of the “grace time”. The objective is to obtain these calculation results by end of 2016.

3. Developments within the U.S. Department of Energy Project

The developments performed within the U.S. Department of Energy (DOE) project began in 2012 and span a period of ten years. The main goal of this project is to insert fuel into a commercial power reactor by 2022. This section describes that work. It gives an overview of the organization and strategy of the project and then discusses the technical aspects of the components being studied: pellets, cladding, and cladding coatings.

3.1 Organization and strategy

The DOE expects its grant recipients to use scientific advances to develop commercially viable materials and designs, and that expectation is reflected throughout AREVA's project, including the makeup of the team. AREVA Federal Services, the prime recipient, is responsible for project management. Scientific support comes from the research organizations (Electric Power Research Institute, Savannah River National Laboratory, University of Florida, and University of Wisconsin), which have proposed materials and processes for improving accident tolerance. A commercial focus is provided by three utilities (Dominion Resources, Duke Energy, and the Tennessee Valley Authority (TVA)). Development, design, and licensing are being handled by AREVA Inc. The choice of participants is broad and balanced to ensure that all aspects of a new fuel are adequately covered.

The project is divided into three phases. Phase 1A, the completed discovery phase, lasted for two years. It included development of the overall strategy, selection of a large number of approaches for increasing accident tolerance, investigation of the suitability of the approaches, and initial screening. Phase 1B, the current phase, is focused on product development and testing. Phase 1B will also last for two years. Phase 2 will account for the remaining six years of the project and will include additional testing, model development, licensing, and manufacturing.

The two central features of the project strategy are the use of gate reviews [3] and the requirements traceability matrix [4]. Gate reviews are a method for directing research and development projects in which there are many ideas but not enough money to develop them all. The gate review process divides the development project into stages and allocates support to each technology for the current stage. Milestones, such as obtaining specific experimental results, are also assigned. At appropriate times, the approaches are reviewed. Technologies that fail to pass the gate review are stopped, and the funding is allocated to the other technologies. All technologies are given an equal chance, the best technologies move forward, and funding increases are allocated to the most promising technologies. The original intent was to have narrowly defined gate reviews that would focus on specific topics such as manufacturability and performance. However, that was found to be impractical because of the nature of scientific development. It is not appropriate, for example, to focus all efforts on establishing manufacturability of a component if there is no indication that it will provide improved performance. And in a gate review on manufacturability, it is equally inappropriate to ignore the available information on performance. Gate reviews therefore tend to have a broad scope, even if particular aspects are emphasized.

The requirements traceability matrix (RTM) includes a number of non-negotiable requirements that were taken from regulations, regulatory guidance, and a standard for fuel design. In addition to these requirements, an additional set of criteria was developed. Some of these were "metrics" that were derived or taken from Reference [5]. Three additional sources of criteria were used: manufacturability, industry practice, and utility requests. These criteria were classified as either requirements or goals. If failure to meet a particular criterion was judged to pose an insurmountable obstacle for a fuel design, the criterion was called a requirement. In contrast, if failure to meet a particular criterion would only impose a competitive disadvantage, the criterion was called a goal. The inclusion of both requirements and goals recognizes that current fuel designs reflect decades of commercial optimization, so it may be necessary to accept reduced performance in one area (e.g., increased cost, reduced operating cycle length, or reduced power output) in order to obtain improved performance in others.

The RTM was used to allocate requirements to components and to set the evaluation criteria for gate reviews. More recently, it has been used, in planning for post-irradiation examinations, to ensure that all applicable tests and exams have been included.

3.2 Pellets

The University of Florida, a sub-recipient to AREVA, is developing fuel pellets that contain a second phase to improve thermal conductivity. To control chemical reactions between the uranium dioxide and the second phase, spark plasma sintering (SPS) is used. That method involves pressing powders in a graphite die while simultaneously heating the die and powder with pulsed direct current. Additives include silicon carbide powder (SiC-p), silicon carbide whiskers (SiC-w), and diamond. These additives were selected because they have extremely high thermal conductivities, high melting points, and small neutron capture cross sections.

Increasing the thermal conductivity can provide several benefits. First, it will decrease the amount of stored energy at the beginning of a LOCA, which will result in a reduced peak cladding temperature. Second, reducing the pellet temperature is expected to reduce fission gas release during normal operation. Reduced fission gas release, in turn, helps to control pellet-cladding chemical interaction, reduce the required plenum volume, and reduce ballooning and fuel relocation during LOCA. Third, reduced pellet temperatures may limit pellet cracking during normal operation, further improving heat transfer to the cladding and reducing the severity of pellet-cladding interaction.

Figure 3 shows the microstructures of pellets with SiC-w and SiC-p. Densification was achieved either by oxidative sintering or SPS. SPS provides high density with a short processing time. SPS also forces the uranium dioxide matrix into intimate contact with the additive, ensuring good heat transfer between the phases and allowing the additive to serve as a thermal “short circuit”. The thermal conductivity of pellets with additives typically exceeds that of plain uranium dioxide pellets by 50% or more [6].

An obvious question about the performance of these pellets is whether the increase in thermal conductivity will persist under irradiation. To answer that question, pellets with SiC-w and diamond additives are currently being irradiated in the Advanced Test Reactor at Idaho National Laboratory. It is expected that a single pellet type will be selected in a future gate review.

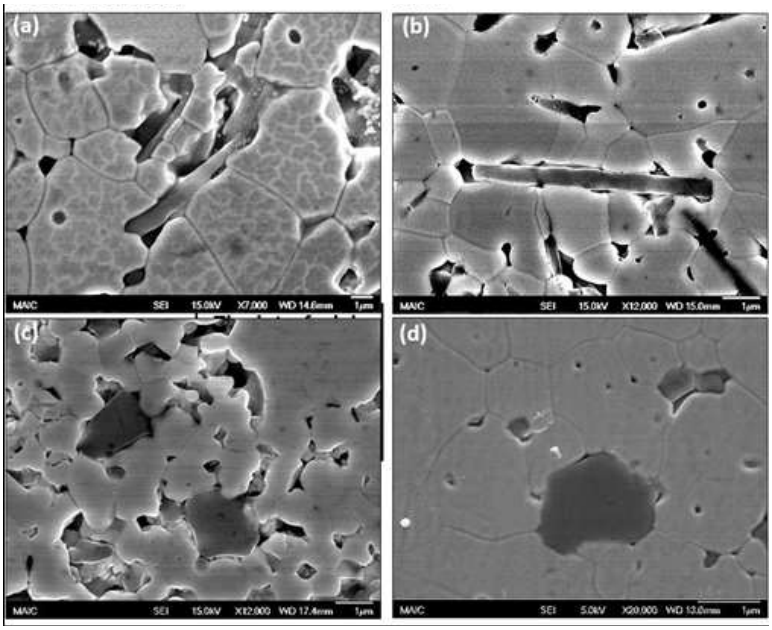

Fig. 3: Microstructures of uranium dioxide pellets with SiC-w (a and b), and SiC-p (c and d), densified by conventional sintering (a and c) or SPS (b and d)

3.3 Cladding

The Electric Power Research Institute, an AREVA teammate, is developing molybdenum alloy tubing for use as fuel cladding [7]. The outstanding feature of molybdenum as a cladding material is that it retains significant strength up to 1500 °C. Because it is a new cladding material, research is needed in various areas, including fabrication of bare tubes, application of coatings, welding, oxidation resistance, and irradiation effects.

Fabrication of bare tubes is the area that is most advanced. Tubes with suitable diameters for fuel cladding have been produced in both unalloyed molybdenum and an oxide dispersion strengthened alloy with 0.3 to 1.0% lanthanum oxide. Lengths up to 1.5 m have been produced, and efforts are in progress to optimize the heat treatment and microstructure.

Bare molybdenum does not have sufficient corrosion resistance under normal reactor operating conditions, so coatings of zirconium alloy and FeCrAl are being investigated to serve as a protective barrier against corrosion. For the current feasibility studies, physical vapour deposition (PVD) and various spray techniques were used successfully. For commercial production, mechanical co-reduction would be desirable to control cost and provide quality control. Tests on co-reduction are planned for 2015.

End caps have been successfully welded to tubing by plasma, gas-tungsten arc, and electron beam techniques. Additional work is in progress to ensure that welding can be done economically and with the extreme reliability required for fuel cladding.

Oxidation tests have shown good oxidation resistance in aggressive tests. Bare molybdenum, molybdenum coated with Zircaloy-2, and molybdenum coated with FeCrAl showed satisfactory performance during 7-day (168 hours) exposures at 1000 °C to steam.

Irradiation tests of molybdenum cladding are scheduled to start in 2015. Rodlets with uranium dioxide fuel pellets were sealed into stainless steel capsules and will be irradiated in the Advanced Test Reactor. Additionally, a test of 4 rodlets forming a 50 cm long fuel rod has been proposed for irradiation at the Halden Test Reactor beginning in 2016. A post-irradiation examination of molybdenum disks and rings in direct contact with uranium dioxide waffles, which were previously irradiated to about 110 GWd/MTU, is in progress to determine the chemical compatibility between the two.

3.4 Cladding Coatings

Savannah River National Laboratory, a sub-recipient to AREVA, is developing methods to apply oxidation-resistant MAX phase coatings to zirconium alloy substrates, and the coated samples are being treated and evaluated at the University of Wisconsin. Coatings are particularly attractive as a near-term measure because the substrate remains a conventional zirconium alloy. Design methods would require only minor changes and licensing would be eased. For example, mechanical design of a fuel assembly could discount the strength of the coating and take structural credit only for the zirconium alloy substrate. That approach is familiar from liner cladding.

Early results were not particularly promising [4]. Electrophoretic deposition produced thin, uniform layers, but the coatings were soft and could not be consolidated. High-velocity oxy-fuel spraying overheated the substrate. Cold-sprayed MAX phase coatings were hard, dense, adherent, and provided good protection during high-temperature steam oxidation, but relatively thick layers (about 100 µm) were needed to produce an impermeable layer, and the surface was rough. Only a few types of MAX phases are commercially available as powder, therefore their investigation as sprayed coatings were limited to Ti_2AlC. That composition has the drawback that titanium has a relatively large thermal neutron capture cross section.

In spite of those results, MAX phase coatings remained attractive because they typically provide good thermal conductivity, good oxidation resistance, radiation resistance, and some ductility. To overcome the problems with sprayed coatings, physical vapour deposition (PVD) by sputtering is now being investigated. Thin (5 µm), dense, adherent layers of Ti_2AlC have been successfully deposited on Zircaloy-4 substrates, as is shown in cross section in Figure 4. The thinness of the layer substantially reduces the neutronic penalty from titanium. Further reductions in the penalty are possible if coatings of Zr_2AlC are used; that material is currently being investigated. The PVD process can use the individual elements as source material, so it is not necessary to obtain powder with the desired composition.

Performance tests on PVD-coated Zircaloy-4 coupons are planned. The tests will characterize the oxidation resistance of both Ti_2AlC and Zr_2AlC coatings, at various thicknesses, and under normal operating and high-temperature steam conditions.

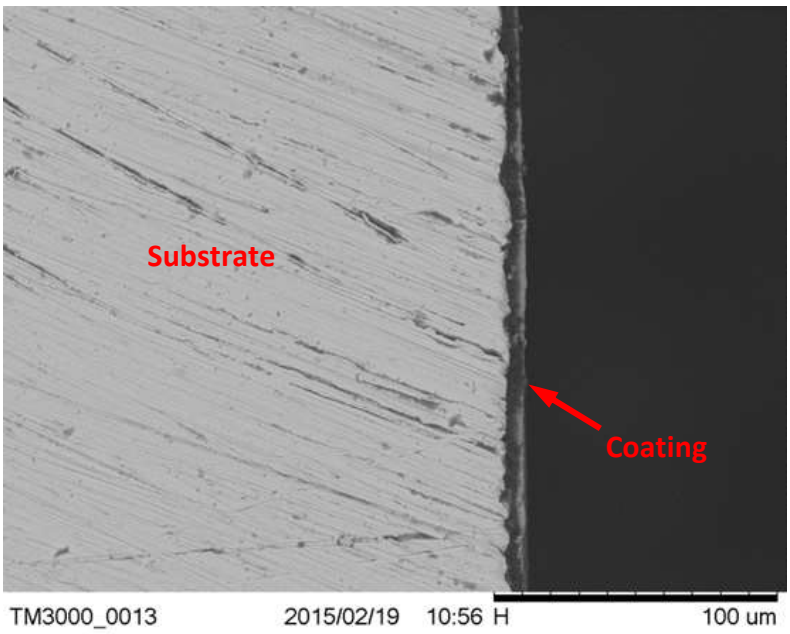

Fig 4: PVD coating of Ti_2AlC on Zircaloy-4

4. Developments within the French Nuclear Institute

Within the French Nuclear Institute framework, with the CEA and EDF, AREVA is developing two potential cladding concepts: chromium coating on zirconium alloys and SiC/SiC composite sandwich cladding. This section gives an overview of these developments.

4.1 Chromium-coating on zirconium alloys

The development of chromium (Cr)-coated zirconium (Zr) alloys is being investigated as a near-term solution since it is an evolution of the standard zirconium alloy cladding. The coating is fabricated using a Physical Vapour Deposition (PVD) process and forms a relatively thin (between 5 and 20 µm), dense layer, which adheres well to the zirconium substrate, and serves as a protective oxidation barrier with the following advantages [8]:

- Significantly improved corrosion resistance under nominal conditions
- Reduced corrosion rates in high temperature steam
- Improved post-quench mechanical behaviour due to a reduced ingress of oxygen and reduction of the amount of α(O)-Zr phase for design basis LOCA and slightly beyond design basis conditions
- Fretting resistance, low activation
- Easier licensing since it is similar to the zirconium alloy standard

The goal for the Cr-coating is to improve the behaviour in nominal conditions and to increase the “grace time” in accident conditions. The current work focuses on determining the potential gains in time and temperature during accident conditions to assess and quantify the benefits of such a solution in the ATF framework. For example, Figure 5 shows the comparison between uncoated and coated Zy-4 tubes after oxidation in 1200°C steam for 6000 s followed by a water quench. The reference uncoated sample exhibits a very thick oxide layer, with a large diffusion of oxygen within the remaining zirconium alloy forming the α(O)-Zr phase, which led to the fragmentation of the tube sample after the quench. On the other hand, the coated sample shows limited oxide formation, with significantly less diffusion of oxygen within the remaining metal, and thus the sample was not broken during the quench. This example shows that the Cr-coating provides additional “grace time” at 1200°C.

Fig 5: Post-Quench overview of uncoated and coated Zy-4 tubes exposed to 1200°C steam for 6000 s [10].

The next major step for the development of this concept is the irradiation of coated samples to evaluate the impact of irradiation on the coating behaviour. The Halden reactor is a potential candidate for such an irradiation, and a white paper was sent in 2014. This would greatly complement the out-of-pile data acquired so far.

4.2 SiC/SiC composite sandwich cladding

At CEA, SiC/SiC composite cladding was investigated at first for Generation IV application in Gas Fast Reactors due to its very good high temperature properties and irradiation resistance. Since the event at Fukushima in 2011, this concept is being adapted for application in light water reactors (LWRs) with the aim to increase safety margins during accidental conditions. The main advantages for using SiC to improve accident tolerance are:

- very low nominal and high temperature steam corrosion kinetics
- high strength at high temperature
- high sublimation temperature (>2700°C)

The CEA sandwich concept contains a thin (50-100 µm) refractory metal liner between two SiC/SiC composite layers. This sandwich design offers many advantages since the metallic liner provides the following key features [9][10]:

- leak-tightness of the cladding
- improved mechanical properties, especially resistance to flexural stress/strain
- easier sealing of the cladding by conventional methods such as welding

Studies were performed to establish the corrosion behaviour of SiC/SiC composite under PWR conditions, such as autoclave and PWR water corrosion loops, and showed very little oxidation compared to conventional zirconium alloys. Furthermore, high temperature tests showed that SiC composite tubes exhibited very little weight change up to 110 h in 1200°C steam whereas a standard Zy-4 tube was decomposed after only 4 h as shown in Figure 6. These results demonstrate the potential of this material, but studies and developments are still necessary due to new failure modes compared to conventional metallic cladding, which would also lead to new design rules, and thus lengthen the licensing process.

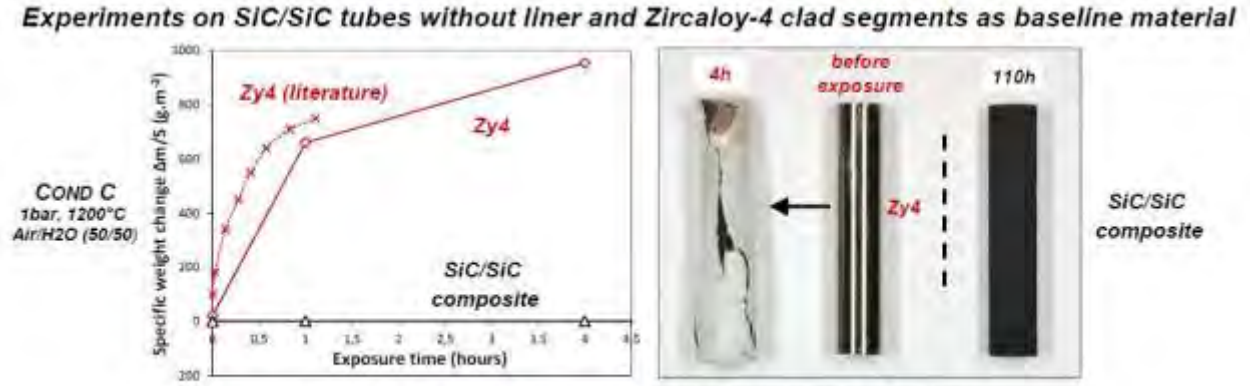

Fig 6: Comparison of the 1200°C air/steam oxidation between Zy-4 and SiC/SiC composite tubes [10].

5. Conclusion

Following the Fukushima-Daiichi accident several international programs were launched to investigate and develop innovative fuel concepts that would exhibit enhanced resistance to accidental conditions. Within this framework, AREVA is actively involved in the development of several cladding and pellet concepts through collaborative projects as part of the DOE EATF program and the French Nuclear Institute for R&D with CEA and EDF. For the cladding, three main concepts are being investigated: coatings on zirconium alloys (Cr coating and MAX phase coatings), EPRI's molybdenum cladding, and the CEA's SiC/SiC composite sandwich cladding. For pellets, AREVA is working with the University of Florida to develop enhanced thermal conductivity pellets containing SiC or diamond particle additives. Overall, the concepts investigated range from evolutionary solutions to longer term revolutionary solutions with gradually increased potential performance in accidental conditions.

6. Acknowledgements

Part of the material in this article is based upon work supported by the U.S. Department of Energy under Award Number DE-NE0000567 with AREVA Federal Services LLC.

7. References

[1] "The Fukushima Daiichi Nuclear Power Plant Accident: OECD/NEA Nuclear Safety Response and Lessons Learnt", NEA N°7161, OECD (2013)

[2] AREVA Federal Services LLC, Final Report for the Enhanced Accident Tolerant Fuels, RPT-3011235-000, Contract No. DE-NE-0000567 (2014)

[3] R. Kochendarfer, K. McCoy, P. Blanpain, "Use of Gate Reviews to Select Approaches for Enhancing Accident Tolerance", *Proceedings of the 2013 LWR Fuel Performance Meeting/Top Fuel 2013*, (September 15-19, 2013, Charlotte, NC)

[4] R. Kochendarfer, K. McCoy, B. Dunn, "Review of Progress on Enhanced Accident Tolerant Fuel", *Proceedings of Fontevraud 8 - Contribution of Materials Investigations*

and Operating Experience to LWRs' Safety, Performance and Reliability, (September 14-18, 2014, Avignon, France)

[5] INL/EXT-13-28090 / FCRD-FUEL-2013-000087, *Enhanced Accident Tolerant LWR Fuels: National Metrics Workshop Report* (January 2013)

[6] S. Yeo, E. Mckenna, R. Baney, G. Subhash, J. Tulenko, "Enhanced thermal conductivity of uranium dioxide–silicon carbide composite fuel pellets prepared by Spark Plasma Sintering (SPS)", *Journal of Nuclear Materials*, vol. 433, pp. 66-73 (2013)

[7] B. Cheng, P. Chou, and Y-J Kim, "Enhancing Fuel Resistance to Severe Loss of Coolant Accidents with Molybdenum-alloy Fuel Cladding, Proceedings WRFPM 2014, Sendai, Japan, Paper # 100075

[8] I. Idarraga-Trujillo, M. Le Flem, J-C Brachet, M. Le Saux, D. Hamon, S. Muller, V. Vandenberghe, M. Tupin, E. Papin, A. Billard, E. Monsifrot, F. Schuster, Assessment at CEA of Coated Nuclear Fuel Cladding for LWRs with Increased Margins in LOCA and beyond LOCA Conditions, Proceedings of 2013 LWR Fuel Performance Meeting/TopFuel, Charlotte, NC, USA, Sept. 15-19, (2013)

[9] C. Sauder, A. Michaux, G. Loupias, P. Billaud, J. Braun, Assessment of SiC/SiC Cladding for LWRs, Proceedings of TopFuel Conference in Charlotte, NC, USA, (2013)

[10] J.C. Brachet, C. Lorrette, A. Michaux, C. Sauder, I. Idarraga-Trujillo, M. Le Saux, M. Le Flem, F. Schuster, A. Billard, E. Monsifrot, E. Torres, F. Rebillat, J. Bischoff, A. Ambard, CEA studies on avanced nuclear fuel claddings for enhanced Accident Tolenrant LWRs Fuel (LOCA and beyond LOCA conditions), Proceedings Fontrevraud 8 SFEN conference, Avignon, France (2014)

INNOVATIVE TESTING METHOD FOR JOINTS OF SILICON CARBIDE TUBES

M.GENTILE, T.ABRAM
School of Mechanical, Aerospace and Civil Engineering,
The University of Manchester, Oxford Road,
M13 9PL, Manchester – UK

ABSTRACT

An innovative test method for joints of silicon carbide tubes is presented. Many research projects are focusing their attention on the development of silicon carbide – silicon carbide joints that have application in the nuclear industry. However there is a lack of consolidated test methods for the produced joints. The presented testing methodology addresses the weakness of the currently used test methods identifying the factors that determine the performance of the bond. The test method is based on mathematical calculations of the joint strength. The presented testing methodology is compared with the testing methodology currently employed. The results demonstrate that the proposed method improves the testing performance in terms of accuracy.

Introduction

All commercial Light Water Reactors (LWRs) fuel cladding is currently made from zirconium-based alloys. Zirconium alloys have been used as fuel cladding material for water-cooled reactors for over 50 years. However, in a severe accident scenario, such as the recent accident at the Japanese Fukushima site, zirconium alloys corrode rapidly in high temperature steam causing an extensive gaseous hydrogen generation, which compromises the safety of nuclear plants.

Therefore, after the Fukushima accident, extensive research has focused on the development of a new generation of nuclear fuels, which are accident tolerant. Accident Tolerant Fuels (ATF) offer significantly improved high temperature capability, due largely to the adoption of novel cladding materials[1].

Ceramic SiC-SiC composite claddings, for instance, have excellent thermal and radiological properties [2-4], offering significant improved oxidation resistance and the absence of hydrogen generation at high temperatures [5]. However, it has not been possible to utilise this great potential as a technology for manufacturing high temperature resistant joints of ceramic materials has not yet been adequately developed [6].

Another issue related to joining of SiC is the lack of a widely accepted standard methodology to test silicon carbide joints. Diverse technologies have been developed to join ceramics, although comparison of the strength of the joints produced using various bonding techniques is confounded by the variety of test types used [7-9]. Measuring the shear strength of the same joining material with different test methods could lead to different results.
The development of a reliable test method, capable of yielding reproducible shear strength data, would be beneficial to the entire research community.

This paper reviews previous testing standard in the research community, addressing their strength and weakness. It additionally presents a new testing methodology for silicon carbide joints, which improves results in terms of accuracy. The proposed testing methodology could be used to assess the strength of the joints after proton irradiation, which could be used to emulate reactor irradiation.

2. Fuel Cladding in LWRs

The fuel rods in LWRs, which comprise around 90% of the world's nuclear generating capacity, are 4m long and have a diameter of 9mm. The fuels pins are loaded with 2kg of uranium dioxide in the form of cylindrical pellets. Nuclear fuel rods operate in the temperature range of 300-330°c and in the pressure range of 70-170 bar.

The heat generated is about 20-30kW/m. The length of the operating life of nuclear fuel in a LWR ranges from 4 to 7 years [6]. Figure 1(a) shows an image of the typical design of a LWR's nuclear fuel and a schematic representation of the isotropic pressure distribution inside a nuclear fuel pin.

The gap between the cladding, the nuclear fuel pellets, and the plenum of the nuclear fuel rod, is filled with helium. During operation of the nuclear power reactor, the pressure inside the cladding varies due to the development of temperature gradients and the generation of xenon and krypton gases due to the fission of uranium dioxide pellets [10]. Figure 1(b) provides an overview of proposed nuclear fuel end-cups designs [11]. In addition, the swelling of nuclear fuel pellets stresses the cladding.

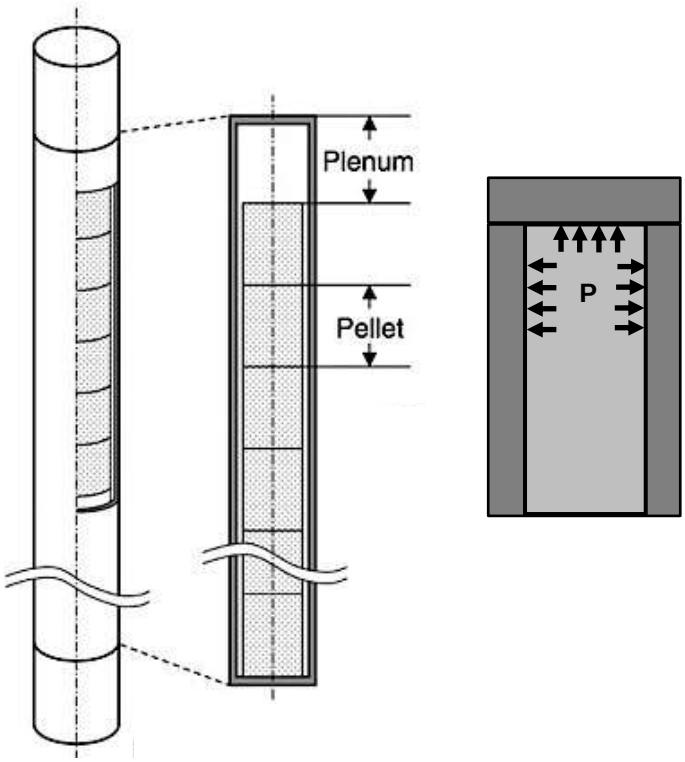

(a)

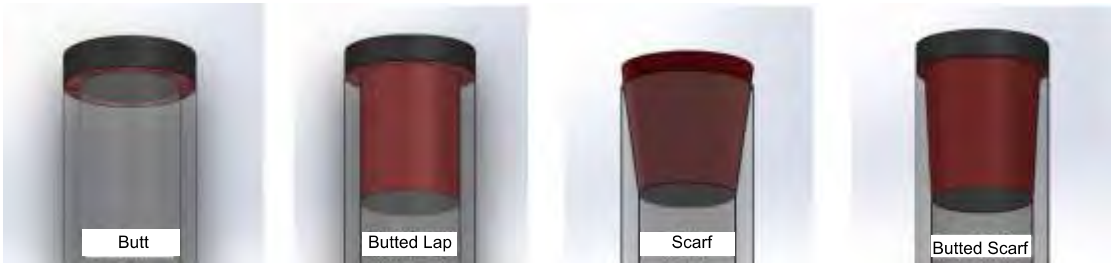

(b)

Fig.1 shows: a) schematic diagram of LWR fuel rod pressure distribution near the end-cup of the nuclear fuel rod; b) proposed lid geometries for silicon carbide cladding [11].

Depending on the joining process, the joint region may be the weakest part of the nuclear fuel cladding. While the joints between similar materials have similar thermal expansion coefficients, joints involving dissimilar materials are subject to thermal stresses due to different thermal expansion coefficients.

Additionally, forces generated by the gas pressure inside the cladding, and by the swelling of the nuclear fuel, have directions, which have a radial distribution inside the cylindrical cladding tube and are perpendicular to the top plane of the cylinder, as shown in Fig.1(a). Finally, the load transferred across the joints depends upon the geometry of the silicon carbide cladding lid, which can determine the mixed-mode load for the joining area. This can be observed in the lid geometries proposed in Fig.1(b).

3. Testing methods of ceramics joints

There is a lack of standards for ceramic joints. Therefore, researchers have measured the properties of the ceramic joints using standards for adhesive bonds, polymer matrix composite materials, reinforced plastics, and composite materials. A summary of the standards used to measure the strength of the joints in reported by Y.Katoh et al. [12] Shear testing of composite materials has proven to be one of the most difficult areas of mechanical property testing. The presence of edges, material coupling, non-pure shear loading, non-linear behavior, imperfect stress distributions or the presence of normal stresses, make shear strength determination questionable. It is presently stands that none of the available test methods are without their inaccuracies. Therefore, application of shear strength data to structural applications should be reviewed carefully on a case-by-case basis to understand the consequence of the potential inaccuracies of the value being used. Table 1 summarises the testing methods currently used to evaluate the properties of silicon carbide joints. The standards, D3846, D3518, D4255 and D905 measure apparent shear strength, while the ASTM standards D5448, D2344, F1362, D5379 and C1469 measure the pure shear strength of ceramics joints.

Tab.1 Summary of the methods used to evaluate the properties of silicon carbide joints.

P_{max} is load carried by the test specimen. A is cross sectional area at test section. T_{max} is the maximum torque applied to the cylinder. J is the polar moment of inertia and r_{max} is the maximum radial distance. S_o and S_i are the outer and the inner span respectively. In all of the ASTM standards, the shear strength is measured in MPa, except for the ASTM D905 standard, in which it is measured in kPa. P_{max} is measured in N, and A is measured in mm^2.

ASTM Standard		Specimen geometry	Value measured	Mathematical equation
D3846	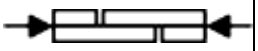	Lap-joined double-notched coupon	Mixed shear strength	$\tau = P_{max}/A$
D3518		Slant-butt-joined beam	Mixed shear stress	$\tau = P_{max}/2A$
D4255	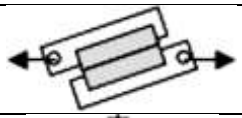	Lap-joined coupon	Mixed shear stress	$\tau = P_{max}/A$
D2344		Lap-joined beam	Mixed shear strength	$\tau = 0.75 \times P_{max}/A$
D5379	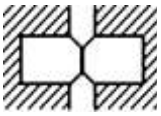	Butt-joined notched beam	Shear stress	$\tau = P_{max}/A$
D905	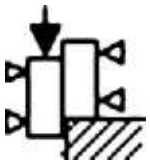	Offset lap-joined coupon	Mixed shear strength	$\tau = P_{max}/A$
C1469	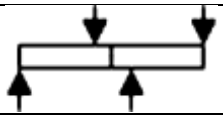	Butt-joined beam	Shear strength	$\tau = P_{max}(S_o - S_i)/A(S_o - S_i)$
F1362	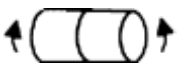	Lap or butt-joined rod	Shear strength	$\tau = T_{max} r_{max}/J$
D5448		Butt-joined hollow rod	In-plane shear strength	$\tau = T_{max} r_{max}/J$

The ASTM standard D3846 measures the in-plane shear strength of the analysed material in compression in flat sheet, with a thickness ranging between 2.54mm and 6.6mm. Conversely, the ASTM standard D3518 measures the in-plane shear strength in tension for laminated composites with a symmetric lay-up, composed only of +45° plies and −45° plies.

The ASTM standard D4255 determines the in-plane shear properties of high-modulus fiber-

reinforced composite materials by either of two procedures. In the first procedure, laminates clamped between two pairs of loading rails are tested. When loaded in tension, the rails introduce shear forces to the specimen. In the second procedure, laminates are clamped onto opposite edges, with a tensile or compressive load applied to a third pair of rails in the center, and are subsequently tested. The ASTM D2344 standard measures the shear strength loading a beam in three points bending.

The application of the ASTM D2344 testing methods is limited to materials for which the elastic properties are balanced and symmetric, with respect to the longitudinal axis of the beam. In most cases, because of the complexity of internal stresses and the variety of failure modes that can occur in this specimen, it is not generally possible to relate the short-beam strength to any one material property. The ASTM standard D5379 determines the in-plane and inter-laminar shear properties, depending upon the orientation of the material coordinate system, relative to the loading axis. The application of the ASTM standard D5379 is limited to composite materials.

The ASTM standards D3846, D3518, D4255, D2344 and D5379 are easier to do and the shape of the specimens is, usually, closer to the components working conditions. However, they do not measure shear strength properly. They underestimate the joint strength for pure shear, as they give “apparent shear” resulting from a mixed state of stress, including sometime shear bending, and tensile stresses. Due to the various complex stress states in different test configurations, comparison of data obtained by different test methods is not possible.
The ASTM standard D905 is intended primarily as an evaluation of adhesives for wood. It cannot be assumed that this test method measures the true shear strength of the adhesive bond. Many factors including the strength of the wood, the specimen, the shear tool designs themselves, and the rate of loading interferes with or adds bias to the measurement. One of the major drawbacks with this method is its limited measurement range: although samples are easy to obtain and be broken in the joint, due to the relatively weak joining materials, many difficulties have been encountered when measuring moderately strong joints. In this case, the failure always occurs between the fixtures and the specimen and never inside the joined area, independently from the kind of joined ceramic. This test cannot be used, when the apparent shear strength of the joined samples approaches 50MPa.

The ASTM standard C1469 is the only ASTM standard designed for ceramics joints. However, the C1469 standard presents two pitfalls. If the flexural strength of the joined material is higher than 50% of the base material, the asymmetrical four-point bending test cannot be used. To obtain reliable pure shear strength of joined ceramics with this test, the joint must be perfectly aligned to ensure proper loading. A lateral shift of a few micrometres to the aligned positioning of the sample can result in a mixed shear plus bending load in the joint, with a consequent lower apparent shear measured.

Torsion results were considered more reliable than those obtained by standard lap tests. A pure shear stress distribution is obtained with torsion tests: the stress distribution is non uniform, since the shear stress acts in the tangential-axial plane and is proportional to the distance from the cylinder axis.

Finally, the ASTM standard F1362 (TC) measures the shear strength and the shear modulus of interlayer materials. Torsional shear forces are applied to the interlayer through a circular section, which produces a peripherally uniformed stress distribution. The ASTM standard D5448 measures, in torsion, the in-plane shear properties of wound polymer matrix composites reinforced by high- modulus continuous fibres. Specimens tested with the procedure described in the ASTM standard D5448 showed failure of the tubes inside the fixtures due to the stress concentration on the edges caused by the specimen fixture. Specimens tested using the ASTM standard F1362 gave more satisfactory results.

However, it was found that the shear strength measured with the proposed torsion shear fixture is higher than that measured with the conventional step lap specimen. Improved results were obtained using miniaturised torsion tests [13] although the proposed miniaturised torsion tests are suitable to measure the pure shear strength of a joined component only if the joining material is purely brittle and if the fracture propagates in the joined area.

4. Proposed testing method

The mechanical performance of silicon carbide joints is a crucial factor for the safety in nuclear power reactors. Therefore, it is necessary to use appropriate testing methodologies to assess the performance of new and improved joining techniques.

The proposed testing method is based on the local measurement of the mechanical proprieties of the joints. This testing method has general application.

A testing method based on local measurements presents several advantages. In fact, a testing method based on local measurements correlates the effective properties of the joining material to the overall performance of the joint. The manufacturing process of the joints usually generates bubbles, crack and voids. These defects introduced by the manufacturing process affect the strength of the joints.
Additionally, local measurements can determine the properties of irradiated materials. Proton irradiation has proved to be a valuable substitute to neutron irradiation [14 - 15]. The great advantage of proton irradiation is that it can be carried out in a relatively short time compared to neutron irradiation. Although, ion-beam irradiation has a rather limited penetration depth and therefore drastically limits the amount of material available to be investigated. Consequently, mechanical tests of proton irradiated joints cannot be carried out with conventional testing methods.

The proposed testing method consists of three steps. Firstly, the micro-tensile specimens and micro-cantilevers are prepared using the focused ion beam technique. Secondly, the properties of the micro-tensile specimens and the micro-cantilever are measured through micro-tensile testing. Thirdly and finally, the strength of the entire joint is calculated through differentiation.

The tensile strength is measured using micro-tensile tests. The specimens are tested using micro-tensile tests and micro-cantilever beam bending tests. Fig.2 shows examples of micro-tensile test specimens.

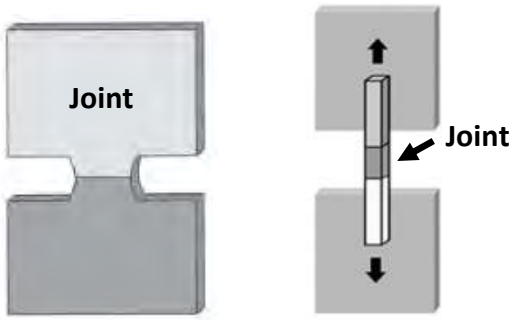

Figure 2: Examples of micro-tensile test specimens.

The tensile strength is calculated according to the formula: $\sigma = P/A$ in which σ is the tensile strength, P is the load and A is the cross-sectional area of material with area parallel to

the applied force vector. The shear strength is measured using a cantilever beam bending test. Fig.3 reveals an example of this test.

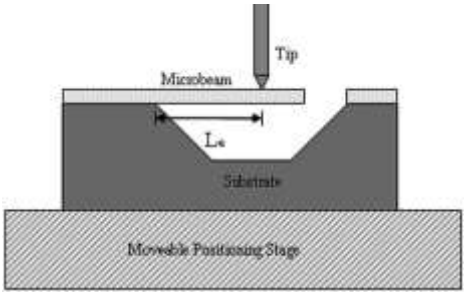

Figure 3: Schematic representation of cantilever bending test.

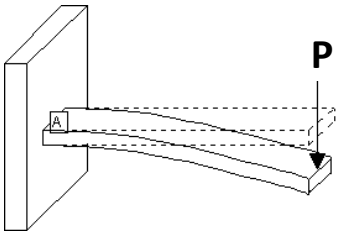

Figure 4: Examples of cantilever beam under load.

According to the Jourawski formula:

$$\tau_{xy} = \frac{VQ}{It}$$

In which V is the total shear force at the location in question, Q is the statical moment of the area, I is moment of inertia of the entire cross sectional area, and t is the thickness in the material perpendicular to the shear. The Jourawski formula can be simplified using the formula:

$$\tau_{xy} = \chi \frac{V}{A}$$

Where χ is the shear coefficient, which is 6/5 for a rectangular cross-section. Finally the overall strength of the joints is calculated by integration.

The method based on local measurements presents several advantages:

1) This method can be easily implemented.
2) The method can be used to measure the strength of irradiate materials, when handling large samples presents safety issues.
3) The small volume of the specimens is advantageous to obtain more data points on a given volume of material and increase the accuracy of the measurement.

5. Conclusions

The current test methods do not correlate the joint performance to the properties of the analysed material. In order to understand the behavior of silicon carbide joints, and to improve their performance, a method based on local measurement is suggested. This method improves the testing performance in terms of accuracy.

References

1) Zinkle, S.J.; Terrani, K.A.; Gehin, J.C.; Ott, L.J.; Snead, L.L. Journal of Nuclear Materials 448 (2014) 374 –379
2) Slack, G.A. Journal of Applied Physics 1964, 35, 3460
3) Barret, D.L.; Campbell, R.B. Journal of Applied Physics 1973
5) Ford, L.H.; Hibbert, N.S.; Martin, D.G. Journal of Nuclear Materials 1973, 45, 139 149.
5) Snead, L.L.; Nozawa, T.; Katoh, Y.; Byun, T.; Kondo, S.; Petti, D.A. Journal of Nuclear Materials 2007, 371, 329 377.
6) Hallstadius, L.; Johnson, S.; Lahoda, E. Progress in Nuclear Energy 57 (2012) 71-76
7) Katoh, Y.; Snead, L.L.; Cheng, T.; Chunghao, S.; Lewis, W.D.; Koyanagi, T.; Hinoki, T.; Henager, C. H. Jr.; Ferraris, M. Journal of Nuclear Materials 448 (2014) 497-511
8) Henager Jr, C.H.; Kurtz, R.J. Journal of Nuclear Materials 417 (2011) 375–378
9) Henager Jr, C.H.; Shin, Y.; Blum, Y.; Giannuzzi, Y.L.A.; Kempshall B.W.; Schwarz, S.M. Journal of Nuclear Materials 367–370 (2007) 1139–114
10) Olander,D.;Journal of Nuclear Materials 389 (2009) 1–22
11) Khalifa, H.E.; Deck, C.P.; Gutierrez, O.; Jacobsen, G.M.; Back, C.A.; Journal of Nuclear Materials 547, (2015), 227– 240
12) Katoh,Y.; Snead, L.L.; Cheng,T.; Shih, C.; Lewis, W.D.; Koyanagi, T.; Hinoki, T.; Henager Jr, C.H.; Ferraris, M.; Journal of Nuclear Materials 448 (2014) 497– 511

13) Monica, F.; Milena, S.; Casalegno, V.; Ventrella, A.; International Journal of Applied Ceramic Technology 9, (2012), 795–807

14) Was, G.S.; Journal of Materials Research 30, (2015),1158-1182

15) Hosemann, P.; C. Shin, C.; Kiener,D.; Journal of Material Research 30, (2015),1-16

PWR Operating Experience

IN-REACTOR PERFORMANCE OF HIPER16^{TM} FUEL DESIGN

S. Y. JEON, J. S. Yoo, H. J. Kim, K. S. Choi, J. I. KIM, K. L. JEON
Nuclear Fuel Development Group, KEPCO Nuclear Fuel
242, Daedeok-Daero 989Beon-Gil, Yuseong-Gu, Daejeon, 305-353, Korea

ABSTRACT

KEPCO Nuclear Fuel(KNF) developed the HIPER16^{TM} (High Performance with Efficiency and Reliability) fuel design in 2010, accomplishing a series of out-of-pile tests. The mechanical integrity and safety of HIPER16^{TM} fuel design has been verified based on the final verification test and evaluation results. The eight HIPER16^{TM} Lead Test Assemblies(LTAs) were loaded in HANUL Unit 6 for 3 cycles from 2011 to 2015. The poolside examinations have been performed after 1st and 2nd irradiation cycle of LTAs to verify the in-reactor performance of HIPER16^{TM} fuel design. The visual examinations and dimensional measurements were performed on the LTAs using poolside examination equipment. The in-reactor verification test results showed that the HIPER16^{TM} fuel design met the irradiation related design requirement. The poolside examinations after 3rd irradiation cycle of LTAs will be performed at the end of 2015.

1. Introduction

KEPCO Nuclear Fuel (KNF) developed the HIPER16^{TM} (High Performance with Efficiency and Reliability) fuel design in 2010, accomplishing a series of out-of-pile tests. The main design objectives of HIPER16^{TM} fuel development include high burn-up capability, high thermal performance, and high mechanical performance, such as hold-down force optimization, fretting wear margin increase and debris filtering efficiency increase, etc. The out-of-pile tests were performed either in air or in a hydraulic loop and at room temperature or operating temperature conditions. The test results include the required physical and thermal-hydraulic data needed to verify the HIPER16^{TM} fuel design. The mechanical integrity and safety of HIPER16^{TM} fuel design has been verified based on the final verification tests and evaluations[1].

The HIPER16^{TM} LTAs were loaded in HANUL Unit 6 for 3 cycles from 2011 to 2015. The four reference alloy LTAs and the other four HANA^{TM} alloy LTAs were loaded in symmetric positions in the core. The reference alloy is a conventional zirconium-based alloy(Zr-1.0Nb-1.0Sn) which has enough commercial reactor irradiation experience. The HANA^{TM} (High performance Alloy for Nuclear Application) alloy is an advanced zirconium-based alloy(Zr-1.1Nb-0.07Cu) developed in Korea in order to meet the global demand for an extension of the fuel discharge burn-up. The HANA^{TM} cladding has higher corrosion resistance compared to commercial claddings. And, it has similar creep and LOCA resistance with commercial claddings. The LTAs were located at the vicinity of the shroud during 1st irradiation cycle and located at the center of the core during 2nd irradiation cycle. The poolside examinations have been performed after 1st and 2nd irradiation cycle of LTAs to verify the in-reactor performance of HIPER16^{TM} fuel design. The visual examinations and dimensional measurements were performed on the LTAs using poolside examination equipment. The in-reactor verification test results showed that the HIPER16^{TM} fuel design met the irradiation related design requirement. The poolside examinations after 3rd irradiation cycle of LTAs will be performed at the end of 2015.

In this paper, the in-reactor verification test results for HIPER16^{TM} fuel design were described. The in-reactor performance of the fuel assembly growth, fuel assembly bow, spacer grid growth, fuel rod growth, fuel rod outer diameter and fuel rod oxide thickness were evaluated based on the in-reactor verification test results. Based on the measured data and evaluation results, the in-reactor performance of HIPER16^{TM} fuel assembly and fuel rod design have been verified.

2. HIPER16^{TM} Fuel Design Characteristics

The HIPER16^{TM} fuel design is a 16X16 type fuel assembly with 236 fuel rods, and 150 inches fuel stack length for CE-NSSS Type Nuclear Power Plants. The fuel assembly contains reference alloy or HANA^{TM} alloy fuel rods that have same outer diameter, inner diameter and cladding thickness. Table 1 identifies the main design parameters of the HIPER16^{TM} fuel design and Figure 1 shows the key design features of the HIPER16^{TM} fuel assembly. As indicated in Figure 1, the HIPER16^{TM} fuel design features include: Removable Top Nozzle, Reduced Rod Bow (RRB) Inconel top grid, reference alloy or HANA^{TM} alloy mid and IFM grids, high debris filtering Inconel bottom grid, low pressure drop Bottom Nozzle, reference alloy or HANA^{TM} alloy guide tubes and instrument tube, and fuel claddings[2].

Tab 1. Main Design Parameters of HIPER16^{TM}

Items	Reference alloy	HANA^{TM} alloy
Fuel Array	16x16	16x16
Fuel Assembly Pitch (in.)	8.180	8.180
Number of Rods per Assembly (EA)	236	236
Guide Tubes OD (in.)	0.980	0.980
Fuel Rod Pitch (in.)	0.506	0.506
Fuel Rod OD (in.)	0.374	0.374
Fuel Stack Length (in.)	150	150
Number of Guide Tubes (EA)	4	4
Number of Instrument Tube (EA)	1	1
Number of MID Grids	9	9
Number of IFM Grids	2	2

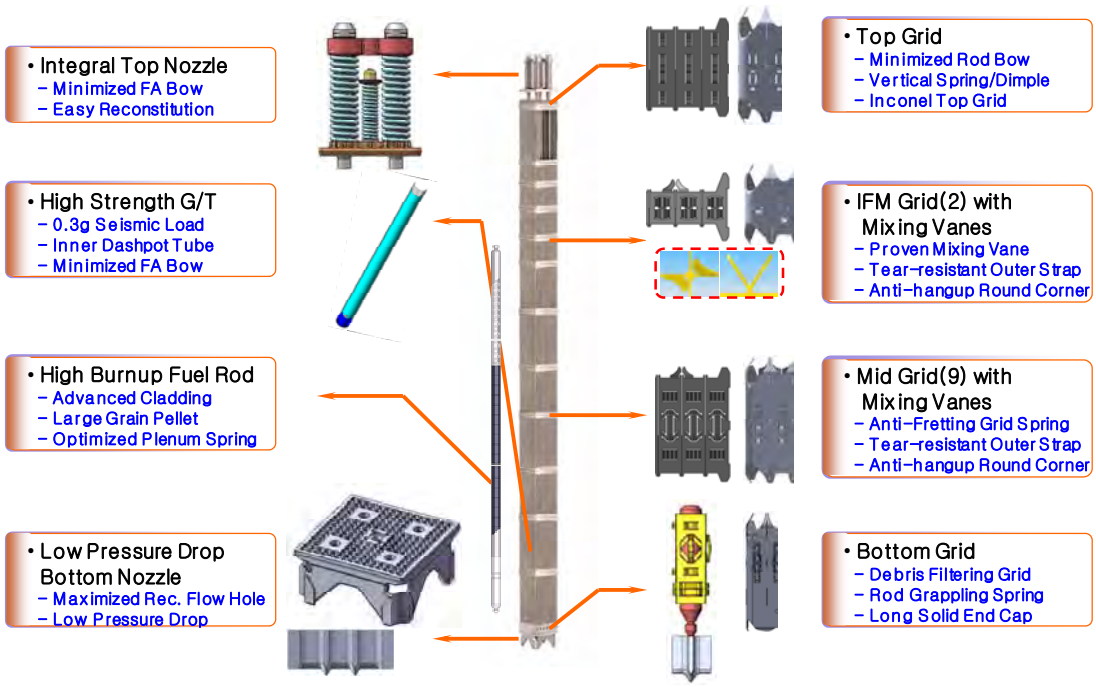

Fig 1. Key Design Features of HIPER16^{TM}

The structural skeleton is comprised of four guide tubes and one center instrumentation tube with a 0.980 inch diameter. The guide tubes are quite different in respect that the uniform outer diameter guide tubes are used in the HIPER16^{TM} fuel assembly. The dashpot region is implemented using a separate dashpot tube which is spot-welded to the outer guide tube. The outer diameter and thickness of the guide tube and instrumentation tube is same as that of PLUS7^{TM} fuel design. At the lower end of the assembly, there is a low pressure drop bottom nozzle with large square holes. Then, an Inconel 718 bottom grid with debris filtering capability is utilized. Nine reference alloy or HANA^{TM} alloy mid-grids with mixing vanes and two intermediate flow mixers are then utilized, followed at the very top of the assembly by an Inconel 718 vaneless structural top grid. All the grids are fabricated from slotted, interlocked straps which are attached by either laser welding or brazing. The top and bottom nozzles are fabricated from Type 304 stainless steel. The top nozzle is designed to have an on-off type coil spring and a removable attachment feature. The total pellet stack length is 150 inches in which large grain pellets are loaded. The fuel stack is contained within the fuel tube, which is pressurized with helium gas. There is a plenum at the top of the fuel rod, and a variable pitch rod plenum spring is used for high burnup capability.

3. In-Reactor Performance of HIPER16^{TM}

The eight LTAs were manufactured using qualified processes that are applied for the existing commercial fuel manufacturing processes at KNF. The LTAs and their components were pre-characterized prior to irradiation to obtain reference values for the post irradiation examination. The LTAs were loaded in HANUL Unit 6 for 3 cycles. The four reference alloy LTAs and the other four HANA^{TM} alloy LTAs were loaded in symmetric positions in the core. The LTAs were located at the vicinity of the shroud during 1st irradiation cycle and located at the center of the core during 2nd irradiation cycle. The fuel assembly average burnup of 1st and 2nd irradiation cycle of LTAs were about 18,000 MWD/MTU and 38,700 MWD/MTU, respectively.

The 1st and 2nd cycle of the LTAs irradiation has been successfully completed in 2012 and 2014, respectively. The poolside examinations have been performed after 1st and 2nd irradiation cycle of LTAs to verify the in-reactor performance of HIPER16^{TM} fuel design. During the fuel outage period after the 1st and 2nd irradiation cycle, visual examinations and dimensional measurements were performed on the LTAs using poolside examination equipment as shown in Figure 2. The items for the visual examination and dimensional measurements are as follows:

- Visual examinations
  - Assembly outside visual inspection
  - Rod outside visual inspection
- Dimensional measurements
  - Assembly length
  - Grid width
  - Rod length
  - Rod shoulder gap
  - Rod diameter
  - Rod oxide thickness
  - Other performance parameters, etc.

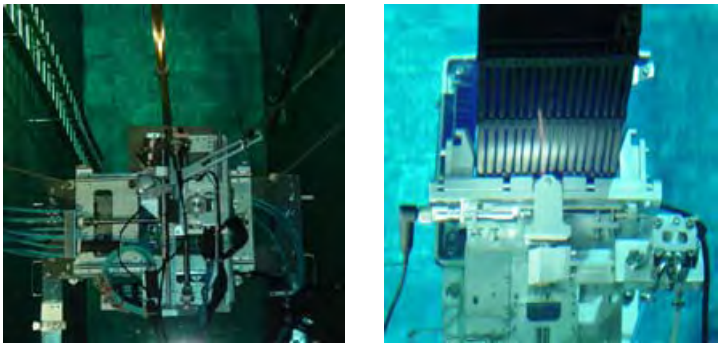

Fig 2. Poolside Examination Equipments

The in-reactor verification test results showed that the HIPER16^{TM} fuel design met all of irradiation related design requirement. The HIPER16^{TM} LTAs are now in the 3rd irradiation cycle and the poolside examination after 3rd irradiation cycle of LTAs will be performed at the end of 2015.

3.1 Fuel Assembly Growth

The fuel assembly growth measurements were performed for the HIPER16^{TM} fuel assemblies with reference alloy and HANA^{TM} alloy in HANUL Unit 6. Figure 3(a) shows the relative fuel assembly growth to allowable growth for PLUS7^{TM} and HIPER16^{TM} fuel design. The growth characteristics of PLUS7^{TM} and HIPER16^{TM} fuel assembly design are very similar except a little higher growth for HIPER16^{TM} fuel assembly design after 1st cycle. The fuel assembly growth for PLUS7^{TM} and HIPER16^{TM} fuel design are very similar because the nominal dimensions of guide tube and fuel rod designs are same and the hold-down forces for both fuel assembly designs are almost same. Figure 3(b) shows the relative fuel assembly growth to allowable growth of HIPER16^{TM} fuel assembly design for reference alloy and HANA^{TM} alloy. The fuel assembly growth of HIPER16^{TM} with HANA^{TM} alloy is lower than that of HIPER16^{TM} with reference alloy. Based on the measured data and evaluation results, the HIPER16^{TM} fuel design has very similar fuel assembly growth characteristics with PLUS7^{TM} fuel design which has enough in-reactor experience and it was confirmed that the in-reactor performance of HIPER16^{TM} with HANA^{TM} alloy is better than that of HIPER16^{TM} with reference alloy.

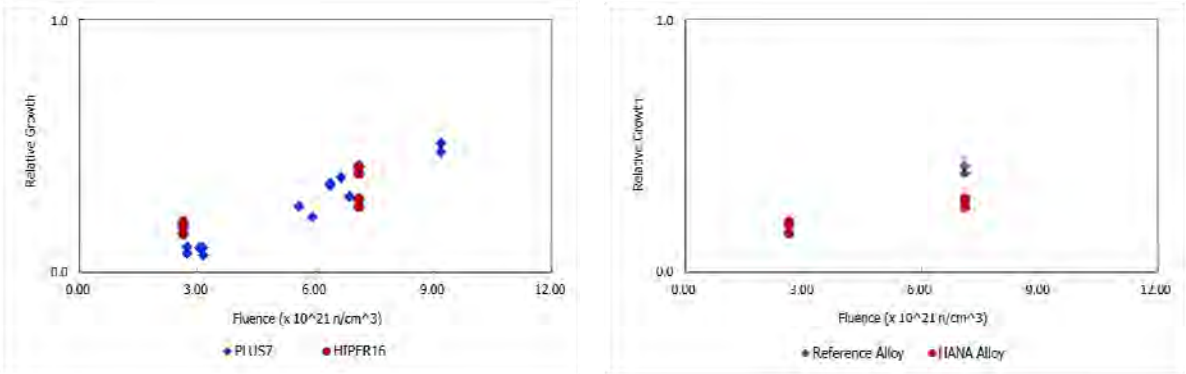

(a) PLUS7^{TM} vs. HIPER16^{TM} (b) Reference alloy vs. HANA^{TM} alloy

Fig 3. Fuel Assembly Growth

3.2 Fuel Assembly Bow

The fuel assembly bow measurements were performed for the HIPER16^{TM} fuel assemblies with reference alloy and HANA^{TM} alloy in HANUL Unit 6. The measured fuel assembly bow data for the reference alloy and HANA^{TM} alloy HIPER16^{TM} fuel assemblies have been analyzed to investigate the characteristics of fuel assembly bow for the HIPER16^{TM} fuel assembly design.

Figure 4, 5 and 6 show the fuel assembly bow plotted on the same scale. Figure 4 shows the fuel assembly bow for each face of the HIPER16^{TM} fuel assembly with reference alloy for cycle 1 and 2. Figure 5 shows the fuel assembly bow for each face of the HIPER16^{TM} fuel assembly with HANA^{TM} alloy for cycle 1 and 2. The typical shape of the HIPER16^{TM} fuel assembly bow is “C” shape and the direction of fuel assembly bow was changed as the number of cycle increase. Based on the measured data and evaluation results, the bow characteristics of HIPER16^{TM} fuel assembly design for reference alloy and HANA^{TM} alloy are very similar and the HIPER16^{TM} fuel assembly bow requirement is met based on the measured data. The fuel assembly bow requirement has been established based on the loading and unloading performance of fuel assembly in the core. The maximum values of the measured fuel assembly bow data for the HIPER16^{TM} fuel assembly design with reference alloy and HANA^{TM} alloy are about 25% of the allowable fuel assembly bow requirement. Based on the evaluation results, it was confirmed that there are enough margin on the fuel assembly bow of the HIPER16^{TM} fuel design.

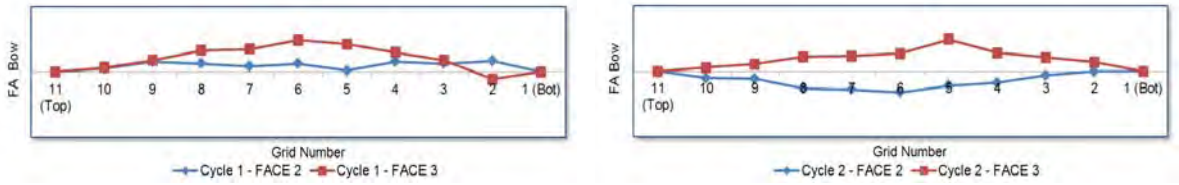

(a) Cycle 1 (Face 2 and 3) (b) Cycle 2 (Face 2 and 3)

Fig 4. HIPER16^{TM} Fuel Assembly Bow (Reference alloy)

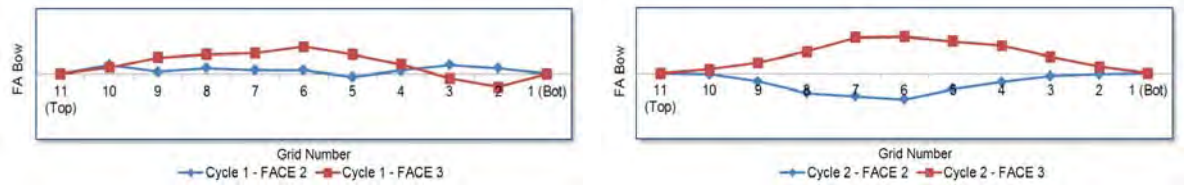

(a) Cycle 1 (Face 2 and 3) (b) Cycle 2 (Face 2 and 3)

Fig 5. HIPER16^{TM} Fuel Assembly Bow (HANA^{TM} alloy)

Figure 6 shows the measured bow of PLUS7^{TM}[3] and HIPER16^{TM} fuel designs. There are some differences on the shape of fuel assembly bow between PLUS7^{TM} and HIPER16^{TM} fuel designs. The maximum fuel assembly bow occurs at the upper part of the fuel assembly for the PLUS7^{TM} design and at the middle part of the fuel assembly for the HIPER16^{TM} design.

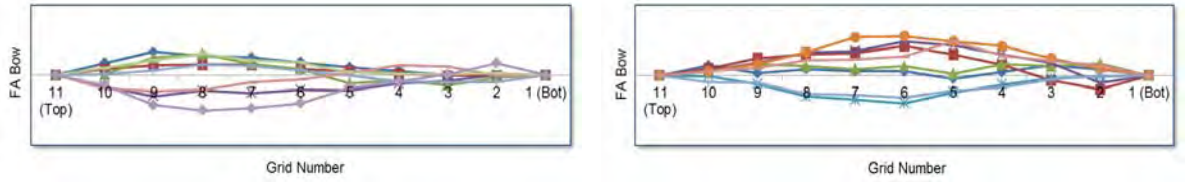

(a) PLUS7^{TM} (Cycle 1~2, Reference) (b) HIPER16^{TM} (Cycle 1~2, Reference/HANA^{TM})

Fig 6. Fuel Assembly Bow (PLUS7 ^{TM} vs. HIPER16^{TM})

The shape of the fuel assembly bow can be affected by the fuel assembly lateral stiffness distribution along the fuel assembly length. The main design parameters to increase the fuel assembly lateral stiffness are the guide thimble stiffness, fuel rod stiffness and the number of joints between guide tubes and spacer grids. The guide thimble stiffness and fuel rod stiffness of HIPER16^{TM} fuel design are almost same as that of PLUS7^{TM} fuel design. There are two IFM grids at the upper part of the HIPER16^{TM} fuel assembly. The two IFM grids at the upper part of the HIPER16^{TM} fuel assembly increase the lateral stiffness of the HIPER16^{TM} at the upper part of the fuel assembly due to the additional joints between guide tubes and spacer grids. Based on the evaluation results, it seems that the differences of the fuel assembly bow shape are mainly due to the two IFM grids of HIPER16^{TM} fuel design. The maximum fuel assembly bow of PLUS7^{TM} and HIPER16^{TM} fuel designs are almost same regardless of the location of maximum fuel assembly bow.

3.3 Spacer Grid Growth

The spacer grid growth measurements were performed for the HIPER16^{TM} fuel assemblies with reference alloy and HANA^{TM} alloy in HANUL Unit 6. Figure 7(a) shows the relative spacer grid growth to allowable growth for PLUS7^{TM} design with reference alloy and HIPER16^{TM} design with reference alloy and HANA^{TM} alloy. The growth characteristics of PLUS7^{TM} and HIPER16^{TM} spacer grid design are very similar except a little higher growth for HIPER16^{TM} fuel assembly design after 2nd cycle. The grid growth of HIPER16^{TM} design with reference alloy is higher than that of PLUS7^{TM} design with reference alloy. It is evaluated that the higher grid growth of HIPER16^{TM} design with reference alloy is mainly due to the increased grid spring force of HIPER16^{TM} design compared to PLUS7^{TM} design. Figure 7(b) shows the relative spacer grid growth to allowable growth of HIPER16^{TM} fuel assembly design for reference alloy and HANA^{TM} alloy. The spacer grid growth of HIPER16^{TM} with HANA^{TM} alloy is lower than that of HIPER16^{TM} with reference alloy. Based on the measured data and evaluation results, the HIPER16^{TM} fuel design with HANA^{TM} alloy has very similar spacer grid growth characteristics with PLUS7^{TM} fuel design which has enough in-reactor experience and it was confirmed that the in-reactor performance of HIPER16^{TM} with HANA^{TM} alloy is better than that of HIPER16^{TM} with reference alloy.

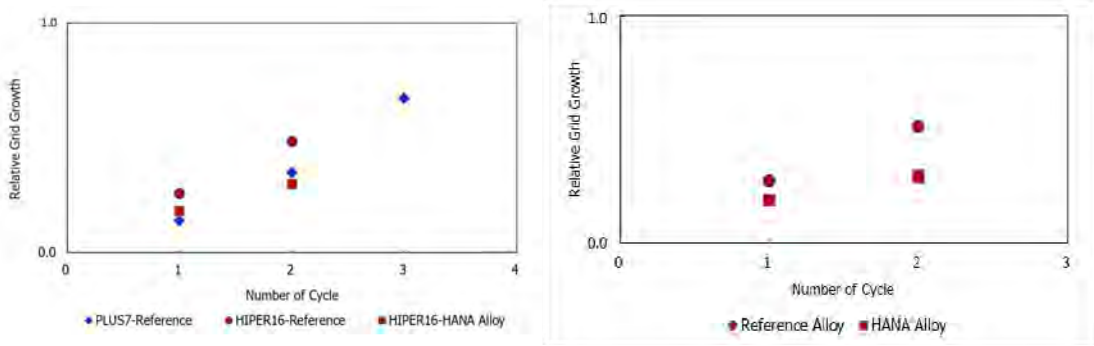

(a) PLUS7^{TM} vs. HIPER16 ^{TM} (b) Reference alloy vs. HANA^{TM} alloy

Fig 7. HIPER16^{TM} Spacer Grid Growth

3.4 Fuel Rod Growth, Diameter Change and Oxide Thickness

The fuel rod growth, fuel rod outer diameter and fuel rod oxide thickness were measured for the HIPER16^{TM} fuel assemblies with reference alloy and HANA^{TM} alloy in HANUL Unit 6. Figure 8 (a) and (b) show the relative fuel rod growth and oxide thickness to design requirement of HIPER16^{TM} fuel assembly for reference alloy and HANA^{TM} alloy, respectively. The fuel rod growth of HIPER16^{TM} with HANA^{TM} alloy is a little higher than that of HIPER16^{TM} with reference alloy. The fuel rod oxide thickness of HIPER16^{TM} with HANA^{TM} alloy after 2nd cycle is much lower than that of HIPER16^{TM} with reference alloy. Based on the measured data and evaluation results, it was confirmed that the in-reactor performance of fuel rod oxide

thickness for HIPER16™ with HANA™ alloy is much better than that of HIPER16™ with reference alloy. And, the characteristics of fuel rod outer diameter changes along the fuel rod length for HIPER16™ fuel assembly design with reference alloy and HANA™ alloy are very similar within 0.2% differences.

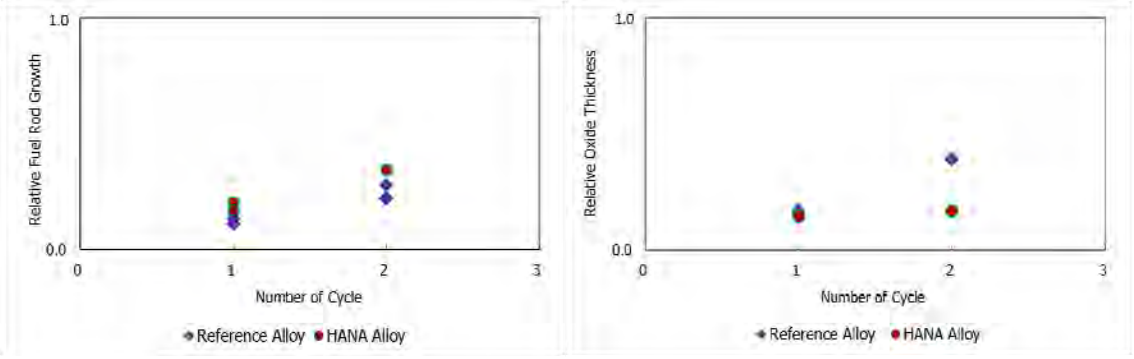

(a) Fuel Rod Growth (b) Fuel Rod Oxide Thickness

Fig 8. HIPER16™ Fuel Rod Growth and Oxide Thickness

4. Conclusions

KEPCO Nuclear Fuel (KNF) developed the HIPER16™ (High Performance with Efficiency and Reliability) fuel design in 2010 and the Lead Test Assemblies (LTAs) were loaded in HANUL Unit 6 for 3 cycles from 2011 to 2015. The poolside examinations have been performed after 1st and 2nd irradiation cycles of LTAs to verify the in-reactor performance of HIPER16™ fuel design. The visual examinations and dimensional measurements were performed on the LTAs using poolside examination equipment.

(1) The in-reactor performance of HIPER16™ fuel design has been verified based on the in-reactor verification test results. Based on the measured data and evaluation results, the HIPER16™ fuel design has very similar in-reactor performance with PLUS7™ fuel design which has enough in-reactor experience.

(2) The HIPER16™ fuel design with HANA™ alloy has better in-reactor performance than that of HIPER16™ fuel design with reference alloy.

The poolside examinations after 3rd irradiation cycle of HIPER16™ LTAs will be performed at the end of 2015 and HIPER16™ fuel will be supplied commercially after obtaining the license for commercial supply from 2019.

References

[1] Sang-Youn Jeon et al., “Verification of HIPER16™ Fuel Design for 16x16 CE-NSSS Type Nuclear Power Plants”, Transactions of the 19th Pacific Basin Nuclear Conference(PBNC 2014), Canada, 2014.
[2] Sang Youn Jeon et al., “HIPER16™ Fuel Assembly Development for 16x16 CE-NSSS Type Nuclear Power Plants”, 2013 LWR Fuel Performance Meeting/Top Fuel 2013, Charlotte, NC, USA, Sep. 15~19, 2013.
[3] Sang-Youn Jeon et al., “An Investigation on the Bow Characteristics of the PWR Fuel Assembly”, Transactions of the Korean Nuclear Society Autumn Meeting, Gyeongju, Korea, 2011.

Q12™ ULTRA LOW TIN QUATERNARY ALLOY FOR STRUCTURAL COMPONENTS IN PWR FUEL ASSEMBLIES.

V.CHABRETOU
AREVA NP, Fuel Business Unit, 10 rue Juliette Récamier, F-69456 LYON Cedex 06, France

S.TRAPP-PRITSCHING
AREVA GmbH, Paul-Gossen-Str. 100, D-91052 ERLANGEN, Germany

ABSTRACT

A fuel assembly (FA) structure stable to deformation is a key point for fuel robustness. Among the numerous factors influencing the FA deformation in a PWR, creep strength of the structural components is involved in this phenomenon. In this context, AREVA has developed the Q12™ alloy. The high creep resistance of the Q12™ alloy allows for a high degree of dimensional stability, regardless of the fuel assembly design or operating conditions. In this paper, the operating experience of Q12™ alloy is reported. Guide tubes, spacer grids and test tubes were manufactured in different geometries. Irradiation experiments up to 6 cycles confirm the significant improvement in irradiation creep strength and show a low and stable free growth behaviour. Good corrosion resistance for structural component application has been measured. First lead fuel assemblies with Q12™ guide tubes were introduced in 2010 and in 2011 for FAs with Q12™ guide tubes and spacer grids. Today, more than 170 FAs with Q12™ structural components have been or are irradiated in 10 PWRs including 2 reloads in 2 different PWRs.

1- Introduction

A fuel assembly (FA) structure stable to deformation is a key point for fuel robustness [1,2]. Among the numerous factors influencing the FA deformation in a PWR, creep strength of the structural components is involved in this phenomenon. In this context, an extensive AREVA R&D program on Zr1NbSnFe quaternary alloys was developed to support increasing creep resistance while maintaining high burnup capability. Examinations were done with alloys varying the tin content in the range from 0.3 to 0.5wt.% and the iron content from 0.1 to 0.2wt.% [3,4]. The Q12™ alloy has been chosen as the best candidate for structural applications in relation with its improvement in creep resistance combined with acceptable corrosion and hydriding resistance. This Q12™ ultra-low tin ZrNbSnFe quaternary alloy is based on M5™ and thus benefits from the extensive industrial experience already gained with the latter. Q12™ alloy is differing only by a small addition of tin and a slightly increased content of iron. These modifications provide higher irradiation creep strength and suitable corrosion resistance for structural applications. The high creep resistance of the Q12™ alloy allows for a high degree of dimensional stability, regardless of the fuel assembly design or operating conditions. Guide tubes, spacer grids and test tubes were manufactured in different geometries. In this paper, the operating experience of Q12™ alloy is reported.

2- Material and characterizations

The chemical composition of the Q12™ alloy is given in Table 1. This alloy is derived from M5™, with 1 wt.% niobium controlled sulfur and oxygen additions, by adding low amounts of tin (0.5 wt.%) and iron (0.1 wt.%).

The manufacturing process of Q12™ products is the same as for the material M5™, in particular with the same low temperature process which leads to fully recrystallized products with fine grains (Figure 1) and uniformly distributed precipitates. Further details on out-of pile properties could be found in previous publication [3] and will not be discussed here.

Alloy	Nb	Sn	Fe
Q12™	1	0.50	0.1
M5™	1	< 100 ppm	0.035

Table 1: Nominal compositions of the studied alloys (in wt.% except where indicated).

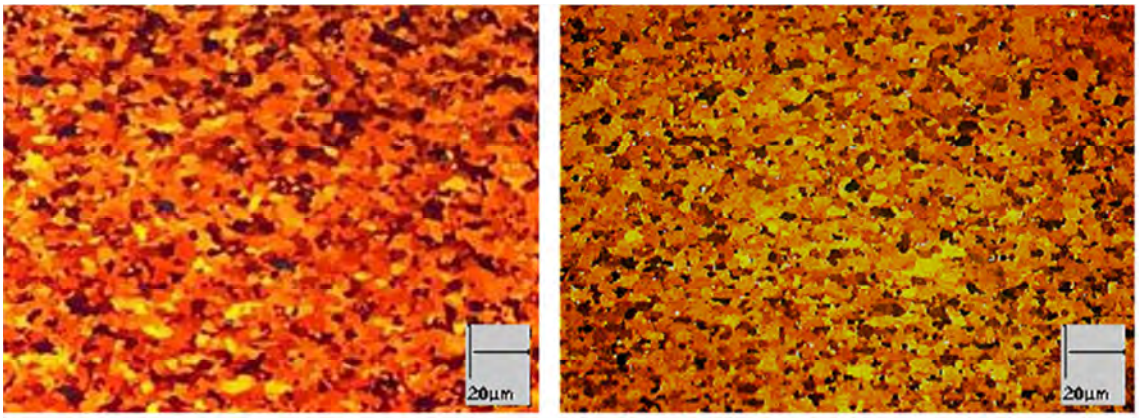

sheet guide tube

Figure 1: Optical micrographies on Q12™ sheet and guide tube (transverse cut from rolling direction)

3- Experimental irradiation programs

Two experimental irradiation programs have been carried out.

As is classically the case, the first irradiation program concerned demo fuel rods in two European reactors. Q12™ was inserted as part of R&D program development on ultra-low tin quaternary ZrNbSnFe alloys. Both plants operate with different fuel management strategies leading to five 12-month cycles (D40, Germany) and four 18-month cycles (D71, France). FA burnup of 53.1 GWd/tU and 62.7 GWd/tU were achieved.

The second irradiation program was a specific one in PWR (D24) on empty material test tubes to assess free growth, creep and corrosion. The test rods were irradiated inside guide tubes of host FAs and located at axial high flux positions. The free growth and axial creep specimens were designed to enable water flow inside and outside the test tubes avoiding radial differential pressure and leading to double side corrosion. The irradiation conditions were therefore representative of those experienced by structural components. Mid 2014, 6 cycles were achieved with equivalent burn up about 95 GWd/tU.

Irradiation of Q12™ structural components began in 2010 with 8 lead use assemblies (LUA) with Q12 guide tubes in two different German plants (D18 and D20). The following year 4 additional LUAs with both Q12™ guide tubes and spacer grids were inserted in a third plant (D21). Beginning of 2015, more than 170 FAs with Q12™ structural components (138 FAs with Q12™ guide tubes and 34 FAs with both guide tubes and spacer grids) are under irradiation or have been irradiated in 10 PWRs including 2 reloads in 2 different plants. Maximum achieved FA burnup are 57.6 GWd/tU on guide tubes and 48.1 GWd/tU on spacer grids.

4- Corrosion resistance of Q12™ products

Oxide thicknesses were measured on fuel rods, material test tubes and spacer grids. Results on fuel rods are considered for oxide layers formed outside the active length (plenum) with low heat flux which gives an indication of the oxidation of structural components. Results are presented on Figure 2. The measured oxide thicknesses are limited till high burn-up with a maximum of 23 µm measured on a fuel rod plenum at 56 GWd/tU after 5 annual cycles in D40 high duty plant. On test tubes, a maximum oxide thickness of 16 µm for an equivalent burn-up of 90 GWd/tU after 5 annual cycles in 2nd cycle host FAs. On spacer grids oxide thicknesses are lower than 20 µm at 48.1 GWd/tU after 3 annual cycles. All those results show that of Q12™ shows good corrosion resistance for structural component application.

The hydrogen uptake was measured at the hottest span of a fuel rod irradiated during 2 18-month cycles (36.7 GWd/tU) and on material test tubes irradiated 5 annual cycles (~90 GWd/tU). A maximum content of about 250 ppm was measured on a test tube, in line with its longer irradiation time its low wall thickness (0.4 mm) and the double side corrosion of the tube. Results indicated a hydrogen pick-up fraction around 20% similar to the one measured on Zy-4. Taking into account the moderate corrosion of Q12™ structural components, this leads to acceptable end-of-life hydrogen contents.
Besides, metallographic examinations performed on corrosion test tubes (no stress, double-side corrosion) irradiated in conditions representative of those of guide tubes show circumferential hydrides uniformly distributed in the tube thickness (Figure 3).

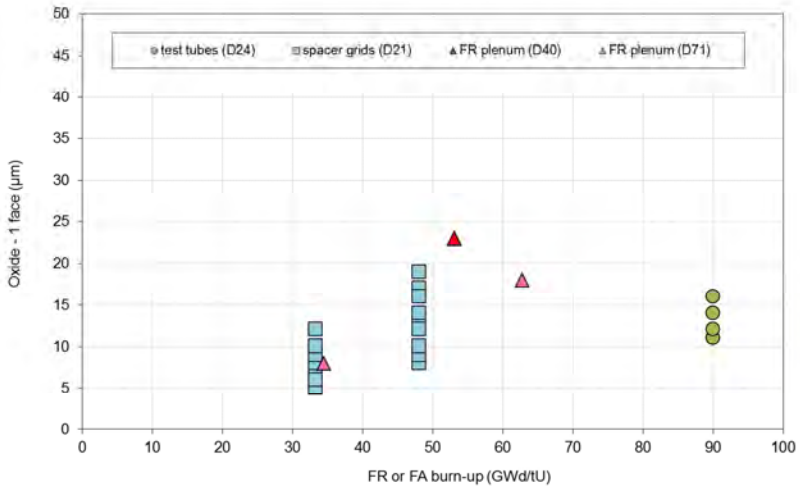

Figure 2: Evolution of oxide thickness on Q12™ products versus mean fuel rod (FR plenum) or mean fuel assembly (test tubes, spacer grids) burn up.

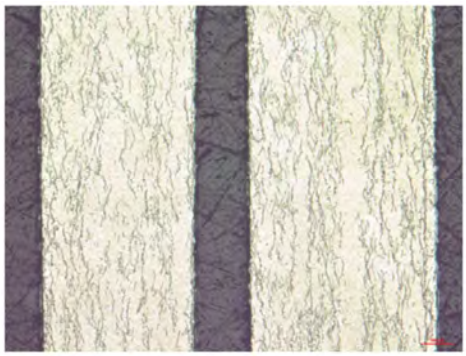

Figure 3: Hydride distribution in Q12™ corrosion test tubes (cross section of the tubes)

5- Free growth and axial creep of Q12™ material test tubes under irradiation

5.1- Free growth

A specific experimental irradiation in D24 power plant was started in 2008 with Q12™ empty material test tubes inserted inside guide tubes of host FAs and located at axial high flux positions. The design of the free growth specimens leads to double side corrosion of the tubes. For comparison, M5™ specimens of the same design were also inserted in this irradiation. The evolution of axial elongations (normalized by the maximum M5™ free growth measured in D24-2008 experimental irradiation) versus fluences is presented Figure 4. M5™ free growth results obtained in previous experimental irradiations (one in the same D24 plant started in 2003 and another one in the D65 plant [5]) are also included and show good agreement between the different experiments. Results show low and stable free growth strains for Q12 till high fluences and similar to M5™ elongations at least within the usual PWR fuel assembly irradiation levels (< 12-14 E+25 n/m², E > 1 MeV).

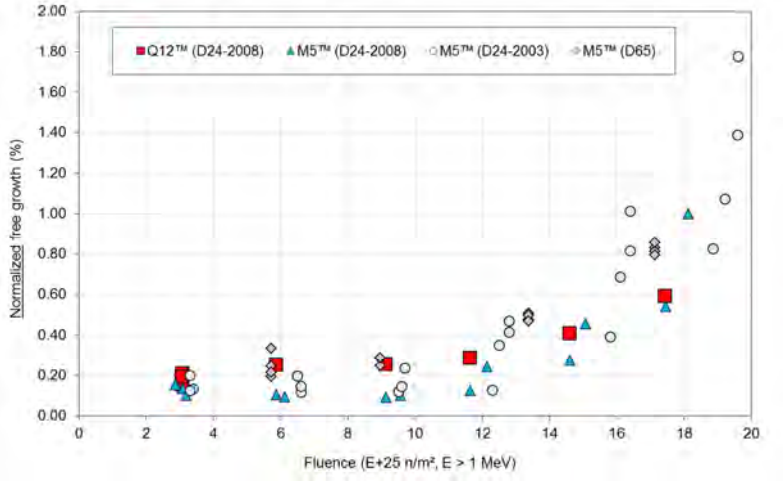

Figure 4: Free growth of Q12™ and M5™ test tubes under irradiation

5.2- Axial creep

In the same experimental irradiation in D24 plant started in 2008, Q12™ and M5™ empty test tubes loaded in compression were also inserted. Those test rods were subjected to double-face corrosion. The creep induced strains (where the irradiation free growth has been subtracted) are presented in Figure 5. The creep strain values presented in Figure 5 have been normalized taking into account the absolute value of the maximum M5 creep strain in this irradiation. Lower strains and strain rate are measured on Q12™ compared to M5™. The creep strength of Q12™ is clearly improved.

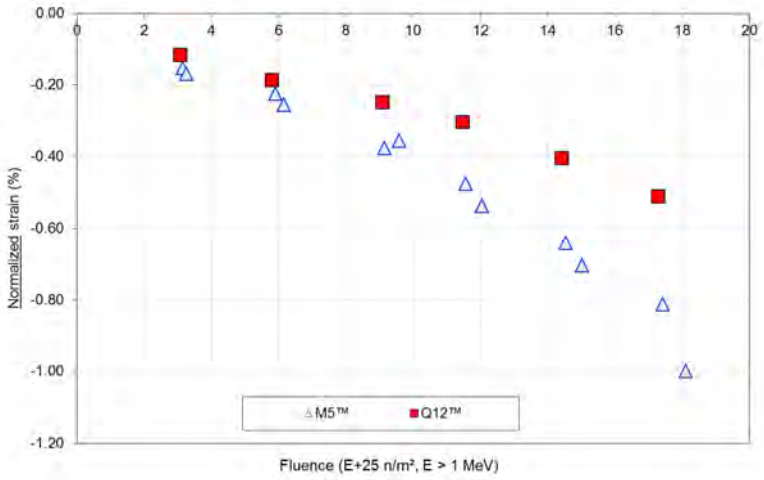

Figure 5: Axial creep strains of Q12™ and M5™ test tubes (-10MPa) under irradiation

6- Irradiation experience on LUAs with Q12™ structural components

The first lead use assemblies with Q12™ guide tube were introduced in 2010 in two different German PWRs (D18 and D20). In 2011, additional LUAs with both Q12™ guide tubes and spacer grids have started their irradiation in another PWR (D21).

Beginning of 2015, more than 170 FAs with Q12™ structural components (among which 34 FAs with both Q12™guide tubes and spacer grids) are under irradiation or have been irradiated in 10 PWRs including 2 reloads in 2 different plants. 2 further reloads in those plants are already scheduled. Therefore end of 2015 more than 300 FAs will be under irradiation or have been irradiated (Table 2). Maximum achieved FA burnup are 57.6 GWd/tU on guide tubes and 48.1 GWd/tU on spacer grids (Figure 6).

Reactor	Array	FA number	Q12 products	Date of introduction	Maximum cycle number
D18	18	4	GT	2010	5 achieved*
D20	18	4	GT	2010	5 on going
		4	GT & grids	2012	3 on going
D21	18	4	GT & grids	2011	4 on going
		8	GT & grids	2012	3 on going
		8	GT & grids	2013	2 on going
D35	16	4	GT & grids	2012	2 on going
D14	16	4	GT & grids	2012	3 on going
D25	15	4	GT	2012	3 on going
D26	17	2	GT	2012	3 on going
D24	15	2	GT & grids	2013	2 on going
D80	17	68	GT	2013	1 achieved
		68		*2015*	*scheduled*
D61	17	56	GT	2014	1 on going
		64		*2015*	*scheduled*

Table 2: Operational experience of FAs with Q12™ structural components

** including a short cycle (13 equivalent full power days)*

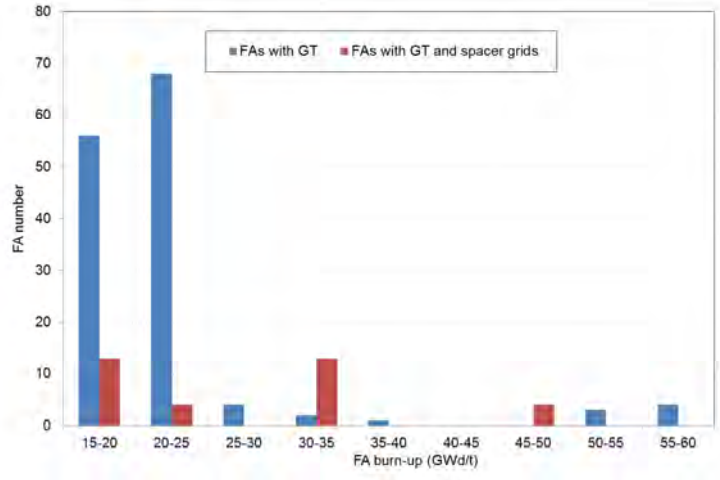

Figure 6: Burn-up distribution of FAs with Q12™ guide tubes or guide tubes and spacer grids (status March 2015)

In several plants the irradiation behavior of the fuel assemblies containing Q12™ was monitored during the outages. The surveillance programs contained measurements of fuel assembly length and fuel assembly bow. In the case of fuel assemblies with spacer grids made of Q12™, visual inspection, spacer width, spacer oxide layer thickness and friction force were also performed.

The fuel assembly growth was measured on several assembly designs of FAs equipped with Q12™ guide tubes and also Q12™ spacer grids in some cases (Figure 7). All FAs equipped with Q12™ guide tubes show a low positive length change up to 0.1% axial growth till high burn-up (57.6 GWd/tU) as expected considering the free growth and axial creep behavior of Q12™ alloy.

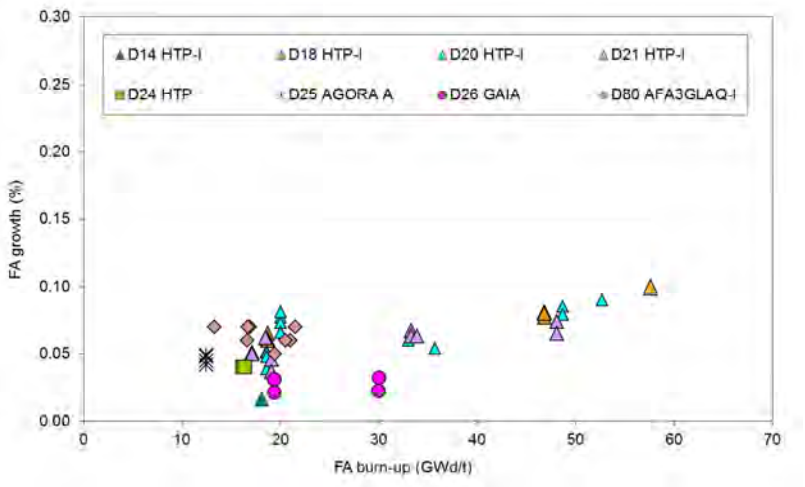

Figure 7: FA growth of FAs equipped with Q12™ guide tubes

Fuel assembly lateral deformation was monitored on LUAs (thus inserted in small quantities) and also on one of the reload (irradiation cycle of the reload in the other PWR is still on-going). First results are encouraging as FAs equipped with Q12™ structural components show bow behavior in the lower range of the measurements. As the lateral distortion of FAs depends on many parameters (neighboring FAs, FA core position, thermo-hydraulic, FA hold down spring force…), and as each plant shows an individual pattern, the efficiency of Q12™ structural components against FA lateral deformation will be progressively validated with the increasing number of reloads inserted.

Visual inspection, spacer width and oxide layer measurements were performed on Q12™ HTP™ spacer grids after two (33.3 GWd/tU) and three cycles (48.1 GWd/tU). Results after 4 cycles with a burn-up about 60 GWd/tU are awaited for mid-2015.
The visual appearance of the spacer grids is good (Figure 8).

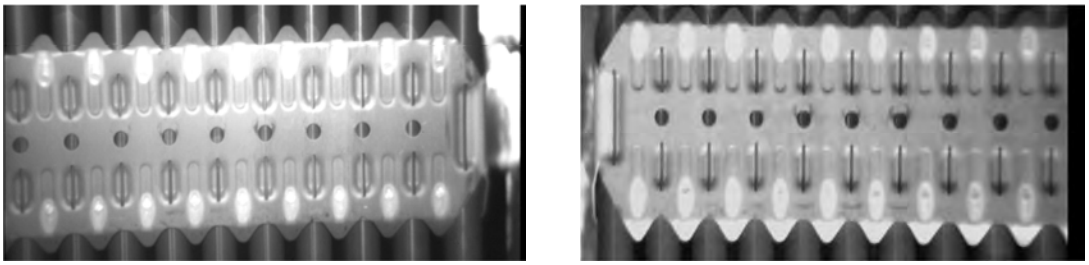

2 cycles - 33.3 GWd/tU

3 cycles - 48.1 GWd/tU

Figure 8: Visual appearance of Q12™ spacer grids (hottest span in full flux) after 2 and 3 cycles

Spacer grid growth is low below 0.20% after 2 cycles and 0.26% in maximum after the 3rd cycle. Comparing the results with the experience made with M5™ and HPA-4 HTP™ grids (Figure 9), Q12™ grid growth is comparable to that of M5™ and a bit below that measured on HPA-4 (~Zr0.5Sn0.5Fe0.3V) spacer grids.

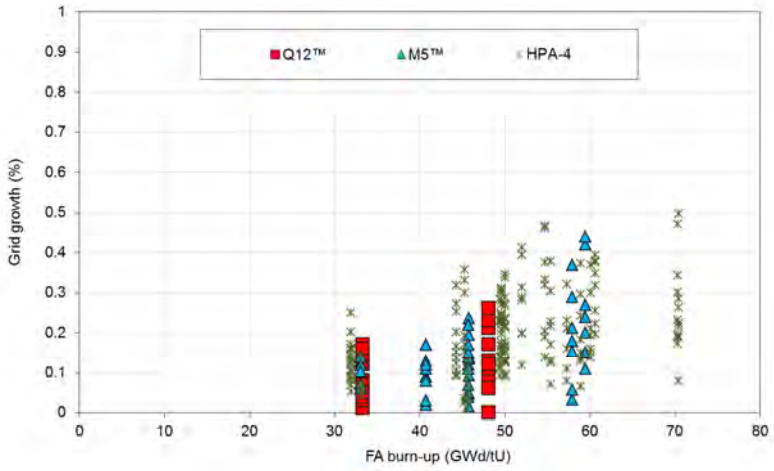

Figure 9: Grid growth of Q12™ HTP™ spacer grids. Comparison to M5™ and HPA-4 HTP™ grid growth.

Oxide layer on Q12™ spacer grid straps remains thin after the third cycle (48.1 GWd/tU) with a maximum oxide thickness just below 20 µm. This maximum oxide thickness is measured at the grid level 8 (hottest span in full flux) in line with the axial temperature profile. The comparison of Q12™ spacer oxide to M5™ and HPA-4 is shown Figure 10. As expected due to the tin addition in Q12™ alloy compared to M5™, the oxide thicknesses measured on Q12™ spacer grids are a bit higher than those observed on M5™. Q12™ oxide thicknesses are comparable to that of HPA-4 spacer grids.

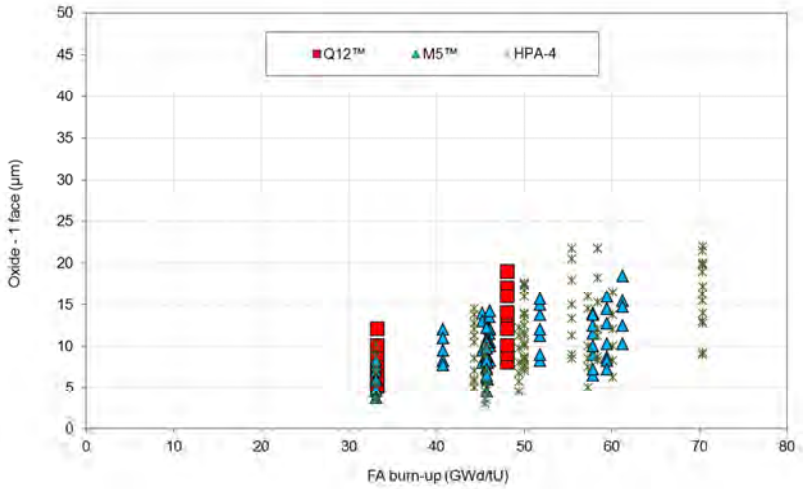

Figure 10: Oxide thicknesses of Q12™ spacer grids. Comparison to M5™ and HPA-4 oxide on spacer grids. (Pool results)

Friction forces were measured by extracting and inserting numerous fuel rods in HTP™ FAs irradiated 1 cycle (~16 GWd/tU). Higher friction forces are measured on the FA equipped with Q12™ spacer grids than on the FA equipped with HPA-4 spacer grids (Figure 11). A global friction force of approximately 15 N is measured on FA equipped with Q12™ spacers (from position 2 to 7, leading to about 2 N for each Q12™ grid - Figure 11a) whereas no detectable friction force is measured on FA equipped with HPA-4 spacer (Figure 11b). This indicates that the Q12™ spacers show slower relaxation behavior than HPA-4 spacers, which is consistent with the high creep strength of Q12™ alloy.

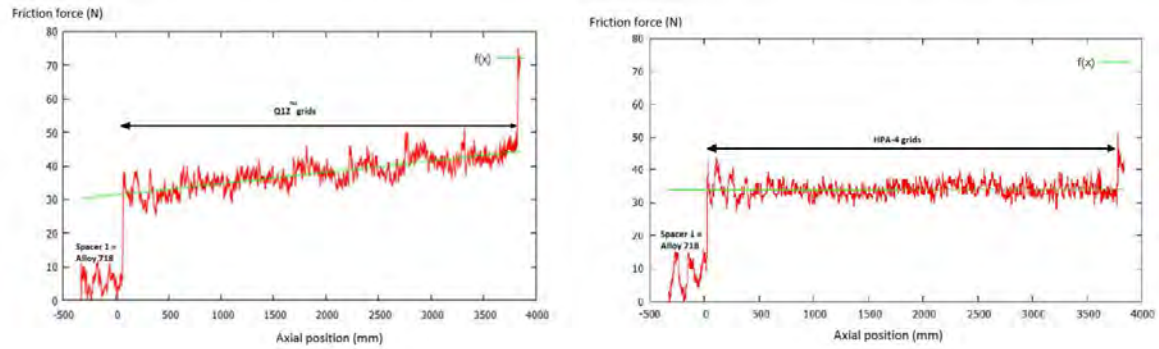

a- Q12™ spacer grids

b- HPA-4 spacer grids

Figure 11: Spacer grid friction force after the first irradiation cycle

7- Conclusion

Experimental irradiations on fuel rods and material test tubes allowing assessing oxidation, hydriding, free growth and irradiation axial creep behavior of Q12™ alloy have been performed. One irradiation on test tubes is still on going in order to increase the data base. Additional hot cells examinations are also scheduled. Q12™ alloy shows good corrosion resistance for structural components application. Low and stable free growth behavior is measured for this alloy. Improvement in the creep strength is clearly observed.

Beginning of 2015, more than 170 FAs with Q12™ structural components (guide tubes only or both guide tubes and spacer grids) are under irradiation or have been irradiated in 10 PWRs including 2 reloads in 2 different plants. Two further reloads are already scheduled in those 2 PWRs. Currently, maximum achieved FA burnup are 57.6 GWd/tU on guide tubes

and 48.1 GWd/tU on spacer grids. Mid 2015, a burn-up about 60 GWd/tU is expected after 4 cycles on FA equipped with both guide tubes and grids. The experience feedback indicates a low FA growth till high burn-up and confirms the expected improved behavior. After 3 cycles, spacer measurements show a moderate Q12™ grid growth similar to the one observed on M5™ and a bit below that of HPA-4 grids. Friction forces in HTP™ FAs irradiated 1 cycle show slower relaxation of Q12™ behavior than HPA-4, which is consistent with the high creep strength of Q12™ alloy. First results of FA lateral deformation measurements are encouraging. The efficiency of Q12™ structural components against FA lateral deformation will be progressively validated with the increasing number of reloads inserted.

Acknowledgments
AREVA would like to thank the customers who contribute and support this development and lead use assembly program.

References

1. J.Stabel, B.Dressel, V.Marx, CJ.Muench, A.Horvath, C.Brun, E.Montigny, C.Song, "Advanced methodology to predict in-reactor bow of PWR fuel assemblies for efficient design optimization: background, validation, examples", Top Fuel, September 11-14, 2011, Chengdu, China
2. C.Lascar, J. Champigny, A. Châtelain, B.Chazot, N. Goreaud, E. Méry, H. Salaün, "Advanced predictive tool for fuel assembly bow based on a 3D coupled FSI approach", Top Fuel, September 13-17, 2015, Zurich, Switzerland
3. V.Chabretou, P.B.Hoffmann, S.Trapp-Pritsching, G.Garner, P.Barberis, V.Rebeyrolle, J.J.Vermoyal, “Ultra Low Tin Quaternary Alloys PWR Performance – Impact of Tin Content on Corrosion Resistance, Irradiation Growth, and Mechanical Properties”, Journal of ASTM International Vol. 8 (5), 2011, paper ID JAI103013
4. S.Trapp-Pritsching, V.Chabretou, C.P.Scott, H.J.Sell, N.Teboul, "Ultra low tin Zr1NbSnFe quaternary alloys - Perspectives for structural components in PWR fuel assemblies", Top Fuel, September 2-6, 2012, Manchester, UK
5. P.Bossis, B.Verhaeghe, S.Doriot, D.Gilbon, V.Chabretou, A.Dalmais, JP.Mardon, M.Blat, A.Miquet, "In PWR comprehensive study of high burn-up corrosion and growth behavior of M5® and recrystalised low-tin Zircaloy-4", Journal of ASTM International Vol 6 (2), 2009, paper ID JAI101314

POST IRRADIATION EXAMINATIONS OF GAIA LEAD FUEL ASSEMBLIES

P.-H. LOUF, G. GENTET
AREVA NP
10, rue Juliette Récamier, 69456 Lyon – France

H.-J. LIPPERT, M. MINDT, J. PEUCKER
AREVA GmbH
Paul-Gossen Str. 100, 91052 Erlangen – Germany

A. JASIULEVICIUS
VATTENFALL NUCLEAR FUEL AB
Evenemangsgatan 13C, SE-16956 Solna - Sweden

ABSTRACT

To address further demands of the utilities worldwide, AREVA has developed the PWR fuel design GAIA. GAIA provides more resistance to fuel assembly bowing, higher thermal hydraulic performance, an intrinsically safe behaviour under seismic conditions, more burnup capability and more Uranium loaded in fuel assembly thanks to its High Performance Fuel Rod. The GAIA development took benefit from improvements and upgrades in codes & methods and computational capabilities that made the fuel design optimization faster and more secure.

In 2009, GAIA lead fuel rods were loaded in host assemblies for a 5 year irradiation program at the Ringhals nuclear power plant, unit 4, in Sweden. This program was completed in 2014 and post-irradiation examination results from rods extracted after 4 irradiation cycles are already available. Growth and oxide are identical to standard M5® clad rods and diameter change confirms the intended earlier pellet to clad gap closure. The pin pressure measurement performed at 52 GWd/tHM burnup confirms that fission gas release in the High Performance Fuel Rod is in the lower bound compared to standard UO_2 fuel rods, thus providing a higher burn-up capability. The results of investigations after 5 cycles shall be available in 2016.

GAIA lead fuel assemblies, completely loaded with GAIA fuel rods, have been in operation since 2012 at the Ringhals nuclear power plant, unit 3. During the reactor outages in 2013 and 2014, visual inspections and post-irradiation examinations of the lead fuel assemblies have been performed at burn-ups of 20 and 30 GWd/tHM. The primary focus of these examinations was on cladding oxide thickness, fuel rod axial and radial dimensions, fuel assembly growth, and fuel assembly bow. The results of the rod inspections are in line with the expectations and fully consistent with the 2009 GAIA lead fuel rod program. The growth behaviour of the GAIA lead fuel assemblies lies within the expected range of the experience feedback already available on similar structures irradiated in various types of reactors covering 15x15 to 18x18 lattices. This is true for both designs: the one with PCAm structural tubes as reference to the design of the resident HTP™ assemblies delivered by AREVA in the same reactor, and the one with Q12™ guide tubes, which corresponds to the reference structural design for GAIA future batches. The GAIA lead fuel

assembly distortion measurements are on the same low level as resident HTP™ assemblies. The post-processing of the video records confirmed the absence of fuel rod bow after 2 cycles.

The GAIA lead fuel assemblies are currently under irradiation for a third cycle. The post-irradiation examination program will be continued during next reactor outages.

1 INTRODUCTION

The Ringhals 4 lead fuel rod irradiation program that started in 2009 consisted in irradiating 6 different test rod designs in two HTP host assemblies during 5 cycles. Among the test rods, the high performance GAIA fuel rod (larger pellet, reduced pellet to clad gap, Cr_2O_3 doping, see [1]) was present together with variants, making it possible for AREVA to decouple the effect of several design features like the reduced gap, initial He pin pressure, pellet diameter and presence of Cr_2O_3 doping in UO_2 pellets. After each cycle the lead rods were inspected according to the Post Irradiation Examination (PIE) program agreed with VATTENFALL: growth, oxide and rod diameter changes were measured. The results of the 5th cycle examination will be available in 2016.

In 2012 the first four GAIA lead fuel assemblies were introduced in the reactor of Ringhals unit 3. These assemblies feature 6 GAIA mixing spacers and 3 intermediate flow mixers, all cladding made of M5®, a GRIP™ bottom nozzle and a HMP™ lower end grid. Their guide thimbles and instrumentation tube were reinforced compared to the standard products and have an outer diameter of 12.6 mm. For two of the lead assemblies, the guide thimble material is PCAm, and the top end grid is an M5® GAIA spacer. The structure of these two assemblies is similar to the one of the HTP™ reloads delivered by AREVA to the same reactor. The two other lead assemblies use Q12™ as structural tube material and an upper HMP™ spacer with reduced spring forces. Except the enrichment, the characteristics of the fuel rods are identical to the high performance fuel rods previously introduced in the GAIA lead fuel rod program in Ringhals-4. A description of the GAIA design and supporting testing performed to justify GAIA technology can be found in [2].

Irradiation and examination planning is depicted in Figure 1. Examination results are available for the four first cycles of the Ringhals 4 lead fuel rod program and the two first cycles of the Ringhals 3 lead fuel assembly program.

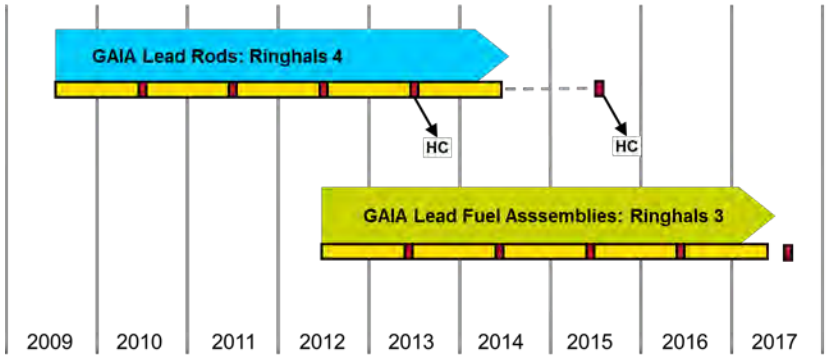

Fig 1. Irradiation and examination planning:
yellow = irradiation periods; red = PIEs during outages; HC = Hot Cell examinations

The results of the measurements performed on GAIA high performance rod are detailed in chapter 2, the examinations performed on the GAIA lead fuel assemblies are shown in chapter 3.

2 High Performance Fuel Rod Examination Results

2.1 Growth

Fuel rod axial growth shall be taken into account to justify that no interference between nozzles and fuel rods will occur during the operation of the fuel assembly. New fuel rod designs might grow differently than previous fuel rods. Therefore, measurements of the fuel rod growth kinetic are mandatory to validate the high performance fuel rod design.

Figure 2 shows the results of the growth measurements performed after the first four irradiation cycles on the high performance lead fuel rods of Ringhals 4 (red diamonds) as well as the measurement performed on the GAIA lead assembly peripheral fuel rods after their first two cycles (blue circles) as a function of the fuel rod burn-up. Some scattering is observed on the GAIA fuel assembly rods after the 2nd cycle, which is due to the burn-up gradient associated with the loading history of the assemblies.

The growth of these high performance fuel rods lies within the overall M5® cladding rods database. These results show that the advanced fuel rod designs are not inducing any penalty regarding the axial clearance requirement, thus allowing using them in place of the current M5® rods, for the same design burn-ups and without any additional axial dimensioning concern on the structure.

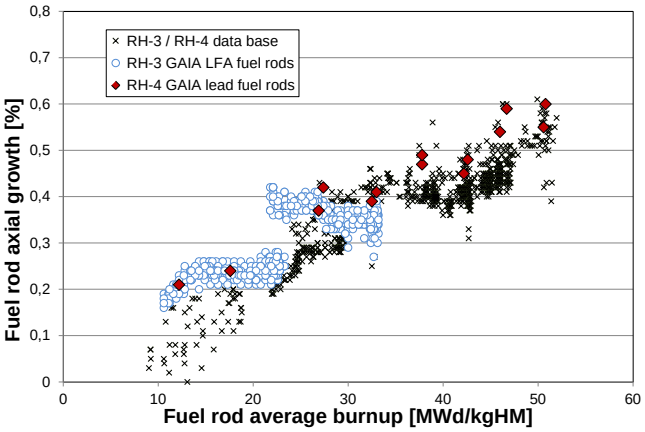

Fig 2. High Performance Fuel Rod Axial Growth Behaviour

2.2 Oxide

The corrosion of the fuel rod can become a limiting factor for fuel assembly operation, typically restricting the operation range (e.g. maximum allowed burn-up) since oxide and hydrogen build-up affect the mechanical properties of the cladding. For a new fuel rod design, it is required to verify that corrosion remains acceptable.

Oxide thickness was measured on the surface of all the peripheral test fuel rods of the Ringhals 4 program and at several axial elevations. The maximum was systematically recorded for each rod and the results can be seen on Figure 3 where they are compared to the database obtained in the same reactor on M5® claddings. The maximum oxide thickness measured on some peripheral fuel rods of GAIA lead fuel assemblies at Ringhals 3 were below or equal to 15 µm for rod burnups up to 33 GWd/tHM (not shown on the figure), fully consistent with the previous observations despite the increased power of the Ringhals 3 reactor.

The oxide build-up on M5® does not depend on the type of rods since oxide thickness measurements are corresponding to the now well-known behaviour of this advanced cladding material. Therefore the high performance fuel rod still benefits from the full M5® oxidation resistance in operation (see [3]).

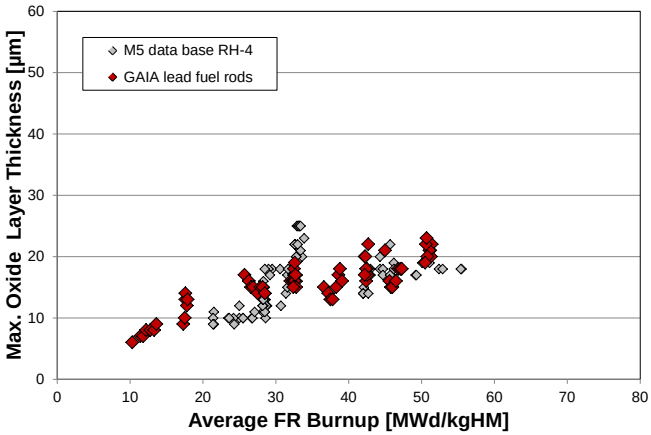

Fig 3. High Performance Fuel Rod Maximum Measured Oxide Thickness

2.3 Diameter

Fuel rod cladding strain must be shown to be limited in order to rule out any risk of cladding defect. The normal operation strain is essentially consisting in tangential deformation that can be quantified by fuel rod diameter measurements.

Figure 4 shows the results of the rod diameter measurements performed after the first three irradiation cycles on the high performance lead fuel rods of Ringhals 4 (red diamonds) as well as the measurement performed on the GAIA lead assembly peripheral rods after their first two cycles (blue circles) as a function of the rod burn-up. Both data sets appear to be very consistent. These data reflect the early pellet to clad gap closure, which was anticipated for the large pellet (with already reduced pellet to clad gap per design at begin of life) of the high performance rod design: the contact occurs during the first irradiation cycle. Diameter evolution of the rod doesn't show any risk of reaching excessive strain.

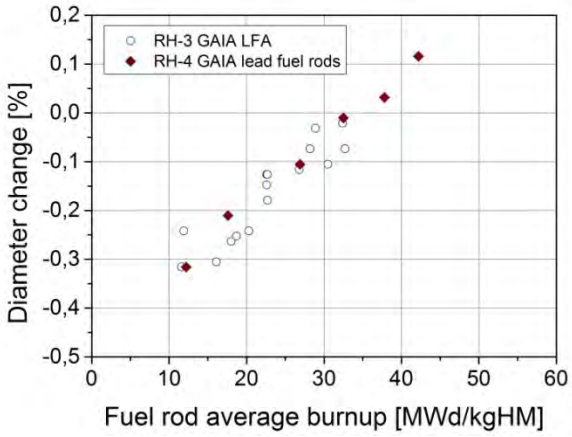

Fig 4. High Performance Fuel Rod diametric behaviour

2.4 Fission Gas Release

The internal rod pressure increases progressively during operation as a consequence of the production of gaseous fission products. Excessive pressure increase could lead to internal overpressure with potential consequences of too fast cladding strain increase.

Two GAIA lead fuel rods of a host assembly were extracted for hot cell examinations after having reached an average burn-up of 52 GWd/tHM. On these two rods, following examinations were performed in hot cell:

- Fuel rod internal pressure
- Fission gas release and analysis
- Gamma scan and burnup evaluation (after cutting in 4 pieces)

The GAIA high performance fuel rod fission gas release measurements are coherent with the experience feedback already acquired on the doped fuel, i.e. in the lower bound of the UO_2 database (see Figure 5). This lets us believe that the gains observed on the other large burn-up specimens will be confirmed by the next Ringhals 4 hot cell examinations that will be performed on rods at burn-up around 60 GWd/tHM.

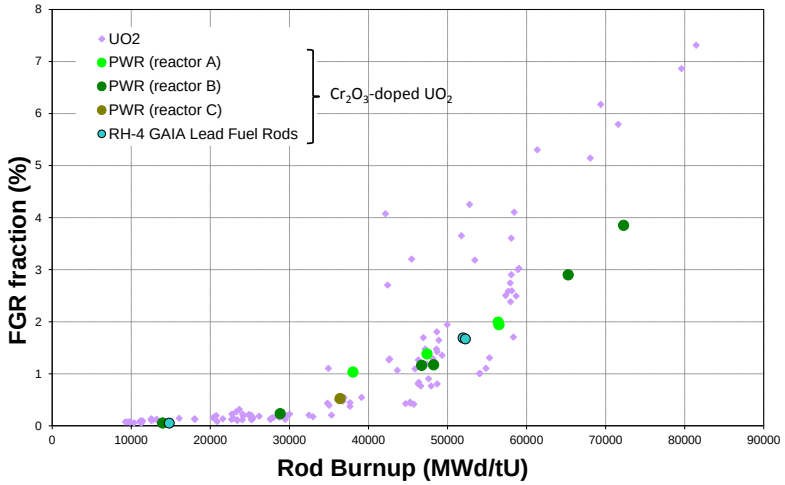

Fig 5. Fission Gas Release (FGR) of Cr_2O_3-Doped Fuel (green / blue circles) compared to Standard UO_2 Fuel (violet diamonds)

3 GAIA lead fuel assemblies Examination Results

3.1 Fuel Assembly Growth

The fuel assembly length evolution must be taken into account in order to verify that no lift-off will occur during normal operation and that positive clearance between assembly and reactor internals is ensured during the assembly lifetime.

The growth behaviour of the GAIA lead fuel assemblies lies within the expected range of the experience feedback already available on similar structures irradiated in various types of reactors covering 15x15 to 18x18 lattices. This is true for both design variants: the one with PCAm structural tubes as reference to the design of the resident HTP™ assemblies delivered by AREVA in the same reactor, and the one with Q12™ guide tubes, which corresponds to the reference structural design for future GAIA batches.

The small and positive growth of the GAIA structures will contribute to refine the growth law that will be used for future reloads licensing.

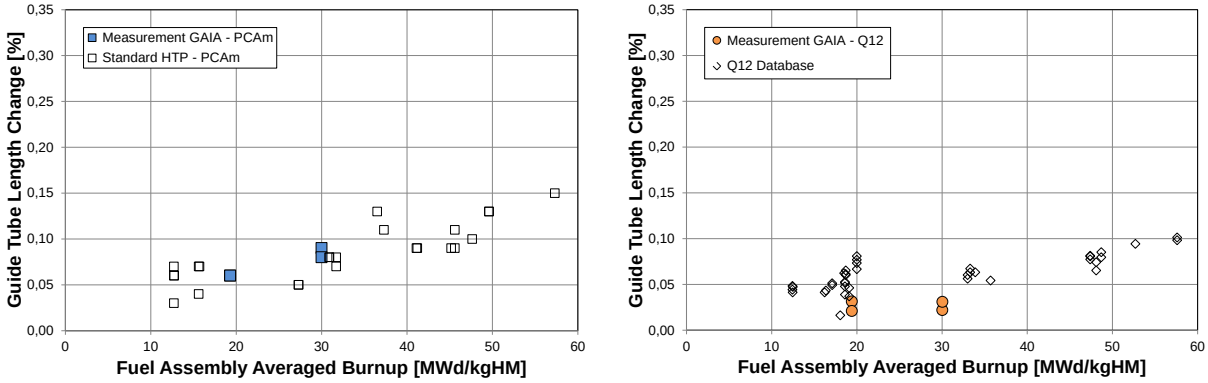

Fig 6. Growth of GAIA lead fuel assemblies: PCAm Guide tubes (blue squares on the left) and Q12™ (orange circles on the right, compared to the overall Q12™ growth database)

3.2 Fuel Assembly resistance against lateral deformation

The GAIA fuel assemblies were developed with the objective of improving the fuel assembly resistance against lateral deformation:

- Reinforcement of guide tube geometry : thick guide tube with enlarged cross section increasing lateral stiffness while reducing creep response by reducing stresses in the guide tubes;
- Additional enhancement of guide tube creep resistance by the deployment of so-called Q12™ material (Zr1Nb0.5Sn0.1Fe Ultra Low Tin Quaternary alloy, see [4]);
- Further increase in lateral stiffness by reinforcing spacer to guide tubes connections.

The distortion behaviour of lead fuel assemblies in a reactor cannot be assumed representative of the resistance against lateral deformation of the new design. Indeed, the distortion is known to be a result of interactions between all fuel assemblies present in the core and the flow. Four or eight lead fuel assemblies – even reinforced – are a too limited amount to show a measurable impact on the core deformation pattern.

Straightness measurements were performed on all four GAIA fuel assemblies after each irradiation cycle and have been compared to the data available on the Ringhals 3 reactor. The GAIA LFAs show in the same low level of fuel assembly bow as resident HTP™ assemblies. GAIA fuel assemblies inserted in reloads quantities will decrease the bow level of the core further.

3.3 Fuel Assembly Visual Examinations

The visual appearance of the components shows no anomaly and no crud deposition was detected on the surface (see photos on Figure 7). The rod axial position evolution shows that the upper end grid design plays a major role. These observations correspond to the experience already acquired on similar structures.

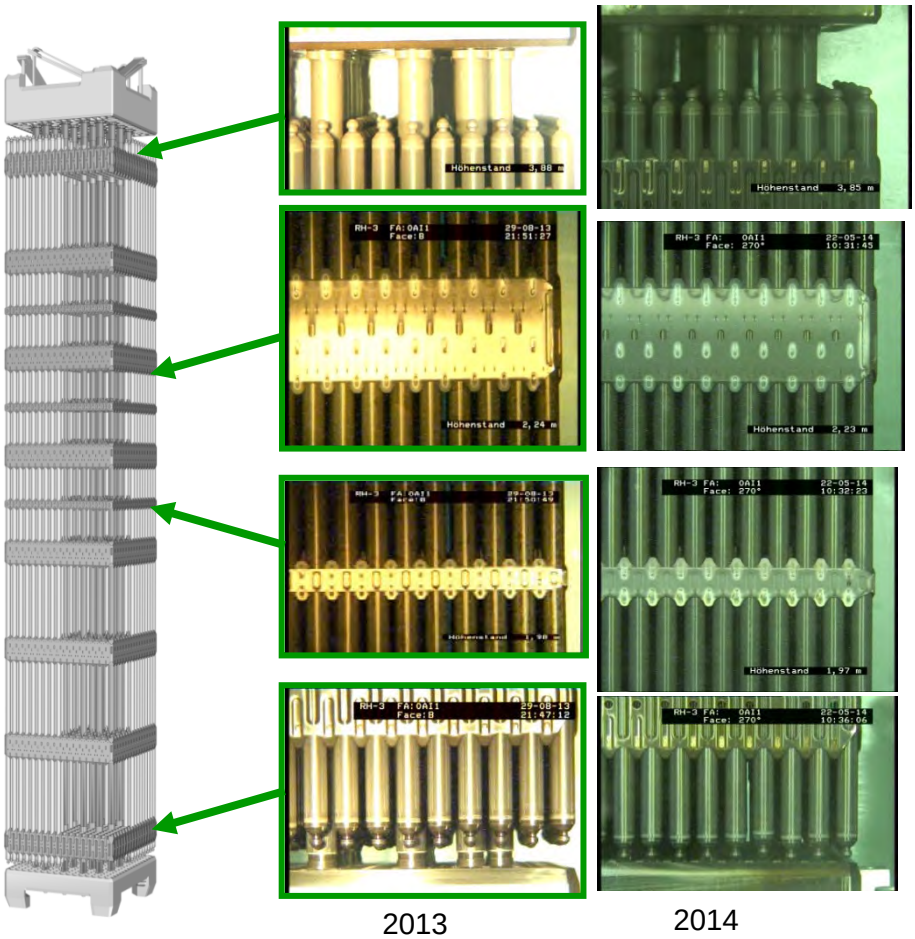

Fig 7. GAIA Fuel Assembly Visual Examinations

The video records were post-processed to derive rod to rod gap closure statistics on peripheral rods in the three lowermost spans, non-equipped with intermediate flow mixers. Excessive gap closure could induce thermal-hydraulic penalties on the fuel assembly design. The gap closure ratio (GCR) is determined according to the following formula:

$$GCR\,[\%] = \frac{M_0 - (M - K \cdot \sigma)}{M_0}$$

With:

- M_0 nominal rod-to-rod distance;
- M average rod-to-rod distance;
- K Owen coefficient taken from statistical table, dependent on sample size;
- σ standard deviation of rod-to-rod distance;

The gap closure ratios evaluated at each span of each GAIA fuel assemblies are all below the design limit, which demonstrates the absence of fuel rod bow after 2 cycles. No significant difference can be seen between the Q12™ and PCAm GAIA designs.

4 Conclusion

The GAIA lead fuel rod program in Ringhals 4 has been completed in 2014. The irradiation of four GAIA lead fuel assemblies is on-going since 2012 in Ringhals 3. The post-irradiation examination results available to date on these two programs are consistent with experience obtained on similar products and validate the GAIA high performance fuel rod design until burnup of 52 GWd/tHM and the GAIA assembly behaviour until burnup of 30 GWd/tHM.
In the next years, the measurements on lead rods and fuel assemblies will be completed for higher burn-ups, thus supporting the GAIA technology reload readiness. A new fuel type will be ready to use in reload scale in Ringhals from 2017 onwards provided that remaining inspections and hot cell evaluation confirm positive trends.

5 Acknowledgments

The authors wish to thank Vattenfall Nuclear Fuel AB and Ringhals AB involved within these two AREVA's fuel irradiation programs. Their involvement, support and contributions to the project are gratefully acknowledged.

6 References

[1] S.E. COLE, C. DELAFOY, R.F. GRAEBERT, P-H. LOUF, N. TEBOUL "AREVA Optimization of fuel rod design for LWRs" Light Water Reactor Fuel Performance Meeting, Manchester UK, September 2012

[2] G.A. THOMAS, J.S. D'ORIO, G. GENTET, P-H LOUF, M. MINDT "GAIA: AREVA'S ADVANCED PWR FUEL DESIGN "Light Water Reactor Fuel Performance Meeting 2013, Charlotte NC US, September 2013

[3] J-P. MARDON and al. "M5® a breakthrough in Zr alloy", Light Water Reactor Fuel Performance Meeting, Proc. ANS Con. Orlando, 2010

[4] S. TRAPP-PRITSCHING, V. CHABRETOU, C.P. SCOTT, H-J. SELL "Ultra Low Tin Zr1NbSnFe Quaternary Alloys – Perspectives for structural components in PWR Fuel Assemblies" Light Water Reactor Fuel Performance Meeting, Manchester UK, September 2012

PWR FUEL PERFORMANCE AND KEY DEVELOPMENTS IN MATERIAL AND MECHANICAL DESIGN

J.R. HALLIGAN, G. PAN, A. GARDE, J. NORRELL
Nuclear Fuel, Product Engineering, Westinghouse Electric
5801 Bluff Road, Hopkins SC, 29061, USA
Nuclear Fuel

ABSTRACT

Significant performance improvements for Westinghouse Pressurized Water Reactor (PWR) fuel have been obtained over the last ten years through a focused fuel reliability improvement process that includes targeted design enhancements, incorporation of advanced alloys and ongoing learnings about advanced alloy behavior. Westinghouse's fuel reliability improvement (FRI) process established and drove a comprehensive global strategy to ensure operations feedback on fuel reliability was trended and used to guide research and development investments.

A key indicator used to evaluate fuel performance is the percentage of power plants operating without leaking fuel rods or percent leak free (%LF). Considering the last ten years, a large number of improvements were developed and implemented during the first portion of this time period (2004 through 2009). As previous designs were discharged over several cycles and enhanced designs were loaded, improved fuel performance was observed in the period between 2010 and 2014. Demonstrated design enhancements have been incorporated across the Westinghouse design family. From 2004 through 2009, Westinghouse-supplied power plants averaged approximately 81%LF in these years. From 2010 through 2014, the overall average was approximately 95%LF in each year with a high of 96%LF in 2014.

In PWR fuel the two largest concerns for fuel performance have been grid to rod fretting (GTRF) and debris fretting. In order to improve margin for GTRF, some designs received multiple enhancements to address vibration and reduce fretting wear, with much of the fuel performance improvement attributable to these changes. Mechanical features to mitigate the effects of foreign material (debris) have also been incorporated in several fuel designs.

In addition to mechanical design enhancements, the development and implementation of advanced zirconium alloys also play major role in the robust performance of Westinghouse PWR fuel. From ZIRLO® cladding to **Optimized ZIRLO**™ cladding, extensive irradiation experience has been achieved in the last ten years on advanced zirconium alloys to burnups over 62 GWD/MTU rod average. Excellent performance has been demonstrated in areas including corrosion, mechanical properties and dimensional stability. Substantial understanding in alloy development including oxide surface peeling (OSP) phenomenon, improved ductility in Nb-containing alloy, creep and growth mechanism, etc., was obtained from detailed post irradiation examinations (poolside and hot cell), which ensures continuous improvement.

1. Introduction

The nuclear industry has been driving improvements in fuel performance. This has resulted in a number of design changes in fuel assemblies in order to prevent fuel leaks. Westinghouse has reviewed the fuel performance and related design changes for the last ten years (2004 through 2014). The design changes include several enhancements to the mechanical design of the fuel assemblies. The most effective enhancements are related to the reduction of GTRF. These design changes have addressed fuel assembly and fuel rod vibration, as well as wear surfaces on the fuel rod support structures. Other enhancements have addressed debris fretting. These changes incorporated more effective debris filtering, and coating on a wear surface.

In addition to these significant mechanical design enhancements, the development and implementation of advanced zirconium alloys also play major role in the robust performance of Westinghouse PWR fuel. The last ten years of alloy development included the evolution from ZIRLO® cladding to **Optimized ZIRLO** cladding. By the late 1990s, ZIRLO cladding had replaced Zircaloy-4 in almost all the Westinghouse plants operating worldwide. For Optimized ZIRLO cladding, the first full region was delivered in 2008 and first full core achieved in 2011. Extensive irradiation experience has been achieved to rod average burnups over 62 GWD/MTU. Robust performance has been demonstrated by Optimized ZIRLO cladding, with 40% improvement in corrosion resistance compared to ZIRLO cladding (Ref. 1). Substantial understanding in alloy development was obtained from detailed post irradiation examinations (poolside and hot cell) in areas including oxide surface peeling phenomenon, improved ductility in Nb-containing alloy, creep and growth mechanism, etc. The performance experience of advanced zirconium alloys and the findings in the alloy development study will be discussed in this paper.

2. Fuel Performance Review

In order to determine the performance of the fuel, the coolant activity at the operating plants is monitored. If coolant activity indicates the presence of leaking fuel, the plants will normally continue to operate to the scheduled end of the cycle. Following the end of the cycle, a Post Irradiation Examination (PIE) is performed. Data from the PIE, along with operating and manufacturing data are used to determine the mechanism that caused the fuel assembly to leak. This information is then used to target design enhancements.

There are several indicators used to determine fuel performance. As described above %LF is an important indicator. This indicates the extent to which leak mechanisms have been eliminated. This indicator is important to the industry because the presence of one leaking fuel rod would result in radiological exposure to personnel in an operating plant, and would disrupt the refueling outage. Examinations during the outage are needed to find the leaking fuel assembly, and the leaking fuel rod within the assembly.

Another important indicator is the total number of leaking fuel rods. This indicator provides information into the nature of the leak mechanism. Some mechanisms, such as GTRF, typically result in multiple leaking fuel rods in core, and sometimes in a single fuel assembly. Other leak mechanisms tend to result in more isolated leakers. Tracking the total number of leaking fuel rods could indicate the reduction or elimination of a specific leak mechanism. See Figures 1 and 2 for these indicators by year.

In order to evaluate the total number of leaking rods, it is important to consider the number of PWR plants fueled by Westinghouse. This number has increased significantly in the time period of interest. In 2004 63 PWR plants were fueled by Westinghouse. In 2009 this

number increased to 80. In 2010 the number of PWR plants was 88, and this increased to 119 in 2014.

2.1 Fuel Performance from 2004 through 2009

In 2004 the average percentage of PWR plants, fueled by Westinghouse, that were operating leak free was approximately 81%. In the period following 2004 the indicator (%LF) was observed to be as low as 75%. Following 2007 %LF for the PWR plants began to increase. In 2009 the average %LF was approximately 87%. The average %LF for the period between 2004 and 2009 was approximately 81%.

In 2004 the total number of leaking fuel rods was 58 rods in 63 plants. In the years following 2004, the number of leaking fuel rods increased. The average for the years 2004 through 2009 was 103 leaking rods. At the end of this time period (2009) 88 PWR plants were fueled by Westinghouse.

2.2 Fuel Performance 2010 through 2014

In 2010 the average percentage of PWR plants, fueled by Westinghouse, that were operating leak free was approximately 93%. In the period following 2010 the indicator (%LF) increased to 96% in 2013 and in 2014. The average for this time period was 95%LF.

In 2010 the total number of leaking rods was 63 rods in 88 PWR plants. In the years following 2010, the number of leaking fuel rods decreased and the number of PWR plants increased. The average number of leaking rods for the years 2010 through 2014 was 40 rods. The low for this period was 14 rods in 2014. The number of PWR plants fuel by Westinghouse increased to a total of 119 in 2014.

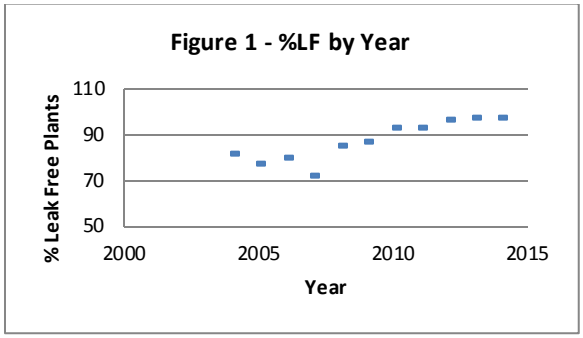

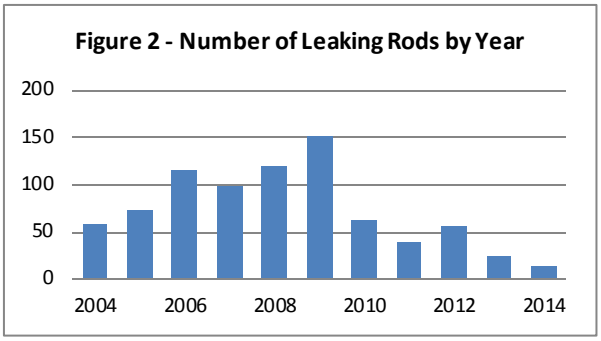

3. Fuel Reliability Improvement Process

Westinghouse brings a continuous improvement focus to fuel reliability, utilizing operating experience, technology expertise, a strong corrective actions process, and senior leadership oversight to drive ever higher levels of fuel performance. Capitalizing on the global fuel business, Westinghouse is able to, through a disciplined fuel reliability improvement process, leverage operating and manufacturing experience from across the globe (Ref: 7).

Leak mechanisms are determined by performing PIEs in plants where coolant activity indicates that leaking fuel is present. The leaking fuel assembly is identified by a process called sipping that detects fission gas escaping from a leaking rod. The leaking fuel rod within the fuel assembly is identified by an ultrasonic inspection of the fuel rods that detects the presence of water inside the rod. Visual inspections are then conducted on the leaking fuel rod. In many cases the visual inspection allows identification of the leak mechanism. In

some cases manufacturing and operating data are needed for this identification. With the leak mechanisms identified, needed design modifications for the fuel assemblies can be determined.

3.1 Targeted Design Enhancement

A review of the number of leaking fuel rods, and the identified leak mechanisms show the areas targeted for enhancement. Two areas were identified for enhancement. In the period from 2004 through 2009, the most prevalent leak mechanism was GTRF. This accounted for an average of about 76% of the leaking fuel rods in that time period. The second leak mechanism targeted was debris fretting. Debris fretting was the leak mechanism for an average of about 13% of the leaking fuel rods in the period from 2004 through 2009. See Figure 3 for a trend for these leak mechanisms in the time period.

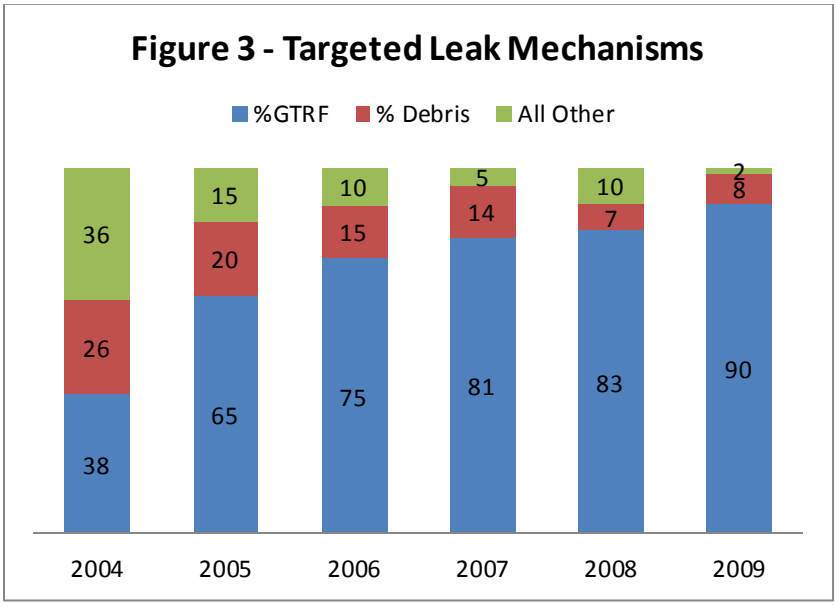

3.1.1 Enhancements to Address GTRF

GTRF performance was identified as a target for enhancements. It was noted that this mechanism sometimes occurred in multiple rods in one fuel assembly in some fuel assembly designs. Flow testing reveled a fuel assembly vibration could occur in some fuel assembly designs when subjected to axial flow. This vibration was eliminated by redesign of the mixing vanes that are designed to increase turbulence in certain areas of the fuel assembly. This eliminated the fuel assembly vibration, and improved resistance to GTRF.

It was discovered that in some fuel assembly designs a fuel rod vibration occurred. Changes to some spacer grid designs eliminated local flow conditions that caused the fuel rod vibration. In some fuel assembly designs both conditions (fuel assembly vibration and fuel rod vibration) existed. These design enhancements significantly increased resistance to GTRF.

Additional margin was added in some designs by increasing the contact area on the fuel rod support surfaces in the spacer grids. In the event fretting may occur, this provides a larger wear area. Testing shows this significantly reduces the wear volume of the cladding material. Therefore, the wear depth is lower.

3.1.2 Enhancements to Address Debris Fretting

The area of the fuel assembly most vulnerable to debris is the bottom of the assembly. Foreign material carried by the primary coolant flow can be carried to the bottom of the fuel rods and become trapped in the bottom grid. In this position the foreign material can fret and wear through fuel rod cladding. The first defense incorporated into fuel assemblies is a debris filter incorporated into the bottom nozzle. This is a design of the flow holes that, in addition to providing the necessary flow and structural conditions, will capture foreign material before it enters the area of the fuel rods.

A protective grid (called a Guardian™ grid in some designs) has been added to enhance the debris filtering capability of the fuel assembly. This is a spacer grid assembly that is located just above the bottom nozzle, and is designed specifically to capture foreign material. Fuel assemblies with a protective grid also have fuel rods with lengthened bottom end plugs. The longer end plugs extend through the protective grid and are solid zirconium alloy. If a piece of foreign material becomes trapped in the protective grid it may fret and cause some wear on the solid bottom end plug. There will be no wear on the cladding, and no potential to cause a leaking fuel rod.

Fuel rods are most vulnerable to fretting when first operated in a core because the oxide coating has not yet formed. Zirconium oxide, which forms on the fuel rod cladding during operation, is a very hard material. Fuel rod cladding with oxide formed on the surface is more resistant to debris fretting. A process has been developed that forms a protective oxide coating on the lower portion of fuel rods during manufacture. Fuel assemblies that have this oxide coating on the lower portion of the fuel rods are less vulnerable to debris fretting in the early part of operation.

3.2 Implementation and Development of Advanced Alloys

In the last ten years ZIRLO cladding has been in full operation in all the Westinghouse plants, replacing Zircaloy-4. Westinghouse continues to gain considerable burnup experience with ZIRLO clad nuclear fuel delivering over 607 Regions (over 40,000 assemblies) since the introduction of the first full region of ZIRLO in 1991. Currently about 80 plants worldwide have utilized ZIRLO cladding. ZIRLO cladding has a robust performance record in corrosion, growth and creep. It has demonstrated robustness in high lithium environments, and has shown significant improvements over Zircaloy-4. Work on the development of more advanced alloys has resulted in a significant irradiation experience.

3.2.1 Implementation of Advanced Alloys

An advanced alloy, **Optimized ZIRLO** has emerged in the last ten years. **Optimized ZIRLO** cladding is an improved version of ZIRLO cladding, developed based on the vast experience of ZIRLO cladding to retain the favorable properties of ZIRLO cladding, while further improving the corrosion resistance. Table 1 shows the chemical composition of Zircaloy-4, ZIRLO cladding and **Optimized ZIRLO** cladding.

Alloy	**Microstructure**	**Nb**	**Sn**	**Fe**	**Zr**
Zircaloy-4	SRA	0	1.3	0.2	Bal.
Optimized	PRXA	1	0.67	0.1	Bal.
ZIRLO	SRA	1	1	0.1	Bal.

Table 1**:** Zircaloy-4, **Optimized ZIRLO** and ZIRLO cladding alloy chemical compositions (nominal weight %) and microstructure from final heat treatment.

Since the introduction of the first **Optimized ZIRLO** cladding Lead Test Assembly (LTA) in 2002, Westinghouse is rapidly gaining burnup experience with **Optimized ZIRLO** clad fuel rods. As of December 31, 2014 thirty six plants worldwide contain **Optimized ZIRLO** fuel rods. Twenty three plants have full regions in operation. Five plants have cores exclusively loaded with **Optimized ZIRLO** clad fuel rods. There are currently 61 Regions or over 3,700 assemblies representing over 893,000 rods currently in operation or discharged. Also, **Optimized ZIRLO** cladding is quickly becoming the fuel cladding of choice for 17x17 Robust Fuel Assembly (RFA) fuel design, a fuel design with excellent performance record. **Optimized ZIRLO** cladding has achieved high burnup levels of over 70 GWD/MTU rod average, significantly higher than the licensed burnup in the United States of 62 GWD/MTU rod average. Figure 4 shows the total number of rods with **Optimized ZIRLO** cladding versus burnup as of December 31, 2014.

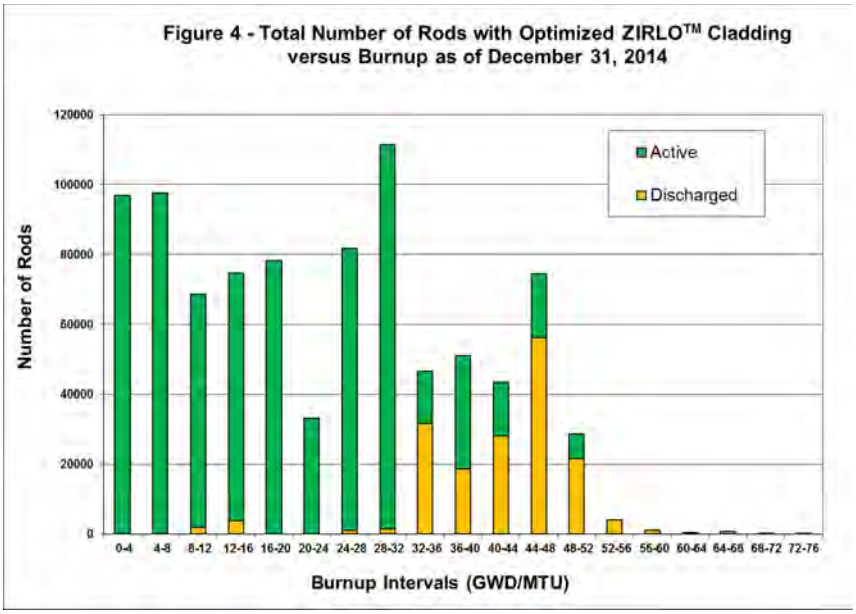

Extensive post irradiation exams (PIE) data for **Optimized ZIRLO** cladding and ZIRLO cladding are available from various LTA programs at various burnup levels. **Optimized ZIRLO** cladding has proved to retain the robustness of ZIRLO cladding. It has similar creep and growth behavior and hydrogen pickup fraction. As designed, the oxide thickness of **Optimized ZIRLO** cladding are reduced by about 40% compared to ZIRLO cladding at higher burnups, as shown in Figure 5. The oxide thickness for Optimized ZIRLO cladding is less than 70 microns at burnup of about 70 GWD/MTU. Overall at high burnups, there is no accelerated corrosion observed for **Optimized ZIRLO** cladding. The calculated hydrogen uptake ratio of **Optimized ZIRLO** cladding is similar to that of ZIRLO cladding. However, since the Optimized ZIRLO cladding has lower oxide thickness, the overall hydrogen level in **Optimized ZIRLO** cladding is less than in ZIRLO cladding.

Figure 5 - Measured oxide thickness for Optimized ZIRLO and ZIRLO clad fuel rods as a function of burnup

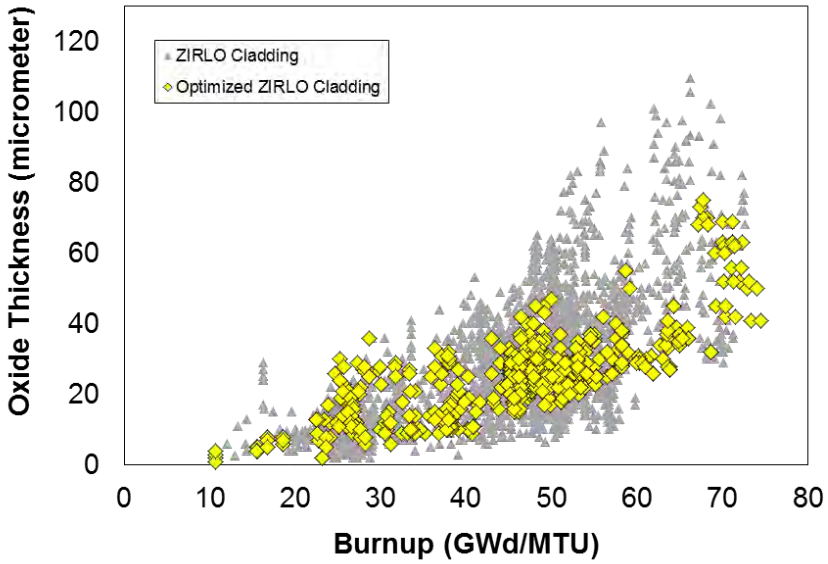

3.2.2 Findings of Alloy Development Study

Microscopic examinations of advanced zirconium alloy cladding irradiated to burnups over 70 GWD/MTU have revealed de-lamination of surface layers of the thin oxide, termed as 'oxide surface peeling'. Although first discovered and analyzed by Westinghouse in high corrosion resistance Westinghouse cladding alloys (Ref.2), OSP is now observed in all high corrosion resistance zirconium cladding alloys from other sources as recently confirmed for high corrosion resistance cladding manufactured by three non-USA cladding vendors. Although the non-uniform visual appearance of thin-oxide OSP during poolside examinations may resemble that of thick oxide spalling seen several decades ago for low corrosion resistance Zircaloy cladding, OSP does not lead to hydride embrittlement as was seen with thick oxide spalling. The available limited data indicate that **Optimized ZIRLO** cladding, due to its intermediate corrosion resistance, has a very low level of OSP compared to high corrosion resistance alloys (Ref. 1 and 2). The minor degree of OSP, occasionally encountered for **Optimized ZIRLO** cladding, has no adverse effect on fuel or grid-to-rod-fretting (GTRF) performance. Only high level of OSP may reduce the GTRF margin (Ref. 2). All the **Optimized ZIRLO** cladding performance data confirm the lack of connection between OSP and fuel leakers. No ductility reduction or hydrogen localization due to OSP is observed. This result is confirmed by the optical microscopy and mechanical tensile test results discussed below.

The hot cell mechanical tests (Ref. 1 and 3) show that **Optimized ZIRLO** alloy and ZIRLO alloy have superior ductility compared to Zircaloy-4. For a burnup level over 70 GWD/MTU, the total plastic strain is in the range of 3.9% to 18.8% for **Optimized ZIRLO** cladding and 1.3 to 6.8% for ZIRLO cladding. While for Zircaloy-4 specimen, even with a lower burnup level of about 55 GWD/MTU, the total plastic strain is only in the range of 0.1 to 1.9%. Based on the surface visual examination of deformed axial tensile test samples, it was speculated that the multiple fine deformation bands within individual grains could be a macroscopic manifestation of the nucleation of large numbers of dislocation channels as a result of niobium induced work hardening preventing deformation concentration in a limited number of dislocation channels. Limited TEM examination was unsuccessful in establishing a connection between macroscopic deformation bands on specimen surface and dislocation free dislocation channels in the microscopic dislocation structure within grains. Research in this area is continuing.

Vogtle creep and growth program is the most comprehensive study on creep and growth behavior of irradiated zirconium materials (Ref. 4-6), covers all advanced zirconium cladding at different processing condition. It gives an in-depth understanding of the effect of chemical composition, microstructure, processing, hydrogen, etc. on the creep and growth behavior in both axial and diametrical direction. It has been found that when the total in-reactor diameter strain is split into growth and creep components. The deviatoric hoop stress component correctly correlates with the data and therefore is the driving force for irradiation creep of zirconium cladding. The total hoop stress is not the driving force for irradiation creep. In-reactor and out-reactor diameter creep directly correlate for **Optimized ZIRLO** material fabricated with different final anneal temperatures (or different microstructures such as PRXA, RXA and SRA).

4. Conclusion

A review of fuel performance shows that the percentage of leak free PWR plants fueled by Westinghouse averaged about 81% for the time period between 2004 and 2009. During this time period design enhancements to address GTRF and debris fretting were implemented. As the new designs were placed into cores and older designs discharged, improvement in fuel performance was observed. The percentage of leak free plants averaged about 95% in the time period from 2010 through 2014. Several design enhancements improved fuel performance. At the end of 2014 a small number of legacy design assemblies were still operating, and some leakers are still observed. There have been no GTRF leakers in any of the enhanced designs. Further improvement in the fuel performance indicators is expected as these fuel assemblies are discharged.

The extensive irradiation experience of ZIRLO cladding and **Optimized ZIRLO** cladding has demonstrated robust performance record. Ongoing learning about advanced alloy behavior ensures the continuous performance improvement. OSP phenomena have been fully studied and well understood by Westinghouse. OSP does not lead to hydride embrittlement and therefore it is not a fuel performance concern. **Optimized ZIRLO** cladding has the optimum combination of performance properties: adequate corrosion resistance, good irradiated ductility and good OSP resistance.

5. Acknowledgements

The authors would like to acknowledge the support of utilities and test facilities for supporting the generation of data presented in the paper.

6. References

1. Pan, G., Garde, A. M., Atwood, A. R., “Performance and Property Evaluation of High-Burnup Optimized ZIRLO Cladding,” Zirconium in the Nuclear Industry: 17th International Symposium on Zirconium in the Nuclear Industry, February 3-7, 2013, Hyderabad, India. STP 1543, Robert Comstock and Pierre Barberis, Eds., doi: 10.520/STP1543201300058, ASTM International, 2014.

2. Garde, A. M., Pan, G., Mueller, A. J., and Hallstadius, L., “Oxide Surface Peeling of Advanced Zirconium Alloy Cladding after High Burnup Irradiation in Pressurized Water Reactors,” Zirconium in the Nuclear Industry: 17th International Symposium, February 3-7, 2013, Hyderabad, India. STP 1543, Robert Comstock and Pierre Barberis, Eds., doi:10.520/STP154320130005, ASTM International, 2014.

3. Garde, A. and Mitchell, D., “Comparison of Ductility of Irradiated ZIRLO® and Zircaloy-4,” Topfuel 2012 Reactor Fuel Performance Conference, Manchester, UK, September 2-6, 2012; Paper 2012-A0149

4. Foster, J. P., and Rita Baranwal, “ZIRLO® Irradiation Creep Stress Dependence in Compression and Tension,” 16th International Symposium on Zirconium in the Nuclear Industry, Chengdu, China, May 9-13, 2010, STP 1529, Pierre Barberis and Magnus Limback, Eds, doi:10.1520/JAI103297, ASTM International, 2011.

5. Foster, J. P., Pulver, Ed., Pan, G., Baranwal, R., “Reduction of AXIOM™ Alloy and ZIRLO® Cladding Irradiation Growth and Creep,” Topfuel 2011 Water Reactor Performance Meeting, Chengdu, China, September 11-14, 2011; Paper T2-024

6. Foster, J. P., Yueh, K., and Comstock, R. J., “ZIRLO Cladding Improvement,” ASTM STP 1505, B. Kammenzind and M. Limback Eds., ASTM International, West Conshohocken, PA, 2009, pp.457-469.

7. R. Buechel, A. Reparaz, J. Bradfute, and J. Norrell, Fuel Reliability: How it affects the industry and one fuel vendor’s journey to flawless fuel performance, Nuclear Power International Magazine, July/August 2014).

PERFORMANCE OF M-MDA™, RELIABLE CLADDING MATERIAL FOR ADVANCED FUEL

SEIICHI WATANABE, YUJI OKADA, DAIKI SATO, HIDEYUKI TESHIMA

Fuel Designing and Core Engineering Dept., Mitsubishi Nuclear Fuel CO., LTD.

622-1, Funaishikawa, Tokai-Mura, Naka-gun Ibaraki 319-1197 - JAPAN

TOSHIYA KIDO, YASUNARI SHINOHARA

Fuel and Core Engineering Dept., Nuclear Development CO., LTD.

622-12, Funaishikawa, Tokai-Mura, Naka-gun Ibaraki 319-1197 - JAPAN

YASUSHI KAMEDA

Nuclear Fuel Engineering Group, Nuclear Power Division, The Kansai Electric Power Co., Inc.

8, Yokota, 13, Goichi, Mihama-cho, Mikata-gun, Fukui 919-1141 - JAPAN

ABSTRACT

Modified MDA (M-MDA™) is a reliable cladding material for PWR fuel with high performance, developed by Mitsubishi Nuclear Fuel Co., Ltd. This cladding material was developed based on MDA which has been widely used for high burn-up PWR fuel cladding. M-MDA is applicable to higher duty operations of NPPs and contributes to enough safety margins for safety limits.

M-MDA has been irradiated in lead test assemblies operated in a commercial reactor to over 70 GWd/t of rod average burn-up, and the on-site examinations demonstrated its superior corrosion resistance and dimensional stability. The irradiated rods were subjected to hot cell examinations and the results demonstrated that hydrogen absorption into M-MDA was less than, and mechanical strength of M-MDA was higher than, conventional materials. Furthermore, the power ramp tests with the irradiated rods showed sufficient resistance to Pellet-Cladding Interaction (PCI) of M-MDA.

This paper summarizes M-MDA performance based on results of on-site examinations, hot cell examinations, power ramp tests and out-of-pile tests.

1. Introduction

For safe operation of nuclear power stations, robustness is strongly required in fuel cladding under severe conditions such as high temperature, corrosive environment and high stress. In Japanese PWRs, some types of Zr-based alloys improved from conventional Zircaloy-4 are utilized as cladding material for high burn-up usage up to 55 GWd/t (assembly average). MDA (Mitsubishi Developed Alloy ; Zr-0.8Sn-0.5Nb-0.2Fe-0.1Cr) is an improved Zr-based cladding produced by Mitsubishi Nuclear Fuel (MNF), and has been used for high burn-up fuel in Japanese PWRs.

MNF has developed the new cladding material M-MDA^{TM} (Modified MDA; Zr-0.5Sn-0.5Nb- 0.3Fe-0.4Cr) expected to have even higher performance than MDA, and has demonstrated its in-core performance in collaboration with Japanese PWR utilities and foreign organizations.

2. Characteristics

Alloying metal elements (nominal values) of M-MDA, in comparison with MDA and Zircaloy-4, are shown in Tab. 1. For realizing further corrosion resistance, the percentage of tin (Sn) is decreased and the total percentage of iron (Fe) and chromium (Cr) is increased. Increase of Fe and Cr is expected to enhance mechanical strength in order to compensate the negative effect of decreased Sn on it.

To maintain high mechanical strength, the final heat treatment of M-MDA cladding tube is stress relieved as well as MDA and Zircaloy-4.

Tab. 1. Alloying metal elements and final heat treatment

	Sn	Nb	Fe	Cr	Zr	Final Heat Treatment
M-MDA	0.5	0.5	0.3	0.4	Balance	Stress Relieved
MDA	0.8	0.5	0.2	0.1	Balance	Stress Relieved
Zircaloy-4*	1.3	-	0.2	0.1	Balance	Stress Relieved

* Low tin Zircaloy-4

Out of pile tests were conducted to examine the basic properties of M-MDA that were necessary for fuel rod design. Elastic moduli and thermal properties such as melting point, phase transformation temperature, thermal conductivity, specific heat and thermal expansion were all similar to those of MDA and Zircaloy-4 as expected.

3. In-core performance

Fuel rods with M-MDA cladding (hereinafter M-MDA rods) were irradiated in 17×17 lead test assemblies (LTAs), together with MDA rods as reference. The LTAs were irradiated in Vandellõs unit 2 in Spain. The power histories of the M-MDA and MDA rods during four 18 month cycles operation are shown in Fig. 1, and the coolant outlet temperature was between 324 and 327 °C.

After the four cycles of operation, the maximum burn-up of the M-MDA rods reached 73 GWd/t. After each cycle operation, oxide thickness (corrosion) of M-MDA rods was inspected on site. The maximum oxide thickness of the M-MDA rods is plotted against fuel rod burn-up in Fig. 2 together with that of MDA rods in the same LTAs. In addition, oxide thickness of MDA and Zircaloy-4 previously obtained are plotted for comparison. As shown in this figure, in-core corrosion resistance of M-MDA is superior to MDA and Zircaloy-4.

At the end of 3rd and 4th cycle, fuel rod length was measured and fuel rod growth was evaluated. The results are shown in Fig. 3 in comparison with MDA and Zircaloy-4. As shown in this figure, fuel rod growth of M-MDA rod is smaller than MDA and Zircaloy-4.

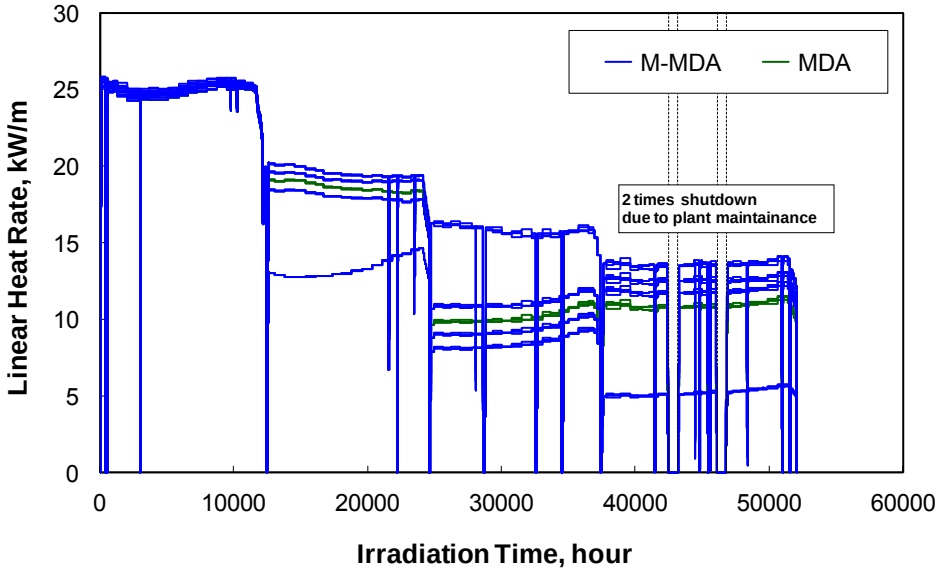

Fig. 1 Power histories of M-MDA and MDA rods irradiated in Vandellõs unit 2 [1]

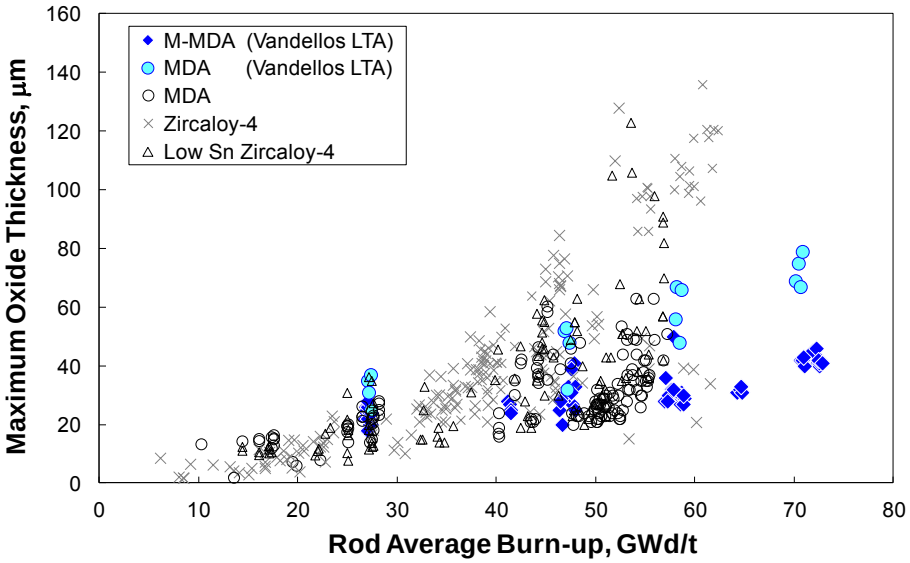

Fig. 2 Oxide thickness of M-MDA rods operated in commercial PWR [1][2]

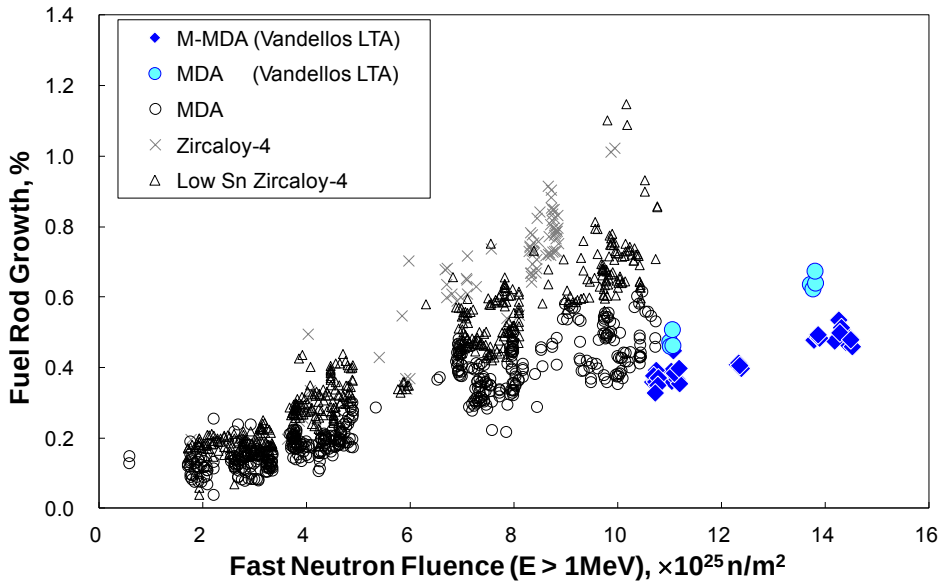

Fig. 3 Fuel rod growth of M-MDA operated in commercial PWR [1][2]

After four cycles of irradiation, several M-MDA rods were transported to hot cell facilities and subjected to post irradiation examinations. Hydrogen analyses were conducted on the specimens, without any oxide peelings, from the rods and the results are shown in Fig. 4 together with the local oxide thickness. The maximum hydrogen absorption of M-MDA during the four-cycle operation was less than 400 ppm.

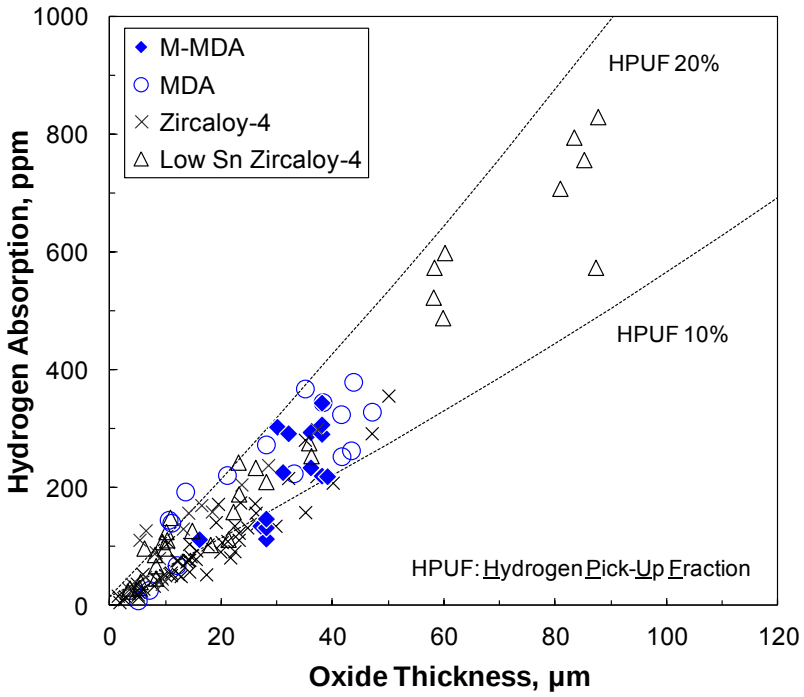

Fig. 4 Correlation between oxide thickness and hydrogen concentration

Axial tensile test was carried out with dog-bone shape specimens at 385 °C. The correlation between fast neutron fluence and 0.2 % yield strength is shown in Fig. 5. As shown in this figure, the 0.2 % yield strength of irradiated M-MDA is higher than those of MDA and Zircaloy-4. Fig. 6 shows the correlation between fast neutron fluence and total elongation. As shown in this figure, M-MDA, irradiated up to high burn-up, maintains higher ductility than MDA and Zircaloy-4. This is because the hydrogen concentration of M-MDA is lower than that of MDA as shown in Fig. 7, in which the total elongations are plotted against hydrogen concentration.

Fig. 8 shows results of fatigue tests, in which cyclic stress in the hoop direction was applied to C-ring specimens at 316 °C. This figure also contains the best-fit curve for fatigue test data of unirradiated and irradiated Zircaloy-4 by Langer and O'Donnell [3]. As shown in this figure, the fatigue strength of M-MDA is comparable to Zircaloy-4.

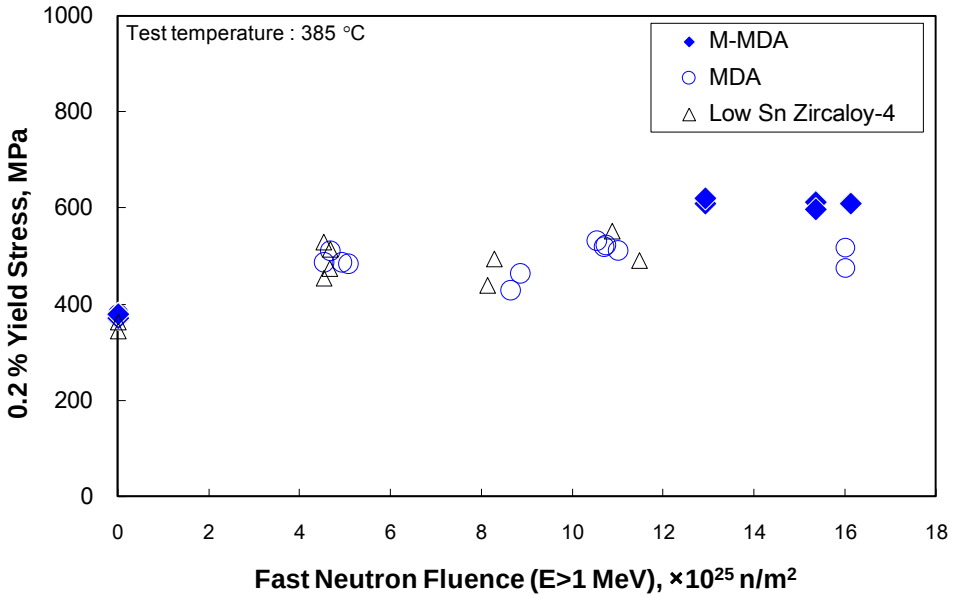

Fig. 5 Correlation between fast neutron fluence and 0.2 % yield strength as a result of axial tensile test at 385 °C [2]

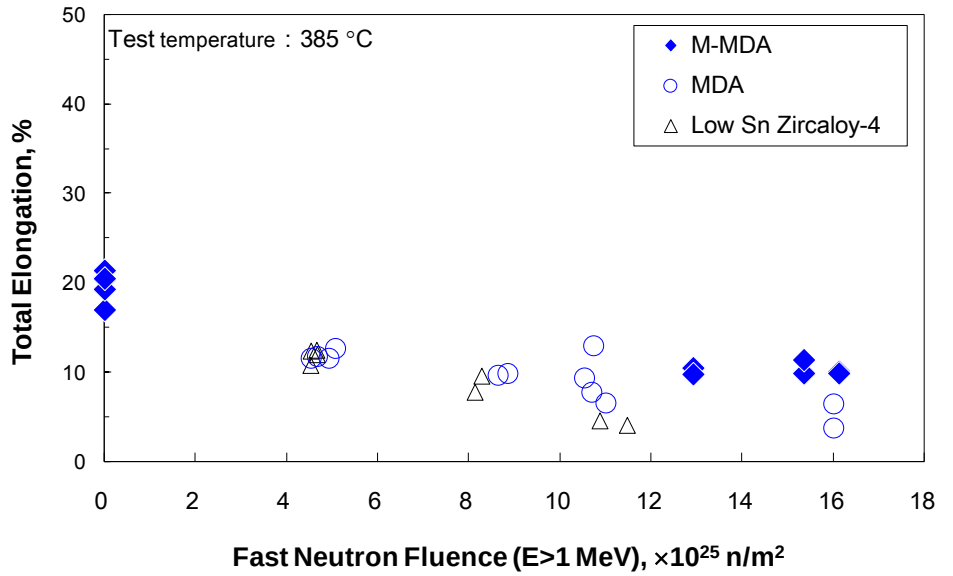

Fig. 6 Correlation between fast neutron fluence and total elongation as a result of axial tensile test at 385 °C [2]

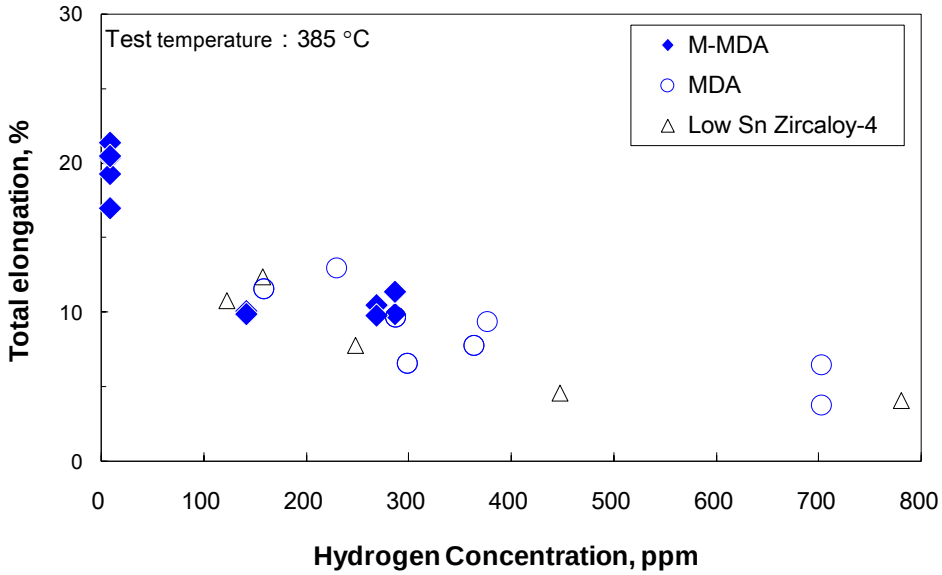

Fig. 7 Correlation between hydrogen concentration and total elongation as a result of axial tensile tests on unirradiated and irradiated specimens at 385 °C [2]

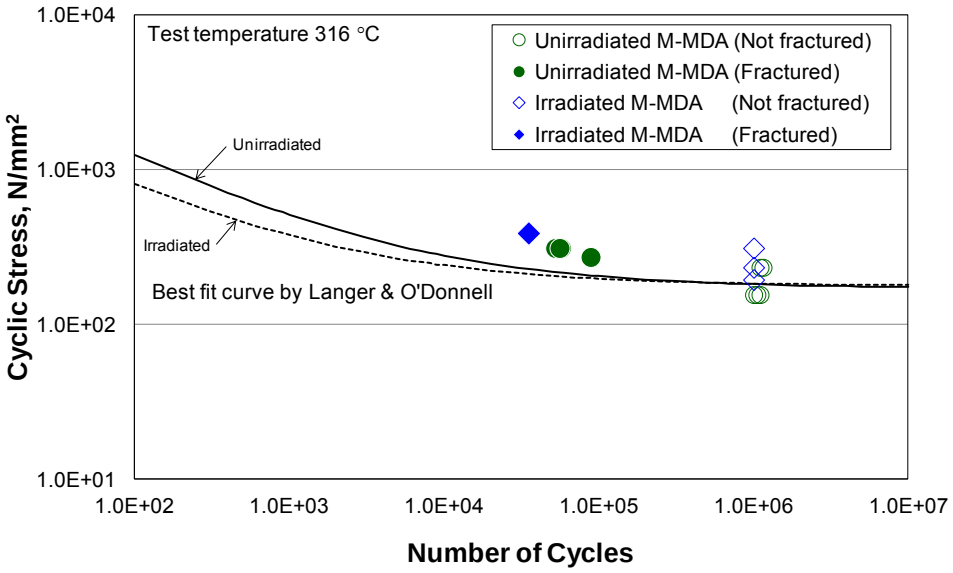

Fig. 8 Results of fatigue test at 316 °C compared to the best-fit curve by Langer & O'Donnell [2][3]

4. Performance against PCI

Resistance to PCI failure of M-MDA was expected to be comparable to MDA, because the mechanical strength of irradiated M-MDA was higher than MDA, the ductility of M-MDA is higher than MDA due to a smaller oxide layer and lower hydrogen concentration, and out of pile tests demonstrated that M-MDA had enough resistance to iodine SCC. To demonstrate resistance to PCI failure of M-MDA, two ramp test rodlets fabricated from the M-MDA rod and a rodlet fabricated from MDA rod were subjected to the power ramp test in Halden reactor in which hydraulic conditions simulated a typical PWR.

Achieved power levels and results of the power ramp tests are shown in Tab.2 Prior to the power ramp, the test rod was irradiated at medium power (Pre-conditioning LHR) for enough time to simulate pellet - cladding mechanical interactions (PCMI) under normal operation, and followingly the test rod power was rapidly ramped up to the target power level and kept with this power level (Ramp Terminal LHR) for 12 hours. As a result, all three rods were intact. The test results are plotted in terms of the maximum power (P_{max}) versus local burn-up and power increase (ΔP) versus local burn-up as shown in Fig. 9. In these figures, results of the ramp test with MDA previously obtained are plotted as well and the current threshold to PCI failure for Japanese PWR fuel is drawn. It demonstrates that the present threshold to PCI failure is applicable to M-MDA.

Tab. 2 Power ramp test results of M-MDA and MDA in Halden reactor

Cladding	M-MDA	M-MDA	MDA
Burn-up, GWd/t	81.2	70.0	74.0
Pre-conditioning LHR, kW/m	24.6	20.0	20.0
Ramp Terminal LHR (P_{max}), kW/m	41.6	44.9	44.6
Ramp power increase (ΔP), kW/m	17.0	24.9	24.6
Failure or Intact	Intact	Intact	Intact

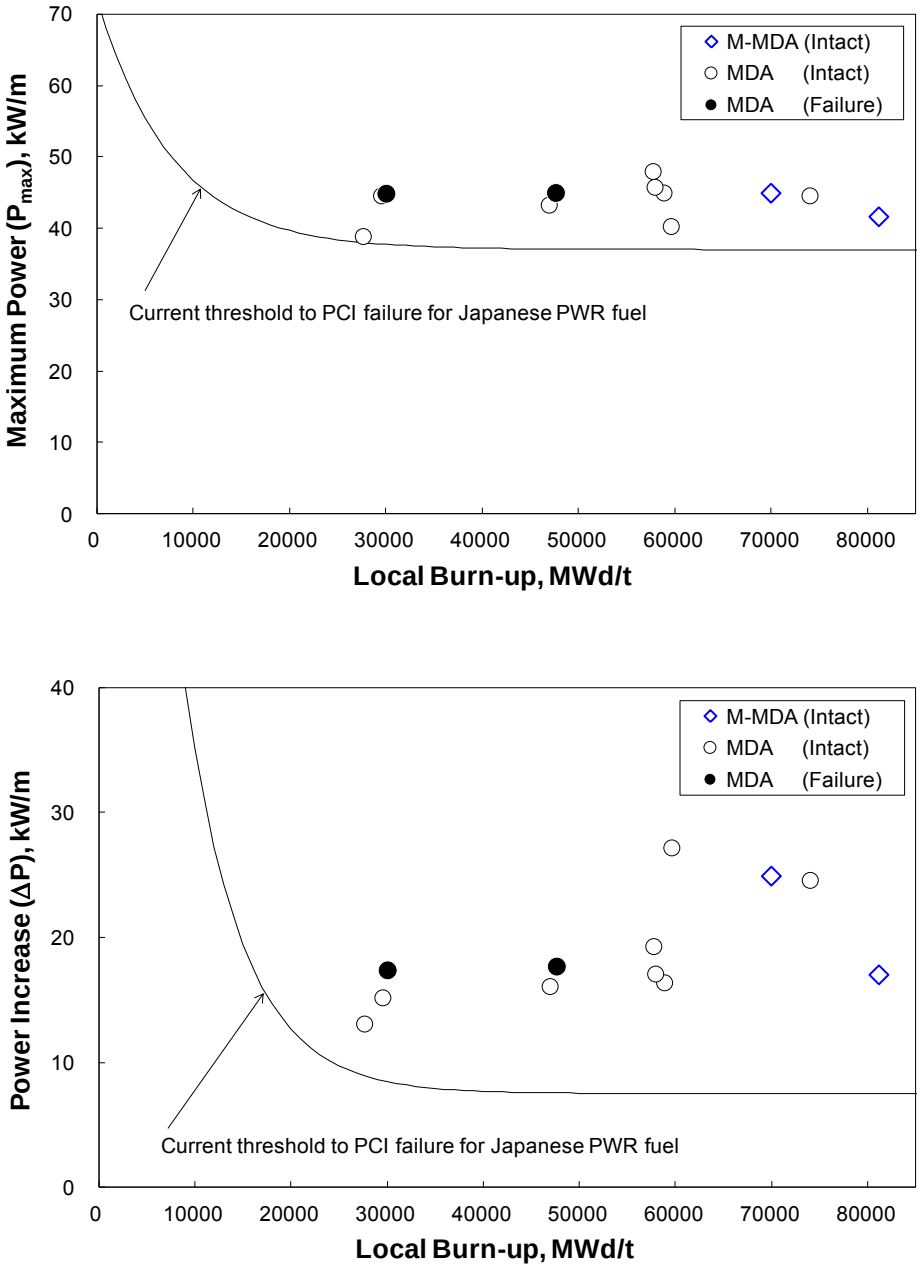

Fig. 9 Ramp test results of M-MDA and MDA, compared with the present threshold to PCI failure for Japanese PWR fuel [2]

5. Behaviour under accidental conditions

Cladding behaviour under high temperature simulated accidental conditions was examined. The results of oxidation tests at high temperature are shown in Fig. 10. The figure is in terms of an Arrhenius plot with the Baker-Just (BJ) correlation [4] and the Cathcart-Pawel (CP) correlation [5] for reference. The parabolic rate constant at each temperature of M-MDA is lower than both the BJ correlation and the CP correlation. This means that both correlations are conservatively applicable for evaluation of oxidation rate of M-MDA during LOCA.

Burst tests simulating LOCA were conducted at ramp rates between 2 °C/sec and 28 °C/sec. Correlation between burst stress (engineering hoop stress applied to cladding when burst) and burst temperature (cladding temperature at burst position) are shown in Fig. 11, together with a correlation of NUREG-0630 model for the ramp rate of 14 °C/sec [6]. As shown in this figure, the correlation between burst stress and burst temperature of M-MDA under LOCA conditions is comparable to the correlation in the NUREG-0630 model.

To confirm the maintenance of coolable geometry after quenching by ECCS, integral thermal shock tests simulating cladding thermal sequence during LOCA were done. As a result, M-MDA cladding survived after quench which had been subjected to double-side oxidation in steam at 1200 °C to over 17 % ECR.

In addition to above examinations with unirradiated cladding, the M-MDA rod irradiated in the LTA has been segmented and transported JAEA for examinations simulating LOCA and RIA.

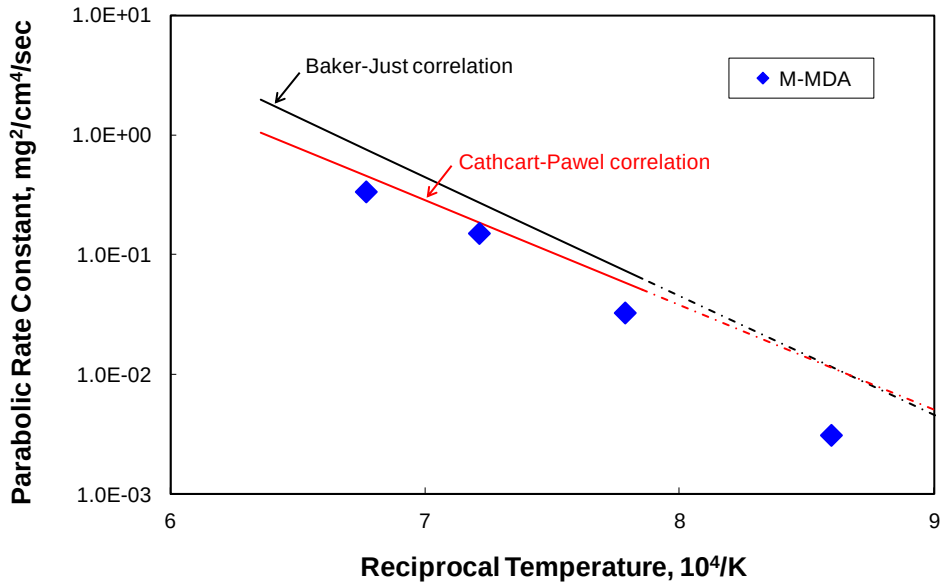

Fig. 10 Correlation between reciprocal temperature and parabolic rate constant of M-MDA as a result of H.T. oxidation test [4][5]

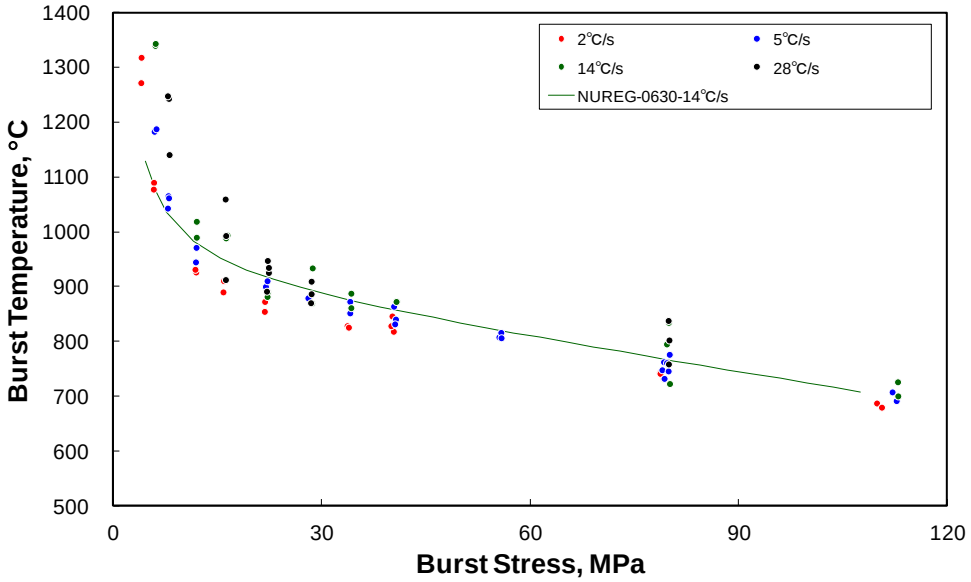

Fig. 11 Correlation between burst stress and burst temperature of M-MDA [6]

6. Summary

To demonstrate the performance of M-MDA cladding, material properties examination, irradiation test in a commercial reactor, post irradiation examinations, power ramp tests and examinations under accidental conditions have been carried out. The advantages of M-MDA in comparison with the conventional cladding (Zircaloy 4, Low tin Zircaloy 4 and MDA) are superior corrosion resistance, superior dimensional stability (smaller rod growth), lower hydrogen concentration and higher mechanical strength. The other performances of M-MDA, including PCI resistance and behaviour under accidental conditions, are comparable to the conventional cladding.

7. Acknowledgments

The irradiation in a Spanish commercial reactor was realized thanks to ENUSA, ENDESA and ANAV. The post irradiation examinations were carried out by CEA and Studsvik, and the power ramp tests were carried out by IFE. The authors are grateful to these organizations for their technical cooperation.

8. References

[1] D. Sato, T. Kido and Y. Mazaki, "In-pile behavior of M-MDA^{TM}, advanced PWR fuel cladding irradiated up to 73 GWd/t(R) in a commercial reactor", 2011 Water Reactor Fuel Performance Meeting, Chengdu, China, (2011)

[2] Mitsubishi Nuclear Fuel Co, Ltd., "Mechanical Design of Mitsubishi High Burn-up Step-2 Fuel for PWR" (in Japanese), Revision 1 to MNF-1001, March 2011

[3] W. J. O'Donnell, B. F. Langer, "Fatigue Design Basis for Zircaloy Components", Nuclear Science and Engineering 20, 1-12 (1964)

[4] L. Baker and L. C. Just, "Studies of Metal-Water Reaction at High Temperatures III. Experimental and Theoretical Studies of the Zirconium-Water Reaction", ANL-6548, Argonne National Laboratory (1964)

[5] J. V. Cathcart, R. E. Pawel, R. A. McKee, R. E. Druscel, G. J. Yurek, J. J. Cambell and S. H. Jury, "Zirconium Metal-Water Oxidation Kinetics IV. Reaction Rate Studies", ORNL/NUREG-17, Aug. 1977, pp. 168-181.

[6] D. A. Powers and R. O. Meyer, "Cladding Swelling and Rupture Models for LOCA Analysis", NUREG-0630 (1980)

FIRST DNB TESTS AT THE WESTINGHOUSE ADVANCED LOOP TESTER (WALT)

G. WANG[1], W. A. BYERS[1], Z. E. KAROUTAS[2]
S. RAY[2], R. L. OERICH[2], and B. N. BURGOS[1],
[1]*Westinghouse Electric Company LLC, Pittsburgh, Pennsylvania, U.S.A.*
[2]*Westinghouse Electric Company LLC, Hopkins, South Carolina, U.S.A.*

wangg@westinghouse.com, byerswa@westinghouse.com, karoutze@westinghouse.com, rays@westinghouse.com, oelricrl@westinghouse.com, burgosbn@westinghouse.com

ABSTRACT

The Westinghouse Advanced Loop Tester (WALT) at the Science and Technology Center of Westinghouse was completed in October 2005. Recently, a number of upgrades of the test loop have been made to increase the pressure and thermal stabilities, and the data acquisition system has been improved for performing Departure from Nucleate Boiling (DNB) tests. With the improvements, the WALT test loop has been designed to meet current and future requirements for measuring fuel cladding temperatures with and without crud deposition, evaluating effects of plant chemistry on crud deposition on Pressurized Water Reactor (PWR) fuel pins, as well as performing DNB tests at PWR conditions.

This paper describes the first laboratory test program to measure the cladding temperature jump at DNB conditions within the WALT loop test facility with and without surface treatments. This DNB measurement study is necessary to allow more accurate predictions of DNB for different surfaces with and without crud that initiated from realistic PWR operating conditions. Currently, the WALT loop is also being used to explore the connection between a base DNBR value and improved DNB margin.

1. Introduction

The objective of this paper is to present the improvements and the first set of Departure from Nucleate Boiling (DNB) test results on the WALT loop [1,2]. In general, the WALT test loop has been improved [3,4] to meet the requirements for DNB tests at PWR conditions, and make evaluations of chemistry effects for crud deposition on PWR fuel rods.

The WALT loop located at the Westinghouse Churchill site, Pennsylvania, USA has a single heater rod and is being used to simulate a fuel rod in the upper region of a PWR. Normally, the rod is uniformly heated except at each ends where the rods are terminated with two Zircaloy plugs. In the first set of planned DNB tests, the rod section between the plugs had two different thicknesses, and thus operated at different heat fluxes. Basically, the majority of the center section of the heater rod is thinned down to allow higher heat flux. The two small sections at ends of the heater rod have regular cladding thickness. Thermocouples are placed in the thinned section of the heater rod, which can be utilized for the DNB test.

Typically, there are at least two standard ways to increase DNB margins. The first one is to improve the grid designs or extend the grid structure, e.g. putting wires surrounding the fuel or heater rods. The second way is to conduct fuel rod surface treatment, e.g. cold spray or forming a fine deposit layer on the heater rod surfaces. Heat transfer benefits are suggested by possible decreased cladding corrosion in plants with advanced grid design or surface treatments. If these heat transfer benefits can be proven, many benefits can be utilized. These benefits may include plant power uprate and associated operation and safety analysis improvements. Plants will benefit from having more operating margin, higher powered cores,

and lower overall fuel cycle costs. For a new plant, this will also significantly increase existing safety margins, or enhance the new plant rated power.

As the first step, a clean surface heater rod was designed and manufactured in the presented work, i.e. without surface treatments or grid structure changes. After a clean surface DNB test, a wire was spiraled to the heater rod surface to simulate an extended grid design. Then, another DNB test was conducted with the wired heater rod. This simple extended grid, i.e. the spiral wires, has contributed not only to improve heat transfer at normal PWR operating conditions but also to improve DNB margin at any postulated transient conditions. Thermal-fluid characterizations were carried out by controlling the pitch of the spiral wire. The preliminary DNB test results have shown that the extended grid design as a simple approach can contribute DNB margin to nuclear power plant core and safety systems.

2 WALT DNB Test Method

Based on previous WALT loop experimental data [2,3], boiling heat transfer was investigated to determine the operating condition, especially heat flux and effects on cladding temperatures of the heater rod. Normally, the WALT test data span the full range of non-boiling and boiling conditions expected in a PWR. For WALT DNB tests, the test data will cover a wider range up to the CHF point. Figure 1 shows a typical boiling curve to explain the observed behavior of the DNB test conditions.

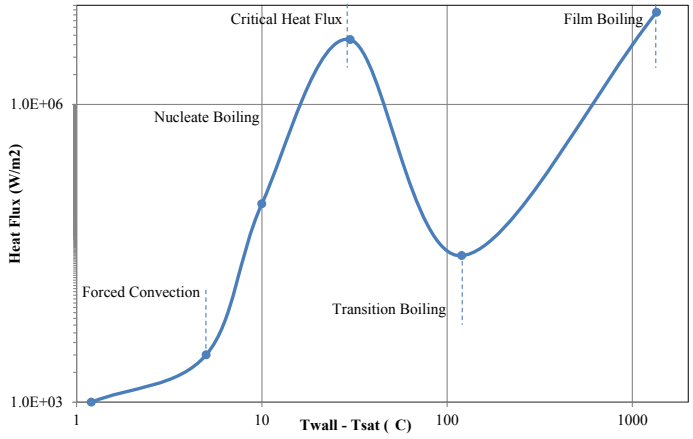

Figure 1 A Typical Boiling Curve

The CHF point shown in Figure 1 is the focus in the WALT DNB test methodology. This typical boiling curve shows the cladding temperature behavior, when reaching the CHF point. Typically, there are two types of Critical Heat Flux (CHF) mechanisms, i.e. DNB and dryout. At postulated accident conditions, annular flow regime surrounding a fuel pin may exist. When heat flux increases, the liquid film layer becomes thinner and thinner. Eventually, dryout may occur at high heat flux. Normally, dryout is quality driven, and the process is relatively slower. On the other hand, Departure from Nucleate Boiling may also occur at postulated accident conditions in PWRs. DNB is heat flux driven, and the process is faster.

As shown in Figure 1, heat transfer is by forced convection at lower heat flux. When heat flux increases, heat transfer is enhanced due to nucleate boiling. On the fuel pin surface with nucleation sites, subcooled nucleate boiling becomes pronounced as a result of non-wetting surface or deposit [5]. At the subcooled nucleate boiling region under PWR operation conditions, vapor bubbles grow at active nucleation sites leaving, as they grow, a very thin

‘micro-layer’ of liquid beneath the bubble. This thin layer is totally evaporated leaving the solid content (i.e. corrosion products) of the micro-layer deposited on the surface. The bubble detaches and water contacts the surface again, removing some of the deposit. When heat flux increases further, more bubbles will be generated. At high heat flux, these bubbles will eventually collapse into vapor film. Heat transfer becomes worse due to the formation of the vapor film. Then, DNB occurs, and the CHF point is reached (Figure 1).

It is very important utilizing Figure 1 to identify the flow regimes and heat transfer mechanisms. The WALT DNB test methodology describes three heat transfer mechanisms or phases, i.e. forced convection, nucleate boiling, departure from nucleate boiling (DNB). These three phases are shown in Figure 1: (a) the forced convection phase is typical for the normal inlet temperature operating conditions in PWRs. It is selected as the initiating point for the WALT loop DNB test. (b) when the heat flux is increased gradually, the heater rod in the WALT test section will go through the nucleate boiling phase. (c) with much finer steps to increase the heat flux, the phase of DNB will occur at a higher heat flux level. With high speed data acquisition system, the DNB process can be observed and controlled by the engineers and operators of the WALT loop. After a successful DNB test, the heater rod from the WALT loop shall be preserved for post DNB test exam.

3. WALT Loop Description and Heater Rod Design

The Westinghouse Advanced Loop Tester (WALT) is located in the Westinghouse Churchill site in Pittsburgh, Pennsylvania. The WALT loop is a single heated rod facility and has been used for convection, sub-cooled boiling and other heat transfer tests. The original WALT loop was completed in October 2005 in Building-401 of the Westinghouse Churchill site. A completed picture is shown in Figure 2. Even though the WALT loop has now been relocated to Building-301, the WALT loop DNB tests reported in this study were conducted in Bldg-401.

Figure 2 Picture of the WALT (October 2005)

3.1 WALT Loop Equipment and Systems

The entire test loop, as shown in Figure 3, includes heater rod, valves, pumps, heat exchangers, make-up tank, flow meter, pressure control system, and protection system. All thermocouples are isolated from the power supply. Thermocouples, flow meters, pressure gauge, current and voltage meters are reset/calibrated and recorded for each test.

An immediate power shutdown system was installed and improved in the test facility, based on the measured heater rod cladding temperature, pressure, power (current), and flow rate, that would immediately trip the power supply to the heater rod. For example, if the heater rod surface temperature is approximately 40.0 to 60.0 ºC superheated at specified pressure (e.g. 15.5 MPa), the power shutdown system would also immediately trip the Rectifier DC power supply. If either the system pressure is too high/low (e.g. 13.6 MPa ≤ Pressure ≤ 20.7 MPa) or the flow rate is too low (e.g. Flow ≤ 3.15x10-4 m3/s), the Rectifier DC power supply to the heater rod will be also shutdown. The general idea is to maintain the integrity of the test loop and to preserve the heater rod surface for post-test examinations.

The heater rod of the WALT loop has a total heated length of 336 mm. The end plugs and connection parts add another 139 mm for a total length of 380 mm. The heater rod is utilized to model one of the top grid spans of a PWR fuel assembly. As can be seen in Figure 3, a large diameter pipe was used as the inlet to the autoclave in order to allow for better mixing of water flowing into the inner chimney tube that surrounds the heated rod. The inner tube was a tube-in-tube design with an air gap. The air gap reduces the heat loss from the water in the flow channel to the bulk autoclave solution. As shown in Figure 3, there are two thermocouples for measuring the flow chimney inlet and outlet temperatures. The WALT loop can be operated with either forced flow or natural circulation.

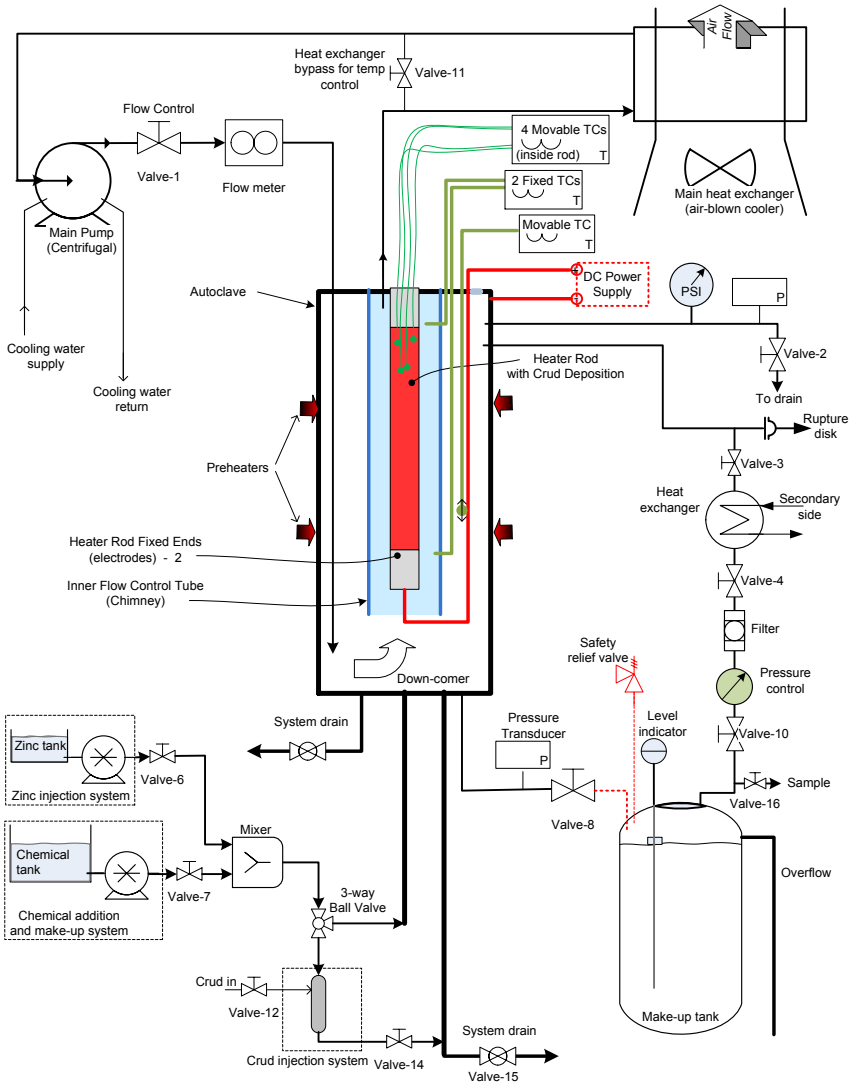

Figure 3 Layout of the WALT Loop

Heater rods having a thermal power of up to 31.8 kW can be used in the WALT loop. The maximum operating pressure is 20 MPa. The maximum linear velocity rate can be as high as 6 m/s in the WALT loop test section. Key parameter upper limits of the WALT loop are summarized in Table 1.

As shown in Figure 3, the test loop pressure is controlled by a pressure control system and an independent pressurizing pump. The heat is removed from the loop by a heat exchanger with an air-blown cooler. The autoclave in the WALT loop is surrounded by electrical heaters that control the temperature of the coolant entering the flow chimney.

The main pump can be powered off and the air-blown cooler fan is turned on during natural circulation tests. The top right corner in Figure 3 shows the main heat exchanger, which is located at a higher elevation than the heater rod section in order to have natural circulation flow. The natural circulation flow rate can be adjusted by closing or opening Valve-1 in the main loop. In addition, the flow can be accurately measured by means of the flow meter in the main loop. The heater rods are typically constructed from standard PWR fuel cladding tubes, i.e. ZIRLO® tubes. The WALT loop can simulate the typical PWR operating conditions as given in Table 2.

PARAMETERS	UPPER LIMITS
System pressure, MPa	20.00
DC power supply, kW	100.00
Heat exchanger, kW	31.80
Flow velocity, m/s	6.00
Inlet temperature, °C	<Tsat
Axial Power Shape	Typically Uniform
Heater rod material	**ZIRLO®**
Heater rod length, m	<1.35 (0.33 heated typical)
Heater rod OD, mm	9.50
Heater rod ID, mm	8.36
Test section shroud ID, mm	23.5
Test section flow area, mm^2	362.6

Table 1Key Parameters in WALT Loop

PARAMETERS	NORMAL VALUES
Reactor System Pressure, MPa	15.50
Reactor Core Power, MWth	3411, or about 23 kW/m
Core Inlet Flow, m/s	4.50
Core Inlet Temperature, °C	290.50
Axial Power Shape	Non-Uniform
Fuel Rod Cladding Material	**ZIRLO®**
Fuel Rod Heated Length, m	3.66
Top Grid Span Length (w/IFM), m	0.25~0.305
Fuel Rod OD, mm	9.50
Fuel Rod ID, mm	8.36

Table 2 Typical PWR Operating Conditions

3.2 DNB Test Articles

In this section, a general description for the WALT Loop DNB test article is provided. There will be two test articles. Each will be a ZIRLO® heater rod that has been altered to create different simulated fuel rod surface conditions, which are clean, and wired surfaces.

A clean surface thinned heater rod design is shown in Figure 4. Each test article used in the WALT loop DNB tests is a thinned ZIRLO® heater rod. For a DNB test, it is important to design a heater rod to meet the requirements for approaching the CHF point as shown in the boiling curve in Figure 1. There are four thermo-wells built in the heater rod. Four thermocouples are inserted to the thermowells to measure the heater rod inner surface cladding temperatures. The power distribution is uniform in the section with the same cladding thickness. The heater rods are constructed from standard PWR fuel ZIRLO® cladding. As shown in Figure 4, four thermo-wells are supported by a ceramic ring, which is

located at about 5 inches from the end of the plug. Movable Type-J thermocouples are placed in these thermo-wells to measure the inside wall temperatures axially. The thermocouples length is typically 36 inches. The heater rod design for the WALT loop has several unique features, which are summarized below:

- uniform axial power shape distribution for the section with the same OD,
- Movable thermocouples in the four thermo-wells to measure the inside wall temperatures,
- heated length is long enough to model the PWR fuel assembly top grid span,
- short copper rings are inserted into the heater rod ends to reduce the electric resistance,
- ceramic ring and sleeve coatings are used to electrically isolate and support the TCs.

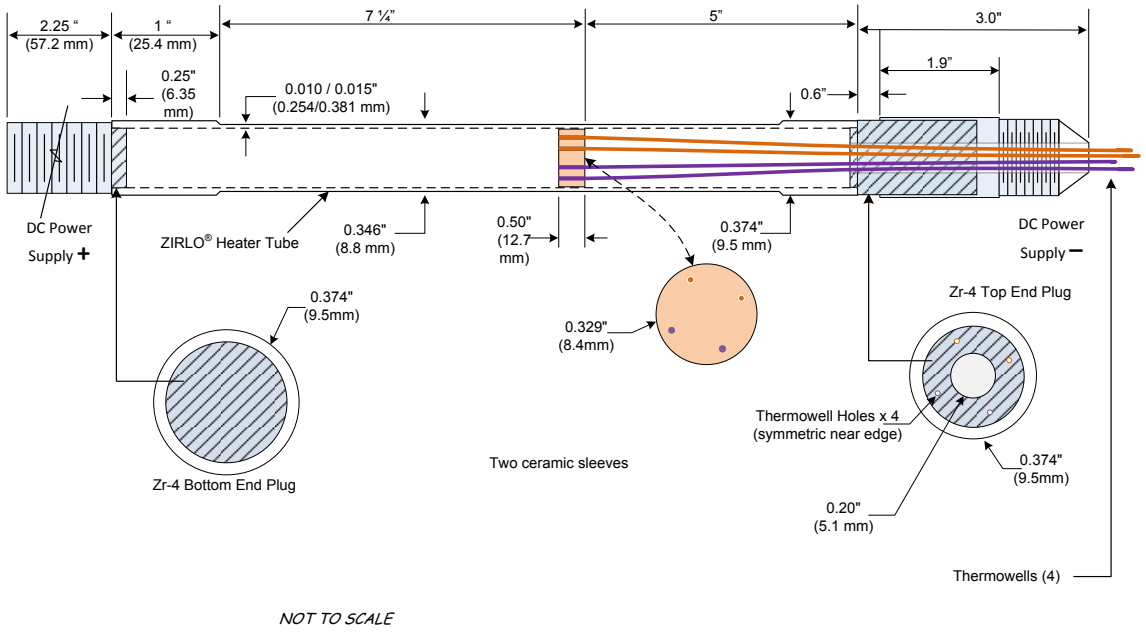

Figure 4 A Heater Rod Design with Two Different ODs

3.3 Heat Flux Calculations

As described in a separate paper [2,3], there is an alternating current (AC) component in addition to the direct current (DC) component in the electric current supplied to the WALT heater rod. Therefore, the heater rod in the WALT loop is heated by both AC and DC power. In direct current resistive conductor instantaneous electrical power (PDC) is calculated using Joule's Law combined with Ohm's law,

$$P_{DC} = I_{DC}^2 R_{elec} \qquad (1)$$

For AC current, rather than using instantaneous power, it is more practical to use a time averaged power (PAC), where the averaging is performed over any integer number of cycles. Therefore, AC voltage or current is often expressed as a root mean square (RMS) value, written as Vrms or Irms. Then, the time averaged power for the AC component, PAC, is given below.

$$P_{AC} = I_{rms}^2 R_{elec} \qquad (2)$$

In the WALT loop, the current root mean square (RMS) value, Irms is measured and recorded together with the DC current value, IDC. Then, the total heat flux (q″) generated

through the heater rod cladding of the WALT loop by electric current is calculated using Equations (1) and (2) as the following.

$$q'' = \frac{P_{total}}{S_{clad}} = \frac{(I_{rms}^2 + I_{DC}^2) \times R_{elec}}{2\pi \times r_2 \times L_H} = \frac{(I_{rms}^2 + I_{DC}^2) \times \rho}{2\pi^2 \times r_2 \times \left(r_2^2 - r_1^2\right)} \quad (3)$$

All parameters or dimensions used in the above equations are listed and described in the nomenclature section. From Equation (3), the total heat flux (q″) is calculated and utilized in the DNB test results, i.e. the DNB test curves of cladding temperatures and heat flux vs time as discussed in Section 4.3.

4. DNB Test Data and Results

As mentioned previously, the method employed in the WALT DNB tests is discussed in Section 2. In this section, the test data obtained, and test results are presented and discussed for the first set of WALT DNB test cases.

4.1 Heater Rod Surface Condition

Departure for Nucleate Boiling (DNB) tests have been performed with the following conditions on the same heater rod in order to make appropriate comparisons for a DNBR margin gain:

- Using a clean surface ZIRLO® heater rod.
- Putting wires surrounding same ZIRLO® heater rod after clean surface DNB test.

4.2 WALT DNB Test Operating Conditions

As shown in Figure 4, the heater rod used in the DNB test is designed to have the majority of the center section thinned down (with an OD of 8.8 mm). The two ends (about 63 to 76 mm long) of the ZIRLO® heater rod are with a standard OD of 9.5 mm at the end. The hydraulic diameter in (HD) the WALT loop test section is the same or very close to the HD in a typical PWR fuel assembly channel. The two plugs are laser welded to the end of the ZIRLO® heater rod. The heated length of the heater rod is about 336 mm with the end plugs contributing an additional 139 mm to the total length. The heater rod is long enough to simulate a typical PWR top grid span of about 250 to 305 mm as listed in Table 2.

The initial parameter values for coolant temperature, pressure, flow rate, Reynolds number and heat transfer rates can be adjusted throughout the range of actual PWR conditions, which are shown in Table 2. Accordingly, geometric data and steady state operating parameters used in a DNB test are given in Table 3.

PARAMETERS	NORMAL VALUES
System Pressure, MPa	15.5
Heat Flux (Thinned section), W/cm^2	163.6
Chimney Inlet Flow Velocity, m/s	2.85
Chimney Inlet Temperature, °C	333.4
Axial Power Shape	Non-Uniform
Heater Rod Cladding Material	**ZIRLO®**
Heater Rod Heated Length, mm	336
Heater Rod OD (Two ends), mm	9.5
Heater Rod OD (Thinned section), mm	8.8
Flow chimney hydraulic diameter, mm	14.7

Table 3 Steady State Operating Conditions Before DNB

The WALT DNB test of Rod #108 was conducted with a ceramic chimney. The chemistry conditions are close to the typical PWR coolant chemistry conditions with 1000 ppm boron and 2.2 ppm lithium. The DNB test of Rod #135 was conducted with a new stainless steel chimney with a chimney ID of 23.5 mm. The chemistry conditions are also close to the typical PWR coolant chemistry conditions with 1000 ppm boron and 2.2 ppm lithium. A VIPRE-W model was also built [6,7] where the VIPRE-W predicted DNBR results were used to guide the first DNB test at the WALT loop.

4.3 DNB Data Reduction and Results for Rod #108 and Rod #135

WALT DNB test Rod#108 was a successfull test for clean surface conditions only. The CHF point was approached closely for WALT DNB test Rod #108. Pictures of the ZIRLO® heater rod for before (Case (a)) and after (Case (b)) the DNB test are shown in Figure 5.

As the result of this DNB test, a curve of cladding temperature and heat flux vs time was generated in Figure 6. As can be seen, the cladding temperature was increased to a very high value at the end of the DNB test. Since the power supply was shut down near DNB, the heater rod was not damaged. The recorded results for Rod #108 are summarized in the second column of Table 4.

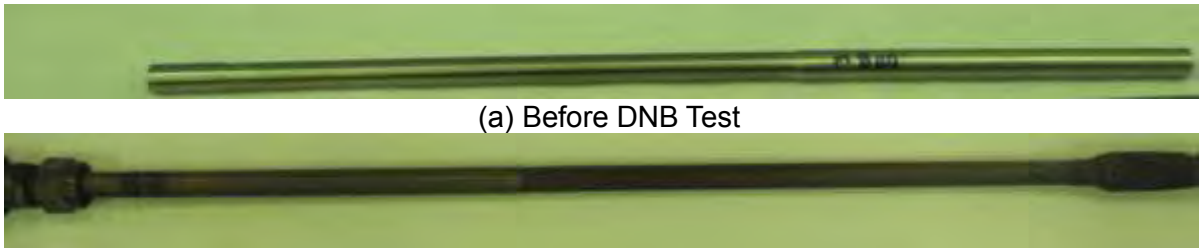

(a) Before DNB Test

(b) After DNB Test

Figure 5 ZIRLO® Heater Rod #108

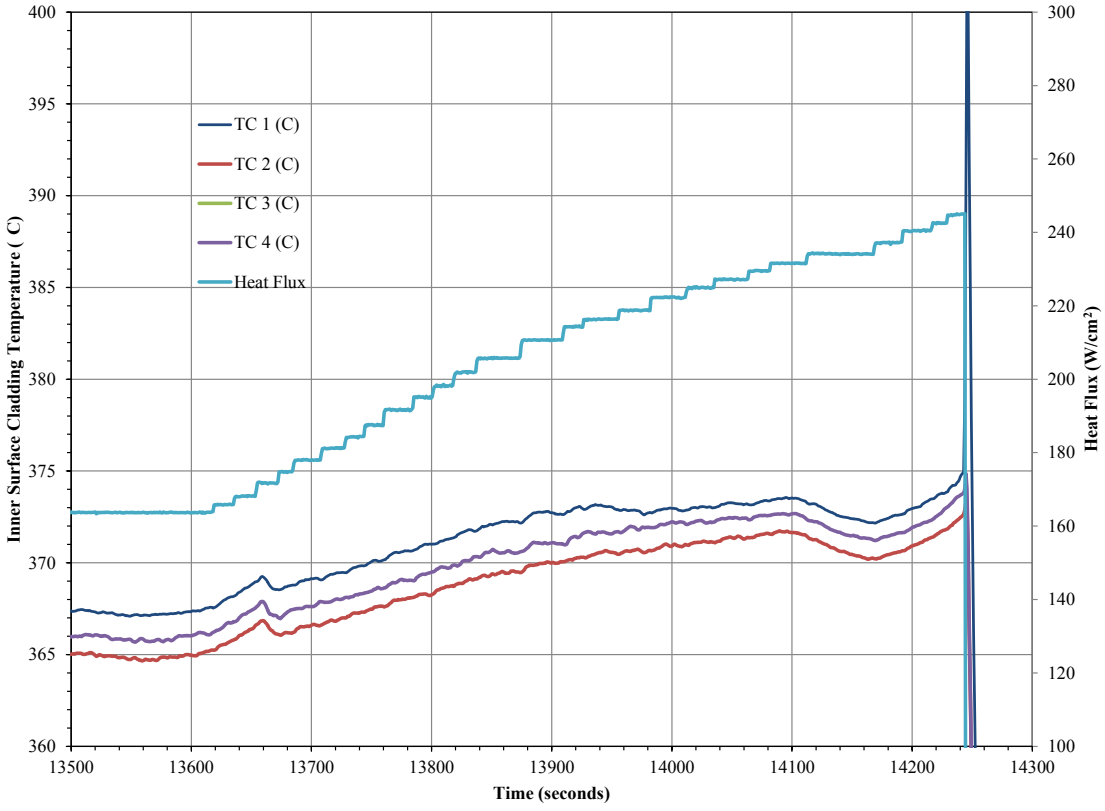

Figure 6 Clean Surface DNB Test Boiling Curve for Rod#108

PARAMETERS	Rod #108 CLEAN SURFACE	Rod #135 CLEAN SURFACE	Rod #135 WIRED SURFACE
System Pressure, MPa	15.5	15.8	15.5
Heat Flux (Thinned section), W/cm^2	245.1	202.4	227.3
Chimney Inlet Flow Velocity, m/s	2.85	2.53	2.53
Chimney Inlet Temperature, °C	333.4	334.1	333.2
Axial Power Shape	Non-Uniform	Non-Uniform	Non-Uniform
Heater Rod Cladding Material	**ZIRLO®**	**ZIRLO®**	**ZIRLO®**
Heater Rod Heated Length, mm	336	336	336
Heater Rod OD (Two ends), mm	9.5	9.5	9.5
Heater Rod OD (Thinned section), mm	8.8	8.8	8.8
Flow chimney hydraulic diameter, mm	14.7	14.7	14.7

Table 4 DNB Test Results for Rods #108 and #135

WALT DNB test Rod #135 was successfully conducted with the following two test conditions. All other geometric conditions and dimensions are identical for both DNB tests. In addition, all initial fluid condition, including parameter values for coolant temperature, pressure, flow rate, and Reynolds number are the same for both DNB tests.

- At clean surface conditions,
- Wired ZIRLO® heater rod surface conditions.

Pictures of the ZIRLO® heater rod for before and after the DNB test are shown in Figure 7. As can be seen in Figure 7, the heater rod is still reasonably clean after the two DNB tests with clean (Case (b)) and wired (Case (c)) ZIRLO® heater rod surfaces, respectively. Since the surfaces are still relatively clean, it is reasonable to exclude any crud or deposition effects. Accordingly, reasonable comparisons can be made between Cases (a) and (b).

(a) Before DNB Test

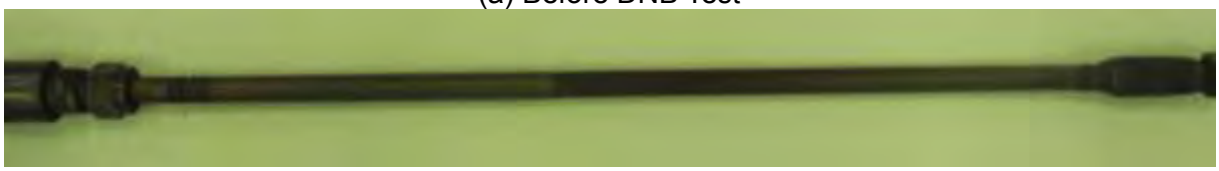

(b) After Clean Surface DNB Test

(c) After Wired Surface DNB Test

Figure 7 ZIRLO® Heater Rod #135

As the result of the clean and wired surface DNB tests, two boiling curves were performed. Accordingly, the heat flux and cladding temperature vs time are plotted in Figures 8 and 9.

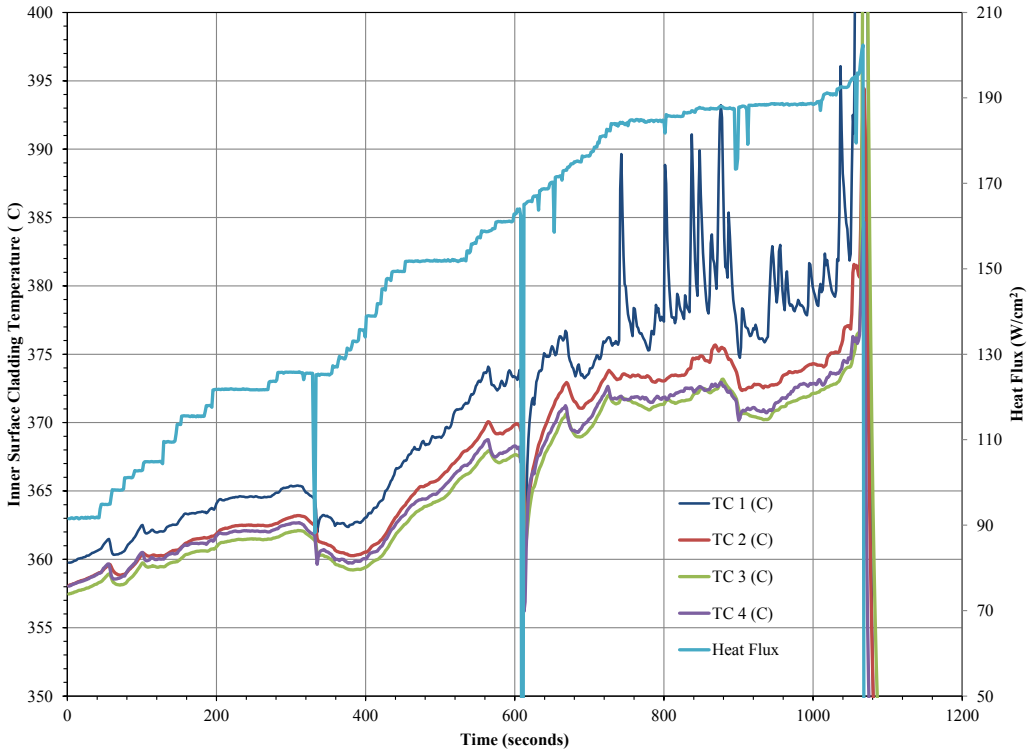

Figure 8 Clean Surface DNB Test Results for Rod #135

As can be seen in both figures, the cladding temperature was increased to a reasonably high value without damaging the heater rod yet. After seeing the cladding temperature jumped, the WALT power supply was shut down and the DNB test were completed. The recorded results for the two cases for Rod #135 are presented in the last two columns of Table 4, respectively. A quick comparison between these two columns is made and the differences on system pressure, flow, and heat flux are listed in Table 5.

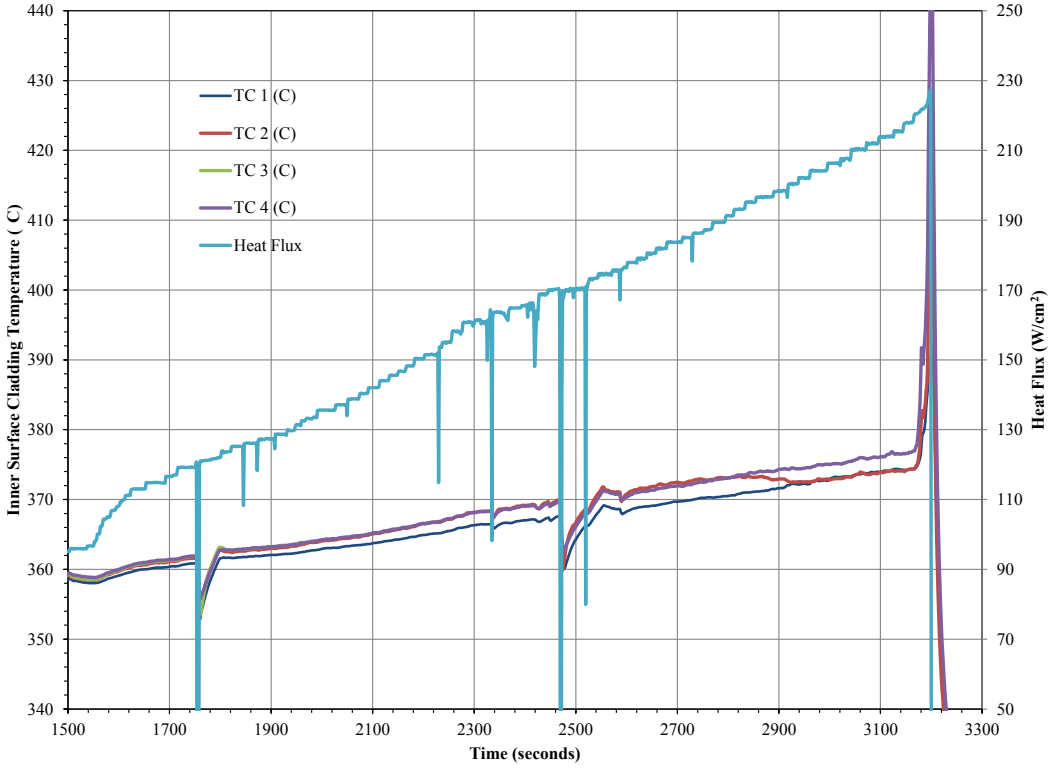

Figure 9 Wired Surface DNB Test Results for Rod #135

Table 5 shows that the differences for system pressure and inlet temperature between the clean and wired surface cases are very small. In fact, the wired surface case has about 2% and 0.3% lower values in pressure and inlet temperature, respectively. Based on past experiences [6], the WALT DNBR effects from these two small differences will be cancelled out. Thus, the only significant difference between these two DNB test cases is the heat flux. The wired surface case has a higher heat flux than the clean surface case. This 12.3% difference (Table 5) in heat flux will translate to at least 12.3% DNBR margin gain for the wired surface ZIRLO® heater rod.

PARAMETERS	CLEAN SURFACE	WIRED SURFACE	WIRED/ CLEAN (%)
System Pressure, MPa	15.8	15.5	2%
Chimney Inlet Temperature, °C	334.1	333.2	0.3%
Heat Flux (Thinned section), W/cm^2	202.4	227.3	12.3

Table 5 Result Differences between Clean and Wired Surface DNB Tests for Rod #135

5. Conclusions and Recommendations

A variety of experiments has been performed in the WALT loop, since the loop was completed in October 2005. Basically, the WALT Loop has been utilized to simulate the PWR operating conditions, and the first set of DNB tests has been successfully conducted on the WALT loop. The main goal of this study was to demonstrate that the WALT loop can be utilized to perform a DNB test. Meanwhile, the WALT loop has been used to explore the connection between a base DNBR value and improved DNB margin. This goal has been met through the following achievements.

- The WALT facility at the Westinghouse Churchill site was improved to allow reliable measurement of the cladding temperature of electrically heated fuel rods. The WALT facility was qualified for making DNB tests. This qualification showed that reproducible DNB results were obtainable.
- The preliminary DNB test results show that significant DNBR margin was obtained for the wired DNB test case. A more comprehensive test matrix will be developed in the future. This will very likely generate a new fuel rod and assembly designs, e.g. with extended grid structure.
- WALT tests also show repeatability of DNB test results, which demonstrate that the DNB results and comparisons using the WALT loop are reliable.

This paper presented the first set of DNB tests on the WALT loop, and explored the connection between one of the proposed means (i.e. wired surface) and improved DNB margin. The available preliminary results show a DNBR margin of 12.3% by comparing wired heater rod surfaces against clean heater rod surfaces. The preliminary DNB test results have shown that extended grid design as a simple approach can contribute DNB margin to nuclear power plant core and safety systems.

Based on relevant observations [8,9,10] and DNB test results obtained from the WALT loop, it is recommended that further studies be performed in these areas.

- DNB effects of a crud deposit shall be studied in the WALT loop.

- More generically, DNB test shall be conducted with different surface treatments or modifications.
- Further DNB tests on wired heater rods with optimized pitches.
- Cold spray on fuel rod surface
- Ribbed heater rod surface
- Investigate transient effects on DNB for different rod surfaces and deposits

Nomenclature

CHF	Critical Heat Flux
DNB	Departure from Nucleate Boiling
DNBR	Departure from Nucleate Boiling Ratio, CHF / q''
PWR	Pressurized Water Reactor
WALT	Westinghouse Advanced Loop Tester
HD	hydraulic diameter
OD	Outer Diameter
TC	Thermocouple
AC	Alternating Current
DC	Direct Current
P_{DC}	Heater Rod Electric DC Power (W)
I_{DC}	Heater Rod Electric DC Current (A)
R_{elec}	Heater Rod Electric DC/AC Resistance (ohm)
P_{AC}	Time Averaged AC Power (W)
I_{rms}	Root Mean Square AC Current (A)
V_{rms}	Root Mean Square AC Voltage (V)
q''	Surface Heat Flux (W/m^2)
P_{total}	Average Heater Rod Power (W)
S_{clad}	Outer Surface Area of the Heater Rod Cladding (m^2)
L_H	Heated Length of Heater Rod (m)
ρ	Measured Electric Resistivity (ohm-m)
r_1	Cladding Inner Surface Radius (m)
r_2	Cladding Outer Surface Radius (m)

Acknowledgements

Kevin Harding, Walt Profota and Mike Peck for making preparations and running WALT DNB tests, Bob Rees and Chuck McGuire for metallographic sample preparation, Allan Neville and Greg Kustra for welding and machining of heater rods, Jim Skutch for making some of the drawings, Jerry Galiszewski for project management, as well as suggestions or comments from Nuclear Fuel and Nuclear Service managements of Westinghouse Electric Company, your efforts are gratefully acknowledged.

6. References

1. W. A. Byers, et al., July 7 – 11, 2014, “Simulation of PWR Crud”, 22nd International Conference on Nuclear Engineering, Prague, Czech Republic.
2. Wang, G., et al., May 2011, “Best Estimate Probabilistic Safety Assessment Results for the Westinghouse Advanced Loop Tester (WALT)”, 19th International Conference on Nuclear Engineering.
3. J. Deshon, G. Wang, W. A. Byers, M. Y. Young, October 2011, “Simulated Fuel Crud Thermal Conductivity Measurements under PWR Conditions.”. Product ID #1222896.
4. Wang, G., et al., May 2008, “WESTINGHOUSE ADVANCED LOOP TESTER (WALT) UPDATE”, 16th International Conference on Nuclear Engineering.
5. James H. Rust, “Nuclear Power Plant Engineering”, Haralson Publishing Company, Buchanan, Georgia, copyright © 1979 by James H. Rust.
6. Sung, Y. X., Schueren, P. and Meliksetian, A., “VIPRE-01 Modeling and Qualification for Pressurized Water Reactor Non-LOCA Thermal-Hydraulic Safety Analysis”, WCAP-14565-P-A (Proprietary) and WCAP-15306-NP-A (Nonproprietary), October 1999.

7. Stewart, C. W., et al., “VIPRE-01: A Thermal/Hydraulic Code for Reactor Cores”, Volumes 1,2,3 (Revision 3, August 1989), and Volume 4 (April 1987), NP-2511-CCM-A, Electric Power Research Institute, Palo Alto, California.
8. Zhao, Xiong, et al., July 7 – 11, 2014, “Study on DNB-Type Critical Heat Flux with “Chopper”-Cosine Axial Heat Flux Distribution”, ICONE22-30945, 22nd International Conference on Nuclear Engineering, Prague, Czech Republic.
9. Lee, Y. H., Kim, D. H. and Chang, S. H., 2004, An Experimental Investigation on the Critical Heat Flux Enhancement by Mechanical Vibration in Vertical Round Tube, Nucl. Eng. Des., Vol. 229, pp. 47-58.
10. Wieckhorts, Kronenberg, et al., July 7 – 11, 2014, “AREVA’s Test Facility KATHY: Robust Critical Heat Flux Measurements, a Prerequisite for Reliable CHF Prediction”, ICONE22-30761, 22nd International Conference on Nuclear Engineering, Prague, Czech Republic.

Modelling, analysis methods

Modelling cladding response to changing conditions

V. TULKKI, T. IKONEN
VTT Technical Research Centre of Finland ltd
P.O. Box 1000, FI-02044 VTT - Finland

ABSTRACT

The cladding of the nuclear fuel is subjected to varying conditions during fuel reactor life. Conventionally the effect of the changing conditions to cladding creep are modelled using strain hardening law: using creep curves obtained from single stress experiments and assuming the strain is invariant when translating between curves representing different external conditions. While even the original works showed that the strain hardening law applies to zirconium alloys in only a limited set of conditions, it has been applied quite universally in fuel behaviour codes. The situations where strain hardening law fails are the load drop and the reversal of load direction; as a consequence modelling both creep and stress relaxation with the same model has proven to be problematic.
In our paper we show that the load drops and reversals can be modelled by taking cladding viscoelastic behaviour into account. Viscoelastic contribution to the deformation of metals is usually considered small enough to be ignored, and in many applications it merely contributes to the primary part of the creep curve. With nuclear fuel cladding the high temperature and irradiation as well as the need to analyse the variable load all emphasise the need to also inspect the viscoelasticity of the cladding.
A simple model is constructed using tools of linear viscoelasticity. We show it can explain the observed creep behaviour from variable stress tests and improve the description of stress relaxation tests without resorting to dedicated models for the two different situations. The model development and the investigation of individual cases have been originally published in References [1-3].

1 Introduction

Creep is defined as time-dependent strain occurring under stress which is lower than the yield point. Creep processes require elevated temperatures, and affect the long term behaviour of metallic structures. Creep behaviour is a complex material dependent problem and, in the case of a nuclear fuel cladding, the various engineering level correlations in common use are usually fitted to a limited set of data.

The creep response of a cladding tube to changing conditions is conventionally modelled using the strain hardening rule. The rule assumes accumulated strain to be invariant during changes in conditions, and is relatively simple to utilize. However, original experiments by Lucas and Pelloux [4], which are used to justify the use of the strain hardening rule show that it applies only to a restricted set of conditions. Later on, in-pile creep experiments with on-line instrumentation performed at the Halden experimental reactor further challenged the use of the strain hardening rule [5, 6].

Yet the use of the strain hardening is widely spread in fuel behaviour codes. This is probably due to its ease of use, as the fuel behaviour codes require models that are both computationally efficient and easily understandable. In order for a new methodology to replace the strain hardening rule it needs to be similarly easily adoptable. The understanding of the cladding stress state and mechanical response to changing conditions affects both performance and safety analysis of nuclear fuel, but a model too complex to be implemented in engineering level application will not be widely adopted.

2 Cladding response to transient stresses

According to investigations of Lucas and Pelloux [4] the thermal creep deformation at temperatures below 375 ˚C can be described by a strain hardening rule when the stress is increased. In strain hardening, it is assumed that the creep response follows a curve as seen in single stress level experiments and the changing stress state is taken into account by moving to the new stress/strain curve at the point where the accumulated strain is retained, thus keeping the strain invariant during change. This is illustrated in the Figure 1. Lucas and Pelloux do note that the strain hardening rule fails in situations where load is reduced or reversed. Yet their work is used as a justification for the use of the strain hardening rule in most of the models since, e.g. Refs [7, 8].

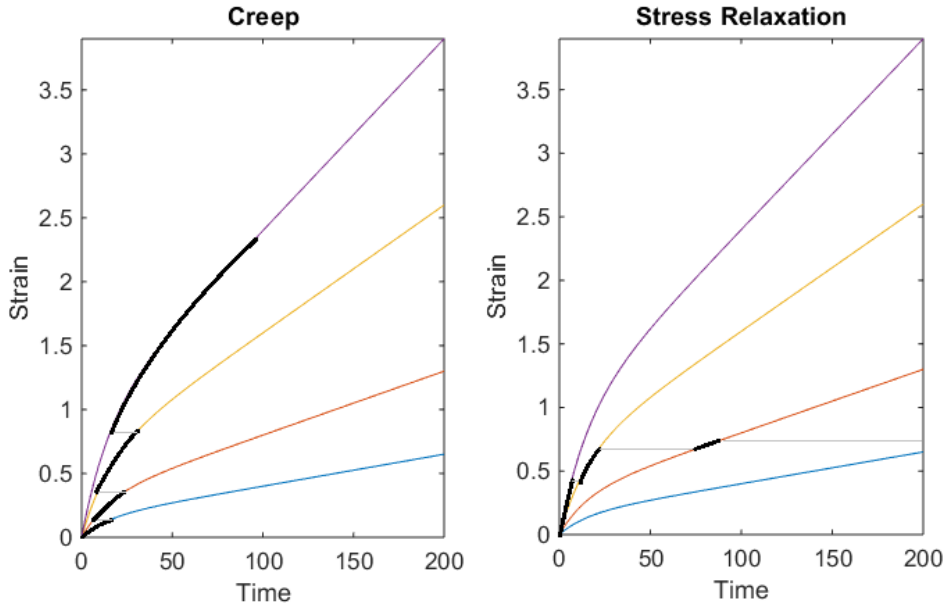

Figure 1: Illustration of creep and stress relaxation behaviour according to strain hardening rule.

Murty and Yoon investigated strain transients following stress changes [9] in laboratory conditions and proposed a creep model which assumes an anelastic strain component in addition to the traditional elastic and plastic contributions. This anelastic component is used to successfully explain the observed accumulation of reverse strain at load drop, while the traditional plastic contribution from creep is assumed to follow the strain hardening rule. Also Matsuo investigated the creep behaviour of Zircaloy-4 under variable conditions [7] and formulated a set of rules for stress reversal situations based on reversible creep hardening surfaces.

Several experiments investigating cladding creep response to stress transients have been performed at the Halden Boiling Water Reactor, the most successful to date being IFA-585 [5] and IFA-699 [6]. Halden reactor features the ability for on-line measurements of in-pile experiments, and these provide a valuable asset for model development and validation. It was observed in both IFA-585 and IFA-699 experiments that the total saturated primary creep is proportional to the change in the applied stress. This observation challenges both the use of the strain hardening rule as well as the both models proposed by Murty and Yoon [9] and by Matsuo [7] as the initial primary creep is similar to the consequent re-initiated primary creep without evidence of a subsequent hardening behaviour.

Modelling stress relaxation using creep correlations has been challenging with models using the strain hardening rule. In a stress relaxation experiment a forced strain is applied to a

segment and the stress is measured as a function of time. Stress relaxation refers to the observation that the stress imposed by a forced strain gradually relaxes. In the stress relaxation experiment, the highest stresses are encountered when the deformation is applied, and then the stresses reduce as the elastic strain turns into a plastic strain. If the strain hardening rule is applied to the constantly diminishing stress case, all the changes advance the apparent time towards the steady state creep region. Effectively, in a stress relaxation experiment nearly all of the deformation would be accounted for by the steady state creep, as the initial high stress provides enough strain for lower stress primary creep to saturate, as illustrated in Figure 1.

Results obtained from stress relaxation experiments have been successfully used to obtain information on the cladding creep properties in the region where creep stress dependency is linear, meaning the region of less than 150 MPa of stress [10]. These stresses are encountered after the initial fast relaxation, and it is implicitly assumed that all the transient behaviour similar to the primary creep has already happened during the loading of the sample and the initial fast relaxation. Recent studies [11, 12] claim that by increasing the stress exponent in the creep correlations originally derived from the creep experiments of Matsuo [7], the loading and the initial relaxation can be also described. However, in these studies it is assumed that all the cladding behaviour can be described with equations originally describing only the steady state behaviour, which is curious considering the transient nature of the stress relaxation experiments.

Formulations of increasing complexity for describing the exact state of cladding do exist. Of interest here is the work of Delobelle et al. [13] where a complex model with kinematic variables is created. They concentrate on describing the anisotropy of the material and intentionally leave the description of the anelastic properties from the model. However, they note that its inclusion would be warranted to describe the cladding response to changing temperature.

3 Development of viscoelastic model

Anelastic deformation is originated from several sources, such as point defects which move or rotate in response to stresses to new positions, dislocations that move to accommodate the external stresses and interfaces of the larger scale structures such as grain boundaries, and the relaxation may originate from grain boundary sliding or movement in normal direction (grain growth). Thermoelastic relaxation also produces anelastic deformation as spatially heterogeneous thermoelastic stresses produce temperature gradients that relax by heat flow. Some of these mechanisms are accounted for in the mechanistic formulations of creep, such as the build-up of internal stresses by pinning of dislocations. Yet in practice this has led to ignoring the anelastic component in engineering models. In this work we separate the creep and the anelastic deformation. Adding the effect of non-recoverable creep to the anelastic component makes the whole model behaviour viscoelastic.

In studies of viscoelastic properties of solids, a common method of describing models is via so-called mechanical analogues. These combine springs representing the elastic component of the material to dashpots representing the viscous components. The springs' displacement ϵ_i is linearly proportional to stress σ ($\epsilon_i = \sigma/\kappa_i$) and the dashpots' displacement rate is linearly proportional to stress ($\dot{\epsilon}_i = \eta_i \sigma$).

An analogue with a spring and a dashpot in parallel is called a Kelvin, Voigt-Kelvin or Voigt model in literature. For clarity this two component construct is called a Kelvin unit in this work. A general Kelvin model is a serial arrangement of *n* Kelvin units and a spring. The individual Kelvin units model various relaxation processes that take place at different time scales. Higher *n* provides more accurate representation of a system with multiple relaxation modes at the cost of increasing model complexity. It should be noted that the individual

Kelvin units are not meant to represent individual physical processes but instead a macroscopic aggregate of various microscopic processes acting on similar time scales.

A model is constructed with a spring for elastic response, *n* number of Kelvin units and a dashpot for creep deformation, all in series. While conventionally the creep deformation includes the primary creep, in this model the primary creep is as a whole given by the Kelvin units. This is in line with observed in-reactor creep behaviour [5, 6]. The system for *n* = 2 is displayed in Fig. 2.

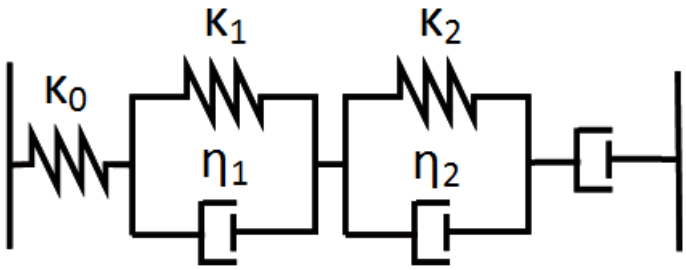

Figure 2: A mechanical analogue for the viscoelastic model.

The number of the components in a system as depicted in the Fig. 2 as well as the non-linearity of most creep deformation correlations makes finding an analytical solution to the system challenging. A common engineering solution is to use the internal variable approach, where the strain of each individual component is calculated.

For stress relaxation an explicit numerical solution is used, calculating the stress arising from the elastic deformation of the lone spring based on the difference between the imposed strain and the strain of Kelvin units and the lone dashpot as per Eq. (1). This stress determines the system stress as a whole. Then the strains of the Kelvin units and the lone dashpot are calculated assuming the stress stays constant for the duration of the time step. The strains of the Kelvin units are calculated based on Eq. (2) and the steady state creep strain from Eq. (3):

$$\sigma(t) = (\epsilon_{tot}(t) - \epsilon_s(t) - \sum_{i=1}^{n} \epsilon_i(t))\kappa_0 \quad (1)$$

$$\epsilon_i(t + \Delta t) = \epsilon_i(t) + (\sigma(t) - \epsilon_i(t)\kappa_i)\left(1 - e^{-\frac{\Delta t}{\tau_i}}\right)\kappa_i^{-1} \quad (2)$$

$$\epsilon_s(t + \Delta t) = \epsilon_s(t) + f(\sigma(t))\Delta t \quad (3)$$

where ϵ_{tot} is the total (imposed) strain, κ_0 the elastic spring constant, ϵ_i, κ_i and τ_i are the strain, spring constant and characteristic time of the *i*th Kelvin unit, ϵ_s is the steady state creep strain, Δt the time step used and $\sigma(t)$ the stress. The function $f(\sigma(t))$ denotes the steady state creep rate, which may be a simple function of stress or a more complex function such as the ones used by Matsuo [7]. This solution scheme requires using very short time steps.

For solving the system during imposed stress (creep experiment), Eqs. (2) and (3) can be directly used as the stress $\sigma(t)$ is known and each Kelvin unit as well as the lone spring and the lone dashpot experiences the same stress. In order to find out the strain of the whole system ϵ_{tot} the individual strain components are combined:

$$\epsilon_{tot}(t) = \frac{\sigma}{\kappa_0} + \epsilon_s(t) + \sum_{i=1}^{n} \epsilon_i(t) \quad (4)$$

For the simulations initial values for the internal strains ϵ_i are needed. In this work an assumed value of $\epsilon_i(0) = 0$ has been used unless otherwise specified.

The contribution of the anelastic strain component is demonstrated with the investigation of the qualitative behaviour of two models, a reference model with elastic and creep components, and the viscoelastic model with elastic, anelastic and creep components. The former model corresponds in behaviour to traditional strain hardening models in situations where enough strain has been accumulated for the primary creep to be fully developed. The anelastic component is modelled with a single Kelvin unit yielding slow recoverable deformation, whereas the elastic and creep components are the same in both models.

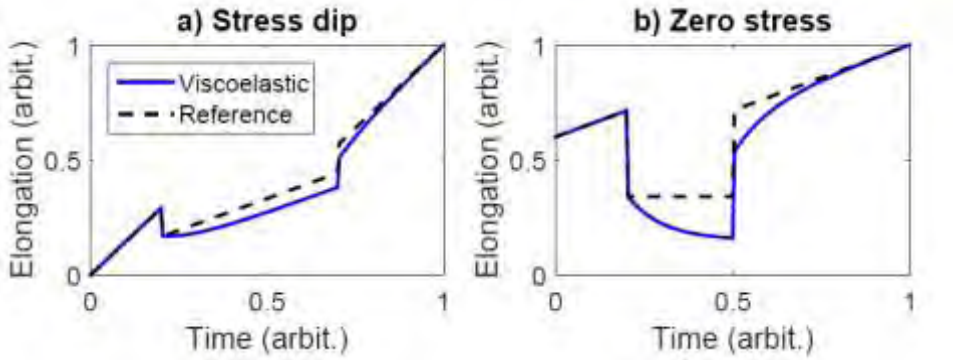

Figure 3: Qualitative behaviour of the viscoelastic model as compared to a reference model with purely elastic and creep components. The solid line denotes the viscoelastic model and the dashed line the reference model results. In the simulation shown in the left plot (a), the stress of the sample has first been held until the steady state creep has been obtained. Then the stress is reduced for a while, and finally returned to its original value. The viscoelastic model shows an apparent stop at stress dip, and faster elongation at return to stress. The right plot (b) features similar situation, but with the stress reduced to zero. The apparent deformation continues in the viscoelastic model, but will return to match the previously achieved rate as is seen in several experiments.

One technique for investigating the metal transient response is called the stress dip experiment. In the experiment, a load is first applied to a sample until a steady strain rate is achieved. Then, the load is reduced for a while and finally increased to its original value. In the experiments the sample deformation appears to stop for a while at the load reduction before it starts to creep at the rate corresponding to the reduced stress. After the subsequent increasing of the stress the strain rate increases for a while before returning to the strain rate corresponding to the applied stress. Models not taking anelastic contribution into account do not explain these observations, but as illustrated in the Fig. 3a, the observed behaviour is well in line with the one provided by the viscoelastic model.

Several authors of experimental papers [14, 15] describe issues encountered when during a creep experiment the stress is reduced to zero while the sample is still at the experimental temperatures. Limbäck and Andersson [14] describe the need to quickly cool down the sample before the creep recovery sets in and Kozar et al. [15] measure the change in strain during the zero stress period. Fig. 3b shows the difference between traditional and viscoelastic interpretation following a prolonged zero stress period. It is common to clean up such periods of zero stress from experimental results, as according to strain hardening rule they should not have any effect on the sample strain. However, this results in fast dips in measured strain, which is subsequently recovered, as seen for instance in Fig. 3 of Kozar et al. [15].

4 Model testing

The cases investigated with the developed model were the in-pile experiments IFA-585 (BWR segment) [1, 5] and IFA-699 (Zircaloy-4 segment) [2, 6], and laboratory experiments by Delobelle et al. (stress relaxation) [3, 13].

IFA-585 experiment featured a pre-irradiated BWR cladding tube that was pressurized to several stress states, both compressive and tensile, while under irradiation in the Halden research reactor. The cladding deformation was measured with on-line diameter gauges which were calibrated to unpressurized reference segments on the end plugs. The BWR rod sample was irradiated prior to the Halden experiment in a commercial reactor to a fast neutron dose of $6*10^{21}$ n/cm^2. Also, during the first experimental cycle there were issues with rod pressurization which are not included in the analysis. For the simulations it was assumed that the cladding had been conditioned to the effective stress of 52 MPa at t = 0, which was the planned stress on the cladding in the initial cycle. The temperature of the cladding sample varied between 575–595 K.

IFA-699 investigated the creep of Zircaloy-4, E110, M5 and M-MDA cladding tube segments containing fuel pellets for realistic temperature gradient. The experiment was still on-going during the writing of recently declassified Halden Work Report HWR-882 [6] but at the time it had lasted for nearly 3000 full power hours and had subjected the cladding samples to hoop stress levels of 0, -75, -50 and +30 MPa of hoop stress, with negative values indicating compression and positive values tension. This was achieved by alternating the segment internal pressure (to 18.2, 8.5, 11.6 and 22.7 MPa) while the external pressure was at steady 16.2 MPa simulating PWR conditions. The model was compared with the measurements of Zircaloy-4 segment. The mid-wall cladding temperature was estimated to be 625 K.

Delobelle et al. [13] performed various experiments in laboratory conditions, including both creep and stress relaxation, for Zircaloy-4 samples with two different experimental heat treatments. As they performed both experiments using similar samples it was possible to use the creep experiment to determine the required material-dependent coefficients for the viscoelastic model and use them to simulate the stress relaxation experiment. While Ref. [13] provides a wealth of experimental data, most of it focuses on investigation of material anisotropy. Uniaxial data from the publication was used. It concerned the experiments in the axial direction for recrystallized Zircaloy-4 at 623 K (350 °C). The data for the creep experiment was taken from Fig. 16 and for the stress relaxation from Fig. 15 of Ref. [13]. In the creep experiments the stress was stepwise increased and the elongation measured. The stress steps used were 125, 135, 150 and 170 MPa. In the stress relaxation experiments the sample was deformed to a desired strain at the rate of $6.6 *10^4$ s^{-1}. Then the strain was held constant for 48 hours and the stress measured. The strain steps were 0.4 %, 0.8 %, 1.2 %, and 4 % for the sample.

Model coefficients used are listed in Table 1. Model with n=1 was considered sufficient for creep experiments, but model with n=2 was also investigated in stress relaxation case. The model coefficients for the in-pile experiments were fitted to experiments. For Delobelle experiment the fitting was done with the creep experiment and the same model coefficients were used for the stress relaxation experiment. Steady state creep rate has a strong effect on the results as all the possible errors are compounded. Steady state creep rate is also affected by material composition and the final heat treatment and as all the cases investigated featured different samples and conditions, different steady state creep models were used in the analysis. Validation of the in-pile creep models using independent data sets was not possible due to the lack of published online measurements of in-pile transient creep with similar materials in similar conditions. In general, the lack of detailed data of the in-pile creep transients in the public literature may prove to be the greatest challenge in generalizing the presented model for various conditions.

Table 1: Coefficients for the anelastic model used in this work.

Cladding	κ_0 (MPa)	κ_1 (MPa)	κ_2 (MPa)	τ_1 (h)	τ_2 (h)
IFA-585 n = 1	N/A	$5.2*10^5$	–	100	–
IFA-699 n = 1	N/A	$2.0*10^5$	–	40	–
Delobelle n = 0	$3.9*10^4$	–	–	–	–
Delobelle n = 1	$3.9*10^4$	$2.52*10^4$	–	26	–
Delobelle n = 2	$3.9*10^4$	$4.80*10^4$	$4.49*10^4$	6.5	65

For the analysis of the IFA-585 and IFA-699, the FRAPCON-3.4's steady state correlation was used [16]. There were uncertainties in the IFA-585 test results [5], especially related to the effect of the different rates of oxide layer growth between the sample and the end plugs and experimentally measured secondary creep rate [5]. For the steady state creep it has been noted that the IFA-585 experiment features very high secondary creep rates [5] compared to other creep experiments. This was also seen in the initial analysis. For IFA-585 analysis the FRAPCON-3.4 correlation used for secondary creep rate was multiplied by a factor of 2 in order to better match the experimental results.

The analysis of the experiments by Delobelle et al. used a simple engineering model for the modelling of the steady state creep:

$$\dot{\epsilon}_s = F \sinh G\sigma \tag{5}$$

where coefficients $F = 4.5168*10^6$, and $G = 4.2416*10^7$ are fitted to the steady state creep data obtained from Fig. 16 of [13]. The use of hyperbolic sine function is a common engineering approximation used to cover both low stress region below 100 MPa where $\dot{\epsilon}_s \sim \sigma$ and high stress region where $\dot{\epsilon}_s \sim \sigma^5$. Delobelle et al.'s experiments were performed in the axial direction, so axial stress was used.

5 Results

The comparison between the simulated and measured strain, along with the applied effective stress for IFA-585 experiment, is shown in Fig. 4. The mid-wall effective stress with positive values signifying tension and negative values compression is also shown in Fig. 4. The match between the experiment and the simulation is good, especially at the beginning of the experiment. However, errors compound during the simulation. These can be mostly attributed to the uncertainties in the secondary creep rate. It can thus be argued that as the error seen in Fig. 4 is mostly due to the uncertainty in the secondary creep rate, the creep response to stress reversal can be modelled using the viscoelastic model.

For IFA-699 Zircaloy-4 experiment the measured values are shown as dots and the base simulation as the solid line in Fig. 5. The measured values in Fig. 5 consistently trend toward the positive (or tensile, outward) direction. An oxide growth contribution was included to the simulations according to Eq. (6) [17]

$$w = Ke^{-Q_0/RT}t^{1.02474}, \tag{6}$$

where w is the oxide layer thickness in micrometres assuming a constant temperature, K = 23663.76 $\mu m \cdot h^{-1}$, Qo/R = 8645.4 K is the activation energy for the oxide formation, T = 625 K is the interaction layer temperature and t is time in hours. As the oxidation replaces metal with less dense oxide, the net effect is the increase of the apparent diameter by a fraction of one third of the oxide layer thickness. The creep with oxide layer contribution is shown with

dashed line in Fig. 5. This case would represent a situation where the Zircaloy-4 segment is heated by the fuel inside and thus oxidises faster than the measurement calibration piece which was assumed to be at coolant temperature (approximately 50 K lower than the test sample). The used oxide layer equation is a simple formula fitted to publicly available post-irradiation data for PWR fuels with Zircaloy-4 cladding, and as such caution should be used when utilizing it for samples in the Halden flask conditions.

The simulation of the Delobelle et al. creep and stress relaxation experiments are shown in Fig. 6 for the recrystallized samples. The simulations are performed with models with 0, 1 and 2 Kelvin units. The model with 0 Kelvin units is shown only for the stress relaxation plot, where it represents the traditional strain hardening rule behaviour. The ability of the model to describe stress relaxation behaviour is improved with the increasing number of Kelvin units. The model overpredicts the stress at the beginning of the strain step, which would indicate either plastic deformation due to the fast strain rate or relatively quick relaxation mechanisms that are not modelled.

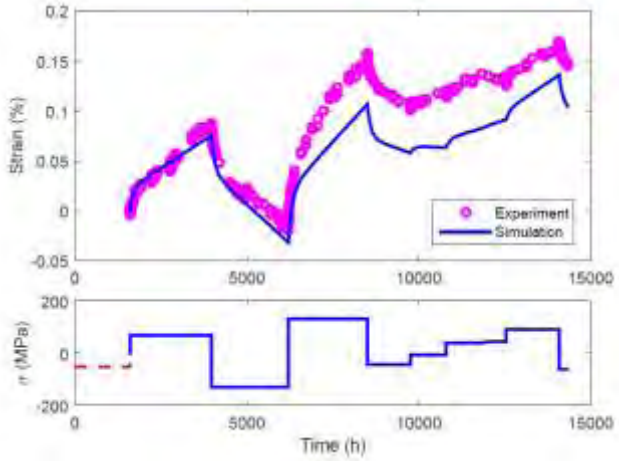

Figure 4: Comparison between IFA-585 measurements (circles) and the simulation (line).

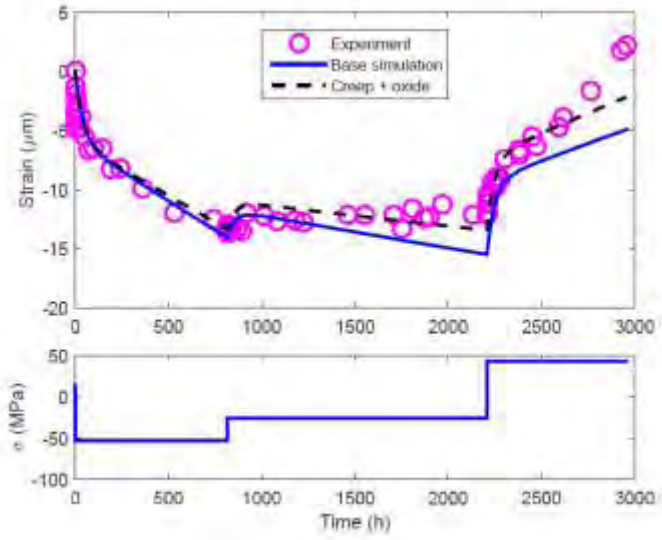

Figure 5: Comparion between IFA-699 Zircaloy-4 measuments (circles) and the simulated values (lines). Blue line corresponds to base simulation, the dashed black line includes an addition of an oxide layer contribution.

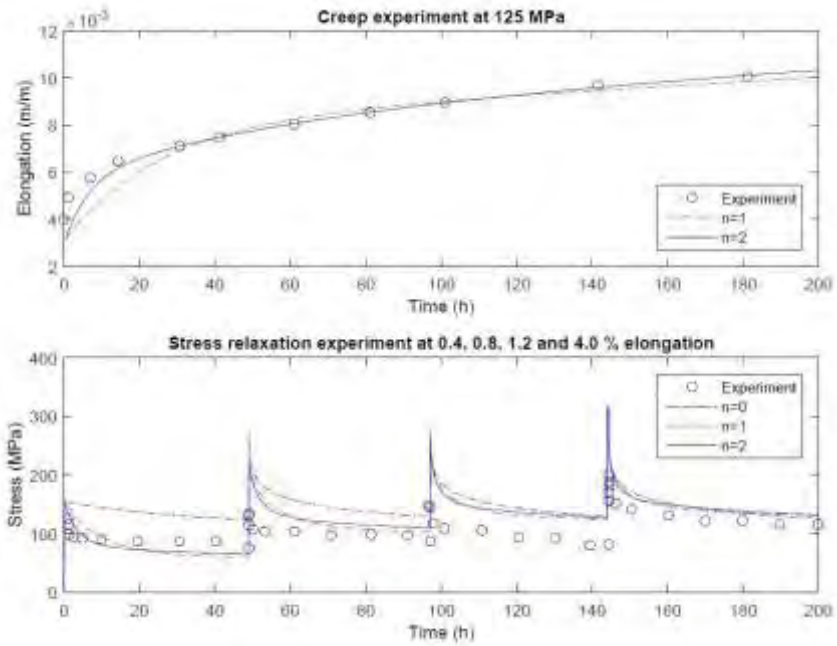

Figure 6: Creep (top plot) and stress relaxation (bottom plot) experiment by Delobelle et al. on recrystallized Zircaloy-4 sample. Plots display measurements (circles) and modelling (lines) using various number of Kelvin units.

6 Conclusions

The anelastic contribution to cladding mechanical behaviour has been investigated and accounted for in some models in the 1970s and 1980s [9, 10]. However, later on it has been neglected [4, 7, 11-16], either implicitly or explicitly, and several experimentally observed cladding transient responses have remained unexplained. Yet the viscoelastic model described in this work is able to provide a qualitative interpretation of the observations on the cladding response to transient stresses such as load drops, creep reversal and stress relaxation. In scenarios where a commonly used strain hardening rule is known to work, such as stress increases, the viscoelastic model behaves similarly to strain hardening models. The observed time evolution of the primary creep can be explained by various concurrent processes operating at different time scales and approximated by a series of relaxation processes. The model can be used to simulate various creep experiments performed both in laboratory conditions and in-pile. The model is self-consistent in the sense that the creep and the stress relaxation are simulated with the single model.

The major difference of the model presented in this work to the conventional approach is the addition of the anelastic component. The anelastic component is modelled with the Kelvin units, an approach which is known to be able to model the behaviour of various substances for small deformations. As this limitation is also inherent in the 1D approach for the cladding modelling in engineering level codes, it should not decrease the usability domain of the fuel behaviour codes. The successful replication of the IFA-585 and IFA-699 results by the model (Figs. 4 and 5) demonstrate the validity of the chosen approach.

Figure 6 shows that by including Kelvin units also the stress relaxation modelling is improved. Increasing the number of Kelvin units enhances the correspondence between the measurements and the simulation results.

In general, the lack of detailed data of the in-pile creep transients in the public literature may prove to be the greatest challenge in generalizing the presented model for various conditions and cladding materials. As it is the current work should be considered as a demonstration of the viability of the viscoelastic approach instead of a creation of a full creep model.

7 References

[1] V. Tulkki and T. Ikonen, “Modeling of Zircaloy cladding primary creep during load drop and reversal”, Journal of Nuclear Materials 445, 98–103 (2014).

[2] V. Tulkki and T. Ikonen, “Viscoelastic modeling of Zircaloy cladding in-pile transient creep ”, Journal of Nuclear Materials 457, 324–329 (2015).

[3] V. Tulkki and T. Ikonen, “Modelling anelastic contribution to nuclear fuel cladding creep and stress relaxation”, Journal of Nuclear Materials 465, 34–41 (2015).

[4] G. Lucas and R. Pelloux, “Some observations on time-hardening and strain-hardening rules for creep in Zircaloy-2,” Nuclear Technology, vol. 53, pp. 46–57, 1981.

[5] J. Foster and M. McGrath, “In-reactor creep behavior of zircaloy-2,” Proceedings of the 2007 LWR Fuel Performance Meeting, 2007.

[6] S. Hanawa, “In-reactor creep behaviour of LWR fuel claddings: Initial results from IFA-699,” HWR-882, 2008.

[7] Y. Matsuo, “Creep behaviour of Zircaloy cladding under variable conditions,” ASTM STP, vol. 1023, pp. 678–691, 1989.

[8] G. Rossiter, “Development of the ENIGMA fuel performance code for whole core analysis and dry storage assessments”, Nuclear Engineering and Technology, vol. 43, no. 6, 2011.

[9] K. Murty and K. Yoon, “Prediction of creep transients in Zircaloy fuel cladding using anelastic strain model,” Transactions of the 5th International Conference on Structural Mechanics in Reactor Technology (SMiRT-5), vol. C3/6, 1979.

[10] A. Causey, F. Butcher, and S. Donohue, “Measurement of irradiation creep of zirconium alloys using stress relaxation,” Journal of Nuclear Materials, vol. 159, pp. 101–113, 1988.

[11] Y. Long, C. Beard, S. Henk, and G. Zhou, “ZIRLO high performance fuel cladding material high stress creep model,” Proceedings of 2010 LWR Fuel Performance Meeting, p. Paper 054, 2010.

[12] G. Zhou, L. Hallstadius, G. Wikmark, Y. Long, and J. Foster, “Evaluation and modeling of in-reactor creep and stress-relaxation tests of ZIRLO fuel cladding under wide stress conditions,” Proceedings of 2011 Water Reactor Fuel Performance Meeting, pp. Paper T2–038, 2011.

[13] P. Delobelle, P. Robinet, P. Geyer, and P. Bouffioux, “A model to describe the anisotropic viscoplastic behaviour of Zircaloy-4 tubes,” *Journal of Nuclear Materials*, vol. 238, pp. 135–162, 1996.

[14] M. Limbäck and T. Andersson, “A model for analysis of the effect of final annealing on the in- and out-of-reactor creep behavior of zircaloy cladding,” ASTM STP, vol. 1295, pp. 448–468, 1996.

[15] R. Kozar, A. Jaworski, T. Webb, and R. Smith, “In situ monitored in-pile creep testing of zirconium alloys,” Journal of Nuclear Materials, vol. 444, pp. 14–22, 2014.

[16] K. Geelhood, W. Luscher, and C. Beyer, “FRAPCON-3.4: A computer code for the calculation of steady-state thermal-mechanical behavior of oxide fuel rods for high burnup,” NUREG/CR-7022, Vol.1, 2011.

[17] J. Kättö, “Corrosion and its modeling in nuclear reactor fuel cladding,” 2013. M.Sc thesis, Aalto University.

THERMODYNAMIC MODELLING OF MOLYBDENUM BEHAVIOUR IN CHLORIDE MOLTEN SALT

S. NICHENKO, M. STREIT
Isotope and Elemental Analysis, Department Nuclear Energy and Safety,
Paul Scherrer Institut,
5232 Villigen PSI, Switzerland

ABSTRACT

In the presented work a thorough review of the available literature data has been done attempting to acquire experimental and theoretical information on molybdenum (Mo) behaviour in selected molten salt (LiCl-KCl). Thermodynamic modelling was used to study, first, speciation in the selected melts and, second, formation Gibbs energies of different species in the selected melts. Information on formation Gibbs energy in the melts was used to assess standard potential for different species in the selected melts. Further, information on the standard potential of different species was used to build E-pO^{2-} stability diagrams for Mo in LiCl-KCl.

This information should help to downsize the experimental work on inert matrix fuel performance and serve as a complementary source of information for pyro-electrochemical processing of nuclear wastes.

1 Introduction

There are several reasons why behavior of molybdenum (Mo) in molten salt media is of a great interest. On one side molybdenum (Mo), on one side, serves as a possible metal matrix for the CERamic-METallic (CERMET) fuels [1, 2], that is a ceramic fuel compound embedded in an inert metallic matrix. On the other side molybdenum is one of the most abundant fission products and, thus, present in significant amounts in molten salt media in molten salt reactors (MSR) and in spent nuclear fuels [3, 4]. At the same time molten salts are promising media for pyro-electrochemical reprocessing process of nuclear waste [5, 6].

From this perspective the understanding of Mo behaviour in alkali metal chlorides is of a great importance. First of all, to be able to design and optimize a safe pyro-electrochemical reprocessing process employing molten salts and involving Mo matrices, a detailed knowledge is required on properties, speciation and behavior of Mo species in these media. But the acquisition of experimental information on irradiated fuel behavior in molten salts is a difficult task due to high dose rates and high temperatures. In this case thermodynamic modelling, based on the Gibbs energy minimization approach, is a powerful technique for studying the behavior of Mo species, as well as actinides and fission products, in molten salts. This approach allows modelling of Mo behaviour and speciation in ideal and non-ideal media.

In addition, thermodynamic modelling can provide a deep and broad understanding of the systems at different conditions and serves as a complementary tool to experimental data. But to be able to perform thermodynamic modelling and model the behaviour and speciation in the fuel/salt melt, information on the thermodynamic functions for the pure compound as well as on the binary interactions between all the species in the system are needed. There is no issue with the data on the pure compounds. This information is available and is presented in numerous databases. At the same time the information on binary interactions between the species in the system are very limited and are of a great importance. This information is necessary for the correct modelling of speciation and phase equilibria in the system of interest.

The results of the present work should help to downsize the experimental studies on the inert matrix fuel performance and should serve as a complementary source of information for optimisation and safety assessment for pyrochemical processes for treatment of nuclear waste.

2 Review of Molybdenum Species

This review is done with a goal to define possible stable species in LiCl-KCl melt as a starting point for E-pO^{2-} diagram development.

$MoCl_2$ is known to decompose at around 780 K [7, 8] into solid $Mo_{(s)}$ and gaseous $MoCl_{4(g)}$ [9]. Thus $MoCl_2$ is the most stable among the molybdenum chlorides with the highest melting/decomposition point.

$MoCl_3$ has a lower decomposition point, which is about 680 K [7, 8]. At this temperature $MoCl_3$ disproportionates into solid $MoCl_{2(s)}$ and gaseous $MoCl_{4(g)}$ [9].

At the temperature about 590 K solid $MoCl_{4(s)}$ undergoes the solid-liquid phase transition. At the same time the solid $MoCl_{4(s)}$ sublimes on heating [9] and the gaseous $MoCl_{4(g)}$ decomposes to solid $MoCl_{3(s)}$ and gaseous $MoCl_{4(g)}$. From a thermodynamic modelling the equilibrium temperature for the liquid-gas phase transition is estimated to be about 680 K.

According to the data of Haynes [8] $MoCl_{5(s)}$ undergoes solid-liquid phase transition at the temperature of 467 K. This data is with agreement with the equilibrium temperature obtained from the thermodynamic calculations. Moreover, the thermodynamic calculations showed that the boiling point of $MoCl_{5(s)}$ is about 536 K. This result is in good agreement with the boiling point presented by Haynes [8] which is 541 K. Thus the boiling point of $MoCl_{5(l)}$ is about 540 K. In the gaseous phase $MoCl_{5(g)}$ dissociates with formation of $MoCl_4$ [9].

Review of the available literature data on the $MoCl_6$ behaviour [10] has shown that $MoCl_6$ is very unstable and decomposes even at room temperature (298 K). Thus, among the simple molybdenum chlorides $MoCl_6$ appears to be the less stable. Apparently it decomposes to more simple chlorides, $MoCl_5$ and $MoCl_4$, and to solid Mo.

In contrast to simple molybdenum chlorides, MoO_2 is stable in a much wider temperature range. According to Haynes [8] solid $MoO_{2(s)}$ is stable up to the temperature of about 2050 K, at which solid $MoO_{2(s)}$ decomposes.

As in the case with molybdenum dioxide, MoO_2, MoO_3 is much stable then simple molybdenum chlorides but, according to Haynes [8], solid $MoO_{3(s)}$ has significantly lower melting temperature than in the case of MoO_2, which is 1075 K. The boiling point for liquid $MoO_{2(l)}$ is 1428 K. The phase transition temperatures are in good agreement with the results of thermodynamic modelling performed with the available thermochemical data.

According to the data presented in [11] $MoOCl_{3(s)}$ melts temperature of 583 K. This temperature is coincides with the calculated equilibrium temperature for the solid-liquid equilibrium transition.

$MoOCl_{4(s)}$ undergoes solid-liquid phase transition at the temperature of 378 K according to the data presented in the Landolt-Börnstein Database [11]. This data is with agreement with the equilibrium temperature obtained from the thermodynamic modelling.

At the same time thermodynamic calculations have shown that there is almost no temperature range of liquid $MoOCl_{3(l)}$ and $MoOCl_{4(s)}$ existence, which means that $MoOCl_{3(s)}$ and $MoOCl_{4(s)}$ are volatile and sublimates almost without formation of liquid phase. This conclusion agrees with the literature review [7].

According to the Haynes [8] MoO_2Cl_2 has a melting point of 449 K. The results of thermodynamic modelling shows almost no region of liquid phase existence. Thus, MoO_2Cl_2 is volatile and undergoes solid-gas phase transition at 449 K.

In Table 1 the review of the main characteristic of molybdenum chlorides and oxychlorides is presented. This review allows to conclude which species are stable at the temperatures of interest for the study of molybdenum behavior in molten salts, in particular in LiCl-KCl.

Table 1: Molybdenum oxy-/chlorides

Species	T_b, K	T_m, K	$S^o, J/K/mol$	$\Delta_f H^o, kJ/mol$	Ref.
$MoCl_2$	780 K (d)		95.0	-290.0	[11, 12]
$MoCl_3$	680 K (d)		158.155	-424.0358	[11, 12]
$MoCl_4$	590 K	680 K	223.844	-476.976	[11, 12]
$MoCl_5$	470 K	540 K	238.488	-527.184	[11, 12]
$MoCl_6$	298 K (d)		255.224	-523.0	[11, 12]
MoO_2	2050 K (d)		46.510	-589.30	[11, 12]
MoO_3	1075 K	1428 K	77.660	-744.60	[11, 12]
$MoOCl_2$	—		125.0	-530.0	[11, 12]
$MoOCl_3$	583 K (s)		163.8	-616.0	[11, 12]
$MoOCl_4$	378 K	432 K	202.0	-655.0	[11, 12]
MoO_2Cl_2	449 K	523 K	135.6	-724.0	[11, 12]

T_b is boiling point, T_m M.p. is melting point
(d) - decomposes, (s) - sublimates

3 Molybdenum chemistry in LiCl-KCl

The information on thermochemical functions presented in [11, 12, 13] was used for thermodynamic modelling and calculations of Gibbs energy of formation for redox reactions of interest.

3.1 $MoCl_3$/Mo in LiCl-KCl melt

In case of $MoCl_3$ species behavior in LiCl-KCl melt first the redox half-reaction for the Mo^{3+}/Mo couple has to be specified. The redox system in this case can be represented as follows:

$$MoCl_3 + 3e^- \leftrightarrow Mo + 3Cl^- \tag{1}$$

In this case the Nernst equation for this system can be written as follows:

$$\begin{aligned} E_{Mo^{3+}/Mo} &= E^o_{Mo^{3+}/Mo} + \frac{2.3RT}{(-3)F}\log[Mo^{3+}]^{-1} \\ &= E^o_{Mo^{3+}/Mo} + \frac{2.3RT}{3F}\log\gamma_{Mo^{3+}} + \frac{2.3RT}{3F}\log X_{Mo^{3+}} \\ &= E^{o\prime}_{Mo^{3+}/Mo} + \frac{2.3RT}{3F}\log X_{Mo^{3+}} \end{aligned} \tag{2}$$

where $X_{Mo^{3+}}$ is a molar fraction of $MoCl_3$ species in LiCl-KCl.

In this case the standard potential, $E^o_{Mo^{3+}/Mo}$, has been replaced by the apparent standard potential, $E^{o\prime}_{Mo^{3+}/Mo}$, under assumption that at low molar fractions the $MoCl_3$ activity coefficient, $\gamma_{Mo^{3+}}$, is constant:

$$E^{o\prime}_{Mo^{3+}/Mo} = E^o_{Mo^{3+}/Mo} + \frac{2.3RT}{3F}\log\gamma_{Mo^{3+}} \tag{3}$$

The electrochemical behavior of $MoCl_3$ and $MoCl_2$ species in LiCl-KCl system has been described by Smirnov *et al.* [14]. Some results for the $MoCl_3$ behavior in alkali chloride melts are presented in the report of ENRESA [15]. In particular, Smirnov *et al.* presented in his work expression for the Mo^{3+}/Mo apparent standard potential, $E^{o\prime}_{Mo^{3+}/Mo}$:

$$E^{o\prime}_{Mo^{3+}/Mo} = -1.48 + 4.9\cdot 10^{-4}T \tag{4}$$

And the results presented in the ENRESA report [15] can be expressed by the following equation:

$$E^{o\prime}_{Mo^{3+}/Mo} = -1.1436 + 2.4 \cdot 10^{-4} T \tag{5}$$

The standard potential for the Mo^{3+}/Mo couple can be defined using the available in the literature thermodynamic functions [11, 12, 13]. The standard potential for the Mo^{3+}/Mo couple can be then expressed as follows:

$$E^{o}_{Mo^{3+}/Mo} = \frac{\Delta_f G^{o}_{MoCl_3}}{3F} \tag{6}$$

The formation Gibbs energy for the $MoCl_3$ species, $\Delta_f G^{o}_{MoCl_3}$, was determined using the literature data on thermochemical functions [11, 12, 13]. The standard potential for the Mo^{3+}/Mo couple can then be expressed as follows:

$$E^{o}_{Mo^{3+}/Mo} = -1.414 + 6.144 \cdot 10^{-4} T \tag{7}$$

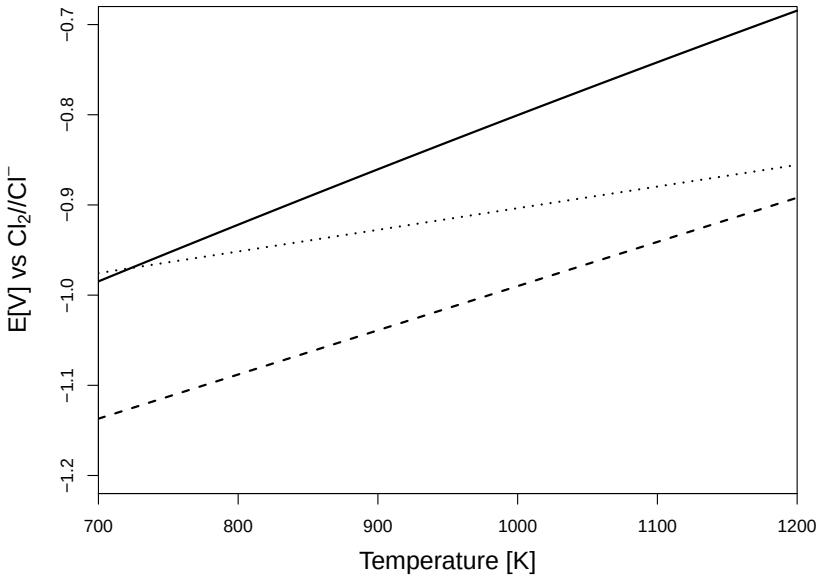

Figure 1: Mo^{3+}/Mo standard potential.

In Figure 1 the apparent standard potentials, $E^{o\prime}_{Mo^{3+}/Mo}$, according to Smirnov *et al.* [14] and report of ENRESA [15] are presented together with a calculated standard potential, $E^{o}_{Mo^{3+}/Mo}$ calculated with equation 7. As it can bee seen a quite significant discrepancy between the results is observed. The difference between the calculated and literature results can be explained by the activity of the $MoCl_3$ species in LiCl-KCl system related to the apparent standard potential and standard potential by the expression 3. Using this equation it is possible to assess the activity coefficient of $MoCl_3$ species in LiCl-KCl:

$$\log \gamma_{Mo^{3+}} = \frac{3F(E^{o\prime}_{Mo^{3+}/Mo} - E^{o}_{Mo^{3+}/Mo})}{2.3RT} \tag{8}$$

The calculated activity coefficients for the Mo^{3+} species in LiCl-KCl melt based on the data of Smirnov *et al.* [14] and report of ENRESA [15] are shown in Figure 2.

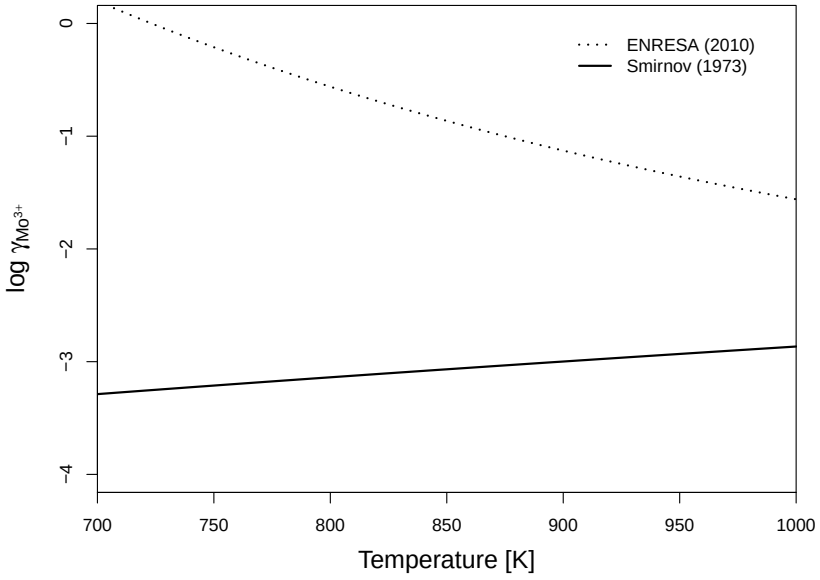

Figure 2: Mo^{3+} activity coefficient in LiCl-KCl melt.

In the Figure 2 a significant discrepancy between the data of Smirnov and ENRESA is observed. Unfortunately, the data presented in ENRESA report is very limited and does not allow making any conclusions about the possible nature of such a pronounced difference between results.

Thus, on the basis of results presented by Smirnov *et al.* [14], the recommended value for $MoCl_3$ activity coefficient in LiCl-KCl in a temperature range 700-1000 K can be expressed by the equation 9 :

$$\log \gamma_{Mo^{3+}} = -9.818398 + 0.003233T \tag{9}$$

3.2 $MoCl_2$/Mo in LiCl-KCl melt

The redox system for the case of Mo^{2+}/Mo couple is as follows:

$$MoCl_2 + 2e^- \leftrightarrow Mo + 2Cl^- \tag{10}$$

The Nernst equation for the Mo^{2+}/Mo couple is expressed as follows:

$$\begin{aligned} E_{Mo^{2+}/Mo} &= E^o_{Mo^{2+}/Mo} + \frac{2.3RT}{(-2)F}\log[Mo^{2+}]^{-1} \\ &= E^o_{Mo^{2+}/Mo} + \frac{2.3RT}{2F}\log\gamma_{Mo^{2+}} + \frac{2.3RT}{2F}\log X_{Mo^{2+}} \\ &= E^{o\prime}_{Mo^{2+}/Mo} + \frac{2.3RT}{2F}\log X_{Mo^{2+}} \end{aligned} \tag{11}$$

where $X_{Mo^{2+}}$ is a molar fraction of $MoCl_2$ species in LiCl-KCl.

And, as in the case of Mo^{3+}/Mo couple, the standard potential, $E^o_{Mo^{2+}/Mo}$, is replaced by the apparent standard potential, $E^{o\prime}_{Mo^{2+}/Mo}$, under assumption that at low molar fractions the $MoCl_2$ activity coefficient, $\gamma_{Mo^{2+}}$, is constant:

$$E^{o\prime}_{Mo^{2+}/Mo} = E^o_{Mo^{2+}/Mo} + \frac{2.3RT}{2F}\log\gamma_{Mo^{2+}} \tag{12}$$

Smirnov *et al.* [14] studied an electrochemical behaviour of $MoCl_2$ species in LiCl-KCl system. Unfortunately these are the only results for the $MoCl_2$ species behaviour in LiCl-KCl system. The apparent standard potential, $E^{o\prime}_{Mo^{3+}/Mo}$, according to Smirnov *et al.* [14] can be expressed by the following equation:

$$E^{o\prime}_{Mo^{2+}/Mo} = -1.32 + 5.1 \cdot 10^{-4} T \tag{13}$$

To be able to define the activity coefficient of $MoCl_2$ species in LiCl-KCl system we need first to define the standard potential for the $MoCl_2$. The standard potential can be defined using the formation Gibbs energy of $MoCl_2$ using the following expression:

$$E^{o}_{Mo^{2+}/Mo} = \frac{\Delta_f G^{o}_{MoCl_2}}{2F} \tag{14}$$

The calculated standard potential, $E^{o}_{Mo^{2+}/Mo}$, can be described by the following equation:

$$E^{o}_{Mo^{2+}/Mo} = -1.469 + 7.487 \cdot 10^{-4} T \tag{15}$$

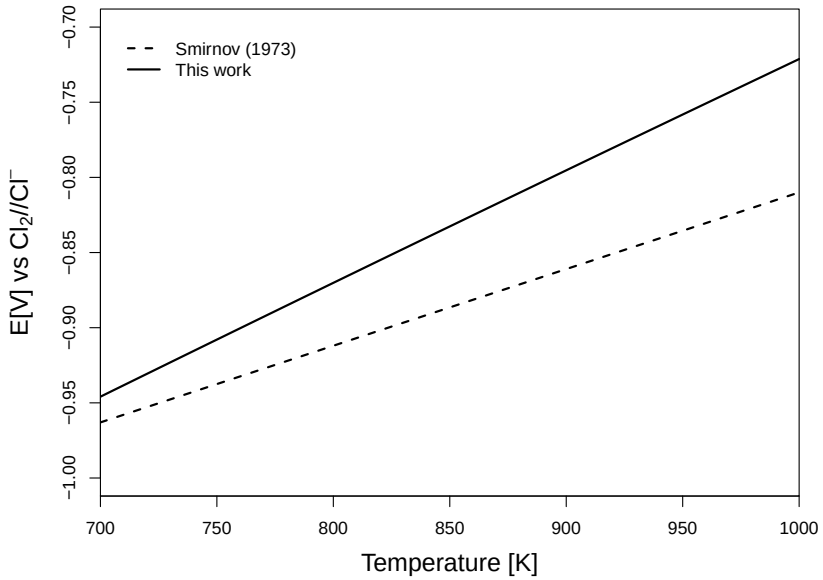

Figure 3: Mo^{2+}/Mo standard potential.

In the Figure 3 the apparent standard potential, $E^{o\prime}_{Mo^{2+}/Mo}$, according to Smirnov *et al.* [14] together with the standard potential, $E^{o}_{Mo^{2+}/Mo}$, calculated with equation 14 are presented. The presented information in Figure 3 allows assessment of Mo^{2+} species activity coefficient in LiCl-KCl using the following equation:

$$\log \gamma_{Mo^{2+}} = \frac{2F(E^{o\prime}_{Mo^{2+}/Mo} - E^{o}_{Mo^{2+}/Mo})}{2.3RT} \tag{16}$$

The calculated activity coefficient for the Mo^{2+} species in LiCl-KCl melt based on the data of Smirnov *et al.* [14] is shown in Figure 4 and can be described by the equation 17 in a temperature range 700-1000 K.

$$\log \gamma_{Mo^{2+}} = 7.738 - 1.677 \cdot 10^{-2} T + 6.985 \cdot 10^{-6} T^2 \tag{17}$$

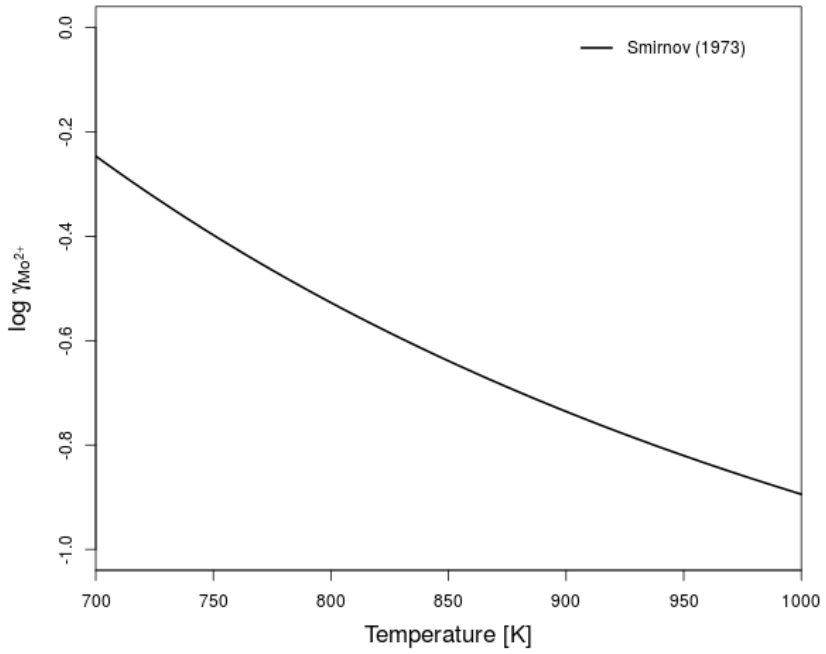

Figure 4: Mo^{2+} activity coefficient in LiCl-KCl melt.

3.3 MoO_3/MoO_2 in LiCl-KCl melt

The MoO_2/MoO_3 couple the standard potential can also be calculated using the thermodynamic data available in the literature [11, 12, 13]. The redox system in the case of MoO_2/MoO_3 couple can be described as follows:

$$MoO_3 + 2e^- \leftrightarrow MoO_2 + O^{2-} \tag{18}$$

The Nernst equation for this system can be written as follows:

$$E_{MoO_3/MoO_2} = E^o_{MoO_3/MoO_2} + \frac{2.3RT}{-2F}\log\frac{[MoO_2][O^{2-}]}{[MoO_3]} = E^o_{MoO_3/MoO_2} + \frac{2.3RT}{2F}pO^{2-} \tag{19}$$

The standard potential, $E^o_{MoO_3/MoO_2}$, was calculated using the information from the section 2. Thus, the estimated standard potential $E^o_{MoO_3/MoO_2} = -0.547V$.

3.4 $MoCl_3$/MoO_2 in LiCl-KCl melt

In case of $MoCl_3$/MoO_2 couple the standard potential can be calculated using the published thermodynamic data [11, 12, 13] and using the obtained in section 3.1 information of $MoCl_3$ activity in LiCl-KCl melt. The redox system in the case of $MoCl_3$/MoO_2 couple is:

$$MoO_2 + 3Cl^- + e^- \leftrightarrow MoCl_3 + 2O^{2-} \tag{20}$$

In this case the Nernst equation for this system can be written as follows:

$$E_{MoO_2/Mo^{3+}} = E^o_{MoO_2/Mo^{3+}} + \frac{2.3RT}{(-1)F}\log\frac{[MoO_2][Cl^-]^3}{[Mo^{3+}][O^{2-}]^2} =$$
$$E^o_{MoO_2/Mo^{3+}} + \frac{2.3RT}{F}\left(\log\gamma_{Mo^{3+}} + \log X_{Mo^{3+}} + 2\log X_{O^{2-}}\right)$$
$$= E^{o\prime}_{MoO_2/Mo^{3+}} + \frac{2.3RT}{F}\log X_{Mo^{3+}} + \frac{2\cdot 2.3RT}{F}pO^{2-} \quad (21)$$

In this case the standard potential, $E^o_{MoO_2/Mo^{3+}}$, has been replaced by the apparent standard potential, $E^{o\prime}_{MoO_2/Mo^{3+}}$, as in the case of Mo^{3+}/Mo couple described in section 3.1. Assuming that at low molar fractions the $MoCl_3$ activity coefficient, $\gamma_{Mo^{3+}}$, is constant:

$$E^{o\prime}_{MoO_2/Mo^{3+}} = E^o_{MoO_2/Mo^{3+}} + \frac{2.3RT}{F}\log\gamma_{Mo^{3+}} \quad (22)$$

where $X_{Mo^{3+}}$ is a molar fraction of $MoCl_3$ species in LiCl-KCl.

3.5 $MoCl_3$/MoO_3 in LiCl-KCl melt

As in the case of $MoCl_3$/MoO_2 couple, the $MoCl_3$/MoO_3 couple the standard potential can be calculated using the thermodynamic data available in the literature [11, 12, 13] and using the obtained in section 3.1 information of $MoCl_3$ activity in LiCl-KCl melt. The redox system in this case can be expressed as follows:

$$MoO_3 + 3Cl^- + 3e^- \rightarrow MoCl_3 + 3O^{2-} \quad (23)$$

And the redox half-reaction is:

$$Mo^{3+} + 3e^- \rightarrow MoO_{3(s)} \quad (24)$$

In this case the Nernst equation for this system can be written as follows:

$$E_{MoO_3/Mo^{3+}} = E^o_{MoO_3/Mo^{3+}} + \frac{2.3RT}{(-3)F}\log\frac{[MoO_3][Cl^-]^3}{[Mo^{3+}][O^{2-}]^3} =$$
$$E^o_{MoO_3/Mo^{3+}} + \frac{2.3RT}{3F}\left(\log\gamma_{Mo^{3+}} + \log X_{Mo^{3+}} + 3\log X_{O^{2-}}\right)$$
$$= E^{o\prime}_{MoO_3/Mo^{3+}} + \frac{2.3RT}{3F}\log X_{Mo^{3+}} + \frac{3\cdot 2.3RT}{3F}pO^{2-} \quad (25)$$

In this case the standard potential, $E^o_{MoO_2/Mo^{3+}}$, has been replaced by the apparent standard potential, $E^{o\prime}_{MoO_2/Mo^{3+}}$, as in the case of Mo^{3+}/Mo couple described in section 3.1. Assuming that at low molar fractions the $MoCl_3$ activity coefficient, $\gamma_{Mo^{3+}}$, is constant:

$$E^{o\prime}_{MoO_2/Mo^{3+}} = E^o_{MoO_2/Mo^{3+}} + \frac{2.3RT}{F}\log\gamma_{Mo^{3+}} \quad (26)$$

where $X_{Mo^{3+}}$ is a molar fraction of $MoCl_3$ species in LiCl-KCl.

3.6 Diagram of molybdenum

The stability domain of the Mo-O-Cl compounds in the molten LiCl-KCl eutectic can be defined by the E-pO^{2-} diagram. The construction of the diagram for molybdenum species in LiCl-KCl system is based on the data of pure compounds, presented in section 2, together with the information on activity of the molybdenum species in LiCl-KCl system obtained in section 3. Also in section 3 the review of stable species in LiCl-KCl melt was performed.

The preliminary $E - pO^{2-}$ diagramm for the Mo-O-Cl system in the LiCl-KCl eutectic at 850 K is presented in Figure 5.

As it was shown in sections 2 and 3 among the stable in LiCl-KCl system species are: $MoCl_3$, MoO_2 and MoO_3. Higher chlorides and oxychlorides are unstable and thus are not present in the melt. In the Figure 5 the stability domains of the above mentioned species are presented.

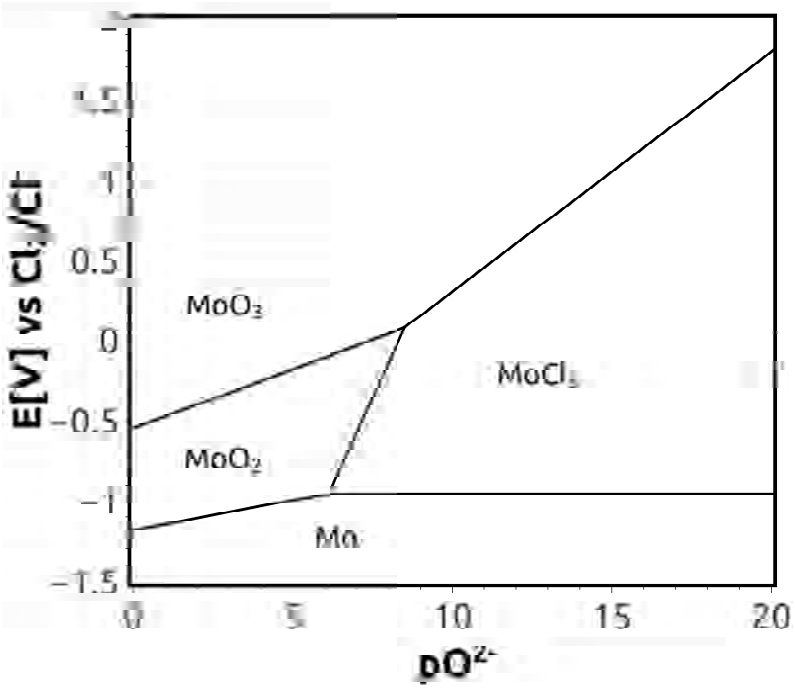

Figure 5: The $E - pO^{2-}$ diagramm for the Mo-O-Cl system in LiCl-KCl eutectic at 750 K.

Currently this is a preliminary diagram and the regions of stability are being verified.

4 Conclusion

In the presented work a thorough review of the available literature data has been done attempting to acquire experimental and theoretical information on molybdenum (Mo) behaviour in selected chloride melt (LiCl-KCl). First, the review of different molybdenum species was done attempting to define stable and unstable species and provide necessary information for further thermodynamic modelling.

Further, the information on phase equilibria for binary systems was used to asses binary interaction parameters in terms of excess Gibbs energy for binary mixture. Excess Gibbs energy behaviour has been described using the Legendre form polynomials. Obtained information on excess Gibbs energy allowed correct description of phase equilibria for binary systems. The idea behind was to use an established theoretical approach where knowledge on binary interaction parameters allows to study complex systems (ternary and higher orders) assuming that interaction parameters of higher orders are negligible.

The information on excess Gibbs energy for binary systems together with the information on thermophysical properties of pure compounds was used to study complex systems. Such an approach allowed to study, first, speciation in the selected melts and, second, formation Gibbs energies of different species in the selected melts. Information on formation Gibbs energy in the melts was used to assess standard potential for different species in the selected melts. Further, information on the standard potential of different species was used to build E-pO^{2-} stability diagrams for Mo in LiCl-KCl.

Therefore, performed theoretical study provides a broad and thorough picture of Mo speciation and electrochemical behaviour in LiCl-KCl and LiF-AlF_3 melts. This information may be used to support experimental study of electrochemical reprocessing of CERMET fuels in the presented melts. Of course further experimental study for approval and optimization of the presented results would be desirable.

Acknowledgement

The present work was carried out with the financial support of the European Commission within the 7th framework program under the collaborative project "Safety of ACtinide Separation proceSSes - SACSESS", project agreement No. 323282.

References

References

[1] C Degueldre and J.M Paratte. Concepts for an inert matrix fuel, an overview. *Journal of Nuclear Materials*, 274(1-2):1–6, August 1999.

[2] Klaas Bakker, Frodo C. Klaassen, Ronald P. C. Schram, Alfred Hogenbirk, Robin Klein Meulekamp, Arjan Bos, Hubert Rakhorst, and Charles A. Mol. The Use of Molybdenum-Based Ceramic-Metal (CerMet) Fuel for the Actinide Management in LWRs. *Nuclear Technology*, 146(3):325–331, June 2004.

[3] H. Kleykamp. The chemical state of the fission products in oxide fuels. *Journal of Nuclear Materials*, 131(2-3):221–246, April 1985.

[4] Philippe Martin, Michel Ripert, Gaëlle Carlot, Philippe Parent, and Carine Laffon. A study of molybdenum behaviour in UO2 by X-ray absorption spectroscopy. *Journal of Nuclear Materials*, 326(2-3):132–143, March 2004.

[5] R. W. Benedict, C. W. Solbrig, Brian R. Westphal, T. A. Johnson, S. X. Li, K. C. Marsden, and K. M. Goff. Pyroprocessing progress at Idaho National Laboratory. In *Advanced Nuclear Fuel Cycles and Systems, Global 2007*, pages INL/CON–07–12983, 2007.

[6] K. Nagarajan, B. Prabhakara Reddy, Suddhasattwa Ghosh, G. Ravisankar, K.S. Mohandas, U. Kamachi Mudali, K.V.G. Kutty, K.V. Kasi Viswanathan, C. Anand Babu, P. Kalyanasundaram, P.R. Vasudeva Rao, and Baldev Raj. Development of Pyrochemical Reprocessing for Spent Metal Fuels. *Energy Procedia*, 7:431–436, 2011.

[7] D. L . Perry. *Handbook of Inorganic Compounds, Second Edition*. CRC Press, 2011.

[8] W. Haynes. *CRC Handbook of Chemistry and Physics*. CRC Press; 95 edition (June 4, 2014), 2014.

[9] C. K. Gupta. *Extractive Metallurgy of Molybdenum*. CRC Press, 1992.

[10] L. Brewer, R. H. Lamoreaux, R. Ferro, R. Marazza, and K. Girgis. *Molybdenum: Physico-Chemical Properties of Its Compounds and Alloys*. IAEA, 1980.

[11] Collaboration: Scientific Group Thermodata Europe (SGTE). Thermodynamic Properties of Compounds, MgCl2H2O to RhCl2. In *Landolt-Börnstein - Group IV Physical Chemistry*.

[12] M. W. Chase. *NIST-JANAF Thermochemical Tables, Fourth Edition*. 1998.

[13] H. L. Kiwia and E. F. Westrum. Low-temperature heat capacities of molybdenum tri- and tetrachlorides. *The Journal of Chemical Thermodynamics*, 7(6):523–530, June 1975.

[14] V.A. A Smirnov, M.V. and Khokhlov. *Electrode Potentials in Molten Chlorides*. Nauka, Moskov, 1973.

[15] J. Astudillo and J. Farias. Desarrollo y resultados del 5 Plan de I+D de ENRESA 2004-2009. Technical report, 2010.

[16] S. Senderoff and A. Brenner. The Electrolytic Preparation of Molybdenum from Fused Salts. *Journal of The Electrochemical Society*, 101(1):28, January 1954.

[17] S. Senderoff and A. Brenner. The Electrolytic Preparation of Molybdenum from Fused Salts II. The Preparation of Reduced Molybdenum Halides. *Journal of The Electrochemical Society*, 101(1):28, January 1954.

[18] S. Senderoff and A. Brenner. The Electrolytic Preparation of Molybdenum from Fused Salts III. Studies of Electrode Potentials. *Journal of The Electrochemical Society*, 101(1):31, January 1954.

EFFECT OF POWER VARIATIONS ACROSS A FUEL BUNDLE AND WITHIN A FUEL ELEMENT ON FUEL CENTERLINE TEMPERATURE IN PHWR BUNDLES IN UNCREPT AND CREPT PRESSURE TUBES

E. N. ONDER, D. ROUBTSOV, Y.F. RAO
Canadian Nuclear Laboratories
Chalk River, Ontario Canada K0J 1J0
Nihan.Onder@cnl.ca, Dan.Roubtsov@cnl.ca, Yanfei.Rao@cnl.ca

B. WILHELM
University of Guelph
Guelph, Ontario Canada N1G 2W1
wilhelmb@mail.uoguelph.ca

ABSTRACT

The neutron flux and fission power profiles through a fuel bundle and across a fuel element are important aspects of nuclear fuel analysis in multi-scale / multi-physics modelling of Pressurized Heavy Water Reactors (PHWRs) with advanced fuel bundles. Fuel channels in many existing power PHWRs are horizontal. With ageing, pressure tubes creep and fuel bundles in these pressure tubes are eccentrically located, which results in asymmetric flow distribution between the top and bottom of the fuel bundles. The diametral change of the pressure tube due to creep is not constant along the fuel channel; it reaches a maximum in the vicinity of the maximum neutron flux location. The cross-sectionally asymmetric positioning of fuel bundles in a crept pressure tube contributes to an asymmetric power distribution within a ring of fuel elements. In this work, rigorously validated physics and thermalhydraulics codes are applied to quantify the effect of eccentricity of a fuel bundle in a pressure tube, on power variations across a fuel bundle and within a fuel element and ultimately on the fuel temperature distribution and fuel centerline temperature, which is one of the indicators of fuel performance.

INTRODUCTION

Knowledge of fuel temperature and fuel temperature distribution is essential for accurately predicting fuel performance characteristics. Besides thermal conductivity, the power distribution within an element and power distribution across the fuel bundle can affect the fuel temperature distribution within an element. In Canadian PHWRs, pressure tubes develop a creep deformation with aging [1], and the creep is distributed non-uniformly along the fuel channel. As a result, in aged horizontal pressure tubes, fuel bundles are eccentrically located, which results in asymmetric flow distribution between the top and bottom of fuel bundles in the channel. The cross-sectionally asymmetric positioning of fuel bundles in a crept pressure tube contributes to an asymmetric power distribution within a ring of fuel elements.

For this study, the reactor physics lattice cell code WIMS-AECL [2] was used to predict the power distribution within an element and across the bundle; and with the calculated powers, the thermalhydraulics subchannel code ASSERT-PV [3],[4] was applied to calculate fuel and sheath temperatures and cross-section averaged fluid temperatures.

The objective of this study is to investigate the impact of non-uniformity of the power distributions across a fuel bundle and within a fuel element on fuel centerline temperatures in uncrept and crept pressure tubes.

Background

The existing fleet of Canadian PHWRs are pressure tube type reactors, where pressure tubes are located horizontally in calandria tubes (see Figure 1 (a)). Figure **1** (b) shows the cross sectional geometry of a 43-element bundle with appendages: end-plates, bearing pads, CHF enhancement buttons and spacers. The 43-element bundle consists of two types of fuel elements: the diameter of centre element and inner ring elements is slightly larger than the diameter of middle and outer ring elements. Figure 2 (a) shows the reference (uncrept) pressure tube whereas Figure 2 (b) shows an axially non-uniform crept pressure tube where fuel bundles are eccentrically located. This eccentricity results in an asymmetric flow distribution between the top and bottom of fuel bundles in a crept pressure tube (see the flow by-pass region in Figure 2 (b)), which in turn can result in power differences within the same ring between the top and bottom of a bundle, depending on the creep ratio, which is defined as

$$CR = (D_{creep} - D_{ref}) / D_{ref} \quad (1)$$

where D_{creep} is the local inner diameter (ID) in a crept pressure tube and D_{ref} is the ID of the reference (uncrept) pressure tube.

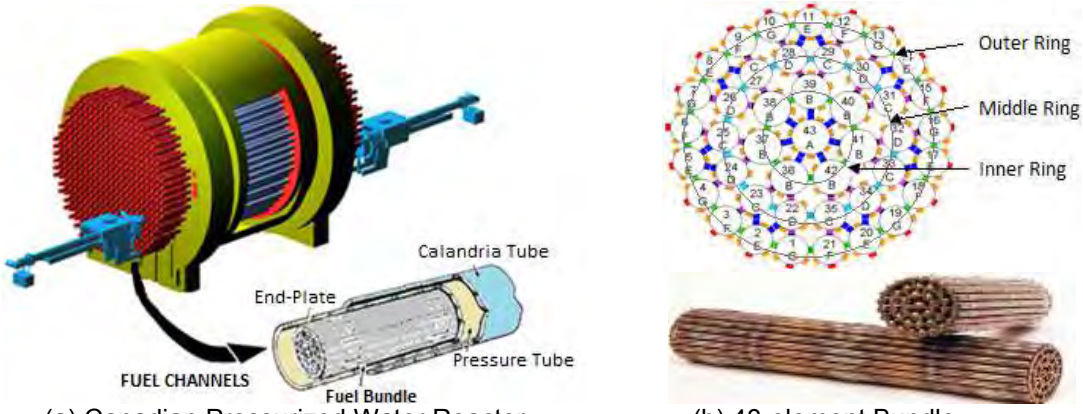

(a) Canadian Pressurized Water Reactor (b) 43-element Bundle

Figure 1 – Canadian Pressurized Water Reactor with a Fuel Channel and a Fuel Bundle

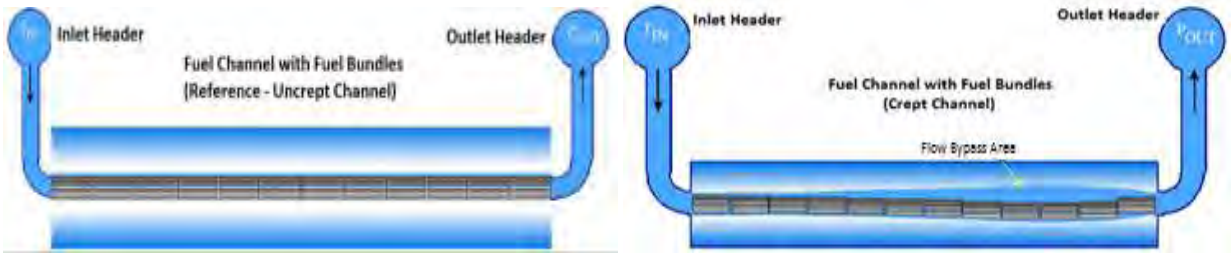

(a) Reference Pressure Tube (b) Crept Pressure Tube

Figure 2 – Pressure Tubes (a) Reference (Uncrept) and (b) Crept

From foil activation experiments in nuclear reactors [5] and from reactor physics simulations [6], it is well-known that the thermal neutron flux inside the bundle in a pressure tube decreases

toward the bundle center. As a result, there is a neutron flux gradient in the fuel elements and a similar fission power distribution in the fuel pellets (see Figure 3). This effect is known as "flux tilt" [7] and can be modelled as follows:

$$pow(r,\theta) = q''' \times (1 + \varepsilon \times (r/R_f) \times \cos\theta) \quad (2)$$

where q''' is the power density, R_f is the fuel pellet radius, r and θ are local cylindrical coordinates associated with the fuel element, and $\varepsilon > 0$ is the tilt parameter. The element power (per unit length) is given by

$$q' = q''' \times \pi R_f^2. \quad (3)$$

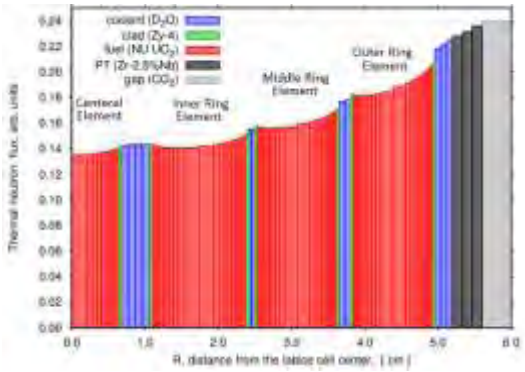

Figure 3 – Thermal neutron flux in a reactor lattice cell for 43-element bundle (WIMS-AECL 3.1)

WIMS-AECL Physics code

WIMS-AECL [2], a two-dimensional lattice physics code, uses multi-group integral transport theory and collision probability methods to solve for the neutron flux distribution within a given lattice cell design. The WIMS-AECL neutron transport code has become a standard tool for analyzing the lattice physics characteristics of Canadian PHWR-type fuel bundles [6].

ASSERT-PV Thermalhydraulics Subchannel Code

AECL has developed the ASSERT-PV code for subchannel thermalhydraulics analysis of Canadian fuel bundles [3], [4]. It provides detailed flow and phase distributions in subchannels of a fuel bundle. The current release version of ASSERT-PV is ASSERT-PV 3.2 [3], [4] which was used to predict fuel temperatures in the present analysis. The fuel temperature was calculated at different specified radial locations. The material properties of fuel and sheath are user defined values, and for this analysis, the material properties were obtained from IAEA-TECDOC-1496 [8].

simulations

The WIMS-AECL [2] lattice physics code was applied to calculate element powers in a 43-element fuel bundle located concentrically and eccentrically in uncrept and 5.1%[1] crept pressure tubes of a Canadian PHWR. The concentric arrangement of bundles in a pressure tube provides a uniform distribution of powers among fuel elements in a given ring, while the

[1] This is the creep ratio that has been tested at the Stern Laboratories, Canada for different Canadian fuel bundle simulators for safety and licensing applications.

eccentric arrangement leads to element power variations within the same ring. Despite an uncrept channel providing a high symmetry, there is still a small eccentricity due to gravity.

The power tilt due to non-uniform distribution of thermal neutron flux in an element (relatively high powers in segments facing outer subchannels and relatively low powers in segments facing inner subchannels) was also taken into account in this study using the results from [9] (see Figure **4**). It is expected that slight changes in flow conditions will not affect the distribution of power within an element. This effect was included to simulate more realistic conditions within the fuel element.

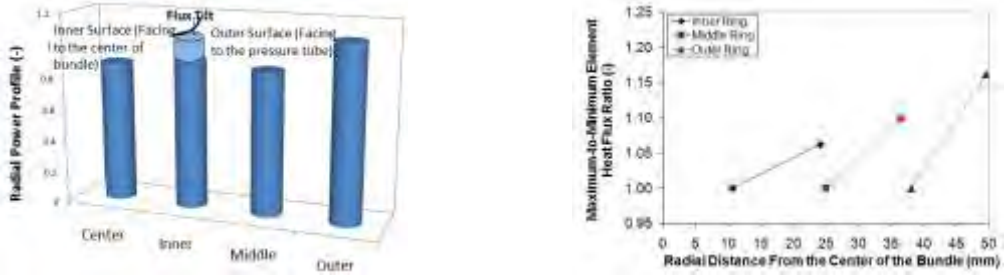

(a) (b)

Figure 4 - (a) Direction of Flux Tilt, (b) Degree of Flux Tilt in Elements of Different Rings

Once uniform and non-uniform element power distributions (EPD) within rings were obtained by WIMS-AECL from concentric and eccentric cases, respectively, ASSERT-PV [3] was employed with a cosine axial power profile (see Figure **8**) to calculate fuel and sheath temperatures in the uncrept and 5.1% non-uniform crept channels. The predicted fuel and sheath temperatures obtained with element power variations were then compared with the predictions without considering these effects (uniform element powers in a given ring). Simulations were performed at the normal operating condition of interest to Canadian PHWR: outlet pressure of 9.9 MPa, inlet temperature of 265°C, mass flow rate of 23 $kg \cdot s^{-1}$, and fuel channel power of 5.5 MW. The radial power profiles (or ring powers) obtained using WIMS-AECL [2] are compared with the previous profiles [9] and similar results were obtained (see Figure **5**).

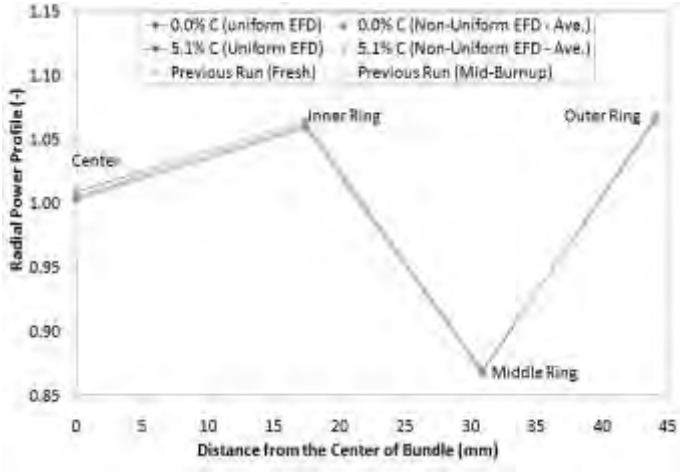

Figure 5 - Comparison of Radial Power Profiles Between Previous and Recent WIMS-AECL Calculations

Variation of element power within a ring is insignificant (see empty symbols in Figure 6) for bundles with uniform EPD regardless the channel creep. However, once the bundles are

placed in fuel channels asymmetrically (i.e., eccentricity is imposed), element powers vary in a given ring; highest powers are obtained at the bottom of the bundle (elements 33 and 34 in the outer ring; elements 15 and 16 in the middle ring; elements 5 and 6 in the inner ring) and lowest powers are obtained at the top of the bundle (element 23 in the outer ring; elements 9 and 22 in the middle ring; element 2 in the inner ring). Element power variation within a ring is largest in the 5.1% crept channel as compared to that in the uncrept channel and in the outer ring as compared to the inner ring.

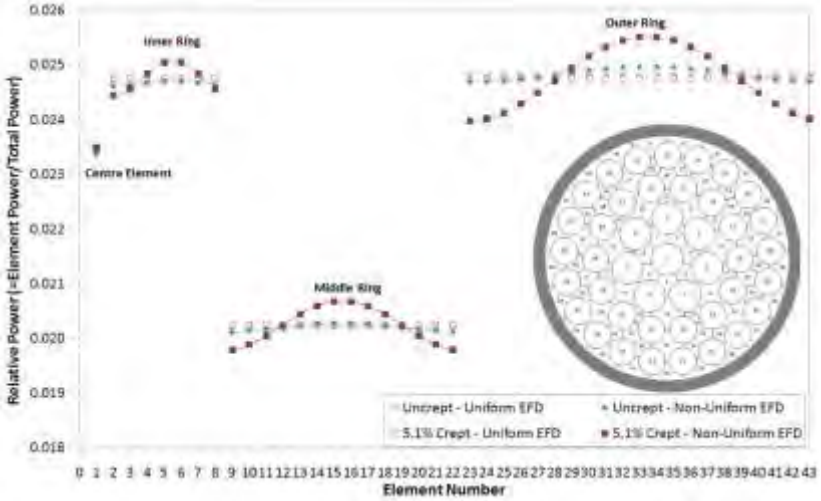

Figure 6 – Relative Power Distribution in Different Rings for Uncrept and 5.1% Crept Channels with Bundle Geometry Showing Locations of Elements in a Fuel Channel

RESULTS

For the conditions given above (i.e., the channel power and the element power distribution), the linear element power (LEP) at any ring elements varies between 28 and 35 kW/m at the high power region (i.e., close to the middle of the fuel channel for a cosine axial power distribution), with the highest LEP (34-35 kW/m) in the outer ring elements, and between 4 and 5 kW/m at the low power region (i.e., inlet), with the highest LEP (5 kW/m) in the outer ring elements.

Figure 7 shows the critical element (i.e., elements with the highest centreline temperatures) locations for a 43 element bundle with uniform and non-uniform element power distributions (EPD) in the uncrept and 5.1% crept channels: in all cases, critical elements are in the outer ring at the bottom of the bundle at the peak axial power location; in the case of uniform and non-uniform EPD in the uncrept channel and uniform EPD in the 5.1% crept channel, critical elements are 25.7° away from the bottom, and in the case of non-uniform EPD in the 5.1% crept channel, critical elements are at 6 o'clock (or 8.6° relative to the bottom) position. For most of the cases, maximum sheath temperatures happened to occur at the critical elements.

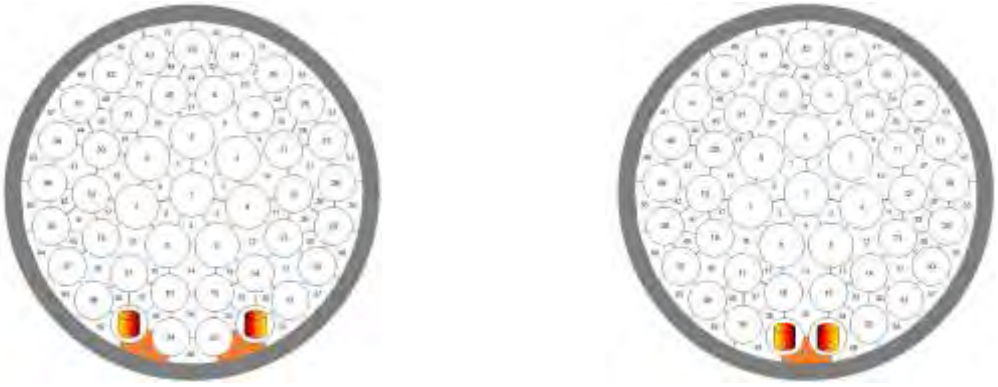

(a) (b)

Figure 7 – Critical (Hot) Element and Maximum Sheath Temperature Locations in a 43-Element Bundle with : (a) Uniform and Non-Uniform EPD in the Uncrept Channel and Uniform EPD in the 5.1% Crept Channel, (b) Non-Uniform EPD in the 5.1% Crept Channel

Figure 8 shows the variation of cross section average coolant and sheath temperatures along the fuel channel for 0.0% (i.e., uncrept) and 5.1% crept channels (CC) together with the axial power distribution and pressure tube creep. In Figure 8, the cross section average coolant temperatures for the uncrept and crept channels are provided. It should also be noted that there is no difference in coolant temperature variations along the fuel channel between uniform and non-uniform EPD cases, and also the difference in sheath temperatures between uniform and non-uniform EPD in the uncrept channel is insignificant. Coolant temperatures increase gradually in both fuel channels but, due to higher enthalpy imbalance for the 5.1% crept channel, the downstream of the critical location (beyond the peak in the axial power distribution and downstream the maximum pressure tube diametral creep), the cross section average coolant temperature at the outlet of the channel is lower as compared to that in the uncrept channel. Coolant temperatures in the subchannels of a bundle in the uncrept pressure tube are more homogenously distributed: e.g., for the uniform EPD, coolant temperatures in the subchannels at the outlet vary between 305.0°C and 312.7°C in the uncrept channel, and between 295.3°C and 310.3°C in the 5.1% crept channel.

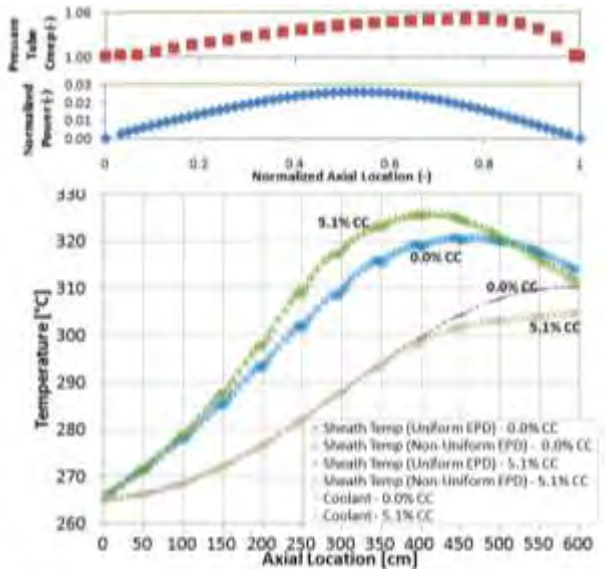

Figure 8 – Variation of Critical Element Sheath and Cross Section Average Coolant Temperatures along the Fuel Channel in Uncrept and 5.1% Crept Channels (CC)

Maximum sheath temperatures occur at critical elements facing outer subchannels (as identified/coloured in orange in Figure **7** with subchannels 59 - 61) and reach a peak value downstream of the peak power location. Maximum sheath temperature is reached in the 5.1% crept channel earlier as compared to that in the uncrept channel (i.e., at an axial location of 408 cm in the 5.1% channel compared to 448.5 cm in the uncrept channel). This is due to a higher enthalpy imbalance in the 5.1% crept channel. The maximum sheath temperature in the 5.1% crept channel (~325°C) is slightly higher than that in the uncrept channel (320°C); however, at the outlet, the sheath temperature for the uncrept channel (314°C) is slightly higher as compared to that in the 5.1% crept channel (311°C), similar to the coolant temperatures.

Figure 9 shows the axial distribution of fuel centerline temperatures in the critical elements for elements with linear powers of 4-5 kW/m at the low power region (i.e., at the inlet) and 28-35 kW/m at the high power region. Fuel centerline temperatures reach a maximum at the peak power location (~323 cm). A fuel centerline temperature of 1248°C for the uniform EPD in the uncrept channel, of 1255°C for the non-uniform EPD in the uncrept channel, of 1260°C for the uniform EPD in the 5.1% crept channel and of 1302°C for the non-uniform EPD in the 5.1% crept channel is reached in the critical elements that are located in the outer ring with linear element powers of 35 kW/m at the high power region.

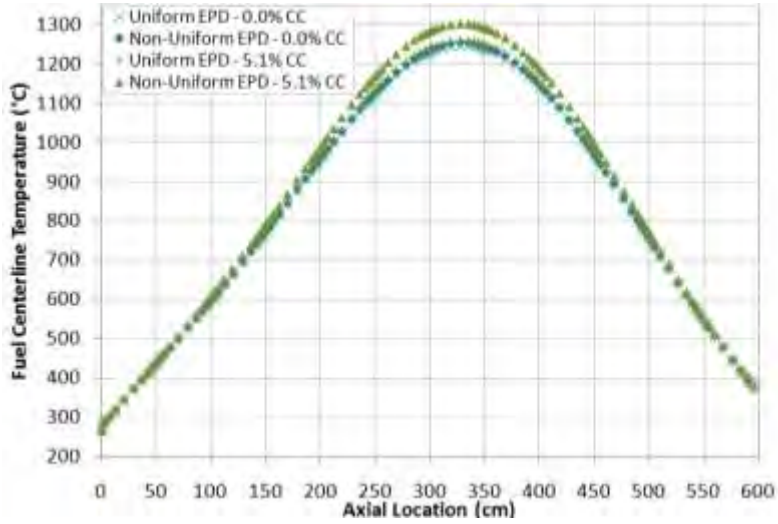

Figure 9 – Variation of Fuel Centerline Temperatures along the Fuel Channel in Uncrept and 5.1% Crept Channels (CC)

There is no significant difference among uniform EPD (taken as the reference case) and non-uniform EPD in the uncrept channel and uniform EPD in the 5.1% crept channel: an increase in temperature from the reference case by 7.3°C (or 0.59%) for the non-uniform EPD in the uncrept channel, and by 11.4°C (or 0.91%) for the uniform EPD in the 5.1% crept channel. However, the temperature difference for the non-uniform EPD in the 5.1% crept channel is 54.1°C (or 4.33%) as compared to the reference case and 42.7°C (or 3.39%) as compared to uniform EPD in the 5.1% crept channel

It has been expected that the temperature distribution may show angular dependency, as 1) the flux tilt is imposed to fuel elements, and 2) non-uniform subchannel coolant temperatures occur due to enthalpy imbalance and flow (re)distributions between subchannels due to turbulence. Therefore, Figure 10 (a) is plotted for the variation of fuel temperatures in the fuel pellet at the mid-channel location (axial location where the highest fuel centerline temperatures are observed) as a function of distance from the fuel center in the segment facing outer subchannels and in the segments facing inner subchannels. It should be noted that temperatures in Figure 10 are averaged for a segment facing outer subchannels (e.g., see Figure 10 (b) for element 35 in sub-segments facing subchannels 36, 37 and 38) and for a segment facing inner subchannels (e.g., see Figure 10 (b) for element 35, in sub-segments facing subchannels 61 and 62). In segments facing outer subchannels, slightly higher temperatures are observed as compared to the segments facing inner subchannels. Table 1 summarizes temperature distributions in different segments (facing different subchannels) in the critical elements.

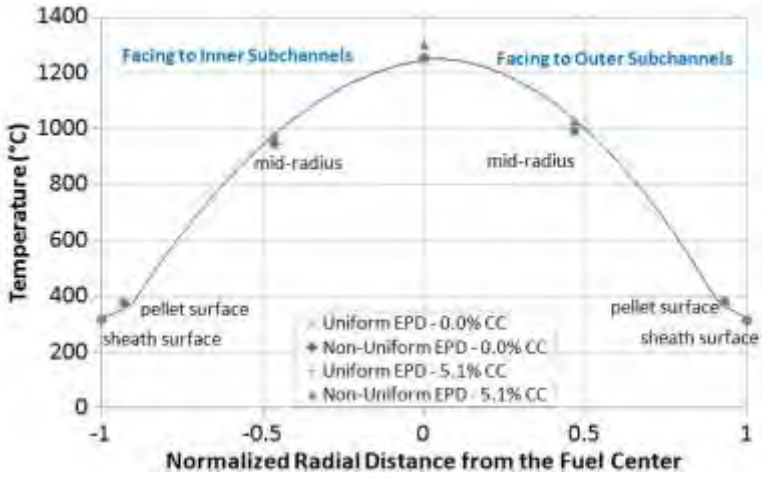

(a)

(b)

Figure 10 – Variation of Fuel Temperatures with Normalized Radial Distance in Uncrept and 5.1% Crept Channels (CC) (a), and Segmentation of Fuel Element 35 (b)

Table 1: Summary of Temperature Distribution in the Critical Segment of Fuel Pellets for Uniform and Non-Uniform EPD in Uncrept and 5.1% Crept Channels

Channel Creep (%)	Element Power Distribution	Critical Element	SC #	Inner or Outer SC	Temperatures (°C)			
					Fuel Centre	Mid-Radius	Pellet Surface	Sheath Surface
0	uniform	35	36	Inner	1248	948.2	376.3	316.3
			37	Inner	1247	934.4	373.7	315.5
			38	Inner	1248	947.4	375.4	315.3
			61	Outer	1248	989.1	379.9	314.1
			62	Outer	1248	988.4	379.1	313.3
0	Non-uniform	32	32	Inner	1255	952.6	376.5	316.3
			33	Inner	1255	938.9	374.1	315.7
			34	Inner	1255	952.3	376	315.7

			58	Outer	1255	993.7	379.9	313.7
			59	Outer	1255	993.8	380.2	314.1
5.1	uniform	35	36	Inner	1259	958.2	383.1	323.4
			37	Inner	1259	944.8	381.4	323.6
			38	Inner	1259	957.6	382.5	322.7
			61	Outer	1260	999.3	387.1	321.7
			62	Outer	1260	998.6	385.9	320.4
5.1	Non-uniform	34	35	Inner	1302	976.4	382.9	322.2
			36	Inner	1302	982.4	385.1	324
			60	Outer	1302	1028.6	389.5	322.1
			61	Outer	1302	1029.3	390	322.5

Figure **11** shows the variation of fuel centerline temperatures with locations (i.e., top and bottom and different rings). The largest temperature difference of 112°C is observed between top and bottom in the outer ring elements with non-uniform EPD in the 5.1% crept channel; the temperature difference between top and bottom elements in the middle ring is 50°C and in the inner ring is 36°C. The temperature variations between top and bottom elements in the other configurations (i.e., 43-element bundle in the uncrept channel with uniform and non–uniform EPD and in the 5.1% crept channel with uniform EPD) are lower than 30°C at any given ring.

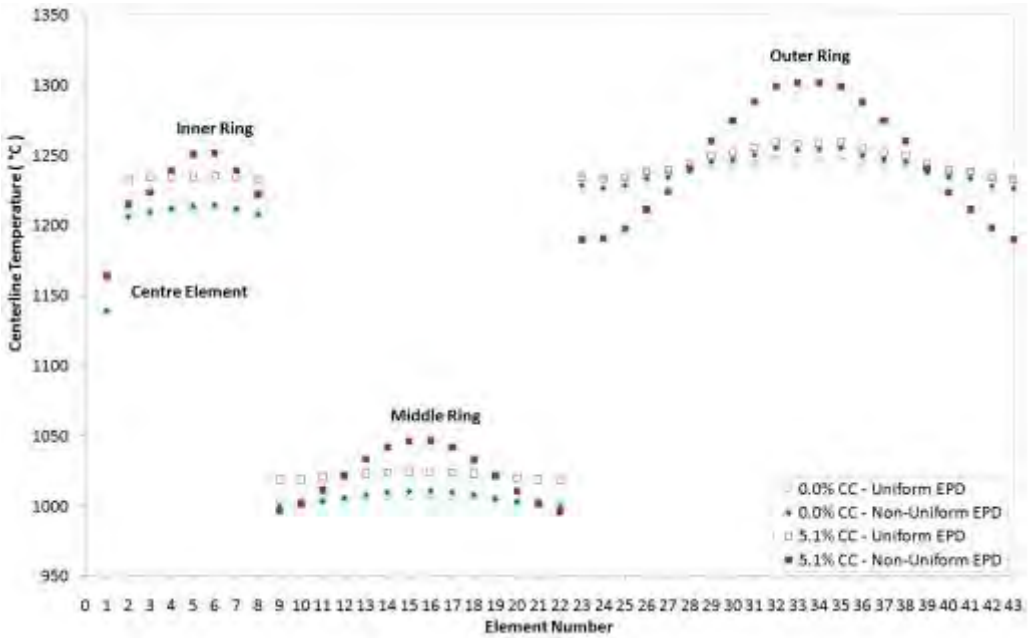

Figure 11 – Centerline Temperature Variations between Top and Bottom Elements

CONCLUSIOn

With ageing, pressure tubes develop a non-uniform creep deformation along the fuel channel resulting in fuel bundles being located eccentrically in the horizontal pressure tubes of a Canadian PHWR. This results in asymmetric flow and enthalpy distributions between the top and bottom of the fuel bundles in a crept pressure tube, which in turn can contribute to an

asymmetric power distribution within a ring of fuel elements. This study quantified the effect of eccentricity on the fuel centerline temperatures for a 43-element bundle in uncrept and 5.1% crept channels. The WIMS-AECL physics lattice cell code was used to predict power distribution within an element and across the bundle, and the ASSERT-PV thermalhydraulics subchannel code was used to describe inhomogeneous power distribution within and across fuel elements, which was then applied to calculate the temperatures of fuel, sheath and coolant.

The findings are summarized as follows:

- The effect of bundle eccentricity on element power variations in a given ring is insignificant in an uncrept channel of a Canadian PHWR, but may become noticeable in a 5.1% crept channel: The element power variation within a ring is larger in the 5.1% crept channel than in the uncrept channel, and it is the highest in the outer ring and the lowest in the inner ring.
- High element powers and hence high fuel centerline temperatures at critical elements are observed in the outer ring at the bottom (or close to the bottom) of the bundles for all cases. Critical segments in critical elements were found to be facing outer subchannels.
- There is no difference in cross-section averaged coolant temperatures between uniform and non-uniform EPD cases. Cross-section averaged coolant temperatures increase gradually in both fuel channels, but due to higher enthalpy imbalance for the 5.1% crept channel as compared to the uncrept channel, the cross-section averaged coolant temperature is lower in the 5.1% crept channel than in the uncrept channel downstream of the axial location where the channel power reaches a maximum.
- The maximum sheath temperature is reached at an upstream location in the 5.1% crept channel as compared to the uncrept channel. This is due to higher enthalpy imbalance in the 5.1% crept channel. The maximum sheath temperature in the 5.1% crept channel (~325°C) is slightly higher than that in the uncrept channel (~320°C); however, approaching the channel outlet, the maximum sheath temperature for the uncrept channel (314°C) is slightly higher than that (311°C) for the 5.1% crept channel, similar to the coolant temperatures.
- Fuel centerline temperatures reach a maximum at the peak power location (~323 cm from the inlet). A fuel centerline temperature of 1248°C for the uniform EPD in the uncrept channel, of 1255°C for the non-uniform EPD in the uncrept channel, of 1260°C for the uniform EPD in the 5.1% crept channel and of 1302°C for the non-uniform EPD in the 5.1% crept channel is reached in the critical elements that are located in the outer ring with linear element powers of 35 kW/m at the high power region.
- A centerline temperature difference of 112°C is observed between top and bottom elements in a bundle with non-uniform EPD in the 5.1% crept channel. In the other rings, the temperature difference is equal or less than 50°C. For the other configurations (i.e., 43-element bundle hosted in the uncrept channel with uniform and non–uniform EPD and in the 5.1% crept channel with uniform EPD), the centerline temperature difference between top and bottom elements is lower than 30°C at any given ring.

REFERENCES

[1] R.A. Holt, “In-Reactor Deformation of Cold-worked Zr-2.5Nb Pressure Tubes”, Journal of Nuclear Materials, 372, pp. 182-214, 2008.

[2] D. Altiparmakov, “New Capabilities of the Lattice Code *WIMS-AECL”*, *Proceedings of PHYSOR 2008*, Interlaken, Switzerland, 2008 September 14-19.

[3] Y.F. Rao, Z. Cheng, G.M. Waddington and A. Nava-Dominguez, “ASSERT-PV 3.2: Advanced Subchannel Thermalhydraulics Code for CANDU Fuel Bundles”, Nuclear Engineering and Design, 275, pp. 69–79, 2014.

[4] Y.F. Rao and N. Hammouda, “Recent Development in ASSERT-PV Code for Subchannel Thermalhydraulics”, *Proceeding of the 8th CNS Int. Conf. on CANDU Fuel*, 2003 September 21-24, Honey Harbor, Ontario.

[5] K.J. Serdula and R.E. Green, “Lattice Measurements with 28-Element Natural UO_2 Fuel Assemblies, Part II: Relative Total Neutron Densities and Hyperfine Activation Distribution in a Lattice Cell”, Atomic Energy of Canada Limited Report AECL-2772, 1967 August.

[6] D. Altiparmakov, W. Shen, G. Marleau and B. Rouben, “Evolution of Computer Codes for CANDU Analysis”, *Proceedings of PHYSOR 2010,* Pittsburgh, Pennsylvania, USA, 2010 May 9-14.

[7] L.S. Tong and J. Weisman, “Thermal Analysis of Pressurized Water Reactors”, 2nd Ed., American Nuclear Society, LaGrange Park, IL (1979).

[8] IAEA, “Thermophysical Properties Database of Materials for Light Water Reactors and Heavy Water Reactors”, IAEA-TECDOC-1496, 2006.

[9] E.N. Onder, D. Roubtsov, Y.F. Rao, “The Effect of Burn-Up on CHF for a CANFLEX Bundle in Uncrept and Crept Flow Tubes”, *Proceedings of the 15th International Topical Meeting on Nuclear Reactor Thermal - Hydraulics, NURETH-15*, 2013 May 12-17, Pisa, Italy.

AREVA'S ARCADIA® CODE SYSTEM – IMPLEMENTATION BENEFITS

F. CURCA-TIVIG[2], K. MAUPIN[3], D. PORSCH[2], S. KUCH[2], S. OPEL[2], F. LE BARS[1], G. SIMONINI[1], R. BROCK[3], D. DEVENEY[3]

[1]AREVA NP, 10 rue Juliette Récamier, F-69456 Lyon Cedex 06, FRANCE
[2]AREVA GmbH, Paul-Gossen-Str. 100, D-91052 Erlangen, GERMANY
[3]AREVA Inc, 3315 Old Forest Road, Lynchburg, VA, USA

ABSTRACT

AREVA is implementing ARCADIA®, a new advanced 3D coupled neutronics/thermal-hydraulic/thermal-mechanical code system using a software architecture that supports nodal and pin-by-pin calculation capability. ARCADIA® is applied to Light Water Reactor (LWR) fuel assembly and core design calculations as well as transient safety analysis. An expanded verification and validation basis, with significant improvements to each of the integral solver modules, and 3D transient analysis with pin-by-pin power and temperature distribution capability provides improved margin to key elements of the fuel cycle design space.

The spectral code of ARCADIA® is APOLLO2-A, while ARTEMIS™ is the 3D coupled neutronics/thermal-hydraulic/thermal-mechanical steady-state and transient core simulator. Both APOLLO2-A and ARTEMIS™ are validated and verified over a wide range of conditions. AREVA's extensive and unique database of tests includes critical experiments, core physics results from start-up testing, and transient benchmarks.

Transient 3D core simulation is a significant advancement relative to the point model core representation, still commonly used in transient safety analysis today. Because the core is modeled explicitly in three dimensions throughout the transient, it is no longer necessary to impose unrealistic combinations of penalizing conditions that do not, in fact, exist simultaneously. In the absence of such layered penalizations required to compensate for a lack of resolution in the method, the result is a more realistic assessment of the proximity to fuel safety limits through direct simulation of relevant phenomena.

Implementation of ARCADIA® expands the available fuel cycle design space through:

- Reduced calculation uncertainty
- Reduced maximum local power prediction
- Reduced bounding conservatisms (3D coupled transient solutions)
- Reduced failure predictions for accidents (explicit pin-by-pin calculation)

Design space expansion removes obstacles to plant or cycle design modifications and provides additional flexibility to support design initiatives, such as:

- Increase in discharge assembly burnup
- Core power uprates
- Verification of compliance with evolving regulatory requirements
- Fuel designs with optimized poison loading and arrangement
- Cycle reload batch size reduction

1. Brief Description of the ARCADIA® Code System

ARCADIA® [1, 2, 3] is an advanced 3D coupled neutronics/thermal-hydraulic/thermal-mechanical code system for steady state and transient core design using a software architecture allowing for both nodal and pin-by-pin calculation capability. It encompasses the following main components depicted in Figure 1-1 multi-group spectral lattice code APOLLO2-A, core simulator ARTEMIS™, core thermal-hydraulics code COBRA-FLX™, fuel rod module FRM (fully consistent with the advanced fuel rod performance code GALILEO™), and a comprehensive user environment system LADON™ with business and integration

services, for automating calculation sequences using a modern graphical user interface with powerful pre- and post-processing tools.

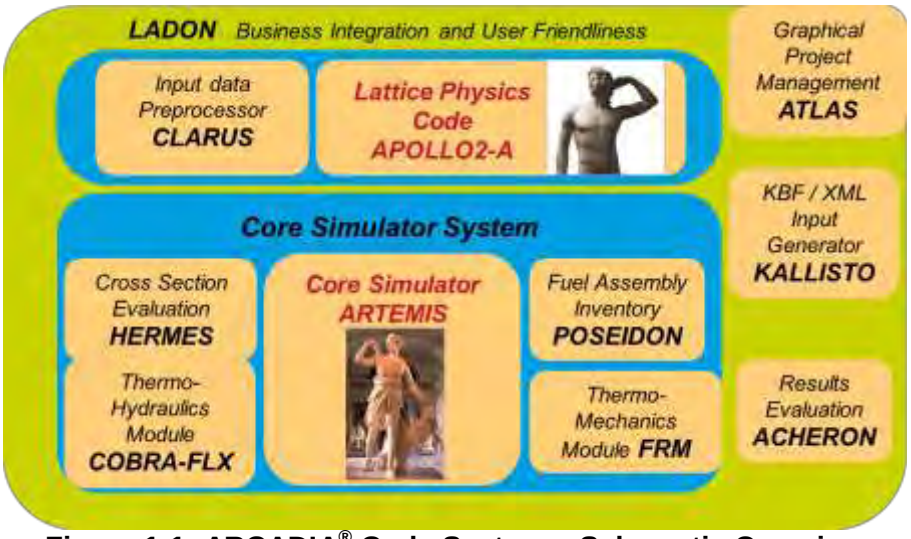

Figure 1-1: ARCADIA® Code System – Schematic Overview

A basic rule of ARCADIA® development was to use first-principle approaches to the highest degree possible and to avoid approximations and simplifications. The goal was to meet the current and future challenges of in-core fuel management and safety analyses.

In addition to state-of-the-art physical modelling, the ARCADIA® system features state-of-the-art software engineering, numerical performance, and industrial functionality. A decisive achievement in this regard is the implementation of a model-driven iterative development methodology with supporting tools for software design and code generation.

1.1. The Spectral Code APOLLO2-A

APOLLO2-A is AREVA's adaptation of CEA's APOLLO2 [4] for industrial LWR application and is used for reference fuel assembly design calculations and for generation of the nuclear data (cross sections, discontinuity factors, heterogeneous form functions) for use with the reactor simulation code ARTEMIS™. APOLLO2-A also supports the generation of cross-sections for radial (shroud/water or heavy steel) and axial reflectors. The master nuclear and gamma libraries used with ARCADIA® are based on JEFF3.1.1 and include up to 281energy groups, 26 fissile isotopes and actinides, and 131 fission products. APOLLO2-A describes the resonance self-shielding of several nuclides (U, Pu, Th/Zr, Fe/Gd, Er, Dy, Ag, In, Hf/Co, Rh) and treats resonance self-shielding below 23 eV neutron energy explicitly. In addition, it performs explicit calculation of γ-transport (local and non-local energy deposition). More details on the features of APOLLO2-A and examples of applications can be found in [5]. With its advanced physical models, APOLLO2-A displays the first level of margin gains for ARCADIA®.

1.2. The Core Simulator ARTEMIS™

The core simulator ARTEMIS™ describes the multi-physics of the reactor core (neutronics/thermal-hydraulic/thermal-mechanical) with full 3D resolution. ARTEMIS™ includes high performance multi group diffusion and transport flux solvers and is designed for both PWR and BWR applications. The main features of ARTEMIS™ are described in [6, 7]. The advanced capability to perform 3D coupled steady-state and transient calculations on pin-by-pin (sub-channel by sub-channel) geometries is an asset for the development of innovative, more accurate safety analysis methodologies.

ARTEMIS™ determines full-core pin-by-pin (sub-channel by sub-channel) parameters such as Departure from Nuclear Boiling Ratio (DNBR) and fuel rod temperature distribution by passing through two separate execution steps that can be run in parallel or in series, depending on the application of interest. The first step is a nodal core calculation. This is a coupled neutronics/thermal-hydraulic/thermal-mechanical calculation with a typical radial nodalization of four radial nodes per fuel assembly. This step determines the core power response and core power distribution throughout the transient, with all of the relevant feedback mechanisms present. A de-homogenization method is then applied to the nodal results giving rise to the full-core pin-by-pin power distribution. The de-homogenized pin powers are then available for use in the second step where the composition-specific fuel rod model along with the sub-channel thermal hydraulic model are used in conjunction to determine important local parameters such as DNBR, probability of DNB, fuel temperature, and clad temperature for each fuel rod in the core.

2. Validation of the Relevant Elements of ARCADIA®

2.1. The Spectral Code APOLLO2-A

The validation of APOLLO2-A for single fuel assembly up to high burnup and 2x2 colorset calculations was demonstrated in previous publications [8]. In addition to these standard applications a validation was pursued for applications to core geometries. The core in this example is composed of two fresh fuel assembly types (2.60 weight-% (w/o) ^{235}U and 3.95 w/o ^{235}U). The higher enriched assemblies are located on the core main axis directly adjacent to the outer shielding assemblies (light blue areas), resulting in large flux gradients. Figure 2-1 demonstrates the accuracy of the APOLLO2-A core calculation in comparison to a Monte-Carlo solution with MCNP5 for this demanding benchmark problem. In this example, the largest relative deviations of 2.3 % occur directly at the outer edge of the active core for pins with very low fission rates. The root mean square of the relative deviations between APOLLO2-A and MCNP5 is 0.4 %. Considering the uncertainty of the MCNP5 solution of 2σ ≤ 1 % the two solutions are in excellent agreement for the pin fission rates. This comparison and other supplemental analyses confirm the reference quality of APOLLO2-A for core size applications and unstructured meshes in core and reflector.

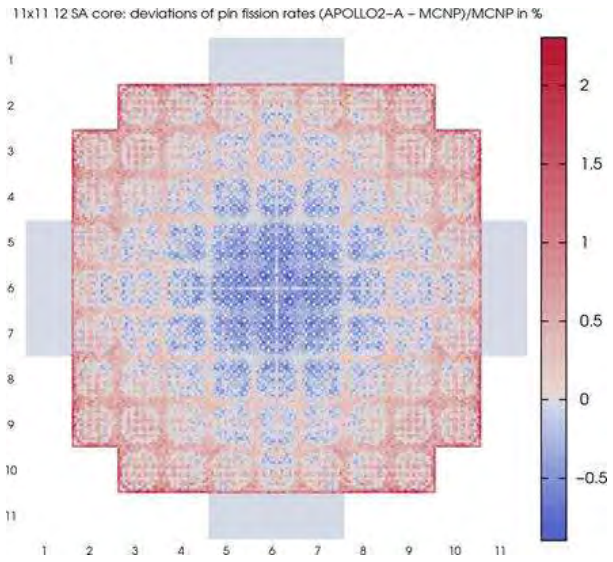

Figure 2-1: Core Benchmark Problem – Deviation of the Fission Rate Distribution between APOLLO2-A and MCNP5

2.2. ARTEMIS™ Steady State Validation

The validation of ARTEMIS™ was already demonstrated in previous publications [8, 9]. The current status of validation includes calculation to experiment (C/E) comparisons for more than 210 cycles of 18 LWR plants. Table 2-1 shows the range and extent of the parameters covered by these comparisons.

Parameter	Range in studied cycles
U235 enrichment (w/o)	1.80 – 4.95
MOX content (% Pu_{fiss}, FA averaged)	3.05 – 4.65 (equals 7.5% Pu-tot)
U235 enrichment in ERU (w/o)	up to 4.60
Core power (MW_e)	800 – 1450
Instrumentation	Aeroball Measurement System Fixed In-core Detector Movable In-core Detector Self-Powered Neutron Detector
Core height (cm)	299 – 427
Number of fuel assemblies	157 – 217
Fuel assembly lattices	14x14 – 18x18
Absorber materials	Gd_2O_3, boron silicate, B_4C, IFBA, WABA
Number of absorber pins	up to 1544 Gd pins in FAs in the core
Measured boron concentrations (ppm B_{nat})	up to 2224
Cycle lengths (EFPD)	129 - 600

Table 2-1: Validation Range for ARTEMIS™ Comparisons

2.3. Transient Validation of ARCADIA®

Demonstrations of transient validation of ARCADIA® have been included in previous publications [10, 11]. The overall validation plan includes recalculation of a selected set of transient cases using the transient application modes of ARCADIA®. This set of validation cases (Table 2-2) contains international benchmarks such as the NEACRP rod ejection benchmark as well as experiments, special tests performed at power plants, and available data for actual accident transients. The types of accidents include reactivity transients like the rod ejection accident, flow transients, and main steam line break (MSLB). Both fast and slow transients are included. The application modes validated include core-only nodal calculations as well as system-coupled calculations combining a detailed simulation of the core behaviour with ARTEMIS™ and simulation of the plant response using a system code (S-RELAP5 or CATHARE 2).

The validation concept is complemented by specific functionality tests and comparisons with licensed codes. These code-to-code comparisons allow performance of plausibility checks for features, models, and functionalities of ARCADIA® that are not accessible with measured or benchmark data. These include the capability to penalize input data for conservative safety analysis as well as parameters that are not easily measured in a real core (e.g. DNBR, local fuel temperatures etc.).

1	International Code and Analytical Benchmarks	Status
1.1	TWIGL-2D Ramp Transient Analytical Benchmark	Done
1.2	NEACRP Rod Ejection UOX Benchmark	Done
1.3	NEACRP Rod Ejection MOX Benchmark	Done
1.4	NEA/NSC Bank Withdrawal Benchmark	In Progress
1.5	MSLB Benchmark (Exercise 2 and 3)	In Progress
2	**Benchmarks against Measurements**	
2.1	PQY 1300 MW_e Rod Drop Transient	Done
2.2	SPERT Rod Ejection Measurements (HZP and HFP)	Done
2.3	German Design 1000 MW Coolant Pump Shaft Break	Done
3	**Benchmarks against Measurements with System Code Coupling**	
3.1	German Design 1300 MW_e, Load Rejection Transient	Done
3.2	German Design 1300 MW_e, Load Rejection with Temporary Loss of one Reactor Coolant Pump	In Progress

Table 2-2: ARCADIA® Transient Validation Plan

In Figure 2-2, preliminary example results for two subcases of the NEA/NSC bank withdrawal benchmark [12] are shown. This benchmark contains several different cases for a zero power control rod bank withdrawal event. In the different cases, different subsets of control banks are withdrawn until a scram is triggered at a pre-set power level. The left plot in Figure 2-2 compares the fission power calculated with ARTEMIS™ for case A from the benchmark to the reference solution, the right plot shows the power response for case B. In both cases the ARTEMIS™ solution is strongly consistent with the benchmark reference solution.

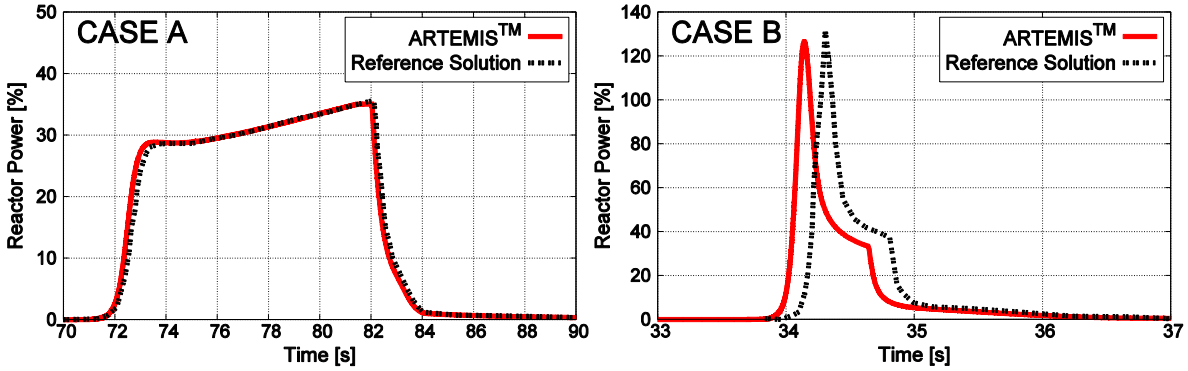

Figure 2-2: Preliminary Example Results for the NEA/NSC Bank Withdrawal Benchmark

3. ARCADIA® IMPLEMENTATION BENEFITS

The use of ARCADIA® defines a new state-of-the-art in coupled neutronics/thermal-hydraulic/thermal-mechanical safety analysis. Accurate theoretical models and new capabilities implemented in ARCADIA® are for example:

- In APOLLO2-A
  - Explicit gamma transport calculation

    - Modelling up-scattering in the self-shielding calculation
    - Method of Characteristics for determination of heterogeneous 2D pin values (power, flux, burnup, detector reaction rates)
    - Nuclear data based on JEFF3.1.1

- In ARTEMIS™
    - One set of nuclear data for continuous coverage of the application domain from hot to cold conditions with consistent accuracy
    - Consistent steady-state and transient calculations resulting in consistent initial core conditions for transient applications
    - Internal coupling of nodal and pin-by-pin (sub-channel by sub-channel) calculation
    - Explicit calculation of fuel rod conditions consistent with the fuel rod design code GALILEO™ in nodal and pin-by-pin calculations
    - Improved multi-group pin power/flux reconstruction technique for mixed cores with UO_2 and MOX assemblies
    - Explicit spacer grid model for local flux depressions
    - More than 100 explicitly treated heavy nuclides and fission products

From these enhancements follows an improved accuracy of predictions and a reduction of calculation uncertainties compared to legacy core design systems. Evaluation of a large variety of core designs (see section 2.2) and a comprehensive uncertainty analysis reveal a reduction of predicted peaking factors ($F_{\Delta H}$ and F_Q) in the range of 1-2 %. These gains can be converted into more optimized core designs and, for example, into a reduction in reload batch size.

In addition, more gains can be realized by applying the ARCADIA® code system for the development of advanced 3D coupled neutronics/thermal-hydraulic/thermal-mechanical safety analyses methodologies with realistic transient simulations.

4. 3D Transient Simulation

When the ARCADIA® 3D transient simulation functionality is used for plant safety analysis, the results for many transient events are significantly different than those obtained from traditional methods where the core power response is based on a simple kinetics model. In addition to this, the ARCADIA® advanced simulation provides information for all of the fuel rods in the core. This is particularly important when acceptance criteria are specified as a function of fuel rod condition, such as burnup or oxide thickness. Application of the ARCADIA® advanced simulation method gives a better understanding of the real margin to the applicable safety limits and liberates existing margin by removal of modelling simplifications and reduced conservatisms. Several examples follow that highlight these benefits.

4.1. Reactor Coolant Pump Rotor Seizure (Locked Rotor)

The Locked Rotor event is postulated to be caused by the instantaneous seizure of a reactor coolant pump rotor. Flow through the affected coolant loop is rapidly reduced and the event continues until the protection system initiates a reactor trip. DNBR safety limits are frequently challenged by the resulting combination of operation at or near full power and dramatically reduced reactor coolant system flow.

ARCADIA® 3D transient simulation of this event allows for important phenomena affecting its severity, such as moderator feedback and dropping of the rods to insert negative reactivity upon reactor trip, to be modelled dynamically. When compared to traditional methods using a constant value for moderator feedback and steady-state derived scram reactivity insertion

curves, the differences are significant even though the core was initially biased to the same initial (positive) moderator temperature coefficient (MTC) and total scram worth.

Figure 4-1: presents core power and minimum DNBR (MDNBR) comparisons of two different simulation methods for this event. Both models include equivalent key parameter biases consistent with those typically applied to safety analysis grade calculations (moderator/Doppler feedback, delayed neutron fraction, scram worth, etc.). Inspection of Figure 4-1: clearly shows that the event is modelled with positive moderator feedback. As the moderator temperature increases the effective moderator feedback coefficient decreases and this effect is captured by the ARTEMIS™ simulation. A substantial improvement in the MDNBR response is attributed primarily to the dynamic nature of the reactor scram.

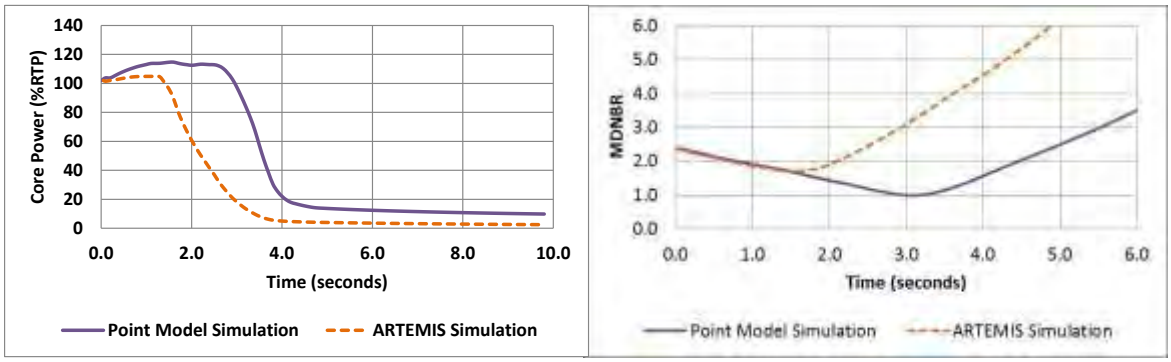

Figure 4-1: Locked Rotor Event
Core Power and MDNBR Comparison (Traditional 0D vs. 3D Transient Simulation)

4.2. Control Rod Ejection

A postulated failure of a control rod drive mechanism leading to the ejection of a control element presents a scenario in which positive reactivity may be added to the core very rapidly. When the worth of the ejected element is large enough, a prompt power excursion will result. The design of a reactor must protect the integrity of the core and the reactor coolant system by limiting the mechanical energy produced as a result of prompt energy deposition. Regulatory acceptance criteria for prompt fuel element rupture and prompt energy deposition vary from a specific calorie per gram energy deposition limit for all of the rods in the core, to energy deposition limits functionalized to individual fuel rod corrosion levels such as clad oxide thickness or clad hydrogen content.

Simulation of the rod ejection event with ARCADIA® where traditional decoupled 0D and 1D methods are replaced with 3D transient simulation brings benefits in reducing the severity of the event, similar to those that were seen for the locked rotor, due to the dynamic treatment of feedback mechanisms. Preliminary analysis has shown a significant reduction in maximum fuel enthalpy and maximum fuel enthalpy rise compared to traditional methods. In addition, and of significant importance, simulation with ARCADIA® provides full-core pin-by-pin results with important phenomena such as thermal conductivity degradation and gap conductivity explicitly modelled. This level of detail also delivers full-core pin-by-pin results for fuel rod energy deposition and fuel rod temperature profile.

Figure 4-2 shows full-core pin-by-pin enthalpy deposition as a function of individual pin burnup for two different exposure and power level combinations. Inspection of Figure 4-2 shows that the energy generated in this event is distributed over a wide range of pin burnup conditions (clad oxide thickness, clad hydrogen content). Each fuel rod with its particular clad composition, pellet composition, and operating history can be compared to the

functionalized acceptance criteria with ease and without the penalizing simplifications that are necessary when this level of detail is not available.

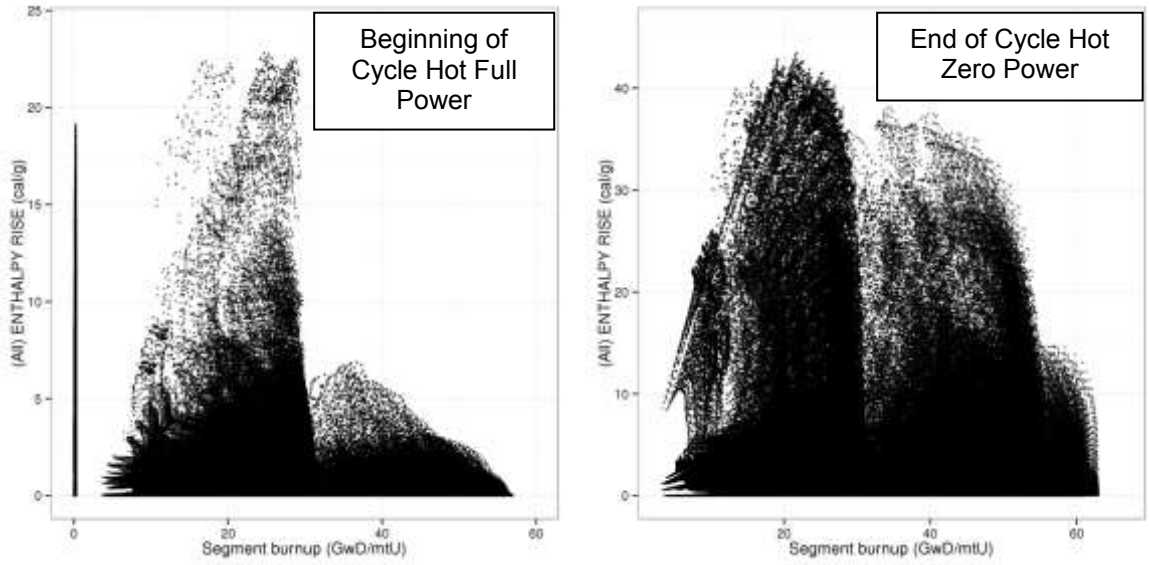

Figure 4-2: Control Rod Ejection Deposited Enthalpy as a Function of Pin Burnup

4.3. Hot Zero Power Excess Steam Demand

Opening of steam dump and bypass valves or opening of turbine control valves when the plant is in the hot zero power condition gives rise to a power mismatch between the primary and secondary plant systems. Steam generator pressure and temperature rapidly decrease and, in the presence of a negative moderator coefficient, the subsequent primary system temperature reduction represents a positive reactivity insertion to the core.

ARCADIA® 3D transient simulation of this event allows for important phenomena affecting its severity, such as moderator feedback, Doppler feedback, and maximum local power peaking to be modelled dynamically. Figure 4-3 presents a comparison between representative traditional methods using a constant moderator feedback coefficient and steady-state derived constant maximum peaking factor and a 3D ARTEMIS™ transient simulation. Both models include equivalent key parameter biases consistent with those typically applied to safety analysis grade calculations (moderator/Doppler feedback, delayed neutron fraction, scram worth, etc.). Inspection of Figure 4-3 shows a significant difference in the core power response. As the moderator temperature decreases the effective moderator coefficient becomes less negative and this effect is captured by the ARTEMIS™ simulation. The approach to sensible power production slows considerably when the 3D moderator feedback is evaluated explicitly and the magnitude of the peak power is reduced significantly. The tail in the point model core power response results from the conservative use of a steady-state-derived scram reactivity insertion correlation which is not present in the ARTEMIS™ simulation as the scram is dynamically simulated.

An additional benefit from the use of ARCADIA® is found in the direct computation of the maximum local power peaking conditions for each pin in the core. Where traditional methods may be compelled to simplify the determination of the maximum local peaking factor (F_Q), by assuming a constant value based on a separate steady-state calculation exists throughout the transient, ARCADIA® includes this calculation as part of its solution (See Figure 4-3). The result is a significant reduction in the maximum fuel temperature experienced during the transient.

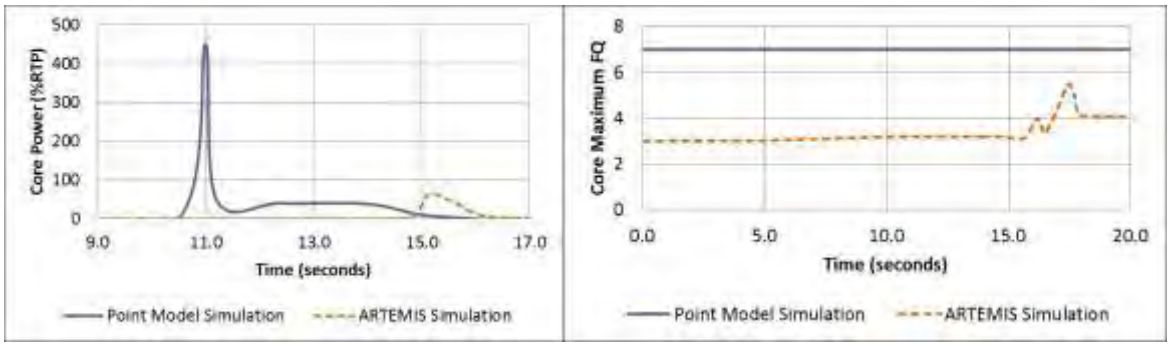

Figure 4-3: Excess Load From Hot Zero Power – Core Power and Core Maximum Local Peaking Comparison

5. Design Space Expansion

The collection of design limitations that limit flexibility in the cycle design process typically are imposed by a combination of stakeholders including the utility, the regulator, and the fuel vendor. Together, these limitations define a design space and a given cycle design must "fit" within this space to be acceptable. An assessment of a given plant for a typical cycle design would provide the needed information to determine the plant's current position within the acceptable design space. This concept is illustrated in Figure 5-1 where the normalized acceptable design space is the area shaded in scarlet, the current position of a virtual plant design within this space is shaded in grey, and the distance from the borders of the grey region to the borders of the scarlet region represents available margin or flexibility relative to each design limitation.

Figure 5-1: Normalized Design Space (Scarlet)
Representative Plant Position within Normalized Design Space (Grey)

Implementation of ARCADIA® restores margin and design flexibility to key areas that are typically limiting today. In the context of Figure 5-1 this is equivalent to an increase in separation between the borders of the plant position within the design space and the acceptable design space itself (i.e. increased margin to key design limits). Benefits, such as reduced calculation uncertainty and reduced maximum local power peaking prediction, increase primary cycle design margins in an immediate fashion. Application of 3D coupled transient methods removes "obstacle" transients such as the locked rotor, control rod ejection, and main steam line break, by facilitating the removal of bounding conservatisms in

traditional methods. In addition, the use of the fully benchmarked 3D transient modelling capability can be used to build solid justification for relaxation of excessive conservatisms in steady-state methods for events such as the uncontrolled bank withdrawal at power. Hence, with the implementation of ARCADIA®, the acceptable design space is expanded. This removes obstacles to plant or cycle design modifications and provides additional flexibility to support design initiatives such as:

- Increase in discharge assembly burnup
- Core power uprates
- Verification of compliance with evolving regulatory requirements
- Fuel designs with optimized poison loading and arrangement
- Cycle reload batch size reduction

6. Conclusions

AREVA's advanced 3D coupled neutronics/thermal-hydraulic/thermal-mechanical code system for LWR applications, ARCADIA®, is ready for implementation. The new code system is applied to core design calculations as well as transient safety analysis. The validation basis for key aspects of application is extensive and its development has placed strong emphasis on first principle approaches and uniform application with no plant specific adaptation of the code system. In addition, ARCADIA® is applied as a single code and a single model for steady-state and transient analysis. These development and application principles combine to deliver more accurate determinations of safety margin and significant design flexibility. This design flexibility can then be used to generate customer-specific value in areas that are indeed valuable to them. Examples include core power uprate support, reload batch size reduction, and compliance with evolving regulatory requirements.

REFERENCES

1. F. Curca-Tivig et al., "ARCADIA®- A New Generation of Coupled Neutronics/ Core Thermal-Hydraulics Code System at AREVA", Proc. of the 2007 Int. LWR Fuel Performance Meeting, San Francisco, California, Sept. 30 – Oct. 3, 2007
2. D. Porsch et al, "ARCADIA® – AREVA NP's Next Generation Nuclear Design System", Jahrestagung Kerntechnik 2009, Dresden, Germany, May 12-14, 2009
3. M. Leberig et al, "AREVA NP's Advanced Thermal Hydraulic Methods for Reactor Core and Fuel Assembly Design", TopFuel 2010, Orlando, Florida, USA, September 26-29, 2010
4. R. Sanchez et al., "APOLLO2 Year 2010", *Nuclear Engineering and Technology*, Vol.42 No.5, October 2010
5. E. Martinolli et al., "APOLLO2-A AREVA's New Generation Lattice Physics Code: Methodology and Validation", *PHYSOR 2010*, Pittsburgh, USA, May 9-14, 2010
6. G. Hobson et al., "ARTEMIS™: The core simulator of AREVA NP's next generation coupled neutronics/thermal-hydraulics code system ARCADIA®", PHYSOR 2008, Interlaken, Switzerland, September 14-19, 2008
7. G. Hobson et al., "ARTEMIS™ Core Simulator: Latest Developments", Joint International Conference on Supercomputing in Nuclear Applications and Monte Carlo 2013 (SNA + MC 2013), Paris, France, October 27-31, 2013
8. D. Porsch et al., "Status of Verification & Validation of AREVA's ARCADIA® Code System for PWR Applications", PHYSOR 2012, Knoxville, Tennessee, U.S.A., April 15-20, 2012

9. B. HARTMANN et al., ”Advanced PWR Core Analysis with ARCADIA®“, Jahrestagung Kerntechnik 2014, Frankfurt, Germany, May 6-8, 2014
10. G. HOBSON et al., “ARCADIA® Transient Capabilities and Recent Validation Experience”, Proceedings of 2013 LWR Fuel Performance Meeting / Top Fuel, Charlotte, North Carolina, USA, September 15-19, 2013
11. S. KUCH et al., “Transient Validation of AREVA’s new ARCADIA® code system”, Proceedings of the 2014 22nd International Conference on Nuclear Engineering, ICONE 22, Prague, Czech Republic, July 7-11, 2014
12. R. Fraikin, “PWR Benchmark on Uncontrolled Rods Withdrawal at Zero Power”, NEA/NSC/DOC(96)20

GLOBAL SENSITIVITY ANALYSIS IN FUEL PERFORMANCE MODELLING

T. IKONEN
VTT Technical Research Centre of Finland Ltd.
P.O. Box 1000, FI-02044 VTT - Finland

ABSTRACT

Fuel performance codes have two characteristics that make their sensitivity analysis challenging: large uncertainties in input parameters and complex, non-linear and non-additive structure of the models. The complex structure of the code leads to interactions between inputs that show as cross terms in the sensitivity analysis. Due to the large uncertainties of the inputs these interactions are significant, sometimes even dominating the sensitivity analysis. For the same reason, standard linearization techniques do not usually perform well in the analysis of fuel performance codes.

We discuss the practical aspects of performing an uncertainty and sensitivity analysis for a fuel performance code. We compare the performance of several analysis methods in the analysis of a steady state FRAPCON simulation. For the analysis of maximum fuel temperature, even the simplest methods are shown to work well. However, for the gap conductance, sophisticated methods are needed. Based on our example, we also present an importance ranking of the input uncertainties.

1. Introduction

Light water reactor fuel performance codes model the behaviour of the fuel rod under irradiation, either in the steady state or in transient conditions. The purpose of the modelling is to provide understanding how the thermal, mechanical and materials properties interact and how the rod responds as a whole to the boundary conditions imposed by the environment. An important aspect of the analyses is to support the rod design and safe operation, so that the cladding remains intact and various safety margins are respected. In addition to the usual difficulty of representing a complex system with soluble mathematical models, there are also large uncertainties in many of the system and model parameters. Therefore analyses are often coupled with uncertainty analyses, which take into account the uncertainties in the code input, and produce an estimate of the uncertainty of the calculated result. To take the analysis one step further, one may ask how to reduce the uncertainty of the results, or which of the code inputs is (most) responsible for the uncertainty of the result. These questions can be addressed by sensitivity analysis.

The goal of a sensitivity analysis is to find the most influential input parameter to the computed model output. The method chosen for the sensitivity analysis depends on the computational cost of the model, the number of inputs to be considered, and the specific question to be answered by the analysis. Computationally the most inexpensive method is the one-at-a-time (OAT) method, where each parameter is varied independently while keeping the others fixed. Although simple, the method suffers from poor coverage of the parameter space and from lack of control over the quality of the analysis. For a typical fuel performance code, such as FRAPCON [1,2], the computational time per run is of the order of seconds or minutes. In this case it is feasible to use Monte Carlo based sensitivity analysis methods that require several hundreds or thousands of model runs. In addition to OAT, these are the types of methods that we study in this work. Specifically, we apply global variance based methods, including the Pearson correlation analysis (see, e.g., Ref. [3]) and the Sobol' variance decomposition [4]. The methods are based on estimating the influence of a given input on the output variance. In some cases it is possible that the variance is not a good

measure of uncertainty, in which case moment-independent methods can be used [5]. These methods are outside the scope of the present work.

Another consideration when choosing the method is the specific question posed to the analysis. Questions such as “If we could eliminate the uncertainty of one input parameter, which one should we choose in order to reduce the variance of the output as much as possible?” and “Which of the input parameters are so non-influential that they can be fixed?” define the *setting* of the sensitivity analysis (see, e.g., Refs. [6,7]). The first one corresponds to factor prioritization (FP) and the second one to factor fixing (FF) setting. In the FP setting, it is sufficient to determine the main (first order) effect of an input parameter, while in the FF setting one has to consider the interactions between different inputs (uncertainties in the output that only arise as a result of changing more than one variable simultaneously). These can be quantified, for example, by the total effect sensitivity index, discussed in Section 3.

For a fuel performance code, the role of interactions in the model can be significant [8]. This is because of two characteristics of fuel performance codes: large uncertainties in input parameters and complex, non-linear and non-additive structure of the models. A famous example of the latter is the gap conductance, which couples together the thermal, mechanical and microstructural (e.g., fission gas release) models in the fuel performance code. The intertwined structure of the code leads to interactions between inputs that show as cross terms in the sensitivity analysis. Due to the large uncertainties of the inputs these interactions are significant, sometimes even dominating the sensitivity analysis. For the same reason, standard linearization techniques do not usually perform well in the analysis of fuel performance codes.

A thorough sensitivity analysis of a fuel performance code requires methods that can cope with the large uncertainties and interactions. On the other hand, the simplicity and computational ease of the OAT method is very appealing. In this work, we attempt to address the choice between different methods by comparing their performance in the sensitivity analysis of a steady state scenario modelled with the FRAPCON-3.4 code. In our analysis we focus on the gap conductance computed for a mid-burnup (22 MWd/kgU) PWR rod, which is particularly challenging to analyse.

2. Fuel performance model and the simulated scenario

We study the propagation of uncertainties under steady-state irradiation with the FRAPCON-3.4 fuel performance code [1,2]. FRAPCON is a deterministic fuel performance code that calculates the steady-state response of light-water reactor fuel rods during long-term burn-up. Boundary conditions such as the power history and the coolant properties, in addition to the rod fabrication parameters, are supplied as input. Additionally, several model parameters can be re-defined in the input both in the PNNL and in the VTT’s modified versions. The output of the code comprises several observables. A thorough analysis of the most important ones has been done previously with the Sobol’ variance decomposition method [6]. In this work, we focus only on the pellet centreline temperature, and the gap conductance. Based on the previous work, we expect the gap conductance to be more difficult to analyse. The intuitive reason for this is that in solving the gap conductance, the fuel performance code takes into account both the thermal and mechanical behaviour models, which essentially leads to cross terms in the sensitivity analysis that may be difficult to pin-point. The centreline temperature, on the other hand, is much more straightforward to analyse, and even simple methods should be quite effective.

The analysed scenario is a hypothetical steady-state irradiation of a UO_2 fuel rod in the Three Mile Island 1 (TMI-1) PWR reactor. The scenario is designed to bring the fuel rod to a relatively high burn-up of 50–60 MWd/kgU (depending on the input values), using a simplified power history, where the average linear heat rate is 23.39 kW/m from the beginning of the

irradiation until 550 days, 19.69 kW/m until 1200 days and 15.0 kW/m until the end of irradiation at 1800 days. The axial power profile is given in Table 1.

Table 1. The axial power profile of the considered scenario

Position (mm)	0.0	304.8	609.6	914.4	2743.2	3048.0	3352.8	3657.6
Relative power	0.63	0.83	1.03	1.08	1.08	1.03	0.83	0.63

Table 2. The nominal values of the input parameters and their uncertainties (see text). For the FRAPCON correlations and the average linear power, only the uncertainties are shown, because the nominal value is a function of several variables or changes with time.

Parameter	**Value**
Clad outer diameter	(10.92 ± 0.06) mm
Clad thickness	(0.673 ± 0.025) mm
Pellet outer diameter	(9.40 ± 0.02) mm
Fuel enrichment	(4.85 ± 0.003) atom-%
Density (% of theoretical)	(93.8 ± 1.6) %
Coolant pressure	(15.51 ± 0.31) MPa
Coolant inlet temperature	(561 ± 3) K
Coolant mass flux	(3460 ± 69) kg/m^{2}s
Fuel thermal conductivity	± 10 %
Fuel thermal expansion	± 15 %
FGR diffusion coefficient	+ 200 % / - 67 %
Fuel swelling	± 20 %
Clad creep	± 30 %
Clad axial growth	± 50 %
Clad corrosion (waterside oxide)	± 40 %
Clad H concentration	± 80 ppm
Clad thermal conductivity	± 5 W/mK
Clad thermal expansion	± 30 %
Gas thermal conductivity	± 0.02 W/mK
Coolant heat transfer	± 5 %
Average linear power	± 5 %

The varied input parameters are listed in Table 2. The uncertainties reported in the OECD Benchmark for Uncertainty Analysis in Best-Estimate Modeling for Design, Operation and Safety Analysis of LWRs [9] have been used as a guideline for the rod fabrication and system parameters. The uncertainties in the material correlations and models were determined based on a recent model evaluation [10] and the recommendations given in the FRAPCON-3.4 manual [1,2]. For all variables, the probability distribution is assumed Gaussian, with a cut-off at the lower and upper 2.5 % percentiles. The uncertainty limits corresponding to these cut-offs are given in Table 2. The input parameters are assumed mutually independent. In addition to the varied inputs, the fuel height and pellet height were assumed (fixed) at 3657.6 mm and 11.43 mm, respectively, the rod was assumed filled with helium at 1207 kPa, and the Zircaloy-4 correlations were used for the cladding. Default FRAPCON-3.4 models were used in the simulations.

3. Analysis methods

3.1 One-at-a-time (OAT) analysis

Arguably the simplest sensitivity analysis strategy is to vary one model input parameter at a time while keeping the others fixed. Typically such a one-at-a-time (OAT) sampling is done around the nominal (most probable, or best estimate) values of the input parameters. It is possible to choose the sampling points in many ways, but one of the most common ones is

to choose the extreme values of the distribution. Another typical way would be to evaluate the effect of infinitesimal changes to the inputs by choosing a very small deviation from the nominal value. However, in the case of a fuel performance code, where we do not expect the model to linearize effectively and where the uncertainties are large, we choose to sample the parameters at their extreme values. One could of course increase the number of points to sample intermediate values of the parameter. While this increases the likelihood of catching non-monotonic effects of the input parameters, it also quickly increases the number of required function evaluations, and is unlikely to cover the parameter space efficiently [11].

The change in the model output is evaluated at all the sampled points, and the input causing the largest change in the output is given the highest rank in the sensitivity analysis. In this work, we define the OAT sensitivity measure for input x_i as

$$OAT_i = \frac{\max\limits_{\Delta_i} \left| f(x+\Delta_i) - f(x) \right|}{\sum\limits_j \left(\max\limits_{\Delta_j} \left| f(x+\Delta_j) - f(x) \right| \right)}, \quad (1)$$

where x is the vector of inputs, and Δ_i is a vector of zeros, except for the *i*:th element, which is chosen at the extrema of the distribution of x_i. The denominator serves to normalize the measure so that it can be easily compared to the global sensitivity measures discussed below, which are normalized between 0 and 1 by construction. The normalization has no effect on the parameter ranking.

The computational cost of the method is very small, as the number of required simulation runs is only $2k+1$, where *k* is the number of inputs.

3.2 Global sensitivity analysis

The goal of global sensitivity analysis is to characterize the dependence of the model output on its inputs in the whole input parameter space. Usually the analysis involves some kind of the Monte Carlo sampling of the inputs, either by simple random sampling or by quasi random sampling. In quasi random sampling, the sample points are chosen in a way that avoids clusters and results in more effective sampling and faster convergence. In this work, the Sobol' quasi random sequence [12] is used to generate the sample points. The error estimates for the correlation coefficients and sensitivity indices (see below) are calculated by the bootstrap method [13] over at least one hundred bootstrap samples.

3.2.1 Pearson correlation analysis

The simplest global sensitivity analysis of a model is the calculation of linear correlation between an input x_i and the output $f(x)$ from (quasi) randomly sampled data. In practice this is done by calculating the Pearson correlation coefficient R_i. The square R_i^2 of the Pearson coefficient also gives the portion of the output variance attributable to input x_i, and it can be used as a normalized sensitivity measure,

$$R_i^2 = \frac{\mathrm{cov}(x_i, f(x))^2}{V(x_i)V(f(x))}, \quad (2)$$

where $V(\cdot)$ denotes the variance and $\mathrm{cov}(\cdot)$ the covariance. R_i^2 is normalized so that $\sum R_i^2 \leq 1$, with the equality exact if the model is linear. The sum also gives the overall degree of determination, so it is easy to control that the sensitivity analysis is comprehensive. If the value of the sum remains significantly below unity, the model contains nonlinearities and interactions that can only be analysed with higher order methods. The ability to check the quality of the sensitivity analysis *a posteriori* is an important advantage of the Pearson correlation analysis over the OAT methods.

The computational cost of the method is relatively low and (almost) independent of the number of inputs. The number of model runs required for reasonable statistical accuracy depends on the nature of the model, but is typically of the order of $N \approx 1000$.

3.2.2 Variance decomposition analysis

A model such as a fuel performance code that has significant interactions between input parameters can be analysed only incompletely with linear correlation methods. A simple rank transform of the data (for example, the Spearman correlation method) is not sufficient to analyse a fuel performance model comprehensively [8]. A method that can extract information about the interactions is necessary. One such method is the Sobol' variance decomposition analysis [4].

In the variance decomposition method, the idea is to express the variance $V(f(x))$ of the output as a finite sum of terms of increasing order. Each of these terms represents the contribution of one input variable to the output variance (first order terms) or the variance due to interactions of several variables (higher order terms). For independent variables, this decomposition is unique [4]. The Sobol' sensitivity indices are then defined as these partial variances normalized by the output variance. For example, the first order effect of input x_i is defined as

$$S_i = \frac{V(E(f(x) \mid x_i)}{V(f(x))}, \tag{3}$$

where $E(f(x) \mid x_i)$ is the conditional expectation value of $f(x)$ with a fixed value of the input x_i. The measure S_i is very similar to R_i^2, the difference being that the latter is based on linear regression on the data. However, both measure the portion of output variance that can be directly traced back to the uncertainty in the value of x_i. The index S_i is also normalized so that $\sum S_i \leq 1$, with the equality becoming exact if the model is additive (has no interactions).

The analysis of model interactions can be done by computing the higher order terms in the variance decomposition. For computational reasons one typically only analyses the first and possibly the second order terms, and the so-called total effect index, T_i. The index T_i describes the combined effect of the *i*:th variable on the output including the first order effect and all the higher order interaction terms between the variable x_i and the other variables, up to the term describing the interactions of all the *k* inputs of the model. The formal definition for the total effect is

$$T_i = \frac{E(V(f(x) \mid x_{-i})}{V(f(x))}, \tag{4}$$

where $V(f(x)|x_{-i})$ denotes the output variance conditional to fixing all the variables except x_i. Since the interaction terms are included in the total effects of more than one variable (for example, the interaction between variables x_i and x_j is included in both T_i and T_j), the sum of the total effects is not normalized to unity. In fact, $\sum T_i \geq 1$. The equality becomes exact if there are no overlapping terms in the total effects of different inputs (that is, the model has no interactions).

The calculation of the higher order terms can be done efficiently by Monte Carlo integrals for the first order, second order and total effect indices [8,14,15]. Here one uses a special sampling design to estimate the indices (for the details of the numerical implementation used in this work, we refer the reader to Section 3.4.3 of Ref. [8], and Ref. [14]). To evaluate the conditional expectations and variances in Eqs. (3) and (4), the design reduces the required computational effort from exponential in *k* (the number of inputs) to linear in *k*. Compared to the correlation coefficient analysis, for which the computational cost does not inherently depend on *k*, even the linear scaling remains a limitation for models with tens of uncertain inputs. The required number of model runs is $N(2k+2)$, where *N* depends on the desired accuracy, but is typically of the order of $N \approx 1000$.

4. Results and discussion

4.1 Uncertainty analysis

Before going into the sensitivity analysis, we take a look at the results from the uncertainty analysis of the scenario described in Section 2. The scenario was simulated with FRAPCON-3.4 on a Linux cluster. The input parameters were sampled independently from their respective probability distributions, with a sample size of $N = 50000$. In addition, for the Sobol' sensitivity indices an additional 22 sample sets were generated, bringing to total number of simulation runs to 1.15×10^6, which took approximately 20 CPU-days on the Linux cluster. It should be noted that for most purposes satisfactory accuracy could be achieved with, say, $N = 1000$. However, the large sample size allows very precise determination of the sensitivity indices. This is advantageous for the present comparative study of different methods, as it practically eliminates the effect of statistical variation in the comparison. A more detailed analysis of the effect of the sample size is outside the scope of this paper.

From the calculated results, we choose just two for further analysis: the maximum fuel temperature $T_{\max}$ and the gap conductance h_{gap} at the central axial node, both evaluated at the burnup of approximately 22 MWd/kgU, where the gap can be either open or closed, depending on the values of inputs [8]. The evolution of the mean values and uncertainties of $T_{\max}$ and h_{gap} with increasing burnup are shown in Fig. 1. Their probability distributions at 22 MWd/kgU are also shown in the insets.

Already from the probability distributions of $T_{\max}$ and h_{gap}, it is possible to make some deductions. The distribution of $T_{\max}$ is almost Gaussian. Therefore it is likely that the model that produces the distribution of $T_{\max}$ from the (almost Gaussian) input distributions is quite simple. On the contrary, the distribution of h_{gap} is very complex (two large peaks, corresponding to the open and closed gap states, and a long tail towards zero). It is not likely that such a distribution could be produced by any simple function, so we may expect to find significant nonlinear and interaction terms. For both $T_{\max}$ and h_{gap} the uncertainty in the value is high.

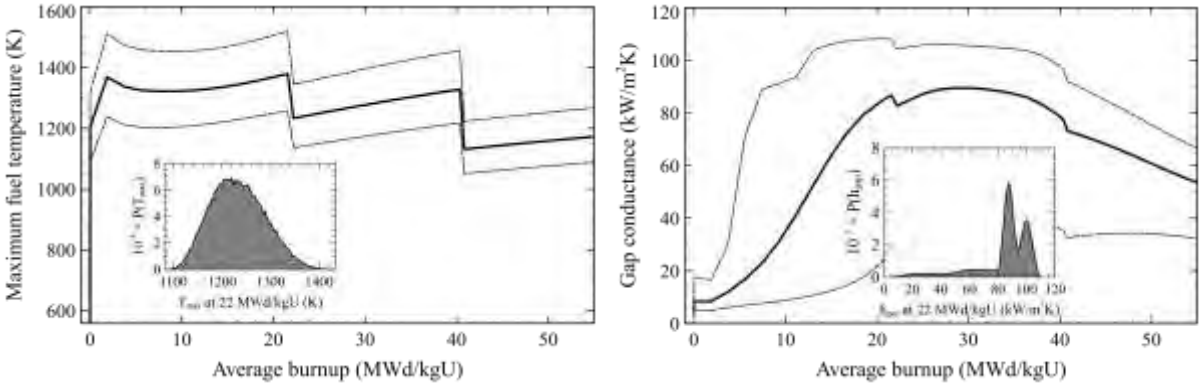

Figure 1. Left: The maximum fuel temperature (solid line) and its 95 % confidence limits (dashed lines) as a function of burnup. Right: The corresponding plot for the gap conductance at the central axial node. The insets show the probability distributions of maximum temperature and gap conductance at 22 MWd/kgU.

4.2 Sensitivity analysis

4.2.1 Maximum fuel temperature

The sensitivity analysis on the maximum fuel temperature has been done with the methods described in Section 3: one-at-a-time sampling, Pearson correlation analysis, and by variance decomposition. The results are gathered in Fig. 2, where the computed sensitivity measures are shown for each of the considered inputs. The results are almost the same for all the global methods (R_i^2, S_i and T_i). This is a clear indication that the computation of the maximum temperature by FRAPCON is almost linear with respect to the input parameters. At least, the nonlinear and nonadditive parts of the model do not have a strong influence on the maximum fuel temperature. This result is true also for low and intermediate-to-high burnups [8], and agrees with a previous study focusing on fuel thermal properties [16].

Compared to the global variance based methods, the OAT analysis gives somewhat different results, although the most important factors (fuel thermal conductivity and average linear heat rate) are identified by all methods. For some of the low-ranking factors there are differences, but overall the agreement is quite good.

4.2.2 Gap conductance

The gap conductance computed at the central axial node by FRAPCON was also analysed similarly to the maximum fuel temperature. In this case, there is considerably more scatter in the results (see Fig. 3). The Pearson correlation coefficient R_i^2 and the first order Sobol' index S_i generally agree very well. However, compared to the total effect index T_i, their values are considerably lower. This is a sign on nonadditive interactions between the inputs, which can be analysed by taking into account the higher order terms in the variance decomposition. In a previous study [8] it was shown that the first order terms can identify only about 60 % of the uncertainty, but including the second order and total effect terms brings the count to practically 100 %.

The OAT analysis gives somewhat similar results. However, the values are not consistently close to S_i (R_i^2) or T_i, but sometimes tend to mimic the first order effects and in other cases the total effects. Although it seems that the OAT method gives a fair indication of the inputs' importance, the somewhat erratic behaviour makes it difficult to draw definite conclusions, or to define the exact question (setting) the OAT method should give an answer to.

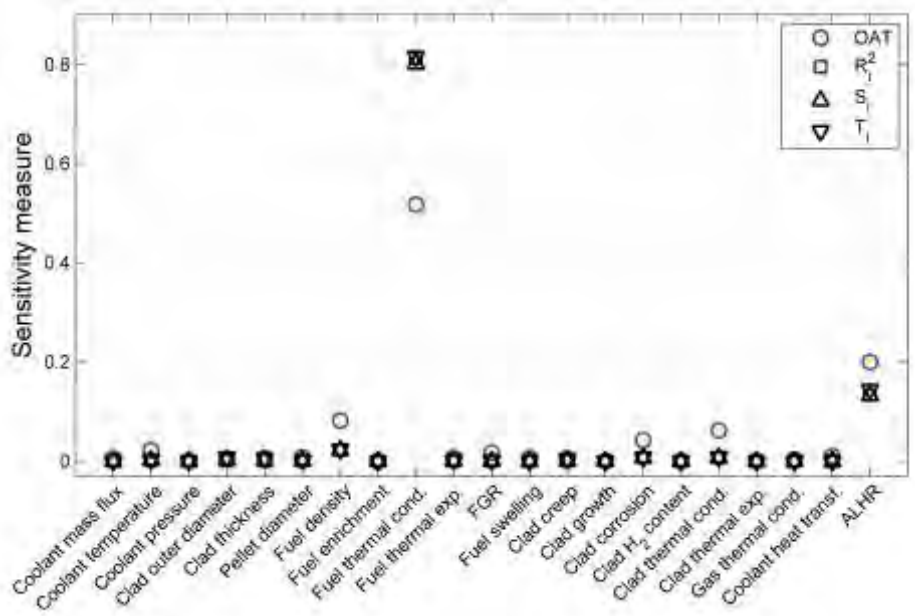

Figure 2. The sensitivity measures for the maximum fuel temperature at 22 MWd/kgU estimated for the different inputs. The statistical error is smaller than the size of the symbols. The different symbols correspond to the different methods (see Section 3).

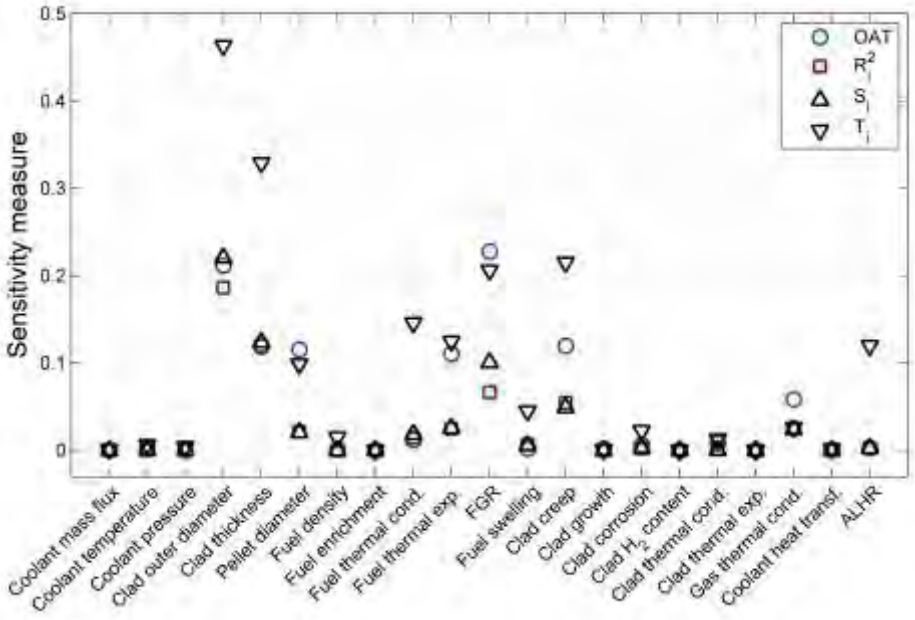

Figure 3. The sensitivity measures for the gap conductance at 22 MWd/kgU estimated for the different inputs. The statistical error is smaller than the size of the symbols. The different symbols correspond to the different methods (see Section 3).

To make a more transparent comparison of the methods, the inputs have been ranked according to the values obtained with each of the methods. The rankings are shown in Table 3. For the most part, the rankings are very similar. The cladding diameter, thickness and creep model rank high with all methods, as well as the uncertainty in the FGR model. Also the set of inputs receiving lowest rankings is very similar. Nevertheless, there are also clear differences. For example, the OAT method ranks the FGR diffusion coefficient first, while the global methods give a ranking between 3 and 4.

The question then arises, whether the difference in the rankings is significant or not. This depends on the intended use of the sensitivity analysis. If the purpose is to identify the most influential input so that its estimate can be improved and the output uncertainty reduced

(factor prioritization setting), then the OAT analysis can be misleading by focusing too much effort on the FGR diffusion coefficient. On the other hand, the set of, say, five topmost inputs is quite similar, so a more loose interpretation of the ranking is still a good indication of their importance. At the same time, in a factor fixing setting, where one wants to rule out non-influential variables, one should not rely on the OAT or the first order measures. Because the first order effects do not detect interactions, it is easy to make false judgements. This is especially true in the present case, where interactions are responsible for about 40 % of the total variance in gap conductance. For example, based on the OAT and first order effects one would be tempted to judge the ALHR insignificant, but examination of the total effect reveals that the ALHR is involved in interactions causing more than 10 % of the total variance.

Table 3. The importance ranking of the inputs for the gap conductance at 22 MWd/kgU.

Parameter	OAT	Pearson	Main effect	Total effect
Clad outer diameter	2	1	1	1
Clad thickness	4	2	2	2
Pellet outer diameter	5	7	7	8
Fuel enrichment	19	19	19	19
Density (% of theoretical)	15	16	21	12
Coolant pressure	18	13	14	15
Coolant inlet temperature	11	14	13	14
Coolant mass flux	17	15	20	17
Fuel thermal conductivity	8	8	8	5
Fuel thermal expansion	6	6	5	6
FGR diffusion coefficient	1	3	3	4
Fuel swelling	14	9	9	9
Clad creep	3	4	4	3
Clad axial growth	13	17	16	18
Clad corrosion	10	11	11	11
Clad H concentration	19	21	17	20
Clad thermal conductivity	9	12	12	13
Clad thermal expansion	19	20	17	20
Gas thermal conductivity	7	5	6	10
Coolant heat transfer	16	18	15	16
Average linear power	12	10	10	7

5. Conclusions

We have analysed a FRAPCON-3.4 simulation of a steady state irradiation scenario of a TMI-1 PWR rod with different sensitivity analysis methods. The methods include a one-at-a-time (OAT) sampling method that is a commonly used simple sensitivity analysis method, the Pearson correlation analysis, and the Sobol' variance decomposition analysis. Apart from the first one, the methods are so-called global sensitivity analysis methods, which sample the whole space of input parameters, and calculate the sensitivity measures as Monte Carlo estimates. We have analysed two outputs from the simulation, the maximum fuel temperature and the gap conductance, both evaluated at the burnup of 22 MWd/kgU.

The analysis of the maximum temperature $T_{\max}$ reveals that with respect to $T_{\max}$, the fuel performance model is almost linear and additive. As a result, the global methods give very similar results. The OAT method performs similarly in ranking, although the absolute values of the sensitivity measures are different. However, an important advantage of the global methods is the ability to control the quality of the analysis by checking the normalization of the sensitivity measures.

Contrary to the temperature, the analysis of the gap conductance h_{gap} reveals strong input interactions, which were already suspected on the basis of the shape of the probability distribution of h_{gap}. These interactions make the OAT, Pearson and first order Sobol' measures largely incomplete and it is difficult to make reliable judgements based solely on these sensitivity measures. Including the total effect index makes the analysis more reliable. Despite the interactions, the overall rankings given by the different methods are quite similar. However, relying on the simpler methods can lead to wrong conclusions. For example, the average linear heat rate would be rated insignificant by all measures except for the total effect, which reveals that it has a significant role in the h_{gap} uncertainty through interactions with other inputs.

6. Acknowledgments

This work was funded by the Finnish Research Programme on Nuclear Power Plant Safety 2015 – 2018 (SAFIR2018).

7. References

[1] Geelhood, K., Luscher, W. and Beyer, C., FRAPCON-3.4: A computer code for the calculation of steady-state thermal-mechanical behavior of oxide fuel rods for high burnup, NUREG-CR-7022 Vol 1, Pacific Northwest National Laboratory (2011).
[2] Geelhood, K., Luscher, W. and Beyer, C., FRAPCON-3.4: Integral assessment, NUREG-CR-7022 Vol 2, Pacific Northwest National Laboratory (2011).
[3] Draper, N. and Smith, H., Applied Regression Analysis, 3rd edition, John Wiley & Sons, New York (1998).
[4] Sobol', I., Sensitivity analysis for non-linear mathematical models, Math. Model. Comput. Exp. 1, 407 (1993).
[5] Borgonovo, E., A new uncertainty importance measure, Reliability Eng. Syst. Safety 92, 771 (2007).
[6] Saltelli, A. and Saisana, M., Setting and methods for global sensitivity analysis – a short guide, Proc. Appl. Math. Mech. 7, 2140013 (2007).
[7] Saltelli, A. *et al.*, Global sensitivity analysis. The Primer., John Wiley & Sons, Chichester (2008).
[8] Ikonen, T. and Tulkki, V., The importance of input interactions in the uncertainty and sensitivity analysis of nuclear fuel behavior, Nucl. Eng. Des. 275, 229 (2014).
[9] Blyth, T., Avramova, M., Ivanov, K., Royer, E., Sartori, E. and Cabellos, O., Benchmark of uncertainty analysis in modeling (UAM) for design, operation and safety analysis of LWRs, Volume II: Specification and support data for the core cases (Phase II) [draft version 1.0], Nuclear Energy Agency, to be published.
[10] Geelhood, K., Luscher, W., Beyer, C., Senor, D., Cunningham, M., Lanning, D. and Adkins, H., Predictive bias and sensitivity in NRC fuel performance codes, NUREG-CR-7001, Pacific Northwest National Laboratory (2009).
[11] Saltelli, A. and Annoni, P., How to avoid a perfunctory sensitivity analysis, Environ. Model. Softw. 25, 1508 (2010).
[12] Sobol', I., Distribution of points in a cube and approximate evaluation of integrals. USSR Computational Mathematics and Mathematical Physics 7, 86 (1967).
[13] Efron, B., Bootstrap methods: another look at the jackknife, Ann. Stat. 7, 1 (1979).
[14] Glen, G. and Isaacs, K., Estimating Sobol' sensitivity indices using correlations, Environ. Model. Softw. 37, 157 (2012).
[15] Saltelli, A., Making best use of model evaluations to compute sensitivity indices, Comput. Phys. Commun. 145, 280 (2002).
[16] Bouloré, A., Struzik, C. and Gaudier, F., Uncertainty and sensitivity analysis of the nuclear fuel thermal behavior, Nuclear Engineering and Design 253, 200 (2012).

FEM MODELLING OF THE PWR CONTROL ROD DRAG FORCES IN DEFORMED GUIDE TUBES

J. KLOUZAL, M. DOSTÁL*
Department of Severe Accidents and Thermomechanics, ÚJV Řež, a. s.
Husinec-Rez 130, 250 68 Rez – Czech Republic

** corresponding author: martin.dostal@ujv.cz*

ABSTRACT

The analysis of mechanical friction force during withdrawal/insertion of control rods into deformed guide tubes in the fuel assembly can be facilitated by the application of the finite element modelling. In order to be able to evaluate the measured data several models of varying complexity were developed at ÚJV Řež using the ABAQUS 6.12 code. A 3D model of single guide tube and absorber rod was found to provide a good compromise in terms of computational speed and model reliability.
This mechanical model can quantify, with certain used assumptions, the friction force between the rod and guide tube for different shapes and amplitudes of the deformation. The results of performed calculations prove that the form of the measured force vs. extraction curve indicates the type of the deformation of the guide tube. It is also shown that global guide tube bow (C-, S-, or W-shape) corresponding to the fuel assembly bow as measured during the poolside inspections may be quite large without reaching critical friction forces. On the other hand, local grid-to-grid bow could increase the probability of incomplete RCCA insertion even for low bow magnitude because the frictional forces are substantially higher than for only global bow applied. The effect of the superposition of these types of the bowing is also discussed.

1. Introduction

The operability of control rods is required to ensure requested shutdown margins and the insertion of negative reactivity within the time interval postulated in the safety analysis. The excessive deformations of the fuel assemblies may result in delayed or incomplete control rod insertion. Several fuel parameters related to this phenomenon may be directly measured, namely the fuel assembly bow and twist, control rod drop times and forces required to withdraw / insert control rods either in the core or in the spent fuel pool. However, these measurements require further analysis of the results in order to assess the margins.

Modelling is quite good instrument for such an analysis. Several ways on how to model control rod drop were published during last decades (e.g. [1]-[6]). These models consider complete process by calculation of mechanical and hydraulic forces during drop to get rod drop time and drag forces, the mechanical forces calculation is a part of coupled calculation approach to get rod drop times. Another issue is the guide tube deformation which can either be prescribed in the model or its evolution during irradiation calculated. The approach presented in this paper is purely mechanical and uses FEM software ABAQUS [7] to calculate friction forces during control rod insertion and removal in the guide tubes with prescribed deformed shape. The influence of guide tube shape on the friction force is shown and a newly proposed methodology is formulated for estimation of the shape and magnitude of the guide distortion based on the forces measured during the shuffling of the rod cluster control assemblies (RCCA) in the spent fuel pool. The model was developed as a supplemental tool to the poolside measurements of the fuel assembly deformations in response to longer than usual RCCA drop times in the assemblies where the distortion measured during the inspections was within the previously encountered area.

The first part of the paper describes used modelling approach, the second section contains examples of calculation results and comparison to other model. In the last section we propose the methodology for estimation of guide tube shape based on the measured forces during control rods removal/insertion from fuel assembly with deformed guide tubes.

2. Modelling approach

The control rod drop can be described by hydraulic and mechanical forces using the equation [3]:

$$ma = mg - F_{fr} - F_{fl},$$

where m is the mass of the rod cluster assembly, a is the acceleration, g is the gravity acceleration, F_{fr} is the mechanical frictional drag force and F_{fl} are the fluid forces (hydraulic drag force and buoyancy force).

Our model calculates F_{fr} using FEM system Abaqus [6] under the assumption that this component is static (independent on rod velocity or acceleration). Symmetrical 3D model of tube-in-tube situation was prepared having the control rod and deformed guide tube. The initial deformation of the guide tube in the model is prescribed to correspond to the state expected at the end of the cycle based on the poolside measurements of the fuel assembly distortions. From the technical point of view, the initial shape is defined either geometrically during guide tube model generation (any shape can be prescribed) or via modelling of creep of the guide tube in the first step of the simulation (before control rod begins moving). In the latter case, forces or displacements in certain points are prescribed as boundary conditions simulating the loading of the guide tube in the core.

The model uses a mirror symmetry along the longitudinal axis, i.e. only half of the circumference of one Guide Tube (GT) is modelled. Insertion or withdrawal is simulated by application of displacement on the top of control rod. The calculated force needs to be multiplied by the number of control rods in the assembly to get the force for the whole cluster. The control rod is assumed to be solid cylinder and the guide tube is modelled as a tube with both ends fixed (no displacement is allowed).

Standard C3D8R (3D Stress) 8-node linear brick finite elements with reduced integration were used in the calculations. Quite rough mesh is used to have short computational time and good convergence (many computations with different meshes were run to show that such a quite coarse mesh is sufficient to get almost the same results with lower computational time cost).

Simple model with beam and pipe elements (as was introduced e.g. in [1]) was also prepared giving very similar results to standard 3D elements.

Materials of the guide tube and control rod are assumed to be elastic only with Young´s modulus of GT 95 GPa and for control rod 205 GPa, Poisson numbers are 0.34 and 0.3). The value of friction coefficient was used 0.3 which lies in the expected range of 0.1 to 0.6 for contact of metal (zirconium) tubes during tube-in-tube contact (e.g. the value used in [1] is 0.5). There were also some calculations with different friction coefficients as shown in chapter 3 to evaluate its influence on calculated forces.

The model was based on the TVSA-T fuel assembly dimensions (VVER-1000) which were used as follows: control rod outer diameter is 8.2 mm, guide tube outer diameter is 12.6 mm and wall thickness 0.9 mm. The lengths are assumed slightly shorter than in reality as no deformation is expected in the area of the top nozzle of the assembly: control rod length is 4.1 m and guide tube length 4 m. Any dimensions can be adopted to verify the model with the measured data.

The example of model with deformed guide tube with C-shape and straight with local bows (between spacer grids) is shown in the Figure 1. Many basic shapes of GT such as C, S, W etc. as well as buckling with the number of the maxima corresponding to the number of the

Spacer Grids (SGs) were considered in calculations. The shape and geometry of GT, whose calculation results are presented in this paper, are summarized in Tab. 1.

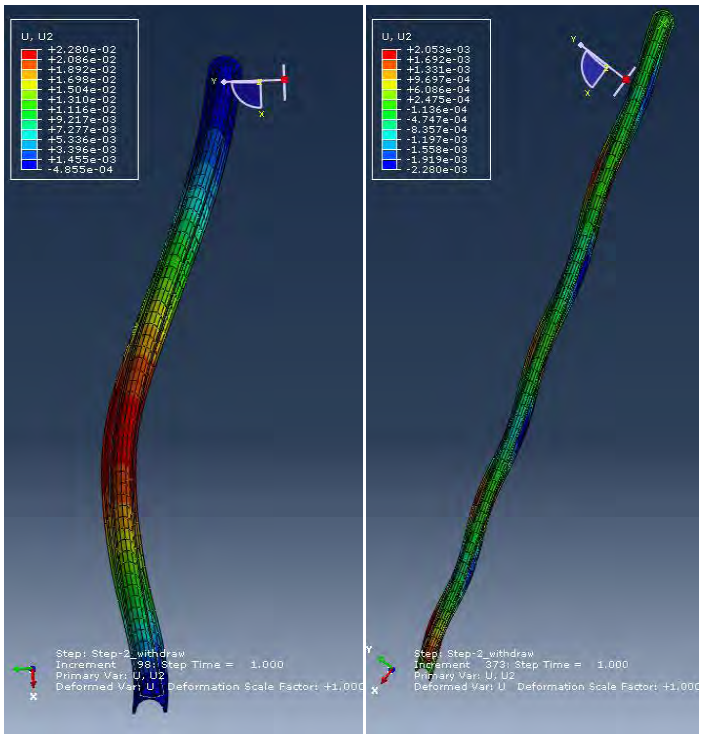

Fig. 1 Example of the deformed guide tube (C-shape bow - left, local bows - right).

Number of bow maxima	1	2	3	4	5	6	7	8
Shape	C	S	W	SS				
Global bows	1x30 mm	2x24 mm	3x13 mm	4x6 mm	5x4 mm	6x3 mm	7x2 mm	8x2 mm
	1x20 mm	2x13 mm		3-10-7-3 mm				
	1x14 mm	7.5mm-5.0mm						
		8mm-4mm						
Local bows	8x1 mm	8x1 mm						
	8x2 mm	8x2 mm						

Tab. 1 Guide tube shapes considered in presented results.

3. Calculation results

The friction forces were calculated for different assumed modes of the guide tube deformation. We have considered basic shapes such as C, S, W as well a buckling with the number of the maxima corresponding to the number of the spacer grids (the summary is given in Tab.1). The calculated force using above described 3D half-model is multiplied by factor of 2 to get the force of one control rod and subsequently by 18 to get the force of whole RCCA which is plotted in the graphs. Calculated friction forces for C-shape of 30 mm bow, S-shape of 24 mm bow, W-shape of 13 mm bow and double S-shape of 6 mm bow are plotted in Fig. 2 (please note that the deformation axes are not the same). It can be seen that pure C-shape even with 30 mm leads to only 130 N force, while a force of around 300 N is achieved for S-shape of 24 mm and W-shape of 13 mm. Please note that force peaks are calculation artifacts due to coarse mesh used.

There are differences in case of pure C-shape where it depends between which spacer grids it is formed. If we assume guide tube with 9 grid positions, the pure C-shape can be constructed between first and last SG which leads to relatively smooth increase of friction force during insertion (the curvature of the GT is smooth) - see Fig. 3. When considering the C-shape between 2nd and 8th SG there are three force increases along the GT length which cause clearly distinguished peaks in frictional force - Fig.3. These increases stem from the curvature change of the GT which are just three (the first one after the 2nd SG, second one in the middle /5th SG/ and the last one in the 8th SG).

Other shapes with 5 to 8 guide tube deformation maximums were assessed as well - Fig. 4 - 5x4 mm means five local bows of 4 mm magnitude. It can be clearly seen that with increasing number of local bows the number of friction force increase steps also grows. The maximum friction force is higher for more local bows with the same magnitude (8x2 mm vs. 7x2 mm).

A uniform buckling (local deformation between the spacer grids) was superimposed on the global deformation (two figures Fig. 5 and Fig. 6 show a combination of 1mm and 2mm local bow with a 14mm C-shape global deformation and 1 and 2 mm on nonsymmetrical 8 and 4 mm “S”). The maximum friction force for the local bow of 2 mm is 10 times higher than for 1 mm local bow which indicate that "threshold" lies between 1 and 2 mm.

Example of non-symmetrical double S-shape with 3-10-7-3 mm bow (Fig. 7) confirms that the friction force increase is proportional to bow magnitude - second force increase is larger than third one (~100 N vs. ~70 N) because the third local bow is larger than the second one (10mm vs. 7mm). The calculated values are very close during simulated insertion and removal (see Fig. 7) which allows to model only rod insertion to reduce computational time and compare it with data from in reactor RCCA insertion/removal.

Different friction coefficients were also assessed for different cases. The impact of higher friction coefficient (0.1; 0.3; 0.5; 0.7 and 0.9 were used) resulted in nearly linear increase of calculated friction force.

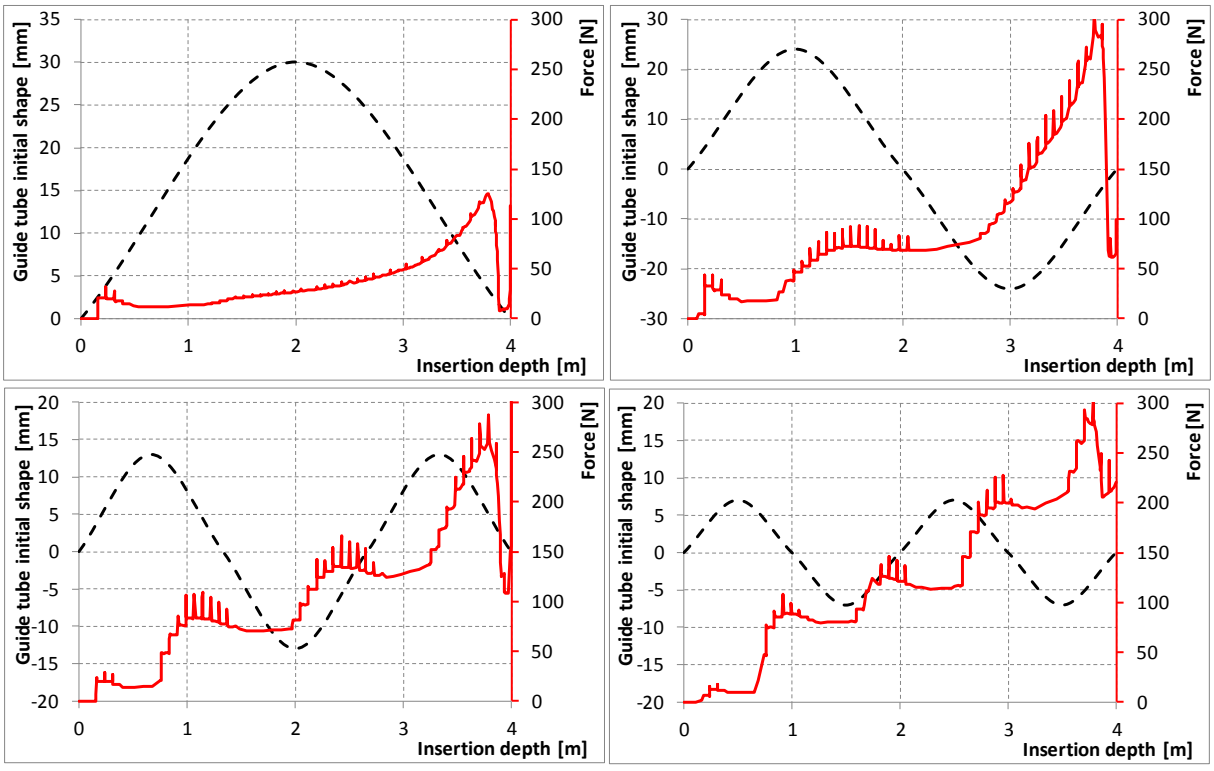

Fig. 2 Calculated friction force for C-bow of 30 mm, S-bow of 24 mm, W-bow of 13 mm and double S-bow of 6 mm.

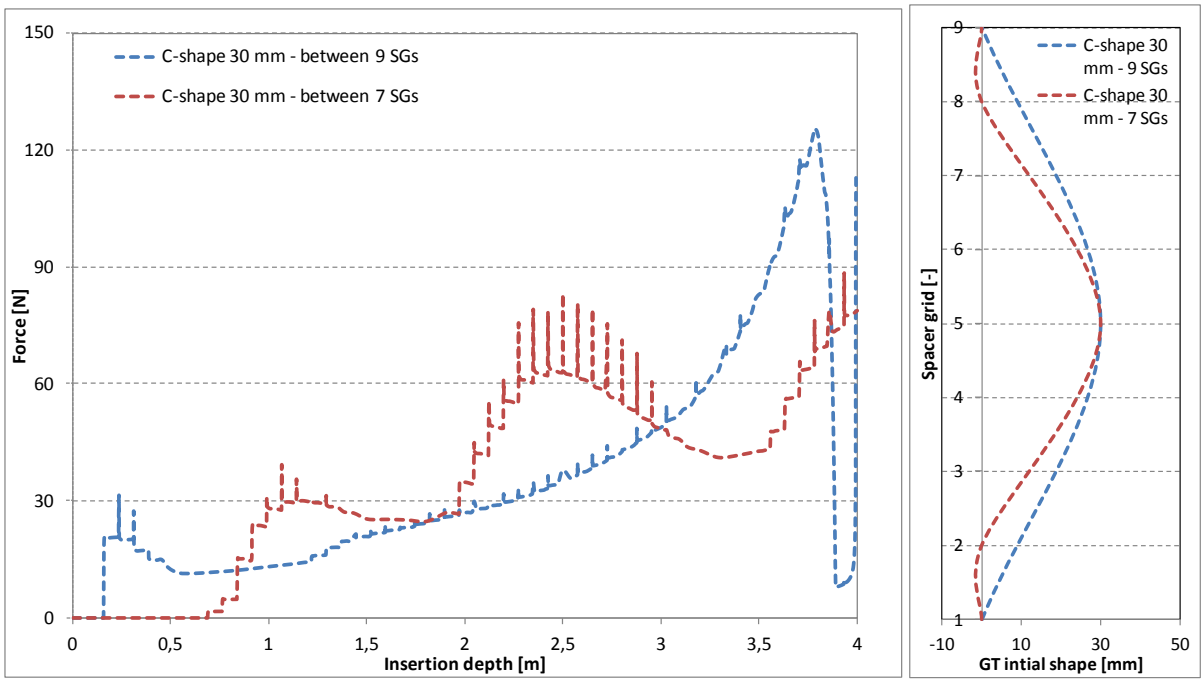

Fig. 3 Calculated friction force for C-shape (between 7 and 9 SGs) bow of 30 mm.

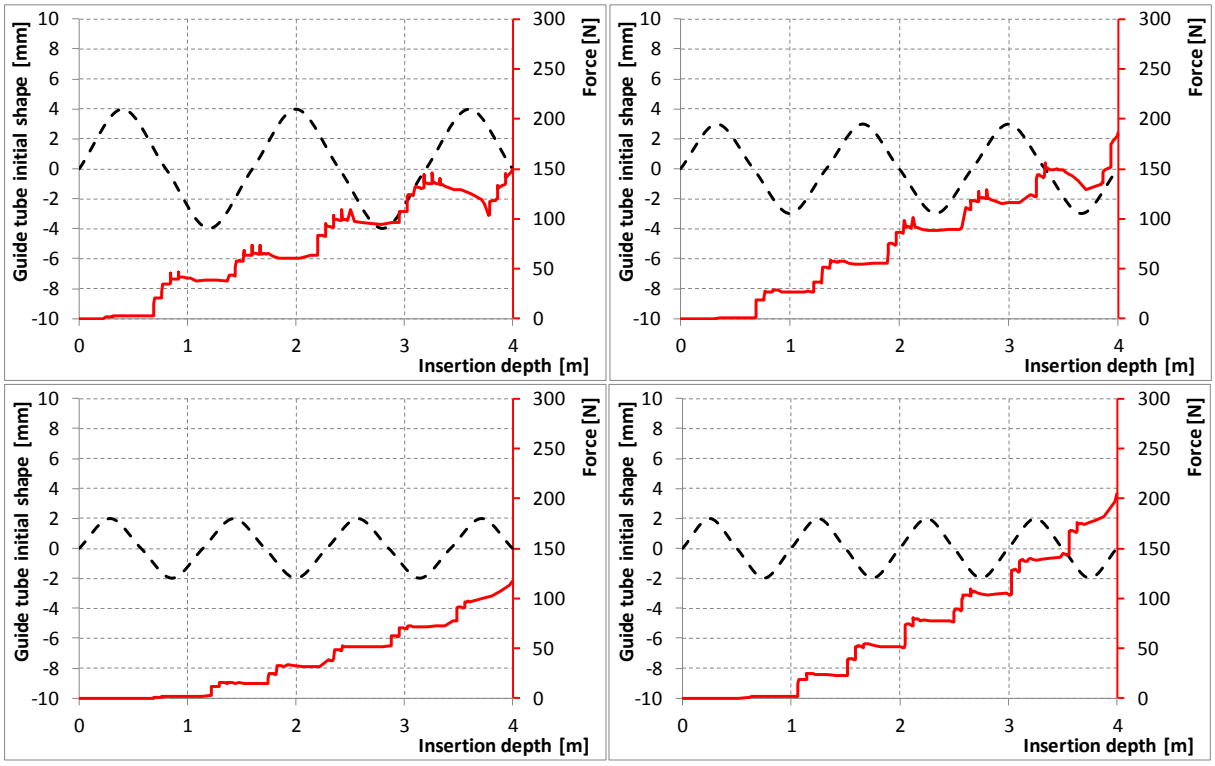

Fig. 4 Calculated friction force for GT bow of 5x4 mm, 6x3 mm, 7x2 mm and 8x2 mm.

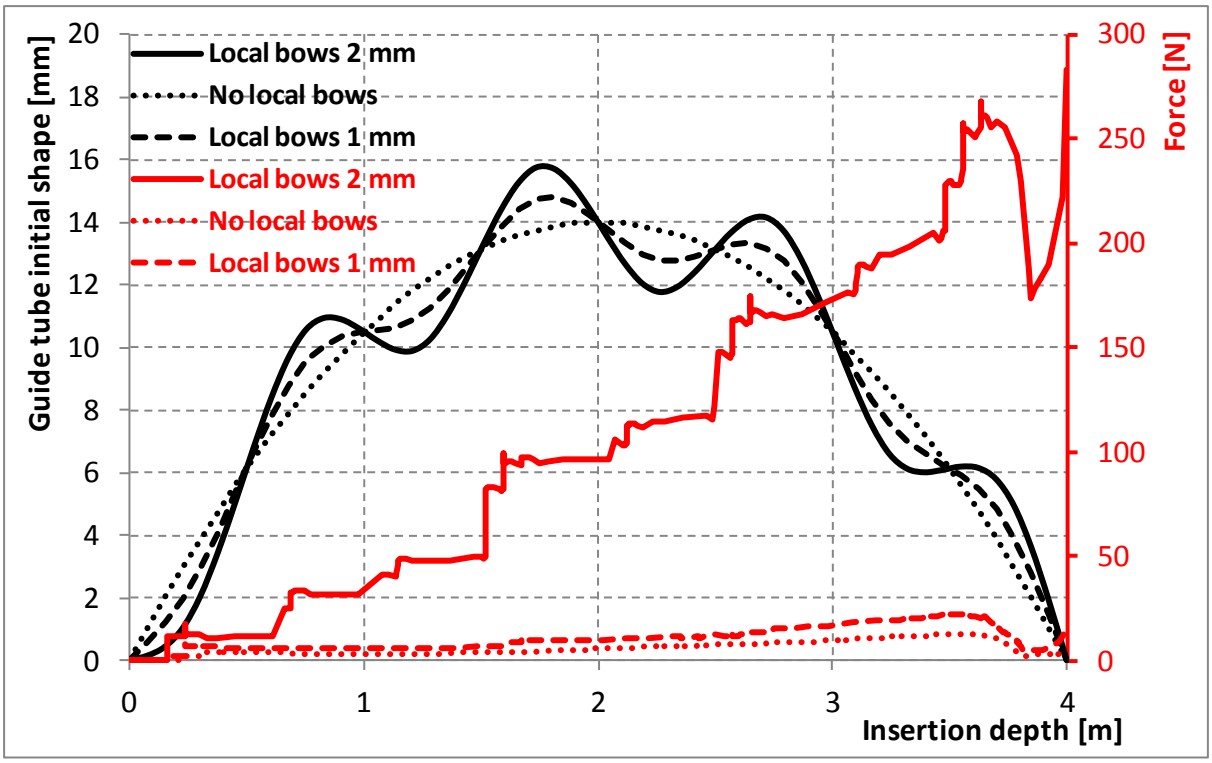

Fig. 5 Calculated friction force for C-shape bow 14 mm /dotted lines/ and for 8 local bows of 1 mm /dashed lines/ and 2 mm /solid lines/ superimposed on C-shape.

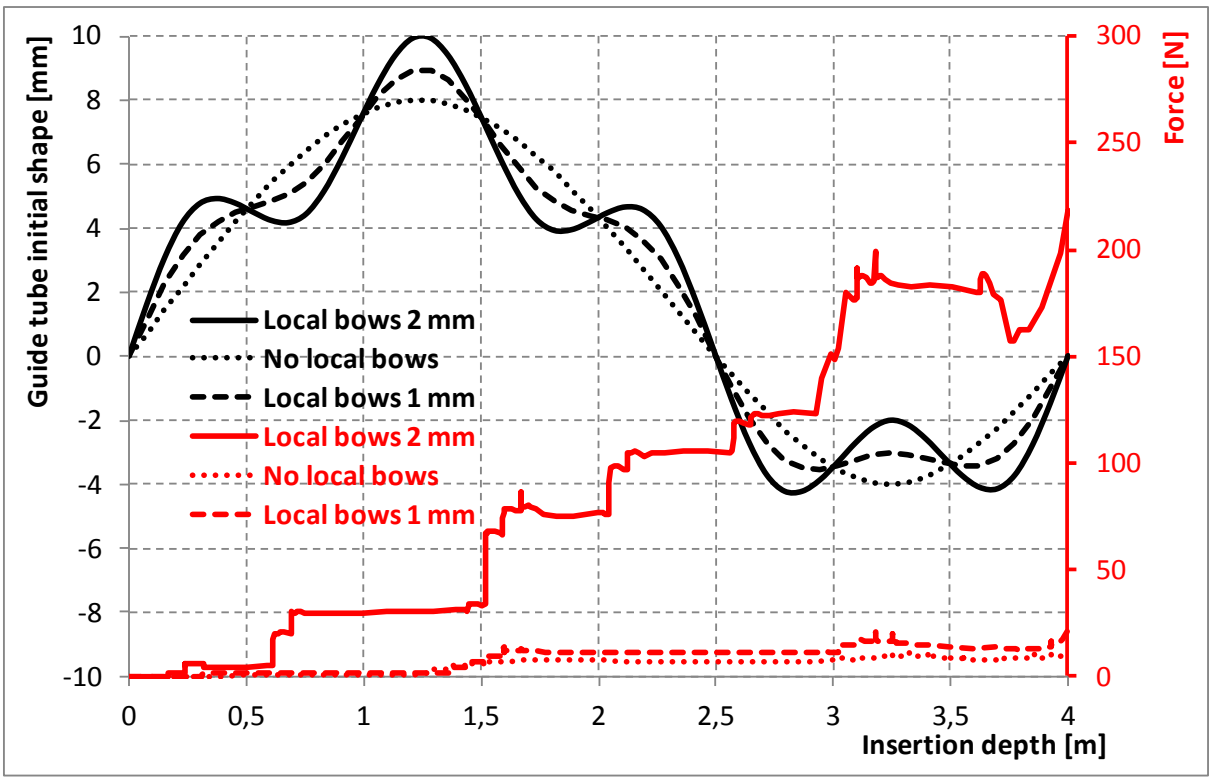

Fig. 6 Calculated friction force for S-shape bow (non-symmetrical 8 and 4 mm) /dotted lines/ and for 8 local bows of 1 mm /dashed lines/ and 2 mm /solid lines/ superimposed on S-shape.

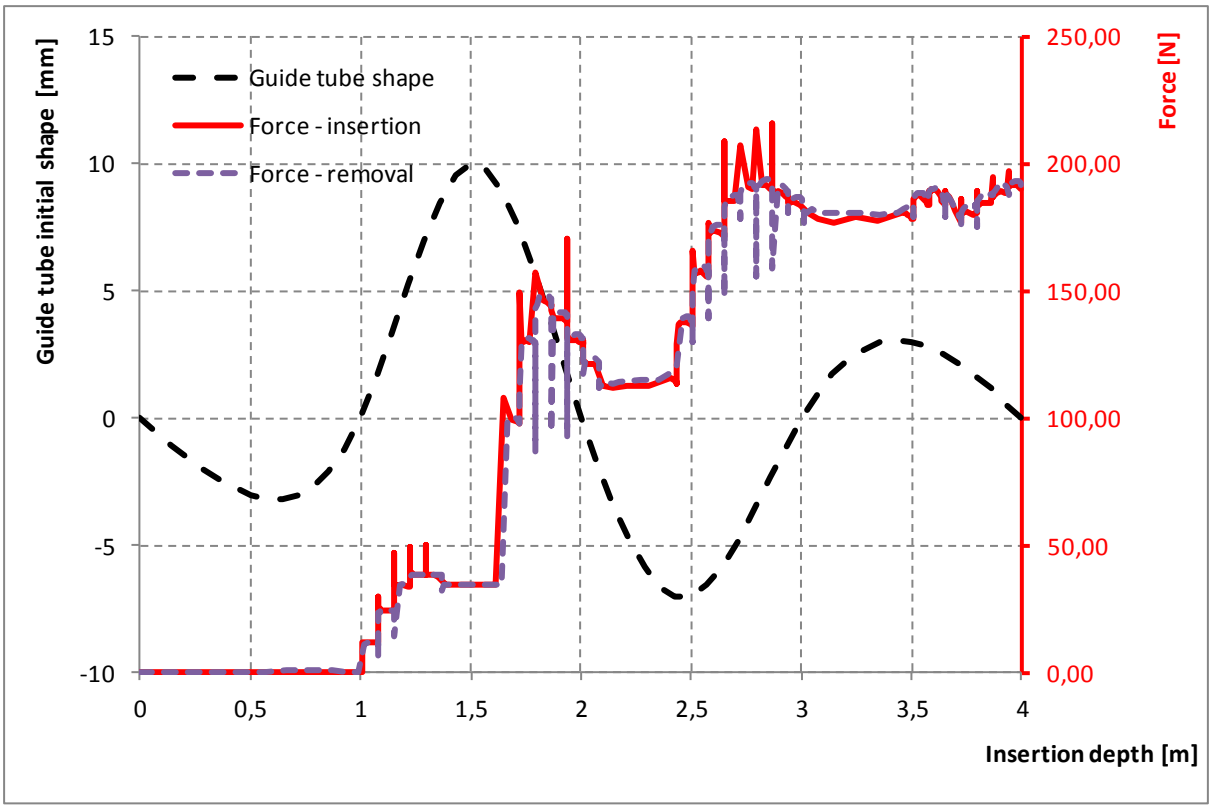

Fig. 7 Double S-shape with 3-10-7-3 mm bow - control rod insertion and removal from guide tube.

Measured data of friction force are usually not publicly presented which makes validation hardly possible and closed data from e.g. NPP measurements from rod drop test or RCCA reshuffling must be used. Ren and Münch [6] presented predictions and measurements of friction forces during RCCA rod drop tests in AREVA´s DISTU test facility for two shapes of fuel assembly bow - C-shape with 20 mm and S-shape with -7.5/+5.0 mm bow. We have used our FEM model (tube-in-tube case) with the same height (3.5 m) and guide tube shape (C-shape bow of 20 mm and S-shape bow of -7.5/+5.0 mm - see Figure 8) and calculated friction force in the assembly is shown in Figure 8 (considering 24 control rods). The comparison with results presented in [5] (these are shown in Fig. 9) shows quite good agreement in the shape of calculated friction force, however, the absolute values of friction force are different because the diameters of rod and guide tube are not known to us (as well as friction coefficient used in [5]).

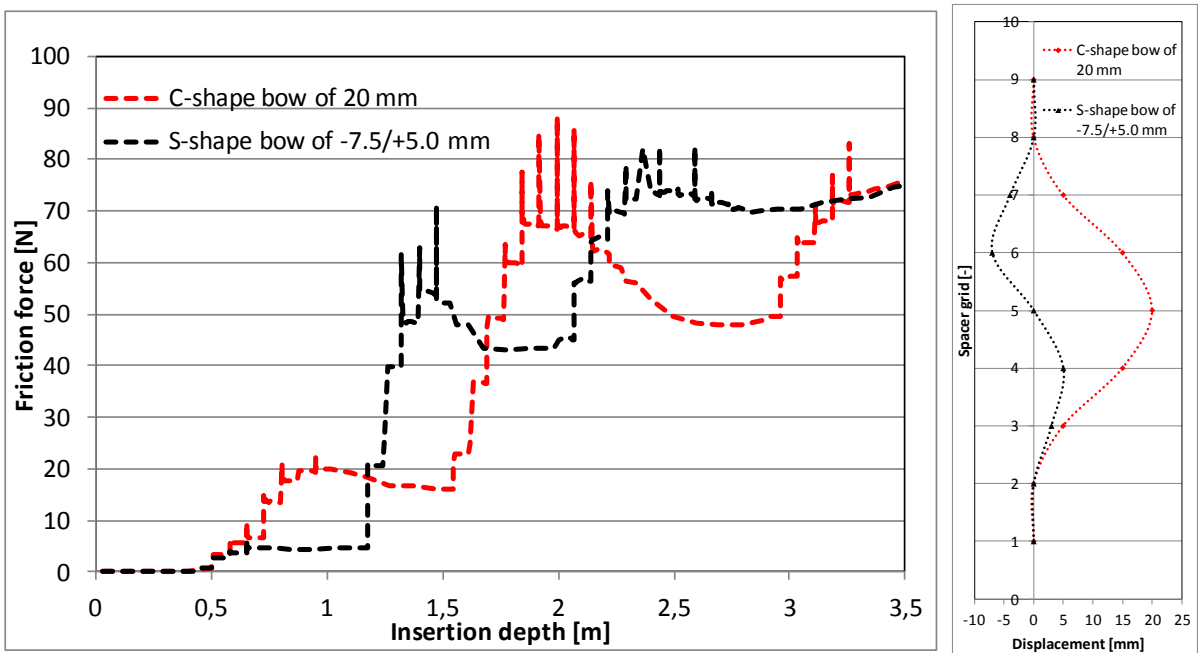

Fig. 8 Calculated friction force for C-shape bow of 20 mm and S-shape bow of -7.5/+5.0 mm and considered bow shape according to [6]; friction coefficient 0.3.

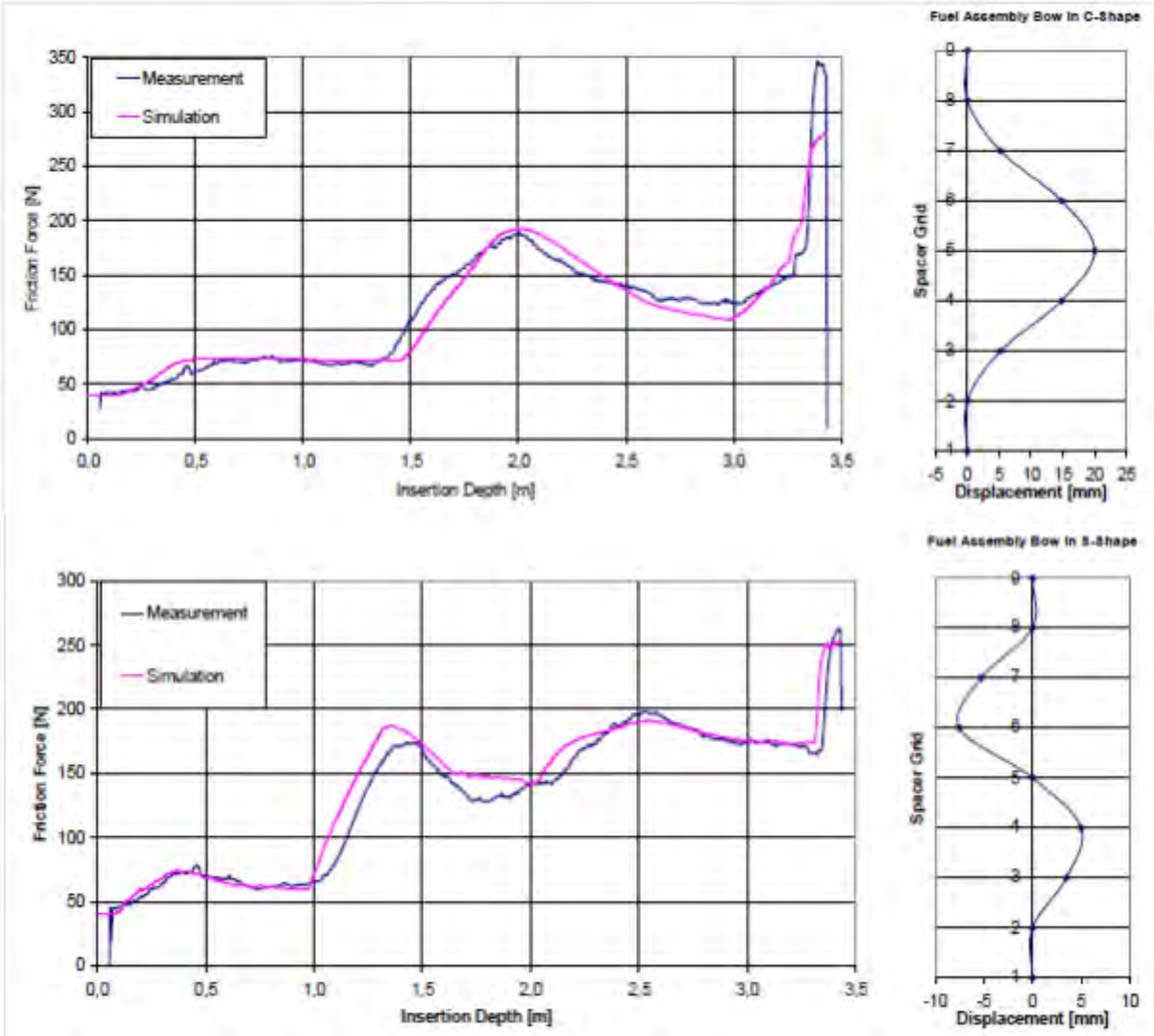

Fig. 9 DISTU quasi-static test with a FA bow of 20 mm in C-shape (upper figure) and bow of -7.5/+5.0 mm in S-shape (lower figure). Picture taken from [5].

4. Methodology of the guide tube deformed shape deduction

Based on the calculations discussed above, it seems possible according to our calculation experience to deduce the probable deformed shape of the guide tube from the measured drag forces during the RCCA withdrawal from the core or during the RCCA reshuffling in the spent fuel pool.

Each sudden change in the drag force is connected with shape curvature change - see e.g. Figure 2 above with the W-shape of GT and corresponding calculated force. It is obvious that during curvature change the force has its increase steps.

The methodology of shape and magnitude deduction from measurement based on FEM mechanical calculations can thus be summarized as follows:

- count number of increase steps of force

- draw them according to their height

- plot a curve with counted number of curvature changes

- make first calculation with default magnitudes of bow

- change the bow magnitudes to get rough agreement with the measurement.

- calculated shape and magnitude is the average for the whole assembly (e.g. 18 guide tubes).

This approach may be used to assess the probable guide tubes bow and, for example, compare it with the poolside fuel assembly bow measurements, compare the difference between the in core guide tube deformation with the one measured in the spent fuel pool on a single assembly or to set up rules restricting high drag force fuel assemblies from the RCCA positions in order to avoid slow or incomplete control rods insertion.

5. Conclusions

The developed 3D FEM mechanical model can quantify the friction force between the rod and guide tube for different prescribed shapes. The results of the performed calculations, with used assumptions, proved that the form of the measured force vs. extraction curve indicates the type of the deformation of the guide tube and the methodology for guide tube deformation shape was deduced. It was also shown that global guide tube bow (C-, S-, or W-shape) corresponding to the fuel assembly bow as measured during the poolside inspections may be quite large without reaching critical friction forces. On the other hand, local grid-to-grid bow could increase the probability of incomplete RCCA insertion even for low bow magnitude because the frictional forces are substantially higher than for only global bow applied.

The developed numerical approach needs to be further validated against the measured data (drag force) for known guide tube deformation. Our next steps will be development of the model for calculation of guide tube deformation development during the fuel assembly irradiation.

6. References

[1] Preliminary Evaluation of Factors Leading to Control Rod Insertion Difficulties. EPRI report TR-110690, May 1998.
[2] A semi-empirical mechanical model for the assessment of control rod insertion problem. AVN Annual Report 1996.
[3] Collard, B. RCCA drop kinetics test, calculation, and analysis. Abnormal friction force evaluation. 7th International Conference on Nuclear Engineering (ICONE), Tokyo, Japan, April 19-23, 1999.

[4] Ren, M., Stabel, J. Analytical Modeling of Control Rod Drop Behavior. Transactions of the 15th International Conference on Structural Mechanics in Reactor Technology (SMiRT-15), Seoul, Korea, August 15-20, 1999.
[5] Ren, M., Münch, C. Predictions of RCCA drop times under consideration of fuel assembly distortions. Transaction of SMiRT-22, San Francisco, California, USA, August 18-23, 2013.
[6] Liu, T. et al. A Method for RCCA Drop Analysis. Proceedings of the 2013 21st International Conference on Nuclear Engineering, ICONE21, July 29-August 2, 2013, Chengdu, China.
[7] ABAQUS 6.12-3. SIMULIA, 2012.

A STUDY ON EFFECTS OF CRYSTALLOGRAPHIC TEXTURE ON THE IRRADIATION GROWTH OF ZIRCONIUM ALLOY USING VISCO-PLASTIC SELF CONSISTENT MODELING APPROACH

W. LIU[1], C.N. TOMÉ[2], R.O. MONTGOMERY[3], and C. STANEK[2]

[1]ANATECH Corp.
5435 Oberlin Dr, San Diego, CA 92121, U.S.A.
wenfeng.liu@anatech.com
[2]Los Alamos National Laboratory
[3]Pacific Northwest National Laboratory

ABSTRACT

A Visco-Plastic Self-Consistent (VPSC) polycrystal plasticity model representing polycrystals by weighted orientations of single crystals has been implemented as a constitutive law in a finite element fuel code BISON-CASL to model the deformation of α-phase zirconium alloy cladding. This paper presents the study of the effects of crystallographic texture on irradiation growth using the VPSC model in BISON-CASL. Texture representations with reduced number of grains are used in the current study. VPSC results have been compared to the $1\text{-}3f_z$ (f_z is the Kearns factor in the axial direction) law, as used in the MATPRO model and the crystallographic texture effects in Franklin's model which is based on in-reactor deformation data. VPSC results have shown that the irradiation growth strain of polycrystal deviates from the $1\text{-}3f_z$ relationship. In comparison to the Franklin's model, the VPSC model has captured the effects of f_r, (the Kearns factor in the radial direction) on the irradiation growth, but suggests a weaker dependency on f_r than that used in the empirical models.

1. Introduction

Irradiation growth has been an important in-reactor deformation mechanism of zirconium-alloy based structure components and fuel cladding materials in Light Water Reactors. The α-phase zirconium has a hexagonal closed-packed (HCP) crystallographic structure. Because of the anisotropy of the microstructures and the anisotropic distributions of the irradiation produced defects in different sinks, zirconium alloys exhibit anisotropic irradiation growth and creep. This results in the strong dependency of irradiation growth on crystallographic texture. It is important to understand the role of as-fabricated texture and irradiation damage on the dimensional change of cladding tube.

The Visco-Plastic Self-Consistent (VPSC) polycrystal plasticity modeling approach, developed by Lebensohn and Tomé [1], has the ability to represent the mechanistic material processes controlling the deformation behavior of the cladding. A critical component of VPSC is the representation of the crystallographic orientation of the grains within the matrix material and the ability to account for the role of texture on deformation. More recently, the irradiation growth model for single crystal Zr developed by Golubov et. al. [2][3] at ORNL has been incorporated into the VPSC framework; the VPSC model has been implemented as a constitutive law in the engineering scale code BISON-CASL (formerly known as Peregrine [4][5]), a fuel performance code developed for US DOE's CASL program [6].

This paper gives the results of modeling irradiation growth using the VPSC model with emphasis on the effects of crystallographic texture on irradiation growth.

2. Methodology

2.1 VPSC Model

The fully anisotropic VPSC polycrystal plasticity model was originally developed by Lebensohn and Tomé [1] and has seen continuous improvements since then. VPSC treats each grain as an ellipsoidal visco-plastic inclusion embedded in an effective visco-plastic medium. Both, inclusion and medium have fully anisotropic properties. The effective medium represents the 'average' environment 'seen' by each grain. When boundary conditions of stress or strain rate are applied to the effective medium, an interaction between medium and grain (embedded inclusion) takes place, and local stresses are induced in the inclusion and its vicinity, which drive the deformation of the inclusion. The stresses, which follow from solving the stress equilibrium equations, are uniform inside the inclusion but deviate from the average stress in the medium depending on the relative properties of medium and inclusion. The 'self consistency' of the approach relies on enforcing the condition that the average stress and strain rate over all the grains has to be equal to the boundary values imposed on the medium.

The propagation of slip dislocations induces plastic shear and no volumetric dilatation. Denoting n^s the normal to the slip plane, and b^s the direction of shear (Burgers vector), the resolved shear stress on the shear plane and along the shear direction associated with the stress tensor σ_{ij}^c acting on the grain is given by [1]

$$\tau_{res}^s = b_i^s n_j^s \sigma_{ij}^c = m_{ij}^s \sigma_{ij}^c \tag{1a}$$

$$m_{ij}^s = \tfrac{1}{2}(b_i^s n_j^s + b_j^s n_i^s) \tag{1b}$$

The strain rate tensor associated with shear rate $\dot{\gamma}^s$ in system *s* is

$$\dot{\varepsilon}_{ij} = m_{ij}^s \dot{\gamma}^s \tag{1c}$$

Neutron irradiation produces vacancies, interstitials and interstitial clusters in Zr alloys, with concentrations far greater than their thermal equilibrium concentrations. These defects eventually are absorbed by sinks, such as forest dislocations and dislocation loops, and produce dimensional changes in the material. When dislocations preferentially absorb vacancies or interstitials, they climb. Dislocation climb may be followed by glide (climb assisted glide) in the presence of a resolved shear stress. Both mechanisms induce dimensional changes, and are called irradiation growth and irradiation creep, respectively, and are driven by a high concentration of irradiation-produced defects.

Irradiation growth is the irradiation-induced dimensional changes that take place in the absence of applied stresses, and is caused by the trapping of vacancies and interstitials by sinks present in the crystal such as dislocations and grain boundaries. Each sink makes a directional contribution to the macroscopic strain, such that the final deformation is anisotropic and volume conserving. In Zr alloys, point defects tend to aggregate into either mobile (glissile) dislocations or immobile (sessile) dislocation loops, making them climb and grow in size, and thereby changing the crystal dimension perpendicular to the plane of the loop.

The strain rate associated with climb of forest and loop dislocation segments is given by [7]:

[1] Unless stated otherwise, throughout this text we use the implicit summation convention: repeated indices in equations denote summation over the range of such indices.

$$\dot{\varepsilon}_{ij}^{(\text{climb})} = \sum_s \rho^s (\hat{l}^s \times \mathrm{v}^s)_i b_j^s \tag{2}$$

Where ρ^s is the dislocation density of class 's', v^s is their climb velocity, b^s is Burgers vector, and $\hat{l}^s$ is the tangent vector along the dislocation line.

Next, for incorporating irradiation creep into the model, we adopt the relatively simple climb-controlled-glide model [8-10]. In this model, the shear rate of a dislocation segment is proportional to the resolved shear acting on the segment and inversely proportional to the time it takes to climb over obstacles. The latter is taken here as the average radius of loops r_{mean} divided by the climb velocity v^s. The shear contributed by a dislocation system is also proportional to the availability of segments, namely, to the density.
The total irradiation creep that results from all dislocations that climb-glide is:

$$\dot{\varepsilon}_{ij}^{\text{creep}} = \sum_s m_{ij}^s \rho^s \frac{m_{kl}^s \sigma_{kl}}{\mu} \frac{v^s}{r_{\text{mean}}} \tag{3}$$

Where μ is the shear modulus; r_{mean} is the mean radius of dislocation loop; r_{mean}/v^s defines the average time it takes for a dislocation to climb over obstacles; σ_{kl} is the stress in the grain; m_{ij}^s is the Schmid tensor that projects the stress onto the slip plane of system s; ρ^s is the glissile dislocation density for this system; and v^s is the climb velocity of the glissile dislocations.

For describing thermal creep, we use a power law in which the shear rates are given by a power of the ratio between resolved shear stress and a threshold stress.

$$\dot{\gamma}^s = \dot{\gamma}_o \left(\frac{m_{kl}^s \, \sigma_{kl}}{\tau_{thres}^s} \right)^n \tag{4}$$

Here $\dot{\gamma}_o$ is a normalization factor and *n* is the rate-sensitivity exponent. When several systems are active in a grain, the strain rate is given by the sum of their shear rates as

$$\dot{\varepsilon}_{ij} = \sum_s m_{ij}^s \, \dot{\gamma}^s = \dot{\gamma}_o \sum_s m_{ij}^s \left(\frac{m_{kl}^s \, \sigma_{kl}}{\tau_{thres}^s} \right)^n \tag{5}$$

Linearizing Eq. (5) inside the domain of a grain gives:

$$\dot{\varepsilon}_{ij} = M_{ijkl}(\sigma) \sigma_{kl} + \dot{\varepsilon}_{ij}^o + \dot{\varepsilon}_{ij}^{growth} \tag{6}$$

where M_{ijkl} and ε_{ij}^o are the viscoplastic compliance and the back-extrapolated term for a given grain, respectively. The linearization of the constitutive response is required to solve the equilibrium conditions between inclusion and medium, and is actually a tangent approximation to the non-linear law Eq. (5). In Ref.[6], we have shown that irradiation creep, thermal creep, and instantaneous plasticity can be expressed in the form of Eq. (5). In Eq. (6) a stress-independent extra term is added in order to account for the irradiation growth rate of the grain. The constitutive law giving the response of the effective medium (polycrystal) is given by a linear relation analogous to Eq. (6):

$$\bar{\dot{\varepsilon}}_{ij} = \bar{M}_{ijkl} \, \bar{\sigma}_{kl} + \bar{\dot{\varepsilon}}_{ij}^o \tag{7}$$

where $\bar{\dot{\varepsilon}}_{ij}$ and $\bar{\sigma}_{kl}$ are overall (macroscopic) magnitudes and $\bar{M}_{ijkl}$ and $\bar{\dot{\varepsilon}}^{o}_{ij}$ are the macroscopic visco-plastic compliance and back-extrapolated rate, respectively. The growth of the polycrystal cannot be separated from the back-extrapolated parameter and the term $\bar{\dot{\varepsilon}}^{o}_{ij}$ accounts for both. The macroscopic moduli are unknown a priori and need to be adjusted self-consistently by enforcing the condition that the stress and strain rate averaged over all grains has to be equal to the stress and strain rate of the effective medium

$$\bar{\dot{\varepsilon}}_{ij} = \left\langle \dot{\varepsilon}^{c}_{ij} \right\rangle \quad and \quad \bar{\sigma}_{kl} = \left\langle \bar{\sigma}^{c}_{kl} \right\rangle \tag{8}$$

2.2 Interface with BISON-CASL

Finite element solution of a mechanical problem involves solving the weak-form equation of the mechanical equilibrium condition. In the BISON-CASL code, which is based on the MOOSE and BISON code systems [11][12], the global residual associated with the weak-form equation is minimized using a variant of the Newton iteration method. To solve the nonlinear deformation problem which involves creep and plasticity, the increment of total strain at each time step is passed to a material model which would compute a trial stress tensor. The trial stress tensor would be used to update the weak form solution until the convergence is reached, i.e., both the weak-form equilibrium equation and the constitutive relationship between stress and strain are satisfied. Such a computational process requires the VPSC model to compute a stress tensor for the increment of total strain. The calculation of the stress at each integration point involves a second, local Newton iteration to solve for the trial stress tensor.

At each time step, knowing the old stress tensor at time t, the problem is to provide an update of the trial stress, the stress computed using the increment of total strain regardless of the code's convergence, at current time t+Δt as shown in following equations.

$$\sigma_{t+\Delta t} = \sigma_t + C\Delta\varepsilon_e \tag{9}$$

$$\Delta\varepsilon_e = \Delta\varepsilon - \Delta\varepsilon_p \tag{10}$$

where, σ_t is the old stress tensor at time t, C is the elastic stiffness tensor of the polycrystal, $\Delta\varepsilon_e$ is the elastic strain increment at time t, $\Delta\varepsilon$ is the total strain increment at time t, $\Delta\varepsilon_p$ is the plastic strain increment computed in VPSC. Residua R is defined in Eq. (11) as:

$$R = C^{-1}\Delta\sigma + \dot{\varepsilon}_p\Delta t - \Delta\varepsilon_t \tag{11}$$

where, $\Delta\sigma = \sigma_{t+\Delta t} - \sigma_t$, $\Delta\varepsilon_t$ is the total strain increment computed by BISON-CASL, and $\Delta\varepsilon_p \equiv \dot{\varepsilon}_p\Delta t$. Newton iteration method is used to compute the trial stress.

$$\Delta\sigma_{k+1} = \Delta\sigma_k - \left(\frac{\partial R}{\partial\Delta\sigma_k}\right)^{-1} R(\Delta\sigma_k) \tag{12}$$

Subscript *k* represents the k_{th} iteration in the local Newton iteration loop to compute the trial stress.

The convergence is determined by following quantities.

$$e_1 = \left|\Delta\varepsilon_t - \Delta\varepsilon_p(\sigma_{tr}) - \Delta\varepsilon_e(\sigma_{tr})\right| \tag{13}$$

$$e_2 = \left|\Delta\varepsilon_t - \Delta\varepsilon_p(\sigma_{tr}) - \Delta\varepsilon_e(\sigma_{tr}) / |\Delta\varepsilon_t\|\right| \tag{14}$$

$$e_3 = \left|\Delta\varepsilon_{t,k} - \Delta\varepsilon_{p,k}(\sigma_{tr,k}) - \Delta\varepsilon_{e,k}(\sigma_{tr,k})\right| / \left|\Delta\varepsilon_{t,1} - \Delta\varepsilon_{p,1}(\sigma_{tr,1}) - \Delta\varepsilon_{e,1}(\sigma_{tr,1})\right\| \tag{15}$$

where, σ_{tr} is the trial stress computed in VPSC, $\Delta\varepsilon_t$ is the total strain increment, $\Delta\varepsilon_e$ is the elastic strain increment, and $\Delta\varepsilon_p$ is the plastic strain increment. In the iteration loop, convergence is detected if any of the three quantities are lower than prescribed tolerances. If a prescribed maximum number of iteration is reached but none of these quantities are lower than prescribed tolerances, the code is considered to be diverged and stops running.

A typical VPSC texture can have a few thousand orientations, which would incur significant computational cost in the finite element code. To optimize running times of BISON-CASL, reduced number of orientations is used. The benchmarking of the implementation of the constitutive models and examples of modeling deformations have been reported in Ref. [6][13].

3. Results

3.1 Comparison with the MATPRO model

A linear relationship between irradiation growth strain and f_z is given as $1-3f_z$, which essentially assumes the projection of the growth strain in the axial direction of each individual grain is linear additive. Such linear relationship has been used to describe the texture effects in terms of the fraction of basal poles in the axial directions f_z in the MATPRO model[14][15]. VPSC calculations for both the single grain and two-grain textures are performed in absence of external stress in a single element with dislocation density of 1.67e11/m^2 and a dose rate of 1.0e-7 dpa/sec, and results are compared with the $1-3f_z$ law as shown in Figure 1.

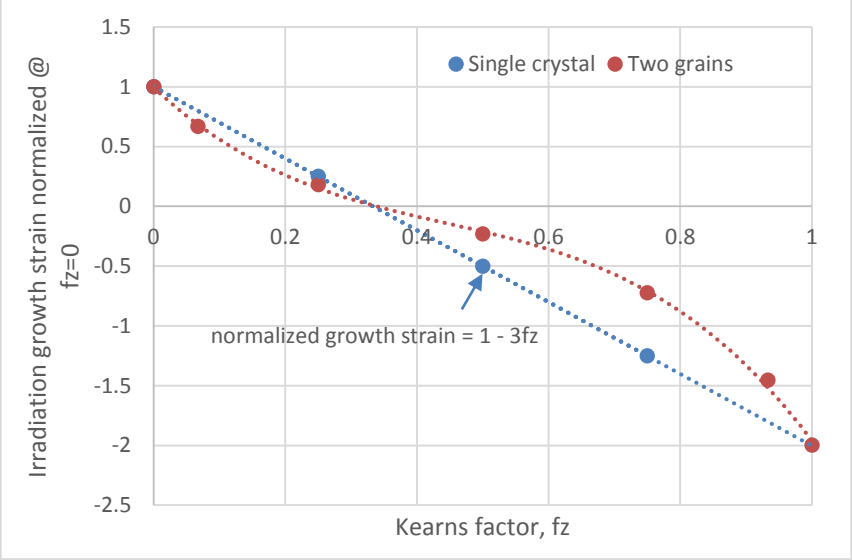

Figure 1 Irradiation Growth Strain (normalized @ f_z=0) versus f_z by VPSC Calculation (one-grain and two-grain results)

The single crystal growth strains match perfectly with the $1-3f_z$ law; however, the irradiation growth strains computed for two-grain texture deviate from the $1-3f_z$ law indicating the effects of the grain-grain interactions.

The irradiation growth of a grain induces reaction stresses that result from the grain interaction with its neighbors. These stresses, in turn, induce creep in the grains, even if at the macroscopic level the material is stress-free. The two phenomena of irradiation creep and irradiation growth become coupled in polycrystalline materials. The VPSC approach having accounted explicitly for these internal stresses and the creep-growth coupling, therefore, is capable of capturing the grain-grain interactions.

3.2 Comparison with Engineering Models

3.2.1 Engineering Approach to Model Clad Elongation

The models derived from the data analysis in a irradiation program on Zircaloy-4 cladding in-reactor deformation [16] are used to compare with the VPSC modeling results. Franklin performed the regression analysis on 72 LWR rods (60 fuel rods and 12 non-fueled rods) from the CE irradiation program and 65 characterized rods from Westinghouse irradiation program [16]. Several empirical models were developed correlating the fractional length change of the cladding tube with the rod average fast neutron fluence and a number of design and material parameters. The correlation that has included the texture effect can be summarized in the following equation:

$$\frac{\Delta L}{L} = A(\phi t)^m [\cos(\theta_{\max})]^n \sigma_y^k \tag{16}$$

Where, ΔL is the rod length change (m), L is the rod length (m), ϕ is fast neutron flux (n/cm^2/sec), E >1 MeV, θ_{max} is the angle between the maximum intensity of basal pole and the radial direction in the radial-circumferential plane (degree), σ_y is clad yield stress (MPa), A, m, k, and n are fitting constants determined by regression analysis.

The reported $\cos(\theta_{max})$ of the characterized test rods ranges from 0.6427 to 0.8746 as shown in Table 1 and Table 2.

Table 1: Elongation data from characterized fuel rods [16]

Vendor	Type	Number of rods[a]	Fluence X10^{-21} n/cm^2 E> 1MeV	Cos(θ_{max})	Yield Stress (MPa)	Hoop Stress (MPa)	ΔL/L
CE	SSM	4	3.07	0.857	497.6	79.82	0.00315
CE	SSM	8	4.28	0.857	497.6	79.82	0.00414
CE	SSM	4	3.06	0.857	497.6	114.27	0.0044
CE	SSM	8	4.28	0.857	497.6	97.05	0.00503
CE	SSM	8	3.97	0.857	497.6	79.82	0.00435
CE	SSM	3	3.05	0.857	497.6	97.05	0.00409
CE	SSM	3	3.86	0.857	497.6	79.82	0.00523
CE	SSM	3	3.85	0.857	497.6	97.05	0.00556
CE	SSM	15	4.16	0.857	497.6	79.82	0.00435
W	W	24	6.72	0.766	612.1	76.77	0.0067
W	W	7	2.88	0.766	612.1	76.77	0.00332
W	W	28	5.11	0.766	612.1	76.77	0.00532
W	W	6	1.61	0.766	612.1	76.77	0.00173

[a] Average value of irradiation growth (ΔL/L) was reported when multiple rods were measured

Table 2: Elongation data from characterized non-fueled rods [16]

Vendor[a]	Type	Number of rods	Fast Fluence X10^{-21} n/cm^2	Cos(θ_{max})	Yield Stress (MPa)	Hoop Stress (MPa)	ΔL/L
CE	SSM	1	3	0.8746	497.6	131.5	0.00413
CE	SSM	1	4.19	0.8746	497.6	131.5	0.00591

CE	SSM	1	3.04	0.8746	497.6	97	0.00351
CE	SSM	1	4.21	0.8746	497.6	97	0.00474
CE	SSM	1	4.19	0.8746	497.6	79.8	0.00466
CE	SSM	1	4.21	0.8746	497.6	79.8	0.00371
CE	WOLV	1	3.05	0.848	440	131.5	0.00368
CE	WOLV	1	4.29	0.848	440	97	0.0038
CE	WOLV	1	4.18	0.848	440	79.8	0.00347
CE	Zirt	1	3.02	0.6427	467.2	131.5	0.00181
CE	Zirt	1	4.18	0.6427	467.2	131.5	0.00281
CE	Zirt	1	4.29	0.6427	467.2	131.5	0.00299

[a] The B&W rods were not individually characterized for length and were not included.

The correlation in Eq. (17) shows that the fractional length increase is proportional to $\cos(\theta_{max})^{1.75}$ when only fast fluence and $\cos(\theta_{max})$ are used as independent variables; the fractional length increase is proportional to $\cos(\theta_{max})^{2.44}$ when the clad hoop stress is also used as an independent variable in the correlation [16].

$$\frac{\Delta L}{L} = 3.69e-17(\phi t)^{0.655}[\cos(\theta_{\max})]^{1.75} \quad (17)$$

A regression analysis to include the effect of yield stress was also performed:

$$\log_{10}\frac{\Delta L}{L} = b + m\log_{10}(\phi t) + n\log_{10}\cos(\theta_{\max}) + k\log_{10}\sigma_y \quad (18)$$

The results of the fitting parameters are provided in Table 3.

Table 3: Fitting parameters in the irradiation growth model determined from regression analysis

	k	***n***	***m***	***b***
All rods	0.725	1.822	0.853	-4.69
Non-fueled rods	1.118	1.629	0.663	-5.66

3.2.2 VPSC Analysis using Two Grain Representation

The material characterization information in the elongation data [16] did not provide sufficient details, but only the θ_{max} or $\cos^2(\theta_{max})$ (the Kearns factor in the radial direction). Therefore, the texture effect on the irradiation growth was examined using the two-grain texture representation without basal poles in the axial direction. Table 4 shows the input crystallographic parameters for the different textures used for the simulation.

Table 4: Input crystallographic parameters for different texture

θ_{max} (degree)	f_r[a]	Euler angles (degree) of rotation[b]
30	0.7500	(150, 90, 0), (210, 90,0)
35	0.6710	(145, 90, 0), (215, 90, 0)
40	0.5868	(140, 90, 0), (220, 90, 0)
45	0.5000	(135, 90, 0), (225, 90, 0)
50	0.4132	(130, 90, 0), (230, 90, 0)

[a] Fraction of basal poles in radial direction

[b]The texture file describes the fraction of crystals with basal poles in certain direction in terms of Euler angles in three consecutive rotations: a) The first angle is the angle of rotation around the axis Z; b) The second angle is the angle of rotation around the axis X in the new coordinate system; and c) The third angle is the angle around the axis Z in the new coordinate system.

Different initial dislocation densities (ρ_d=1.67e11/m^2 and ρ_d=1.67e12/m^2 respectively) are used to represent cladding alloys with different degree of cold work; a constant dose rate of 1.0e-7 dpa/sec is used in the calculations. At the irradiation dose of 5 dpa (neutron dose equivalent to a fast fluence of ~1x10^{22} n/cm^2), all irradiation growth strains are normalized by the growth strain computed at θ_{max}=30°.

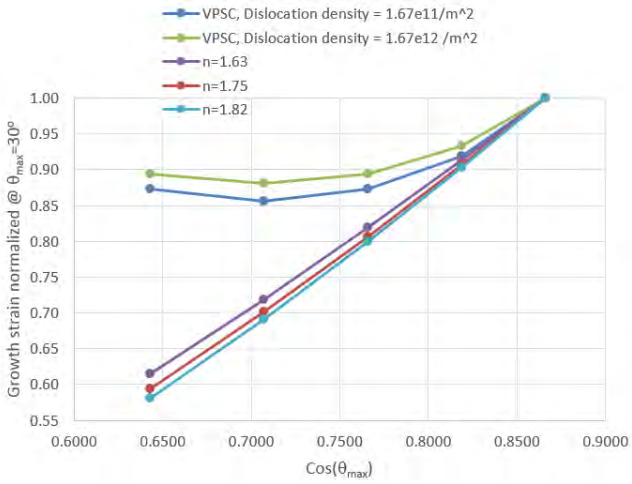

Figure 2: Comparison between results of engineering models and VPSC calculations in modeling irradiation growth with different θ_{max} at 5 dpa

A comparison between the engineering models (*n*=1.63, 1.75, and 1.82 respectively) and VPSC calculations is shown in the Figure 2. It appears that the two modeling approaches only have agreement in a limited range of θ_{max} with higher values of cos(θ_{max}), and a large discrepancy is noticeable at lower values of cos(θ_{max}) or larger θ_{max} for the zirconium alloys with different degree of cold work as represented by different initial dislocation densities.

The strong dependency on the cos(θ_{max}) is not observed in the VPSC modeling results, which indicates the power law function of cos(θ_{max}) in the empirical correlation of irradiation growth model may not be applicable.

Using the information gained from the VPSC model, an attempt was made to modify the empirical correlation using the following equation:

$$\frac{\Delta L}{L} = 8.14\times10^{-8}(\phi t)^{0.85}[\cos(\theta_{\max} - \pi/4)]^{0.503}\sigma_y^{1.73} \qquad (19)$$

The comparison between the measured strain and the calculated strain using the model parameters in Table 3 for all rods is shown in Figure 3; and the comparison between the measured strain and the calculated strain using the new model Eq. (19) is shown in Figure 4. The fitting results are still comparable to the old regression analysis results; the new equation (Eq. 19) indicates a strong dependency on the yield stress (k=1.73 as compared to k=0.725 in the old model), and a similar dependency on the fast neutron fluence (m=0.850 as compared to m=0.853 in the old model).

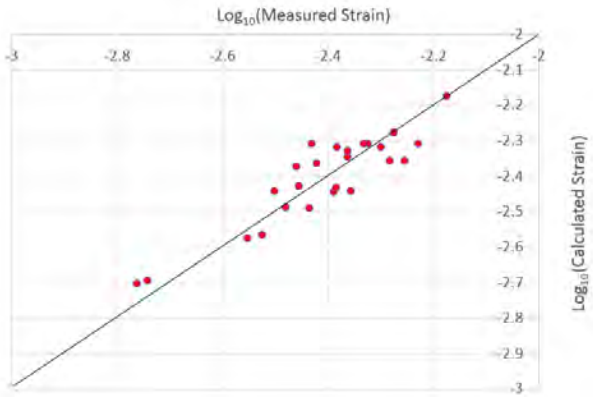

Figure 3: Comparison between the Log_{10}(Calculated Strain using Franklin model) and Log_{10}(Measured Strain)

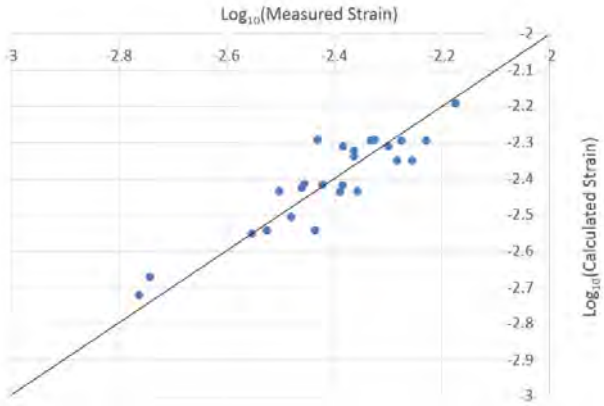

Figure 4: Comparison between the Log_{10}(Calculated Strain using New regression model) and Log_{10}(Measured Strain)

Examination of the measurement data has shown that among all the non-fueled rods, only three out of the twelve non-fueled rods have $\cos(\theta_{max}) = 0.6427$; and all the other cases have $\cos(\theta_{max})$ in the values of 0.848 and 0.8746. The measured clad elongation of the fuel rods however may have included some effects due to the pellet-clad interaction. Those limitations in measurements could also have limited the fidelity of the empirical models.

4. Summary and Conclusions

A VPSC polycrystal plasticity model representing polycrystals by weighted orientations of single crystals has been implemented as a constitutive law in a finite element fuel code BISON-CASL to model the deformation of α-phase zirconium alloy cladding. This paper describes a multi-scale modelling approach to study the irradiation growth of zirconium alloys with an emphasis on the effects of crystallographic texture on irradiation growth. Texture representations with reduced number of grains are used in the current study.

VPSC results have been compared to both the $1\text{-}3f_z$ law, as used in the MATPRO model and the crystallographic texture effects observed in Franklin's model which is based on in-reactor deformation data. VPSC results have shown that the irradiation growth strain for polycrystals deviates from the $1\text{-}3f_z$ relationship. In comparison to the Franklin's model, the VPSC model has captured the effects of f_r, (the Kearns factor in the radial direction) on the irradiation growth, but suggests a weaker dependency on f_r than that used in the empirical models.

5. Acknowledgements

The submitted manuscript has been authored by a contractor of the U.S. Government under Con tract DE-AC07-05ID14517. Accordingly, the U.S. Government retains a non-exclusive, royalty-fr ee license to publish or reproduce the published form of this contribution, or allow others to do so , for U.S. Government purposes.

References:

1. R. Lebensohn and C.N. Tomé, Acta Metallurgica et Materialia, Vol. 41, No. 9, (1993).

2. S.I. Golubov, A.V. Barashev, R.E. Stoller, B.N. Singh, "Breakthrough in Understanding Radiation Growth in Zirconium", 17th International Symposium on Zirconium in the Nuclear Industry, ASTM STP (2013).

3. S.I. Golubov, A.V. Barashev, R.E. Stoller, “On the Origin of Radiation Growth in HCP Crystals”, ORNL/TM-2011/473, (2011).

4. R.O. Montgomery, et. al., “Peregrine: Advanced Modeling of Pellet-Cladding Interaction (PCI) Failure in LWRs,” Proceedings of the TopFuel 2012 Reactor Fuel Performance Meeting, Manchester, U.K., Sep. 2-6, (2012).

5. R.O. Montgomery, C. Stanek, W. Liu, and B. Kendrick, “US DOE CASL Program Fuel Performance Modeling for Steady State and Transient Analysis of LWR Fuel,” IAEA Technical Meeting “Modelling of Water-Cooled Fuel Including Design-Basis and Severe Accidents” Chengdu, China, (2013).

6. W. Liu, R.O. Montgomery, and C.N. Tomé, “Demonstration of Atomistically-informed Multiscale Zr Alloy Deformation Models in Peregrine for Normal and Accident Scenarios”, CASL-U-2014-201-000, (2014).

7. C.H. Woo, “Polycrystalline Effects on Irradiation Growth and Creep in Textured Zirconium,” Journal of Nuclear Materials, v131, p.105, (1985).

8. J.H. Gittus, “Theory of Dislocation Creep for a Material Subjected to Bombardment by Energetic Particles,” Philosophical Magazine, v30, p.751-764, (1974).

9. J.H. Gittus, "Theory of Dislocation-creep Due to the Frenkel Defects or Interstitialcies Produced by Bombardment with Energetic Particles," Philosophical Magazine, v25, p.345-354, (1972).

10. P.T. Heald and J.P. Harbottle, “Irradiation Creep due to Dislocation Climb and Glide,” Journal of Nuclear Materials 67, p. 229 (1977).

11. D. Gaston, C. Newman, G. Hansen, and D. Lebrun-Grandie, “MOOSE: A parallel computational framework for coupled systems of nonlinear equations,” Nuclear Engineering and Design, v239, p. 1768–1778, (2009).

12. R.L. Williamson, J.D. Hales, S.R. Novascone, M.R. Tonks, D.R. Gaston, C.J. Permann, D. Andrs, and R.C. Martineau, “Multidimensional Multiphysics Simulation of Nuclear Fuel Behavior,” Journal of Nuclear Materials., 423, p. 149-163, (2012).

13. W. Liu, R.O. Montgomery, C.N. Tomé, C. Stanek, and J.D. Hales, “VPSC Implementation in BISON-CASL Code for Modeling Large Deformation Problems,” International Conference on Mathematics and Computation (M&C), Nashville, TN, U.S.A., April 19-23, (2015).

14. R.B. Adamson, R.P. Tucker, and V. Fidleris, “High-Temperature Irradiation Growth in Zircaloy,” ASTM STP 754, American Society for Testing and Materials, p. 208-234, (1982).

15. D.T. Hagrman, “MATPRO - A Library of Materials Properties for Light Water Reactor Accident Analysis,” SCDAP/RELAP5/MOD3.1 Code Manual, Vol 4, NUREG/CR-6150, EGG-2720, June (1995).

16. D.G. Franklin, “Zircaloy-4 Cladding Deformation during Power Reactor Irradiation,” ASTM STP 754, American Society for Testing and Materials, p.235-267, (1982)

FUEL ASSEMBLY SEISMIC AND LOCA SAFETY ANALYSIS UNDER END OF LIFE CONDITIONS AND FLOWING WATER DAMPING EFFECTS

R. Y. LU, N. E. MARSHALL, J. X. JIANG and P. M. EVANS
Nuclear Fuel, Westinghouse Electric Company
5801 Bluff Road, Hopkins, SC 29061 USA

ABSTRACT

For a fuel assembly with zirconium alloy grids, irradiation causes small gaps to form between rods and grid supports. Therefore, an irradiated fuel assembly has different dynamic characteristics compared to a fresh fuel assembly. The gapped grids reduce grid dynamic impact stiffness, local impact stiffness and crush strength. Also, due to gapped grids, both the fuel assembly natural frequencies and stiffness are reduced. All these parameter changes have a combined effect on fuel assembly seismic and loss of coolant accident (LOCA) impact forces and safety margins. The NRC issued IN 2012-09, "Irradiation Effects on Fuel Assembly Spacer Grid Crush Strength", [1] in June 2012 which challenges approved assumptions based on the beginning of life conditions in seismic and LOCA analysis. The NRC is currently in the process of clarifying the guidance provided in Standard Review Plan 4.2 to require consideration of the end of life condition effects on fuel assembly seismic/LOCA evaluations.

Low fuel assembly natural frequencies will increase fuel assembly impact forces under seismic events but decrease impact forces in LOCA events in general. Westinghouse currently uses the fuel assembly damping value equivalent to that in still water in seismic/LOCA analysis. The fuel assembly damping in flowing water is significantly higher than in still water. The damping in flowing water can be applied to reduce impact forces in seismic events. Fuel assembly damping vs. flow rate curve is important when reactor coolant pump coast-down is considered in a seismic event. Some parametric studies are presented in the paper.

1. Introduction

For a fuel assembly with zirconium alloy grids, irradiation causes small gaps to form between rods and grid supports. Therefore, an irradiated fuel assembly has different dynamic characteristics compared to a fresh fuel assembly. The gapped grids change grid and fuel assembly mechanical and dynamic characteristics. All of these changes have a combined effect on fuel assembly seismic and loss of coolant accident (LOCA) impact forces and safety margins. The NRC issued IN 2012-09 [1] in June 2012 which challenges approved assumptions based on the beginning of life (BOL) conditions in seismic and LOCA analysis. The NRC is currently in the process of clarifying the guidance provided in Standard Review Plan 4.2 to require consideration of the end of life (EOL) condition effects on fuel assembly seismic/LOCA evaluations.

2. Effects of Irradiation on Grid and Fuel Assembly

NRC Information Notice (IN) 2012-09 was issued in June 2012. The IN raises questions that extend beyond current licensed seismic/LOCA methodologies (NUREG-0800, Section 4.2 Appendix A) [2], which are based on Beginning-Of-Life conditions. The IN questions that the strength of the fuel assembly spacer grids may decrease during the irradiation of a fuel assembly.

For a fuel assembly with zirconium alloy grids, irradiation causes grid growth, grid cell spring relaxation and fuel rod creep. Therefore, a small gap to form between the rod and grid supports at early EOL and EOL. The primary EOL fuel assembly effect is gap formation between the grid and rod, which decreases grid buckling (or crush) strength and changes the dynamic properties of a fuel assembly. Both of these effects act to reduce margin to grid buckling under seismic loads. Therefore, an irradiated fuel assembly has different dynamic characteristics than a fresh fuel assembly.

2.1 Grid Mechanical Characteristics at End of Life Conditions

Irradiation not only forms the cell gaps for zirconium alloy grids, but also causes some material property changes, such as material ductility due to hydrogen pickup, material thinning due to oxidation and material strength increasing due to irradiation. For irradiated zirconium material, yield strength increases significantly.

Reference [3] reported “there are no indications that the strength reduction results from material property degradation. In fact, the irradiated grids have a more pronounced elastic response that reflects a material hardening due to irradiation. The main contributor to the decrease in buckling strength appears to be a reduction in grid spring force with irradiation.” “The EOL grid condition is well simulated by the spring relaxation method, i.e., the test results are well correlated between actual and simulated EOL grids, and grid ductility is retained as was observed in the hot cell testing.” [4]

The primary EOL effect is gap formation between the grid and rod. The grid dynamic buckling/crush tests with gapped cell sizes are performed. Figure 1 shows the test apparatus. The grid cells were thermally sized in a furnace with proper stainless steel pins in each cell. The target value of cell sizes were based on cell size post irradiation examination (PIE) data.

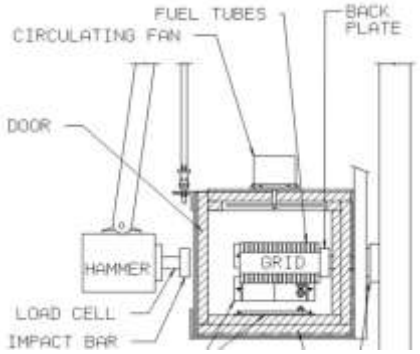

Fig. 1: Grid Dynamic Buckling/Crush Test Apparatus

Grid dynamic buckling/crush tests show that the buckling/crush strength of EOL decreases more than 20% compared to BOL and stiffness is also decreased. The grid buckling mode of EOL is the same as that of BOL. Grid straps buckled at the strap intersections and cells change from square to parallelogram as in Figure 2. Thimble tube inner diameters were measured before and after tests and had no elastic deformation.

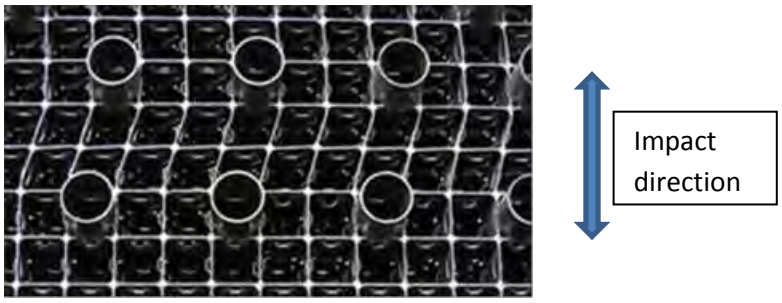

Fig. 2: Grid buckling model

2.2 Fuel Assembly Dynamic Characteristics at End of Life Conditions

The fuel assembly dynamic characteristics, stiffness, modal frequencies and modal shapes, are obtained by fuel assembly mechanical and dynamic tests with a full size fuel assembly. The test results are the key parameters used to benchmark fuel assembly analytic models, which are used in seismic/LOCA analysis code. When fuel assembly grids reduce or lose the preload and friction force on fuel rods at EOL conditions, the rods significantly reduce their contribution to the fuel assembly stiffness, which results in significant fuel assembly modal frequency reduction.

Fuel assembly mechanical tests are performed in air and room temperature conditions. The grid cells were thermal relaxed as described in grid impact tests before fuel assembly was built in order to simulate EOL conditions. The test setup is shown in Figure 3. The fuel assembly is held by simulated lower and upper core plates with a typical axial hold down force. The comparisons fuel assembly modal frequencies at BOL and EOL are shown in Figure 4.

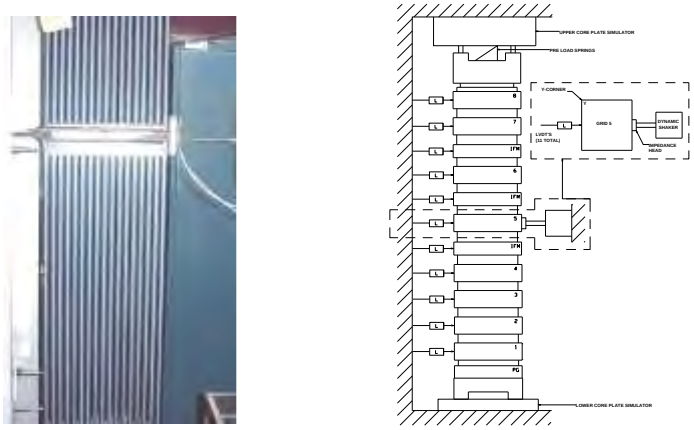

Fig. 3: Fuel assembly mechanical and dynamical test setup

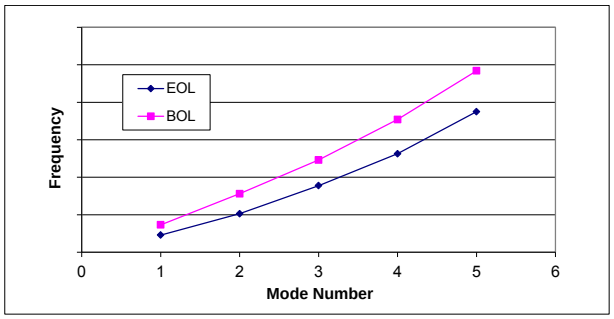

Fig. 4: Modal frequency comparison, BOL and EOL

Fuel assembly lateral impact tests were performed to determine the fuel assembly grid to baffle impact characteristics with the top and bottom nozzles constrained with in core boundary conditions. The test was designed to simulate assembly to baffle impacting at the central mid grids and IFM grids. These grids were positioned to impact into rigid plates. The testing procedure consisted of displacing the central structural grid of the fuel assembly to a predetermined amount relative to its initial equilibrium position. The fuel assembly was then suddenly released and allowed to impact against solid constraints. This test measured the fuel assembly grid impact force and corresponding impact time, and determined the fuel assembly grid impact characteristics.

The comparison of the impact test results between the assembly with EOL conditions and with BOL conditions are shown in Figure 5. Due to gapped cells (lower grid stiffness), the local grid impact force reduced and the impact duration time increased. The main reason for lower impact force at EOL is the lower elastic potential energy. A softer assembly stores less energy than a stiffer assembly for the same displacement. The impact test results will provide the benchmark for fuel assembly impact models.

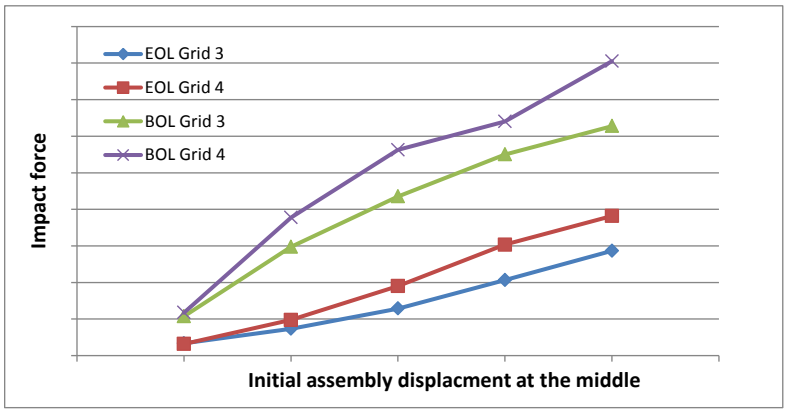

Fig. 5: Impact force comparison, BOL and EOL

3. Flowing Water Damping

PWR fuel assembly damping is a key parameter in seismic/LOCA safety analysis. The damping coefficients of a fuel assembly in air, still water and flowing water are significantly different. Several researchers and engineers have published their results and methods in the past [5, 6, and 7]. Typical fuel assembly damping values in different medium including air, still water and flowing water are shown in Figure 6. The fuel assembly damping in air gives the damping component of assembly structural damping. The damping in still water is the summation of structural damping and viscous damping. The viscous damping component is the effect of still water on damping. The damping is significantly affected by flowing water. For relatively low flow velocities, the damping coefficient is around two times the damping in still water. For high velocities and large displacement, the damping coefficient can be over 3 times higher than that in still water. The flow velocity appears to be acting on the system by suppressing the motion of the assembly. Additional damping due to flowing water is called hydraulic damping, which is generated by hydraulic force. When a fuel assembly vibrates in flowing water, the assembly is trying to change the flow direction and momentum, but the flow mass wants to retain its pure axial direction which suppresses the motion of the assembly.

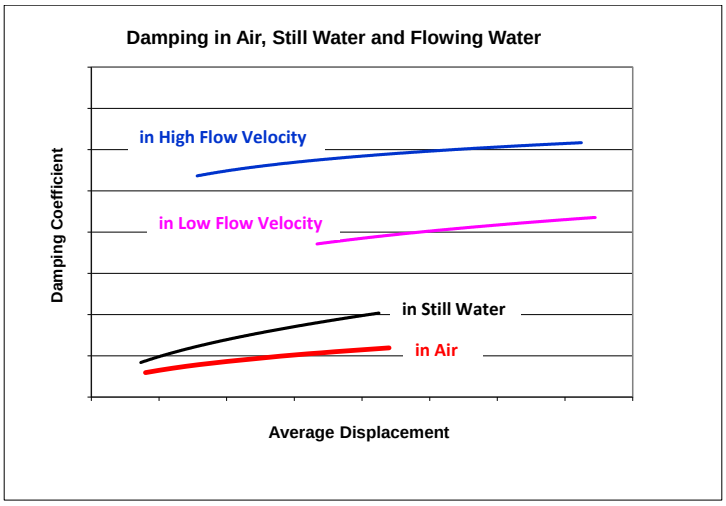

Fig. 6: Typical fuel assembly damping values in air, still water and flowing water

Applying higher damping due to the flowing water effect can significantly reduce fuel assembly impact forces. However, during a seismic event the reactor coolant pumps may trip resulting in a coast-down. As such, reduced flow rates that occur during the pump coast-down must be considered. The worst situation is a loss of AC power from both the grid and the plant turbine generator. Conservative damping values should be used in seismic analysis to demonstrate the control rod insertability.

4. Fuel Assembly Seismic and LOCA Analysis

Three 17x17 Westinghouse standard fuel models were generated to perform seismic/LOCA parametric analyses and evaluate EOL and flowing water damping effects. Table 1 gives a summary of the three models. Two typical seismic/LOCA loading core plate motions, corresponding to a 3-loop and a 4-loop nuclear plants, are used in the parametric study.

Table 1: Summary of 17x17 Westinghouse standard fuel models

Model ID	Model Name	Model main Characteristics
1	BOL-SW	BOL condition, still water damping
2	EOL-SW	EOL condition, still water damping
3	EOL-FW	EOL condition, flowing water damping

In the parametric studies, the impact forces and displacements of three models, with different numbers of fuel assemblies in a row, were calculated for two Safety Shutdown Earth Quake (SSE)/LOCA loading cases (core plate motions). The grid impact force results are presented in Figures 7 and 8. Grid impact forces due to a LOCA event are just shown in one horizontal direction since the forces are small in the other direction. Grid impact forces due to a seismic event are normally similar in both horizontal directions and only the results in one direction are shown. The results of a 4-loop plant with moderate seismic/LOCA loads are shown in Figure 8.

In general, the existing 3-loop plant designed by Westinghouse has relatively large LOCA loads. Under LOCA core motion, the two EOL models (assuming with still water and flowing water damping) have lower impact forces than the BOL model for any row. High damping has no significant effect on the results of EOL model impact forces under LOCA loads. By reviewing spectrum of LOCA core plate motion, the dominant frequencies of the motion are much higher than the fundamental frequency of a fuel assembly. When the fuel assembly stiffness is decreased due to EOL conditions, the fundamental frequency is reduced and is more away from

the excitation frequency. Therefore, the impact forces of EOL assemblies tend to be lower than those of a fuel assembly. This conclusion is consistent with vibration theory. A LOCA event normally occurs in a short duration and the reactor core plates and internal experience shock load due to sudden pressure change, therefore, fuel assemblies have no time to build up motion. Damping, which dissipates energy, has less effect on the motion with short period.

For seismic events, the dominant frequency range is close to the fundamental frequency of a fuel assembly. A typical seismic spectrum shows that the dominant frequency range is around 0.25 ~2.5 Hz (see Figure 9, [8]). Compared with the BOL assemblies, the EOL assemblies have higher impact forces because the exciting frequencies are close to the assembly fundamental frequency. The EOL models with still water damping have significantly higher impact forces than the BOL models especially for rows with a high number of assemblies. In seismic events, the damping coefficient of flowing water is applied to the EOL-FW model, which effectively reduces the impact forces.

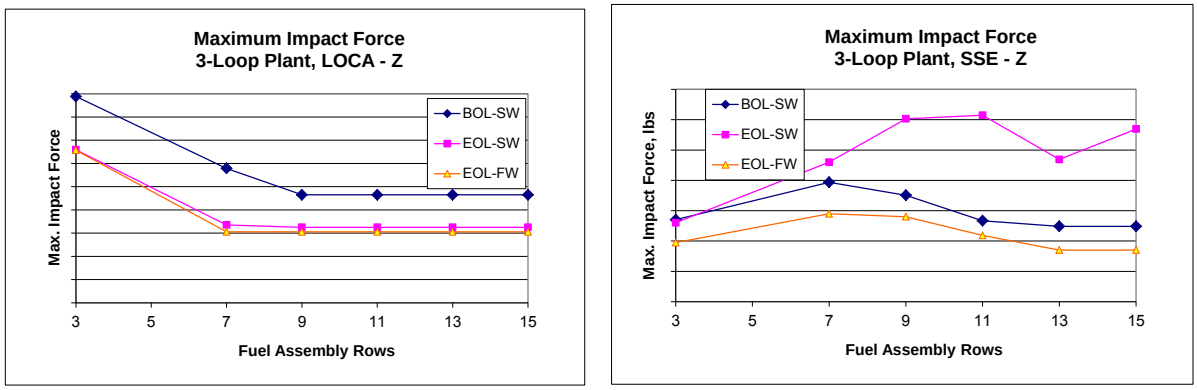

Fig. 7: Maximum mid grid impact forces, a typical 3-loop plant

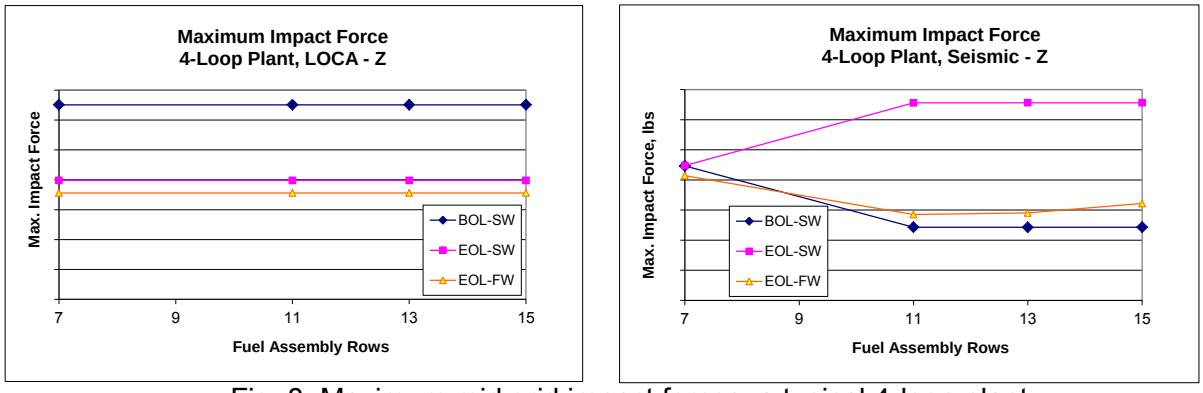

Fig. 8: Maximum mid grid impact forces, a typical 4-loop plant

Under LOCA core motion, the 4-loop EOL models have lower impact forces than the BOL models, which is the same as the 3-loop plant models. For seismic loads, the EOL-FW models have slightly lower maximum impact loads as compared to the corresponding cases of the BOL-SW models. The EOL-FW case with flowing water damping will gives similar results as the BOL-SW model with still water.

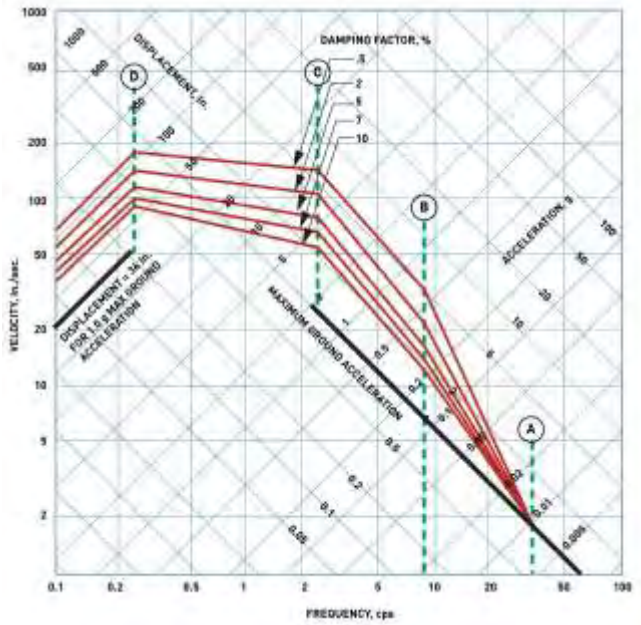

Fig. 9: Horizontal design response spectra scaled to 1 g horizontal ground acceleration

5. Conclusions and Future Work

Westinghouse is working with PWROG (PWR Owners group) to address EOL issue for all Westinghouse fuel fleet. Grid impact tests, fuel assembly mechanical/dynamic tests and fuel assembly flowing water damping tests will be performed for several fuel designs. Based seismic/LOCA parametric analyses, several conclusions are obtained.

1) Fuel assembly grid cell gaps due to irradiation reduce grid buckling/crush strength, fuel assembly stiffness and modal frequencies.
2) Flowing water damping coefficient can be applied with consideration of pump coast down.
3) Normally, a LOCA event is a rapid transient, which has short time duration. LOCA events generate core plate motion waves dominated by higher frequency components which are higher than the fundamental frequency of fuel assemblies. When the fuel assembly stiffness is decreased due to EOL conditions, the fundamental frequency is reduced and is further away from the excitation frequencies. The impact forces of EOL assemblies will be lower than those of BOL assemblies. This conclusion is consistent with vibration theory.
4) For seismic events, the fundamental core motion frequency is close to the fundamental frequency of a fuel assembly. Compared with the BOL assemblies, the EOL assemblies have higher impact forces because the exciting frequencies are close to the assembly fundamental frequency. The EOL models with still water damping have significantly higher impact forces than the BOL models especially for rows with larger number of assemblies. In seismic events, the damping coefficient of flowing water is applied to the EOL-FW model and the damping significantly reduces the impact forces.

References

1. NRC INFORMATION NOTICE 2012-09, “Irradiation Effects on Fuel Assembly Spacer Grid Crush Strength”, June 28, 2012.
2. NRC NUREG-0800, “Standard Review Plan for the Review of Safety Analysis Reports for Nuclear Power Plants: LWR Edition,” (SRP) Section 4.2, “Fuel System Design,” Revision 3, March 2007, Appendix A, “Evaluation of Fuel Assembly Structural Response to Externally Applied Forces”.
3. Framatome ANP Letter to NRC, NRC:02:031, “Interim Report of Evaluation of a Deviation Pursuant to 10 CFR 21.21(a)(2),” July 10, 2002, J. F. Mallay.
4. Framatome ANP Letter to NRC, NRC:03:051, “Closure of Interim Report 02-002, Spacer Grid Crush Strength – Effects of Irradiation”, August 8, 2003, J. F. Mallay.
5. F. E. Stokes and R. A. King, “PWR Fuel Assembly Dynamic Characteristics,” International Conference On Vibration In Nuclear Power Plants. Keswick, United Kingdom, May 9-12, 1978 (BNES).
6. R. Y. Lu and D. D. Seel, Westinghouse USA, “PWR Fuel Assembly Damping Characteristics,” Proceedings of ICONE 14, 14th International Conference on Nuclear Engineering, July 17-20, 2006, Miami, Florida, USA.
7. S. Pisapia, et al. “Modal Testing and Identification of a PWR Fuel Assembly,” Transactions of the 17th International Conference on Structural Mechanics in Reactor Technology (SMiRT 17), Paper #C01-4, Prague, Czech Republic, August 17-22, 2003.
8. NRC REGULATORY GUIDE 1.60 Revision 2, “Design Response Spectra for Seismic Design of Nuclear Power Plants”.

AREVA SOLUTIONS TO LICENSING CHALLENGES IN PWR & BWR RELOAD AND SAFETY ANALYSIS

FLORIN CURCA-TIVIG

AREVA, AREVA GmbH, Paul-Gossen-Str. 100, D-91052 Erlangen, GERMANY

ABSTRACT

Regulatory requirements for reload and safety analyses are evolving: new safety criteria, request for enlarged qualification databases, statistical applications, uncertainty propagation… In order to address these challenges and access more predictable licensing processes, AREVA is implementing consistent code and methodology suites for PWR and BWR core design and safety analysis, based on first principles modeling and extremely broad verification and validation data base.
Thanks to the high computational power increase in the last decades methods' development and application now include capabilities not available in the past. For example 3D coupled transient core power distribution characterization allow more realistic modeling of plant behavior and removal of inaccuracies by high resolution allowing for access to local information, which improves overall safety and operating margins. The paper provides an overview of the main AREVA codes & methods developments covering PWR and BWR applications in different licensing environments. It illustrates AREVA's capability of smoothly and promptly addressing licensing challenges.

1. Introduction

Fuel suppliers are expected to improve their technologies in order to increase (1) availability factors (flawless fuel operation, short time reloading…), (2) fuel performance (reliability, flexibility, burn-up, thermal hydraulic performance…),and (3) safety margins. The present evolution of fuel assembly and core designs towards greater heterogeneity, higher enrichments and burnup, Gadolinium-loading, MOX loading, low leakage, etc., challenges codes & methods (C&M) development.

Safety Authority (SA) requirements are evolving, e.g. new Reactivity Induced Accident (RIA) criteria, request for enlarged qualification database…; fuel suppliers have to anticipate this evolution and come up with methods properly meeting the new needs, such that penalties on products or on limits in operation are avoided. In this context, AREVA took up the challenge to significantly advance the state-of-the-art in nuclear methods and started a selection of large R&D programs to prepare for the next generation of C&M for fuel assembly and core design, safety analysis and core monitoring that are now mostly accomplished [1].

An overview is provided on new AREVA basic codes (Section 2) and new methodology suites (Section 3). Section 4 shows how these developments can contribute to successful licensing of high-performance fuel products in the currently strongly moving regulatory environment. Conclusions are drawn in section 5.

2. The new basic AREVA codes

AREVA's code development program was practically completed in 2014. The basic codes supporting a new generation of advanced methods are the followings:

- GALILEO™ state-of-the-art fuel rod performance code for pressurized water reactor (PWR) and boiling water reactor (BWR) applications. Development is completed, implementation started in France and the U.S.A. [2].

- ARCADIA®-1 state-of-the-art neutronics/thermal- hydraulics (TH)/thermal-mechanics (TM) code system for PWR applications. Development is completed, implementation started in France, the Netherlands, the U.S.A. and other countries [3].
- F-COBRA-TF advanced TH sub-channel code [4]. Development is completed; the code is in use in AREVA for reference analyses and fuel design optimization studies.
- AURORA-B state-of-the-art neutronics/TH/TM code system for BWR applications. Development is completed, implementation started in the U.S.A. [5].
- ARGOS™ universal core monitoring system providing solution to any type of LWR [6]; the first off-line parallel run started in 2014 in a plant in the U.S.A.
- System thermal-hydraulic codes S-RELAP5 and CATHARE-2 are not really new but still represent state-of-the-art in the domain. S-RELAP5 was completely re-structured and re-coded such that its life cycle increases by further decades. CATHARE-2 will be replaced in the future by the new CATHARE-3.

2.1 GALILEO™ - State-of-the-art fuel rod performance code

AREVA has developed the new global fuel rod performance code GALILEO™ that will be industrially used to accurately predict fuel performance in a wide range of irradiation conditions, for UO_2, Gadolinium and MOX fuels at high burnup or power, for both PWR and BWR reactors. A licensing topical report was submitted in 2013 to the U.S. NRC for review.

GALILEO™ incorporates state-of-the-art models to adequately simulate fuel behavior at high burnup, multi-dimensional effects, fuel's thermal conductivity degradation with burn-up, etc. The code is supported by a large experimental database including both publically available international data and also proprietary data, global and separate-effects test, and irradiation programs. The data base covers high burnup, low and high duty plants, for both PWR and BWR reactors and for UO_2, UO_2-Gd_2O_3 and MOX fuel. It is continuously updated by the newest experimental feedbacks. Today more than 2000 rods with measurements of temperature, fission gas release, dimensional changes, and other parameters, up to a maximum rod burnup of 100 GWd/tHM are included.

GALILEO™ will be deployed with the best-estimate realistic methodology for fuel rod performance evaluation during normal operating and Anticipated Operational Occurrences (AOO) conditions. The methodology was originally developed at AREVA based on its RODEX4 BWR fuel rod code and was approved by the U.S. Nuclear Regulatory Commission (NRC) for use in BWR licensing analysis. This realistic methodology is based on a Monte Carlo type random sampling of all relevant input variables, i.e. inputs related to reactor operating conditions, fuel rod manufacturing and thermal-mechanical model uncertainties. The best-estimate GALILEO™ code is then used in conjunction with non-parametric order statistics to evaluate the propagation of these uncertainties to the design analysis results. Statistical calculations provide accurate design margins assessment. Reference [2] illustrates results obtained with the AREVA realistic thermal-mechanical methodology applied to representative design sample cases.

2.2. ARCADIA® - State-of-the-art neutronics/ thermal-hydraulic/ thermal-mechanic code system

The new code system, named ARCADIA®, is an advanced 3D coupled code system for steady state and transient core design. The new software architecture allows for nodal and pin-by-pin calculations. ARCADIA® encloses the following main sub-systems: spectral code APOLLO2-A, core simulator ARTEMIS™, core thermal-hydraulics code COBRA-FLX™, Fuel Rod Module (FRM) and LADON™, a comprehensive user environment (Figure 1).

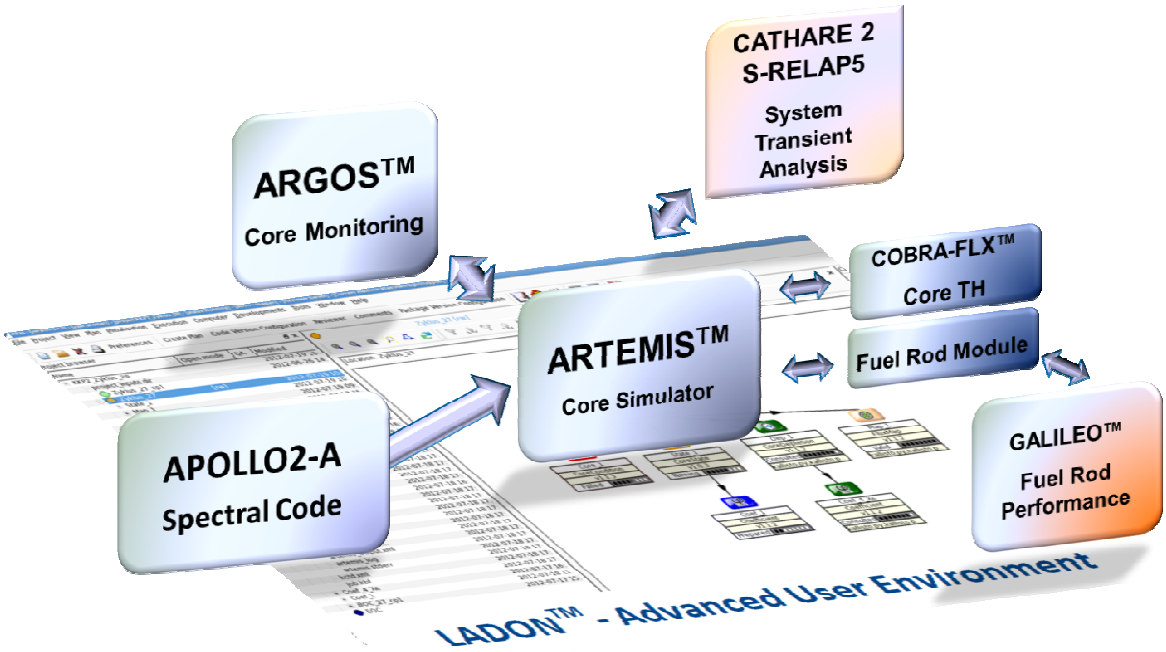

Figure 1: ARCADIA® - Modular architecture (the main modules)

The U.S. NRC has approved in 2013 the use of ARCADIA®-1 for PWR core performance analysis. ARCADIA®-1 can now progressively replace the legacy code systems used by AREVA worldwide for PWR applications.

A basic rule of ARCADIA® development was to use first principle approaches to the highest degree possible and to avoid approximations and simplifications. The goal was to meet the current and future challenges of in-core fuel management and safety analyses. Increased prediction accuracy is demonstrated by using the extensive validation database available worldwide at AREVA as well as test data accessible through the cooperation with the French Commissariat à l'Energie Atomique (CEA).

The spectral code system APOLLO2-A was developed in close cooperation with CEA [7]. The newest nuclear data library JEFF3.1.1 is used. Qualification file covers a large range of LWR applications.

ARTEMIS™ is the 3D core simulator within the ARCADIA® code system [8-10]. It unifies our most advanced computational methodologies and provides state-of-the-art analysis capabilities. It includes high performance multi-group diffusion and transport flux solvers and is designed for PWR and BWR applications. The capabilities to perform 3D coupled steady-state and transient calculations on pin-by-pin (sub-channel by sub-channel) geometries are an asset for development of high accuracy safety analysis methodologies.

The thermal-hydraulic sub-channel code COBRA-FLX™ is integrated in ARTEMIS™ and has the capability of performing 3D steady-state and transient analyses with full-core subchannel-by-subchannel spatial discretization [11]. This way, complex two-phase flow problems can be solved and access to local physical parameters is made possible.

The Fuel Rod Module (FRM) of ARTEMIS™ resolves the nonlinear heat transfer equation in representative fuel rods, both in steady state and transient conditions, in order to evaluate the Doppler feedback in fuel pins. It is fully consistent with the fuel rod performance code GALILEO™. The FRM also supports pin-by-pin calculations.

The business and integration services shell LADON™ covers input generation and pre-processing, output evaluation and post-processing. It includes a graphical user interface, job automation and many kinds of post-processing tools needed for fuel assembly and core design. It is also the frame for setting up methodologies for any kind of applications.

Basically, three major ARCADIA® releases have been achieved or are respectively planned:
1. ARCADIA®-1 for standard PWR applications (used to generate the Licensing Topical Report approved by the US NRC)
2. ARCADIA®-2 for standard PWR and BWR applications (development on-going)
3. ARCADIA®-3 for reference 3D pin-by-pin calculations (development on-going).

The code system ARCADIA®-1 has been validated for a very large number of reactor cycle conditions covering many of the PWRs served by AREVA as well as many transient cases. Recent validation experience of ARTEMIS™ for transient modeling is provided in [12-16].

2.3. F-COBRA-TF – An advanced thermal-hydraulic sub-channel code

F-COBRA-TF is AREVA's advanced subchannel code applicable for both PWR and BWR. F-COBRA-TF is based on a heterogeneous two-fluid representation of the two-phase flow in the reactor core, solving the transport equations for mass, momentum, and energy for the three separate fields - continuous liquid, vapor, and entrained liquid - in a transient way. Different flow regimes are described to take into account phenomena like wall and interfacial drag, wall and interfacial heat transfer, turbulent mixing, void drift, droplet entrainment and deposition, etc. This refined modeling allows for a more detailed description of two-phase flow phenomena and reduces the dependency on empiric correlations, e.g. void and two-phase pressure drop correlations. An individual film model explicitly treats each liquid film on any rod or unheated structural surface within a subchannel. In combination with an advanced spacer grid model, F-COBRA-TF allows for an enhanced prediction of dryout with a standard deviation < 3.3 %. Thus, it supports BWR dryout correlation development by generation of reliable numerical data for non-tested boundary conditions [17]. In the future F-COBRA-TF will be integrated in ARCADIA®-2.

2.4. AURORA-B - State-of-the-art neutronics/ thermal-hydraulic/ thermal-mechanic code system for BWR applications

AREVA's code system, AURORA-B, is an advanced transient and accident simulator that is under review by the U.S. NRC for licensing applications. AURORA-B has been built on three separately NRC approved computer codes:

- S-RELAP5 – A two-phase thermal hydraulic code with a large validation and assessment base including updates to address recent fuel performance data. It has been comprehensively reviewed by international safety authorities for application to the entire spectrum of PWR and BWR applications and has been used in design and licensing of the EPR™ and Generation III+ reactor designs.

- RODEX4 – Best estimate code which realistically evaluates the local thermal-mechanical behavior of fuel rods during normal operation and anticipated operational occurrences.

- MB2-K – The neutron kinetics extension of the steady state core simulator MICROBURN-B2 which provides best-estimate predictions of neutron flux excursions, including pin-power reconstruction to assess performance of individual fuel rods. The code utilizes the advanced nodal expansion method and an advanced frequency transformation time integration technique to increase the code's accuracy and speed.

By integrating each of these separate code capabilities into the AURORA-B evaluation model, AREVA established a robust foundation for transient simulations that has been extended to address both Control Rod Drop Accident (CRDA) and Loss Of Coolant Accident (LOCA) simulations. Reference [5] gives an overview of the AURORA-B code capabilities, selected event validation and analytical examples that highlight the code capabilities to address expected changes in the regulatory safety requirements such as the BWR CRDA.

2.5. ARGOS™ – AREVA universal core monitoring system

The ARGOS™ Core Monitoring System (CMS) utilizes live plant data to perform detailed physics calculations, compares these calculations to allowed technical specifications and provides summary reports to plant operators and engineers. The system also provides robust core follow and prediction capabilities.

Because of the diversity of plant types in the AREVA portfolio, ARGOS™ must easily and efficiently accommodate different sources of data. Consequentially, ARGOS™ has been designed as a highly modular universal platform for monitoring a wide variety of commercial light-water reactor types – PWR and BWR - and also, different nodal simulators.

The Graphical User Interface (GUI) can be configured to customer-specific requirements and needs. The state-of-the-art framework technology provides the ability to adjust the information and data display at any moment during run time based on individual preferences and/ or online requirements. The data backbone of ARGOS™ consists of a relational database which stores all the relevant information associated with core monitoring. The database contents can be queried by the ARGOS™ GUI or by external processes.

2.6. System thermal-hydraulic codes S-RELAP5 and CATHARE-2

AREVA currently uses two similar thermal-hydraulic system codes: CATHARE-2, developed by CEA, and S-RELAP5, developed by AREVA. Both codes are at state-of-the-art and their performance is equivalent. S-RELAP5 was recently completely recoded and modernized in terms of software architecture. On the other side, CEA is developing the next CATHARE generation: CATHARE 3 that may become in the long-term the converged code of AREVA. Both, CATHARE and S-RELAP5, were successfully coupled with ARCADIA®-1.

3. Advanced AREVA methodologies for core design and safety analysis

Computational capability has increased enormously in the last 20+ years; methods' development and application now include options that were not available in the past, e.g. in the 1990th. In the past physical phenomena would have been modeled separately and simple technics of sequential calculations relying on external file transfer between the single codes were common because of computational costs. The associated application methodologies had to envelop the uncertainty of such "chains" by artificial "uncertainty factors", means to ensure conservatism of the analysis. However, the physical "reality," notably the local behavior was obfuscated by the simplifications and assumptions in the methodology. Today, full integration (full coupling) of the main physical models becomes possible and opens new ways for even predictive calculations (see schematic in Fig. 2).

Advanced features such as 3D coupled transient core power distribution characterization allow (1) more realistic modeling of plant behavior, (2) removal of overall uncertainty by high resolution and access to local information, (3) maintaining and improving overall safety and operating margins. AREVA's main developments in the domain of new methodologies are summarized in this section.

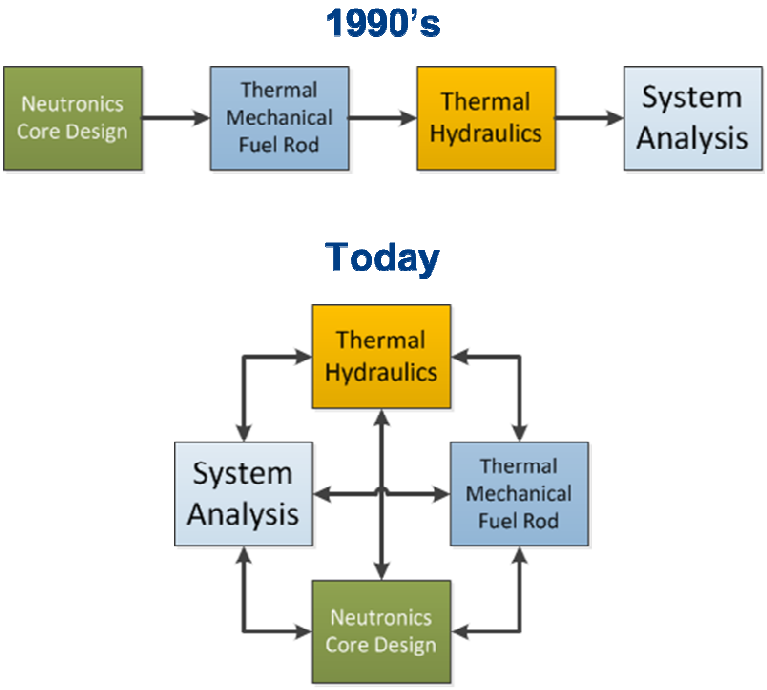

Figure 2: Evolution of codes and methods used for safety analysis

3.1 Methods for PWR core design and safety analysis

AREVA is converging to a new suite of methods for PWR applications, based on: ARCADIA®-1 code system, GALILEO™ fuel performance code and the system TH codes S-RELAP5 and CATHARE 2 (either of them, depending on country and customer).

For core transient calculations, ARCADIA®-1 automatically couples neutronics, thermal-hydraulics and thermal-mechanical modules (internal coupling). Details on internal coupling and its validation can be found in [14]. For specific transients like the main steam line break, ARCADIA®-1 was coupled externally with both S-RELAP5 and CATHARE system codes.

Taking as an example the U.S.A. nuclear market, the advanced methodologies based on the new code suite will be (see red triangle in Fig. 3):

- ARCADIA®/S-RELAP5 integrated transient methodology (non-LOCA)
- Control Rod Ejection Accident (CREA) methodology
- (S-RELAP5) Small break LOCA analysis methodology
- (S-RELAP5) Realistic large break LOCA analysis methodology.

3.2 BWR core design an safety analysis

For BWR applications the full new suite of AREVA codes & methods is under review at the U.S. NRC. The following new methodologies have been developed based on the AURORA-B code system (see blue triangle in Fig. 3):

- AURORA-B AOO analysis methodology
- AURORA-B CRDA analysis methodology and
- AURORA-B BWR LOCA analysis methodology.

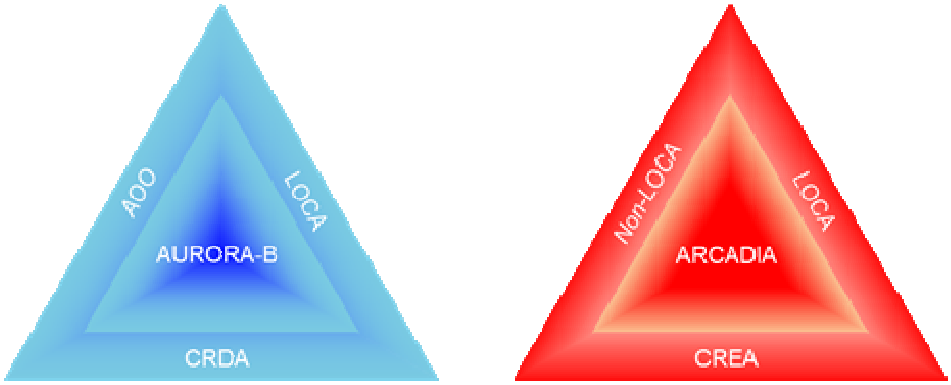

Figure 3: AREVA new codes & methods suits for PWR (red) and BWR (blue) applications (example U.S. market)

4. AREVA solutions to licensing challenges in a moving regulatory environment

A clear message was sent in 2011 from the U.S. NRC to the industry that there is an expectation that methods and codes must progress to be more in line with current regulations and technologies. Predictable licensing requires (a) meeting current SAs expectations, (b) being prepared to support licensing efforts brought on by licensing rule changes and (c) incorporating feedback received over a number of years from SAs. The currently main regulatory evolutions refer to the following items:

1. New RIA acceptance criteria. Notably the U.S. NRC proposes new RIA acceptance criteria and guidance in NUREG-0800 “Standard Review Plan (SRP) for the Review of Safety Analysis Reports of Nuclear Power Plants: LWR Edition”, SRP Chapter 4.2, “Fuel System Design”, Appendix B, “Interim Acceptance Criteria and Guidance for RIA”.
2. U.S. NRC 10 CFR 50.46c rule change aiming to revise Emergency Core Cooling System (ECCS) acceptance criteria to reflect recent research findings and to replace prescriptive analytical requirements with performance-based requirements
3. Explicit SAs request for first-principle physics with comprehensive code and methods validation. Focus is more and more on coupled codes and on a high level of confidence.
4. Explicit SAs request for more data when developing correlations or empirical models, and many others…

The new AREVA codes & methods are largely based on first principles modeling with an extremely broad international verification and validation (V&V) data base, both for UO_2 and MOX fuel (above items 3 and 4). Not only does this data base combine all AREVA’s world-wide sources but also benefits of a huge feedback of operational experience from diverse customers, with different operation strategies and histories. As a representative example, Figure 4 shows an excerpt of data used to validate integrated methods. Worth to notice are the real plant data recorded during planned or unplanned transients, e.g. load rejection with temporary loss of one Reactor Coolant Pump (RCP), RCP shaft break, rod drop transient, etc. They are unique data with high value for meeting SA’s requirements: both the integrated code system ARCADIA® as well complex externally coupled codes like ARCADIA®/S-RELAP5 and ARCADIA®/CATHARE 2 can be validated for their application domains.

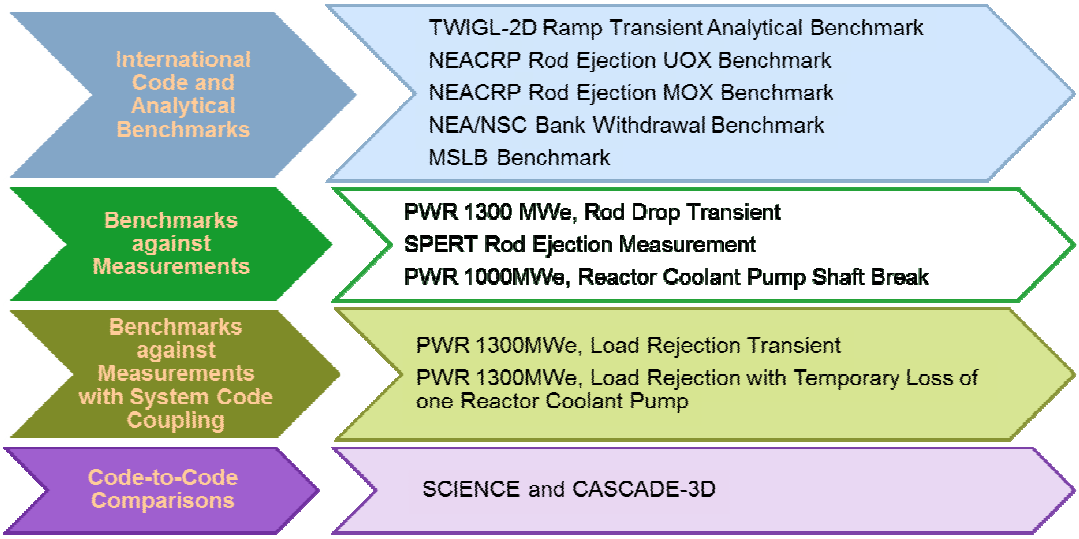

Figure 4: AREVA validation data for advanced PWR codes & methods

Furthermore, AREVA systematically performs code-to-code comparisons with the two mature and already well validated legacy integrated code systems SCIENCE (used in France, Asia and many other markets) and CASCADE-3D (mainly used in Germany, U.S.A. and some other countries in Europe). This is an additional, reliable means to increase the level of confidence of the new AREVA codes and methods. To complete the picture on AREVA's validation of the advanced codes and methods suits one need mentioning the hundreds of fuel cycles used to qualify ARCADIA® for reload analysis. The conclusions supports items 3 and 4: ARCADIA® accurately predicts the behavior of a large range of reactor core types.

The new PWR and BWR codes and methods suites cover per definition (i.e. as part of the original technical specifications for this development) the new RIA and ECCS acceptance criteria and guidelines (items 1 and 2). Some example can be given:

- Hydrogen pick-model was integrated from the beginning in the corresponding methodologies (answer to item 1).
- A new rod swell, rupture and relocation model was integrated in the realistic large break LOCA methodology (answer to item 2).
- Fuel thermal conductivity degradation as a function of burnup is modeled throughout the advanced AREVA methodologies and the impact on the parameters of interest (e.g., fuel centerline temperature, peak cladding temperature, rod internal pressure) is determined (answer to item 2).

Another sensitive domain always under SA's scrutiny is related to critical heat flux (CHF) correlations. The ability to properly and confidently predict CHF for a fuel assembly (FA) design is a regulatory requirement for safety analysis applications. Taking the opportunity of developing the advanced fuel designs GAIA [18] and ATRIUM™-11 [19], AREVA established two new CHF correlations:

- The ORFEO correlation for AREVA's advanced PWR FA GAIA [20]. It has an advanced functional form including more mechanistic modelling based on a very large data base. Comprehensive CHF testing has been performed at Karlstein Thermal Hydraulic Test Facility (KATHY), in Germany. Tests covered large ranges of TH conditions such that application of the correlation to the full domain encountered in safety analysis is performed on a sound and reliable basis.

- The ACE critical power correlation is used to predict thermal-hydraulic performance of AREVA's BWR ATRIUM™-10 and ATRIUM™-11 fuel assembly families. The foundation

for the correlation is a theoretical model that describes more mechanistically the point of maximum heat transfer in boiling conditions.

All these facts enable AREVA and its customers to access more predictable licensing processes in a challenging regulatory environment.

5. Conclusions

After a phase of intensive R&D investment in reactor physics, thermal-hydraulics and thermal-mechanics, AREVA has accomplished the development of state-of-the-art codes in all of these domains and is now implementing a new generation of advanced methodologies for fuel assembly design, core design, safety analysis and core monitoring. Advanced features such as 3D coupled transient core power distribution characterization allow more realistic modeling of plant behavior and removal of overall uncertainty by high resolution and access to local information.

The new AREVA codes & methods are largely based on first principles modeling with an extremely broad international verification and validation data base. This enables AREVA and its customers to access more predictable licensing processes in a moving regulatory environment (new safety criteria, requests for enlarged qualification databases, statistical applications, uncertainty propagation…). In this context, the advanced codes & methods and the associated verification and validation represent the key to avoiding penalties on products, on operational limits, or on methodologies themselves. Advanced and integrated methods (coupling all the relevant disciplines) are keys to maintaining and improving overall safety and improving operating margin.

References

1. F. Curca-Tivig, “Advanced Codes & Methods – AREVA’s Key to Successful Licensing of High-Performance Fuel Products and Full Support to Customer”, Proceedings of Water Reactor Fuel Performance Meeting (Top Fuel 2011), Chengdu, China, Sept. 11-14, 2011
2. J.H. Strumpell et al., “Application of GALILEO™: AREVA’s Advanced Fuel Performance Code and Methodology”, Proceedings of 2013 LWR Fuel Performance Meeting / Top Fuel, Charlotte, North Carolina, USA, September 15-19, 2013
3. F. Curca-Tivig et al., “ARCADIA®- A New Generation of Coupled Neutronics/ Core Thermal- Hydraulics Code System at AREVA”, Proc. of the 2007 Int. LWR Fuel Performance Meeting, San Francisco, California, Sept. 30 – Oct. 3, 2007
4. M. Glück, “Sub-channel Analysis with F-COBRA-TF – Code Validation and Approaches to CHF Prediction”, Nuclear Engineering Design, vol. 237 (6), pp. 655-667 (2007).
5. K. Quick et al., “AREVA’s Advanced BWR Transient and Accident Methodologies”, Proceedings of 2013 LWR Fuel Performance Meeting / Top Fuel, Charlotte, North Carolina, USA, September 15-19, 2013
6. ARGOS™ Product Bulletin, AREVA, ANP:U-563-V1-15-ENG
7. E. Martinolli et al., “APOLLO2-A – AREVA’s New Generation Lattice Physics Code: Methodology and Validation”, Proc. of. PHYSOR 2010, Pittsburgh, Pennsylvania, USA, May 9-14, 2010

8. A. Pautz et al., “The ARTEMIS™ Core Simulator: A Central Component in AREVA NP’s Code Convergence Project”, Joint Int. Topical Meeting on Mathematics & Computation and Supercomputing in Nuclear Application, (M&C + SNA 2007), Monterey, California, April 15-19, 2007
9. G. Hobson et al., “ARTEMIS™: The Core Simulator of AREVA NP’s next Generation Coupled Neutronics/ Thermal-Hydraulics Code System ARCADIA®”, PHYSOR 2008, Interlaken, Switzerland, September 14-19, 2008
10. G. Hobson et al., “ARTEMIS™ Core Simulator: Latest Developments”, Joint International Conference on Supercomputing in Nuclear Applications and Monte Carlo 2013 (SNA + MC 2013), Paris, France, October 27-31, 2013.
11. M. Leberig et al., “AREVA NP's Advanced Thermal Hydraulic Methods for Reactor Core and Fuel Assembly Design”, Top Fuel 2009, Paris, France, September 6-10, 2009
12. G. Hobson et al., “ARCADIA® Transient Capabilities and Recent Validation Experience”, Proceedings of 2013 LWR Fuel Performance Meeting / Top Fuel, Charlotte, North Carolina, USA, September 15-19, 2013
13. S. Kuch et al., “Transient Validation of AREVA’s new ARCADIA® code system”, Proceedings of the 2014 22nd International Conference on Nuclear Engineering, ICONE 22, Prague, Czech Republic, July 7-11, 2014
14. S. Zheng, K. Segard, “Validation of ARCADIA® Transient Model with Rod Drop Test Benchmarking“, PHYSOR 2010, Pittsburgh, USA, May 9-14, 2010
15. B. Hartmann et al., ”Advanced PWR Core Analysis with ARCADIA®“, Jahrestagung Kerntechnik 2014, Frankfurt, Germany, May 6-8, 2014
16. D. Porsch et al., “Status of Verification & Validation of AREVA’s ARCADIA® Code System for PWR Applications”, PHYSOR 2012 – Advances in Reactor Physics – Linking Research, Industry, and Education Knoxville, Tennessee, USA, April 15-20, 2012, on CD-ROM, American Nuclear Society, LaGrange Park, IL (2012)
17. S. Opel et al., “Advanced CHF Prediction by F-COBRA-TF and CFD Analysis to Support PWR and BWR Fuel Product and Methodology Development”, Proceedings of 2013 LWR Fuel Performance Meeting/ Top Fuel, Charlotte, NC, USA, September 15-19, 2013
18. G.A. Thomas et al. “GAIA: AREVA’S ADVANCED PWR FUEL DESIGN “Light Water Reactor Fuel Performance Meeting 2013, Charlotte NC US, September 2013
19. N.L. Garner, S.E. Cole et al “ATRIUM™ 11 – The transition from development to in-services qualification of an advance fuel design for boiling water reactors”, Light Water Reactor Fuel Performance Meeting 2012, Manchester (UK) September 2012
20. O. Wieckhorst et al., ORFEO – A CHF Correlation for GAIA, AREVA’s Advanced Fuel Assembly Design”, 16th International Topical Meeting on Nuclear Reactor Thermal Hydraulics (NURETH-16), August 30th – September 4th 2015, Chicago, IL, USA

A WESTINGHOUSE LOCAL FUEL DUTY PCI RISK MONITOR AND ANALYSIS TOOL

W.A. BOYD[1], G. MANGHAM[2]
Westinghouse Electric Company LLC, [1]Methods & Technology, [2]Core Engineering
1000 Westinghouse Drive, Cranberry Township, Pennsylvania 16066, USA

ABSTRACT

Pellet Clad Interaction (PCI) is a potential failure mechanism for nuclear fuel that occurs during a power increase where the thermal expansion of the fuel pellet places excessive stress on the fuel cladding. To minimize the risk of PCI fuel failures, global power ramp rate guidelines have been typically applied during startup after refueling and after extended periods of reduced power operation. While these historical guidelines have proven very efficient in avoiding PCI failures by the long-time successful operating experience of Westinghouse modern PWR fuel they can overly restrict power ascension, place stringent controls on the axial power distribution and restrict control rod withdrawal rates. Westinghouse has developed a Local Fuel Duty Risk Monitor (LFDRM) methodology and tool that integrates with the BEACON™ On-line Core Monitoring System to continuously monitor the risk of PCI failure locally throughout the core. The LFDRM tool can show real time information on the current risk of a PCI induced fuel failure and also provide engineers an off-line dynamic planning tool to evaluate PCI risks for a startup or drop rod recovery strategy before actual implementation. This will allow the ramp rates and hold times to be a function of the actual plant fuel loading and past operation.

1. Introduction

To protect against a potential PCI fuel failure mechanism general or global power ramp rate guidelines are typically applied during startup after refueling and after extended periods of reduced power operation. These guidelines can overly restrict power ascension, place stringent controls on the axial power distribution and restrict control rod withdrawal rates to ensure adequate margin to potential PCI fuel failures. Westinghouse has developed a Local Fuel Duty Risk Monitor (LFDRM) methodology and tool that integrates with the BEACON™ On-line Core Monitoring System to continuously monitor the risk of PCI failure locally throughout the core. The tool will allow plant engineers and operators to evaluate the risk of a PCI fuel failure for a startup or drop rod recovery strategy before actually performing the maneuver. They can then monitoring the PCI risk during the actual maneuver.

The LFDRM methodology includes a very fast fuel conditioning analytical model that was previously developed and benchmarked to a stand-alone fuel performance code (FPC) [1]. This model continuously calculates and tracks the clad stress for every axial fuel pin-node in the core in a few seconds. The local clad stress is changing based on local power, the effective conditioned local power, and the local clad temperature. These parameters are a direct function of the core power level and the local power distributions that are being monitored by the BEACON core monitoring system. The potential increase in clad stress from Missing Pellet Surface (MPS) Areas (MPSA) is calculated from the known probability distribution of MPSA data for the fuel

manufacturing plant. The overall risk of PCI failure is determined using a stress-failure probabilistic model and is compared to a threshold limit to determine if the PCI failure risk is acceptable. The calculated core power margin is a straight forward way of showing plant engineers and operators how much core power can be increased before the PCI failure risk exceeds the threshold limit.

2. Methodology Overview

The clad stress increase from a power change is highly dependent on the pellet-clad geometry prior to the power increase. Only the power increase above the point where the pellet to clad gap is closed will be associated with the clad stress increase and potential failure. The fuel as manufactured has a small pellet-clad gap at cold conditions. During operation, the hot gap gradually closes due to the high system pressure and the irradiation creep of the clad. The pellet will initially experience some densification, but then has irradiation swelling due to the production of the fission products.

If operated at a constant power, the fuel will eventually reach an equilibrium point with hot gap closure and equilibrium stresses. This is defined as the fully conditioned state of the fuel. Any change of power from that fully conditioned state will result in a gradual transition to a new conditioned state.

The PCI process occurs locally, so any PCI analysis must consider the 3-D distribution of powers and conditioned states of the fuel. A PCI analysis is therefore best performed as part of the 3-D neutronic calculations. While a fuel rod code could be used for this analysis, its models are typically 1-D, and each fuel pin would have to be analyzed separately. This becomes cumbersome with the power history being important. What has been developed to address these issues is a set of models that are integrated together to run very quickly and provide accurate results for reactor plant operations to evaluate limiting stresses and total failure probability.

A fuel conditioning model was developed to track the effective conditioned power or state of the fuel during the initial clad creep down phase from fresh conditions through the transient conditions of a power increase to a new equilibrium conditioned power. The model is benchmarked to a FPC which itself was benchmarked to ramp rate test results to establish a fuel failure threshold stress limit. This model is designated the Westinghouse Nuclear Fuel (WNF) model. The threshold limit is the approximate stress level below which there is no significant probability of fuel failures.

Once the effective conditioned power for every pin-node is determined with the WNF model the fuel pin-node clad stress ratio is then calculated using a clad stress model based on delta power above the conditioned power and the clad temperature. The stress data used to generate the WNF conditioning model are obtained directly from the FPC results. The clad stress is dynamically changing based on the pin-node power, the effective conditioned power level, and the clad temperature. These parameters are all a direct function of the core power and the core axial and radial power distributions.

With the clad stress ratio known for each “perfect” pin-node pellet (no MPS), the increase in the stress ratio due to the MPSA frequency distribution data of the manufacturing plant is then determined. The probability of each pellet failing is then determined using a failure probability model. The total probable number of pellets failing is summed for each assembly and for the core. The total probable core pellet failures are then compared to a defined limit.

The core power margin to the total pellet failure limit is then determined by uniformly adjusting the core wide pin-node power distribution until the clad stress results in a total core pellet failure probability that matches the limit. This provides the core power limit to the pellet failure limit.

2.1. Fuel Conditioning Model

The WNF model includes a PCI model based on previous work [1] that is benchmarked to a series of FPC calculations. In this model, the local conditioned power level is inferred from the local power required to reach the failure stress. This is a different approach from the simplified models that focus on using a surrogate variable such as the cold clad gap as the independent variable representing the fuel conditioned state or utilize clad stress as a parameter that can be translated into a conditioned power level. The PCI model is based on the premise that if the initial fully conditioned state power is known, then the limiting power can be determined.

Figure 1 shows a simplified drawing of the fuel state behavior and the phases of the PCI model. During fuel depletion the clad will creep down and gradually close the hot gap. The fully conditioned state power would then correspond to an equilibrium condition. If there were a power increase while in that state then stress would be applied to the clad and as the clad creeps outward, the stress is relieved, hence the effective equilibrium state power is gradually increased.

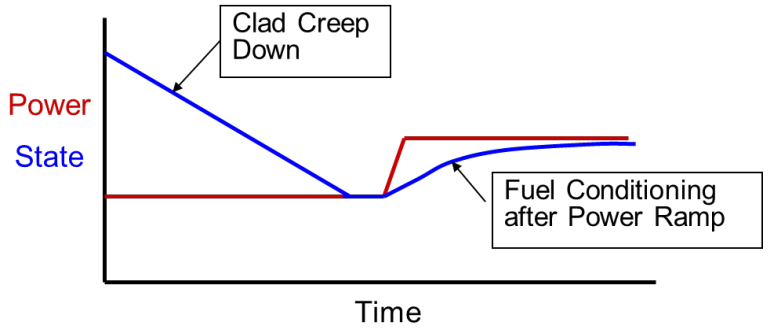

Figure 1: Power vs. Fuel Condition State Behavior

A FPC model is setup representing the fuel rod geometry of interest. Cases are run to 60K MWD/MTU burnup in 2K burnup increments, for power ranges between 2 and 13 kW/ft and coolant temperatures from the hot zero power inlet temperature to 610 ºF (321 ºC). At each burnup step for each combination of rod power and coolant temperature a power spike is performed to ensure the fuel failure threshold is reached. Determination of the PCI threshold was previously determined using a FPC feeding a finite element model (FEM) [2]. These fuel failure threshold points are used to define the fuel deconditioning or the effective conditioned state, when there is an open gap between the pellet and clad. The deconditioning formulation in the WNF model is applicable for the initial clad creep down phase and for the creep down after a power reduction. This formulation gives the effective conditioned state power as a function of clad temperature, fuel burnup and rod power.

There is a transition phase as the clad contacts the pellet. To generate data to represent this transition, FPC cases are run at initial power levels of 4 to 13 kW/ft to certain burnups and then down power ramps are performed over the same coolant temperature range used for the creep down phase. After the down power maneuver a power spike is performed every few hundred MWD/MTU in burnup to determine when the fuel failure threshold is reached. This failure threshold

condition is correlated with the failure threshold condition from the creep down phase to determine the effective conditioned state. An asymptotic approach to the conditioned power level is assumed for this transition as illustrated in Figure 2. This is accomplished through an exponential formulation with the change in the effective conditioned power being a function of the change in fuel rod burnup, rod power, clad temperature, and the initial conditioned power state.

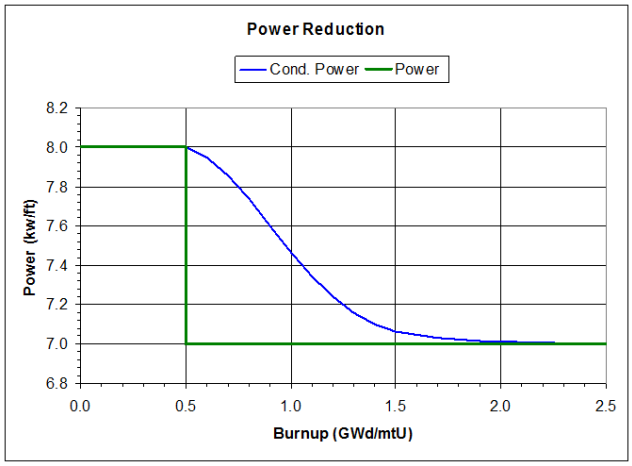

Figure 2: Transition of Conditioned Power with Power Reduction

Once the clad gap is fully closed the clad stress will increase with increasing rod power. The stress on the fuel cladding for a power increase is proportional to the power increase above the effective conditioned power state for normal operation. The stress will cause strain, and the clad creep will reduce the stresses on the clad over time. The stress relaxation is directly proportional to the clad creep in this regime.

To generate data to represent the fuel conditioning phase, FPC cases are depleted at initial power levels of 2 to 11 kW/ft to an extended burnup and then power ramps are performed over the same coolant temperature range used for the creep down phase. After each power ramp a power spike is performed every few hours to determine where the fuel failure threshold is reached. This timing is used because the fuel conditioning happens much faster than the fuel deconditioning. The failure threshold condition is correlated with the failure threshold condition from the creep down phase to determine the effective conditioned state. A complex multi-component formulation was developed to represent the change in the effective conditioned power as a function of the change in fuel rod power, clad temperature, and the initial conditioned power state

2.2. Clad Stress Model

Since the limiting clad stress is not a constant but is a function of MPSA, the concept of clad ‘stress ratio’ is introduced. The stress ratio is the ratio of the clad stress to the performance code fuel failure threshold stress. Then, failure risk is correlated to stress ratio rather than to absolute stress. The data used for the clad stress ratio model generation is taken directly from the FPC runs used to generate the data for the WNF clad creep down model. These cases simulated power spikes in small increments from the initial power level up to 20 kW/ft. This ensures the fuel failure threshold stress determined from the ramp rate test will be exceeded. The stress ratio, power level, and clad temperature are saved for each power spike increment.

Figure 3 shows a stress ratio data set at 50K MWD/MTU with a conditioned power of 6 kW/ft. The delta power above the condition power ranges from 0 to 6 kW/ft. The clad temperature ranges from 600 to 670 ºF (315.5 to 354.4 ºC). The simple cubic fit shown in the figure has a correlation coefficient of basically 1.0 and a standard error of 0.0031 which illustrates the uniform behavior of this data.

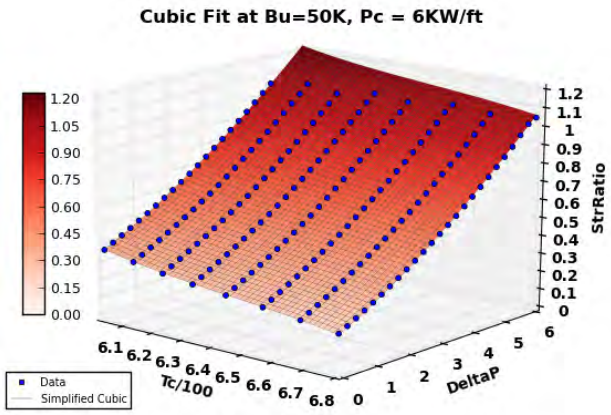

Figure 3: Surface Fit of Clad Stress Data at 6 kW/ft

2.3. Missing Pellet Surface Area Stress Penalty Model

A MPS causes a clad temperature re-distribution. FEM analysis results of MPS with areas from small to full pellet length show a significant reduction in the temperature of the cladding located around the MPS [2]. The distorted temperature distribution affects pellet and cladding thermal expansion and influences clad stresses. The MPS impacts the clad stress distribution with a higher stress area at the location of the MPS. This stress has a bending nature because the cladding is not supported over the MPS. The impact of the MPSA on the clad stress as rod power is increased is clearly illustrated in Figure 4.

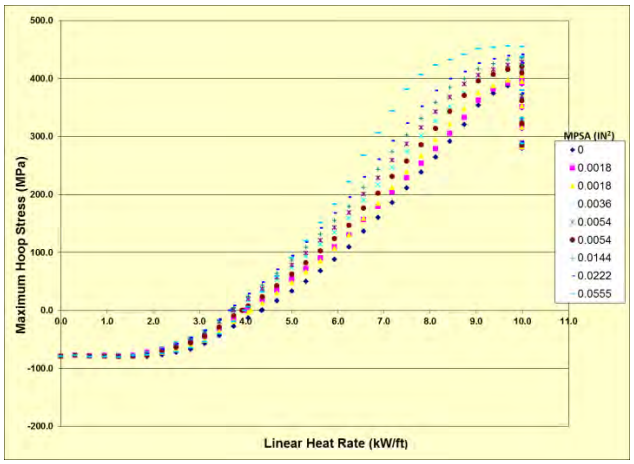

Figure 4: Clad Stress vs. Power and MPSA

To use this MPSA and stress related data it must be correlated to the zero MPSA stress ratio. The delta increase in stress can then be plotted as a function of the zero MPSA data as shown in

Figure 5 [2]. These results show that the stress penalty for a MPSA increases with stress until the zero MPSA stress ratio is approximately 0.6 after which the size of stress penalty begins to decline.

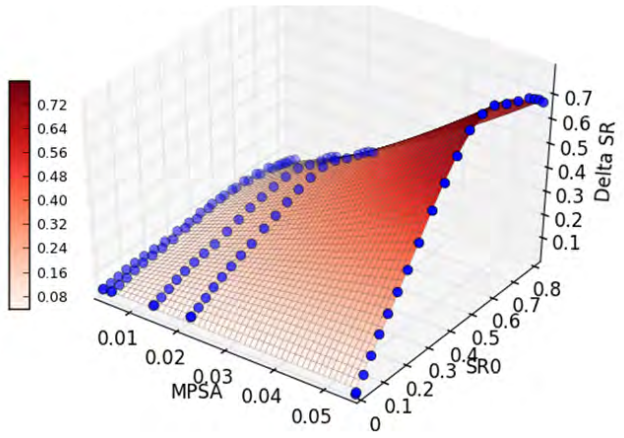

Figure 5: Delta Stress Ratio vs. Zero MPSA Stress Ratio and MPSA

2.4. Failure Probability Model

Power ramp test failure data was sorted according to increasing power and used to create a failure probability distribution. This distribution describes the probability of a rod failure, or the proportion of failed rods in a population of rods when subjected to a range of stresses and is fit with a 3 parameter Weibull function as shown in Equation 1

$$F_F(S) = 1 - \exp\left[-\left(\frac{S - S_T}{\alpha_S}\right)^{\beta_S}\right] \qquad \text{Eq. 1}$$

A key part of the failure probability model is the pellet MPSA probability distribution for the fuel manufacturing plant. For the Westinghouse Columbia manufacturing plant two MPSA probability distributions were generated using pre-2005 and post-2005 pellet manufacturing data. The post-2005 MPSA probability distribution data shows much lower probabilities of MPS and a smaller distribution of MPSA as a result of improvements in the manufacturing process. As will be seen in the benchmark results, the MPSA is a major factor in determining the probable risk of fuel failures and cannot be ignored when evaluating the risk of PCI fuel failures in the reactor core.

3. Benchmark Results

The startup of Plant A Cycle N resulted in three failed fuel rods in three different assemblies in 2003. Measurements and later analysis show that the coolant activity began to increase approximately 50 hours after the startup begin, indicating that the fuel failures started at or before this time. Figure 6 shows the three core locations that had failed fuel rods and previous cycle core locations. A hot cell examination of the failed rod in the assembly in core location C-9 confirmed it to have a large full length MPS. The other failed rods are suspected from MPS but not confirmed.

In addition to the MPS in Cycle N, Cycle N-1 exhibited a crud induced power shift (CIPS) that resulted in the core axial offset (AO) swinging from an excessive negative value to an excessive

positive value at the end of the cycle. This fuel was then shuffled into Cycle N and experienced a relatively rapid startup that resulted in an axial oscillation of 5.5% after reaching full power.

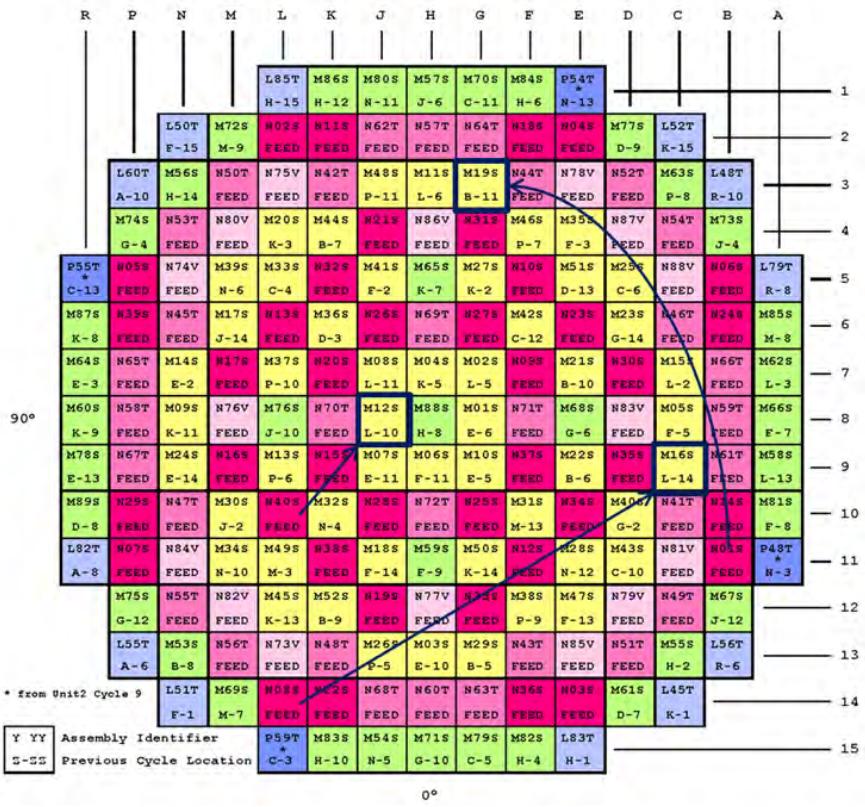

Figure 6: Plant A Cycle N Failed Assembly Locations and N-1 Shuffles

In order to capture this effect on the conditioned powers, the Westinghouse Advanced Nodal Code (ANC) was used to model the observed AO behavior in Cycles N-2 and N-1, and these models were then input to the Local Fuel Duty Risk Monitor (LFDRM) prototype code to generate the end-of-cycle assembly pin-node conditioned powers to shuffle into Cycle N-1 and then into Cycle N. The Cycle N startup was simulated with 138 ANC cases to model the first 81 hours of the startup maneuver shown in Figure 7. The detailed startup history was obtained from the BEACON system cycle history data. Based on the date of the startup the pre-2005 MPSA probability distribution data was used in the LFDRM code.

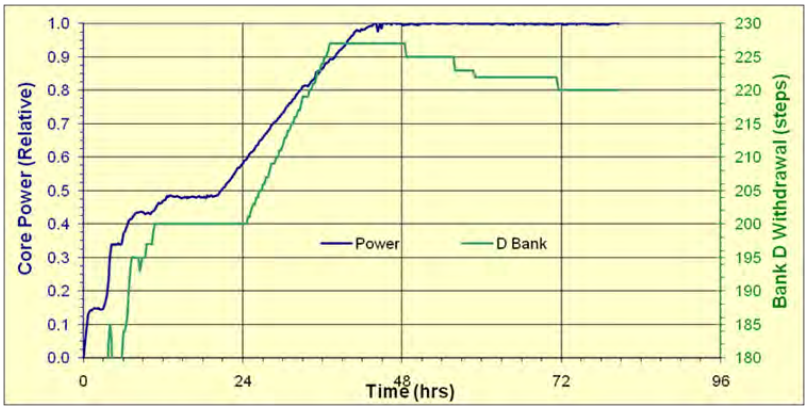

Figure 7: Plant A Cycle N Startup Power and Lead Rod Position

Figure 8 shows the core power level, PCI failure limiting core power and the probable number of failed pellets from the LFDRM prototype code. The time between 40 and 50 hours shows the total core pellet failure probability exceeding the prescribed limit of 0.05. These results indicate that the power should have been held at approximately 90% for 12 hours (to allow clad stress relaxation) before continuing to ramp to full power to minimize the risk of PCI fuel failure.

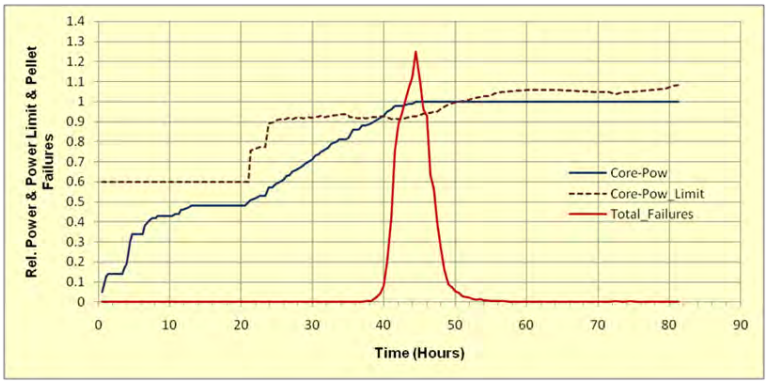

Figure 8: Plant A Cycle N Conditioned Power and Failure Probability

One of the limiting fuel pin-nodes in failed assembly symmetric core location J-3 was tracked during the startup. This location is symmetric to location G-3 and C-9 and is a once burned fuel assembly. Figure 9 shows the power and stress ratio for ANC axial node 8 of pin 13-6 (X-Y location) during the startup. The pin-node conditioned power starts at approximately 6 kW/ft and ends at approximately 7.6 kW/ft. The pin-node power crosses the conditioned power level about 30 hours into the startup. The stress ratio from the LFDRM code reaches a maximum value of ~0.5 about 42 hours into the startup.

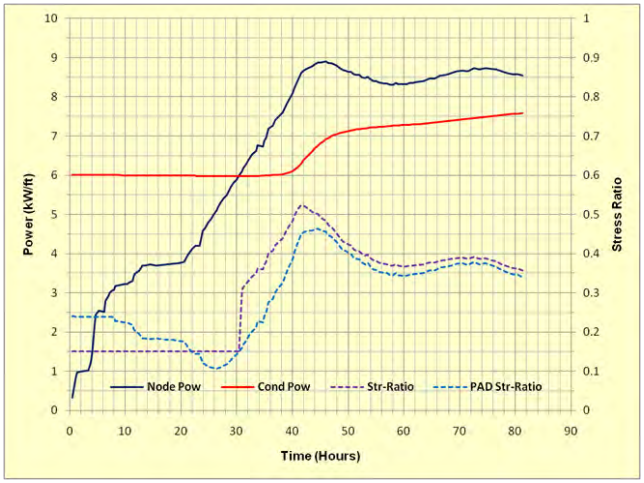

Figure 9: Plant A Cycle N Assembly J-3, Pin 13-6, Node 8 Power and Stress Ratio

Comparison with a FPC model that was depleted through Cycle N-1 to achieve the correct conditioned power shows that the LFDRM startup stress results are conservative with respect to the FPC results but then come together after the peak stress point. The time when the FPC results rise above a stress ratio of 0.15 agrees very well with the timing of the LFDRM stress increase above 0.15 indicating that the effective conditioned power between the two methods is in good agreement. The rise of the FPC stress ratio results above 0.15 indicates that the pellet and clad are in full contact.

There is inherent conservatism in the clad stress model results due to the way the FPC is run to generate data for the model. In each power ramp case very short time steps are used and the clad creep effects from the initial fuel contact are not included. Therefore the initial slow creep effect on the clad after the initial pellet contact is not captured in the model. As a result the LFDRM clad stress results are naturally higher since there is no initial relaxation from the creep model. The stress model assumes that this high stress is applied as soon as the node power exceeds the effective conditioned power with no initial clad relaxation. The conservatism in this approach can be seen in Figure 9. The FPC stress results begin to increase at the same time as that from the stress model but the stress results from the model initially have a step increase because there is no gradual clad relaxation. The results from the stress model will always be higher than the FPC results until the benefit of the initial relaxation from the clad creep is conditioned out of the fuel. The size of the initial difference is dependent on the conditioned power level.

The clad temperature between the two models also has good agreement. After the peak stress point is reach the FPC clad temperature rises to about 8 ºF (4.4 ºC) higher than the temperature from the LFDRM code. The difference would have a very small impact on the stress results and would actually bring the stress results closer together.

The oscillation of the pin-node power is evidence of the core AO oscillation that occurred after reaching full power. This resulted in an oscillation in the pin-node stress as seen in Figure 9 and more clearly in Figure 10 that shows the axial stress ratio for fuel pin 13-6 at 42, 50 and 58 hours from the beginning of the startup.

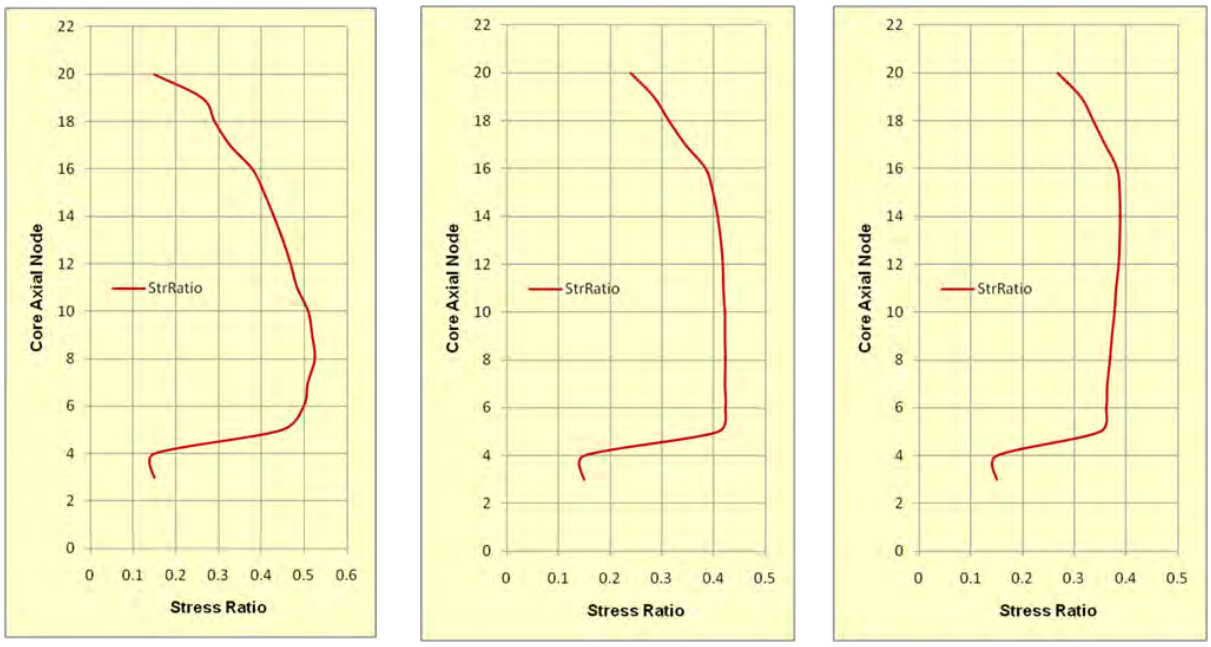

Figure 10: Plant A Cycle N Assembly J-3, Pin 13-6 Stress Ratio at 42, 50 and 58 Hours

A question arises regarding the sensitivity and impact of assuming the post 2005 Columbia plant MPSA probability distribution on the startup PCI failure probability. Figure 11 shows the Plant A Cycle N startup PCI failure limiting power level and the probable number of fuel pellet failures assuming the post 2005 MPSA probability distribution. The results show that the probable pellet failures are significantly reduced and the plant is limited to 98% power for only about 6 hours with a much smaller fuel failure risk.

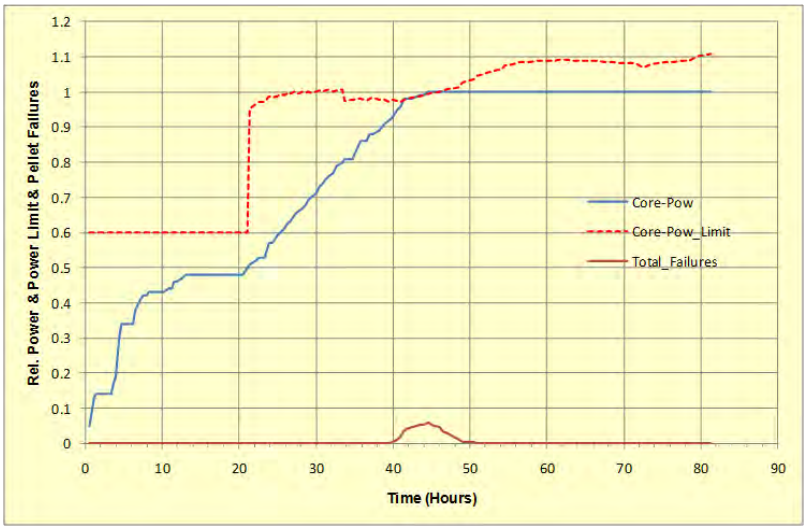

Figure 11: Plant A Cycle N Conditioned Power and Failure Probability Using Post-2005 MPSA Data

These results show that MPSA is a key component when determining the risk of PCI fuel failures. It is clear that without the added stresses from the MPS there is no predicted risk of PCI fuel failures during the Cycle N startup. Therefore it is highly desirable to be able to use a probability distribution of MPSA when determining the risk of PCI failure in the core.

4. Conclusion

The LFDRM methodology is based on the very fast WNF conditioning and clad stress model that is benchmarked to a FPC. Results from the LFDRM methodology are based on an evaluation of the local pin-node conditioned power and clad stress. The evaluation is fast enough that every fuel rod axial node in a four loop core can be evaluated and the risk of PCI failure determined in two to three seconds. The increased risk of higher clad stress due to MPSA is statistically applied to the stress results at a pellet level using the MPSA probability distribution from the fuel manufacturing plant. These results are translated into a core power limit that can be used by the plant reactor engineers or operators when planning power maneuvers or monitoring the core conditions.

Benchmark results with an actual core startup that incurred PCI type fuel failures showed excellent agreement with the timing of the peak risk and the actual measurement of increased coolant activity in the core. The local pin-node stress results also agree well with the FPC results. The capability to shuffle the local fuel conditioned state from cycle to cycle along with the fuel assembly will ensure the correct fuel conditioning at the start of each cycle. The core power limit data will provide guidance for establishing core power ramp rates, hold periods and dropped rod recovery pull rates to reduce the risk of PCI failures. The BEACON core monitoring system will continuously update the fuel conditioning state and enable monitoring of the core PCI fuel failure risk.

5. References

1. Y. Aleshin, A.R. Atwood, D.B. Mitchell, R.E. Sears, PCI Margin Assessment in **AP1000®** Plant, Top Fuel 2012, Paper A0150, September, 2012.
2. Y. Aleshin, C. Beard, D. Mitchell, E. Malek, M. Young, The Effect of Pellet and Local Power Variations on PCI Margin, Paper 041, Top Fuel 2010, Orlando, Florida, September 26-29, 2010.

EFFECTS OF FUEL ROD UNCERTAINTY IN PWR HZP RIA ANALYSIS

Joosuk Lee and Swengwoong Woo

Korea Institute of Nuclear Safety

62 Gwahak-ro, Yusong-gu, Daejeon, 305-338, Republic of Korea

Tel: +82-42-868-0784, Fax: +82-42-868-0045 Email: jslee2@kins.re.kr

ABSTRACT

Effects of fuel rod uncertainties to the rod performance during reactivity initiated accidents (RIAs) in PWR hot zero power (HZP) condition have been analyzed. Considered uncertainties are totally 45 parameters, and these are related to the manufacturing, models in computer code, power pulse and thermal-hydraulic boundary condition. Westinghouse-type 17x17 fuel with Zircaloy-4 cladding, and FRAPCON-3.4a/FRAPTRAN-1.5 code were utilized. Gaussian shape of power pulse with changing the full width half maximum (FWHM) from 10 to 100 ms was used. Considered initial fuel burnup before RIA initiation was 0.5 and 30 MWd/kgU. Radially averaged injected energy at the axially hottest spot of fuel rod was set as 100 cal/g, irrespective of FWHM and fuel burnup. Results of base case analysis indicated that the smaller FWHM has induced more conservative performance values than the larger one. And as fuel burnup moved from 0.5 to 30 MWd/kgU, except for the peak fuel enthalpy, the fuel performance such as the peak fuel and clad temperature, clad permanent strain showed more conservative results. Sensitivity studies revealed that power related uncertainties such as the peak power and FWHM showed relatively strong influences to the rod performance. And several uncertainty parameters in manufacturing and models also have showed strong impacts. Effects of combined uncertainty evaluated by utilizing a non-parametric order statistics approach are also assessed and described in this paper.

1. Introduction

In the mid-1990s, it was discovered that the acceptance criteria of reactivity initiated accidents (RIAs) such as the 170 cal/g, departure from nucleate boiling (DNB) or critical power ratio (CPR) were not always adequate to protect the fuel rod failure, especially for the high burnup fuel. Thereafter, extensive experimental works for the establishment of new safety criteria have been conducted in CABRI, NSRR, BIGR [1]. Based on these data, interim acceptance criteria were established by U.S. NRC in 2007 [2]. The interim criteria contain more stringent limits than previous ones. For example, pellet-to-cladding mechanical interaction (PCMI) was introduced as an additional failure criterion. And incipient fuel melting, fuel-to coolant interaction, rod burst, fuel rod ballooning and flow blockage phenomena should be addressed for core coolability assurance. For dose assessment, transient-induced fission gas release has to be accounted. Since these new criteria tend to reduce the margins to the criteria, licensees are trying to improve the margins by utilizing a less conservative approach in licensing applications. For example, detailed 3D kinetic analysis methodology has been utilized [3].

On the other hands, along with these experimental studies, for the simulation of fuel behaviors during RIAs, modeling works by use of the computer codes have been also conducted. But some differences between the experiments and code analysis results were founded. For example, the residual hoop strain of the tested cladding in CABRI and NSRR showed about 1~2 % differences. And maximum fuel enthalpy revealed about up to 12 cal/g differences as the experimental results were simulated by FRAPTRAN 1.4 code [4]. Furthermore, recently performed RIA code benchmark results in OECD/NEA showed a large scatter of rod performance among the computer codes, and it recommended the assessment

of the initial state of the fuel rod for the transient analysis [5]. These discrepancies seem to be partly due to the various kinds of uncertainty such as fuel dimensions, models used in the computer codes, power pulses, heat transfer phenomena, thermal-hydraulic boundary conditions (THBC) etc.
Several parametric sensitivity studies have been conducted to find out which parameters are affecting the fuel performance during RIA [6,7,8]. But, they do not consider every uncertainty parameter that can be conceivable. Thereby, in this paper, sensitivity studies based on the various kinds of uncertainty have been carried out to identify the relative importance to the rod performance. And effects of combined uncertainty have been evaluated by utilizing a non-parametric order statistics approach as well.

2. Analysis Details

2.1 Base case analysis

In this study, Westinghouse-type 17x17 fuel with Zircaloy-4 cladding was utilized. Design parameters of fuel rod and operating conditions of PWR are listed in Table 1. For the generation of initial state of fuel rod before RIA, applied steady-state power history was such that the linear heat rate (LHR) of 10.18 kW/ft (rod average) was maintained up to 30 MWd/kgU fuel burnup, and it reduced continuously with burnup increase. This information is described in NUREG-1754 [9].
Initiation of RIA was supposed to be occurred in a hot zero power (HZP) condition at the fuel burnup of 0.5 and 30 MWd/kgU. Gaussian shape of power pulse was used with changing full width half maximum (FWHM) from 10 to 100 ms. A single strongly bottom-skewed axial power profile was used. This axial power profile was obtained from the hottest pin power evolution in condition of APR1400 HZP RIA [10]. Radially averaged injected energy at the axially hottest spot of the fuel rod was 100 cal/g, and it was set to be an invariant with considered FWHM and fuel burnup. Applied rod averaged power pulses and axial power profile were shown in Fig.1.
For the fuel performance assessment, FRAPCON-3.4a and FRAPTRAN-1.5 code were used

Table 1. Design information of fuel rod and operational conditions of PWR [9].

Description(units)			
Cladding material	Zircaloy-4	Cladding inner diameter(mm)	8.18
Cladding thickness(mm)	0.61	Cladding roughness (micron)	0.5
Pellet outer diameter(mm)	8	Pellet density(TD)(%)	95
Pellet re-sinter density(%)	0.9	Pellet roughness(micron)	2
Pellet dish diameter & depth(mm)	4.01, 0.287	Rod fill pressure(MPa)	2.41
Rod plenum length(mm)	254	Active fuel length(m)	3.66
Mass flow rate(kg/m^2)	12.47x10^6	Coolant inlet temperature, (^{o}C)	288
System coolant pressure(MPa)	15.5	Pitch(mm)	12.6

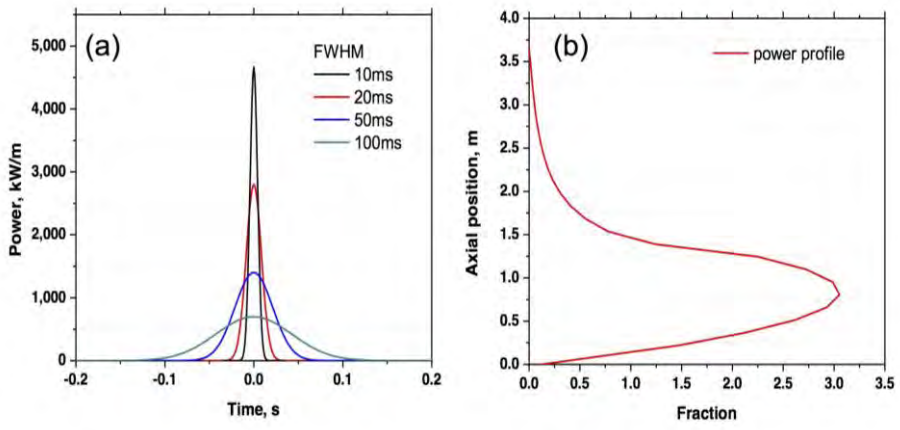

Fig. 1 (a) Applied rod averaged power pulse with changing FWHM, and (b) axial power profile for RIA analysis. Peak power was injected at the time of t=0 s.

[11,12]. FRAPCON and FRAPTRAN code can evaluate the thermo-mechanical performance of fuel rod during steady-state and transient, respectively. 20 evenly spaced axial nodes in the fuel rod and 20 equal-area radial nodes in a pellet were used. 'Coolant option' in FRAPTRAN code was turned on to specify the coolant conditions for RIA analysis.

2.2 Considered fuel rod uncertainty

Authors have already identified many uncertainty parameters of fuel rod such as related to the manufacturing, models used in computer code and power for the assessment of loss of coolant accident (LOCA) safety analysis with limiting fuel burnup change [13]. In this study we utilized those parameters again, and additional parameters were newly introduced. Additional parameters are related to the heat transfer phenomena from cladding to coolant, THBC and power pulse during RIA. All parameters were listed in Table. 2. In manufacturing uncertainties, 10 different parameters were used. In model uncertainties, along with 24 different parameters, which were already identified, five additional parameters were newly introduced. These are Dittus-Boelter(liquid and vapor), Tom, Grenoveld-5.9 and critical heat flux (EPRI-1) correlation. Uncertainty ranges of those parameters were basically chosen based on the information of audit calculation methodology of LBLOCA analysis in Korea (KINS-REM) [14]. But some models adapted in FRAPTRAN code are different with the KINS-REM. Therefore exact uncertainty range should be determined for further in detail analysis. Coolant inlet temperature, system pressure, mass flow rate were also newly selected as uncertainty parameters, and uncertainty of those parameters were chosen based on the operating experiences.

Radial power profile in a pellet, peak power and FWHM of RIA power pulse were considered as power uncertainties. Uncertainty of radial power profile was set as +/- 10%. And uncertainty of peak power and FWHM was set as +/- 5%. In this way, 45 uncertainty parameters were selected.

2.3 Combined uncertainty analysis

Effects of combined uncertainty were evaluated by utilizing a probabilistic approach, so called a non-parametric order statistics approach. Non-parametric order statistics based on the Wilks' formula is a well-known statistical method for the best-estimate LOCA safety analysis, and its validity is already proven through the OECD/NEA BEMUSE program [15]. Several sets of 124 inputs for the running of FRAPCON/FRAPTRAN were produced by utilizing a simple random sampling (SRS) technique [16].

In the statistical treatment, probability density function (PDF) is an important factor to the rod performance. In this study, the PDF on each parameter was assigned in accordance with the authors' previous works [13]. The PDF of newly introduced parameters was assumed as a uniform distribution, except for the power related uncertainties. The PDF of power uncertainties were assumed as a normal.

3. Results and Discussion

3.1 Base case

Fig. 2 shows the evolution curves of radial averaged peak fuel enthalpy, peak cladding permanent strain, peak fuel and cladding temperature with changing fuel burnup and FWHM. These peak values were obtained at the axial node number of 5 or 6 from the bottom position of fuel rod. As can be seen in Fig. 2(a), the shorter FWHM resulted in the higher peak enthalpy values. At the 0.5 MWd/kgU burnup, the peak enthalpy was 116.8 cal/g in 10 ms FWHM condition and it continuously reduced as the FWHM changed to 100 ms. It was 115.7, 113.2 and 110.2 cal/g when the applied FWHM was 20, 50 and 100 ms, respectively. This reduction is due to the relatively sufficient time of heat conduction from fuel to coolant. At the 30 MWd/kgU burnup, it was 115.0, 113.3, 110.2, 107.0 cal/g as the applied FWHM was 10, 20, 50, 100 ms, respectively. These results also indicate that at the given analysis condition, results of 30 MWd/kgU fuel burnup showed a little bit lower peak enthalpy than the results of

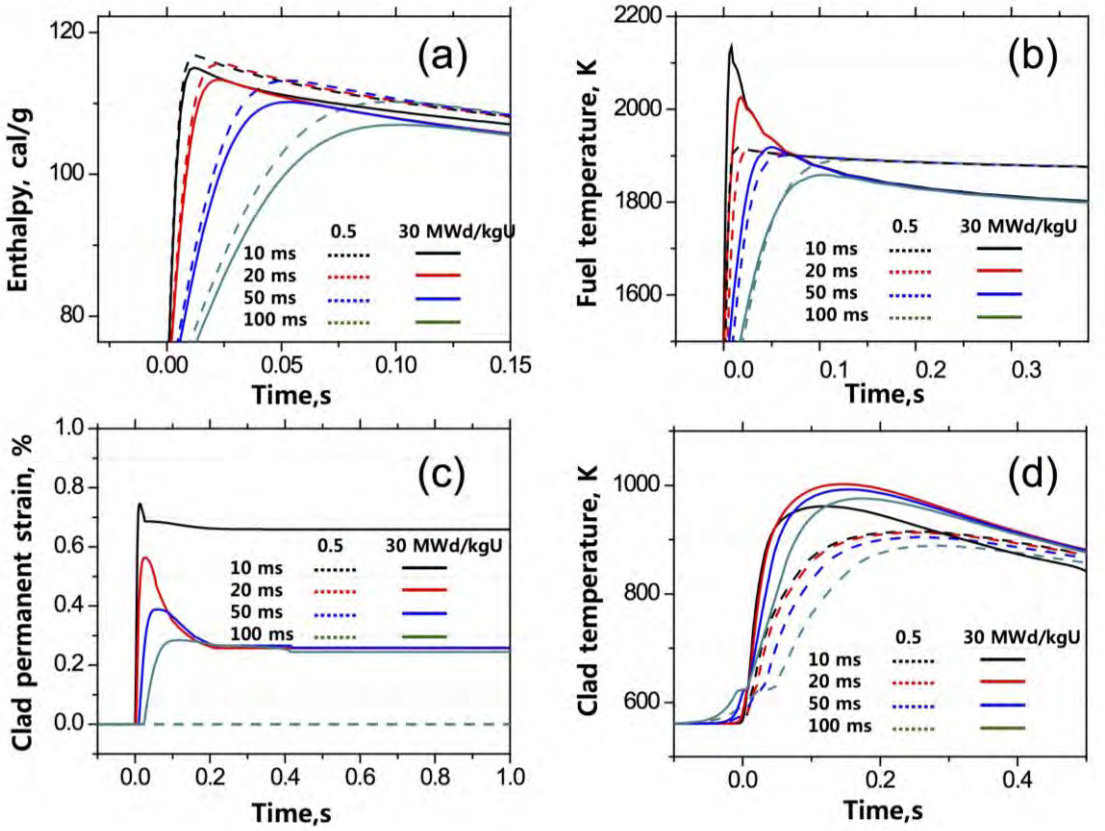

Fig. 2. Evolution curves of (a) radial averaged peak fuel enthalpy, (b) peak fuel temperature, (c) peak cladding permanent hoop strain and (d) peak cladding temperature with changing fuel burnup and FWHM. Peak power pulse was injected at the time of t=0 s.

0.5 MWd/kgU condition. This is related to the heat conduction due to the differences of initial gap width and radial power peaking.

Fig. 2(b) shows the evolution of peak fuel temperature. At the 0.5 MWd/kgU fuel burnup, peak fuel temperature was 1917, 1911.2, 1900.8, 1890.5 K when the FWHM was assigned as 10, 20, 50, and 100 ms, respectively. And at the 30 MWd/kgU condition, it was 2134.1, 2025.9, 1918.3 and 1858.8 K. The reduction of maximum fuel temperature with increasing the FWHM is also related to the heat conduction from fuel to coolant. And the higher peak fuel temperature at the fuel burnup of 30 MWd/kgU is related to the radial power peaking. Basically peak fuel temperature in a pellet was observed at the pellet periphery due to the radial power peaking. And as fuel burnup moved to 30 MWd/kgU, even stronger radial power peaking occurred. Therefore, much higher peak fuel temperature appeared at the fuel burnup of 30 MWd/kgU.

Fig. 2(c) shows the evolution of clad permanent hoop strain. At the fuel burnup of 0.5 MWd/kgU, permanent hoop strain was not observed. This is caused by the relatively large size of initial gap. But fuel burnup moved to 30 MWd/kgU, it was observed. Maximum permanent hoop strain was 0.74 % at the 10 ms FWHM condition, and it reduced to 0.56, 0.39 and 0.28 % as the applied FWHM changed to 20, 50 and 100 ms, respectively. This reduction is explained by the lower thermal expansion of fuel pellet due to the lower fuel temperature. The permanent residual hoop strain was 0.66, 0.26, 0.26 and 0.24 % for 10, 20, 50 and 100 ms FWHM condition, respectively.

Fig. 2(d) shows the evolution of peak cladding temperature. At the fuel burnup of 0.5 MWd/kgU, peak cladding temperature was 914.9, 912.9, 904.4 and 888.7 K as applied FWHM was 10, 20, 50 and 100 ms, respectively. And as fuel burnup moved to 30 MWd/kgU, it was 961.2, 1002.1, 992.4 and 975.7 K, respectively. These changes of peak cladding temperature are similar with the peak fuel temperature variations with changing FWHM and fuel burnup.

Table 2. Effects of fuel rod uncertainty on the peak fuel enthalpy (Δh), peak permanent residual hoop strain (Δε_res), peak fuel (ΔPFT) and peak cladding temperature (ΔPCT) with changing FWHM.

	Parameter	Tolerance or Bias	0.5 MWd/kgU												30 MWd/kgU											
			Δh, cal/g				Δε_res, %	ΔPFT, K				ΔPCT, K				Δh, cal/g				Δε_res, %				ΔPFT, K				ΔPCT, K			
			FWHM,ms					FWHM,ms								FWHM,ms											
			10	20	50	100	10~100	10	20	50	100	10	20	50	100	10	20	50	100	10	20	50	100	10	20	50	100	10	20	50	100
Manufacturing	1. Cladding inner diameter, mm	±0.04	1.9	2.3	2.9	3.3	0.0	3.5	2.8	2.9	2.7	88.5	90.3	116.8	143.6	0.7	0.8	1.0	1.4	0.4	0.7	0.6	0.4	67.6	40.6	25.1	22.0	57.1	64.9	41.4	27.8
	2. Cladding thickness, mm	±0.04	0.0	0.0	0.0	0.0	0.0	0.0	0.0	0.1	0.1	49.6	48.7	43.8	31.7	0.0	0.0	0.1	0.1	0.2	0.0	0.0	0.1	2.0	1.5	1.2	1.5	50.4	31.1	30.8	30.2
	3. Cladding roughness, micron	±0.3	0.0	0.0	0.0	0.0	0.0	0.0	0.0	0.0	0.0	0.0	0.0	0.0	0.0	0.0	0.0	0.0	0.0	0.0	0.0	0.0	0.1	0.4	0.1	0.1	0.1	0.8	0.2	0.0	0.1
	4. Pellet outer diameter, mm	±0.013	1.5	1.6	1.7	1.7	0.0	8.9	8.6	8.7	8.6	45.1	37.3	33.2	31.0	0.8	0.8	0.9	0.9	0.1	0.1	0.1	0.1	40.5	29.6	18.7	14.9	44.7	15.7	14.9	14.1
	5. Pellet density, %	±0.91	1.8	1.7	1.7	1.6	0.0	21.6	21.8	22.2	22.4	5.3	5.1	4.7	4.7	1.9	1.8	1.8	1.7	0.1	0.0	0.0	0.0	44.1	33.9	26.7	23.7	46.3	2.1	2.0	1.8
	6. Pellet re-sinter density increase, %	±0.4	0.1	0.1	0.1	0.2	0.0	9.5	9.6	9.3	9.2	42.9	42.6	37.8	36.3	0.8	0.7	0.6	0.5	0.2	0.4	0.2	0.1	3.8	4.6	4.8	4.4	52.4	56.8	1.2	1.3
	7. Pellet roughness, micron	±0.5	0.0	0.0	0.0	0.0	0.0	0.0	0.0	0.0	0.0	0.3	0.2	0.2	0.1	0.3	0.3	0.3	0.3	0.1	0.0	0.0	0.0	27.6	11.8	4.3	2.3	11.6	7.8	8.0	8.1
	8. Pellet dish diameter & depth, mm	±0.5, +0.05	0.0	0.0	0.0	0.0	0.0	0.0	0.0	0.0	0.0	2.1	1.8	1.1	0.6	0.0	0.0	0.0	0.0	0.1	0.0	0.0	0.0	0.3	0.1	0.1	0.1	8.6	0.1	0.1	0.2
	9. Rod fill pressure, Mpa	±0.07	0.0	0.0	0.0	0.0	0.0	0.0	0.0	0.1	0.1	4.3	3.8	2.4	1.4	0.0	0.0	0.0	0.0	0.0	0.1	0.0	0.0	0.6	0.3	0.6	0.7	2.2	0.8	0.7	0.7
	10. Rod plenum length, mm	±11.4	0.0	0.0	0.0	0.0	0.0	0.0	0.0	0.0	0.0	1.6	1.4	0.9	0.5	0.0	0.0	0.0	0.1	0.0	0.0	0.0	0.0	2.3	1.6	0.8	1.0	10.4	0.4	0.7	0.5
Model	11. Fuel thermal conductivity	±2σ	0.1	0.2	0.4	0.6	0.0	1.7	2.0	3.4	4.1	58.2	57.6	51.9	46.8	1.0	1.2	1.6	1.9	0.4	0.2	0.1	0.1	113.3	69.0	42.3	32.6	129.0	77.2	52.9	55.1
	12. Fuel thermal expansion	±2σ	1.6	1.9	2.4	2.6	0.0	2.1	1.2	1.5	1.4	108.7	112.8	130.1	152.3	0.1	0.1	0.1	0.3	0.9	0.8	0.5	0.4	10.5	8.1	6.1	6.1	71.3	46.2	9.4	2.4
	13. FGR	±2σ	0.0	0.0	0.0	0.0	0.0	0.0	0.0	0.0	0.0	0.0	0.0	0.0	0.0	0.7	0.8	0.9	1.0	0.6	0.2	0.2	0.0	61.8	31.8	17.1	13.6	97.3	47.4	16.5	16.7
	14. Fuel swelling	±2σ	0.0	0.0	0.0	0.0	0.0	0.0	0.0	0.0	0.0	0.0	0.0	0.0	0.0	0.1	0.1	0.1	0.2	0.1	0.1	0.1	0.1	7.4	5.8	4.6	4.6	46.9	0.3	0.3	0.4
	15. Fuel relocation	±2σ(±34%)	0.0	0.0	0.0	0.0	0.0	0.0	0.0	0.0	0.0	0.1	0.2	0.1	0.1	0.0	0.0	0.0	0.1	0.1	0.1	0.1	0.1	2.5	2.4	1.8	1.8	2.9	0.2	0.5	1.4
	16. Fuel specific heat capacity	±1se	0.5	0.5	0.6	0.6	0.0	22.3	22.2	22.0	21.8	12.0	11.5	10.2	10.0	0.4	0.4	0.5	0.5	0.0	0.0	0.0	0.1	19.9	20.9	20.6	20.4	3.2	4.6	4.6	5.0
	17. Fuel emissivity	±1se	0.0	0.0	0.0	0.0	0.0	0.0	0.0	0.0	0.0	0.0	0.0	0.0	0.0	0.0	0.0	0.0	0.0	0.0	0.0	0.0	0.0	0.1	0.0	0.0	0.0	0.1	0.0	0.0	0.0
	18. Cladding corrosion(oxide thickness)	±2σ	0.1	0.1	0.1	0.1	0.0	0.1	0.0	0.1	0.1	5.1	4.4	2.7	1.6	0.0	0.0	0.0	0.0	0.1	0.0	0.0	0.0	1.9	0.1	1.1	1.4	6.7	3.1	3.2	3.2
	19. Creep of cladding	±2σ	0.1	0.1	0.1	0.2	0.0	0.1	0.1	0.1	0.1	6.2	5.9	5.3	5.3	0.1	0.1	0.2	0.4	0.2	0.2	0.3	0.2	13.6	11.5	8.9	8.9	2.5	1.2	0.6	0.7
	20. Cladding axial growth	±2σ	0.0	0.0	0.0	0.0	0.0	0.0	0.0	0.0	0.0	2.7	2.4	1.5	0.8	0.0	0.0	0.0	0.0	0.0	0.0	0.0	0.0	0.3	0.7	0.4	0.5	7.1	0.2	0.2	0.0
	21. Hydrogen pickup	±2σ	0.0	0.0	0.0	0.0	0.0	0.0	0.0	0.0	0.0	0.0	0.0	0.0	0.0	0.0	0.0	0.0	0.0	0.0	0.0	0.0	0.0	0.0	0.0	0.0	0.0	0.0	0.0	0.0	0.0
	22. Cladding thermal conductivity	±2σ	0.0	0.1	0.1	0.1	0.0	0.0	0.0	0.1	0.1	8.0	7.8	7.5	8.3	0.1	0.1	0.2	0.2	0.0	0.0	0.0	0.0	5.8	3.1	1.5	1.0	9.7	7.4	7.9	8.3
	23_1 Cladding axial thermal expansion	±30%	0.0	0.0	0.0	0.0	0.0	0.0	0.0	0.0	0.0	0.8	0.7	0.4	0.3	0.0	0.0	0.0	0.0	0.0	0.0	0.0	0.0	0.5	0.0	0.3	0.1	0.2	0.0	0.3	0.0
	23_2 Cladding diametral thermal expansion	±30%	0.5	0.7	0.8	0.8	0.0	0.2	0.4	0.5	0.5	44.8	44.5	41.8	37.3	0.0	0.0	0.1	0.1	0.2	0.5	0.2	0.2	3.3	2.8	2.8	3.1	23.7	38.2	0.0	0.6
	24. Cladding elastic modulus	±1se	0.2	0.2	0.2	0.2	0.0	0.1	0.1	0.1	0.2	13.2	12.6	11.1	10.7	0.0	0.0	0.0	0.0	0.5	0.3	0.0	0.0	1.2	0.9	0.8	0.9	97.1	31.3	0.7	0.5
	25. Cladding specific heat	±1se	0.0	0.0	0.0	0.1	0.0	0.0	0.0	0.1	0.1	9.5	8.9	7.7	7.0	0.0	0.0	0.1	0.1	0.0	0.0	0.0	0.0	1.8	1.1	0.6	0.5	12.3	9.1	8.2	8.8
	26. Cladding yield stress	±30%	0.0	0.0	0.0	0.0	0.0	0.0	0.0	0.0	0.0	30.2	30.1	29.2	27.8	0.0	0.0	0.0	0.0	0.4	0.0	0.0	0.0	0.0	0.2	0.1	0.0	39.7	0.5	0.1	0.6
	27. Cladding surface emissivity	±1se	0.0	0.0	0.0	0.0	0.0	0.0	0.0	0.0	0.1	0.2	0.2	0.1	0.2	0.0	0.0	0.0	0.0	0.0	0.0	0.0	0.0	0.1	0.1	0.0	0.1	0.4	0.0	0.0	0.1
	28. Zirconium oxide thermal conductivity	0.5~1.1	0.0	0.0	0.0	0.0	0.0	0.0	0.0	0.0	0.0	0.0	0.1	0.0	0.0	0.0	0.0	0.0	0.0	0.0	0.0	0.0	0.0	2.1	1.0	0.3	0.3	4.1	0.6	0.6	0.7
	29. Gas conductivity (He)	±2σ	0.0	0.0	0.1	0.1	0.0	0.0	0.0	0.1	0.1	2.0	2.0	1.9	2.1	0.0	0.0	0.0	0.0	0.0	0.0	0.0	0.0	2.0	0.7	0.2	0.5	2.1	0.6	0.7	0.4
	30. Cladding failure stress, MPa	-30 ~ +90	0.0	0.0	0.0	0.0	0.0	0.0	0.0	0.0	0.0	0.0	0.0	0.0	0.0	0.0	0.0	0.0	0.0	0.0	0.0	0.0	0.0	0.0	0.0	0.0	0.0	0.0	0.0	0.0	0.0
	31. Cladding failure strain	0.2~1.6	0.0	0.0	0.0	0.0	0.0	0.0	0.0	0.0	0.0	0.0	0.0	0.0	0.0	0.0	0.0	0.0	0.0	0.0	0.0	0.0	0.0	0.0	0.0	0.0	0.0	0.0	0.0	0.0	0.0
	32. High temperature oxidation (C-P)	±6%	0.0	0.0	0.0	0.0	0.0	0.0	0.0	0.0	0.0	0.0	0.0	0.0	0.0	0.0	0.0	0.0	0.0	0.0	0.0	0.0	0.0	0.0	0.0	0.0	0.0	0.0	0.0	0.0	0.0
	33. Crud thermal conductivity	0.5~1.5	0.0	0.0	0.0	0.0	0.0	0.0	0.0	0.0	0.0	0.0	0.0	0.0	0.0	0.0	0.0	0.0	0.0	0.0	0.0	0.0	0.0	0.0	0.0	0.0	0.0	0.0	0.0	0.0	0.0
	34. Crud thickness(accumarated), micron	0~30	0.0	0.0	0.0	0.0	0.0	0.0	0.0	0.0	0.0	0.0	0.0	0.0	0.0	0.0	0.0	0.0	0.0	0.0	0.0	0.0	0.0	0.0	0.0	0.0	0.0	0.0	0.0	0.0	0.0
	35. Dittus-Boelter HTC(liquid)	0.6~1.4	0.0	0.0	0.0	0.0	0.0	0.0	0.0	0.0	0.1	0.1	0.1	0.5	0.6	0.0	0.0	0.0	0.0	0.0	0.0	0.0	0.0	0.0	0.1	0.0	0.4	1.2	0.4	0.4	1.3
	36. Dittus-Boelter HTC(vapor)	0.6~1.4	0.0	0.0	0.0	0.0	0.0	0.0	0.0	0.0	0.0	0.0	0.0	0.0	0.0	0.0	0.0	0.0	0.0	0.0	0.0	0.0	0.0	0.0	0.0	0.0	0.0	0.0	0.0	0.0	0.0
	37. EPRI-1 CHF	0.2~1.8	0.0	0.0	0.2	0.8	0.0	0.0	0.0	0.0	0.1	278.1	277.0	296.1	289.3	0.0	0.1	0.5	1.4	0.1	0.3	0.1	0.0	0.0	0.2	1.1	2.7	202.9	212.4	242.2	296.8
	38. Tom HTC	0.5~1.5	0.0	0.0	0.0	0.0	0.0	0.0	0.0	0.0	0.0	22.7	20.9	16.9	14.1	0.0	0.0	0.0	0.0	0.0	0.0	0.0	0.0	0.0	0.0	0.1	0.0	19.1	21.9	30.8	23.2
	39. Groenveld HTC	0.5~1.5	0.0	0.0	0.0	0.0	0.0	0.0	0.0	0.0	0.0	184.9	184.2	180.9	171.8	0.0	0.0	0.0	0.1	0.7	0.2	0.2	0.1	0.0	0.0	0.0	0.0	176.2	165.3	154.3	158.7
TH BC	40. Coolant temp.,K	±3	0.4	0.4	0.4	0.4	0.0	4.7	4.8	4.8	4.8	17.9	17.2	16.1	17.5	0.4	0.4	0.4	0.5	0.0	0.0	0.0	0.0	4.5	4.9	4.9	5.0	11.1	11.6	12.5	13.8
	41. Coolant pressure, MPa	±0.15	0.0	0.0	0.0	0.0	0.0	0.0	0.0	0.0	0.1	9.7	9.6	9.6	10.2	0.0	0.0	0.0	0.0	0.0	0.0	0.0	0.0	0.3	0.3	0.2	0.1	5.6	10.1	10.6	10.7
	42. Mass flow rate	0.98~1.02	0.0	0.0	0.0	0.0	0.0	0.0	0.0	0.0	0.0	9.1	8.9	8.4	8.8	0.0	0.0	0.0	0.0	0.0	0.0	0.0	0.0	0.0	0.0	0.1	0.0	5.6	6.3	6.8	7.5
Power	43. radial power profile	0.9~1.1	0.7	0.7	0.6	0.5	0.0	66.2	50.5	24.4	0.1	43.8	41.6	28.8	22.8	0.6	0.7	0.8	0.9	0.5	0.3	0.0	0.0	159.1	89.1	31.7	4.3	56.5	4.6	39.8	40.6
	44. Power(peak power)	0.95~1.05	9.4	9.3	9.1	8.8	0.0	120.4	120.2	119.8	119.4	83.3	83.2	82.8	101.5	9.8	9.7	9.4	9.1	0.2	0.4	0.1	0.1	139.3	129.1	121.9	118.1	6.4	3.3	47.1	49.3
	45. FWHM	0.95~1.05	9.3	9.0	8.7	8.3	0.0	119.4	119.5	118.5	117.6	82.7	82.8	81.1	92.8	9.6	9.4	9.0	8.6	0.2	0.4	0.1	0.0	118.3	115.0	112.7	110.3	0.4	4.8	45.1	45.8
	Base case		h, cal/g				ε_res, %	PFT, K				PCT, K				h, cal/g				ε_res, %				PFT, K				PCT, K			
			116.8	115.7	113.2	110.2	0.00	1917.0	1911.2	1900.8	1890.5	914.9	912.9	904.4	888.7	115.0	113.3	110.2	107.0	0.66	0.26	0.26	0.27	2134.1	2025.9	1918.3	1858.8	961.2	1002.1	992.4	975.7

3.2 Sensitivity Analysis

3.2.1 Peak fuel enthalpy

Analysis results of fuel rod uncertainty to the changes of peak fuel enthalpy (∆h) were summarized in Table 2. Generally, power related uncertainties have strong impact and several uncertainties in the manufacturing and models showed a moderate influence on the ∆h. At the fuel burnup of 0.5 MWd/kgU, cladding inner diameter, pellet outer diameter, pellet density and fuel thermal expansion in a pellet showed a moderate influence to the ∆h. They induced about 1.3~3.3 cal/g ∆h. Uncertainties of peak power and FWHM have induced a significant impact. They resulted in about 8.3~9.4 cal/g ∆h. But, as fuel burnup moved to 30 MWd/kgU, pellet density and fuel thermal conductivity only have induced a moderate influence. They resulted in 1.0~1.9 cal/g ∆h. Peak power and FWHM still showed a strong influence. They resulted in about 8.6~9.8 cal/g ∆h.

3.2.2 Peak permanent residual hoop strain

At the fuel burnup of 0.5 MWd/kgU, change of peak permanent residual hoop strain (∆ε_res) due to fuel rod uncertainty was not observed. But burnup moved to 30 MWd/kgU, many parameters were identified. Pellet re-sinter density increase, fuel thermal conductivity, creep of cladding, cladding diametral thermal expansion, cladding elastic modulus, cladding yield stress, radial power profile, peak power and FWHM showed a moderate impact. The ∆ε_res was about 0.2~0.5 %. Cladding inner diameter, fuel thermal expansion, fission gas release (FGR), Groenveld-5.9 heat transfer correlation induced a relatively strong influence. The ∆ε_res was about 0.6~0.9 %. But the importance was varied depending on the considered FWHM.

3.2.3 Peak fuel temperature

Change of peak fuel temperature (∆PFT) was also summarized in Table 2. At the 0.5 MWd/kgU burnup, pellet density and fuel specific heat capacity showed a moderate influence to the ∆PFT. It was about 20K. Radial power profile showed 66.2K ∆PFT at the 10 ms FWHM, but as the FWHM changed to 100 ms, it was almost zero. Peak power and FWHM have induced a strong influence. ∆PFT was about 120K. As fuel burnup moved to 30 MWd/kgU, cladding inner diameter, pellet outer diameter, pellet density, pellet roughness, FGR, fuel specific heat capacity resulted in a moderate influence. Maximum ∆PFT was about 20~70 K. Fuel thermal conductivity, radial power profile, peak power and FWHM showed strong impact such that maximum ∆PFT was about 110~160 K. The ∆PFT was also dependent on the FWHM.

3.2.4 Peak cladding temperature

Many parameters showed a moderate impact to the change of peak cladding temperature (∆PCT). At the fuel burnup of 0.5 MWd/kgU, cladding inner diameter, cladding thickness, pellet outer diameter, pellet re-sinter density increase, fuel thermal conductivity, cladding diametral thermal expansion, cladding yield stress, radial power profile, peak power and FWHM showed a moderate influence. The maximum ∆PCT was about 30~140 K. But fuel thermal expansion, EPRI-1 CHF correlation, Groenveld-5.9 have induced about 150~300 K ∆PCT. As fuel burnup moved to 30 MWd/kgU, cladding inner diameter, cladding thickness, pellet outer diameter, pellet density, pellet re-sinter density increase, fuel thermal conductivity, fuel thermal expansion, FGR, fuel swelling, cladding elastic modulus, radial power profile, peak power and FWHM have induced a moderate influence. And EPRI-1 CHF correlation and Groenveld-5.9 still showed a strong impact.

3.3 Combined uncertainty

Fig. 3(a) shows a set of 124 fuel enthalpy evolution curves analyzed at the 20 ms FWHM condition. The peak enthalpy was obtained at the time of 0.022~0.024s after peak power insertion. At the 0.5 MWd/kgU condition, the minimum and maximum peak enthalpy was 110.8 and 121.9 cal/g, respectively. And at the 30 MWd/kgU, it was 108.3 and 119.1 cal/g.

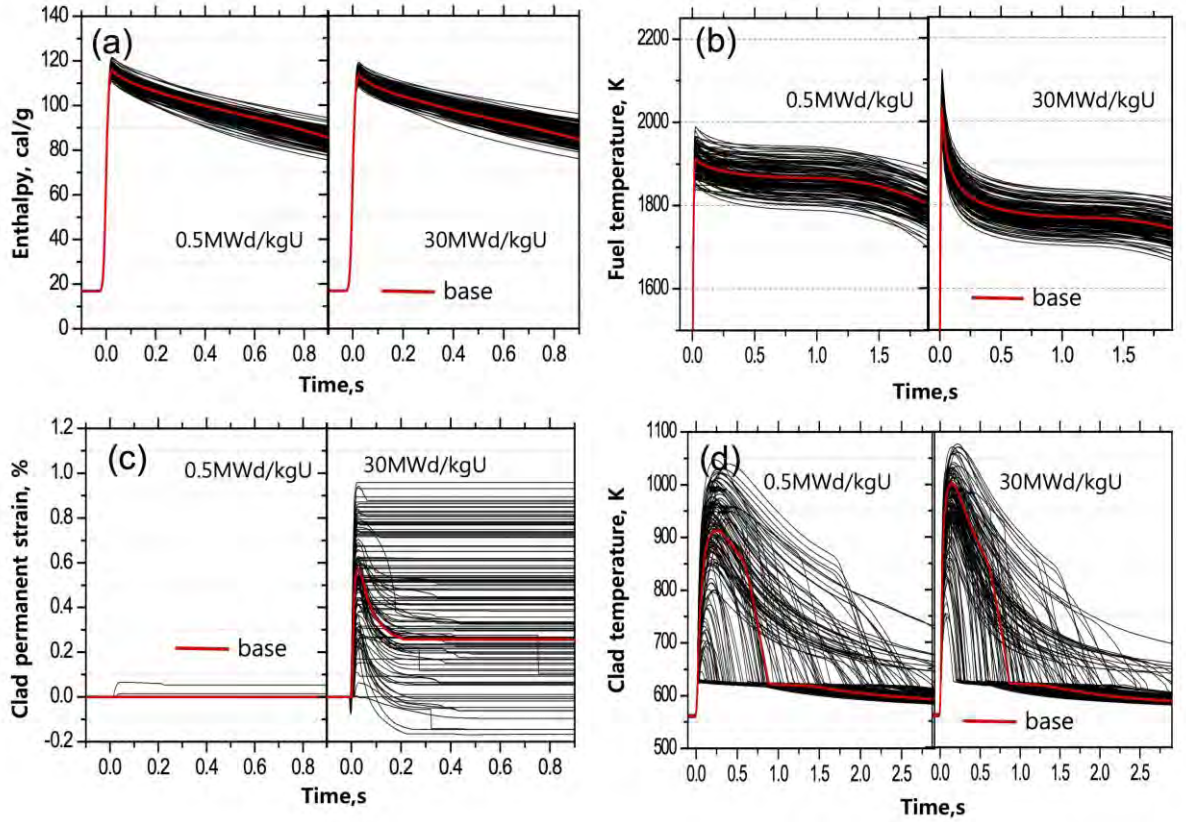

Fig. 3. A set of 124 fuel performance evolution curves. (a) peak enthalpy, (b) peak cladding permanent hoop strain, (c) peak fuel and (d) peak cladding temperature with burnup change. FWHM was 20 ms and peak power was injected at the time of t=0 s. These curves were obtained from axial node number of 5 or 6.

Thus the change of peak enthalpy with respect to the base case was about +/-5 % at both fuel burnups.

Fig. 3(b) shows the peak fuel temperature evolution curves. Peak fuel temperature appeared at the time of 0.02~0.03 s after peak power insertion. At the 0.5 MWd/kgU condition, the minimum and maximum peak fuel temperature was 1838.2 and 1989.6 K, respectively, and at the 30 MWd/kgU condition it was 1941.2 and 2124.9 K. Thus compared to the base case it varied about +/- 4% at both fuel burnups.

Fig. 3(c) shows cladding permanent hoop strain evolution curves. At the fuel burnp of 0.5 MWd/kgU, permanent hoop strain was not observed, except for two cases. And hoop strain of these two cases was also very small, less than 0.1 %. However, as burnup moved to 30 MWd/kgU, it was ranging from -0.16 to 0.96 %. Thus permanent hoop strain varied from -160 to 270 % with respect to the base case.

Fig. 3(d) shows the peak cladding temperature evolution curves. Peak cladding temperature was observed at the time of 0.04~0.47 s and 0.06~0.27 s after peak power insertion for the 0.5 and 30 MWd/kgU condition, respectively. At the 0.5 MWd/kgU condition, the minimum and maximum peak cladding temperature was 624.6 and 1043.0 K, respectively. And it was 741.6 and 1080.2 K for the 30 MWd/kgU condition. Thereby, with respect to the base case it varied from -32 to 14% and from -26 to 8% for the 0.5 and 30 MWd/kgU burnup condition, respectively.

Analysis results of combined uncertainty revealed that about 10 percent of uncertainty appeared in the fuel enthalpy and fuel temperature performance. But much significant uncertainty effects on clad hoop strain and clad temperature were discovered. These results also indicate that with the fuel enthalpy point of view, the beginning of life fuel will give conservative performance results, but with the fuel temperature, cladding temperature and clad strain point of view, burnt fuel will result in more conservative results.

4. Summary

As many as uncertainty parameters that may influence the fuel rod performance during HZP RIA in PWR have been identified. Based on this information, sensitivity and combined uncertainty studies have been carried out. Main findings are as follows.

- In general, as the same energy was injected into the fuel, the smaller FWHM resulted in more conservative fuel performance results than the larger one.
- With the fuel enthalpy point of view, the 0.5 MWd/kgU fuel condition gave more conservative results than the 30 MWd/kgU condition. But with the fuel temperature, clad strain and clad temperature point of view, 30 MWd/kgU condition showed more conservative results.
- Uncertainties of peak power and FWHM have induced a strong influence to the fuel enthalpy.
- Cladding inner diameter, fuel thermal expansion, fission gas release (FGR), Groenveld-5.9 heat transfer correlation induced a relatively strong influence to the cladding permanent hoop strain.
- EPRI-1 CHF correlation and Groenveld-5.9 heat transfer correlation have induced strong impact to the cladding temperature.
- Analysis results of combined uncertainty revealed that about 10 percent of uncertainty appeared in the fuel enthalpy and fuel temperature evolution. But much significant uncertainty effects were discovered in clad permanent hoop strain and clad temperature.

Above results are valid only at the PWR HZP RIA condition. Therefore if initial conditions before RIA as well as utilized computer codes are changed, the results will be varied also.

References

1. OECD/NEA, “Nuclear Fuel Behavior Under Reactivity-initiated Accident (RIA) Conditions”, ISBN 978-92-64-99113-2, NEA/CSNI/R(2010)1, 2010
2. U.S. NRC, “Standard Review Plan for the Review of Safety Analysis Reports for Nuclear Power Plants: LWR Edition”, NUREG-0800, May 04, 2012
3. EPRI, “RETRAN-3D Analysis of BWR Control Rod Drop Accidents”, 1015206, June 2007
4. Geelhood, K.J., Luscher, W.G., Beyer, C.E., 2011, “FRAPTRAN1.4: Integral Assessment”, NUREG/CR-7023, Vol.2, March 2011.
5. OECD/NEA, “RIA Fuel Codes Benchmark – Volume 1”, NEA/CSNI/R(2013)7, November 2013.
6. Lars Olof Jernkvist, “Sensitivity Study on Clad Tube Failure under Reactivity Initiated Accidents in Light Water Reactors”, SKI Report 2004:34, August 2004.
7. Javier Riverola et. al., “RIA Analysis for PWR at both HZP and HFP Operation and all Cycle Fuel Exposure with 3D Techniques”, Proceedings of the 2004 International Meeting on LWR Fuel Performance, Orlando, Florida, September 19-22, 2004
8. F. Anchel et. al., “Uncertainty and sensitivity analysis in the neutronic parameters generation for BWR and PWR coupled thermal-hydraclic-neutronic simulations”, Nuclear Engineering and Design 246 (2012) 98-106
9. O’Donnell, G.M., Scott, H.H., Meyer, R.O., 2001, “A New Comparative Analysis of LWR Fuel Designs”, NRC, NUREG-1754
10. JoosukLee, Gwanyoung Kim, Swengwoong Woo, “Development of Audit Calculation Methodology for RIA Safety Analysis”, Transactions of the Korean Nuclear Society Spring Meeting Jeju, Korea, May 7-8, 2015

11. Geelhood, K.J., Luscher, W.G., Beyer, C.E., 2011, “FRAPCON-3.4: A Computer Code for the Calculation of Steady-State Thermal-Mechnical Behavior of Oxide Fuel Rods for High Burnup”, NRC, NUREC/CR-7022; PNNL-19418
12. Geelhood, K.J., Luscher, C.E., Cuta, J.M., 2014, “FRAPTRAN 1.5: A Computer Code for the Transient Analysis of Oxide Fuel Rods”, NRC, NUREG/CR-7023, Vol.1, Rev.1.
13. Joosuk Lee, Swengwoong Woo, “Effects of fuel rod uncertainty on the LBLOCA safety analysis with limiting fuel burnup change, Nuclear Engineering and Design 273 (2014) 367–375
14. Kim, I.-g., Kim, B.H., Bang, Y.S., Oh, D.Y., Shin, A.-d., Seul, K.W., 2005, “Improvement of the ECCS Best Estimate Methodology and Assessment of LOFT L2-5 Experiment”, KINS, KINS/RR-279 (in Korean).
15. OECD/NEA, “BEMUSE PHASE III REPORT; Uncertainty and Sensitivity Analysis of the LOFT L2-5 Test”, NEA/CSNI/R(2007)4, 2007
16. Iman, R.L., Shortencarier, M.J., 1984, “FORTRAN 77 Program and User's Guide for the Generation of Latin Hypercube and Random Samples for Use with Computer Models”, NRC, NUREG/CR-3624

BWR Operating Experience

GNF FUEL PERFORMANCE 2015 UPDATE (A0081)

P. CANTONWINE, R. SCHNEIDER, R. DUNAVANT, K. LEDFORD, R. FAWCETT

Global Nuclear Fuel – Americas

3901 Castle Hayne Road, Wilmington, NC, 28411 - USA

ABSTRACT

As of late 2014 GNF2 surpassed GE14 and has the largest number of bundles in the operating fleet. Utilities in the US and Europe are reaping the benefits of improved performance as well as the highest reliability of any design in GNF history. The transition to GNF2 is nearly complete with only a few plants continuing to receive GE14 fuel. Over 1,000 GNF2 bundles have been discharged, and inspections have been completed on GNF2 bundles operated to over 61 MWd/kgU (bundle average) and over 7.5 years. Reliability has been excellent with no manufacturing, PCI-type, or corrosion-related failures. The combination of the Defender™ debris filter and the Alloy X-750 spacer design has resulted in fewer failures by debris relative to GE14 with Defender™. A key element of this performance success is GNF's Zircaloy-2 cladding that has been shown to be tolerant of shadow corrosion. Poolside fuel inspections of GNF2 bundles have been performed after various irradiation cycles, providing valuable evidence of fuel behavior during irradiation to high exposure. The fuel inspection data is well predicted by the GNF fuel performance code PRIME. Looking ahead GNF has developed a channel-bow resistant material called NSF that is considered the material solution to channel distortion issues that have plagued the industry for almost 15 years.

1. Introduction

The history of GNF fuel design and performance provides a textbook example of how learning promotes continuous improvement. In the early 1970's in 7x7 fuel designs, GNF learned the hard lesson of the importance of controlling hydrogenous material during manufacture after the occurrence of primary hydride failures. Manufacturing procedures for controlling hydrogenous materials developed over 40 years ago continue to provide protection against primary hydride failures today.

In the late '70's and 80's, corrosion failures spurred the improvement of processing to control the second phase particle (SPP) size and distribution in the Zircaloy-2 cladding and the understanding that controlled chemistry within the ASTM specification improved corrosion - eventually leading to the development of GNF Ziron, a high Fe version of Zircaloy-2 (Ref 1). In parallel, risk factors at the plants that correlated with corrosion failures were identified and corrected, including replacing brass condensers and improving condensate treatment systems performance.

In the 1980s, GNF introduced barrier cladding, which has a thin zirconium layer on the inner surface of a fuel rod, as a material solution to failures by pellet cladding interaction (PCI) linked to the release of iodine in the fuel during a power ramp. In the early 1990's after some primary failures in barrier fuel experienced secondary degradation (from a combination of hydrogen generated as a result of corrosion of the liner, and aggressive post-failure operation,) GNF increased the Fe content in the Zr liner (improving corrosion resistance and decreasing hydrogen generation) and developed guidance to identify bundles with fuel failures so power ramps that cause fuel degradation could be avoided. The GNF failed fuel management guidelines rapidly became the industry standard and are nearly universally applied today.

Also in the 1990s, PCI-type failures associated with missing pellet surface (MPS) occurred under lower duty conditions than previously observed and resulted in GNF tightening the

pellet quality requirements, improving pellet inspection capabilities, and updating operational guidelines to account for MPS.

By around 2004, virtually the only remaining failure mechanism was fretting from debris (see for example, Ref 2) despite introduction of first generation debris filters. This experience led to the evolutionary development of the lower-tie-plate Defender™ filter that dramatically decreased the size of debris that can enter the bundle and has reduced debris failures by ~5X. GNF also worked with GEH to develop a high-performance strainer for the feedwater/condensate system to reduce debris ingress into the primary system.

Besides fuel failures, the observation of channel–control blade interference has been the most significant fuel performance issue in BWRs over the last 15 years. GNF was the first to link observations of interference to early-life control and shadow corrosion and coined the term shadow corrosion-induced bow (Ref 3). This understanding that a new channel bow mechanism added to the already well-understood fluence gradient-induced bow was critical to being able to respond with mitigating actions to minimize plant operational issues that included monitoring guidance for plant operators, developing methodologies for minimizing susceptibility in core design (Ref 4) and the eventual development of the channel bow resistant material called NSF (Ref 5).

As materials & manufacturing technology evolved to solve and prevent problems, GNF's BWR fuel designs also evolved to deliver more energy at higher power with increased margins at lower cost. Nuclear design techniques were developed to tailor the axial reactivity distribution of the fuel considering the unique characteristics of the BWR to support simple control rod patterns. The lattice number grew to support increased nodal power for spectral shift, and partial length fuel rods were pioneered by GNF to provide the necessary stability margins as the fuel rod diameter decreased with higher lattice number. Spacers evolved to harvest as much of the available liquid as possible while conforming to mechanical requirements and constraints on hydraulic resistance (pressure drop). As reactor owners increased capacity factors from ~70% to >90%, doubled their operating cycle lengths from 12 to 24 months, and increased power densities by as much as 20%, GNF's fuel technology rose to the occasion by delivering substantially increased burnups and remarkable power producing capability at reduced cost.

Over the past 50 years of developing, manufacturing and operating BWR fuel, GNF has remained vigilant in understanding and improving fuel performance. The following sections provide a current status of our vigilance in this area. The specific topics discussed are the GNF 10x10 operational experience, GNF2 fuel inspections, improvements to GNF's thermal/mechanical fuel-performance code called PRIME and GNF channels. Previous status updates on GNF fuel performance were documented in References 6 and 7.

2. Operational Experience and Fuel Reliability

GNF's 10x10 bundle designs have powered a large percentage of the world-wide BWR fleet for decades. It is the world's largest 10x10 experience base, operating in the entire spectrum of BWR conditions: annual, 18, and 24 month cycles; residence times at discharge from nominally 4 years to 8 years; power densities from <3.5 to >5.5 MWt/bundle, with correspondingly wide ranges of nuclear designs (enrichment and Gd concentration); and every BWR water chemistry environment, from NWC "Normal Water Chemistry" through OLNC "On-Line Noble Chem" and in ultra-low as well as higher feedwater metals (crud) environments.

Table 1, GNF 10x10 experience base

	GE12	GE14	GNF2	TOTAL
Reloads	31	186	54	271
Bundles	~4,300	~35,000	~11000	~50,000
Rods	~400 K	~3.2 M	~1M	~4.7 M

Fuel reliability performance of GNF 10x10 fuel has been excellent, with several evolutionary modifications made within the designs or in the next designs as they were introduced. Performance relative to each of the main classifications of BWR failure mechanisms is discussed separately, roughly in the order or extent to which they have occurred in plants.

Dryout or Transition boiling: no occurrences

Crud or corrosion related failures: no occurrences

Under-spacer shadow corrosion related failures: no occurrences

Manufacturing defects: 1 suspected rod at one European BWR, 2009; several (~2-3) "PCI-type" or duty related failures likely due to missing pellet surface (2001 fabrication, US.)

PCI type or "duty-related": no occurrences in GNF2; within GE14, 4 failures in one plant maneuver in 2003 and 4-5 in higher exposure/residence time bundles. Largely based on these events, GNF developed PCI-risk reduction fuel-operating guidelines that have proven to be 100% effective and have minimal capacity factor impact. Cycle specific studies consistently indicate just a few hours of mandatory ramping required for most two-year fuel cycles.

Debris fretting: This mechanism continues to be the main source of fuel failures in BWRs. Improvements in bundle lower tie plate filters have successfully reduced the rate of failures, but have not reduced failures to the extent hoped for by the BWR fleet. From the vast operational experience of the GNF 10x10 designs, some observations include:

- Table 2: Debris Failure rates, per 1,000 bundles operated

No Filter	First generation filter	Defender
~6	~3.6	~0.8

- Table 3: Debris failure rate per 1,000 bundles operated, GE14 vs. GNF2, with Defender filter

GE14 (>13,000 bundles)	GNF2 (>10,000 bundles)
~1.1	~1.0

- In the 10x10 designs, approximately 75% of the debris fretting perforations have occurred in spacers in the upper half of the bundle.

- For the largest/most mature design, GE14, the failed pin within the 10x10 lattice has been remarkably random; for edge rods, interior rods, partial length rods, Gd rods, etc. the # of debris failures is within 1 to 3 % of the number of rods of that type that exist in the bundle.

- GE14 has operated in reload quantities in over 40 plants. There are ~65 GE14 debris fretting failures, yet over 53% are in only 4 plants. All four of these plants are "pumped forward drains" plants and in several cases there were major steam plant modifications done just prior to multi-failure cycles. 18 plants have no debris failures in GE14. The correlation with more frequent

debris failures in pumped-forward plants (as well as with steam plant repairs/ modifications work) extends into GE12, GNF2, and other vendor fuel designs as well.

It is clear that achieving and maintaining zero debris leakers is more difficult in certain plants, and that susceptibility is dependent on plant design as well as foreign material exclusion practices.

GNF2 is performing very well with respect to every fuel failure mechanism, including debris, the only mechanism to affect this fuel design. To date, it is the most reliable fuel design (lowest fuel rod failure rate) in GNF history, with several plants now operating full cores and reloads starting to be discharged (>1,000 bundles as of summer 2015.) Over 20 plants are operating GNF2; 4 plants account for all (six) suspected failures, 3 of the 4 plants are pumped forward drain plants and/or performed modifications work or other work that could have been a source of debris.

Finally, when failures do occur, GNF fuel operating practices recommendations and customer support in the core design and operational support areas come together to minimize the consequences of failures. It has come to be "expected" that cycles can be completed without degradation or fuel pellet material loss, for periods up to 18 months or more, including for entire 24-month cycles in recent cases. GNF, in the 1990's, pioneered the modern approach to failed fuel management that has become the industry standard in nearly all of the BWR fleet. To illustrate the effectiveness of this integrated approach, 19 out of the past 20 GNF fuel failures in US plants (2009 to today) have been operated for the balance of the operating cycle with no fuel pellet material washout and no long term plant contamination or increased background activity. Several of the recent cases exceed 12 months in duration and two are greater than 20 months. Improvements to the cladding degradation resistance help to ensure that there is adequate time to identify the core location of failures and apply softer operation to failed/hydrided cladding, as well as provide more margin for long-term operation.

3. GNF2 Fuel Inspections

GNF maintains an active fuel inspection program to investigate failure events, verify expected performance of fuel design changes and lead use assemblies, and support utility compliance with EPRI/INPO/WANO or other regulatory guidance. Some examples of the fleetwide (most or all BWRs) benefits obtained from the GNF inspection experience include:

- Establishing the feedwater Zn injection guidance that has been adopted by EPRI BWR VIP and Fuel Reliability Programs for the BWR water chemistry guidelines and the crud/corrosion guidelines, to minimize the extent of tenacious crud formation and crud spalling.
- Justification of removing a lower limit of 0.1 ppb for feedwater Fe in the guidelines, as many plants have adopted full flow condensate filtration systems and have achieved "ultra low" feedwater Fe inputs.

One of the most important inspection activities is to confirm adequate corrosion performance when either the fuel product or cladding changes, the environment changes (i.e. new chemistry additive programs) or there are large or unusual transients. It is also very important to confirm that "newer" or "unusual" fuel failure mechanisms do not occur, such as under-spacer shadow corrosion. Some example photographs of the GNF2 design with all-Inconel spacers are shown in Fig 1 to illustrate that shadow corrosion does occur as expected, but that the extent has not resulted in any significant oxide spalling in either challenging environments or at end of life conditions, which is necessary precursor to metal thinning that would threaten fuel integrity in GNF2. Fig 2 provides quantification of the magnitude of the shadow corrosion localizations, via diameter measurements, in multiple cycles of operation. The 8 spacers are approximately 20 inches (500 mm) apart in the plot.

Similar conclusions were made based on inspections of GE14 that had Inconel springs in a Zircaloy-2 ferrule spacer and the GE12 version with an all-Inconel spacer.

a) GNF2 LUA operated 4X24 months, ~50 MWd/kgU, 7 OLNC applications, Zn injection (Spacer 3 slightly raised to view shadow corrosion affected area)

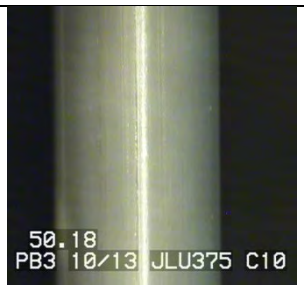

b) GNF2 LUA operated 4X24 months, ~50 MWd/kgU, 7 OLNC applications, Zn injection (mid-span clad, high exposure rod, at ~peak exposure/ peak expected crud elevation)

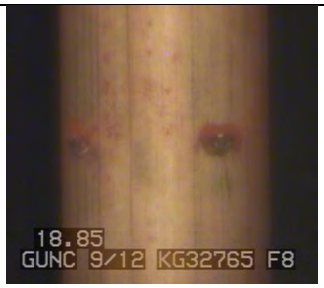

c) GNF2 LUA operated 3X12 months, ~32 MWd/kgU, NWC with high FW Fe, spacer 1 shadow corrosion & spring contact area.

d) GNF2, 3X24 month cycles, ~51 MWd/kgU, spacer 1, NMCA and 4 OLNC, numerous condenser leaks in last ~2 cycles.

Fig 1 GNF2 cladding corrosion/shadow corrosion observations

4. PRIME Fuel Performance Code

GNF developed the PRIME fuel performance code to provide predictions of fuel rod thermal-mechanical performance up to, and beyond, current licensed burnup limits to support the industry trend toward increased uranium utilization. PRIME includes new or updated models relative to previous GNF thermal-mechanical codes to explicitly address specific high burnup mechanisms and to reflect current understanding of relevant material properties. Some specific updates include modeling of high burnup (rim) structure formation at the pellet periphery, explicitly considering burnup dependency of fuel pellet thermal conductivity, and updated Zircaloy creep, fuel pellet relocation, and fuel fission gas release models. These new models are based on, and qualified to, results of in-pool and post irradiation examination (PIE) of commercial, and LUA, BWR fuel rods at high burnup and results from international experimental programs. The results of continuing fuel inspection activities are evaluated to ensure fuel performance is within expectations. GNF also regularly validates PRIME predictions against fuel inspection data to continue to prove PRIME's predictive capabilities and to expand the PRIME qualification database. Given the industry trend toward increased uranium utilization, there is high interest in high exposure fuel inspection data at, and beyond, current licensed burnup limits.

An example comparison is given illustrating measured fuel inspection data for GNF2 LUAs that operated to very high burnup, (bundle average exposure of 61 MWd/kgU, relative to PRIME predictions. PRIME predictions of fuel rod deformation and measured deformation, taken from fuel rod profilometry data, are shown in Fig 2. The PRIME predictions of fuel rod deformation shown in Fig 2 account for the effects of irradiation in-reactor and include measured cladding oxide thickness. Power histories are also given in Fig 3 illustrating peak

and rod average LHGR. Axial exposure profiles for this rod are given in Fig 4, at the cycles where inspections were performed, illustrating that the peak nodal exposure for this rod reached 76 MWd/kgU.

During operation, cladding diameter tends to increase due to thermal expansion and decrease due to the combined effects of creep-down, overpressure, and axial elongation from pellet stack thermal expansion combined with pellet-clad locking. The net effect is an observable decrease in clad diameter at mid-life exposures. Fig 2 illustrates that rod diameter was slightly less than "as built" after 4 annual cycles. As irradiation continues, fuel pellet diameter increases due to fuel pellet irradiation swelling, relocation, and thermal expansion, but decreases due to densification. At some burnup, dependent on operating history, the pellet-cladding gap completely closes due to these effects and further expansion of the fuel pellets causes the cladding diameter, now reduced from initial fabrication dimensions due to the effects described above, to increase. These effects compete with one another as the fuel rod burnup increases. For profilometry data, GNF has observed that, at very high exposures, the permanent effects of pellet-clad contact can result in a slight increase beyond as fabricated dimensions in fuel rod diameter as shown in measurements after 6 and 7 cycles (see Fig 2). As illustrated in Fig 2, PRIME predicts rod diametral deformation well, for both the middle of life and for higher exposures. These types of comparisons provide confidence that PRIME predictions of pellet-clad interaction are valid at high burnups.

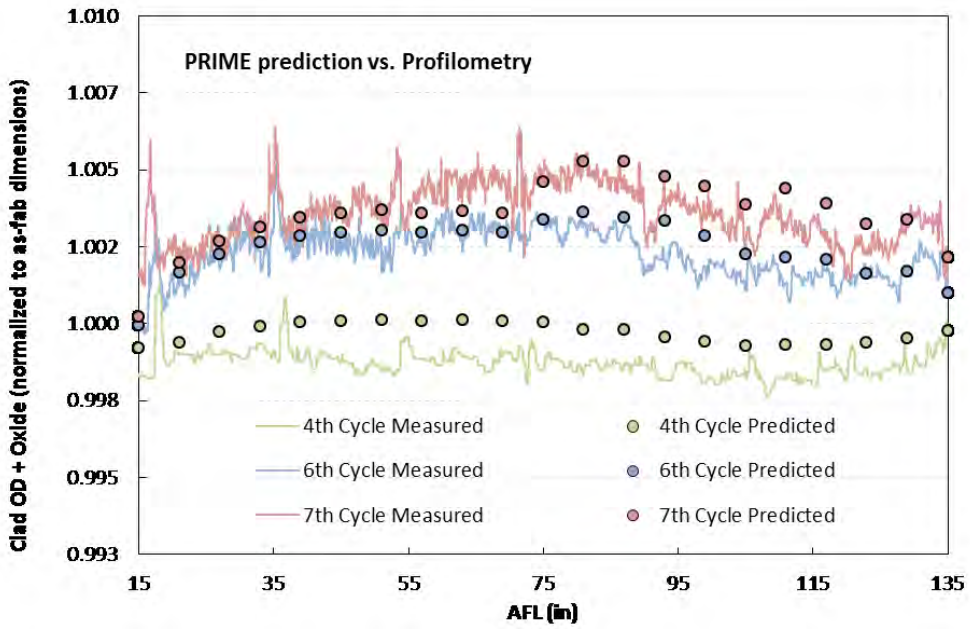

Fig 2. Predicted and Measured Fuel Rod Deformation (diameter) for High Burnup GNF2 Fuel Rod

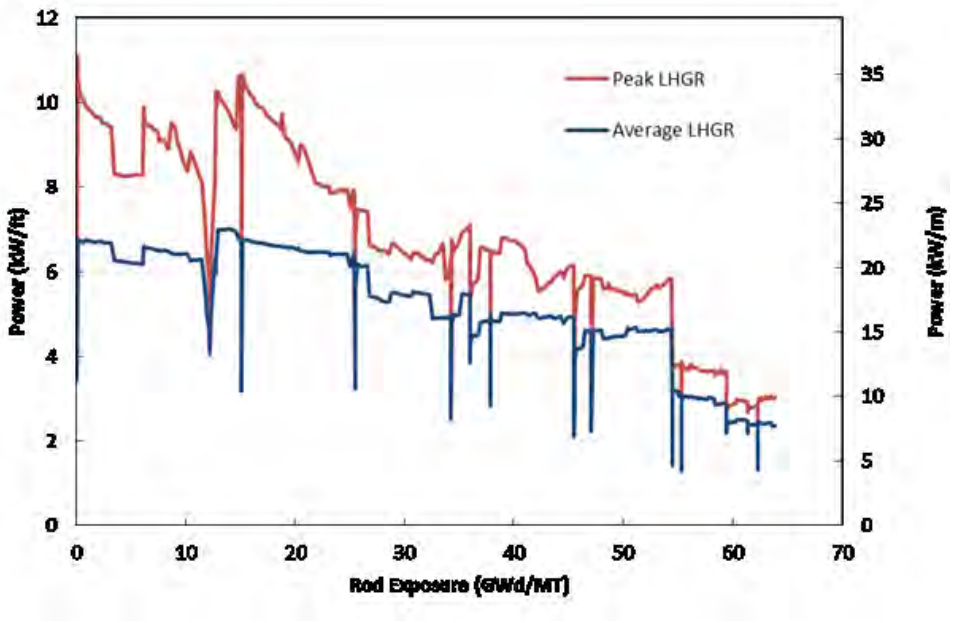

Fig 3. Power History for High Burnup GNF2 Fuel Rod

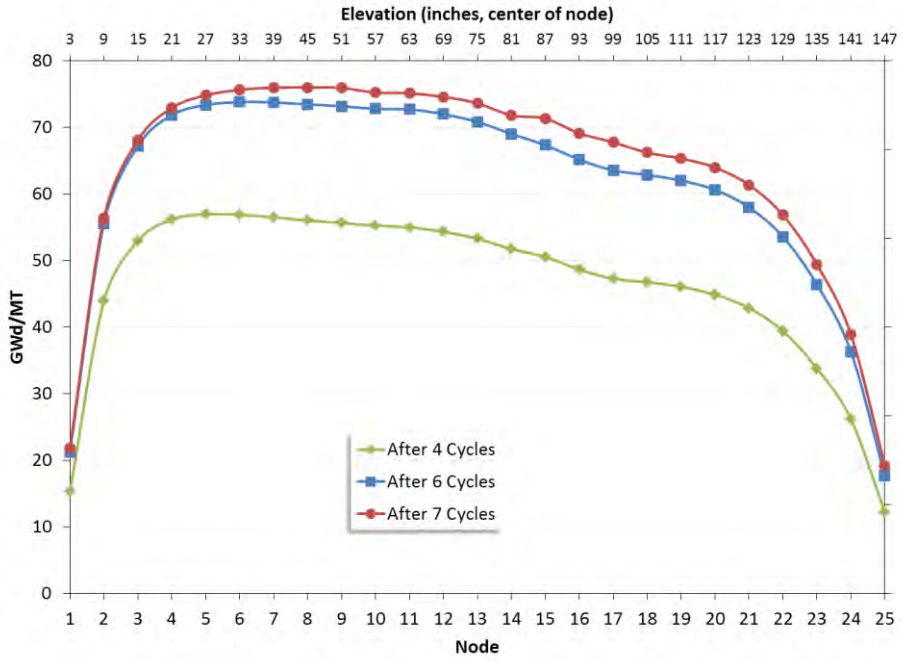

Fig 4. Axial Exposure Profile for High Burnup GNF2 Fuel Rod

5. GNF Channels

Channel – control blade interference caused by channel distortion continues to be an operational concern in BWR plants (see Fig 5). Observations of interference occur when the control blade fails to settle into a notch location within 30 seconds (there are 48 notch locations from full-out to full-in). Initially the observations were a result of distortion problems with Zircaloy-2 channels that were controlled early in life, and thus susceptible to shadow corrosion-induced bow. Discharge exposures greater than 45 MWd/kgU also contributed to greater fluence-gradient induced bow. More recently, the observations of interference have been in cells with Zircaloy-4 channels that were viewed as an interim material mitigation to

distortion because it is less susceptible to shadow bow than Zircaloy-2. Clearly to return to the days when there are no observations of channel – control blade interference, a new channel bow resistant material is needed. That material is NSF.

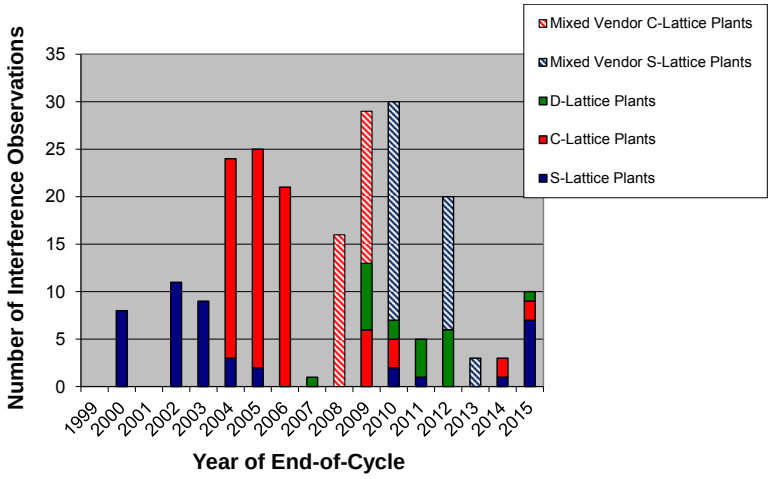

Fig 5 Observations of interference in Boiling Water Reactors with GNF fuel. The time axis is in terms of the year when the cycle ends rather than in terms of when the observations were made.

NSF is a Zr-Nb-Sn-Fe alloy with a nominal composition of 1.0% Nb, 1.0% Sn, 0.4% Fe and Zr in balance. While NSF has been found to be resistant to both fluence gradient-induced bow and shadow corrosion-induced bow, only the resistance to fluence bow is discussed in detail herein. NSF is resistant to fluence bow because it is resistant to breakaway irradiation growth, in contrast to Zircaloy-2 and Zircaloy-4, as shown in Fig 6. Irradiation growth data from BOR60 indicated that NSF does not exhibit breakaway characteristics out to a fluence of ~2.2E+22 n/cm^2, which is more than twice the typical end-of-life (EOL) fluence in a channel. The channel length data for NSF is consistent with the BOR60 data and is representative of the very lowest growth data in the Zircaloy-2 channel database. In contrast to NSF, Zircaloy-2 exhibits breakaway growth at fluences that can range from 6E+21 to 9E+21 n/cm^2, which results in significant variability in channel growth at EOL fluences (from 0.1515% to almost 0.3%). This variability in channel growth translates to a large uncertainty in bow of Zircaloy-2 channels at high exposures (see Fig 7). Based on experience evaluating the operational conditions of channels in cells where channel-control blade interference has occurred, it is the uncertainty in the predictive models of fluence bow for Zircaloy-2 (and Zircaloy-4) channels that make accounting for distortion in core designs difficult – subsequently making it difficult to eliminate such observations. In contrast to Zircaloy-2, the residuals for NSF channels in Fig 7 are much lower. Thus, in addition to NSF suppressing fluence bow compared to Zircaloy-2, it is expected to significantly decrease the uncertainty in the predictive model for fluence bow – making it easier to eliminate observations of channel–control blade interference. As more NSF channels are operated and measured for channel distortion, the expectation of low fluence bow and decreased uncertainty will be confirmed in statistical terms.

Because NSF is a new material for BWR fuel component applications there are licensing considerations. In the US, a licensing topical report that provides a technical justification for insertion of full reloads of NSF channels was submitted to the US NRC in 2013. NRC approval is expected in the fall of 2015. GNF has also supported licensing of full reloads of NSF channels in other countries.

6. Summary

The fuel reliability of GNF 10x10 fuel is excellent. While remaining constantly vigilant to avoid all fuel failure mechanisms, the major mechanism that continues to cause failures in

GNF fuel is debris fretting. Debris failures are strongly correlated with plant-specific issues that include whether there were recent plant modifications (i.e. for EPU) and whether the plant has a pumped-forward drain configuration.

When GNF2 was introduced as a replacement for GE14, one of the concerns was the use of an all-Inconel spacer because of increased susceptibility to shadow corrosion on the fuel rods. Thus, when inspecting the leading GNF2 bundles, the corrosion performance under the spacers was thoroughly investigated. While shadow corrosion does occur as expected, the extent has not threatened fuel integrity in GNF2, including under challenging water-chemistry environments out to end of life exposures.

In parallel with the development of the GNF2 fuel design, GNF developed the PRIME fuel performance code to provide improved predictions of fuel rod thermal-mechanical performance – especially at higher exposures to support the industry trend toward increased uranium utilization. Specific improvements include modeling of high burnup (rim) structure formation at the pellet periphery, explicitly considering burnup dependency of fuel pellet thermal conductivity, and updated Zircaloy creep, fuel pellet relocation, and fuel fission gas release models.

Finally, the NSF channel offers the best hope of eliminating channel–control blade interference that is caused by channel bow – including channel bow at high exposures where it is difficult to predict the performance of Zircaloy channels because of uncertainty. It is expected that NSF will be fully licensed in the US to support full reloads in 2016. Full reloads of NSF are also being inserted in European plants.

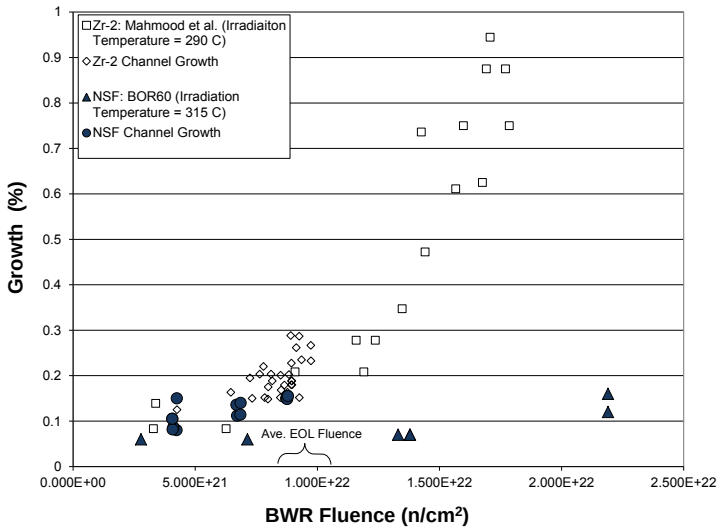

Fig 6 Irradiation growth of NSF and Zircaloy-2 as a function of BWR Fluence. The channel growth data is based on length measurements of BWR fuel channels. The Mahmood data for Zircaloy-2 is from Ref 8, and the NSF data irradiated in BOR60 is from Ref 9; where both fluences were normalized to the neutron energy distribution in a BWR.

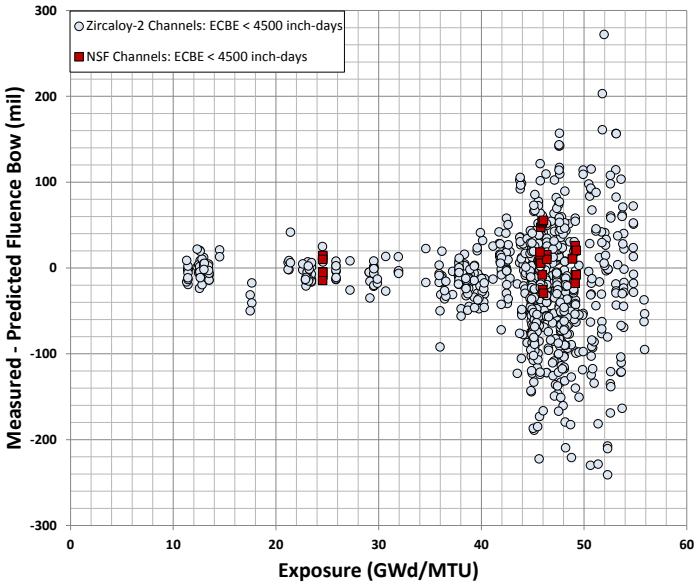

Fig 7 The residual in the predicted fluence bow for both Zircaloy-2 and NSF channels that have low susceptibility to shadow bow as defined by a low value of Effective Control Blade Exposure (ECBE).

7. References

1. Ishimoto et al., "Improved Zr Alloys for High Burnup BWR Fuel," *TopFuel 2006 International Meeting on LWR Fuel Performance*, Salamanca, Spain, European Nuclear Society, (2006).
2. J. Siphers and R. Schneider, "Brunswick Fuel Failure Reduction," *Proceedings of 2010 LWR Fuel Performance/TopFuel/WRFPM*, Orlando, Florida, USA, September 26-29, 2010
3. S.T. Mahmood, et al., "Channel Bow in Boiling Water Reactors – Hot Cell Examination Results and Correlation to Measured Bow," *Proceedings of the 2007 International LWR Fuel Performance Meeting*, San Francisco, CA, American Nuclear Society, (2007).
4. A.A. Karve, et al., "A Methodology for Calculating and a Process for Mitigating Channel Distortion and Cell Friction (Part I)," *TopFuel 2006 International Meeting on LWR Fuel Performance*, Salamanca, Spain, European Nuclear Society, (2006).
5. P.E. Cantonwine et al., "BWR Corrosion Experience of NSF Channels, " *LWR Fuel Performance Meeting / TOPFUEL 2013,* Charlotte, NC, USA, American Nuclear Society, (2013).
6. K.L. Ledford et al., "GNF Defense in Depth 2010 Update," Proceedings of 2010 LWR Fuel Performance/TopFuel/WRFPM, Orlando, Florida, USA, September 26-29, 2010
7. A. Lingenfelter et al., "GNF Defense in Depth 2009 Update," *Proceedings of the 2009 TOPFUEL,* Paris, France, September 6-10, (2009)
8. Mahmood, S. et al., "Post-Irradiation Characterization of Ultra-High-Fluence Zircaloy-2 Plate," Zirconium in the Nuclear Industry: 12th International Symposium, ASTM STP1354, p. 139, (1998).
9. G.P. Kobylyansky et al., "Irradiation-Induced Growth and Microstructure of Recrystallized, Cold Worked and Quenched Zircaloy-2, NSF, and E635 Alloys," 15th International Symposium on Zirconium in the Nuclear Industry, ASTM STP 1505, p. 564, (2009).

MONITORING THE INTEGRITY OF CONTROL RODS ON-LINE WITH A HELIUM LEAK DETECTOR

K. AMMON, H. LONER, R. BIELI, G. LEDERGERBER
Kernkraftwerk Leibstadt AG, 5325 Leibstadt – Switzerland

ABSTRACT

Control rods are safety relevant systems in a BWR, but due to irradiation and corrosion together with the swelling of the absorber material boron carbide (B_4C), control rods can form cracks. Through small cracks only helium will be released but with sufficient ^{10}B depletion also boron can be washed out of the blade.
In recent years the discussion about leaking control rods became more and more important. The problem is that codes to calculate the mechanical end of life for a control rod tend to have large uncertainties because they depend on so many variables and unknowns.
At KKL an on-line helium leak detector with a built-in mass spectrometer was installed in 2008. It is part of a combined system for detection of fuel and control rod failures. The sampling points are located in the off-gas system after the condenser and gas coolers, and before the charcoal filters. When measuring before the delay line for short response time, the time it takes for the gas to be transported from the core to the sampling point is 2–4 min. This makes the helium detecting system very well suited to detect leaking control rods. Moving a cracked control rod will release helium, which will be detected immediately by the mass spectrometer. The data are displayed in our on-line core monitoring system where the helium signal will show a peak in case of a failure.
Knowing the relative ^{10}B depletion when control rods start to form cracks cannot only help to improve codes to calculate the end of life, it will also help to reduce waste without risking large boron leaking cracks.
At KKL an empirical study has been conducted to test a series of control rods to determine their mechanical end of life. In this paper we will show how the helium mass spectrometer can be used to determine leaking control rods and to monitor the integrity of control rods on-line.

1. Introduction

BWR control rods are filled with boron carbide (B_4C). Due to neutron capture ^{10}B transforms to ^{11}B, which then decays to ^{7}Li (lithium) and ^{4}He (helium). This leads to a swelling of the B_4C matrix and to a pressure increase in the blade, which in turn can lead to the cracking of the steel confinement and in a final consequence to the wash-out of boron into the reactor water. Control rod integrity in BWRs therefore can be monitored via helium measurements and/or the determination of the boron concentration in the reactor water.
However, B_4C will only dissolve after a certain depletion of ^{10}B [1]. Small cracks, through which helium will be released, occur as precursor to boron leakage. Being able to detect the helium gives not only the opportunity to early detect defective control rods, it will also define the relative ^{10}B depletion for the mechanical end of life of each type of control rod.

Only recently, the discussion about leaking control rods in BWRs became more and more important. Regulators tend to demand a zero boron leaking tolerance. This means that the established surveillance tool for control rods, the boron concentration in the reactor water, can no longer be used. Utilities therefore depend on ^{10}B depletion calculations and exchange suggestions by the vendors.
The problem is firstly, that simplified models have been applied to design the control rods in early days. Today, more sophisticated reactor calculation tools are used to monitor these rods. Calculating the limits with different models can lead to substantial differences in ^{10}B depletion for the mechanical end of life. Therefore, the limits, to which the control rods are designed, should be re-evaluated with modern tools.
Secondly, even modern codes employed to monitor the end of life of a control rod are still not very precise, which lead to large discrepancies between different codes. Consequently, using a different code than the vendor will cause some problems for the development of an exchange strategy for control rods.
Being conservative, operators are forced to off-load control rods before they reach their actual mechanical end of life, which creates a lot of unnecessary waste.
In the following we will show how KKL has used the on-line helium leak detector to develop a safe, but also waste-limiting strategy of control rod exchange. Additionally, the neutron flux distribution below the core was calculated with a MCNP model that was validated against gamma flux measurements in this region obtained by KKL's TIP[1] system [2]. Implementing this neutron flux profile in the nodal codes of KKL and Westinghouse resolved the discrepancy in depletion calculations for Westinghouse supplied control rods to a large extent.

2. Control Rod Leak Detection

2.1 On-line Helium Mass Spectrometer

To perform a prompt detection of control rod failures, on-line helium monitoring is the most useful method. In 2008 the on-line detection system for fuel failures at KKL was complemented with a helium leak detector, working with a mass spectrometer, to be able to detect also control rod failures. The sampling points of the combined system are located in the off-gas system after the condenser and gas coolers, and before the charcoal filters of the stack, as shown in Figure 1. There are two different measuring modes, depending on the location of sampling. The first mode is a fast response mode, taking off-gases directly after the condenser and gas coolers. The second mode is a delayed response mode, where the sample gas is taken from the main off-gas line after an additional delay line. During normal operation the second mode is used to allow the short lived fission products to decay. This is mainly important for the detection system of fuel failures for a better sensitivity. For special tests the first mode is used to get a faster response.
To prevent the helium detector from contamination and for stable operational conditions, a gas separation cell is connected to the detector inlet. The separation cell is a small stainless steel container, which consists of two plates separated by a PTFE membrane, as shown in the lower right part of Figure 1. Helium penetrates through the PTFE membrane by diffusion and is transported to the helium detector inlet, while other gases with larger and heavier molecules cannot penetrate the membrane. The off-gas from the sample line is flowing through the upper part of the gas separation cell with a flow of 2 l/min at an absolute pressure of 500 mbar. Constant flow and pressure in the sampling line are reached by

[1] TIP = Traversing Incore Probe used to calibrate the local power range monitors (LPRM) in the core.

electronic flow and pressure regulator valves. The exhaust of the helium detector is connected to the ventilation system.
The data is directly read from the detector into an SQL data base on a local computer which is also used for the on-line gamma spectroscopy system. The data from the helium measurement and the pressure and flow regulator valves are transferred to KKL's process data base from where they can be retrieved for visualisation in the core monitoring system MinuteMan[2].

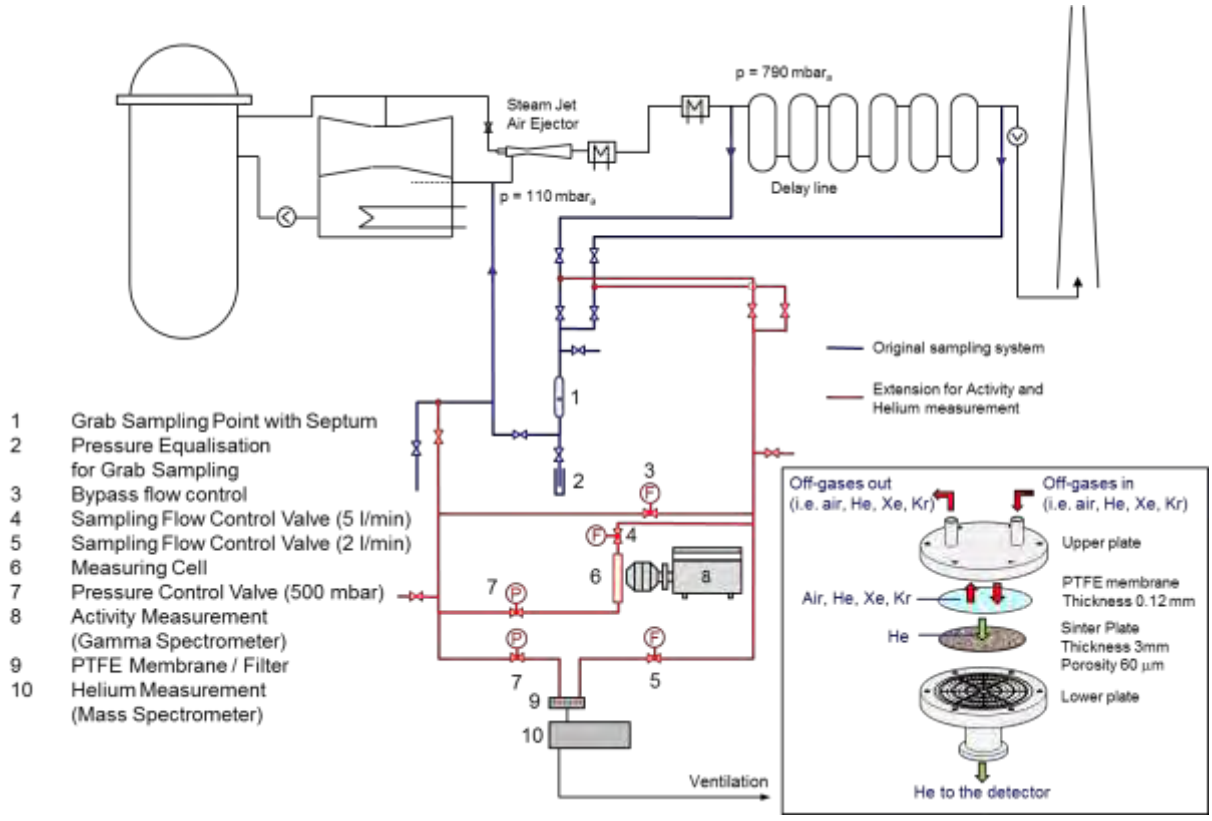

Figure 1: Schematic set up of the gamma and helium measuring system at KKL including the gas separation cell.

2.2 Procedure

Helium concentration in the off-gas, measured by the on-line helium mass spectrometer, is plotted against time in the core monitoring system MinuteMan (Figure 2). With an update every minute this plot always shows the actual status in the core. When a control blade cracks or a cracked control rod is moved, helium will leak out of the blade. The concentration of helium in the off-gas will increase and immediately show a peak in the on-line monitoring system. The larger the peak, the more helium has leaked out, which also gives a hint on how severely the blade is cracked [3], [4].
To use the on-line helium mass spectrometer as a surveillance tool it has to be considered that the helium concentration also depends on different process parameters like off-gas flow, hydrogen feed rate[3], the helium pollution in the hydrogen trailers and feed water refill [4], [5]. These parameters are also displayed in the on-line monitoring system. As shown in Figure 2, the helium concentration (black line) follows the feed rate of hydrogen (blue line). The hydrogen feed rate depends on reactor power (red line).

[2] MinuteMan is a product of K Effective LLC
[3] KKL applies hydrogen water chemistry and on-line NobleChem (HWC/OLNC).

As can be seen in Figure 2, the helium concentration dropped substantially when hydrogen injection was interrupted between 6 and 8 am. This is due to the helium traces present in the hydrogen trailers used for HWC/OLNC. Since the hydrogen trailers contain variable amounts of helium, a trailer exchange leads to a step change of helium. The dependence on the off-gas flow is reverse, because the increasing off-gas flow dilutes the helium concentration. However, helium peaks due to cracked control rods can still be clearly identified, but the concentration has to be considered as a relative measure.

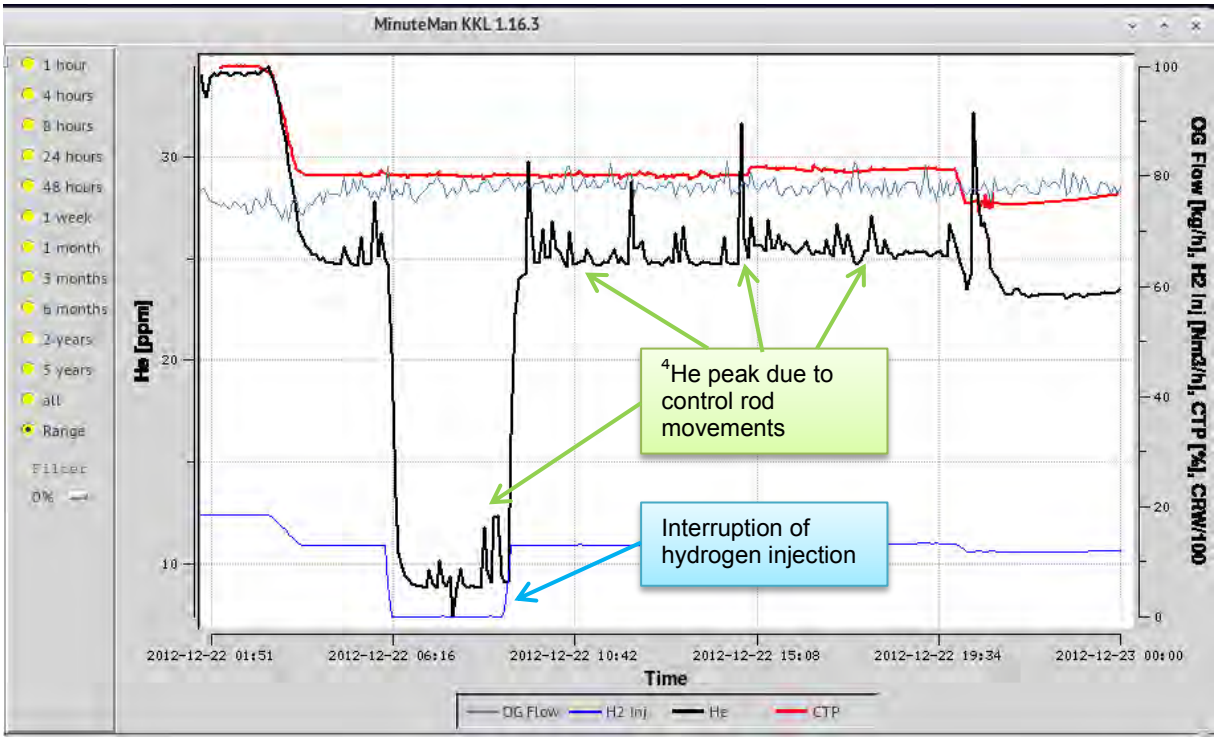

Figure 2: Helium concentration in the off-gas as shown in the core monitoring system.

With an immediate feedback on the helium concentration, it is possible to detect damaged control rods in a similar way as leaking fuel rods in a flux tilt test. Table 1 shows how the leak tests for control rods have been performed at KKL.

Step	Action	Remarks
1	Decrease reactor power to 80%	Wait about 20 minutes before starting the test
2	Individually insert control rod to 50%	
3	Let control rod inserted for at least 2 minutes	Wait for the helium signal in the on-line monitoring system
4	Pull control rod to fully withdrawn position	
5	Wait about 10 minutes before the next movement	Depending on how much helium has been released the waiting time until the next movement has to be adjusted. Do not start before the helium concentration is back to the starting level.
6	Start with the next movement and repeat steps 2 - 6	

Table 1: Procedure for the control rod leak test as performed at KKL.

In Figure 3, typical signals from a control rod leak test are shown. By moving a leaking control rod, clear peaks can be observed shortly after the control rod is inserted 50% into the core.

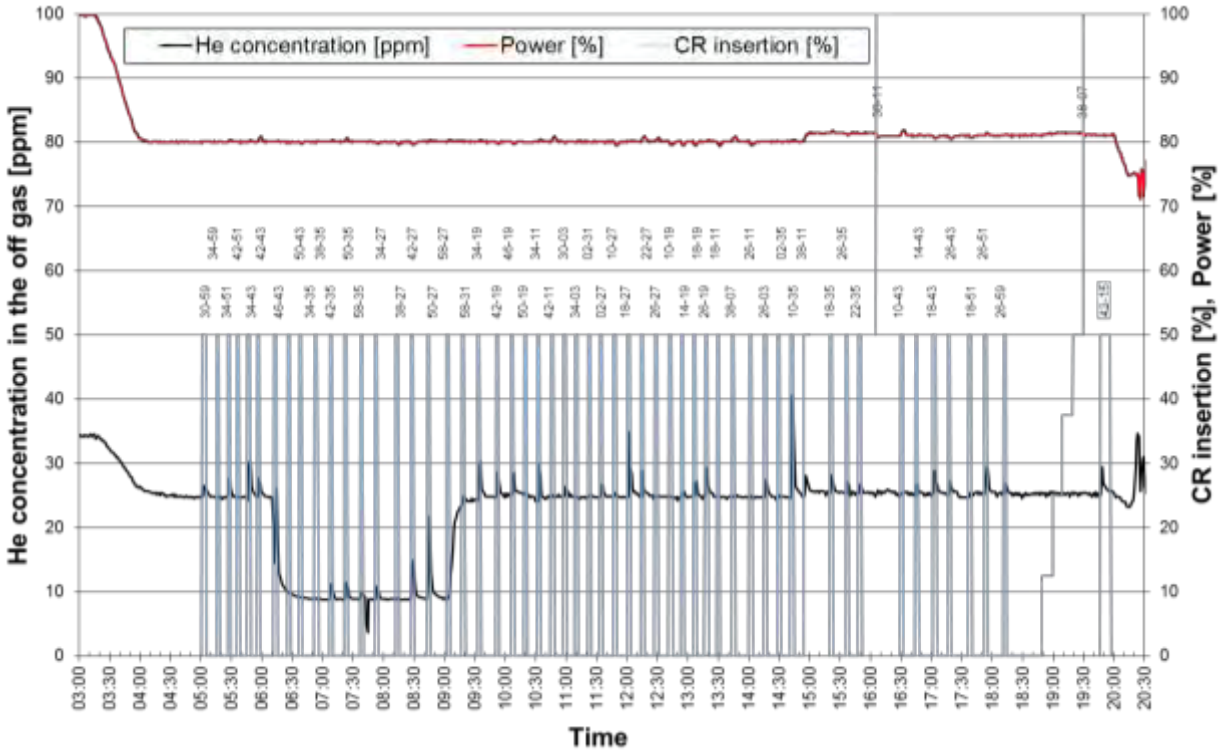

Figure 3: He signals during a control rod leak test.

2.3 Test Results

A total of 86 control rods (type original equipment, OE, from GEH) have been moved during 6 independent tests. 46 control rods have been moved more than once in consecutive cycles and therefore with increasing ^{10}B depletion. Rods which showed clear helium signals (release of > 20 ml) in the first test also showed clear signals in the following tests. In some cases rods with low signals (5 – 10 ml release) showed higher release with higher ^{10}B depletion. For these rods the mechanical end of life could be directly narrowed down. Due to uncertainties in the measurements, releases below 5 ml are not counted as crack indications. Figure 4 shows the helium release for all data plotted against the relative[4] ^{10}B depletion of the respective control rod. Interestingly two groups can be distinguished: Control rods located at the periphery of the core and control rods located in the center of the core. Figure 5 shows the division of the control rod positions into peripheral and central locations as used for the plot in Figure 4.

The data indicate that peripheral rods tend to crack at higher ^{10}B depletion than central rods. This is an artefact of the codes probably resulting from their inability to correctly model the neutron flux and its spectrum at the periphery and below the core. To overcome the problem we defined two separate end-of-life ^{10}B depletions for each group of control rods. To do so, two curves have been manually fitted into the data to define the ^{10}B depletion when helium

[4] Calculated ^{10}B depletion strongly depends on the code used for the calculation. Therefore only relative ^{10}B depletion values are given in this paper. All ^{10}B depletions are divided by the highest calculated value.

release by movement of the control rods increases. However, the actual end-of-life limits do not only depend on the code used for the calculations, they also differ for each type of control rod.

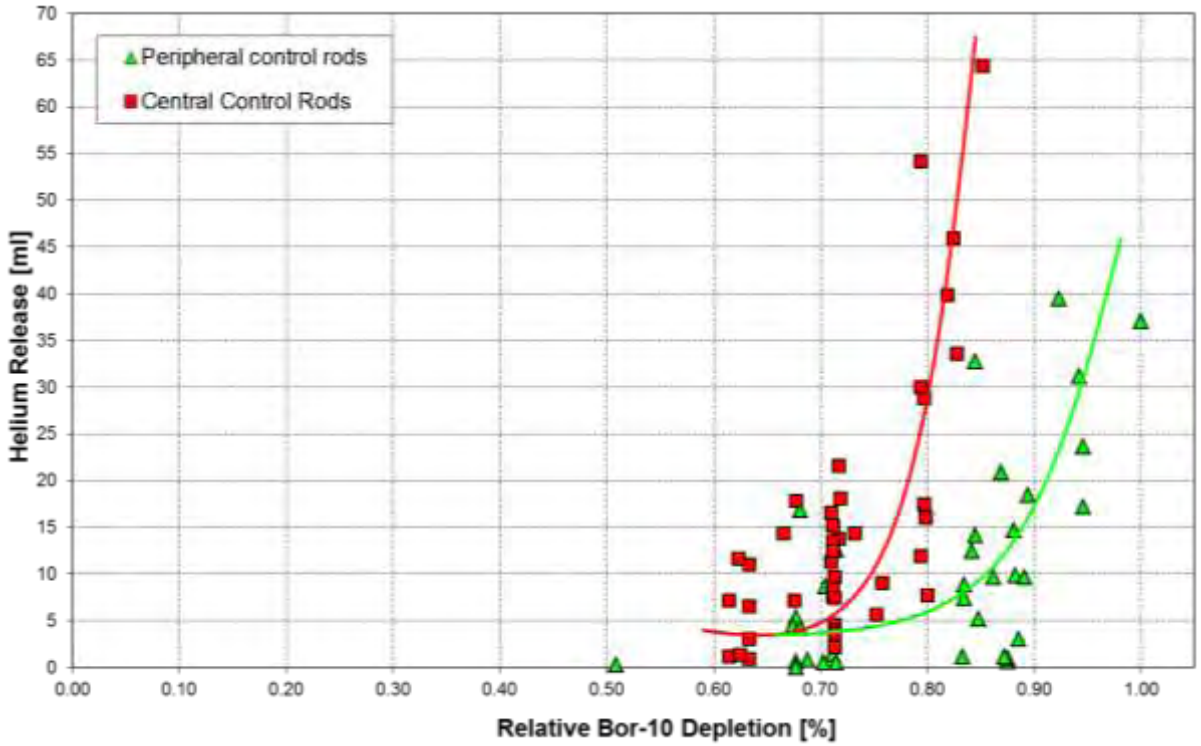

Figure 4: Helium release of all moved control rods plotted against the relative ^{10}B depletion calculated with Presto-2.

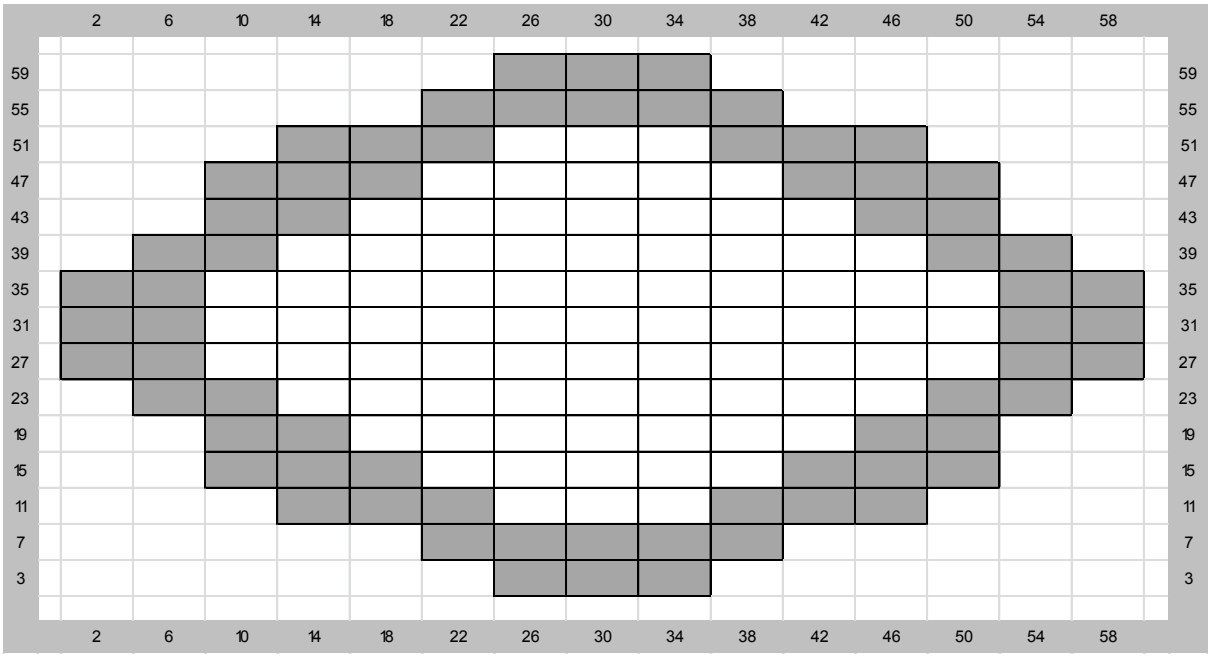

Figure 5: The core has been divided into peripheral control rod positions shown in grey and central positions shown in white.

Repeated movements of the same control rod during a single test showed decreasing helium releases. This proves that helium is pumped out of the blade due to operational demand.

Very clearly this phenomenon could be seen during a flux tilt test performed shortly after a SCRAM[5] in July 2014 (Figure 6).

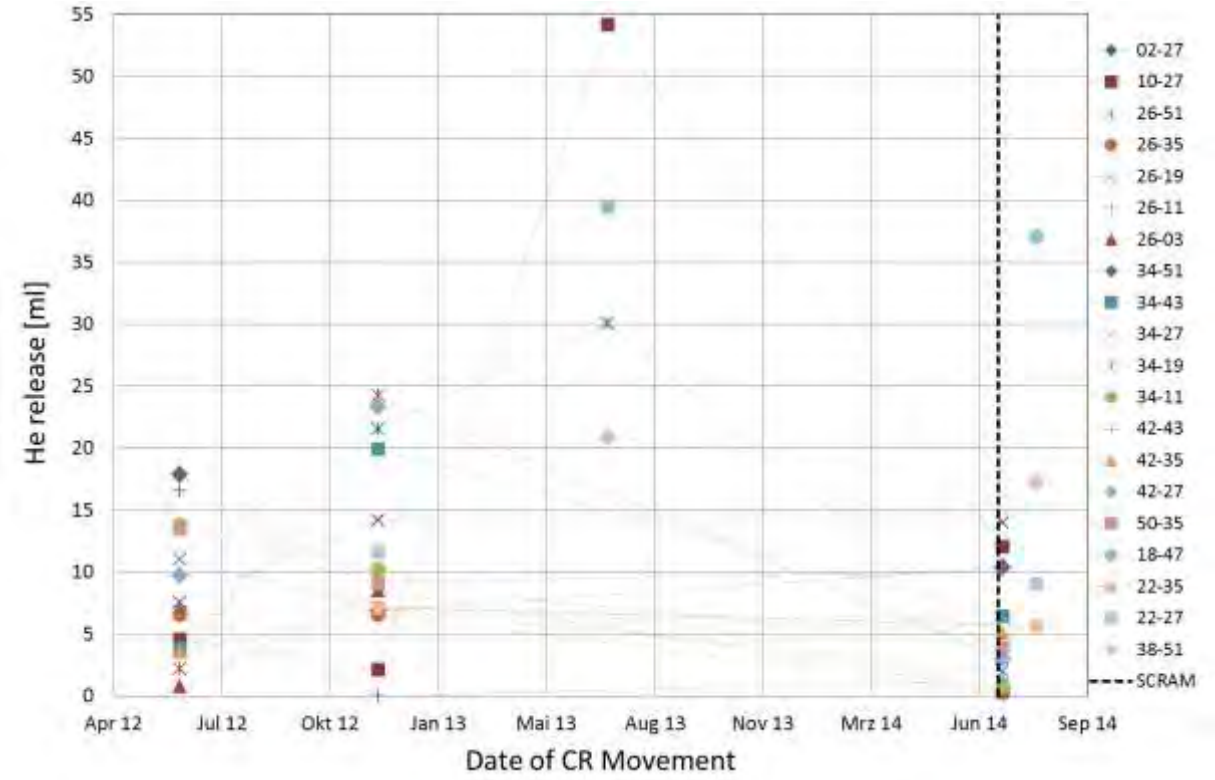

Figure 6: Control rod movements in July 2014 have been performed shortly after a SCRAM. During this flux tilt test the helium release of most control rods is lower than in earlier tests. (The numbers in the legend give the control rod position in the core).

A representative group of control rods, which have been moved in at least two previous tests before the one in July 2014, are displayed in Figure 6. All moved control rods, independent of ^{10}B depletion or core position, showed very little helium release (< 15 ml). Also control rods that have shown clear helium signals in earlier tests (e.g. control rods at position 10-27, 26-51, 34-19, 42-27 and more) and have therefore clearly reached their mechanical end of live, did not show any significant releases. One month later the helium inventory has been built up again, but was not yet fully recovered. Therefore, a control rod leak test should, whenever possible, only be performed at least two month after a SCRAM or regular start up.

3. Improvement of models and codes

In addition to the only rather heuristically modelled neutron leakage at the core periphery the poorly known profile of the neutron flux below the core causes large modelling uncertainties in the depletion of absorber segments that are withdrawn from the core. A comparison of the code Presto-2[6] used by KKL with POLCA7 used by Westinghouse showed differences of the ^{10}B depletion for shut-down rods of up to a factor of 2. Therefore, carelessly applying the life-time limits derived by the vendors, using their code system, to develop an exchange strategy for control rods, based on depletion values delivered by a core monitoring system that uses a different code, would lead to either a lot of unnecessary waste or leaking control rods in the core.

[5] Unscheduled trip of the reactor
[6] Code system of Studsvik Scandpower

The problem with modelling shut-down rods is that they are depleted almost exclusively in the fully withdrawn state where the entire absorber section is located below the core. The core simulator, on the other hand, does not explicitly calculate the fluxes in this region. What is currently done in both Presto-2 and POLCA7 is that the neutron fluxes at core bottom are simply extrapolated into the region below the core using a predefined polynomial in the distance from core bottom. The models for KKL in both nodal codes assumed a linear decline of the neutron fluxes but with different gradients. It turned out that this difference in the extrapolated fluxes accounted for the main part of the observed differences in the ^{10}B depletion of shut-down rods.

In order to improve the flux extrapolation model and base it on empirical grounds, two TIP machines at KKL were re-configured such that measurements could be extended to positions below the core support plate. In this configuration four TIP traces each at different radial positions were obtained including a common trace for machine inter-calibration. Since the TIP system at KKL uses gamma detectors this measurement yielded the gamma flux distribution below the core. The gamma fluxes were also calculated with a MCNP model of the lowermost two fuel nodes and the structures below the core. The MCNP model was then used to calculate detailed neutron fluxes in the region of interest that were validated by the agreement between measured and calculated gamma fluxes. By means of the two-group neutron fluxes obtained in this way it was possible to improve the flux extrapolation model in Presto-2 as well as in POLCA7. Details on the method and results can be found in [2]. Since the depletion tracking in both nodal codes is quite similar this resolved most of the discrepancies for Westinghouse control rods. However, the discrepancies for OE control rods remained nearly unchanged which makes the empirical study even more important.

For GEH control rods of type Ultra HD, which are currently inserted as lead assemblies at KKL and are planned to be deployed in reload quantities for the next cycle, it was necessary to go one step further. The reason is that GEH's core monitoring system, 3D Monicore, tracks control rod depletion in a very different way than Presto-2 does. To make a connection between the Presto-2 calculated depletion values and the vendor supplied life-time limits relevant for 3D Monicore tracking, GEH provided a set of well-specified MCNP benchmark calculations. These benchmark cases were re-calculated with KKL's lattice code Helios in order to validate the control rod model implemented there. For each depletion step of the MCNP benchmark cases, GEH also provided an equivalent control rod depletion value that 3D Monicore would calculate under the given circumstances. These values could be used to establish a mapping between Presto-2 depletions and 3D Monicore equivalent depletions. Moreover, inspection results from plants monitoring their Ultra HD control rods with 3D Monicore or reported by GEH in terms of 3D Monicore calculated depletions become directly applicable in this way.

4. Summary

The on-line helium mass spectrometer combined with an on-line monitoring system is very well suited to detect small cracks in control rods. The control rod leak tests have been performed according to the flux tilt test used to determine leaking fuel rods.
Developing an exchange strategy for control rods using the on-line helium mass spectrometer first of all pointed to some important weaknesses in the codes. We learned that the ^{10}B depletion has to be considered as a relative number which is subject to the respective code used for the calculation. However, determining the neutron flux profile below the core

and implementing the extrapolation coefficients accordingly lead to a substantial improvement of the codes Presto-2 and POLCA7 [2].
Not being able to overcome the problem with the uncertainty of the neutron leakage at the core periphery we decided to divide the core into peripheral control rod positions and central control rod positions (Figure 5). For both groups we defined a separate end-of-life ^{10}B depletion (Figure 4).
Another important finding was that helium is pumped out of the control rods due to operational demand. Therefore it is important to meet a recovery time of at least 2 months after start up or any other maneuver using control rods, before doing a leak test.

5. Conclusion

Even though the codes used by KKL and the control rods suppliers (Westinghouse and GEH) could be improved due to this investigation the calculation of absolute ^{10}B depletion for the end of life of a control rod is not possible so far. If a plant uses another code than the control rod vendor, their suggestion for the end of life should be considered as a relative number. In this case, an empirical determination of the end-of-life ^{10}B depletion for each control rod type would be helpful, to prevent either boron leakage or an early off-load of the control rods.
Based on our control rod leak tests we developed an exchange strategy for our OE control rods. The empirical method, presented in this paper, is independent on the construction of the blade and on the code used by the utility. Therefore it can be performed for all types of control rods with any code.

6. References

[1] N. Eickelpasch and R. W. Seepolt: Operational Experience and Postirradiation Examinations on Boiling Water Reactor Control Rods, Nuclear Technology, Vol. 60, March 1983, p. 362-366.

[2] T. Beran, R. Bieli, P. Seltborg, G. Ledergerber, S.-Ö. Lindahl, MCNP Evaluation of Top Node Control Rod Depletion below the Core in KKL, Proceedings of the Water Reactor Fuel Performance Meeting (WRFPM 2014/TOP FUEL), Sendai, Japan, Sep. 14-17, 2014, 100042.

[3] I. Larsson, H. Loner, K. Ammon, L. Sihver, G. Ledergerber, On-line monitoring of control rod integrity in BWRs using a mass spectrometer, Nuclear Instruments and Methods in Physics Research A 698 (2013) 249–256.

[4] I. Larsson, Helium measuring system for on-line fuel and control rod integrity surveillance in BWRs, PhD Thesis, Chalmers University of Technology, Sweden, CTH-NT- 264, ISBN 978-91-7385-738-3, 2012.

[5] I. Larsson, H. Loner, B. Schnurr, L. Sihver, G. Ledergerber, On-line detection of fuel and control rod failures in BWR, in: Proceedings of the 2009 Water Reactor Fuel Performance Meeting (WRFPM 2009/TOP FUEL), Paris, 2009.

CORROSION AND HYDROGEN PICKUP IN ZIRCALOY-2 CHANNELS WITH AND WITHOUT PROXIMITY TO CONTROL BLADE

DAVID SCHRIRE
Vattenfall Nuclear Fuel
SE 162 87 Stockholm, Sweden
Tel: +46-76 809 6596, Email: david.schrire@vattenfall.com

KRISTINA KARLSSON
Forsmarks Kraftgrupp AB
SE 742 03 Östhammar, Sweden
Tel: +46-173 81293, Email: kka@forsmark.vattenfall.se

GÖRAN BLOMBERG
Studsvik Nuclear AB
SE 611 82 Nyköping, Sweden
Tel: +46- 155 221653, Email: goran.blomberg@studsvik.se

ANDREAS MOECKEL
AREVA GmbH
Paul-Gossen-Straße 100, 91052 Erlangen, Germany
Tel: +49-9131-900 95316, Email: andreas.moeckel@areva.com

ABSTRACT

The hydrogen pickup behaviour in BWR fuel channels is an important characteristic not least because the hydrogen is implicated in the irradiation growth behaviour which can lead to distortion. It has been observed that fuel channels with extensive control blade exposure (i.e. adjacent to a partially or fully inserted control blade for a significant amount of time) early in life tend to bow towards the control blade side late in life. Since bow is understood to result from a difference in growth between opposite sides of a channel, it can be assumed that the sides adjacent to a control blade early in life tend to grow more later in life. Another consequence of operation adjacent to a control blade is that the outer surface of the channel facing the control blade (or control blade handle) develops what is commonly known as “shadow corrosion”. Shadow corrosion occurs on Zr-base alloys in contact with or in close proximity to other metallic alloys in the reactor core radiation field in BWRs or other reactors with similarly oxidising water conditions.

Due to an issue with thermal fatigue of the control blade shafts, the Forsmark 3 plant operated for 7 months with all the control blades inserted 500 mm into the core. The bottom sections of fuel channels at all burnup levels were thus continuously adjacent to control blades during this time. Taking advantage of this unique opportunity, at the end of this cycle it was decided to cut out samples from a 1-cycle and a 6-cycle Zircaloy-2 channel that both experienced this unusual control blade exposure without any significant prior control blade exposure, for post-irradiation hydrogen measurements and metallographic examination at the Studsvik hot cell laboratory.

The results of the post-irradiation examinations showed that:

- The shadow corrosion rate was somewhat higher on the 6-cycle channel than on the 1-cycle channel.
- For the 1-cycle channel the side adjacent to the control blade and the opposite side at the same elevation had the same low hydrogen concentration, showing that the early-in-life control blade exposure did not cause any significant increase in hydrogen pickup.
- For the 6-cycle channel the samples on the side adjacent to the control blade had far higher hydrogen concentrations than the opposite side at the same elevations. This difference was higher at the higher elevation samples than at the elevation directly adjacent to the control blade.

Since the 1-cycle sample from the side adjacent to the control blade had significant shadow corrosion on the outer surface but about the same low hydrogen content as the sample at the same elevation from the opposite side (without any shadow corrosion), it is concluded that the shadow corrosion from the proximity to the control blade *per se* did not make any significant contribution to the hydrogen

pickup. For the 6-cycle channel there was a larger increase in the hydrogen concentration between the control blade side and the opposite side at higher elevations, well above the zone in direct proximity to the control blade. Since this could not be due to shadow corrosion, it is concluded that the higher hydrogen pickup on the control blade side of the 6-cycle channel is probably due to some other effect of the different conditions on the two sides of the assembly, for instance the local power, fast neutron flux and void distribution.

1. Introduction

1.1. Background: impact of control blade exposure on channel behaviour

The hydrogen pickup behaviour in BWR fuel channels is an important characteristic not least because the hydrogen is implicated in the irradiation growth behaviour which can lead to distortion. It has been observed that fuel channels with extensive control blade exposure (i.e. adjacent to a partially or fully inserted control blade for a significant amount of time) early in life tend to bow towards the control blade side late in life [1]. Since bow is understood to result from a difference in growth between opposite sides of a channel, it can be assumed that the sides adjacent to a control blade early in life tend to grow more later in life. Another consequence of operation adjacent to a control blade is that the outer surface of the channel facing the control blade (or control blade handle) develops what is commonly known as “shadow corrosion”. Shadow corrosion occurs on Zr-base alloys in contact with or in close proximity to other metallic alloys in the reactor core radiation field in BWRs or other reactors with similarly oxidising water conditions.

1.2. Unique operating condition in Forsmark 3 cycle 24B

Vattenfall’s Swedish BWRs are normally operated such that medium burnup fuel assemblies (typically in their 3rd year of operation) are placed in control cells with extensive control blade exposure, while fresh and high burnup fuel have a minimum of control blade exposure during normal operation. However, due to an issue with thermal fatigue of the control blade extender shafts, the Forsmark 3 plant operated for seven months (cycle 24B) with all the control blades inserted 500 mm (14 %) into the core [2]. The lowest 500 mm of fuel channels at all burnup levels were thus continuously adjacent to control blades during this time.

Taking advantage of this unique opportunity, at the end of this cycle it was decided to examine samples from a 1-cycle and a 6-cycle Zircaloy-2 channel that both experienced this unusual control blade exposure without any significant prior control blade exposure.

2. Channel design and operating history

Both the fuel channels were from ATRIUM^{TM} 10B fuel, with nominally identical channel design and material. The channels were fully recrystallized Zircaloy-2, with a constant wall thickness of 2.3 mm. In the Forsmark 3 lattice the channel-channel water gap is nominally 19.4 mm on the control blade sides and 12.9 mm on the opposite sides. Forsmark 3 operates with normal water chemistry (NWC), i.e. with no injection of hydrogen, zinc or noble metals.

Assembly ID	KU8127	KU7485
Channel ID	F07163	F03155
Cycles with no control (CB fully withdrawn)	c24A	c19-c23, c24A
Time of operation with no control (days)	70	1799
Time of operation with CB inserted 14 % in c24B (days)	212	212
EOL assembly average burnup, MWd/kgU	9.7	41.1

Table 1. Fuel channel operating history

The assembly and channel overall operating history is summarised in Table 1. The node-wise axial burnup distributions of the 1-cycle fuel bundle KU8127 and 6-cycle fuel bundle KU7485 are shown in Figure 1 together with the equivalent controlled exposures for each node. The nodal controlled exposure is the cumulative burnup for the node for that time in which the control blade (or its handle) has been inserted into that node. This metric is equally weighted irrespective of when in life the control blade has been present in the node. As can be seen in Figure 1, for both assemblies/channels there was zero control blade exposure above the lowest 5 nodes at any time in the fuel lifetime. In the lowermost node (node 1) the controlled exposure is equal to the total burnup in that node – this is because with the control blade fully withdrawn (parked position) the control blade handle extends into the first node, so irrespective of the control blade position this node experiences “control”. The shadow corrosion formed from proximity to the control blade handle in the withdrawn position is clearly seen in the lower part of the 6c channel (Figure 3). For the 1c assembly KU8127 the controlled exposure in nodes 2-5 is almost as much as the total burnup, since those nodes only experienced about 70 days of uncontrolled operation prior to the partial blade insertion. For the 6c assembly KU7485 the controlled exposure in nodes 2-5 is much lower than for the 1c assembly since this assembly operated at a much lower power during cycle 24B (it had a higher burnup and was on the core periphery), and represents only a very small fraction of the total burnup for these nodes, see Table 2. It should be noted that the 6c assembly KU7485 was located on the core periphery for its last 3 cycles, so the control blade corner faced inwards. The assembly achieved a burnup of 35.2 MWd/kgU during its first 3 cycles, but only an additional 5.9 MWd/kgU in its last 3 cycles on the periphery. Nonetheless, the fuel rods at both sides of the assembly (adjacent to the channel sampling positions) had similar end of life burnups and so the channel fast neutron fluences were probably relatively similar on both sides during the first 3 cycles and only differed much in the last 3 cycles.

Figure 2 shows the axial power profile in the lower part of the corner fuel rod adjacent to the control blade corner (a1 rod) during the last cycle of operation, based on Nb-95 gamma spectrometry. The effect of the partially inserted control blade, as well as the control blade handle, are clearly seen.

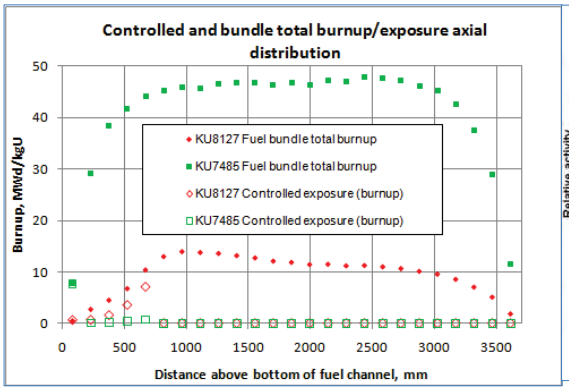

Figure 1. Axial burnup and controlled exposure profile for 1c assembly KU8127 and 6c assembly KU7485.

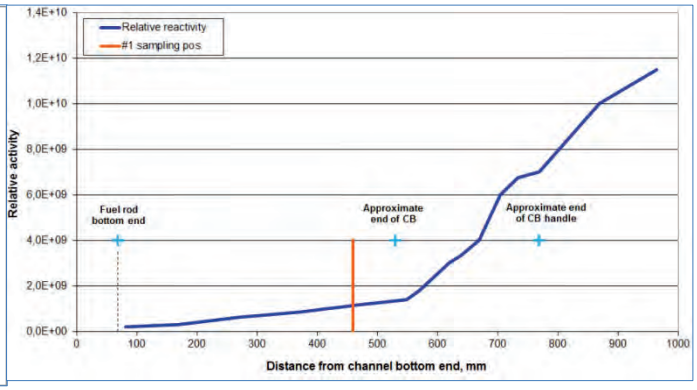

Figure 2. Axial power profile at bottom of corner fuel rod adjacent to control blade in 6-cycle assembly, based on Nb-95 gamma.

Axial node / Assembly	1	2	3	4	5	6-25
KU8127 (1 cycle)	0.63	0.67	1.59	3.58	7.16	0.00
KU7485 (6 cycle)	7.74	0.09	0.18	0.38	0.73	0.00

Table 2. Nodal controlled exposure, MWd/kgU

3. Poolside inspection and sampling

Circular samples (coupons) were cut from the CB (Control Blade) side (Face 4) and the non-CB side (Face 2) beside the longitudinal weld seam, see Figures 4 and 5 below. On each side, coupons were cut at three axial positions: 460 mm, 1930 mm and 3290 mm above the bottom of the channel. A new replacement channel was obtained for the continued operation of the 1-cycle bundle, since its original channel had to be scrapped after the coupons had been cut out.

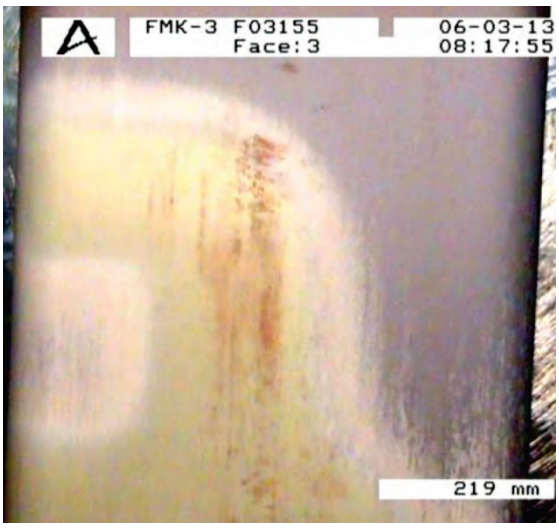

Figure 3. KU7485 channel showing the shadow corrosion from the control blade (in the parked position for most of its life).

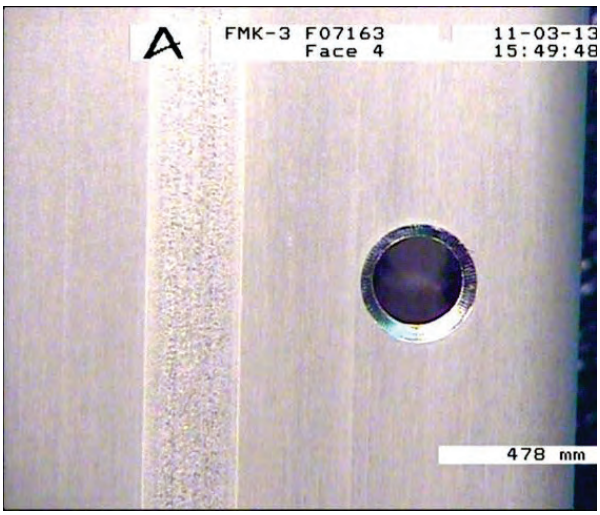

Figure 4. KU8127 (1 cycle assembly) channel after cutting out coupon.

The coupons were positioned by drilling a pilot hole through the channel wall, marking the upper end with the pilot drill, and then cutting out the coupons with a core drill, see Figure 6 below.

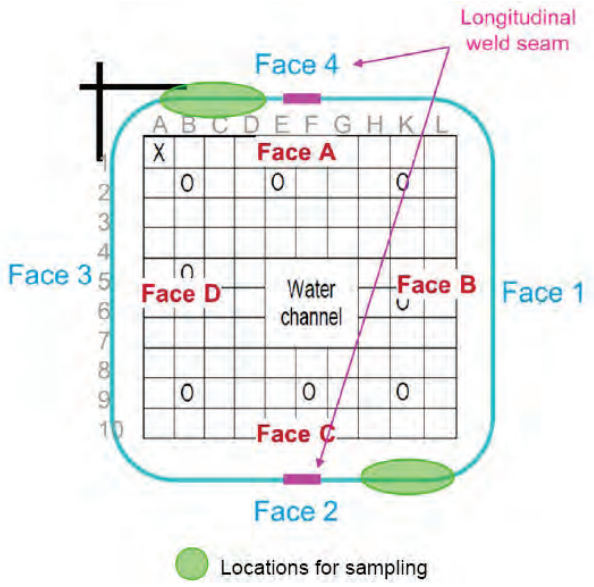

Figure 5. Sampling positions on fuel channel.

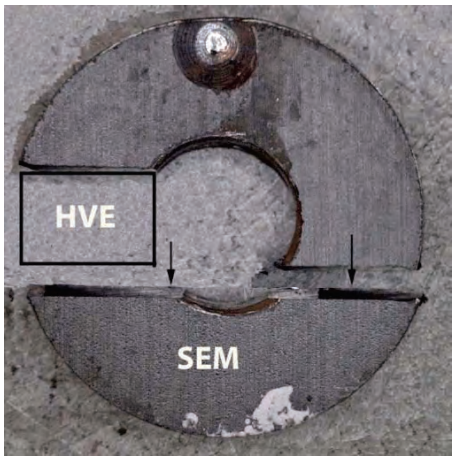

Figure 6. Coupon after cutting out samples for destructive PIE.

Channel bow measurements were performed on both channels before the sample cutting. The maximum bow was as follows, where a negative value is away from the CB.
KU8127 (1 cycle) x-direction -0.35 mm y-direction -0.46 mm
KU7485 (6 cycle) x-direction +0.98 mm y-direction +2.26 mm

4. Hot Cell Post-Irradiation Examination (PIE)

4.1. Experimental methods

The channel coupons were retrieved from the shipping container, and photographed to record the inner and outer surface appearance. Hot vacuum extraction (HVE) and scanning electron microscopy (SEM) samples were cut out as shown in Figure 6.

The hydrogen content was measured by HVE using an ELTRA OH-900 Hydrogen Determinator as follows: The samples (weighing about 0.1 g) were placed in a graphite crucible and heated up to about 2000 °C with argon as carrier gas. Any CO that might be present was removed by passing the gas mixture through Schütze's reagent (I_2O_5) to oxidize the CO to CO_2 which was subsequently removed by chemical reaction with NaOH. The gas mixture of argon and hydrogen then passed through a thermal conductivity detector with low drift, high resolution and wide measuring range. The hydrogen concentration was determined by an integrator. Before the measurements, the HVE equipment was calibrated using certified Ti-based standards with 62.5 ± 3.2 ppm hydrogen content. Although the absolute accuracy of the hydrogen determination using HVE is no better than the relative accuracy of the calibration standards (in this case about 5 %), the reproducibility/precision has previously been found to be better than this, except at very low concentrations. The measurements were performed on samples which included any attached oxide, so the reported hydrogen concentrations refer to the total evolved hydrogen relative to the total sample weight.

Cross-sectional arcs were cut out for scanning electron microscopy (SEM), where the inner and outer surface could be examined along a plane just above the word "SEM" in Figure 6. The samples were embedded in epoxy resin, ground and polished with 0.04 µm colloidal SiO_2 suspension as a final oxide polishing step. The examinations were performed in a JEOL 6300 SEM. Micrographs were taken in BEI-mode (Backscatter Electron Imaging) using different instrument settings for optimised imaging of the oxide or the hydrides. The oxide thickness was evaluated from the micrographs acquired in the SEM. The average thickness was determined by measuring the total oxide area in each micrograph using a Leica QWin image analysis software. The oxide area was divided by the width of the measured oxide layer in each micrograph to obtain the average oxide thickness. This method takes into account variations in oxide thickness and delamination or separation of oxide layers.

4.2. Results

The hydrogen concentrations measured by HVE are shown in Figure 7. The red symbols represent the measurements on the control blade side (face 4 in Figure 5) and the black symbols represent the measurements on the non-control blade side (face 2 in Figure 5). The 1-cycle channel (diamond-shaped symbols in Figure 7) had a low concentration of just over 20 ppm for both the CB side (face 4 in Figure 5) and the non-CB side (face 2 in Figure 5) at the lowest elevation (460 mm above the bottom of the channel). At this elevation the control blade was adjacent to the CB side during cycle 24B. At the mid-height elevation (1930 mm) the hydrogen was only measured on the CB side and was essentially the same as at the lower elevation.

The 6-cycle channel (square symbols in Figure 7) had very much higher hydrogen levels in all the samples measured. On the non-CB side, the hydrogen concentration increased with elevation from just over 40 ppm at the lowest position to just over 70 ppm at the top sample. On the CB side, the hydrogen concentration was very much higher, increasing with elevation from just over 100 ppm at the lowest position to just over 240 ppm at the top sample.

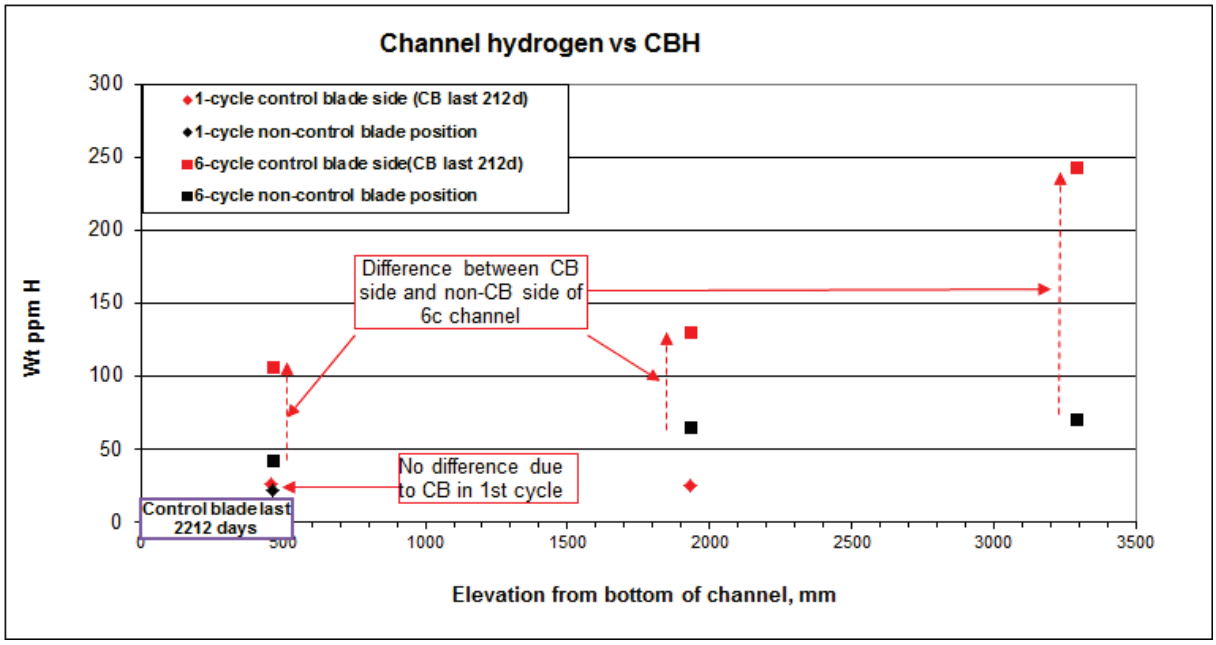

Figure 7. Channel sample hydrogen concentration vs. channel elevation.

The average oxide thicknesses measured in the SEM are shown in Figure 8. The red symbols represent the measurements on the control blade side (face 4 in Figure 5) and the black symbols represent the measurements on the non-control blade side (face 2 in Figure 5). The filled symbols are the oxide thickness on the outside of the channel wall and the open symbols are the oxide thickness on the inner surface. The oxide layer appearance (topography) varied between the samples and frequently between the inner and outer surface of the same coupon. The oxide appearance is described qualitatively below.

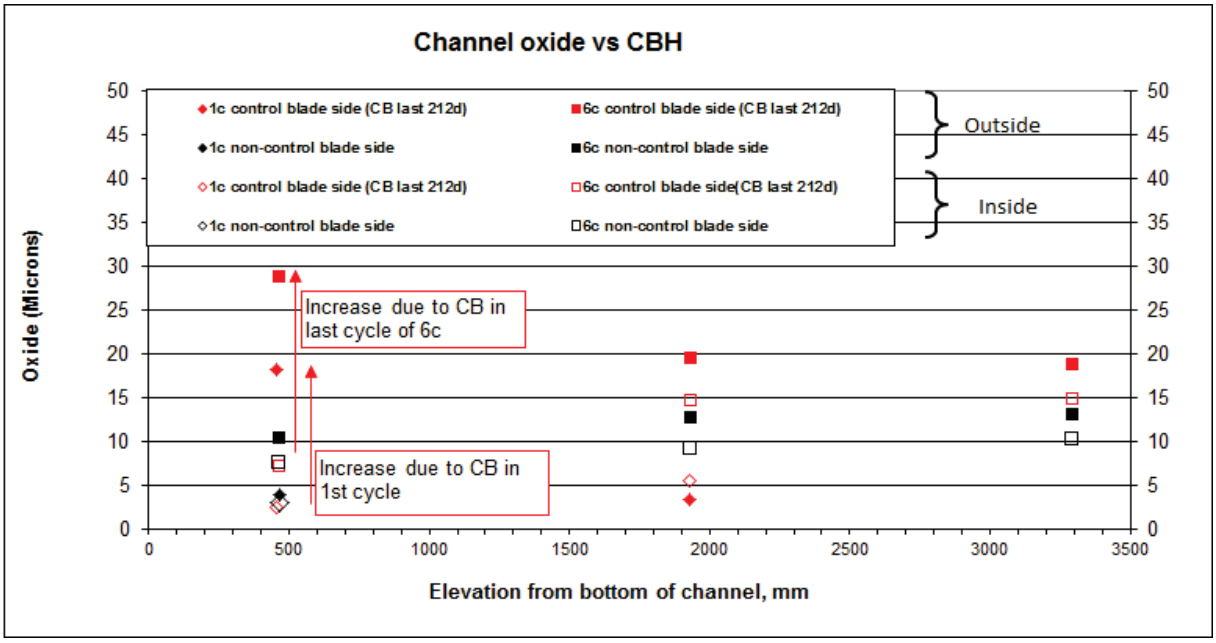

Figure 8. Channel sample oxide thickness vs. channel elevation.

1-cycle channel. The inner oxide layer was rather uniform in both the 1-cycle samples at the lowest elevation but thicker nodules were present at the 1930 mm elevation (Figures 9a and 9b). The outer surface oxide layer was much thicker, and relatively uniform, in the sample that had been adjacent to the control blade (460 mm elevation on CB-side), compared to the other samples (Figures 10a and 10b).

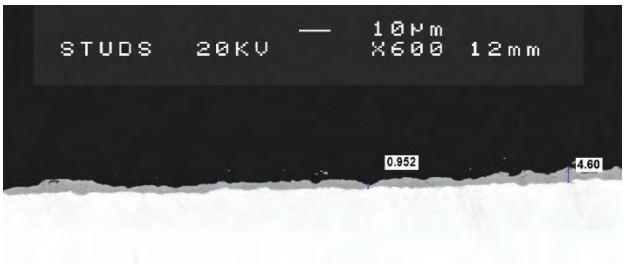

Figure 9a. 1-cycle channel. Inner surface oxide 460 mm elevation, CB-side.

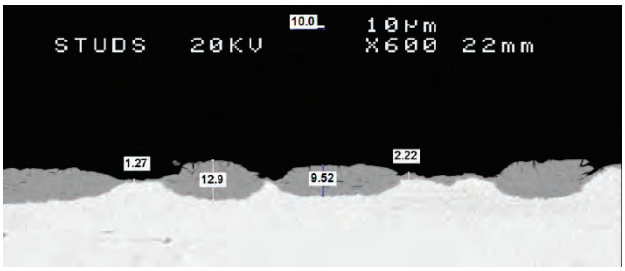

Figure 9b. 1-cycle channel. Inner surface oxide 1930 mm elevation, CB-side.

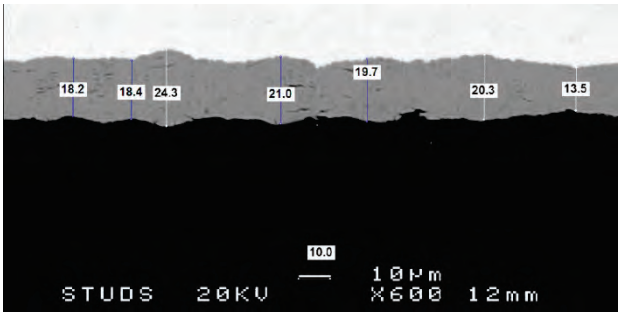

Figure 10a. 1-cycle channel. Outside oxide 460 mm elevation, CB-side.

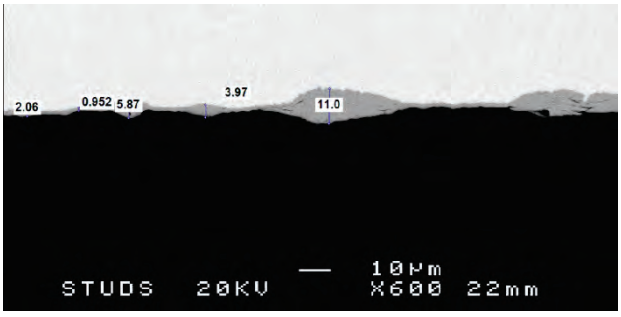

Figure 10b. 1-cycle channel. Outside oxide 460 mm elevation, non CB-side.

6-cycle channel. The inner oxide layer was rather even in the 6-cycle samples (Figures 11a and 11b). The average thickness was the same on both sides at the 460 mm elevation, and thicker higher up. The outer surface oxide layer was thicker in the sample that had been adjacent to the control blade (460 mm elevation on CB-side), compared to the other samples. (Figures 12a and 12b). Both the inner surface and outer surface oxide showed some apparent tendency to delamination (cracks) which was not seen in the 1-cycle samples.

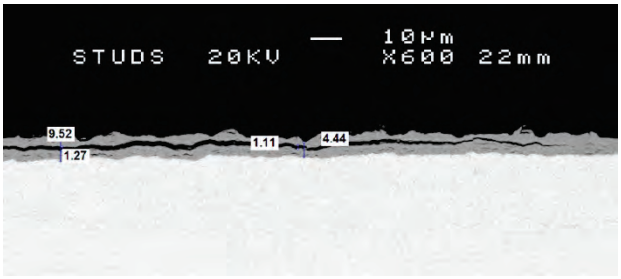

Figure 11a. 6-cycle channel. Inner surface oxide 460 mm elevation, CB-side.

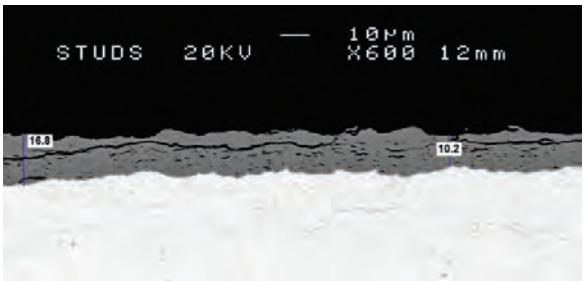

Figure 11b. 6-cycle channel. Inner surface oxide 1930 mm elevation, CB-side.

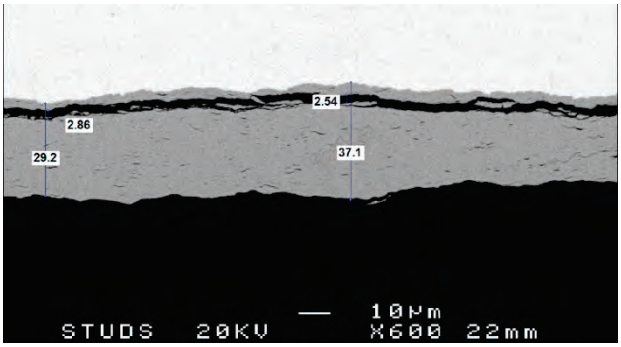

Figure 12a. 6-cycle channel. Outer surface oxide 460 mm elevation, CB-side

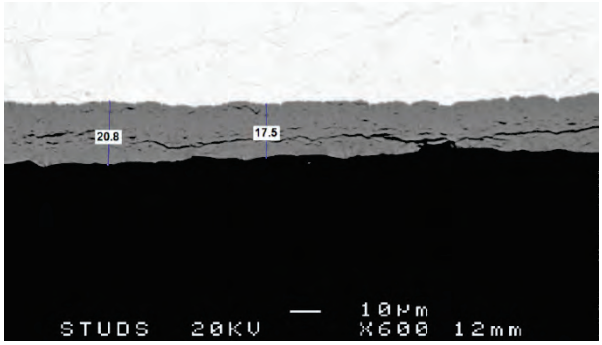

Figure 12b. 6-cycle channel. Outer surface oxide 1930 mm elevation, CB-side.

5. Discussion

The **oxide appearance** has been broken down into the following rough categories, and the different sample surfaces are characterized accordingly in Table 3:

- "Wavy" where there is a continuous oxide coverage, but the thickness varies significantly with a wavy appearance, see e.g. Figure 9a.
- "Nodular" " where the individual nodules are about an order of magnitude thicker than the thin oxide separating them, see e.g. Figures 9b and 10b.
- "Uniform" where the thickness varies less than about a factor 2, irrespective of the actual thickness or condition of the layer, see e.g. Figures 11b and 12b.

It is considered likely that the wavy or nodular oxide appearance seen in the 1-cycle channel would eventually progress to the continuous oxide film categorised as "uniform".

Shadow corrosion. The shadow oxide thickness (oxide attributable to the shadow corrosion) can be estimated from the difference in oxide thickness between the CB-side outer surface at the 460 mm elevation, compared to the non-CB side at the same elevation. The shadow corrosion can also be estimated from the difference in oxide thickness between the outer surface (facing the control blade) and the inner surface, at the 460 mm elevation. In both cases for the 1-cycle channel, this results in an apparent shadow corrosion during cycle 24B of about 15 µm, as indicated in Figure 8. For the 6-cycle channel, the shadow oxide thickness estimated in the same way results in an apparent shadow corrosion during cycle 24B of 18-22 µm, as indicated in Figure 8. It thus seems that the 212 days of exposure to the partially inserted control blade resulted in a somewhat thicker shadow corrosion on the 6-cycle channel than on the 1-cycle channel, despite the fact that the latter had only operated for 70 days prior to the control blade exposure and thus not built up a thick oxide layer prior to the control blade exposure.

This observation is notable when bearing in mind the fact that the 6-cycle channel operated in a far lower radiation field during cycle 24B when the shadow corrosion occurred. Although not a perfect measure of the radiation field, the difference in "controlled exposure" (fuel bundle nodal burnup accumulation while adjacent to the control blade) gives some indication of this difference between the two channels. In the controlled node 3 (corresponding to the 460 mm elevation coupons) this parameter was almost an order of magnitude lower for the 6-cycle assembly than for the 1-cycle assembly. Since shadow corrosion is believed to be a form of radiation assisted galvanic corrosion [3], if the radiation field intensity plays a role it might have been expected that the shadow corrosion should have been equal or greater in the 1-cycle channel. However, the exact distance between the control blade surface and the channel might vary slightly from case to case, which could potentially explain the faster shadow corrosion in the 6-cycle channel.

General corrosion. The corrosion on all the sample surfaces from the 1-cycle channel, apart from the surface exposed to the control blade with shadow corrosion, had average oxide thicknesses ranging from just under 3 µm to just over 5 µm at both the 460 mm and the 1930 mm elevation (Figure 8). For the 6-cycle channel, however, there was a more noticeable (factor 2) increase in the general oxide thickness from the 460 mm to the 1930 mm elevation (Figure 8). At the 1930 mm elevation both the inner and outer surfaces of the 1-cycle channel had characteristically nodular oxide appearance, see Figure 9b and Table 3. The oxide on the 6-cycle channel at the same elevation had a more uniform appearance, see Figure 11b and 12b. Assuming that the 6-cycle channel had a similar oxide layer at the end of its first cycle to the 1-cycle channel then the subsequent growth of the oxide in the later cycles primarily consisted of "filling in" the oxide layer between the nodules, rather than a further increase in the depth of the nodules.

Hydrogen pickup. The measured hydrogen content in three coupons from the 1-cycle channel all showed low and similar levels of 22-26 ppm, despite the 3-times thicker total oxide thickness (inner and outer surface) for the 460 mm sample exposed to the control blade, see Figure 7. There was thus no indication of any additional hydrogen pickup due to shadow corrosion in these channel samples. The 6-cycle channel sample exposed to the control

blade, however, had a far higher hydrogen content than the sample from the opposite side at the same elevation, see Figure 7. The difference between the control blade side (face 4) and the opposite side (face 2) was even more striking for the two higher elevations. Since the higher elevations were never exposed to control blade presence, the higher hydrogen level in face 4 cannot be explained by shadow corrosion due to control blade proximity, which has been claimed in other cases [1, 4, 5]. The apparent "hydrogen pickup fraction" for the sample positions where both hydrogen concentration and inner and outer surface average oxide thickness were measured, is shown in Table 3, assuming the oxide has 100% theoretical density.

Channel	Side (face)	Elevation mm	Oxide appear-ance	Total inte-grated oxide (µm)	Hydrogen (ppm)	"Hydrogen Pick-up frac-tion" (%)
1-cycle	CB (4)	460	Wavy (inner) Wavy (outer)	21	26	10
	NoCB (2)	460	Wavy (inner) Nodular (outer)	7	22	25
	CB (4)	1930	Nodular (inner) Nodular (outer)	9	25	22
6-cycle	CB (4)	460	Uniform (inner) Uniform (outer)	36	107	23
	NoCB (2)	460	Uniform (inner) Nod/unif (outer)	18	43	19
	CB (4)	1930	Uniform (inner) Uniform (outer)	35	130	30
	NoCB (2)	1930	Uniform (inner) Nod/unif (outer)	22	65	23
	CB (4)	3290	Uniform (inner) Uniform (outer)	34	243	57
	NoCB (2)	3290	Uniform (inner) Nod/unif (outer)	24	71	24

Table 3. Hydrogen "pickup fraction"

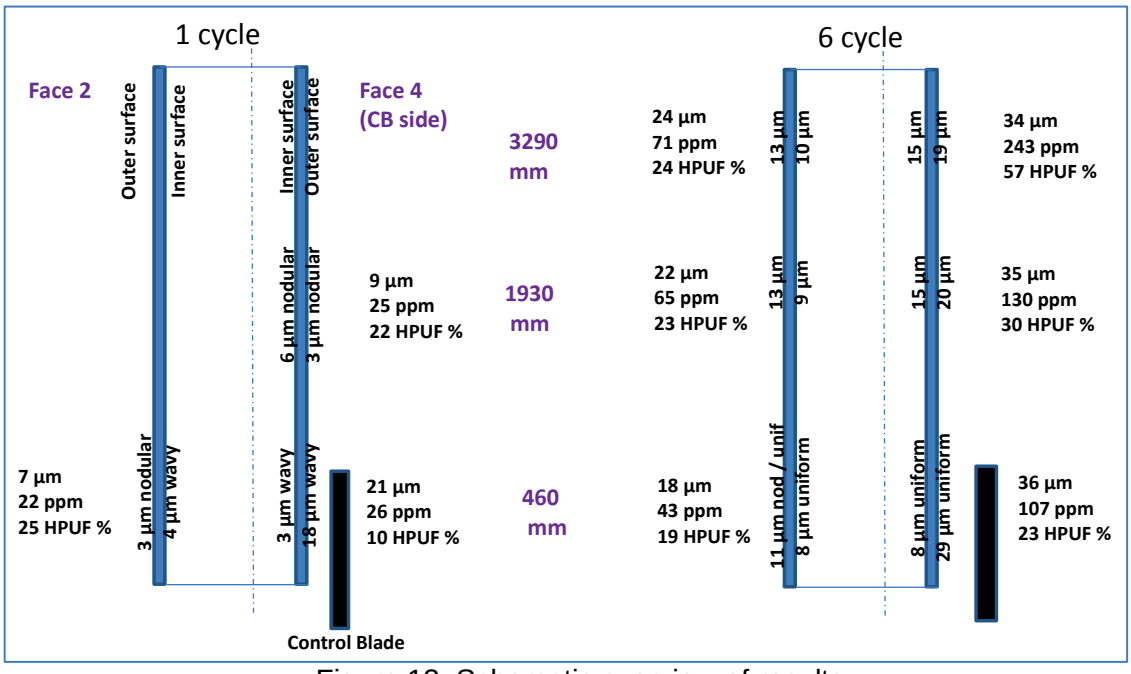

Figure 13. Schematic overview of results

As explained above, it would seem that the shadow corrosion (estimated to be about 15 µm for the 1-cycle channel) did not result in significant hydrogen pickup. Similarly, for the 6-cycle channel, the total hydrogen content in the CB side at 460 mm elevation (which experienced control blade proximity and shadow corrosion) is lower than for the higher elevations on the same side. So what could have caused the higher total hydrogen pickup (and apparent pickup fraction) on the CB side of the 6-cycle assembly compared to the opposite side?

One difference between the two channel sides is that the channel-channel water gap is larger on the CB-side (see section 2 above). However, it is not evident that this would affect the hydrogen pickup, since the non-boiling bypass water was about the same temperature on both sides when the assembly operated in more central positions in the core in the first three cycles. Instead, it is more likely that the last 3 cycles when the assembly was in the same core position on the periphery may have had some effect.

The entire assembly had a very low average void in the last three cycles (exit void of about 25 %), with no bulk boiling calculated for the lowest 13 nodes including the 1930 mm elevation, so presumably what void there was occurred mainly on the side facing the core centre (towards the CB sides). The inlet temperature was 275-277 ºC, and since there was no bulk boiling in the bypass the exit temperature on both sides was below 286 ºC. Since the bypass flow area is larger, and the heat flux lower, on the outer facing surface the bypass water temperature (and thus channel temperature) was somewhat lower compared to the inboard-facing sides. However, it does not seem likely that the slightly higher bypass water temperature on the CB-side than the opposite side could explain the difference in hydrogen pickup, since the hydrogen content at both the 460 mm and 1930 mm levels on the CB-side were higher than the hydrogen content in the opposite side at higher elevations (where the channel temperature would also have been higher).

The non-CB side had a lower fast neutron fluence than the CB-side during the last three cycles, which may provide an explanation for the difference in behaviour. It is possible that although both sides of the channel had experienced substantial irradiation damage during the first three cycles of operation, the outer-facing sides experienced insufficient fast neutron flux in the last three cycles to undergo the rapid increase in hydrogen uptake that is typical for irradiated Zircaloy-2 in in-pile BWR conditions after high exposure.

Neither channel had appreciable bow. The 1 cycle channel had a very small negative bow (i.e. away from the CB corner), remaining from the as-fabricated condition (Forsmark 3 channels are oriented such that any existing bow is away from the control blade). The 6 cycle channel has a small bow towards the CB sides, which is not surprising considering the higher neutron fluence and hydrogen content on those sides.

6. Conclusions

The results of the post-irradiation examinations showed that:

1. The shadow corrosion rate was somewhat higher on the 6-cycle channel than on the 1-cycle channel.
2. For the 1-cycle channel the side adjacent to the control blade and the opposite side at the same elevation had essentially the same low hydrogen concentration, showing that the early-in-life control blade exposure did not cause any significant increase in hydrogen pickup.
3. For the 6-cycle channel the samples on the side adjacent to the control blade had far higher hydrogen concentrations than the opposite side at the same elevations. This difference was higher at the higher elevation samples than at the elevation directly adjacent to the control blade.
4. Since the 1-cycle sample from the side adjacent to the control blade had significant shadow corrosion on the outer surface but about the same low hydrogen content as the sample at the same elevation from the opposite side (without any shadow corrosion), it is concluded that the shadow corrosion from the proximity to the control blade *per se* does not make any significant contribution to the hydrogen pickup.

5. For the 6-cycle channel there was a larger increase in the hydrogen concentration between the control blade side and the opposite side at higher elevations, well above the zone in direct proximity to the control blade. Since the difference at the higher elevations could not be due to shadow corrosion, it is concluded that the higher hydrogen pickup on the control blade side of the 6-cycle channel is probably related to thicker oxide and is due to some other effect of the different conditions on the two sides of the assembly, for instance the local power, fast neutron flux and void distribution.

Acknowledgements

The authors are grateful to Jesper Kierkegaard for assistance in selecting the candidate channels and insights into relevant aspects of their operation.

References

1. “Shadow Corrosion Resulting in Fuel Channel Bowing”. USNRC Information Notice 89-69 Supplement 1, 25 August 2003.
2. Operating Experience from Swedish Nuclear Power Plants 2008. Kärnkraftsäkerhet och Utbildning AB, 2009.
3. G Lysell, A-C Nystrand and M Ullberg, “Shadow Corrosion Mechanism of Zircaloy”, ASTM STP 1467, 2005.
4. S. T. Mahmood et al., “Channel Bow in Boiling Water Reactors – Hot Cell Examination Results and Correlation to Measured Bow”, Proc. Int. LWR Fuel Performance Meeting San Francisco, California, Sept. 30 – Oct. 3, 2007.
5. S. T. Mahmood et al., “Shadow Corrosion-Induced Bow of Zircaloy-2 Channels”. 16th Int. Symposium on Zirconium in the Nuclear Industry, 13 May, 2010, Chengdu, China.

ATRIUM™ 11 – Validation of Performance and Value for BWR Operations

Steven E. Cole[1],
Norman L. Garner[1]
[1] *AREVA Inc, 2101 Horn Rapids Road 99354 Richland WA - USA*

Rüdiger-Frank Graebert[2]
[2]*AREVA GmbH, Paul-Gossen-Str. 100, D-91052 ERLANGEN - Germany*

Pierre Mollard[3]
[3] *AREVA NP, 10 rue Juliette Récamier, F-69456 LYON Cedex 06 - France*

ABSTRACT

AREVA's ATRIUM™ 11 advanced fuel design for Boiling Water Reactors (BWRs) is the result of a product development program designed to realize a strict set of performance and reliability objectives. These objectives were established based on the projected industry demand for value, considering the evolution of the market and the always present expectation for flawless fuel performance. Early in the development it became clear that an 11x11 array would be necessary to deliver the required breakthrough level of performance and that the ATRIUM™ platform was ideally suited to accommodate this evolution. Maintaining a direct link to proven design concepts and materials allowed for faster validation of the mechanical design and confidence in the analytical predictions of value. The validation of ATRIUM™ 11 performance and reliability is given by two steps; the now completed out of pile thermal hydraulic and mechanical tests, and the initiated lead fuel assembly programs in different plants and regions covering a large spectrum of operating conditions. In this paper, the results of fuel cycle analyses will be presented to provide an example of the cost reduction to be realized with the ATRIUM™ 11. The gains in fuel reliability and operational flexibility will be translated into economic value. Finally, the results of poolside examinations of irradiated ATRIUM™ 11 fuel assemblies will be provided as evidence for validation of the mechanical design.

1. Introduction

A decade ago, AREVA decided to develop an upgraded BWR fuel design to address the anticipated future market needs. The capability to responsively address reactor power uprates from 10% up to 30% was considered as one main requirement of this development. Another main requirement was the improvement of fuel efficiency and fuel cycle economy. Reinforced protection against debris fretting was also a key goal, as debris related fuel failures and associated outages cost the industry millions of euros in lost generation and negatively impact the working area of plant site personnel.

The exploration of a wide range of 10x10 geometries confirmed that only little additional performance could be gained while staying with this basic array constraint. The key to making further performance gains was requiring a more significant improvement in thermal-mechanical margin. Therefore, the decision to develop an 11x11 array design was taken. An extensive design development, testing and verification program was conducted validating the design prior to its first insertion in a reactor [1]. A structured Lead Fuel Assembly program began in 2012 and first results are now available and presented in the following as well as some quantified examples of the impact of the utilization of ATRIUM™ 11 on the fuel cycle economy.

2. Overview of the ATRIUM™ 11 Fuel Assembly Design and Performance

The 11x11 lattice of the ATRIUM™ 11 provides a fully symmetric array of 112 fuel rod positions vs. the 91 to 96 rods in currently available 10x10 configurations (Fig. 1). When accounting for the part-length fuel rods (PLFRs), the total fuel column length within the bundle is increased by ~20% relative to the ATRIUM™ 10XM design. Increasing the total length of fuel rod within a bundle significantly reduces the average linear heat generation rate (LHGR) of the individual fuel rods for a given bundle power. A lower average LHGR in turn has the benefits of reducing power load related stress on the fuel rod cladding, pellet temperatures and fission gas release. In practice, the LHGR operational limit applied for the ATRIUM™ 11 is scaled down from that used on the 10x10 in order to ensure that part of the inherent gains are used to increase design flexibility while retaining a net increase in the safety margin. As demonstrated in [2] the reduced LHGR of the ATRIUM™ 11 enhances margins to limits and is beneficial for the safety analysis.

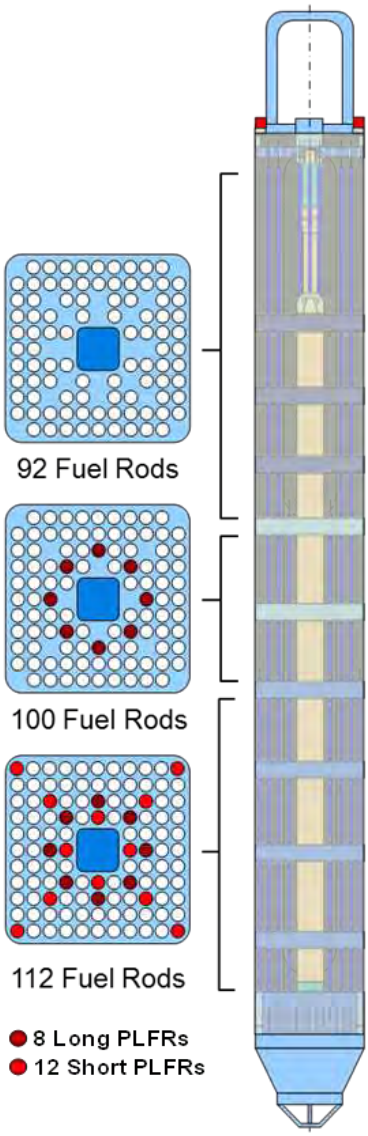

Fig. 1 ATRIUM™ 11 Axial and Radial Configuration

The BWR fuel rod array has increased at regular intervals over the last several decades. In order to apply past experience to new designs, AREVA scales the cladding thickness to maintain the same cladding thickness-to-outside diameter ratio (t/OD) across the ATRIUM™ 9x9, 10x10 and 11x11 products. Reducing the t/OD, with or without a change in the fuel rod array, would represent a real reduction in mechanical safety margin and would bring into question the relevance of prior operating experience. Maintaining this mechanically sound reference parameter assures that the cladding strain for a power change proportional to the bundle average power will result in comparable stress regardless of the fuel rod dimension. AREVA's benchmarking data base includes successful irradiation of millions of such rods with zirconium alloy cladding with similar characteristics to those of the ATRIUM™ 11 fuel rods. The well proven t/OD parameter assures that peak cladding stress levels are accurately predicted with AREVA's benchmarked thermal mechanical methodology. A statistical evaluation of cladding strain response, including both steady state and bounding transient strain effects, shows an improvement in the median strain experienced by the ATRIUM™ 11 fuel rods relative to the ATRIUM™ 10XM [2].

The ATRIUM™ 11 fuel rods are loaded with Cr_2O_3 doped fuel pellets. Testing has demonstrated that Cr_2O_3 fuel provides enhanced protection against pellet-clad interaction failure (PCI) comparable to that brought by liner-cladding [3]. Fuel pellets doped with Cr_2O_3 bring direct relief of peak cladding stress by virtue of pellet yielding deformation during a power ramp after pellet-to-clad gap closure when pellet expansion rates exceed the creep rate of the cladding. In contrast, liner cladding only delays the onset of combined axial and hoop stress arising from pellet stack expansion during a power ramp after which the expansion strain is borne almost entirely by the structural portion of the cladding wall. The transfer of protection against PCI failure from the cladding to the Cr_2O_3 doped fuel makes liner redundant. Considering that the non-liner part of the cladding provides the primary mechanical structure (i.e., the structural wall), combining Cr_2O_3 doped fuel with non-liner cladding in the 11x11

results in a greater absolute thickness of the cladding structural wall relative to a 10x10 fuel rod with liner cladding, making available the potential for increased mechanical margin.

The ATRIUM™ 11 features a total of 9 ULTRAFLOW™ spacer grids manufactured from alloy 718. The version of the ULTRAFLOW™ spacer developed for the ATRIUM™ 11 retains the primary design elements responsible for the excellent critical power performance of the ATRIUM™ 10x10 product line. In particular, the closed strip egg-crate style construction and the basic geometry and orientation of the spacer mixing vanes are consistent with the ULTRAFLOW™ spacer design used on more than 34000 ATRIUM™ 10x10 assemblies delivered since 1992. With the ATRIUM™ 11, Computational Fluid Dynamics (CFD) analysis allowed an optimization of the ULTRAFLOW™ spacer by identifying features that were contributing to bundle pressure drop without significantly impacting critical power performance [1]. Furthermore, the fuel rod spring and dimple supports were integrated into the spacer strip and formed in a manner to reduce pressure drop [4]. These design optimizations resulted in a highly effective spacer with respect to coolant mixing, but with an overall low pressure drop. In addition, the total mass of alloy 718 was reduced relative to the ATRIUM™ 10XM spacer resulting in improved neutron economy.

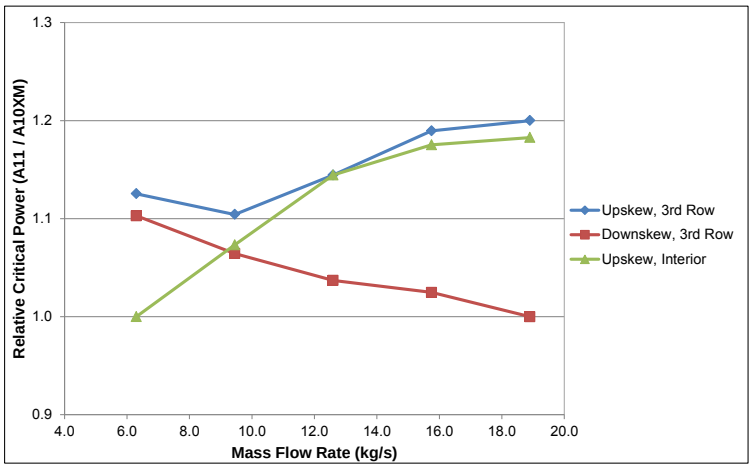

Fig. 2 Relative Critical Power Performance for Comparable Rod Locations

As in the ATRIUM™ 10XM design, the positioning of the ATRIUM™ 11 spacer grids varies axially to concentrate the coolant mixing in the upper, two-phase region of the assembly where it is most essential for rod cooling [5]. Measurements from the ATRIUM™ 11 full bundle critical power tests are shown in Fig. 2 relative to the ATRIUM™ 10XM for comparable fuel rod positions as a function of mass flow rate. Applications of the ATRIUM™ 11 critical power correlation in fuel cycle design studies confirm that the critical power capability of the design is comparable or better than the ATRIUM™ 10XM [2]. The critical power test measurements and the resulting correlation demonstrate that the design objective to maintain or to improve the critical power capability relative to the ATRIUM™ 10XM was realized. At the same time the overall bundle pressure drop was reduced and the two-phase to single-phase pressure drop rebalanced to improve thermal-hydraulic stability relative to the ATRIUM™ 10XM [2].

Several elements of the ATRIUM™ 11 fuel assembly contribute to its comprehensive defence against debris fretting. The 3rd Generation FUELGUARD™ lower tie plate (Fig. 3) ensures a higher filtration target for the inlet debris to exclude wires greater than 8 mm in length and 0.3 mm in diameter. Debris with a dimension below this threshold is not expected to harm the cladding [5]. So called ‘twister’ features at the inlet of the filtration cartridge (Fig. 3) provide an additional level of protection against thin wire filaments that pose a particular threat to BWR fuel. The closed grid upper tie plate (Fig. 3) aims to protect the fuel rod array from debris with a spherical diameter larger than 8 mm from entering from above, e.g. during refuelling operations. Assuming that debris may eventually be introduced into the fuel rod array, a low entrapment spacer grid design becomes the next line of defence. For the ATRIUM™ 11 it was decided to remain with a closed strip egg-crate style spacer grid structure, as this structure provides for relatively large unobstructed areas for debris to bypass the spacer in the sub-channel between the fuel rods. The leading edge of the ATRIUM™ 11 ULTRAFLOW™ spacer is fabricated with a scalloped, or zig-zag shape

(Fig. 3) that works to move wire shaped debris away from the fuel rod contact points and orient it such that it can safely pass through the open sub-channel areas between the fuel rods. Furthermore, the shape of the spacer-to-fuel rod contact area was redesigned into a smooth form in order to remove debris pinch points. Finally the total number of spacer-to-fuel rod contact points in the ATRIUM™ 11 fuel assembly was reduced by 20% relative to the standard ATRIUM™ 10XM design to decrease the statistical probability of debris entrapment within the rod array. This means that while there are more fuel rods to protect in the ATRIUM™ 11 bundle, there are fewer debris catch points than in the prior 10x10 design.

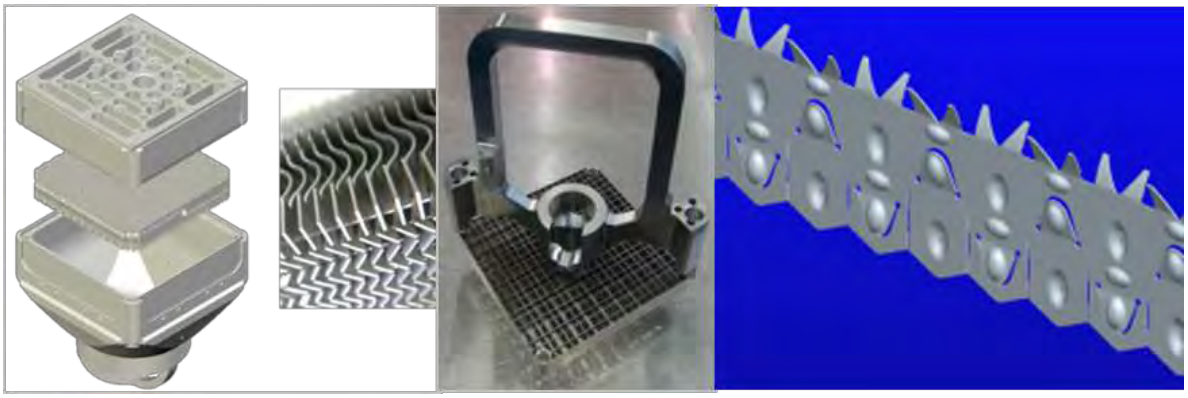

Fig. 3 (from left to right): 3rd Generation FUELGUARD™ lower tie plate (exploded view) - Close-up of the 'twister' inlet features – Closed grid upper tie plate – ATRIUM™ 11 ULTRAFLOW™ spacer strip

The design features of the ATRIUM™ 11 are complemented by the use of AREVA's Z4B™[1] alloy [7] for both the internal water channel and the external fuel channel structures. Z4B™ is a derivative of Zry-4 with iron and chromium levels above the reference ASTM specification to improve corrosion resistance relative to Zry-4. Additionally, the external fuel channel material receives a beta-quench heat treatment in the final thickness to randomize the crystal structure, erasing grain distortion artefacts from the sheet rolling process. The combination of Z4B™ and beta-quenching effectively eliminates fluence-induced growth to improve dimensional stability and minimize risk of control blade interference.

3. ATRIUM™ 11 Lead Fuel Assembly Program

3.1. Program Overview

The primary ATRIUM™ 11 lead fuel assembly (LFA) program consists of 40 fuel assemblies operating in 5 reactors worldwide. As shown in Table 1, the program scope accounts as much as possible for the potential different reactor types, power densities, cycle lengths, water chemistries and licensing environments to be experienced by the ATRIUM™ 11 in future reload applications. The first 8 LFAs were introduced in 2012 and have completed 3 irradiation cycles. The second set of 8 LFAs began operating in 2013 and has now completed 2 irradiation cycles. The third set of 8 LFAs started operation in 2014 and has completed 1 irradiation cycle. In spring 2015 the fourth and fifth sets of 8 LFAs were inserted into two plants and are operating in their first cycle. All 40 ATRIUM™ 11 fuel assemblies in operation have performed flawlessly and the multiple poolside inspection campaigns conducted thus far confirm the excellent behaviour.

To date, a total of 5 post irradiation examinations (PIE) have been conducted to collect measured data and to visually assess the mechanical integrity of the ATRIUM™ 11 assemblies.

[1] Z4B™ was developed by AREVA under the working name Zry-BWR

Table 1 ATRIUM™ 11 LFA Program Scope

Plant	Power Uprate	Cycle Length	Water Chemistry[2]	LFA Quantity	LFA Cycles completed as of July 2015
C05	N/A	12 mo.	NWC	8	3
C22	14.7%	12 mo.	HWC+OLNC	8	2
C17	25%	12 mo.	NWC	8	1
A40	5%	24 mo.	HWC+OLNC	8	<1
A23	20%	24 mo.	HWC+OLNC	8	<1

Generally all PIE campaigns include a comprehensive visual assessment of the fuel assembly and fuel channel to confirm the general mechanical appearance, to verify fuel rod straightness and fuel rod support, and to check the spacer positioning and integrity. The LFAs are also subjected to periodic detailed inspections to collect geometric data and to assess corrosion.

3.2. Results from Visual Inspections

Example results from the visual inspections are provided (Figs. 4 through 8). To date, the visual inspection of the ATRIUM™ 11 lead fuel channels (Fig. 4) exhibits a normal mechanical status and a low level of uniform corrosion as expected from the Z4B™ alloy. The 3rd Generation FUELGUARD™ lower tie plate appearance, including the visible portions of the filtration cartridge, is fully as expected (Fig. 5). Detailed visual examination of the ATRIUM™ 11 ULTRAFLOW™ spacer (Fig. 6) reveals as expected axial positioning and demonstrates that the rod support features and other mechanical aspects are perfectly sound. Visual inspection of the ATRIUM™ 11 upper tie plate (Fig. 7) shows normal behaviour for the fuel rod support function with uniform support of the fuel rod upper end caps and otherwise as expected mechanical performance. Fig. 8 shows the results of a standard visual inspection for fuel rod straightness mid-span between the spacer grids. In all cases, the rod-to-rod spacing is completely normal as expected. Visual inspections of single fuel rods after one cycle show normal appearance; in particular the areas immediately beneath the spacer grids indicate low levels of shadow corrosion at the spacer-to-fuel rod contact points (Fig. 8).

Fig. 4 ATRIUM™ 11 PIE Result: Fuel Channel Visual Inspection

[2] NWC = Normal Water Chemistry, HWC = Hydrogen Water Chemistry and OLNC = On-Line NobleChem, a trademark of GE Hitachi Nuclear Energy

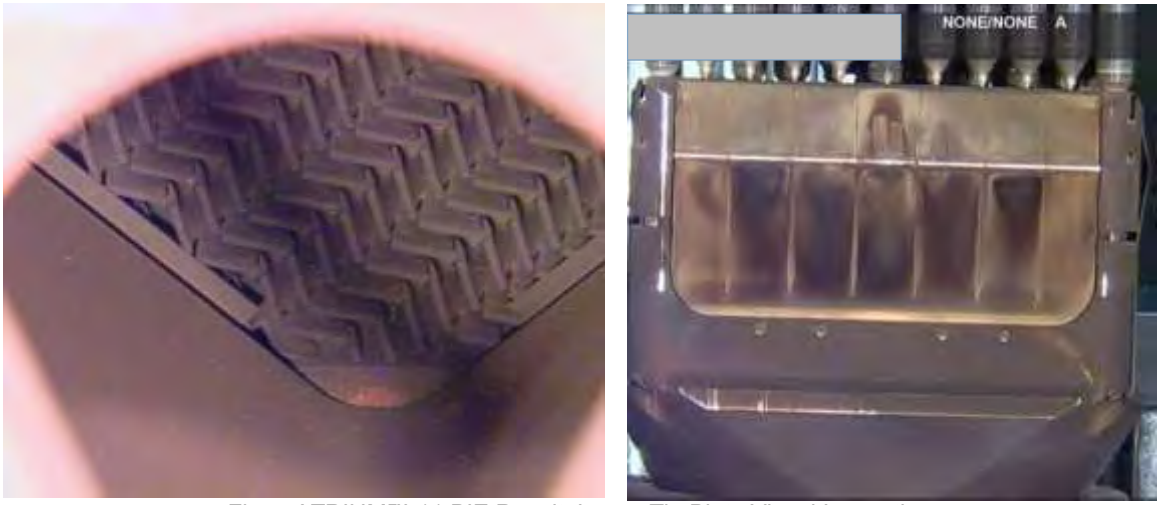

Fig. 5 ATRIUM™ 11 PIE Result: Lower Tie Plate Visual Inspection

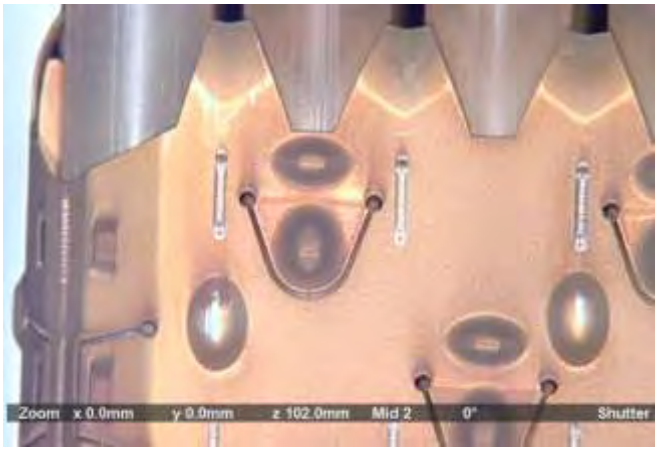

Fig. 6 ATRIUM™ 11 PIE Result: Spacer Grid Visual Inspection

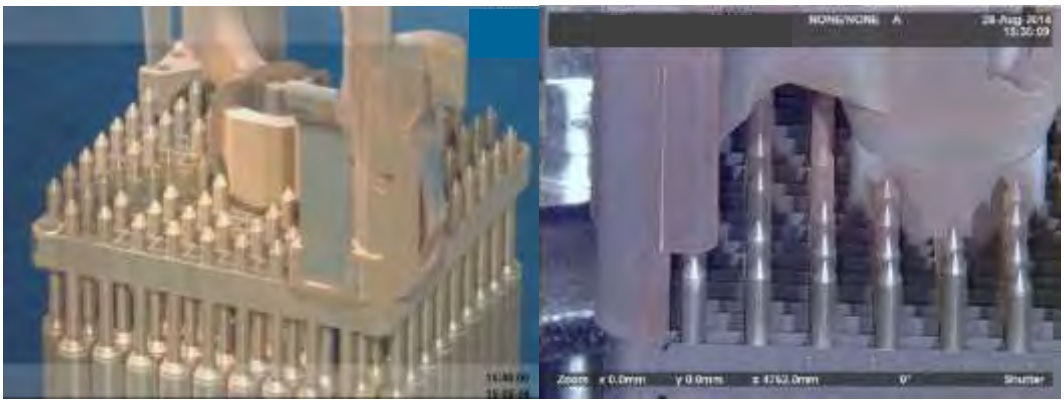

Fig. 7 ATRIUM™ 11 PIE Result: Upper Tie Plate Visual Inspection

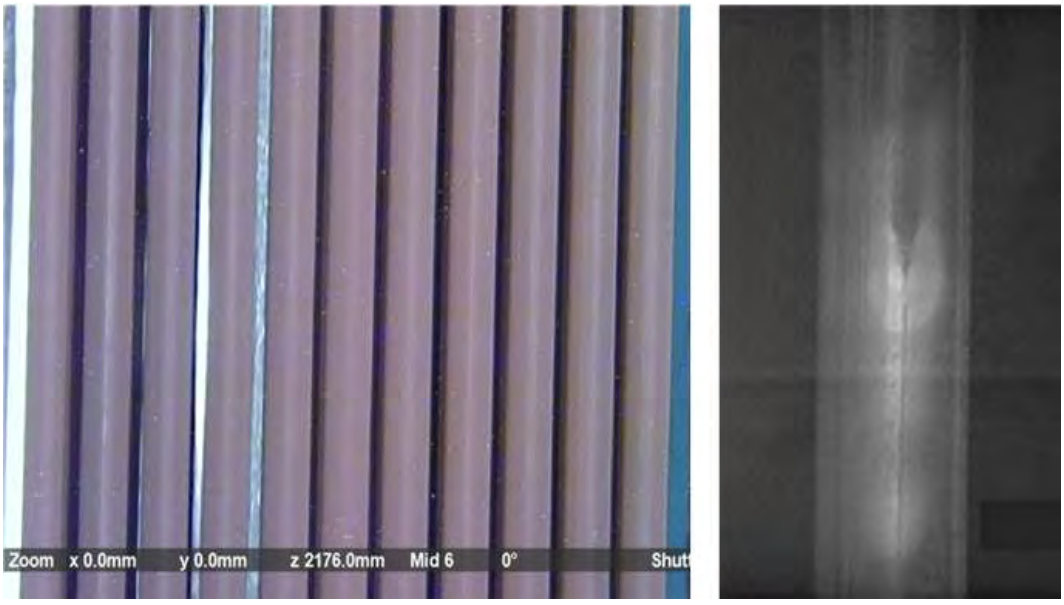

Fig. 8 ATRIUM™ 11 PIE Result: Visual Assessment of Fuel Rod Straightness & Single Rod Assessment of Spacer Grid Induced Shadow Corrosion

3.3. Results from Detailed Measurements

The available detailed measurement trends are presented and are shown next to results of AREVA 10x10 fuel measurements for comparison (Figs. 9 through 13)[3]. The measured data consist of fuel channel and fuel assembly growth, individual fuel rod growth and diameter change, and maximum mid-span fuel rod liftoff (i.e., tenacious CRUD plus oxide). As shown in the figures, the measured data are fully consistent with the similarly operated 10x10 fuel and reveal no adverse trend or anomaly. ATRIUM™ 11 fuel channel growth data are presented in Fig. 9. The measured ATRIUM™ 11 fuel channels in Fig. 9 are non-beta quenched Z4B™ alloy. The early ATRIUM™ 11 fuel channel growth and fuel assembly growth (Fig. 10) are generally low (<<1%) and are in line with the 10x10 measurements as expected. Similarly the ATRIUM™ 11 fuel rod growth and diameter measurements to date are trending as expected (Figs. 11 and 12). The reference 10x10 fuel rod dimensional data contain measurements from different initial fuel rod diameters, further demonstrating the already known fact that fuel rod growth and diameter change are not strongly dependent on the initial diameter. The fuel rod diameter measurements are corrected for oxide thickness. The measured ATRIUM™ 11 fuel rod data consist of a mix of Cr_2O_3 non-liner rods and standard UO_2 liner rods and there is no relevant performance difference between these two populations at this early burnup stage. The ATRIUM™ 11 utilizes the same cladding alloy as the previous 10x10 and as such the general corrosion trend is similar as is shown in Fig. 13.

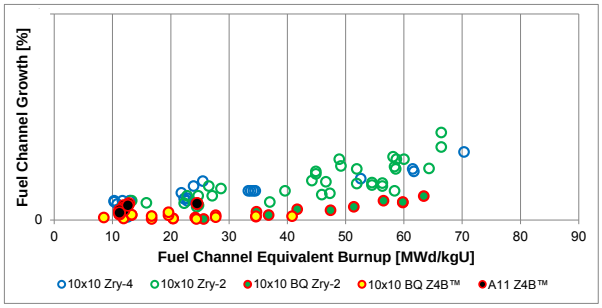

Fig. 9 ATRIUM™ 11 PIE Result: Fuel Channel Growth Compared to Reference 10x10 Data

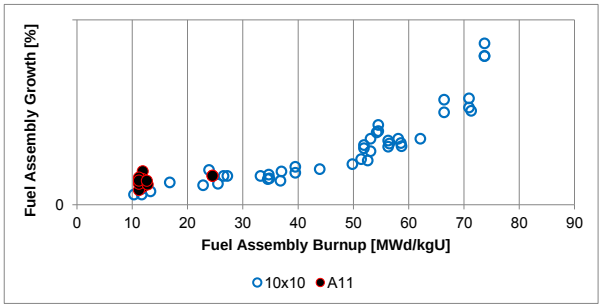

Fig. 10 ATRIUM™ 11 PIE Result: Fuel Assembly Growth Compared to Reference 10x10 Data

[3] Due to proprietary reasons the scale is omitted, but the trend against 10x10 performance is clearly shown.

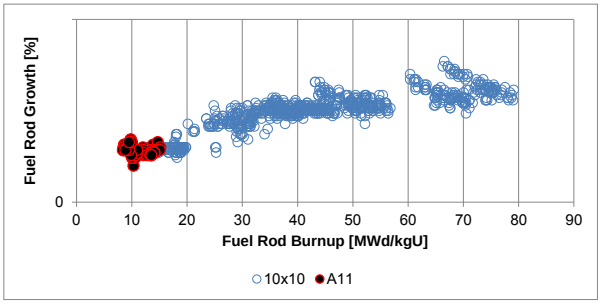

Fig. 11 ATRIUM™ 11 PIE Result: Fuel Rod Growth Compared to Reference 10x10 Data

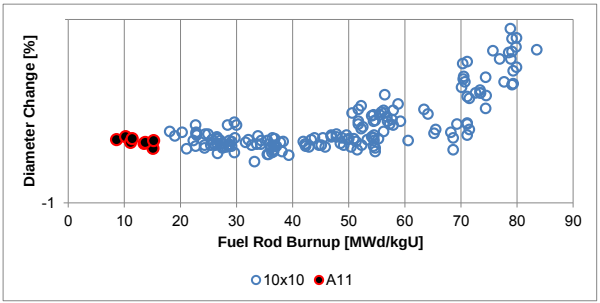

Fig. 12 ATRIUM™ 11 PIE Result: Fuel Rod Diameter Change Compared to Reference 10x10 Data

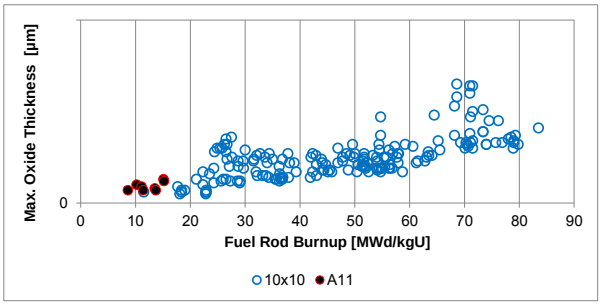

Fig. 13 ATRIUM™ 11 PIE Result: Fuel Rod Oxide Compared to Reference 10x10 Data

4. Fuel Cycle Economy and Economic Value

The ATRIUM™ 11 has been developed to deliver a step change in fuel cycle economics across the full range of the current BWR fleet, delivering significant economic value over a wide range of core geometries, power densities, operating strategies, and cycle lengths.

Calculating only the theoretical maximum efficiency of a bundle lattice design is insufficient to assess the economic gains possible for a given reactor as the final enrichment distribution within a bundle and loading of fuel within the core may diverge significantly from the ideal for maximum theoretical efficiency. For example, in BWRs operating on annual cycles, fuel cycle optimization is primarily constrained by thermal-mechanical operating limits (TMOL) and/or thermal-hydraulic stability. In plants where 18- to 24-month operating cycles are the norm, dryout capability and cold shutdown reactivity margin tend to be the limiting criteria for optimizing fuel efficiency. Any deficiency in a bundle design in one or more of these limiting characteristics requires compromises in the enrichment distribution and core loading pattern to assure that adequate operating margins are maintained throughout the cycle. With regard to the respective limiting conditions noted above, the ATRIUM™ 11 provides increases in all categories relative to AREVA's current primary BWR fuel design.

In application, the manner in which the beneficial characteristics of the ATRIUM™ 11 are utilised differs depending on the cycle operating length. In annual cycle operations, the improved TMOL is utilised to support higher radial peaking values arising from optimised core loading and reload batch size. In cycles of 18-months or longer, the TMOL capability is utilised to optimise spectral shift operations by allowing a strong bottom peaked power shape during the first 80% of the operating cycle. Operating with a bottom peaked profile increases the amount of plutonium transmuted from ^{238}U in the top of the fuel column which is then consumed in the last 20% of the operating cycle, significantly reducing the initial uranium enrichment required to generate a given cycle energy.

In order to quantify the benefits for a specific plant, equilibrium cycle designs are generated with both the ATRIUM™ 10XM and ATRIUM™ 11 using common design margin and cycle energy requirements. In establishing the TMOL limits, specifically the Linear Heat Generation Rate (LHGR), the respective limits are established such that the ATRIUM™ 11 yields equal or greater margin to the underlying criteria, such as cladding strain and end-of-life fission gas pressure. Fig. 14 provides the comparison of the ATRIUM™ 10XM and ATRIUM™ 11 fuel performance for a BWR operating on 24-month cycles. As seen in the comparison of fraction of LHGR limits for the respective designs on the left, the ATRIUM™ 11 inherently yields a substantial gain in margin to limit as the power shifts to a top peaked power shape at the end of the operating cycle. The combined benefits of the inherent lattice reactivity and use of optimised spectral shift capability of the ATRIUM™ 11 substantially improve the enrichment utilization efficiency (GWd/kg-^{235}U) while both total batch weight and enriched uranium product costs are reduced, as seen in the right hand chart.

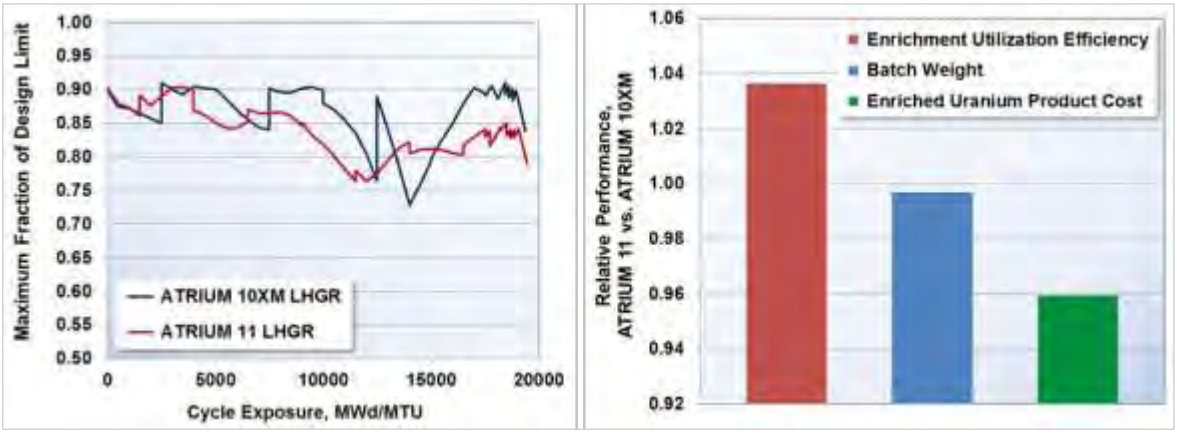

Fig. 14 Comparison of ATRIUM™ 10XM and ATRIUM™ 11 equilibrium cycle designs for a common 24-month reactor cycle. Left: margin to respective LHGR limits; Right: comparative efficiency and reload batch requirements

In addition to improvements in steady-state efficiency, the enhanced thermal-mechanical margin realised with the 11x11 fuel rod array will also allow plant power manoeuvres to be more rapidly executed, minimizing lost generation during plant startup or during control blade exchange sequences. Generation gains in excess of 2 effective full power days can be realized over long operating cycles through relaxed manoeuvring constraints.

Moreover, the comprehensive defence against debris of the ATRIUM™ 11 design brings an additional fuel cycle cost optimization by reducing the risk and costs resulting from the debris fretting failure of one or more fuel rods. The comprehensive design against all failure mechanisms will benefit BWR operators with avoidance of dose issues arising from higher coolant activity levels, contamination of plant systems and components, the burden of hosting failure location and repair activities, and potential mid-cycle outages to remove failed fuel.

5. Conclusion and perspectives

The ATRIUM™ 11 Lead Fuel Assembly program is running in Europe and in the USA since 2012 and the first irradiation experience data give as-expected results in terms of mechanical and thermal-mechanical behaviour as well as levels of corrosion. The gains in term of fuel cycle economy are being fine-tuned case after case and confirm the pertinence of the decision to develop an 11x11 BWR fuel design. The in-service qualification program is confirming the design leading to the anticipated reload readiness in the 2017 timeframe.

6. References

[1] *ATRIUM™ 11 – The Transition from Development to In-Service Qualification of an Advanced Fuel Design for Boiling Water Reactors*, N. Garner, S. Cole & al, Light Water Reactor Fuel Performance Meeting 2012, Manchester (UK), September 2012.

[2] *ATRIUM™ 11 – The Utilization of Reduced LHGR for Optimized BWR Operations*, N. Garner & al, LWRFPM 2013, Charlotte NC (USA), September 2013.

[3] *AREVA Cr_2O_3-Doped Fuel: Increase in Operational Flexibility and Licensing Margins*, C. Delafoy & al, Topfuel Reactor Fuel Performance 2015, Zurich (Switzerland), September 2015.

[4] A*TRIUM™ Fuel – Continuous Upgrading for High Duty BWR Plants*, R. Koch & al, Topfuel 2009, Paris (France), September 2009.

[5] *Protecting AREVA ATRIUM™ BWR Fuel from Debris Fretting Failure*, S. Cole & al, WRFPM 2014, Sendai (Japan), September 2014.

[6] *Development and Application of ATRIUM™ 10XM BWR Fuel Assemblies*, S.E. Cole & al, LWR Fuel Performance/TopFuel/WRFPM 2010, Orlando FL (USA), September 2010.

[7] *AREVA's Integrated Solution to Fuel Channel Performance*, A. Zbib & al, LWRFPM 2013, Charlotte NC (USA), September 2013.

WESTINGHOUSE BWR FUEL – EXPERIENCE UPDATE AND EVOLUTION OF HARDWARE AND METHODS DEVELOPMENT

JEREMY KING
BWR Product Management, Nuclear Fuel Strategy, Westinghouse Electric Company LLC
5801 Bluff Road, Hopkins SC, 290161 – USA

UFFE BERGMANN, ULF BENJAMINSSON
Nuclear Fuel Engineering, Westinghouse Electric Sweden AB
SE-72163 Västerås – Sweden

ABSTRACT

The Westinghouse BWR fuel evolution is based on the SVEA water-cross design, with its proven high reliability and superior uranium utilization. The most recent design step is the SVEA-96 Optima3 design that today has been widely licensed and has taken over as preferred product from its SVEA-96 Optima2 predecessor. The new design features, a new spacer concept and an improved debris filter, were jointly designed to mitigate debris fretting which is the only remaining failure mode for Westinghouse BWR fuel. The superior debris mitigation of the combined features has been qualified in loop testing, and its verification in actual fuel operation is in progress.

The fuel design is based on evolutionary development and also includes the proven liner concept (with a perfect PCI track record), LK3 cladding material, the advanced ADOPTpellet concept and the distortion-resistant **Low Tin ZIRLO™** fuel channel.

The hardware product development goes hand-in-hand with the evolution of software methods. A good example is the MEFISTO code that was presented recently at Top Fuel. That code allows more accurate prediction of thermal margins, at both normal and transient conditions. MEFISTO is used to support a new Critical Power correlation concept that was introduced for Optima3. The new concept gives improved robustness in thermal margin prediction, in particular for transients, which is translated into improved fuel utilization. Similarly, the McSLAP code assists in core optimization and assessing proper thermal margins in cycle-specific core analyses.

1. Introduction

The SVEA-96 Optima3 BWR fuel design (or simply Optima3) is the latest member of the SVEA fuel design series.

Based on the well-proven SVEA-96 Optima2 design (Optima2), with the SVEA water-cross and optimized part-length rods that enable superior neutron moderation and uranium utilization, the most important new features of Optima3 are the following:

- Better protection against harmful debris
- Less channel growth and consequent bow

Optima3 has been thoroughly evaluated to fulfill the requirements of all Westinghouse's BWR customers. The evolutionary features of the design build on the basic, proven SVEA 10×10 fuel design introduced in 1986. This basic design has been delivered in reload quantities to 23 reactors all over the world with a total of more than 24 000 delivered fuel assemblies.

2. BWR Fuel Design Development

2.1 Evolutionary development

Figure 1 shows the evolution of the Westinghouse BWR fuel designs. The first generation of 10×10 designs includes SVEA-100, SVEA-96, and SVEA 96+. The second generation of 10×10 designs includes SVEA-96 Optima, Optima2, and Optima3, which incorporate design refinements such as part-length rods and mixing vane grids. All of these designs share a basic mechanical structure with incremental changes for improved performance.

Optima2 builds on the successful operating experience of its predecessors and includes an optimized fuel rod lattice, additional part-length rods, **TripleWave™** debris filter, and spacer grids with mixing vanes. Optima3 is a further evolutionary design based on the same principles as Optima2. With this design, fuel reliability is further improved by a new spacer design and the **TripleWave+™** debris filter. The **Low Tin ZIRLO** channel material, developed to mitigate the effects of channel bow, is a standard feature of Optima3.

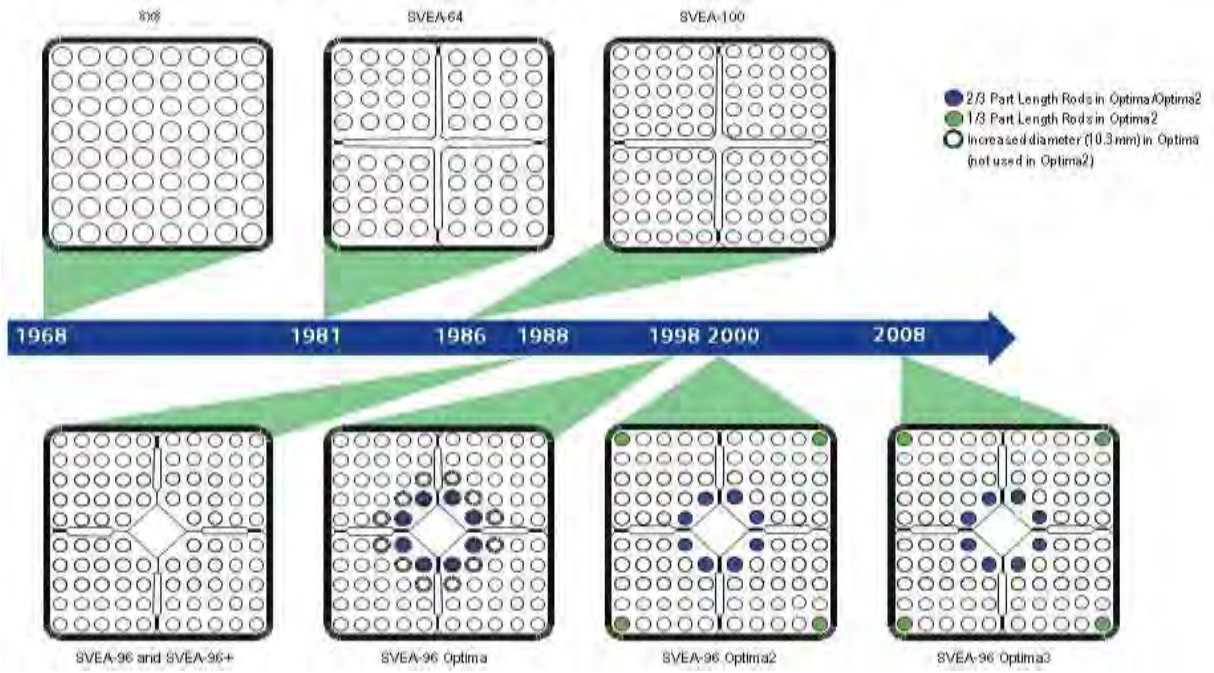

Figure 1. BWR Fuel design evolution leading to Optima3.

2.2 Optima3 design features

Optima3, described in full detail in [1], has been developed with the main objective of mitigating the two most important fuel reliability issues in the BWR industry, debris fretting and channel bow. While achieving these objectives, the mechanical design has been simplified. The key features of Optima3 for enhanced reliability and a strong fuel cycle economy are summarized below, and Figure 2 shows a schematic illustration of the design and its different components.

- **TripleWave+ debris filter**: The already highly effective **TripleWave** debris filter has been refined to further improve the capturing efficiency of small and medium size debris, which poses the primary risk for fuel rod fretting.

- **New spacer grids**: Optima3 fuel features a new, sleeve-type spacer design, which has a minimum number of edges and protrusions.

- **Low Tin ZIRLO channel material**: Superior resistance to channel bow is achieved by use of **Low Tin ZIRLO** channel material that is proven to be less susceptible to both irradiation growth and hydrogen pickup compared to standard Zircaloy-2 and Zircaloy-4 channels. The much reduced channel bow of Optima3 leads to enrichment savings as a result of reduced reactivity losses, improved thermal margins and reduced measurements uncertainties.

- **ADOPT pellet**: The development of the ADOPT pellet has combined higher density, reduced transient fission gas release, better pellet-cladding interaction (PCI) performance, and improved secondary degradation behavior.

- **Water cross and part-length fuel rods**: The basic Optima3 design with water cross and optimized part-length fuel rods retains superior uranium utilization due to the improved moderation, lower radial power peaking and thinner channel.

- **Simplified mechanical design:** The sub-bundle top tie plate is replaced with a top spacer and the bottom tie plate is simplified. All fuel rods, except the tie rods, which also have the spacer capture function, rest freely on the bottom tie plate.

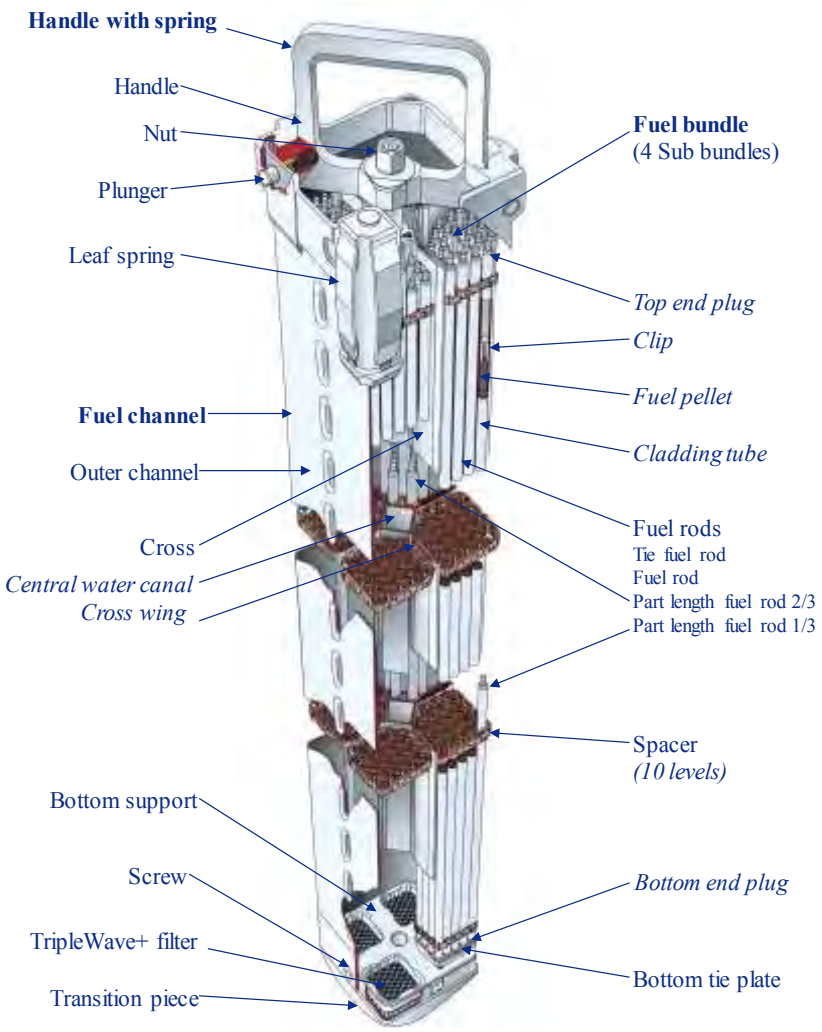

Figure 2. Optima3 fuel assembly. Four sub-bundles are separated by a cruciform water cross in the channel

3. Validation of Optima3 Features

3.1 Debris Failure Mitigation

Studying the operating data of Westinghouse 10x10 liner fuel with the current fuel cladding material, we could conclude that all determined failures originate from debris fretting. In most cases the debris enters the fuel assembly with the coolant and can potentially get caught by a spacer grid on its way through the fuel assembly. Once captured by a spacer, the debris can be brought to very rapid oscillation by the coolant flow. If such debris is in contact with a fuel rod, the high frequency of the oscillations can rupture the cladding within a few days. Long and slender debris, such as small pieces of metal wire, are particularly harmful.

The Optima3 design includes the **TripleWave+** debris filter, which has been designed to effectively capture slender debris exceeding 10 mm in length. Operating experience clearly indicates a significant decrease of the debris-induced failures in fuel assemblies equipped with this filter. However, due to the required margins to clogging and pressure drop limitations the debris filter could not be designed to capture even smaller size debris.

To address smaller size slender debris, Westinghouse realized that the design of the spacer had to be changed. The new spacer design of Optima3 resembles the shape of a honeycomb, consisting of almost identical thin straps that are formed into individual cells

shown in Figure 3. The cells are placed side-by-side inside a frame and welded together. The manufacturing process has been completely automated, which has enabled excellent precision. The flexible walls of each spacer cell replace the dimple-spring concept used in traditional spacers, and thereby the contact points and openings with potential to catch debris have been eliminated. Moreover, each cell is curve-shaped to guide debris away from the fuel rod. The debris will immediately pass the spacer, or may rest at a safe location underneath the spacer where the curved cell provides efficient protection of the fuel rod. From that location, the debris is too short to reach a neighboring fuel rod (large debris will not pass the **TripleWave+** filter).

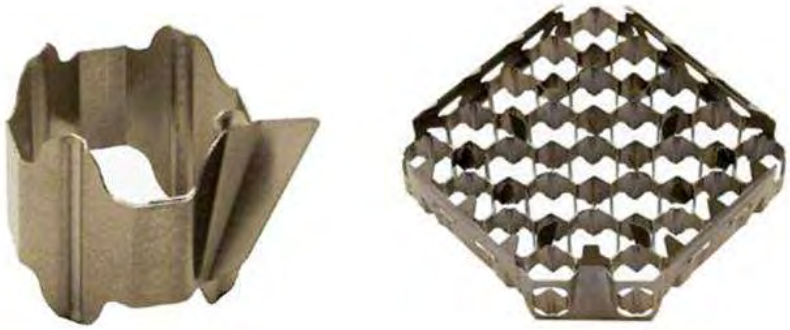

Figure 3. Optima3 Spacer Cell and Assembly

Figure 4 shows the results of debris testing that demonstrates the benefit in debris mitigation using Optima3. The area to the right of the purple Optima2 line and under the blue **TripleWave** curve indicates that there is a risk that debris (of a particular size index) can pass through the **TripleWave** filter and potentially get stuck in the spacer grid. In contrast, the test results for the combination of the **TripleWave+** debris filter and the Optima3 spacer show that if debris is small enough to pass through the filter, it will also pass through the spacer grid.

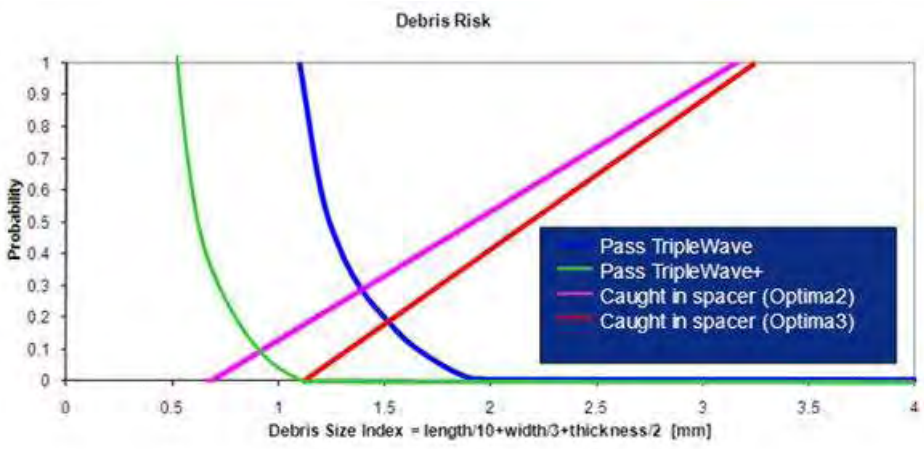

Figure 4. Debris Testing Results for Optima2 and Optima3.

What makes the Optima3 fuel design unique is the combination of the two features: the **TripleWave+** debris filter and the new spacer design. By adding the functionality of the two, the ultimate goal of zero fuel failures is further approached.

3.2 Minimized channel distortion

The fuel family name “SVEA” was introduced in 1980 in conjunction with the implementation of a water cross structure inside the fuel channel. The main purpose of the cruciform structure and its central water canal was to improve the moderation of the fuel assembly, but

it was also found to provide excellent mechanical support. The SVEA channel has also proven to have less bulge (since the free length of the wall is only half as long) and better flexibility (due to a thinner channel wall). The flexibility is important, since it means that the fuel channel will easier give way in case of mechanical contact with a control rod during maneuvering.

Today, many utilities are struggling with channel distortion issues as a result of higher average burnup and 24-month cycle operation with control rods inserted adjacent to fresh fuel. The most obvious consequence of excessive bow is mechanical interference with the control rods. Since a distortion changes the geometry of the core, there is also an impact on the power distribution, which leads to a less effective fuel utilization, as well as reduced dryout and other thermal margins. The extra management of the channels due to distortion, and sometimes also premature replacement, cause the utilities significant costs.

Following the transition, especially in the U.S., of many reactors from annual to 24-month cycle operation, some BWR units started to report observation of enhanced channel bow. This type of bow could not be explained by the regular (fluence gradient-driven) differential growth only. Instead, it was concluded to be caused by the presence of a control rod early in life of the fuel assembly, which is common for cores operating 24-month cycles. The control rod causes shadow corrosion to the two sides of the channel it is facing, which leads to hydrogen uptake of the channel. This early-life hydrogen pickup causes an enhanced irradiation growth later in life, that is, an increased differential growth and consequently an enhanced bow. The mechanisms are only partially understood, but the phenomenon was clearly demonstrated under the Nuclear Fuel Industry Research Program managed by the Electric Power Research Institute.

Westinghouse's solution to address channel bow, in particular the enhancement caused by early life shadow corrosion, was to introduce a new **Low-Tin ZIRLO** material, known from pressurized water reactor (PWR) experience [2] to have very low rate of irradiation-induced growth and hydrogen pick-up. As shown in the next section in Figures 6 and 7, this effect has been shown to be particularly important for higher burnup levels with the channel growth and channel bow shown not to exceed 4 mm and 3 mm, respectively. It can therefore be concluded that the **Low-Tin ZIRLO** channel of Optima3 has the properties needed to keep the channel distortion at a minimum.

3.3 Operating experience confirms the anticipated behavior

By 2015, more than 800 Optima3 fuel assemblies will have been delivered to nine BWR units, with the leading fuel assemblies at an average burnup of between 50 and 55 MWd/kgU. Several inspections and measurements have been performed, verifying the expected behavior of Optima3's new mechanical features such as free standing rods and the new spacer. Figure 5 confirms the anticipated behavior and function of the leading assemblies after 4 annual cycles.

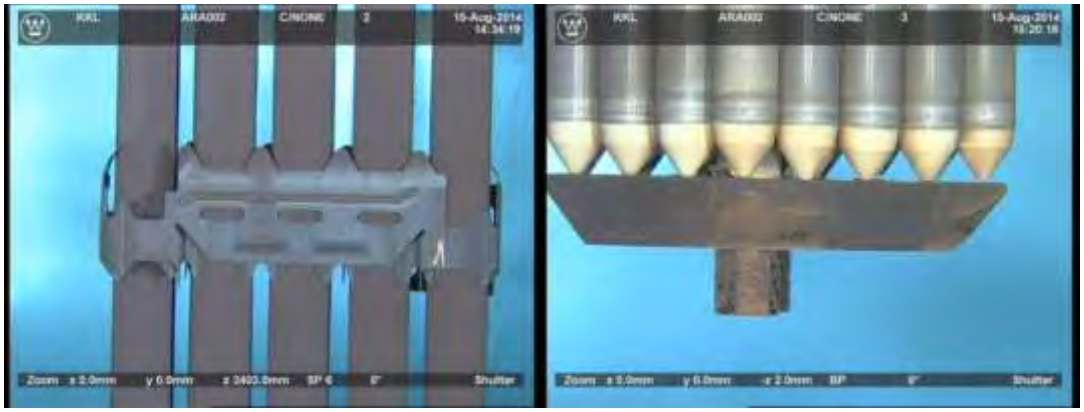

Figure 5. SVEA-96 Optima3 inspections after 4 cycles

The first full reload with **Low-Tin ZIRLO** channels was delivered in 2011, and the experience base now encompasses over 700 channels. The **Low-Tin ZIRLO** channel material has been verified to very high burnup (more than 70 MWd/kgU), as well as full lives in 24-month cycle operation in locations with extensive control rod presence early in life. Figure 6 below shows that, despite the challenging operating conditions, the growth of the **Low-Tin ZIRLO** channels has been limited to 4 mm which indicates low hydrogen pickup.

Figure 7 shows channel bow up to 3 mm, even after the most severe early control conditions. These channels experienced high-inch days in their first 24-month cycle and high fluence gradients for the second and third cycles. After the second cycle, fresher fuel was inserted into one of the channels so it would reach higher burnup during the third cycle. These data were in a BWR-6 plant and considered to bound operations in other plants. The 12-month cycle data is showing virtually no bow to ~1 mm.

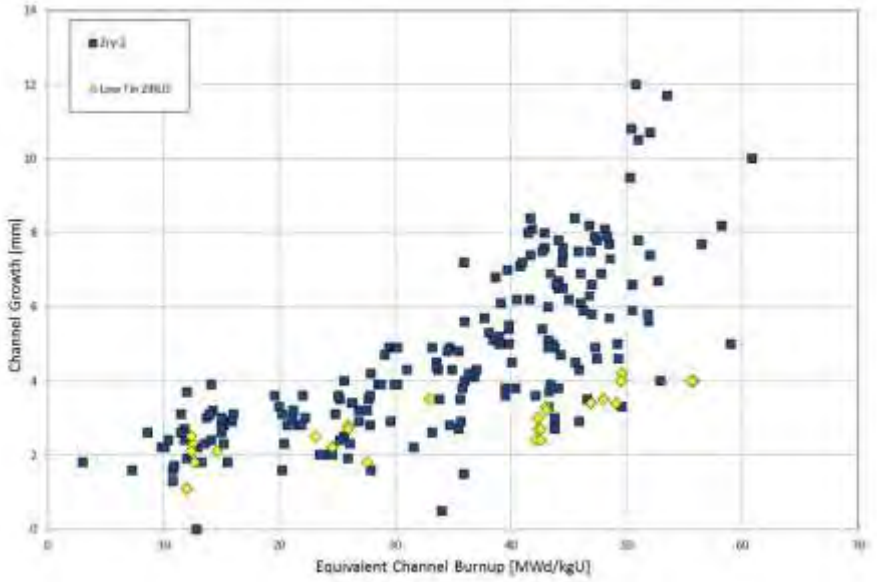

Figure 6. SVEA 10×10 channel bow growth data

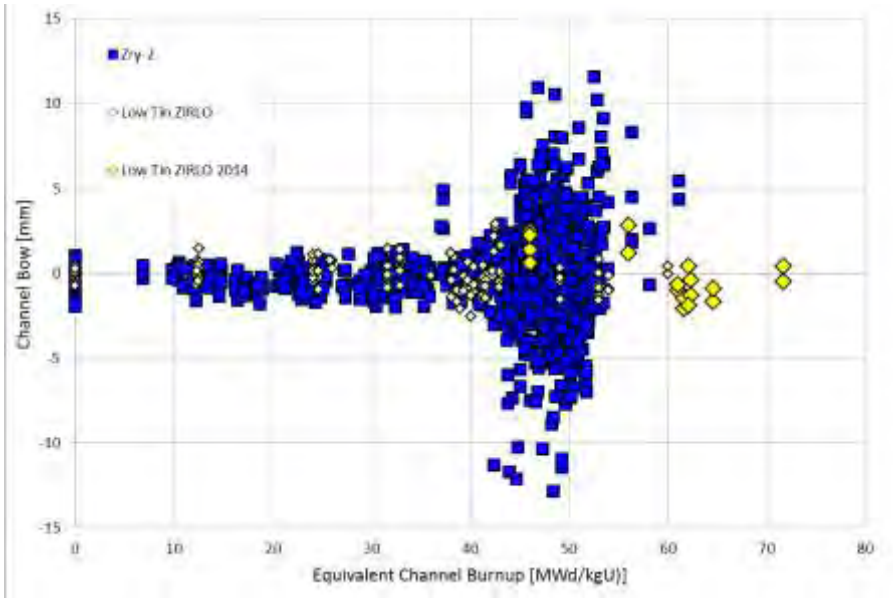

Figure 7. SVEA 10×10 channel bow measurements in symmetric lattice plants

4. BWR Fuel Methods Development

The BWR fuel design evolution has gone hand-in-hand with methods evolution, driven by the need for higher fidelity and more challenging fuel operation due to power uprates, burnup increase and long cycles. All code areas are affected and have required further development. Some areas have been of particular interest to support the latest fuel product Optima3, and an overview of methods and methodology achievements is given below.

4.1 Critical Power Prediction

The fuel assembly maximum heat transfer capability, or its “Critical Power”, has always been a very important driver for Westinghouse BWR fuel development. The performance evolution of the SVEA fuel designs relative to the original 8x8 fuel design is depicted in Figure 8. Steady, gradual improvements have been obtained, with the most advanced product Optima3 being on top. This has been achieved by careful optimization of designs features, in particular the spacer grids and mixing features to improve drop deposition that enhance the fuel rod cooling. The FRIGG loop is the basis for this development and has been used extensively for product development and verification.

Critical Power Ratio correlations are based on comprehensive FRIGG loop measurements on full-scale simulated fuel lattices. The correlation concept for SVEA-96 Optima3 is novel, and based on a robust formulation that takes into account the variation in power profile, rod powers and operation conditions included in the test data-base. Extrapolation to other conditions is done smoothly and robust predictions are achieved also for transients. The correlation is implemented in the BISON and POLCA-T codes for transient prediction.

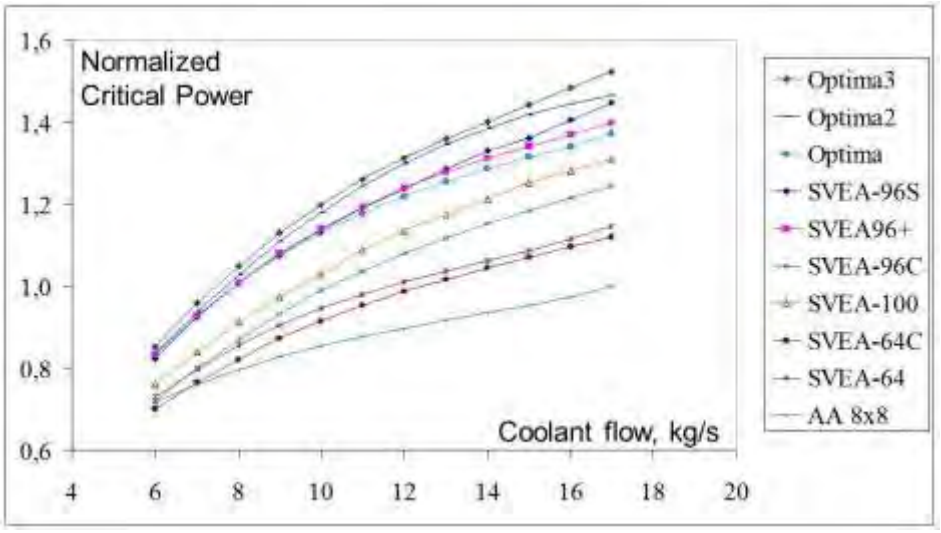

Figure 8. SVEA Fuel Critical Power performance evolution as measured in the FRIGG thermal-hydraulic test loop

A mechanistic dryout prediction code has been developed to support the correlation development. This code, MEFISTO (Mechanistic Film flow simulation tool), was presented at Top Fuel 2013 [3] and has since then been further developed and validated for transient conditions. The code can reproduce the Optima3 FRIGG data with similar statistics as the correlation, and provides a tool to support the prediction for conditions outside the tested range. The code also runs with transient conditions. Examples from the several Optima3 fast transient tests performed in the test loop are given in Figure 9.

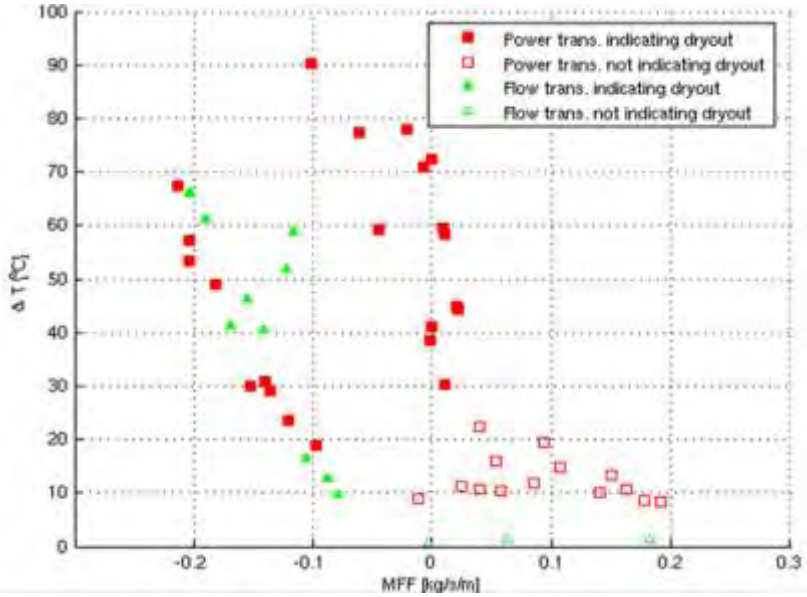

Figure 9. FRIGG rod temperature increase vs Minimum predicted Film Flow (MFF)

The transient dryout tests are repeated with gradually increased initial power, until dryout is indicated as rapid cladding temperature increase. Thus the transients can be divided into two groups, with and without indicated dryout. The MEFISTO code predicts the film flow that cools the individual fuel rods, and the minimum predicted flow, MFF, equals zero at dryout. The predicted dryout fits the measured onset of dryout well, thus demonstrating that the MEFISTO film model is also relevant for transient conditions, c.f. Figure 9.

4.2 Channel bow impact on thermal margin

Traditionally, the impact of channel bow on dryout margins (or CPR, Critical Power Ratio) has been evaluated using analytical methods, treating the channel bow as a core average property and applying a conservative penalty factor to each fuel assembly. However, such methods are inappropriate when the susceptibility to channel bow varies significantly across the core, e.g. due to varying burnup and operating history, and the results tend to be overly conservative. Even if channel bow is small for Optima3 fuel assemblies, the CPR of Optima3 assemblies may be affected by a potentially larger bow in neighboring assemblies.

McSLAP (Monte Carlo Safety Limit Analysis Program) was developed by Westinghouse to statistically determine lower limits for the core minimum critical power ratio (MCPR) corresponding to given dryout criteria. A unique advantage of this Monte Carlo method is its ability to accurately account for the effects of channel bow, as illustrated in Figure 10 for the Safety Limit MCPR (SLMCPR). The statistical influence of channel bow is determined by random sampling of the magnitude of channel bow in two directions for each individual bundle in the core, according to statistical distribution functions determined by measurements. The lateral power tilt, caused by the perturbed water gaps on all four sides of each fuel bundle, is then accurately accounted for in the CPR, determined for each fuel rod by the use of detailed 2-D neutron transport calculations with the PHOENIX4 code.

The McSLAP code can properly verify the traditional criterion of 0.1% fraction of fuel rods expected in dryout which defines the SLMCPR, provide and evaluate a more appropriate dryout criterion for normal operation, and account for the detailed effects of channel bow on dryout risk while avoiding the excess conservatism from assumptions that are necessary in an analytical approach [4]. In the following two graphics in Figure 10, results from McSLAP evaluations of SLMCPR are shown with and without the impact from channel bow accounted for. For comparison, results from the previously used analytical code (MASL) are also provided.

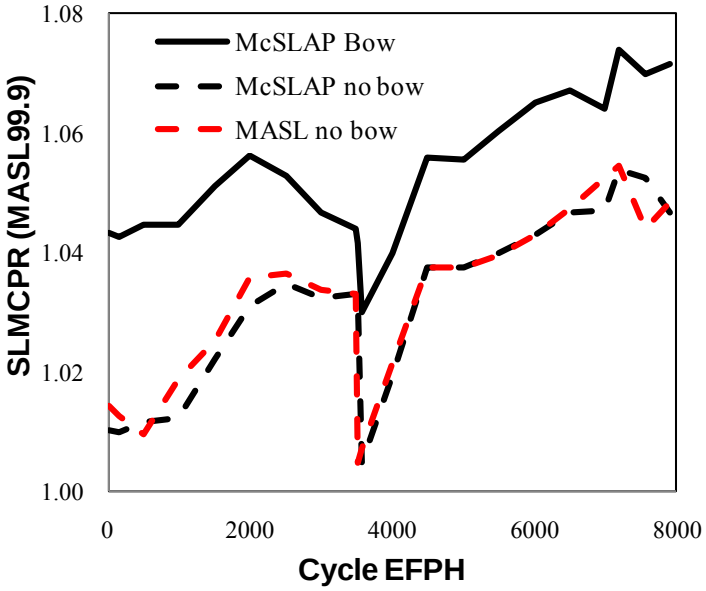

Figure 10. Evolution of the SLMCPR throughout a cycle with and without channel bow.

As compared to analytical methods used for safety analysis, the Monte Carlo approach with McSLAP provides a much more rigorous evaluation of channel bow, whose impact can be directly included in both the SLMCPR and the steady-state OLMCPR and with no need for further penalties [4].

5. Conclusion

A long-term ambition of the Westinghouse Electric Company has been to create a fuel product that addresses the reliability concerns raised by the BWR utilities. With Optima3, a fuel design that has the potential to operate flawlessly both with regard to fuel failures and channel distortion has become a reality. Methods to support current more stringent requirements on core design and safety analyses are available as well, enabling our customers to get the maximum value out of Optima3.

6. References

1. U.C. Bergmann et al., Westinghouse SVEA Fuel Evolution and Management, Top Fuel 2012, Manchester, UK

2. J.R. Halligan et. al., PWR Fuel Performance and Key Developments in Material and Mechanical Design, Top Fuel 2015, Zurich, Sept 13-17, 2015

3. J-M Le Corre, Advanced Dryout Prediction Methods at Westinghouse, Top Fuel 2013, Charlotte, North Carolina, Sept 15-19, 2013, pp. 1008-1016

4. U.C. Bergmann et al., CPR Methodology for Statistical Treatment of Channel Bow, Nuclear Technology Vol. 183, Sept 2013, pp. 298-307.

FLAKING OF SHADOW OXIDE ON BWR CLADDING ASSOCIATED WITH PRE-EXISTING SURFACE SCRATCHES

DAVID SCHRIRE
Vattenfall Nuclear Fuel
SE 162 87 Stockholm, Sweden
Tel: +46-76 809 6596, Email: david.schrire@vattenfall.com

GUIDO LEDERGERBER
Kernkraftwerk Leibstadt,
CH-5325 Leibstadt, Switzerland 5325
Tel: +41 56 267 7395, Email: guido.ledergerber@kkl.ch

KRISTINA KARLSSON
Forsmarks Kraftgrupp AB
SE 742 03 Östhammar, Sweden
Tel: +46-173 81293, Email: kka@forsmark.vattenfall.se

KARIN CARLING
Ringhals AB
SE-432 85 Varöbacka, Sweden
Tel: +46-340 667 504, Email: karin.carling@vattenfall.com

ABSTRACT

In connection with the routine inspection and repair of a leaking fuel assembly, long and narrow white flakes were noticed caught in a spacer. Further inspection of the fuel, and examination of retrieved flakes, revealed that these were zirconium oxide originating from the “shadow corrosion” in the vicinity of the nickel alloy spacer. Detailed inspection showed that the strip-like flakes corresponded exactly to the spacing between pre-existing axial scratches in the cladding surface caused by the spacer contact during the fuel rod loading in the bundle manufacturing process. The scratches are clearly visible on the oxidized cladding surface after operation, both in areas where shadow corrosion occurs as well as on mid-span surfaces without shadow corrosion, as long as the fuel rod surface is not covered in crud.

Shadow corrosion occurs on Zr-base alloys in contact with or in close proximity to other metallic alloys in the reactor core radiation field in BWRs. The oxide growth rate in the shadow is typically accelerated compared to the oxide that forms on the Zr-base alloys in the same environment (temperature, water chemistry and radiation field) but without proximity to other metals. Shadow corrosion on the fuel cladding within the spacer region is normally observed in all BWR fuel, especially where the entire spacer is made of a non-zirconium alloy (typically Ni-base). However, the strip-like flakes had not been observed before, and a review was initiated in order to establish the root cause. In the course of this review, examples of a similar pattern of flaking of shadow oxide, where the flaking correlated with pre-existing surface scratches in the cladding surface, were found for various BWR fuel designs manufactured by different vendors. Examples were found from fuel operated in different BWRs, under different operating conditions and widely differing water chemistry conditions.

It is believed that the predominantly axial scratches introduced in the cladding surface during the loading of the fuel rods into the bundles possibly result in the formation of an initiation site for the flaking. Where the lateral spacing between the scratches is optimal, these flaws are thought to lead to the formation and propagation of cracks in the oxide layer, presumably during the cool-down at the end of an operating cycle. A tendency to delamination (formation of cracks in the circumferential direction) is fairly common in oxide layers formed on fuel rod cladding during normal operation; however, it is thought that the existence of suitably spaced axial cracks assists the oxide to flake off in strips.

Since there are potential negative consequences of such flaking, there is a strong incentive for the fuel vendors to modify the fuel rod loading processes so as to prevent the formation of scratches with a spacing that promotes the strip-like flaking. We are confident that by avoiding such scratches, the occurrence of such flaking will be reduced or its onset delayed.

1. Introduction

1.1. Background: observed flaking of shadow oxide

In connection with the routine inspection and repair of a leaking fuel assembly, long and narrow white flakes were noticed caught in a spacer. Further inspection of the fuel, and examination of retrieved flakes, revealed that these were flakes of oxide originating from the "shadow corrosion" in the vicinity of the nickel alloy spacer.

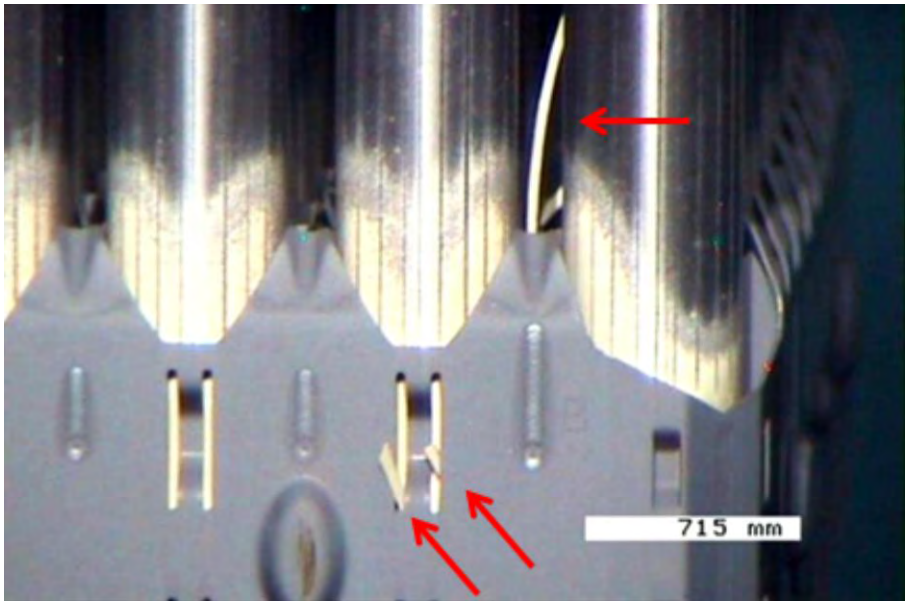

Figure 1. Flakes of oxide caught in spacer.

The flakes were robust enough to be retrieved, see Figure 2 and it was possible to examine individual flakes in the SEM. Energy dispersive X-ray spectrometry (EDS) was performed on a cross-section of a flake. The results of an area scan (see Figure 3) are given in Table 1. The ratio of the Zr to O corresponds exactly to ZrO_2 (the Al is believed to be due to background from the collimator of the EDS detector). Line-scans across the thickness of the flake showed no significant variation in composition.

Figure 2 Retrieved flakes

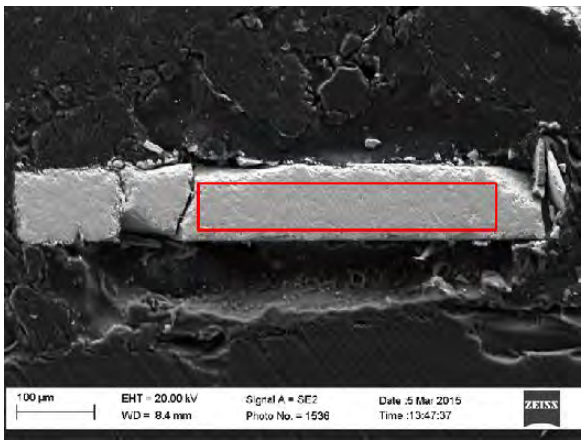

Figure 3. Cross-section of flake in SEM indicating area of EDS analysis.

ELEMENT	Zr	O	Sn	Al
Composition (weight %)	72.62	25.53	1.12	0.73

Table 1. Composition of cross-section measured by EDS

Detailed inspection measurements showed that the strip-like flakes corresponded exactly to the spacing between pre-existing axial scratches in the cladding surface caused by the spacer contact during the fuel rod loading in the bundle manufacturing process. The scratches are clearly visible on the cladding (oxide) surface after operation, both in the shadow corrosion region as well as on surfaces without shadow corrosion, as long as the fuel rod surface is not covered with crud.

The flakes had a thickness reaching up to almost 100 µm (see Figure 3), corresponding to a large fraction of the total shadow oxide thickness in the flaked regions.

1.2. Shadow corrosion under spacers

Increased corrosion occurs on Zr-base alloys in contact with or in close proximity to other metallic alloys in the reactor core radiation field in BWRs or other reactors with similarly oxidising water conditions. The oxide growth rate in the so-called shadow is typically accelerated compared to the oxide that forms on the Zr-base alloys in the same environment (temperature, water chemistry and radiation field) but without proximity to other metals. Shadow corrosion on the fuel cladding within the spacer region is normally observed in all BWR fuel, especially where the entire spacer is made of a Ni-base alloy.

The shadow corrosion rate is roughly inversely proportional to the distance between the corroding Zr-alloy and the “shadow-casting” other metal, resulting in a peak oxide thickness at the points of contact between the Zr-alloy and the other metal. Also, the shadow corrosion rate has been observed to decrease with time [3], although there is a paucity of shadow corrosion data from BWRs for times shorter than about 1 year of operation.

In the absence of flaking, the shadow oxide thickness on the cladding in the region of an all-Ni-base alloy spacer typically has the appearance of a contour relief map, where the oxide thickness reflects the proximity of the cladding surface to the spacer features, see Figure 4.

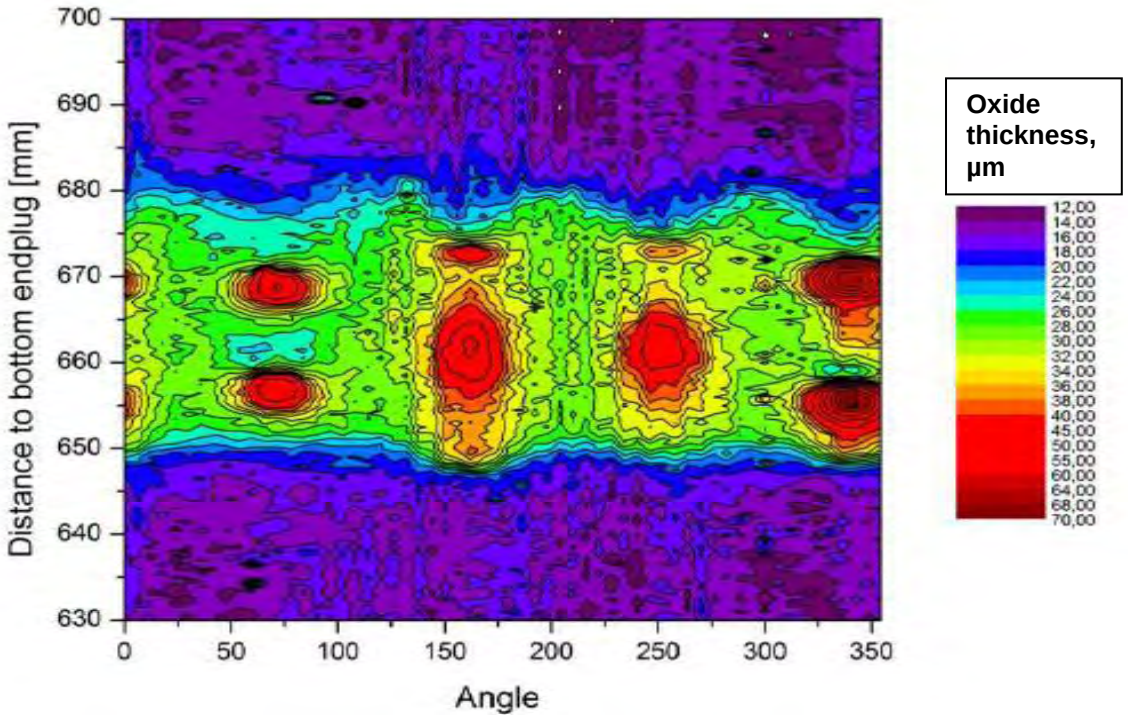

Figure 4. Contour map of shadow oxide thickness in a typical spacer position showing peaks at the spacer-cladding contact positions.

2. Observations of flaking shadow oxide associated with scratches

The strip-like flakes still present in the spacer (Figure 1) had not been observed before, and a review of available post-irradiation examination (PIE) data was initiated in order to establish the root cause of the flaking shadow oxide. In the course of this review, examples of a similar pattern of flaking of shadow oxide, where the flaking correlated with pre-existing surface scratches in the cladding surface, were found for various BWR fuel designs manufactured by different vendors. Examples were found from fuel operated in different BWRs, under different operating conditions and widely differing water chemistry conditions.

Examples of the onset of significant flaking, after 2 or 3 annual cycles of operation, are shown in Figures 5a and 5b below. Although the flaking occurs adjacent to the scratch marks, in this case the possibility that the flaking occurred during the removal of the fuel rod(s) from the spacer cannot be excluded.

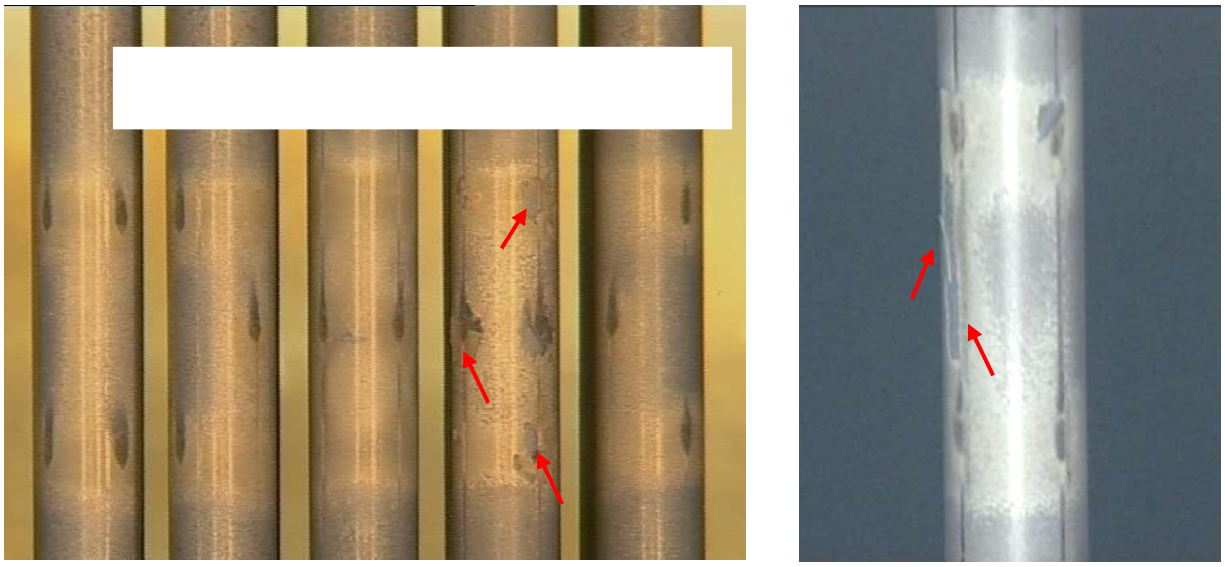

Figure 5 a) and b). Onset of flaking shadow corrosion near the spacer contact points.

Figure 6 below shows an example of flaking oxide in the region of a fuel rod where shadow corrosion is not caused by a spacer but instead by proximity (but not contact) with a steel component. In this case the possibility that the flaking occurred due to movement of the fuel rod in a spacer can be excluded.

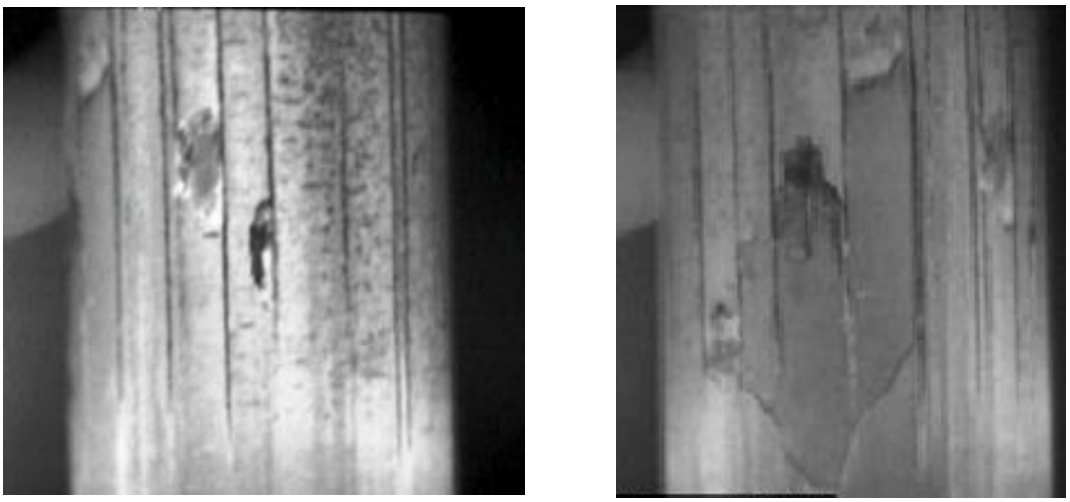

Figure 6. Flaking shadow oxide on a fuel rod in proximity to a steel component.

In some cases, flaking shadow oxide in connection with pre-existing scratches on the cladding surface has been observed even with relatively thin shadow oxide layers. In Figure 7 below, an example is shown of such flaking locally in the limited shadow corrosion caused by a Ni-based spring in an otherwise entirely Zr-alloy spacer. The oxide thickness measured by EC liftoff on 4 orthogonal generatrices along the rod is shown below the photograph – the 45º curve (magenta) represents the trace that passes directly along the side shown in the photograph. It can be seen that the oxide flake despite being no more than about 30 µm thick at most.

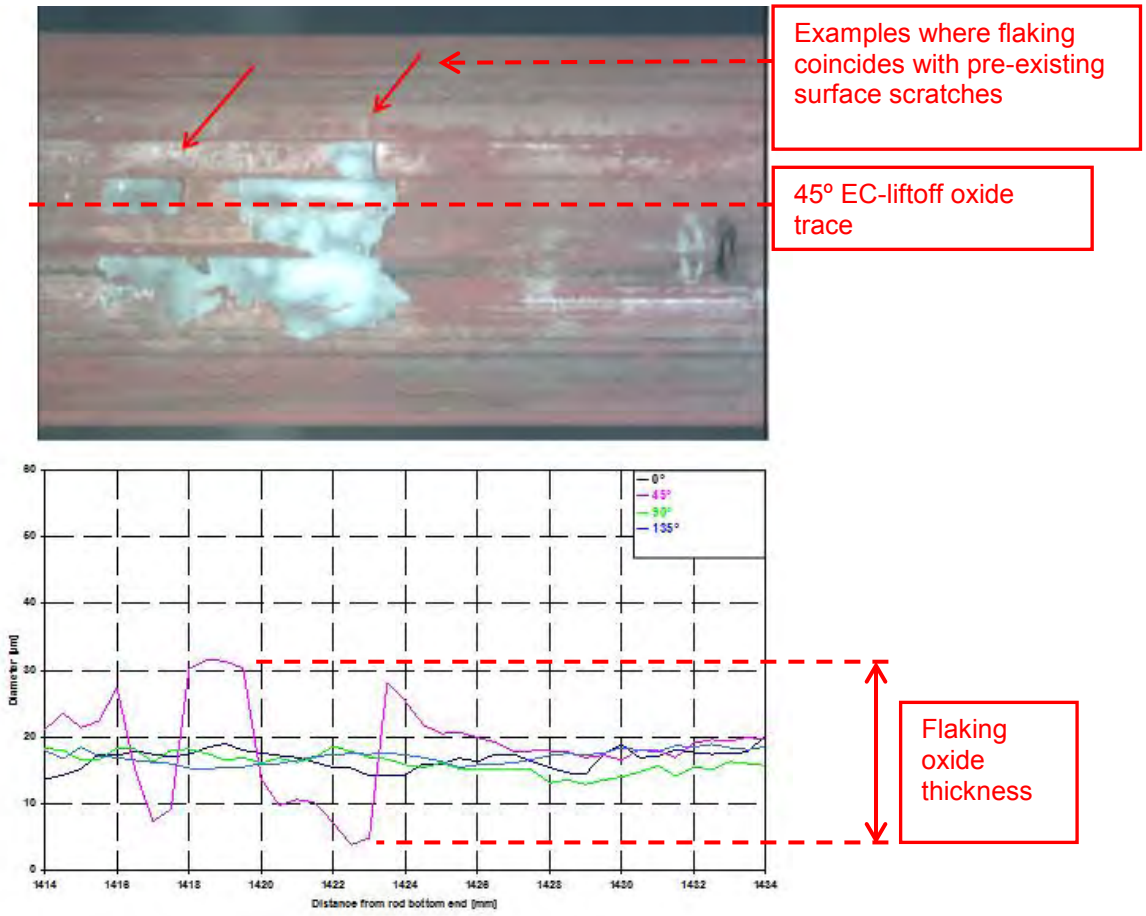

Figure 7. Flaking shadow oxide in the vicinity of a spacer spring, and oxide thickness trace.

3. Discussion

3.1. Effect of scratches on the original surface on flaking

The initial scratches in the cladding metal surface are typically shallow compared to the shadow oxide thickness, and fuel vendors ensure that the scratches due to spacer contact during fuel rod loading are within specified limits. Exactly how the presence of relatively shallow scratches can affect the flaking of an oxide film that is far thicker, is not intuitively obvious.

A possible explanation is that the scratch represents a discontinuity in the cladding surface, somewhat like a V-notch, that results in two separate oxide films forming. As the two oxide films grow they tend to collide and push each other apart, since the oxide volume is larger than the equivalent volume of the metal consumed by corrosion. This in turn induces stresses in the metal and the oxide, that could result in a discontinuity or crack in the oxide roughly along a direction extending from the boundary of the two meeting oxide layers. An example of such a discontinuity is shown in Figure 8 below – note that this is not an example of shadow corrosion at a cladding scratch but is from in-reactor corrosion of a completely

different type of Zr-base component. However, it illustrates a possible mechanism whereby a pre-existing notch-like surface discontinuity (scratch) could lead to a crack or flaw that propagates much deeper into the oxide.

Another possible explanation is that a discontinuity arises when the oxide film grows on a convex corner or edge, where the outer part of the oxide layer is put into a tensile stress due to the larger volume of oxide than consumed metal near the metal-oxide interface at the bend. An example of such a discontinuity is shown in Figure 9 below – note that this is again not an example of shadow corrosion at a cladding scratch but is from in-reactor corrosion of a completely different type of Zr-base component. This illustrates a possible mechanism whereby a pre-existing edge-like surface discontinuity (at the edges of a scratch) could lead to a crack or flaw in the oxide. However, the observation that shadow corrosion itself falls away to zero in a 90º corner, interpreted to be due to the vanishing (due to geometrical considerations) of the electrostatic field that is assumed necessary for the galvanic corrosion mechanism believed responsible for shadow corrosion [3], speaks against this idea.

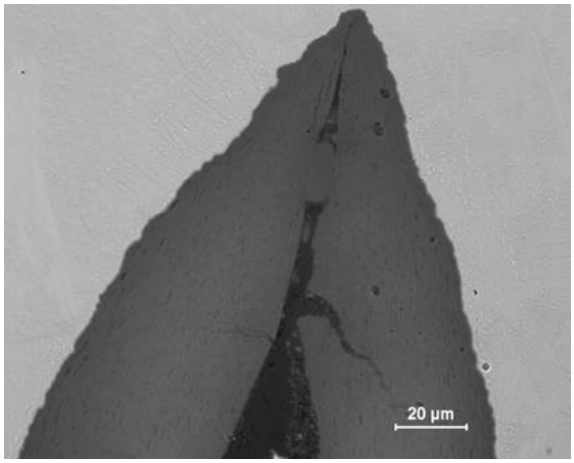

Figure 8. Illustration of oxide film at a V-notch.

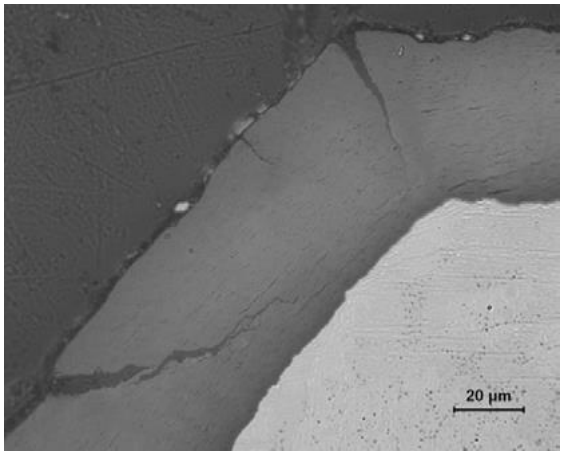

Figure 9. Illustration of oxide growing on a sharp corner

Some theoretical studies of the stress state and decohesion (flaking) of an oxide layer suggest that a depression in the underlying material can promote decohesion, i.e. delamination of the oxide layer from the metal under some conditions [4]. However, the stress state responsible for this would likely be reduced if there are cracks perpendicular to the interface such as discussed in the above examples.

3.2. When does the flaking occur?

The fact that oxide flakes were observed caught in a spacer when a fuel bundle was inspected after an outage suggests that they flaked off during or after the reactor shut down while the fuel surface cooled down. Flakes released during power operation would most likely have dislodged and broken due to the high coolant flow velocity.

In some other materials, where the oxide film has a lower thermal expansion than the metal, delamination is observed during cooling, and is believed to be due to buckling caused by the compressive stresses arising in the oxide film [5]. However, this is not the case for ZrO_2 which has a higher thermal expansion than Zircaloy metal (in the circumferential direction) in the temperature interval from operating temperature (roughly 300 ºC) to cold shutdown conditions [6]. Since the ZrO_2 film should contract more than the cladding metal (if both are free-standing, i.e. not under an elastic stress during operation), cracks through the oxide film might occur due to tensile stresses during cooling. Flaking could then occur if there already exists some decohesion between the oxide and the metal, or between a thin cohesive inner layer of oxide and a thicker outer layer prior to the cool-down.

3.3. At what thickness does flaking occur?

There does not appear to be a very strong correlation between shadow oxide thickness and the onset of flaking. Figure 4 shows an example without any flaking, where the peak oxide thickness reached about 70 µm. On the other hand, Figure 7 shows an example where flaking was observed despite a lower peak oxide thickness. There are numerous examples of non-flaking spacer shadow corrosion where the peak local oxide thickness at or very near the contact positions reaches over 100 µm. Figure 10 below shows measurements on 4 orthogonal traces in the region of a spacer position of a 3-cycle fuel rod (assembly burnup of 25 MWd/kgU). There was no flaking of the oxide in any spacer location of this rod, and the oxide profiles represent the variations that would be expected for these angles due to the spacer cell geometry and distance to the Ni-base metal. Figure 11 below shows an identical type of measurement at the same spacer position on a rod with the same type of cladding and spacer materials and design, operated in the same reactor for only 1 cycle (assembly burnup of 10 MWd/kgU). In this case there was clear flaking of the shadow oxide at several spacer locations, despite a lower unflaked shadow oxide thickness than the 3-cycle rod.

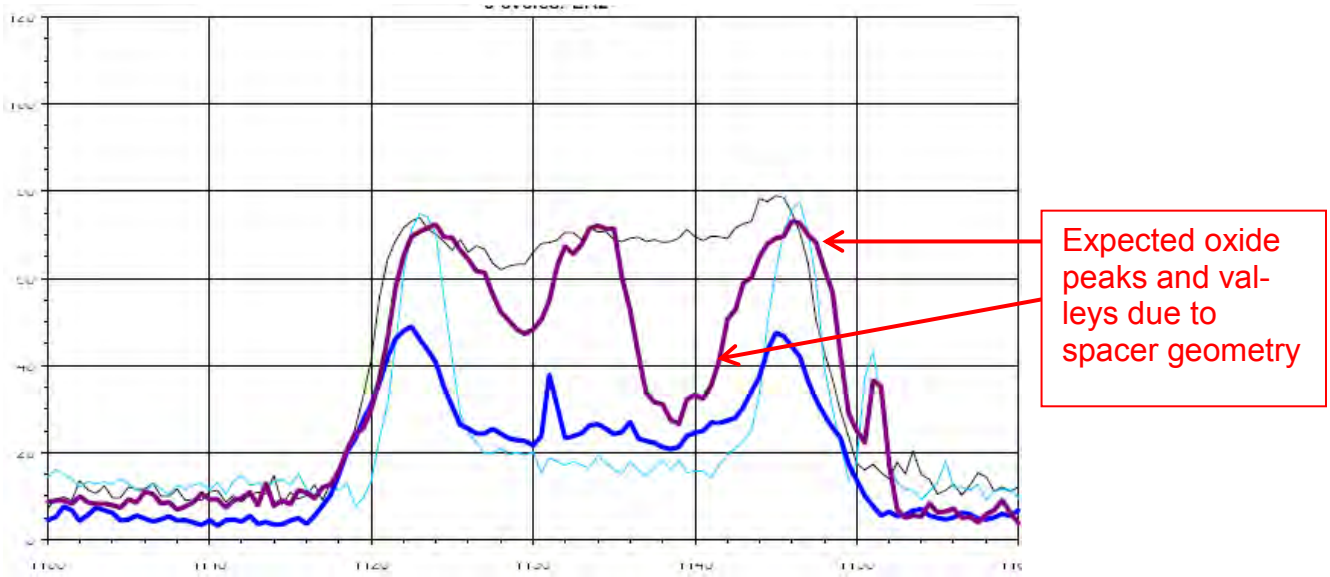

Figure 10. 3-cycle fuel rod, oxide thickness in µm, traces at 4 angles.

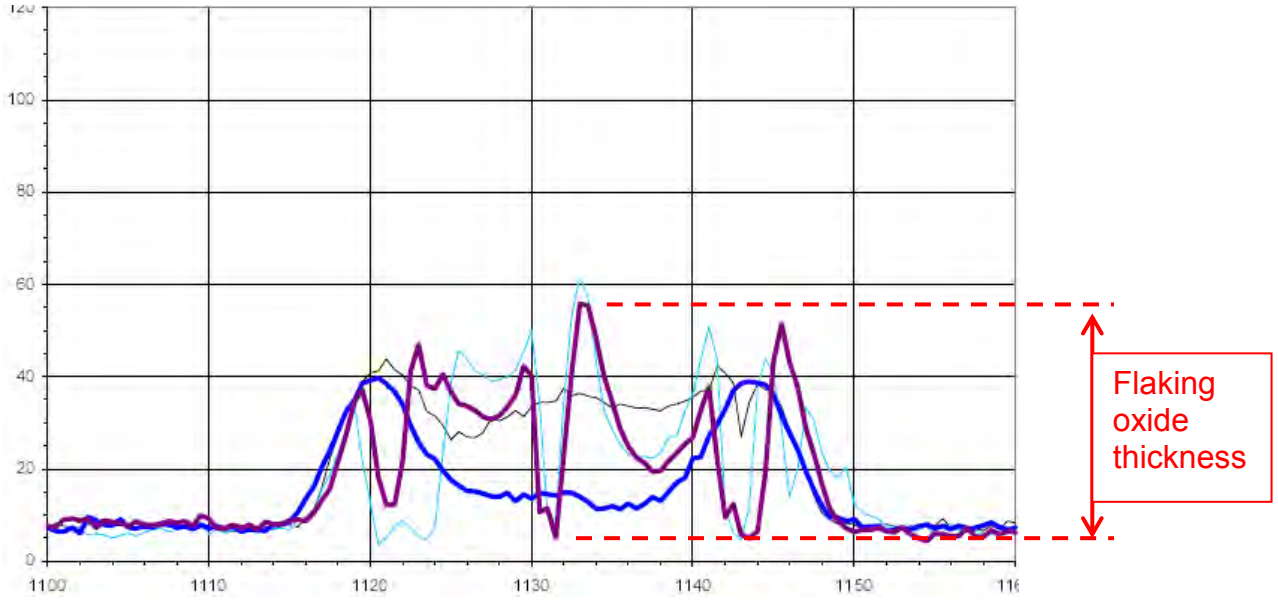

Figure 11. 1-cycle fuel rod, oxide thickness in µm, traces at 4 angles.

In the course of the review of PIE data, similar patterns of flaking of oxide, where the flaking correlated with pre-existing surface scratches in the cladding surface, were not observed for the non-shadow oxide. Generally, the non-shadow oxide was thinner than the shadow oxide thickness for which this particular type of flaking was seen, but for a few cases with thick non-shadow oxide limited spot-wise flaking (small point-like flakes) was occasionally seen.

3.4. Potential significance of flaking shadow corrosion

The flaking of the shadow oxide could potentially lead to two undesirable effects.

The first potential risk is that it could result in an acceleration of the oxidation process following the loss of the oxide barrier by flaking. As noted in section 1.2, the normal shadow corrosion rate has been observed to decrease with time; however, from a mechanistic point of view it is likely that the reduction in corrosion rate is due to the increase in the oxide layer thickness [3]. Repeated cycles of flaking followed by accelerated corrosion could potentially lead to significantly higher cladding metal wall loss than without flaking. However, extensive fuel surveillance has verified that the cladding integrity has not been threatened by early-in-life flaking of the shadow oxide.

The second risk arises from the fact that partial flaking of the shadow oxide results in localised areas where the cladding temperature during operation is lower than in adjacent areas where there is still a thick oxide layer, due to the poor thermal conductivity of the oxide. Hydrogen could then migrate down the temperature gradient from adjacent hotter areas to such “cold” spots or areas [7]. This would then lead to locally increased levels of hydrogen in the cladding wall below the places where the oxide has flaked off. If the local hydrogen content exceeds the hydrogen solubility limit then hydrides are formed, and if the local volume fraction of hydrides becomes excessive it can lead to a reduction in cladding ductility locally at the area where the cladding surface temperature is cooler than surrounding areas due to the locally thinner oxide. In the worst case, if a high enough local hydrogen content is reached a blister-shaped zone of almost massive hydride phase can form at the cladding surface; such a hydride blister can result in a significant reduction in the cladding ductility and failure threshold under fast strain-rate pellet-cladding mechanical interaction, for example under simulated Reactivity Initiation Accident (RIA) conditions [8].

In order to confirm the integrity of fuel with flaked shadow oxide under RIA conditions, high strain-rate mechanical testing using the EDC-method [9] was performed on cladding samples with such flaking (see Figure 12 below). The testing confirmed the ability of the cladding to withstand the level of strain that could be expected for fuel with this exposure, despite some reduction in the strain to failure in one of the specimens, with non-liner cladding, compared to similar cladding without such flaking.

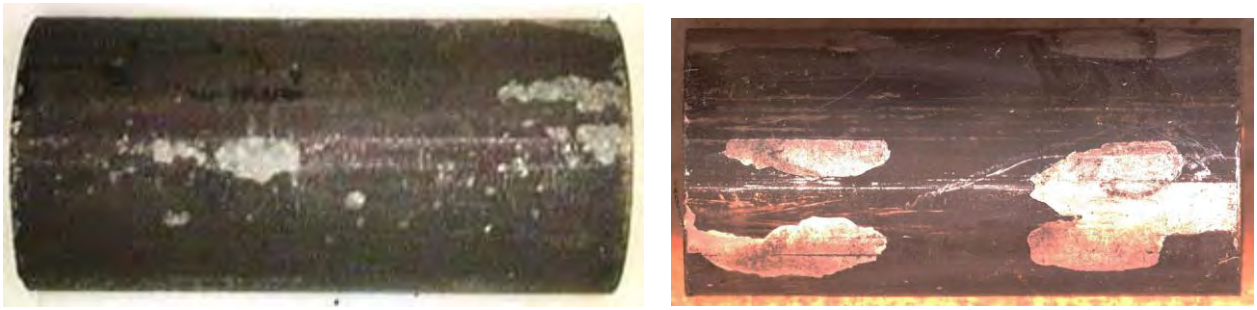

Figure 12. Cladding samples tested by the EDC method.

An additional potential consequence of very high local levels of hydrides at the cladding surface is that the hydride phase may lead to an acceleration of the corrosion rate compared to the corrosion rate of the metal under the same conditions [10]. In the past, a runaway form of shadow corrosion (termed Enhanced Spacer Shadow Corrosion, or ESSC) has occasionally

been observed, leading to rather severe local corrosion and wall-thinning in the spacer regions [11]. In this case, it is quite possible that the corrosion enhancement effect of hydrides played an important role, since the cladding material which showed the worst behaviour was known to be susceptible to accelerated uniform corrosion and hydrogen pickup at higher exposure, and was of the non-liner type.

The modern BWR cladding materials have significantly reduced hydrogen uptake in general, compared to the material that exhibited the worst ESSC [11]. Since the shadow corrosion itself usually generates no significant hydrogen pickup [12], the reduced general hydrogen pickup rate in modern cladding provides a much improved margin to ESSC. Furthermore, modern BWR cladding has a generally low oxidation rate and a low-alloyed liner as an inner layer. Since hydrogen tends to preferentially migrate to the liner-base alloy interface where it is trapped, this results in a reduced amount of hydrogen available to form a hydride-rich layer at the outer surface of the cladding where it is most detrimental to the cladding ductility and the corrosion rate.

4. Conclusions

Flaking of shadow oxide on BWR fuel cladding, where the flaking correlates with pre-existing surface scratches in the cladding surface, has been observed for various fuel designs manufactured by different vendors. Examples were found from fuel operated in different BWRs, under different operating conditions and widely differing water chemistry conditions.

The initial scratches in the cladding metal surface are typically smaller than the shadow oxide thickness. So far it has not been established exactly how the presence of relatively shallow scratches can affect the flaking of an oxide film that is far thicker than the depth of the scratches. Nonetheless, since there are potential negative consequences of such flaking, there is a strong incentive to reduce the susceptibility to flaking. For this reason, and since there are no known or anticipated benefits of such scratches, it is recommended that fuel vendors modify the fuel rod loading processes so as to prevent the formation of scratches with a spacing that promotes the strip-like flaking. We are confident that by avoiding such scratches, the occurrence of such flaking should be reduced or its onset delayed.

Acknowledgements

The authors are grateful to Björn Hall and Roots Madis for performing the SEM and EDS on retrieved flakes. We acknowledge the assistance of fuel vendors for poolside inspections and in retrieving fuel rods for hot cell examination, and Studsvik and PSI for performing hot cell examinations.

References

1. “Shadow Corrosion Resulting in Fuel Channel Bowing”. USNRC Information Notice 89-69 Supplement 1, 25 August 2003.
2. Operating Experience from Swedish Nuclear Power Plants 2008. Kärnkraftsäkerhet och Utbildning AB, 2009.
3. G Lysell, A-C Nystrand and M Ullberg, “Shadow Corrosion Mechanism of Zircaloy”, Proc. Zirconium in the Nuclear Industry: 14th International Symposium, ASTM STP 1467, 2005.
4. M. Y. He et al., “Effect of morphology on the decohesion of compressed thin films”, Phys. Stat. Sol. a, 166, 19 (1998).
5. H. E. Evans et al., ” A Numerical Analysis of Oxide Spallation”, Proc. Royal Soc. 440, 1993.

6. MATPRO- A library of materials properties for light-water-reactor accident analysis, INEEL/EXT-02-00589 rev. 2.2, 2003.
7. A. Sawatsky and C. E. Ells, ”Understanding Hydrogen in Zirconium”, Proc. Zirconium in the Nuclear Industry: 12th International Symposium, ASTM STP 1354, 2000.
8. R. Meyer, “An assessment of fuel damage in postulated reactivity initiated accidents”, Nucl. Techn. 155, 293 (2006).
9. V. Grigoriev et al., “RIA Failure of High Burn-up Fuel Rod Irradiated in KKL: Out-of-Pile Mechanical Simulation and Comparison With Pulse Reactor Tests”, Proc. Zirconium in the Nuclear Industry: 16th International Symposium, ASTM STP 1529, 2012.
10. M. Blat and D. Noel, “Detrimental Role of Hydrogen on the Corrosion Rate of Zirconium Alloys”, Proc. Zirconium in the Nuclear Industry: 11th International Symposium, ASTM STP 1295, 1996.
11. H.-U. Zwicky et al., ” Enhanced spacer shadow corrosion on SVEA fuel assemblies in the Leibstadt nuclear power plant”, Proc. ANS Int. Top. Mtg. on LWR Fuel Performance, Park City, Utah, April 10-13, 2000.
12. R. B. Adamson et al., “Hot cell observations of shadow corrosion phenomena”, Proc. Fachtagung der KTG-Fachgruppe, Brennelemente und Kernbautelle, 29 Feb. 2000.

Advances in designs, materials and manufacturing

CF3: AN ADVANCED FUEL ASSEMBLY DESIGN FOR PWR

JIAO YONGJUN, RU JUN, GUO XIAOMING, XIAO ZHONG, LI HUA

Nuclear Power Institute of China

P.O.Box 436-75, Chengdu Sichuan P.R.C (610213)

Abstract: CF3 fuel assembly is recently developed for PWR reactor core by China National Nuclear Corporation for 18-months fuel cycles. The advanced design features are utilized in CF3 fuel assembly, such as the guide thimbles improves the fuel assembly stiffness, the excellent hang-up resistance performance and thermal characteristic based on the grid design, and the anti-debris bottom nozzle.

For high burnup demand, the advanced N36 alloy (Zr-based alloy) is adopted as cladding. It allows the burnup of CF3 to be increased showing outstanding resistance against corrosion and hydriding.

Large scope of out-of-pile tests were performed, which confirms CF3 design ensure mechanical, thermal-hydraulic characteristic and compatibility. Furthermore, for in-pile performance verification，4 CF3 lead assemblies have already been loaded in Qinshan phase II Unit 2 in China in July 2014.

Keywords: CF3 fuel assembly, N36 alloy, High burnup, Hang-up resistance, Anti-debris bottom nozzle

1. Introduction

As the amount of nuclear power plants is growing fast in China, that brings a great demand for nuclear fuel assemblies. Nowadays, most of fuel assemblies are imported, including technologies, materials and equipments. The China National Nuclear Corporation (CNNC) has started CF3 fuel assembly development, aiming to meet the demand for fuel assemblies, especially for HUALONG 1# nuclear power plant.

CF3 fuel assembly design utilized the advanced design features such as improved “tube-in-tube” guide thimbles which have reinforced structure to improve the fuel assembly bowing resistance, excellent hang-up resistance behavior based on the anti-hang up grid

design, intermediate mixing grids to increase thermal performance, and effective anti-debris bottom nozzle. N36 alloy is used as cladding material, to achieve a 62 GWd/tU rod burnup. CF3 is expected to achieve the burnup of 52 GWd/tU for 18 months cycles.

2. Design parameters

The CF3 fuel assembly is composed of 264 fuel rods arranged within a 17×17 supporting structure. The supporting structure (or skeleton) is composed of 24 guide thimbles, one instrumentation thimble, a top nozzle and a bottom nozzle, 8 grids and 3 intermediate mixing grids. The active length is 3.657m(12ft).

The operating environment of CF3 may vary for different reactors, such as CNP600, CNP1000 and HUALONG 1#. A comparison of the principal design parameters is shown in Table 1.

CF3 lead assemblies are under irradiation in CNP600, and would be irradiated in CNP1000 lately.

Design Parameters	CNP600	CNP1000	HUALONG 1#
Reactor core heat output(MWt)	1930	2895	3050
Reactor coolant system pressure, nominal (MPa)	15.5	15.5	15.5
Reactor coolant average velocity(m/s)	4.34	4.94	4.39
Number of fuel assemblies	121	157	177
Fuel rod array	17×17	17×17	17×17
Number of fuel rods per assembly	264	264	264
Active core height (m)	3.657	3.657	3.657
Average linear power(W/cm)	160.9	186	173.8

Table 1: Comparison of Principal Reactor Design Parameters

3. Material and Component design features

3.1 N36 alloy

N36 zirconium alloy is developed as material of fuel rod cladding, guide thimble and spacer grid, to meet the requirements of higher burnup (more than 60 GWd/tU fuel rod burnup).

Chemical compositions of the materials were given in Table 2, metallurgical state is fine recrystallized.

Composition	Sn	Fe	Nb	Zr
Mass fraction%	1.0	0.3	1.0	residual

Table 2 Chemical composition of N36

In four lead CF3 fuel assemblies, N36 is used as cladding material, while Zr-4 is used as material of guide thimble and spacer grid.

Research on composition of N36 started several years ago. Based on previous studies, the technological processes have been designed and mastered commercially for fabricating of tubes, bars and fuel rod claddings with this alloy. Effect of low-temperature processing, annealing parameters, chemical composition on the cladding properties are studied and optimized.

Out of pile properties, such as autoclave corrosion, hydrogen uptake, physical properties, welding, hydride stress reorientation, burst, tensile, low-cycle and high-cycle fatigue, creep, Iodine-induced corrosion cracking (ISCC) and high temperature oxidation, etc, are tested.

Creep, fatigue, corrosion and high temperature oxidation properties are shown in Figure 1 to figure 5, Burst intensity is shown in table 3. The results show that the N36 alloy has excellent or equivalent out-of-pile properties compared with Zr-4.

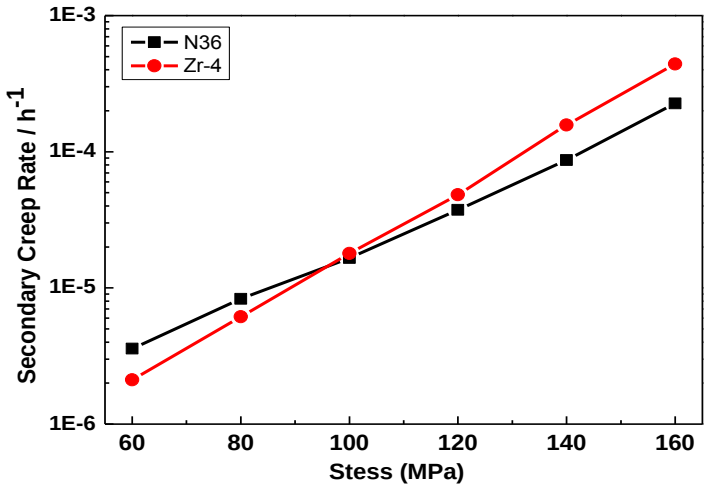

Figure 1. Creep of N36

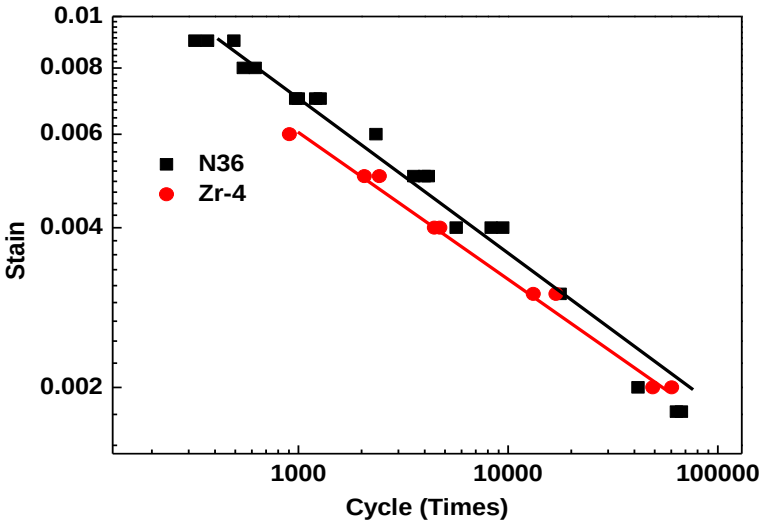

Figure 2. Low-cycle fatigue property of N36

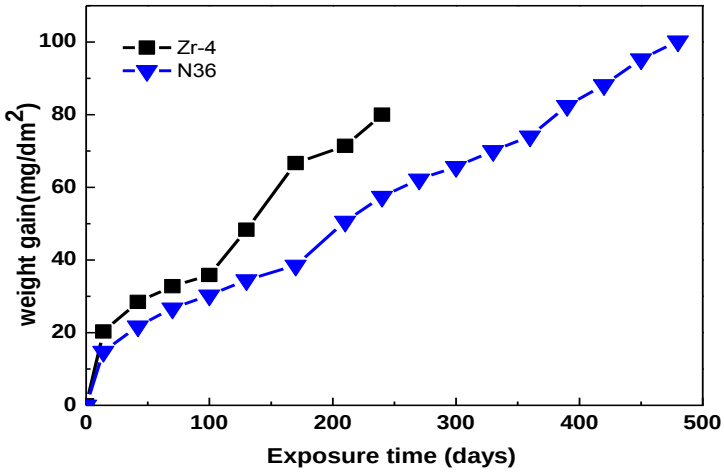

Figure 3. Corrosion in 360°C ionized water

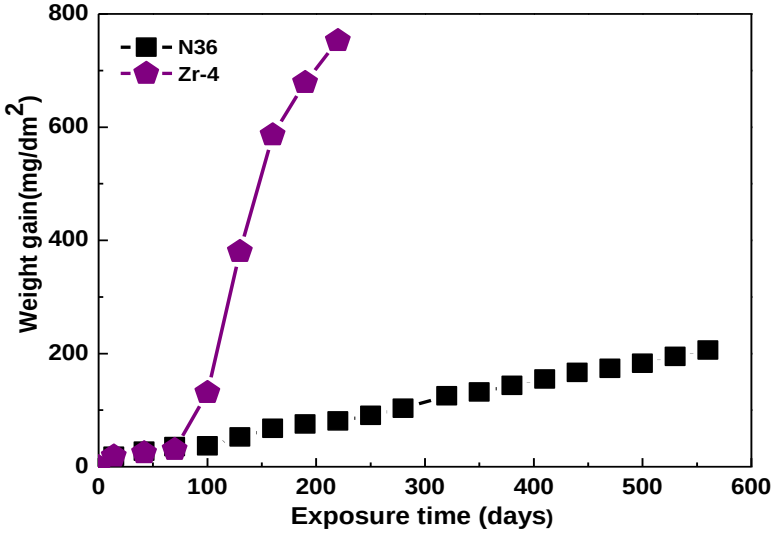

Figure 4. Corrosion in ionized water with 70 ppm LiOH

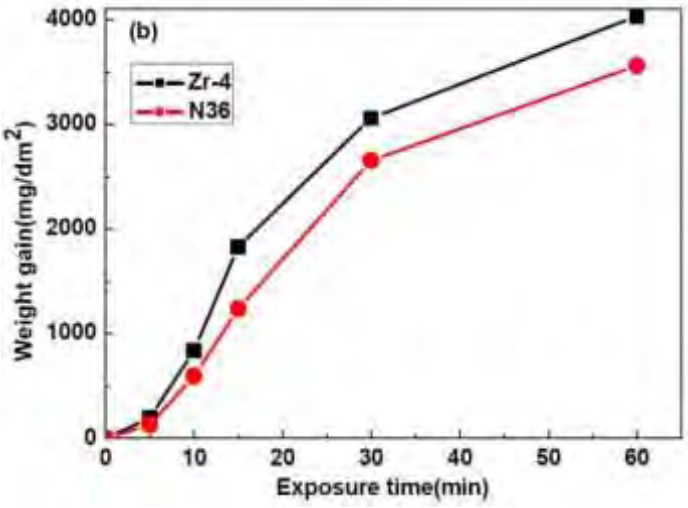

Figure 5. Oxidation at 1200°C, high temperature steam

Temperature(℃)	Burst intensity (MPa)	
	N36	Zr-4
23	686.4	736.4
200	613.4	—
300	514	—
350	454.6	369.6
375	398.4	—
400	379.7	349.6

Table 3. Burst intensity of N36 and Zr-4 tube

3.2 Top nozzle and Bottom nozzle

Top nozzle is an integral welded assembly, which has four sets of hold-down springs and spring bolts mounted on its top plate. The material is 304L stainless steel.

The adaptor plate features flow slots with optimized array and geometry, increasing the flow area while satisfying the mechanical strength criteria.

The CF3 bottom nozzle consists of bottom nozzle structural components, leaves, reinforcements, guide thimble bases and instrumentation tube bases. They are connected by brazing. Indexing and positioning of the fuel assembly is controlled by alignment holes in two diagonally opposite legs which mate with locating pins in the lower core plate. The leaves and reinforcements are arranged closely so as to form the coolant channels, and also they have anti-debris ability and can prevent accidental downward ejection of the fuel rods from the fuel assembly. Analysis show that debris with diameter higher than 3 mm could be stopped by the

filter, diameter between 1.8mm and 3mm could get through partially. The flow channel is shown in figure 6.

The guide thimbles are firmly attached to the ribbed plate by shoulder screws. The instrumentation thimble of each assembly is constrained in hole located at the center of bottom nozzle.

CFD and FEM stress analyses are performed on the structure design, to obtain a uniform flow distribution, proper press drop and sufficient mechanical strength. Pressure drop of bottom nozzle measurement is performed on fuel assembly. The measured pressure drop is in accordance with CFD analysis.

Mechanical test is performed on bottom nozzle with maximum 100kN load. The structure remains undamaged. In the mechanical test, 24 short tubes are connected to the mockup to simulate the guide thimbles of fuel assembly.

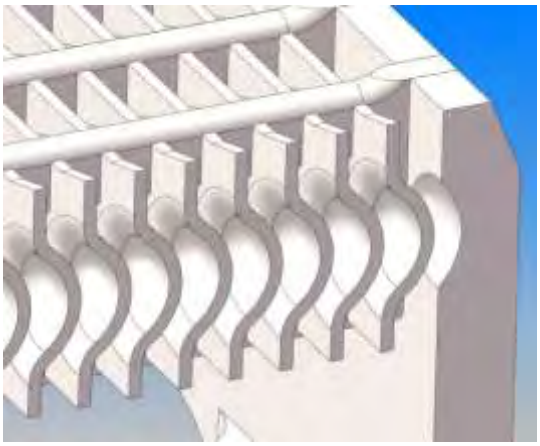

Figure 6. Bottom Nozzle flow channel

3.3 Guide and instrumentation thimbles

The CF3 guide thimble adopts an improved tube-in-tube design, Zr-4 is used as material. The guide thimble consists of a constant diameter outer guide thimble tube, a dashpot tube and plugs. The thickness of outer tube is 0.6mm which improves the fuel assembly stiffness. The outer tube is terminated with individual welded plugs. Restraint bulges between the guide thimbles and the dashpot tube provide the constraint for them.

The larger inner diameter of the upper part (11.25mm) provides a relatively large annular area to permit rapid insertion of the control rod during a scram and to accommodate the flow of coolant during normal operation. The lower part acts as a dashpot to slow down the motion of the control rod at its travel limit.

The tube-in-tube design coupled with swage process minimizes the difficulty to produce a tube with different inner diameters. The swage process is a result of abundant

experimentation, to maintain the linearity of guide thimble and sufficient strength. Minimum strength of 1200N is assured for every swage.

The guide thimble is closed at the bottom by means of an end plug, the joint with the bottom nozzle being achieved by a screw. The screw is provided with a small flow hole to avoid fluid stagnation in the dashpot volume during normal operation.

Control rod drop time test was performed on the tube-in-tube guide thimble design, which showed an accordance with expectation.

3.4 Spacer Grid

The CF3 fuel rods are supported along their length by 8 structural grids (1 top grid, 1 bottom grid, 6 structural mixing grids) which maintain the lateral spacing between the rods. Recrystallized Zr-4 is used as strap of structural grids.

Guiding vanes on the outer strap are arranged continuously, which improved the handling performance. However, the height of every other guiding vane is lower than normal one, as well as 16 flow holes are set at the upper part of outer strap so as to enhance the coolant mixing between nearby fuel assemblies.

In order to get a fuel assembly with high thermal-hydraulic performance, the proposed CF3 fuel assembly features 3 intermediate mixing grids(IMGs), located mid-way along the three highest heated spans of the assembly. The main function of IMGs is to increase the coolant mixing effect and improve the DNB performance. They are made of straps stamped and formed from Zr-4 strips. The mixing vane array of the IMG is similar to the mixing grids.

Anti hang-up test, strength test, stiffness test and CHF test are performed on the grid.

Figure 7. Spacer grid hang-up test

4. Out-of-pile tests

4.1 Spacer grid tests

Handing tests are performed to verify any risk of hang-up and the grid strength exceeds the applied load in reactor handing condition. The result of the test exhibits excellent anti hang-up performance.

To determine the static stiffness and crush strength of the grid, cold static crush tests are performed. Hot dynamic crush tests are also performed to determine the dynamic crush strength and lateral stiffness of the grid, which could be used in LOCA/Seismic accident analysis.

Static buckling load at room temperature is 19500N, dynamic buckling load at 315℃ is 16800N.

4.2 Fuel assembly mechanical tests

To verify mechanical performance of CF3 fuel assembly, several tests are performed, including fuel assembly lateral stiffness test, fuel assembly axial stiffness test, fuel assembly lateral dynamic test, fuel assembly axial dynamic test and fuel assembly natural frequencies and mode shape test. The results could be used in LOCA/Seismic accident analysis of fuel assembly.

Lateral stiffness is approximately 72kN/m, axial stiffness is approximately 35000kN/m.

4.3 Control rod drop test

Control rod drop test are conducted in different coolant flux and drop height conditions to measure control rod drop time, impact force and verify structural design of tube-in-tube design.

Measured T5 and T5+T6 are 1.31s, 1.76s respectively, while calculated nominal time are 1.38s, 1.74s. The rod drop time meet the requirement of nuclear power plant.

The results demonstrate that the tube-in-tube design satisfy the control rod drop time and impact force requirements.

4.4 Endurance test

One full size fuel assembly mock-up is placed in a test section testing for 1000 hours. The test condition is 15.5MPa, 315℃. The flow rate is 510m^3/h.

After the endurance test, several rods are removed and examined at spacer grids locations and the result indicated no obvious fretting wear was found. Fuel assembly remains integrated.

4.5 Hydraulic tests

To gain hydraulic characteristics of components and whole assembly, and provide input date for CF3 fuel assembly design, hydraulic tests are performed with a full size fuel assembly mock-up. The results of the tests provide the variation of the fuel assembly total resistance with Re, the nozzle resistance characteristics and the grids resistance characteristics. Resistance coefficient of fuel assembly is approximately 21 at $Re=2.2\times10^5$.

4.6 Critical heat flux tests

CHF tests are performed at high temperature and high pressure test facility using 5×5 full length bundle with non-uniform radial heating power. The heat rod diameter is 9.5mm and the rod pitch is 12.6mm. Power ratio between internal hot rod and external cold rod is about 1:0.85. The CHF test provides adequate test data to develop CHF correlation of CF3 fuel assembly, which is used for DNBR calculation in the reactor core thermal hydraulic design and safety analysis.

5. In-pile tests

To gain the CF3 fuel assembly in-pile performance, four CF3 lead assemblies have already been loaded in Qinshan phase II Unit 2(CNP600) in China in July 2014. The lead assemblies are in operation without any abnormal indication.

Design parameters of CF3 lead assemblies are as introduced in section 2. N36 is used as material of rod cladding. Recrystallized Zr-4 is used as material of guide thimble and grid strap.

Figure 8. N36 rod assembly into the pool

6. Conclusion

In this paper, the advanced design features which are utilized in CF3 fuel assembly are described, the out-of-pile and in-pile irradiation are also presented. Some conclusions can be obtained as follows:

(1) N36 alloy, which used as the fuel rod cladding, had excellent out-pile and in-pile properties compared with commercial claddings.

(2) The fuel assembly performance is improved by the advanced design features which are utilized in the guide thimbles, the grid and the bottom nozzle design.

(3) Out-of-pile tests have been done to confirm the design of CF3 fuel assembly and in-pile tests are under way.

References

[1] M. Aullo, W.D. Rabenstein. European fuel group experience on control rod insertion and grid to rod fretting, Structural behaviour of fuel assemblies for water cooled reactors(IAEA-TECDOC-1454), Proceedings of a technical meeting held in Cadarache, France, 22–26 November 2004.

[2] ZHAO WJ. Development of Chinese advanced zirconium alloys[J]. Atomic Energy Science and Technology, 2005, 39(Suppl): 2-9(in Chinese).

THE MISSION AND ACCOMPLISHMENTS FROM DOE'S FUEL CYCLE RESEARCH AND DEVELOPMENT (FCRD) ADVANCED FUELS CAMPAIGN

J. CARMACK AND L. BRAASE
Idaho National Laboratory
PO Box 1625, Idaho Falls, ID, 83415 – USA

F. GOLDNER
Department of Energy – USA
1000 Independence Ave. SW
Washington DC, 20585

ABSTRACT

The mission of the Advanced Fuels Campaign (AFC) is to perform Research, Development, and Demonstration (RD&D) activities for advanced fuel forms (including cladding) to enhance the performance and safety of the nation's current and future reactors, enhance proliferation resistance of nuclear fuel, effectively utilize nuclear energy resources, and address the longer-term waste management challenges. This includes development of a state of the art Research and Development (R&D) infrastructure to support the use of a "goal oriented science based approach." AFC uses a "goal oriented, science based approach" aimed at a fundamental understanding of fuel and cladding fabrication methods and performance under irradiation, enabling the pursuit of multiple fuel forms for future fuel cycle options. This approach includes fundamental experiments, theory, and advanced modeling and simulation.

One of the most challenging aspects of AFC is the management, integration, and coordination of major R&D activities across multiple organizations. AFC interfaces and collaborates with Fuel Cycle Technologies (FCT) campaigns, universities, industry, various DOE programs and laboratories, federal agencies (e.g., Nuclear Regulatory Commission [NRC]), and international organizations. Key challenges are the development of fuel technologies to enable major increases in fuel performance (safety, reliability, power and burnup) beyond current technologies, and development of characterization methods and predictive fuel performance models to enable more efficient development and licensing of advanced fuels. Challenged with the research and development of fuels for two different reactor technology platforms, AFC targeted transmutation fuel development and focused ceramic fuel development for Advanced Light water reactor (LWR) Fuels.

1. Introduction

In support of the Fuel Cycle Research and Development (FCRD) program, AFC is responsible for developing advanced fuels technologies to support the various fuel cycle options defined in the Department of Energy (DOE) Office of Nuclear Energy, "Development of Light Water Reactor Fuels with Enhanced Accident Tolerance," Report to Congress, April 2015. [1]

AFC uses a "goal-oriented, science-based approach" aimed at a fundamental understanding of fuel and cladding fabrication methods and performance under irradiation,

enabling the pursuit of multiple fuel forms for future fuel cycle options. This approach includes fundamental experiments, theory, and advanced modeling and simulation. The modeling and simulation activities for fuel performance are carried out under the Nuclear Energy Advanced Modeling and Simulation (NEAMS) program, which is closely coordinated with AFC. The word "fuel" is used generically to include fuels, targets, and their associated cladding materials. [2]

1.1 Science-Based Approach

Fuel development and qualification is a lengthy and expensive process. The traditional empirical approach to fuel development is not amenable to conducting research on multiple fuel forms and types with very aggressive performance objectives. In addition, limited budgets, human resources, and research facilities further complicate the situation. Fortunately, the advances made in fundamental understanding of materials, instrumentation, measurement techniques, and development and growth of high performance computing provide a means to overcome these barriers and implement a new approach to R&D. This "science-based" approach involves small-scale experiments, coupled with theory development and advanced modeling and simulation, to reduce the number and cost of engineering-scale tests (
Figure 2).

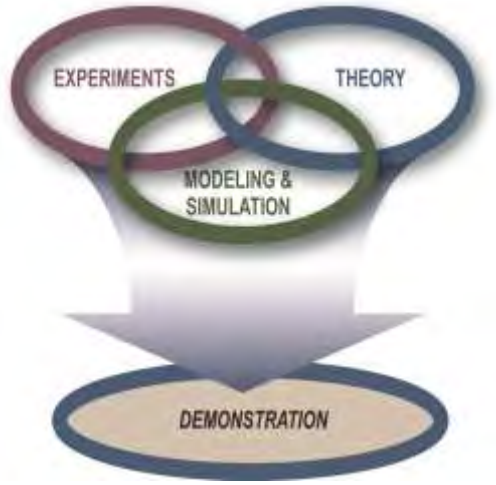

Figure 1. Goal-Oriented Science-Based Approach

Experiments. The focus on experiments for a science-based approach shifts from large-scale, integrated experiments typical of demonstration-based programs, to smaller-scale, phenomenological, fundamental mechanisms, and integral effects testing aimed at measurement of fundamental properties. This approach provides a fundamental understanding of targeted phenomena and the data needed for model development. New and innovative experimental design and novel measurement techniques will be incorporated into experimental programs. In some cases, targeted integral experiments will also be needed. However, small-scale integral testing combined with scientifically developed scaling laws may alleviate the need of full-scale experiments. Novel measurement techniques with high spatial resolution (micron to sub-micron scale characterization) are needed for science-based fuel development. Finally, in situ instrumentation for in pile experiments will be valuable to understand the transient in pile behavior of the fuels and materials.

Theory. Essential elements of the science-based approach are to build upon existing theories and to develop new theories that explain the various phenomena of interest based either on first principles or observations made during phenomenological testing or uncovered through analysis of modeling results. In the long-term, theory must span from quantum mechanics to continuum mechanics in explaining the behavior of physical systems. A well-integrated science-based approach is needed between experiments and theory development. For advanced fuels, the near-term theory development will be a mesoscale (microstructural) understanding of fuels and materials under irradiation conditions.

Modeling and Simulation. The knowledge and data gained under experimental and theoretical elements of the science-based approach will be incorporated into advanced modeling and simulation programs that take advantage of state-of-the-art computing capabilities. Due to the very complex nature of the licensing process for nuclear fuels, a formal science-based approach must be developed and implemented to demonstrate the validity of newly developed simulation tools to address the behavior of fuels and materials in

realistic situations and qualify these tools to be used in the licensing process. The technical objective of the modeling and simulation effort is to provide insight into highly non-linear, coupled, multi-physics processes that occur during fuel fabrication and fuel performance. The practical objectives are to:

- Minimize the number of empirical iterations during fabrication and high-dose irradiation testing of fuels by designing the performance into the fuel at the early development phases
- Reduce the number of prototypes and large-scale experiments needed before demonstration and deployment
- Quantify uncertainties for design and operational parameters.

Demonstrations. Nuclear energy systems are large-scale, complex facilities characterized by phenomena that can span ten orders of magnitude in space and time. Financing these systems requires the synthesis of complex business considerations and long-term financial commitments. Plant construction requires the use of large amounts of basic commodities such as concrete and steel. Facility operation requires adherence to a plethora of regulations at the local, state, and federal levels. At the same time, the United States regulatory process still relies heavily on experiments to confirm the ultimate safety of nuclear power systems (including the fuels). Ultimately, the amelioration of these risks requires that new nuclear energy systems must be thoroughly demonstrated before commercial deployment. Therefore, new technologies, regulatory frameworks, and business models must be integrated into first-of-a-kind system demonstrations and prototypes. Then construction and operation will provide sufficient top-level validation of system technical and financial performance to enable deployment. For fuels, demonstration means fabrication of test assemblies, typically referred to as lead test assemblies using prototypic processes and tested in a prototypic environment. At the end of testing, it must be demonstrated that the behavior of the Lead Fuel Assemblies (LFA) are within the bounds of the established safety and operational envelopes. Historically, the safety-acceptability of advanced fuels in LFAs requires prior transient testing of those fuels.

2. AFC Organization

AFC has the specific responsibility to develop advanced nuclear fuel technologies for the Fuel Cycle R&D program. There are three overall technical areas with research focused on advanced LWR fuels, transmutation fuels, and capability development. Modeling and simulation capability is provided by the Nuclear Energy Advanced Modeling and Simulation (NEAMS) program. NEAMS and AFC work closely together to develop and validate fuel and cladding performance under irradiated conditions. AFC technical areas are shown in

Figure 2 and described below.

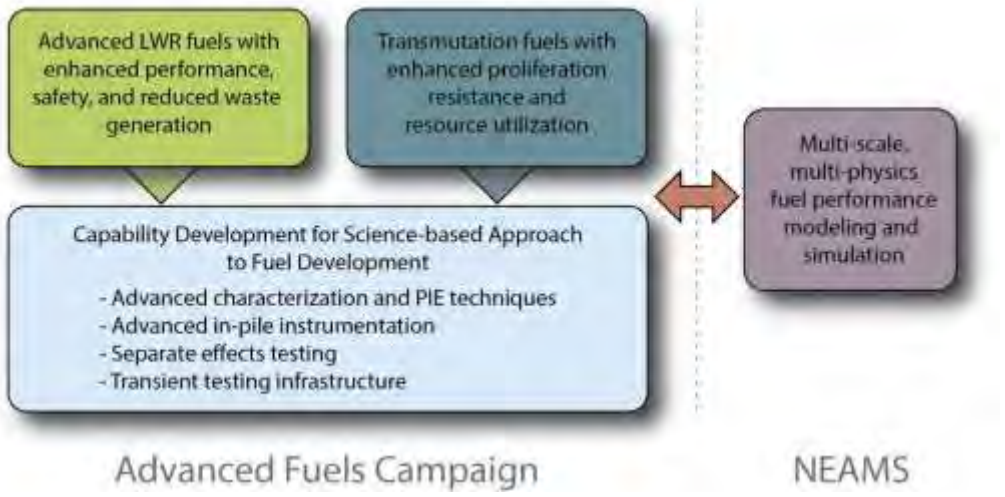

Figure 2. Advanced Fuels Campaign organization and interface with NEAMS.

2.1 Advanced Light Water Reactor (LWR) Fuels

LWR fuels, with enhanced accident tolerance, are designed to achieve significantly higher fuel and plant performance to allow operation to significantly higher burnup, and to provide enhanced safety during design basis and beyond design basis accident conditions. The overarching goal is to develop advanced nuclear fuels and materials that are robust, have high performance capability, and are more tolerant to accident conditions than traditional fuel systems.

Researchers are investigating a number of potential fuels and cladding technologies to improve fuel system performance in both normal and accident conditions. Significant progress has been made on establishing oxidation, corrosion, and materials property characterization capabilities and techniques that can be used to assess the performance of potential advanced LWR fuel technologies. In addition, AFC has initiated the first irradiation of Accident Tolerant Fuel (ATF) technologies in Idaho National Laboratory's (INL) Advanced Test Reactor (ATR) in FY 2015.

2.2 Transmutation Fuels

Transmutation fuels have enhanced proliferation resistance and resource utilization. Research is ongoing to gain a fundamental understanding of metallic fuels, such as low-loss fabrication methods and capability and on developing a fundamental understanding of the phase, microstructure, and chemical migration behavior of metallic fuel constituents. The desired outcome is to develop an understanding of the key phenomena affecting metallic fuel performance and behavior under irradiation.

Primary RD&D areas include casting technology development; fabrication and characterization of minor actinide and lanthanide bearing fuel samples; fundamental property measurement and fuel cladding chemical interaction (FCCI) tests; and irradiation performance testing.

2.3 Capability Development

Performing research on irradiated and highly radioactive fuel materials is difficult, time intensive, and technically challenging. Couple this with the desire to study the microstructural evolution of fuels and materials under irradiation provides the opportunity for the development of advances in nuclear fuels and materials R&D science. Innovative and

creative science and engineering are utilized by the technical scientific and engineering staff to develop cross-cutting research tools and capabilities. This includes fabrication process development; advanced modeling and simulation analysis of fuel systems and fabrication processes; characterization technique and instrument development; and unique in-pile and out-of-pile material property measurements.

3. AFC Accomplishment Highlights

The accomplishments below showcase a sampling of the achievements made by AFC scientists and engineers. A more comprehensive summary is available in the AFC 2014 Accomplishments Report [3].

3.1 Accident Tolerant Fuels Strategy

The Congressionally driven goal of accident tolerant fuel development is to identify alternative fuel system technologies to further enhance the safety, competitiveness, and economics of commercial nuclear power. The development of an enhanced fuel system supports the sustainability of nuclear power, allowing it to continue to generate clean, low-CO_2-emitting electrical power in the United States. Details on the applicable development phases, key ATF attributes, and proposed evaluation metrics are included in previous publications [4, 5].

The ATF development effort adopts a three-phase approach to commercialization (Figure 3). Phase 1 includes feasibility assessment and down-selection to develop, test, and evaluate fuel concepts. Feasibility assessments of the new concepts will be performed to reduce the number of concepts for further development. These assessments include laboratory scale experiments, e.g., fabrication, preliminary irradiation, material properties measurements; fuel performance code updates; and analytical assessment of economic, operational, safety, fuel cycle, and environmental impacts. In Development and Qualification, Phase 2, will expand to industrial scale for Lead Fuel Rods (LFRs) and LFAs. Finally, the industry led Phase 3 establishes commercial fabrication capabilities.

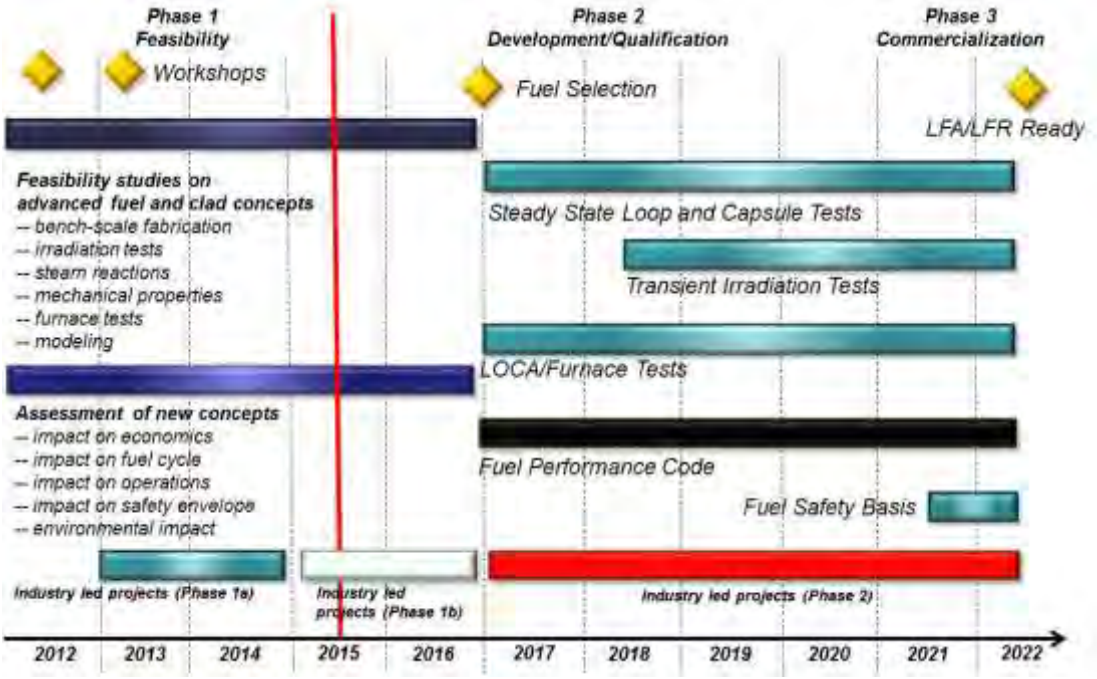

Figure 3. RD&D Strategy for Enhanced Accident tolerant Fuels - 10 Year Goal

Accident Tolerant LWR fuel research made significant progress in FY 2014 through completion of Phase 1A activities by the three industry-led Funding Opportunity Announcement (FOA) awards and initiation of Phase 1B for two additional years of activity. These projects are integrated into the DOE laboratory funded research, development, and infrastructure activities in AFC with the Nuclear Energy University Program (NEUP) and university-led Integrated Research Projects (IRP). In addition, ATF fabrication support resources were established and demonstrated at Oak Ridge National Laboratory (ORNL), INL, and Los Alamos National Laboratory (LANL). Research quantities of ATF compositions were fabricated, demonstrating the capability to support industry FOA fuel fabrication needs as well as the capability to fabricate novel ATF fuel compositions. Design of the initial irradiation of ATF concepts, designated as the ATF-1 test series, was completed. The ATF-1 experiment was inserted into INL's ATR on February 10, 2015. The experiment includes fuel concepts from Westinghouse Electric Company (WEC), AREVA, and General Electric (GE); irradiation will continue over the next two years, and additional concepts will be added when available

3.3 Fabrication of Metallic Fuel Samples

To support fuel characterization and irradiation testing, additional fuel tests were made to supplement the ATR AFC-4A irradiation test. The fuel slugs were cast, machined to final diameter and encapsulated in the standard AFC-OA irradiation hardware. The Bench-scale Casting II furnace was upgraded to provide better atmospheric contamination control. The original furnace designed called for the use of plastic tubing and compression fitting because a high vacuum level was not needed at the time. However, due to further testing and programmatic changes higher vacuum level was needed so the furnace was upgraded to utilize O-ring sealed vacuum fittings and stainless steel hoses.

The goal was to determine which transmutation fuel samples were needed for characterization to fill in gaps in the fuel property database. An extensive inventory of the legacy fuel samples was undertaken to determine which samples were appropriately packaged to prevent excessive oxidation, the form of the samples, and which pieces could be used as feedstock to cast other samples needed for further characterization. Figure 4 shows an example of a fuel slug and feedstock samples. Following this inventory 12 alloys were identified that need to be cast for further characterization. The alloys are from the AFC-1 and AFC-2 series of irradiation tests as well as basic characterization samples that are needed for further phase diagram development. Currently three of the alloys have been cast; Pu-60Zr, Pu-40Zr, and Pu-30Zr. During casting it was observed that the casting hardware used was contaminating the melt, and possibly hindering the casting process. To avoid this contamination a new series of casting hardware was developed and used, which has proven to produce less contamination and improve overall castability.

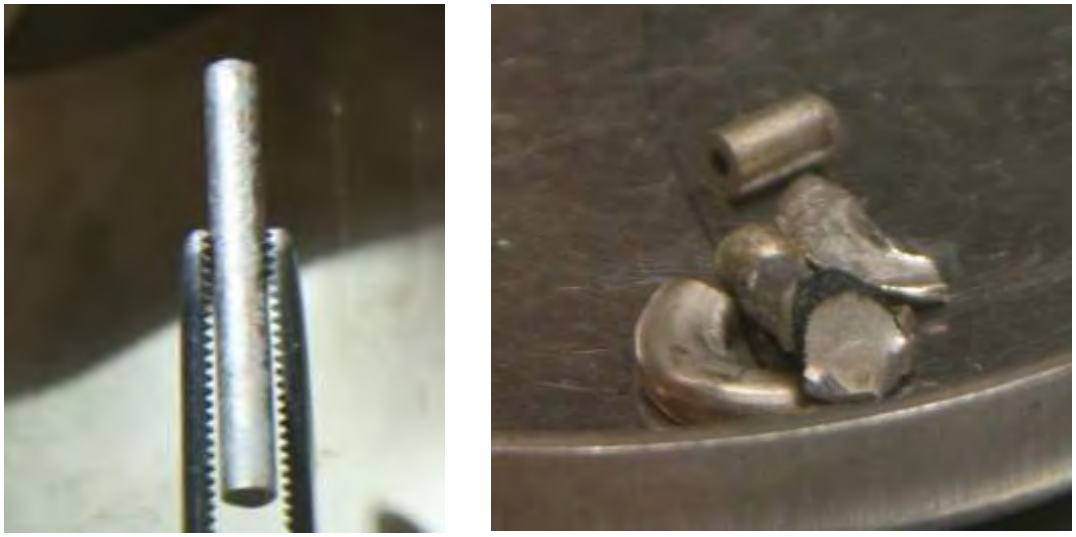

Figure 4. Legacy AFC-1 material: (Left) Archive slug which can be used as-is for further characterization and Right) remaining casting heel pieces which can be re-cast into a usable sample.

3.4 Capability Development: Thermal Property Measurements

The Thermal Conductivity Microscope (TCM) is designed to operate in a radiation hot cell environment via remote control manipulation.[6] The TCM provides micron-level thermal property information that is commensurate with microstructure heterogeneity. Development of the microscope connects closely with INL's larger post-irradiation examination (PIE) effort to provide new validation metrics for fundamental computational material science models. The TCM is being used to provide important data on uranium bearing surrogate fuel samples.

One example of this work on surrogate fuel, shown on the upper right side of Figure 5, investigates the reduction in thermal conductivity of polycrystalline UO_2 irradiated with 4 MeV He^{++}. The conductivity of the thin surface layer corresponding to the plateau region of the damage profile was isolated by tuning the penetration depth of the thermal waves. Another example, shown in the lower right side of Figure 5, involves using the TCM to measure thermal anisotropy. Currently the TCM is being used to confirm the existence of thermal anisotropy in UO_2 caused by phonon-spin coupling. Plans are underway to benchmark the accuracy and reproducibility of the TCM using known thermal conductivity standards. Preliminary test conducted in FY 2014 indicate that conductivity results are accurate within $\pm$5% and the reproducibility is less than 2%.

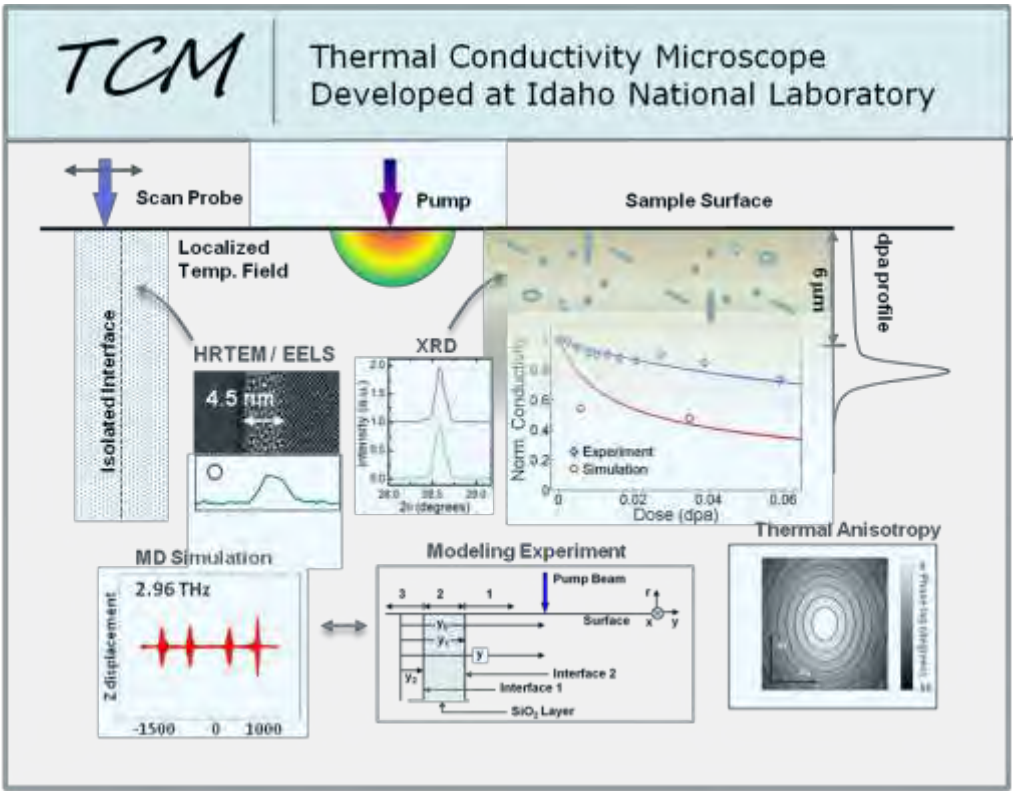

Figure 5. TCM measures local changes in thermal conductivity. The left side illustrates measurement of the Kapitza resistance of an individual, highly characterized interface. The right side demonstrates the use of the TCM to measure the conductivity of a thin surface layer damaged by energetic ions.

3.5 Transient Testing Capability

A transient testing research program is being developed to support assessment of ATF designs being proposed for LWR applications. Transient testing of ATF fuels under both overpower (e.g. Reactivity Initiated Accident (RIA) simulation) and undercooling (e.g. LOCA simulation) conditions will be done to support the 2022 ATF goal. This series of ATF transient tests have been termed ATF-3.

The Transient Reactor Test (TREAT) facility is a versatile test facility able to subject experimental specimens to various transient nuclear conditions of interest. TREAT resides at the Materials and Fuels Complex (MFC) at INL. The reactor first achieved criticality in 1959 and was operated successfully until 1994, when its operations were suspended. Resumption of operations is an active project underway to facilitate reactivation of the TREAT facility by 2018.

In parallel to the effort to resume operations at TREAT, the transient testing strategy to support ATF concept screening, development, and qualification is being developed. A proposal for the first set of transient experiments has been prepared for discussion with the ATF concept design leads. These tests emphasize assessment of the relative performance of the fuel designs under various enthalpy additions anticipated under pulse and ramp conditions.

3.6 Minor Actinide Casting Experiments

The Glovebox Advanced Casting system (GACS) was developed, installed and now operates in a minor actinide qualified glovebox at INL's MFC. This furnace was designed to provide a flexible casting development platform where both gravity casting into a permanent

mold and counter gravity casting into a glass mold could be developed and studied. In addition to casting development the GACS will also be used to study melt properties, americium volatility studies, and general sample fabrication. The furnace was designed to be a flexible platform in which a number of experiments, alloys, and configurations can be run. The modular design of the furnace makes it possible to change out components, such as coils, crucibles, and molds to accommodate a variety of sizes or techniques as required.

The solid model of the GACS is currently configured for gravity casting and is contained in a stainless steel shell, which used standard ISO style vacuum flanges for all sealing surfaces. The mold and crucible are independently inductively heated allowing the ability to rapidly heat the crucible and mold which may be necessary to decrease the total amount of time the fuel alloy is heated thereby reducing volatility losses.

4. Summary

The mission of AFC is to perform RD&D activities for advanced fuel forms (including cladding) to enhance the performance and safety of the nation's current and future reactors, enhance proliferation resistance of nuclear fuel, effectively utilize nuclear energy resources, and address the longer-term waste management challenges. Achievement of the mission relies on effective management, integration, and coordination of major R&D activities across multiple organizations. Challenged with the research and development of fuels for two different reactor technology platforms, AFC targeted transmutation fuel development and focused ceramic fuel development for Advanced LWR Fuels.

The funding source had no role in the research or writing of this paper, or the decision to submit it for publication.

5. References

[1] U.S. DOE Office of Nuclear Energy, "Development of Light Water Reactor Fuels with Enhanced Accident Tolerance," *Report to Congress,* April 2015.

[2] U.S. DOE, "Advanced Fuels Campaign Execution Plan," Revision 4, June 30, 2015, FCRD-FUEL-2011-000105.

[3] U.S. DOE, "Advanced Fuels Campaign 2014 Accomplishments Report," October 2014, INL/EXT-14-33515, FCRD-FUEL-2015-000002.

[4] S.M. Bragg-Sitton, "Metrics for the Evaluation of Light Water Reactor Accident Tolerant Fuel," in proceedings of the 2014 Water Reactor Fuel Performance Meeting, Sendai, Japan, paper 100143 (2014).

[5] S.M. Bragg-Sitton, et al. "Advanced Fuels Campaign: Enhanced LWR Accident Tolerant Fuel Performance Metrics," February 2014, INL/EXT-13-29957, FCRD-FUEL-2013-000264.

[6] D. H. Hurley, “Status Report on the Development of the Thermal Conductivity Microscope,” Idaho National Laboratory, May 2015, INL/LTD-15-35366.

TECHNOLOGY READINESS LEVEL (TRL) ASSESSMENT OF ADVANCED NUCLEAR FUELS

D.J. SHEPHERD, G.D. ROSSITER, I.D. PALMER, G. MARSH, M. FOUNTAIN
Fuel & Radioisotope Technology, National Nuclear Laboratory
NNL Preston Laboratory, Springfields Works, Salwick, Preston, Lancashire, PR4 0XJ – UK
Correspondence: daniel.shepherd@nnl.co.uk

ABSTRACT

High performance nuclear fuel technology is essential for the safe, reliable, sustainable, secure and economic operation of nuclear stations worldwide. This paper presents a broad ranging technology readiness level (TRL) assessment of potential advanced nuclear fuel concepts relevant for Generation III, III+, IV and small modular reactors (SMRs) including those considered to be potential accident tolerant fuels (ATF).

Assessed fuel concepts include advanced UO_2, advanced MOX, advanced dopants and burnable absorbers, annular and dual-cooled fuel (DCF), carbides and nitrides (U & U,Pu-based), advanced metallic fuels, uranium silicide intermetallics, dispersion and inert matrix fuel (IMF), zirconium hydride matrix fuel, coated particle and microencapsulated fuel, thorium-based fuel, those bearing minor actinides and finally molten salts.

The assessment takes into account the extent of previous nuclear industry experience with these concepts following an extensive literature review combined with conference attendance, relevant facility visits and discussion with key contacts in the international nuclear industry. This paper develops upon a short summary that was published in Nuclear Engineering International in 2014. A similar companion assessment of advanced cladding materials was previously presented at the 2013 OECD NEA SMINS-3 (Structural Materials for Innovative Nuclear Systems) international workshop. This work has been funded by the UK Department of Energy and Climate Change (DECC).

Overall, a sizeable number of advanced fuel concepts are being developed worldwide with some being significantly closer to commercial deployment than others. In particular, in two areas where advanced fuels could potentially provide very significant benefits, ATF for Gen III reactors and fuels for Gen IV reactors, a significant degree of further development is required. In the case of Gen IV fuels, this must take place alongside the development of the reactor system.

1. Introduction

Reliable nuclear fuels are essential for achieving the safe, sustainable and economic operation of nuclear stations. Therefore, this paper presents a worldwide assessment of the technology readiness levels (TRLs) of advanced nuclear fuels. The paper is aimed at highlighting various advanced fuels and their current status with regards to commercialisation in order to allow comparison. This paper develops upon a short summary that was published in Nuclear Engineering International in 2014 [1]. A similar companion assessment of advanced cladding materials was previously presented at the 2013 OECD SMINS-3 (Structural Materials for Innovative Nuclear Systems) international workshop [2]. The work has been funded by the UK Department of Energy and Climate Change (DECC).

The assessment has considered both 'evolutionary' fuels (i.e. improvements to existing and past commercial fuels including geometrical improvements) as well as radically different 'revolutionary' fuels. The nuclear reactor systems considered to deploy these advanced fuels are current Generation III / III+ light and heavy water reactors (LWRs and HWRs) as well as the more revolutionary Gen IV systems which are aimed at generating nuclear energy in a significantly more sustainable and secure manner [3]. For Gen IV systems, the deployment of the entire reactor designs is dependent on the qualification of advanced fuels in order to fully realise their goals. Small modular reactors (SMRs) are based on either larger Gen III / III+ reactors (i.e. LW SMRs) or on larger Gen IV reactors (e.g. HTR, SFR or LFR). Therefore the fuel concepts for SMRs and their TRLs would be similar to the larger variants. Only TRLs for commercial power applications are assessed and hence marine propulsion, space and research and test reactors (RTRs) are not considered except where RTRs are used as the means to qualify fuels for commercial operation.

2. Method

2.1 Down-selection of advanced fuel concepts

In order to conduct a TRL assessment, it was first necessary to down-select candidate advanced fuels for deployment in Gen III / III+ and IV systems including Gen III / III+ accident tolerant fuel (ATF) concepts. These down-selections were made by applying pre-existing knowledge of the relevant systems. Dispersion, inert matrix, coated particle fuels and molten salts are considered alongside more traditional bulk material fuel forms. These down-selections are summarised below under a series of broader groupings of these fuels by common characteristics, with standard commercial fuels included for comparison.

- Standard fuels
  - UO_2
  - MOX (mixed uranium-plutonium oxide <12% PuO_2)
- New geometries
  - Annular pellets in LWRs (exc. VVER)
  - Dual-cooled fuel (DCF)
- Evolutionary materials
  - Advanced UO_2
  - Advanced MOX
  - Advanced metal
- New compounds
  - Carbide
  - Nitride
  - Uranium silicide
- Including new elements
  - Thorium-based fuels
  - Minor actinide (MA) bearing fuels
- Including other materials
  - Inert matrix fuel (IMF)
  - Dispersion fuel
  - Zirconium-hydride based
  - Coated particle-based
- Liquid-based
  - Molten salt

2.2 Technology Readiness Levels (TRLs)

The TRL system is a means of measuring technology maturity, with a degree of standardisation, which allows for comparison between different technologies. Originally defined by Mankins (1995) of NASA [4], TRLs have become adopted by many industries around the world. As the technology matures from the lower TRLs to the higher TRLs, it moves from a scientific idea through to a fully developed application that has demonstrated its usefulness by being deployed in an operational situation. Figure 1 illustrates where the development of technologies at different TRLs may be conducted in order to advance their TRL in a typical national technology supply chain.

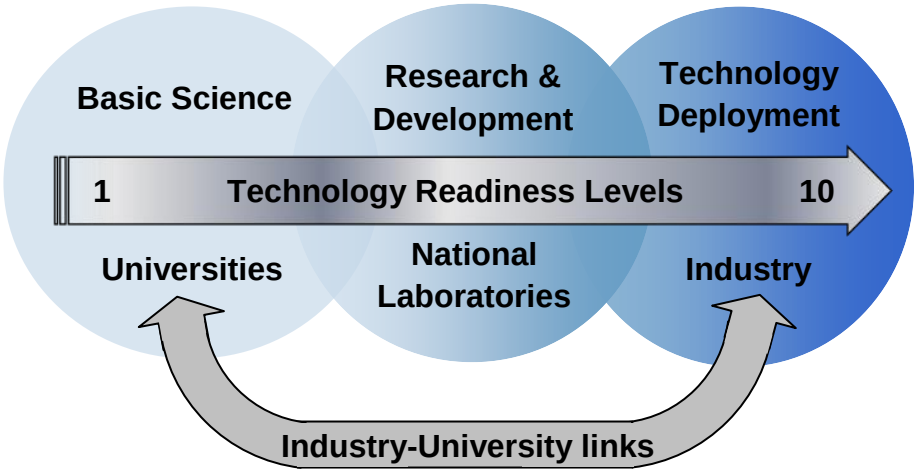

Figure 1. TRLs and a typical national technology supply chain

It should be emphasised that the NASA TRLs were defined for systems for individual space missions (often electronic) and the terminology is not always suitable for nuclear industry applications. Hayes and Porter (2007) of INL (Idaho National Laboratory) [5] reported an adaptation of the TRL system for application to fast reactor fuel.

There is some apparent inconsistency between the NASA and the INL definitions (which both have TRLs 1 to 9). For example, INL TRL 1 seems to correspond more closely with NASA TRL 2, due to INL not including basic principles research at the bottom of the scale. Furthermore at the top of the scale, INL TRL 9 could feasibly correspond to an assumed NASA TRL 10, if their definitions were extrapolated to operation of many actual systems as opposed to single missions. Therefore overall, the INL scale appears to be shifted by one TRL with respect to NASA's.

For the fuel TRL assessments in this paper, a combined approach has been used that includes elements of both the NASA and the INL definitions. Some additional simplification and generalisation was also employed to allow a flexible approach to what is in reality a highly complex situation. Consistency has been maintained with the NASA scale, with TRL 1 still corresponding to basic principles research. In addition, aspects of the more precise INL approach have been incorporated including their guidelines regarding out-of-reactor/in-reactor testing, lead assemblies and core reloads. A TRL 10 has also been defined based on the INL TRL 9 to consider long term operation of many actual systems.

The TRL definitions used for this paper are presented in Table 1 using a 'traffic light' colour coding that is employed throughout.

TRL	Definition and Description
10	**Widespread, reliable and long-term operation of many actual systems** e.g. long-term use of fuel within a commercial reactor fleet / fleets with many thousands of hours of operating experience and data
9	**Successful operation of actual system** e.g. assemblies have performed successfully under irradiation in reload quantities (demonstrated by surveillance programme)
8	**Actual system constructed and commissioned** e.g. assemblies fabricated in reload quantities; may include irradiation with only limited success
7	**Prototype successfully demonstrated** e.g. lead use assemblies have performed successfully in a prototype or commercial reactor (demonstrated by PIE and/or in-core monitoring)
6	**Prototype construction (much more representative than the basic system)** e.g. lead use assemblies have been fabricated, and potentially irradiated in a prototype or commercial reactor but with only limited success
5	**Basic system successfully demonstrated** e.g. test rods have been irradiated and performed successfully in a test reactor (demonstrated by in-reactor instrumentation and/or post-irradiation examination (PIE) and/or post-irradiation mechanical testing)
4	**Integration of components into a basic system** e.g. representative assembly sections have been manufactured and subjected to out-of-reactor tests and/or test reactor irradiation trials of individual rods have been conducted with only limited success
3	**Basic components fabricated and successfully demonstrated** e.g. fuel and/or cladding components have been manufactured and tested out-of-reactor and/or irradiated as a component only
2	**Practical applications suggested and concepts formulated** e.g. fuel, cladding and/or fuel assembly designs have been established
1	**Research identifies the basic principles that underlie the technology** e.g. promising materials and/or geometry have been identified

Table source: This table represents an amalgamation of those presented in [4] and [5].

Table 1: TRL definitions for nuclear fuels and claddings

2.3 Assessing the TRL of the fuel concept down-selections

For each down-selection, a literature search was performed seeking papers in peer-reviewed journals, conference proceedings and reports produced by international nuclear organisations (IAEA, OECD NEA, WNA) as well as the work of national nuclear institutions. Further information was sought where appropriate through attending various conferences and by contact with partners in the international nuclear community. Using this information, it was then possible to use the TRL definitions in Table 1 to assess the TRL of the down-selections.

The ascribed TRLs in Table 2 represent an international best case scenario for each technology with the TRL being representative of its most developed form in the country or countries that have progressed it to the greatest extent. These international TRLs do not necessarily equate to the TRL applicable to individual countries. Table 2 also considered TRLs with respect to the reactor type(s) for which the fuel concept is most developed. A lower TRL may apply to the use of the same fuel concept in a different reactor type. TRLs with respect to reactor type are given in Table 3.

2.4 Limitations of TRL assessments

It should be emphasised that a TRL assessment is at best a crude measure of a complex and ever changing international technological situation. Interpretation and use of the definitions in a TRL assessment is inevitably somewhat subjective and challenging to apply consistently.

TRL assessment gives no indication of the amount of time/effort/cost required to increase a technology's TRL. For example, if two technologies are currently at the same TRL, then there is no guarantee that these will continue to be developed successfully at the same rate. Indeed, a technology currently with a lower TRL may reach deployment sooner than another technology which currently has a higher TRL due to increased R&D effort, fewer feasibility issues, etc. Importantly, there is no guarantee that any technology will ever reach the highest TRL as it may ultimately be found to be unfeasible during further development. TRLs themselves also give no indication of the relative benefits of the different technologies if they were fully deployed, though this weakness can be overcome by plotting TRLs against appropriate measures of benefit.

In spite of these limitations, a TRL assessment remains useful as a guide for further study. It should be noted that TRL values are potentially more useful for comparisons between technologies than they are when considered individually as absolute values.

3. Results

The full details of the TRL assessment of each fuel concept down-selection are given in an NNL report produced for the UK Department of Energy and Climate (DECC) [6]. Details include a full description of each concept and its benefits, a written justification for each ascribed TRL, and the most important literature references (typically 4-8 per technology). A summary of the assessments from the full report is given in this paper using the same 'traffic light' colour coding as Table 1.

Table 2 gives the ascribed international best case TRLs for the down-selected fuel concepts alongside a brief justification and a reference if appropriate. Figure 2 then plots these international best case TRLs in a more visual manner. Finally, Table 3 shows which reactor types the fuels are relevant to and gives TRLs with respect to each. The reactor types considered are Gen III / III+ reactors (LWRs and HWRs) and the six Gen IV systems as listed below [3]:

- SFR, LFR & GFR – sodium, lead & gas-cooled fast reactor respectively
- HTR/VHTR – high and very high temperature reactor
- SCWR – super critical water reactor
- MSR – molten salt reactor

Fuel categories		Best case TRL	Justification and reference
Standard	UO_2	10	Vast majority of fuel that has been used in almost all commercial reactors worldwide for decades [7].
	MOX (<12%PuO_2)	10	Used in many commercial LWRs [7].
New geometries	Annular pellets in LWRs (exc. VVER)	7	Lead assemblies successfully irradiated in Japanese commercial boiling water reactor (BWR) [8]
	Dual Cooled Fuel (DCF)	5	Test rods irradiated in Korean commercial PWR [9]
Evolutionary materials	Advanced UO_2	9	AREVA Cr_2O_3 doped and Westinghouse Cr_2O_3-Al_2O_3 doped fuel are now commercial products [7].
	Advanced MOX	9	High PuO_2 content MOX used in commercial scale SFR in Russia [7].
	Advanced Metal	7	Hundreds of U-Pu-Zr fuel rods irradiated in prototype SFR in USA [10].
New compounds	Carbide	7	Manufacture and irradiation of (U,Pu)C on a prototype scale for SFR especially in India [11].
	Nitride	7	Manufacture and irradiation of UN on a prototype scale for SFR in Russia [12].
	Uranium silicide	4	U_3Si_2 LWR rodlet irradiation programme by Westinghouse-led consortium [13].
New elements	Thorium	8	Significant amount of Th-bearing fuel irradiated in commercial PHWRs in India [14].
	Minor Actinides (MAs)	4	A number of test irradiations of MA fuel have been carried out, targeting SFR application [10].
Including other materials	Inert Matrix Fuels (IMFs)	5	Successful test irradiations of various IMF types targeting Pu and/or MA disposition [10].
	Dispersion	5	Successful irradiation of dispersion fuels based on research reactor designs have been performed [15].
	Zirconium hydride-based	5	Widespread use in TRIGA research reactors with concept development for LWRs [16].
	Coated particle-based	7	Significant manufacturing and irradiation experience for prototype HTRs [17].
Liquid-based	Molten salt	4	Experience of the use of U-based molten salt fuels in test reactors in the USA in the 1950s and 60s [18].

Table 2: International best case TRL assessments for advanced fuels

4. Discussion

Unlike the cladding materials TRL assessment published previously [2], where maximum operating temperature was considered, it was not appropriate to consider different fuel concepts with respect to a figure of merit that can be easily compared in terms of their relative benefit. This was because fuel concepts are required to perform more complex functions than a cladding material, whose primary function is to contain the fuel and fission products. For example, in addition to the release of nuclear energy, fuel concepts may also be required to perform a fuel cycle function. Such functions can include the breeding of fresh fissile material (Pu, or U-233 in the case of a thorium fuel cycle) for use in recycled nuclear fuel and/or the destruction of transuranics (Pu and/or MAs). As a result, considering a figure of merit for fuel concepts such as heavy metal density or melting temperature was not attempted, as it would not take account of the fuel cycle benefits of adopting a

given fuel. Therefore the horizontal axis in Figure 2 has no numerical significance other than ease of presentation, with concepts arranged broadly in order of decreasing TRL from left to right with the exception of the 'new geometries' concepts (annular pellets in LWRs and DCF).

For a number of the fuel concepts (advanced UO_2, MOX and metals as well as Th-based and coated particle), such a large range of sub-concepts within these broader types have been proposed, that it was not appropriate to conclude a single TRL and instead a range was more appropriate. These ranges have been plotted on Figure 2 with TRLs of some of the individual concepts within the range identified. No further explanation of these concepts is given in this paper due to space constraints.

It is difficult to identify an overall trend from Figure 2. Pre-assessment, it might have been expected that the more revolutionary concepts compared to standard fuels would have a lower TRL. However, whilst this trend is in evidence to an extent, there are significant exceptions in the form of the better developed thorium-based and coated particle concepts. Broadly speaking, the TRL results seem to correspond to the relative amount of international effort that has been put into developing the particular fuel concept. However, this would take a much larger study to confirm.

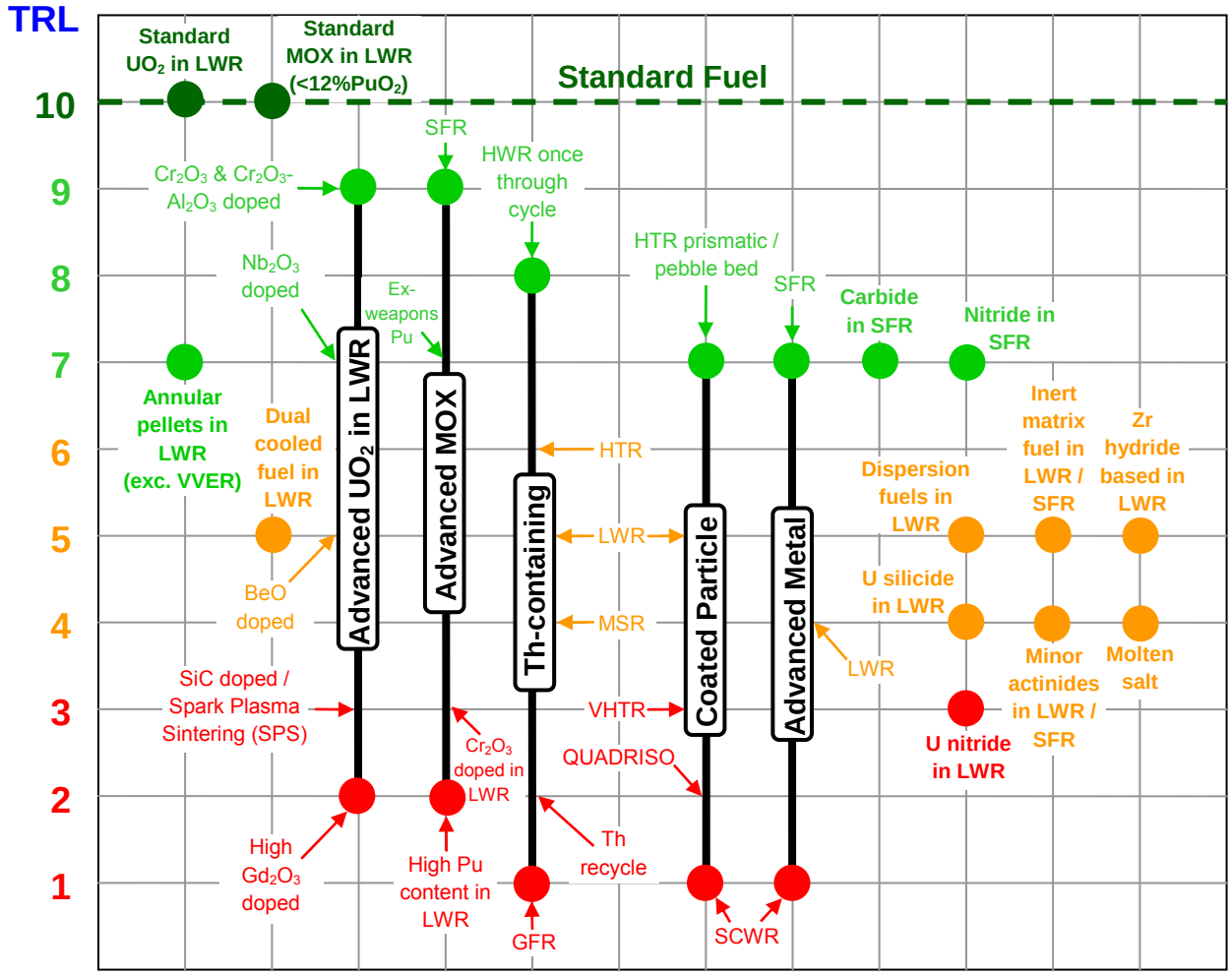

Figure 2. Advanced fuel TRLs

Table 3 shows the complex relationship between fuel TRLs and reactor types. The TRLs for Gen III / III+ L/HWRs show a large range which likely reflects the large amount of R&D effort that has been and continues to be made into developing fuels for these highly successful commercial reactors, with various concepts at different stages in the development pipeline. In general, as might be

expected, fuels for Gen IV systems are less well developed, though fuel materials for SFRs and HTRs have quite high technology readiness (TRL 9 and 7 in the best case respectively), as might be expected from the two Gen IV systems nearest to widespread commercial deployment. The fuel concepts for the other Gen IV systems require significant further development if they are ever to be deployed commercially, as these currently score no better than TRL 4.

Ordered by increasing maximum operating temperature	**Generation**	**III / III+**	**IV**					
	Reactor	**L/HWR**	**SFR**	**SCWR**	**LFR**	**MSR**	**GFR**	**HTR / VHTR**
Advanced fuel categories	**Outlet temperature (°C)**	~325 (PWR)	550	510 – 625	480 – 800	700 – 800	850	650 – 1000
Standard	UO_2	**10**		**3**				**7 in coated particles**
	MOX (<12%PuO_2)	**10**		**2**				**4 in coated particles**
New geometries	Annular pellets in LWRs	**7 (10 in VVER)**		**1**				
	Dual Cooled Fuel (DCF)	**5**		**1**				
Evolutionary	Advanced UO_2	**9 – 2**		**2**				**2 in coated particles**
	Advanced MOX	**7 – 2**	**9**	**2**	**4**		**3**	**2 in coated particles**
	Advanced Metal	**4**	**7**	**1**	**4**			
New compounds	Carbide	**2**	**7**	**1**	**2**		**3**	**6 as oxycarbide in coated particles**
	Nitride	**3**	**7**	**1**	**4**		**1**	**2 in coated particles**
	Uranium silicide	**4**		**1**				
New elements	Thorium	**8 – 5**	**4**	**2**	**2**	**4 in molten salt**	**1**	**6 in coated particles**
	Minor Actinides (MAs)	**4**	**4**	**2**	**3**	**2 in molten salt**	**2**	**2 in coated particles**
Including other materials	Inert Matrix Fuels (IMFs)	**5**	**5**	**2**	**3**		**2**	**2 in coated particles**
	Dispersion	**5**		**1**				
	Zirconium hydride-based	**5**		**1**				
	Coated particle	**5**		**1**			**2**	**7 – 2**
Liquid-based	Molten salt					**4**		

Table 3: TRLs of advanced fuels vs. reactor systems

5. Conclusions

A number of the fuel concepts were found to have higher TRLs than their associated cladding materials, assessed previously [2], which suggests that cladding material development may be the more limiting factor in terms of the deployment of some advanced fuel concepts and possibly even reactor designs. However, such a conclusion should be treated with caution as potential fuel-clad interaction (FCI) must also be investigated in operating and credible accident conditions.

For Generation III / III+ reactors, a number of proposed accident tolerant fuel (ATF) concepts still have relatively low TRLs and hence represent an urgent development priority if their potential safety benefits are to be realised in the shortest possible timeframe in current and soon to be operating reactors.

Finally, the R&D effort required to deploy higher radioactivity fuel concepts – those containing plutonium, minor actinides and recycled thorium – should not be underestimated. Consideration should be given to the widely reported difficulties that have been experienced in deploying new commercial-scale production facilities for even relatively well developed fuel materials with higher radioactivity such as MOX. Deployment may be even more difficult for non-oxide forms of such highly radioactive fuels as some production methods require inert atmospheres.

6. Acknowledgements

This work has been funded by the UK Department of Energy and Climate Change (DECC) under an 'Initial UK National Nuclear R & D Programme'. The authors would also like to thank the following for their assistance:

- **NNL** – Walter Weaver, Dr. David Goddard, Andy Nickson, Dr. Emma Johnston, Alex Brooke, Dan Mathers, Paul Glenville, Aiden Peakman, Robbie Gregg, Mike Thomas, Kevin Hesketh, Dr. Richard Stainsby, Carol Bullen, Paul Smith and Keith Miller.

- **Others** – Dr. Megan Cooper and Rob Arnold of DECC; Prof. Tim Abram, Joel Turner, Matthew Gill, Dr. Maria-Luisa Gentile of Manchester University; Maxime Zabiego, Marion Le Flem, Christian Poette of CEA; Lars Hallstadius and Ed Lahoda of Westinghouse; Prof. James Marrow and Prof. Steve Roberts of Oxford University.

7. References

[1] D. Shepherd (NNL), "TRLs for fuel and cladding", Nuclear Engineering International, p32-33, January 2014.

[2] D. Shepherd (NNL), "Technology readiness level (TRL) assessment of cladding alloys for advanced nuclear fuels", NEA/NSC/WPFC/DOC(2015)9, p108-116, Structural Materials for Innovative Nuclear Systems (SMINS-3), Idaho Falls, USA, 7-10th October 2013.

[3] US DOE and GIF, "A Technology Roadmap for Generation IV Nuclear Energy Systems", GIF-002-00, 2002.

[4] J.C. Mankins (NASA), "Technology Readiness Levels", NASA White Paper, 6th April 1995.

[5] S.L. Hayes and D.L. Porter (INL), "SFR Fuel Performance and Approach to Qualification", Presentation to DOE/NRC Seminar Series on Sodium Fast Reactors, 27-28th November 2007.

[6] D. Shepherd, G.D. Rossiter, I.D. Palmer, G. Marsh, M. Fountain (NNL), “Technology Readiness Level assessment of advanced fuels, cladding and associated manufacturing technology”, NNL (13) 12502, 2013.

[7] IAEA, “Manufacturing technology of uranium and mixed uranium plutonium oxide fuels”, Experiences and Trends of Manufacturing Technology of Advanced Nuclear Fuels”, IAEA-TECDOC-1686, Chapter 2, 2012.

[8] H. Oguma et. al. (Hitachi, Toshiba and JNC), “Technology developments for Japanese BWR MOX fuel utilization”, IAEA-TECDOC-941, p155-170, Technical Committee meeting on Recycling of plutonium and uranium in water reactor fuel, Windermere, UK, 3rd–7th July 1995.

[9] Y.H. Koo et. al. (KAERI), “Status of Dual Cooled Annular Fuel Development in KAERI”, Enlarged Halden Programme Group Meeting, March 2013

[10] OECD-NEA, “State-of-the-art Report on Innovative Fuels for Advanced Nuclear Systems”, NEA No. 6895, 2014.

[11] IAEA, “Carbides and Nitrides”, Status and Trends of Nuclear Fuels Technology for Sodium Cooled Fast Reactors, Nuclear Energy Series, NF-T-4.1, Chapter 4, 2011.

[12] V.M. Poplavsky et. al. (IPPE, VNINNM and RIAR), “Fuels for advanced sodium cooled fast reactors in the Russian Federation: State of the art and prospects”, IAEA, Proceedings of Fast Reactors and Related Fuel Cycles (FR09), p261-275, Kyoto, Japan, 7-11th December 2009.

[13] S. Bragg-Sitton (INL/US DOE), “Overview of International Activities in Accident Tolerant Fuel Development for Light Water Reactors”, Presentation to IAEA Technical Working Group on Fuel Performance and Technology, 24th April 2014

[14] D. Greneche (Nuclear Consulting) and M. Chhor (AREVA), “Development of the thorium fuel cycle”, Nuclear Fuel Cycle Science and Engineering, ISBN 978-0-85709-073-7, Chapter 8, 2012.

[15] IAEA, “Development status of metallic, dispersion and non-oxide advanced and alternative fuels for power and research reactors”, IAEA-TECDOC-1374, Chapters 5 and 6, 2003.

[16] K.A. Terrani et. al. (University of California), “Investigation of liquid metal bonded hydride fuels for LWRs: a review”, Advanced Fuel Pellet Materials and Fuel Rod Design for Water Cooled Reactors, IAEA-TECDOC-1654, p215-228, 2009.

[17] IAEA, “High Temperature Gas Cooled Reactor Fuels and Materials”, IAEA-TECDOC-1645, 2010.

[18] J. Uhlir (UJV Rez), “Chemistry and technology of Molten Salt Reactors – history and perspectives”, Journal of Nuclear Materials, Volume 360, Issue 1, p6-11, 2007.

PILOT PROCESS DEVELOPMENT TO CHANGE SURFACE PROPERTIES PROVIDING THE INCREASED STABILITY OF LWR ZIRCONIUM COMPONENTS IN NORMAL OPERATION CONDITIONS AND IN EMERGENCY SITUATIONS

S.V. IVANOVA, E.M. GLAGOVSKY, I.I. BELUGIN,
Institute of Industrial Nuclear Technologies of National Research Nuclear University "MEPhI"
Kashirskoe sh., 31, 115409, Moscow - Russia

M.S. KHOMICH, O.P. KOROGODA
Scientific-Engineering Enterprise "Polimag"

I.A. KHAZOV
Joint Stock Company "Krasnaya Zvezda"

ABSTRACT

The process and the facility are developed for magnetic abrasive modification that can be used at the same time for both an external and an internal surfaces of tubes of zirconium components. The coatings and the method of their plasma-assisted sedimentation in the initiated gas discharge allowing applying coatings on zirconium components of any form and size are developed. It is determined that simultaneous use of both methods of surface processing (magnetic abrasive modification and coating application) allows achieving a synergetic effect (a summarizing effect surpassing the effect of each type of processing in the form of a simple sum).

1. Introduction

The necessity to increase properties of zirconium components of Light Water Reactor (LWR) fuel assemblies (FA) is caused, on the one hand, by life extension and operation condition toughening of evolutionary and innovative reactors, on the other hand, by increase of requirements for FA components, first of all, to fuel element claddings in accident conditions. These circumstances make new demands to operability of FA components both in normal operation conditions and in emergency modes.

The important operability factors of FA zirconium components are their corrosion stability, hydrogen permeability and wear resistance in normal operation conditions, as well as their behavior (oxidation level) in emergency situations (in accident conditions).

Development of new alloys and their reactor validation require long time (dozens of years) and cause considerable difficulties as the achieved properties of zirconium alloys approached their physical limit. Besides, zirconium alloy composition and structural condition necessary to provide the best "chemical" properties (corrosion stability in water and steam-water mixture) differ from zirconium alloy composition and structural condition necessary to provide the best "physical" properties (deformation resistance, creep, etc.). That is, any, even insignificant, change of existent zirconium alloy composition with the purpose, for example, to decrease corrosion and hydrogenation, may result in decrease in other important operation properties (strength, creep, radiation stability, etc.) [1].

Elimination of these contradictions is possible with change of only zirconium component surface condition (surface structural condition modification, coating application) to increase their operation capacity without changing the zirconium alloy basis properties.

2. Surface magnetic abrasive modification

Now the production uses 2 methods of zirconium product surface finishing processing: 1) mechanical cleaning (abrasive processing, grinding and polishing by abrasive tapes) and 2) etching in hydrofluoric solutions. Grinding disadvantage is presence of residual tensile stresses in a product surface layer after processing which may be the reason of poor cohesion with the surface of protective oxide films. When polishing by abrasive tapes or abrasive processing of surface the abrasive particles can remain in a surface layer of a processed product, having in the subsequent an adverse effect on its long-term corrosion stability. Negative consequences of etching operation are: difficulties at a product cleaning after etching, and also environmental problems [2, 3].

As an alternative to used now finishing operations of mechanical and chemical cleaning of surface of zirconium products the magnetic abrasive modification (MAM) is developed. This processing method lacks the specified disadvantages and can play a double role: 1) to clean a surface of zirconium components from production products and to be used as surface finishing processing instead of grinding, abrasive processing and etching; 2) to improve surface properties: to modify and to microalloy surface.

The essence of MAM process consists in magnetic abrasive powder impact on a processed product surface. Powder is elastically fixed in a magnetic field created in an operating clearance between magnetic poles of an installation. Magnetic abrasive powder particles are a ferromagnetic matrix with abrasive grains interspersed in it, the particles are arranged along the direction of power lines of the operating magnetic field. At that the chains of particles create similarity of a brush which rigidity is defined by magnetic field induction. During MAM under the influence of magnetic field the particles are condensed, nestled on the processed surface, clear, grind and polish it. The process is close to traditional methods of abrasive processing and grinding, however, it has one basic advantage. That is, during MAM the particle cutting edges are constantly renovated as in process of outwearing the particle are "turned over" in the magnetic field holding them, therefore, during the whole processing there is an abrasive cutting (by a sharp edge) rather than abrasive peeling. At that, the processed surface uniform relief is formed consisting of rather shallow parallel microgrooves of cutting. Depth of deformable layer is less than from sanding belts and other abrasive materials. The fundamental difference of MAM from usual grinding by sanding belts with rigidly fixed abrasive grain consists in possibility of flexible management of orientation and effort of cutting of abrasive particles in a processing area.

Surface roughness after MAM is different as per structure: R_a value is less, and ridges are not smoothed as after an abrasive paper, and sharper. As a result, after MAM another microrelief is formed on the processed item surface. Feature of the formed surface microrelief is such that during operation of zirconium components processed in that way there will be a coolant stream turbulization in their surface layer that will improve heat pick up and heat exchange. It is determined that unlike usual abrasive processing and grinding after MAM in a surface layer there are not tensile but compression stresses which promote forming a passive film on a product surface under corrosion slowing down corrosion processes.

The first and most important argument when comparing abrasive methods of processing (grinding by tapes, jet-abrasive processing) and the MAM method is essentially different mechanisms of material removal and processed product surface layer formation. Under grinding and abrasive processing the macro- and micro-processes of product abrasive wear-scratching prevail. These processes at a traverse speed of abrasive grains more than 5 m/s cause high local temperatures (up to 1500 °C) in a contact area of an abrasive grain and a processed product that can be the reason of forming the defects - burns, micro- and submicrocracks in a product surface layer which are potential centers of emergence of nodular corrosion and mechanical destruction. The

processes of submicroscratching, elastic-plastic shift of metal and microsmoothing of a surface prevail during MAM. The temperature in a contact area of a ferroabrasive grain and a processed product does not exceed 150 °C, at that the surface defects peculiar to abrasive processing are not formed.

The role of the applied pulse magnetic field is very important during MAM. It modifies a surface layer causing an action of magnetic-plastic, magnetic-electric and magnetic-striction effects in a processed part surface layer. Under their influence the weakly-fixed defects of a structure (dislocations, disclinations, rotations, etc.) formed on the previous operations of product processing are set in motion (similar to Brownian). The considerable part of the moving defects comes to a surface and is removed by "a soft brush" from ferroabrasive powder. In the course of the subsequent processing there is a modifying of a product surface structural and phase condition, the surface layer is formed with a minimum of structure defects - the potential centers of product material destruction. When using for MAM the special process liquids the other physical and chemical processes of energy exchange and mass transfer at a nuclear and molecular level become more active. These phenomena promote reduction of the processed material structure in an equilibrium condition, "heal" many structure defects. This results in creation of a surface nanorelief with minimum of structure defects and with minimum roughness.

If elements badly influencing the corrosion resistance can be transferred on a surface of a processed product under processing by sanding belts and other abrasive materials, then under MAM specially selected elements can be used as an abrasive which transfer on a surface layer of a processed product will promote improvement of mechanical, chemical and corrosion properties of a product in general.

So, under MAM along with cleaning and modifying of a structural and phase condition of a surface there is a microalloying of a processed product surface layer by an abrasive material that can be considered as a special type of surface modification. The combination under MAM of the above-stated processes of material removal and surface cleaning with removal of undesirable defects of structure, surface modification and introduction of useful elements to a surface layer (microalloying) is a basis of magnetic and abrasive modification process surpassing known analogs by process capabilities, economic and ecological parameters. MAM gives the possibility to process not only one of surfaces of fuel element claddings and other FA components: external or internal, but also allows to process simultaneously external and internal surfaces, at that after MAM the roughness of external surface does not exceed 0.2 microns, and internal - 0.4 microns.

Now we have developed:

- the most optimum compositions of abrasive powders: ferrosilicium (FS) and silicium aloy (FT);
- an installation prototype which allows performing the process of magnetic abrasive modification of simultaneously external and internal surface of zirconium pipes (including fuel element claddings) at magnetic induction values in an operating area up to 1 Tesla.

2.1 The installation technical characteristics

- diameter of the processed tubes, mm – 6-15;
- length of the processed tubes, m – 0.7-5.0;
- processing of simultaneously external and internal surface of tubes;
- surface roughness: external – Ra $\leq$ 0.2 microns, internal – Ra $\leq$ 0.4 microns;
- metal dimensional removal, micron – 10-30;
- power consumption, kW – 2.5;
- the installation overall dimensions: Length $\times$ Width $\times$ Height, m – 11.5 x 0.6 x 1.3;
- the installation weight, kg – 200.

2.2 Corrosion resistance investigation for zirconium products with modified surface

For comparative evaluation of surface quality after different methods of finishing processing, and also properties of oxide films formed on this surface under corrosion, the corrosion tests of fuel element cladding samples from an alloy E110 (Zr-1%Nb) were performed after grinding, etching and MAM in steam-and-water environment in autoclaves at temperature 400º C and pressure of 20.3 MPa. To characterize sample surface condition after tests, beside an weight gain we used measurements of electrolytic capacity. Investigation results are given in Tab 1.

Tab 1: Influence of processing method of alloy E110 fuel rod cladding surface on properties of oxide films formed thereon during corrosion tests at temperature 400^0C and pressure 200 atm. within 30 days

Surface processing method	Weight gain W, mg/dm^2	Index of protective properties 1/CW, $cm^4/mg \cdot microfarad$
Grinding	46.02	2.9
Etching	42.53	3.8
MAM FT	40.46	13.3
MAM FS	35.77	16.5

To estimate of properties of oxide film formed on the sample surface during corrosion tests, index 1/CW was used (applied as characteristic of protective properties of corrosion films [4]), representing the ratio between protective (nonporous) part of film 1/C (where C is electrolytic capacity) and overall thickness of oxide film as per weight gain W. After electrolytical capacity measurements, barrier voltage of oxide layer on a specimen, i.e. voltage when there is a dielectric breakdown of barrier part of oxide film was identified. For that, the current with density 0.2 mA/cm^2 was supplied on the cell with measured specimen using potentiostate and the origination moment of voltage oscillations indicating the dielectric breakdown was determined.

The implemented tests shows that MAM results in increase of zirconium item corrosion stability and raises protective properties of oxide films formed thereon in 4,5-5,5 times, that it's very important for long-term corrosion stability during operation.

With the purpose to study influence of MAM of a surface of zirconium products on their corrosion stability during operation in a reactor we have performed tests of cladding samples in autoclave condition closed to operation condition in water at temperature 360°C (maximal temperature of fuel rod cladding operation of VVER-1200 type reactors) and pressure 18 MPa.

The test results, see Fig 1, have shown that MAM results in increase of zirconium item corrosion stability, the greatest positive influence is caused by MAM by abrasive powder FS. And, if after 3 days of tests the weight gains of grinded samples and samples after MAM are close by value, with increase in test time the corrosion resistance of grinded samples decreases in comparison with the corrosion resistance of samples after MAM. If in the range from 120 to 280 days of tests a tilt angle of corrosion curves of samples after grinding and MAM is almost identical, only values of weight gains differ which is less for samples after MAM, after 280 days of tests on a curve of grinded samples there is an inflection and the tilt angle increases. At that, the tilt angle of corrosion curves after MAM does not considerably change. We may conclude that the long-term corrosion resistance of grinded samples concedes to the long-term corrosion resistance of samples after MAM.

Hence, if we use MAM as finishing processing of zirconium items, we can raise their long-term corrosion stability.

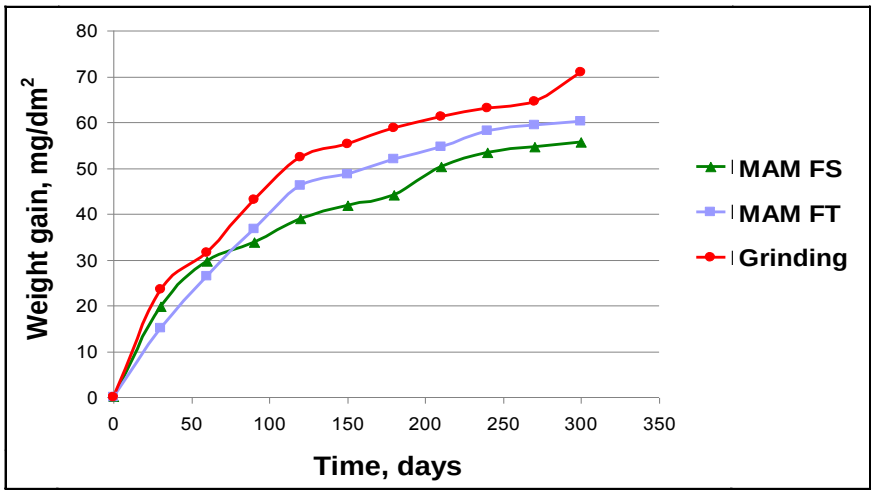

Fig 1. Results of corrosion tests in water at temperature 360°C and pressure 18 MPa of fuel element cladding samples with surface different processing: grinding and MAM by various composition powders

3. Protective coatings to increase corrosion resistance of zirconium components during operation and in emergency situations

It was necessary to find such coating compositions which would allow increasing the corrosion resistance of zirconium components not only in operational conditions, but also in the conditions of emergency situations (maximum design accident like LOCA and beyond design accident). Functional properties of coatings are defined not only by their composition, but also by coating application method, and also by adhesion.
3 coating options were investigated:
1) multilayer chromium based coating – XP;
2) two-component chromium based coating – X-XA;
3) two-component titanium based coating with ion mixing – TU mix;
4) electrolytic and plasma coating – EPP.

Characteristics of developed coatings are given in Tab 2. Tab 2 shows average values obtained for 3-5 samples.

Tab 2: Characteristics of developed coating

Coating	Coating thickness, micron	Coating density, g/cm^3	Surface roughness, Ra, micron	Microhardness, HV_{50}, kg/mm^2	Microhardness, HV_{100}, kg/mm^2
Without coating	–	–	0.60	210.5	198.6
XP	4.0–4.3	5.3	0.26	276.0	253.7
X-XA	4.5–5.0	4.6	0.40	413.3	328.0
TU mix	2.0–2.5	4.6	0.40	413.3	328.0
EPP	5.0–5.5	3.2	0.36	226.7	224.9

3.1 Corrosion resistance of developed coatings in operation conditions

To investigate corrosion stability of developed coatings we have performed autoclave tests of fuel element cladding samples of alloy E110 without coating and with protective coatings in water at temperature 360 °C and pressure 18 MPa. Corrosion test results are given in Fig 2.

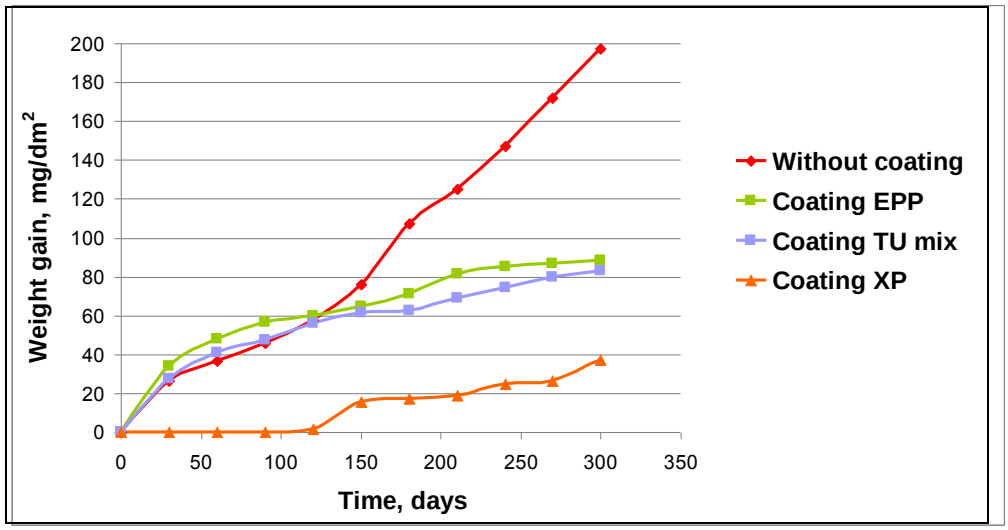

Fig 2. Results of corrosion tests in water at temperature 360°C and pressure 18 MPa of fuel element cladding samples with different types of coatings

Under the results the developed protective coatings considerably (in 2 times and more) increase corrosion stability of zirconium products. The greatest protective anticorrosive effect has the coating XP. Scanning electronic microscopy method (Fig 3) allowed to find out traces of destruction of oxide film formed on a surface of zirconium samples without coating (Fig 3a and 3b) after corrosion tests which are shown in the form of cracks and swellings (shown in figure by white arrows). On samples with coatings at this stage of corrosion tests we did not reveal traces of de-

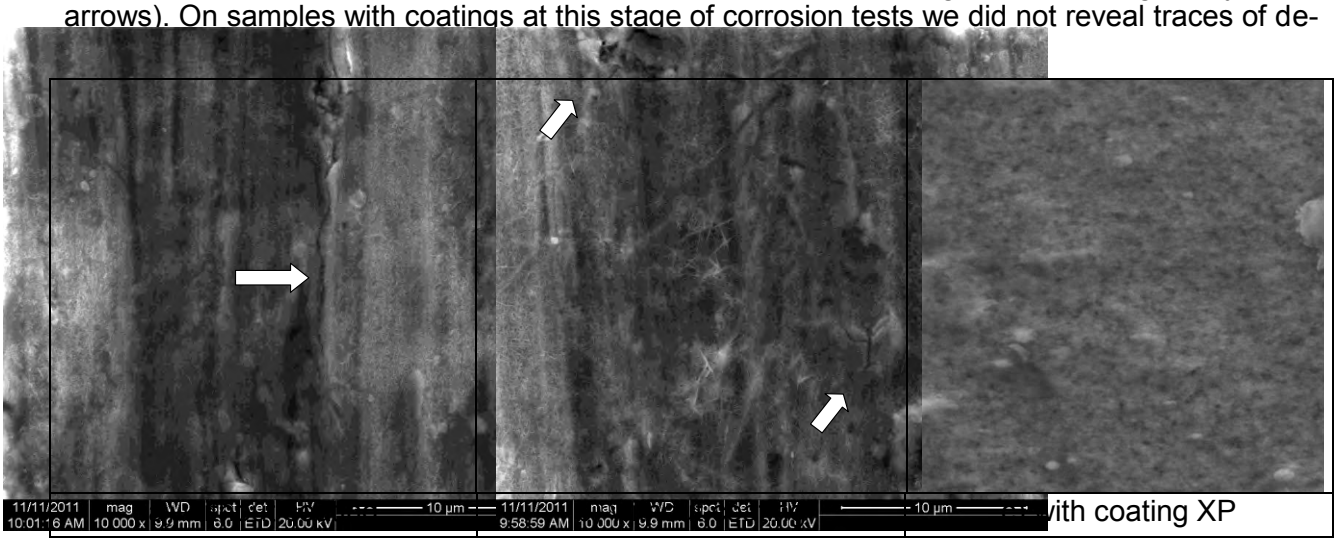

	ith coating XP
after 72 h of corrosion tests	after 144 h of corrosion tests

Fig 3. Electron-microscopic images of sample surface without coating after corrosion tests (x10000)

3.2 Corrosion resistance of developed coatings in emergency situations

Tests were performed under two scenarios:

1. Imitation of maximum design-basis accident (MDBA) with exposure at maximal temperature 33 and 69 sec.
2. Imitation of beyond design-basis accident with long exposure at maximal temperature during 1 and 4 h.

High-temperature exposures from 1 to 4 hours simulated design failure development into beyond design-basis accident when occurrence and course of failure take place within several hours

down to failure localization and temperature decrease up to 30...50 ºC. At that on samples without coatings the maximum permissible depth of cladding oxidation was achieved making 18% from thickness of a cladding wall. Such long impacts of high temperature may occur also during local overheats of fuel element claddings under corrosion product precipitations, during fuel element contacts and flow section reduction, and also in cases of leak formation.

Modes and results of sample tests are given in Tab 3 and in Fig 4. According to the investigation results, the developed coatings essentially protect fuel element claddings from corrosion not only in operation conditions, but also in conditions of various emergency situations (design-basis accident with coolant loss and beyond design-basis accident). The surface of initial samples not protected by coating, essentially corroded during tests, and with increase in exposure time at maximal test temperature friable thick white showered oxide film was formed on their surface (see Tab 3), and samples with protective coatings tested simultaneously in the same conditions preserved a rigidly adherent film on the surface. Corrosion stability of samples after deposition of protective coatings has increased from 2 up to 7 times depending on coating composition and test mode.

Tab 3: Modes and results of sample tests

Processing type	Test temperature, °C	Test time	Gain, mg/dm^2	Increase of corrosion stability of samples with coatings	Sample appearance after tests
Without coating	1100	33 sec	126.94		Black, shining
Coating X-XA			39.09	3.3 times	Yellow-blue, shining
Without coating	1100	69 sec	270.00		Sample is covered with white oxide film
Coating XP			54.25	5.0 times	Green, shining
Coating X-XA			46.79	5.8 times	Yellow-blue, Shining
Without coating	1100	1 hour	1200.00		Sample is covered with white showered oxide film
Coating XP			413.36	2.9 times	Green
Coating X-XA			175.52	6.8 times	Dark-green
Without coating	1100	4 hours	2800.00		Very strongly showered white oxide film
Coating X-XA			780.17	3.6 times	Grey-blue

It means that the contribution of steam-zirconium reaction to thermal emission at MDBA will decrease equally (in 2–7 times), that will reduce temperature of surface of FA zirconium components and develop more sparing conditions for them during MDBA. This fact has proved to be true during tests as under indications of gauges (on external and internal surface of samples) during tests the temperature on samples with coatings was less than on samples without coatings at identical temperature in the test chamber.

And it means that deposition on fuel element claddings of the developed protective coatings will allow to increase reliability of fuel elements at MDBA and will enable FA designers to reasonably reduce wall thickness of fuel element claddings with the purpose to increase uranium loading in them and increase reactor technical and economic parameters.

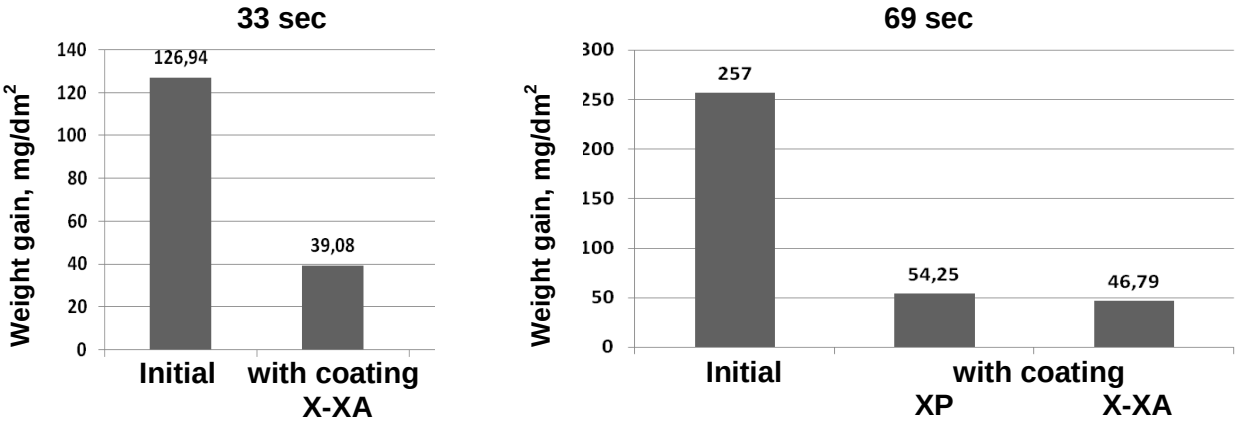

a) Test results in conditions of maximum design-basis accident

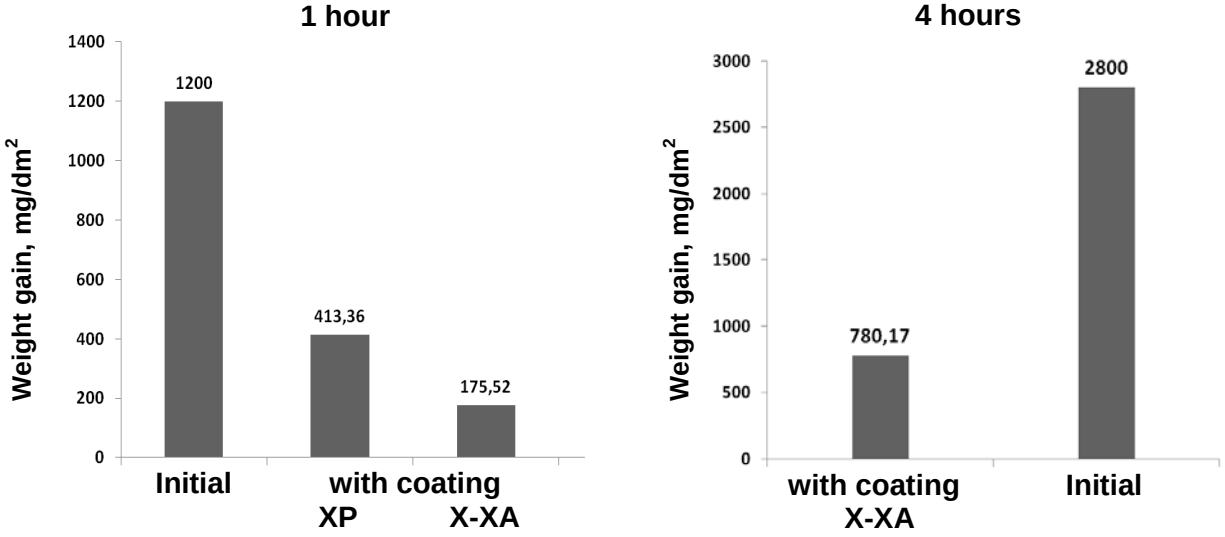

b) Test results in conditions of beyond design-basis accident

Fig 4. Test results of fuel element cladding samples with protective coatings in emergency situations

3.3 Coating application method

Except composition of protective coatings, the method of its application is of great importance which should provide a good adhesion of coatings, application of coatings on FA full-scale components and to be realized in industrial conditions. To solve this task the method was used to apply coatings in the initiated gas discharge with the filament cathode created in three-electrode system (the filament cathode, the intermediate anode, the anode). The spraying installation developed for this purpose has a number of advantages in comparison with the installations using widespread magnetron, arc and other discharges with cathode which is at the same time a sprayed target. In the initiated gas discharge the sprayed surfaces and the sprayed target (the sprayed targets) are located in the field of the gas discharge (in plasma volume), but functions of plasma creation and management of its parameters and a function of ion impact on the sprayed target (the sprayed targets) are separated. It allows realizing a number of operations in the initiated discharge which implementation in discharges of other types is possible in the narrow range of parameters or impossible in general.

Advantages and opportunities of method and installation for coating application in initiated gas discharge with filament cathode:

1. The developed method of coating application allows applying coatings both on an external surface of zirconium components and on the internal.
2. Coatings can be applied on components of any shape and the size.
3. Temperature of coating application can vary according to requirements to products on which the coatings are applied.
4. The method allows applying coatings at the same time on several products, i.e. to organize line production.
5. The developed method of coating application and the installations for its realization can be used in mass industrial production.

4. Combination of magnetic abrasive modification and coating application method in initiated gas discharge with filament cathode

4.1 Investigation of adhesive properties

As it was already said above, except composition of protective coating and a method of its application the adhesive properties of a coating are also of great importance which in many respects depend on a surface condition on which the coating is applied.

To define how the method of finishing processing of a fuel element cladding surface influences adhesive properties of the coating applied on it, comparative investigations were performed of adhesive properties of a coating TU mix which was applied on fuel element cladding samples from alloy E110 with a grinded surface and with a surface after MAM. Adhesive properties of coatings were investigated on the CSEM MicroScratchTester installation with 2 load options of F1 and F2. The results are given in Fig 5 and 6 and in Tab 4.

a) 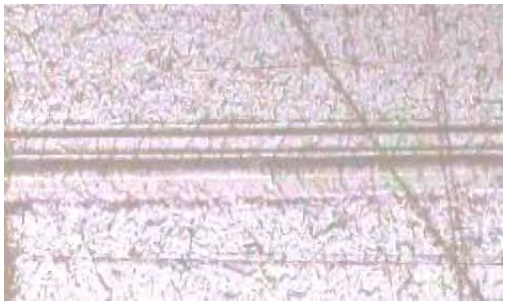 b) 

Fig 5. Photos of scratches at critical loading F1 for TU mix coating
a) coating is applied on fuel element cladding from E110 alloy with grinded surface
b) coating is applied on fuel element cladding from E110 alloy after MAM

a)  b) 

Fig 6. Photos of scratches at critical loading F2 for TU mix coating
a) coating is applied on fuel element cladding from E110 alloy with grinded surface
b) coating is applied on fuel element cladding from E110 alloy after MAM

Tab 4: Results of adhesive characteristics of coatings

Sample	Critical force F1, H	Critical force F2, H
Coating is applied on grinded surface	0.8	1.48
Coating is applied on surface after MAM	2.9	3.83

It follows from investigation results of adhesive properties that coating destruction for samples when it is applied on a grinded surface begins with smaller critical force of F1, than for samples with the coating applied on a surface after MAM. Also peeling and chipping of coatings with the critical force of F2 for samples with a grinded surface begins with smaller loading than for samples with a surface after MAM that speaks on a greater adhesive ability of a coating TU mix applied on a surface after MAM.

4.2 Investigation of corrosion properties

Corrosion properties were investigated of fuel element cladding samples from E110 alloy with TU mix coating applied: on grinded surface and on surface after MAM. Under the investigation results the corrosion weight gains for samples which coating was applied on grinded surface, were 25% more than for samples with coatings applied on surface after MAM. Thus, it was shown that simultaneous use of both methods of surface modification (magnetic abrasive modification and coating application) promotes the synergetic effect (summarizing effect surpassing effect of each type of processing).

5. Conclusion

1. We have developed the process bases and the facility for MAM of at the same time an external and an internal surfaces of tubes of zirconium components.
2. The coatings and the method of their plasma-assisted sedimentation in the initiated gas discharge with the filament cathode allowing applying coatings on zirconium components of any form and size are developed. At that, the developed coatings allowed to increase corrosion resistance of zirconium components both in normal operation conditions and in emergency situations: maximum design accident like LOCA and beyond design accident.
3. It is determined that simultaneous use of both methods of surface processing allows achieving a synergetic effect (a summarizing effect surpassing the effect of each type of processing in the form of a simple sum).

6. References

1. Ivanova S.V., Glagovsky E.M. Khazov I.A., Orlov V.K., Shlepov I.A., Nikitin K.N., Dubrovsky Y.V., Denisov E.A. Modification of a surface of zirconium components of thermal reactor FA with the aim to increase their operation properties. J. Physics and chemistry of material processing, 2009, No.3, p.5-7.
2. Zenguil E. Physics of a surface. Transl. from English, M.: Mir, 1990, 535 p.
3. Pankov L.A., Kostin N.V. Processing by grinding sandpaper tools, L.: Mechanical engineering, 1988, 235 p.
4. Wanklyn J.N., Silvester D.R. // J. Electrochem. Soc. 1958. Vol. 105. No.11. P. 647-654.

HIGH-RESOLUTION CHARACTERIZATION OF CORROSION AND HYDROGEN PICKUP OF ZR CLADDING ALLOYS

J.Hu*, B. Setiadinata, T. Aarholt, P. Bagot, M. Moody, S. Lozano-Perez, C. Grovenor
Department of Materials, University of Oxford, Parks Road, Oxford, UK
A. Garner, A. Harte, K. Moore, P. Frankel, M. Preuss
Materials Performance Centre, School of Materials, University of Manchester, Manchester, UK
N. Ni
Department of Materials, Imperial College London, Royal School of Mines, London, UK
*Tel: +44 (0)7583260056 Email: jing.hu@materials.ox.ac.uk

ABSTRACT

As part of the MUZIC-2 project, several state-of-the-art high resolution analysis techniques are being used to study the microstructure of a range of commercial and developmental Zr alloys corroded under autoclave simulated PWR conditions. Samples were chosen to be representative of the early, pre-transition, transition and post-transition stages of the oxidation process. We have studied the development of the equiaxed-columnar-equiaxed grain structure, and observe that the columnar grains are both longer and show a stronger preferred texture in more corrosion-resistant alloys. Fresnel imaging revealed the existence of both parallel interconnected pores and some vertically interconnected pores along the columnar oxide grain boundaries, which become disconnected near the metal-oxide interface. Analytical (Scanning) Transmission Electron Microscope ((S)TEM) has been used to study two types of second phase particles (SPPs): β-Nb and $Zr(Nb,Fe)_2$. The $Zr(Nb,Fe)_2$ SPPs are present at a lower number density and tend to become amorphous quickly once incorporated into the growing oxide. Atom Probe Tomography (APT) was used to study finer Nb and Fe clusters in the suboxide and metal regions, Fe clusters are also found at the oxide grain boundaries. Electron Energy Loss Spectroscopy analysis (EELS) and automated crystal orientation mapping with TEM have also revealed Widmanstatten-type suboxide layers in some samples with compositions in different regions of either the hexagonal ZrO structure predicted with *ab initio* modelling or Zr_3O_2. Some of these layers are much thicker than observed previously in other oxidised zirconium alloys. Hydrogen pickup mechanisms have been studied by high resolution Secondary Ion Mass Spectrometry (NanoSIMS) analysis of deuterium-spiked samples, showing that at different stages of oxidation the penetration of deuterium occurs in quite different patterns. These observations are discussed in the context of current models for oxidation and hydrogen pickup in zirconium alloys.

1. Introduction

For the past five decades, Zr alloys have been selected for use as nuclear fuel cladding and major components of the fuel assembly in nuclear reactors. These alloys show a low thermal neutron absorption cross section and reasonable mechanical properties. However, the major problems associated with cladding applications are high temperature aqueous corrosion and hydrogen pickup (HPU)[1].

The oxidation kinetics of Zr alloys start with an initial pre-transition period of parabolic growth kinetics followed by cycles of increased oxidation rate, and eventually an abrupt increase called ‘‘breakaway’’ to almost linear kinetics[2]. Some of the liberated hydrogen from the corrosion process is absorbed into the metal, which can lead to further problems such as delayed hydride cracking (DHC). Careful kinetics studies have shown that the hydrogen pickup(HPU) rate is related to the oxidation rate and alloying chemistry of Zr alloys[3].

In recent years, developments of modern microscopy and sample preparation techniques have allowed us to understand the microstructural and microchemistry changes during the

oxidation and HPU processes in unprecedented detail. In this work, the same Zr-1Nb alloys were treated in the autoclave with periodic measurements of oxidation weight gain. Samples from early, pre-transition, transition and post-transition stages were studied using state-of-the-art microscopy techniques including (Scanning) Transmission Electron Microscope((S)TEM), Electron Energy Loss Spectroscopy (EELS), Energy-dispersive X-ray Spectroscopy (EDX), automated crystal orientation mapping with TEM (ASTAR), Atom Probe Tomography (APT) and high resolution Secondary Ion Mass Spectrometry (NanoSIMS).

2. Materials and Method

In this work, Zr cladding tubes from a Westinghouse developmental alloy were selected. The composition of the Zr-1Nb alloys was measured by EDF using inductively coupled plasma atomic emission spectrometry (ICP-AES) as Zr-0.9Nb-0.01Sn-0.08Fe (wt%) and all samples were in the recrystallized state. The bulk Zr cladding tube samples were oxidised in an autoclave at EDF under simulated Pressurized Water Reactor (PWR) water conditions at 360°C for up to 540 days and some samples then received an additional exposure to deuterated water for further 45 days. Details of autoclave testing and oxidation kinetics are reported elsewhere[4]. The weight gain data in Fig.1 shows that, although the weight gain data show no obvious signs of transition after 360 days, the HAADF image of 360day sample in Fig.1 reveals a first layer of cracks next to the metal-oxide interface which might suggest that transition has just started. The 585-day sample shows two layers of cracks which suggests two transitions have happened.

In order to observe the microstructural changes during the oxidation process, four samples were selected for detailed analysis, as shown by the circles in Fig.1. Sample A from the early stage of pre-transition was oxidised for 120 days. Sample B which represents the early stage of pre-transition has been oxidised initially for 180 days and received an additional exposure to deuterated water for a further 45 days. Sample C is close to first-transition and was oxidised for 360 days. Sample D which represents the post-transition stage was initially oxidised for 540 days and then exposed to deuterated water for a further 45 days. The inserts in Fig.1 are Scanning Transmission Electron Microscope (STEM) High Angle Annular Dark Field (HAADF) images of the samples showing the general microstructural changes at different stages of the oxidation process.

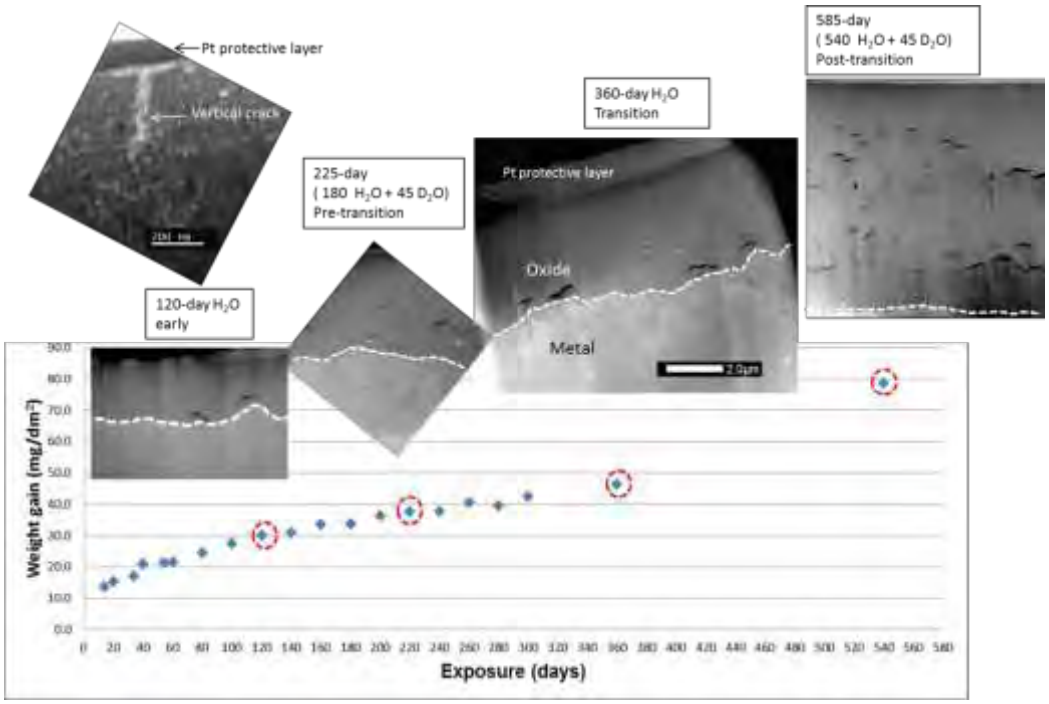

Figure 1: Autoclave corrosion weight gain profiles showing averaged weight gain values for Zr-1Nb samples. Samples selected for further study are circled in red, with STEM HAADF images of the samples inset (scale bar applies to all images) Top corner TEM-BF image shows vertical crack from the sample surface till oxide for about 400nm in length..

The four tube samples around 30 mm long and 9.5mm in diameter were cut into small pieces with a diamond saw. TEM samples were prepared by the *in-situ* lift out method on an FEI FIB200 and further thinned down to a thickness below 100nm in a Zeiss Nvision 40 dual beam FIB to create a homogeneous and electron-transparent sample for TEM and STEM analysis. The samples were further thinned down to ~50nm using low-voltage conditions for final EELS analysis on selected regions of interest. TEM and STEM analysis were performed on a JEOL 2100 LaB_6 microscope operated at 200kV. EELS spectrum imaging was performed on a JEOL ARM microscope operated at 200kV and equipped with a Gatan image filter. The convergence half-angle α was 20mrad and collection half-angle β was 30mrad with an energy dispersion of 0.5eV per channel and a step size of 7.7nm. Automated crystal orientation mapping with TEM was performed in an FEI Tecnai F30 Field Emission Gun Transmission Electron Microscope (FEG-TEM) operating at 300 keV with precession angle of 0.8° and 5nm step size. Data analysis was carried out using a NanoMEGAS ASTAR automated crystal orientation mapping system.

APT specimens from 225-day and 585-day Zr-1Nb samples were also prepared by *in-situ* lift out using a Zeiss NVision 40 dual-beam FIB. Needle-like samples with tip diameter less than 100nm were prepared for analysis near the oxide/suboxide-metal interface. The needles were tested in a Cameca LEAP3000X with laser energy of 0.5nJ and repetition rate 200kHz and the data reconstruction was carried out using iVAS 3.6.6 software.

The materials selected for NanoSIMS analysis were 225-day and 585-day Zr-1Nb, samples were set in epoxy resin and metallurgically polished in cross-section to a 40nm colloidal silica finish to reveal the metal-oxide interface. Immediately thereafter, 5nm of platinum was deposited onto the surface to ensure conductivity and minimise oxidation of the metal surface.

Samples were analysed on a CAMECA NanoSIMS50 with a 16keV primary Cs^+ beam. The ^{16}O signal was detected to indicate the exact location of the metal-oxide interface, and the ^{2}H signal was detected to show deuterium localisation[5]. As hydrogen was present in the vacuum chamber, in carbon contaminants and in the previously oxidised material, the use of deuterium showed how hydrogenic species interact with the microstructure during the 45 days of deuterated oxidation. As deuterium is only present with a natural isotopic abundance of only 0.01%, it was assumed that any deuterium detected was from the 100% heavy-water oxidation stage.

3. Results and discussions

3.1 Overview of Oxide Morphology

Fig. 1 shows STEM HAADF images of the four selected Zr-1Nb samples. In the pre-transition samples oxidised for 120, 225 and 360 days, the oxide grows from 1.5 µm in overall thickness to about 3.0 µm overall when it reaches the transition point, and to 5.4 µm in the 585-day sample. In all the pre-transition samples, macro-cracks around 0.6-1.2um in length parallel to the metal-oxide interface are scattered near the metal-oxide interface as reported in previous studies[6,7]. In addition, much smaller micro-cracks or flake-like porosity 40-50nm in length cuts through the columnar grains or is located near the metal-oxide interface. In the post-transition 585-day sample, there are two distinct layers of cracks parallel to the metal-oxide interface, although the two layers are not exactly parallel which suggests the local transition happens at different times in different locations, in agreement with previous observation[6]. Although there is no available autoclave data between 360 and 585 days, the two layers of cracks suggest that the sample has gone through two transitions. There is

another 1.5 μm thick region with small oxide grains between the second layer of crack and the metal-oxide interface, showing that the sample may still be in the fast oxidation rate region after the second transition.

The top ~700nm layer of pre-transition samples consists of equiaxed grains with a grain size ~20nm. In the post-transition sample, equiaxed grains near the two layers of cracks were also observed. Cracks and pores are found around these small equiaxed grains near the sample surface. It is worth mentioning that at a much lower density there are vertical cracks from the sample surface about 400nm in length as shown in the inserted image in Fig.1. This type of cracks provides the best paths for oxygen towards the metal-oxide interface. Since this type of cracking is observed very rarely, we do not believe that it is a general feature of FIB-prepared TEM samples. Other authors have observed similar vertical cracks[8]. Under the equiaxed layer in the pre-transition samples, and between the two layers of cracks in the post-transition samples, there are larger columnar grains around 30-50nm wide and 500nm in length.

3.2 Porosity in Fresnel Imaging

By using Fresnel imaging in the TEM, different types of porosity can be easily identified. The outer equiaxed part of all the oxides is very porous, with individual pores around 10nm in diameter at oxide grain boundaries. Around 500nm further into the oxide, small flake-like pores around 200nm in length start to appear parallel to the metal-oxide interface between equiaxed and columnar oxide grains. The columnar oxide grains have flake-like porosity 50nm wide at the top and 20nm wide across the middle of grains. There are also individual pores inside columnar grains, which suggests that bulk lattice migration is a possible path for oxygen transport. Some of the individual pores are connected, creating an interconnected array of nanocracks around 20nm in width as shown in Fig 2. (a) ~200 nm away from the metal-oxide interface of the 225-day sample. Near the metal-oxide interface, columnar grain boundaries are more commonly seen to be decorated with vertically interconnected pores, as seen in the Fig. 2(b) which is taken close to (a). Towards the end of the vertical connected porosity, the pores gradually become disconnected as we move closer the metal-oxide interface. In Fig. 2(c) there are disconnected pores along the columnar grain boundaries and also individual pores at the metal-oxide interface and the suboxide region underneath which is the oxygen sink for the most recent oxidation process. In Fig. 2(d), at the end of the columnar grains, another type of connected porosity is seen along the metal-oxide interface. This kind of complex interconnected porosity is proposed to play an important role in the rate determining oxygen diffusion process[9].

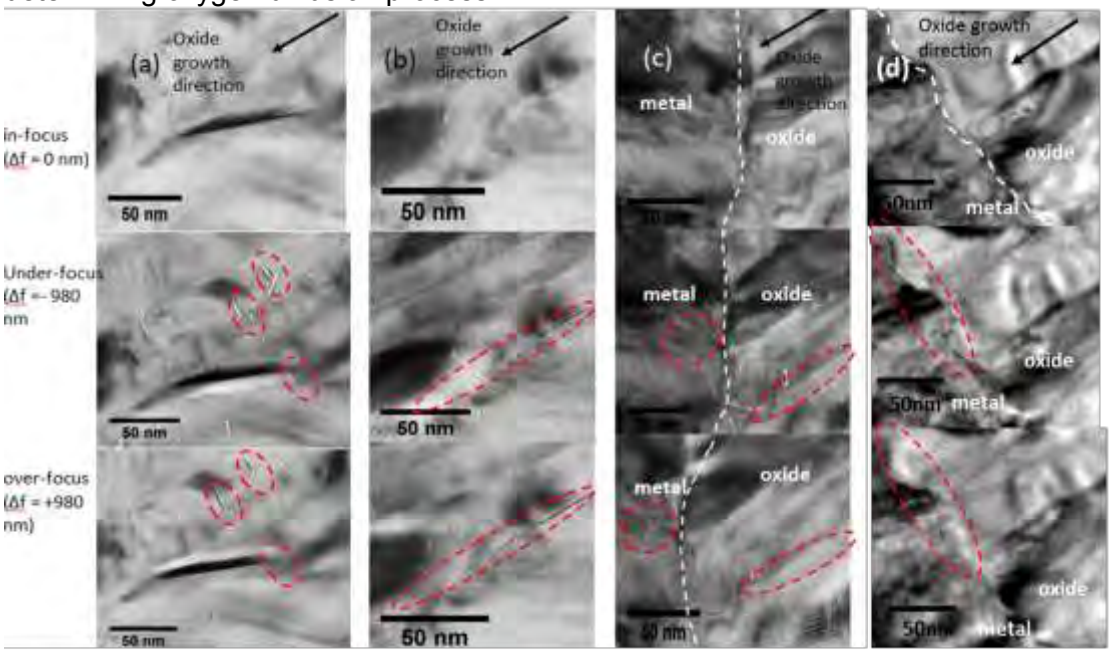

Figure 2: Through-focal imaging of fine pores (circled) close to the metal-oxide interface in the 225-day Zr-1Nb sample. The pores are invisible in the top in-focus images (Δf = 0 nm), but show Fresnel contrast in the middle under-focussed images (Δf = -980 nm) and in the lower over-focussed images (Δf = +980 nm). Three different types of porosity are revealed at different locations: (a) 100nm from the metal-oxide interface: parallel interconnected pores; (b) 100nm from the metal-oxide interface: vertically interconnected pores along the columnar oxide grain boundaries; (c) near the metal-oxide interface: disconnected pores. (d) connected porosity under the columnar grains right at the metal-oxide interface.

3.3 Second Phase Particles

We have studied SPPs in some details because they are proposed to offer cathodic sites for hydrogen penetration and also become oxidised and release aliovalent elements which can affect the local electronic conductivity in the oxides.

3.3.1 EELS mapping of SPPs

Analytical (S)TEM revealed two types of second phase particles: β-Nb and $Zr(Nb,Fe)_2$. The $Zr(Nb,Fe)_2$ SPPs are present at a lower number density and tend to become amorphous quickly as the oxide grows.

EELS spectrum imaging was carried out on the 120-day sample. Fig. 3(a)-(d) shows the EELS core loss results. In Fig.3 (a), STEM HAADF image of three SPPs is taken around 300-500 nm from the metal-oxide interface where there is a parallel crack. EDX mapping of the same region has shown that both the top and middle SPPs (SPP1 and 2) contain Fe and Nb, and the bottom one (SPP3) contains Nb only. Fig.3 (b)-(d) shows different oxidation stages for these three SPPs: SPP1 is fully oxidised, SPP2 is partially oxidised with the bottom part remaining metallic, while SPP3 has the lowest oxygen content (metallic). This illustrates the gradual oxidation process of the SPPs as they move away from the metal-oxide interface during oxide thickening.

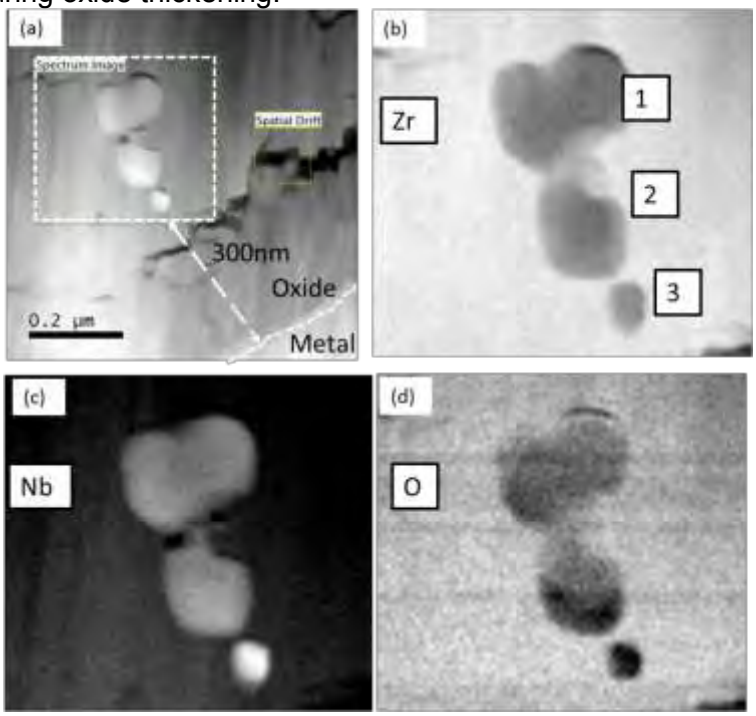

Figure 3: (a) STEM HAADF image of an area containing three SPPs about 300nm away from the metal-oxide interface. (b)-(d) Core loss EELS mappings of Zr, Nb and Oxygen respectively. These three SPPs are labelled as SPP1, SPP2, SPP3 in (b). SPP1 is fully oxidised, SPP2 is partially oxidised, and SPP3 is metallic.

3.3.2 Atom Probe Tomography of SPPs

We have used APT to study the chemistry of the metal-oxide interface at the atomic scale. The sensitivity of this technique means that the distribution of even dilute impurity elements like Fe can be studied in detail.

The APT results in Fig. 4 show the presence of two β-Nb particles. These particles have similar concentration profiles, containing ~85at% Nb and ~13at% Zr at the core. Fe atoms decorate the precipitate-metal interface with a maximum concentration of ~0.9at%, but very little Fe is found inside the precipitates.

A partially-oxidised Nb-rich particle similar to those observed in Fig. 3 is observed in the ZrO suboxide adjacent to the metal-oxide interface. This particle is about ~4nm in diameter with the core containing ~50at% Nb, ~30at% Zr, and ~20at% O. Fe is now present inside the precipitate rather than at the periphery of the particle, with maximum Fe concentration of ~3.5at%.

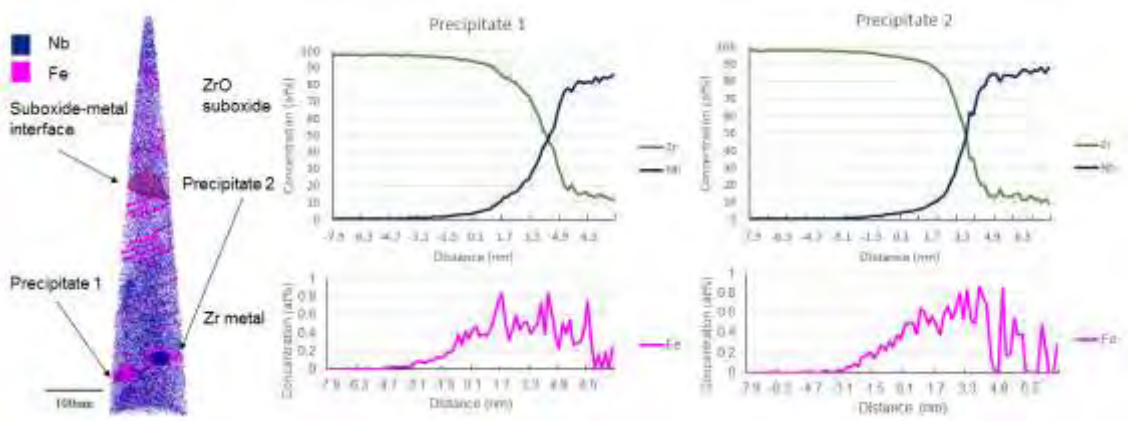

Figure 4: Atom map showing Nb and Fe distributions near the suboxide-metal interface of the 225-day Zr-1Nb sample. Two β-Nb particles are found in the metal with similar concentration profiles across the precipitate-metal.

Group of Nb clusters have also been observed in the ZrO and metal regions, as seen in Fig. 5 (a) and (b), but only a few of them was found in the bulk ZrO_2. Many Fe clusters were found in O-saturated metal (Fig. 5 (c)) and only a few in ZrO_2. This indicates that both Fe and Nb clusters can be dissolved into bulk oxide during oxidation. In addition, it has been observed that grain boundaries were found to be enriched in Fe, as has been observed by other authors[10,11].

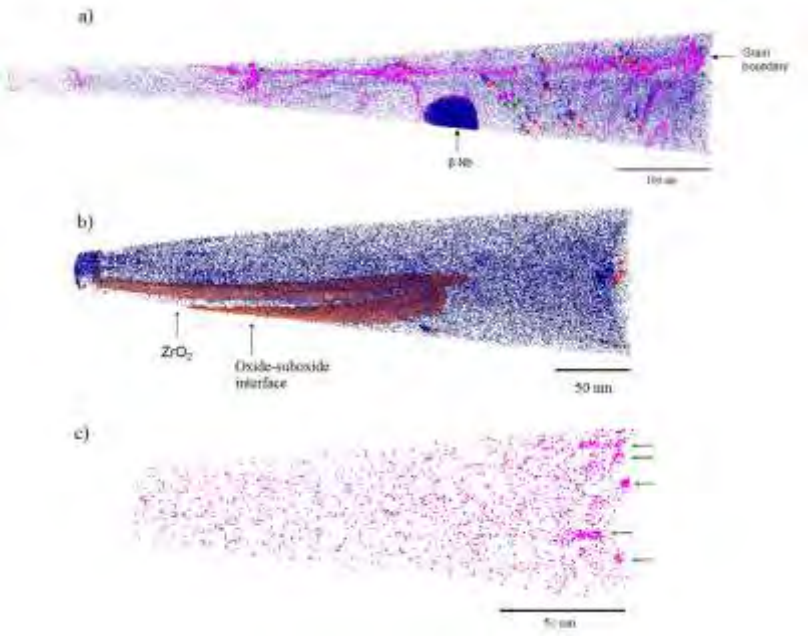

Figure 5: a) Fe (pink) and Nb (blue) concentration profiles in the O-saturated metal showing Fe (green arrows) and Nb (red arrows) clusters, b) Nb clusters in the ZrO region, and c) Fe clusters in bulk ZrO_2.

3.4 Suboxide growth

3.4.1 EELS and ASTAR mapping

EELS analysis and automated crystal orientation (ASTAR) mapping in the TEM have been used to study the metal-oxide interface in order to provide a comprehensive view of microstructure and micro-chemistry.

Fig.6 (a) shows the HAADF STEM image of a 120-day Zr-1Nb sample after further thinning down to around 50nm in order to do accurate ASTAR and EELS mapping. Fig.6 (b) shows a phase map of the TEM lamella. Columnar oxides with monoclinic-ZrO_2 (m-ZrO_2) structure are clearly seen, and scattered equiaxed tetragonal-ZrO_2 (t-ZrO_2) grains. The top layer of t-ZrO_2 is considered to be a result of FIB damage. At the metal-oxide interface, there is a continuous layer of Widmanstatten-type suboxide with the hexagonal ZrO structure predicted with *ab initio* modelling[11], which agrees with previous findings[6] using Transmission Kikuchi Diffraction but with a higher matching rate. The undulating area under a parallel crack shows a more uniform saw-tooth shape with metal underneath intact. This same area was analysed in the EELS mapping in Fig. 7.

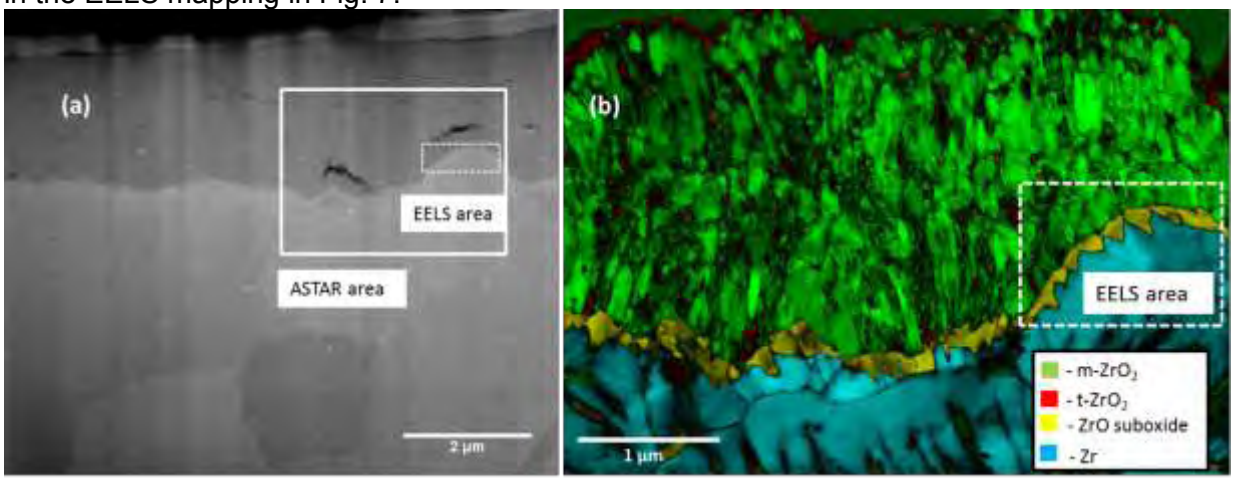

Figure 6: (a) HAADF STEM image of the 120-day Zr-1Nb sample. The areas for automated crystal orientation (ASTAR) and EELS mapping are highlighted. (b) Phase map in ASTAR mapping with the area for EELS mapping highlighted.

A higher magnification HAADF STEM image of the highlighted area in Fig.6 is shown in Fig. 7(a). The Z-contrast in the image shows the saw-tooth shaped suboxide as seen in the ASTAR map, and the Oxygen and Zr concentration maps in Fig. 7 (b1, b2) confirm an ~86nm thick ZrO suboxide followed by oxygen saturated metal with ~25 at% oxygen.

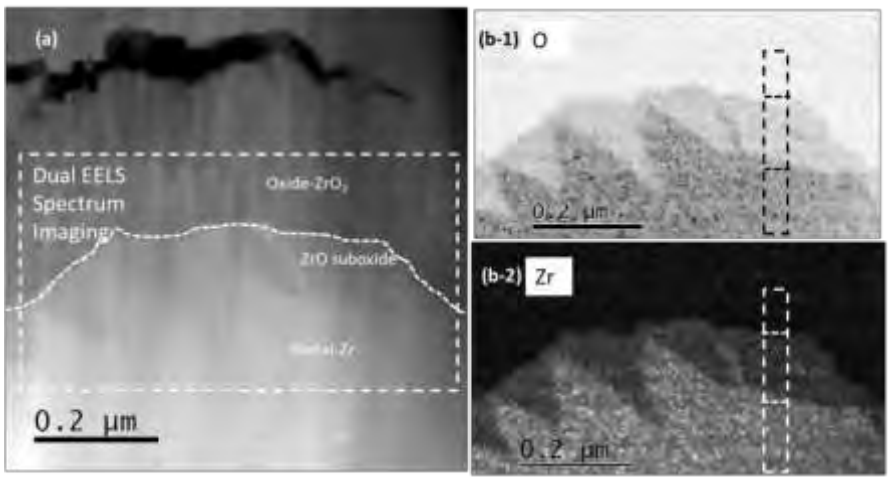

Figure 7: (a) HAADF STEM image of the area for EELS mapping of the 120-day Zr-1Nb sample, (b-1) Oxygen concentration map, (b-2) Zr concentration map.

EELS mapping of the suboxide was carried out on a series of Zr-1Nb samples. The suboxide thickness grows with oxidation time before transition. Some of these suboxide layers are much thicker than observed previously in other oxidised Zr alloys[12]. We concluded that the suboxide forms only during the slow stages of oxidation and is rapidly consumed at transition as the metal-oxide interface moves much faster to consume the underlying metal.

3.4.2 Atom Probe Tomography of ZrO layers

ZrO suboxide layers were found by APT in both 225-day and 585-day samples. In both cases, a ZrO layer of 100nm or more in thickness was found. This initially contradicts the observations by Ni et al[12], showing that no suboxide is present in post-transition specimens. However, our TEM results also found a suboxide in the 540-day sample, indicating that these regions may still be in pre-transition state. In the 225-day sample, as illustrated in Fig. 5, Fe-decorated dislocation lines were found at the metal adjacent to the suboxide-metal interface. They are oriented in the direction perpendicular to the oxide growth direction. These may form due to the compressive stress in that region originating from volume expansion during oxidation. As the deformed metal transforms to ZrO and the dislocation lines disappear, but the Fe atoms often remain decorating linear features.

In the 585-day sample, as seen in Fig.8, a thick ZrO layer was also found. This particular saw-tooth shaped suboxide-metal interface had a composition profile similar to that reported in previous atom probe studies: 68at% Zr and 32at% O[14]. The presence of Fe accumulation along the suboxide-metal interface suggests that Fe is rejected from the suboxide to the metal during oxidation.

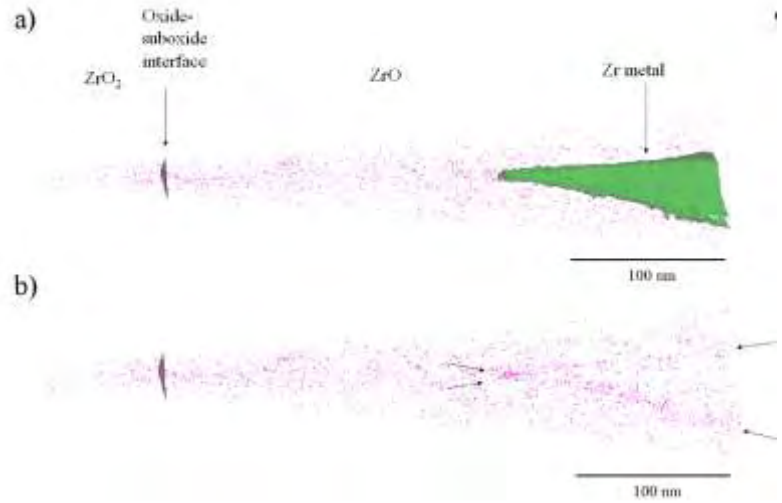

Figure 8: a) Fe distribution in oxide, suboxide, and O-saturated metal with saw-tooth shape suboxide-metal interface in the 585-day sample, b) arrows showing Fe segregation to the interface.

3.5 NanoSIMS analysis of deuterium distribution

SIMS results from the 225-day and 585-day Zr-1Nb show higher intensities of deuterium in the oxide as seen in Fig. 9. Linescans drawn across the metal-oxide interface of the 225-day sample show particularly high intensities of deuterium in the top 1 μm of the oxide, rapidly dropping off further towards the metal-oxide interface. The 585-day sample, whilst still showing the initial strong peak in the first micron of oxide, shows significantly more deuterium throughout the bulk oxide, suggesting that the transition event enables the propagation or trapping of deuterium while the pre-transition sample is a good barrier to deuterium penetration. In the metal, the 225-day sample shows very low deuterium counts, whilst the 585-day sample shows regions of strong intensity which can be identified as zirconium deuterides.

The high deuterium signal at the oxide surface is thought to be due to trapping in the extensive porosity seen by TEM in the equiaxed top layers. The relatively dense bulk oxide in the 225-day sample then offers few preferential sites for trapping deuterium and the measured ratio is not much higher than natural isotopic background. The more cracked and porous 585-day sample offers a much easier route for deuterium penetration down to the zirconium metal.

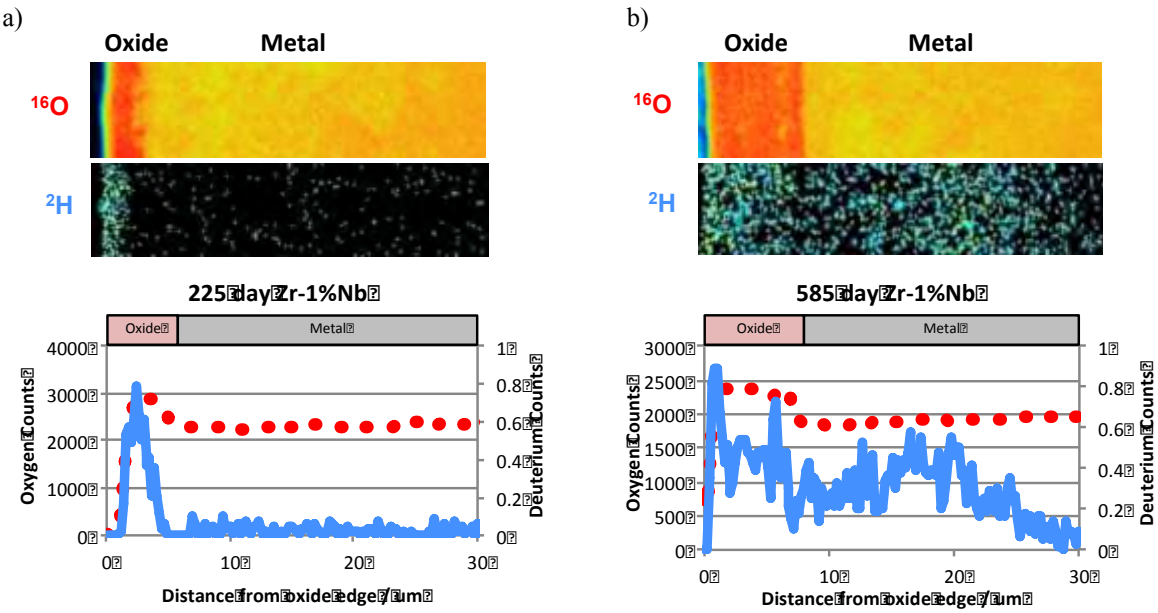

Figure 9: Typical SIMS maps and line scans comparing the oxygen (dotted line) and deuterium (solid line) signals from the (a) 225-day and (b) 585-day Zr-1Nb samples.

4. Conclusions

Here we present a detailed microstructural and microchemistry study of oxidised Zr-1Nb alloys. Samples were chosen to represent the early, pre-transition, transition and post-transition stages of oxidation.

(1) Fresnel imaging revealed the existence of both parallel interconnected pores and some vertically interconnected pores along the columnar oxide grain boundaries, which become more disconnected near the metal-oxide interface. For the first time, we report similar porosity at the metal-oxide interface itself.

(2) Analytical (S)TEM revealed two types of second phase particles: β-Nb and $Zr(Nb,Fe)_2$. The $Zr(Nb,Fe)_2$ SPPs are present at a lower number density and tend to become amorphous quickly as the oxide grows. APT was used to study finer Nb clusters and Fe clusters in the suboxide and metal regions, Fe clusters are also found at the oxide grain boundaries. These observations help us understand how different aliovalent elements (Nb^{5+}, Fe^{3+}, Fe^{2+}) can be redistributed in the oxide during oxidation and potentially alter the electronic conductivity.

(3) APT, EELS and automated crystal orientation mapping have revealed Widmanstatten-type suboxide layers in some samples with compositions in different regions of either ZrO structure or Zr_3O_2. Some of these layers are much thicker than observed previously in other oxidised zirconium alloys[13]. And this may be an important feature in understanding the different overall corrosion rates on the basis of local environment in oxidation kinetics at the micron scale.

(4) Hydrogen pickup mechanisms have been studied by high resolution SIMS analysis, showing that at different stages of oxidation the penetration of deuterium occurs in quite different patterns. This data can be correlated to the overall oxide microstructure revealed by ASTAR mapping in the TEM.

Acknowledgements:

This project is part of the MUZIC-2 collaboration studying oxidation and hydrogen pickup in Zr alloys. The authors gratefully acknowledge support from EDF, Westinghouse, EPRI and Rolls Royce, and many useful discussions within the consortium. The authors wish to acknowledge EDF, Dr. Jianfei Wei and Dr. Peng Wang for previous autoclave testing and deuterium spiking work in MUZIC-1. Jing Hu is supported by the China Scholarship Council.

References:

1. Olander, D. R. & Motta, A. T. *Waterside Corrosion and Hydriding of Zr Alloy Cladding*. *Light Water Reactor Materials* (2006).

2. Garzarolli, F., Cox, B. & Rudling, P. *Corrosion and hydriding*. (2012).

3. Couet, A., Motta, A. T. & Comstock, R. J. Hydrogen pickup measurements in zirconium alloys: Relation to oxidation kinetics. *J. Nucl. Mater.* **451,** 1–13 (2014).

4. Wei, J. *et al.* Autoclave study of zirconium alloys with and without hydride rim. *Corros. Eng. Sci. Technol.* **47,** 516–528 (2012).

5. Yardley, S. S. *et al.* An investigation of the oxidation behaviour of zirconium alloys using isotopic tracers and high resolution SIMS. *J. Nucl. Mater.* **443,** 436–443 (2013).

6. Ni, N. Study of oxidation mechanisms in zirconium alloys by electron microscopy, D.Phil thesis, Department of Materials, University of Oxford. (2011).

7. Hu, J. *et al.* Identifying suboxide grains at the metal-oxide interface of a corroded Zr-1.0%Nb alloy using (S)TEM, transmission-EBSD and EELS. *Micron* **69,** 35–42 (2015).

8. Ortner, S. *et al.* Study Of Zircaloy Corrosion To Develop Mechanistic Understanding. in *Fontevraud 8 - Contribution of Materials Investigations and Operating Experience to LWRs' Safety, Performance and Reliability France, Avignon – 2014, September 14* (2014).

9. Ni, N. *et al.* Porosity in oxides on zirconium fuel cladding alloys, and its importance in controlling oxidation rates. *Scr. Mater.* **62,** 564–567 (2010).

10. Hudson, D. & Smith, G. D. W. Initial observation of grain boundary solute segregation in a zirconium alloy (ZIRLO) by three-dimensional atom probe. *Scr. Mater.* **61,** 411–414 (2009).

11. Sundell, G., Thuvander, M. & Andrén, H.-O. Enrichment of Fe and Ni at metal and oxide grain boundaries in corroded Zircaloy-2. *Corros. Sci.* **65,** 10–12 (2012).

12. Nicholls, R. J. *et al.* Crystal Structure of the ZrO Phase at Zirconium/Zirconium Oxide Interfaces. *Adv. Eng. Mater.* (2014). at <http://doi.wiley.com/10.1002/adem.201400133>

13. Ni, N. *et al.* How the crystallography and nanoscale chemistry of the metal/oxide interface develops during the aqueous oxidation of zirconium cladding alloys. *Acta Mater.* **60,** 7132–7149 (2012).

14. Dong, Y., Motta, A. T. & Marquis, E. a. Atom probe tomography study of alloying element distributions in Zr alloys and their oxides. *J. Nucl. Mater.* **442,** 270–281 (2013).

Test Reactor Evaluation of Zirconium Alloy NMCA Corrosion Behavior

D. LUTZ
Global Nuclear Fuel - Americas
6705 Vallecitos Road, Sunol, CA 94586 - USA

Y-P. LIN, P. CANTONWINE
Global Nuclear Fuel - Americas
3901 Castle Hayne Road, Wilmington, NC 28402 - USA

J. VARELA
GE HITACHI NUCLEAR ENERGY
6705 Vallecitos Road, Sunol, CA 94586 - USA

A. KUCUK, K. EDSINGER
Electric Power Research Institute
3420 Hillview Avenue, Palo Alto, CA 94304 - USA

ABSTRACT

A test reactor experiment has been conducted to investigate the corrosion behavior of zirconium alloy materials used in Boiling Water Reactor (BWR) fuel assemblies. The experiment was conducted to better understand the impact of modern water chemistry operating regimes on fuel performance, namely noble metal chemical addition (NMCA). NMCA corrosion was evaluated in the Massachusetts Institute of Technology (MIT) reactor using a test rig comprised of Zircaloy material variations that were pre-exposed to different treatments that resulted in either a low or high amount of Pt or Rh, which are the active species used in NMCA treatments. The corrosion responses were generally small and variable, which made it challenging to identify meaningful differences and effects. Test results showed that deposition of Pt or Rh on Zircaloy-2 cladding by sputter coating or a simulated NMCA process resulted in increased corrosion for some samples and conditions, which is contrary to BWR field experience where corrosion performance has been very good. A possible contribution to this laboratory versus in-reactor performance difference may be related to differences in noble metal deposition characteristics for laboratory versus in-plant applications.

1. Introduction

In 1996 GE Hitachi Nuclear Energy (GEH), formerly GE Nuclear Energy, conducted a BWR water chemistry technology demonstration program that added, for the first time, a solution containing dissolved Pt and Rh to the coolant of a commercial BWR during hot standby near the end of its planned cycle. This process is known as Noble Metal Chemical Addition (NMCA) or NobleChem™. The solution was added because it renders the surfaces of reactor internal surfaces catalytic, which lowers the amount of dissolved hydrogen in the coolant that is needed to create a low oxygen reducing environment in order to mitigate stress corrosion cracking [1-4]. The lower hydrogen content in the coolant then lowers the release of volatile N-16, which has a large effect on personnel dose rates and is very beneficial for site operations [4].

Incidental deposition of Pt and Rh onto the fuel rods that were present in the core occurred from the application, and the possible side effect of that deposition on fuel rod corrosion was evaluated periodically during subsequent end of cycle fuel inspections and hotcell examinations. The fuel rods that were exposed directly to the Pt and Rh during the application had a well-developed reactor-formed oxide on them that would mitigate possible deleterious effects of increased corrosion and hydriding that might be caused by direct contact with the catalytic noble metals. To help determine whether an initial reactor-formed oxide was even necessary or not to prevent noble metal incidental effects on the fuel, a special bundle containing six "pre-treated" fuel rods was placed in the core in the outage immediately following the first end of cycle application. Noble metals were applied to the pre-treated rods directly to a bare metal surface in a laboratory environment, and then operated along with the fuel that received the hot standby application. Fuel inspection one cycle later, about 18 months, indicated slightly elevated corrosion for some of the bare metal pre-treated rods but not for the irradiated rods that had a well-formed oxide prior to the application [5, 6].

This observation and other considerations led to an experimental program to further investigate whether or not noble metals applied directly to a fresh bare metal surface of Zircaloy cladding were likely to affect fuel cladding corrosion in BWRs, and if factors such as cladding fabrication process variations, pre-oxidation, and noble metal application amount were important controlling parameters. To this end, Global Nuclear Fuel (GNF), GEH, and Electric Power Research Institute (EPRI) initiated a zirconium alloy corrosion test program using MIT's MITR-II research reactor. The objective of the program was to evaluate the effect of noble metals on zirconium alloy corrosion that complemented the field surveillance and hotcell programs related to fuel performance in NMCA that were on-going at the time.

GNF prepared and sent samples with various conditions to MIT for the simulated BWR corrosion tests. In particular, several different cladding materials with various water chemistry and surface condition treatments were tested in an in-core section of the capsule. Upon completion, the test samples were shipped back to the GE Hitachi Vallecitos Nuclear Center hotcells to characterize the corrosion test results. The hotcell examination work scope includes documentation of the visual appearance, sectioning of each sample, measurement of the oxide thickness and estimation of the hydrogen content by metallographic techniques. Results of these tasks are presented in this paper.

2. Experimental Design

2.1 Specimen Matrix

The experimental matrix included three types of Zircaloy-2 barrier fuel cladding with fabrication process variations designated P5, P6, and PP8. The claddings originated from ASTM B350 grade ingots and were fabricated by GNF using standard production processing from tubeshells for 9X9 or 10X10 designs that resulted in intermetallic particle sizes that increase in order from P5 to P6 to PP8, respectively. Processing for P5 and P6 included a penultimate induction heat treatment, and all types were subjected to a final recrystallization anneal. The samples were then exposed to either a Pt sputter coating of 4 different amounts, a Pt, Rh, or Pt+Rh simulated 165°C aqueous NMCA exposure at two different noble metal loading levels, very much like that which is applied in operating BWRs, and NMCA controls. The NMCA controls were prepared with the same autoclave cycle but without the noble metal in the water. A pre-oxidized sample condition was included, which was obtained by 1500 psig (10.34 MPa) autoclave steam exposure at 400°C for 7 days. No detailed post-treatment analysis was performed to characterize the noble metal particle deposition characteristics.

All cladding samples were cut lengthwise from a parent fuel cladding tube. The length of a sample was nominally 1.25 inches (31.75 mm). Holes 0.118 inches (3.00 mm) in diameter

were drilled in both ends of all samples for fixturing purposes. Samples were positioned in eleven (11) tiers within the core of the reactor. A complete factorial design was not possible due to space limitations, however some replicate samples were included throughout the capsule tiers. The matrix in Table 1 lists each sample and its position in the experiment.

The samples are identified with a shorthand notation that is used to describe the type and condition of each sample. Some examples are given here to illustrate:

- "6138 P6 OX 20 Pt": The first numbers or letters are the sample identification that is stamped on each sample. For the cladding samples, the first number is a 5, 6, or 8 and indicates whether the sample is the P5, P6, or PP8 cladding manufacturing process. "OX" means that the material was pre-oxidized in 400°C steam at 1500 psig (10.34 MPa) for 7 days. "20 Pt" means that the sample was exposed to a simulated aqueous NMCA application process at 165°C for 225 hours which yielded a nominal target[1] Pt loading level of 20 μg/cm^2 Pt. Thus, the P6 cladding sample was pre-oxidized and then loaded with a nominal 20 g/cm^2 Pt by the simulated NMCA process. Variations of this condition exist for P5 and PP8 cladding, an AR condition that is not pre-oxidized, a condition with nominal 20 g/cm^2 Rh (nominal target), 20 μg/cm^2 Pt + 20 μg/cm^2 Rh (nominal target), as well as conditions with nominal 5 μg/cm^2 Pt (nominal target), 5 μg/cm^2 Rh (nominal target), and 5 μg/cm^2 Pt + 5 μg/cm^2 Rh (nominal target) for which the samples were exposed to the simulated 165°C aqueous NMCA application for 36 hours.
- "6055 P6 AR + 225 hrs": The "AR" means that the as-manufactured and cleaned surface was exposed to a simulated NMCA application but without any noble metals. This condition serves as a control for the nominal 20 μg/cm^2 noble metal loading condition. A similar control condition exists for P5 and PP8 cladding, a pre-oxidized condition, and a 36 hour simulated condition to correspond to the 5 μg/cm^2 nominal target loading level.
- "6240 P6 OX SP 100 Rh": The "SP" means that noble metal was deposited on the sample by sputter coating on only the outer surface. Thus, a P6 cladding sample was pre-oxidized in 400°C steam at 1500 psig (10.34 MPa) for 7 days and then sputter coated with a nominal 100 μg/cm^2 Rh. Variations of this condition exist that had 5 and 40 μg/cm^2 Rh and 5, 40, or 100 μg/cm^2 Pt, as well as a condition that was not pre-oxidized.

2.2 Specimen Holder Design

A system of insulating holders was designed to position the samples accurately in the reactor core and in specific relationship to the flow channels. Each sample holder was made from alumina rod 0.92" (23.4 mm) in diameter with a central hole for a titanium spine that extended the entire length of the irradiation fixture. Samples were positioned adjacent to the spine with the concave side (cladding inside surface) towards the spine. Samples were arranged six to a level. Flow separators were positioned between pairs of samples on each level. Flow separators were used to maintain different water chemistries within each capsule.

An example capsule is shown schematically in Figure 1 that illustrates six samples, colored brown, with three flow separators shown in green. Flow separators are keyed into the upper and lower insulating ceramics and into the central spine that passes through the central hole (spine not shown).

2.3 MITR-II Test Loop System

The main out-of-pile components of the test loop include a fluid delivery system comprised of a main recirculation loop, loop heater, charging system, letdown system, cleanup system,

[1] The nominal target loading levels are based on scoping tests that were performed to determine the exposure time or sputtering time necessary to achieve a desired loading level. No additional confirmatory loading measurements were performed on samples from test batch materials.

bubbling system, chemical injection system, pressurizer, auxiliary cooling water system and other instrumentation. The in-pile components of the test loop include an autoclave, thimble, and dummy fuel element to irradiate the samples using a specified circulating light water test condition of 288°C and 10 MPa within the autoclave in the reactor core. These conditions were implemented through the use of a pressure vessel/autoclave made from 1.25 inch (31.75 mm) outside diameter titanium tubing, a 2 inch (50.8 mm) diameter aluminum thimble tube, and an aluminum, parallelogram-shaped dummy fuel element. The autoclave provided the pressure boundary for the experiment, and the thimble separated the autoclave from the reactor core water with an insulating gas gap. Thimble and autoclave extended from above the reactor lid through the lid to the bottom of the reactor core. The dummy fuel element was used to position the thimble in a central position within the core. The overall useable length of the element is 24 inches (609.6 mm).

A charging tank provides a supply of 70 liters of cleaned water to supply the main feed water charging pump. Water chemistry in the charging tank is carefully controlled to achieve the desired water chemistry in the main loop. A metering pump is used to pressurize water from the charging tank up to system pressure for injection into the main loop. The pump provides a constant flow rate. Main loop water volume is about 5 liters and water is supplied at 0.5 L/min, resulting in a refresh cycle of 10 minutes.

Loop coolant water flows through the main loop at a rate of about 20 L/min. Water flows down outside of the sample stack between the stack and autoclave wall, to the bottom of the autoclave where it enters the bottom of the sample stack and flows up across the specimens and out of the autoclave. When the water reaches the chemistry control and measuring system some 10% of the water is bled out of the main stream through the letdown system. This water is analyzed for water chemistry, cleaned with an ion exchange column and returned back to the main loop by the charging pump. Before passing through the heater the main loop flow is mixed with incoming water from the chemistry control system.

2.5 Irradiation History and Loop Conditions

The test achieved slightly more than 1600 hours irradiation (~67 days). Maximum powers were about 4.5 MW and were slightly lower in the second half of the irradiation period. Coolant temperature was maintained near 275°C, and conductivity in the letdown system varied between 0.1-0.3 µS/cm during the length of the run. The oxygen concentration in the letdown system was between 150-200 ppb and the dissolved hydrogen content was always less than 0.07 ppb.

3.0 Results

Post-irradiation examination included a visual inspection and metallographic oxide thickness measurements. Following completion of the oxide examination, the samples were etched for hydrides. Results are summarized in Figure 2 for the simulated NMCA corrosion test results and in Figure 3 for the sputter coated corrosion test results.

3.1 Simulated NMCA Results

Ten control samples were used to represent the P5, P6, and PP8 cladding in various pre-oxidized and initially unoxidized conditions with a 36 hour or 225 hour simulated NMCA aqueous exposure. Figure 2A shows the oxide thickness results for the simulated NMCA controls. Typical visual appearance of P6 control samples in AR and PreOx 225 hour conditions are shown in Figures 2D and 2E. Although the controls do not have noble metal on them, the equivalent position on the x-axis is shown for the amount of noble metal that they would have had if noble metal had been present in their autoclave control exposure with a single noble metal species. The oxide thickness of all control samples ranges between about 1.5 and 3.5 microns. Variability between replicate control samples can be up to about 2 microns. No significant variation in cladding type is observed.

The effect of core position is shown in Figure 2B for all control coupons. All controls were either in Tier 6, 7, or 16 (Tier 1 at very bottom of core, Tier 16 at core top). Although there is a significant axial variation in the flux and gamma dose within the core, core position did not have a large effect on the corrosion response.

Results of the simulated NMCA treated samples are shown in Figure 2C for the oxide thickness and in Figures 2F and 2G for examples of the visual appearance of the P6 samples in AR and PreOx 225 hour Pt-treated conditions. The oxide thickness data are grouped into various categories and plotted against the target noble metal loading for either the 36 or 225 hour noble metal exposure. The oxide thickness ranges for the controls are highlighted as in Figure 2A. Again, it must be noted that the controls do not have noble metal but for comparison to the noble metal treated samples the controls are assigned noble metal loadings of 5 $\mu g/cm^2$ for the 36 hour exposure and 20 $\mu g/cm^2$ for the 225 hour exposure. 36 hours is sufficient to deposit about 5 $\mu g/cm^2$ of Pt or 5 $\mu g/cm^2$ of Rh when applied separately, or a total of 10 $\mu g/cm^2$ when both Pt and Rh are present during the exposure, as was the case. 225 hours is sufficient to deposit about 20 $\mu g/cm^2$ of Pt or 20 $\mu g/cm^2$ of Rh if applied separately as was the case, or 20 $\mu g/cm^2$ of Pt and 20 $\mu g/cm^2$ for a total of 40 $\mu g/cm^2$ Pt and Rh when applied together, as was the case. Thus, the 36 hour control is applicable to the 36 hour 5 Pt + 5 Rh $\mu g/cm^2$ series (10 $\mu g/cm^2$ total) and the 225 hour control is applicable to the 225 hour 20 $\mu g/cm^2$ Pt condition, the 225 hour 20 $\mu g/cm^2$ Rh condition, or the 225 hour 20 Pt + 20 Rh $\mu g/cm^2$ Pt+Rh series (40 $\mu g/cm^2$ total).

As a group, the oxide thickness of all samples in Figure 2C ranges between about 1.5 and 12 microns. A majority of the samples have oxide thicknesses that exceed those of the control samples, while the remaining samples are within the control ranges.

The effects of noble metal type, noble metal loading amount, cladding type, and pre-oxidation can be ascertained to some extent by examination of subgroups of samples. The following observations are made from graphs of the data subgroups:

- The oxide thickness of many samples is greater than that of the control samples. These results indicate that the simulated NMCA treatments had a broad effect on the corrosion response of the Zircaloy cladding.
- The effect of Pt alone exhibits significant variability that overlaps the controls and rises to 12 microns which is the thickest oxide that was observed. Both P6 and PP8 exceed the control condition, whereas P5 is within the range of the controls. Pre-oxidation did not prevent Pt treated samples from having corrosion that was higher than the controls.
- The effect of Rh alone was less than that of Pt alone but the oxide thickness of some samples still exceeded that of the controls by up to 3.5 microns. PP8 exceeds the control condition, P6 is similar to or slightly above the control condition, and P5 is within the range of the controls. Pre-oxidation did not prevent Rh treated samples from having corrosion that was higher than the controls.
- The effect of Pt + Rh at 10 $\mu g/cm^2$ and 40 $\mu g/cm^2$ was similar to that of Rh alone at 20 $\mu g/cm^2$ and less than that of Pt alone at 20 $\mu g/cm^2$. The oxide thickness of some Pt + Rh treated samples still exceeded that of the controls by up to 2.5 microns. Both P6 and PP8 exceed the control condition, whereas P5 is within the range of the controls. Pre-oxidation did not prevent Pt + Rh treated samples from having corrosion that was higher than the controls.
- A P6 sample has the thickest oxide of all samples, however P6 was the most widely used test material. The oxide thickness of many of the P6 samples exceeds that of the controls although this is most notable at the 20 $\mu g/cm^2$ Pt loading level. The P6 material was affected by all three types of simulated NMCA conditions whether it was pre-oxidized or not. Pt had the greatest effect on P6.

- For P6 and PP8, Pt alone had a stronger effect than the Pt + Rh condition, and Rh alone had a similar but slightly greater effect than the Pt + Rh condition. P5 was not affected by the noble metal treatments.
- The oxide thickness of four of the six PP8 samples exceeds that of the controls. The PP8 material was affected by the Pt, Rh, and Pt + Rh condition.
- The oxide thicknesses of the P5 samples all fall within the range of the controls. P5 was affected by the Pt, Rh, and Pt + Rh conditions less than the P6 and the PP8 materials were.

Hydrogen contents were differentiated most strongly by whether a sample had been pre-oxidized in steam or not. Unoxidized samples have hydrogen contents that are estimated to be less than 100 ppm. Pre-oxidized samples have higher hydrogen contents (due to the pre-oxidation cycle) that are estimated to be between about 100 and 200 ppm. Hydriding does not have a strong dependence on the noble metal loading amount, the type of noble metal, or the cladding type. The differences between samples were deemed too small to warrant quantitative analysis and further comparisons.

3.2 Noble Metal Sputter Coating Results

Only P6 cladding was used for the sputter coating series. Four nominal loading levels were used at 5, 20, 40, or 100 μg/cm^2. Duplicate samples were used for each loading level. Samples were in the pre-oxidized condition at each loading level and in the unoxidized condition only at the highest loading level.

The oxide thickness measurements for the sputter coated samples are summarized in Figure 3A, and the visual appearance of a series of Pt sputter coated samples ranging in loading amount from 5-100 μg/cm^2 are shown in Figures 3B-3F. The oxide thickness ranges between about 2 and 12 microns. Taken as a whole there is an upward trend in oxide thickness with noble metal loading, however the correlation is quite low due to large variability in the replicate P6 samples at 5 and 20 μg/cm^2 Pt. Replicates at all other conditions were more similar to each other. The highest linear correlation is for the Rh group of samples, which has an R^2 correlation of 0.57. At 100 μg/cm^2 both Pt and Rh treated sample groups have elevated corrosion but the effect of Pt is greater than that of Rh. There is no apparent effect of pre-oxidation on the post-test oxide thickness for either the Pt or Rh treated samples. The visual appearance is not a reliable differentiator of corrosion, as Figure 3B for 5 μg/cm^2 sputtered Pt appears dark and uniform and yet this sample has the maximum amount of corrosion in the series of 12.1 microns.

As discussed above, cladding control samples for the NMCA portion of the experiment, including pre-oxidized P6, have between about 1.5 and 3.5 microns of oxide. Although these samples in Figure 3A included a 36 or 225 hour aqueous exposure that the sputter coated samples did not experience, many of the sputter coated samples have greater oxide thickness than the NMCA control samples, which provides another comparative indication that the sputter coating affected the corrosion response. Similar to the NMCA treated samples, hydrogen contents of the Pt and Rh sputter coated samples based on metallographic observation did not have a strong dependence on the amount of noble metal loading, and the differences were deemed too small to warrant quantitative analysis.

4.0 Discussion

The test response varied due to indeterminate factors, however, the test does indicate that noble metal deposited on Zircaloy-2 cladding by simulated NMCA treatments applied in the laboratory and by sputter coating can increase oxidation rates a relatively small amount for some conditions in a short-term, simulated BWR environment test. When the noble metal deposit is applied by sputter coating the effect is consistently greater for replicate samples of both Pt and Rh at the highest loading tested (100 μg/cm^2). Similarly, Pt and Rh simulated NMCA treated samples exhibit slightly higher corrosion than control samples, particularly for

P6 at 20 μg/cm^2 Pt. Apparent test results indicate that Pt had a greater effect than either Rh or Pt + Rh, that the P5 with the finest intermetallic particle size provided more resistance to the effect than the P6 or PP8 materials, and that pre-oxidation did not prevent the effect. Surface analysis to investigate post-test noble metal particle size distributions, and possible differences among samples, was not performed.

Isolated instances of atypical BWR fuel performance early in the introduction of NMCA have placed application constraints even though the cause and effect role of NMCA in those instances has never been completely understood [5, 6]. The first instance was slightly elevated lift-off (using eddy current that measures combined thickness of corrosion oxide and surface crud) of Pt + Rh NMCA pre-treated rods following the first cycle of NMCA operation in the lead commercial demonstration plant. The slightly elevated lift-off was confirmed in a hotcell examination to be due to elevated corrosion [5, 6]. A 90 day in-reactor pre-conditioning requirement was placed on fuel following this observation. The second instance was elevated corrosion and “tree barking” of third cycle fuel at low elevations following one cycle of operation with the highest noble metal input amount in the BWR fleet (62 μg/cm^2) [6]. A 30 μg/cm^2 input limit was placed on fuel following this observation. Both observations are counter to unirradiated laboratory corrosion tests that show no effect of small noble metal depositions [7, 8].

In the years since the MIT noble metal effects test was conceived and set in motion, numerous NMCA applications and reapplications have continued across the BWR fleet, and an extensive database of poolside fuel performance information has been accumulated. The vast majority of the fuel performance observations from “real world” BWR experience have shown no significant adverse effect of NMCA on BWR fuel performance within the application constraints that have been imposed. In light of this BWR NMCA fuel performance record, the current test results, combined with the Duane Arnold noble metal pre-treated rod experience, suggest that there may be a significant difference in the effect of Pt and Rh whether they are applied in a laboratory environment rather than a BWR environment. The cause of the difference is unknown, but may be related to the absence of crud in laboratory applications or the size and distribution of noble metal particles under laboratory vs. in-reactor applications. Nonetheless, the MITR-II test results do indicate that there may be some conditions under which NMCA could cause increased corrosion.

5.0 Summary

A test reactor experiment has been conducted to investigate the corrosion behavior of commonly used BWR zirconium alloy fuel cladding materials that have a range of intermetallic particle sizes. The experiment was conducted to better understand the impact of NMCA in light of some early, but isolated, adverse field corrosion responses when NMCA was in the early stages of commercial demonstration. NMCA corrosion was evaluated in the MIT reactor using a test rig comprised of Zircaloy material variations that were pre-exposed to different treatments that resulted in either a low or high amount of Pt or Rh, which are the active species used in NMCA treatments. The test response varied due to indeterminate factors, however, the test clearly showed that deposition of Pt or Rh on Zircaloy-2 cladding by sputter coating or a simulated NMCA process could result in slightly increased corrosion. Trends indicated that Pt had a greater effect than either Rh or Pt + Rh, that the P5 with the smallest intermetallic particle size provided more resistance to the effect than the P6 or PP8 materials, and that pre-oxidation did not prevent the effect.

In light of the proven BWR NMCA fuel performance experience, the current test reactor corrosion results suggest that there may be a significant difference in the effect of Pt and Rh whether they are applied in a laboratory environment rather than a BWR environment. The cause of the difference is unknown, nonetheless, the MITR-II test results do indicate that there may be some conditions under which NMCA could cause increased corrosion.

6.0 Acknowledgements

This work was funded by EPRI's Fuel Reliability Program (FRP).

The authors are appreciative of the overall effort that the MIT staff applied to design and complete the test, in particular Principal Investigators Professor Ron Ballinger and Pete Stahle.

7.0 References

1. Andresen, P., Kim, Y., Hettiarachchi, S., and Diaz, T., "On-Line NobleChem™ Mitigation of SCC," in Proc. of the 12th int. Conference on Environmental Degradation of Materials in Nuclear Power Systems Water Reactors, Salt Lake City. The Minerals, Metals and Materials Society (TMS), 2005.
2. Andresen, P. L., Diaz, T. P., and Hettiarachchi, S., "Mitigation of SCC By On-Line NobleChem™," in Proc. of the 13th int. Conference on Environmental Degradation of Materials in Nuclear Power Systems Water Reactors, Whistler. Canadian Nuclear Society (CNS), 2007.
3. Hettiarachchi, S., Horn, R. M., Kim, Y. J., and Andresen, P. L., "Electrochemical Corrosion Potential (ECP) Reduction and Crack Mitigation Experiences with NobleChem™ and On-Line NobleChem™," in Proc. of the 14th int. Conference on Environmental Degradation of Materials in Nuclear Power Systems Water Reactors, Virginia Beach. American Nuclear Society (ANS), 2009.
4. Hettiarachchi, S., Diaz, T. P., Varela, J. A., Seeman, R. A., and Tran, L. C., "NobleChem™ Application During Power Operation for Crack Mitigation and Dose Rate Reduction of BWRs," in Proc. of the 13th int. Conference on Environmental Degradation of Materials in Nuclear Power Systems Water Reactors, Whistler. Canadian Nuclear Society (CNS), 2007.
5. Cheng, B., Smith, D., Armstrong, E., Turnage, K., Bond, G., "Water Chemistry and Fuel Performance in LWRs," Proceedings of the International Meeting on LWR Fuel Performance, Park City, UT, April 10-13, 2000.
6. Cheng, B., Turnage, K.G., Potts, G.A., Lutz, D. R., Pathania, R., Rohrer, R. J., Eyre, M., Armstrong, E., "Effects of Noble Metal Chemical Application on Fuel Performance," Proceedings of the 2004 International Meeting on LWR Fuel Performance, Orlando, Florida, Paper 1069, September 19-22, 2004.
7. Lin, Y-P., Kim, Y, Lutz, D., Kucuk, A., Cheng, B., "Effect of Water Chemistry Variations on Corrosion of Zr-Alloys for BWR Applications," Proceedings of Water Reactor Fuel Performance Meeting, Chengdu, China, Sept. 11-14, 2011.
8. Lutz, D.R., Levin, H.A., "Influence of Noble Metal Additions to Water on Corrosion of Zircaloy," Proceedings Eighth International Symposium on Environmental Degradation of Materials in Nuclear Power Systems – Water Reactors, Amelia Island, FL, August 10-14, 1997.

16	6238 P6 OX SP 100 Pt	6177 P6 AR SP 100 Pt	6240 P6 OX SP 100 Rh	6123 P6 AR SP 100 Rh	6323 P6 OX + 36 hrs	6313 P6 AR + 36 hrs
15	6128 P6 AR SP 100 Pt	6239 P6 OX SP 100 Pt	6131 P6 AR SP 100 Rh	6257 P6 OX SP 100 Rh	6215 P6 OX 20 Pt 20 Rh	6119 P6 AR 20 Pt 20 Rh
14	6231 P6 OX SP 40 Pt	6232 P6 OX SP 40 Pt	6109 P6 OX SP 40 Rh	6162 P6 OX SP 40 Rh	8013 P8 OX 20 Pt 20 Rh	8039 P8 OX 20 Pt 20 Rh
13	5013 P5 OX 20 Pt	6080 P6 OX 20 Pt	5016 P5 OX 20 Rh	6103 P6 OX 20 Rh	5018 P5 OX 20 Pt 20 Rh	5025 P5 OX 20 Pt 20 Rh
12	6202 P6 OX 20 Pt	6151P6 OX SP 20 Pt	6219 P6 OX 20 Rh	6208 P6 OX SP 20 Rh	6147 P6 OX 20 Pt 20 Rh	6120 P6 AR 20 Pt 20 Rh
11	6056 P6 AR 20 Pt	6057 P6 AR 20 Pt	6289 P6 AR 20 Rh	6059 P6 AR 20 Rh	-	-
10	6159 P6 OX SP 20 Pt	6079 P6 OX 20 Pt	6228 P6 OX SP 20 Rh	6087 P6 OX 20 Rh	6167 P6 AR 5 Pt 5 Rh	6062 P6 AR 5 Pt 5 Rh
9	6138 P6 OX 20 Pt	5014 P5 OX 20 Pt	6263 P6 OX 20 Rh	5024 P5 OX 20 Rh	6093 P6 OX 5 Pt 5 Rh	6212 P6 OX 5 Pt 5 Rh
8	8027 P8 OX 20 Pt	8030 P8 OX 20 Pt	8032 P8 OX 20 Rh	8031 P8 OX 20 Rh	-	-
7	6225 P6 OX SP 5 Pt	6207 P6 OX SP 5 Pt	6158 P6 OX SP 5 Rh	6104 P6 OX SP 5 Rh	8026 P8 OX + 225 hrs	8023 P8 OX + 225 hrs
6	6074 P6 OX + 225 hrs	6055 P6 AR + 225 hrs	6330 P6 OX + 36 hrs	6308 P6 AR + 36 hrs	5029 P5 OX + 225 hrs	5027 P5 OX + 225 hrs

Table 1: Sample matrix for MITR-II noble metal corrosion test showing location of cladding in Tiers 6 (bottom) through 16 (“div” means flow separator)

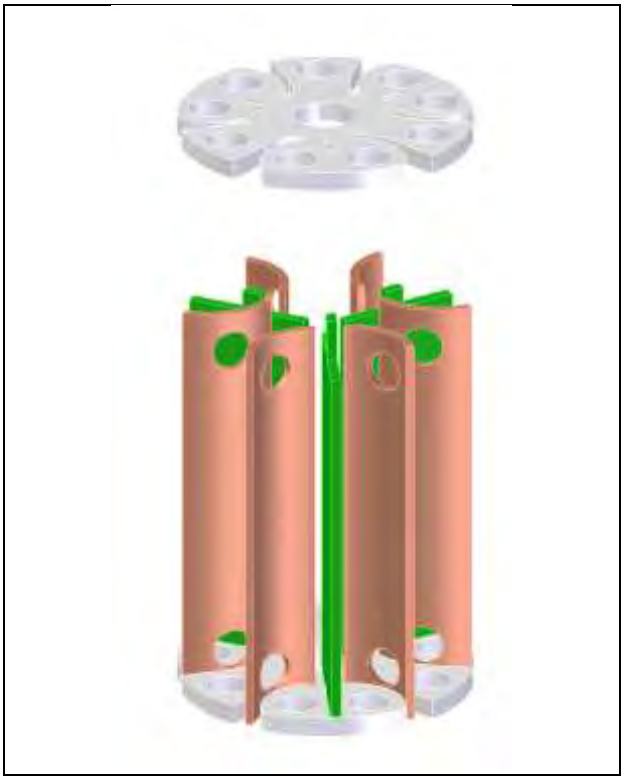

Figure 1: Schematic of NMCA corrosion module used in GNF MITR-II tests showing cladding coupon samples surrounded by flow separators and alumina fixture parts

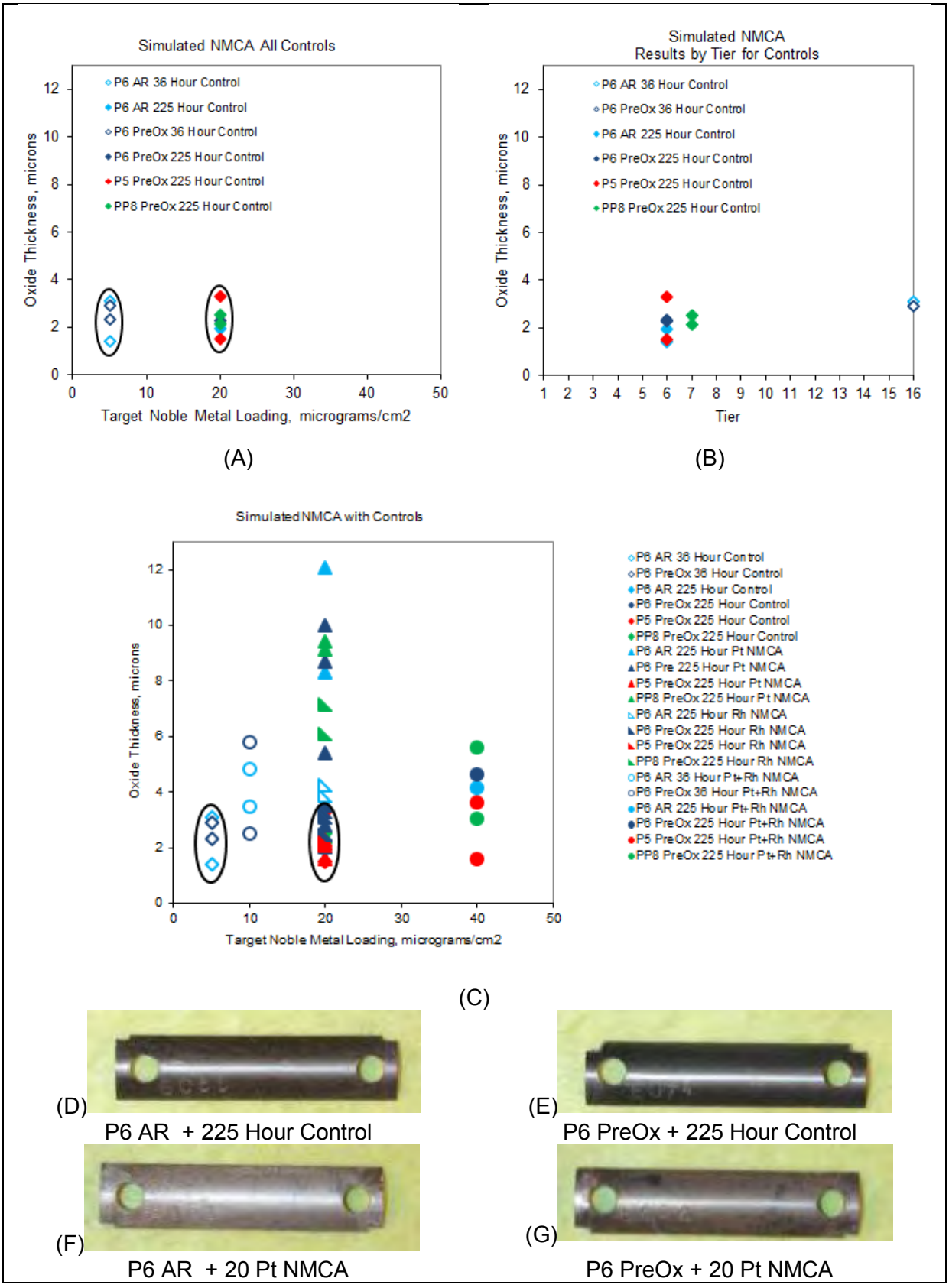

Figure 2: Oxide thickness and visual appearance of simulated NMCA treated cladding samples tested in MITR-II corrosion test loop

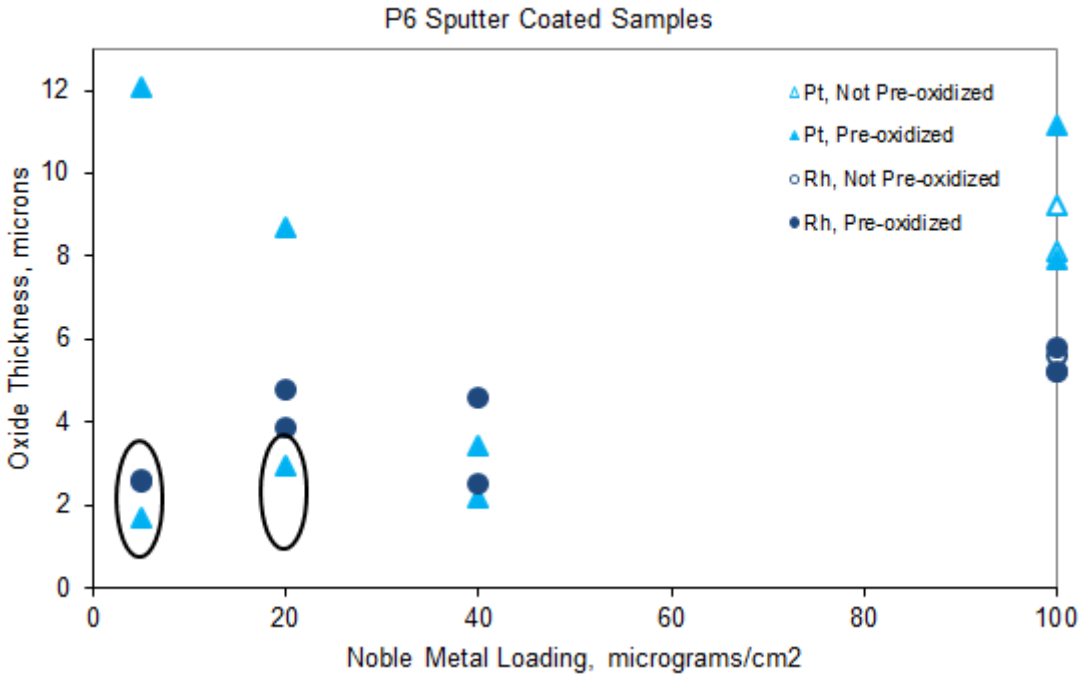

(A)

(B) P6 PreOx Sputter 5 Pt

(C) P6 PreOx Sputter 20 Pt

(D) P6 PreOx Sputter 40 Pt

(E) P6 PreOx Sputter 100 Pt

(F) P6 AR Sputter 100 Pt

Figure 3: Oxide thickness and visual appearance of P6 sputter coated cladding samples tested in MITR-II corrosion test loop

Test Reactor Evaluation of Zirconium Alloy Shadow Corrosion Behavior

D. LUTZ
Global Nuclear Fuel - Americas
6705 Vallecitos Road, Sunol, CA 94586 - USA

Y-P. LIN, P. CANTONWINE
Global Nuclear Fuel - Americas
3901 Castle Hayne Road, Wilmington, NC 28402 – USA

J. VARELA
GE HITACHI NUCLEAR ENERGY
6705 Vallecitos Road, Sunol, CA 94586 - USA

A. KUCUK, K. EDSINGER
Electric Power Research Institute
3420 Hillview Avenue, Palo Alto, CA 94304 - USA

M. McGRATH
Halden Reactor Project
Halden, P.O. Box 173, Norway

ABSTRACT

The shadow corrosion behavior of zirconium alloy materials used in Boiling Water Reactor (BWR) fuel assemblies was evaluated in test reactor experiments. The experiments were conducted to better understand the effect of material variations on shadow corrosion. Shadow corrosion experiments in the Massachusetts Institute of Technology (MIT) and Halden test reactors included test rigs comprised of material variations that exposed Zircaloy-2 and Zircaloy-4, and the alternate zirconium alloy NSF to stainless steel and X-750 that are known to cause shadow corrosion in BWRs when in close proximity to Zr-based fuel cladding and channels. The corrosion responses were generally small and variable, which made it challenging to identify meaningful differences and effects. In fact, two shadow corrosion tests in Halden showed no meaningful shadow corrosion effect, contrary to expectations, before successful rig design adjustments were made in a third test that resulted in reliable detectable effects, and provides some insight into the corrosion mechanism and experimental design. For shadow corrosion, the effects of cladding process type, counter electrode material, counter electrode spacing, or pre-oxidation were difficult to discern but results suggested that Rh is the stronger shadowing agent among those tested. NSF, a promising new zirconium alloy that is proposed to mitigate fuel channel bow, developed similar or slightly less maximum shadow corrosion levels compared to the Zircaloy-2 control.

1. Introduction

The zirconium alloy enhanced corrosion phenomenon referred to as shadow corrosion has been well known for many years. This corrosion enhancement mechanism results from the interaction between the zirconium alloy and nearby dissimilar metals such as X-750 and stainless steel. The corrosion enhancement on the zirconium alloy is localized and therefore the dissimilar nearby component appears to cast its “shadow”. A number of occurrences of

local corrosion enhancement of zirconium-based alloys in proximity to other components have been reported [1, 2].

Common examples of shadow corrosion are of stainless steel control blade handle shadows on Zircaloy fuel channels, and X-750 fuel assembly spacer grids on fuel cladding. It has not been until relatively recently that shadow corrosion has had a significant impact on fuel performance. Specifically, shadow corrosion-induced channel bow has caused interference with control blade motion [3, 4, 5], and in a very severe case shadow corrosion from X-750 spacers acting on Zircaloy fuel cladding has led to rod failure [6, 7].

As a result of this operating experience, the mechanism of shadow corrosion is of interest and has been the focus of experimental studies and investigations in the nuclear industry [8-13]. Châtelain et al., who conducted an experiment in a loop in the MITR-II reactor, showed that shadow corrosion could occur in reasonably short times when non-contacting counter and working electrodes are insulated from each other, and that the effect of various counter materials could be differentiated [12, 13]. Pt and X-750 counter electrodes had a strong effect, while a beta emitting Nitronic 32 and Zircaloy-2 had a negligible effect. Châtelain also observed shadows in ex-core locations while shadows have not been demonstrated in laboratory autoclave tests without radiation. In addition, they noted the shadow effect scaled with the inverse of the distance between the zirconium alloy and the counter material (that is, the smaller the distance the larger the shadow effect).

Early efforts by GNF to mitigate the channel shadow bow phenomenon consisted of exploring various material solutions that included pre-oxidation, low growth beta quenched Zircaloy-2, use of low hydrogen pickup Zircaloy-4, and the alternate zirconium alloys VB and NSF. To help evaluate these options, Global Nuclear Fuel (GNF) and GEH in collaboration with the Electric Power Research Institute (EPRI) and MIT, prepared samples with various conditions to provide early screening of them in a simulated BWR corrosion test loop in MIT's 5 MW test reactor. The test design and conditions were much like that used by Châtelain, with modules of samples and tapered counter electrodes facing each other, and separated in tiers by insulating ceramics.

Interestingly, the possible influence of noble metals, which are being used in BWRs to mitigate stress corrosion cracking of plant materials, on Zircaloy corrosion might share similarities to the shadow corrosion mechanism in some way. Since Châtelain demonstrated that platinum could cause shadow corrosion on Zircaloy [12, 13], the question of whether or not thin layers of Pt deposited on the surface of Zircaloy fuel components, or on the surface of nearby non-Zircaloy components, would affect the Zircaloy corrosion by a shadow corrosion-like mechanism was also of interest. To help explore this question, noble metal treated counters and solid noble metal counters were also included in the shadow corrosion screening test.

Upon completion of the GNF MIT test, all samples were shipped to the GE Hitachi Vallecitos Nuclear Center to characterize the corrosion test results. The hotcell examination work scope included documentation of the visual appearance of each sample, sectioning of each sample, measurement of the oxide thickness and estimation of the hydrogen content by metallographic techniques.

Results of the GNF MIT shadow corrosion screening test and characterization are reported in this paper. In addition, a similar material screening and mechanism test program was conducted by GNF in a corrosion loop in the Halden test reactor. Selected results of this GNF Halden shadow corrosion test program are useful to help interpret the MIT results and are also discussed on a limited basis in this paper.

2. Experimental Design

2.1 Specimen Matrix

The experimental matrix included three types of Zircaloy-2 barrier fuel cladding with fabrication process variations designated P5, P6, and PP8. The claddings originated from ASTM B350 grade ingots and were fabricated by GNF using standard production processing from tubeshells for 9X9 or 10X10 designs that resulted in intermetallic particle sizes that increase in order from P5 to P6 to PP8, respectively. Processing for P5 and P6 included a penultimate induction heat treatment, and all types were subjected to a final recrystallization anneal.. The inner zirconium barrier that is standard for GNF cladding was removed by machining. Channel materials used in the test included Zircaloy-2 in the recrystallized and beta quenched (BQ) states originating from ASTM B350 grade ingots, and recrystallized NSF, an Zr-Nb-Fe-Sn alloy. The recrystallized Zircaloy-2 channel materials also had two types of pre-oxidation, one a 400°C autoclave steam treatment at 1500 psig (10.34 MPa) for 7 days, and the other an oxide that resulted from an in-process Ar/Air annealing step.

Counter electrodes included solid Pt sheet, solid Rh sheet, a thin Pt coating on an inert alumina base, X-750, X-718, and stainless steel. An inert alumina counter electrode was included as a control condition. The solid Pt counter was used most extensively because of the strong effect that it had in Châtelain's tests [12, 13].

All cladding samples were cut lengthwise from a parent fuel cladding tube into a ¼ arc. The length of a sample was nominally 1.125 inches (28.58 mm) long. Holes 0.118 inches (3.00 mm) in diameter were drilled in both ends of the cladding samples for fixturing purposes. A change was made in the length of cladding shadow samples after the end holes were drilled, resulting in one of the fixturing holes being cut in half. Flat channel samples were 1.125 inches (28.58 mm) long by 0.271 inches (6.88 mm) wide. Channel samples did not have fixturing holes, but they did have bevels applied to form a trapezoid shape that provided the extra space that was needed to fit the samples into the small test fixture. Samples were positioned in five tiers within the bottom section of the reactor core. The matrix in Table 1 lists each sample, its position in the core, and its counter electrode. Additional noble metal corrosion samples were included in tiers above the shadow corrosion test tiers.

2.2 Specimen Holder Design and MITR-II Test Loop System

A system of insulating holders was designed to position the samples accurately in the reactor core and in specific relationship to the flow channels and shadow counter electrodes. Each sample holder was made from alumina 0.92" (23.4 mm) in diameter with a central hole for a spine that extended the entire length of the fixture. Four samples were mounted around the central spine. Cladding samples were positioned adjacent to the spine with the cladding inside surface towards the spine. The half hole on the cladding samples was specified to be positioned on the narrow gap end of the counter electrode. Channel samples were positioned with the beveled side facing towards the spine. A tapered, non-contacting counter electrode was positioned adjacent to the outward facing side of the specimens.

The counter electrodes had a tapered shape (10 degrees) so that the gap between the counter electrode and the test sample varied from top to bottom. Counters were 1 inch (25.4 mm) high by 0.25 inches (6.35 mm) wide. On one end of the counter there is an untapered area 0.195 inches (4.95 mm) long that would form a constant gap of 0.02 inches (0.5 mm) between the counter electrode and the sample. At the other end of the electrode the maximum gap would be about 0.12 inches (5 mm). An example of a tier design and layout illustrating cladding samples and counters is shown in Figure 1. The illustration of the shadow capsule shows two platinum sheet metal counter electrodes in blue, a rhodium counter electrode in cyan and an inert alumina counter electrode in pink.

The MITR-II test loop system is comprised of a number of out-of-pile and in-pile components designed to deliver circulating light water at 288°C and 10 MPa to an in-core autoclave that

contains the sample train. Additional details of the loop system are provided in related work discussed in Reference 14.

2.4 Irradiation History and Loop Conditions

The test achieved slightly more than 1600 hours irradiation (~67 days). Maximum powers were about 4.5 MW and were slightly lower in the second half of the irradiation period. Coolant temperature was maintained near 275°C, and conductivity in the letdown system varied between 0.1-0.3 µS/cm during the length of the run. The oxygen concentration in the letdown system was between 150-200 ppb and the dissolved hydrogen content was always less than 0.07 ppb.

3.0 Results

Post-irradiation examination included a visual inspection and metallographic oxide thickness measurements. Photomicrographs were taken of key representative areas of interest and oxide thickness measurements were made from the photomicrographs. Photomicrographs were taken at 3 elevations on both the counter electrode shadow face and the back face. The three locations are 1) narrow counter gap area (approx. 0.5 mm gap), 2) mid-sample height (approx. 2 mm gap), and 3) large counter gap (approx. 4-5 mm gap). For the longitudinal cladding samples, photomicrographs of the oxide were taken at these three elevations on the shadow face but only at the mid-height elevation on the back face. The back face on the cladding coupons is the cladding inner surface that was machined to remove the barrier. Machining created an irregular, variable surface condition that is not comparable to the outer surface. Following completion of the oxide examination, the samples were etched for hydrides.

The oxide thickness measurements and selected visual appearance photos are summarized in Figure 2 for the cladding samples and Figure 3 for the channel samples. The oxide thickness ranges between about 1 and 8 microns for all samples and conditions. Shadow corrosion effects on the counter side are expected to appear as a gradient in oxide thickness from one end of the specimen to the opposite end, with the thickest oxide occurring at the sample end where the gap is the smallest. When the oxide thickness on the top and bottom on the counter side are compared, there is very little difference and consistent trends are difficult to identify. For the initially unoxidized cladding samples, the oxide thickness at Gap 1 is similar to the gap at the opposite end (Gap 3) for 7 of the 9 samples exposed to a counter electrode, similar to samples exposed to inert controls. For the typical in-reactor shadow corrosion coupling of X-750 next to Zircaloy-2 cladding, there is no difference between the two ends of the sample (e.g., sample 6039). Likewise, the strong effect of a Pt counter electrode observed by Châtelain [12, 13] is not observed.

The two samples that have a distinct end-to-end difference of about 2.5-4.5 microns are a P6 (6034) and a PP8 (8005) that were exposed to a Rh counter electrode. The slightly thicker oxide is reportedly at the sample bottom where the counter gap is expected to be the largest and corresponds to the location of small oxide patches that are visible in the sample macrophotos (Figure 2). Oxide patches were not visible to the eye for the other samples. The size and position of the oxide patches and greater oxide thickness are at the end with the full hole. The orientation of the sample is established by the position of the half hole, whereby the half hole was specified to be on the end with the narrow gap, i.e. full hole is specified to be on the end with large gap. All cladding coupons were examined and results compiled according to this specified design. However, in light of questionable post-test results that were contrary to expectations, some available photographs of the pre-test assembly steps were inspected closely. Two of these photographs are shown in Figure 1 and clearly show that at least one sample is oriented with the half hole by the narrow gap and at least one other is oriented with the half hole towards the larger gap. The reported sample orientations are therefore unreliable and it is presumed that the two observed patches are in fact at the narrow gap position rather than the reported large gap position and

are due to shadow corrosion from the Rh counter electrode. In this light, these results then suggest that Rh is a stronger shadow agent than Pt or X-750 and that P5 is more resistant to shadow corrosion than P6 and PP8.

End-to-end shadow effects on the channel/strip materials were also weak. No isolated localized patches were observed at either end of any sample, however the beta quenched Zircaloy-2 had an irregular patch running from one end to the other. For the channel materials, an inert counter electrode was not used as a control, however the back side of the samples serves as a self-contained control for each sample. All of the channel samples were exposed to a solid Pt counter except for one Zircaloy-2 channel sample, which was exposed to stainless steel. A positive differential between counter side and back side oxide thicknesses at the same elevation for a given sample indicates shadow corrosion. The average side-to-side differentials for five of seven samples have small positive differentials, which implies a weak shadow effect. Counter-to-back side differentials are less than 0.5 microns except for the beta quenched Zircaloy-2 material, which has an average positive differential of about 3.5 microns. With such weak shadow effects, drawing broad conclusions about the effect of material type, counter type, counter spacing, or pre-oxidation for the channel materials is not practical.

Sample hydrogen contents are estimated to be less than 100 ppm for the initially unoxidized samples and between about 100 and 200 ppm for the non-beta quenched pre-oxidized samples. Hydrogen contents were found to be similar at both top and bottom and thus no distinction can be made related to counter spacing, nor does the hydrogen content have a strong dependence on the counter material type. The basket weave microstructure of the beta quenched sample is different than the recrystallized materials which affects the hydride distribution, nonetheless it appears to have a hydrogen content that is less than 50 ppm. Steam pre-oxidized samples have the highest hydrogen contents.

4.0 Discussion

Shadow corrosion was reported to occur in the MITR-II reactor in the short 1999 ABB test program performed by Châtelain [12, 13], and extensive GNF commercial BWR experience indicates that shadow corrosion appears in visual examinations and eddy current lift-off measurements within one annual cycle under a variety of water chemistry conditions. No commonly used cladding materials, which are essentially like those currently tested, are immune to shadow corrosion in BWRs. Thus stronger shadow corrosion effects were anticipated to occur in the current GNF MIT test and the reason(s) that they were not stronger is surprising and suggests the test condition did not capture certain key test parameters.

The basic design of the GNF MITR-II loop test is very similar to Châtelain's design. Structural and insulating materials were nominally the same, that is mainly titanium and alumina, respectively. The total sample surface areas and counter electrode dimensions and pitch and gap, as well as the overall size of the test thimble, were similar. Use of an oxidizing water chemistry was also similar. Radiation and radiolytic species in the water were present in both cases. In the absence of simple explanations for the weak effects based on these basic test comparisons, consideration of results from related shadow corrosion tests conducted by GNF in Halden and work by Lysell [15] has led to a hypothesis that could rationalize the observations.

In parallel with GNF's MIT shadow corrosion test, a similar material screening and mechanism test program was conducted by GNF in a corrosion loop in the Halden test reactor. Results of this GNF Halden test program were also weak in two of three tests, and adaptive measures resulted in a stronger response in a third test. .

The first Halden test was performed with 250 ppb oxygenated water conditions over 111 days with the same class of channel materials used in the GNF MIT test. The test rig had

coupons in stacks with all 316 stainless steel counter electrodes “sandwiched” between them with a 1 mm spacing. Electrical isolation between all coupons and counter electrodes was a critical design characteristic that was specified, and implemented through pre-oxidation of Zircaloy fixture hardware. Shadow corrosion was minimal to non-existent.

In an attempt to produce the expected stronger effects, a second test was conducted with essentially the same design and materials but with the coupon/counter gap reduced from 1 mm to 0.5 mm, doubling of the total irradiation time, inclusion of one X-750 counter electrode, use of a small section notched out of some counter electrodes to provide a visual indication of shadow corrosion, and fixture hardware that had direct contact with the sample used without pre-oxidation of the hardware. With these changes, post-test eddy current measurements of the oxide thickness again indicated extremely weak to non-existent shadow effects. Interestingly, similar to GNF’s MIT test, the beta quenched Zircaloy-2 had the most noticeable effect, which was no more than about 2 microns on average.

As the expected stronger shadow corrosion effects were still not produced in the second Halden test, a third test with several very different design variations was conducted. The third test ran for 157 days and doubled the oxygen content of the coolant to 400-500 ppm. The design variation that most succeeded in developing a shadow effect was one that had a 316SS counter electrode that contacted the test coupon in a local spot and had a 0.5 mm gap elsewhere. This design is shown in Figure 4, compared to a non-contacting module very much like that used in the second test. Eddy current oxide thickness measurement results for the Zircaloy-2 coupons in the third Halden test for the contacting and non-contact counter electrodes are also shown in Figure 4. The non-contact module had maximum oxide thicknesses that were no more than about 2 microns on the counter side, and a little less on the back side. No big effect of the counter notch was observed. In contrast, the back side measurements on the contact module were about 3-4 microns, but up to 12.5 microns on the counter side directly under the contact point, and a decrease in thickness moving away from the contact point. The alternate channel material NSF with the spring-type contact design had slightly less shadow corrosion than its Zircaloy-2 counterpart.

Lysell conducted a shadow corrosion test that demonstrated that shadow corrosion could be impeded when the working and counter electrodes are well isolated electrically [15]. Lysell designed a shadow corrosion test rig that had three Zircaloy-2 cladding samples in series inserted within a stainless steel flow shroud. Stainless steel counter electrodes were spot welded to the shroud near the center of each cladding sample to form a 0.5 mm gap between the counter and cladding. The top and bottom cladding samples were physically contacting the rig’s stainless steel end pieces, while the center 15 mm long cladding sample was placed on a 90 mm long sapphire tube that isolated it from the stainless steel end pieces, shroud, and counter electrodes. The rig was then tested for 432 hours with 285°C flowing oxygenated conditions in Studsvik’s test reactor INCA loop. There was no indication of shadow corrosion on the isolated center sample on the sapphire rod, whereas the top and bottom specimens had clear indications of shadow corrosion that was about 2 microns thicker beneath the counter electrode versus away from the electrode. Lysell’s convincing explanation is that the shadow corrosion mechanism is fundamentally galvanic in nature and that an electrical connection between the Zircaloy and counter electrode is necessary to complete the electrical circuit for the anodic and cathodic charge transfer reactions. The sapphire rod provided complete, or nearly complete, electrical isolation and disrupted the oxidation/reduction circuit and prevented shadow corrosion.

A hypothesis is proposed to rationalize the weak shadow corrosion response in the GNF MIT test based on consideration of aspects of Châtelain’s [12, 13] MIT test, GNF’s Halden tests, and Lysell’s isolation experiment [15]. The hypothesis is that the alumina materials used in the Châtelain [12, 13] and GNF MIT tests are different, and that the alumina in the Châtelain test was more conductive under irradiation than the alumina used in the GNF test. It is

known that the alumina used for the GNF test was not the same as the Châtelain test, because a pre-test by GNF used a high silica alumina that dissolved in the test loop, and new low silica alumina was then purchased and used for the GNF test reported here. Unfortunately, electrical conductivity information for the alumina materials for all of the tests, under irradiation, is not available to confirm the hypothesis, nor are electrical conductivities of rig components commonly reported in the literature for shadow corrosion tests. The three GNF Halden tests that had contacting and non-contacting test modules support the hypothesis that weak physical and electrical connection between the coupons and counter electrodes existed and could inhibit completion of the electrical circuit that is necessary for forming shadow corrosion.

6.0 Summary

The shadow corrosion behavior of zirconium alloy materials used in BWR fuel assemblies was evaluated in test reactor experiments to provide material screening information. Shadow corrosion experiments in the Halden and MIT test reactors included test rigs comprised of material variations that exposed Zircaloy-2 and Zircaloy-4, and the alternate zirconium alloy NSF to the common BWR shadowing materials stainless steel, X-750, and Pt that are known to cause shadow corrosion. The corrosion responses were generally small and variable, which made it challenging to identify meaningful differences and effects. For shadow corrosion, the effects of cladding process type, counter electrode material, counter electrode spacing, or pre-oxidation were difficult to discern but results suggested that Rh is the stronger shadowing agent among those tested. Beta quenched Zircaloy-2 generally had the largest effect in multiple tests.

The lack of strong shadow corrosion effects was perplexing in light of earlier results from tests in MIT by Châtelain [12, 13] that used nominally the same test design. Work by Lysell [15] convincingly demonstrated the need for electrical connection between the counter electrode and the test coupon in irradiation test fixtures. In light of Lysell's results, a hypothesis is proposed to rationalize the current test results whereby 1) alumina intended to be electrically insulating under irradiation and used in the Châtelain MIT tests was more electrically conductive than the alumina used in the GNF tests, and 2) test fixtures used in Halden did not provide sufficient electrical contact until intentional physical contact was ensured by a series of rig design changes. The results presented here provide some cautionary experience for the industry about important design questions that should be considered prior to conducting future shadow corrosion test programs.

7.0 Acknowledgements

This work was funded by EPRI's Fuel Reliability Program (FRP).

The authors are appreciative of the overall effort that the MIT staff applied to design and complete the MITR-II test, in particular Principal Investigators Professor Ron Ballinger and Pete Stahle.

8.0 References

1. Chen, J. S.F. and Adamson, R. B., "Observations of Shadow Phenomena on Zirconium Alloys", Proceedings of the International Topical Meeting on LWR Fuel Performance, ANS, West Palm Beach, Florida, 1994, pp. 309-317.
2. Adamson, R. B., Lutz, D. R., Davies, J. H., "Hotcell Observations of Shadow Corrosion Phenomena," KTG Conference Verifikation des Brennelementverhaltens durch Nachbestrahlungsuntersuchhungen und Experimente, Fachtagung der KTG-Fachgruppe, February 29-March 1, 2000, Karslruhe, Germany.
3. Cantonwine, P.E., Karve, A.A., Lin, Y.P., Mahmood, S.T., White, D.W., and Crawford, D.C., "GNF Channel Performance and Success in Mitigating Channel Distortion and Cell Friction," 2008 Water Reactor Fuel Performance Meeting (WRFPM 2008), Paper No. 8078, October 19-23, 2008, Seoul, Korea (2008).

4. Cantonwine, P., Paustian, H., Hahn, G., Tusar, J., Reitmeyer, M., and Mader, E., “Channel – Control Blade Interference in GE Boiling Water Reactor, D-Lattice Plants with Zircaloy-2 Channels,” 2010 LWR Fuel Performance/TopFuel/WRFPM Conference, Paper No. 079, September 26-29, Orlando, Florida, (2010).
5. Mahmood, S.T., Cantonwine, P., Lin, Y.P., Crawford, D., Edsinger K., and Mader, E.V., “Shadow Corrosion-induced Bow of Zircaloy-2 Channels”, 16th International Symposium on Zirconium in the Nuclear Industry,Chengdu, China, ASTM STP 1529, (2010).
6. Andersson, B, “The Enhanced Spacer Shadow Corrosion Phenomenon,” Verifikation des Brennelementverhaltens durch Nachbestrahlungsuntersuchungen und Experimente, Fachtagung der KTG-Fachgruppe, February 29-March 1 2000, Karlsruhe, Germany.
7. Zwicky, H-U., Loner, H., Andersson, B., Harbottle, J., “Enhanced Spacer Shadow Corrosion Phenomenon on SVEA Fuel Assemblies in the Leibstadt Nuclear Power Plant,” ANS International Topical Meeting on Light Water Reactor Fuel Performance, April 10-13, Park City, Utah, 2000.
8. Nystrand, A., Lysell, G., “On the Shadow Corrosion Mechanism for Zirconium Alloys,” TopFuel 2001, Stockholm, Sweden, May 27-30, 2001.
9. Lemaignon, C., “Impact of Beta Radiolysis and Transient Products on Irradiation-Enhanced Corrosion of Zr Alloys”, J. Nuc. Mat. 187, 1992, p. 122-130.
10. Kim, Y.-J., Rebak, R., Lin, Y.-P., Lutz, D., Crawford, D. C., Kucuk, A. and Cheng, B., “Photoelectrochemical Investigation of Radiation-Enhanced Shadow Corrosion Phenomenon,” J. ASTM Intl., Vol. 7, No. 7. doi:10.1520/JAI102952.
11. Andersson, B., Limback, M., Wikmark, G., Hauso, E., Johnsen, T., Ballinger, R. G., and Nystrand, A.-C., "Test Reactor Studies of the Shadow Corrosion Phenomenon," Zirconium in the Nuclear Industry: Thirteenth International Symposium, ASTM STP 1423, G. D. Moan and P. Rudling, Eds., ASTM International, West Conshohocken, PA, 2002, pp. 583-615.
12. Châtelain, A., Enhanced Corrosion of Zirconium-Base Alloys in Proximity to Other Metals: The “Shadow Effect”, Master’s Thesis, Massachusetts Institute of Technology, Cambridge, MA, February 2000.
13. Châtelain, A., Andersson, B., Ballinger, R. G., Wikmark, G., “Enhanced Shadow Corrosion of Zirconium-Base Alloys in Proximity to Other Metals: The ‘Shadow Effect’,” Proceedings of the International Topical Meeting on Light Water Reactor Fuel Performance, American Nuclear Society, Park City, Utah, April 2000, pp. 485-498.
14. Lutz, D, Lin, Yang-Pi, Cantonwine, P, Kucuk, A, Edsinger, K, “Test Reactor Evaluation of Zirconium Alloy NMCA Corrosion Behavior,” Paper A0159, TopFuel 2015 Reactor Fuel Performance, Zurich, Switzerland, September 13-17, 2015,
15. Lysell, G., Nystrand, A.-C., Ullberg, M., “Shadow Corrosion Mechanism of Zircaloy,” Journal of ASTM International, June 2005, Vol. 2, No. 6, Paper ID JAI12374.

	6 O'Clock		9 O'Clock		12 O'Clock		3 O'Clock	
Tier	**Sample**	**Counter**	**Sample**	**Counter**	**Sample**	**Counter**	**Sample**	**Counter**
5	P5 Clad	Pt (solid)	P5 Clad	Rh (solid)	P5 Clad	Inert (alumina)	PP8 Clad	Pt (solid)
4	P6 Clad	Pt (solid)	P6 Clad	Rh (solid)	P6 Clad	Inert (alumina)	PP8 Clad	Rh (solid)
3	P6 Clad	Thin Pt coating over inert (alumina)	P6 Clad	X-750 sheet	P6 Clad	X-718 sheet	VB Strip	Pt (solid)
2	BQ Zr2 NoOx Chan	Pt (solid)	NSF NoOx Chan	Pt (solid)	Zr2 NoOx Chan	Pt (solid)	Zr2 NoOx Chan	Stainless
1	Zr2 NoOx Chan	Pt (solid)	Zr2 TSA Ox Chan	Pt (solid)	Zr2 PreOx Chan	Pt (solid)	Empty	Empty

Table 1: Sample matrix for MITR-II shadow corrosion test showing location of cladding and channel strip samples and corresponding counter electrodes in Tiers 1 (bottom) through 5

Figure 1: Shadow corrosion modules used in GNF MITR-II tests; left, schematic showing cladding coupon samples surrounded by tapered counter electrodes; right, in-process assembly of cladding test modules

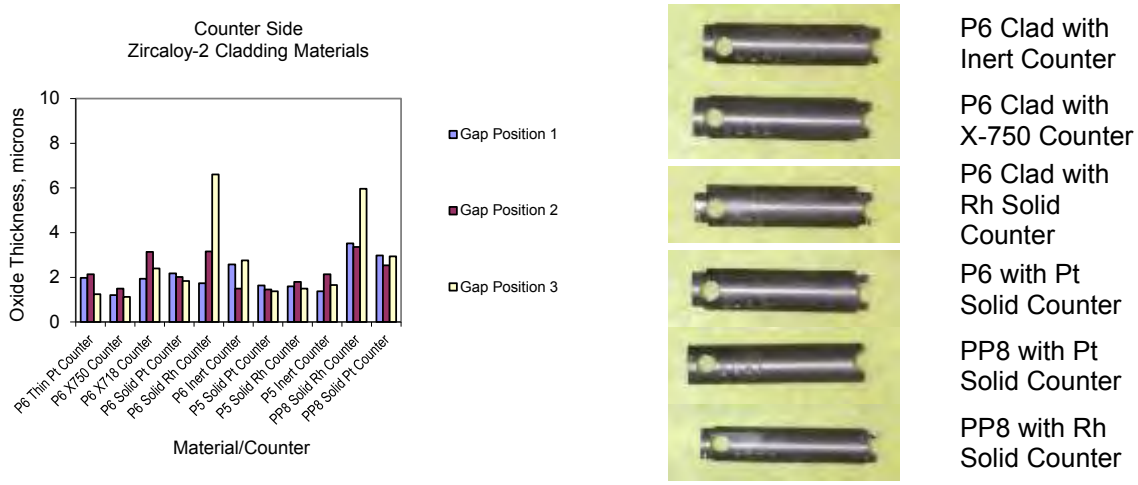

Figure 2: Post-test oxide thickness and visual appearance of P6 and PP8 cladding exposed to various counter electrode materials in MIT test

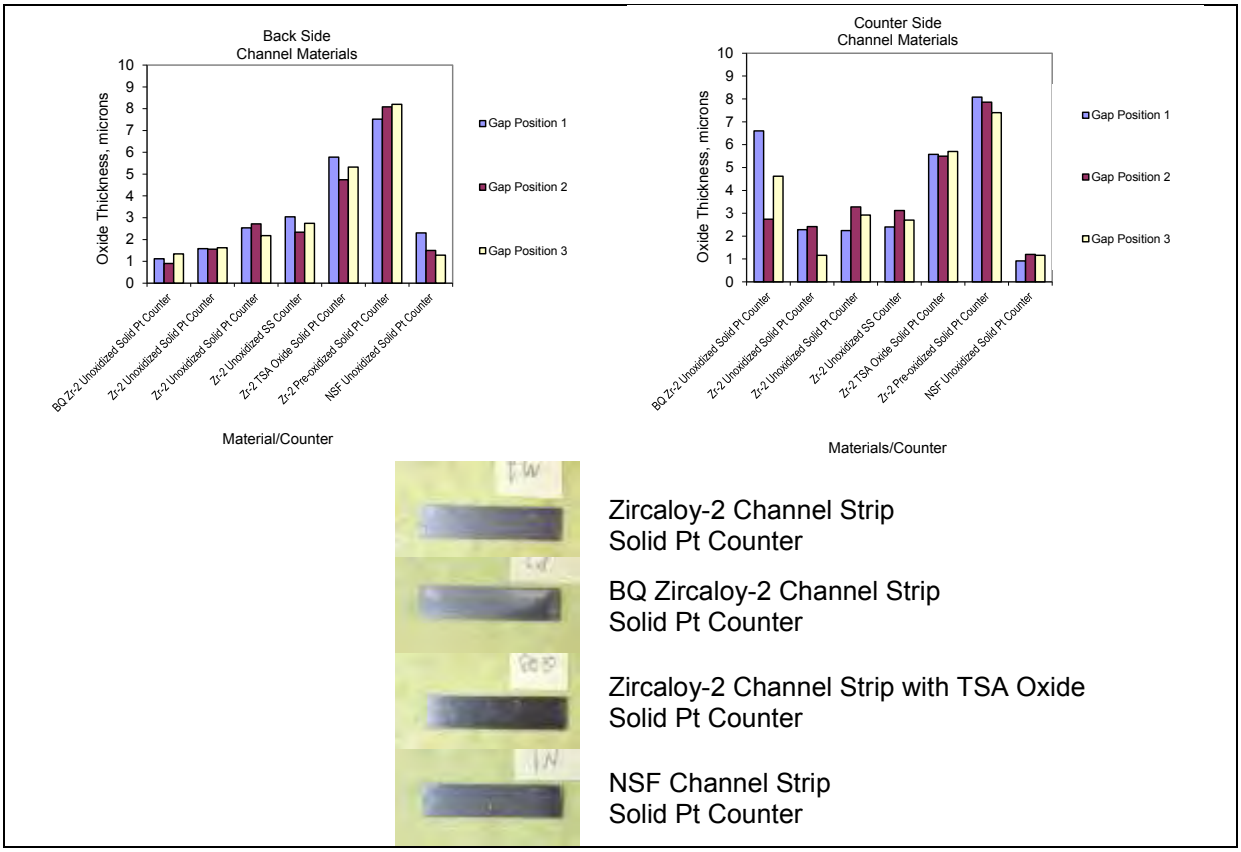

Figure 3: Post-test oxide thickness and visual appearance of various channel materials exposed to solid Pt counter electrodes in MIT test

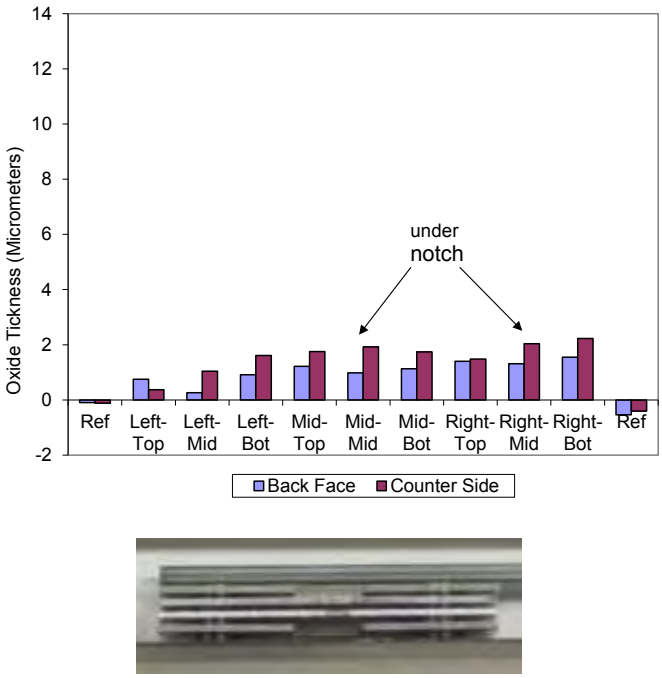

(a) Non-Contact Counter Electrode

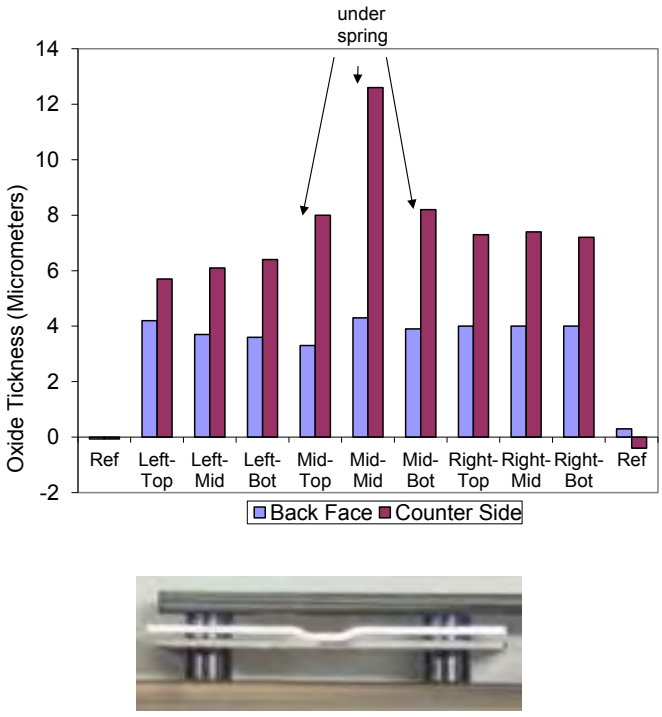

(b) Contact Counter Electrode

Figure 4: Eddy current oxide thickness comparison of two test modules with and without stainless steel counter electrode contact on Zircaloy-2 in third Halden test

XANES ANALYSIS OF IRON IN ZIRCALOY-4 OXIDES FORMED AT DIFFERENT TEMPERATURES STUDIED WITH MICROBEAM SYNCHROTRON RADIATION

BRENDAN M. ENSOR*, ARTHUR T. MOTTA
Department of Mechanical and Nuclear Engineering, The Pennsylvania State University
227 Reber Building, University Park, PA 16802 – USA

RAM BAJAJ, JOHN R. SEIDENSTICKER
Bettis Atomic Power Laboratory, Bechtel Marine Propulsion Corporation
814 Pittsburgh-McKeesport Boulevard, West Mifflin, PA 15122 – USA

ZHONGHOU CAI
Advanced Photon Source, Argonne National Laboratory
9700 South Cass Avenue, Argonne, IL 60439 – USA

*Corresponding Author - *Email Address:* bme133@psu.edu *Phone*: 814-865-9709

ABSTRACT

The different corrosion rates observed in zirconium alloys are attributed to differences in alloying element content and how these elements affect the microstructure of the protective oxide layers formed in these alloys. In this study, six thin oxide layer samples formed on Zircaloy-4 at four autoclave corrosion temperatures between 274°C and 400°C were examined using a microbeam at the Advanced Photon Source (APS) in Argonne National Laboratory (with 0.2 μm resolution) to perform fluorescence and X-ray absorption near-edge spectroscopy (XANES). The X-ray fluorescence capabilities and high spatial resolution permitted by the microbeam allowed for detailed analysis of the microstructure of the oxide layers to give insight into the growth mechanism of these oxides. Because second-phase precipitates are known to strongly affect overall corrosion behavior, it is important to better understand their oxidation kinetics when incorporated into the oxide layer. To that end, the iron X-ray absorption edge was analyzed using XANES. The results show that zirconium corrodes preferentially compared to iron both in precipitates and in the matrix, with iron atoms becoming completely oxidized ~2 μm from the oxide metal interface in samples corroded in water, and slightly farther in samples corroded in steam.

1. Introduction and Background

Zirconium alloys are widely used in water-cooled nuclear reactors as fuel cladding due to their low neutron cross-section, suitable mechanical properties, and excellent corrosion resistance. Corrosion resistance in these alloys is important because a typical nuclear reactor operates in water at temperatures and pressures as high as 360°C and 15.5 MPa, respectively. These alloys must remain in these harsh environmental conditions for years and, therefore, the fuel cladding, which encapsulates the fuel, must be as resistant to corrosion as practically possible. This is because as zirconium alloys oxidize, in addition to decreased heat transfer through the greater thermal resistance of the oxide layer, hydrogen from the corrosion reaction ingresses into the metal where it may precipitate as hydrides causing embrittlement [1].

Early testing from the 50's and 60's demonstrated that unalloyed zirconium metal, made from crystal bar or sponge exposed to high temperature, exhibits a deleterious oxidation behavior, known as breakaway corrosion, in high temperature water conditions, where accelerated corrosion and oxide spalling occur [2-3]. What makes zirconium alloys more resistant to corrosion

than pure material is the intentional addition of small amounts of alloying elements to the material. Although alloying elements exist in crystal bar and sponge zirconium, their levels are low and they are not properly controlled. Because some alloying elements suppress accelerated corrosion (e.g. Fe), it is logical that studying the behavior of the alloying elements themselves when incorporated into the protective oxide layer can lead to insights into the corrosion of zirconium alloys.

The common commercial zirconium alloys in use today contain tin, niobium, iron, chromium, and nickel, although other elements, including oxygen, have been used [1]. Whereas niobium and tin have reasonable solubility in alpha Zr, the transition alloying elements iron, chromium and nickel dissolve only to a few hundred ppm before forming intermetallic precipitates [1]. There is evidence from numerous studies using both transmission electron microscopy (TEM) and X-ray absorption near-edge structure (XANES) analysis that the second phase particles (SPPs) oxidize later than the Zr matrix [4-10]. XANES analysis has been used by other researchers to determine chemical state, measure atomic distances, and describe local bonding of alloying elements in zirconium alloys [11-13]. Recently, the work of Couet et al. has claimed that Fe and Nb atoms oxidize later than the Zr matrix [4]. The incorporation of second phase particles in the metallic state in the oxide layer could play a role in the oxidation kinetics and hydrogen pickup of the alloy as a whole, since the oxide conductivity and hydrogen transport could be affected by the incorporation of the alloying elements in the metallic state in the oxide layer or by the oxidation of these elements to different oxidation states than those of Zr [4]. Also, the specific role of precipitates in providing cathodic/anodic sites for hydrogen ingress or short circuit paths for electron migration through the oxide would be affected by their oxidation state. In this study, we investigate the oxidation of Fe in zirconium alloy oxide layers as a function of corrosion temperature using microbeam synchrotron radiation, which allows tracking of the evolution of the XANES signal with distance from the metal-oxide interface, in order to understand how temperature plays a role in Fe oxidation.

2. Experimental Methods

2.1. Materials

The alloy of interest for this study was Zircaloy-4, which has a composition of 1.2-1.7 wt.% Sn, 0.18-0.24 wt.% Fe, 0.07-0.13 wt.% Cr, and 1000-1400 ppm oxygen with the remainder as zirconium. The six Zircaloy-4 samples examined in this study are listed in Table 1.

Table 1- Samples examined at the 2-ID-D beamline at the APS

Sample	Alloy	Exposure Condition*	Time (days)	Oxide thickness (μm)**	Heat Treatment [14]
H1190R	Zircaloy-4	274°C water	3003	2.35	β-quenched
N2513	Zircaloy-4	316°C water	3113	13.1	Rx α-annealed
H1405J	Zircaloy-4	360°C water	20	1.14	Rx α-annealed
H1406J	Zircaloy-4	360°C water	120	2.09	Rx α-annealed
H1312J	Zircaloy-4	400°C steam	41.3	3.5	Rx α-annealed
H1313J	Zircaloy-4	400°C steam	259.4	9.1	Rx α-annealed

Five samples in Table 1 were in the recrystallized alpha annealed condition processed in the same manner as described by Bajaj and Kammenzind [14], while the other sample was in the beta quenched and annealed condition and produce smaller precipitates as shown by Anderson and Bajaj [15]. The second phase particles, C14 Laves phase precipitates $Zr(Fe_xCr_y)_2$, in the five alpha annealed Zircaloy-4 samples were intragranularly distributed globular particles that had an

*H1190R, H1312J, and H1313J were corroded for 3 days at 360°C prior to listed exposure, <0.8 μm of the oxide for all
**Oxide thickness is average thickness based on the weight gain of the sample

average diameter of 0.24 μm as described in Kammenzind et al. [16]. The precipitates in the β-quenched sample were of irregular shape and were present at the lath boundaries [15]. Anderson and Bajaj show morphologies, chemical characteristics (Fe/Cr ratio) and crystal structures of the particles for both types of samples [15].

The samples were tested in autoclaves in the form of ~2.5 cm x ~2.5 cm x ~1 mm thick coupons in either single phase water (274-360°C) or steam (400°C) and had film thicknesses ranging from ~1 μm to ~13 μm. Note that some coupons were exposed in the autoclaves in a single exposure run (as short as 20 days) and others multiple exposures to as long as 3113 days. The samples were judiciously selected to study oxidation behavior of Fe in Zircaloy-4 as a function of: (1) exposure temperature from 274°C to 360°C in the same medium (water) in post transition films, (2) environment (water vs. steam), (3) pre-transition vs. near transition film thickness (H1405J at 1.14 μm vs. H1406J at 2.09 μm) at the same temperature in water, (4) same temperature but with different thickness (H1313J and H1312J) in steam, (5) similar exposure times at different temperatures and texture (N2513 vs. H1190R), and (6) same film thickness but different heat treatment (H1190R vs. H1406J), which may reveal different behavior due to differences in particle shapes and chemistries for different heat treatments [15].

Figure 1 shows weight gain (mg/dm^2) vs. exposure time (in days) for the six samples listed in

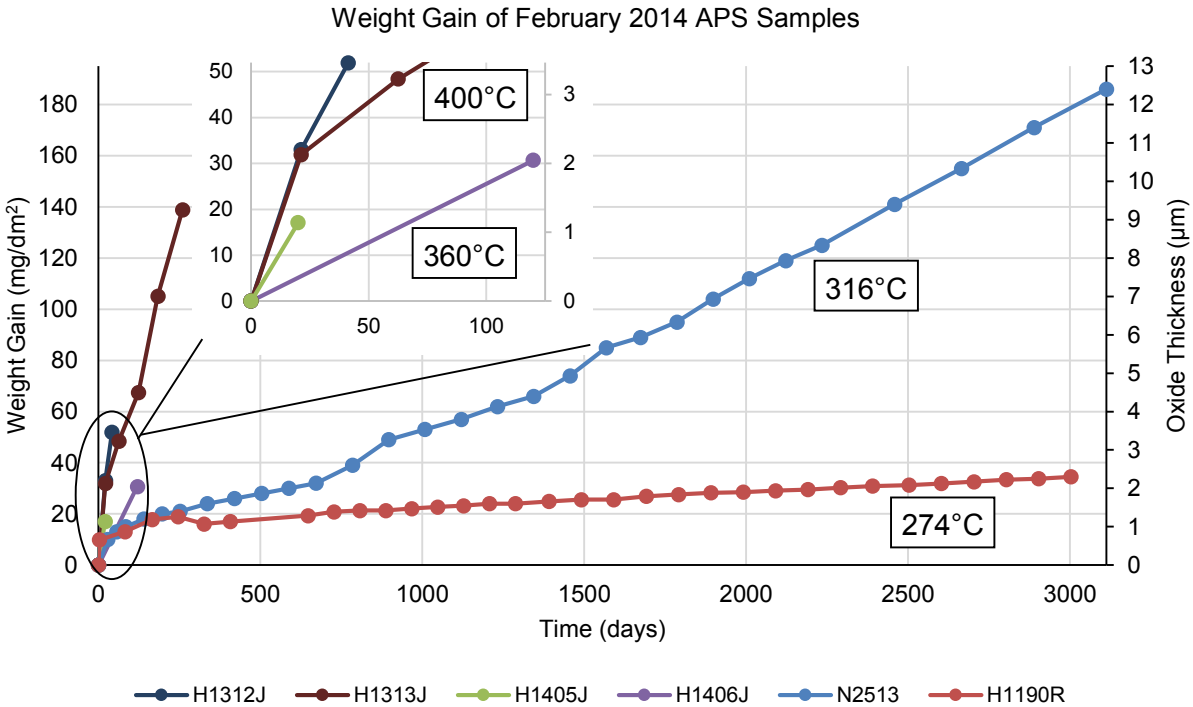

Figure 1- Weight gain data for the six samples examined at the 2-ID-D beamline at the APS in Feb 2014.

Table 1. The average oxide thicknesses are based on the weight gain with a conversion of ~15 mg/dm^2 to 1 μm of oxide. There is a large difference in corrosion rate and exposure times across the samples including samples in both the pre-transition and post-transition regime. Only a few measurements were made for some of the samples corroded over a short time, thus some of the finer aspects of the progression of weight gain were missed.

2.2. Experimental Techniques

The Advanced Photon Source (APS), a national synchrotron radiation light source research facility at the Argonne National Laboratory (ANL), was used to investigate the oxidation behavior of iron

in zirconium alloys corroded at various temperatures. The microdiffraction x-ray source at the APS (2-ID-D beamline) features high beam brilliance, small 0.2 μm x 0.2 μm spot size, and tunable energy from 5 to 32 keV, permitting precise investigation of the Fe x-ray absorption edge using XANES [11-12,17]. The samples were in the form of a segment of the coupon prepared by sectioning, mounting in cross section, and polishing to a final finish in a composite of Mo and epoxy in a brass tube. Sample preparation was identical to that done in Spengler et al. and by other researchers [4,10,18]. At the beamline, each sample was affixed onto an aluminum stud parallel to the beam and then tilted into the beam's path. A Ge(Li) Canberra solid state detector was used to acquire fluorescence data at each step, which allowed precise positioning of the beam relative to the oxide-water and metal-oxide interfaces. Figure 2 shows a fluorescence scan of one of the samples.

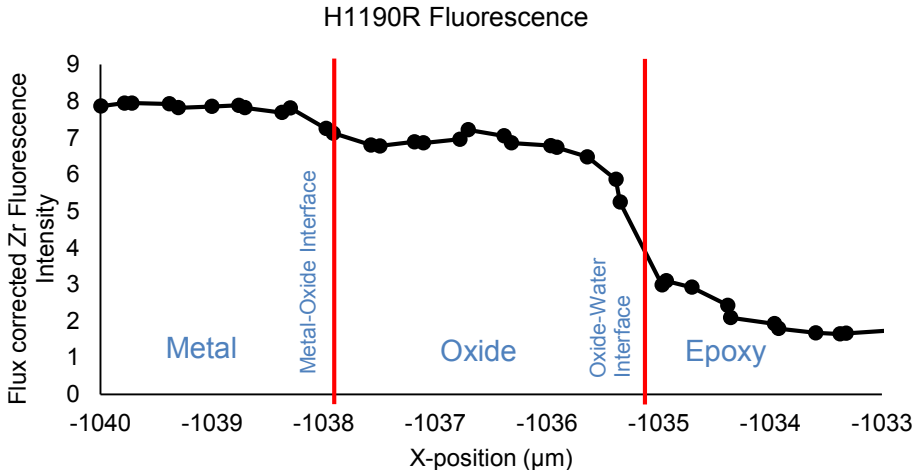

Figure 2- Example of the flux corrected zirconium fluorescence counts from sample H1190R (274°C) taken at the 2-ID-D beamline at the APS used to determine the metal-oxide and oxide-water interfaces.

The Zr fluorescence counts were used to determine the metal-oxide interface and the oxide-water interface. The Zr counts were normalized to the incoming beam flux, which varied slowly during acquisition. The interfaces were then determined by finding the midpoint of the line between the regions on the fluorescence graph, as seen in Figure 2. In Figure 2, on the left, the beam is in the metal; a small drop is seen at the metal-oxide interface (since the oxide provides slightly less Zr fluorescence than the metal) and a larger drop is observed at the oxide-water interface, as indicated. It should be noted that the oxide thickness, measured by fluorescence, does not always match the average oxide thickness based on weight gain due to the variability of the local oxide thickness. Figure 3 shows SEM micrographs of samples corroded in steam (a) and water (b), with

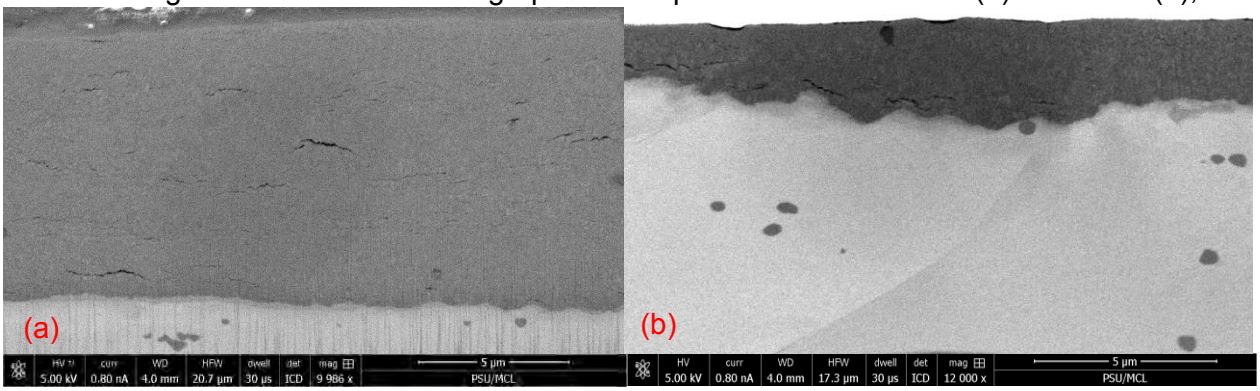

Figure 3- SEM images of (a) H1313J (Zircaloy-4, 400°C for 259.4 days) and (b) H1406J (Zircaloy-4, 360°C for 120 days) taken using a FEI Helios NanoLab™ 660 SEM/FIB showing the oxide (dark gray) and the metal (light gray).

oxide thicknesses of 9.1 μm and 2.09 μm respectively. The oxide layer in (b) illustrates the variability in oxide thickness.

For each scan, the sample was moved in steps of 0.1-0.25 μm across the oxide layer as fluorescence and XANES data were simultaneously acquired. Although the steps were not always equidistant, due to the mechanics of the stage setup and motor, the actual position of the beam was well known. For each sample, one full XANES scan was acquired at each location in the oxide layer. This means that the beam traversed the sample and at each stop a XANES scan near the Fe absorption edge (encompassing a range of 100 eV, from 7.078 keV to 7.178 keV) was obtained. Because XANES examines the structure of the x-ray absorption spectra for a particular element, which is caused by photoabsorption of an electron promoting it to a higher energy state and a subsequent photon emission [17,19], the absorption edge and shape of the spectra are affected by the local bonding of the element in question, providing a means to determine the chemical state of the alloying elements at each location by matching the spectra obtained from a sample to a linear combination of spectra from standards [4,9,13].

The Fe fluorescence counts were used to examine the Fe absorption edge. Examples of the flux-corrected Fe fluorescence counts are shown in Figure 4a. The main point to be observed in Figure

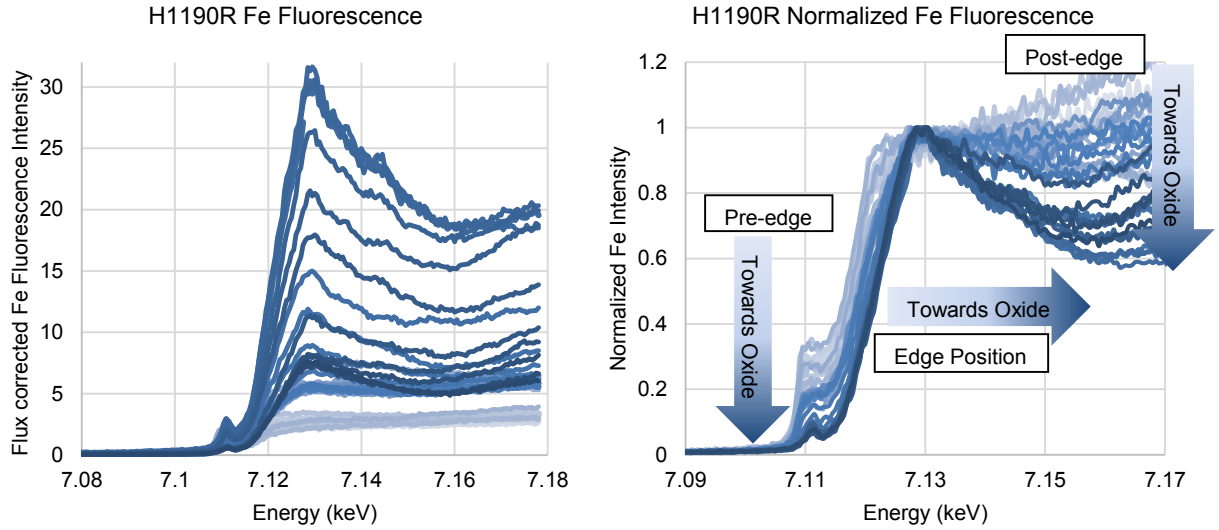

Figure 4- (a) Flux corrected Fe fluorescence counts obtained as the beam is scanned from the metal into the oxide layer cross section for sample H1190R (Zircaloy-4 corroded at 274°C) and (b) normalized to the maximum value between 7.12 and 7.135 keV; examined at the 2-ID-D beamline at the APS.

4a is the change in the shape of the absorption curve as one moves from the metal (lighter) to the oxide (darker lines). Note that the variation in absorption intensity is not physically significant, since it primarily depends on the number of Fe atoms hit by the beam and each spectrum is analyzed individually. Based on a 0.5% volume percentage of precipitates, with an average spherical precipitate diameter of 0.24 μm [14], 0.2 μm x 1 μm footprint of the beam, and at least a 50 μm beam penetration (from mass attenuation of photons at these energies), on average at least four full precipitates are captured in each scan (the four could be composed fractionally of many more than four precipitates). Over the course of a 10 micron scan, there is a >99.7% probability of hitting at least one precipitate at every point [4]. The actual number of precipitates contributing to the signal is higher. The XANES spectra shown in Figure 4a were taken from a 2.35 μm thick oxide formed at 274°C. Here the colors indicate the translation of the microbeam from the metal (lighter lines) into the oxide until the oxide-water interface. Figure 4b shows a normalization of the flux corrected Fe fluorescence intensity shown in Figure 4a. The spectra were normalized to the maximum value for an individual scan between 7.12 keV and 7.135 keV. The spectra acquired from locations in the oxide that are furthest from the metal-oxide interface are darkest. It is clear that a systematic variation of the Fe x-ray absorption edge occurs as one moves

away from the metal-oxide interface through the oxide. Note the evolution of edge energy[1], pre-edge maximum intensity[2], and post-edge minimum intensity[3] in Figure 4b.

It is clear that the XANES spectra evolve considerably as the beam travels across the oxide, but in order to analyze this quantitatively, it is necessary to use standards. Thus, standards of bcc-Fe, Fe_2O_3, Fe_3O_4, Fe in Zircaloy-4, and $Zr(Fe,Cr)_2$ were examined to create fluorescence plots around the Fe absorption edge. Except for Fe in Zircaloy-4, the standards were in the form of powders acquired from Alfa Aesar, used previously in other XANES studies [4]. These standards were normalized in the same manner as described above for Figure 4b. They were then examined using the Demeter software package, part of the Athena Suite [20]. Plots of the standards used can be seen in Figure 5. Note that the edge of the metallic standards is lower in energy than that of the

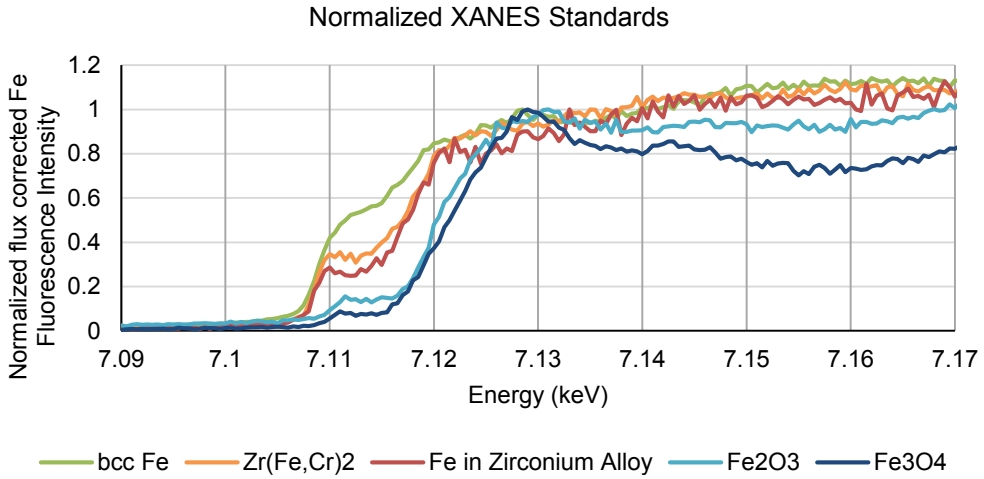

Figure 5- Fe fluorescence data of the standards used to perform XANES on the six samples examined at the 2-ID-D beamline at the APS.

oxidized standards. Also, the pre-edge maximum intensity and the post-edge minimum intensity vary between metallic and oxidized Fe. The differences between individual metallic and oxide standards being less substantial, the focus of the analysis is mostly on the overall sum of oxidized Fe versus metallic Fe.

XANES analysis was performed on oxide layers formed on the six samples shown in Table 1. The fluorescence patterns were fit as a linear combination of the standards to determine how much of the Fe in the alloys was in metallic form (bcc Fe, Fe in Zircaloy-4, and $Zr(Fe,Cr)_2$) or in an oxidized state (Fe_2O_3, and Fe_3O_4). Thus, the best overall fit (as described by Couet et al. [4]) provided our best estimate of the fraction of Fe atoms oxidized at the particular location. The Fe XANES done here cannot determine the difference between Fe in solid solution and that in precipitates. In the oxide, the extent of Fe oxidation is estimated by comparing to powder Fe_2O_3 and Fe_3O_4 standards. Goodness of fit is shown in terms of error bars in the figures produced. Finally, the maximum of the pre-edge peak, the edge position, and post-edge minimum intensities were also analyzed and plotted as a function of distance from the metal-oxide interface to serve as additional indicators of the Fe oxidation process.

3. Results

Figure 6 shows similar data from the oxide layer shown in Figure 4, but showing the different spectra stacked as one moves across the oxide layer for 2 samples, N2513 and H1313J. The shift

[1] The edge position here is defined here as the energy where the normalized Fe counts cross 0.5
[2] The pre-edge maximum intensity here is defined as the maximum of the normalized Fe counts between 7.108 and 7.112 keV
[3] The post-edge minimum intensity here is defined as the minimum of the normalized Fe counts between 7.152 and 7.162 keV

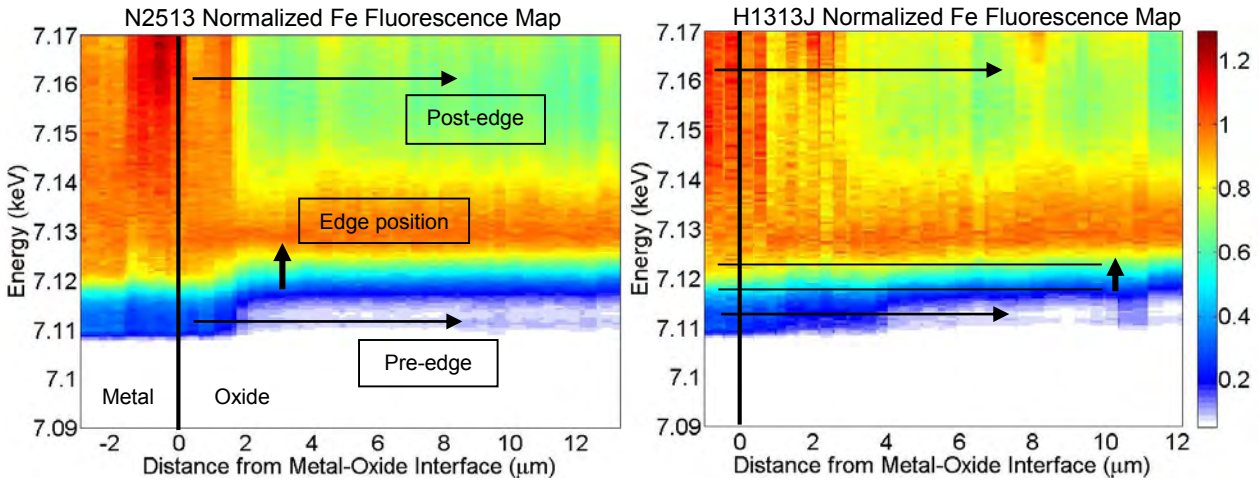

Figure 6- An intensity map of N2513 (Zircaloy-4, 316°C 3113 days) and H1313J (Zircaloy-4, 400°C 259.4 days) showing the movement of the edge position, pre-edge peak intensity, and post-edge minimum as the microbeam travels from the metal-oxide to the oxide-water interface (right most edge of each map)

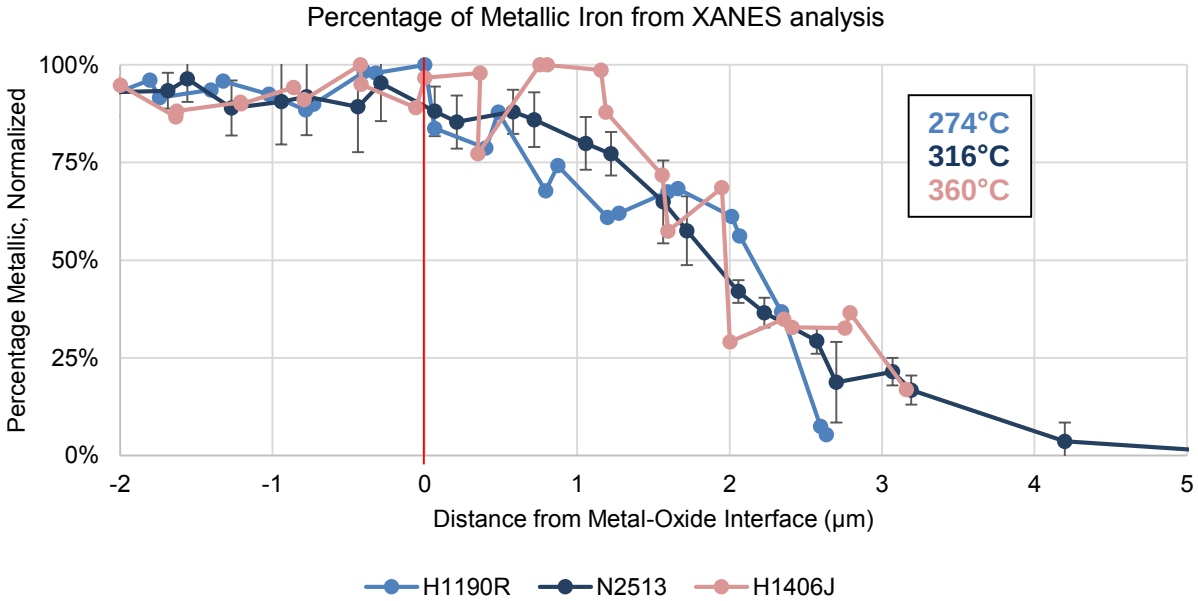

Figure 7- Fe XANES analysis of three Zircaloy-4 samples corroded in water between 274°C and 360°C showing the percentage of the fit to the spectrum data coming from metallic standards, error bars are mostly ≤10% and are shown for N2513 as an example

of the absorption edge to a higher energy value in the oxide is clearly seen. To analyze these results, each individual spectrum is fitted with a linear combination of the standards as described previously [4]. Although the spectra from different oxide and metal phases are difficult to distinguish between each other (e.g. Fe_2O_3 from Fe_3O_4), it is easy to distinguish the oxide phases from the metal (e.g. Fe_2O_3 from $Zr(Fe,Cr)_2$). All the scans were analyzed in this manner and the sum of all the oxide phases in the fits gives the fraction of oxidized iron atoms. Figure 7 shows a comparison between samples corroded in water at different temperatures that have undergone transition (>2 μm oxide), showing a remarkable similarity in behavior. Figure 8 shows a comparison between samples corroded at the same temperature in water (360°C) but at different thicknesses, pre and post-transition. The difference shown is due to the effect of complete oxidation of Fe occurring at the outer oxide edge in contact with the water. Figure 9 compares the samples corroded to a similarly thick oxide (>9 μm) but in different environments, 316°C water vs. 400°C steam. Note the remarkable difference between the steam and water corroded samples.

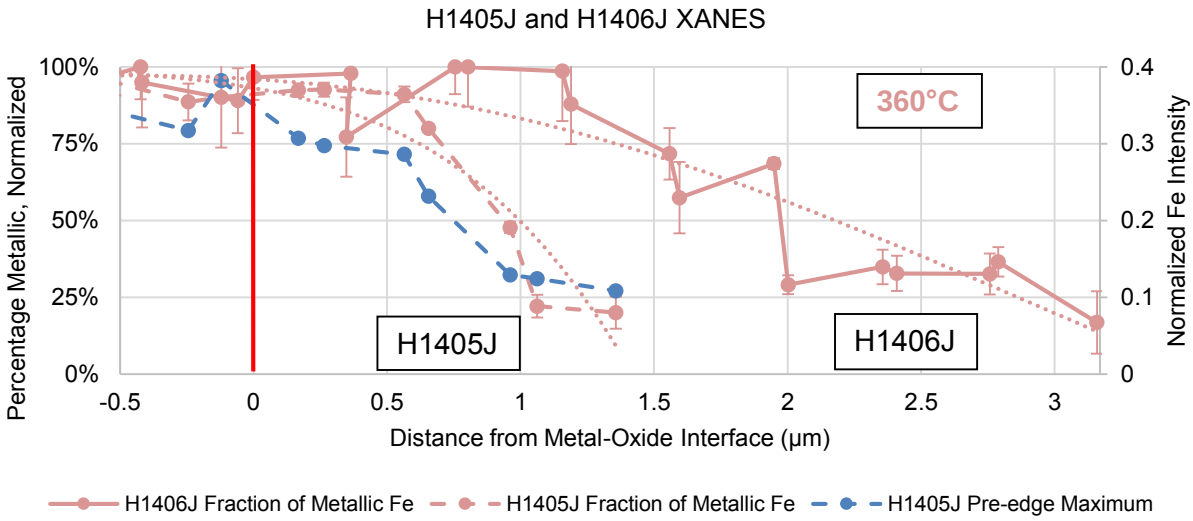

Figure 8- Comparison between H1405 (Zircaloy-4, 360°C 20 days) and H1406J (Zircaloy-4, 360°C 120 days) with the pre-edge maximum intensity of H1405J overlaid

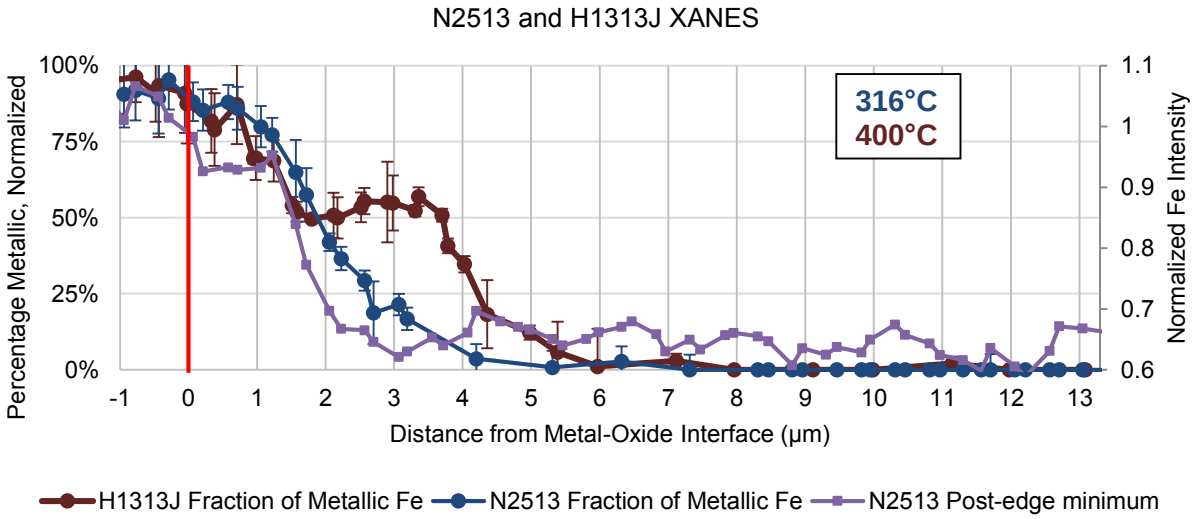

Figure 9- Comparison between N2513 (Zircaloy-4, 316°C water for 3113 days) and H1313J (Zircaloy-4, 400°C steam for 259.4 days) with the post-edge minimum of N2513 overlaid

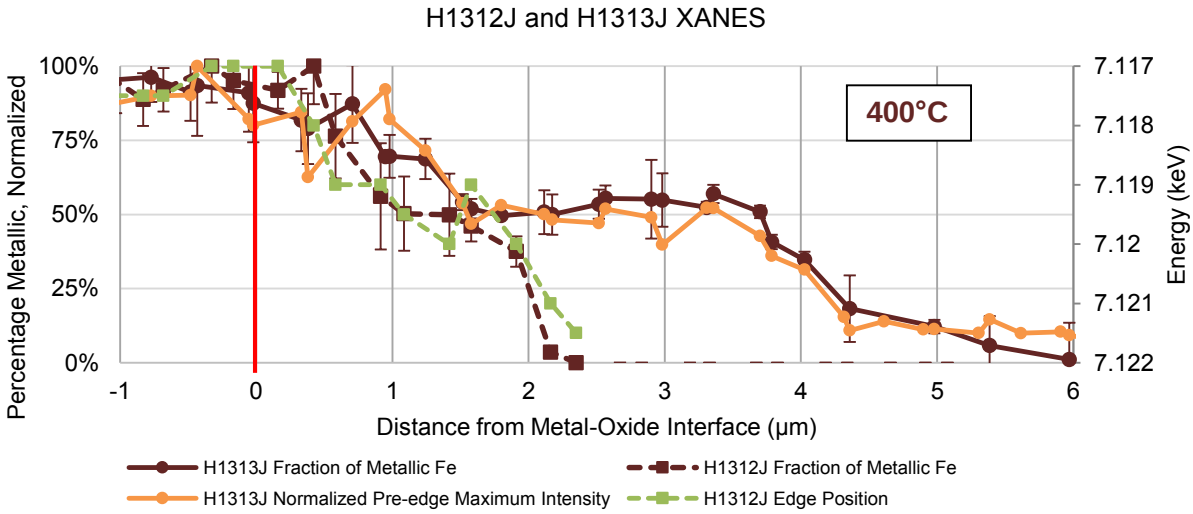

Figure 10- Comparison between H1313J (Zircaloy-4, 400°C steam for 259.4 days) with the pre-edge maximum intensity overlaid and H1312J (Zircaloy-4, 400°C steam for 41.3 days) with the edge position overlaid

Figure 10 shows a comparison between samples corroded at the same temperature in steam (400°C) but at different thicknesses. In these figures the metal-oxide interface is at zero. In the negative region (metal) Fe is completely metallic.

Although we note that a significant degree of scatter exists on the plots indicating some uncertainty on the measurements, at the metal-oxide interface Zr goes from completely unoxidized to completely oxidized, but within the first micron or so this is not true for Fe, which retains a significant metallic fraction. However, looking further into the layer, within ~2 μm of the metal-oxide interface, analysis of the XANES spectra shows that the Fe has been mostly oxidized, showing a metallic fraction less than 50%, and at about ~3 μm, for most cases, Fe is completely oxidized such that the XANES spectra can be fitted entirely using a combination of oxide standards. Comparing the spectra obtained from oxide layers grown at different temperatures, it is possible to note that the complete oxidation of Fe in the samples formed at 400°C appears to take place further away from the metal-oxide interface than in the oxide layers formed at lower temperature. It is possible that differences in oxidation kinetics can account for this behavior, since the faster kinetics at higher temperature would allow the oxide front, the average radial position of the metal-oxide interface, to advance further into the metal before oxidation of Fe would occur. The plateau could also be related to corrosion in steam rather than in water. These results will need to be confirmed with further analysis. Overall, the XANES spectra appear remarkably similar, in spite of the wide difference in exposure times (from 20 to 3113 days), suggesting that the corrosion mechanism does not significantly change over this temperature range.

The analysis of the oxide layers using the other parameters (edge position, pre-edge maximum and post-edge minimum) mostly confirms the analysis above. Figure 10 shows a plot of the edge position plotted versus position in the oxide. It is clear that as the metallic fraction decreases, the edge energy increases. Figure 8 and 10 show the pre-edge maximum, again plotted together with metallic fraction versus position in the oxide. Again, it is clear that the pre-edge maximum decreased in accordance with the decrease in metallic Fe fraction. Finally, Figure 9 shows the post-edge minimum which also follows well the decrease in metallic Fe. The consistency of these results gives further confidence that the analysis is valid.

4. Discussion

As seen in Figures 8-10, the three parameters - pre-edge maximum intensity, absorption edge position, and post-edge minimum – change as the beam moves from the metal through the oxide to the outside edge. This behavior correlates well with the metallic fraction determined from the fitting analysis of the full spectra. The behavior is a result of bonding differences between metallic Fe atoms (either in a precipitate or in solid solution) versus those in Fe_2O_3 and Fe_3O_4. As the Fe atom shares electrons with the oxygen atom, it also becomes more difficult to excite its inner shell electrons. Thus, the edge position moves to a slightly higher energy level. Similarly, the pre-edge peak intensity and post-edge intensity also decrease with increasing oxidation. Therefore, these may be good additional metrics for characterizing the oxidation of alloying elements, especially Fe. In fact this is to be expected, as the XANES analysis that fits the sample spectra to the linear combination of standard spectra is heavily influenced by all three parameters, as seen in Figure 4. The caveat with this method is it does not allow the determination of specific chemical state (oxidation state) of Fe, just a relative measure of how oxidized it has become.

The preferential oxidation of Zr compared to Fe is driven by the oxygen potential across the oxide. Once the oxygen potential has increased enough, there is enough driving force to cause Fe oxidation, as stated previously [6]. When chromium oxidizes at a lower oxygen potential than Fe, the Fe in precipitates forms locally as bcc Fe due to dissolution from the precipitates [5]. The bcc Fe was detected in the samples examined, primarily from the metal-oxide interface up to the point

that the Fe became oxidized. Previous XANES examinations of oxide layers formed on Zr alloys have shown that the point in the oxide where the precipitates are mostly oxidized roughly coincides with the point where interconnected microporosity has reached [4,21].

No change in the oxidation of Fe was observed between the different liquid water corrosion in the temperature ranges studied (274°C-360°C), suggesting that the corrosion process is similar for these temperatures, in spite of the wide differences in exposure times. Despite these similarities, some differences were seen in the distance from the metal-oxide interface for full Fe oxidation in the steam samples. The full Fe oxidation appeared to occur further into the oxide during autoclave corrosion at higher temperature in steam than at lower temperature in water. The much faster kinetics at high temperature (see Figure 1) would leave less time for Fe to oxidize and thus create a non-equilibrium situation where a driving force for Fe oxidation exists, but the actual transformation has not yet occurred. As seen previously by Couet et al. [4], in the spectra of the steam samples, the metallic fraction shows an initial “plateau”, at a lower percentage of metallic Fe than in the metal, suggesting that a fraction of the Fe was oxidized while another population is still metallic. A possible interpretation would be to ascribe the first population to early oxidation of the Fe to the Fe in solid solution and the second population in the plateau to the Fe in precipitates. It is also possible that Fe oxidation during corrosion in steam occurs differently than in water. It would be useful to be able to compare samples corroded in both steam and water at the same temperature to test this, as the effect is observed in a 40°C increase from the 360°C samples, yet no similar change in Fe oxidation behavior is observed from 274°C to 360°C. It also could be that the precipitates oxidize first on the edges, leaving the inside metallic, but this needs to be confirmed by TEM observations. Finally, it is possible that precipitates of different composition (Fe/Cr ratio or possibly Zr_3Fe) corrode at different rates. Additional experiments would need to be performed to confirm the means of the difference in behavior observed in 400°C samples in this study. Because the fraction of metallic Fe in the oxide can affect the oxide electronic conductivity, and this in turn can affect the hydrogen pickup fraction, these different kinetics of oxidation may be important in determining cladding behavior.

5. Conclusions

The oxidation state of Fe within the oxide layers formed in Zircaloy-4, corroded at a range of temperatures (274°C-400°C), was examined using XANES. The XANES spectra of Fe were acquired and analyzed as a function of distance from the metal-oxide interface using synchrotron radiation from the 2-ID-D microbeam at the APS with a spatial resolution of ~ 0.2 μm. The following conclusions resulted from the analysis of the linear combination fits from XANES standards to the XANES data and characteristics of the Fe fluorescence spectra:

- Zirconium oxidizes preferentially with respect to iron as the oxide front advances into the metal, with the fraction of oxidized Fe atoms becoming 100% at about ~2 μm from the metal-oxide interface for water oxidation conditions.
- The overall similarity of the Fe oxidation in water suggests that the corrosion mechanism is similar in this temperature range (274°C-360°C).
- The corrosion temperature does not show a significant effect on Fe oxidation in samples corroded at temperatures from 274°C to 360°C in water, but, a slight difference is seen in the Fe oxidation in samples corroded at 400°C in steam in which the Fe atoms appear completely oxidized at a slightly larger distance from the oxide front than in samples corroded at lower temperatures. This could be caused by the fact that oxidation of the matrix occurs faster at a higher temperature such that the oxide front can travel farther before iron oxidation can occur.
- Additionally, three spectrum parameters – edge position, pre-edge maximum intensity, and post-edge minimum – are identified that match reasonably well with the analysis of the

spectra in determining Fe oxidation and provide additional insight into the behavior of iron as studied by XANES.

Acknowledgements

This research was performed under appointment to the Rickover Fellowship Program in Nuclear Engineering sponsored by Naval Reactors Division of the U.S. Department of Energy (B. Ensor). This research was performed under contract by Bettis Atomic Power Laboratory of the Bechtel Marine Propulsion Corporation. This research used resources of the Advanced Photon Source, a U.S. Department of Energy (DOE) Office of Science User Facility operated for the DOE Office of Science by Argonne National Laboratory under Contract No. DE-AC02-06CH11357. The authors would also like to thank Ashley Lucente of Knolls Atomic Power Laboratory for her role as an adviser and helpful participation in discussions.

References

[1] Lemaignan, C. and A.T. Motta. "Zirconium alloys in nuclear applications." *Materials Science and Technology, A Comprehensive Treatment*. Ed. B.R.T. Frost. Vol. 10B. VCH, (1994): 1 - 51.

[2] Cox, B. "Some thoughts on the mechanisms of in-reactor corrosion of zirconium alloys." *Journal of Nuclear Materials* 336 (2005): 331-368.

[3] Ahmed, T. and L. H. Keys. "The breakaway oxidation of zirconium and its alloys a review." *Journal of the Less-Common Metals* 39 (1975): 99-107.

[4] Couet, Adrien, et al. "Microbeam X-ray absorption near-edge spectroscopy study of the oxidation of Fe and Nb in zirconium alloy oxide layers." *Journal of Nuclear Materials* 452 (2014): 614-627.

[5] Pecheur, Dominique, et al. "Oxidation of intermetallic precipitates in ZIrcaloy-4: Impact of irradiation." *Zirconium in the Nuclear Industry: Tenth International Symposium, ASTM STP 1245*. Ed. A. M. Garde and E. R. Bradley. Philadelphia: American Society for Testing and Materials, (1994): 687-708.

[6] Pecheur, D., et al. "Precipitate evolution in the Zircaloy-4 oxide layer." *Journal of Nuclear Materials* 189 (1992): 318-332.

[7] Hatano, Yuji, et al. "Role of intermetallic precipitates in hydrogen transport through oxide films on Zircaloy." *Zirconium in the Nuclear Industry: Twelfth International Symposium, ASTM STP 1354*. Ed. G. P. Sabol and G. D. Moan. West Conshohocken, PA: American Society for Testing and Materials, (2000): 901-917.

[8] de Gabory, Benoit, Arthur T. Motta and Ke Wang. "Transmission electron microscopy characterization of Zircaloy-4 and ZIRLO oxide layers." *Journal of Nuclear Materials* 456 (2015): 272-280.

[9] Sakamoto, Ken, Katsumi Une and Masaki Aomi. "Chemical state of alloying elements in oxide layer." *2010 LWR Fuel Performance, TopFuel 2010*. Orlando, (2010): 101-106.

[10] Yilmazbayhan, Aylin, et al. "Transmission electron microscopy examination of oxide layers formed on Zr alloys." *Journal of Nuclear Materials* 349 (2006): 265-281.

[11] Degueldre, C., et al. "Nuclear material investigations by advanced analytical techniques." *Nuclear Instruments and Methods in Physics Research B* 268 (2010): 3364-3370.

[12] Degueldre, C., et al. "Zircaloy-2 secondary phase precipitate analysis by X-ray microspectroscopy." *Talanta* 75 (2008): 402-406 [13] Bianconi, Antonio. "Surface X-ray absorption spectroscopy: surface EXAFS and surface XANES." *Applications of Surface Science* 6 (1980): 392-418.

[13] Sakamoto, K., et al. "Depth profile of chemical states of alloying elements in oxide layer of Zr-based alloys." *Progress in Nuclear Energy* 57 (2012): 101-105.

[14] Bajaj, R., B. F. Kammenzind, and D. Farkas, "Effects of neutron irradiation on the microstructure of alpha-annealed Zircaloy-4." *Zirconium in the Nuclear Industry: Thirteenth International Symposium, ASTM STP 1423*. G. D. Moan and P. Rudling, Eds., West Conshohocken, PA: American Society for Testing and Materials, (2002): 400-426.
[15] Anderson, Ken. R. and Ram Bajaj, “Microstructural and microchemical analyses of extracted second-phase precipitates in alpha-annealed and beta-quenched Zircaloy-4.” *Microscopy ad Microanalysis*, 20 (Suppl. 3), (2014): 500-501.
[16] Kammenzind, B. F., K. L. Eklund, and R. Bajaj, "The influence of in-situ clad straining on the corrosion of Zircaloy in a PWR water environment." *Zirconium in the Nuclear Industry: Thirteenth International Symposium, ASTM STP 1423*. G. D. Moan and P. Rudling, Eds., West Conshohocken, PA: American Society for Testing and Materials, (2002): 524-560.
[17] Eisenberger, P. and B.M. Kincaid. "EXAFS: New Horizons in Structure Determinations." *Science* 200 (1978): 1441-1447.
[18] Spengler, David J., et al. "Characterization of Zircaloy-4 corrosion films using microbeam synchrotron radiation." *Journal of Nuclear Materials* 464 (2015): 107-118.
[19] Bianconi, Antonio. "Surface X-ray absorption spectroscopy: surface EXAFS and surface XANES." *Applications of Surface Science* 6 (1980): 392-418.
[20] Ravel, B. and M. Newville. "Athena, Artemis, Hephaestus: data analysis for X-ray absorption spectroscopy using IFEFFIT." *Journal of Synchrotron Radiation* 12 (2005): 537-541.
[21] Ni, N., et al. “Porosity in oxides on zirconium fuel cladding alloys, and its importance in controlling oxidation rates” Scripta Mater. 62 (2010) 564–567.

ADVANTAGES GAINED BY INTRODUCING LOW TIN ZIRLO™ AS BWR CHANNEL MATERIAL

B. ANDERSSON[1], U. BERGMANN[1], M. DAHLBÄCK[1], L. HALLSTADIUS[1], W. HASKINS[2], M. LIMBÄCK[1]

(1) Westinghouse Electric Sweden, SE-721 63, Västerås, Sweden

(2) Westinghouse Electric Company, Western Zirconium Plant, 10,000 West 900 South Ogden, Utah 84404-9760

ABSTRACT

Boiling Water Reactor (BWR) channel distortion is an industry issue, aggravated in long cycles with operation next to an inserted control rod early in life. Channel bow is a consequence of differential channel growth, potentially induced by different irradiation exposures (fast neutron fluences) on opposite channel sides. The length increase is also strongly dependent on the hydrogen content. Shadow corrosion resulting from operation next to an inserted control rod may lead to increased hydrogen pickup on the sides facing the control blade, which by volume expansion could lead to channel growth and bow. In addition, hydrogen pickup early in life, driven by early life control rod exposure, may lead to accelerated irradiation growth and bow later in life. Westinghouse has continuously developed the channel to minimize growth and bow, while maintaining very good corrosion and hydrogen pick-up resistance. The enhancements have included development of materials chemical composition as well as fabrication processes. Westinghouse, consequently, has a wide experience of BWR channels made of Zircaloy-4, Zircaloy-2 and final dimension β-quenched (FDBQ) Zircaloy-2 and Zircaloy-4. In the current development step Westinghouse introduces Low Tin ZIRLO™ as channel material.

Since 2004, close to 700 Low Tin ZIRLO channels have been inserted in eleven different reactors worldwide, covering a wide range of operating conditions, including 24 month cycles and early control. Leading channels have attained an equivalent burnup of 72 MWd/kgU with very good performance. Detailed poolside and hot cell examinations have provided evidence of the superior performance of Low Tin ZIRLO channels. Channel growth is less than 50% of that observed for standard Zircaloy-2 channels, and for burnups above 50 MWd/kgU Low Tin ZIRLO has lower growth than FDBQ Zircaloy-2. The advantage is explained by very low irradiation induced growth in combination with absence of the type of accelerated growth caused by early hydrogen uptake that may be observed for Zircaloy-2 and Zircaloy-4. The bow of Low Tin ZIRLO channels is, therefore, small, even after early control conditions.

The present paper provides high burnup performance data and elucidates the advantages gained by introducing Low Tin ZIRLO as BWR channel material. The advantages of geometrically more stable channels at high burnup range from improved margins to control blade interference, better thermal margins, higher reactivity, and improved quality of readings from in-core instrumentation. Straighter channels provide opportunity for lower fuel cycle costs via further optimized fuel and core designs and improved operational flexibility while ensuring a safe shutdown of the reactor.

1 Introduction

Channel distortion is the change of shape of Boiling Water Reactor (BWR) fuel channels during in-reactor service. Channel growth, bow, bulge and twist are manifestations of channel distortion. Channel bow, i.e. loss of straightness, is caused by differential growth of opposite sides of the channel. Irradiation growth is the dimensional changes at constant volume that occurs during irradiation of an unstressed material [1]. Zirconium alloy components in Light Water Reactors (LWRs) are particularly subjected to pronounced growth behaviour during reactor operation [2]. Hence the growth aspect must be accommodated in their design and improvement in product performance is highly desirable in regard to extending their service life. Factors impacting irradiation growth include reactor operating condition such as irradiation history and temperature, as well as parameters reflecting the material design (chemical composition) and fabrication history or processing of the Zr based product [3].

Irradiation growth in monocrystalline zirconium consists of expansion along the ***a***-axis and the corresponding contraction along the ***c***-axis of the hexagonal crystal. In polycrystalline Zr alloys the growth process is more involved. The grain boundaries act as sinks for point defects; therefore, the grain size, shape and orientation influence the irradiation growth. Nevertheless, on the whole, growth behaviour of polycrystalline Zr alloys also comprises expansion along the ***a***-axis and contraction along the ***c***-axis [3]. Irradiation growth is due to the diffusion of interstitials and vacancies to different sinks that are anisotropically distributed in the material. The sinks can be cold-work or irradiation–induced dislocations of <***a***> or <***c***> or <***c***+***a***> type, and grain boundaries of different orientations [3]. Growth can occur in cold-worked microstructures containing <***c***+***a***> as well as <***a***> dislocations by partitioning of vacancies to the former and self interstitial atoms (SIAs) to the latter [4]. For annealed Zircaloy, the growth acceleration observed at high fluences can be due to the appearance of basal plane loops acting as strong vacancy sinks [4].

Irradiation growth is very sensitive to metallurgical conditions and growth behaviour varies from one Zircaloy material to another depending on the detailed chemical compositions and the microstructure evolved during fabrication processes as mentioned above. The important metallurgical factors are, (i) crystallographic texture, (ii) degree of recrystallization, (iii) grain size and morphology and (iv) chemical composition. The operational factors are temperature and fast neutron fluence. Fast neutrons cause displacement of Zr atoms from their stable positions by collision. The conversion factor for the fast neutron fluence ($E \geq 1$ MeV) to displacement per atom is around 2 dpa for each 10^{25} neutrons/m^2 [3], assuming the neutron energy spectrum of a commercial LWR.

The continuous development of the Westinghouse BWR fuel channel material has included multiple evolutionary steps, with the focus maintained on dimensional stability as well as corrosion and hydrogen pickup resistance. Zircaloy-2 early on replaced Zircaloy-4 to provide improved corrosion resistance. Efforts were subsequently focused on further improving the dimensional stability, resulting in the development and introduction of the final dimension β-quenched (FDBQ) Zircaloy-2 channel [5]. More recently Low Tin ZIRLO has been introduced to further improve the hydrogen pickup resistance as well as the high burnup dimensional stability [6]. In the present study recent high burnup data for Low Tin ZIRLO is presented and compared with the performance of earlier channel versions, including FDBQ Zircaloy-2.

2 Materials

The development of Low Tin ZIRLO for BWR applications is based on the earlier experience with ZIRLO in PWRs as well as Anikuloy/E635 in PWRs and BWRs. The initial goal was to develop a channel material that outperforms FDBQ Zircaloy-2 both with respect to hydrogen pickup and dimensional stability at high burnups, without requiring the technically more complex FDBQ process. Table 1 provides an overview of the nominal compositions of the different materials.

Table 1: *Chemical compositions of the various Zr-based alloys.*

Alloy	Sn	Nb	Fe	Cr	Ni
ZIRLO	1.0	1.0	0.1		
Low Tin ZIRLO	0.7	1.0	0.1		
Anikuloy/E635	1.2	1.0	0.4		
Zircaloy-2	1.3		0.19	0.12	0.06

Mechanical requirements for Low Tin ZIRLO channel material are the same as for standard Zircaloy-2 material, consistent with ASTM B352.

3 Channel design

All the experience with Low Tin ZIRLO channels has been acquired in Westinghouse SVEA-96 Optima2™ or SVEA-96 Optima3™ fuel assembly designs. These designs are based on a 10x10 rod lattice in the SVEA™ water cross channel, which consists of an outer shroud with a square cross section and an internal double-walled cruciform structure that forms a central canal accommodating non-boiling water. The family name SVEA was introduced already in 1980 in conjunction with the implementation of the water cross structure inside the fuel channel. The main purpose of the cruciform structure and its central water canal was to improve the moderation of the fuel assembly, but it was also found to provide excellent mechanical support. The mechanical design helps mitigating the consequences of channel distortion, since it features relatively low bow stiffness due to the thinner outer channel wall, thus yielding more easily to lateral forces than other designs, and mitigating control rod interference. Furthermore, thanks to the water cross, the SVEA design has significantly less bulging than conventional designs.

A simplified drawing of a cross-section of typical SVEA-96 channel is shown in Figure 1, along with a bottom view photo. Each SVEA-96 channel contains four fuel sub-assemblies.

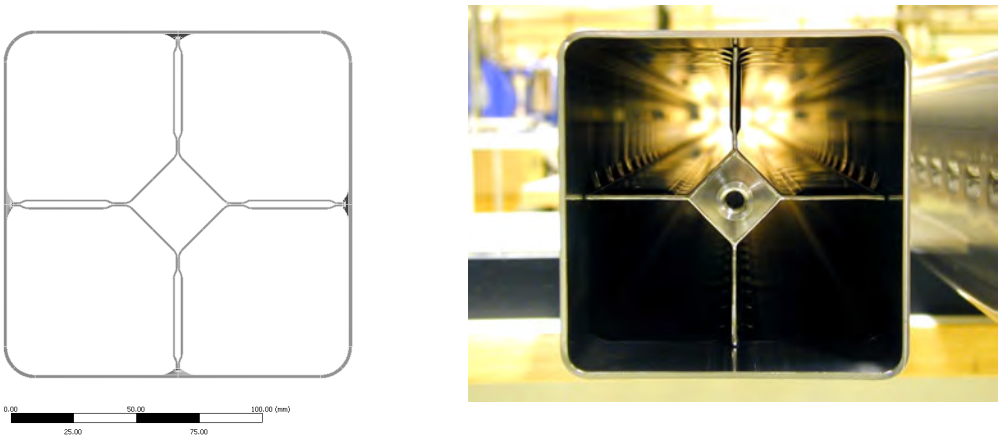

Figure 1: *Cross-section and bottom view photo of a Westinghouse BWR fuel channel.*

4 Measurements & Results

The data presented here are plotted as a function equivalent channel burnup. In most cases the equivalent burnup is identical to the assembly average burnup. To evaluate ultra-high burnup properties, fuel channels that have been irradiated during one full assembly life have in some cases been used for a second life, with an initially fresh fuel bundle. In these cases the equivalent channel burnup is the sum of the assembly average burnup of the original fuel bundle and the average burnup attained by second bundle.

4.1 Oxidation

Oxide layer thickness on channels irradiated in various BWRs to different exposures has been measured using eddy current (EC) technique. Commonly, the oxide layer thickness of a channel is measured along the whole length and on all sides of the fuel channel. Figure 2 presents the average oxide thickness as function of equivalent channel burnup.

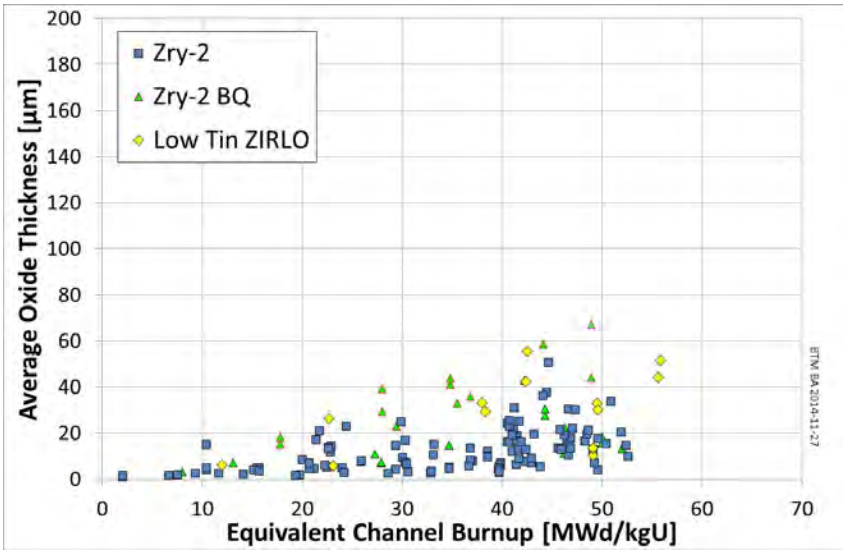

Figure 2: *Oxide layer thickness versus burnup.*

4.2 Growth

Length of channels irradiated in various BWRs to different exposures has been measured using Westinghouse standard channel length measurement procedure. The measuring equipment consists of a gauge of a known length (about 4 m long), a perforated index plate and a dial indicator. The channel axial growth is evaluated in terms of axial strain versus burnup (Fig. 3).

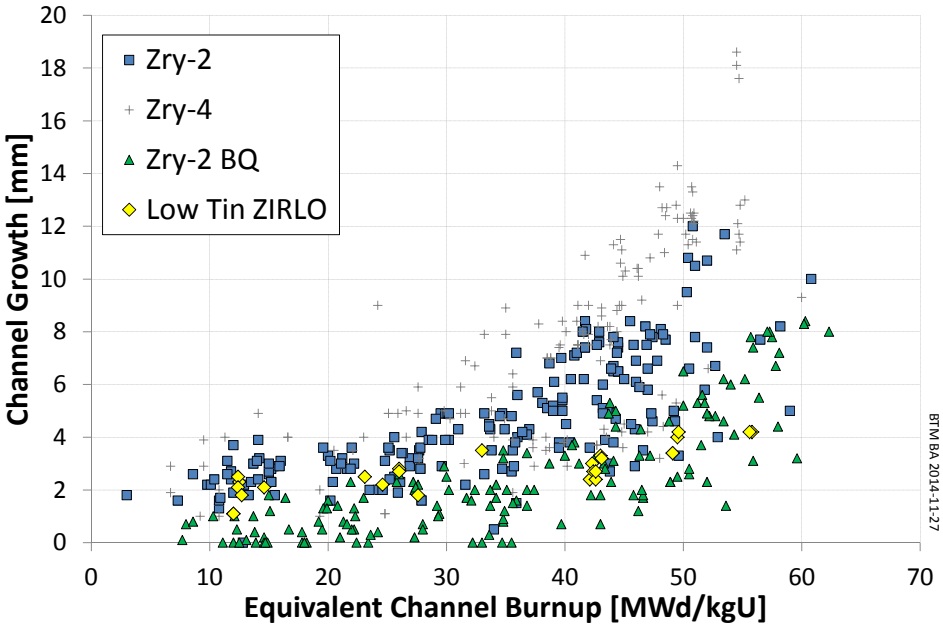

Figure 3: *Channel growth versus burnup.*

4.3 Bow

Irradiation–induced lateral displacements (bowing) of channels irradiated in various BWRs to different exposures have been measured using Westinghouse standard channel deformation measurement procedure. The measuring equipment consisted of a fixture (about 4.4 m long) with ultrasonic probes and an electronic package that monitors and performs signal analysis. The results of BWR fuel channel bow measurements are presented in terms of the maximum lateral displacements in the (x,y)-coordinates versus burnup (Fig. 4). The data represent bending towards (+) and away from (-) the control rod position.

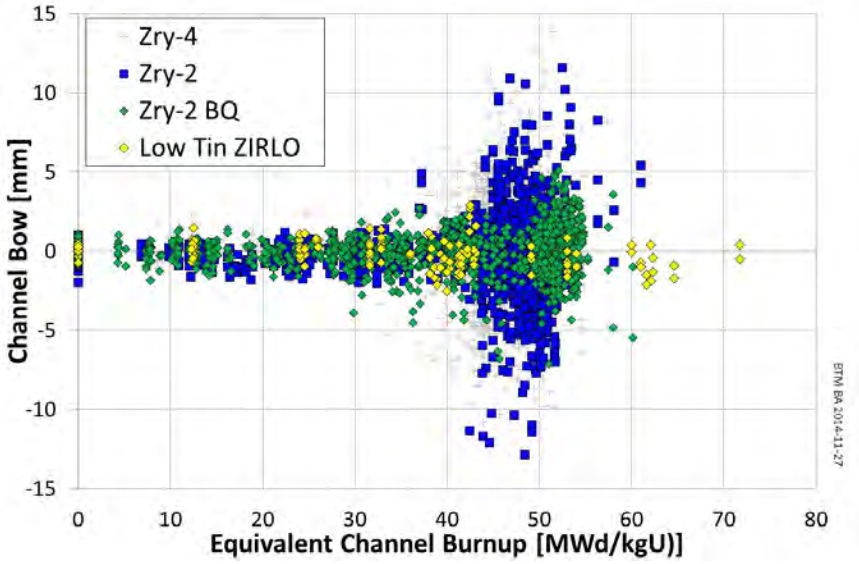

Figure 4: *Channel bow versus burnup.*

5 Discussion

Today, many utilities are struggling with channel distortion issues as a result of higher average burnup as well as 24-month cycle operation with control rods inserted adjacent to fresh fuel. The most severe consequence of excessive bow is the mechanical interference with the control rods. In addition, since a distortion changes the distribution of moderator in the core, there is significant impact on the power distribution, which results in less efficient fuel utilization (lower reactivity), and reduced rod power margins, e.g., with respect to CPR (Critical Power Ratio) and PCI (Pellet-Cladding Interaction).

Reactivity losses due to channel bow require loading fuel with higher enrichments worth $k 500 or more per reload. Similar added costs can be associated with losses in thermal margins and less accurate core monitoring readings. Hence, an added fuel cycle cost of $M 1.0 per reload in a 24-month cycle can be associated with channel bow. This cost is not visible in standard fuel cycle cost evaluations and needs to be accounted for separately. In addition, the needs of performing measurements on channels and regular supervision of control blade friction due to channel distortion, and sometimes also premature channel replacement, cause the utilities significant burden and costs.

The main distortion mode of the channel is bowing. Bowing was first observed when increasing the burnup of the fuel assemblies, and was a result of differential growth - meaning that one side of the channel grows faster than the opposite side, which forces the channel to bow. The differential growth is caused by gradients in the fast neutron flux in the core, e.g., the channel wall facing the core periphery usually experiences a lower flux than the side facing the centre of the core. Although there are means to counteract the effects from the differences in the neutron flux, the variation of neutron flux is a difficult condition to handle.

Following the transition, especially in the US, of many reactors from annual to 24-month cycle operation, some BWR units started to report observation of excessive channel bow. This type of bow could not be explained only by the regular fluence gradient-driven differential growth. Instead, it was concluded to be caused by the presence of a control rod early in life of the fuel assembly which is common for cores operating in 24-month cycles. The control rod induces shadow corrosion on the two sides of the channel it is facing, which leads to additional hydrogen pickup in the channel material. This early-life hydrogen pickup may cause an accelerated irradiation growth later in life, i.e., an increased differential growth resulting in channel bow. The mechanisms are only partially understood, but the phenomenon was clearly demonstrated under the EPRI-managed NFIR program [7].

Westinghouse's solution to address channel bow, in particular the enhancement caused by early life shadow corrosion, was to introduce Low Tin ZIRLO material, known from PWR experience to have very low irradiation induced growth as well as low hydrogen pickup with an optimized manufacturing process.

Since 2004, close to 700 Low Tin ZIRLO channels have been inserted in eleven different reactors worldwide, covering a wide range of operating conditions, including 24 month cycles, early control and water chemistries including:

- Normal water chemistry (NWC)
- Hydrogen water chemistry (HWC)
- Zinc addition
- On-line noble chemical addition (OLNC)

The main advantage of the Low Tin ZIRLO channel is the high burnup dimensional stability, which can be observed both in terms of channel bow (Fig. 4) and growth (Fig. 3). The channel bow data includes two-life Low Tin ZIRLO channels that have reached equivalent average burnups of 72 MWd/kgU in 12-month cycles and 56 MWd/kgU in 24-month cycles, the latter with extensive control rod exposure starting from beginning of life. While the

channel bow of Low Tin ZIRLO is within ±3 mm for all data points, the channel bow for Zircaloy-2 and FDBQ Zircaloy-2 starts diverging at burnups above 40 MWd/kgU and 50 MWd/kgU, respectively (Fig. 4). The increase in channel bow for Zircaloy-2 and FDBQ Zircaloy-2 correlates to the burnup level where an increase in growth rate can be observed for the two considered channel types (Fig. 3). This type of increased growth rate has not been observed for Low Tin ZIRLO channels, on the contrary the growth rate remains constant and the channel bow insignificant to very high burnups (>70 MWd/kgU).

The oxidation performance of Low Tin ZIRLO is similar to that of Zircaloy-2 and FDBQ Zircaloy-2. The hydrogen pickup is, however, lower for Low Tin ZIRLO than for the Zircaloy-2 materials [5], providing generally better high burnup corrosion resistance as well as further improved margin to increased growth and bow.

6 Conclusions

Since 2004, close to 700 Low Tin ZIRLO channels have been inserted in eleven different reactors worldwide, covering a wide range of operating conditions, including 24-month cycles and early control. The first full reload with Low Tin ZIRLO channels was delivered in 2011. Detailed poolside and hot cell examinations have provided evidence of the superior performance of Low Tin ZIRLO channels. Channel growth is less than 50% of that observed for standard Zircaloy-2 channels, and for burnups above 50 MWd/kgU Low Tin ZIRLO has even lower growth than FDBQ Zircaloy-2. Since channel bow is a result of differential growth, an equivalent reduction in channel bow is obtained. The advantage is explained by very low irradiation induced growth in combination with absence of the type of accelerated growth caused by early hydrogen uptake that is observed for Zircaloy-2 and Zircaloy-4 channels.

The Low-Tin ZIRLO channel material has been verified to very high burnup (>70 MWd/kgU) as well as to end of life in 24-month cycle operation with extensive early control, i.e., the mode of operation where Zircaloy channels have been routinely replaced to avoid interference with control blade movement. The data show that in no case did the bow of the Low Tin ZIRLO channels exceed 3 mm after three consecutive 24-month cycles.

The advantages of geometrically more stable channels at high burnup range from improved margins to control blade interference, better thermal margins, higher reactivity, and improved quality of readings from in-core instrumentation. Straighter channels provide opportunity for lower fuel cycle costs via further optimized fuel and core designs and improved operational flexibility while ensuring a safe shutdown of the reactor.

7 References

[1] Fidleris, V., “The Irradiation Creep and Growth Phenomena,” Journal of Nuclear Materials, Vol. 159, 1988, pp. 22-41.

[2] Franklin, D. G. and Adamson, R. B., “Implications of Zircaloy Creep and Growth to Light Water Reactor Performance,” Journal of Nuclear Materials, Vol. 159, 1988, pp. 12-21.

[3] Lemaignan, C. and Motta, A. T., “Zirconium Alloys in Nuclear Applications,” in Materials Science and Technology, R. W. Cahn, P., Haasen, E. J.,Kramer, Eds.,Vol. 10B, pp. 1-51, 1994, VCH, Weinheim.

[4] Holt, R.A., “Mechanisms of Irradiation Growth of Alpha-Zirconium Alloys”, Journal of Nuclear Materials, Vol. 159, 1988, pp. 310-338.

[5] Dahlbäck, M., Limbäck, M., Hallstadius, L., Barberis, P., Bunel, G., Simonot, C., Andersson, T., Askeljung, P., Flygare, J., Lehtinen, B., and Massih, A. R., ”The Effect of Beta-Quenching in Final Dimension on the Irradiation Growth of Tubes and Channels”, Presented at ASTM Symposium on Zirconium in the Nuclear Industry: Fourteenth International Symposium, Stockholm, Sweden, June 13-17, 2004, ASTM STP 1467, pp. 276-304, and Journal of ASTM International, June 2005, Vol. 2, No. 6, Paper ID JAI12337.

[6] Romero, J., Dahlbäck, M., and Hallstadius, L., ”Mitigating BWR Channel Distortion: Westinghouse Low Tin ZIRLO™ Channel”, Paper 8310, TopFuel 2013, Charlotte, NC, USA, September 15-19, 2013.

[7] Garcia Sedano, P. J., Iglesias Ayuela, J., Albendea, M., and Mader, E., “Channel Measurement Campaign at EOC18 in Cofrentes NPP”, Paper 7906, TopFuel 2013, Charlotte, NC, USA, September 15-19, 2013.

EVOLUTION OF HYDROGEN PICKUP FRACTION WITH OXIDATION RATE ON ZIRCONIUM ALLOYS

J. ROMERO[1], J. PARTEZANA[2], R. J. COMSTOCK[2], L. HALLSTADIUS[3], A. MOTTA[4], A. COUET[5]

[1]*Westinghouse Electric Company, 5801 Bluff Rd., Hopkins, SC 29061, USA*
[2]*Westinghouse Electric Company, 1332 Beulah Rd., Churchill, PA 15235, USA*
[3]*Westinghouse Electric Sweden, Fredholmsgatan 22, 721 36 Västerås, Sweden*
[4]*Pennsylvania State University, 138A Reber Building, University Park, PA 16082, USA*
[5]*EDF, Avenue des Renardières – Ecuelles, 77818 Moret-Sur-Loing Cedex, France*

ABSTRACT

Hydrogen pickup during aqueous corrosion of zirconium-based alloys is currently the most important life-limiting phenomenon for operation of cladding and structural components of fuel in light water reactors, especially at high burnup where embrittlement due to hydriding becomes a significant factor. A fraction of the hydrogen generated by the corrosion reaction is absorbed by the metal, which is known as the hydrogen pickup fraction. The current understanding of the fundamental mechanisms driving hydrogen absorption and governing the hydrogen pickup fraction, and crucially its relationship with the oxidation rate, is very limited and semi-empirical at best. For many practical purposes and analytical methods it has been assumed that the hydrogen pickup fraction of zirconium-based components is constant over the entire in-reactor exposure. In this study, tubing and strip specimens of zirconium alloys, using a wide range of commercial and model chemical compositions and final heat treatments to produce different microstructures, have been subjected to long-term autoclave testing simulating in-reactor conditions. Alloy systems studied include Zircaloy-2, Zircaloy-4, ZIRLO®+ and zirconium-niobium. The corrosion kinetics and the hydrogen content and pickup fraction were closely followed during exposure. A consistent correlation between the oxidation rate and the hydrogen pickup fraction has been observed whereby the hydrogen pickup fraction increases when the corrosion rate decreases, such that the hydrogen pickup fraction is not constant during exposure. The hydrogen pickup fraction evolves following a correlation with the oxidation rate, while being strongly influenced by alloy composition and final heat treatment of the material. The correlation between hydrogen pickup fraction and oxidation rate has been attributed to changes in the electronic conductivity of the zirconium oxide, which in turn is linked to the characteristics of the oxide and the base metal. The results from this study are consistent and supported by observations made under a broader research program to understand the fundamental mechanisms of hydrogen pickup in zirconium alloys, called MUZIC-2. MUZIC-2 is led by Westinghouse in collaboration with industrial partners: EPRI, EDF, Rolls-Royce, Amec Foster Wheeler, Sandvik, Vattenfall, Studsvik, Paul Scherrer Institute and NNL; as well as academic institutions: University of Oxford, University of Manchester, Imperial College London, Chalmers Institute of Technology and Pennsylvania State University. Under this collaboration program, the samples produced in this study are being characterized with state-of-the-art techniques, aiming to understand the interaction and evolution of oxidation rate, chemistry/microstructure/conductivity of the oxide, transport paths and eventually the evolution of the hydrogen pickup fraction. In this paper these interactions are put into context by reporting and analyzing industry relevant oxidation rates and hydrogen pickup data produced by Westinghouse.

1. Background

Zirconium-based alloys are widely used for fuel cladding and structural components in light water nuclear reactors. For these components, hydrogen pickup due to aqueous corrosion during operation is currently the most important life-limiting phenomenon. This is most

noticeable at high burnup towards the end of life of the fuel, where embrittlement of the material due to hydriding becomes a significant factor for its performance. It is therefore of utmost importance to the nuclear industry to optimize materials to minimize hydrogen pickup during operation.

The propensity of a material to absorb hydrogen is commonly expressed as the hydrogen pickup fraction, defined as the ratio of the hydrogen absorbed by the metal to the total amount of hydrogen generated during corrosion. The hydrogen pickup fraction of zirconium based materials is affected by multiple factors. The current understanding of the fundamental mechanisms driving hydrogen absorption and governing the hydrogen pickup fraction, and crucially its relationship with the oxidation rate, is very limited and semi-empirical at best.

In order to gain understanding on the fundamental mechanisms involved during aqueous corrosion of zirconium alloys, a large international collaborative research program started in 2006. The program is called Mechanistic Understanding of Zirconium Corrosion, abbreviated as MUZIC. The first phase of MUZIC provided important insights into corrosion mechanisms and the evolution of the zirconium oxide during transition of oxidation kinetics, examples of publications in [1,2].

The second phase of MUZIC, which started in 2010, is focused on hydrogen pickup mechanisms. MUZIC-2 is led by Westinghouse in collaboration with industrial partners: Electric Power Research Institute, Electricite de France, Rolls-Royce, Amec Foster Wheeler, Sandvik, Vattenfall, Studsvik, Paul Scherrer Institute and National Nuclear Laboratory; together with academic institutions: University of Oxford, University of Manchester, Imperial College London, Chalmers Institute of Technology and Pennsylvania State University. The approach of MUZIC-2 is a combination of experimental and theoretical/modeling studies using complementary techniques.

For many practical purposes and analytical methods for nuclear fuel design it has been assumed that the hydrogen pickup fraction of zirconium-based components is constant over the entire in-reactor exposure. Recently within MUZIC-2, it has been demonstrated that the hydrogen pickup fraction is not constant during the corrosion process and has a close relationship with the corrosion kinetics. A correlation between the oxidation rate, the onset of corrosion transitions and the hydrogen pickup fraction has been consistently observed whereby the hydrogen pickup fraction increases when the corrosion rate decreases, such as the hydrogen pickup fraction is not constant during exposure. The correlation between hydrogen pickup fraction and oxidation rate has been attributed to changes in the electronic conductivity of the zirconium oxide, which in turn is linked to the characteristics of the oxide and the base metal. Indeed, the pickup of hydrogen has been hypothesized to have an inverse relationship to the rate of electronic conductivity of the oxide, i.e. the higher the electronic conductivity of the oxide, the lower the hydrogen pickup fraction [3,4].

The study reported in this paper consists of long-term autoclave testing of tubing and strip material of zirconium-based alloys using a wide range of commercial and model chemical compositions and final heat treatments to produce different microstructures. During testing, the corrosion kinetics and hydrogen pickup fraction were closely followed as a function of exposure, aiming to independently test the hypothesis that the hydrogen pickup fraction has an inverse relationship with the oxidation kinetics, and that different conditions in the base metal affect the hydrogen pickup fraction, most probably due to changes in the conductivity of the oxide.

The samples produced in this study are being characterized using state-of-the art techniques, with results reported elsewhere [5,6], aiming to understand the interaction and evolution of oxidation rate, chemistry/microstructure/conductivity of the oxide, transport paths and eventually the evolution of the hydrogen pickup fraction. In this paper these interactions are put into context by reporting and analyzing oxidation rate and hydrogen pickup data produced by Westinghouse.

2. Autoclave Testing

In order to test the multiple factors that affect the hydrogen pickup fraction in zirconium-based alloys, a selection of materials and conditions was made using the following criteria:

- Include industry relevant alloy systems such as Zircaloy-2 (Zr-Sn-Fe-Cr-Ni), Zircaloy-4 (Zr-Sn-Fe-Cr), ZIRLO (Zr-Nb-Sn-Fe) and Zr-Nb. Alloying elements are likely to segregate in the zirconium matrix and in the oxide, and also form second phase particle (SPP) precipitates in the metal (e.g. Laves phases and β-Nb). Some elements (e.g. Nb and Sn) may distribute in solid solution. Different chemical compositions were included to confirm and gain insights on known effects such as the beneficial effect of Nb and Fe, and the detrimental effect of Ni on hydrogen pickup.
- Some of the materials were obtained as strip and others as cladding tubes. The type of specimen is indicated in Table 1 below. All the specimens were tested in as-fabricated condition. Buffed surface for strips and belt polished outer diameter with grit blasted inner diameter for tubing were employed.
- All the materials studied were obtained in fully recrystallized condition. To study the effect of SPP size/density and phase transformation, some of the materials (designated as -A) were subjected to an additional anneal at 720°C for 24 hours.

All the materials listed were subjected to corrosion testing in pure water at 360°C in static stainless steel autoclaves. The tubing and strip specimens were tested in two separate autoclaves. The number of coupons in each autoclave at a given time was limited to maintain the level of hydrogen dissolved in the water below 40 cc/kg H_2O. Enough coupons were prepared to extract samples after 1, 3, 7 and then approximately every 15 days until a total corrosion time of 225 days was achieved. After extraction, specimens were weighed and hydrogen content measurements were performed using inert gas diffusion.

3. Corrosion Kinetics and Hydrogen Pickup Fraction

For all the specimens tested, the weight gain as a function of exposure time follows a power law of the form $W = At^n$ from the start, where W is the weight gain, t is the exposure time, and A and n are constants. The value of n, in particular, is characteristic of each material and condition. Table 1 presents a summary of the specimens tested and the overall results for the pre-transition regime. At different points during the tests all the specimens reached a corrosion transition, where the oxidation rate increases. In some cases the post-transition oxidation reproduces the initial kinetics with periodicity, while in others the oxidation kinetics deviate from a power law after the first transition. An example of this is shown for ZIRLO, with and without the additional heat treatment, in Figure 1.

Table 1 shows the constants describing the pre-transition oxidation kinetics for all the materials tested, as well as the total hydrogen pickup fraction at the end of the test. The main observations from this table are the following:

- The pre-transition oxidation kinetics and onset of corrosion transition for the LK2+ and LK3 variants of Zircaloy-2 are very similar.
- All the Zr-Nb specimens without additional anneal showed corrosion transition late in the tests.
- For all the alloy systems, the annealing treatment accelerates the onset of the corrosion transition, and increases the oxidation rate post-transition. In some cases, for example for ZIRLO-A in Figure 1, the corrosion rate is almost constant after the first transition.

Table 1 Pre-transition oxidation kinetics and total hydrogen pickup fraction

Alloy	Designation	Heat treated (720°C/24hrs)	Pre-transition oxidation kinetics			Hydrogen pickup fraction at end of test (225 days)
			A	*n*	Oxide thickness at transition (μm)	
Zircaloy-2	LK2+[(1)]	-	6.9	0.29	2.2	20%
	LK3[(1)]	-	7.1	0.28	2.1	20%
	LK3-A[(1)]	Yes	6.7	0.33	2.2	25%
Zircaloy-4	Zr-4[(2)]	-	8.1	0.29	2.1	20%
	Zr-4-A[(2)]	Yes	6.9	0.32	1.9	17%
ZIRLO	ZIRLO[(2)]	-	7.0	0.34	2.5	16%
	ZIRLO-A[(2)]	Yes	5.5	0.41	2.1	10%
Zr-Nb	Zr-0.5Nb[(1)]	-	6.9	0.36	3.1	9%
	Zr-1.0Nb[(1)]	-	5.7	0.41	3.4	12%
	Zr-1.0Nb-A[(2)]	Yes	5.9	0.47	3.1	9%
	Zr-2.5Nb[(1)]	-	7.7	0.34	3.2	11%

(1) Cladding Tube (2) Strip

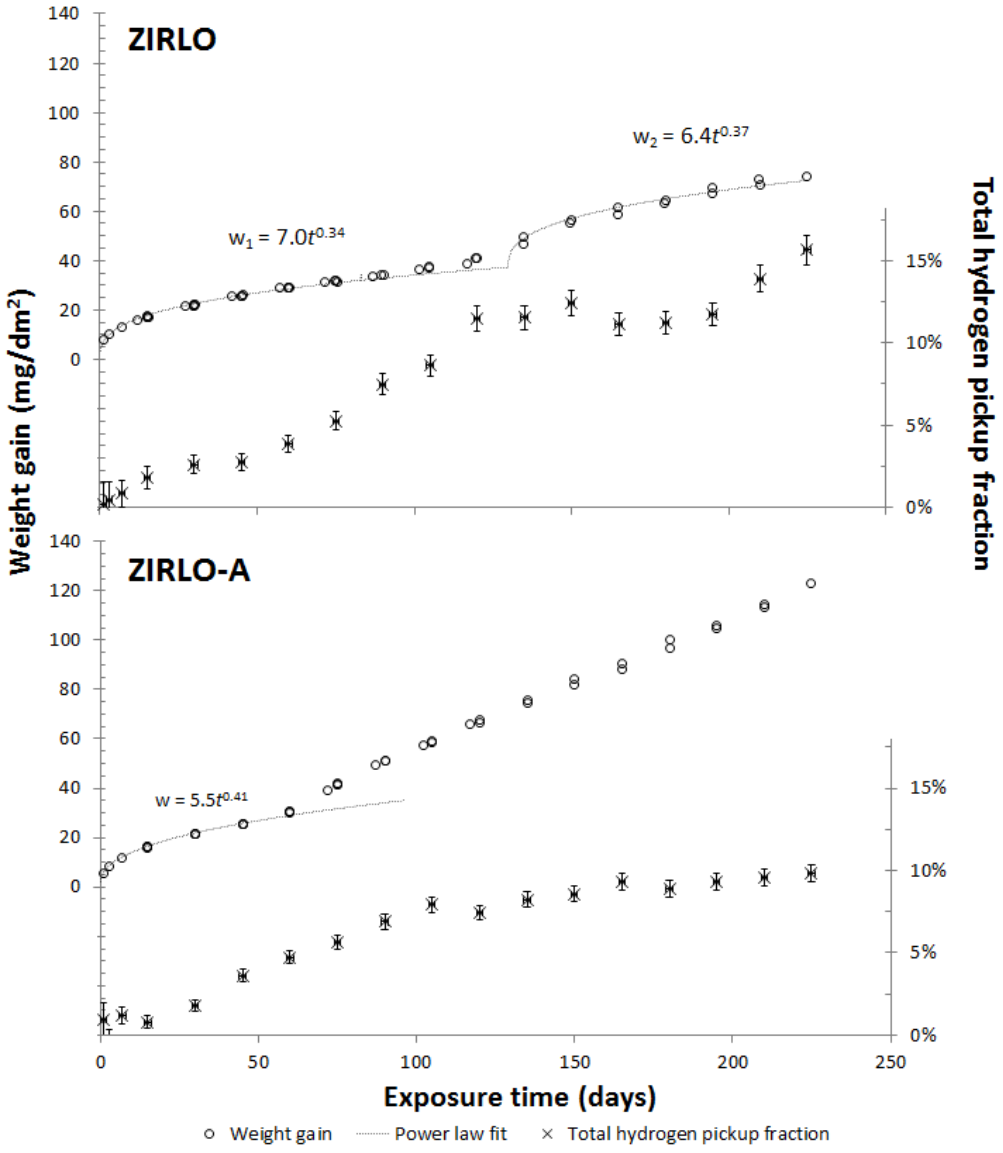

Figure 1 Weight gain and total hydrogen pickup fraction of ZIRLO tubes (with and without additional anneal) as function of exposure time. Regimes where a power law applies are indicated

Figure 1 shows the oxidation kinetics for ZIRLO specimens with and without the additional anneal. In the initial pre-transition regime and in some samples in a second pre-transition regime, the kinetics can be described by a power law. The total hydrogen pickup fraction at different exposure times is also shown in the figure. Crucially, the total hydrogen pickup fraction varies as a function of exposure time. Annealed samples of Nb-containing alloys (ZIRLO-A and Zr1.0Nb-A), show oxidation kinetics approximately linear after the first transition, while the hydrogen pickup fraction remains reasonably constant.

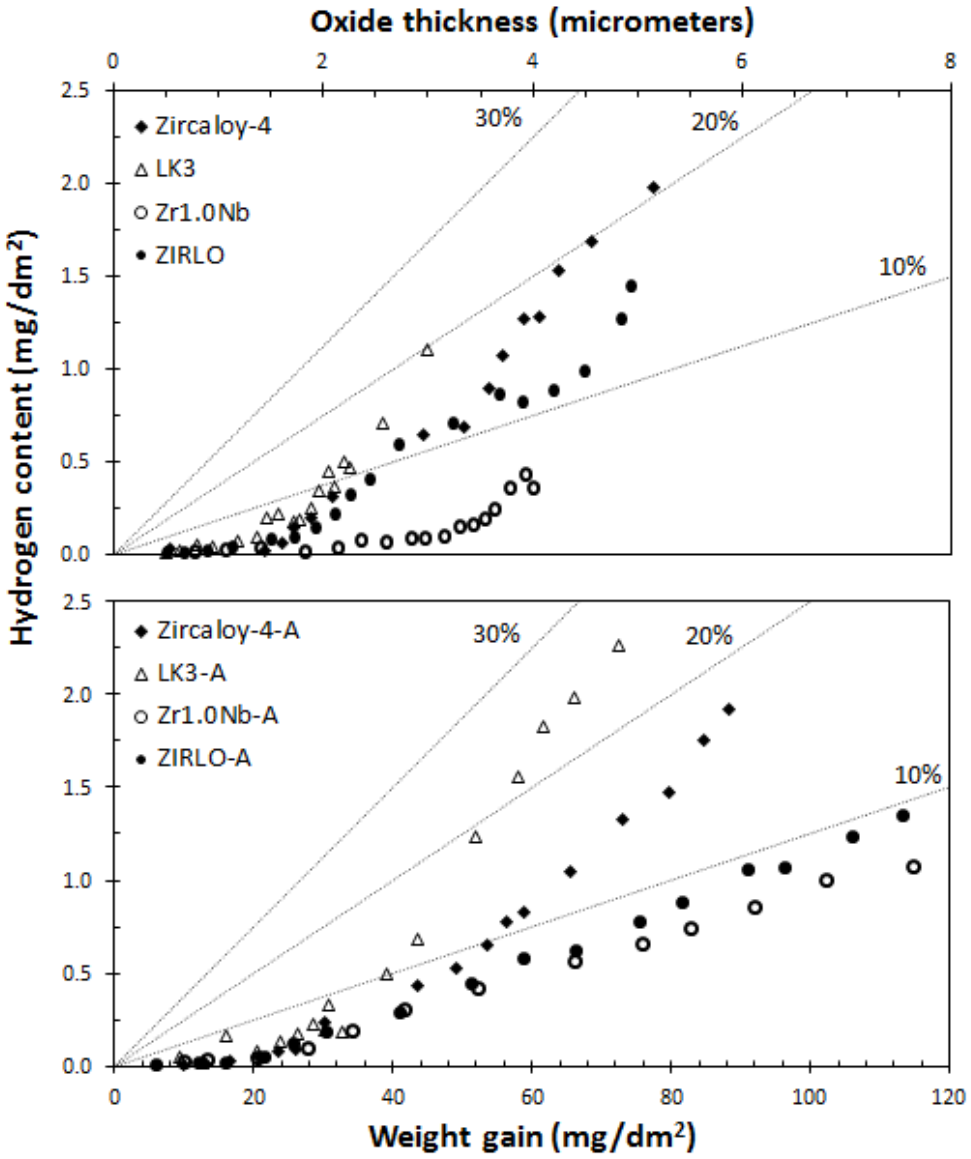

Figure 2 Hydrogen content as a function of weight gain (and oxide thickness) for different alloys. Materials with additional anneal (designated as –A) at the bottom. The straight dashed lines correspond to constant total hydrogen pickup fraction of 10%, 20% and 30%

Figure 2 shows the hydrogen content in each alloy tested versus total corrosion weight gain and oxide thickness. In such a graph, if the hydrogen pickup fraction is constant during corrosion the data points should follow a straight line. Constant hydrogen pickup fractions of 10, 20 and 30% are indicated in the figure. The data shows that the hydrogen pickup does not follow a straight line, and increases as the corrosion proceeds. For example, Zircaloy-2 (LK3) has a total hydrogen pickup fraction of less than 10% at 20 mg/dm^2 (about 1.4 micron thick oxide layer) but about 20% at 40 mg/dm^2 (2.8 microns). The differences between the alloys are clear, with Zr-1.0Nb showing the lowest hydrogen pickup fraction, followed by

ZIRLO and Zircaloy-4. Zircaloy-2 (LK3) shows the highest hydrogen pickup fraction. The additional annealing treatment does not change this ranking, but modifies the distance between alloys with the hydrogen pickup fraction of LK3-A remaining high, while that of ZIRLO-A decreases. The figure illustrates that the hydrogen pickup fraction increases with exposure time for all the materials. For the specimens without anneal the hydrogen pickup fraction steadily increases following the periodicity of the corrosion kinetics. The additional anneal makes the evolution of hydrogen content after the first corrosion transition more linear, resulting in an almost constant hydrogen pickup fraction. At the same time the oxidation rate deviates from a power law and also remains relatively constant. ZIRLO-A and Zr-1.0Nb-A show a hydrogen pickup fraction close to constant after the first oxidation transition, just below 10%.

It is important to note at this point that the testing conditions for the autoclave tests performed are most relevant for in-reactor performance of pressurized water reactor (PWR) materials. Relevance of the observations reported here for boiling water reactor (BWR) phenomena such as nodular or shadow corrosion remains to be tested.

To illustrate the correlation between oxidation kinetics and hydrogen pickup fraction and confirm the observations in [3], the total hydrogen pickup fraction is plotted in Figure 3 as a function of the exponent n, which describes the change in corrosion rate when a power law applies before the first corrosion transition. Although specimens with additional anneal (-A) do not show periodic power law oxidation kinetics, the correlation remains valid since the hydrogen pickup fraction remains reasonably constant after the first transition. The figure clearly illustrates the inverse relationship between the hydrogen pickup fraction and the oxidation kinetics for the wide range of alloy systems tested in this study. For example, most Zr-Nb alloys have kinetics close to parabolic (n close to 0.5) and show the lowest hydrogen pickup fraction.

The results support the notion in [3] that a common oxidation and hydrogen pickup mechanism exists for all the alloys, and that the hydrogen pickup must be described within a general corrosion mechanism. The correlation between hydrogen pickup fraction and oxidation rate has been attributed to changes in the electronic conductivity of the zirconium oxide, which in turn is linked to characteristics of the oxide and the base metal [7]. All the samples produced in this study have been made available to the MUZIC-2 program to study the interaction of chemistry, microstructure and conductivity of the oxide with the oxidation rate and the hydrogen pickup fraction.

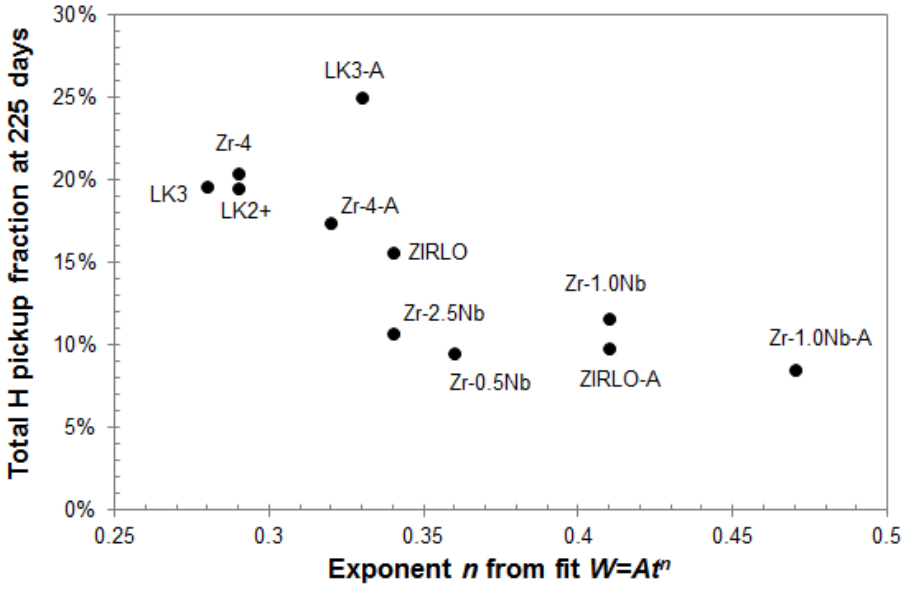

Figure 3 Total hydrogen pickup fraction at the end of autoclave tests (225 days) as function of the exponent *n* from the power law fit of the pre-transition weight gain $W=At^n$ for various zirconium alloys

4. Conclusion

A wide range of industry-relevant alloys have been tested in identical conditions to closely follow oxidation kinetics and hydrogen pickup. The study confirms that the hydrogen pickup fraction is clearly not constant throughout the corrosion process of zirconium-based alloys and correlates with oxidation kinetics. The hydrogen pickup fraction decreases with increasing the exponent n, such that it is the lowest for materials with oxidation kinetics close to parabolic, consistent with the observations in [3].

The base hydrogen pickup fraction and its variation during corrosion both depend on the composition of the material, with the highest fractions observed in Zircaloy-2 and the lowest in Zr-Nb systems. Thermal treatments, which increase the size of second phase particles in Zircaloy-2 and Zircaloy-4, and induce phase transformations in ZIRLO and Zr-Nb; accelerate the onset of the oxidation transition, increase the oxidation rate after transition, and change the subsequent evolution of the hydrogen pickup fraction.

The results obtained in this study are consistent with the hypothesis in [3] and [7] that the mechanisms for oxidation and hydrogen pickup are the same for all the alloys, and that they are closely coupled, so a mechanistic model of zirconium corrosion must include both phenomena.

Acknowledgement

The support and fruitful collaboration of all the members of the MUZIC-2 program is gratefully acknowledged.

References

1. N. Ni et al., “How the crystallography and nanoscale chemistry of the metal/oxide interface develops during the aqueous oxidation of zirconium cladding alloys”, *Acta Materialia*, **60**, *20*, (2012)
2. E. Polatidis et al., “Residual stresses and tetragonal phase fraction characterization of corrosion tested Zircaloy-4 using energy dispersive synchrotron X-ray diffraction”. *Journal of Nuclear Materials*, **432**, *1-3*, (2013)
3. A. Couet et al., “Hydrogen pickup measurements in zirconium alloys: Relation to oxidation kinetics”, *Journal of Nuclear Materials*, **451**,*1-3*, (2014)
4. A. Couet et al., “Oxide electronic conductivity and hydrogen pickup fraction in Zr alloys", in 2014 Annual Meeting on Transactions of the American Nuclear Society and Embedded Topical Meeting: Nuclear Fuels and Structural Materials for the Next Generation Nuclear Reactors, (2014)
5. J. Hu et al., “Identifying suboxide grains at the metal–oxide interface of a corroded Zr-1.0%Nb alloy using (S)TEM, transmission-EBSD and EELS”, *Micron*, **69**, (2015)
6. A. Garner et al., “The microstructure and microtexture of zirconium oxide films studied by transmission electron backscatter diffraction and automated crystal orientation mapping with transmission electron microscopy”, *Acta Materialia*, **80**, (2014)
7. A. Couet et al., “The coupled current charge compensation model for zirconium alloy fuel cladding oxidation. I. Parabolic oxidation of zirconium alloys”, *Accepted in Corrosion Science*, (2015)

ELIMINATION OF SOLUBLE BORON IN PWR WITH THE BigT BURNABLE ABSORBERS

MOHD-SYUKRI YAHYA, HWANYEAL YU, YONGHEE KIM*
Department of Nuclear and Quantum Engineering (NQe), Korea Advanced Institute of Science and Technology (KAIST), 291 Daehak-ro, Yuseong-gu, 305-701 Daejeon, Republic of Korea
** Corresponding author. Email: yongheekim@kaist.ac.kr*

HYEONG HEON KIM
NSSS Division, KEPCO Engineering & Construction Company (KEPCO E&C), 989-113 Daedeokdaero, Yuseong-gu, 305-353 Daejeon, Republic of Korea

ABSTRACT

Elimination of soluble boron in a pressurized water reactor (PWR) core offers a number of potentially significant improvements. Firstly, boric acid-induced corrosion in the primary system can possibly be eliminated in the soluble boron-free (SBF) PWR. Secondly, plant operation and maintenance can greatly be simplified. Thirdly, crud and liquid radioactive waste in the primary loop can drastically be reduced. Fourthly, an SBF PWR always maintains a desirably 'large negative' moderator temperature coefficient (MTC) at all times. All these help improving economics and safety of the PWR.

This paper investigates feasibility of equilibrium SBF PWR designs with a new burnable absorber (BA) concept named "Burnable absorber-Integrated Guide Thimble" (BigT). The research focuses on two state-of-the-art PWR designs, namely AP1000 and OPR1000 reactors. The equilibrium cores were directly searched via repetitive Monte Carlo depletion calculations until convergence. The analyses clearly demonstrated promising SBF PWR designs with the BigT absorbers. In the model BigT-loaded AP1000 core, burnup reactivity swing over the equilibrium cycle was quite small (~2,000 pcm). Fairly consistent radial power peaks (<1.82) with strongly negative MTC were obtained throughout the cycle, with a sufficiently high shutdown margin (>1,000 pcm) at beginning-of-cycle. In the model BigT-loaded OPR1000 core, preliminary results indicate a promising burnup reactivity swing of <3,000 pcm. In conclusion, SBF PWR designs were neutronically-feasible with the BigT absorbers. All simulations were completed using the Monte Carlo Serpent2 code with ENDF/B-VII.0 nuclear data library.

1. Introduction

There are a number of potential advantages of removing soluble boron from primary system of a pressurized water reactor (PWR) [1-3]. Firstly, typical concerns related to boric-acid induced corrosion and crud depositions can almost entirely be eliminated in a soluble boron-free (SBF) PWR design. Secondly, without the needs to borate and deborate coolant during normal operation, the SBF PWR system may require fewer piping and circuitries, thereby significantly simplifying the core design, operation and maintenance. Thirdly, accumulation of radioactive liquid wastes in the primary loop can greatly be reduced since 90% of total tritium in PWR coolant are consequences of mixing boric acid with lithium hydroxide for the coolant pH control. Fourthly, an SBF PWR yields constantly high negative moderator temperature coefficients (MTC), which is a desirable characteristics of an inherently safe PWR. All these possibly enhance economics and safety of the PWR.

The aforementioned advantages justify the pursuits for modern SBF PWR designs [1-3]. Standard approach to realize the SBF core is by actively maximizing use of burnable absorber (BA) while limiting worth of regulating control rods <1,000 pcm in the absence of soluble boron. Previous studies concluded that the SBF PWR design is 'less restrictive' for small reactor cores. As of yet, there is still no successful deployment of commercial SBF PWR designs.

This paper aims to reassess neutronic feasibility of modern SBF PWRs with the newly-proposed "Burnable absorber-Integrated Guide Thimble" (BigT) [4-5] absorber. In this research, the model PWR designs are based on AP1000 [6] and OPR1000 [7] cores. All simulations were completed using Monte Carlo Serpent2 [8] code with ENDF/B-VII.0 nuclear data library.

2. The BigT Burnable Absorber

The BigT absorber offers significant advances over state-of-the-art PWR thimble-occupying BA technology, in that it still allows insertion of control rod in its thimble, is replaceable during refueling and is neutronically very flexible. Since only minor modifications are required to the existing lattice design, the BigT is possibly retrofittable to most modern PWR configurations.

The BigT comes in three different design variants. This research, however, focuses on only two: BigT-AHR ('Azimuthally Heterogeneous Ring') and BigT-Pad concepts as depicted in Figure 1. Figure 2 illustrates how the BigT absorbers are loaded into representative PWR fuel assembly lattices. The BigT-AHR is a zircaloy ring inserted separately into the PWR guide thimble. The ring, which must be thin enough to enable insertion of control rod in its annulus hole, houses azimuthally-heterogeneous BA materials. The BigT-Pad, on the other hand, is a *modified* guide thimble with expanded corner pockets that contain azimuthally-heterogeneous BA materials. Geometrical aspect ratios of these BA materials strongly affects its effectiveness as neutron poisons. This is because a lumped poison with a large *exposed surface* area has small spatial self-shielding, and vice versa. One notes control rod in the BigT-AHR thimble is slightly smaller than conventional. Nonetheless, its worth can easily be enhanced by simply replacing the rod material with a "blacker" absorber or by selectively enriching highly-absorbing isotopes in the rod [4-5].

The BigT absorbers have previously been demonstrated to perform as well as the commercial BA technologies [4-5]. While the potential flexibility and replaceability of the BigT may enable many operational specifications, this paper specifically concentrates on one: application of the BigT absorbers in pursuit of modern SBF PWR designs.

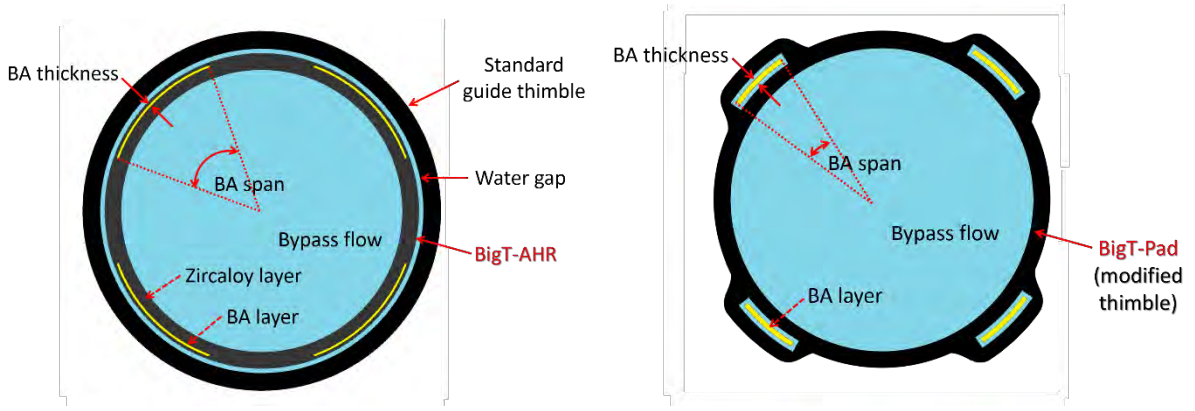

Fig 1. The (left) BigT-AHR and (right) BigT-Pad design concepts

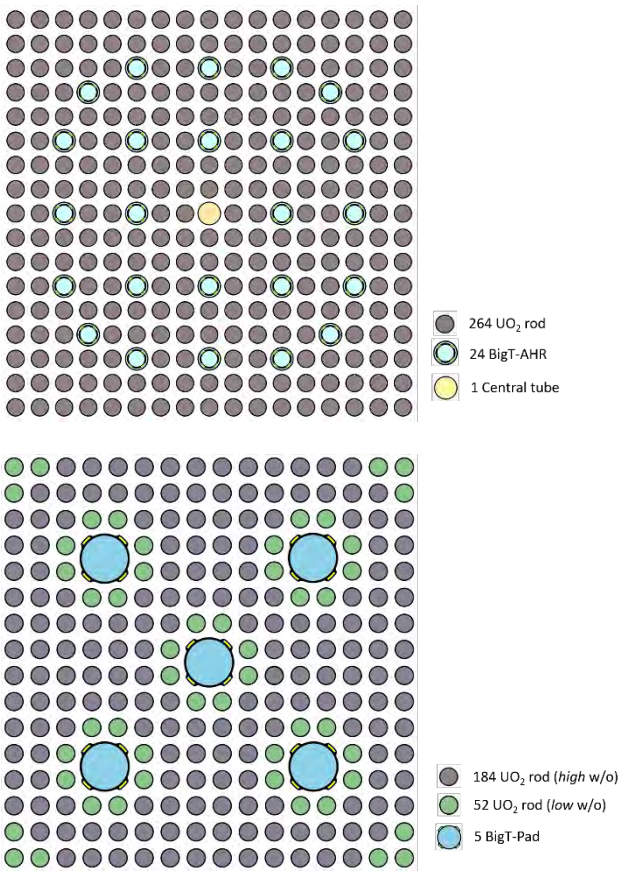

Fig 2. BigT-loaded (top) 17x17 and (bottom) 16x16 fuel assembly lattices

3. The Model Soluble Boron-Free (SBF) PWRs

3.1 BigT-loaded SBF AP1000 Core

Objective of this sub-section is to define a conceptual equilibrium core design of a model SBF AP1000 [6], which uses standard 17x17 fuel assembly lattices. The 3,400 MWt rated reactor is operated for a 490-EFPD (effective full power day) cycle on a three-batch fuel management as shown in Figure 3. The fresh assemblies are composed of 4.95-w/o UO_2 fuel rods.

The SBF AP1000 core utilizes batch-wise BigT-AHR B_4C absorbers as tabulated in Table 1. This is because lattice reactivity varies batch-wise due to burnup and xenon content. As such, core reactivity management can be designed batch-wise as well. In this model, specifically, the core criticality is pursued by offsetting super-criticality of fresh assemblies with sub-criticality of twice-burned assemblies, while maintaining once-burned assemblies about critical (Figure 4). One notes *depleted* BigT are replaced with *fresh* BigT absorbers of the next batch configuration every 510 EFPDs (note that simulation cycle of the assembly lattice calculation differs from that of the 3-D core calculation, i.e. 490 EFPDs).

Equilibrium cycle of the SBF core was searched via repetitive Monte Carlo depletion calculations until convergence as depicted in Figure 5. 300 active and 100 inactive cycles, with 360,000 particles per cycle, were simulated to assure sufficient convergence (standard deviations of reactor neutron multiplication factor about ±7 pcm). To minimize the required computing resources, material compositions were defined assembly-wise and batch-averaged. Four vertical stacks of fixed core-averaged temperatures were modeled in this scoping study, with an assumption that there is no significant axial effect which would invalidate general conclusions of the simulations.

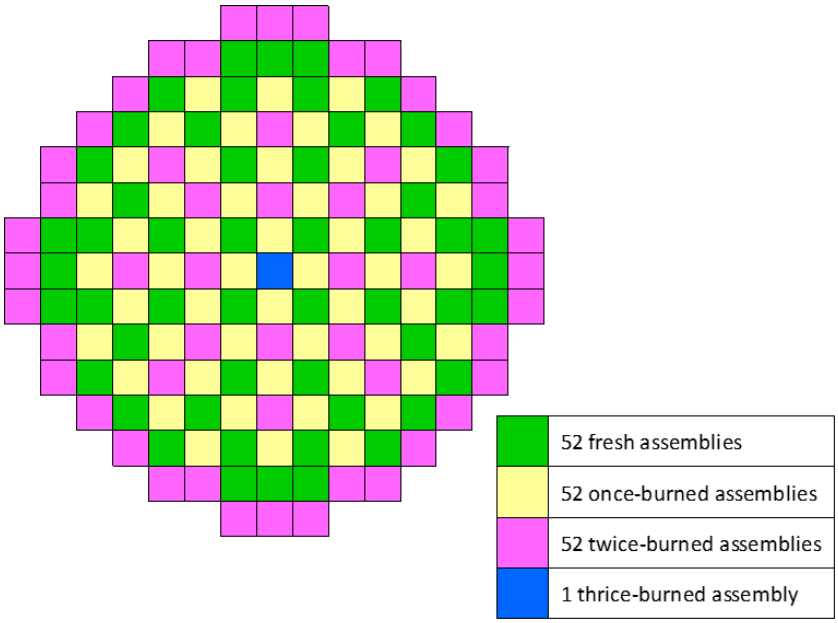

Fig 3. The model BigT-loaded SBF AP1000 core

BigT-AHR B_4C	**Thickness (mm)**	**Span**
Fresh Assembly	0.17 mm	50˚
Once-burned	0.28 mm	25˚
Twice-burned	0.02 mm	88˚

Tab 1: Batch-wise BigT-AHR Absorbers for the SBF AP1000 Core

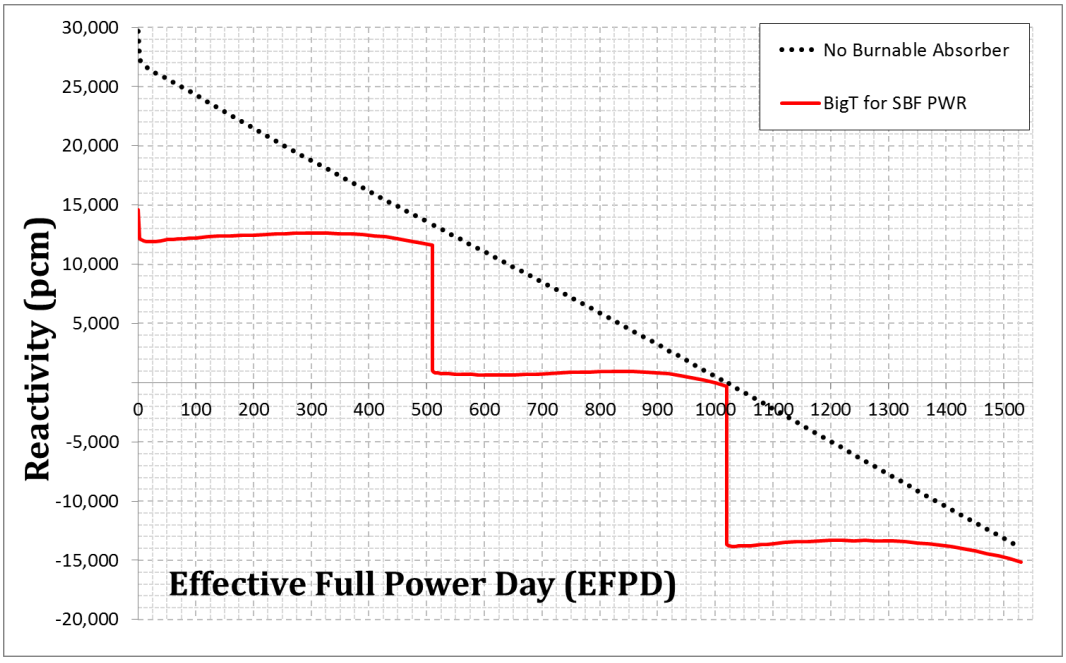

Fig 4. Three-cycle depletion of a representative SBF AP1000 lattice

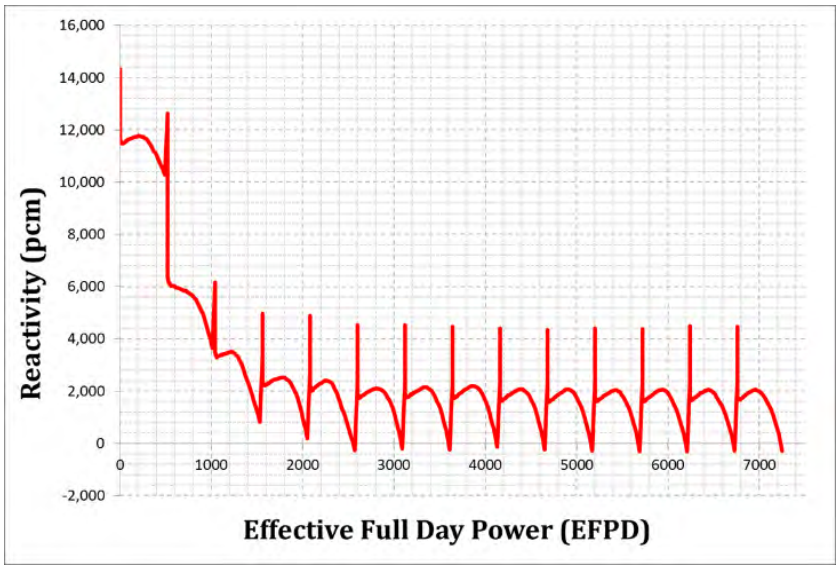

Fig 5. The search for equilibrium core: repetitive depletion calculations until convergence

Figure 6 depicts resulting burnup-dependent core reactivity over the equilibrium cycle. A gradual hike of ~400 pcm during the first 250 EFPDs and a noticeable quicker drop of ~2,000 pcm over second half of the cycle are observed. This reasonably well-controlled core reactivity depletion is attained due to the optimal spatial self-shielding adjustment of the batch-wise BigT absorbers. Burnup reactivity swing (BRS) is ~2,000 pcm, fairly promising against target <1,000 pcm [1-3].

Figure 7 shows the core normalized assembly radial power at different burnup. The core leakage is moderately low, despite the non-optimized loading pattern, as power peaks at sub-periphery. One also notes 'Assembly 0602' is consistently the hottest lattice as highlighted, with normalized power <1.60.

Figures 8 depict normalized pin power of the 'Assembly 0602'. BOC and EOC pin peaking factors are 1.158 and 1.108, respectively. Radial peaking factors of the core are 1.83 at BOC and 1.75 at EOC, as estimated from the following approximation:

$$F_{xy}^{\text{Total}} = \text{Max}\left[F_{xy}^{\text{Assembly}} \cdot F_{xy}^{\text{Pin}}\right]$$

Figure 9 depicts normalized radial power peaking factors throughout the cycle. Radial peaks hover ~1.60 assembly-wise, and <1.20 pin-wise in 'Assembly 0602', clearly demonstrating potential of the BigT absorber in properly controlling the core radial power distributions.

Table 2 lists selected neutronic characteristics of the SBF AP1000 equilibrium core. At hot full power (HFP) operating condition, the MTCs are always strongly negative, -60.0 pcm/K. The fuel temperature coefficients (FTC) span between -2.7 to -3.2 pcm/K, within typical range of those of conventional PWR with similar comparable enrichment and burnup.

Table 3 tabulates BOC shutdown margin of the BigT-loaded SBF PWR core, based on rodding pattern documented in Ref. 6. A sufficiently high margin is obtained even with the *smaller* Ag-In-Cd rods. B_4C control rods can provide a higher margin, if necessary. As such, shutdown from HFP to hot zero power (HZP) condition can safely be performed in the BigT-loaded SBF AP1000 equilibrium design.

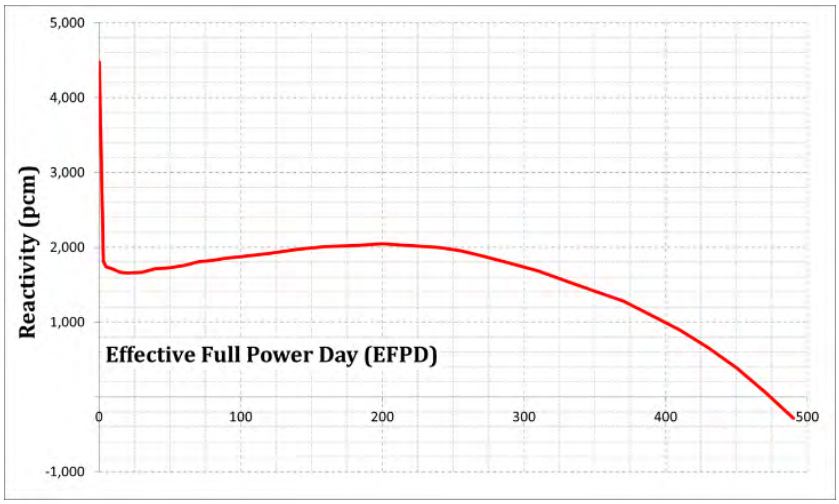

Fig 6. Reactivity depletion over equilibrium cycle of the SBF AP1000 core

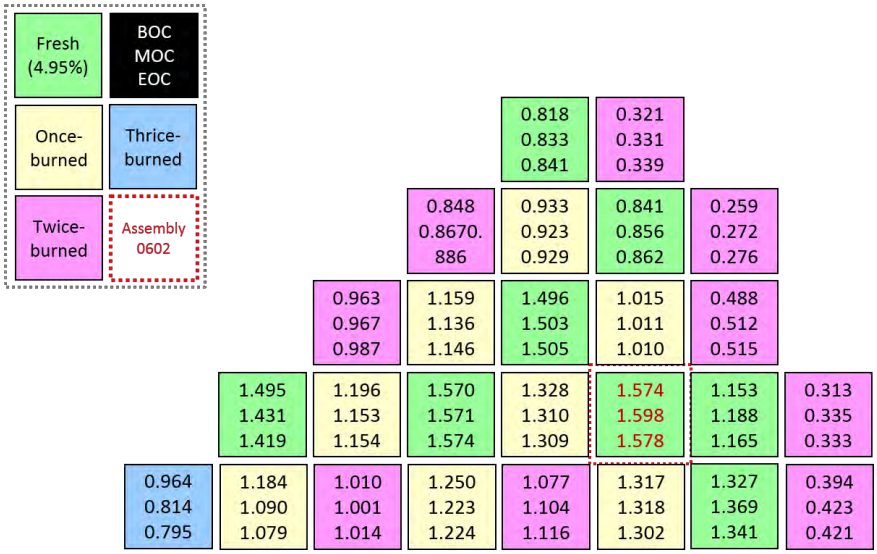

Fig 7. Normalized radial assembly power profile at different burnup of 1/8th of the equilibrium SBF AP1000 core

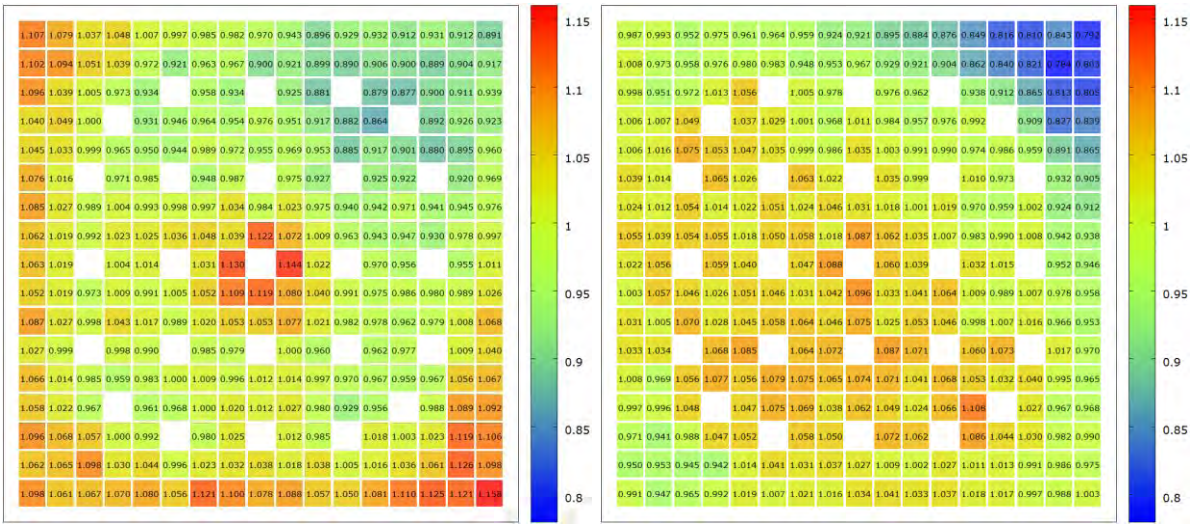

Figs 8. Normalized radial pin power profiles of ‘Assembly 0602’ at (left) BOC and (right) EOC

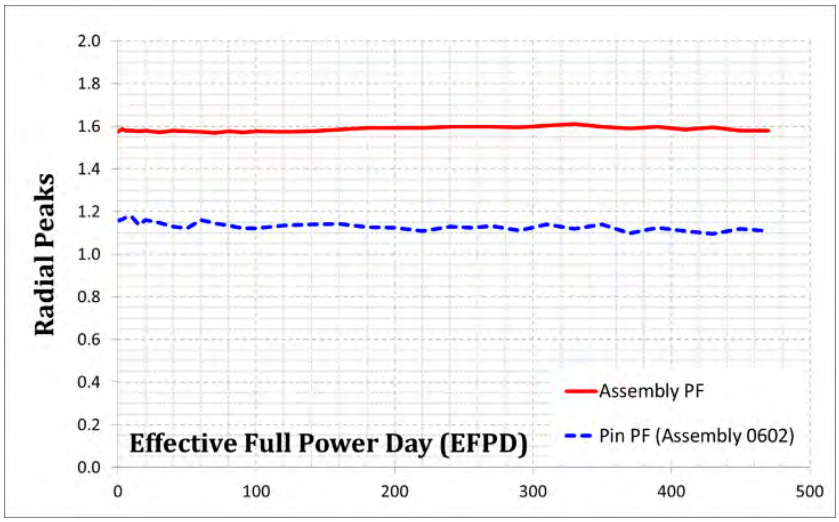

Fig 9. Radial peaks of the equilibrium SBF AP1000 core

Parameters	BOC	EOC
F_{xy}^{assembly}	1.574	1.578
F_{xy}^{pin}	1.158	1.108
$\boldsymbol{F_{xy}^{\text{total}}}$	**1.82**	**1.75**
FTC (HFP), pcm/K	**-2.67**	**-3.22**
MTC (HFP), pcm/K	**-59.4**	**-60.0**

Tab 2: Nuclear Characteristics of Equilibrium SBF AP1000 Core

Reactivity Insertion (HFP to HZP)	****Ag-In-Cd Rod (pcm)**	****Natural B_4C Rod (pcm)**
Total power defect*	2,009	2,009
Void content*	50	50
(1) Total rod requirement*	**2,059**	**2,059**
Estimated Rod Worth (HZP)		
All rods inserted	5,616	7,113
N-1 rods inserted	5,055	6,615
(2) N-1 worth less 10%	**1,303**	**1,763**
Shutdown Margin		
Calculated Margin [(2) – (1)]	**2,995**	**4,555**
Required Shutdown Margin*	**1,770**	**1,770**

* Based on Yonggwang NPP Unit 1 Cycle 12 Nuclear Design Report (1999) [9]
** 0.351 cm control rod (20% smaller in radius than conventional) to fit the BigT-AHR

Tab 3: BOC Shutdown Margin of Equilibrium SBF AP1000 Core

3.2 BigT-loaded SBF OPR1000 Core

This sub-section aims to demonstrate neutronic feasibility of model equilibrium SBF OPR1000 cores [7] with the BigT absorbers. In this study, the 2,815 MWt core was modeled as follows:

- 16x16 lattices that employ 4.80 and 4.27 w/o enrichment-zoning of admixed 0.5 w/o erbia-urania (UO_2-Er_2O_3) fuel rods,
- three-batch fuel management as shown in Figure 10, and
- operational cycle of 510 EFPDs with 10 cooling days for refueling.

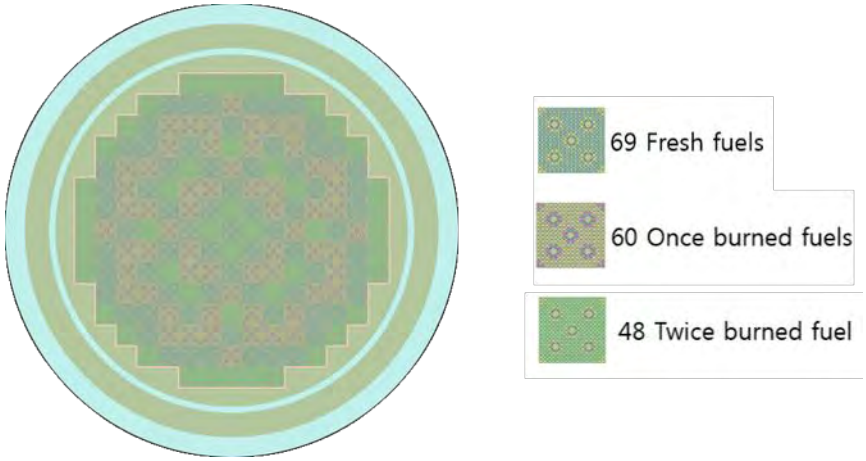

Fig 10. The SBF OPR1000 core

The simulated core adopts similar loading strategy as described in Section 3.1; i.e. batch-wise BigT absorbers. The BigT are mostly of Gd variants, except for twice-burned assemblies which may use either Gd or B_4C, as shown in Figure 11. This is because reactivity swing in the twice-burned assemblies is particularly volatile due to its considerably higher plutonium content.

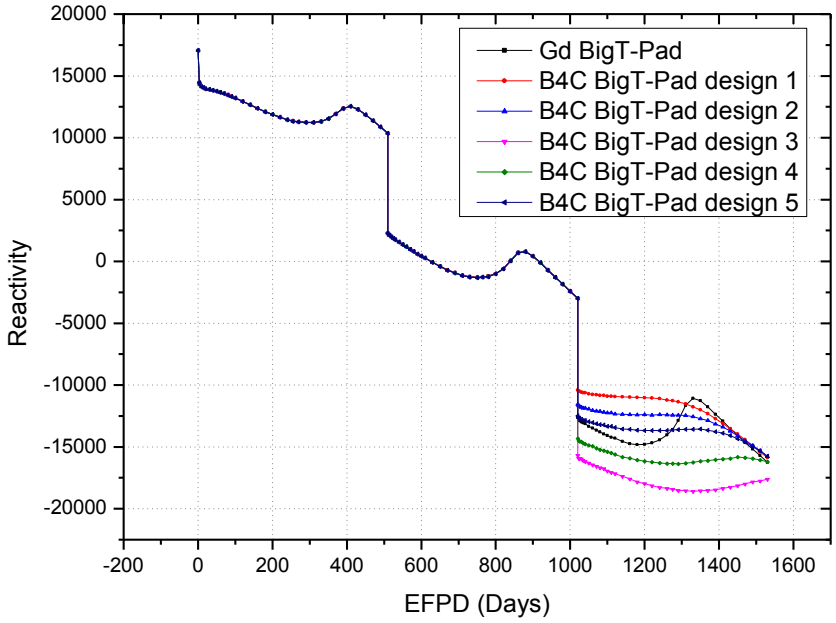

Fig 11. Three-cycle depletion of representative multi-material OPR1000 lattices (*note*: BA variations of either Gd or B_4C are loaded into twice-burned assemblies)

Figure 12 illustrates the search for equilibrium cycle of the SBF OPR1000 core. One notes reactivity oscillates due to gadolinium spatial self-shielding peaks at BOC and due to xenon burn-up during refueling.

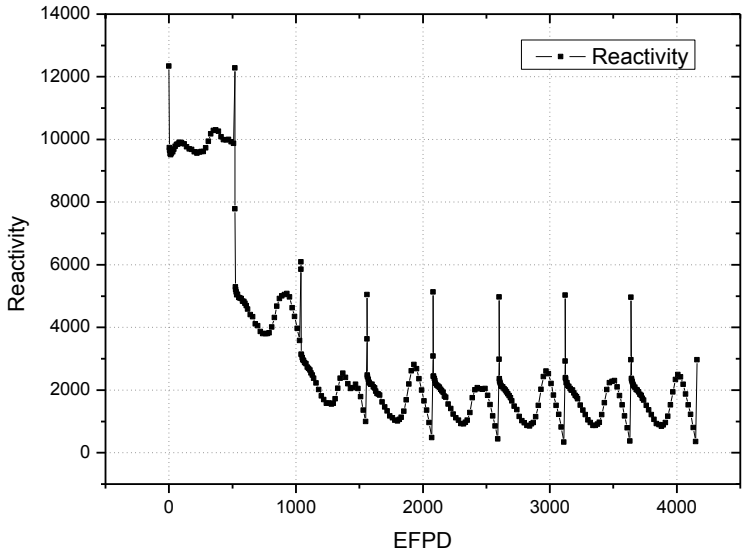

Fig 12. The search for OPR1000 equilibrium core

Figure 13 depicts reactivity evolution throughout the equilibrium cycle of the cores. 'Gd BigT only' denotes core that uses Gd exclusively, while the other two load BigT-Pad Gd in fresh and once-burned assemblies, and BigT-Pad B_4C in twice-burned assemblies (as depicted in Figure 11). The multi-material configurations (i.e. combination of BigT-Pad Gd and B_4C) yield *flatter* reactivity swing between 100 and 350 EFPDs. More importantly, BRS of the 'BigT-Gd only' design is ~2,700 pcm, clearly demonstrating potential of the BigT-loaded SBF OPR1000 core.

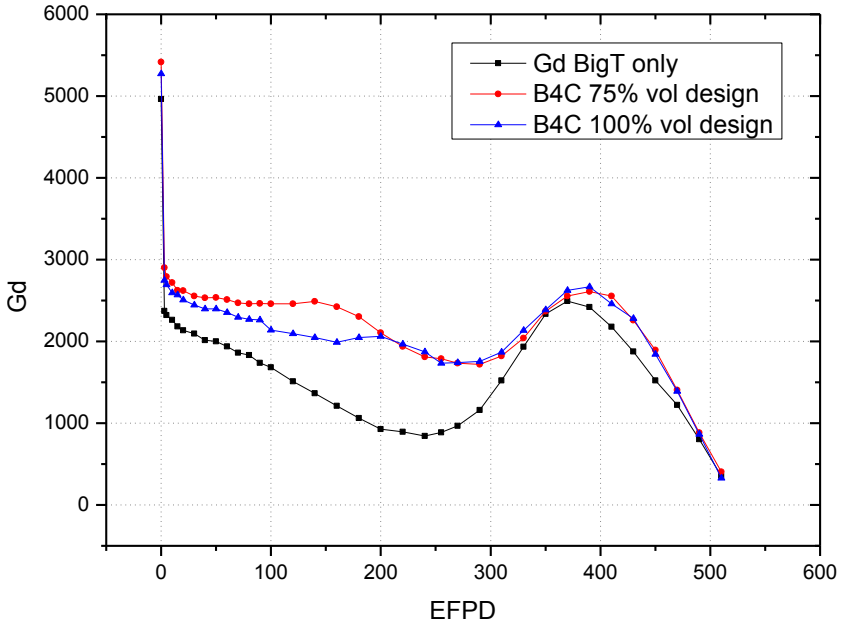

Fig 13. Reactivity depletion over equilibrium cycle of the SBF OPR1000 cores

4. Conclusions

Removal of soluble boron in a PWR offers many significant improvements, chiefly in the simplification of core design and operation, elimination of boric acid-induced corrosion, reduction of liquid radioactive waste accumulation, and assurance of consistently negative moderator temperature coefficient (MTC). This research aims to define soluble boron-free (SBF) PWR equilibrium core designs with a newly-conceptualized BigT absorbers. Reference PWR designs are based on AP1000 and OPR1000 cores. This approach uniquely requires replacing spent with fresh batch-wise BigT-AHR absorbers during refueling interval.

Preliminary analyses imply promising feasibility of the SBF AP1000 and OPR1000 cores as burnup reactivity swing (BRS) over equilibrium cycles are reasonably small, ~2,000 pcm and ~2,700 pcm respectively. For the SBF AP1000 core, in particular, fairly consistent radial power peaks, strongly negative MTCs at all times and sufficiently high shutdown margins are attained throughout the cycle.

This research is, however, far from complete. Further optimization is needed to fine-tune the solution, especially the BigT detailed designs and core loading pattern. Quantifications of other vital neutronic parameters, such as axial power distribution and cold shutdown capability, are also needed to fully assess technical feasibility of the design.

5. Acknowledgements

This work was supported by the Nuclear Power Core Technology Development Program of the Korea Institute of Energy Technology Evaluation and Planning (KETEP), granted financial resource from the Ministry of Trade, Industry & Energy, Republic of Korea (20131610101850).

6. References

[1] A. GALPERIN, M. Segev and A. Radkowsky, “Substitution of the Soluble Boron Reactivity Control System of a Pressurized Water Reactor by Gadolinium Burnable Poisons”, Nuclear Technology, volume 75, pp. 127 – 133 (1986).
[2] Elimination of Soluble Boron for a New PWR Design, Report No. EPRI NP-6536, Electric Power Research Institute (EPRI), USA (1989).
[3] P. THOMET, “Feasibility Studies of a Soluble Boron-Free 900-MW(electric) PWR, Core Physics – I: Motivations, Assembly Design, and Core Control”, Nuclear Technology, volume 127, pp. 259 – 266 (1999).
[4] M.S. YAHYA, H. Yu and Y. Kim, “BigT – A New Burnable Absorber Concept for PWR”, Proc. of PHYSOR 2014, Kyoto, Japan (2014).
[5] M.S. YAHYA and Y. Kim, “Application of the BigT Burnable Absorber to AP1000 Core for a Soluble Boron Free Operation”, Transaction of American Nuclear Society, volume 111, pp. 1208-1210, Anaheim, CA, USA (2014).
[6] Public version of AP1000 Design Control Document rev. 19, Report No. APP-GW-GL-702, Westinghouse Electric Corp., USA (2011).
[7] The Nuclear Design Report for Yonggwang Nuclear Power Plant Unit 6 Cycle 8, Report No. KNF-Y6C8-11029 Rev. 0, KEPCO Nuclear Fuel Company, Republic of Korea (2011).
[8] J. LEPPÄNEN, Serpent – A Continuous Energy Monte Carlo Reactor Physics Burnup Calculation Code, VTT Technical Research Centre of Finland, Finland (2012).
[9] The Nuclear Design Report for Yonggwang Nuclear Power Plant Unit 1 Cycle 12, Report No. KNF-Y1C12-99019, KEPCO Nuclear Fuel Company, Republic of Korea (1999).

RESEARCH ON MANUFACTURING TECHNOLOGY OF LARGE GRAIN SIZE FUEL PELLETS

PENG Wang, CHEN Xiaoxiang

CNNC Jianzhong Nuclear Fuel Co., Ltd

YinBing Road , YiBin city, SiChuan Province ,China , 644000

ABSTRACT

In order to improve the economy of nuclear power, nuclear power plants are gradually increasing the fuel burn-up and extending reload cycle. The reload cycle of TianWan nuclear power plant would be extended from 12 to 18 months, and it changed the type of the fuel assembly. Based on manufacturing former fuel pellet, CJNF(CNNC Jianzhong Nuclear Fuel Co., Ltd) had completed the development of large grain fuel pellet after research and technology improvement. The diameter of central hole and chamfer height of the pellet were changed, so the main difficulty in manufacturing was the grain size which is indeed more than 25μm, while the thermal stability remains unchanged. A large number of projects were made through the orthogonal test to investigate the UO_2 powder preparation process, the content of additives (nanoscale-Al_2O_3, nanoscale-SiO_2 and U_3O_8) and thermal stability. The test results showed that the pellet grain size increased as the increasing of nanoscale-Al_2O_3, when the content of nanoscale-Al_2O_3 reached a certain level, the grain size growth was slow, but nanoscale-SiO_2 had little effect on the pellet grain size compared with Al_2O_3; It needed more nanoscale-Al_2O_3-SiO_2 to obtain large grain size pellet for wet process UO_2 powder than that for dry process UO_2 powder.

In the process of the verification, we analyzed the thermal stability, physical and chemical properties, which all met the design requirements. Results showed the large grain UO_2 fuel pellet for nuclear power plant had been studied and manufactured successfully in CJNF.

Keywords: nanoscale-Al_2O_3-SiO_2, large grain, pellet

1 Introduction

With the rapid development of science and economy, we are longing for more energy, nuclear energy as a green, economical efficiency one will increase in the proportion of China's energy. In recent years, the domestic industry was accelerating the development of nuclear power. To and improve the economy, nuclear power plants aimed to improve the burn-up of the fuel assemblies and extend refueling cycle.

Higher burn-up pellets could generate problems, the typical one is the increasing pressure of the fuel rods, it can be fixed by designing the inner rod gas chamber volume, reducing pre-charge pressure helium, we are using large grain fuel pellets inside the rods to solve the problem.

Practical experience shows that the main factors influencing the performance of fuel assembly include: fuel cladding corrosion, component deformation, fission gas releasing, Pellet-Cladding Interaction (PCI), coolant in the wear debris, and so on. Single in terms of

fuel pellets, the fission gas release in the process of irradiation reduced with the increase of grain size. Therefore, it is of great significance to develop large grain pellets study on nuclear economy and nuclear operation reliability.

The large grain size fuel pellets required an average grain size greater than 25 microns, which can reduce the releasing of fission gas, thereby significantly reducing the pressure of the fuel rods.

Russian TVL used methods by doping Al_2O_3-SiO_2 to increase the grain size of the pellet, the added amount is about 800ppm, the Al_2O_3 and SiO_2 ratio is 3: 1. SAYASHIN [1] pointed that using 50ppm Al_2O_3-SiO_2 mixed to powder of UO_2, when the grain growth to (12 to 14) microns, the sintered shrink process will stop, the grain will further grow. When the (Al + Si) / U reached 0.010% (100ppm), the average grain size to (20 to 30) microns. When added (250 ~ 1000) ppm, the core is formed on the grain boundaries of the eutectic point of the block to promote the grain boundary sliding and improve the creep rate. SAYASHIN recommended, when the content of Al_2O_3-SiO_2 is not more than 0.010wt%, the boron content met the technical requirements of the equivalent. If the addition was greater than 250ppm, the pellet density would be reduced.

Guanren Zhu[2]noted that when the sintering temperature reached 1300°C, the change of not adding additives powder was larger than the adding one, but added Al_2O_3-SiO_2 one was rapidly concentrated at 1400°C, which shows early in the sintering additives inhibit the compact in the early process of sintering, Al_2O_3-SiO_2 and other additives approximately played a role in promoting the sintering of pellets at 1400°C.

TianWan nuclear power plant will extend the refueling cycle to 18 months, the fuel assemblies had been changed. Compared to the older fuel assemblies, not only the number of fuel rods, but the fuel column length had been changed. The pellet loading of new assemblies was changed, it required the development of new fuel UO_2 pellets, which can meet the requirements of new fuel assemblies.

Annular pellets on fuel, which can reduce the temperature in the center of the pellet and decrease PCI. Compared with the traditional solid ceramic pellets, annular uranium oxide fuel pellets into the internal cooling, reducing the fuel temperature, increasing the fuel rods inside the cavity volume and reducing the PCI action, it can ensure the economy and safety of the reactor when making the reactor power increase.

Compared with the new developed and the former fuel pellet, the center of the hole diameter is reduced, it had an increase in diameter and an increase in pellet loading weigh, the average grain size increased to more than 25μm.

2 Experiment

2.1 The design of orthogonal experiment

Orthogonal test commonly is used to study the impact of multiple factors on an index, using fewer tests that we can get more comprehensive information, which optimize test parameters. Specific test programs must be carried out strictly in accordance with orthogonal

design.

Table 1. The orthogonal test $L_{16}(2\times3^7)$

number	1	2	3	4	5	6
	condition	SiO_2(ppm)	Al_2O_3(ppm)	UO_2 powder	U_3O_8(%wt)	A.O(wt%)
1	1(W.H)	1(0)	1(0)	1(D.P)	1(5)	1(0.1)
2	1	1	2(25)	2(W.P)	2(8)	2(0.2)
3	1	1	3(50)	3(MIX)	3(12)	3(0.3)
4	1	2(25)	1	1	2	2
5	1	2	2	2	3	3
6	1	2	3	3	1	1
7	1	3(50)	1	2	1	3
8	1	3	2	3	2	1
9	1	3	3	1	3	2
10	2(D.H)	1	1	3	3	2
11	2	1	2	1	1	3
12	2	1	3	2	2	1
13	2	2	1	2	3	1
14	2	2	2	3	1	2
15	2	2	3	1	2	3
16	2	3	1	3	2	3
17	2	3	2	1	3	1
18	2	3	3	2	1	2

Remark:

1) SiO_2 (PPM), Al_2O_3 (PPM), UO_2 powder, U_3O_8 (%wt), A.O (wt%)all have three levels;

2) Re-sintering atmosphere has two levels: dry and wet hydrogen;

3) Sintered pellets of each test sample is not less than 12 pieces;

4) The addition amount of the AKL is stabled;

5) JB/T 7510-94 (process parameter optimization method of orthogonal test method).

6) W.H=wet hydrogen, D.H=dry hydrogen, D.P=dry process, W.P=wet process, MIX=mixture

Combined with the actual situation of the production process, we used orthogonal experiment to test factor, like UO_2 powder type, Al_2O_3, SiO_2, block U_3O_8, oxalate, complex burn test in the sintering atmosphere to study pellets of operating parameters on grain structure and thermal ability. According to JB/T 7510-94 (process parameter optimization method - orthogonal test method) select the mixed orthogonal test. The detail of orthogonal test is in Table 1.

2.2 The test process

2.2.1 Equipment and materials

(1) equipment

A) 300 DX hydraulic material testing machine or the WE-300B hydraulic testing machine;

B**)** NFHD sintering furnace;

(2) the materials

A) dry process UO_2 powder, wet process UO_2 powder, mixing dry process UO_2 powder ;

B) U_3O_8 powder (enrichment 2.40%, 3.10%, 3.60%);

C) nanoscale-Al_2O_3, nanoscale-SiO_2;

D) pore forming material(ammonium oxalate);

E) lubricants (zinc stearate, AKL).

2.2.2 Test method

(1)Mixing

According to the test condition of additives and mixing uniformity;

(2) Molding

Used for molding powder with 300 DX hydraulic material testing machine or the WE-300B hydraulic testing machine;

Die diameter: 10.10mm;

The green density: (5.80±0.05) g/cm^3.

(3) Sintering

The sintering time is stable;

The sintering temperature is stable.

2.2.3 Sample analysis

1) Each test used 2 sintering pellets for grain size and microcosmic structure analysis;

2) Each orthogonal experiment took 10 sintering pellets after sintering performance inspection, measuring the complex pellet density changes before and after burning.

3 Result

The focus of the paper will be the analysis of the pores, the average grain size and thermal stability of the pellet. Influenced factors is obtained by orthogonal analysis, with image analyzer KS400, the statistics of (0 ~ 100)μm and total porosity are classified, porosity percentage and total porosity percentage are given. The shares of various factors on the large pore volume are given in Table 2, so is the results of the distribution of the pores,the average grain size and thermal stability. The influence of various factors on the pellet grain

size was shown in Figure 1. The relationship between grain size and thermal stability in hydrogen is shown in Figure 2.

Table 2. **The pores, average grain size and thermal stability**

Number	The distribution of the pores					Grain size (μm)	thermal stability (%T.D)
	（1~10）μm （%Vol）	（1~100）μm （%Vol）	The total porosity	（1~10）μm （%pore）	>500μm		
1	1.83	2.74	2.74	97.63	none	20.6	0.46
2	2.64	4.12	4.12	97.91	none	14.5	0.53
3	1.83	3.00	3.00	97.01	none	35.1	0.21
4	1.83	2.84	2.84	97.82	none	20.9	0.46
5	3.03	6.02	6.02	97.28	none	12.7	0.58
6	1.96	3.85	3.85	96.02	none	19.6	0.66
7	2.53	4.49	4.49	97.80	none	12.4	0.60
8	2.25	3.13	3.13	97.98	none	21.1	0.34
9	2.23	3.33	3.33	96.20	none	27.3	0.27
10	2.55	4.73	4.73	97.50	none	14.5	0.39
11	1.78	2.82	2.82	98.07	none	28.1	0.05
12	2.74	4.57	4.57	98.30	none	22.3	0.22
13	3.02	2.84	2.84	96.05	none	10.6	0.54
14	1.75	4.22	4.22	97.21	none	22.1	0.18
15	1.94	3.22	3.22	94.98	none	31.4	-0.07
16	2.17	3.03	3.03	97.93	none	14.9	0.23
17	2.45	3.74	3.74	97.97	none	24.4	0.12
18	2.52	4.54	4.54	97.32	none	21.6	0.21

We can see from Table 2, the factor like nanoscale-Al_2O_3, nanoscale-SiO_2 and U_3O_8 don't influence the number of large pores like the additive A.O does. Not pores larger than 500 microns was detected, and the percentage of the（1~10）μm also meets the technical requirements.

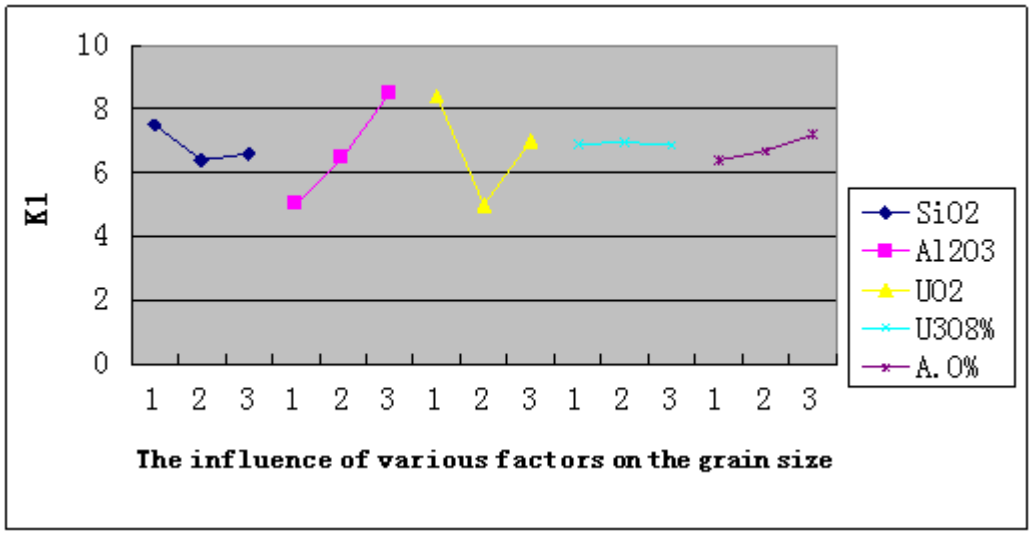

Figure 1. Effects on the average grain size of each factor

The No.3, 9, 11, 15 testing results show that it has significant effects on the grain size of the five factors, adding Al_2O_3 and the category of UO_2 are the key method, the other three factors have little effect on the grain size, adding U_3O_8 factors is the minimum. It can be seen from table 2, with the increase of adding Al_2O_3, dry process powder is the most obivious on the influence of the grain size, followed by mixing materials, minimal impact is wet powder.

In the orthogonal experiment, dry process powder (mixing material is dry powder mixing) when Al_2O_3 content is 25 PPM, the grain size of pellet can reach above 25μm. In the wet process powder when addition Al_2O_3 is 50ppm or more, grain size of the pellets to achieve 20μm, Even if the adding Al_2O_3 is 50ppm, the grain size of pellets could not be above 25μm.

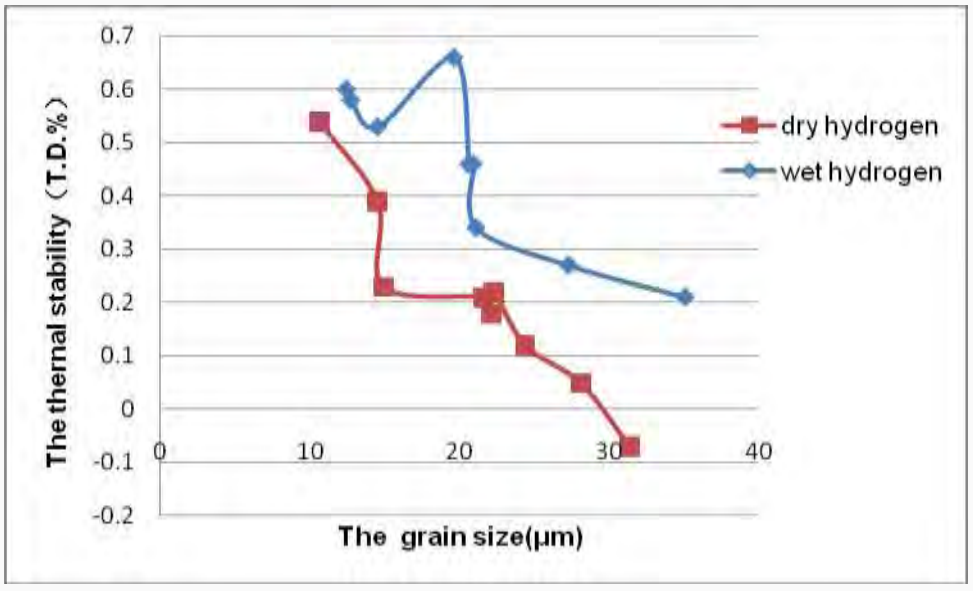

Figure 2. **The relationship between grain size and thermal stability in hydrogen**

From Figure 2 we can see the big impact of wet hydrogen atmosphere on thermal stability than dry hydrogen atmosphere. In the grain size equal, the stability of the complex burned in a dry hydrogen atmosphere is better than wet hydrogen gas. The grain size and the degree of thermal stability of the existence of a great relationship, in the same

atmosphere, with the increase of the thermal stability , the grain size is also more stable.

Other physical and chemical properties, such as porosity, density and open porosity and thermal ability, which all meet the design requirements, here we were not to do concrete analysis.

4 Process verification

We had an added test that nanoscale-Al_2O_3-SiO_2 were added 1: 1 ratio. In order to ensure nuclear-grade requirements and pellet density was under control (test showed more than 100ppm nanoscale-Al_2O_3 and SiO_2 were added will have an impact on pellet density). During the test the following amounts of nanoscale-Al_2O_3-SiO_2 have been added : 25ppm, 50ppm, 75ppm, 100ppm.

Because the addition of nanoscale-Al_2O_3-SiO_2 powder is in a low percentage, if they were directly pumped into the blender, which would result in the nanoscale-Al_2O_3-SiO_2 powder mixed inhomogeneous. Once that happened, the grain size and other properties of the product were not under control.

We sampled the batch before, during and after the test for measuring physical and chemical properties of the pellets. Table 3 shows the results of the sample analysis.

Table 3. **Large grain pellets verification test**

Items		addition	Grain size (μm)	Thermal stability (%T.D)	Al content (μg/g)	Si content (μg/g)
Dry process	240P13P1+	25	27.2 24.4 26.3	0.17 0.20 0.15	12 <5 10	<23 28 <23
	240P13P2+	50	27.9 31.3 29.2	0.09 0.10 0.08	17 13 14	<23 <23 32
	240P13P3+	75	32.2 28.7 31.5	0.12 0.07 0.09	13 22 <5	34 <23 <23
	240P13P4+	100	30.4 32.7 31.9	0.04 0.03 0.07	10 27 24	29 <23 25
Wet process	310P13P1+	25	12.7 13.9 11.4	0.41 0.53 0.47	10 9 <5	<23 <23 24
	310P13P2+	50	26.3 24.0 25.7	0.34 0.45 0.37	13 24 19	<23 <23 <23
	310P13P3+	75	28.4 29.7 27.9	0.33 0.26 0.29	17 <5 25	33 <23 27
	240P13P4+	100	27.1 29.4 28.6	0.27 0.18 0.22	15 9 23	31 <23 <23

From the test results of Table 3 we can see:

(1) It would have little impact adding less than 100ppm nanoscale-Al_2O_3-SiO_2 , the pellets could meet the technical requirements of impurities;

(2) With the increasing of the nanoscale-Al_2O_3-SiO_2 powder, the thermal stability is under control;

(3) The addition of nanoscale-Al_2O_3-SiO_2 should be higher than 25ppm to manufacture pellet that grain size is larger than 25μm. In the dry process, the addition of nanoscale-Al_2O_3-

SiO_2 should not be less 25ppm, the wet process should be higher than 25ppm,

(4) CJNF today's technology is fully able to manufacture large grain size fuel pellets meet the technical requirements.

The grain of large grain size pellet is shown in Figure 3, and the appearance of produced pellet is shown in Figure 4.

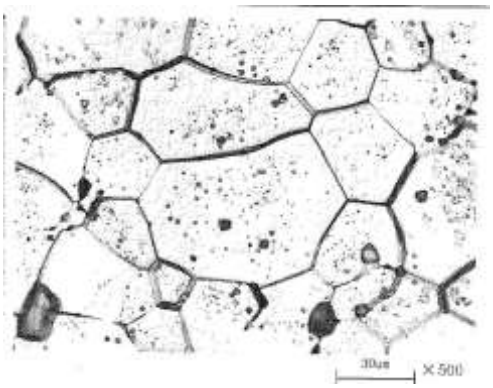

Figure 3. Grain

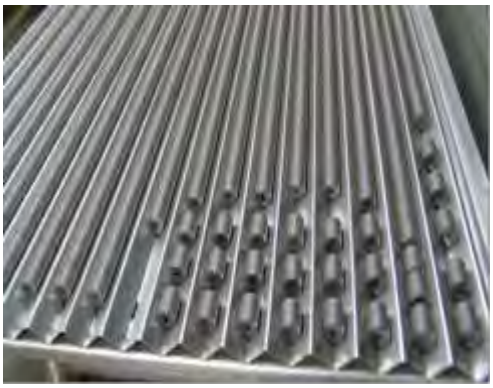

Figure 4. Appearance

5 Conclusions

（1） In SiO_2, Al_2O_3, U_3O_8 and ammonium oxalate these factors, the influence of the grain size, the largest was Al_2O_3.Under the same conditions, the dry process powder of grain size was larger than the wet process powder.

（2） When addition was less than 100ppm, with the increasing of the amount of Al_2O_3, the grain size increased, too.

（3） To prepare the pellet that grain size is larger than 25μm, the amount of nanoscale-Al_2O_3-SiO_2 powder should be higher than 25ppm in dry process powder, the addition in wet process powder should be higher than 50ppm.

（4） With the grain size increasing, the thermal stability was more and more stable. When the grain size reached 30μm or more, the thermal stability is close to zero.

（5） When addition of nanoscale-Al_2O_3-SiO_2 is within 100ppm, the pellets will meet the technical requirements of impurities;

（6） CJNF technology was fully able to make large grain size fuel pellets.

References

[1] S.A.YASHIN, et al. Development Of Technologies Of Nuclear Ceramic Grade Production, IAEA 2004.

[2] Guanren Zhu and Chengxin Liu, “The Manufacturing And Properties Of Japanese High Burn-up Pellet With Large Grain Size”. Nuclear Engineering And Technology. 1999,12(2).

[3] 08JTT1010/5. The technology requirement of large grain size pellets.

[4] JB/T 7510-94. optimization method - orthogonal test method.

POSITRON ANNIHILATION SPECTROSCOPY STUDY OF LATTICE DEFECTS IN NON-IRRADIATED DOPED AND UN-DOPED FUELS

M. CHOLLET, V. KRSJAK, C. COZZO, J. BERTSCH
Nuclear Energy and Safety Department, Paul Scherrer Institut
5232 Villigen PSI – Switzerland

ABSTRACT

Fission gas behavior within the fuel structure plays a major role in the safety of nuclear power plant in operation. Fission gas distribution and retention is determined by both, micro- and lattice-structure of the fuel matrix. The ADOPT (Advanced Doped Pellet Technology) fuel, containing chromium and aluminum additives, shows larger grain sizes than standard (undoped) UO_2 fuel, enhancing the fission gas retention properties of the matrix. However, the additions of such trivalent cations shall also induce defects in the lattice.
In this study, we investigated the microstructure of such doped fuels as well as a reference standard UO_2 by positron annihilation spectroscopy (PAS). Although this technique is particularly sensitive to lattice point defects in materials, a wider application in the UO_2 research is still missing.
The PAS-lifetime components were measured in the hotlab facility of PSI using a ^{22}Na source sandwiched between two 500-μm-thin sample discs. The values of lifetime at the center and the rim of both samples, examined to check at the radial homogeneity of the pellets, are not significantly different. The mean lifetimes were found to be longer in the ADOPT material, 220 ps, than in standard UO_2, 190 ps, which indicates a larger presence of additional defects, presumably generated by the dopants. While two-component decomposition (bulk + one defect component) could be performed for the standard material, only one lifetime component was found in the doped material. The absence of the bulk component in the ADOPT sample refers to a saturated positron trapping (i.e. all positrons are trapped at defects).
In order to associate a type of lattice defect to each PAS component, interpretation of the PAS experimental observations was conducted with respect to existing experimental and modeling studies. This work has shown the efficiency of PAS to detect lattice point defects in UO_2 produced by Cr and Al oxides. These additives create lattice irregularities, which are acting as sinks for fission products on one hand and trapping positrons on the other hand. Fitting of the obtained experimental data with a suitable theoretical model can provide a valuable qualitative assessment of these defects. At this stage of the research, some of the existing models were used for this purpose.

1. Introduction

It is well established that the addition of chosen dopants in UO_2 fuel, the most popular being Cr_2O_3, enlarges grain sizes contributing to a better fission gas retention and improves pellet-cladding interaction behavior [1]. While the oxidation state of Cr has been recently assessed to be +3 only [2], the mechanism of accommodation of such cation in the face centered cubic (*f.c.c.*) structure of the UO_2 is still not entirely understood: is Cr accommodated in substitution? Of oxygen? Uranium? In interstitials? In vacancies or clusters of vacancies already present in the lattice? Whatever the mechanism, dopants are likely to induce point defects. In this study, we have investigated the occurrence of such lattice defects by positron annihilation spectroscopy (PAS).

PAS is a powerful technique to probe defects and has already widely been used for nuclear structural materials [3,4]. However, the number of published work on UO_2 is shy. Even less papers have addressed the issue of radiation effects [5–9] and there is only one study on doped-material by PAS where dopants were actinides [10]. The present study focuses for the first time on PAS characterization of UO_2 fuel with a microstructure modified by dopants.

2. Experimental

The doped UO_2 ADOPT (Advanced Doped Pellet Technology) and conventional UO_2 Standard Optima2 (Std Opt2) fuels manufactured under similar conditions by Westinghouse (Västeras, Sweden) have been investigated in this study. Details of the fabrication process are given in Arborelius *et al*. [11]. Both initial powders were pressed into green pellets with a force of 50kN and then sintered in a H_2/CO_2 gas mixture at 1800 °C during 14 hours. Additives of Cr and Al are limited to 1000 ppm in the ADOPT material. The pellet densities are respectively 10.67 and 10.60 g/cm^3, corresponding to 97.3 and 96.7% of the theoretical values, showing the effect of additives.
For both materials, two thin slices of the pellets of 8.36 cm in diameter were cut and one face polished to obtain discs of 500 μm thickness.
We used the decay of ^{22}Na generating positrons as a source, described as following: $^{22}Na \rightarrow {}^{22}Ne + \beta^+ + \nu_e + \gamma$. This source of 3.7 MBq, obtained from an evaporated drop of aqueous solution containing ^{22}Na salt, has an effective diameter of 2 mm and is embedded between Kapton foils. Thanks to the small size of the source relative to the pellet slices, two separate measurements could be performed, both, in the center and at the rim of the pellets to investigate the radial homogeneity. The source is sandwiched between the two pieces of each sample and detectors are placed at each side of the set-up (Figure 1).
The positron lifetime measurements were performed using a conventional two-detector spectrometer with a resolution of 195 ps. Contribution of positrons annihilating within the source was determined by calibration measurements to have 20% intensity and 390 ps lifetime. A typical lifetime spectrum, as obtained for the both UO_2 materials, calibration Fe sample and calibration ^{60}Co source, can be seen in Figure 2.

3. Results

Analytical data processing was performed using the LT 9.0 program [12] and two-component decomposition of the spectra (bulk + defect component) according to the standard trapping model [13]. The lifetime spectra were fitted with a variance of fit (FV) ranging better than 1.06 (Table 1). In the case of the ADOPT sample, the bulk component could not be identified, which means that the positron trapping at defects reached its saturation (i.e. all positrons trapped). In this case the variance was slightly worse. All experimental data are listed in Table 1. Two different values (250 and 300 ps) fixed for the defect component have been selected based on the previously published studies [9,10] to examine scenarios with different types of defects.

Mean lifetimes are homogeneous at the center and the rim of the pellet at 190 and 220 ps for both materials ADOPT and Std Opt2, respectively. It means that the microstructure along the pellet radius is not affected by the production process from a point defect perspective. Both pellets are radially isotropic. Mean lifetimes were found to be higher in the ADOPT material than in Std Opt2, indicating a higher number of point defects in the doped material. This is highly probably the consequence of the incorporation of trivalent cations (Cr^{3+}) in the structure.

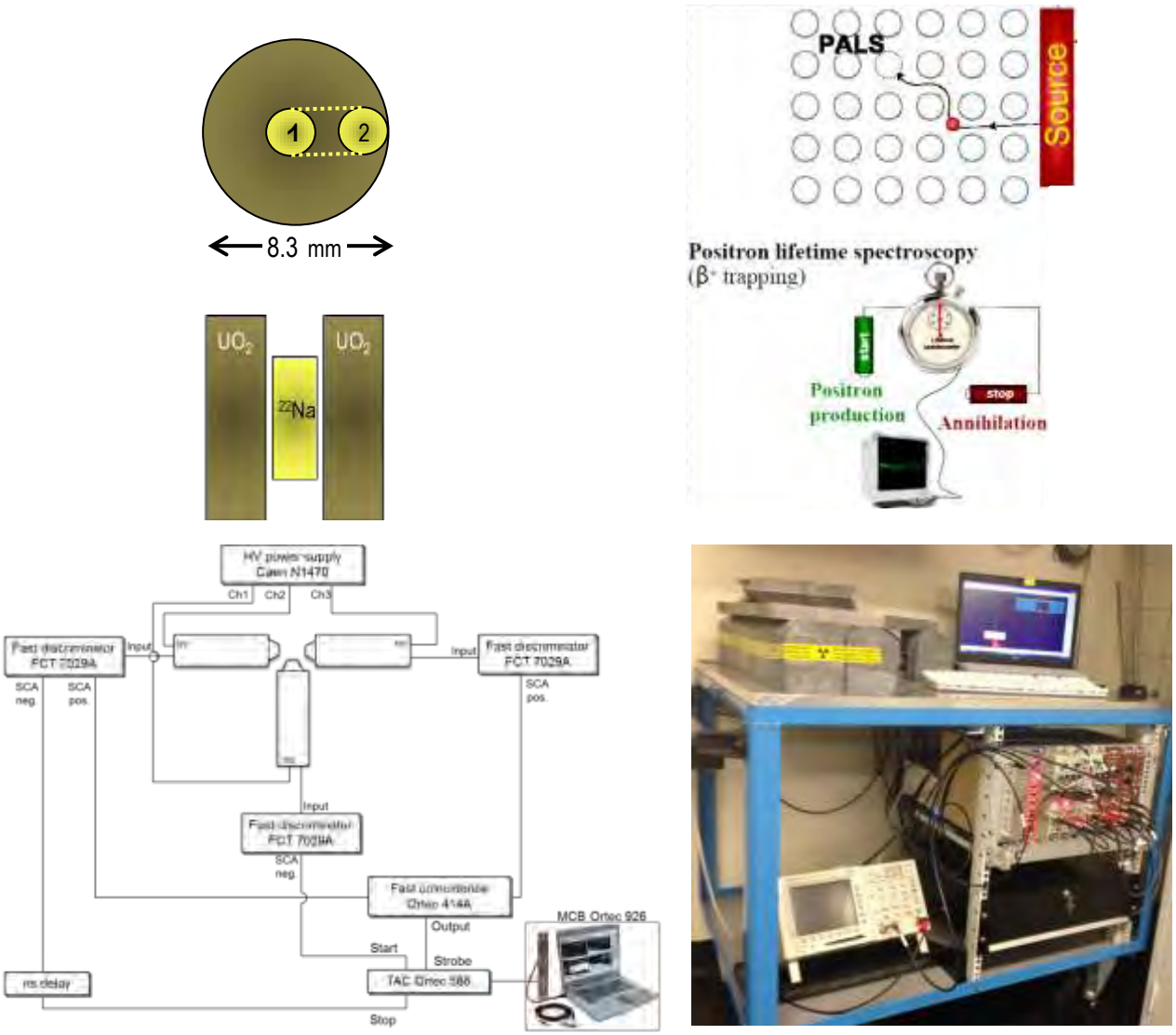

Figure 1: Schematic drawings of the experimental setup (top and bottom left) and picture of the positron lifetime spectrometer facility (right). In this case, the spectrometer was used in 2-detector mode [3].

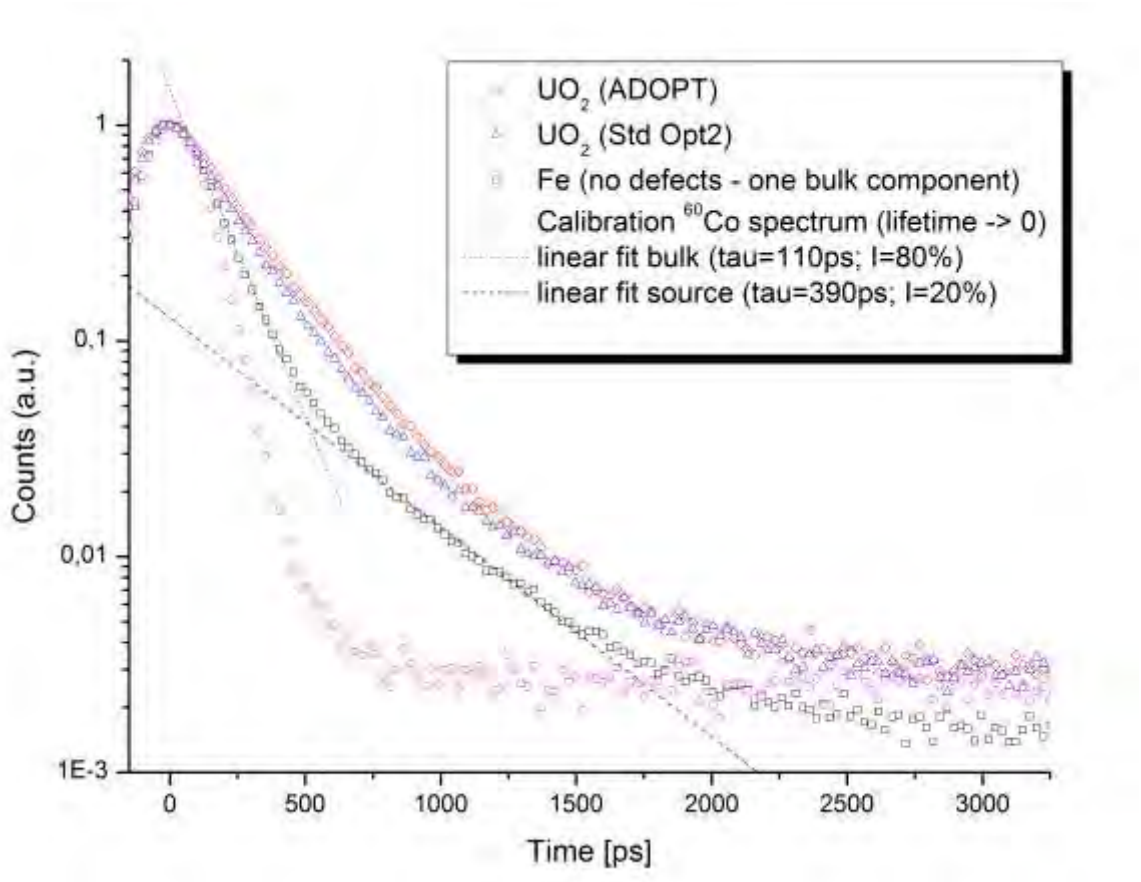

Figure 2: Positron lifetime spectrum of the two investigated UO_2 materials, defect-free Fe sample and calibration ^{60}Co source.

As mentioned above, the spectra have been decomposed into two lifetimes τ_1 and τ_2. Two lifetime components are generally reported for UO_2 [5,9,10]. Such decomposition enables to calculate the lattice lifetime τ_{bulk}. For the Std Opt2 sample, τ_{bulk} = 180 ps was obtained. The first measured component τ_1 of the Std Opt2 sample is by 10 ps slightly lower than τ_{bulk}, which is in agreement with the standard trapping model. This component could correspond either to a reassessment of a defect-free bulk or a mix of bulk and some shallow defects. In addition to this component, 15-33% of the positrons are trapped in defects with a life time of 250-300 ps. The nature of this trapping site will be discussed in the next section. Larger defect structures as clusters with higher lifetimes (e.g. porosity) are not observed in either of the samples.

In the ADOPT fuel, positrons are trapped at defects (saturated positron trapping). Table 1 shows also some proposed fits with a fixed τ_2 value at 250 or 300 ps. As can be seen, these fits result in a significantly reduced intensity of this component (as compared to the Std Opt2 sample) and suggest that such defects, if existent, are less attractive to positrons (so called shallow traps).

sample	mean τ (ps)	τ_1 (ps)	I_1 (%)	τ_2 (ps)	I_2 (%)	F.V.	τ_{bulk} (ps) calc.
Std Opt2 center	188	159	69.1	252	30.90	1.0315	179
	189	170	85.13	*300*	14.87	1.0318	182
Sdt Opt2 rim	189	158	66.3	*250*	33.70	1.0217	180
	191	171	84.78	*300*	15.22	1.0305	183
ADOPT center	218	218	100			1.0064	
	218	208	75.5	*250*	24.50	1.0045	
	218	213	94	*300*	6.00	1.0035	
ADOPT rim	221	221	100			1.0349	
	222	218	88.5	*250*	11.50	1.0673	
	221	220	98.29	*300*	1.71	1.0368	

Table1: mean lifetimes τ, first and second components τ_1 and τ_2 and their associated intensity I_i. Italic values of τ_2 indicate fixed parameters during the decomposition. Reduced chi squares F.V. are given for each fit. Bulk lifetimes were calculated from the experimentally measured data according to the standard trapping model [13].

4. Discussion – interpretation of the PAS components

The PAS signals of the standard and doped material are material-specific and indicate different microstructures. The few PAS-studies on UO_2 material limit to establish a straightforward identification of the nature of the positron-trapping sites. In this section, we compare and discuss the results in the perspective of the previous experimental and modelling studies [5,7,9,10]. It is worth noting that these three available valuable studies come from the same research group (CEA/CNRS, France). In particular, Wiktor *et al.* [9] have performed DFT + *U* calculations to obtain the positron lifetimes of uranium and oxygen vacancies in UO_2 as well as combination of vacancies (Shottky defect…). They did not consider interstitial defects in their calculations as they are expected to produce lower lifetimes than the bulk one, which is seldom observed in the experiments.

The value of the lattice τ_{bulk} of 180 ps compares well with the previous experimental values of 170-180 ps in Roudil *et al.* [10] and 169 ps in Barthe et al. ([5]. It is possible that our value is slightly enhanced by a polishing effect or others intrinsic defects as no annealing was performed prior to measurements. Roudil *et al.* noticed a reduction of the bulk component from 180 to 170 ps for increasing annealing temperature, showing hence the recovering and removal of the bulk defects in the materials.

As already evoked, the τ_1 at 170 ps component in the standard material is probably a mix of the bulk component lowered by oxygen interstitial which is the most stable interstitial defect in the structure.

The τ_2 component is higher than the mean value τ, indicating positron trapping at vacancy-type defects (e.g. [9]). Several interpretations are likely for this component, but there is a consensus

in the experimental studies [5,10] to attribute the annihilation time between 250 and 300 ps to a displacement of U atoms (U-vacancies). The test-fits for the PAS signal with these imposed and fixed values at 250 and 300 ps as τ_2 component give good results given the FV values (Table 1). However, the formation energy for a uranium vacancy is almost twice that of oxygen [14], and in the literature this kind of point defect was generally detected in irradiated/damaged UO_2 [5,10]. In our fresh non-irradiated sample, the mechanism of creation of such defects could again be polishing, as already proposed by Evans *et al*. [8]. On the other hand, this 2nd lifetime component τ_2 is only observed in the standard sample, whereas both standard and doped samples have been polished; thus it should have also been detectable in the doped sample. Other mechanisms of formation are likely (e.g. intergranular misfits). Nevertheless, one can notice that fits including a fixed τ_2 at 250 or 300 ps for the doped fuel data yield better or comparable variance of fit FV than those without τ_2 (Table 1), so that the possibility of the occurrence of such U-vacancies should not be excluded in the doped material either. Other types of vacancies could also correspond to this τ_2 component. Wiktor *et al*. determined that the well-stable Schottky defect (V_U + $2V_O$) (neutral charge) shows lifetimes varying between 301 and 316 ps depending of the lattice direction arrangement. Moreover, their energies of formation calculated by GGA + *U* at 4.2 eV are comparable to the one of oxygen vacancies [15], such that these defect clusters could also be considered for the τ_2 lifetime component.

The nature of the lifetime at 220 ps recorded for the doped material is more disconcerting than the other found in the standard sample, first because the trapping sites capture the totality of positrons up to saturation, second because this value was never reported in previous studies as a specific lifetime component. This component could be a signature of the defects created by the incorporation of additives in the UO_2 lattice. Indeed, Riglet-Martial *et al*. [2] have shown by X-ray absorption near edge structure (XANES) that the oxidation state of soluble Cr is 3+ only in UO_2, creating obvious charge defects. According to the experimental and calculation work of Cardinaels *et al*. [16], the most favorable site for Cr satisfying the observed variation of lattice parameter of doped UO_2 is the substitution of uranium combined with a bonding with a U^{+5} or one oxygen vacancy in neutral cluster. Oxygen vacancies, the most stable point defects in stoichiometric UO_2 [9], are formally expected to be positively charged, and should therefore in principle be invisible to PAS. However, Vathonne *et al.* [15] has shown by DFT + *U* method that V_O charged -2 could also be stable for Fermi levels lying close to the middle of the band gap, so that the presence and detection of this very-stable defect should not be absolutely excluded. In order to provide a solid interpretation of the experimental data, more theoretical calculations are needed. Recently, a collaboration with the Institute of Nuclear and Physical Engineering, Slovak University of Technology was established aiming to obtain an accurate theoretical interpretation.

5. Conclusion and perspectives

The PAS technique obviously highlights the microstructural particularity of doped *vs*. undoped UO_2. We identified the bulk lifetime at 180 ps in a quite good agreement with previous studies. A second component most probably corresponding to either U-vacancies or Schottky defects has been detected in the undoped material. In the ADOPT UO_2, the defects created by the addition of dopants lead to a strongly localized trapping site up to saturation. If the origin of this 220 ps component remains unclear, the PAS signal evidences the specific lattice particularities of this material. A modeling work using DFT + *U* approach is ongoing in order to support assumptions and interpretation of the PAS signal. First calculations on 4 x UO_2 supercell for U-vacancy result in a good accordance with the present interpretation. The effect of Cr^{+3} incorporation will be studied in larger supercell (32 x UO_2).
We believe this technique, up to now scarcely used for nuclear fuel, provides new valuable data on the UO_2 lattice-microstructure and can be used as a kind of quality assessment tool for fresh

fuel. This is of particular interest, as the doped fuel seemingly exhibits a structural contradiction, i.e. higher general density (i.e. less pores), but also a higher density of point defects. However, the one does not exclude the other; and the higher density is beneficial for the thermo-physical properties whereas the point defects are trapping sites for volatile fission products (i.e. fission gas) atoms. The point defects quantification is well accessible by PAS. Unfortunately, although the analysis of defects in irradiated fuel would be of utmost interest, today PAS can not be used for this case due to the strong activity of the fuel which affects the detector.

Acknowledgments

The authors are very grateful to the financial support of swissnuclear and Westinghouse for providing the samples. The authors also would like to acknowledge useful discussions with Eva Vitkovska and Peter Ballo from the Institute of Nuclear and Physical Engineering, Slovak University of Technology as well as with Claude Degueldre from PSI. Finally they deeply appreciate the sample preparation performed by Andrej Bullemer, PSI.

References

[1] L. Bourgeois, P. dehaudt, C. Lemaignan, A. Hammou, J. Nucl. Mater. 297 (2001) 313–326.

[2] C. Riglet-Martial, P. Martin, D. Testemale, C. Sabathier-Devals, G. Carlot, P. Matheron, X. Iltis, U. Pasquet, C. Valot, C. Delafoy, R. Largenton, J. Nucl. Mater. 447 (2014) 63–72.

[3] V. Krsjak, J. Kuriplach, T. Shen, V. Sabelova, K. Sato, Y. Dai, J. Nucl. Mater. 456 (2015) 382–388.

[4] V. Krsjak, V. Grafutin, O. Ilyukhina, R. Burcl, A. Ballesteros, P. Hähner, J. Nucl. Mater. 421 (2012) 97–103.

[5] M.-F. Barthe, H. Labrim, A. Gentils, P. Desgardin, C. Corbel, S. Esnouf, J.P. Piron, Phys. Status Solidi C 4 (2007) 3627–3632.

[6] N. Djourelov, B. Marchand, H. Marinov, N. Moncoffre, Y. Pipon, P. Nédélec, N. Toulhoat, D. Sillou, J. Nucl. Mater. 432 (2013) 287–293.

[7] H.E. Evans, J.H. Evans, P. Rice-Evans, D.L. Smith, C. Smith, J. Nucl. Mater. 199 (1992) 79–83.

[8] H. Labrim, M.-F. Barthe, P. Desgardin, T. Sauvage, G. Blondiaux, C. Corbel, J.P. Piron, Proc. Tenth Int. Workshop Slow Positron Beam Tech. Solids Surf. SLOPOS-10 Proc. Tenth Int. Workshop Slow 252 (2006) 3256–3261.

[9] J. Wiktor, E. Vathonne, M. Freyss, G. Jomard, M. Bertolus, MRS Proc. 1645 (2014).

[10] D. Roudil, M.F. Barthe, C. Jégou, A. Gavazzi, F. Vella, J. Nucl. Mater. 420 (2012) 63–68.

[11] J. Arborelius, K. Backman, l. Hallstadius, M. Limbäck, J. Nilsson, B. Rebensdorff, G. Zhou, K. Kitano, R. Löfström, G. Rönnberg, J. Nucl. Sci. Technol. 43 (2006) 967–976.

[12] J. Kansy, Nucl. Instrum. Methods Phys. Res. Sect. Accel. Spectrometers Detect. Assoc. Equip. 374 (1996) 235–244.

[13] A. Vehanen, P. Hautojärvi, J. Johansson, J. Yli-Kauppila, P. Moser, Phys. Rev. B 25 (1982) 762–780.

[14] B. Dorado, M. Freyss, B. Amadon, M. Bertolus, G. Jomard, P. Garcia, J. Phys. Condens. Matter 25 (2013) 333201.

[15] E. Vathonne, J. Wiktor, M. Freyss, G. Jomard, M. Bertolus, J. Phys. Condens. Matter 26 (2014) 325501.

[16] T. Cardinaels, K. Govers, B. Vos, S. Van den Berghe, M. Verwerft, L. de Tollenaere, G. Maier, C. Delafoy, J. Nucl. Mater. 424 (2012) 252–260.

Modelling of powder die compaction for press cycle optimization

J-P. Bayle [a]*, V. Reynaud [e], F. Gobin [a], C. Brenneis [a], E. Tronche [a], C. Ferry [a], V. Royet [a]

[a]CEA, DEN, DTEC, SDTC, 30207 Bagnols/Cèze, France
[e]Champalle company, 151 rue Ampère ZI Les Bruyères 01960 PERONNAS, France

* Corresponding author. Tel.: +33 4 66791890; Email address: jean-philippe.bayle@cea.fr (J-P. Bayle)

1. Abstract

A new electromechanical press for fuel pellet manufacturing was built last year in partnership between CEA-Marcoule and Champalle[Alcen]. This press was developed to shape pellets in a hot cell via remote handling. It has been qualified to show its robustness and to optimize the compaction cycle, thus obtaining a better sintered pellet profile and limiting damage. We will show you how 400 annular pellets have been products with good geometry's parameters, based on press settings management. This results are due to according good phenomenological pressing knowledge with Finite Element Modeling calculation. Therefore, during die pressing, a modification in the punch displacement sequence induces fluctuation in the axial distribution of frictional forces. The green pellet stress and density gradients are based on these frictional forces between powder and tool, and between grains in the powder, influencing the shape of the pellet after sintering. The pellet shape and diameter tolerances must be minimized to avoid the need for grinding operations. To find the best parameters for the press settings, which enable optimization, FEM calculations were used and different compaction models compared to give the best calculation/physical trial comparisons. These simulations were then used to predict the impact of different parameters when there is a change in the type of powder and the pellet size, or when the behavior of the press changes during the compaction time. In 2016, it is planned to set up the press in a glove box for UO_2 manufacturing qualification based on our simulation methodology, before actual hot cell trials in the future.

HIGHLIGHTS

- 10 tons electromechanical nuclear press for fuel manufacturing in hot cell,
- Modelling of powder die compaction,
- Compaction cycle optimization for net shape pellets,
- Cam-Clay, Drucker-Prager cap model, Net-shape

GRAPHICAL ABSTRACT

New nuclear press for fuel manufacturing

1. Introduction

The electronuclear closed fuel cycle chosen by France plans the reprocessing of spent fuel and will enable natural uranium resource saving, as well as a reduction in the volume of wastes and their toxicity compared with the choice of direct storage (once-through cycle). The nuclear waste from spent fuel is classified depending on its activity and half-life. The High Activity (HA) waste represents more than 95% of the total radioactivity of French nuclear waste. The liquid extraction process called PUREX enables the Minor Actinides (MAs) to be separated from the Fission Products (FP) in HA waste. The advanced management of the MAs is a goal for the transmutation envisaged in 4th generation reactors or in specially-dedicated reactors. Two approaches to MA transmutation in fast breeder reactors (FBRs) are envisaged, i.e. homogeneous and heterogeneous recycling. The heterogeneous mode consists in concentrating the MAs in special assemblies located in the periphery of the reactor core. The neutronic impact on the core limits the introduction of a higher quantity of MAs, restricted to 10 to 20%. Materials including Americium (Am) located around the reactor core can be of target type if the MA supports an inert matrix, or else part of a Minor Actinide Bearing Blanket (MABB) if the MAs are directly incorporated into fertile UO2 fuels.

2. Context

The manufacturing of fuel pellets incorporating minor actinides by remote handling in hot cells requires simple, effective operations and robust technologies. Rejects must be minimized, which is harder with higher and higher actinide concentrations. The process of pellet shaping is well known from the literature **[1]**, **[2], [3], [4]**. It is generally carried out by uniaxial cold compaction in die to obtain green pellets (rough pellets from the pressing) with a density about 65% of the theoretical density (th.d). This shaping is then followed by a sintering operation which enables the density to reach 95% of the th.d. At present, the pressing technology used in Atalante hot cells (Marcoule, France) is based on a manual process with a radial opening die, compared to the conventional process of a floating die where a downward movement of the die occurs, enabling the ejection of the pellet. Another process with a fixed die enables pellet ejection by the lower punch which pushes with a pressure support from the upper punch. Damages can be present after the ejection stage if the pressure from the two punches is not coordinated, and these are generally revealed during the sintering stage. They can be worsened by the radiological behavior of the pellet, depending on its composition, and by the manufacturing process. Different defect types occur for sintered pellets, in particular cracks, end-capping and spalling **[5]**. Cracks can form down the sides of pellets and be longitudinal or lateral, or happen in the ends and sometimes cause a lateral "dishing" in the top of the pellets. Spalling can be found on the sides or the ends. The green pellets can have defects which depend essentially on the level of support pressure during die ejection. Other sources of damage can also be identified in the process of powder shaping **[6]**. First, the introduction of secondary phases composed of hard inclusions or air pockets leads to an excessive relaxation during ejection, with spalling occurring on the pellets, and to different wear patterns on the internal walls of the die and thus to blocked pellet sliding and to shearing. Secondly, inappropriate press settings for compression level, pressing time, or punch accompanying pressure during ejection can cause damage.

The mechanical stress distribution within pellets during the ejection step influences the surface defects. The mechanical stress induced by the die can be high, in particular at the angle formed by the internal surface of the die when the compact is partially ejected. The stress concentrations are accentuated by springback, which corresponds to the volume expansion of the pellet by relaxation of stress during ejection. Some authors have used digital simulation to estimate the mechanical stresses in pellets during this step. Aydin&Briscoe **[1]** attempted to determine the residual stress distributions in cylindrical pellets. Their study showed that axial residual tensile stress appears at the extremities of the pellet from the axial stress relaxation stage in die (decompression in die). These stresses are due to the friction forces between the die and the pellet, which block the axial springback when the pressure is released. In their study, neither the pellet slide and release phase nor the interactions with the edge of the die were taken into account, as the radial walls of the die were artificially removed. Jonsen & Hagglad **[7]** took into account the compaction and the ejection with the real kinematics of ejection. The distribution of the residual stress consolidated by measurements of neutron diffraction show that the pellet edges are submitted to axial compression over a thin layer (200 - 400 μm), and the part below this layer undergoes traction over a thicker zone (600 μm). From these two studies, it is known that residual stresses after ejection are

strongly influenced by the tool shapes and kinematics of ejection. In this context, an ejection performed by a radial die opening is expected to be less damaging. Therefore, this mode of ejection was used for the manufacturing of the minor actinide fuel pellets considered in this study.

Another issue is that minor actinide fuel pellet grinding after sintering must be minimized in order to limit highly radioactive dust. Consequently, geometrical tolerance for the diameter needs to be rather wide, +/- 50 µm around nominal values (8-10 mm). Pellet geometrical dimension mastery is necessary in order to obtain "net shape" pellets. It is well known that the pressing stage is critical for the shape of the pellet after sintering. For instance, when uniaxial compaction is performed green densities decrease along the height of the compact from the extremity which was in contact with the moving punch. After sintering, the shrinkage follows the density gradient and a conical shaped pellet is formed. With two mobile punches, a double-conical (hourglass) shaped pellet is obtained. In die compression, the heterogeneous density is due to the friction forces between the powder and the wall of the die, as well as the friction between the grains of the powder **[1], [8]**. These friction effects have been extensively studied for perfectly cylindrical dies, but never investigated for a specially shaped die. More particularly, the diametrical profile of the die could be designed in order to counterbalance the effect of friction.

3. Objectives

The density gradients obtained in the compact depend on various parameters such as the tool quality, the powder behavior, the compaction cycles, the lubrication type, etc. Because the powders used for nuclear fuel manufacturing are precious, pellet damage must be minimized and a net-shaped pellet which does not require further grinding is necessary. The main objective of this study was to be able to anticipate the demanding manufacturing factors, which can influence the press settings before the production cycle, and then during the manufacturing, to be able to have the shortest possible response time to correct parameters to ensure finished products with stable quality. Consequently, the study firstly concerned the optimization of the fuel manufacturing cycles of an innovative nuclearized press for nuclear fuel manufacturing in a hostile and restricted environment. To meet this need, a capability study of the press is described, with on the first press regulation results in the inactive conditions of a mock-up. An annular geometry pellet with compulsory manufacturing tolerances is taken into account. From the results of the study, simulations are proposed on the basis of previous simulations where the model parameters of the compaction were characterized for various powders. We can thus act on the cycle compaction parameters of the press, on the model parameters of each powder, and on certain friction coefficients depending on the lubricant type.

4. Materials and methods

Powdered material was used in this study. Alumina powder is considered a reference because its behavior is known from the literature **[4]**, and it is widely used in the compaction field of the nuclear community.

4.1. Alumina powder (Al_2O_3_T195)

Alumina powder was used to guarantee the conformity of the measurement and calculation results which could be compared with those from unpublished works **[3]**. Furthermore, it will be used to carry out qualification trials for a new nuclearized press currently undergoing testing. The particles are spherical, 50 to 200 µm in diameter. These spheres in turn are composed of 1-10 µm grains **[9]**. Main characteristics of the several powders studied are summarized in ***Tab 1***:

Powder	Supplier	Morphology	Size (µm)	Filling density ($g.cm^{-3}$)	Theoretical density ($g.cm^{-3}$)	E_{Th} Theoretical Young's modulus (GPa)	ν_{Th} Theoretical Poisson's ratio
Al_2O_3	Ceraquest	Spherical	50-200	1.24	3.970	530	0.22

Tab 1: characteristics of Al_2O_3 powder.

4.2. New nuclear press description and characteristics

One of the fuel manufacturing processes originates in the conventional process of the powder metallurgy industry and enables pellet shaping in dies, followed by sintering. The shaping of the Minor Actinide Bearing Blanket (MABB) pellets is currently done manually in hot cells. Manufacturing Automation and a better control of the shaping parameters were tested during this study, in order to prepare the way for a new automatic nuclear press under a collaboration set up between the CEA and CHAMPALLE^{ALCEN}. The minimization of criticality risks is an important goal for MABB pellet manufacturing, and is the main reason why the press is being built to operate without oil, and is completely electromechanical. It is a uniaxial automatic mono-punch simple effect press, with a displacement-piloted die. Its capacity is 10 tons, the maximum height is limited to 1200 mm and the production rate is 1 to 5 cylindrical annular

pellets per minute. Installing the apparatus in an existing hot cell for nuclear fuel production required a modular design and simulation studies, which were carried out using 3D software to show the entry of all modules through the airlock. The objective was to validate the modular units' ability to be assembled, dismantled and maintained by remote handling techniques. The thirty separate units making up the press had to go through a 240 mm diameter air-lock to enter the hot cell. To be sure the remote handling scenarios were appropriate, virtual reality simulation studies were carried out, taking into account force feedback and inter-connectability between the different units. In parallel, different radiological software checked that the press components' radiological dimensioning would ensure radiation resistance during operation in a hostile environment. A mock-up simulating the future hot cell and equipped with the real remote handling systems has been built in the CEA/Marcoule HERA facility technological platform, in order to physically test press unit assembly by remote handling, and the apparatus operations. The press, adapted to nuclear conditions, is patented.

The device **[9]**, is a uniaxial mono-punch press, with a single compaction cycle. The upper punch and die are mobile at different velocities and the lower punch is fixed. The die is used for the ejection step with an upper punch pressure support. The hot cell press location imposed the use of an existing hot cell, without modifications or external motors being possible. A transfer of the module units through the 240 mm diameter of the Lacalhene Leaktight Transfer Double Door had to be carried out. To minimize the criticality impact, the use of hydrogenated liquids is not permitted in the hot cell.

This is the main reason why the choice was made of electric motors with transmission systems with a minimum gap, combining rotary and translatory mechanisms for the upper punch and the die. To decrease the height needed, the die motorization was placed to one side and the effort transmitted via a toggle joint to the die plate.

The press production rate is about 4 pellets per minute and its pressure capacity is 10 tons. The base structure has one lower plate. This plate is fixed to a circular rail built into the hot cell floor. The press can therefore be rotated in order to enable access to any of the five main parts as required. The first part includes the rigid frame of the press, consisting of the lower and upper plates connected by 4 guide columns. The plates support respectively the motors of the die and of the upper punch. The lower plate holds the fixed lower punch equipped with a displacement sensor. Between these two plates, the upper punch and the die plates (parts 2 and 3) slide up and down. Plate displacements are monitored by sensors, and the mobile upper punch is also fitted with a force sensor. The powder load system and displacement motor of the filling shoe are set up on the mobile die plate. The filling shoe is moved laterally by an electric motor and a rack system. The powder load system has a tippable powder transfer jar which can be completely connected using remote handling. The press was patented under a CEA and Champalle common patent **[9]**. The nuclear press have enabled the manufacturing of Al_2O_3 anular pellets with a 10 mm die diameter in CEA Marcoule mock-up. The AL_2O_3 powder was used, with a zinc stearate lubrication in the mass measured at 2%.

4.3. Optimization cycle background

The use of the press with slave die displacement (equivalent to a double effect cycle) can enable cycle optimization and operating, in order to reduce the difference between the minimum and maximum pellet diameters. An optimal operating cycle enabling uniform stress distribution throughout the pellet means making the applied and transmitted forces equivalent. The difference between these forces is called Δ. To influence Δ, several parameters were varied in the compaction cycle.

We shown in the previous study **[9]**, the evolution of the measurements of applied and transmitted forces as well as the displacements of the upper punch and the die depending on time during a force piloting. A batch of 3 pellets (1 to 3) was made for each set of parameters (serial 1 to 6), (ex: 308S=Serial 3, Number of pellet 08, S for sintered, letter G is for green pellet). The parameters varied were: die start force (kN), noted SF; the upper punch force slope, noted R, it is the time in seconds to pass from the force at the beginning of compression to the maximal force; the die stroke in mm, noted C, equal to the difference between the position of the height of the powder column and the position of the compression start point; the compaction speed of the die in mm/s, noted Vm. Constants are: the force at the beginning of compression is set (punch) at 2.5 kN; the compressive force (punch) is 46 kN; time to the compression plateau (punch) is 3 seconds; the decreasing slope (punch) is set at 2.5; the maintaining force (punch) at 0.2 kN; the position of the height of the cavity (die) at 25 mm; the extraction speed is set (die) at 9 mm/s.

The interest of using a pressing cycle enabling control of the stress gradients in order to master pellet geometry was mentioned previously. The use of the slave die displacement press (almost double effect) seems preferable to a double effect press, where both punches are mobile. This is because with a mobile die, pellet support pressure given by the upper punch is difficult to manage, which makes the process more complex. It has been shown that having both punches mobile can give the same pressure to both, and minimize and center the shrinkage in the middle of the pellet. With a mobile die, the results are equivalent and the risk of pellet damage during ejection is also minimized. In the sam study, we shown the evolution of the green and sintered pellet diameters depending on the height of the Al_2O_3 powder. The internal diameter of the die is equal to 10 mm. The pellet springback after ejection is often determined by law $\rho_{Out\_die} = a.\rho_{In\_die} + b$ **, [10]**.

The springback reduce the density gradient. This reduction depending on the evolution of the a parameter, high reduction corresponds to a low parameter a.

The radial pellet springback ($\phi_{Out\_die} - \phi_{Die}$) was 1 % under optimal settings for the Al2O3 powder.

The shrinkage after sintering is also often determined by the law $\phi_{S\,int\,ered}(z) = \phi_{Green}(z) - \Delta\delta$, **[10]**.

Where $\Delta\delta$ is the sintered diametral shrinkage. It was 10 % under optimal settings for the Al_2O_3 powder. The relationship for the average diameter and internal tolerances is shown below. We explained that The the springback and all shrinkages depending on the parameters of the pressing cycle and shown the picture of the green pellets manufactured at the top, and the same pellets after sintering at the bottom. Note that the pellet number is used to record the compaction direction of the pellet, and the side with a number is where the upper punch applied the force.

The average diameter is calculated with: $\phi_{Average} = (\phi_{Mini} + ((\phi_{Max} - \phi_{Min})/2)^{+/-(\phi_{Max}-\phi_{Min})/2}$

The compaction cycle settings for a given powder thus require an optimization of the press setting parameters. For the Al_2O_3 powder studied, in order to obtain a geometrical tolerance of +/-0.012 mm for a diameter sintered to 9.015 mm, the choice was made of a die start force of 3.5 kN, an increase slope for the upper punch of 5 seconds to increase from 3.5 to 46 kN, a die compression speed of 7 mm/s, a 25 mm die cavity depth, and a compression height of 19 mm which enables a green pellet height to be compacted to 11 mm. These optimal settings meant the best pellet quality was obtained, with a lubricant inside the powder and with a good flowing powder. We can see the bad result of single effect compaction (101, 102, 103) where the die velocity is equal to 0 and the high shrinkage where the stress is low (lower punch). Comparison between experiment and calculation results shows that a good volumetric expansion (springback) and an important difference concerning shrinkage results.
The results of the serial 3 have been used to calculate size of a new tool. The sintered input dimensions of the sintered pellet are given bellow by: Diameter = 8.45 +/-0 .09 mm, hole diameter = 2.2 mm and, height < 12 mm. We have used the same parameters of the press cycle than the serial 3. The die diameter was of 10.000 mm and the sintered pellet diameter was 9.015+/- 0.012 mm. The proportional law is possible for the small gap and the new calculate diameter is **9.370 mm** with the high tolerance fixed to +/- 0.005 mm. The needle diameter has been not changed. Two new tools have been built, one with needle and one without needle. We decided to shape 400 pellets with hole and 400 pellets without hole but only hole pellet results are presented in this study. Statistical study has been made like next chapter, the main goal is to determine the capability of the press depending on the tolerances given before.

5. Capability study

5.1. Trials

The capability of the machine is the ability of the apparatus to reach the required input performance. This takes into account the statistical process control and permits a measurement of whether the machine can respect the interval tolerances (defined by the top and bottom targets) given in the specifications.The apparatus concerned in this study is the nuclear press described in chapter **4.2** and the diameter of the pellet (with hole) is 8.45 +/-0. 09 mm. Altogether, 400 pellets were shaped with the regulation parameters given in ***Tab 2***.

Parameters	Symbol	Value	Unit
Die start force	**SF**	**3.5**	**kN**
Upper punch force slope	**R**	**5**	**s**
Die stroke	**C**	**6**	**mm**
Die compaction speed	**V_m**	**7**	**mm/s**

Tab 2: Regulation parameters of the cycle press

The ***Fig 1*** shows compaction cycle during 400 annular pellet production.

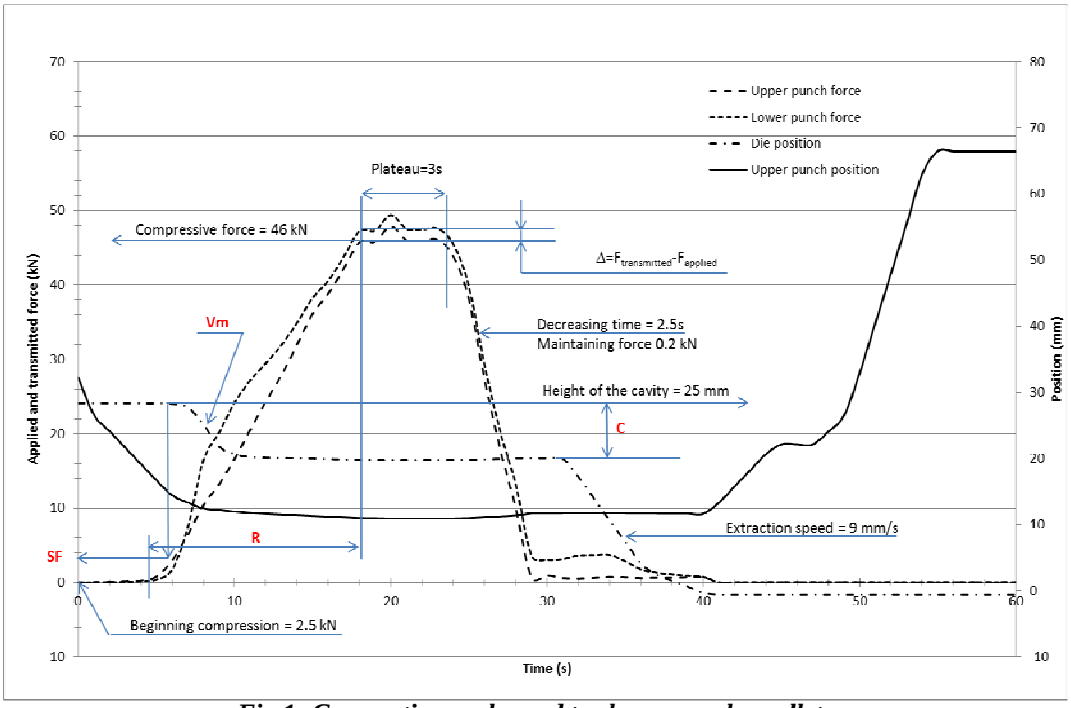

Fig 1: Compaction cycle used to shape annular pellets

The powder density depends on the position of the height of the cavity (**25 mm),** the die diameter (**9.370 mm**) and the weight of the pellet (**2.180 g**). The powder density calculated is about **1.26 g.cm^{-3}**. The volume of the powder necessary to make 400 pellets is **0.689 l** (1723.10^{-6} x 400). For information, the capacity of the jar is **0.751 l** and **0.374 l** between the jar and the die cavity. The pellets were shaped in continuous compaction, and a pathway system was built to keep the order and the direction of the pellet. This order was monitored to check the press variations (drift) and direction, and to see the side where the upper punch applied the force. All the compaction cycles were recorded in the press data base software. The pellets were put into glass tubes containing 37 pellets, see ***Fig 2***.

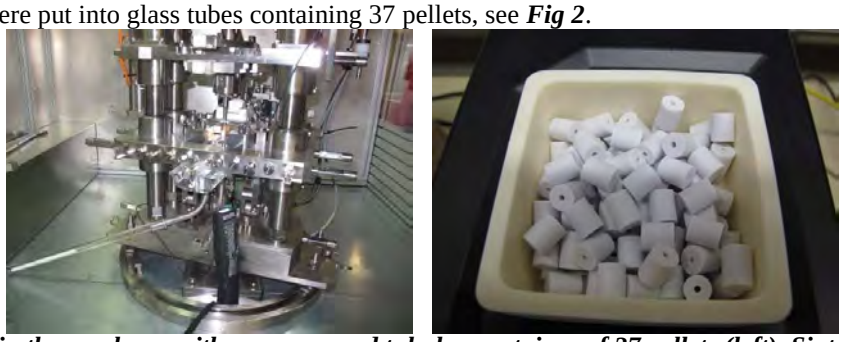

Fig 2: Press in the mock-up, with conveyor and tubular container of 37 pellets (left), Sintered pellets in the alumina container (100 pellets)

After compaction, each green pellet was measured by laser profilometer (height, and diameter corresponding to height) and weighed with precision scales. A chronological number was written on the side directly in contact with the upper punch. All the pellets (100 per batch) were then placed in an alumina crucible and sintered in a furnace under air. To record the pellet number, photos were taken before and after sintering. The written pellet number disappeared after sintering but the photos enabled the numbers of certain pellets to be remembered. The sintering conditions were 1600°C, with 4 °C/min for the heating up, for a duration set at 4 hours, followed by 2 °C/min for the cooling. The same measurements were carried out on pellets after sintering (height, diameter and weight).

5.2. Results

5.2.1. Annular pellets

Fig 3 shows the evolution of diameters as a function of pellet number. Diameters increase slowly after the middle of the production and are less regular than at the start of the production. After 194 pellets, pellet diameters are more random.

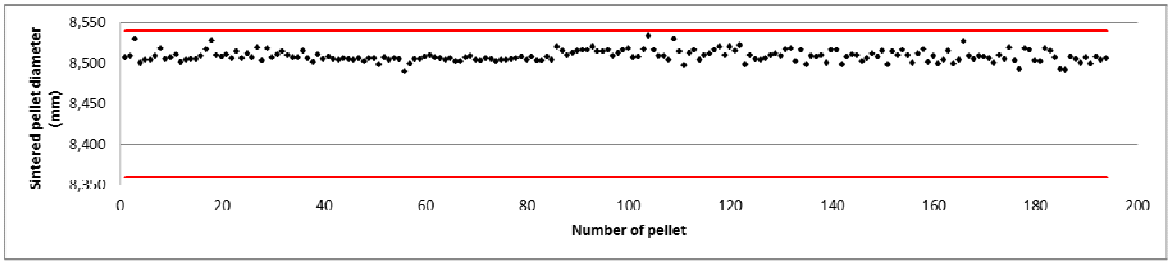

Fig 3: Sintered pellet diameter evolution as a function of pellet number

As shown in ***Tab 3***, the average diameter of the pellets is 8.510 mm, the maximum and minimum diameters are respectively 8.533 mm and 8.487 mm. The project objective was reached, but the diameter of the die must be reduced because the average diameter is still too high.

	Φ_{die} (mm)	$\Phi_{sintered}$ (mm)
trial number 308	10.000	9.015 +/-0.012
Objective		8.450 +/-0.090
Results	9.370 +/-0.005	8.510 +/-0.023

Tab 3: Comparison between objective and result diameter, compared to trial number 308

In ***Fig 4***, we have the evolution of the sintered pellet height as a function of pellet number. Like the previous result, the height increased after 194 pellets and the measurement is more random.

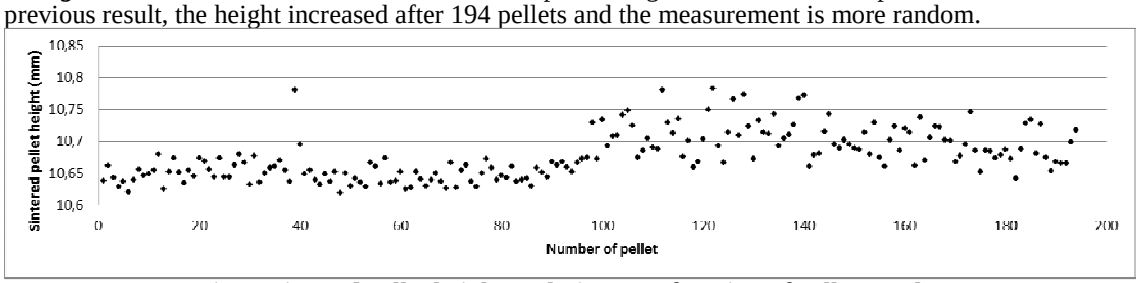

Fig 4: Sintered pellet height evolution as a function of pellet number

To confirm these results, ***Fig 5*** shows the evolution of weight as a function of pellet number. The random evolution after 194 pellets is the same, and is due to press behavior and not to the sensitivity of the sensor.

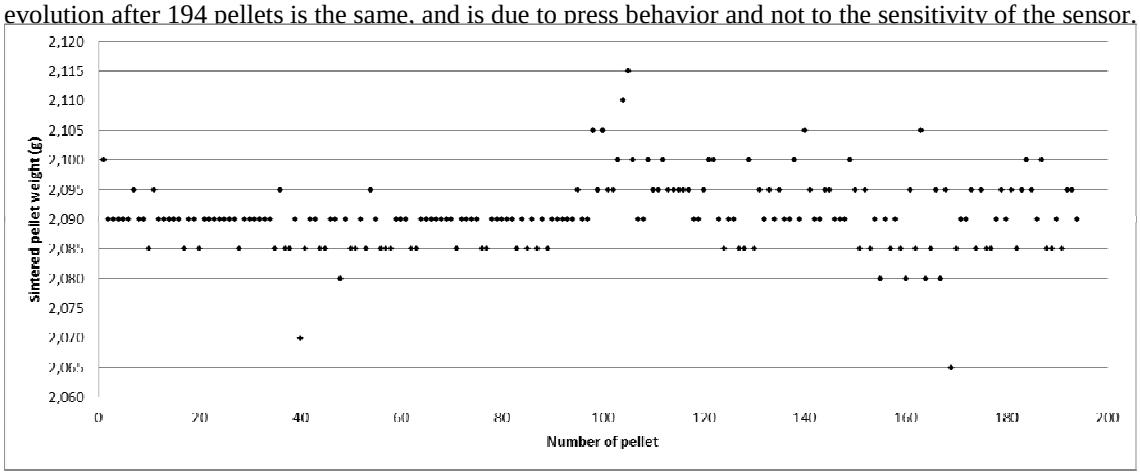

Fig 5: Sintered pellet weight evolution as a function of pellet number

The ***Fig 6*** shows the histogram of the sintered pellet diameters. We can see that the distribution is not centred and the asymmetric coefficient is 0.572. The average is 8.508 mm. The maximum is 8.533 and the minimum is 8.490. The standard deviation is 0.0068 and the variance is 4.75. 10^{-5}. The Alfa coefficient of the confidence gap is 0.05. The Cp capability process is 5.03. The performance process coefficients Pp and Ppk are respectively 4.35 and 1.52 and we must conclude that the process is very capable **[16]**.

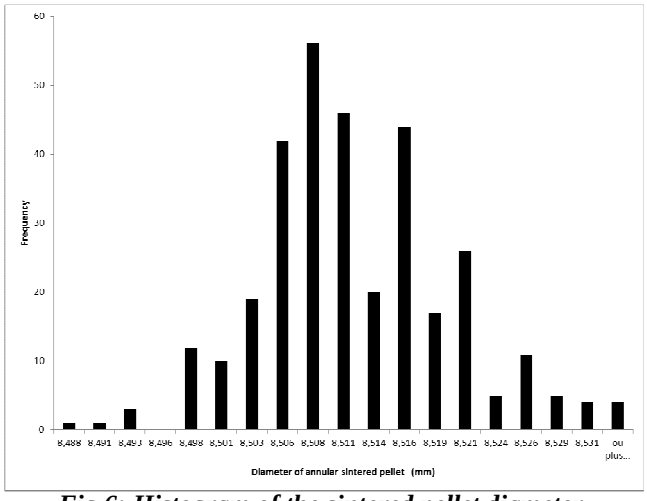

Fig 6: Histogram of the sintered pellet diameter.

6. Simulations

6.1. Geometrical model and meshing

The geometrical model is an axisymmetric 2D type. It is established based on the powder column, the die and the lower and upper punch. The upper punch and the die are mobile. A connector (equation between 2 nodes) was used to ensure the speed ratio between the upper punch and the die (punch with rigid connection for piloting via a reference node), as shown in ***Fig 7 (left)***:

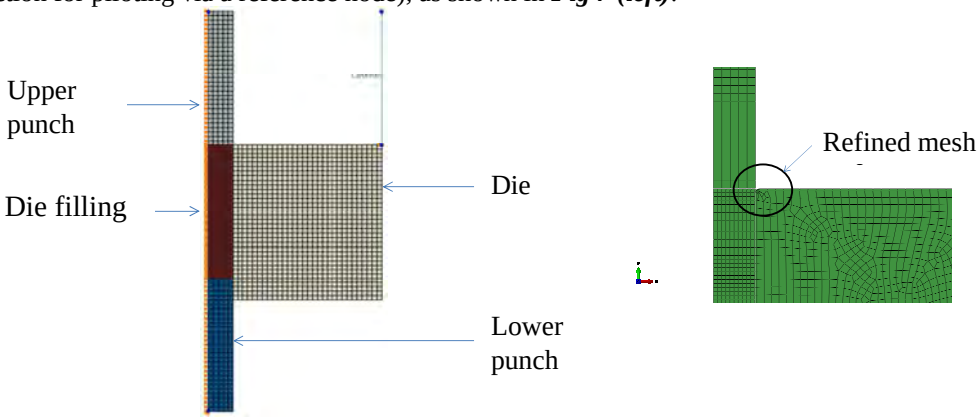

Fig 7: 2D geometrical axisymmetric model (left), Mesh tools (right); greatly improved mesh

The punch mesh is relatively large and uniform. That of the powder is also uniform, and a little finer. On the other hand, that of the die is much more refined, as shown in ***Fig 7 (right)***, in particular at the rounded corners in touch with the powder where the stress concentrations are situated, and where the generation of residual stress can be high during the pellet ejection springback. It is the sensitive point which must be handled carefully to avoid generating problems of convergence during the calculation.

6.2. Materials and Model

Two different models were taken into account, the Cam-Clay (CC) model **[2]**, **[9]**, **[18]** and the Drucker-Prager-Cap model (DPC) in the Finite Element Method (FEM) Abaqus® software **[2]**, **[17]**.

6.2.1. Cam-Clay model

Roscoe et al. **[11]** of Cambridge University first established general relationships of soil behavior based on the theory of elastoplasticity with strain hardening, in the field now described by Cam-Clay Models.

These models are based on four main elements: the study of isotropic compression tests, the concept of critical state, a force relation-dilatancy and the rule of normality for plastic strain. In the Cam-Clay Model, the elliptical load surface (plastic potential), in isodensity, is defined in the plan of invariants (P, Q) by the expression **(1)** :

(1) $$f(P,Q,\rho(\varepsilon_V^P)) = (Q/M(\rho))^2 + P(P-P_C) = 0$$

In this law, $P = (\sigma_{Applied} + \sigma_{Radial})/3$ is the hydrostatic stress. $Q = \left|\sigma_{Applied} - \sigma_{Radial}\right|$ is deviatoric stress. $M = f(\beta, \mu, \sigma_{Applied}, \sigma_{Transmitted}, \sigma_{Radial})$ is the internal powder friction coefficient, it characterizes the

critical state of the constraints and separates de-densification from densification. It depends on flow index β, friction coefficient μ, and applied, transmitted and radial stresses.
The pressure P_C represents the pellet's maximum allowable pressure before densification is activated (consolidation pressure). Its value depends on previous load states and mainly on the density. It follows a shape evolution law **(2)**:

(2) $$dP_c / P_c = k.d\rho / \rho \text{ , hence } P_C(\varepsilon_V^P) = P_0.e^{-(\frac{(1+e_0)}{Lambda-Kappa})\varepsilon_V^P}$$

where e_0 is the void ratio: $e_0 = (1-\rho_{ref})/\rho_{ref}$.

Kappa is the elastic contribution, Lambda the plastic contribution and ρ_{ref} is the reference relative density or non-packed relative initial density: $\rho_{ref} = \rho_{real} / \rho_{theo}$.

P_0 is the initial consolidation pressure and ε_V^P is the plastic volumetric strain.

The relationship between ε_V^P and ρ is : $\rho = \rho_0.e^{-\varepsilon_V^P}$ where ρ_0 is the initial density.

The plastic strain, or density, becomes the strain hardening variable of the model. It goes through the origin and is centered on the hydrostatic pressure axis.
The elastic and plastic modules, respectively Kappa and Lambda, are taken from isotropic (oedometric) compression tests. In these, the powder is compacted in a die and then changes in powder height H are drawn up as a function of the applied pressure P. Next, the void ratio is drawn up as a function of the P logarithm with: $e = n/(1-n)$, where $n = 1-\rho/\rho_{theo}$ is the powder porosity. The isotropic compression test results give curves e=f(ln σ) which can be considered as lines:

- A blank consolidation curve, called the Lambda curve, which describes the load during the test,
- An unloading-reloading curve, called the kappa curve, which describes the non-linear elastic behavior during the test.

The oedometric test is a normalized test stemming from the study of soil behaviors. It is the curve of loading-unloading, called the K curve, that describes the non-linear elastic behavior during the test. Reference **[9]** gives oedometric curves for the alumina powder at four pressures, 150, 300, 450 and 600 MPa. From the essential alumina material data, for example (ρ_{th}), and essential geometrical tool (d), it is possible to calculate the volume of powder loaded. For example for a mass of 0.410 g, a powder column height (h) of 13.82 mm and a diameter of 5.165 mm, V_0 289.73 mm^3 is found.
The filling density ρ was then calculated, followed by the n_0 porosity and by the void ratio e_0, **[9]**.
Two successive versions of the Cam-Clay Model were proposed. The original model enabled a qualitative description of the phenomena observed experimentally, but for paths close to the isotropic compression axis and for low constraint ratios, this model predicted overly-strong deviatoric strains ε_v^P. For that reason, the flow law or Constraint–dilatancy relationship was modified by Burland&Roscoe **[11]**. The load surface passed from a kernel shape to an ellipse for the modified model. According to **[15]**, other improvements were made to the modified model. To describe the cohesion of the pellet during traction or shear, the load surfaces were moved towards the negative mean pressures.
The porous elastic material law (not linear, isotropic) under Abaqus is expressed according to according to the Abaqus user manual. The hydrostatic stress evolves exponentially, with volumetric deformation **(3)**:

(3) $$p = -p_t^{el} + (p_0 + p_t^{el})\exp\left[\frac{1+e_0}{kappa}(1-\exp(\varepsilon_{vol}^{el}))\right], \text{ with } \frac{kappa}{(1+e_0)}\ln(\frac{p_0+p_t^{el}}{p+p_t^{el}}) = J^{el} - 1$$

where J^{el} -1is the volumetric nominal strain and $\varepsilon_{vol}^{el} = \ln(J^{el})$ is the volumetric elastic logarithmic strain. p_t^{el} is the elastic limit traction stress (= 0 in the case of Cam-Clay) and p_0 is the initial pressure when the œdometric test begins. There were not enough points on the elasticated part of the oedometric test, and therefore a position on the part where the elastic return takes place was chosen by making the hypothesis of linear return.
This is translated by a straight line to calculate the kappa=0.0675 parameter. A theoretical Poisson's ratio stemming from data information was also taken, i.e. ν=0.22.
For the strain hardening consideration, another representation is possible in Abaqus. We selected the points on the consolidation pressure evolution curve depending on the plastic volumetric strain, as shown in **[9]**.

The consolidation pressure is the relationship of the force on the pellet section, although strictly speaking it is equal to the geometric average of three stresses (axial, radial and circumferential).

For ε_{Vol}^{Pl} , it is a function of the $J_{plastic}$ natural logarithm. With $J_{total}=J_{elastic}*J_{plastic}$, knowing the J_{total} and $J_{elastic}$ expressions according to respectively **(4)** and **(5)**, it is possible to calculate the expression of $\varepsilon_{Vol}^{Pl} = \ln(J_{plastic})$:

(4) $$J_{elastic} = 1 + \frac{kappa}{1+e_0}\ln(\frac{p_0}{p})$$

(5) $$J_{total} = \frac{V}{V_0} = \frac{(V_0 + \Delta V)}{V_0} = 1 + \frac{\Delta V}{V_0} = 1 + \frac{\Delta H}{H_0}$$

Where *P is* the applied pressure, $\Delta H = H - H_0$

Finally, besides consolidation pressure points and volumetric plastic strain **[9]**, the code needs the stress ratio corresponding to the M parameter (guiding coefficient of the line passing through the summit of the load line (critical state) in the plan (P, Q)), for which an average value was taken according to the identification of the coefficients **[9]**, (for example M=1.7 for Al_2O_3), an initial value of the plastic strain ($\varepsilon_{Vol\,0}^{Pl}$ =1.10^{-5}). ϖ is a constant used to modify the shape of the load surface, see Abaqus® user manual. It was taken to be equal to 1 and is the ¥ calibration parameter which controls the load dependence of the 3rd stress invariant. It is generally between 0.8 and 1, and here it was made equal to 1.

On the other hand, the M module is considered as the critical state of the material, as in the previous study with Cast3M® **[9], [15], [18]**. We had taken ten M values depending on the density, but this possibility was not taken into account in the Abaqus code and will lead to a later improved version.

You can see in ***Tab 4***, the AL_2O_3 powder Cam-Clay model parameters in Abaqus® FEM Code.

Parameters	Type	Unit	Cam-Clay
m	Weight	g	0.410
ρth	Theoretical density	g/cm^3	3.9
d	Die diameter	mm	5.165
h	Powder column height	mm	13.82
V_0	Powder volume in die	mm^3	289.73
ρ	Powder density in die	g/cm^3	1.415
n_0	Porosity		0.637
e_0	Void ratio		1.756
p_t^{el}	Yield stress	MPa	0
p_0	Initial pressure	MPa	0.1
ν	Poisson's ratio		0.22
ε_{Vol_0}	Initial volumetric strain		1.10-5
β			1
K			1
M			1.7
Kappa	Elastic coefficient		0.067
$Pc = f(\varepsilon_{Vol}^{Pl})$	Consolidation pressure	MPa	**[9]**

Tab 4: The AL_2O_3 powder Cam-Clay model parameters in Abaqus® FEM Code

6.2.2. Drucker-Prager Cap model

The characteristics of the Modified Drucker-Prager/Cap model are:

- ✓ This model is intended to simulate the constitutive response of cohesive geological materials,
- ✓ It adds a "cap" yield surface to the linear Drucker-Prager model:
  - o To bind the model in hydrostatic compression,
  - o To help control volume dilatancy when the material yields in shear.
- ✓ The elastic response is followed by a non-recoverable response idealized as being plastic,
- ✓ The material is initially isotropic.

The yield behavior depends on the hydrostatic pressure. There are two distinct regions of behavior:

- ✓ On the failure surface, the material is perfectly plastic,
- ✓ On the cap yield surface it hardens and also stiffens,
- ✓ The hardening /softening behavior is a function of the volumetric plastic strain.

The yield behavior may be influenced by the magnitude of the intermediate principal stress. The inelastic behavior is generally accompanied by volume changes:

- ✓ On the failure surface, the material dilates,
- ✓ On the cap surface, it compacts,
- ✓ At the intersection of these surfaces, the material can yield indefinitely at constant shear stress without changing volume.

Under large stress reversals, the model provides reasonable material response on the cap region. However, on the failure surface region, the model is acceptable only for essential monotonic loading. The material properties can be temperature dependent.

To describe the model, the model can use linear elasticity or nonlinear porous elasticity. It used two main yield surface segments:

- ✓ A linearly pressure-dependent Drucker-Prager shear failure surface,
- ✓ A compression cap yield surface.

The Drucker-Prager failure surface itself is perfectly plastic (no hardening), but plastic flow on this surface produces an inelastic volume increase, which cause the cap to soften. The Drucker-Prager failure surface is:

(6) $$F_S = t - p\tan\beta - d = 0$$

Where β is the angle of friction, d is the cohesion of the material, t is the measurement of the deviatoric stress. This allows matching of different stress values in tension and compression in the deviatoric plane.
The cap yield surface is:

(7) $$F_C = \sqrt{(P - P_a)^2} + \left[Rt/(1+\alpha-\alpha/\cos\beta\right]^2 - R(d + P_a\tan\beta) = 0$$

Where R is a material parameter that controls the shape of the cap, α is a small number and $P_a(\varepsilon_{Vol}^{Pl})$ is an evolution parameter that represents the volumetric plastic strain driven hardening/softening. The Cap yield surface is elliptical with constant eccentricity in the meridional (p-t) plane. It includes dependence on the third stress invariant in the deviatoric plane and hardens or softens as a function of the volumetric plastic strain (volumetric plastic compaction causes hardening, volumetric plastic dilation causes softening). The hardening/softening law is a user-defined piecewise linear function relating the hydrostatic compression yield stress, P_b and the corresponding volumetric plastic strain ε_{Vol}^{Pl} . The volumetric plastic strain axis in the hardening curve has an arbitrary origin. $\varepsilon_{Vol}^{Pl}\Big|_0$ is the position on this axis corresponding to the state of the material when the analysis begins, thus defining the position of the cap (P_b) at the start of the analysis. The evolution parameter Pa is given as: $P_a = \dfrac{P_b - Rd}{(1+R\tan\beta)}$. The parameter a is a small number (typically 0.01 to 0.05) used to define a transition yield surface:

(8) $$F_t = \sqrt{((P - P_a)^2} + \left[t - (1-\alpha/Cos\beta)(d + P_a\tan\beta\right]^2 - \alpha(d + P_a\tan\beta) = 0$$

Thus the model provides a smooth intersection between the cap and the failure surfaces. A larger value of α can be used to construct a more complex (curved) failure surface.

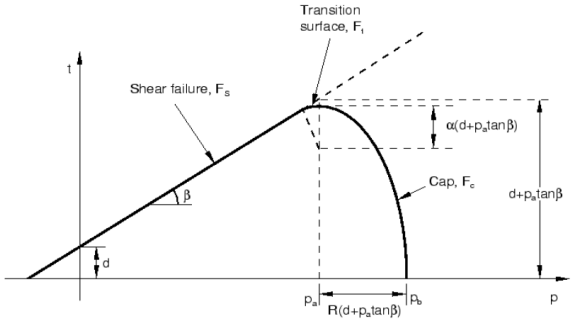

Fig 8: Drucker-Prager load surface

Tab 5 summarizes all Drucker-prager parameters uses in Abaqus® code for Al2O3 powder.

Parameters	Type	Drucker-Prager
d	Material cohesion	80
β	Angle of friction	60
R	Cap shape controller	0.5
Eps	Volumetric plastic strain	0.0001
α	Smaller number	0.1
K	Curvature	1
FV	-	0.6

Tab 5: Drucker-Prager model parameters in Abaqus® FEM Code for AL_2O_3 powders

6.3. Geometric model, meshing, loading and boundary conditions

During the simulation, the uniaxial simple effect cycle of shaping with a floating die is composed of a succession of discrete stages, each run in a succession of iterations. At the beginning of the calculation the die is considered to be full of powder, with the upper punch in contact with the powder. At this stage, there is the first step which consists in powder compaction with the upper punch at the speed of 14 mm/s while exercising a push with the die in the same direction as the upper punch but at a more moderate speed, i.e. 10 mm/s. The step is finished when a plateau of a few seconds is reached at 47 kN (600 MPa). The second step consists in pellet ejection by a vertical die withdrawal and the preservation of a support pressure fixed at 11 kN (150 MPa). During this stage pellet radial springback takes place. The third step consists in withdrawal of the upper punch and complete pellet freeing, when the pellet axial springback occurs. The final step involves the sintering process, and creates shrinkage depending on the density gradients generated during the shaping, see ***Fig 9***.

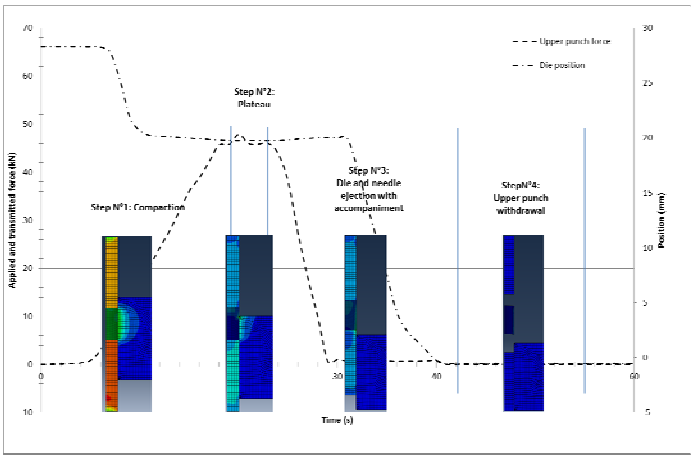

Fig 9: Von-Mises stress during each shaping cycle steps

6.4. Friction contact

For the press contact elements, the model used is based on the non-penetration of the two bodies in contact. Abaqus® uses the Lagrange multipliers method. The algorithm imposes the non-penetration condition on the resolution system by adding unknowns to the system. This greatly increases calculation time. The friction is defined as a Coulomb friction: $\sigma_f = \mu\sigma_r$, where σf is the residual stress of friction between the die and the powder which comes to oppose the die load, σr is the resultant radial stress of the powder on the matrix, and μ is the Coulomb's coefficient. The Coulomb coefficient taken into account in the calculation is equal to 0.094.

6.5. Sintering

As indicated in **[9]**, we used a simple sintering model based on thermal strain to one dimension $\alpha\Delta T = \varepsilon^{th}$, with $\alpha = (\rho_c / 95\%\rho_{th})^{1/3} - 1$. To summarize, for each meshing element of the powder, the green density ρ_c was calculated with the Cam-Clay model as well as the corresponding α coefficient. Next, the thermal dilation model of the green density map, the α coefficient map and a temperature level ($\Delta T = 1$) were entered. Shrinkage was thus calculated. A subroutine was developed in a Piton language in the Abaqus® code to take the sintering step into account.

7. Simulation results, comparisons and discussions

We observed convergence problems during the first calculations, because of the raw curve considerations stemming from the press data acquisition concerning the upper punch load evolution of force as well as the die and needle displacements. This problem was solved by separating compaction and accompaniment into several steps, so as to soften the slope changes.

Another problem of convergence comes from the Cam-Clay model itself, because it cannot represent a tensile stress (no section of the load surface corresponding to the negative hydrostatic pressures). There is thus a 10% failure of convergence in elastic return. Two solutions appeared: either to start again with the modified Cam-clay stemming from calculations carried out in a previous study under Cast3M® **[9]**, taking into account of c (cohesion in the model), or change model and take into account Drucker-Prager's cap model in which the cohesion is considered via the parameters d and β.

This is presented in ***Fig 10*** where we show the evolution of the pellet height depending on the diameter. The calculation converges better and a better model behavior is seen than for previous calculations, even if the parameters taken into account will need to be further identified. The final goal will be to ensure the calculation results a within the tolerance interval.

To better understand the results, the curves in ***Fig 10*** show different experimental and calculation results. The optimization and capability study conclusions are indicated. For each study, you have the green and sintered pellet diameters and the die diameters obtained by the application of the proportionality law (data shown in green for green pellets and red for sintered pellets). We can see the springback between the die and green pellet, as well as shrinkage between green and sintered pellets. Finally, the calculated green and sintered pellet diameters with Cam-Clay and with Drucker-Prager, used for an optimization study without hole and carried out with the Abaqus® software are shown. The calculation results show the model parameters must be optimized. Drucker-Pragger behavior is better than that of Cam-Clay, as the shape of the sintered pellet is conical. The model behavior at the base of the pellet does not suit the requirements. The height of the sintered pellet must be modified, and the sintered densities are weak. The sintering is too high and must be reduced.

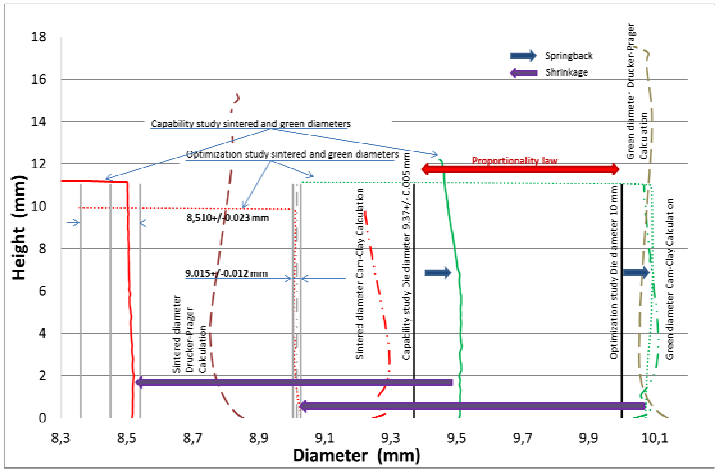

Fig 10: Comparison between optimization and capability studies, experimental and calculated results

8. Conclusions and Perspectives

The modelling of die powder compaction was studied for press cycle optimization. This optimization enables pellet density gradients and shrinkage after sintering to be minimized for better control of pellet tolerances and to avoid grinding pellets.

Based on the press optimization cycle results (optimization study) from a previous study **[9]**, we were able to minimize the density gradients in the pellet and so to minimize shrinkage after sintering and obtain an annular sintered pellet of 9.015 +/-0.012 mm for a die diameter of 10 mm.

Following thus, in the context of a new project to study cladding issues in fuel manufacturing for the Astrid reactor, we carried out a capability study with the nuclearized press to supply 400 annular pellets meeting the manufacturing constraints of 8.450 +/-0.090 mm for the sintered pellet diameter. The optimization study results were used for a new die sizing, implemented in the capability study by taking into account a simple proportionality law.

In the capability study, good quality results were obtained, with a sintered diameter of 8.510 +/-0.023 mm from a die diameter of 9.370 +/-0.005 mm. The press capability was shown to be satisfactory and no diameter and height drifts were found on the 400 pellets produced.

In parallel, a further objective was to be able to compare the experimental results with results from FEM simulations. This took into account the most realistic compaction model and the press cycles as load or displacement boundary conditions, in order to be as close as possible to experimental conditions. We noticed that the Abaqus® code used does not propose a Cam-Clay model with the cohesion consideration enabling a tensile stress to be represented. Rather than implementing this special feature in the initial model, we opted for a better adapted Drucker-Prager type model, for which the coefficient identification is currently being optimized.

In the future, a similar study is planned for the manufacturing of 400 full pellets (without needle holes) for the same cladding program, with a Drucker-Prager model parameter optimization.

Acknowledgements

We would like to thank the Simulia /Abaqus team for their support and in particular C.Geney. Our thanks also to Champalle and all the LTAP team.

References

[1] Aydin I, Briscoe J, Dimensional variation of die pressed ceramic green compacts, comparison of a FEM with experiment. Journal of the European Ceramic Society 17 (1997) p1201-1212.

[2] Brewin PR, Coube O, Doremus P, Tweed JH. Modelling of powder die compaction.

[3] Pizette P, Martin C.L, Delette G, Sornay P, Sans F, Compaction of aggregated ceramic powders: From contact laws to fracture and yield surfaces, Powder technology 198 (2010) 240-250.

[4] Pizette P., Martin C.L., Delette G., et al, Journal European ceramic society, vol.33 (2013) pp.975-984.

[5] Kerboul G, Etude de l'endommagement des produits céramiques crus par émission acoustique, Thèse INSA Lyon-1992.

[6] Zenger DD, Cai H, Handbook of the common cracks in green P/M compacts, Powder Metallurgy Reserch Center, WPI, 1997.

[7] Jonsen P, Haggblad A, Modelling and numerical investigation of the residual stress in a green metal powder body. Powder Technology 155 (2005) p196-208.

[8] Delette G, Sornay Ph, Blancher J. A Finite Element modelling of the pressing of nuclear oxide powders to predict the shape of LWR fuel pellet after die compaction and sintering, AIEA Technical Committee, Brussels, 20-24 October 2003.

[9] Bayle J-Ph et al, Minor actinide bearing blanket manufacturing press and associated material studies for compaction cycle optimization, NuMat 2014 Nuclear Materials conference, 27-30 October 2014, Clearwater Beach, Florida.

[10] Fourcade J, Etude de la mise en forme par pressage uni-axial des poudres de combustible nucleaire, Thèse UMII, 2002.

[11] Pavier E, Caractérisation du comportement d'une poudre de fer pour le procédé de compression en matrice, Thesis INPG/ENSHMG, 1998.

[12] Bonnefoy V, Modélisation du comportement de poudres métalliques et céramiques en compression, Thèse INPG/ENSHMG, 2001.

[13] Gillia O, Modélisation phénoménologique du comportement des matériaux frittants et simulation numérique du frittage industriel de carbure cementé et d'alumine. Thèse INPG, 2000.

[14] Alvain O., Caractérisation, modélisation et simulation numérique de la mise en forme de comprimés MOX par compression et frittage de poudres dures, thèse de doctorat, INPG.

[15] Dellis C et al., PRECAD, A Computer Assisted Design and Modelling Tool for Powder Precision Moulting, HIP'96 Proceeding of the international conference on Hot Isostatic Pressing, 20-22 May 96, Andover, Massachussetts, P75-78.

[16] Desnoyer F., Mémento sur la notion de capabilité, TI, ag1775.

[17] ABAQUS® User manual

[18] CAST3M® User manual

HIGH TEMPERATURE DECOMPOSITION OF URANIUM-BASED MIXED NITRIDES

V.G. BARANOV, A.V. LUNEV, V.V. MIKHALCHIK, A.V. TENISHEV, D.P. SHORNIKOV
National Research Nuclear University MEPhI (Moscow Engineering Physics Institute)
31, Kashirskoe shosse, 115409, Moscow, Russia

ABSTRACT

Specimen of uranium-based mixed nitrides were synthesized by high-temperature nitriding of metal powder composed of uranium and mischmetal. To investigate thermal stability, samples were annealed at 1800–2100 °C in a helium atmosphere. During these experiments, the effect of increasing the exposure temperature is studied. Raising the exposure temperature by 100 °C results in a multifold increase of mass loss. A comparison with data on pure uranium nitride shows that increasing the complexity of the nitride systems also results in higher mass loss. Later microscopic investigation of test samples revealed that metal precipitates may be found on the surface of test samples. Electron probe micro-analysis indicates these precipitates to be uranium metal. Hence, compared to pure uranium nitride, uranium-based mixed nitrides exhibit active evaporation at lower temperatures.

1. Introduction

Nuclear fuel based on mixed uranium-plutonium nitride has been considered as perspective for fast nuclear reactors with recycling fuel cycle. This is primarily due to high thermal conductivity, density and melting point of mixed nitrides compared to conventional MOX fuel. Nevertheless, there is a serious drawback in processing and usage of uranium-based nitrides at high temperatures – namely, thermal decomposition. This process hinders the sintering of pellets to a high density, also leading to dissociation and evaporation of plutonium at 1700–1900 °C. A detailed study of thermal decomposition in uranium-based mixed nitrides is required.

Conducting experiments with fuel containing plutonium and minor actinides requires special working conditions, i.e. gloveboxes with inert atmosphere. This circumstance greatly increases the complexity of research. At a certain point, one may consider using simulated fuel samples instead where active elements (Pu, Am, etc) are replaced by chemically identical simulators (Ce, La, *etc*.). This method was originally developed for oxide fuel and has proven to be very useful.

This paper aims to provide further information for the kinetics of thermal decomposition in uranium-based mixed nitrides.

2. Sample preparation

2.1. Green pellets of uranium mononitride

Powder of uranium mononitride (UN) was produced by nitridation of hydrogenated uranium metal. Cold pressing was performed then to obtain green pellets. Due to the reactive nature of the metal and nitride powders, all materials were handled and stored in argon-filled gloveboxes, which provided an inert atmosphere. Microstructural investigation of uranium

mononitride samples was performed with scanning electron microscope JEOL-6610LV equipped with EDS and WDS for X-ray microanalysis.
Fig. 1. shows the microstructure of the uranium nitride green pellets with open porosity channels. The structure shows no cracks. Powder size is about 100–500 nm.

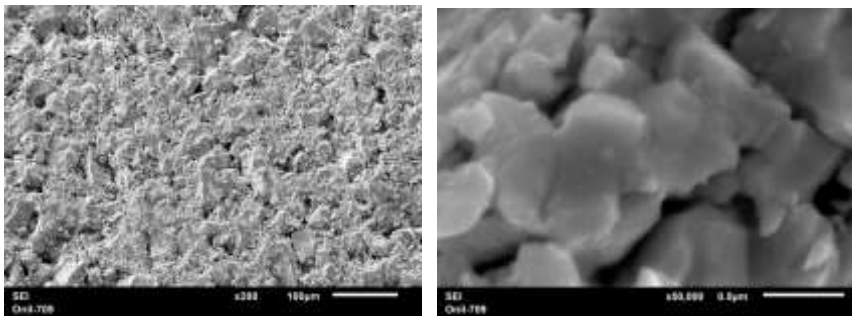

Fig. 1. Microstructure of uranium mononitride green pellets prior to high-temperature tests

2.2. Green pellets of uranium-based mixed nitride

For tests at 1500–2100 °C plutonium mononitride (PuN) may be replaced by yttrium and neodymium mononitrides (YN and NdN) which provide similar nitrogen vapor pressure (Table 1). Thus, YN, NdN and Ce have been selected as simulators for PuN.
Fission products are simulated by Nd, Ce, Mo, Zr, Ba, La, Sr, Y, Pr, Ru. To simplify the alloying procedure, Nd, Ce, La, Pr, and Y were substituted with an equivalent 10 and 20 wt. % amount of mischmetal (Mm). MmN was produced by hydrogenation of mischmetal prior to nitridation. The product was then mechanically admixed to uranium mononitride powder. The composition of green pellets formed from this powder roughly corresponds to spent nuclear fuel with a burn-up of 100 and 200 GWd/tU respectively.

Table 1. Nitrogen partial pressure over nitrides of different metals

	$lgPN_2$,Pa		
T, °C	PuN	YN	NdN
1500	-1.140	-1.380	-0.820
1600	-0.470	-0.640	-0.180
1800	0.660	0.620	0.920
2000	1.580	1.650	1.810

3. Thermal stability tests

3.1. Uranium mononitride samples

Tests using Netzsch STA 449 F1 apparatus with QMS 403 C quadruple mass-spectrometer were performed to determine the threshold temperature of thermal decomposition in uranium nitride samples (temperature range: 1800-2300 °C) Measurements were conducted in high purity helium (6.0 grade) with flow rate of 100 ml/min. Additional helium refinement to <1 ppb was performed using heated catalytic MonoTorr_filter on the basis of metallic getter. Open tungsten crucibles were used with thermogravimetry holders. The following parameters were monitored during the STA test: sample mass change, or thermogravimetry; the rate of sample mass change or the derivative of mass change with respect to time or differential thermogravimetry and the time (*t*) dependence of sample's temperature (T).
Optimal mass for thermogravimetry measurements was determined to be 100–150 mg [1]. Samples with larger mass would intensely interact with the crucible, while lighter samples would contribute to additional measuring errors.
The samples were subjected to annealing at 2000°C (initial mass 116.54 mg) and 2100°C (initial mass 139.96 mg and 142.7 mg) (Fig. 2.). The measurements were conducted in

thermal stability mode. In this mode, the exposure occurs as long as the sample doesn't lose a predetermined mass. The samples exposed at 2100 °C for 35 min lost 2% of their weight.

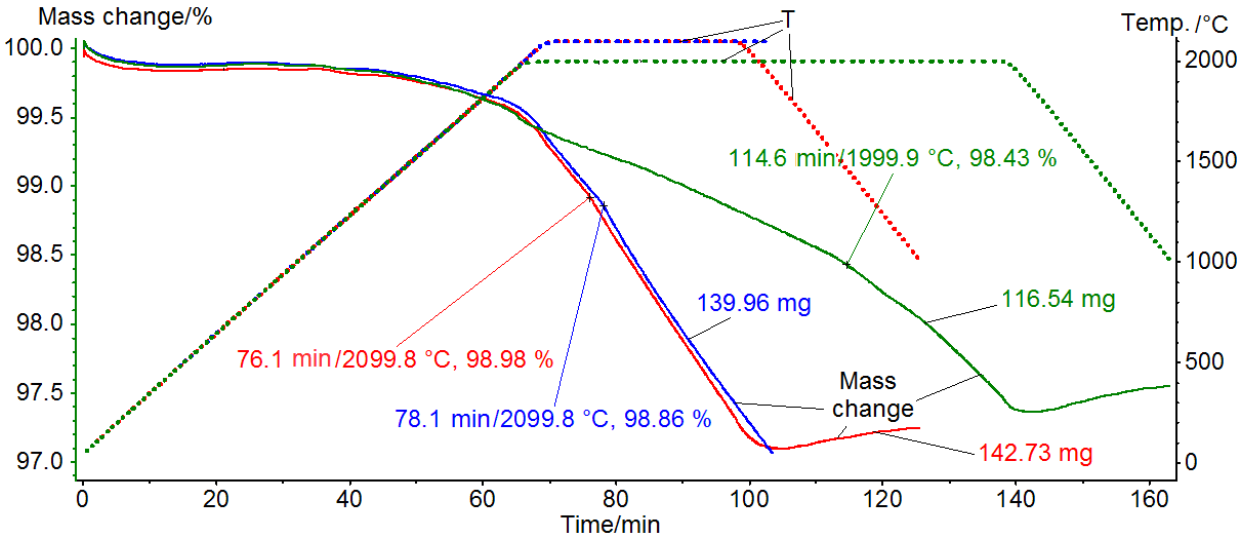

Fig. 2. Dependence of mass change on temperature and isothermal exposure duration for uranium nitride samples

The samples are seen to start losing weight already at the stage of heating at temperatures between 1500°C and 1700°C. After the isotherm is reached, weight loss happens in two stages. First stage consists in increasing the average rate of weight loss (DTG) up to ≈0.06 %/min (Fig. 3.). At half-way of isothermal exposure duration, the rate of weight loss gradually increases up to ≈100 μg/min (≈0.08 %/min). At first stage prior to the acceleration of weight loss, the mass of the samples decreased by approximately 1 mg. The total weight loss of both samples is about 2.8 mg, which is 1.9% of the total weight for each of the samples. At 2100°C increasing the average rate of weight loss begins after 10 min exposure, at 2000°C – after 50 min.

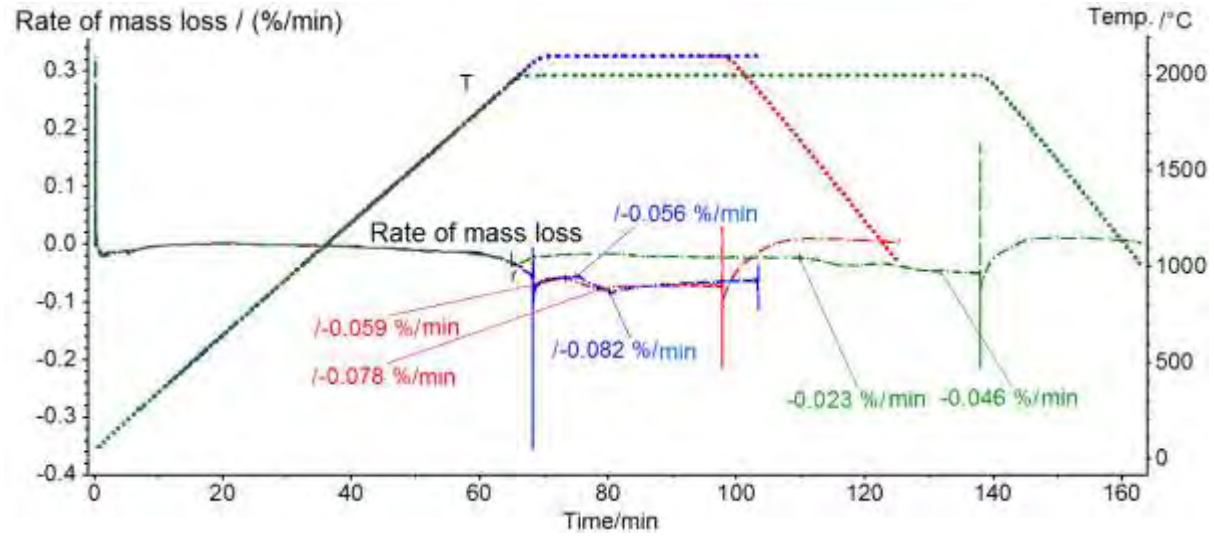

Fig. 3. Dependence rate of mass loss for uranium mononitride samples on temperature and duration of isothermal exposure

After thermal stability tests, UN samples were additionally studied using scanning electron microscopy (Fig. 4). Electron probe micro-analysis (Fig. 5) showed that uranium-rich precipitates were formed. The size of precipitates varied from 0.1 to 6.0 μm. Decreasing exposure temperature from 2100 °C to 2000 °C resulted in lower precipitate sizes.

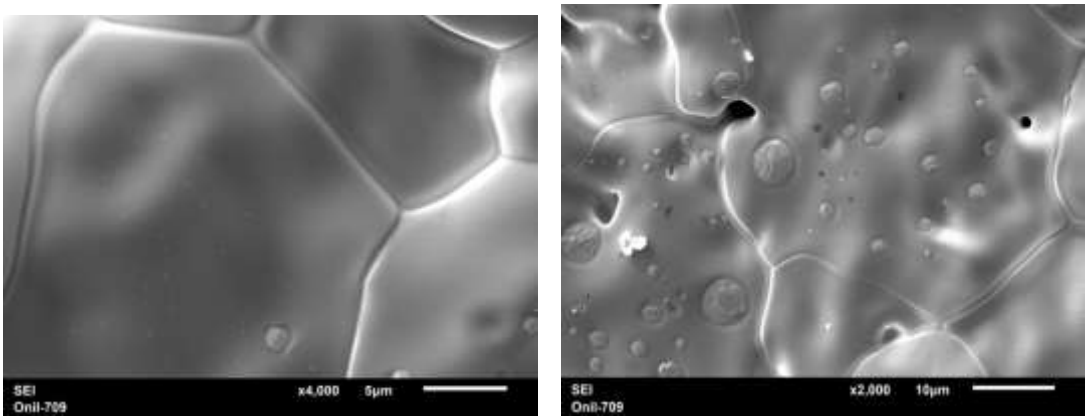

Fig. 4. Microstructure of uranium mononitride sample exposed at 2100 °C: grain size ~30-35 μm, spherical pores as large as 5 μm in diameter, irregularly shaped pores larger than 12 μm

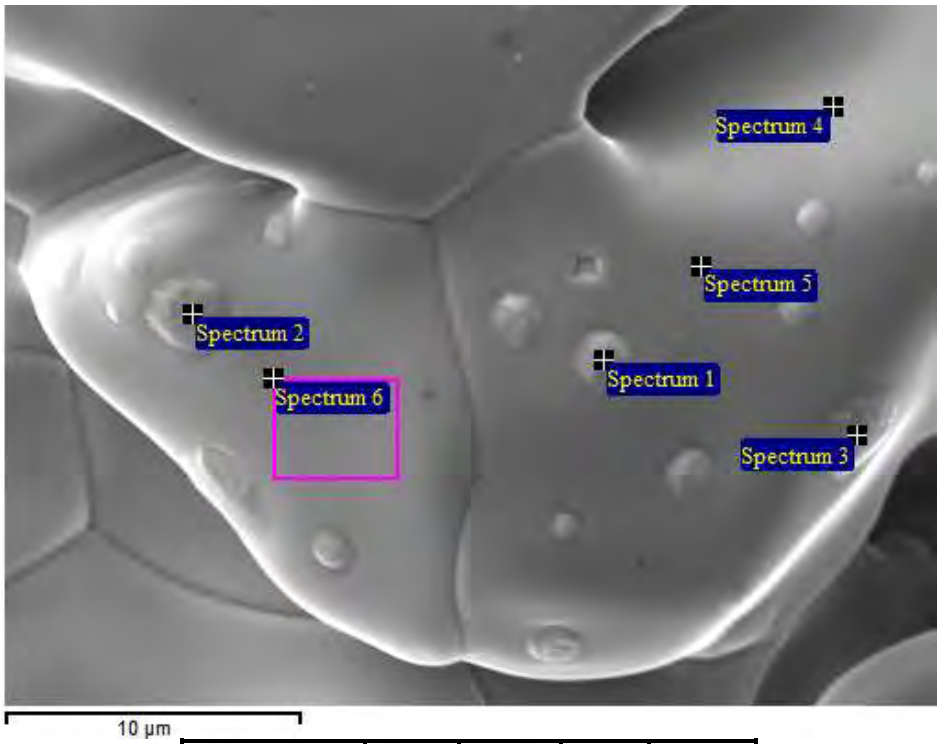

Spectrum	N	O	W	U
1		1.29		98.71
2			1.48	98.52
3	1.28	1.47		97.25
4	5.32			94.68
5	4.05			95.95
6	5.03			94.97

Fig. 5. Electron probe micro-analysis of UN sample after tests at 2100 °C. Data presented in wt. %

Summing up facts mentioned above, the second stage of mass loss may be explained (i.e. severe increase in rate of mass loss during exposure at high temperature – see Fig. 6). Evaporation of uranium mononitride leads to nitrogen depletion: the N/U ratio of uranium mononitride gradually decreases, and dissociation begins when composition reaches equilibrium at given temperature and partial pressure of nitrogen in the gas atmosphere which then leads to precipitation of uranium metal. The precipitated phase remains in liquid

state, since test temperature exceeds the melting temperature of uranium dioxide. Moreover, vapor pressure of uranium is large enough to initiate its evaporation and yet increases the rate of weight loss.
The precipitated phase was distributed evenly over the non-restrained surface of the sample. However, no precipitates were found on sample's surface which was in contact with the crucible during tests. Evidently, the crucible restrained access of helium to the surface of the sample in these areas. This resulted in a higher partial pressure of nitrogen over this surface and stabilized UN.
The other sample was subjected to annealing at 1800 °C. Fig. 6. shows that sample did not lose mass after exposure. Two likely explanations are provided:
- The measurements were conducted in high purity helium. However, an amount of oxygen less than 100 ppb is always present in He. This is sufficient to form UO_2 on the surface. Thus, constant compensation happens: nitrogen is reduced, and oxygen replaces it.
- High partial pressure of nitrogen may prevent decomposition, and mass loss does not occur.

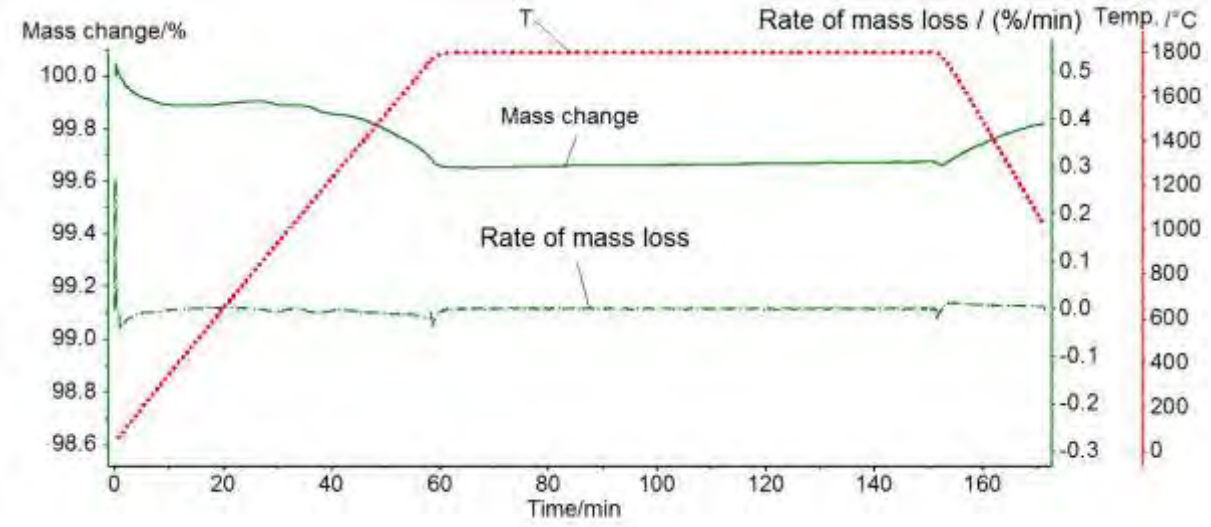

Fig. 6. Dependence of mass change, rate of mass loss on time and temperature for samples exposed at 1800 °C

3.2. Uranium-based mixed nitride samples

Mass loss due to evaporation begin at temperatures above 1480°C in (U,Mm)N samples. Comparing to uranium mononitride, the rate of mass loss is significantly increased in mixed nitrides: 0.08 wt.%/min for UN, 0.45 wt.%/min for UN+10 wt.% MmN, amd 0.51 wt.%/min for UN+20 wt.%MmN (Fig. 7.). During isothermal exposure, the maximum rate of mass loss is about 20% lower. Acceleration of evaporation, nevertheless, does not lead to dissociation.

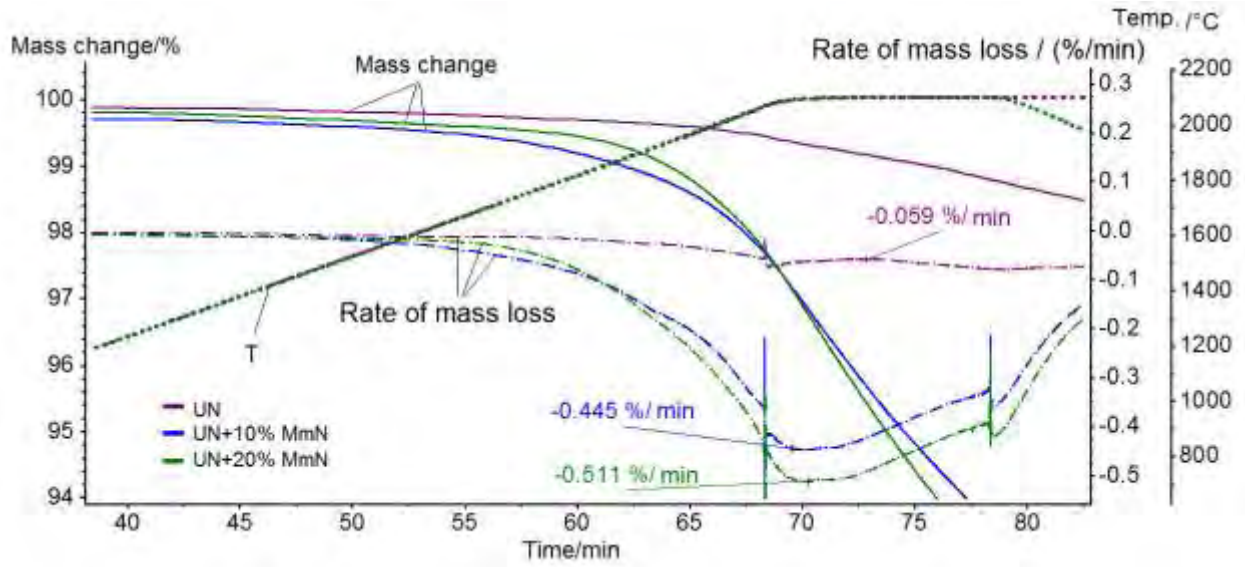

Fig. 7. Dependence of mass loss (TG), rate of weight loss (DTG) for samples on temperature and duration of isothermal exposure: 1 – UN; 2 – UN+10% MmN; 3 – UN+20% MmN

The resulting microstructure of (U,Mm)N after tests is shown on Fig. 8. The distribution of elements in both samples is similar. Ce, La and Nd were evenly distributed along the examined surface.

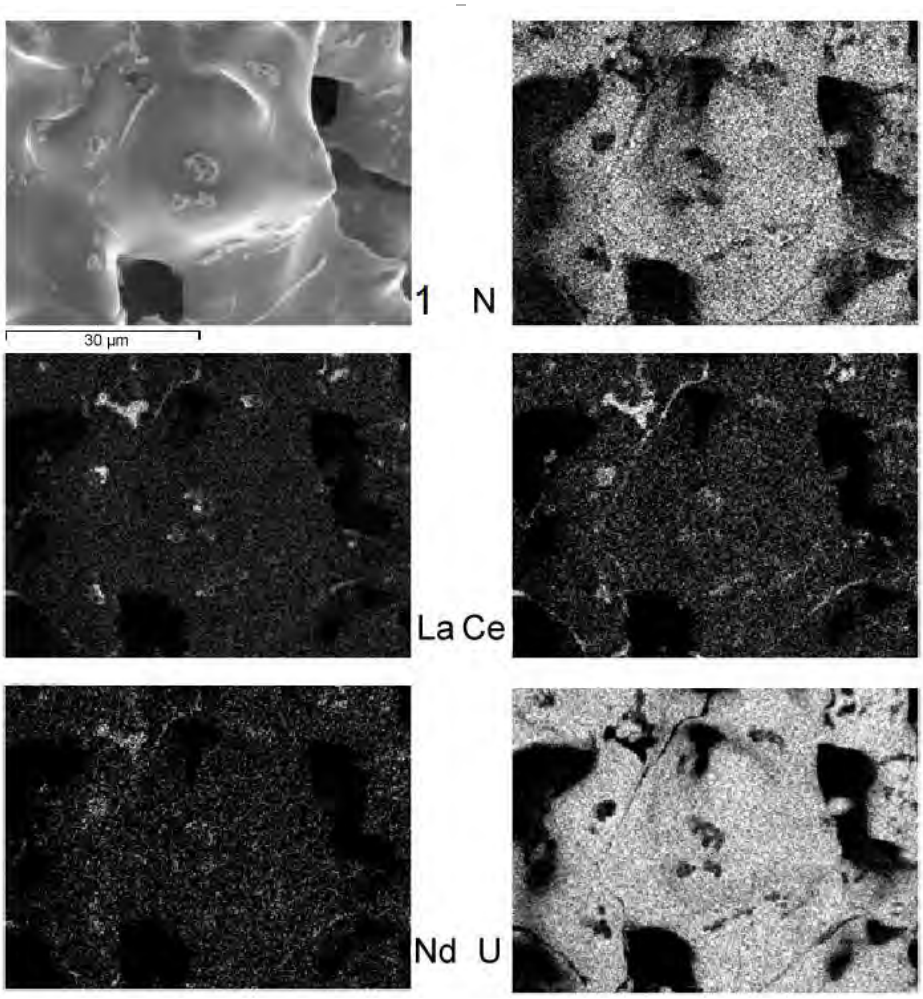

Fig. 8. EPMA maps in UN+20 wt.% Mm samples: 1 – general micrograph

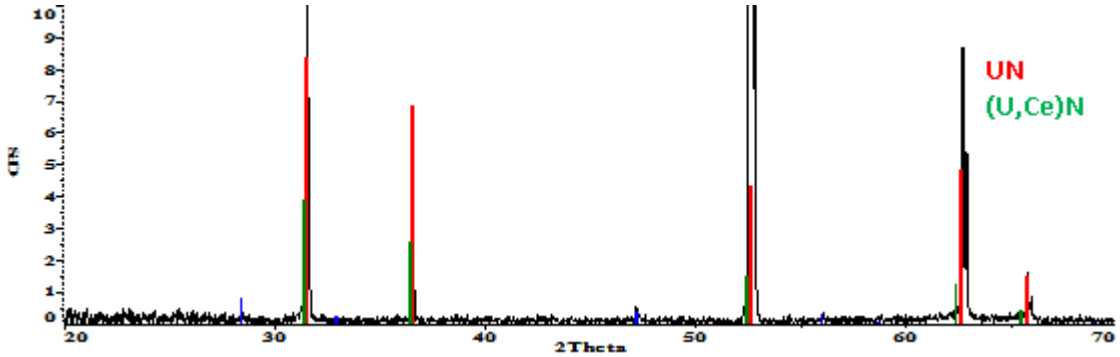

Fig. 9. X-ray pattern of UN+20 wt.% Mm sample

X-Ray analysis showed that lines are split in two: UN and (U,Me)N meaning that MmN dissolved in UN (Fig. 9.). Precipitates of MmN were not observed.

4. Conclusion

This study addressed one of the key problems with using mixed uranium-based nitrides in closed nuclear fuel cycle: namely the influence of minor actinides and fission products on high-temperature sintering of recycled green pellets. Thermal stability tests conducted both with pure uranium nitride (UN) samples and simfuel samples containing 10-20 wt.% mischmetal (Mm) show that samples with complex chemical composition are sufficiently less stable than pure UN. For samples with 10-20 wt. % Mm dissociation temperature drops by 200-300°C. Therefore, it is extremely important to carefully choose the high-temperature processing mode for this fuel so dissociation can be prevented. Both fission products and minor actinides will hinder the performance of mixed nitride fuel. Further work is needed, possibly aimed at selecting proper additives which could increase the dissociation temperature of mixed uranium-based nitrides.

References

1. Mikhalchik V.V., Tenishev A.V., Baranov V.G., Kuzmin R.S. High Temperature Uranium Nitride Decomposition// Advanced Materials Research/ Vol. 1040 (2014) pp 47-52

CAP1400 FUEL ASSEMBLY SELF-RELIANT DEVELOPMENT PROGRESS IN CHINA

Libing Zhu, Jie Ding, Fujun Gan, Qifeng Zeng, Yang Ding, Yixiong Zheng, Junqiang Lu, Yunqing Zhou, Qin Zhou, Jiazheng Liu

Shanghai Nuclear Engineering Research & Design Institute
No.29 Hongcao road, 200233, Shanghai, China

As a result of CAP1400 R&D project in China, the main purpose of CAP1400 fuel assembly development program is to meet the needs of self-sufficient fuel supply to CAP1400 reactor. In 2010 the CAP1400 fuel assembly development program including new zirconium alloy development, fuel assembly mechanical design, fuel assembly and components out-of-pile tests, CHF and TDC tests, irradiation tests in both test reactor and commercial reactor was launched in China.

By now two types of new zirconium alloys have finished composition selection and out-of pile performance tests. A long term test reactor irradiation program will be launched in 2016. Through series of fuel assembly components performance tests, both grid and nozzle will finish design finalization by the end of this year. All of the fuel assembly mechanical and hydraulic tests, TDC and CHF tests will be finished by the end of 2018. A three-cycle LTA program is planned to launch in CAP1400 first core. After transition core analysis and commercial application licensing, the CAP1400 fuel assembly is anticipated to provide adequate burnup capability and operation reliability to CAP1400 reactor in China.

KEY WORDS：CAP1400 Fuel Assembly Development, New Zirconium Alloy Development, UO_2 Pellet Development, Grid Development, Nozzle Development, Fuel Assembly Out-of-pile Tests, TDC and CHF Tests Program, Test Reactor Irradiation and PIE Program, LTA Program in CAP1400 Reactor.

1 Introduction

In 1990s SNERDI developed the first generation of PWR fuel assembly FA300 (as shown in Fig 1-1) for Qinshan Phase one nuclear power plant which is a 300MWe PWR in China. With constantly design improvements over the following 10 years, three types of FA300 fuel assemblies have been developed with max fuel assembly average burnup reach 40000 MWd/tU as shown in Table 1-1, and successfully used in 300MWe PWRs. By now over 1050 fuel assemblies of FA300 series have been successfully operated in three different 300MWe PWRs with satisfied operation reliability. Based on FA300 fuel assembly self-reliant development experience, the CAP1400 fuel assembly development program was launched in 2010. The CAP1400 fuel assembly mechanical design burnup aims at 60000 MWd/tU and through test reactor and commercial PWRs irradiation, the CAP1400 Fuel Assembly is expected to provide adequate performance and reliability at the target burnup, thus meeting the needs of self-sufficient fuel supply to CAP1400 reactors in China.

This paper will mainly describe the overall CAP1400 fuel assembly development program including self-developed zirconium alloy development, UO_2 pellet, SAF Grid, SAFAR and

CARBON Nozzle development, Out-of-pile Test Equipment construction and fuel assembly and components performance tests, TDC and CHF tests, Test Reactor Irradiation and PIE, LTA program in CAP1400 reactor, and the present progress of CAP1400 fuel assembly development will also be introduced.

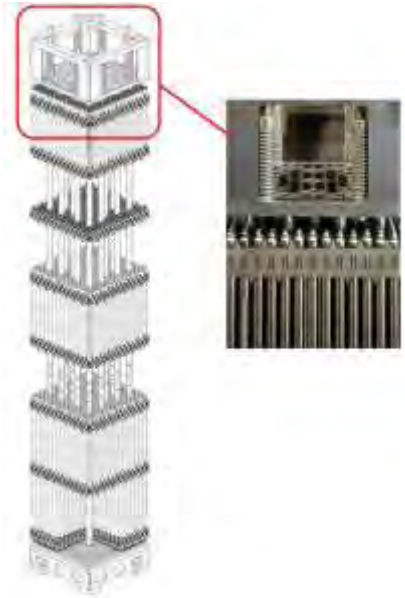

Fig 1-1: FA300 fuel assembly illustration

Table 1-1: FA300 fuel assembly series

	FA300-1	FA300-2	FA300-3
First use time	1991	1999	2003
Main Design Features	1) Zr-4 Tube 2)SS guide thimble 3) Inconel Grid	1) Low tin Zr-4 Clad	1) Anti-debris Bottom Nozzle 2) Chamfered pellets
Batch Average Burnup	25000 MWd/tU	30000 MWd/tU	33000 MWd/tU
Max FA Average Burnup	30000 MWd/tU	36000 MWd/tU	40000 MWd/tU

2 CAP1400 Fuel Assembly Design Feature

As shown in Fig 2-1, CAP1400 fuel assembly design incorporates Self-developed Zirconium Alloy (SZA) fuel rod cladding and guide thimble to improve cladding corrosion resistance performance and reduce fuel assembly irradiation creep and growth, hollow pellets to improve the pellet thermal performance, 2 Inconel End Grids to provide EOL fuel rod holding force, 10 SZA grids (8 SAF Mid Grids and 4 SAF Flow Mixers) aiming to improve the grid thermal performance and reduce fuel rod flow-induce vibration fretting, SAFAR and CARBON reconstruction nozzles as the end fitting components. All of the above design features aim to provide adequate fuel robustness and reliability at the target burnup (CAP1400 fuel assembly mechanical design burnup is expected to reach 60000 MWd/tU).

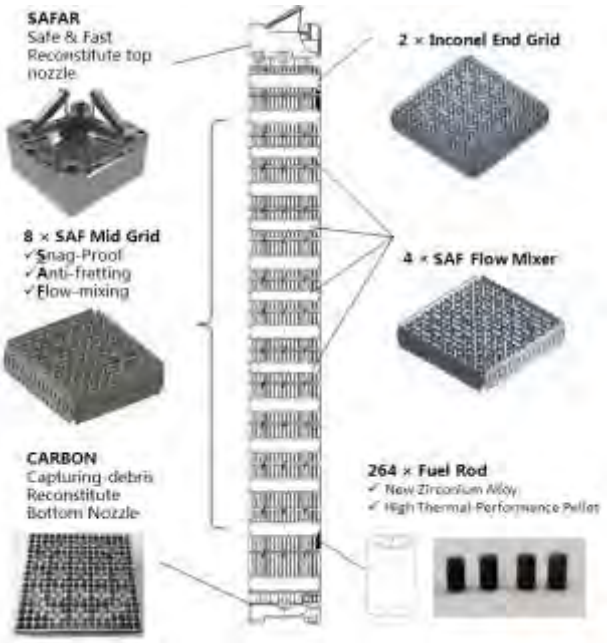

Fig 2-1: CAP1400 fuel assembly structural layout

3 CAP1400 Fuel Assembly Development Progress

3.1 New Zirconium Alloy Development

In order to match the high fuel duty in CAP1400 reactor and the target design burnup, SZA-4 (Zr-(0.1~0.4)Nb-(0.6~1.0)Sn-Fe-Cr-Ge), SZA-6 (Zr-(0.2~0.6)Nb-(0.3~0.7)Sn-Fe-Si) have been selected out of more than 40 of promising candidates by series of out-of-pile tests including long-term corrosion tests, mechanical tests, thermal creep tests and etc. There are three different stages for CAP1400 new zirconium alloys development: composition screening tests in the button ingot stage, composition and manufacturing process screening tests in the small ingot stage, finalized manufacturing process research and out-of-pile performance tests in the industrial ingot stage.

In the button ingot stage, more than 40 alloys with identical manufacturing process were corroded in autoclave with three different water chemistry conditions in two labs. Based on the test results, several model alloys with good corrosion resistance were obtained. In the small ingot stage, the composition and manufacturing process screening tests of different model alloys were done. Several different rolling processes and heat treatments were conducted to study the effects on corrosion resistance of different model alloys. Microstructure analysis, grain structure analysis, uniaxial tensile tests, autoclave corrosion tests and hydrogen pickup measurements were used to study the relationship among heat treatment, microstructure and properties such as corrosion resistance, mechanical property and hydrogen uptake. Autoclave test results showed that rolling processes had little or no effect on corrosion resistance of different model alloys, but heat treatments had a large effect on it. Therefore the critical factor to improve the corrosion resistance of zirconium alloys was to set down reasonable heat treatments. SZA-4 and SZA-6 show good corrosion resistance in different water chemistry conditions. From the present results, the uniaxial tensile properties of SZA-4 and SZA-6 using traditional manufacturing process were equal to Zr-4 alloy. Hydrogen concentration in both two alloys matched design expectation. In the industrial ingot stage, SZA-4 and SZA-6 using different final annealing temperatures show good corrosion resistance, Zr-4 is also tested as reference alloy. Fig 3-1 shows the corrosion weight curves of different alloys in different water chemistry conditions.

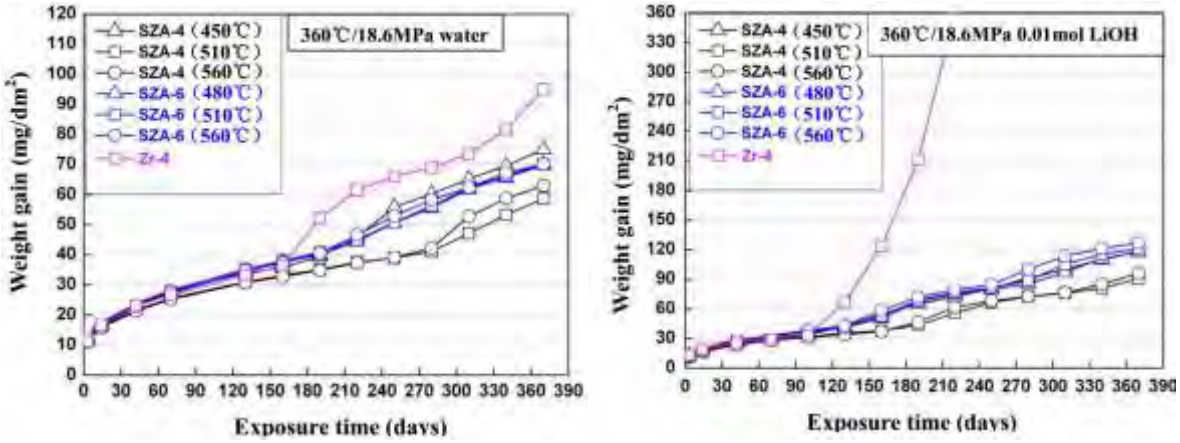

Fig 3-1: Corrosion weight of different alloys in pure water and lithium water

Experimental results of the industrial ingot stage showed that: SZA-4 and SZA-6 using different final annealing temperatures showed good corrosion resistance, commercial Zr-4 Alloy was also tested as reference alloy. Extrusion temperature and intermediate annealing temperature had little effect on corrosion resistance. The only important factor was the final annealing treatment and the recrystallization curve was similar between SZA-4 and SZA-6. Along with the out-of-pile performance tests in the industrial ingot stage continuing, a long-term irradiation test is launching in test reactor using small fuel assembly to obtain the irradiated behavior of SZA-4 and SZA-6.

3.2 UO_2 Pellet Development

CAP1400 fuel rod design incorporates UO_2 pellet with 1.4 mm central hole. The hollow pellet design will help decreasing the pellet center temperature which also increases the PLHR margin in over power accidents. Fuel density is increased to 97% to partially eliminate the loss of uranium loading. Preliminary analysis has shown remarkable decrease of pellet center temperature. As shown in Fig 3-2, the effects of the central hole diameter and the pellet density are taken accounted in the analysis, and pellet density has little affection on the fuel thermal performance while decrease the fission gas release. Thus the increase of the pellet density will compensate the uranium loading loss without affect other fuel performance and cycle length.

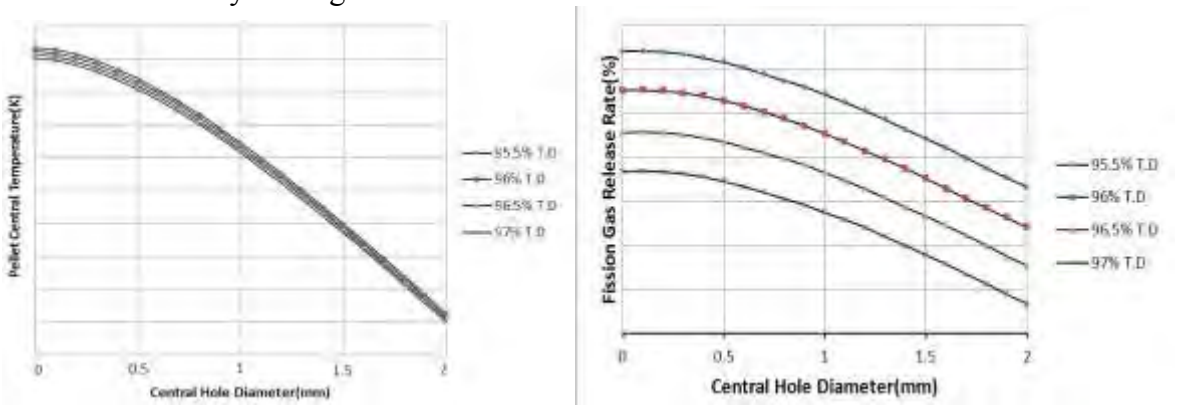

Fig 3-2: Effect of central hole diameter and pellet density on pellet temperature and FGR

In order to further improve the pellet thermal performance, the BeO doped effects on pellet thermal performance improvement are analyzed in parallel. As shown in fig 3-3, the sample UO_2-BeO pellets have been manufactured to show the feasibility of forming BeO "Skeleton" after UO_2 is dissolved in nitric acid and the continuous phase can be observed. UO_2-BeO pellets samples with different BeO content from 1%~5% are also developed to analyze the relationship of thermal diffusivity and BeO content. As shown in Fig 3-4, the thermal

diffusivity increase with the elevated BeO content, while decrease with the temperature rise. Based on the thermal diffusivity, melting temperature and other physical property test results, the BeO content will be further optimized.

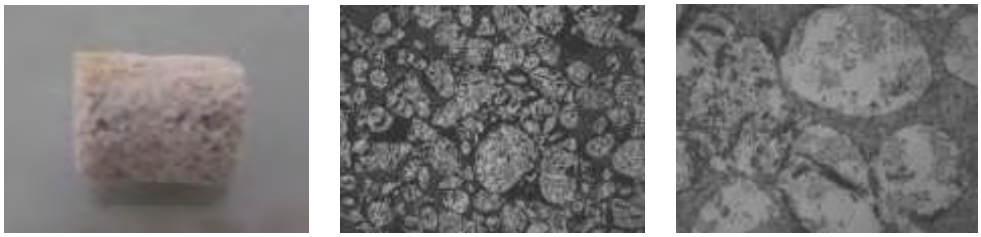

Fig 3-3: BeO "Skeleton" (left) and microstructure of UO_2-BeO pellets (right)

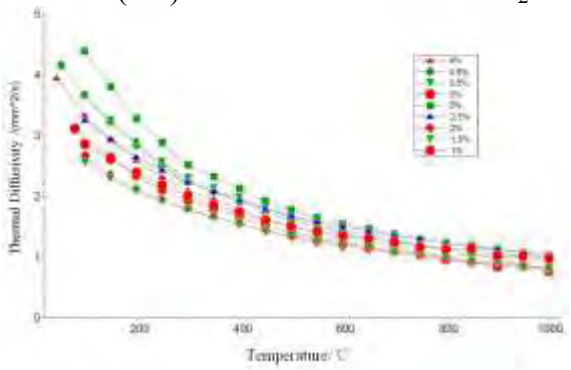

Fig 3-4: Effect of BeO content on thermal diffusivity

3.3 Grid Development

As the main structure components of CAP1400 fuel assembly, the grid design focus on thermal performance enhancement, fuel rod flow-induce vibration fretting reduce and grid anti-snag performance improvement. The Inconel End Grid (Top and Bottom grid) mainly derives from FA300 grid design with wider guide vane settled between every pair of adjacent cell on the outer strap. The wider guide vane design on the strap will reduce the possibility of snag while fuel handling. As shown in Fig 3-5, during fuel assembly worst case handling simulation (the adjacent assemblies misalign one cell size), the guide vane will still function and contact force is well below the yield stress.

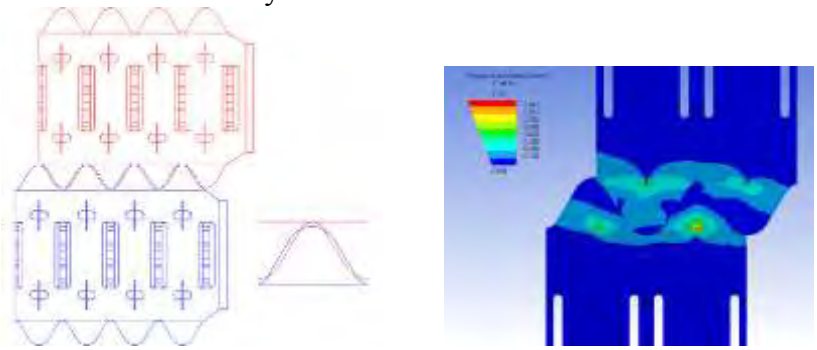

Fig 3-5: Fuel assembly misalignment handling simulation

The SAF Mid Grid and SAF Flow Mixer made by SZA Alloy is expected to have good irradiation growth behavior which will further reduced the grid snag risk together with the enhanced guide vane design. SAF Mid Grid incorporate long spring and wide dimple which will help lessen the fuel rod fretting wear. The fuel rod holding force of the grid cell is optimized which prevent fuel rod buckling while providing sufficient supporting force to reduce the flow induced fretting.

In order to enhance the thermal performance of the fuel assembly, 4 SAF Flow Mixers are evenly located between each SAF Mid Grid in the high temperate flow area. Full-scale CFD

analysis shows rotational flow around rods and acceptable velocity and temperature distribution under the effect of the SAF Mid Grid as shown in Fig 3-6. The temperature of cladding surface are also evaluated using CFD to preliminarily judge the mixing capability, as is shown in Fig 3-7. In addition, FEA simulations of 5×5 grids have been carried out before the full-scale static and dynamic grid crush test to evaluate the static stiffness of the SAF grids, which is shown in Fig 3-8. Now the grid dynamic crush strength test and 5×5 small-scaled assembly flow-induced vibration test are being carried out using the facility shown in Fig 3-9. In addition, full series of grid tests including spring and dimple stiffness test, cell stiffness tests will be finished based on the finalized grid design and test prototypes by the end of 2015.

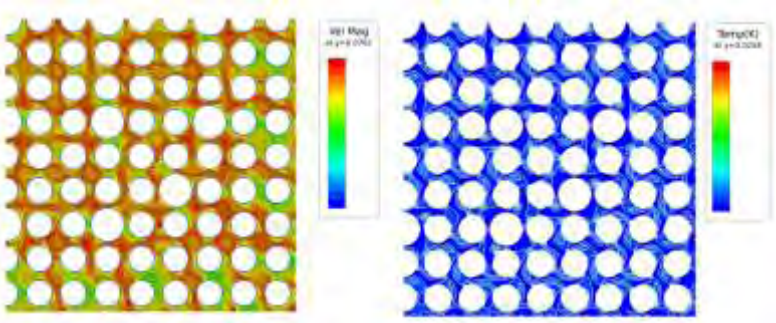

Fig 3-6: Full scaled CFD analysis results of SAF Mid Grid

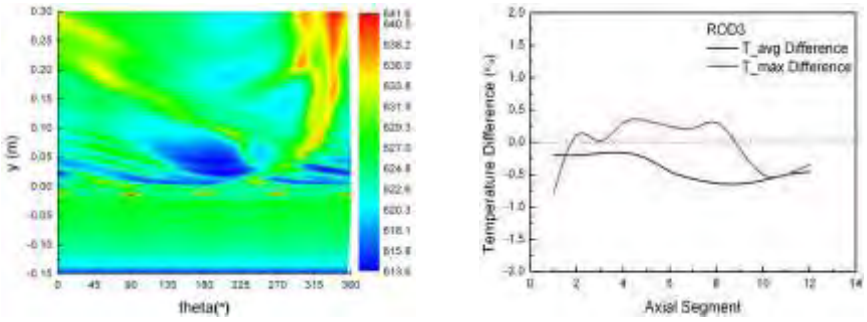

Fig 3-7: Temperature contour on the cladding surface

Fig 3-8: Static stiffness analysis of 5×5 SAF Mid Grid

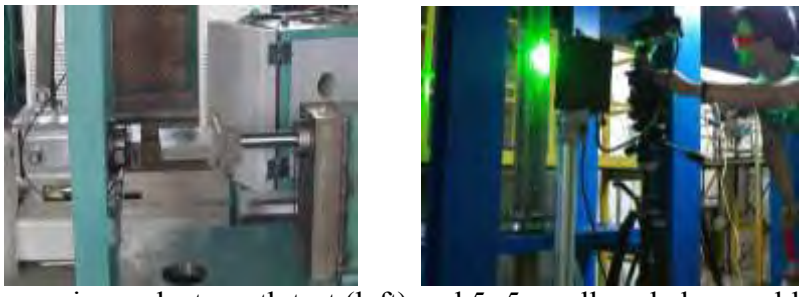

Fig 3-9: Grid dynamic crush strength test (left) and 5×5 small-scaled assembly flow-induced vibration test facilities (right)

3.4 Nozzle Development

CAP1400 fuel assembly adopts Safe & Fast Reconstitute (SAFAR) Top Nozzle and Capturing-debris Reconstitute Bottom Nozzle (CARBON) Bottom Nozzle as shown in Fig 3-10. SAFAR provides a fast connection solution with the flow hole optimized which will provide even flow distribution and stress distribution. CARBON introduces cross-shaped metal slices in the flow holes to minimize every single flow-hole size to enhance the debris capturing capability.

Series of CFD and FEA evaluation, mechanical and hydraulic tests of CARBON and SAFAR have been carried, as shown in Fig 3-11 and Fig 3-12, both SAFARI and CARBON have even stress distribution and acceptable pressure drop. Debris capturing tests using different types of debris have been carried out to verify debris capturing capability of CARBON nozzle using the test flow housing shown in Fig 3-13. The debris capturing test results show that the CARBON nozzle (together with the Bottom Grid) has remarkable debris capturing ability to variety of debris types, which will greatly reduce the possibility of debris induced fuel rod premature leaking.

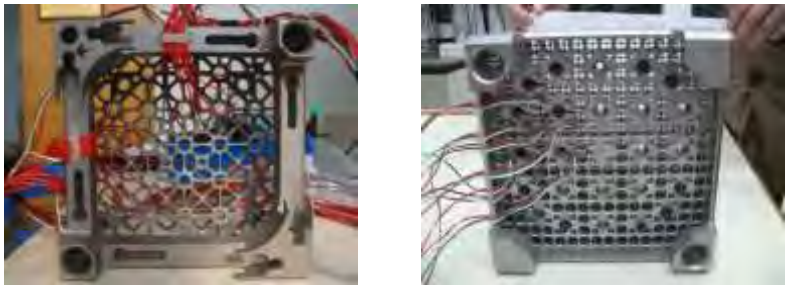

Fig 3-10: SAFAR and CARBON nozzle test prototype

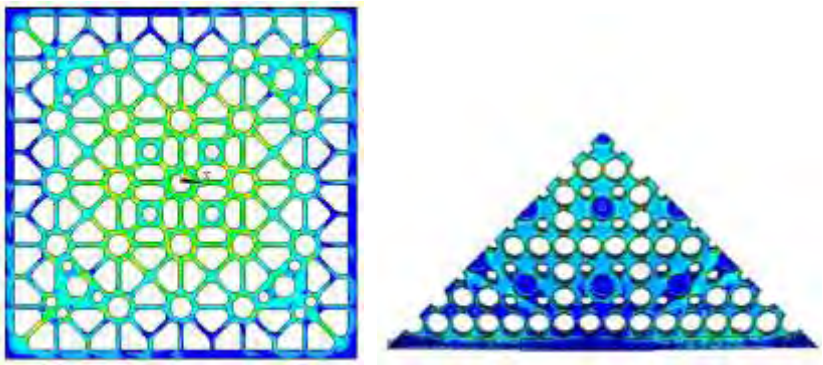

Fig 3-11: Stress distribution of SAFAR (left) and CARBON (right)

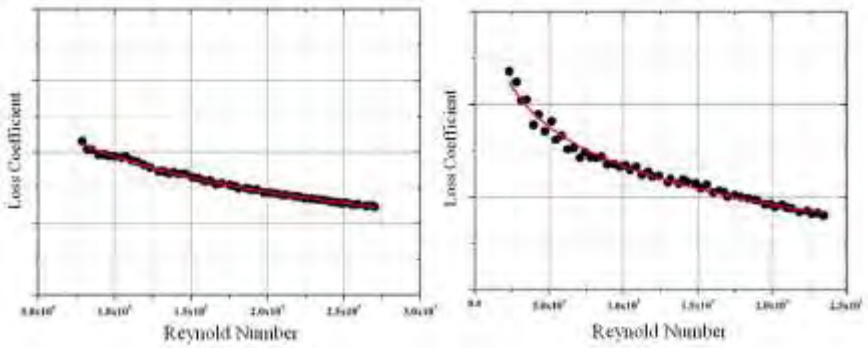

Fig 3-12: Loss coefficient of SAFAR (left) and CARBON (right)

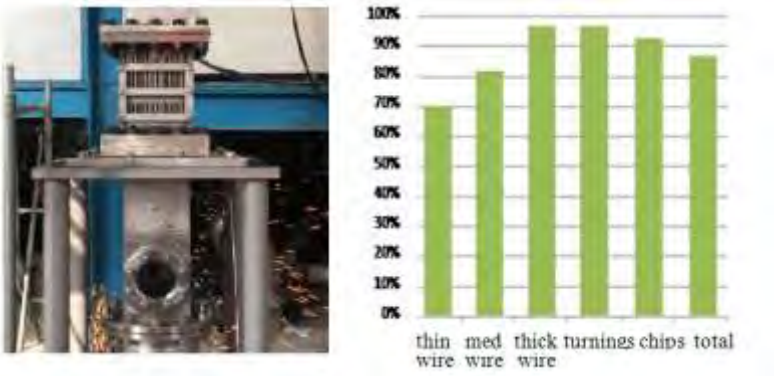

Fig 3-13: Debris Capturing Test Flow housing (left) and CARBON debris capturing efficiency (right)

4 Fuel Assembly Out-of-Pile Test

4.1 Fuel Assembly Mechanical Test

The main purpose of fuel assembly Mechanical tests is to obtain parameters to supply input data for the development of Fuel Assembly Seismic Analysis Code (FASAC), which is a safety-related code to calculate fuel assembly response in seismic and LOCA conditions) and to verify the code model. The test assemblies will be produced to simulate the begin-of-life and end-of-life conditions. The mechanical tests include fuel assembly lateral and vertical stiffness tests, fuel assembly tilt stiffness tests, fuel assembly vibration tests and etc.

Since CAP1400 fuel assembly consist of SAF Grids and guide thimbles produced with SZA alloys, the stiffness and natural frequencies differ significantly from other fuel assembly type. Therefore, multi-fuel assembly shaking table testing is planned with prototype assemblies to support design verification of CAP1400 fuel assembly analytical models for seismic and LOCA conditions. A 0.3g acceleration spectrum will be used to simulate seismic response. Lateral displacement, acceleration and impact force will be obtained with or without water for 1×5 array of prototype assemblies. The results from analytical model shall be compared with shaking table testing results to verify its reliability. Finally the tests results will support the licensing of fuel assembly seismic analysis methodology and FASAC in CAP1400 reactor core.

4.2 Fuel Assembly Hydraulic Test

Along with the fuel assembly mechanical tests, the fuel assembly hydraulic tests will also be finished by 2018. By the end of this year, all of the hydraulic tests loops including fuel assembly pressure drop test loop and fuel assembly long-term fretting wear test loop will finish construction and benchmark tests. The main focus is to enhance the thermal performance (Thermal Diffusion Coefficient and Critical Heat Flux introduced in the following section) while maintaining the pressure drop and flow-induced vibration response as close to the existing value as possible. To reach the target, several steps have been carrying out. In the beginning stage, Computational Fluid Dynamics (CFD) tool is employed to investigate the pressure drop of several component candidates to enhance the following screening 5×5 small-scale test efficiency.

The pressure drop of fuel assembly is obtained through a preliminary 5×5 small-scale test and full-scale fuel assembly final pressure drop test. The former is finished in the Small-Scale Hydraulic Test Loop (SSHL) in Fig 4-1, with the design pressure, maximum loop flow rate and maximum loop temperature 1.2MPa, 60m^3/h and 120℃, respectively. The

full-scale fuel assembly pressure drop test will be carrying out in a Large Hydraulic Test Loop (LHTL) which comprises of two sub-loops, one with maximum flow rate 800 m^3/h and the other 1600 m^3/h. The locations of pressure taps are carefully determined to represent pressure loss of important components, such as Nozzle and Grid, and the inlet/outlet region and the whole pressure drop of the fuel assembly.

To exclude abnormal flow-induced vibration and grid-to-rod fretting (GTRF), three tests are planned to be carried out. The first is a 5×5 small-scale high frequency vibration test in SSHL, with room temperature and pressure test conditions. The second test is a full-scale fuel assembly flow-induced vibration test in LHTL as shown in Fig 4-2 to check no abnormal vibration response of the whole fuel assembly occurs. Finally a 500 hours long-term wear test will be accomplished to verify no series GTRF occurs. Test fuel assembly simulating end-of-life conditions (accounting for grid spring relaxation) will be used. The final verification test will be carried out in a loop with test conditions about 304℃, 15.5MPa and 1250 m^3/h. After the test, fretting wears will be examined to support following data analysis.

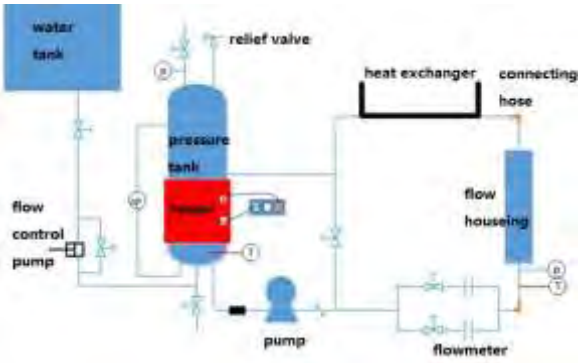

Fig 4-1: Small-Scale Hydraulic Test Loop (SSHL)

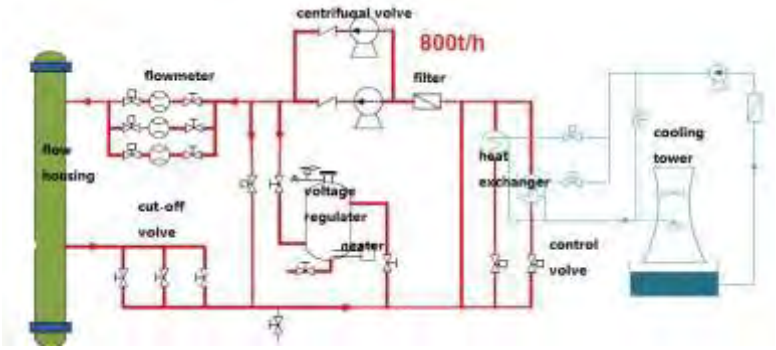

Fig 4-2: Large Hydraulic Test Loop (LHTL)

4.3 TDC and CHF Tests Program

As the critical test of CAP1400 fuel assembly design finalization and the important proof of SAF grid performance, the CHF test is planned to launch in 2018 using the qualified CHF loop. Based on the test data, a new CHF correlation will be developed with self-developed sub-channel code by SNERDI, which also will support the licensing of LTA irradiation program in CAP1400 reactor core. Before the CHF test performed, a TDC (Thermal Diffusion Coefficient) test will be carried out, which used to develop a TDC value for subchannel code. The TDC test is also planned to carry out in 2016.

5 Irradiation Program

Prior to extensive commercial PWR irradiation, a small scaled Irradiation Fuel Assembly (IFA) as shown in Fig 5-1, consisting of SZA-4 and SZA-6 fuel rod claddings will be

irradiated in China Advanced Research Reactor(CARR) to reach the target burn-up (Stage I to 31000 MWd/tU and Stage II above 60000 MWd/tU). The test loop operation parameter and water chemistry are shown in table 5-1 simulating CAP1400 operational environment. At the end of each irradiation stage, several PIE examination including cladding oxide measurement, cladding hydride content measurement, cladding tension and burst test etc, will be carried out to obtain the in-core irradiation data of SZA-4 and SZA-6.

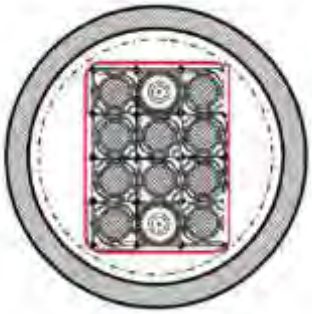

Fig 5-1: Irradiation Fuel Assembly Cross Section

Table 5-1: Test Loop Parameters

Average Linear Power	25~35 kW/m
Coolant Pressure	15.5 MPa
Coolant Velocity	4.5~5.0 m/s
Coolant Temperature	315~325℃
Coolant Chemistry	General PWR water quality

Together with the test reactor irradiation, a LTA program includes a three-cycle in core irradiation program will be launched in CAP1400 first core, 4 or 8 LTAs made by SZA-4 and SZA-6 will be loaded into the core. By pool side examination and PIE examination, more in-core irradiation data will be collected. And the new zirconium alloy performance model will be developed based on test reactor and CAP1400 reactor irradiation data, which will support the licensing process of full core usage of CAP1400 fuel assembly.

6 Summary

Based on the successful self-reliant development of FA300 series fuel assembly, in 2010, SNERDI launched a long term CAP1400 fuel assembly development program including new zirconium alloy development, fuel assembly mechanical design, fuel assembly and components out-of-pile tests, CHF and TDC tests, irradiation tests in both test reactor and commercial reactor.

By now two types of new zirconium alloys have finished composition selection and out-of pile performance tests. A long term test reactor irradiation program with target irradiation burnup to 31000 MWd/tU at stage I, above 60000 MWd/tU at stage II will be launched in 2016. Through series of fuel assembly components performance tests, both grid and nozzle will finish design finalization and the prototype CAP1400 fuel assembly will finish construction by the end of 2015.

All of the fuel assembly mechanical and hydraulic tests, TDC and CHF tests will be finished by the end of 2018, then a three-cycle LTA program is planned to launch to further collect new zirconium alloy irradiation data and prove the in-core performance of CAP1400 fuel assembly in CAP1400 reactor. After transition core analysis and commercial application licensing, the CAP1400 fuel assembly is anticipated to provide adequate burnup capability and operation reliability to CAP1400 reactor in China.

CORROSION BEHAVIOUR OF ALLOY X-750 IN BWR FUEL AT HIGH FLOW RATES

K. GÖRANSSON, L. HALLSTADIUS
Westinghouse Electric Sweden AB
SE-721 63 Västerås, Sweden

C. GUSTAFSSON
Studsvik Nuclear AB
SE-611 82 Nyköping, Sweden

H. LAI, S. TUZI, M. THUVANDER, K. STILLER
Chalmers University of Technology
SE-412 96 Göteborg, Sweden

A. KUCUK
Electric Power Research Institute
3420 Hillview Avenue, Palo Alto, CA 94304 USA

B. JOSEFSSON
Vattenfall Nuclear Fuel AB
SE-162 87, Stockholm, Sweden

ABSTRACT

Corrosion rates of Alloy X-750 have been estimated from autoclaved samples and material exposed in BWR reactor cores by using a combination of weight change measurements, measurements of metals release rates and metallography. Testing under high flow rates is necessary for Ni- and Cr-containing alloys, as these elements form oxides with substantial solubility in BWR reactor water. In that case, the oxide dissolution rates are expected to be influenced by the flow rate and the difference between oxide solubility and the concentration of ions in the reactor water. The formation of mixed oxides with lower solubility than the single-component oxides results in a dependence on the alloy composition for the corrosion rate. In particular, higher alloy Fe content is shown to reduce the corrosion rates, although the mechanism is not fully known. Pre-oxidation under controlled conditions can create a protective oxide that reduces the corrosion rate compared to non-oxidized material. The practical benefit of the pre-oxidation is to create an incubation period during which the corrosion rate is insignificant. The impact of the composition of the oxide on corrosion rate and incubation period is quantified in the present paper. For material in a BWR fuel assembly, the surface oxides may also be exposed to mechanical damage by droplet impact due to two phase flow. The data from autoclave corrosion and in-core measurements have been used to generate an empirical model for the corrosion of Alloy X-750 accounting for the influence of alloy composition, void, linear flow rate and oxide type.

1 Introduction

1.1 Background

Alloy X-750 is used in reactor components and fuel components requiring high mechanical strength and low stress relaxation. It is a Ni base alloy with 14-17% Cr, 5-9 % Fe. Ti, Nb and Al are added for age hardening. To give optimum stress corrosion resistance, the ageing is performed at 700°C. If the ageing is performed in air or another oxidizing environment, this results in a pre-oxidation of the material [1].

The present paper focuses on spacer grids in BWR fuel. In that case, the surface area is large and the thickness is minimized in order to reduce neutron absorption and pressure drop. Therefore, knowledge of the in-core corrosion rates is necessary to avoid excessive activity release and thinning of components. Inside the fuel assembly, the flow rates are relatively high – in the range of 10 m/s or higher at the uppermost spacer level. Radiolysis in combination with boiling results in a high Electrochemical Potential, ECP, within the majority of the assembly length [2]. This means that the corrosion rates for fuel components can be

quite different from those of core components operated under lower flow rates and lower ECP.

The in-core corrosion rate of Alloy X-750 has been shown to vary extensively with the alloy condition and operating conditions: between different spacer elevations and different positions in the same spacer and also between neighbouring areas with similar flow conditions [3]. The corrosion rate increases with reduced Fe content in reactor water [4], and is different for initially pre-oxidized and non-oxidized material [1,5-7]. The flow rate has a strong impact on the corrosion: compare high flow rate data in [8,9] to low flow rate data in [6,7]. Finally, alloy composition variations within the standard specification have a strong impact, especially for pre-oxidized material [3,10]. The most severe conditions occur for high flow rates, low Fe input in reactor water, low alloy Fe and/or non-oxidized material.

The present paper aims at providing a link between on-going research project studying corrosion under high flow rates in autoclaves and the historical database of measured in-core behaviour. The impact of alloy chemistry, pre-oxidation and flow rates on corrosion rates is to be modelled. The models used are empirical and based on data from studies involving variations in smaller subsets of parameters. Only the case of low Fe input from the reactor water will be studied in the present paper, since the focus is to model *maximum* rates. Different hypotheses regarding the observed local variations of corrosion rates in core will be compared in order to understand the main drivers behind locally accelerated corrosion rates.

1.2 Data sets

The following section describes the data that have been used in the modelling.
Present work and [1]: weight change and oxide thickness were measured for non-oxidized and pre-oxidized spacers operated 1-5 years in different BWR reactors in the late 1980's to early 1990's. The measurement technique is referenced in [1]. Non-oxidized spacers were found to corrode more than 10 times faster than pre-oxidized spacers. Maximum corrosion rates for an individual spacer corresponded to approximately 8 µm metals loss/year.

Present work, partially referenced in [3]: measurements were made of local corrosion maxima in spacers operated in commercial reactors using visual inspections pool side and in hot cells as well as metallography in hot cells. The corrosion of the downward facing edges of pre-oxidized spacers was studied. The corrosion rate of the edges on spacers at the top of the fuel assemblies was substantially higher compared to areas parallel to the flow and to corresponding edges of spacers in the bottom half of the fuel assemblies. In addition, the maximum metals loss was shown to vary significantly between spacers with different alloy composition within the Alloy X-750 specification. Specifically, material with low content of Fe had a much higher corrosion rate than material with a high Fe content. The metals loss was also shown to vary by more than a factor of 10 between neighbouring areas in the same spacer, i.e. between areas with very similar composition and operating conditions. The corrosion rates in general were less than 5 µm/year. Locally, in small areas facing the reactor water flow, rates as high as 50 µm/year were shown in [3].

Present work, partially referenced in [4]: in-core corrosion rates were estimated from mass balance calculations for the release of ^{58}Co generated from activation of Ni in X-750 spacers and of ^{51}Cr from activation of Cr in Alloy X-750 spacers. Measurements from five different reactors have been used, relating to non-oxidized and pre-oxidized material with different ranges of Fe content. Since the data refers to full cores of spacers operating under a range of conditions, the values for flow rate, void etc. corresponding to a specific data point are approximate estimates. The functions used in the present work are linear or nearly linear in the relevant variable ranges, which limits the inaccuracy for calculated averages. For core wide averages, the maximum corrosion rate was approximately 2-3 µm/year. The high rates refer to reactors with low Fe input and non-oxidized material or pre-oxidized material with Fe

content <7%. For pre-oxidized material with a Fe content >7% operation in reactors with normal or high Fe input the corresponding rates were approximately 0.5 µm/year or lower.
In [5-7], the corrosion of Alloy X-750 pre-oxidized at 700°C and non-oxidized or autoclaved at 390-400°C was investigated. The tests were performed in autoclaves under chemical conditions and temperature similar to those of a BWR reactor core, but with lower flow rates. Metal release (Fe, Ni, Cr) and oxide thickness was measured at selected exposure times. Non-oxidized and autoclaved material corroded at similar rates, approximately 10 times faster than pre-oxidized material. However, the actual corrosion rates measured in [5-7] were significantly lower than those reported in e.g. [3, 4]. In [5,6] data from experiments with single phase flow and exposure times up to 1420 h is presented. In [7], the measurements were performed with varying void and consequently varying flow rate. The flow rates were not explicitly stated but they can be estimated from information in [7]. Exposure time 500 h.

In [8,9], autoclave testing of non-oxidized Alloy X-750 and other high-Ni alloys was performed under BWR conditions with high flow rates and also turbulent conditions corresponding to leading edges of components. The corrosion rates were significantly higher than in [5-7]: up to more than 30 µm / year. These rates are consistent with the observed maximum in-core corrosion rates [3], but they cannot explain the local variations between points with very similar conditions. Exposure times up to 1512 h.

Autoclave testing at high flow rates of Alloy X-750 with different compositions and pre-oxidation conditions [10]. The same autoclave loop as in [8, 9] was used. The data was used primarily to model the impact of alloy composition and to increase the range of investigated parameters for flow rate. Exposure times up to 840 h.

2. Modelling of corrosion rates

All oxide will be assumed to consist of $NiFe_2O_4$ with a density of 5.4 g/cm^3. Using a porosity of 10% [8], the actual number used is 4.9 g/cm^3. The oxide is assumed to have an ideal composition with 27.3 mass-% oxygen and 72.7 mass-% metal. Most published investigations indicate that the oxide on corroded Alloy X-750 consists of a mixture of oxides where spinel oxides of varying compositions dominate, together with NiO [5-7,9]. Table 1 shows the variable ranges present in the database used for fitting.

Variable	**Autoclave data**		**In-core data**	
	min	max	min	max
Time (t)	380 h	1512 h	0.5 years (release rate) 1 year (weight change)	7 years (weight change)
Linear flow rate (v)	Stagnant	14.4 m/s	Spacer level 1 (1.5-2 m/s)	Top spacer level (8-10 m/s)
Void (α)	0	0.85	Spacer level 1 (approximately 0)	Top spacer level (> 0.8)
Alloy Fe content (x)	5.4 %	8.4 % (18 %*)	<6 % (core wide average)	7.5 % (core wide average)
* Data for Alloy 718 and an experimental alloy with the same composition as X-750 except for a replacement of Ni by Fe.				

Tab 1: Utilized ranges for variables

In general, the metals release and oxide growth is described by the following formulae:
$\Delta m(tot) = \Delta m(MR) + 0.273 * \Delta m(FO)$
$\Delta m(met) = \Delta m (MR) - 0.727 * \Delta m(FO)$, where:
$\Delta m(tot)$ is the weight change per unit area
$\Delta m(met)$ is the change in amount of metal, per unit area due to corrosion (always negative)
$\Delta m(MR)$ is the weight change due to metals release per unit area (always negative)
$\Delta m(FO)$ is the weight of oxide formed per unit area (always positive)
The unit for all mass change measurements is g/m^2.

The metal consumption (in μm) due to corrosion is:
$\Delta d(met) = \Delta m(met)/\rho_{met}$, and similarly for MR and FO. ρ_{met} is 8.28 g/cm^3.
The time dependence is modelled as:
$\Delta m(MR) = A_{MR} * t^{(1/n)}$ $\Delta m(FO) = A_{FO} * t^{(1/p)}$
i.e. for instantaneous corrosion rate:
$\partial\Delta m(MR)/\partial t = (1/n)\ A_{MR} * t^{(1/n)-1}$ $\partial\Delta m(FO)/\partial t = (1/p)\ A_{FO} * t^{(1/p)-1}$
n and p are determined separately for pre-oxidized and non-oxidized conditions.

A depends on composition and flow rate and will in general be different for pre-oxidized and non-oxidized conditions, i.e. there will be four sets of parameters: A_{MR}(pre-ox), A_{MR}(non-ox), A_{FO}(pre-ox), A_{FO}(non-ox).
In general, the A parameters are modelled as a product of three terms: $A = F(v) * G(\alpha) * H(x)$
v is the linear flow rate of the single or two phase flow
α is the void, i.e. the volume fraction of steam in a two phase flow
x is the alloy Fe content

Flow rate dependence (F): the basis for the selected function is the hypothesis that the dissolution behaviour is determined by diffusion over a stagnant boundary layer between the oxide surface and the flowing water. Oxide growth will be indirectly impacted by dissolution but the two phenomena are here modelled independently. The thickness of the stagnant boundary layer is assumed to be proportional to 1/v. The diffusion flow across the layer is inversely proportional the layer thickness, i.e. the dissolution rate is expected to be proportional to v. In addition, the function used allows for finite corrosion rates at zero flow and is modified to allow saturation of the dissolution rate at very high flow rates. For dissolution, F(v) should be multiplied by the difference in concentration of dissolved metals between the oxide surface and the flowing solution, $\{[M]_{surf} - [M]_{sol}\}$. $[M]_{surf}$ is the minimum of the equilibrium solubility of the surface oxide and the maximum diffusion flow through the oxide, $[M]_{sol}$ is the local concentration outside the stagnant layer. In the following we assume that $[Ni]_{surf}$ is constant and much greater than $[Ni]_{sol}$. The data on solubility of Ni containing oxides under BWR conditions, i.e. the maximum in $[Ni]_{surf}$ - is somewhat conflicting, but can be assumed to be greater than 1 ppb [1]. Typically, $[Ni]_{sol}$ in a reactor is of the order 0,2 ppb and the change during passage through the fuel due to evaporation and corrosion release is sufficiently small compared to the difference $[Ni]_{surf} - [Ni]_{sol}$ to allow this to be treated as a constant in the present analysis. For Cr, the oxide solubility is much higher than the reactor water concentration [6] which means that $[Cr]_{surf} - [Cr]_{sol}$ can also be treated as a constant.

Void dependence (G): models the fraction of time that a surface is wetted. G should be approximately proportional to the void, allowing for slightly longer times wetted than for $1-\alpha$.

The impact of alloy Fe content is arbitrarily set to $H(x) = 1-e^{(C*x)}$, $C<0$. The actual Fe dependence is likely to be related to mechanism changes, i.e. for a more complete data set with respect to composition, a model using a step function would probably be more appropriate. However, with the limited data base available, such a function can result in large errors. The current expression is well behaved for extrapolation to high Fe and to model the general trends for the Alloy X-750 range represented by samples (5.4-8.4% Fe). Extrapolation to Fe contents below approximately 5% is not expected to yield realistic values.

3 Results

3.1 Fitting of parameters

Data on release of activation products from spacer material have been analysed. The data was collected from the latter half of 12-month cycles to ensure full activation of the spacer material. The release of Ni [4, 11] was approximately constant. I.e. the parameter n should be close to 1. In contrast, the kinetics for Cr was approximately parabolic, i.e. the total amount released varies as $t^{½}$ and the rate of release varies as $t^{-1/2}$. This indicates that the release of Cr is determined by diffusion through a growing barrier layer. This can be taken as

an indication that the oxide grows approximately parabolically, i.e. that p is close to 2. The total metals release is considered in the following to be dominated by Ni, although the ratio between release of Ni and Cr may change with time.

The expression for the variation of corrosion rate with void, G (α), was selected from an analysis of the flow rate dependence of measurements under single phase conditions [8-10] compared to the data from [7] and the weight change data for spacers at different elevations [1]. In the latter case, void and flow rate vary significantly with time, so approximate averages have been used. The parameters for void dependence have been set to the same values for all four cases: MR/FO and pre-oxidized/non-oxidized material.

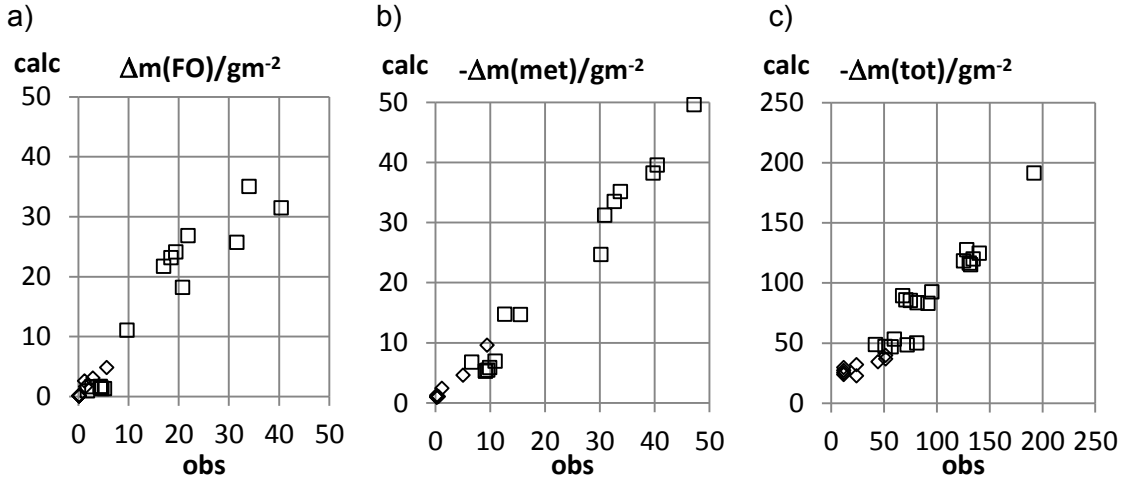

Fig 1. Comparisons of measured (obs) vs, modelled (calc) data. Squares: non-oxidized material, diamonds: pre-oxidized material. a) Autoclave data for Δm(FO), b) Autoclave data for -Δm(met). c) In-core data for -Δm(tot).

Figure 1 summarizes the data on parameter fitting. For the in-core data, the averaging over operating time, flow rate and void introduces a relatively large uncertainty, but the fits are reasonably good also for those cases. This indicates that at least interpolation inside the space spanned by the variables used is expected to give reliable results. For extrapolation, the functions used are selected to be well behaved outside the experimental range. However, step changes will not be captured by the functions F, G and H.

3.2 Examples of calculated trends

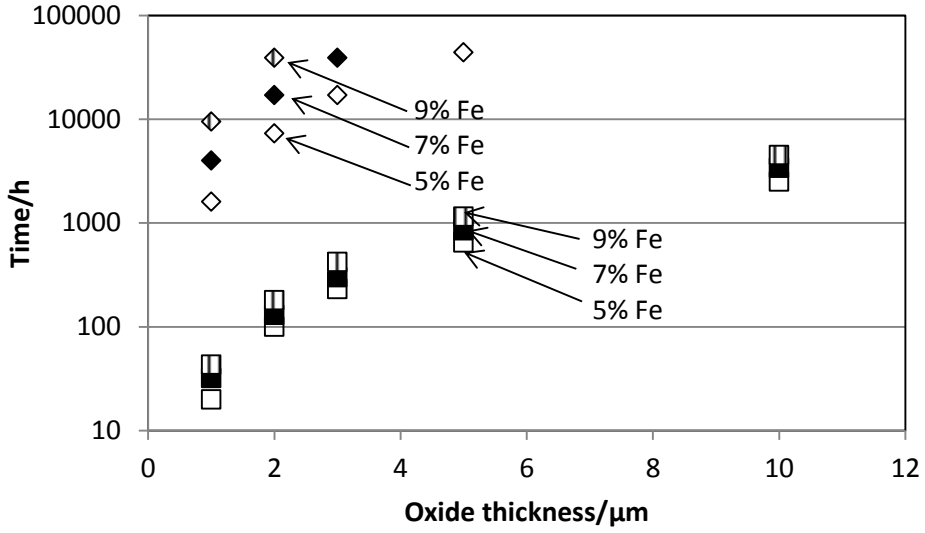

Fig 2. Time to reach a specific oxide thicknesses in single phase flow at 8 m/s. Squares: non-oxidized material, diamonds: pre-oxidized material.

Figure 2 shows the time to reach different oxide thicknesses for different alloy conditions, in single phase flow at 8 m/s. In figure 3, the corresponding total metals loss is shown for 7% Fe. The composition dependence is very small. There is a very large difference in oxide growth rate for pre-oxidized material compared to non-oxidized material. The slow oxide growth for pre-oxidized material shown in figure 2 means that the corrosion of pre-oxidized material is dominated by metals release (cf. figure 3). For non-oxidized material, both oxide growth and metals release contribute significantly to the total corrosion. This is in contrast to the data in [5-7] which shows much greater contribution from metals release in both the pre-oxidized and non-oxidized case. This difference is an effect of the high flow rate, which impacts pre-oxidized and non-oxidized material differently.

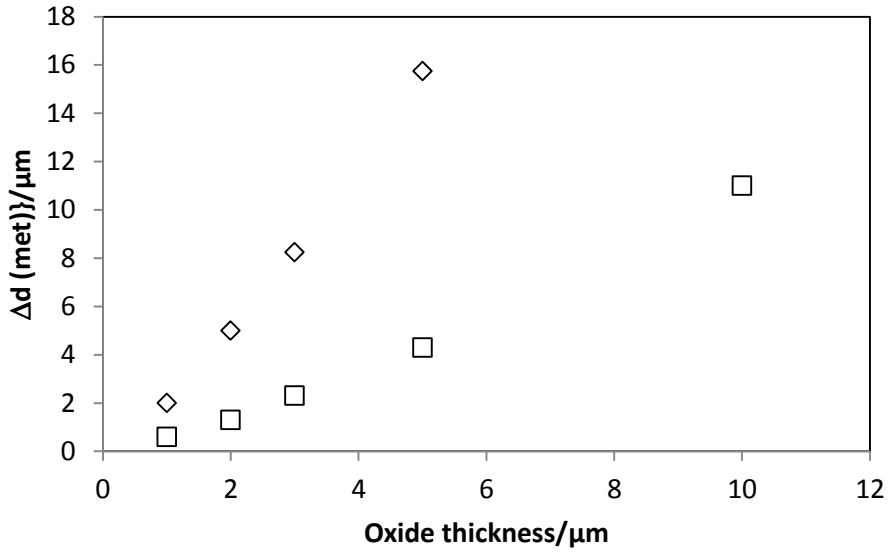

Fig 3. Calculated metals consumption, for specific oxide thicknesses in single phase flow at 8 m/s. Data for 7% Fe. Squares: non-oxidized material, diamonds: pre-oxidized material.

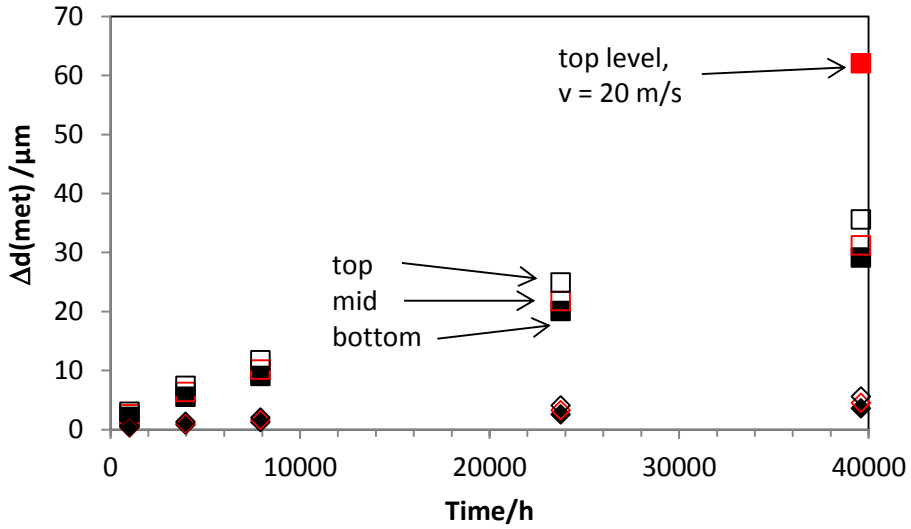

Fig 4. Calculated metals consumption, for conditions corresponding to different spacer levels. Data for 7% Fe. Squares: non-oxidized material, diamonds: pre-oxidized material.

In figure 4, the calculated total metals loss at different spacer levels is shown for pre-oxidized and non-oxidized material with 7% Fe. A substantial reduction in corrosion rate for pre-oxidized material is shown. The predicted levels of metals loss are in the experience range for surfaces that are not facing the flow direction. A comparison for a very high flow rate is also shown in figure 4. The corrosion increase at end of life for this flow rate increase is only by a factor of two, i.e. local flow rate variations cannot explain the local corrosion maxima.

4 Corrosion rate models for local effect of corrosion

In this section, three different hypotheses for local corrosion acceleration will be compared. All three models involve a difference in behaviour between pre-oxidized and non-oxidized material. Initially, the pre-oxidized material corrodes according to the kinetics modelled in previous sections. However, some event occurs that results in a deterioration of protective properties for the pre-formed oxide. After that event, the same kinetics as for an initially non-oxidized material with the same composition are assumed. The three different models differ primarily in the nature of the event causing oxide deterioration.

Some basic observations were made in [3] and references, regarding the oxides found in different areas of pre-oxidized spacers with high local corrosion loss. In areas with high corrosion rates, the oxide was thin compared to the total amount of corrosion and had a composition that was very close to $NiFe_2O_4$. This means that either the oxide growth is very low compared to the metals release or the oxide is removed during operation. In neighbouring areas with minor corrosion loss, the oxide thickness was similar to the total metals loss and the oxide contained Fe and varying amounts of Ni and Cr, i.e. some Cr had been retained in the oxide. These areas were exposed to the same flow conditions as the ones experiencing high metals loss. I.e. in these areas, the metals consumption due to oxide growth was greater or of the same order of magnitude as the metals release.

The oxide on surfaces parallel to the flow was found to consist mainly of Fe oxide. This can be interpreted as a structure formed from a thin protective oxide, covered by a thicker crud layer. Any remnant of the oxide formed in pre-oxidation would be too thin to be analysed in the SEM cross sections used in [3].

4.1 Constant corrosion rate in high flow areas

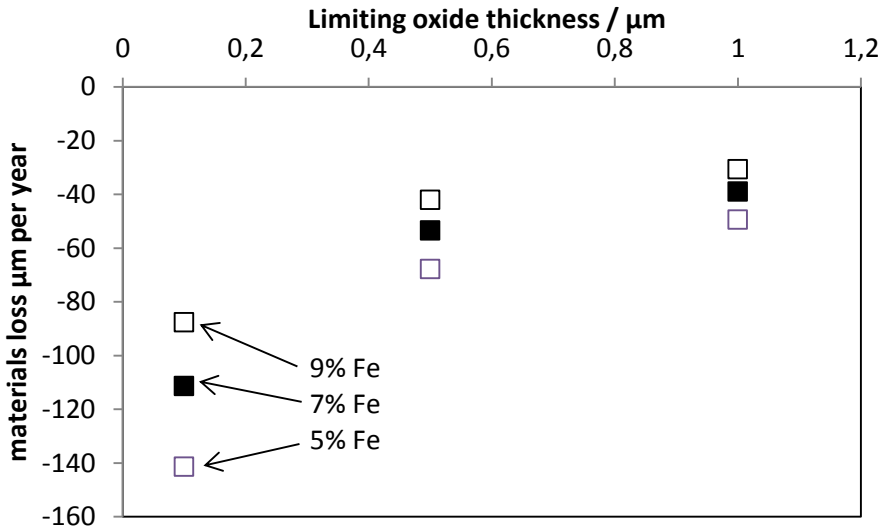

Fig 5. Calculated metals release rates, Δm(MR) per year recalculated to equivalent metals loss, for conditions corresponding to top spacer level. Data for different alloy Fe content.

The basis for the first hypothesis is that the oxide dissolution may become very rapid under very high flow rates or turbulent conditions, i.e. at leading spacer edges. The result is a constant oxide thickness with time. This results in a constant corrosion rate during the propagation phase. For pre-oxidized material, the process involves an initiation step of deterioration of the pre-formed oxide layer, followed by a rapid propagation rate. The current model does not allow the calculation of consumption of pre-formed oxide, i.e. the initiation period cannot be determined, only the propagation rate.

At very high flow rates, the impact of oxide growth and dissolution is incorrectly modelled by the simple models used in the present paper. Therefore, the instantaneous growth rate is set to zero, and the corrosion rate will be modelled by the metals release rate for fixed oxide thickness. In [8], Ni base alloys for which the oxide apparently does not grow during exposure were studied. The oxide thickness in those cases became constant, approximately 1 µm. Therefore the calculations presented here were performed for the range 0.1-1.0 µm oxide thickness.

Figure 5 summarizes the calculated propagation rates for a void corresponding to the top spacer elevation in a fuel assembly at high power. The linear flow rate was set to 20 m/s, i.e. substantially higher than for the average over a fuel assembly at that elevation, in order to model local maxima in flow rates. The calculated corrosion rates are reasonable, at least for the range 0.5-1.0 µm oxide thickness. Therefore, this mechanism is a possible explanation of high local corrosion rates. Since the initiation period is not modelled, the difference between pre-oxidized and non-oxidized is not accounted for. In the data base, there is one point that relates to this condition. It is the examination in [9] of non-oxidized Alloy X-750 exposed to high flow, turbulent conditions in autoclave testing. These data shows a thick oxide forming, indicating that the high flow rate rather increases than decreases the oxide growth. If that result can be reproduced in future tests, this hypothesis can be refuted, at least for initially non-oxidized material.

4.2 Repeated oxide spallation

Oxide spallation can be assumed to occur at a limiting oxide thickness or, more precisely, with an increasing probability with increasing oxide thickness. There may be different driving forces behind the spallation, e.g. generation of interface stresses due to the volume expansion in oxide formation, generation of Kirkendall porosity at the metal-oxide interface of outward growing oxides or depletion of oxide forming elements due to diffusion resulting in a mechanism change. This means that the limiting oxide thickness can depend on the oxide growth rate and diffusion kinetics. This is not accounted for in the present model. The random nature of spallation means that, even for identical conditions, there will be a significant scatter in the limiting thickness. The assumption of constant limiting thickness is therefore expected only to add a minor additional error.

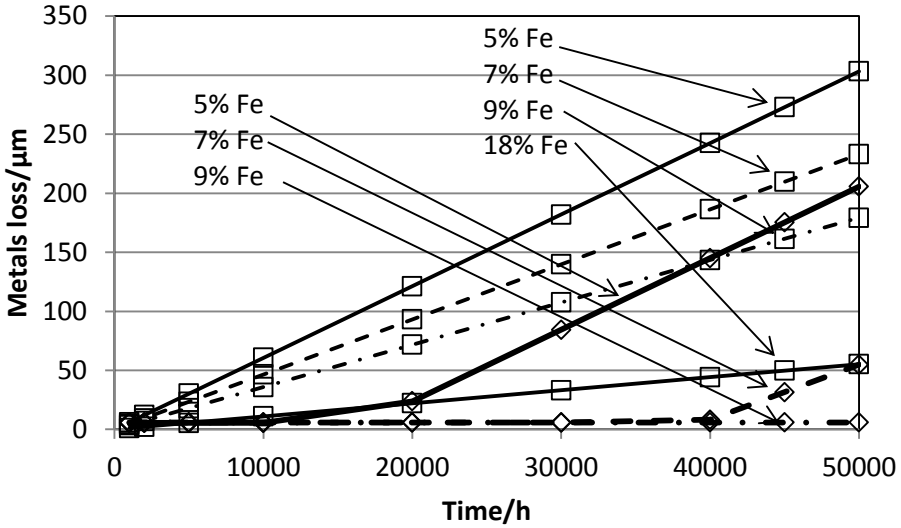

Fig 6. Calculated metals consumption for repeated spallation at a limiting oxide thickness of 2 µm, for conditions corresponding to uppermost spacer level. Squares: non-oxidized material, diamonds: initially pre-oxidized material.

Figure 6 shows the predicted kinetics for a limiting thickness of 2 μm, at operating conditions corresponding to top spacer elevation. It shows a behaviour that is fully consistent with observed maximum corrosion rates for different alloy compositions and the correct difference between pre-oxidized and non-oxidized material. It indicates that for pre-oxidized material with a low Fe content, the initiation period is very short, resulting in essentially the same materials loss as non-oxidized material with the same or slightly higher Fe content. For the example of 7% Fe, pre-oxidized material, changing the limiting thickness to 3 μm means that the oxide will not have spalled once after 50000 h. I.e. small variations in limiting thickness for spallation due to e.g. random variations in oxide composition and structure after pre-oxidation can produce the observed variations in corrosion rates.

4.3 Oxide damage due to droplet impact

An erosion-corrosion mechanism has been suggested in several previous studies, e.g. [3], as the main cause of local variations in corrosion rates. The mechanism would involve droplet impact causing local damage to the protective oxide, resulting in acceleration in corrosion. In terms of the current model this would, for pre-oxidized material, correspond to:

- Initiation that is dependent primarily on droplet impact, i.e. similar initiation period independent of the alloy composition
- Propagation according to the model in previous section for non-oxidized material, but where the oxide may be damaged and the cycle of rapid corrosion rate is restarted more rapidly than predicted from the limiting thickness. The ratio of propagation rate between different alloy compositions is the same as for different non-oxidized conditions.

This model does not result in any composition dependence for the initiation, and for the propagation most likely weaker composition dependence than for the spallation mechanism. Most in-core data do not allow the estimation of the initiation period, only of the total rate. The strong composition dependence of observed localized corrosion fits better to a spallation limited mechanism.

5 Discussion

The relatively small and diverse database used, where the in-core and autoclave data to large extent represent different time periods with little overlap and the relatively large uncertainties in the in-core data means that any model will contain substantial uncertainty.

The data shown in e.g. figure 6 do not correspond to an actual fuel assembly operating history. Instead, a constant value of flow rate and void has been assumed. This results in an overestimation of the corrosion rate, since in actual fuel operation the power and consequently flow rate are reduced in the later part of operation. The current model can however be used together with actual data from fuel operation, including local variations within an assembly.

One obvious limitation of the current model is the lack of combination effects, e.g. the possibility of the alloy composition having an effect on the time dependence of oxide growth or metals release. The data currently available do not allow adequate description of such effects.

With these limitations in mind, all observed behaviour has been possible to explain. Long term corrosion appears most likely to be controlled by oxide spallation at a limiting thickness: the variation of time to spallation caused by minor variations in composition and structure of the oxide together with the expected scatter in actual thickness to spallation also for identical conditions can explain the observed variations.

Exfoliation of oxide has not been observed in the short term autoclave tests even though the suggested limiting thickness of 2 μm in section 4.2 has been exceeded for non-oxidized material. The spallation is probably not a simple exfoliation process, but rather a change in kinetics at some oxide thickness. The actual exfoliation which limits the in-core oxide

thickness in high corrosion areas to approx. 10 µm occurs much later, long after the kinetics change. Also, note that the limiting thickness has been set to the same value for pre-oxidized and non-oxidized material, which is a simplification. The limiting value for non-oxidized material may be substantially higher than for pre-oxidized. For non-oxidized, and hence also for spalled pre-oxidized, material the sensitivity of the calculated corrosion rate to the selected limiting thickness is small, i.e. assuming a limiting thickness for the non-oxidized case of 5 µm reduces the average corrosion rate during the propagation phase by a factor of 2, i.e. still inside the observed range.

6 Conclusions

Corrosion of Alloy X-750 and related Ni base alloys under a wide range of operating conditions and materials conditions is successfully modelled. The difference in corrosion rate between pre-oxidized and non-oxidized material and repeated oxide spallation can fully explain both observed local variations and absolute corrosion rates. The limiting thickness for spallation of a pre-oxidized material is estimated to be approximately 2 µm. Future work will focus on further development of the models for the impact of alloy composition and reactor water chemistry – primarily dissolved Fe and Ni – and on determining the factors that influence limiting thickness for oxide spallation.

7 Acknowledgements

The authors would like to express their sincere gratitude to Professor Jiaxin Chen and Dr Tomas Forsman for valuable discussions and for sharing of ideas and questions.

8 References

[1] E. Ahlberg, B. Rebensdorff, “General corrosion of alloy X-750 under BWR conditions,”, Proc. BNES Conf. Water Chem. Nucl. Reactor Syst, 6, vol. 2, 278-285, 1992

[2] K Lundgren, H Wijkström, G Wikmark, G, “Recent Developments in the LwrChem Radiolysis Code”, Proc. Int. Conf. on Water Chemistry of Nuclear Reactor Systems, 2004

[3] A Jasiulevicius *et al*, “Ni-Base Alloy Spacer Material Corrosion in BWR”, Proc. 2011 Water Reactor Fuel Performance Meeting, Chengdu, China, Sept. 11-14, 2011

[4] K Göransson *et al*, “Water Chemistry Impact on Corrosion of Alloy X-750 in BWR Fuel Spacers”, Proc. Int. Conf. on Water Chemistry of Nuclear Reactor Systems, 2008

[5] Y Hemmi, Y Uruma, N. Ichikawa, “General Corrosion of Materials under Simulated BWR Primary Water Conditions”, J Nucl Sci Technol 31(5) p443,1994

[6] Y Hemmi, N Ichikawa, N Saito, T Masuda, “Protective Oxide Film on Alloy X750 Formed in Air at 973K”, J Nucl Sci Technol 31(6) p552,1994

[7] Y Uruma, T Osato, K Yamazaki, “Development of Alternative Materials for BWR Fuel Springs”, Proc. Chemistry 2002: International conference on water chemistry in nuclear reactor systems – operation optimization and new developments, Paris, 2002

[8] C Gustafsson, J Chen, H Arwin, B Forssgren, ”Corrosion Kinetics of Nickel-Base Alloys in Simulated BWR Conditions under High Flow Velocity”, Proc. 16th International Conference on Environmental Degradation of Materials in Nuclear Power System, 2013

[9] J Chen *et al*, ”High resolution electron microscopy study on oxide films formed on nickel-base alloys X-750, 182 and 82 in simulated high flow velocity BWR water conditions.” , Proc. 15th International Conference on Environmental Degradation of Materials in Nuclear Power System, 2011

[10] C Gustafsson, H Lai, S Tuzi, Chalmers University of Technology, unpublished, 2014

[11] K Göransson, Westinghouse Electric Sweden AB, unpublished, 2015

Multiphysics and thermomechanical modelling

MODELLING OF FUEL BEHAVIOUR DURING LOSS-OF-COOLANT ACCIDENTS USING THE BISON CODE

G. PASTORE, S.R. NOVASCONE, R.L. WILLIAMSON, J.D. HALES, B.W. SPENCER, D.S. STAFFORD

Fuel Modeling and Simulation, Idaho National Laboratory
P.O. Box 1625, Idaho Falls, ID 83415-3840, United States

ABSTRACT

BISON is a modern finite-element based, multidimensional nuclear fuel performance code that is under development at Idaho National Laboratory (USA). Recent advances of BISON include the extension of the code to the analysis of LWR fuel rod behaviour during loss-of-coolant accidents (LOCAs). The new modelling capability incorporated in the thermo-mechanics framework of BISON allows simulation of cladding ballooning during a LOCA, accounting for the mutually interacting effects of creep, oxidation, and crystallographic phase transition. A criterion for assessing cladding failure due to burst is also included. The paper describes the BISON models for the phenomena relevant to LWR cladding behaviour during LOCAs, with emphasis on Zircaloy-4. The new capability is demonstrated by simulating cladding ballooning experiments with BISON, both in 2 and 3 dimensions. Initial comparisons with experimental data of cladding burst are also presented.

1. Introduction

Developing state-of-the-art computational tools for reliably predicting the thermo-mechanical behaviour and integrity of the nuclear fuel rods in current light water reactors (LWRs) during accidents is essential from both safety and economic standpoints. For this purpose, increasingly complex and efficient fuel performance codes [1,2] are developed. Also, fuel performance codes able to simulate accidents can be used for the development of accident-tolerant fuel concepts [3,4].

Generally, separate codes are employed for analysing normal operation and accident reactor conditions, leading to difficulties with code coupling and code management. Developing codes able to simulate both conditions permits one to consistently account for burn-up dependent phenomena, yet requires the implementation of specific models dealing with the additional physics and increased complexity involved in accident behaviour relative to normal operation. For example, during a loss-of-coolant accident (LOCA), the Zr-alloy fuel cladding undergoes high temperatures while exposed to a low-pressure steam environment. The resulting, complex multiphysics response of the cladding includes several mutually interacting phenomena such as rapid steam oxidation, solid-solid phase transformation, and large creep deformation leading to ballooning and possible failure via bursting.

Efforts have been made to extend fuel performance codes originally developed for normal operating conditions to the analysis of fuel rod behaviour during LOCAs, for example the TRANSURANUS code [5]. In this work, recent developments of the fuel performance code BISON of Idaho National Laboratory (INL, USA) regarding analysis of LOCA conditions are presented. BISON [6] is a modern finite-element based, multidimensional fuel performance code that has been under development at INL since 2009. The code is applicable to both steady and transient fuel behaviour and can be used to analyse 1D spherically symmetric, 2D axisymmetric or 3D geometries. Although primarily used for LWR fuel analysis, BISON has been used to analyse TRISO coated-particle fuel [7] and metal fuel [8], design and interpret irradiation experiments [9], and investigate novel fuel concepts [10]. The code features a large-strain mechanics formulation, essential to correctly analyse cladding ballooning during LOCA accidents.

Focusing initially on Zircaloy-4, models have been implemented for the main physical phenomena involved in cladding behaviour during LOCAs, i.e., (1) rapid steam oxidation, (2)

solid-solid phase transition, (3) high-temperature non-linear mechanical behaviour (creep), and (4) failure due to burst. The development and validation against separate effects tests of such cladding models represents a necessary step towards the development of a LOCA simulation capability within the BISON code and is the subject of the present paper.
The outline of the paper is as follows. Section 2 describes the models implemented in BISON for representing cladding behaviour during LOCAs. Section 3 presents applications of the extended BISON code to the simulation (both 2D and 3D) of cladding ballooning experiments, including an initial validation through comparison with experimental data of cladding burst. Conclusions are discussed in Section 4.

2. Modelling

The integrated analysis of cladding high-temperature oxidation, crystallographic phase transformation, creep deformation and failure is needed in order to accurately predict fuel rod behaviour during LOCA accidents. This is accomplished in BISON through the extension of the existing thermo-mechanics framework to include modelling of the above phenomena. The specific models are described in this section.

2.1. Cladding oxidation

The process of oxidation of Zircaloy through exothermic reaction with the coolant (water-side corrosion) affects both thermal and mechanical performance of the cladding. On the one hand, the growth of a zirconium dioxide (ZrO_2) scale on the cladding outer surface adds to the thermal resistance to heat transfer from the fuel to the coolant and leads to thinning of the metallic wall. On the other hand, oxygen uptake affects the mechanical properties (e.g., creep and resistance to burst, Section 2.4) of the zirconium alloy. Concurrent to the oxidation process, a fraction of hydrogen generated during the oxidation reaction can be absorbed into the metal, enhancing cladding embrittlement and affecting the phase transformation kinetics of the material (Section 2.2). In the high temperature range (e.g., LOCA) the coolant has become steam, and oxidation proceeds much more rapidly than at normal LWR operating temperatures. Under these conditions, the kinetics of oxide scale growth and oxygen mass gain can be described by a parabolic law, with the reaction rate constant defined as a function of the temperature through an Arrhenius relation [11]

$$\frac{d\xi}{dt} = A \times \exp\left(-\frac{Q}{RT_I}\right) \quad (1)$$

where ξ is either the oxide scale thickness, $\xi=\delta$ (m), or the oxygen mass, $\xi=\chi$ (kg·m^{-2}), t (s) the time, A (m or kg·m^{-2}) the pre-exponential factor, Q (J/mol) the activation energy, R (J/mol-K) the universal gas constant, and T_I (K) the metal-oxide interface temperature.
Following the recommendations in [11], the BISON model includes correlations for oxide scale growth and oxygen mass gain rates in Zircaloy-2/4 appropriate to different temperature ranges. In particular, the following approach is adopted.

- For metal-oxide interface temperatures from 673 K to 1800 K, the Leistikov [12] correlation is used. The Cathcart-Pawel correlation [13] is also available and can be chosen as an option. The Leistikov correlation has been selected as reference in view of the larger underlying database, the availability of experimentally determined mass gain for all tests, and the better fit for lower temperature relative to the Cathcart-Pawel correlation [11].
- Above 1900 K, the Prater-Courtright correlation [14] is used.
- Between 1800 and 1900 K, a linear interpolation is made. Linear interpolation between two correlations of Arrhenius type is obtained by a third correlation of the same type [11].

The values of the parameters in Eq. 1 relative to the different correlations are given in Table 1. Calculation examples for temperatures of 1100 and 1950 K are illustrated in Fig. 1.

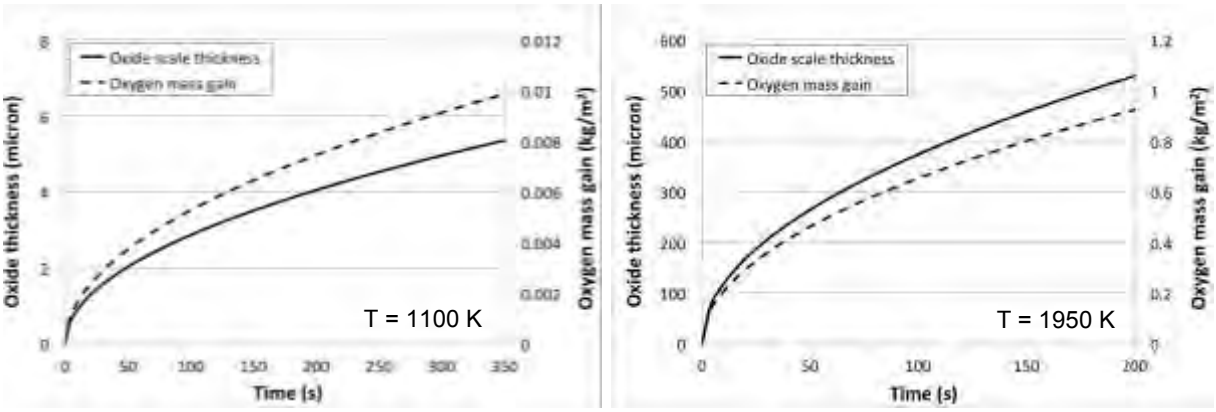

Fig. 1. Oxide scale thickness and oxygen mass gain as a function of time at 1100 K (left) and 1950 K (right), calculated using the Leistikov and the Prater-Courtright correlations, respectively.

For normal operating temperatures below 673 K, the EPRI/KWU/C-E oxidation model [15,16] is used in BISON.

2.2 Phase transformation of the cladding material

The increase in cladding temperature during a LOCA involves time-dependent phase transformation of Zr alloy from hexagonal (α-phase) to cubic (β-phase) crystal structure. Modelling the kinetics of crystallographic phase transformation is pivotal for the assessment of the mechanical properties essential for fuel rod integrity (deformation and burst). The BISON model calculates the evolution of the volume fraction of the new phase in Zircaloy-4 as a function of time and temperature during phase transformation in non-isothermal conditions. The model is based on [17-19]. The phase transformation rate is expressed as

$$\frac{dy}{dt} = k(T)\left(y_s(T) - y\right) \tag{2}$$

where y (-) is the volume fraction of β-phase, t (s) the time, y_s (-) the equilibrium value of y, and k (s^{-1}) the rate parameter. The fraction of β-phase at equilibrium is represented by a sigmoid function of temperature

$$y_s = \frac{1}{2}\left(1 + \tanh\left(\frac{T - T_{cent}}{T_{span}}\right)\right) \tag{3}$$

where T_{cent} and T_{span} are material specific parameters related to the centre and span of the mixed-phase temperature region, respectively. For Zircaloy-4, T_{cent} = 1159 − 0.096w (K) and T_{span} = 44 + 0.026w (K) [17] are used, with w being the hydrogen concentration in the range 0≤w≤1000 wppm (weight parts per million hydrogen). A model for hydrogen uptake and diffusion in the cladding has been recently developed for BISON. The model will be coupled to the present phase transformation model to provide the local hydrogen concentration, but for this work we take w=0. The rate parameter is expressed in the form

$$k = k_0 \times \exp\left(-\frac{E}{k_b T}\right) + k_m \tag{4}$$

Correlation	A_d ($m^2 s^{-1}$)	Q_d / R (K)	A_C ($kg \times m^{-2}$)	Q_C / R (K)
Leistikov	$7.82 \cdot 10^{-6}$	20214	52.42	20962
Cathcart-Pawel	$2.25 \cdot 10^{-6}$	18062	36.22	20100
Prater-Courtright	$2.98 \cdot 10^{-3}$	28420	$3.3 \cdot 10^{3}$	26440

Table 1: Parameters of the oxide scale (δ) and mass gain (χ) correlations [11].

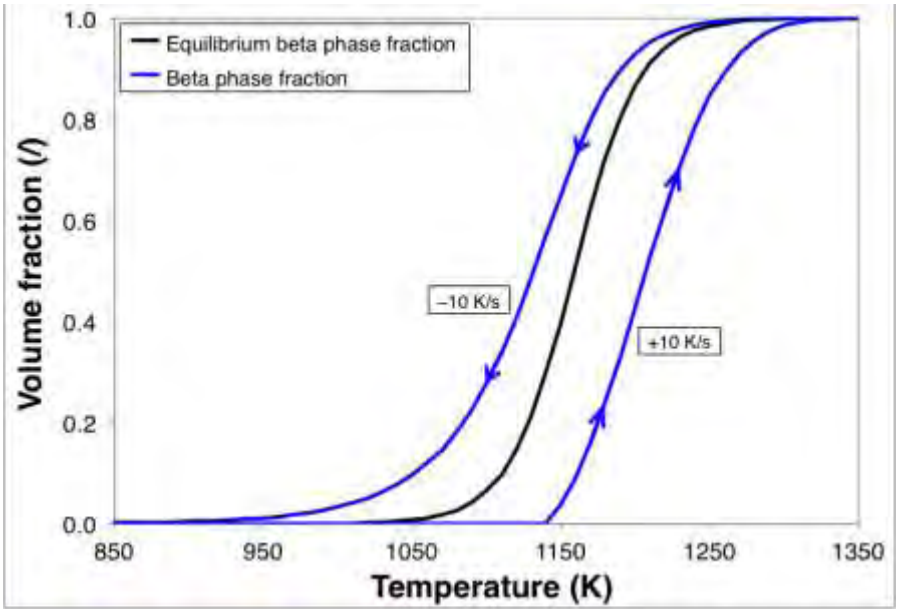

Fig. 2. Calculated volume fraction of β phase as a function of temperature. Equilibrium conditions (slow temperature variation) and temperature variation rates of ±10 Ks^{-1} are considered.

where k_0 (s^{-1}) is a kinetic factor, E (J) an effective activation energy, k_b (J/K) the Boltzmann constant, and k_m (s^{-1}) a constant. For Zircaloy-4, $k_0 = 60457+18129|Z|$ s^{-1} and $E/k_b = 16650$ K [17,19] are used, where Z = dT/dt is the heat rate in the range $0.1 \leq |Q| \leq 100$ Ks^{-1}. The $\alpha \rightarrow \beta$ transformation is purely diffusion-controlled, while the $\beta \rightarrow \alpha$ transformation is partly martensitic. This is represented by the constant k_m given in the form [19]

$$\begin{cases} k_m = 0 & a \rightarrow b \\ k_m = 0.2 & b \rightarrow a \end{cases} \tag{5}$$

The starting temperatures for the onset of $\alpha \rightarrow \alpha+\beta$ and $\beta \rightarrow \alpha+\beta$ phase transformations are calculated as [17]

$$T_{a \rightarrow a+b} = \begin{cases} 1083 - 0.152w & 0 \leq Z < 0.1\,Ks^{-1} \\ \left(1113 - 0.156w\right) Z^{0.0118} & 0.1 \leq Z \leq 100\,Ks^{-1} \end{cases} \tag{6}$$

$$T_{a \rightarrow a+b} = \begin{cases} 1300 & -0.1 < Z < 0\,Ks^{-1} \\ 1302.8 - 8.333\left|Z\right|^{0.477} & -100 \leq Z \leq -0.1\,Ks^{-1} \end{cases} \tag{7}$$

for 0≤w≤1000 wppm. The calculated volume fractions of β phase as a function of temperature at equilibrium and for temperature variation rates of ±10 Ks^{-1} are shown in Fig. 2.

2.3 Cladding creep

During a LOCA, outward creep deformation of the cladding tube under the effect of internal pressurization and high temperature drives cladding ballooning and eventual failure due to burst. In BISON, the stress and strain tensors are updated at each mesh location and time step based on the strain increments due to different contributions, both elastic and non-elastic. The increments of the effective creep or plastic strain can be defined through an optional non-linear function of the effective stress. The large creep deformation of the cladding is defined by a strain rate correlation in the form of a Norton power equation [5,20,21]

$$\dot{\varepsilon}_{eff} = A_{cr} \times \exp\left(-\frac{Q_{cr}}{RT}\right) \times \sigma_{eff}^{n} \tag{8}$$

Phase	$\dot{e}_{eff}$ (s^{-1})	A ($MPa^{-n}s^{-1}$)	Q (J/mol)	n (-)
α	any	8737	321000 + + 24.69·(T-923.15)	5.89
50%-α 50%-β	$\leq 3\cdot10^{-3}$	0.24	102366	2.33
	$>3\cdot10^{-3}$	Lin. Interp. ln(A)	Lin. Interp.	Lin. Interp.
β	any	7.9	141919	3.78

Table 2: Material parameters used to calculate creep of Zircaloy-4 [20,21].

where $\dot{e}_{eff}$ (s^{-1}) is the effective strain rate, A_{cr} ($MPa^{-n}s^{-1}$) the strength coefficient, Q_{cr} (J/mol) the activation energy for the creep deformation, T (K) the temperature, σ_{eff} the effective (Von Mises) stress, and n (-) the stress exponent. The components of the strain tensor are then updated at each time step based on the effective strain increment and a flow rule. The material parameters (Table 2) used in the model were obtained from tension tests on Zircaloy-4 tubes [20,21]. In the mixed phase ($\alpha+\beta$) region, interpolations are made to calculate the Norton parameters. Depending on the strain rate, different approaches are adopted [20]:

- For $\dot{e}_{eff} \leq 3\cdot10^{-3}$ s^{-1}, linear interpolation of ln(A), n, and Q is made between the values for pure α and middle of $\alpha+\beta$ (50%-α 50%-β) phase, and between 50%-α 50%-β and pure β phase.
- For $\dot{e}_{eff} > 3\cdot10^{-3}$ s^{-1}, it is assumed that the values of ln(A), n, and Q vary linearly between the values for pure α and pure β phase.

To perform the interpolation, the fraction of each phase calculated from a dedicated model as described in Section 2.2 is used. The effective creep strain rate as a function of temperature for different stress values is illustrated in Fig. 3.

2.4 Cladding burst criterion

The BISON criterion to model failure due to burst of Zircaloy-4 claddings is based on the work of Erbacher et al. [21]. The criterion assumes that the time of burst is reached when the local hoop stress equals a limiting burst stress. Based on experimental evidence, the burst stress is

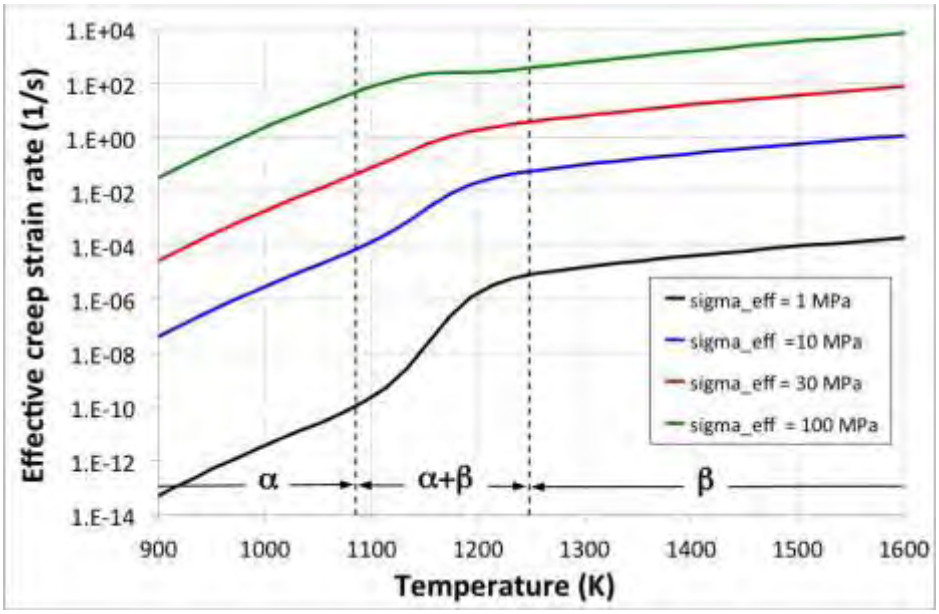

Fig. 3. Effective creep strain rate of Zircaloy-4 as a function of temperature for different values of the effective stress. The approximate temperature regions corresponding to the different crystallographic phases of the material are highlighted.

considered to depend on the temperature and oxygen concentration in the cladding, and is represented by [21]

$$\sigma_b = a \times \exp(-bT) \times \exp\left[\left(\frac{h - h_0}{9.5 \times 10^{-4}}\right)^2\right] \quad (9)$$

where σ_b (MPa) is the burst stress, a (MPa) and b (K^{-1}) are constants determined experimentally, and η (-) is the oxygen weight fraction in the cladding. An oxygen weight fraction at fabrication, $\eta_0 = 1.2 \cdot 10^{-3}$, is considered [21]. The current oxygen weight fraction is computed based on the oxygen mass gain from the oxidation model (Section 2.1) as

$$h = \frac{2 r_{cl,o}}{\rho_{Zy} \times \left(r_{met,o}^2 - r_{cl,i}^2\right)} \times c + h_0 \quad (10)$$

where $r_{cl,o}$ (m) is the cladding outer radius, ρ_{Zy} = 6550 kg·m^{-3} the density of the cladding metal, $r_{cl,i}$ (m) the cladding inner radius, and $r_{met,o} = r_{cl,o} - \delta/R_{PB}$ with R_{PB} = 1.56 being the Pilling-Bedworth ratio for Zr. The values for the parameters a and b are given in Table 3. In the mixed phase ($\alpha+\beta$) region, linear interpolations of ln(a) and b are made between the values for pure α and middle of $\alpha+\beta$ (50%-α 50%-β) phase, and between 50%-α 50%-β and pure β phase [21]. The volume fractions of each phase are calculated by the phase transformation model described in Section 2.2.

3. Simulation of ballooning experiments

The models described in Section 2, and their mutual interactions, have been incorporated in the thermo-mechanics framework of the BISON code. As a first step of validation, the extended version of BISON was applied to the simulation of cladding ballooning and burst experiments, as discussed hereinafter.

3.1. Experiments

The considered experiments are single-rod transient tests in steam performed within the REBEKA program [21-23]. The tests were performed on single PWR-size Zircaloy-4 tubes at a variety of internal pressures and heating rates to establish data with reference to LOCA conditions. The cladding tubes had a fabricated inner/outer diameter of 9.30/10.75 mm, with a 325 mm heated length. The cladding was heated indirectly by conduction heating from inside using an electrically insulated heater rod. The cladding tube, the heater rod and conductive materials that simulate the fuel column in a fuel rod are assembled into the complete fuel rod simulator. For internal pressurization of the cladding tubes, helium was used. The test parameters covered a range of 10 to 140 bar for the internal rod pressure and 1 to 30 K/s for the heating rate. The test atmosphere was almost stagnant steam at atmospheric pressure and 473 K. Each test was initiated after the test assembly was equilibrated at an initial temperature condition of about 573 K, and the helium pressure was adjusted to the desired value. Experimental observations included burst temperature and hoop strain, and the physical appearance of the ruptured tube. In order to achieve well-defined experimental boundary conditions, the internal overpressure and the heating rate were kept constant during the deformation process. The cladding temperatures were measured

Phase	a (MPa)	b (K^{-1})
α	830	$1 \cdot 10^{-3}$
50%-α 50%-β	3000	$3 \cdot 10^{-3}$
β	2300	$3 \cdot 10^{-3}$

Table 3: Material parameters used to calculate the burst stress [21].

by thermocouples spot-welded on the outer surface of the cladding. More details on the experimental apparatus and conditions are given in [21-23]

3.2 Setup of calculations

Both 2D axisymmetric and 3D BISON models of the cladding tubes tested during the REBEKA experiments were built. For simplicity, only the heated length was modelled, and the internal electric heating was simulated by a time-dependent Dirichlet temperature boundary condition applied to the tube inner wall and consistent with the experimental conditions. In particular, a parabolic temperature profile has been considered which results from the uniform axial power generation in the heater rod [23]. To estimate the temperature variation over the heated length of the cladding, calculations of axial heat conduction within the fuel rod simulator and convection to the outer steam atmosphere were performed, based on available information on materials and experimental conditions [21-23]. The considered temperature profile is symmetric with respect to the tube mid-plane. Gas pressure is allowed for by a uniform Dirichlet pressure boundary condition applied to the tube inner wall. Taking advantage of the symmetry of the problem, only the lower half of the heated cladding length was modelled. For the 3D simulations, a quarter of the cladding circumference was modelled.

3.3 Results and discussion

Using the 2D axisymmetric model, BISON simulations were conducted of the REBEKA experiments considering the range of 1 to 14 MPa for the internal cladding pressure and a heating rate of 1 K/s. Fig. 4 shows contour plots of temperature, creep strain magnitude, and locations where the local stress reached the limiting burst stress (Section 2.4) for the case with 10 MPa internal pressure; results are shown at the time of cladding burst. The creep strain magnitude (-) is defined as

$$e_{cr,mag} = \sqrt{\frac{2}{3}\mathbf{e}_{cr} : \mathbf{e}_{cr}} \tag{11}$$

where $\mathbf{e}_{cr}$ is the creep strain tensor. The cladding ballooning effect as reproduced by BISON is

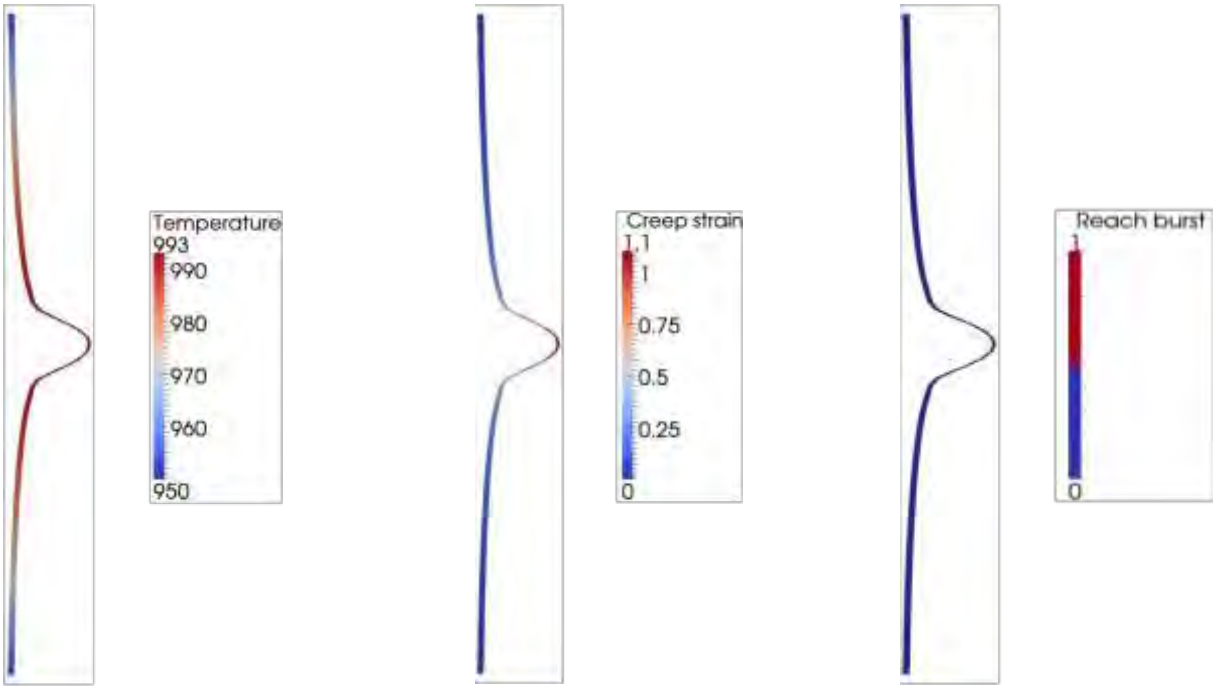

Fig. 4. Contour plots for the BISON 2D simulation of the REBEKA test with 10 MPa internal pressure at the time of cladding burst. The results for the lower half of the heated cladding are mirrored to obtain a full-length view. The plots are magnified 4x in the radial direction for visualization.

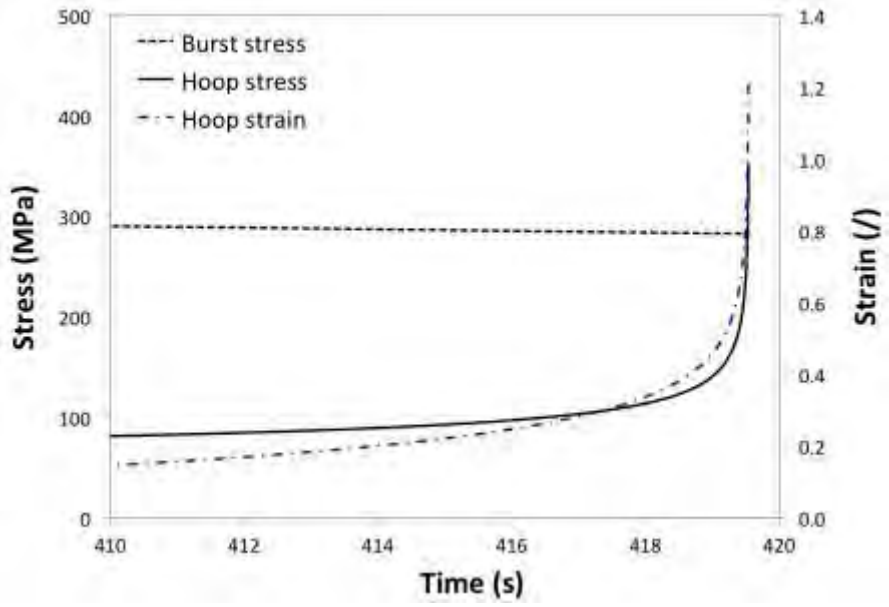

Fig. 5. Time evolution of burst stress, hoop stress, and hoop strain at the cladding mid-section in proximity of time of burst. The results refer to the BISON simulation of the REBEKA test with 10 MPa internal pressure.

obvious. Cladding failure due to burst is predicted at a temperature of about 993 K and a creep strain magnitude of about 1.1, which reasonably conform to experimental observations [21,23]. The burst stress is first reached in the cladding mid-section of the cladding, which is characterized by the largest strain and hence by the highest thinning. The time evolution of the hoop stress and burst stress in the cladding mid-section in proximity of time of burst are plotted in Fig. 5. The corresponding hoop strain is also shown. The stress increases under the effect of the constant inner pressure as the cladding wall thins due to the large creep strain. The burst stress decreases over time due to increasing temperature and progressive cladding oxidation (and in general also due to phase transformation, not observed at the temperatures reached in this specific case). The calculated time evolution of the cladding hoop strain is consistent with the experimental observations [22].

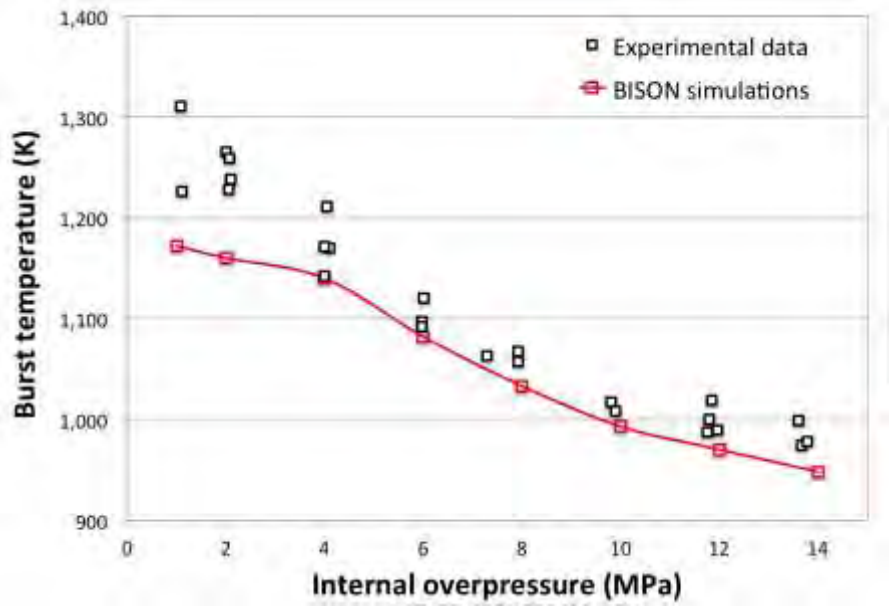

Fig. 6. Comparison between BISON predictions and experimental data of burst temperature for the simulations of the REBEKA tests with heating rate of 1 K/s. The experimental data have been digitized from [23].

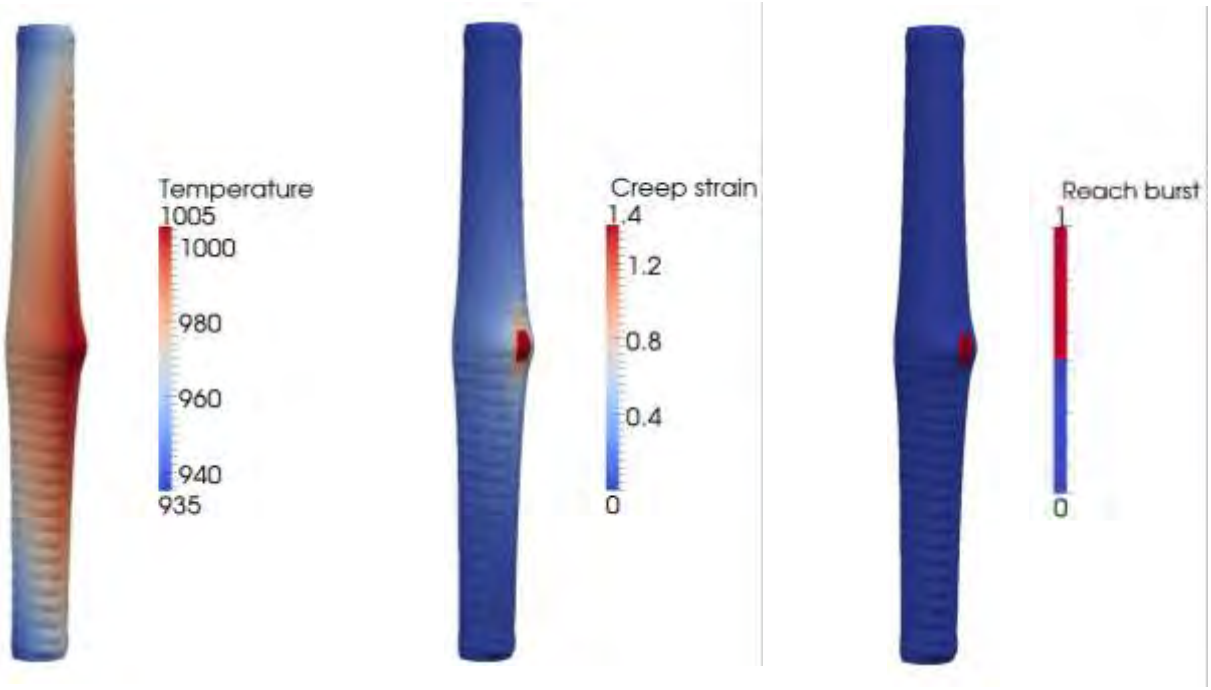

Fig. 7. Contour plots for the BISON 3D simulation of the REBEKA test with 10 MPa internal pressure at the time of cladding burst. The results for the lower quarter of the heated cladding are mirrored to obtain a full-length, half circumference view. The plots are magnified 3x in the radial direction for visualization. The blur zones are due to the adopted visualization tool.

As a first step of validation of the extended BISON code, the predictions of burst temperature for the full 1-14 MPa range of internal cladding pressure are compared to the available experimental data in Fig. 6. The trend of increasing burst temperature with decreasing internal pressure is reproduced, and the quantitative accuracy of predictions is encouraging. Discrepancies may be due to uncertainties inherent in the cladding mechanics, oxidation and phase transformation modelling, 3-dimensional effects (azimuthal temperature differences) that cannot be captured by the 2D model, as well as measurement uncertainties.
To investigate inherently 3-dimensional aspects such as the effect of azimuthal temperature differences, BISON 3D simulations have been conducted. A parabolic axial temperature profile consistent with the corresponding 2D simulation has been considered. In addition, an azimuthal temperature variation has been included with a maximum difference of 30 K, in conformity with available thermocouple measurements [22]. Azimuthal temperature differences are expected to play a significant role in cladding deformation and burst behaviour [21]. BISON results are presented here for exemplifying case of 10 MPa internal pressure at the time of cladding burst. Fig. 7 shows contour plots of temperature, creep strain magnitude, and locations where the local stress reached the limiting burst stress. The 3D simulation reproduces the non-uniform cladding ballooning and a localized burst on the hottest side of the cladding, consistently with experimental observations [22]. Note that the predicted burst temperature (1005 K) is higher than for the corresponding 2D simulation, and closer to the experimental range (1008-1017 K), thus indicating that capturing 3D aspects such as the effect of azimuthal temperature differences may be of importance in terms of accuracy of fuel analyses during LOCA accidents.

4. Conclusions

In this paper, an account was given of recent developments of the BISON fuel performance code relative to modelling of LWR fuel rod behaviour during LOCA accidents. BISON models were described for the behaviour of the Zircaloy cladding under LOCA conditions, including high-temperature steam oxidation, crystallographic phase transition, large creep deformation leading to ballooning, and failure due to burst. BISON simulations of single-rod tests of Zircaloy-4 cladding ballooning and burst under representative LOCA conditions were

performed using two-dimensional axisymmetric models, demonstrating a consistent reproduction of the experimental behaviour. Moreover, the comparison between BISON predictions and experimental data of cladding burst temperature at different cladding internal pressures pointed out an encouraging predictive accuracy. In addition, BISON three-dimensional simulations were carried out, which permit reproduction of the significant effect of azimuthal temperature variations.

Acknowledgements

The submitted manuscript has been authored by a contractor of the U.S. Government under Contract DE-AC07-05ID14517. Accordingly, the U.S. Government retains a non-exclusive, royalty-free license to publish or reproduce the published form of this contribution, or allow others to do so, for U.S. Government purposes.

References

[1] K. Lassmann, *Nucl. Eng. Des.*, 57, 17 (1980).
[2] C. Calvin and D. Nowak, High Performance Computing in Nuclear Engineering, in: Handbook of Nuclear Engineering, vol. 12, pp. 1449-1517, D.G. Cacuci, Ed., Springer Science + Business Media, LLC., New York, NY, USA (2010).
[3] S. Bragg-Sitton, L. Ott, K. Robb, M. Farmer, M. Billone, R. Montgomery, C. Stanek, M. Todosow, N. Brown, Tech. Rep. INL/EXT-13-30226, Idaho National Laboratory, ID, USA (2014).
[4] S.J. Zinkle, K.A. Terrani, J.C. Gehin, L.J. Ott, L.L. Snead, *J. Nucl. Mater.* 448, 374 (2012).
[5] P. Van Uffelen, C. Győri, A. Schubert, J. van de Laar, Z. Hózer, G. Spykman, *J. Nucl. Mater.* 383, 137 (2008).
[6] R.L. Williamson, J.D. Hales, S.R. Novascone, M.R. Tonks, D.R. Gaston, C.J. Permann, D. Andrs, R.C. Martineau, *J. Nucl. Mater.* 423, 149 (2012).
[7] J.D. Hales, R.L. Williamson, S.R. Novascone, D.M. Perez, B.W. Spencer, G. Pastore, *J. Nucl. Mater.* 443, 531 (2013).
[8] P. Medvedev, Tech. Rep. INL/EXT-12-27183 Revision 1, Idaho National Laboratory, ID, USA (2012).
[9] P. Medvedev, Tech. Rep. INL/EXT-13-30006, Idaho National Laboratory, ID, USA (2013).
[10] K.E. Metzger, T.W. Knight, R.L. Williamson, Model of U_3Si_2 fuel system using BISON fuel code, in: Proceedings of the International Congress on Advances in Nuclear Power Plants - ICAPP 2014, Charlotte, NC, USA, April 6–9, 2014.
[11] G. Schanz, Tech. Rep. FZKA 6827, SAM-COLOSS-P043 (2003).
[12] S. Leistikow, G. Schanz, H.v. Berg, A.E. Aly, Comprehensive presentation of extended Zircaloy-4/steam oxidation results 600-1600 C, in: Proc. CSNI/IAEA specialists meeting on water reactor fuel safety and fission product release in off-normal and accident conditions, Riso Nat. Lab., Denmark, 1983.
[13] J.V. Cathcart, R. E. Pawel, R. A. McKee, R. E. Druschel, G. J. Yurek, J. J. Campbell, S. H. Jury, Tech. Rep. ORNL/NUREG-17 (1977).
[14] J.T. Prater, E.L. Courtright, Tech. Rep. NUREG/CR-4889, PNL-6166 (1987)
[15] F. Garzarolli, W. Jung, H. Schoenfeld, A.M. Garde, G.W. Parry, P.G. Smerd, Tech. Rep. EPRI-NP 2789, Palo Alto, CA, USA (1982).
[16] F. Garzarolli, M. Garzarolli, PWR Zr alloy cladding water side corrosion – State of Knowledge on In-PWR Corrosion Analysis Methods of Measured Oxide Data and Oxide Thickness Prediction, Advanced Nuclear Technology International, Mölnlycke, Sweden (2012).
[17] A.R. Massih, *J. Nucl. Mater.* 384, 330 (2009).
[18] A.R. Massih and L.O. Jernkvist, *Modelling Simul. Mater. Sci. Eng.*, 17, 055002 (2009).
[19] A.R. Massih, Tech. Rep. TR11-008V1, Quantum Technologies AB, Sweden (2011).
[20] H. J. Neitzel, H. E. Rosinger, Tech. Rep. KfK 2893, Kernforschungszentrum Karlsruhe, Germany (1980).
[21] F.J. Erbacher, H.J. Neitzel, H. Rosinger, H. Schmidt, K. Wiehr, Burst criterion of Zircaloy fuel claddings in a loss-of-coolant accident, Zirconium in the Nuclear Industry, Fifth Conference, ASTM STP 754, D.G. Franklin, Ed., American Society for Testing and Materials, pp. 271-283, 1982.
[22] M.E. Markiewicz, F.J. Erbacher, Tech. Rep. KfK 4343, Kernforschungszentrum Karlsruhe, Germany (1988).
[23] F.J. Erbacher, H.J. Neitzel, K. Wiehr, Tech. Rep. KfK 4781, Kernforschungszentrum Karlsruhe, Germany (1990).
[24] V. Di Marcello, A. Schubert, J. van de Laar, P. Van Uffelen, *Nucl. Eng. Des.* 276, 19 (2014).

MODELING OF THE RIM-STRUCTURE THERMAL ANNEALING EXPERIMENTS WITH A NEW FGR MODEL FOR START-3A CODE

D.A. CHULKIN, A.A. SHESTOPALOV, V.I. KUZNETSOV, V.V. NOVIKOV
JSC VNIINM
Rogova 5A st., Moscow, Russia

ABSTRACT

Model for the fission gas release for the high burnup structures of UO_2 fuel was developed. The presented model treats the rim-structure as the diffusion media with the same diffusion coefficient as the non-restructured fuel. The specific high-burnup structure parameters, such as increased intergranular porosity and decreased grain size are described by the model parameter of the effective diffusion domain size.
The model was verified against three thermal annealing tests (with burnups of the samples ~ 100 MWd/kgU) and irradiation experiments from the verification matrix of the international project held by IAEA – FUMEX-III (maximum fuel rods average burnup ~ 81 MWd/kgU).
Calculated temperatures and time frames for the increased fission gas release from the thermally treated high burnup structure specimens are in the reasonable agreement with the experiment.
During the first stage of the heating, fission gas release process might be strongly influenced by the microcracking if heating rate exceeds 0.4 K/s. This process was modelled for the samples of high burnup structured fuel that was heated with the rate of 0.5 K/s. Modeling results are in the reasonable agreement with the experiment.

1. Introduction

At the pellet average burnups of about 45-50 MWt·d/kgU and the irradiation temperatures below 1373 K the so-called high burnup structure (HBS, or the rim-structure) starts its formation at the edges of the UO_2 pellets. It differs from the non-restructured fuel by the decreased grain size with diameters of ~0.3 mkm and abundance with large micrometric gaseous pores [1-10]. When the local burnups reach 75 MWt·d/kgU, the structure of the fuel usually is completely transformed into high burnup structure.

There are different opinions on the HBS contribution to the total the fission gas release. Some authors suggest that this contribution is major, since there are additional grain boundaries in the restructured region that increase the ability of the fission gas products to escape from the pellet [11]. Nevertheless, the more common point of view is that the most of the gas, generated in the high burnup structures, remains there [12], since it becomes trapped in the closed porosity.

In the modern fuel codes, the rim-structure is taken into account by means of rather complicated multi-parametric models [13,14].

In this paper, the fission gas release model for the HBS is presented and tested against the results of the several annealing tests. The high burnup structure is treated as the uniform media, in which the spherical grain of the uranium dioxide is taken as the diffusion domain, with the same diffusion coefficient as for the non-restructured fuel. The peculiarities of the rim-structure (e.g. porosity) are taken into account by means of the variation of the diffusion domain size.

The adequacy of this approach is tested with the following criterion – the model must adequately describe the high burnup structure annealing tests and the reactor experiments. This article is focused on the results of the verification against the annealing tests.

2. Porosity distribution and character in the rim

Fig.1 shows the peripheral areas of cross sections of the uranium dioxide pellets irradiated to the average burnups of 40.3, 59.6 and 66.6 MWd/kgU in commercial pressurized water reactor (PWR) from work of Spino et al [5] made with the optical microscope.

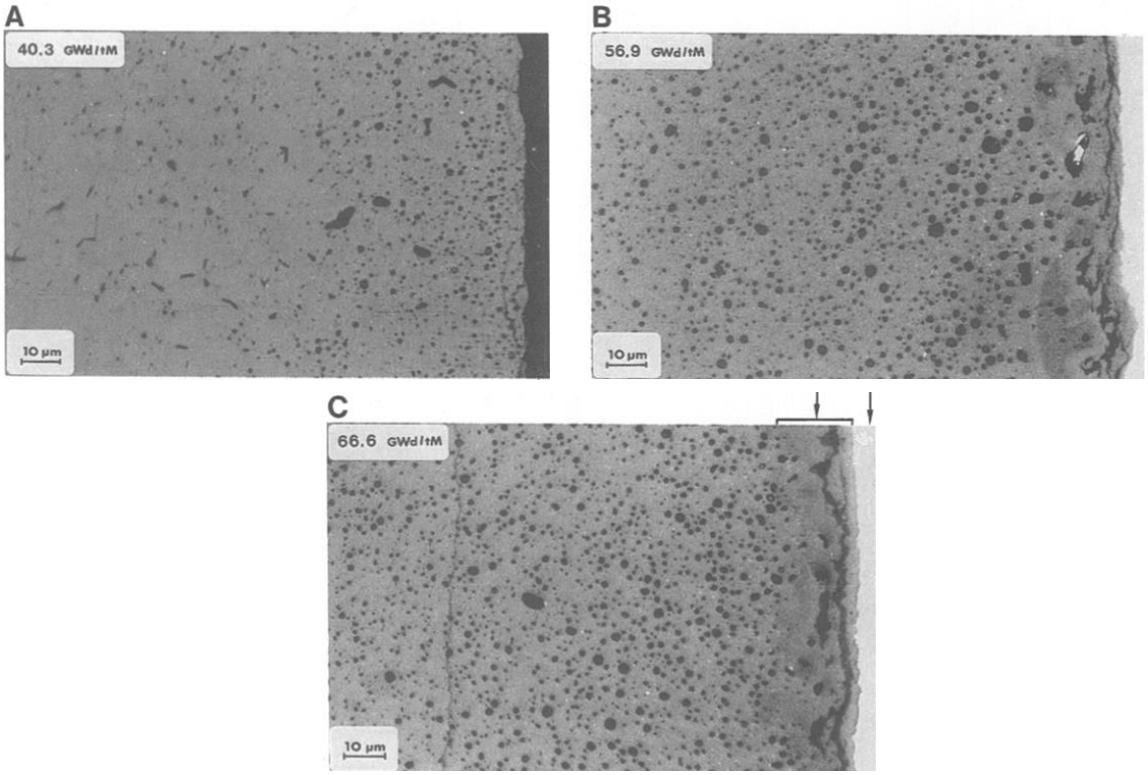

Fig. 1. The peripheral areas of cross sections of the uranium dioxide pellets irradiated to the average burnups of 40.3, 59.6 and 66.6 MWd/kgU, Spino et al [5].

The areas near the pellet edge are highly porous, and the thickness of this area grows with the average burnup.

The porosity of the pellet and the surface density of the pores (number/surface area) were calculated on the basis of these pictures. The characteristic pore size can be calculated using the average pore volume under the assumption that the pores are spherical. The calculated average pore diameter than is

$$D = \frac{\sum_{i=1}^{N} n_{Vi} D_i}{\sum_{i=1}^{N} n_{Vi}}; \qquad (1)$$

here D_i – is the pore diameter of the i-th pore size group; n_{Vi} - the volume density of the pores of the i-th group.

According to the calculations, the pore size is almost constant along the pellet radius for the given average burnup and belongs to the interval of 1.1<L<1.5 mkm. Fig.2a shows the distribution of the pores by size on the different radial distances along the pellet cross section at the average burnup of 40.3 MWd/kgU.

It can be seen that the number of the pores grows with the distance from the pellet center, and the average pore size stays almost the same. Furthermore, the average pore size does not change even with the increasing local burnup.

Figure 2b gives the distribution of the pores in the rim-zone for 3 different burnups. For comparison, the same figure shows the size distribution near the edge of the pellet and it's center [15] for the uranium dioxide fuel at the average burnup of 23 MWd/kgU. The average size of the pore does not change with the local burnup in the rim-zone.

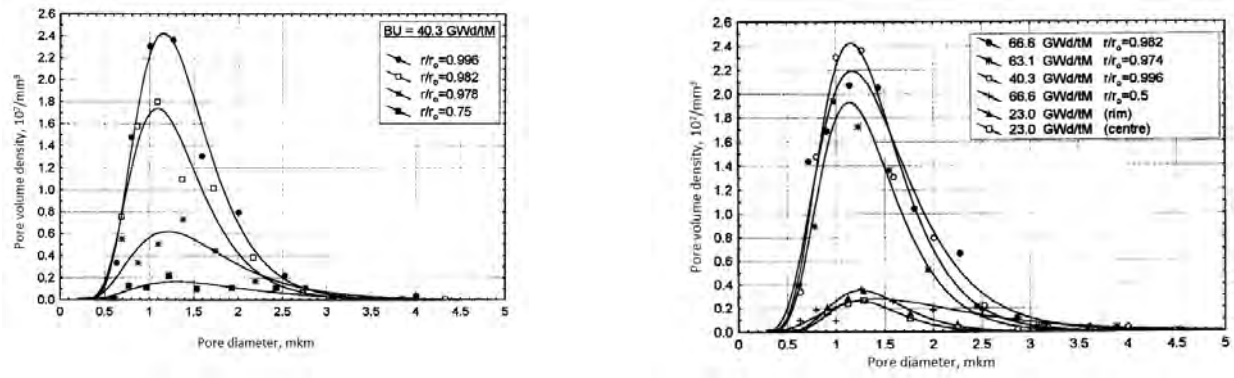

a) b)

Fig. 2. The distribution of the pores by size on the different radial distances along the pellet cross section at the average burnup of 40.3 MWd/kgU [5] (a) and the distribution of the pores in the rim-zone for three different burnups (b).

The solid lines in the figures 2 and 2b are the result of the normal distribution in the log scale fitting for the experimental results:

$$n_V(r) = \frac{N_V}{\sqrt{2\pi}\ln\sigma}\exp\left\{-\frac{\left[\ln r - \ln D\right]^2}{\ln\sigma}\right\} \qquad (2)$$

Here N_V and σ – are the fitting parameters of the approximation curve (2).

Figures 3a and 3b show the distribution of the porosity and the pore density in the uranium dioxide with different burnups. It can be seen that there is a sharp growth of the porosity and pore density at the pellet edge.

Solid lines on the figures 3a and 3b are the results of the approximation with the expression

$$\exp\left\{-\frac{A(r-a)}{r0}+C\right\} \qquad (3)$$

for the experimental points (*A*, *a* and *c* are the fitting parameters). Thus, the porosity at the rim grows exponentially with the distance from the pellet center, and the average pore size is 1-2 mkm.

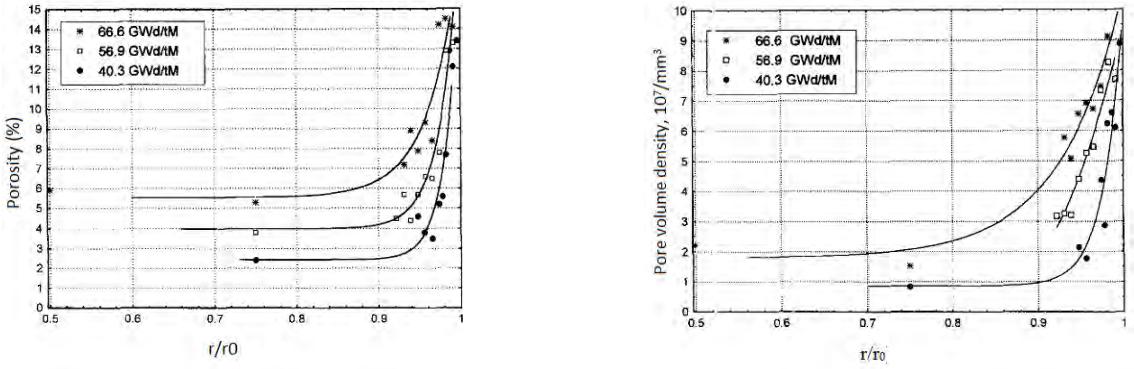

a) b)

Fig. 3. The radial distribution of the porosity in the uranium dioxide with different burnups (a) and the radial pore density distribution in the uranium dioxide with different burnups (b).

3. Fission gas release model

The model describing the fission gas products (FGP) thermal diffusion behavior in the UO_2 is based on the approach of the Lassmann et al. [13] and accounts for the following phenomena affecting the FGR from the pellet: FGP diffusion in the grain, FGP accumulation on the grain boundary, fission gas release through the open porosity and due to the percolation after the saturation of the grain boundary. FGP be behavior inside the grain is described by the following equation:

$$\frac{\partial C_t}{\partial t} = D_{eff}\,\frac{1}{r^2}\,\frac{\partial}{\partial r}\left(r^2\,\frac{\partial C_t}{\partial r}\right) + \beta \qquad (4)$$

here $C_t = C_s + C_b$, C_s – FGP monoatoms concentration, C_b – FGP concentration in the form of gas bubbles, D_{eff} – effective diffusion coefficient, β – source term .

The FGP behavior on the grain boundary is described as the saturation threshold model. As soon as the concentration of FGP at the grain boundary reaches certain value C_{thresh}, the fission gas products are released into the plenum immediately. Before that moment, only the FGR through the recoil, knockout and open porosity takes place.

4. Integral experiments

Figure 4 shows the irradiation histories and the results of the model application for two idealized irradiation histories of PWR fuel rods with high burnups (72 and 81 MWd/kgU) from the verification matrix of the START-3A code. These two high burnup irradiation histories were provided by AREVA during the participation in FUMEX-III, international project held by IAEA. The new model was implemented in the START-3A code alongside with the standard FGR model of the code [12] and its parameters were adjusted to match the results the standard model and the experimental data for integral experiments and the fractional release curve of the first thermal annealing test [16] (see 5.1).

The calculation of the annealing tests made it possible to evaluate the thermal FGR from the high burnup structures. The following set of parameters was finally adopted: threshold grain boundary concentration C_{thresh} = 6.022×10^{19} at/cm^2, effective diffusion coefficient D_{eff} = 5×10^{-9}×exp(-40262/T), diffusion domain size for high burnup structures d_{HBS}=2.0×10^{-8}. The local burnup threshold of ~60 MWd/kgU was used to treat the fuel as HBS at the edge of the pellet (r/r_{pellet}>0.5). The diffusion domain size evolution with burnup was implemented in the code in a form of Heaviside-like step-function with the normal domain size for the local burnup is below the threshold value and d_{HBS} for the local burnups more than ~60 MWd/kgU. Using these parameters, the new model was applied for the calculation of thermal annealing tests, which is described in 5.2 and 5.3. The used approach is somewhat conservative, and even in this case, the thermal fission gas release from the RIM was negligible during the calculation of the given integral cases.

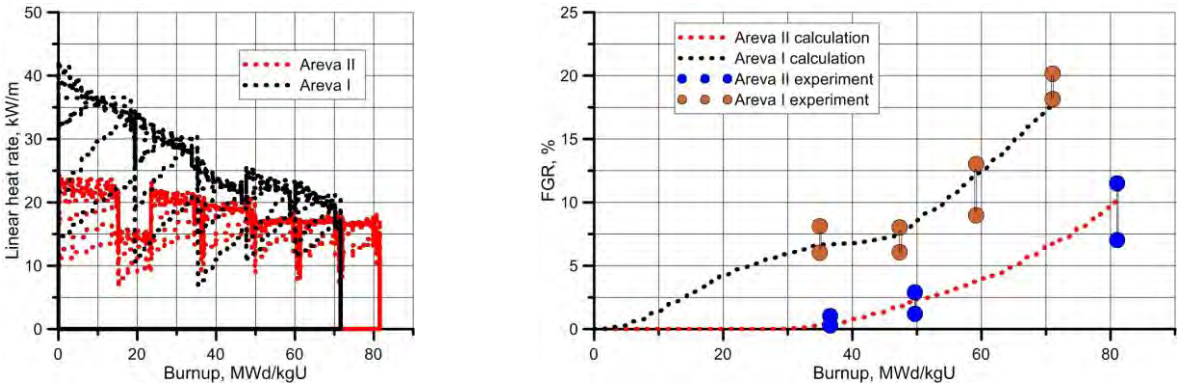

a) b)

Fig. 4. Irradiation histories of AREVA I and AREVA II high burnup cases of FUMEX-III project (a) and the results of the model application in START-3A code (b).

5. Thermal annealing experiments

5.1 Experiment of 2001 year

During the experiment [16] the sample of the rim (~95 MWd/kgU) was heated to the complete vaporization. The sample temperature versus time dependence is given in the figure 5. The model parameter that was varied in order to reproduce the results of the first annealing test was the diffusion domain size. The value of 2.0×10^{-8} for this parameter was derived from the calculation of this experiment and allowed to obtain satisfactory results in the second and the third calculated cases (5.2 and 5.3 correspondingly).

Figure 5 shows the comparison of the calculation results with the experimental data. The complete release of fission gas products occurred in 6000 s. The time of the increased FGP release (~2000 s) and the time when the most of the gas leaves the sample (~3000 s), calculated with the model, is in the reasonable agreement with the experiment.

Nevertheless, the experimental data shows only 80% release at the ~3000 s, unlike the calculation that gives a 100% fractional release. According to the experiment, the rest of the gas releases at the time of ~4500 s, when the temperature reaches the values of ~1800K, which is close to the activation of the gas bubbles movement in the fuel [17]. Possibly, some part of the gas is being held by biggest bubbles so strongly, that the fission gas release from them must be modelled separately.

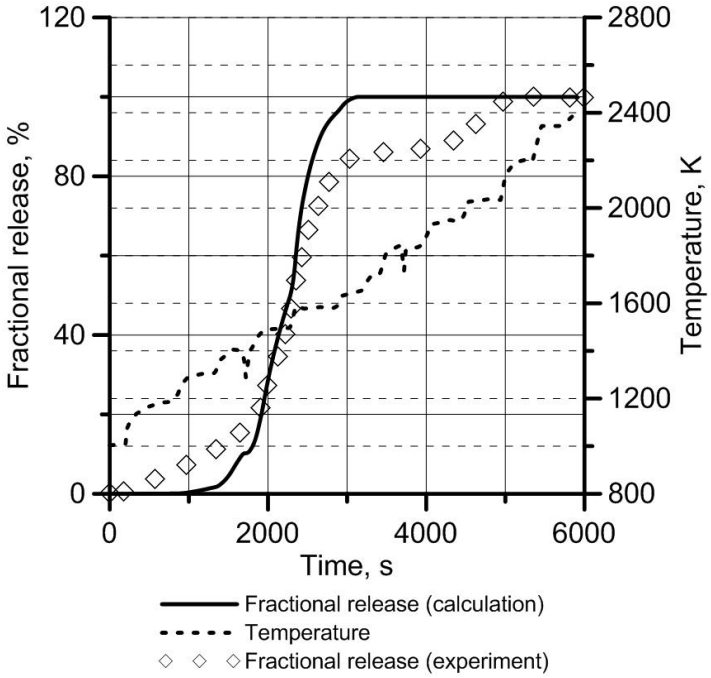

Fig. 5. Comparison of the calculation results with the experiment of 2001 year and the temperature versus time dependence of the rim-sample [16]

5.2 Experiment of 2008 year

During the experiment [18] the sample of the rim (~102 MWd/kgU) was heated to the complete vaporization with the heating rate 0.5 K/s. Figure 6 shows the comparison of the calculation results with the experiment. Experimental data shows that the first significant fission gas release starts at the temperature of 800 K and stops at the 1000 K with the 20% fractional release value. The calculation results that consider no microcracking do not demonstrate the same behaviour. Indeed, the heating rate of 0.5 K/s makes one suspect that the microcraking in the rim-sample has something to do with this 20% gas release step. Une et all. [19] suggest the rim-structure microcraking possibility starting from the heating rates of 0.4 K/s, basing on the series of the thermal annealing experiments.

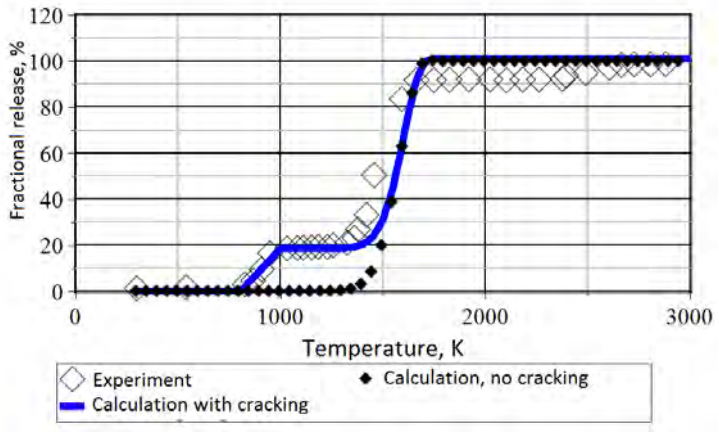

Fig. 6. Comparison of the calculation results with the experiment of 2008 year [18]

In order to model the fission gas release related to the microcraking, the model was supplemented with the following method. The FGP release speed caused by the flow of the

gas to the open surface was modified with the additional term proportional to the sample heating rate:

$$K_{crack} \cdot \frac{\partial T}{\partial t} \qquad (5)$$

here K_{crack} is the parameter that differs from zero only if the heating rate exceeds 0.4 K/s. Figure 6 shows that the result of the calculation with supplemented model is in satisfactory agreement with the experiment with the parameter $K_{crack} = 10^{-2}$. For the current calculation, the parameter was adjusted to fit the fractional release curve. Nevertheless, there are several ideas behind the approach of the fission gas release description in terms of the temperature derivative for microcracking. The common physical background behind them is the presence of the gas bubbles in the fuel that tend to expand during the heating, causing the surrounding material to form microcracks [20,21].

During the later heating, there is a further fission gas release increase that can be seen both on the modelling results and experimental data. Again, as in 5.1, one can see that the experiment shows some amount of the gas that remains trapped in the sample even in the high temperature range ~1700-2700 K, which is not reflected by the modelling, that shows 100% fractional release at the temperatures of 1700 K.

5.3 Experiment of 2014 year

During the experiment [22] several fuel disks were irradiated in the Halden Boiling Water Reactor (HBWR) up to the burnups of ~100 MWd/kgU. To lower the gradient of the temperature during the irradiation, the disks were placed between the molybdenum disks. Two of the irradiated disks were made of UO_2 with standard grain size (3d diameter of 18 mkm). It achieved burnup was 103 MWd/kgU and post-irradiation examination (PIE) results have shown that the high burnup structure with large gaseous bubbles was formed in the whole volume.
The very same disk was heated up to the temperature of ~1200°C. The heating rate (Fig. 9) was slow enough (0.2 K/s) to exclude the effects of microcracking on the fission gas release.

Figure 7 shows the comparison of the calculation results with the experimental data. The model with the parameters that were tested during the previous experiments could adequately predict the time and the duration of the fission gas release, but the predicted fractional release was 70% instead of measured 30%. In order to obtain the correct fractional release, the parameters of the model had to be adjusted, and still, the dynamics of the release was not quite good predicted. Probably, that is caused by the structural differences of the high-burnup structures that were obtained during the irradiation of the disks and during the commercial irradiation of the fuel pellets and some amount of the microcracking that was observed during the test and not yet considered in this simulation. For example, the authors of the experiment claim that the PIE has revealed pores of the larger sizes in the disks which can slow down the mobility of the fission gas products in the rim.

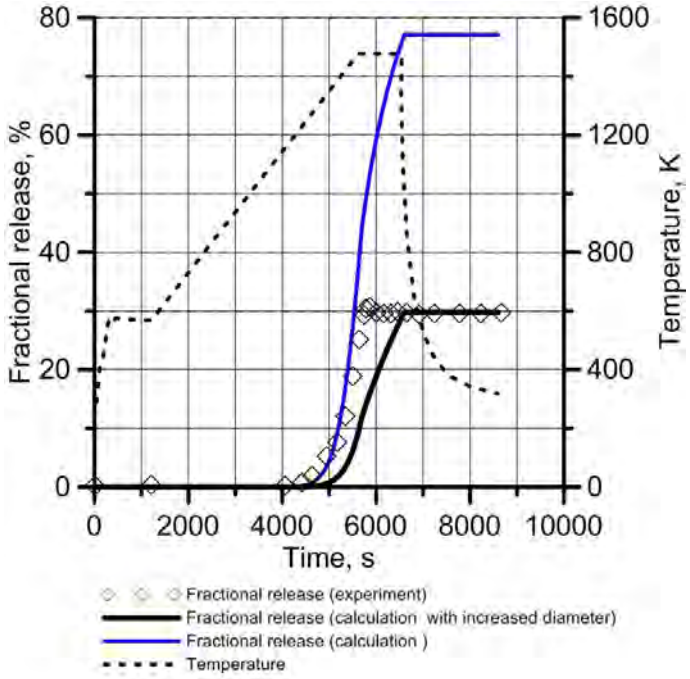

Fig. 7. Comparison of the calculation results with the experiment of 2014 year and the temperature of the rim-sample versus time [22]

6 Conclusion

The new model of the fission gas release from the high burnup structure was developed. This model is applicable in both stationary and transient modes of the fuel irradiation. The model is verified against the irradiation histories of the fuel rods from the START-3A code verification matrix with high burnups (72 и 81 MWd/kgU) and against the thermal annealing tests of the fuel samples with high burnups (95-103 MWd/kgU). The calculation results are in the reasonable agreement with the experiments.

During the calculation of the annealing test the model adequately reflects the fission gas release time and quantity for the commercially irradiated fuel, and it only adequately predicts the time of the release for the high burnup structure obtained during the irradiation of the thin UO_2 disks, which is probably related with the differences in the high burnup structure characteristics between the commercially irradiated fuel and fuel disks (the latter is claimed to have larger pores).

During the first stage of the fuel heating, the microcracking can cause a significant influence on the fission gas release from the rim if the heating rate exceeds 0.4 K/s. The modelling of this process was performed for the HBS sample with the burnup 103 MWd/kgU heated with the rate of 0.5 K/s. The results of the modelling are in the reasonable agreement with the experiment. To improve the model predictive capabilities in future it should be supplemented with the gas bubbles mobility description, since it tends to overestimate the fractional release at the high temperatures.

In general, the modelling results in the present article, and the results of the rim-structure annealing tests (the temperatures of the increased fission gas release start of about ~1400 K) show that the thermal fission gas release from high burnup structures can hardly be considered a dominant process for the usual in-pile temperatures.

7 Acknowledgements

The authors would like to thank Dr. Oleg Khomyakov from the National Research Nuclear University “MEPhI” for a fruitful discussion of the HBS-structure, model assumptions and calculation results.

8 References

1. M. Kinoshita, T. Sonoda, S. Kitajima, A. Sasahara, T. Kameyama, T. Matsumura, E. Kolstad, V. V. Rondinella, C. Ronchi, J. P. Hiernaut, T. Wiss, F. Kinnart, J. Ejton, D. Papaioannou, Hj. Matzke, High burnup rim project: (III) Properties of rim-structure fuel, Proceedings of the 2004 International Meeting on LWR Fuel Performance, Orlando, Florida, Sept. 19–22, 2004
2. N. Lozano, L. Desgranges, D. Aymes, J. C. Niepce, High magnification SEM observation for two types of granularity in a high burnup PWR fuel rim, J. Nucl. Mater., 257, 78 (1998).
3. R. Manzel, C. T. Walker, ‘‘EPMA and SEM of fuel samples from PWR rods with an average burn-up of around 100 MWd/kgHM,’’ J. Nucl. Mater., 301, 170 (2002).
4 H. J. Matzke, M. Kinoshita, ‘‘Polygonization and high burnup structure in nuclear fuels,’’ J. Nucl. Mater., 247, 108 (1997).
5. H. J. Matzke, J. Spino, ‘‘Formation of the rim structure in highburnup fuel,’’ J. Nucl. Mater., 248, 170 (1997).
6. K. Nogita, K. Une, ‘‘High resolution TEM of high burnup UO_2 fuel,’’ J. Nucl. Mater., 250, 244 (1997).
7. I. L. F. Ray, H. J. Matzke, H. Thiele, M. Kinoshita, ‘‘An electron microscopy study of the rim structure of a UO_2 with a burnup of 7.9% FIMA,’’ J. Nucl. Mater., 245, 115 (1997).
8. T. Sonoda, M. Kinoshita, I. L. F. Ray, T. Wiss, H. Thiele, D. Pellottiero, V. V. Rondinella, H. J. Matzke, ‘‘Transmission electron microscopy observation on irradiation induced microstructural evolution in high burn-up UO_2 disk fuel,’’ Nucl. Instrum. Methods B., 191, 622 (2002)
9. J. Spino, D. Papaioannou, ‘‘Lattice parameter changes associatedwith the rim-structure formation in high burn-up UO_2 fuels by micro X-ray diffraction,’’ J. Nucl. Mater., 281, 146(2000).
10. K. Une, K. Nogita, T. Shiratori, K. Hayashi, ‘‘Rim structure ofisothermally irradiated UO_2 fuel discs,’’ J. Nucl. Mater., 288, 20 (2001).
11. G. Khvostov et all, «Modelling of Rim-layer features in frames of START-3 code development» 2001, International conference on WWER fuel performance, modelling and experimental support; Varna (Bulgaria); 1-5 Oct 2001;
12. S. Bogatyr , D. Chulkin, V. Kuznetsov, V.Novikov, «PWR fuel rod modeling in the START-3 code at high burnup and transient conditions in the frameworks of FUMEX-III project», TOPFUEL-2012 transactions, Manchester, United Kingdom, 2-6 September 2012
13. Lassmann K., Schubert A., Van Uffelen P., Győri C., van de Laar J. (2011). TRANSURANUS Handbook, Copyright ©1975-2011, Institute for Transuranium Elements, Karlsruhe, Germany.
14. G. Khvostov, A. Medvedev, S. Bogatyr, ‘‘The dynamic model of grain boundary processes in high burn-up LWR fuel and its application in analysis by the START-3 code,’’ Proceedings of the International Conference on WWER Fuel Performance, Modelling and Experimental Support, Albena-Varna, Bulgaria, Sept. 29–Oct. 3, 2003 (2003)

15. J. Spino, K. Vennix, M. Conquerelle. Detailed characterisation of the rim microstructure in PWR fuels in the burn-up range 40–67 GWd /tM, JNM, 1996, v. 231, p. 179-190.
16. J. P. Hiernaut, C. Ronchi, ‘‘Fission gas release and volume diffusion enthalpy in UO_2 irradiated at low and high burnup,’’J. Nucl. Mater., 294, 39 (2001).
17. Szuta M., «Comparison of bubble diffusion rate during irradiation and annealing in the irradiated UO_2 fuel», Eighth International Conference on WWWR Fuel Performance, Modelling and Experimental Support, Helena Resort near Burgas, Bulgaria, from 26 September to 04 October, 2009»
18. J.-P. Hiernaut, T. Wiss, J.-Y. Colle, H. Thiele a, C.T. Walker, W. Goll, R.J.M. Konings, «Fission product release and microstructure changes during laboratory annealing of a very high burn-up fuel specimen»
19. K. Une, S. Kashibe, A. Takagi, ‘‘Fission gas release behavior from high burnup UO_2 fuels under rapid heating conditions,’’ J. Nucl. Sci. Tech., 43, 1161 (2006).
20. Chulkin et all, “FGR modeling of large grained fuel during transients by START-3A” Proceedings of the TOPFUEL 2013, 5-19 September 2013,
Charlotte, North Caroline, USA
21. Pastore et all, “Modelling of Transient Fission Gas Behaviour in Oxide Fuel
and Application to the BISON Code”, Proceedings of the EHPG meeting Røros Hotel, Norway, 7th-12th September, 2014
22. J. Noirot, Y. Pontillon, S. Yagnik, J.A. Turnbull, T. Tverberg, «Fission gas release behaviour of a 103 GWd/tHM fuel disc during a 1200 C annealing test», Journal of Nuclear Materials 446 (2014) 163–171

MULTIPHYSICS SIMULATION OF FAST TRANSIENTS WITH THE FINIX FUEL BEHAVIOUR MODULE

T. IKONEN, E. SYRJÄLAHTI, V. VALTAVIRTA, H. LOUKUSA, J. LEPPÄNEN, V. TULKKI
VTT Technical Research Centre of Finland
P.O. Box 1000, FI-02044 VTT - Finland

ABSTRACT

FINIX is a recently developed fuel behaviour module that is designed to provide "simple but sufficient" descriptions of the most essential fuel behaviour phenomena in multiphysics simulations. In such simulations, it is possible to obtain significant improvement in the feedback to neutronics or thermal hydraulics modelling even with a relatively simple fuel performance model. In this work, FINIX is used as an internal fuel behaviour module both in reactor physics and in reactor dynamics codes to simulate coupled behaviour in fast transient scenarios. With the Monte Carlo reactor physics code Serpent we model a prompt transient in a VVER-1000 pin cell, and with the reactor dynamics code HEXTRAN, a control rod ejection accident in a VVER-440 reactor.

1 Introduction

In light water reactors, the thermal and mechanical behaviour of the fuel rods strongly influences the behaviour of the reactor in both steady state and transient conditions. For example, the power of the reactor is sharply affected by the fuel temperature due to the absorption of neutrons by Doppler-broadened cross sections. This coupling is important both in the steady state and, even more so, in transients. Similarly, transient heat transfer to the coolant and avoiding departure from nucleate boiling is dependent on the heat conductance of the pellet-cladding gap. The gap conductance is a notoriously complicated function of both thermal and mechanical properties of the fuel rod. Therefore dedicated fuel behaviour codes are often used in multiphysics simulations to solve the heat transfer in the rod self-consistently with, for example, the reactor power calculated by a neutronics code.
However, the fuel performance code or the expertise for its use is not always available for the multiphysics modeller. Therefore a somewhat simpler approach has been studied at VTT, where the fuel behaviour module FINIX has been recently developed. The FINIX module adopts a middle-ground between elaborate fuel performance codes and thermal elements in order to give a "simple but sufficient" description of the fuel rod's thermal and mechanical behaviour. The aim is to make the fuel behaviour modelling more easily approachable to multiphysics modellers without imposing on them the complete fuel behaviour phenomenology, but still provide significant improvements to stand-alone simulation methods.
As examples of multiphysics simulations, we use the FINIX fuel behaviour module integrated into Serpent 2 Monte Carlo reactor physics code and HEXTRAN reactor dynamics code. As a demonstration of the dynamical capabilities of the Serpent-FINIX system we simulate a prompt transient, where the pin power and fuel temperature are solved self-consistently, leading to termination of the transient due to Doppler-broadening of the cross sections. With HEXTRAN-FINIX, we simulate a control rod ejection accident in a full-core geometry, where we use FINIX to evaluate the effect of burnup on the outcome of the transient. We also compare the results to stand-alone HEXTRAN simulations.

2 Description of the FINIX module

2.1 Role in a multiphysics code package

FINIX is a fuel behaviour module designed to be integrated as a subprogram into a larger simulation code, where FINIX replaces the existing fuel model. The main design philosophy of FINIX is to provide a simple but sufficient model of the fuel rod that can be used in different types of simulation codes, including neutronics, reactor dynamics, thermal hydraulics, and system codes. While multiphysics capabilities can also be achieved with direct code-to-code coupling (see, e.g., Refs. [1,2]), such approach is often laborious when highly specialized software is involved. Thus, in the design of the FINIX code, flexibility of the interface between FINIX and the main simulation code has been prioritized. This facilitates integration into a wide range of different simulation codes.

FINIX is integrated into the main simulation code, (the *host code*), at the source code level. This has the benefits of reduced data transfer between the codes, and allows the host code to have direct access to FINIX's functions and data structures. However, FINIX also has a high-level interface, through which the most common functionalities can be used without detailed knowledge of the FINIX data structures. In addition, to reduce the user's need for fuel-specific knowledge, FINIX has an internal database for different fuel types, from which the required fuel simulation parameters can be loaded in by just specifying the desired fuel rod type.

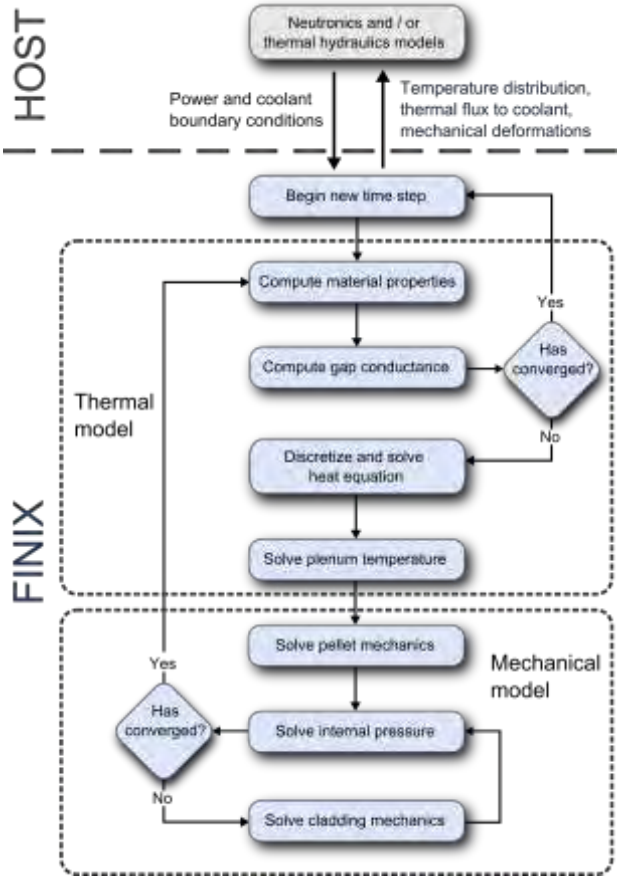

Figure 1. The models of the FINIX module and its role in a multiphysics simulation. The iteration of the thermal and mechanical solutions is indicated by the flowchart. The convergence checks are assumed to automatically fail on the first iteration.

2.2 Overview of models

FINIX is primarily designed as a transient simulation code. Compared full-fledged fuel performance codes such as FRAPTRAN [3], TRANSURANUS [4] and BISON [5], FINIX emphasizes flexibility and the needs of the host code in favour of the fuel performance modelling. For example for neutronics simulations of fast transients, the most important quantity to solve is the time-dependent temperature distribution. On the other hand, many of the phenomena modelled in fuel performance codes such as cladding irradiation growth are less important in this case and are currently not considered in FINIX. However, similar to the work of Ref. [6] and for example the fuel model of RELAP [7], the coupling between the mechanical behaviour of the gap and the radial heat transfer is modelled. Here FINIX takes an approach similar to FRAPTRAN, although some simplifications are done as described below.

The FINIX model itself involves solving both the thermal and mechanical behaviour of the fuel rod, allowing not only thermal effects but also changes in rod geometry to be taken into account in the host code. The thermal and mechanical models are coupled by the gap pressure and conductance, which are functions of both the rod temperature and mechanical dimensions. Both the heat equation and the mechanical behaviour are solved radially in one dimensional, cylindrical and axisymmetric geometry, independently for several axial nodes. The solutions of the different axial nodes are coupled via the gap pressure, which is solved simultaneously for the whole rod. This scheme constitutes what is generally referred to as the 1.5-dimensional model. The main modules of FINIX and their interrelationships are shown in Fig. 1. Properties such as thermal conductivity, thermal expansion, Young's moduli, coolant heat transfer, etc., are solved using publicly available correlations.

Currently FINIX is not equipped with modules to describe long-term evolution of phenomena such as cladding creep and oxidation, fuel swelling, and accumulation of fission products. FINIX thus lacks most of the models needed for simulating the effects of burnup accumulation over a long steady state irradiation. Therefore, for non-fresh fuel, the initial state of the fuel rod prior to the transient should be obtained by other means, for example from a FRAPCON [8] simulation.

For a comprehensive technical description of the FINIX module, the interested reader is referred to Refs. [9-11].

3 Serpent 2 simulation of VVER-1000 prompt transient

FINIX has been integrated into Serpent 2, a 3D continuous-energy Monte Carlo reactor physics burnup calculation code developed at VTT Technical Research Centre of Finland [12]. The development of Serpent 2 has a major focus on multi-physics applications. A universal multi-physics interface for code coupling is complemented with new methodology for the treatment of continuous temperature [13-15] and density [16] distributions. The recently implemented time dependent simulation mode [17] extends the applications of Serpent 2 even further. For further information on Serpent 2 see [18] and for the most recent multi-physics advances in Serpent 2 see [19].

3.1 Integration of FINIX into Serpent

The coupling of Serpent 2 and FINIX is done at the source code level. Serpent is responsible for solving the power distribution in the system while FINIX models the thermal and mechanical response of the fuel rod in transient or steady state conditions. The solution transfer between FINIX and the neutron transport part of Serpent is handled by a set of internal routines that form the fuel behaviour multi-physics interface in Serpent 2.

The fission power in fuel rod is tallied by Serpent and provided to FINIX nodes while conserving the total power generation as well as the local power generation in each node volume. The temperature solution calculated by FINIX can be used in Serpent as is with linear interpolation between the node points, without any mesh transformation. The changes in geometry obtained by FINIX can also be used in the neutron tracking without any transformation.

The multi-physics routines in Serpent 2 provide the neutron transport routines with the correct temperature and density distributions at different points in time and space so that the effect of the realistic temperature and density distributions can be accounted for in the interaction physics. The data transfer between Serpent and FINIX is done internally without disk operations.

For transient scenarios, before calculating the time-dependent solution, the steady state solution is obtained with the coupled system for the power level in question. This fuel behaviour solution is then used as the initial state of the fuel for the transient analysis. The steady state simulation is also used to create the initial neutron source for the transient simulation.

The time-dependent coupled solution is obtained by a sequential and iterative solving of the fission power distribution by Serpent and the temperature and strain distributions by FINIX. At the first iteration of a time step the temperature and strain distributions are taken from the end of the previous step and at the later iterations they are interpolated between the beginning of step (BOS) and end of step (EOS) distributions yielding a semi-implicit scheme. First the neutronics solution is obtained for the new time interval, after which the temperature distribution at the end of the interval is calculated by FINIX. A convergence criterion is applied after this and if the convergence of the coupled solution is not deemed sufficient, the neutronics solution for the next iteration can be obtained. The power distribution is relaxed over the different iterations.

3.2 Results and discussion

The simulation presented here is a prompt super-critical transient for a 2D VVER-1000 pin-cell. The geometry and material properties as well as the fuel rod specifications are taken from the UAM benchmark [20]. The goal of the simulation is to test and present the coupled calculation capabilities of the Serpent 2 – FINIX code system and should not be viewed as a realistic physical transient.

The pellet inner and outer radii were 0.070 cm and 0.378 cm respectively. The cladding inner and outer radii were 0.386 and 0.455 cm. The lattice pitch for the hexagonal unit cell was 1.275 cm. The fuel was pure UO_2 with the enrichment of 3.3 %. The cladding material was Zr + 1 % Nb. The coolant temperature was set to 560 K.

The fuel rod was depleted until the average burnup of 10 MWd/kgU with 10 radial depletion zones to yield the radial burnup distribution shown in Fig. 2(a). The depletion calculation was done without fuel behaviour feedback. The realistic radial burnup distribution affects the radial power density distribution as well as the fuel thermal conductivity in the FINIX thermal model.

For the coupled calculation, the FINIX model of the rod used 101 equally spaced nodes in the pellet and 51 in the cladding. The temperature and strain distributions were brought into Serpent at these nodes. The power distribution was tallied in 20 radial zones with equal area. The cladding outer temperature was set to 570 K as a boundary condition for the thermal model of FINIX.

The power distribution tallied on time interval *i* was used to calculate the end of the interval (EOI) temperature distribution for interval *i* as well as an initial guess for the EOI temperature distribution for interval *i+1.* A pointwise convergence criterion of 1 K was applied to the absolute difference between the temperature fields of subsequent iterations.

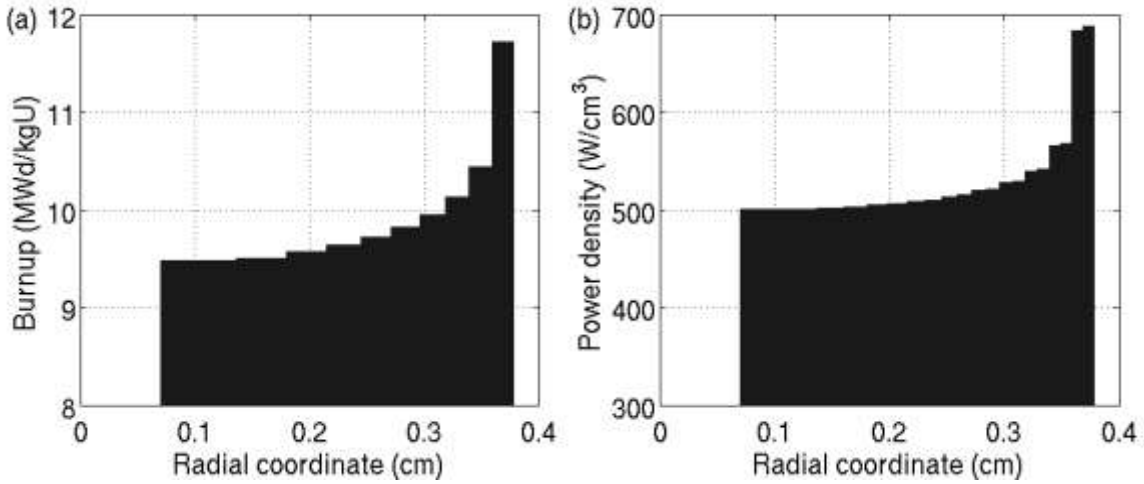

Figure 2. The radial burnup distribution (a) and the resulting power distribution (b) for the VVER1000 pin-cell at 10 MWd/kgU average burnup calculated by Serpent.

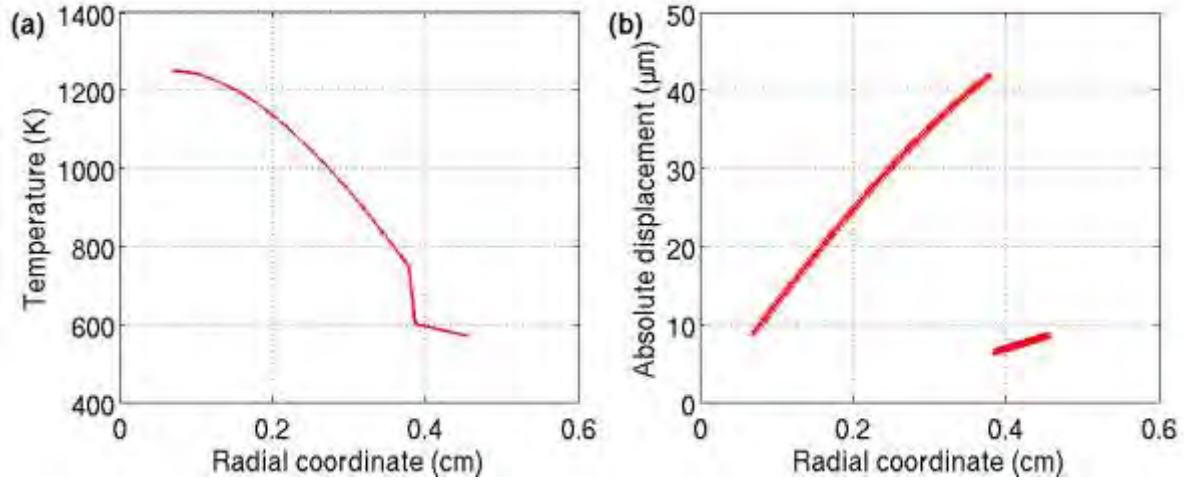

Figure 3. The steady state temperature (a) and strain (b) distributions in the VVER-1000 fuel rod.

An initial steady state coupled calculation was conducted for the depleted system. The system was held critical at 233 W/cm linear power with soluble absorber in the coolant. The resulting radial power density distribution in steady state at 233 W/cm linear power is shown in Fig. 2(b). The critical steady state fuel behaviour solution produces the radial temperature and strain distributions shown in Fig. 3. These were used as the initial conditions for the following time dependent simulation.

For the onset of the transient, the coolant boron concentration was decreased from 413 ppm to 345 ppm. This corresponds to an instantaneous reactivity insertion of 2575 pcm (4.4 $) and makes the system prompt super-critical. After this initial modification, the system was allowed to evolve freely from the initial conditions for 30 ms. Delayed neutron emission was not included in the transient. The prompt super-criticality of the system and the short timescale of the transient mean that the effect of delayed neutrons would be negligible, however.

Figure 4(a) shows the evolution of the system linear power over time. The time behaviour is an initial exponential increase in system power until the increase in fuel temperature shuts down the transient. The development of the centreline and pellet surface temperatures can be seen in Fig. 4(b). The temperature at the centreline reaches its maximum value of 2782 K at 20.9 ms. The temperature of the pellet surface drops sharply after the thermal expansion of the pellet brings it into contact with the inner surface of the cladding greatly decreasing the thermal resistance of the gas gap. The total deposited energy can be integrated from the linear power giving 3.49 kJ/cm.

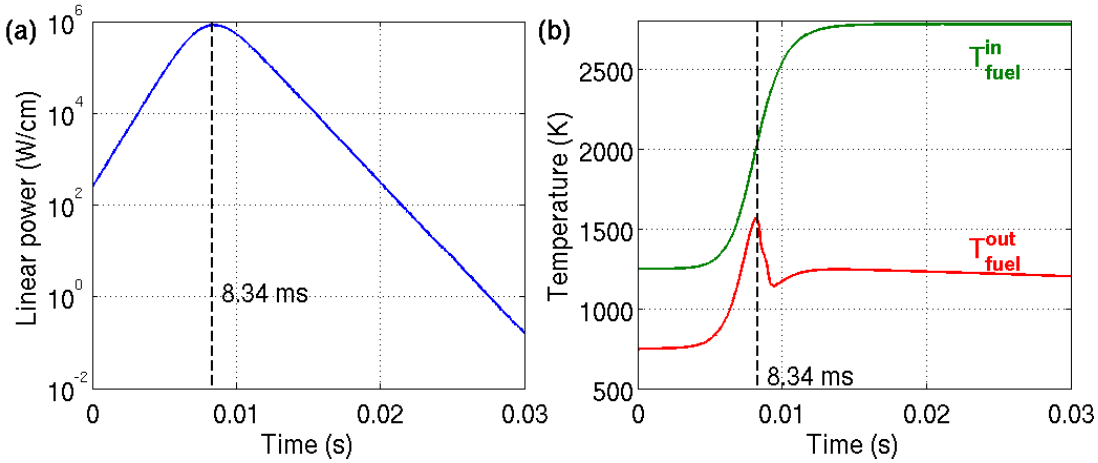

Figure 4. Evolution of system linear power (a) and rod centreline (green) and pellet surface (red) temperatures (b).

This calculation demonstrates the capabilities of the coupled code system to model a prompt power pulse starting from known initial conditions. The fission power and fuel behaviour are solved self-consistently and the code system captures the qualitative behaviour of the system very well. In a more realistic scenario, this simulation technique can solve both the size and shape of the power pulse and the values for interesting safety parameters such as pellet enthalpy and fuel and cladding maximum temperatures.

One of the main limitations of the Serpent – FINIX coupled code system at the moment is the omission of a delayed neutron emission model in the time dependent simulation mode of Serpent, limiting the applicability to fast transients. In longer transients, the coolant behaviour will also pay a greater role and has to be solved with a separate tool as has been done with e.g. the Serpent – SUBCHANFLOW coupled code system [21].

4 HEXTRAN simulation of VVER-440 rod ejection accident

4.1 Integration of FINIX into HEXTRAN

FINIX has also been integrated into the reactor dynamics code HEXTRAN [22] that is a coupled neutronics – thermal hydraulics code developed at VTT for transient and accident analysis of VVER reactors. HEXTRAN solves the two-group neutron diffusion equations with a nodal expansion method in a three-dimensional hexagonal fuel assembly geometry. Thermal-hydraulics of the reactor core is solved in separate one-dimensional hydraulic channels, which can be further divided into axial sub-regions. Usually each channel is coupled with one fuel assembly. Channel hydraulics is based on conservation equations for steam and water mass, total enthalpy and total momentum, and on a selection of optional correlations. During the hydraulics iterations, a one-dimensional heat transfer calculation is done for an average fuel rod of each assembly. HEXTRAN solves the heat transfer in a fuel rod on the basis of one-dimensional axially uncoupled equations using the theta method for time discretization. The heat capacity of the pellet and cladding and the conductivity of the cladding are given in input with temperature dependent correlations, whereas the heat conductivity of the pellet can also depend on burnup. Conductance of the gas gap is in

practice always modelled using linear interpolation from a simple temperature dependent table. It is possible to define several fuel rod types in HEXTRAN and provide separate values for each fuel rod type. In practice, the lack of proper data diminishes the reliability and feasibility of this kind of approach.

In the new coupling with FINIX, HEXTRAN's own fuel heat transfer solution can be replaced with the FINIX module. The choice between FINIX and HEXTRAN's own models is done in the HEXTRAN input. HEXTRAN solves the power distribution in the reactor core and the distribution is transferred to the FINIX module. Also the bulk coolant temperature and the heat transfer coefficient between the cladding outer surface and the coolant are calculated in HEXTRAN and are used as boundary conditions for FINIX. The FINIX calculation is done for one average fuel rod of each fuel assembly, in total 150-500 fuel rods depending on the reactor type. HEXTRAN controls the data for each fuel rod and calls FINIX consecutively with the current state parameters of one fuel rod. FINIX returns the temperature distribution of the fuel rod for the neutronics calculation and other data that has to be stored for the next time step. Deformation of the fuel rod is taken into account in the heat transfer solution but at the moment deformation is ignored in the flow channel modelling. The same axial discretization is used in FINIX and in HEXTRAN. A typical number of axial levels is approximately 20. Radially typically 6 to 10 nodes are used for the pellet and one node for the cladding. The same time step is used in FINIX and HEXTRAN.

4.2 Results and discussion

Here the FINIX module's capability for reactor dynamical simulations is demonstrated with the 3rd dynamic AER benchmark [23,24]. The benchmark concerns a control rod ejection in a VVER-440 reactor. The reactor is at the end of its first cycle. Inlet temperature, inlet and outlet pressures of the core and coolant flow through the whole core are kept constant during the transient calculation. Coolant flow corresponds to conditions in which three of the six main coolant pumps are on. The initiating event of the benchmark is the ejection of the follower-type control rod from hot zero power state of the reactor when all seven rods of one rod bank are inserted 200 cm and all other rods are fully out of the core. Height of the core is 250 cm and the control rod is fully out from the core in 0.16 seconds. No reactor trip is modelled. One average fuel rod from each of the 349 fuel assemblies has been modelled with FINIX.

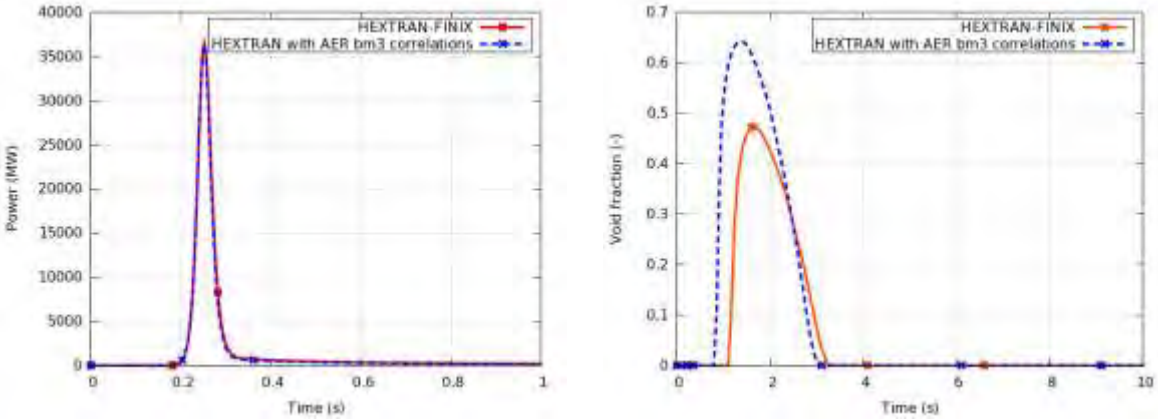

Figure 5. Fission power (left) and maximum void fraction at core outlet (right) during control rod ejection transient with the HEXTRAN code.

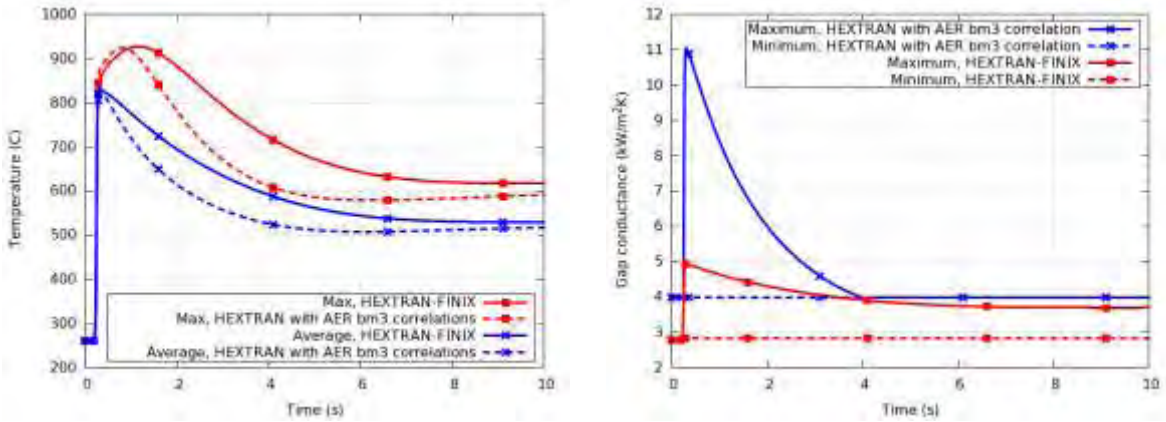

Figure 6. Fuel maximum temperature and maximum of fuel pellet average temperature (left) and the maximum and minimum gas gap conductances (right) during the control rod ejection transient with the HEXTRAN code.

In the reference case, HEXTRAN's own heat transfer model was used for the pellet and cladding temperature-dependent thermal conductivities and heat capacities that were defined in the benchmark specification. The thermal conductance was defined to depend on the average fuel temperature. Gap conductance has a constant value of 4 kW/Km^2 below 800 K, and increases linearly to 20 kW/Km^2 at 1500 K, above which the value is constant.

The control rod ejection induces a strong power increase, which is cut off due to the Doppler effect. Fission power behaves similarly with FINIX and with the reference correlations, as shown in Fig. 5. This is because at the time scale of the power transient, the relevant quantity is the fuel heat capacity, which is very similar in both models. However, the maximum void fraction at the core outlet is higher with the reference model, indicating a difference in heat transfer from the rods to the coolant. The gas gap conductance computed by FINIX is lower, and for that reason heat is transferred more slowly from the rods to the coolant. Consequently, the fuel rod temperature decreases more slowly as shown in Fig. 6.

The power transient is strongly asymmetric in the reactor core and for that reason also the fuel properties vary from one bundle to another. As an example, the maximum gap conductance of each fuel assembly 0.3 seconds after the control rod ejection is shown in Fig. 7(a). Dimensional changes of the gas gap in the fuel assembly in the vicinity of the ejected rod are also shown in Fig 7(b). The dimensions change mainly due to thermal expansion. In the reference calculation the fuel rod dimensions do not change.

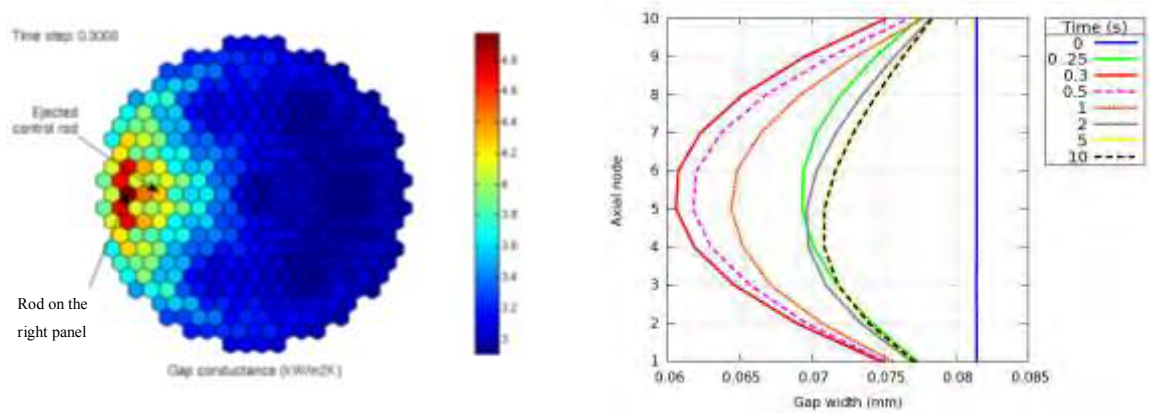

Figure 7. Maximum gas gap conductance in each fuel assembly 0.3 seconds after beginning of the control rod ejection (left) and time evolution of gas gap dimensions in a fuel assembly located near to the ejected control rod (right). The location of the fuel rod is shown on the left panel.

5 Summary

A light-weight fuel behaviour module FINIX has been developed. FINIX is aimed especially for multiphysics simulations, where it takes the role of the simulation's fuel behaviour model. FINIX has been designed to be integrated into a wide array of simulation codes, and to provide an identical description of the fuel thermal behaviour across different disciplines such as reactor physics and thermal hydraulics. In cases where the role of fuel performance simulations has been taken by simple correlations, calculation of the thermal response can be improved by including mechanical feedback and power history dependence.

As a demonstration of the applicability of FINIX to multiphysics simulations, we have integrated FINIX into Serpent 2, a Monte Carlo reactor physics code, and to HEXTRAN, VTT's in-house reactor dynamics code. With Serpent, we model a test case of an initially supercritical VVER-1000 pin-cell, where the exponential increase of power is terminated by the negative reactivity feedback from the increasing fuel temperature. With HEXTRAN, a control rod ejection accident in VVER-440 reactor is simulated combining neutronics, thermal hydraulics and fuel performance simulations. The case involves running multiple (several hundred) instances of FINIX in one simulation, and showcases how FINIX can be used to model the fuel thermal behaviour of a whole reactor.

Development of FINIX is an on-going work. Future developments include enhancing capabilities in fuel modelling such as cladding mechanics, and fission gas release modelling to facilitate modelling of loss of coolant accidents and steady state behaviour in addition to the fast transients discussed in this work. In addition, the development of the FINIX interface to multiphysics simulation packages remains a topic of high interest.

6 Acknowledgments

This work was funded by the Finnish research programmes on nuclear power plant safety SAFIR2014 and SAFIR2018, and the NUMPS project of the Academy of Finland.

7 References

[1] Hämäläinen, A. *et al.*, Coupled Code FRAPTRAN-GENFLO for analysing fuel behaviour during PWR and BWR transients and accidents, in proceedings IAEA Technical Committee Meeting on Fuel Behavior under Transient and LOCA Conditions (IAEA-TECDOC-1320), Halden, Norway 10–14 September 2001, p. 43.
[2] Rossiter, G., Development of the ENIGMA fuel performance code for whole core analysis and dry storage assessments, Nucl. Eng. Technol. 43, 489 (2011).
[3] Geelhood, K., Luscher, W., Beyer, C., Cuta, J., FRAPTRAN 1.4: A Computer Code for the Transient Analysis of Oxide Fuel Rods, NUREG-CR-7023, vol. 1, Pacific Northwest National Laboratory (2011).
[4] Lassmann, K., Transuranus: a fuel rod analysis code ready for use. J. Nucl. Mater. 188, 295 (1992).
[5] Williamson, R.L. *et al.*, Multidimensional multiphysics simulation of nuclear fuel behavior, J. Nucl. Mater. 423, 149 (2012).
[6] Rohde, U., The modeling of fuel rod behaviour under RIA conditions in the code DYN3D, Ann. Nucl. Energy 28, 1343 (2001).
[7] RELAP5/MOD3.3 Code Manual Volume I: Code Structure, System Models, and Solution Methods, Technical Report NUREG-CR-5535 Rev 4, vol. 1, Information Systems Laboratories, Inc. (2010).
[8] Geelhood, K., Luscher, W. and Beyer, C., FRAPCON-3.4: A computer code for the calculation of steady-state thermal-mechanical behavior of oxide fuel rods for high burnup, NUREG-CR-7022 Vol 1, Pacific Northwest National Laboratory (2011).

[9] Ikonen, T., Tulkki, V., Syrjälahti, E., Valtavirta, V., Leppänen, J., FINIX – fuel behavior model and interface for multiphysics applications, in proceedings Fuel Performance Meeting/TopFuel, Charlotte, USA (2013).
[10] Ikonen, T., Loukusa, H., Syrjälahti, E., Valtavirta, V., Leppänen, J. and Tulkki, V., Module for thermomechanical modeling of LWR fuel in multiphysics simulations, Ann. Nucl. Energy, in press (2014).
[11] Ikonen, T., FINIX Fuel Behavior Model and Interface for Multiphysics Applications. Code Documentation for Version 0.13.9, VTT-R-06563-13, VTT Technical Research Centre of Finland (2013).
[12] Leppänen, J., Development of a New Monte Carlo Reactor Physics Code, Ph.D. thesis, Helsinki University of Technology (2007).
[13] Viitanen, T. and Leppänen, J., Explicit Treatment of Thermal Motion in Continuous-Energy Monte Carlo Tracking Routines, Nucl. Sci. Eng. 171, 165 (2012).
[14] Viitanen, T. and Leppänen, J., Target Motion Sampling Temperature Treatment Technique With Elevated Basis Cross Section Temperatures, Nucl. Sci. Eng. 177, 77 (2014).
[15] Viitanen, T. and Leppänen, J., Temperature Majorant Cross Sections in Monte Carlo Neutron Tracking, Nucl. Sci. Eng., Accepted for publication (2014).
[16] Leppänen, J., Modeling of Nonuniform Density Distributions in the Serpent 2 Monte Carlo Code, Nucl. Sci. Eng. 174, 318 (2013).
[17] Leppänen, J., Development of a Dynamic Simulation Mode in Serpent 2 Monte Carlo Code, Proceedings of M&C 2013, Sun Valley, ID, USA (2013).
[18] Leppänen, J. *et al.*, The Serpent Monte Carlo code: Status, development and applications in 2013, Ann. Nucl. Energy, In press (2015).
[19] Leppänen, J. *et al.*, The Numerical Multi-Physics Project (NUMPS) at VTT Technical Research Centre of Finland.
[20] Blyth, T. *et al.,* Benchmark for Uncertainty Analysis in Modelling (UAM) for Design, Operation and Safety Analysis of LWRs, Volume II: Specification and Support Data for the Core Cases (Phase II), OECD/NEA, 2013.
[21] Daeubler, M., Jimenez, J. and Sanches, V., Development of a high-fidelity Monte Carlo thermal-hydraulics coupled code system Serpent/SUBCHANFLOW -- first results, Proceedings of Physor 2014, Kyoto, Japan (2014).
[22] Kyrki-Rajamäki, R., Three-dimensional reactor dynamics code for VVER type nuclear reactors, Tech. Rep. 246, DrTech thesis. Technical Research Centre of Finland, 1995.
[23] Kyrki-Rajamäki, R. & Kaloinen, E., Results of the third three-dimensional hexagonal dynamic AER benchmark problem including thermal hydraulics calculations in the core and a hot channel, in proceedings of the fifth Symposium of AER, Dobogókő, Hungary, 15-19 October 1995. Pp. 255-286.
[24] Kyrki-Rajamäki, R. & Kaloinen E., Definition of the third three-dimensional hexagonal dynamic AER benchmark problem, in proceedings of the fourth Symposium of AER, Sozopol, Bulgaria, 10-15 October 1994. Pp. 417-427.

MICRO-MECHANISTIC MODELING OF BLADE WING SWELLING OF THE WESTINGHOUSE BWR CONTROL ROD CR 99

MAGNUS JINNESTRAND, PER SELTBORG, BJÖRN REBENSDORFF
Westinghouse Electric Sweden AB, SE 721 63, Västerås, Sweden

ABSTRACT

The mechanical performance of the Westinghouse BWR control rod CR 99 has been thoroughly assessed through a long-term program including extensive irradiation and measurement campaigns as well as a number of advanced theoretical analyses of the key mechanisms behind blade swelling of control rods exposed to very high depletion. In this paper, the swelling behaviours of the CR 99 high-density absorber pins and control rod blades as they are exposed to long-term neutron irradiation have been explicitly modelled and assessed in a micro-mechanistic evaluation. By using this information in combination with inspection results of irradiation-assisted stress corrosion cracking (IASCC) on highly depleted test blades, data from blade swelling measurements as well as high-resolution control rod depletion calculations, reliable prediction of the mechanical performance of CR 99 as function of its depletion has been established.

The micro-mechanistic model describes in detail all the main processes relevant for the interaction between the boron carbide absorber pins and the control rod blade. First, the swelling of the pins are modelled as a function of the neutron irradiation, taking into account the effects of the strongly heterogeneous boron depletion resulting in two different types of swelling, here defined as solid swelling and porous swelling. By capturing these behaviours, together with the evolution of the stiffness of the pins, the contact force between the absorber pins and the control rod blade can be modelled, eventually enabling to assess the blade swelling as a result of neutron irradiation.

Finite element modelling has in this study been used to generate and verify a number of mathematical functions describing all of the abovementioned processes. The micro-mechanistic model includes several material parameters, which values need to be determined. As it is not feasible to measure the basic properties of irradiated absorber pins, the measured control rod blade swelling data have been utilized in combination with non-linear optimization when statistically assessing these parameter values. Control rod blade swelling measurement data from several post irradiation programs of CR 99 have been used to build the database resulting in a robust and general model. It is shown that the model predictions are in very good agreement with the measurement data and the developed model is thus justified for application to other CR 99 designs as well.

1. Introduction

The basic design of all Westinghouse BWR control rods consists of four stainless steel blades welded together to form a cruciform-shaped rod. Each blade has horizontally drilled holes containing ^{10}B atoms, which act as neutron absorbers. The absorber material in the latest control rod type CR 99 consists of Hot Isostatic Pressed (HIP) boron carbide pins with nearly 100% of theoretical density. Each absorber hole of the CR 99 rods is loaded with two absorber pins, separated by a thin spring. The general design of CR 99 is depicted in Fig. 1. During control rod operation, neutron irradiation causes boron carbide to swell as ^{10}B atoms are transformed into Li-7 and He-4. With reduced diameter and tapered ends, the HIP two-pin design minimizes swelling-induced mechanical strain on the blade wings and improves the ability to control mechanical behavior.

The contact between the absorber pins and the absorber hole wall results in local deformation of the control rod blade with high stress levels which, in combination with the environment in the core, can cause Irradiation Assisted Stress Corrosion Cracking (IASCC). Furthermore, the force between the absorber pins and the absorber hole wall must be included in the calculations showing that the control rod will not fail structurally during its lifetime.

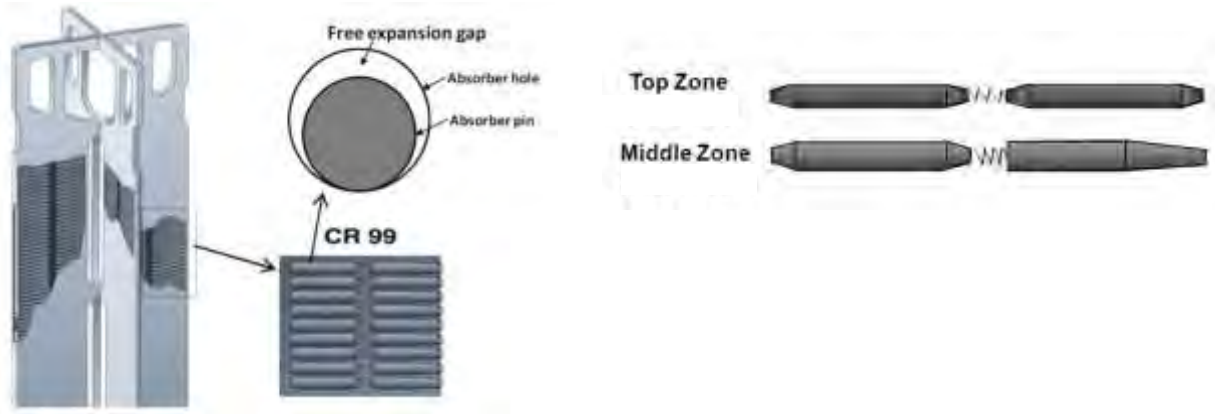

Fig. 1 Schematic views of the CR 99 control rod with its high-density boron carbide pins.

The micro-mechanistic model developed to describe the swelling of the absorber pins needs to be able to predict the local response in the absorber blade caused by irradiation assisted creep as well as the contact force. It is also important that the equations used to describe the properties of the absorber pins are formulated so that they can be utilized predicting the control rod blade swelling. The most limiting position in the control rod blade with respect to the IASCC risk must therefore be captured by the model, as the blade swelling prediction is needed as input to the Westinghouse model for prediction of IASCC risk [1] [2]. Input to the IASCC risk prediction model shall be ^{10}B depletion of the control rod, as the ^{10}B depletion is usually tracked continuously during the lifetime of the control rod, thus facilitating the follow-up of the IASCC risk.

Due to the basic control rod blade design with the absorber pins enclosed in the steel blades, it is impossible to measure directly the mechanical properties of the absorber pins during irradiation. However, the local swelling of the control rod blade can be measured and is suitable as input to the development of the control rod blade swelling model. The ability of the model to predict a set of measured control rod swelling data is best achieved using a statistical approach, allowing the formulation of a best estimate model and a model that is conservative to the chosen level. This is the approach Westinghouse has used developing the model describing the control rod swelling and the contact force between absorber pins and absorber hole wall.

The Westinghouse control rod blade swelling model is divided into two parts. The first part, described in Section 2, models how the stainless steel blade material reacts on the absorber pin to absorber hole wall contact pressure. The second part, described in Section 3, models the absorber pin mechanical properties and how the absorber pin to absorber hole wall contact pressure evolves as a function of the neutron fluence. Section 4 and 5 describe the control rod blade swelling measurements that the model is tuned against and how the parameter estimation is done.

2. Model of local control rod blade response

Detailed mechanical calculation of the local response in the control rod blade is usually done by utilization of finite element simulations. Unfortunately, finite element simulations can be computationally demanding and can be difficult to couple with statistical analysis programs. Westinghouse therefore uses finite element simulations to establish a relation between the pressure in the absorber hole wall and the local response in the control rod blade. Previous experience from finite element calculations and control rod blade swelling measurement has demonstrated that that the path illustrated in Fig. 2 is critical. It is along this path that the maximum stress at the outer surface of the control rod blade is located. The maximum stress state at the outer surface late in life is typically above 100 MPa, but well below the yield strength of highly irradiated austenitic stainless steel 316L (approximately 700 MPa).

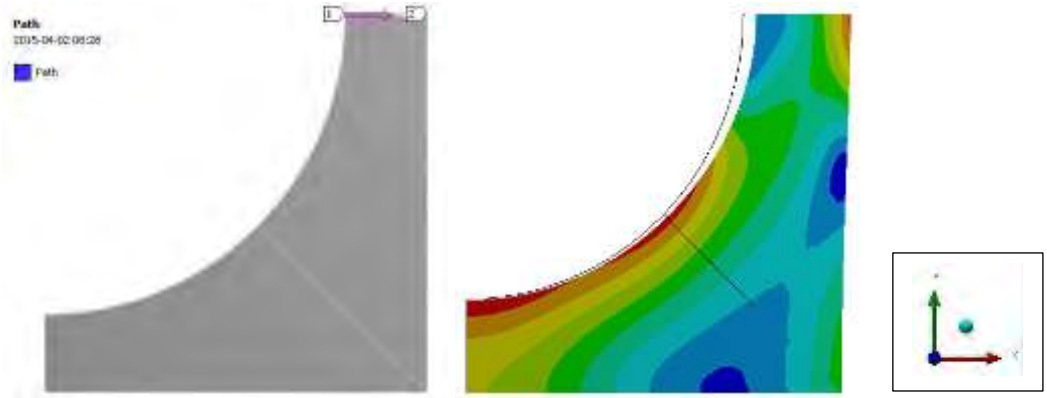

Fig. 2 At left, the path definition (line between point 1 and point 2) used to establish the relation between the pressure load on the absorber hole wall and the local response in the control rod blade. At right, typical stress distribution late in the control rod life, plotted with excessive deformation.

Any concentrations of either stress or strain along the defined path in Fig. 2 have minor influence on the control rod blade swelling and, therefore, the stress/strain have in this study been averaged. Based on linear elastic finite element simulation, the average stress state (σ_m [unit MPa]), the average strain (ε_m [unit mm/mm]) and the average deformation (dx [unit mm]) have here been expressed as a linear function of the contact pressure. The scaling factors Q_1 to Q_3 are calculated as the average response (σ_m, ε_m and dx) in a linear elastic finite element model along the defined path divided by the applied pressure. The following relations are then obtained:

$$\sigma_m = Q_1 \cdot CP$$
$$\varepsilon_m = Q_2 \cdot CP$$
$$dx = Q_3 \cdot CP$$

Here, *CP* [unit MPa] is the pressure on the absorber hole wall. The irradiation induced creep strain is calculated based on the average stress state (σ_m) and by applying the irradiation creep relation:

$$\dot{\varepsilon}^{cr} = C_0 \cdot \sigma_m \cdot \varphi$$

where φ is the fast neutron flux in unit [dpa[1]/s.] and the constant C_0 takes the value $6.0694 \cdot 10^{-10}$ [unit 1/(MPa·dpa)]. The irradiation assisted creep law is based on a work by EPRI, [3], but neglects the constant term describing the primary creep. The elastic response in the blade is calculated by $\varepsilon^{el} = Q_2 \cdot CP$. Thus, the total strain along the critical path in the control rod blade is given by:

$$\varepsilon = \int_0^t 6.0694 \cdot 10^{-10} \cdot Q_1 \cdot CP(t) \cdot \varphi(t) \cdot dt + Q_2 \cdot CP$$

The change of the path length is small compared with the local deformation of the blade and is therefore neglected in the calculation of the control rod blade swelling, *dx*. Thus, the blade swelling can be calculated based on total strain as:

$$dx = \frac{Q_3}{Q_2} \varepsilon$$

3. Model of absorber pin properties

3.1. Solid Pin Swelling

The solid pin swelling describes the volumetric expansion of the B_4C crystals when the ^{10}B atoms capture neutrons. Due to the capture reaction:

$$^{10}_{5}B + ^{1}_{0}n \rightarrow ^{4}_{2}He + ^{7}_{3}Li$$

a helium and lithium atom is created. The helium and lithium atoms occupy more volume compared with the original boron atom and this solid swelling of the absorber pin is described by the following equations:

$$R_{solid} = R_0 \cdot \left(1 + D_1 \cdot \beta^{D_2}\right)$$

$$A_{solid} = \pi \cdot R_{solid}^2$$

β is the relative ^{10}B depletion and R_0 is the original radius of the absorber pin. The solid pin swelling affects the free volume inside the control rod blade and is therefore related to the internal helium pressure in the control rod blade. The values of the parameters D_1 and D_2 are therefore known and do not need to be determined based on control rod blade swelling measurements.

3.2. Total absorber pin swelling

The absorber pin is self-shielding implying that the ^{10}B depletion of the outer part of the absorber pin is faster than the inner part. This uneven distribution of the ^{10}B depletion leads to internal stresses in the absorber pin which results in local cracking above some critical

[1] 15 dpa = 10^{22} n/cm^2

level. The local cracking (or fragmentation) of the absorber pin therefore results in an uneven distributed porosity.

The equation describing the total swelling of the absorber pin is based on the fact that the total cross sectional area of the absorber pin can be described as a sum of the so-called solid area (cross sectional area of the B_4C crystals) and the porosity area (cross-sectional area of the void between the B_4C crystals), according to:

$$A_{pin} = A_{solid} + A_{porosity}$$

The total cross sectional area of the absorber pin is described by the following equation:

$$A_{pin} = A_0 \cdot \left(1 + C_0 \cdot \beta^n\right)$$

where A_0 is the original cross sectional area of the absorber pin and β is the relative ^{10}B depletion. C_0 and n are parameters whose values need to be determined based on a fitting of the model against control rod blade swelling measurements.

The expansion of the total cross sectional area of the absorber pin is physically bounded by the cross sectional area of the absorber hole. The solid pin swelling is a stronger mechanism compared with the evolution of porosity in the absorber pin. Thus, after contact between the absorber pin and the absorber hole wall, the porosity of the absorber pin will decrease as a function of the solid pin swelling.

3.3. Pin stiffness

The micro-mechanistic model of the blade swelling is based on the assumption that the stiffness of the absorber pin can be described by a Young's modulus (*E*) depending on the porosity (*P*) of the absorber pin as:

$$E = E_S \cdot (1 - P)^{n_S}$$

Here, E_S and n_S are parameters whose values need to be determined based on control rod blade swelling measurements. *P* is the porosity of the absorber pin, defined as:

$$P = \frac{A_{porosity}}{A_{pin}} = 1 - \frac{A_{solid}}{A_{pin}}$$

3.4. Pressure exerted by the absorber hole wall on the absorber pin

The contact pressure between the absorber pin and the absorber hole wall causes the total cross sectional area of the absorber pin to decrease. Thus, the inward radial deformation of the absorber pin is calculated as:

$$\delta = \sqrt{\frac{A_{hole} + A_{solid}(\beta) - A_{solid}(\beta_c)}{\pi}} - \sqrt{\frac{A_{hole}}{\pi}}$$

where β is the ^{10}B depletion and β_C the ^{10}B depletion at first contact between the absorber pin and the absorber hole wall. The contact pressure between absorber pin and absorber hole wall, *CP*, is calculated as:

$$CP = \frac{E}{\left(R_{hole} + \delta\right)} \cdot \delta$$

4. Control rod blade swelling measurements

Westinghouse has measured the blade swelling for three CR 99 control rods of the 2nd generation irradiated in the Leibstadt Nuclear Power Plant (KKL). The blade thickness of these control rods were pre-characterized enabling measurements of the change in control rod blade thickness with high accuracy. The measurements clearly showed that the tapered end of the absorber pin effectively mitigates the ^{10}B depletion peak that occurs at the outer edge of the control rod blades, as illustrated in Fig. 3.

Therefore, for control rod blade swelling modelling, the appropriate database is the average measured blade swelling at about 20 mm location from the edge. It is at this position that the maximum swelling and straining of the blade occurs and where the risk for IASCC initiation is largest. The influence of the absorber pin diameter is included in the database, as a smaller diameter is used for the 10 top holes in the control rod. Some data at 10 mm from the control rod blade edge are also used in order to increase the database considering the absorber pin diameter influence.

The local ^{10}B depletion in the control rods has also been calculated [1], and by that, a correlation between the control rod blade swelling and ^{10}B depletion could be established. This is the information used to determine the parameter values in the equations describing the absorber pin properties.

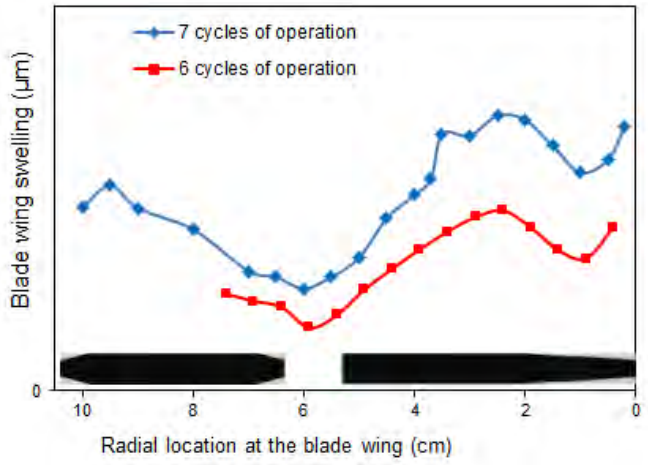

Fig. 3 Typical results showing that maximum control rod blade swelling occurs at about 20 from the control rod blade edge.

5. Parameter estimation

The control rod blade swelling model includes four parameters (C_0, n, E_s, n_s), which values need to be determined. The parameter value estimation has been done by utilization of the general mathematical program MATLAB (R2012b) and its built-in functions for non-linear least square fit of curves towards a set of data.

In order to estimate a 95% conservative parameter set, the control rod wing swelling database has been adjusted based on the error in the best estimate least square fit. The standard deviation of the error, SDEV, and the mean value of the experimental data, MEAN_EXP, were calculated. Then, all experimental data points in the database were scaled with the following factor:

$$factor = 1 + \frac{1.645 \cdot SDEV}{MEAN\_EXP}$$

The number 1.645 has been chosen so that the model predicts larger control rod blade swelling for 95% of the control rod wing swelling data in the database.

The control rod wing swelling model has been compared with the measurement database shown in Fig. 4. The database includes two sets of absorber pin diameters and therefore there are two model predictions of best estimate and 95% conservative prediction plotted in the figure. An alternative comparison between model prediction and measured blade swelling is presented in Fig. 5 showing that the model gives good prediction for a large range of swelling levels and that the model prediction is stable at larger control rod blade swellings.

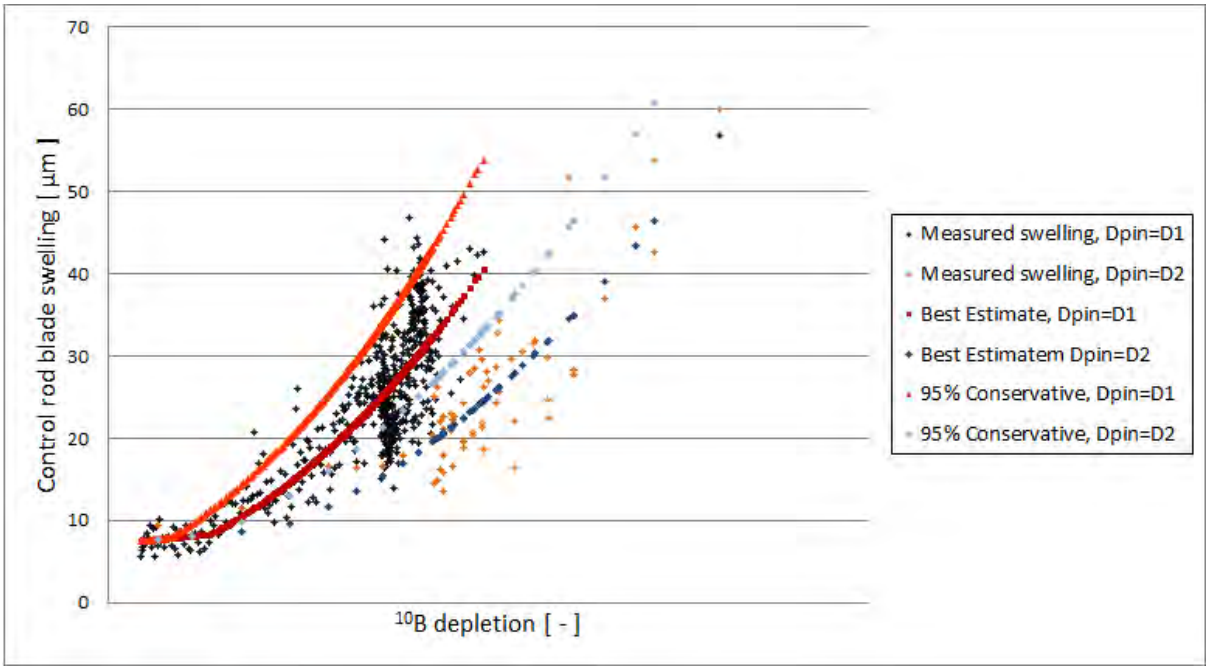

Fig. 4 Prediction of control rod blade swelling model compared with measured control rod swelling data. Two sets of absorber pin diameters are included in the database, Dpin=D1 > Dpin=D2.

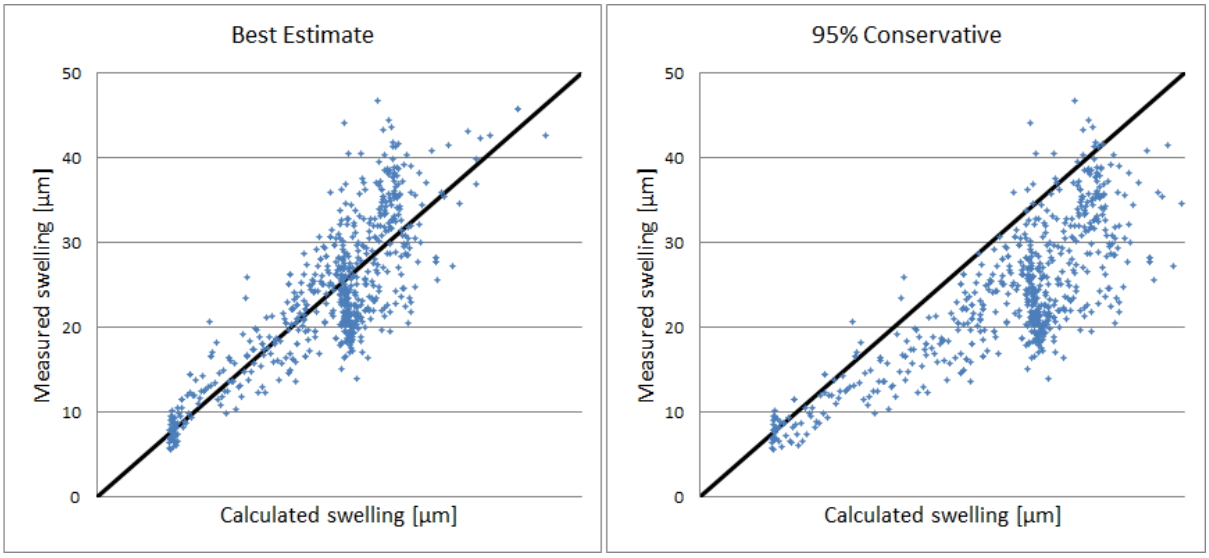

Fig. 5 Comparison between model prediction and measured blade swelling in case of best estimate and 95% conservative parameter sets.

6. Summary

The micro-mechanistic control rod blade swelling model that has been developed is based on a theoretical work of the mechanical properties of the high-density absorber pins in the Westinghouse BWR control rod CR 99. Parameter values needed to complete the model is determined based on mathematical optimization of the model prediction towards measured control rod blade swelling data and the model has then been demonstrated to predict measured control rod wing swellings very well.

This model is one of the basic steps needed in order to build a reliable prediction model for Irradiation Assisted Stress Corrosion Cracking as it correlates calculated ^{10}B depletion to local control rod blade swelling. Furthermore, the model also enables determination of the mechanical absorber pin properties and can be used to calculate the contact pressure between the absorber pin and the absorber hole wall that evolves during the lifetime of the control rod.

7. References

[1] Physor 2012, Assessment of the mechanical performance of the Westinghouse BWR control rod CR 99 at high depletion levels, P. Seltborg and M. Jinnestrand, 2012

[2] TopFuel 2012, Westinghouse BWR control rod CR 99 – Towards flawless operability, P. Seltborg, M. Jinnestrand and B. Rebensdorff, 2012

[3] EPRI report MRP-135-Rev. 1, Material Reliability Program: Development of Material Constitutive Model for Irradiated Austenitic Stainless Steels, 2010

MODELLING OF FISSION GAS RELEASE IN IRRADIATED UO_2 UNDER TRANSIENT CONDITIONS

M. S. VESHCHUNOV, V. I. TARASOV

Nuclear Safety Institute (IBRAE), Russian Academy of Sciences,
52, B. Tulskaya, 115191, Moscow, Russian Federation

ABSTRACT

The mechanistic code MFPR is further developed for modelling of enhanced fission gas release from irradiated UO_2 fuel under conditions of the power ramp tests, along with the microstructure evolution characterised by the formation of a new population of large intragranular bubbles with a rather wide size distribution (from 30 to 500 nm), observed in transient-tested UO_2 fuel samples.

In order to explain the observed microstructure evolution in transient-tested samples, further improvement of the Nelson model for gas atom resolution from bubbles under irradiation is attempted, taking into consideration a tendency of gas atoms ejected from a bubble into surrounding matrix to return back to this bubble by diffusion. The new model, taking this tendency into consideration, predicts a notable reduction of the resolution rate for relatively large bubbles that provokes unrestricted bubble growth owing to gas atom sinking into bubbles, if some critical value of the bubble radius is attained. The attainment of the critical bubble size becomes possible owing to the increased bubble mobility under the transient test conditions enhancing the bubbles collision and coalescence rate.

Results of calculations with the new resolution model implemented in the mechanistic code MFPR show that both mechanisms of random and biased migration of bubbles in the temperature gradient additionally promote the formation of the large bubble population. On the other hand, the main input in the gas release in the transient-tested fuel is associated with the bubble biased migration, whereas the random diffusion mechanism is relatively weak and acts indirectly, accelerating bubbles coalescence and thus reducing the total sink strength of gas atoms to bubbles, to advantage of gas atom transport to grain boundaries.

Besides, the sweeping of gas atoms and bubbles by moving grain boundaries of growing grains also becomes an important mechanism of the gas release at high temperatures attained in the central zone of transient tested pellets. MFPR correctly reproduces the grain growth measured in different local positions of the fuel pellet and thus reliably calculates the swept gas release. Superposition of all these mechanisms: gas atom diffusion, bubbles random and biased migration, and gas sweeping by grain boundaries, results in a reasonable prediction of the measured fractional gas release in the Risø ramp tests with different hold times from 4 to 62 h at the terminal linear power of ≈ 40 kW/m.

1. Introduction

Any model that attempts a realistic description of fission-gas release and fuel swelling as a function of fuel-fabrication variables and in a wide range of reactor operating conditions must treat them as coupled phenomena and must include various mechanisms influencing fission gas behaviour. The key point in such analysis is intragranular bubbles behaviour, which is strongly influenced by irradiation and/or thermal treatment conditions.

A relatively simple behaviour under steady irradiation conditions, characterised by a population of small nanometre bubbles with a relatively narrow size distribution function (SDF), becomes much more complicated under transient conditions (power ramps). For consistent modelling of bubbles behaviour under transient conditions, the critical assessment of available models, their modification and development of more advanced models for implementation in the mechanistic codes, become rather important task. In particular, the improved model for the irradiation induced resolution of gas atoms from bubbles, which allows a reasonable interpretation of a broad bubble size distribution, observed in the

transient-tested fuel pellets, and the additional gas transport mechanisms necessary for correct description of the enhanced gas release in these tests, are developed.

After implementation of the new models in the mechanistic code MFPR, which was developed in collaboration between IBRAE and IRSN (Cadarache, France) [1, 2] and is currently the constituent part of the advanced fuel performance and safety code SFPR [3], the refined code MFPR was applied to the self-consistent consideration of the fuel microstructure evolution and fission gas release under conditions of transient tests.

The main results of the code improvement and verification against the ramp tests [4, 5], recently published in [6], are briefly overviewed in the current paper.

2. An advanced model for gas atoms resolution from bubbles

There are two theories for the mechanism of the re-solution process. Turnbull [8] has proposed a model assuming that small (nanometre) gas bubbles are nucleated heterogeneously in the wake of fission fragments where they grow by collecting gas atoms until they are destroyed when struck by a further fragment. Unfortunately the model must break down at higher temperatures when, within the time between nucleation and encounter with a fragment, the bubble collects sufficient gas such that more than one encounter is necessary for its destruction [9], and in principle cannot describe a wide bubble size distribution function observed in transient tests (described below).

This problem can be overcome by the alternative model of Nelson [10], where the re-solution flux of gas atoms from a bubble relates to the number of atoms in the bubble, N_b, as

$$J_{res} = \omega_{res} N_b , \tag{1}$$

where the resolution rate is proportional to the fission rate G

$$\omega_{res} \approx bG , \tag{2}$$

b is the resolution constant.

In this model the gas atoms are ejected from bubbles by individual binary collisions with fission fragments or U recoils. It is assumed that only a fraction of gas atoms in a bubble within a critical distance from the bubble surface $d \approx$ 1–1.5 nm may escape, therefore, the resolution constant may be represented as

$$b = b_0 \left(\frac{4\pi}{3} R_b^3 - \frac{4\pi \left(R_b - d \right)^3}{3} \right) \left(\frac{4\pi}{3} R_b^3 \right)^{-1} \approx b_0 \frac{3d}{3d + R_b} , \tag{3}$$

where the simplified expression in the right hand side (*rhs*) correctly interpolates the more precise expression in the left hand side at both limits $R_b << d$ and $R_b >> d$. Gas atoms are assumed to have re-dissolved into the matrix if their recoil energy exceeds some threshold value, $E_{\min}$, needed to overcome the surface tension of the bubble and penetrate 'sufficiently far' into the crystal lattice. It was shown in [10] that the resolution rate depends strongly on $E_{\min}$ varying from ~10^{-4} to ~10^{-5} s^{-1} at G = 10^{19} m^{-3} s^{-1} for $E_{\min}$ in the range from 100 to 300 eV.

The resolution rate was studied experimentally in the tests of Cornell and Turnbull [11, 12]. The value ω_{res} at $G \approx 10^{13}$ cm^{-3} s^{-1} was evaluated from the time taken to dissolve a 5 - 7.5 nm radius bubble as $2.6 \cdot 10^{-5}$ – $1.2 \cdot 10^{-4}$ s^{-1} at T = 200°C [12] and $(1.8 – 3.6) \cdot 10^{-4}$ s^{-1} at T = 1200°C [11]. On the base of these results, it was assumed that ω_{res} did not depend on temperature, but depended only on the fission rate being proportional to this value. Results

of these measurements were generally confirmed by other experimental results, and further justified by additional analytical evaluations of experimental data for small bubbles with radius ≈ 1 nm [13], resulting in $b_0 \approx (2–3)\cdot 10^{-23}$ m^3.

On the other hand, it was pointed out by Nelson [10] that ejection of a gas atom into surrounding matrix does not automatically result in its resolution. In accordance with available studies of the thermal desorption of inert gas from solids, it was presumed that those gas atoms received energy from 100 to 250 eV would be knocked to within the first two or three atomic distances from the bubble, and thus would have a rather large probability of returning to the same bubble. In particular, it was inferred that a gas atom must receive some 5–10 keV in order to penetrate sufficiently deep into the lattice to escape from the bubble; however, the probability to receive such energy (that determines ω_{res}, as above explained) from direct or indirect hits considerably decreases.

In order to take this tendency into quantitative consideration, one can assume, at first in the simplest approach (proposed by the authors in [14]), that the influx of the ejected atoms back to the bubble proceeds by diffusion within the re-solution layer δ (of several nm). As a result (see details in [6]), the rate equation for the variation of N_b takes form

$$\frac{dN_b}{dt} = 4\pi D c_g R_b - \omega_{res} N_b \frac{\delta}{R_b + \delta} = 4\pi D c_g R_b - \omega'_{res} N_b , \tag{4}$$

where

$$\omega'_{res} \approx \omega_{res} \frac{\delta}{R_b + \delta} \approx G b_0 \left(\frac{3\lambda}{3\lambda + R_b} \right) \left(\frac{\delta}{R_b + \delta} \right), \tag{5}$$

or

$$b' \approx \frac{\delta}{R_b + \delta} b = \frac{1}{1 + y} b , \tag{6}$$

where $y = R_b / \delta$, thus leading to an additional factor $\delta/(R_b + \delta)$ for the re-solution rate ω_{res} in Eq. (2), which was derived disregarding the back influx of the ejected atoms.

A more sophisticated approach to calculation of ω'_{res} taking into account spatial distribution of resolved gas atoms was presented in [6], which, however, improves Eq. (6) not very significantly thus allowing further employing this simplified equation with a reasonable accuracy.

As seen from Eq. (6), $\omega'_{res} \approx \omega_{res}$ for small bubbles of $R_b \approx$ 0.6–1.2 nm, normally observed under steady irradiation conditions [3, 15]. However, the difference between ω'_{res} and ω_{res} increases for larger bubbles, $R_b >> \delta$; this results in important changes in the bubbles behaviour under transient irradiation conditions, as shown in the next section.

Namely, the notable reduction of the resolution rate for relatively large bubbles provokes unrestricted bubble growth owing to gas atom sinking into bubbles, if some critical value of the bubble radius is attained. It is illustrated in Fig. 1 where the typical dependence of the *rhs* of Eq. (4) on the bubble radius is plotted. The dashed curves correspond to the base irradiation (T = 1273 K, $G = 10^{19}$ fissions/s/m^3 in this example) whereas the solid curves represent the transient conditions ($G = 2\cdot 10^{19}$ fissions/s/m^3, increased temperatures). Open circles mark the stable stationary points (*rhs* = 0, negative slope) which are present for both the resolution models; the unstable points (*rhs* = 0, positive slope) appear for the modified model. It is seen that the temperature increase leads to the rightward shift of the stable point, resulting in some increase of the mean bubble size, whereas the leftward shift of the unstable point facilitates the quick growth of the large bubbles population.

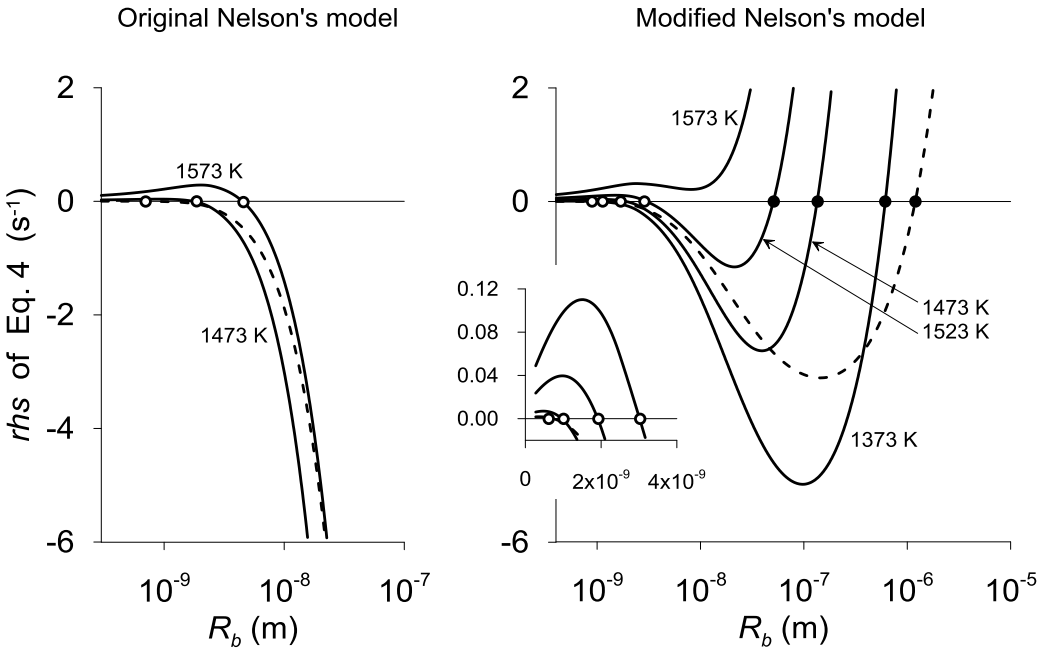

Fig. 1. *Rhs* of the bubble growth rate equation, Eq. (4).

The attainment of the critical bubble size becomes possible owing to the increased bubble mobility under the transient test conditions enhancing the bubbles collision and coalescence rate. As a result, significant microstructure changes characterised by the formation of a new population of large intragranular bubbles with a rather wide size distribution, observed in transient-tested fuel samples, can be described by the mechanistic code MFPR with the new resolution model.

3. Quantitative analysis of transient experiments

3.1. Microstructure evolution

Transmission electron microscopy (TEM) has been used in an extensive study [5] of the microstructure of base-irradiated and transient-tested samples of LWR nuclear fuels. The steady state base irradiation of 3% enriched UO_2 fuel was performed at a maximum linear power of 26 kW/m to an average burnup of 4.5% FIMA. The transient-tested samples came from pellets of the base-irradiated fuel which had been further subjected in reactor to power increases up to a maximum of 42 kW/m with the hold time up to 60 h.

Under the steady-state irradiation conditions most of the fission gas produced was retained in solution in the fuel matrix or precipitated into small fission bubbles with a narrow size distribution and an average diameter of 8 nm. The bubble spatial distribution was homogeneous, with an average concentration of $(1.2–1.9)\cdot10^{22}$ m^{-3}.

The effect of the transient test was to increase the fuel centre temperature from $0.45T_m \approx 1290$°C to about $0.56T_m \approx 1600$°C, causing significant changes to fuel microstructure. The major microstructure change in the fuel centre resulting from the transient was the formation of a new population of large fission bubbles with a broad bubble size distribution (30 to 500 nm in diameter) and an average bubble concentration of $7\cdot10^{18}$ m^{-3}. The temperature rise at the fuel periphery, on the other hand, was small and the microstructure remained essentially similar to that of the base-irradiated fuel, with similar density and distribution of small fission bubbles.

Since the temperature rise was high in the fuel centre and small at the periphery, a relatively large temperature gradient was attained in the fuel pellet. This activates the biased migration of bubbles and may additionally accelerate their coalescence, especially in the high-temperature central zone where bubbles mobility is high, and thus accelerate the bubble size "infiltration" through the unstable stationary point and formation of the large-size bubble population (see Section 2).

Three mechanisms are considered in MFPR that could lead to the bubble biased migration in the fuel: (1) evaporation-condensation across the bubble, (2) bubble surface diffusion, and (3) mass diffusion around the bubbles [7]; these mechanisms are tightly connected with the corresponding mechanisms of the bubble random migration. If the bubbles are small, the surface diffusion process would be expected to dominate at lower temperatures. For relatively large bubbles and at high temperatures the evaporation-condensation process is expected to be the dominant process.

For proper consideration of the bubble population with wide SDF a multimodal option of the MFPR code, rather than the base bimodal option, was used in further calculations. In this approach the problem is formulated in terms of Smoluchowski equation with the coagulation kernel describing the rate of interaction between particles *i* and *j* in the form:

$$K_{ij} = 4\pi\left(D_i + D_j\right)\left(R_i + R_j\right) + \pi\left(R_i + R_j\right)^2\left|\mathrm{v}_i - \mathrm{v}_j\right|, \tag{7}$$

where the first and the second terms in the *rhs* relate to the random and biased bubble migration mechanisms. In this equation D_i and R_i are respectively the bubble diffusivity and radius whereas v_i is the bubble velocity, which is proportional to the external gradients (temperature, vacancy concentration...).

In order to elucidate the effect of the new resolution model, calculations using the MFPR versions with the original Nelson model and the modified one were run. For the steady state irradiation period of the test the code qualitatively correctly reproduced the bimodal bubble size distribution (i.e. gas atoms and a population of small bubble with a narrow size distribution function), however, with bubble concentration ($\approx 10^{24}$ m^{-3}) and bubble mean size ($\approx$ 2 nm) somewhat different from observations in the tests [5], but in a reasonable agreement with observations of the steady state tests [15] (as well as of the earlier tests [18]) performed under similar to [5] temperature and irradiation conditions. This discrepancy in the tests observations was discussed in the literature (e.g. [19]); however, without definite conclusions on its nature. For this reason, only qualitative comparison of the model predictions with the pre- and post-transient stage observations will be further attempted.

Results of the calculations with the original and modified Nelson models are compared in Fig. 2 for two relative distances $x = r / R_{pellet}$ from the pellet centre. In the low temperature pellet periphery (*x* = 1) the both models predict narrow SDFs located near 2 nm, which are close to each other (the both models practically coincide for the small bubbles, see Sect. 2). In this location the SDFs turned out to be close to these calculated for the base-irradiated fuel.

The maximum bubble coalescence effect and the broadest SDF was found at a distance of *x* ~ 0.2 from the pellet centre where some decrease of the temperature (by a few tens of K) in comparison with that in the centreline is compensated with an excess by the nonzero biased migration due to temperature gradient (which is zero at the pellet centreline). In this case the SDFs for the two resolution models differ qualitatively: while the SDF has mainly the unimodal shape for the original model with the bubble sizes restricted by 10–20 nm the modified model distinctly predicts formation of two separate bubble populations. The population of the smaller bubbles (which was not observed in [4]) is characterized by the mean bubble size of 3.1 nm and the total density of ~$1.1\cdot10^{20}$ m^{-3}. The mean bubble size of the second population was found to be of 131 nm whereas the total density turned out to be of ~$2.4\cdot10^{19}$ m^{-3}, which is in a reasonable agreement with the experimental value of

($0.7 \cdot 10^{19}$ m^{-3}), taking into account uncertainties in the model parameters and irradiation conditions.

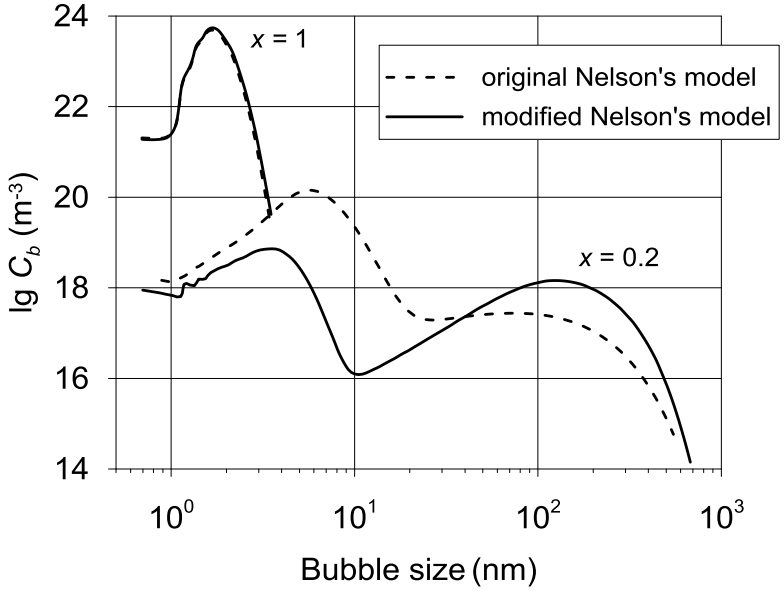

Fig. 2. Bubble SDF calculated with two variants of the resolution model under conditions of the transient test [5].

Besides, MFPR predicts significant fractional fission gas release (up to ≈ 70% in the pellet hot zone); however, it was not controlled in this test. For this reason, gas release measurements in the Risø Project tests performed under similar transient conditions will be analysed in the next Section.

3.2. Fission gas release

Transient tests [4] have been carried out in Risø Project to explore fuel performance at increasing burn-up levels to ~45 GWd/t (~4.7% FIMA) and beyond, especially for power increases (transients) late in life. The tests were performed with the PWR design fuel pellet of diameter 9 mm, pellet density 93.7% TD and grain diameter 6 μm. The fuel had been irradiated in the Biblis-A reactor (Germany) to burn-up of 4.3-4.4% FIMA (pin average). The highest linear power seen by this fuel was 26.7 kW/m. The fuels did not release more than 0.3 % of their fission gas inventory during the base irradiation. Transient test was carried out in the DR3 reactor at Risø. The approach to the terminal power was made either in two large jumps or in multiple steps of 2 or 5 kW/m.

In all of the instrumented tests, the fuel centre temperature and the fission gas pressure in the plenum were simultaneously measured. The temperature of the cladding surface was 613 K in case of PWR fuel and 563 K in the case of the BWR fuel, whereas the conservative upper limits of fuel centreline temperature were estimated in [4] to range from ~1773 K at linear heat rating 30 kW/m to ~2143 K at linear heat rating 40 kW/m. Post-test examinations of the specimens allowed plotting fractional gas releases and grain growth as functions of terminal local fuel temperature, which was calculated in [4].

The modified MFPR code version was applied to calculation of the release curves for two representative sections of transient-tested fuel with the hold times 4 and 62 h at linear heat rating (LHR) ≈ 40 kW/m. The temperature radial profiles in fuel pellets were considered as parabolic with the centreline temperature of $T_c \approx 2100$ K and the pellet outer surface temperature of $T_{surf} \approx 1100$ K, in accordance with temperature evaluation in [4]. High temperatures attained in the fuel centreline induced very steep radial thermal gradient (up to ~$4 \cdot 10^3$ K/cm), which made the bubble biased migration in the temperature gradient an important mechanism of gas release.

Calculation results plotted in Fig. 3 are in a reasonable agreement with experimental results for different hold times (taking into account large uncertainties of ≈ 100-200 K (cf. [4]) in evaluation of local temperatures in the fuel pellet).

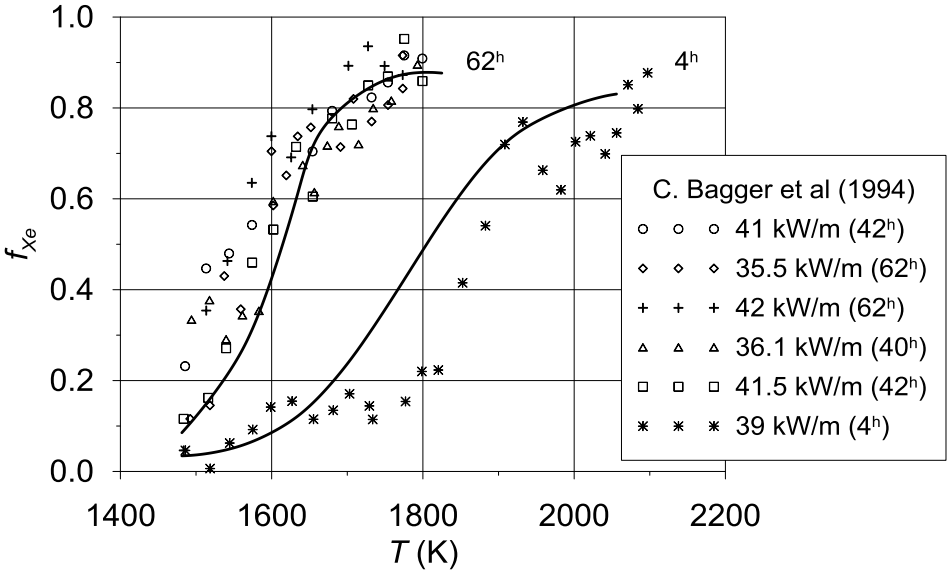

Fig. 3. Comparison of the measured (markers) and calculated (curves) fractional gas releases in the power ramp tests [4]

It should be noted that the bubble biased velocity, which is proportional to the temperature gradient, for the surface diffusion mechanism dominating for the majority of the considered bubbles, has the maximum at the temperature $T_{\max} \approx T_c - 43$ K, located at the radial position $R_{\max} \approx 0.2 R_{pellet}$. Owing to a smooth variation in the vicinity of the maximum, the velocity drops to zero in a relatively thin innermost cell of the fuel pellet (< 100 μm). On the other hand, at such high temperatures in this central zone the release by the other mechanisms becomes significant and efficiently compensates deterioration of the bubble biased migration mechanism. As a result, the fractional release in the innermost zone is calculated as ≈ 47% for the hold time of 4 h and increases up to 58% and 61% at the hold times 40 and 62 h, respectively.

In order to elucidate an input of the various release mechanisms, calculations with different options of MFPR were carried out, Fig. 4. The calculation run with the switched off bubble random migration mechanism, bubble biased migration in the temperature gradient and

sweeping of gas by migrating grain boundaries, characterizes the gas release solely by the gas atom diffusion mechanism, which occurs to be relatively weak ≈ 26% (at $x = 0.2$), curve 1. Switch on of the bubble random migration mechanism with the two other options switched off results in a notable increase of the fractional gas release, curve 2; however, more detailed analysis shows that the enhanced release in this case is associated mainly with the coalescence of bubble, rather than their migration to grain boundaries. Indeed, on heat up the bubbles grow up very quickly following the enhanced coalescence rate, Eq. (7). Simultaneously, the bubbles mean concentration falls down, $C_b \propto R_b^{-2}$, following the gas conservation in coalescing bubbles, resulting in reduction of the total sink strength of gas atoms to bubbles, $k_b^2 \approx 4\pi C_b R_b \propto R_b^{-1}$. This essentially enhances the relative sink strength of gas atoms to grain boundaries, $k_{gb}^2 / k_b^2 \approx 3/(R_{gr} k_b)$ [20] resulting in a notable increase of the fractional gas release (up to ≈ 49% at $x = 0.2$) in calculations via the gas atom diffusion mechanism.

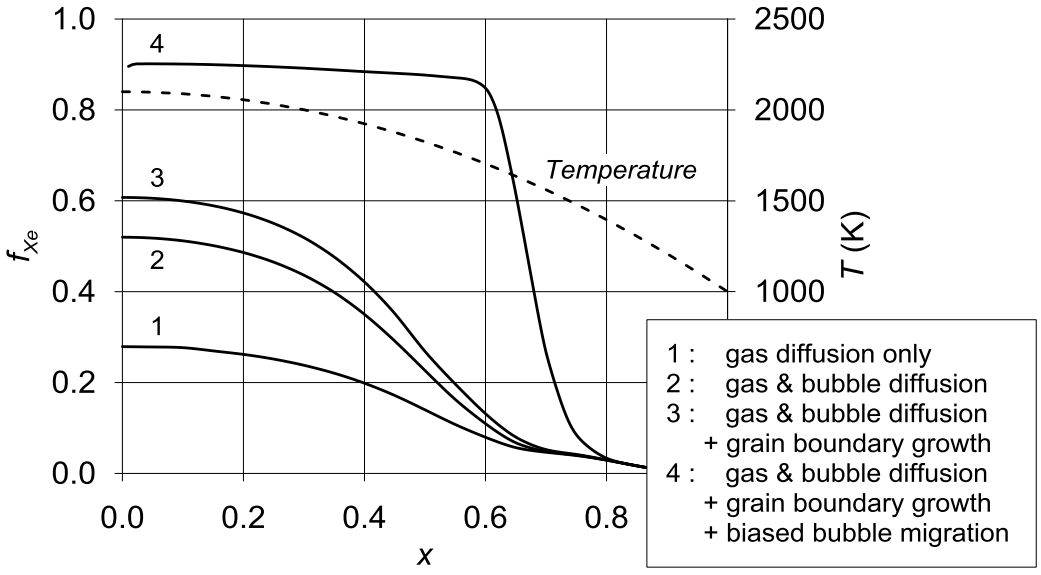

Fig. 4. Radial profiles of the fractional gas release in the 62^h power ramp tests [4] calculated with different options of MFPR code

Subsequent switch on of the sweeping mechanism by grain boundaries results in the further increase of the gas release up to ≈ 56%, curve 3, demonstrating the important contribution of this mechanism to the total gas release. In order to check an adequacy of the MFPR advanced grain growth model [21, 22] used in these calculations, comparison of the local grain sizes measured at different radial positions of the tested fuel pellet [4] to calculations is presented in Fig. 5. It is seen from these calculation results that the grain growth kinetics under transient conditions is also reasonably simulated by MFPR, despite it is somewhat underestimated at very high temperatures.

The additional consideration of the bubble biased migration in the temperature gradient eventually augments the calculated gas release to ≈ 90%, curve 4 in Fig. 4, in a reasonable agreement with the experimentally measured value, Fig. 2. This demonstrates self-consistency of the code calculations for gas release and microstructure evolution.

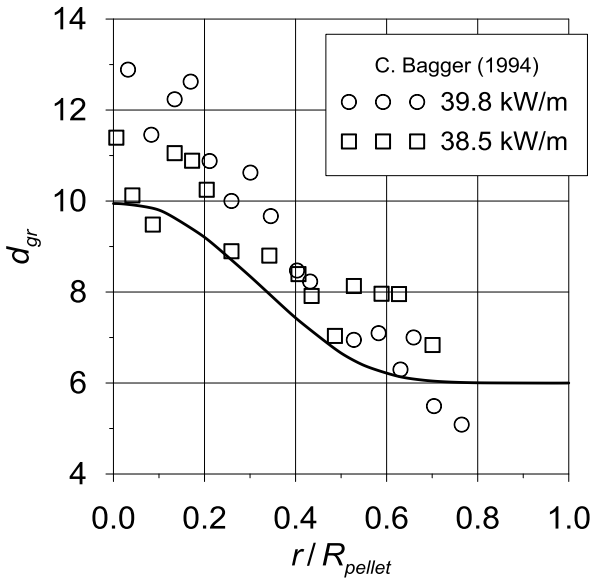

Fig. 5. The radial distribution of UO_2 grain size measured in [4] (markers) and calculated by MFPR (curve)

4. Conclusions

In order to explain the observed microstructure evolution in transient-tested samples, further improvement of the Nelson model for gas atom resolution from bubbles under irradiation was carried out, taking into consideration a tendency of gas atoms ejected from a bubble into surrounding matrix to return back to this bubble by diffusion. The new model, taking this tendency into consideration, predicts a notable reduction of the resolution rate for relatively large bubbles that provokes fast growth of bubbles owing to gas atom sinking into bubbles, if some critical value of the bubble radius is attained. As a result, significant microstructure changes characterised by the formation of a new population of large intragranular bubbles with a rather wide size distribution (from 30 to 500 nm), observed in transient-tested fuel samples [5], are qualitatively correctly reproduced by the mechanistic code MFPR with the new resolution model.

The MFPR calculations show that the main contribution to the gas release in the transient-tested fuel is associated with the bubble biased migration, whereas the random diffusion mechanism is relatively weak and acts indirectly, accelerating bubbles coalescence and thus reducing the total sink strength of gas atoms to bubbles, to advantage of gas atom transport to grain boundaries.

Besides, the sweeping of gas atoms and bubbles by moving grain boundaries of growing grains also becomes an important mechanism of the gas release at high temperatures attained in the central zone of transient tested pellets. MFPR correctly reproduces the grain growth measured in different local positions of the fuel pellet and thus reliably calculates the swept gas release. Superposition of all these mechanisms: gas atom diffusion, bubbles random and biased migration, and gas sweeping by grain boundaries, results in a reasonable prediction of the measured fractional gas release in the Risø ramp tests [4] with different hold times from 4 to 62 h at the terminal linear power of $\approx$ 40 kW/m.

This allows the conclusion that the modification of the mechanistic code MFPR with the advanced models and mechanisms, presented in the current paper, offers the mutually consistent description of the fission gas release and microstructure evolution (bubble size distribution, grain growth) in the UO_2 fuel pellets under the transient conditions.

5. References

1. M.S. Veshchunov, V.D. Ozrin, V.E. Shestak, V.I. Tarasov, R. Dubourg, G. Nicaise. Nucl. Eng. Des., 236 (2006) 179-200.
2. M.S. Veshchunov, R. Dubourg, V.D. Ozrin, V.E. Shestak, V.I. Tarasov. J. Nucl. Mater. 362 (2007) 327.
3. M.S. Veshchunov, A.V. Boldyrev, V.D. Ozrin, V.E. Shestak, V.I. Tarasov. Nucl. Eng. Des. 241 (2011) 2822–2830
4. C. Bagger, M. Mogensen, C.T. Walker. J. Nucl. Mater. 211 (1994) 11.
5. I.L.F. Ray, H. Thiele, Hj. Matzke. J. Nucl. Mater., 188 (1992) 90.
6. M.S. Veshchunov, V.I. Tarasov. J. Nucl. Mater. 437 (2013) 250–260.
7. M.S. Veshchunov and V.E. Shestak, J. Nucl. Mater. 376 (2008) 174–180.
8. J.A. Turnbull. J. Nucl. Mater. 38 (1971) 203.
9. J.A. Turnbull. J. Nucl. Mater. 50 (1974) 62.
10. R.S. Nelson. J. Nucl. Mater. 31 (1969) 153.
11. J.A. Turnbull and R.M. Cornell. J. Nucl. Mater. 41 (1971) 156-160.
12. J.A. Turnbull and R.M. Cornell. J. Nucl. Mater. 37 (1970) 355-357.
13. M.S. Veshchunov. J. Nucl. Mater. 277 (2000) 67.
14. M.S. Veshchunov, A.V. Berdyshev, V.I. Tarasov. Development of Fission Gas Bubble Models for UO_2 Fuel in Framework of MFPR Code. Preprint IBRAE-2000-08, Moscow, 2000.
15. C. Baker, J. Nucl. Mater., 66 (1977) 283-291.
16. P.G. Shewmon, Trans. AIME, 230 (1964) 1134.
17. E.E. Gruber, J. Appl. Phys. 38 (1967) 243.
18. R.M. Cornell, J. Nucl. Mater. 38 (1971) 319.
19. S. Kashibe, K. Une, K. Nogita, J. Nucl. Mater. 206 (1993) 22.
20. A.D. Brailsford, R. Bullough, Philos. Trans. Royal. Soc. A 302 (1981) 87.
21. M.S. Veshchunov, J. Nucl. Mater. 346 (2005) 208-219.
22. M.S. Veshchunov, Materials, 2 (2009)1252-1287.

ASSESSMENT OF STAINLESS STEEL FUEL ROD PERFORMANCE AGAINST LITERATURE AVAILABLE DATA

C. GIOVEDI
LabRisco, University of São Paulo
Av. Prof. Mello Moraes 2231, São Paulo, SP, Brazil

M. CHERUBINI
NINE, Nuclear and Industrial Engineering
Borgo Giannotti 19, 55100, Lucca, Italy

A. ABE
Nuclear and Energy Research Institute - IPEN/CNEN, Nuclear Engineering Center – CEN
Av. Prof. Lineu Prestes 2242, São Paulo, SP, Brazil

F. D'AURIA
UNIPI, University of Pisa
Largo L. Lazzarino 2, 56126, Pisa, Italy

ABSTRACT

Early PWRs (pressurized water reactors) were originally designed to operate using stainless steel as cladding material, but during their lifetime this material was step by step replaced by zirconium-based alloys mainly due to the economic advantages coming from their lower neutron absorption cross section. However, after Fukushima Daiichi Accident, the problems related to the zirconium-based alloys due to the hydrogen production and explosion under severe accident brought the importance to assess different materials in order to improve the safety under these very challenging conditions. In this sense, initiatives as ATF (Accident Tolerant Fuel) program are considering different material as fuel cladding and, one of candidate is iron based alloy as an alternative. In order to assess the fuel performance of fuel rods manufactured using iron based alloy as cladding material, it was necessary to select a specific stainless steel (type 348) and modify properly conventional fuel performance codes developed in the last decades. Then, 348 stainless steel mechanical and physics properties were introduced in the TRANSURANUS code to evaluate the fuel rod performance using this material as cladding. The aim of this paper is to present the obtained results concerning the verification of the modified TRANSURANUS code version against data collected from the open literature, related to reactors which operated using stainless steel as cladding, especially the Yankee Rowe. Yankee Rowe was initially fueled using annealed 348 stainless steel as cladding material. Thus it represents the only large scale fuel experience with this steel type in a commercial PWR. Considering that some data were not available, some assumptions had to be made to carry out the simulations mostly based on engineering judgment. Important differences related to the conventional fuel rods, such as the lack of filling gas and of gap pressurization, were taking into account to perform the analysis. Obtained results regarding the cladding behavior are in agreement with available information: temperature and integrity along with the simulated irradiation period were confirmed by the present analytical work. This constitutes an evidence of the modified TRANSURANUS code capabilities to perform fuel rod investigation of fuel rod manufactured using 348 stainless steel as cladding material.

1. Introduction

The available data shows that the steady state performance of steel cladding in the first PWR was considered excellent [1-2]. The material used in the early PWR was mainly AISI 304 (12% cold worked). Nonetheless, some reactors operated using annealed AISI 348, which presents a better corrosion resistance due to the addition of niobium and tantalum in its composition.

The substitution of stainless steel by zircaloy as cladding material was due to the lower absorption for thermal neutrons of the zirconium based alloys which enables to operate with

lower enrichment cost. Despite of the stainless steel economics penalty, the main advantage of using this material as cladding comes from the reduction of the probability of the violent oxidation reaction that occurs with zirconium-based alloys at high temperatures, as it has occurred in the Fukushima Daiichi accident [3]. As a consequence of this, iron based alloys once again can be considered as a good option to replace zirconium based alloys as cladding material improving the safety under accident scenarios [4]. Considering the previous good experience of AISI 348 as cladding, this material could be again applied to replace zirconium based alloys as PWR fuel cladding.

In order to evaluate the fuel performance of fuel rods using AISI 348 as cladding, it is necessary to modify the current fuel performance codes to insert correlations and properties of this material. In this sense, TRANSURANUS code appears as a good option due to its flexibility for different fuel rod designs and reactor types, time range of the problems to be treated and materials data bank, which includes AISI 316 [5].

The adapted version of the TRANSURANUS code to evaluate the AISI 348 performance under irradiation was assessed using Yankee Rowe available data from open literature. The reason why Yankee Rowe fuel rod was selected is because it was the unique PWR (for which information was available to the authors) in which AISI 348 was used as cladding material. The aim of this paper is present the obtained results in the framework of this activity.

1.1 Transuranus code

TRANSURANUS is a computer code for the thermal and mechanical analysis of fuel rods in nuclear reactors developed at the European Institute for Transuranium Elements (ITU). The code consists of a clearly defined mechanical-mathematical framework into which physical models can easily be incorporated [5].

In order to introduce the AISI 348 data in the TRANSURANUS code, a set of references has been searched and collected. A selection has been made in order to use reliable data, when necessary data are not available either values coming from similar stainless steel (AISI 347) or typical values (i.e. applicable for a variety of stainless steel) were used.

It was assumed that correlations already programmed in TRANSURANUS for the AISI 316 are acceptable and validated enough. In addition the new correlations related to the AISI 348 properties somewhat reflect the same structure of the equivalent formula already programmed for the AISI 316. These correlations similarities should (at least partially) ensure that code numerical stability issue is not to be expected.

The AISI 348 behavior predicted by the modified code version has been compared against AISI 316 behavior which is part of the original (hence validated) code version. In general the two steels present, as expected, similar trends. AISI 316 has shown a bit more conservative results in respect to AISI 348.

1.2 Description of Yankee Rowe NPP features

The Yankee Rowe PWR has been owned and operated since startup in 1960 by the Yankee Atomic Electric Co. at Rowe, Massachusetts. The reactor and its initial core and stainless steel reloads were designed and built by Westinghouse. Yankee Rowe was the first fully commercial PWR of 250 MWe, which started up in 1960 and operated to 1992 [6]. Yankee Rowe produced 44 billion kilowatt-hours of electricity from 1961-1992 when it was permanently shut-down for economic reasons. The plant was successfully decommissioned between 1992-2007 with structures removed and the site restored to stringent federal and state remediation standards [7].

Starting from its 7th cycle of operation, the reactor began to change to Zircaloy cladding, the transition was completed with cycle 12. The stainless steel clad reactor core consisted of 76 assemblies and 24 cruciform control rods. A typical stainless steel assembly was made up of 9 subassemblies each arranged in a 6x6 array, to make up an 18x18 fuel rod array. The subassemblies were tied together along their length to form a complete integral fuel assembly.

The clad material was both seamless and welded annealed AISI 348 and represents the only large scale fuel experience with this steel in a PWR. The chemical composition of the adopted AISI 348 is identical to the niobium stabilized AISI 347, with the exception of a 0.10 % limit on tantalum to reduce the neutron absorption cross section. The fuel rod was also unique in that 6 physically separated fuel stacks spaced by equally spaced stainless steel discs. Each segment contains about 25 pellets. The objective of such design was to minimize differential thermal expansion between fuel and clad. There were no reported stainless steel clad fuel failures. The average fuel rod heat generation rate was 114 W cm^{-1}, the design rate was 353 W cm^{-1} (with a peak as high as 410 W cm^{-1}). The maximum cladding surface temperature was 343ºC. A total of 16 assemblies were examined, all the assemblies were in excellent conditions with a minor amount of crud deposited [1].

2. Methodology

2.1 Yankee Rowe general data

In order to prepare the input deck to perform the simulation considering the Yankee Rowe reactor design and operational parameters, it was collected in the literature all the available data, which are presented in Table 1.

Tab 1: Yankee Rowe general data from open literature [1], [7].

Parameter	Value
Rod Outside Diameter (cm)	0.864
Cladding Thickness (cm)	0.053
Gap size (diametral) (cm)	0.011
Fuel Rod Pitch (cm)	1.153
Fuel Pellet Diameter (cm)	0.747
Fuel Pellet Density (%)	93
Fill Gas Internal Rod Pressure (MPa)	0.1
Active Fuel Length (cm)	229.9
U235 Enrichment Degree (%)	3.4
Coolant flow rate (g h^{-1})	16E+9
Coolant temperature (ºC)	282
Coolant Pressure (MPa)	14
Average LHGR (kW m^{-1})	11.4
Design LHGR (kW m^{-1})	35.3
Maximum Cladding Temperature Surface (ºC)	343
Average Burnup (MWd tU^{-1})	31000
Final Fluence Level (n cm^{-2})	6E+21

2.2 TRANSURANUS model and assumptions

The simulations were carried out adopting the recommended TRANSURANUS models for PWR. The geometric characteristics, thermal-hydraulic parameters and power profile obtained from the literature for the Yankee Rowe fuel rod were implemented in the TRANSURANUS input deck. Table 2 presents some of the parameters fixed in the input deck in order to simulate the Yankee Rowe fuel rod operation, using a modified version of the TRANSURANUS code in which the AISI 348 characteristics have been added.

Tab 2: Yankee Rowe input deck parameters.

Parameter	Description	Value	Remark
IALPHA	Determination of the heat transfer coefficient between fuel rod and coolant	0	Standard option: thermo-hydraulics of the coolant considered
CANF	Concentration of the gas components at the beginning of the calculation	0.8 N_2 0.2 O_2	The fuel rod is not pressurized, then it was considered the air composition [1]
HHREF	Reference heights of axial slices in the cladding	See Figure 1	The Yankee Rowe fuel rod was divided in slices considering the information from the literature [1]
RAB	Outer radius of the fuel (mm)	3.735	[1], [8]
RIH	Inner radius of the cladding (mm)	3.790	[1], [8]
RAH	Outer radius of the cladding (mm)	4.320	[1], [8]
POR000	Average fabrication porosity	0.07	The density of the fuel pellet is 93% [1]
ENRI35	Uranium 235 enrichment (%)	3.4	[1], [8]
PI0EIN	Filling gas pressure (MPa)	0.1	The fuel rod is not pressurized [1]
AOPL	Free volume in the upper plenum available for filling gas and fission gas	0.690	The plenum height assumption considered a conservative value taking into account the fuel stack height
IWERT 2	Linear rod power (kW m^{-1})	35	Design rod power given in the literature for the Yankee Rowe fuel rods [1], [8]
IWERT 3	Neutron flux (cm^{-2} s^{-1})	$6.3x10^{13}$	Average assumed value to achieve the final fluence level and burnup [1], [8]
IWERT 4	Coolant flow rate (g h^{-1})	$7.86x10^{5}$	[8]
IWERT 9	Coolant temperature (°C)	252	[1], [8]
IWERT 10	Coolant Pressure (MPa)	14	[1], [8]
IWERT 18	Hydraulic diameter (mm)	11.53	[1], [8]

Considering that in TRANSURANUS code the analysis is performed slice per slice, it was necessary to assume a discretization for the Yankee Rowe fuel rod, which is presented in the Figure 1. In order to prepare this model, it was considered the following information: the fuel rod had six physically separated fuel stacks with a perforated stainless steel disk between them localized at equally spaced axial locations, each segment contains about 25 UO_2 pellets, the active fuel length is 229.9 cm and the height of the fuel pellet is 1.46 cm [1], [8].
The plenum length is not presented in the literature. Then, for calculation was assumed a value of 14 cm, which represents a conservative value for a PWR fuel rod with an active length of 229.9 cm.
The cladding and pellet roughness are also not presented in the literature for the Yankee Rowe fuel rod, and then it was assumed typical values for PWR. The same was considered for grain diameter, open porosity and plenum spring characteristics.

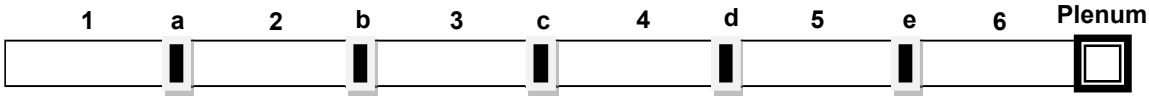

1, 2, 3, 4, 5, 6: 36.5 cm (25 fuel pellets) divided in 4 segments each one of 91 mm (apart the first two meshes of 85 mm); a, b, c, d, e: 40 mm (stainless steel disk); Plenum: 140 mm

Fig 1: Yankee Rowe fuel rod assumed discretization based on the literature data [1].

The simulation to assess the behavior of the Yankee Rowe fuel rod was carried out considering the information related with the rod E6-C-f6 as described in [8]. The selected rod target of the present simulation was irradiated into three core cycles identified as Core I, Core II and Core IV. Boundary conditions and axial power profile have been derived from [8]. Noticeably the axial power profile has been derived considering the average core power reported in Table 1. Data related with E6-C-f6 fuel rod are available in four axial positions, which have been interpreted as average values along the related length. Thus constant piecewise trend has been adopted into TRANSURANUS simulation (Figure 2). The calculated peaking factors have been imposed both to the linear power and to the neutron flux. The resulting profile is bottom skewed for the cycles Core I and II where the power was controlled by control rods, rather in Core IV boron was introduced as chemical shim resulting in a flatter axial profile [9].

The irradiation period is consistent with the information available in [8], adding 24 h for the power rise, 12 h for the power decrease, in addition 48 h has been set as shutdown period between two core cycles.

Finally an average neutron flux equal to 6.3×10^{13} n cm^{-2} s^{-1} has been set in order to achieve a fluence level close to the value available in the literature, i.e. 6.0×10^{21} n cm^{-2}. Regarding the fuel-clad contact model, the perfect slip model has been adopted.

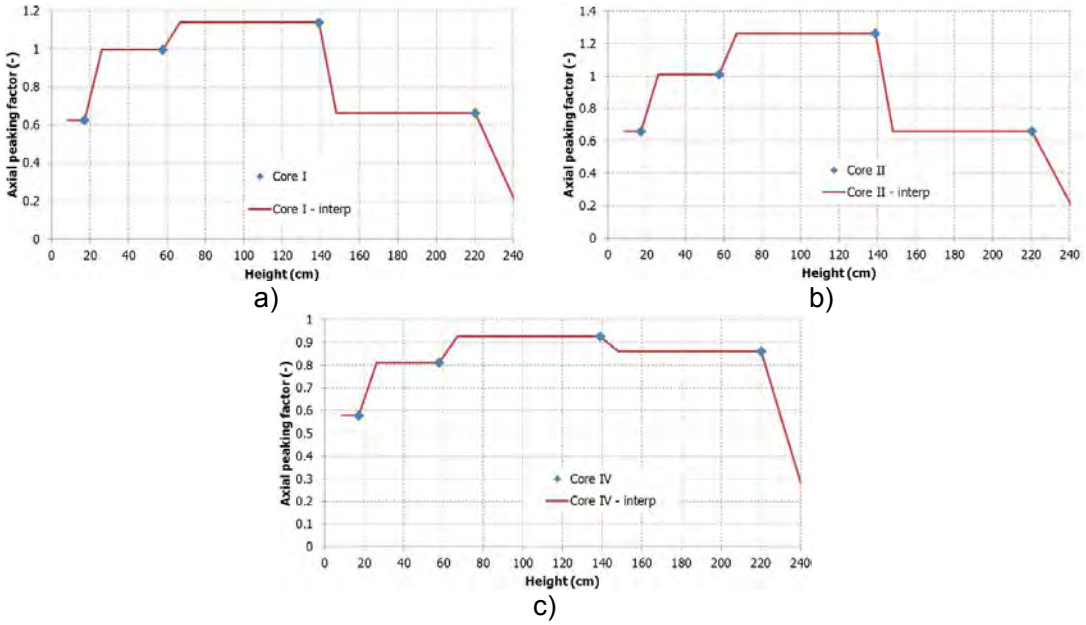

Fig 2: E6-C-f6 fuel rod axial peaking factor for Core I (a), Core II (b) and Core IV(c), available data (blue dots [8]) and related interpolation (red curve).

3. Results and Discussion

The results obtained from the Yankee Rowe fuel model are shown hereafter. Table 3, Table 4 and Table 5 list, respectively, the outcomes of the simulation at the end of the Core I, Core II and Core IV cycle, compared with available information taken from [8]. It should be noted that no tuning has been done for carrying out the simulation.

The parameters attaining to the Core I cycle are reasonably reproduced by the TRANSURANUS code (Table 3). The largest deviation occurs in the burnup of the top part of the E6-C-f6 fuel rod that could be caused by the representation of the power axial profile.

Regarding the fuel temperature calculated by the code, centerline and surface values are provided since for the reference data no specification about the radial position is provided. It can be seen that reference fuel temperature is within the code prediction for all the four axial positions.

The same considerations apply for the clad temperature in relation with both reference data radial position and calculated values.

Additional calculated data are provided in Table 3 regarding fission gas release which remains very low; fuel and clad axial elongation, both are lower than 0.5 %; maximum fluence value and plenum pressure which is double of its starting value.

Tab 3: Yankee Rowe E6-C-f6: comparison between reference and calculated data at the end of Core I cycle.

Position* (cm)	Parameter	Reference [8]	TRANSURANUS	Note
CORE I				
17.02	Cumulative Burnup (MWd tU^{-1})	8.19	8.2	
57.66		13.29	13.058	
138.94		12.53	14.94	
220.22		5.9	8.701	
17.02	Fuel Temperature (°C)	515	655.0	Centerline
			496.6	Surface
57.66		612	878.3	Centerline
			587.2	Surface
138.94		621	961.4	Centerline
			612.8	Surface
220.22		482	700.8	Centerline
			526.8	Surface
17.02	Clad Temperature (°C)	267	275.2	Inner
			266.4	Outer
57.66		278	289.2	Inner
			275.8	Outer
138.94		287	306.6	Inner
			290.1	Outer
220.22		285	295.9	Inner
			287.3	Outer
17.02	Coolant Temperature (°C)	254	252.9	
57.66		258	257.1	
138.94		268	267.0	
220.22		275	273.0	
	Fission gas release (%)	-	0.08	
	Fuel axial elongation (%)	-	0.46	
	Clad Axial elongation (%)	-	0.44	
	Gap size (µm)	-	24.7/36.2	Min/Max value
	Fluence (n/cm^2)	-	2.8e21	Max value
	Plenum Pressure (MPa)	-	0.24	

Table 4 compares reference and calculated data related with the Core II cycle. Also for this irradiation step the code gives reasonable results, showing the same (as in Core I) over prediction of the burnup at the top of the fuel rod.
Calculated values of fuel and clad temperature include the corresponding reference data with a unique exception of the clad temperature at the top position.
Notwithstanding the accumulation of the burnup the fission gas release is still low (0.14%); fuel and clad axial elongation do not change so much from the previous cycle; the gap is reducing but still open; the plenum pressure is slightly increased from the previous cycle.

Tab 4: Yankee Rowe E6-C-f6: comparison between reference and calculated data at the end of Core II cycle.

Position* (cm)	Parameter	Reference [8]	TRANSURANUS	Note
CORE II				
17.02	Cumulative Burnup (MWd tU^{-1})	14.54	14.572	
57.66		23.24	22.864	
138.94		22.78	27.212	
220.22		10.23	15.095	
17.02	Fuel Temperature (°C)	523	664.9	Centerline
			488.8	Surface
57.66		616	852.5	Centerline
			542.8	Surface
138.94		642	964.9	Centerline
			552.7	Surface
220.22		482	694.5	Centerline
			513.5	Surface
17.02	Clad Temperature (°C)	267	275.2	Inner
			266.4	Outer
57.66		279	289.2	Inner
			275.8	Outer
138.94		290	306.6	Inner
			290.1	Outer
220.22		286	295.9	Inner
			287.3	Outer
17.02	Coolant Temperature (°C)	254	256.9	
57.66		258	261.2	
138.94		268	272.0	
220.22		276	277.9	
	Fission gas release (%)	-	0.14	
	Fuel axial elongation (%)	-	0.61	
	Clad Axial elongation (%)	-	0.45	
	Gap size (μm)	-	15.4/32.7	Min/Max value
	Fluence (n/cm^2)	-	5.1e21	Max value
	Plenum Pressure (MPa)	-	0.27	

Table 5 reports the comparison discussed above but at the end of the Core IV cycle. Also at this stage of the simulation the code shows the same discrepancies and capabilities in relation with the burnup, fuel and clad temperature. Coolant temperature is also fairly predicted.
At the end of the whole simulation the fission gas release is below 0.2%; fuel and clad elongation are well below 1%; the gap kept open with a minimum value of about 13 μm (about 1/4 of its initial value) and the plenum pressure is less than the triple of its initial value.
In relation with the fuel and clad relative elongation it can be seen that the code is able to reproduce one of the objective of the particular Yankee Rowe rod design, namely to minimize the differential thermal expansion between fuel and clad.

Tab 5: Yankee Rowe E6-C-f6: comparison between reference and calculated data at the end of Core IV cycle.

Position* (cm)	Parameter	Reference [8]	TRANSURANUS	Note
CORE IV				
17.02	Cumulative Burnup (MWd tU^{-1})	20.19	20.249	
57.66		31.33	30.847	
138.94		30.39	36.322	
220.22		15.95	23.56	
17.02	Fuel Temperature (°C)	504	610.4	Centerline
			452.8	Surface
57.66		574	716.7	Centerline
			468.3	Surface
138.94		575	755.8	Centerline
			458.8	Surface
220.22		525	772.6	Centerline
			512.9	Surface
17.02	Clad Temperature (°C)	270	272.4	Inner
			264.7	Outer
57.66		277	281.9	Inner
			271.1	Outer
138.94		284	292.3	Inner
			280.1	Outer
220.22		288	297.3	Inner
			286.0	Outer
17.02	Coolant Temperature (°C)	258	256.7	
57.66		261	260.0	
138.94		267	267.4	
220.22		276	274.3	
	Fission gas release (%)	-	0.19	
	Fuel axial elongation (%)	-	0.69	
	Clad Axial elongation (%)	-	0.44	
	Gap size (μm)	-	12.6/22.07	Min/Max value
	Fluence (n/cm^2)	-	6.8e21	Max value
	Plenum Pressure (MPa)	-	0.29	

In general the TRANSURANUS code performed reasonably well even facing with a rod design which is quite far from the typical (current) PWR technology (e.g. clad material, filling gas type, lack of gap pressurization, presence of different segments within the fuel rod). Any predicted parameters for the simulated fuel rod are of no concern regarding their corresponding design data.

4. Conclusion

The assessment of the modified TRANSURANUS code benefits of the availability in the open literature of data related with Yankee Rowe NPP, which was one of the few plants in which AISI 348 has been used as cladding material. A specific Yankee Rowe fuel model has been set up, fully considering the available information and doing some assumptions for covering some lacks (e.g. fuel rod upper plenum height). When such assumptions had to be made, conservative values have been adopted.

The carried out calculations show reasonably agreement with available data confirming the modified code capabilities. This constitutes an indication of the modified TRANSURANUS code capabilities to perform fuel rod investigation of fuel rod manufactured with AISI 348 cladding material.

Acknowledgments
The authors are grateful to the technical support of AMAZUL, USP, IPEN-CNEN/SP and UNIPI, and to the financial support of IAEA to attend the meeting.

References
[1] S. M. Stoller Corporation, An Evaluation of Stainless Steel Cladding for Use in Current Design LWRs, NP-2642, EPRI (1982).
[2] V. Pasupathi, Investigations of Stainless Steel Clad Fuel Rod Failures and Fuel Performance in the Connecticut Yankee Reactor, EPRI 2119, Palo Alto (1981).
[3] N. Akiyama, H. Sato, K. Naito, Y. Naoi and T. Katsuta, The Fukushima Nuclear Accident and Crisis Management-Lessons for Japan-U.S. Alliance Cooperation, Sasakawa Peace Foundation, Tokyo (2012).
[4] K.A. Terrani, S.J. Zinkle and L.L. Snead, Advanced oxidation-resistant iron-based alloys for LWR fuel cladding, Journal of Nuclear Materials, 448, 420-435, 2014.
[5] K. Lassman, TRANSURANUS: a Fuel Rod Analysis Code Ready for Use, Journal of Nuclear Materials, 188, 295-302, 1992.
[6] http://www.world-nuclear.org website visit in October 22, 2014.
[7] http://www.yankeerowe.com/pdf/Yankee%20Rowe.pdf website visit in October 22, 2014.
[8] Burnup Credit — Contribution to the Analysis of the Yankee Rowe Radiochemical Assays, 1022910, EPRI (2011).
[9] R. J. Nodvik et al., Supplementary Report on Evaluation of Mass Spectrometric and Radiochemical Analyses of Yankee Core I Spent Fuel, Including Isotopes of Elements Thorium Through Curium, TID 4500, Westinghouse Electric Corporation, Pittsburgh, Pennsylvania, August 1969.

MODELING OF AXIAL DISTRIBUTION OF RELEASED FISSION GAS IN KKL BWR FUEL RODS DURING BASE IRRADIATION

VLADIMIR BRANKOV[1, 2], GRIGORI KHVOSTOV[1], KONSTANTIN MIKITYUK[1], ANDREAS PAUTZ[1, 2], RENATO RESTANI[3], SOUSAN ABOLHASSANI[3]

[1]*Laboratory for Reactor Physics and Systems Behaviour at the Paul Scherrer Institute*
5232 Villigen-PSI, Switzerland

[2]*Swiss Federal Institute of Technology Lausanne (EPFL)*
Route Cantonale, 1015 Lausanne, Switzerland

[3]*Laboratory for Nuclear Materials at the Paul Scherrer Institute*
5232 Villigen-PSI, Switzerland

GUIDO LEDERGERBER

Kernkraftwerk Leibstadt
5325 Leibstadt, Switzerland

WOLFGANG WIESENACK

OECD Halden Reactor Project
Os Allé 5, 1777 Halden, Norway

ABSTRACT

The first part of the paper presents results of a numerical analysis of the fuel behaviour during base irradiation in the Kernkraftwerk Leibstadt Boiling Water Reactor (KKL BWR) using EPRI's FALCON code coupled to the GRSW-A advanced model for fuel swelling and fission gas release. One of the goals of the analysis was to improve the modelling of the fuel-clad interaction under specific conditions of KKL BWR by considering void-dependent fast neutron flux. The post-irradiation examination conducted at the Paul Scherrer Institute's (PSI) hot laboratory for several high-burnup UO_2 rods clearly shows the development of a partial circumferential bonding layer between fuel and cladding at very high burnup (above ~70 GWd/tHM). In some parts of this bonding layer, closed voids are clearly visible on Scanning Electron Microscopy (SEM) images. It is hypothesized, that a part of the released fission gas can be trapped in these voids. In addition, the strong pellet-cladding bond layer may also impede fission gas release from the fuel periphery and thereby increase the quantity of stored fission gas in the high-burnup structure at the fuel pellet rim. A model is suggested to correlate the amount of locally trapped gas with the integral of the local contact pressure. The model is to be calibrated with available measurements of FGR from rod puncturing. In this paper, a simpler approach for fission gas trapping is undertaken which reveals a potential correlation between the position of the rod within the fuel assembly and the degree of fission gas trapping. At the next stages of our work we will extrapolate our hypothesis about the axial distribution of trapped fission gas to the Loss-Of-Coolant Accident (LOCA) analysis, in particular, as an attempt to explain the fission gas release observed in some samples fabricated from the irradiated KKL fuel rods and tested in the OECD Halden Reactor Project's LOCA test program.

1 Introduction

Increase of fuel burnup is a fact in most nuclear power plant operating countries, which is economically well motivated. Different countries operate at different level of burnup. In the United States of America, discharge burnup is around 50 MWd/kgU and in Swiss reactors it can reach as high as 70 MWd/kgU [1]. Longer utilization requires fuel vendors to supply product which will not compromise the plant safety at high burnup with particular focus on design base accidents such as LOCA. With the increase in burnup, virtually all thermo-mechanical properties of the fuel rods degrade. The fuel becomes more fragmented, heat conduction decreases (e.g. [2]) and the cladding becomes more brittle to name a few. Most of the LOCA safety criteria are based on fuel experiments with fresh or low-burnup fuel and this may call for a review of safety criteria before further increases of the fuel burnup at discharge. Although there is currently US NRC driven strong focus on the hydrogen content in the cladding as relevant LOCA criterion, the high burnup properties of the fuel also have to be taken into account. Various research programmes, for example the OECD Halden Reactor Project, Studsvik Cladding Integrity Programme (SCIP) and the EPRI Nuclear Fuel Industry Research (NFIR) programme, are looking into fuel behaviour under transient conditions. Experiments are expensive and time-consuming, experimental programs are few, and efforts should also be invested in fuel modelling in order to transform the experimental test data into validated model data for the calculation of fuel behaviour in nuclear power stations.

A Westinghouse Fuel Performance Programme (FPP) on KKL fuel investigated several properties, including measurement of the fission gas release (FGR) done at PSI by rod puncturing on a large set of high burnup UO_2 BWR fuel rods. The experimental data show considerable scatter among the examined fuel rods. As an example, rods of very similar burnup, power history and rod design differ in the rod puncture data by 400 %, relatively speaking. One explanation for this difference can be the existence of a strong pellet-cladding bond layer, which was observed in the post-irradiation examination (PIE) of selected rods, and which can act as both, fission gas storage in its pores and as barrier for fission diffusion towards the plenum. Furthermore, fission gas – after its release from pores – may also be trapped in a kind of pockets at limited detached pellet-clad areas. The position of the rods within the fuel assembly may be significant for the mechanism of fission gas trapping at the pellet-cladding bond layer and therefore give some explanation for the observed differences in the experimental data. Intact pellet-cladding bond layers were observed on fuel samples of pressurized water reactor (PWR) fuel, too.

Fuel modelling should rely on conservative assumptions because there are uncertainties with respect to the models, power histories and the behaviour under irradiation, to name a few. One assumption, which is backed up by experimental evidence, is the existence of pellet-clad bond layers which can retain some fission gas during the base irradiation phase and additionally suppress the release from the fuel periphery and thereby increase the stored gas in the HBS. The effect of such gas should be considered in a LOCA simulation, because it can be assumed that the rod deformation and fuel fragmentation will facilitate the breakage of the pellet-clad bond layer and therefore the trapped gas will be released which in turn may have impact on the cladding failure. In this paper, an estimation of the axially trapped fission gas is calculated with the output from an advanced FGR model, a simple model for fission gas trapping and available rod puncture measurements as reference.

2 Phenomena and Methods

2.1 FALCON Code Coupled with the GRSW-A Model

The computations are performed with the fuel performance code FALCON MOD01 [3] coupled with the Gas Release and SWelling Advanced model - **GRSW-A** [4] on a number of high burnup fuel rods from KKL that were part of a Westinghouse fuel performance program. A number of post-irradiation examinations were performed on the rods, including FGR measurement from rod puncturing. Relevant fuel rod data such as enrichment, geometry and linear heat generation history, was used to launch a base irradiation simulation on selected rods from that FPP and study the prediction of FGR to the rod plenum. The application of a post-processing model for local fission gas trapping discussed in section 3.1 allows optimizing the calculated FGR with the FALCON code coupled with GRSW-A model.

2.2 Fast Flux Input for the Simulation of Base Irradiation in BWR Fuel

Fast neutron flux is an important parameter in the fuel modeling because it contributes to cladding creep. Consequently, the effects of fast flux on the time of gap closure and on pellet-cladding contact pressure may affect bond layer formation which in turn has hypothesized implication on the trapping of fission gas. The FALCON input system allows for a direct input of tabulated axial distribution of the fast neutron flux as function of time. This option is especially valuable for specification of the appropriate boundary conditions in BWRs, whereas a constant fast-flux-to-power ratio can be assumed for PWR conditions. Open literature models for fast flux calculation in BWR are scarce. In the present BWR-specific analysis, the main relations are adopted from equations reported in [5] and the axially varying void fraction, which is used in the calculation, is derived from FALCON output. The approach, therefore, requires two calculations to be done. The first calculation is used to generate the void fraction profile as function of time, which is then used to prepare the fast flux input for the second calculation. Then the second output is used to extract the fuel-cladding contact pressure history which is necessary for the model described in section 3.1. Fig 1 shows the fast neutron fluence of a BWR fuel rod simulated with constant and void fraction dependent ratio of fast to thermal neutron flux ($\mathbf{R_{FTHF}}$).

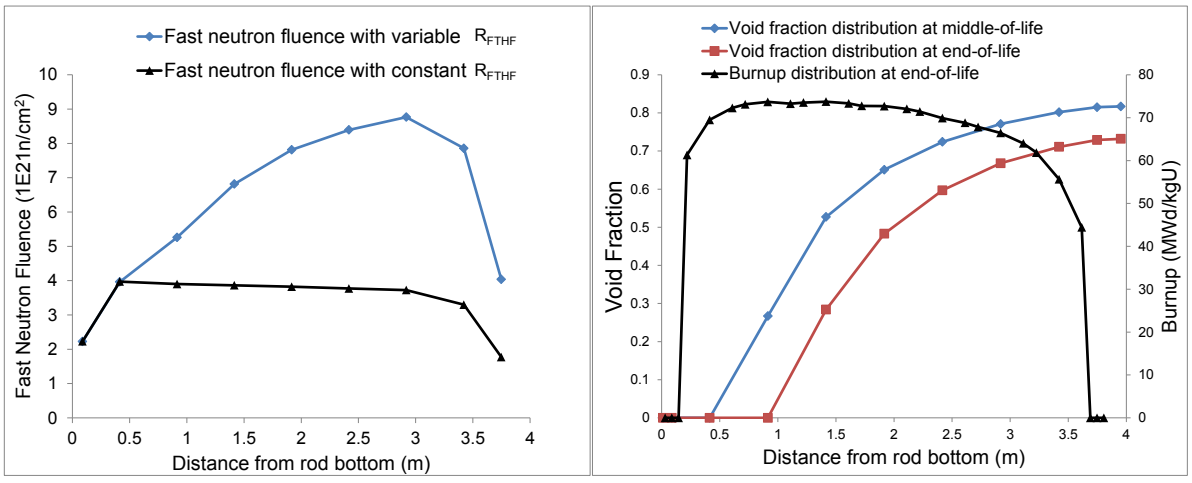

Fig 1: Fast neutron fluence distribution at end-of-life calculated with constant and void-dependent fast to thermal neutron flux ratio (left). Burnup profile at end-of-life and void fraction axial profile distribution at middle-of-life and end-of-life (right)

The fast neutron fluence (the time integral of fast neutron flux) distribution shown in Fig 1 (left) is computed at different elevations of the fuel rod. At the bottom, where the void fraction is zero, there is no difference between the calculations. The two distributions begin to diverge at about 0.5 m from the fuel rod bottom owing to the increase of void fraction of the coolant.

The gradually decreasing trend past the 0.5 m mark in the neutron fluence calculated with constant $\mathbf{R_{FTHF}}$ is explained with decreasing thermal neutron flux due to increasing void fraction and less efficient moderation. With $\mathbf{R_{FTHF}}$ assumed to be constant, the fast flux will decrease as well. The other case is more difficult to interpret. The $\mathbf{R_{FTHF}}$ increases with void fraction and burnup (as it can be inferred from [5]), which favors the fast neutron flux. At the same time, the reduction of power due to the increased void fraction reduces the overall neutron flux population which explains the decreasing trend in the fast neutron fluence distribution. A closer look at the neutron fluence distribution reveals an inflection point in the slope at around 1.5 m, which approximately coincides with the highest point in the burnup distribution shown on Fig 1 (right). After that, the fast neutron fluence distribution has decreasing trend in line with the decrease in burnup and consequently the LHGR from which the neutron flux is calculated. The increase in core voidage favours the R_{FTHF} and therefore the fast neutron flux, but also reduces the thermal neutron flux from which the former is derived and this effect is responsible for the shape of the fast neutron fluence distribution. The simulations done in this paper are performed with the assumption of void-dependent $\mathbf{R_{FTHF}}$, because it is more accurate for a BWR environment.

2.3 Pellet-clad Bonding Layers Observed in Light Water Reactor Fuel

The as-manufactured pellet-cladding gap is about 100 microns. During reactor operation, the fuel thermally expands and fission products build up which contribute to fuel swelling. Due to the reactor pressure and the temperature, the cladding, for its part, creeps down onto the pellet. Eventually, the gap closes and a pellet-clad bonding layer is formed. The fuel performance code FEMAXI-6 uses a pellet-cladding bond model based on the ratio of the time integral of contact pressure from the time of first contact and an empirical parameter characterizing the existence of a bond layer. As soon as the ratio becomes unity, the bonding layer is assumed to be developed as stipulated in [6] .

The paper by Yagnik, Machiels [7] reports that between 25-65% of the circumferential surface area of high burnup (~50 MWd/kgU) samples showed the presence of an interaction layer and strong bonding of the fuel to the cladding inner surface. On the other hand, such observation was absent in the lower burnup samples (< 40 MWd/kgU). From the cladding wall inward, the different phases encountered are pure Zr, ZrO_2, Zr-Cs-O, U-Cs-O and UO_2 [8]. This implies that sufficient time is needed in order for these species to migrate and interact. As the time progresses, and hence burnup increases, the development of bonding layers become stronger. Post-irradiation examinations on high burnup PWR fuel rods reveal level of bonding which makes it difficult to distinguish where the fuel ends and the cladding begins (right image on Fig 2). Once such layer is developed, it may even survive fuel thermally induced contraction during power reduction; a hint for this behaviour is, for instance, the cracks in high burnup fuel in the pellet and not in the bonding layer, as typically revealed by PIE (not shown here).

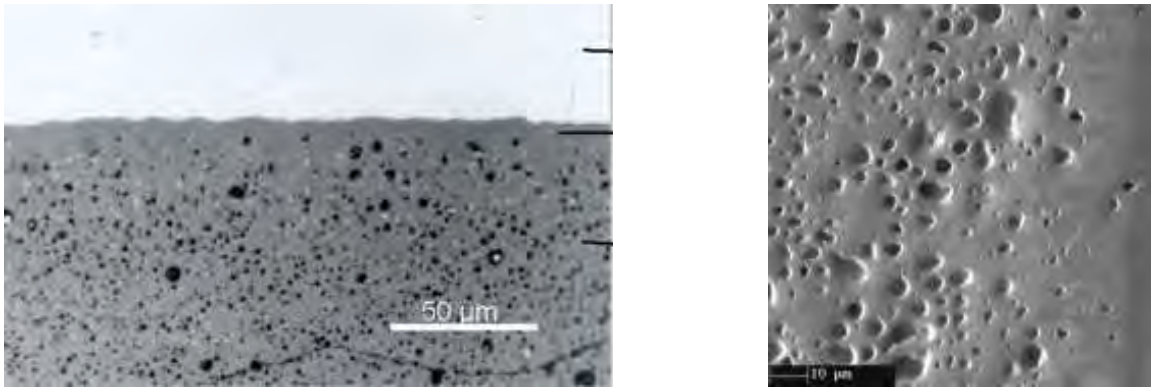

Fig 2: On the left: pellet-cladding bond layer of fuel at 83 MWd/kgU used in a Halden test [9]. On the right: pellet-cladding bond layer observed in a fuel sample from a 10-cycle PWR rod at 105 MWd/kgU average burnup [10].

The formation of a permanent bonding layer may be more pronounced in the case of BWR fuel rods where the radial burnup profile may vary considerably. It is anticipated that rods located next to the water channel will experience higher thermal flux on one side than the other and produce asymmetry in the radial burnup profile as shown on Fig 3 (right). On the other hand, such asymmetries are not expected and also not observed in PWR fuel Fig 3 (left).

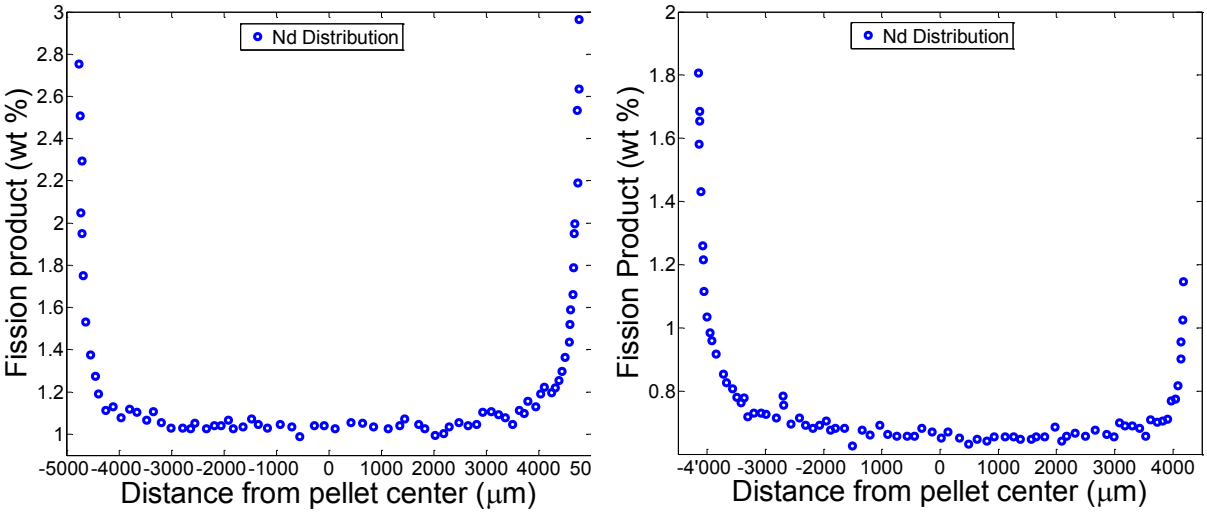

Fig 3: Distribution of Neodymium across the diameter of PWR fuel sample (left) at 105 MWd/kgU burnup [10] and BWR fuel sample (right) at 72 MWd/kgU derived from EPMA [11]

Such asymmetries suggest that bonding layers on the low burnup side may break during power dips in order to account for the thermal contraction, but at the same time keeping the high burnup side bond layer intact. It follows that the anticipated degree of trapping is higher in BWR fuel than in PWR, but that remains to be proven. Another set of SEM images shown on Fig 4 demonstrate strong bonding between fuel and cladding. Voids/pockets located at the pellet-cladding interface (marked by red circles on Fig 4 (left)) are potential sites for local fission gas trapping. The rod-average burnup of this rod was about 65 MWd/kgU where the high burnup side reached burnup of about 100 MWd/kgU.

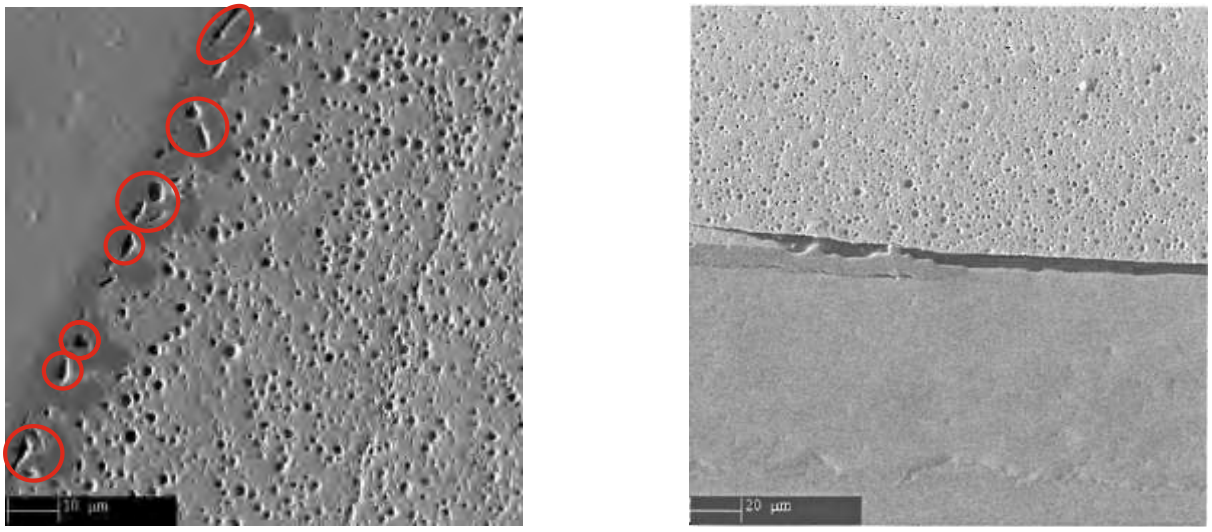

Fig 4: SEM images at the high-burnup side (left) and at the lower burnup side (right) of a 7-cycle BWR fuel rod AEB072-E4, which is also listed in Table 1 and reported in full in [11] and to some degree in [12]

The high burnup side shows an intact bond layer, whereas the lower burnup side shows partial bonding and zirconia layer formation. Experimental evidence of strong pellet-cladding bond layers was observed in both PWR (Fig 2) and BWR (Fig 4) fuel rods at high burn-up, which demonstrates the principal possibility of pellet-cladding bond layer impact on local fission gas trapping or release. The next section presents a simple post-processing model whose aim is to optimize the calculation and measurement of FGR in the rod plenum by considering the pellet-cladding interface as a possible trap for fission gases.

3 Modelling and Experimental Data

3.1 Fission Gas Trapping Model

In the context of fission gas release to the plenum, the presence of a bonding layer will act as an obstacle and may in fact trap fission gas locally. The cladding lift-off experiment IFA-610.10 [13] executed at Halden showed a non-zero hydraulic diameter (or open fuel-cladding gap), which may contradict the claim of strong bond layer. In our paper, the claim is that only fraction of the circumference is closed due to fuel-cladding bond layer and not the whole circumference and as such there is no contradiction of the said lift-off experiment. It is hypothesized that the bias in burnup distribution across a pellet radius in BWR fuel is a strong (perhaps a necessary) factor for development of permanent bond layer. The notion of partial bonding may give some explanation for the low quantity of fission gas measured in the rod plenum from puncture in some BWR rods as shown on Table 1.

As demonstrated in the previous sections, experimental evidence shows the presence of tight bonding layers at the time of examination. These locations are identified as potential sites for the local trapping of fission gas. Following the formulation of the evaluation of bonding of fuel and cladding in [6], a simple post-processing model is presented. The necessary parameters, namely contact pressure and time, are extracted from the output of the FALCON-GRSW-A calculations. A degree of trapping, K, is calculated according to equation (1). The lower bound of K is 0; meaning that the pellet-cladding gap is fully closed and therefore no fission gas is vented to the plenum. The upper bound is 1; meaning that the gap is open and all of the fission gas reaching the fuel periphery is vented to the plenum. The lower bound is a limiting case of full gap closure which may occur at high rod power (K ~ 0). Clearly, when contact pressure (CP) is zero, the gap is open and there cannot be any trapping at the fuel-cladding interface and K is 1. Equations (2) and (3) decompose the FGR into the fraction that reaches the plenum and that remains locally trapped at the interface. The trapping coefficient TC in equation (1) controls the degree of fission gas trapping and it is used as fitting parameter.

$$K = e^{-TR}, where\ TR = \frac{\int_0^{T_{end}} CP(t)dt}{TC} \quad (1)$$

The trapping ratio (TR) is a dimensionless quantity, TC has dimensions of MPa*s and T_{end} is the current time of the analysis. Fission gas release at time step *I* and axial level *Z* is the sum of two components: the fraction that is released to the plenum and the fraction that is trapped locally due to the pellet-clad bond layer.

$$FG_{trapped}(I,Z) = FGR(I,Z) * (1-K) \quad (2)$$

$$FG_{plenum}(I,Z) = FGR(I,Z) * K \quad (3)$$

Using the above formulation, the evolution of the FGR from beginning until end of life can be decomposed to the fraction which is vented to the plenum and the fraction which gets trapped as shown in Fig 5. By optimizing the TC, the fraction that reaches the plenum can be matched to the rod puncture measurement, and the rest of the fission gas is deemed axially trapped.

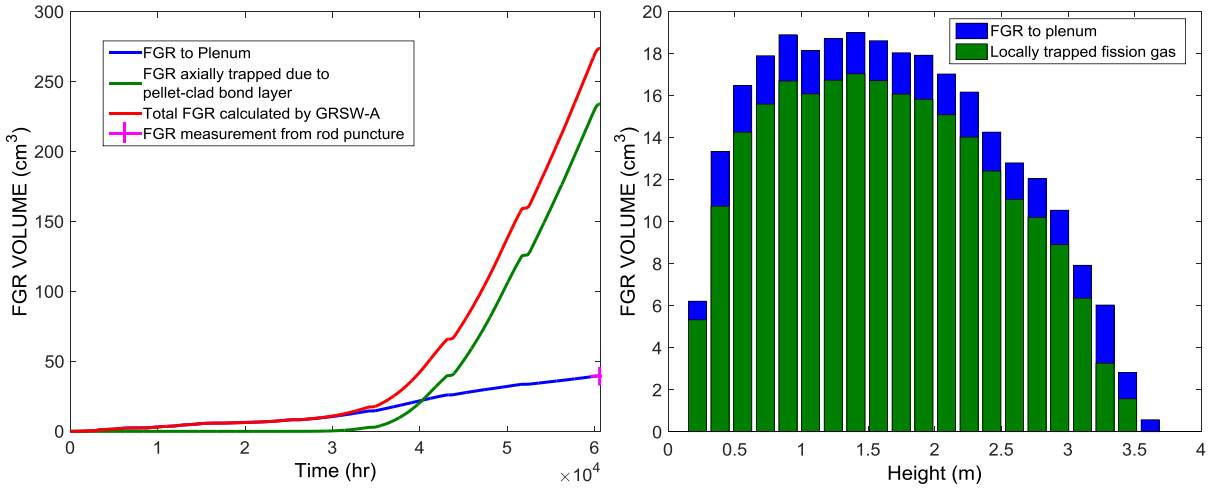

Fig 5: On the left: Time-series of the total fission gas release decomposed into the fraction that reaches the plenum and the fraction that gets trapped. On the right: Bar plot of the distribution of trapped fission gas at the axial levels where the FGR calculation is done. The calculated values are presented at standard temperature and pressure conditions.

The axially trapped fission gas is an important parameter to be considered in the modelling of a LOCA. This gas will stay trapped as long as the bond layer is intact. However, as the cladding begins to balloon, the bond layer will be broken and the trapped gas will be released and move to a region of lower pressure such as the balloon. Based on the experimental data, it is anticipated that the potential for fission gas trapping due to fuel-cladding bond layer increases with burnup while at the same time cladding mechanical properties deteriorate and therefore its resistance to deformation. It is logical to assume that the trapped fission gas may have non-negligible impact on the time to cladding failure, as previously elaborated in [14], and it should be considered in the modelling. In conclusion, contact pressure between fuel and cladding, time and the bias in burnup are deemed important parameters facilitating the creation of locally trapped fission gas and provide a reasonable explanation for the observed rod puncture measurements discussed in 3.2.

3.2 Experimental and validation database

The model for fission gas trapping is tested on a subset of the fuel rods used in the joint fuel performance program between PSI, Westinghouse and KKL. Table 1 summarizes some of the relevant data on the set of fuel rods subjected in this analysis.

Table 1: BWR fuel database of measured fission gas in the rod plenum by rod puncture. Some of this data is already published in [15] and [16]

Rod ID	Number of cycles	Burnup (MWd/kgU)	Generated Fission gas (cm³)	Rod puncture measurement (cm3)	Rod ID	Number of cycles	Burnup (MWd/kgU)	Generated Fission gas (cm³)	Rod puncture measurement (cm3)
AEB067_E4	6	57	3573	39	AEB071_H10	7	61	3896	106
AEB068_E4	6	57	3593	31	AEB071_I6	7	61	3871	207
AEB069_E4	5	51	3217	9	AEB071_J6	7	60	3873	131
AEB071_E4	7	57	3569	52	AEB072_D6	7	63	3946	71
AEB072_E4	7	63	3938	43	AEB072_F9	7	65	4140	220
AEB072_J7	7	63	4021	106	AEB072_I6	7	65	4116	158
AEB073_J9	7	64	4083	133	AGA002_F9	7	62	3779	147
AEB071_D6	7	56	3612	99	AGA002_H10	7	60	3737	158
AEB071_F9	7	62	3922	196	AGA002_I6	7	62	3809	164

All of the fuel rods in Table 1 are qualified as high burnup. The fission gas release measurements show quite inconsistent results. For example, rods AEB072_E4 and AEB072_J7 are at the same level of burnup but the rod puncture measurements differ by 150% relatively speaking. Another example is the pair AEB072_E4 and AEB071_I6 where

the relative difference between measurements is close to 400%. In the last example, the fuel rod pair had similar burnup, power history, rod and fuel assembly design, but it had different coordinates within the assembly. On the other hand, AEB072_J7, AEB072_J9 and AEB071_J8 and AEB071_H10 have comparable FGR measurements but at the same time were located in the periphery of the assembly. It is concluded that the presented evidence suggests strong dependence in the position of the rod within the fuel assembly. The last two digits in the rod identification designate the position within the assembly (please see Fig 7).

4 Results and Discussion

This section discusses the difference in contact pressure in the upper half of the fuel rod due to the two different ways of calculating the fast neutron flux (assuming constant and void-fraction dependent ratio of fast to thermal neutron flux coefficient). Afterwards, the focus is shifted to the grouping of the BWR fuel rods (shown on Table 1) according to their position within the fuel assembly with the aim to look for the optimal values of K that will maximise the agreement between measured and calculated fission gas release in the rod plenum.

4.1 Effect of the void-dependent ratio of fast to thermal neutron flux model on the conditions for local trapping of fission gas

Fast neutron flux affects cladding properties such as cladding creep. The latter may influence the pellet-cladding gap which will be reflected on the pellet-cladding contact pressure. The distribution of fast neutron fluence shown in Fig 1 suggests looking into the upper part of the fuel rod for difference in the behaviour. The effect of the different fast neutron flux models (with constant and void-fraction dependent R_{FTHF}) is reflected on the contact pressure between fuel and cladding in the upper half of the rod (Fig 6 - left) and also leads to differences in the pellet-cladding gap width (Fig 6 - right).

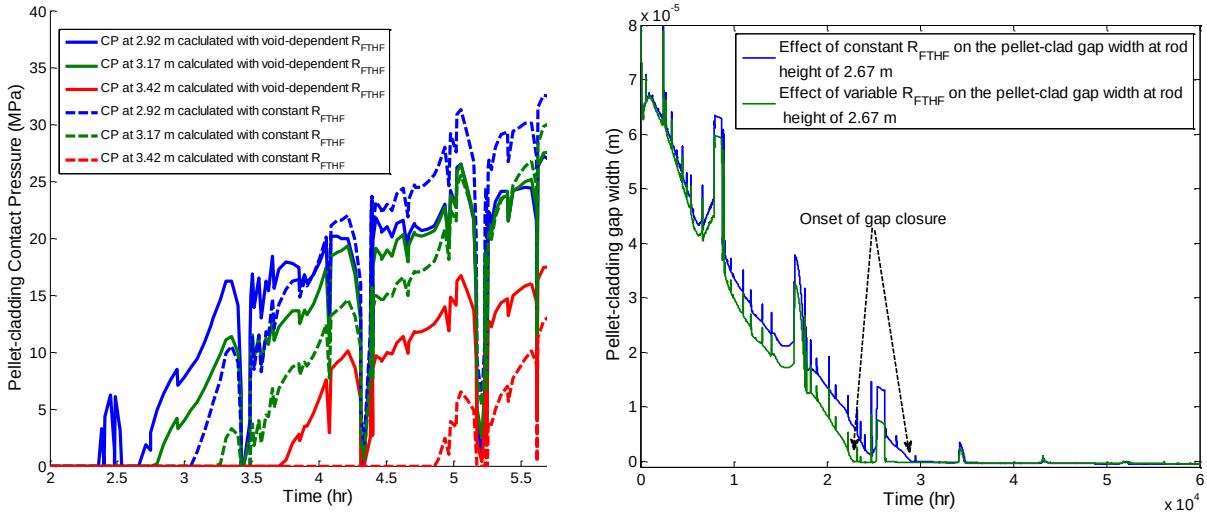

Fig 6: Effect of void-fraction dependent R_{FTHF} on fuel-cladding contact pressure at the upper half of the fuel rod (left) and on the pellet-cladding gap thickness at selected elevation (right)

Contact pressure in the upper part of the rod occurs earlier with the simulation of void-fraction dependent fast neutron flux, and therefore one of the necessary conditions for fuel-cladding bond layer formation according to equation (1). This fact may have direct impact on the amount of locally trapped fission gas. Furthermore, the higher fission rate at the fuel periphery and creation of fission products which diffuse to the gap and the increased development of the local oxygen relation towards hyper-stoichiometry also contribute to the bond layer formation.

4.2 Optimization of calculation and measurement for the database rods

The inconsistencies in the experimental data discussed in 3.2 motivated the grouping of the fuel rods according to their position within the fuel assembly. All of the rods are coming from Westinghouse SVEA96 design which is depicted on Fig 7. The location of the control rod blades is depicted by the black rectangles. Three groups are proposed: the first group includes positions E4, D5 and F7 (those next to the water channel), the second group includes I6 and F9 and the third group includes J7, J8, J9 and H10. According to this grouping, base irradiation calculations were performed and then estimation of the trapped fission gas was done with a single trapping coefficient which maximised the agreement between rod puncture measurement of the fission gas and the simulation. A simpler approach to the trapping of fission gas is to bypass the contact pressure dependence and use a constant value for *K* (eq. (1)). This parameter is between 0 where the gap is fully opened and 1 where the gap is fully closed. Therefore, in order to simulate fission gas trapping due to the bonding layer which covers half of the fuel circumference, *K* is assumed to have a value of 0.5. Using this alternative method to account for trapping and the fuel rod grouping, an optimal *K* for each group is iterated until the agreement between measurement and calculation is maximised. The results are reported in Fig 8.

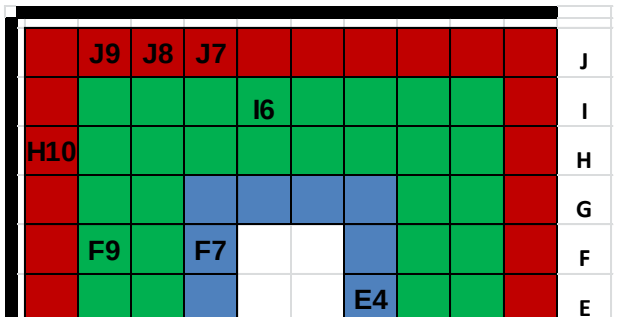

Fig 7: Fuel rod coordinates within SVEA96 fuel assembly design

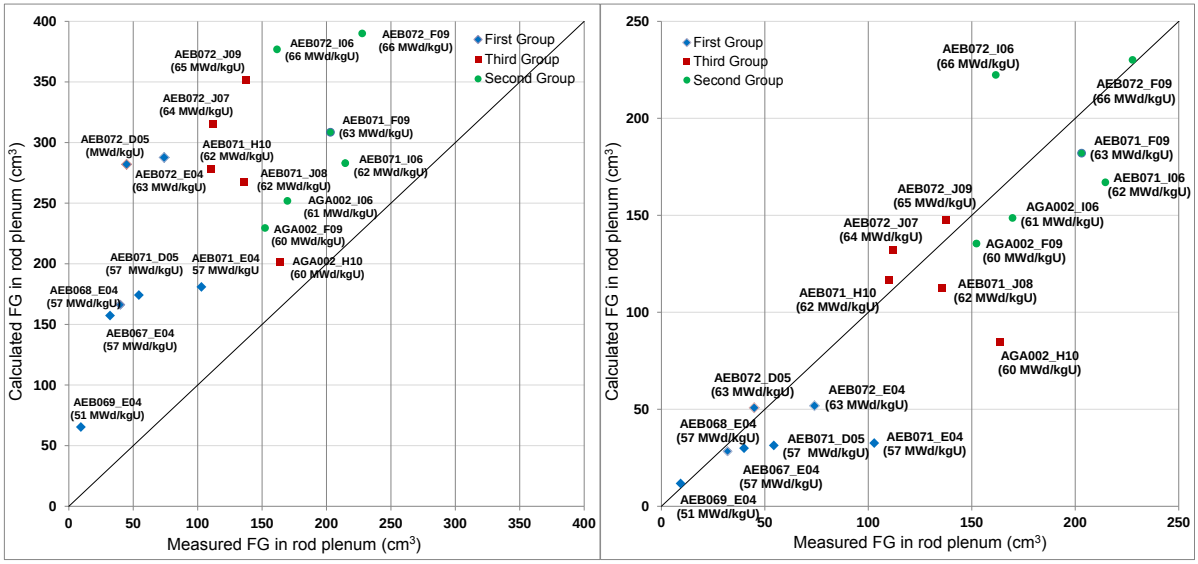

Fig 8: Calculated versus measured fission gas release into the plenum without fission gas trapping (left) and with optimized degree of trapping K (right) for the selected three groups of rods in the SVEA96 fuel assembly design shown in Fig 7.

The optimal *K* for the group of rods with positions E4, D5 and F7 (first group), which are deemed to have the largest burnup inhomogeneity, yielded approximately 0.2, which means that about 20% of the fission gas which is calculated as released is vented to the plenum while the rest is considered trapped in the pellet-cladding bond layer. The second group of rods with coordinates I6 and F9 are deemed to have the smallest burnup inhomogeneity. The

optimal *K* for the second group is approximately 0.6 (more than half of the gap is open) and the third group of rods, which is located at the assembly periphery, with coordinates J7, J8, J9 and H10 is optimized with a *K* of approximately about 0.4. It is apparent that the proposed grouping of the fuel rods and the following optimization with a single group-specific degree of trapping (K) produced better agreement between the calculated FGR at the plenum and the experimental data from rod puncture. Essentially, a qualitative consideration can be put forward that the degree of bias in burnup distribution across a pellet radius, as e.g. shown in Fig 3 (right), must be the highest for the rods at the water channel, and the lowest for the rods from the assembly bulk. This is consistent with the model assumption about an impact of burnup bias on gas trapping.

5 Conclusion and Outlook

The motivation for this paper was to consider some striking discrepancy in fission gas release measurements of high-burnup (above 50 MWd/kgU) UO_2 BWR fuel rods. Larger retention in high-burnup structure, last cycle power, fuel matrix type and other factors can impact the released fission gas. This paper hypothesizes a mechanism for fission gas retention within the pellet-cladding bond layer and increase in the fission gas stored in the HBS of the higher-burnup side of the fuel due to suppression by the bond layer. Post-irradiation examination on both PWR and BWR fuel shows the appearance of strong pellet-cladding bond layers above a certain burnup. Such phenomena present a potential site for local fission gas trapping and it may explain the low FGR on some of the rod-puncture measurements on high-burn fuel rods from the BWR KKL. Due to the higher burnup asymmetry in BWR fuel than PWR, it is hypothesized, that the former develops larger permanent fuel cladding bond layer and therefore has larger potential for fission gas trapping at high burnup. An attempt to quantify the amount of trapped fission products in the cladding inner oxide layer may help to verify or reject this hypothesis. In an attempt to explain the experimental observations of FGR in the plenum, a simple model for fission gas trapping due to pellet-clad bonding was proposed. The model will be applied in a post-processing manner and as such it will neglect any influence that the trapped gas may have on the fuel rod base irradiation simulation (for example, on gap conductance). Nevertheless, the purpose of the model is to roughly estimate the potentially trapped fission gas by adjusting the trapping coefficient with reference to the available rod puncture data. The main assumption behind the model is that partial bonding between the fuel and the cladding is possible in particular for BWR fuel due to the bias in burnup across the fuel diameter. In that respect, there is no violation of experimental observation (e.g. Halden's lift-off experiment IFA-610.10). It must be noted, that the experimental results show, that such assumption is only valid for fuel having a burnup above a threshold, the value of which needs to be determined and it may not be fully burnup related. A simple approach to fission gas trapping was used in this paper, which considered group-wise optimization of the degree of trapping according to the location of the fuel rods within the fuel assembly and resulted in notable improvement in the agreement between the simulations and the measurements. A qualitative consideration can be put forward that the gas trapping must be highest for the rods at a water channel, and lowest for those from the assembly bulk – in line with the degree of azimuthal non-symmetry in burnup distribution across a pellet radius. This is consistent with the model assumption about an implication of burnup bias on gas trapping.

In the upcoming LOCA simulation phase of the work, the estimated trapped gas will be used to study its effect on the progression of cladding failure. Without a doubt, potential for fission gas trapping should be included in the base-irradiation modelling. The modelling results presented in this paper were obtained from FALCON-GRSW-A base irradiation calculations that took into consideration the void-dependent ratio of fast-to-thermal neutron flux in order to improve to improve the fuel modelling in the upper part of a BWR.

6 Acknowledgements

The fission gas release measurements on the high-burnup BWR fuel database that was used in this study was performed at PSI and the fuel rods were manufactured by Westinghouse. They were part of a fuel performance program between PSI, KKL and Westinghouse. The author would like to acknowledge the use of this data. The work presented in this paper is integrated into a research project on fuel fragmentation, relocation and dispersal supported by swiss*nuclear* and conducted at PSI.

References

1. Jatuff, F. *High-Burnup-Fuel Technical and Economical Lessons Learned at Swiss Nuclear Power Plants*. IAEA Technical Meeting on High Burn-up Economics and Operational Experience 2013.
2. Ronchi, C., et al., *Effect of burn-up on the thermal conductivity of uranium dioxide up to 100.000 MWd t−1.* Journal of Nuclear Materials, 2004. **327**(1): p. 58-76.
3. Rashid, R.Y., R.S. Dunham, and R.O. Montgomery, *FALCON MOD01: Fuel Analysis and Licensing Code*. 2004.
4. Khvostov, G., K. Mikityuk, and M.A. Zimmermann, *A model for fission gas release and gaseous swelling of the uranium dioxide fuel coupled with the FALCON code.* Nuclear Engineering and Design, 2011. **241**(8): p. 2983-3007.
5. Loberg, J., M. Österlund, and J. Blomgren, *Neutron Detection-Based Void Monitoring in Boiling Water Reactors.* Nuclear Science and Engineering, 2010. **164**.
6. Suzuki, M., H. Uetsuka, and H. Saitou, *Analysis of mechanical load on cladding induced by fuel swelling during power ramp in high burn-up rod by fuel performance code FEMAXI-6.* Nuclear Engineering and Design, 2004. **229**(1): p. 1-14.
7. Yagnik, S.K., A.J. Machiels, and R.L. Yang, *Characterization of UO2 irradiated in the BR-3 reactor1.* Journal of Nuclear Materials, 1999. **270**(1–2): p. 65-73.
8. Berghe, S.V.d., et al. *Observation of a Pellet-Cladding Bonding Layer in High Power Fuel*. in *Seminar proceedings on Pellet-clad Interaction in LWR Fuels*. 2004. Aix-en-Provence.
9. Oberländer, B.C., M. Espeland, and H.K. Jensen, *LOCA testing of high burnup PWR fuel in the HBWR. Additional PIE on the cladding of the segment 650-5* 2008: Institutt For Energiteknikk (IFE).
10. Horvath, M.I., *Development of a method for Xenon determination in the microstructure of high burn-up nuclear fuel*, M.I. Horvath, Editor. 2007, Zürich : ETH: Zürich.
11. Restani, R. and A. Wälchli, *WA-KKL-PSI Fuel Performance Programme: Electron Probe Microanalyses on Rod AEB072-E4*. 2004, Paul Scherrer Institute (Internal Document TM-43-04-10).
12. Ledergerber, G., *Characterisation of KKL BWR Fuel for Test Series in IFA-610, IFA-629 and IFA-650*, in *HWR-1033*. 2013, Kernkraftwerk Leibstadt AG.
13. Masaki, A., *The Lift-off Experiment IFA-610.10 with a High Burn-up BWR UO2 Fuel Rod: In-pile Results during the First Irradiation Cycle*. 2008: Institutt for Energiteknikk OECD Halden Reactor Project.
14. Khvostov, G., et al., *Analysis of a Halden LOCA Test with the BWR High Burnup Fuel*, in *LWR Fuel Performance Meeting /TopFuel 2013*. 2013: Charlotte, NC, USA.
15. Ledergerber, G., *Fuel Performance Beyond Design - Exploring the Limits*, in *WRFPM 2010*. 2010: Orlando, Florida, USA. p. 12.
16. Ledergerber, G., et al., *Characterization of high burnup fuel for safety related fuel testing.* Journal of Nuclear Science and Technology, 2006. **43**(9): p. 1006-1014.

Improving the Accuracy of PCMI Simulations with More Realistic Geometry and Material Models

R. J. GARDNER[a], S. R. NOVASCONE[a], D. M. PEREZ[a], G. PASTORE[a], R. L. WILLIAMSON[a], J. D. HALES[a], W. LIU [b]

[a]*Fuels Modelling and Simulation Department, Idaho National Laboratory*
PO Box 1625, MS 0340, Idaho Falls, ID 83415-0340 – USA
[b]*ANATECH Corp., 5435 Oberlin Dr, San Diego, CA 92121*

ABSTRACT

Assessment of fuel performance codes is an endeavour that requires re-evaluation as new simulation capabilities become available. BISON, the finite element-based fuel performance code in development at Idaho National Laboratory, has been used to simulate a variety of experiments. Calculations from these simulations are compared to experimental measurements for the purpose of evaluating the progress of code development, in particular with regard to PCMI. One such experiment, from the Risø 3 Fission Gas Project, provides measurements of fission gas release and cladding diameter. A subset of the Risø 3 Fission Gas Project consisted of a base-irradiation period of a full-length fuel rod in the Quad-Cities-1 BWR. The base irradiation test was followed by a "bump test", in which a sub-section of the original rod was subjected to a strongly non-uniform axial power profile. The bump test took place in Risø test reactor DR3 in a water-cooled HP1 rig under BWR conditions. This particular experiment was chosen because it allows for an evaluation of several aspects of BISON, including fully coupled thermo-mechanics, mechanical and thermal contact, several nonlinear material models, and the fission gas release model. A summary of simulation results and comparison to the experiment data has been published previously however, this paper shows new results with recently added features to BISON. These new features include representing the pellets as discrete entities rather than a smeared column, including primary creep in the cladding creep model, a more logical way of combining the effects from multiple nonlinear constitutive models, a new fission gas release model, the coupling of fuel gaseous swelling to fission gas release, a different thermal conductivity model for the fuel, and a more accurate calculation for plenum volume. Comparing to previous results, the addition of these features has narrowed the gap between BISON calculations and experimental measurements for final cladding diameter and fission gas release.

1. Introduction

Pellet-cladding mechanical interaction (PCMI) is an important area of modelling research for fuel performance in general and cladding behaviour in particular. Nuclear fuel performance software can be helpful in studying PCMI. An assessment of how well simulation software performs is important for determining how best to interpret and use simulation results. In this paper, the fuel performance code BISON [1] is used to simulate one well-documented experiment. The salient features of that experiment are measurements of fuel rod diameter before and after a large power ramp and fission gas release. The work presented here is an extension of a prior Top Fuel paper [2] and focuses on the effects of including discrete pellet geometry, the combination of several nonlinear constitutive models in the cladding, a more

accurate calculation for plenum volume, a different thermal conductivity model, a new fission gas release model [3,4] and the coupling of gaseous swelling to the fission gas release model.

BISON is a nuclear fuel performance code developed at Idaho National Laboratory (INL), which is built on the MOOSE (Multi-physics Object Oriented Simulation Environment) framework [5], also developed at INL. BISON can be used to solve the fully coupled energy, species diffusion, and solid mechanics equations. BISON includes material models for thermal expansion, swelling, densification, creep (thermal and irradiation), plasticity, relocation, smeared cracking, and fission gas production and release. Algorithms for mechanical and thermal contact are used to simulate gap conditions between fuel pellets and cladding.

In this paper, pre- and post-bump test measurements of fuel rod diameter and post-experiment fission gas release from a well-known experiment are presented with corresponding calculations from BISON. This experiment was chosen because it allows for evaluation of several aspects of the code. The experiment is believed to be reliable since it was selected as a priority case for the FUMEX-III [6] (FUel Modeling at EXtended Burnup-III) project. The FUMEX-III cases are generally high burnup integral fuel rod experiments and thus involve complex coupled multiphysics behaviour.

2. Experiment

The GE7 bump test was carried out during the third Risø Transient Fission Gas Release Project in 1989 [7]. The test pin (designated as ZX115) was the lower middle segment of four approximately 0.975 m segments. The cladding was stress relieved Zircaloy-2 with a bonded zirconium liner. The fuel segment was base-irradiated in the Quad Cities-1 BWR over four reactor cycles.

The bump-irradiation was performed in a water-cooled rig under BWR conditions. After base irradiation, the power was reduced to zero, then the power history shown in Figure 1A was applied. The power history during the bump included a 6-hour conditioning period at approximately 23 kW/m, a 15 minute power ramp, and then a 4-hour hold, where the peak power at the end of the hold period was 35.5 kW/m. Note that the tabular power data supplied with the test documentation indicated a 2 kW/m power rise during the final hold period. The bump included a strong axial profile, with a peak axial factor of 1.48. Plots of the linear power (Figure 1A) and axial profile (Figure 1B) during the bump are included.

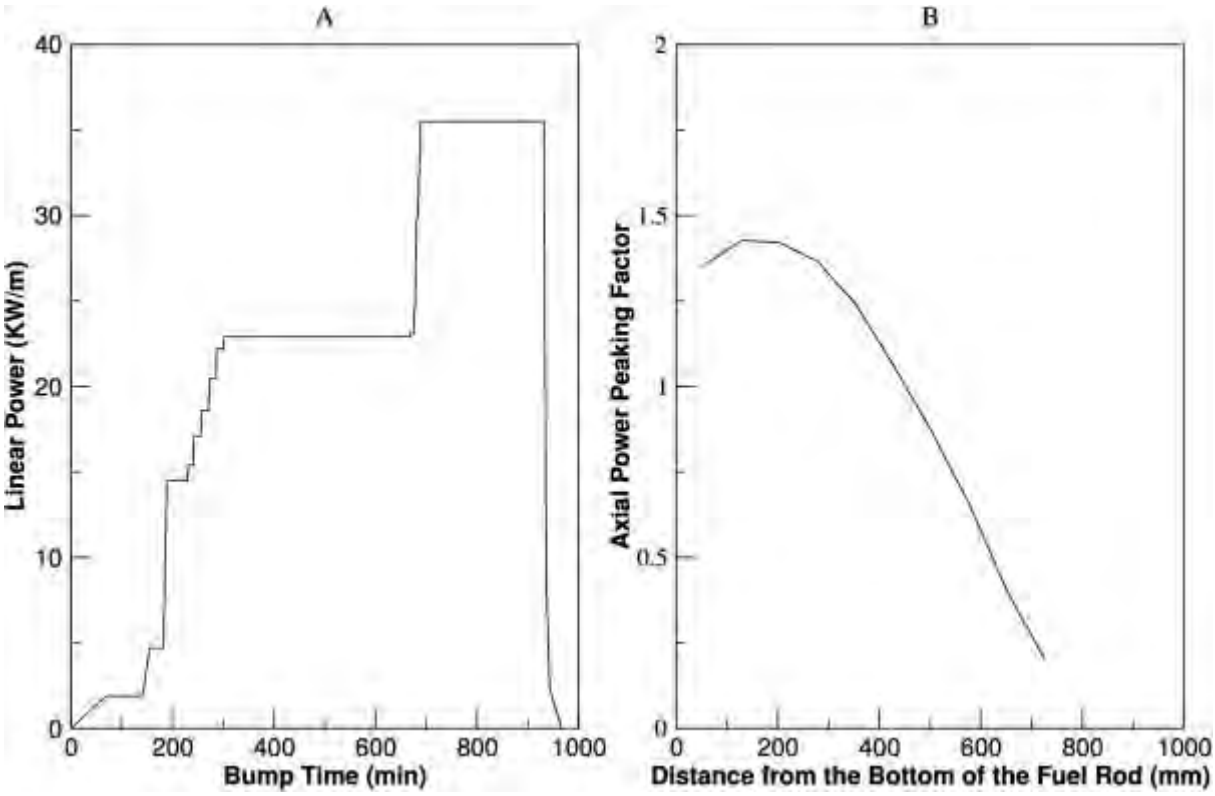

Figure 1 GE7 linear power profile(A) and axial power peaking factors(B) during the bump test.

Conditions were typical for a boiling water reactor during base irradiation. The coolant pressure was held constant at a value of 7.24 MPa throughout the base irradiation, then reduced slightly (~7.22 MPa) during the bump test (according to the experiment data provided). The cladding outer wall temperature was held at ~ 564 K throughout the base irradiation, reduced to 300 K between the base and bump irradiation, then increased back to ~ 564 K. Helium was the rod fill gas, having an initial pressure of 0.29 MPa at room temperature. The axial power profile during the base irradiation was relatively flat, varying over the range of 0.96 to 1.027. The fast neutron flux in the cladding was supplied with other experiment data. This rod was not re-fabricated after base irradiation.

3. Simulation

The fuel pin was modelled assuming 2D axisymmetry, based on the geometry specified in the FUMEX-III [6] project and the Risø GE7 Technical Report [7].

In the prior Top Fuel paper [2], UO_2 thermal conductivity was modelled using the correlation for unirradiated material suggested by Fink [8], modified to account for the effects of irradiation and porosity using a series of multipliers, as outlined by Lucuta et al [9]. In this work, the NIFR [10] thermal conductivity model is used due to more accurate calculations of fuel temperature [11].

Solid swelling in the fuel was described using empirical correlations from MATPRO [12], with densification and relocation specified using models from ESCORE [13]. Relocation strains were applied to the fuel in the radial direction only.

A physics-based model was adopted for the concurrent calculation of gaseous swelling in the fuel and fission gas release. The model incorporates a description of the underlying physical

mechanisms of gas generation, diffusion, bubble growth and interconnection, and accounts for the inherent coupling between gaseous swelling and fission gas release (FGR) [3,4].

While BISON currently has material models for fuel creep and smeared cracking, these effects were ignored in this simulation. The reason for this omission is because programming for the interaction of these two models is still in development. For this simulation, the fuel is modelled as linear elastic.

The cladding was modelled with typical constant thermal properties for heat conduction. Primary thermal creep and secondary thermal and irradiation creep are modelled using the equations from Limbäck and Matsuo [14] [15]. Irradiation growth was described using the model from ESCORE [13]. The thickness of the cladding included the Zr liner such that the inner and outer diameter of the finite element domain of the cladding is the same as the actual cladding, but the entire cladding domain was modelled using Zircaloy-2 material properties.

The cladding creep model was combined with a J_2 plasticity model to simulate rapid deformation during the power ramps. For each stress update, the model first considered only the creep contribution to compute a new effective stress, which is then compared to the yield strength. If the effective stress is above the yield strength, then the effective stress is used to calculate instantaneous plastic strain. A new effective stress is then calculated. The process is repeated until the effective stress stabilizes. This is a feature incorporated after the prior work [2].

A fully coupled thermo-mechanical analysis, with thermal and mechanical contact, was performed with input power and boundary conditions described in the experiment section. The pellet stack was simulated as a single smeared fuel column and as discrete pellets. Cladding oxidation was not considered for either case, so it was expected that calculations would at least slightly under predict final cladding outer-diameter. Mechanical contact between the fuel and cladding was assumed to be frictionless. For more information regarding how the gap is modelled in BISON, see [1].

The meshes for both the smeared and the discrete cases were built using the information provided in the Risø GE7 Technical Report [7]. The smeared pellet model was built as one long fuel column and was meshed as follows: The fuel consists of 11 radial elements and 432 axial elements while the cladding consists of 4 radial elements and 438 axial elements. The total number of elements for the smeared model was 6528. The discrete pellet model accounted for chamfers at the ends of the pellets according to the geometric information provided in the Technical Report [7] and each individual pellet was meshed. The discrete mesh consists of 72 fuel pellets. Each fuel pellet consists of 10 radial elements and 8 axial elements while the cladding consists of 4 radial elements and 582 axial elements. The total number of elements for the discrete model was 8112. The overall mesh density is similar between the discrete-fuel and smeared-fuel simulations. The experiment had an insulator pellet on either side of the fuel stack. These pellets and the plenum spring were not modelled. Due to these items not being included the void volume of the model was larger than the experiment in the prior work. This was corrected by reducing the size of the plenum to account for the volume of the insulator pellets and spring. The experiment void volume for pre- and post- test is reported in the Risø GE7 Technical Report [7]. The void volume (or the volume of gas in the plenum) of the finite element models is consistent with the numbers given in the report. A close up section of the smeared and discrete meshes is shown in Figure 2.

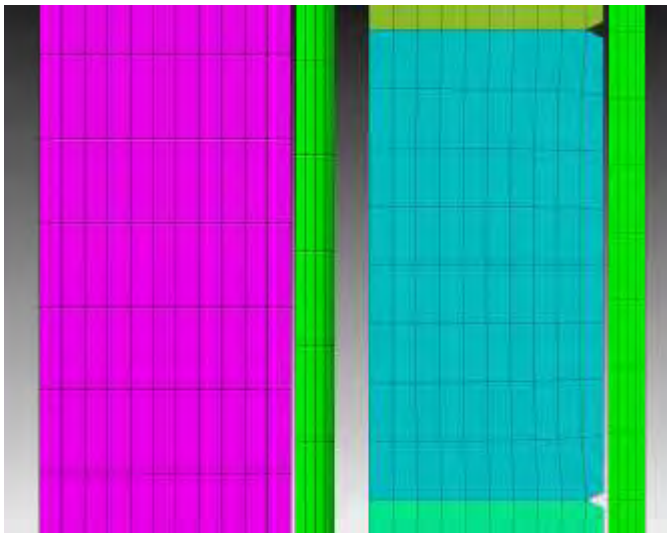

Figure 2 smeared and discrete meshes, close up.

4. Results

Comparisons of rod diameter and fission gas release were the overall figures of merit in this study. Fuel pellet temperature, plenum pressure, and plenum volume calculations and measurements are also shown.

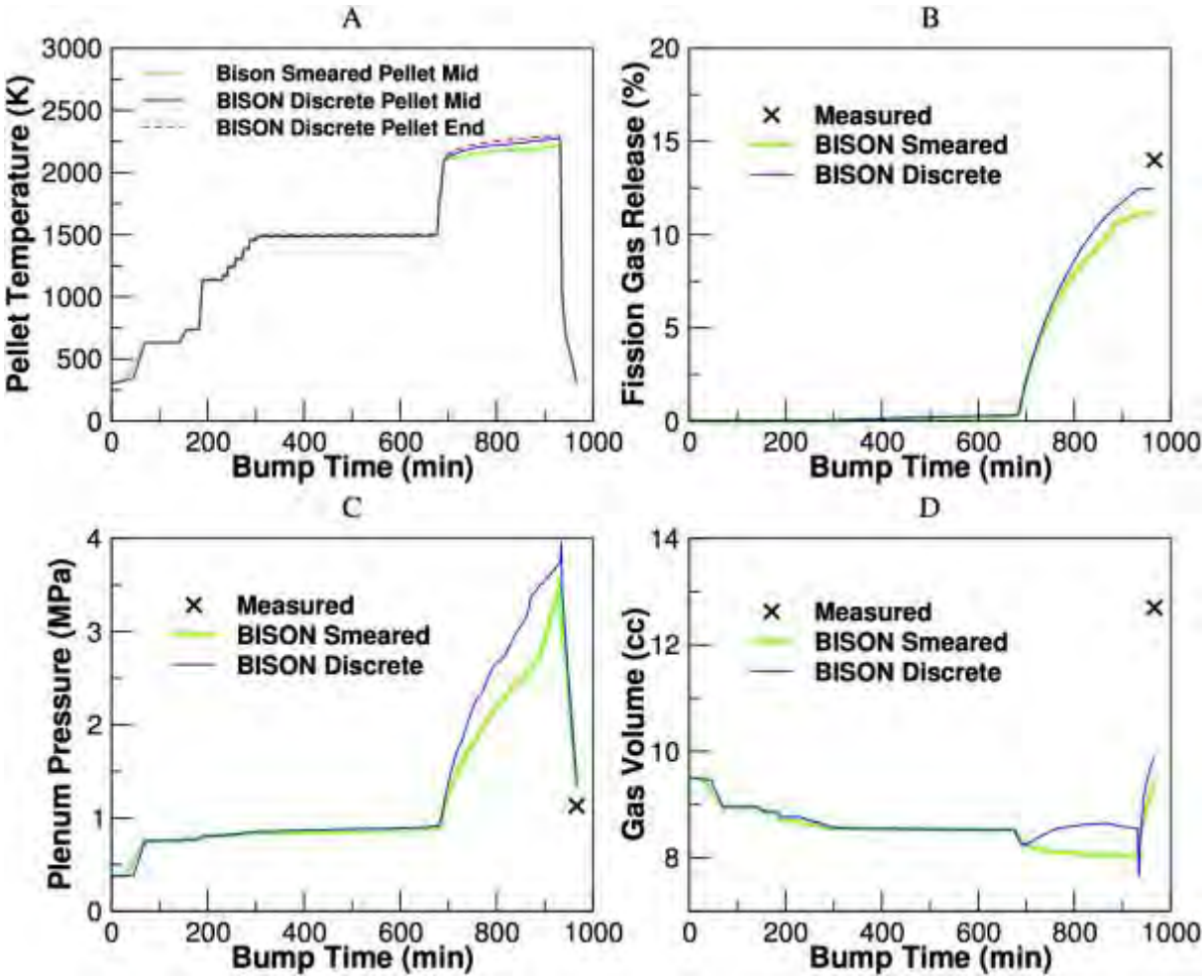

Figure 3 Measured and BISON results for fuel pellet temperature (A), fission gas release (B), plenum pressure (C) and gas volume (D).

The BISON results shown in Figure 3 are for the timeframe of the bump test. Simulation and experiment results for pellet temperature, fission gas release, plenum pressure, and gas volume are shown in Figures 3A-3D respectively. The measured results are from the post irradiation examinations (PIE) performed and are reported in the Risø GE7 Technical Report [7]. The comparisons show that BISON smeared and discrete track very well against each other in general up to about 700 minutes, at which point the power is increased to approximately 35 KW/m (refer to Figure 1A). Figure 3A plots midline pellet temperature for the smeared and discrete cases, as well as the temperature for the end of the discrete pellet where the midline was taken. The temperatures were taken in the high flux region of the fuel rod, at approximately 200 mm from the bottom. Temperature is shown to track well for the two cases until the high power bump at 700 minutes. This difference is thought to be due to the smeared fuel column conducting heat axially more efficiently. Even if the gap between discrete pellets is closed the model does not allow heat transfer because thermal contact was not defined between these surfaces. This difference will lead to the discrete pellets having a higher temperature than the smeared. The higher temperature leads to more fission gas release, which leads to higher cladding interior temperature (due to poor thermal conductivity of the fission gas) and higher plenum pressure. Results in Figures 3A-3C show this expected trend, where the BISON discrete model demonstrates higher temperature, more fission gas release and higher plenum pressure than the smeared model. Both BISON models predict the PIE plenum pressure well, when compared to the measured results, but the discrete model has a better comparison for total fission gas release. Gas volume tracks well between models until the large power ramp at 700 minutes. However, BISON under-predicts gas volume overall. The discrete model shows a rapid decrease in gas volume toward the end of the power ramp. Speculation for the discrete model gas volume behaviour is that as the power is increased the pellets initially swell due to thermal expansion leading to less gas volume at the beginning of the bump. As these pellets swell they elongate and the gap between the pellets opens, creating more gas volume as the bump test progresses. However, the reason for the abrupt volume drop and then subsequent increase in the discrete model is unclear and will be investigated in future work.

A comparison of the predicted and measured rod outer diameter is shown in Figure 4. Depicted in this plot are the data for the experiment and calculations from BISON at both pre- and post-bump. As-built rod diameter is also included in the plot as a reference, and is shown as the horizontal, solid line. The GE7 experiment's post bump diameter was measured at the pellet mid and pellet end and is shown as symbols (x and + respectively). The results for BISON smeared and BISON discrete are the subjects of this study and are shown as lines with symbols and solid lines, respectively.

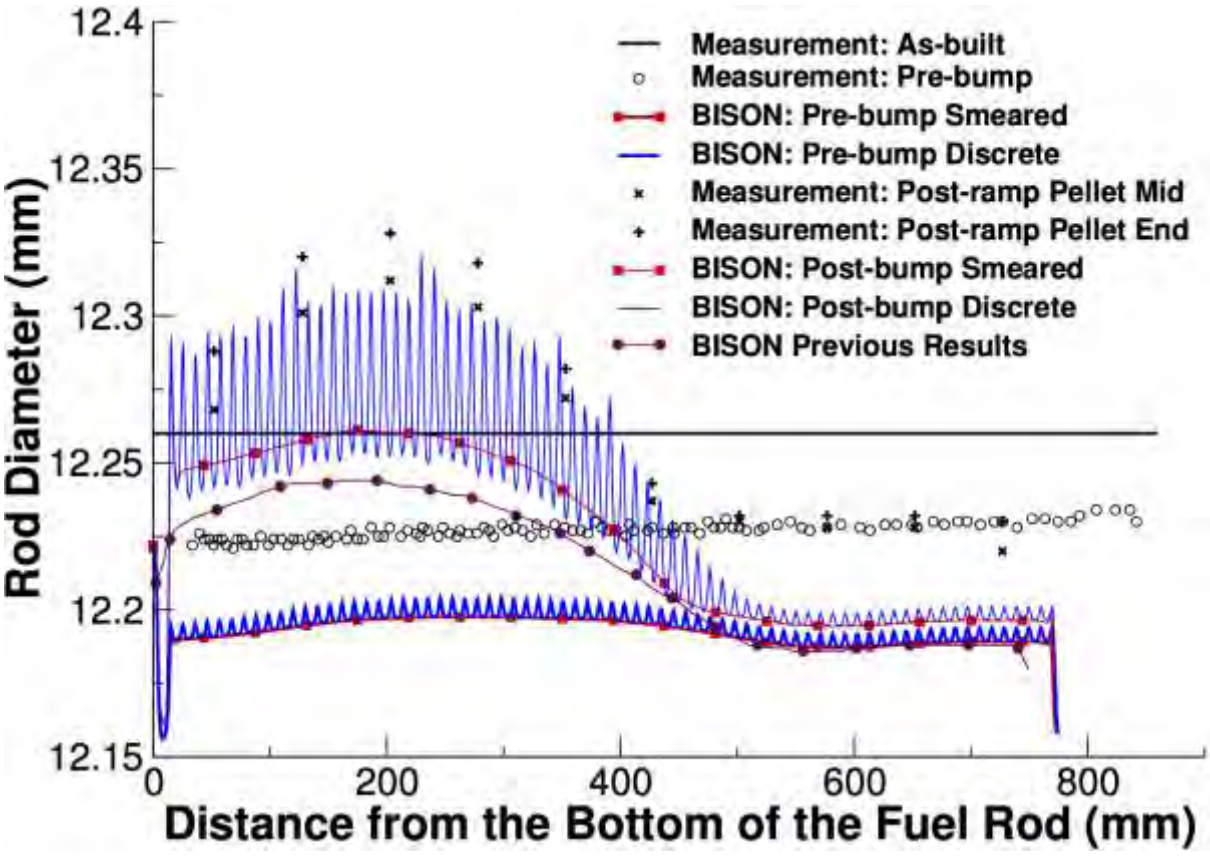

Figure 4 comparison of measured and BISON calculated rod diameter.

Pre-bump

As mentioned in the experiment section, GE7 was base irradiated in a commercial power reactor with a fairly flat axial profile. During this time in the simulation creep is the major contributor to rod diameter. Pre-bump (zero power) measurements and BISON calculations both show a fairly constant rod diameter along the length of the rod. BISON calculates a cold gap size after the base irradiation of about 20 μm. A comparison of pre-bump measured results to BISON calculations shows that BISON overpredicts cladding creep-down, giving a rod diameter of approximately 40 μm less than the measured for both smeared and discrete models. This comparison was made at approximately 600 mm from the bottom of the fuel rod.

Post-bump

The Risø GE7 experiment was designed such that the lower section of the fuel rod experienced higher neutron flux and temperature during the bump test (refer to Figure 1B for axial power profile). Due to this design, the lower region is affected by instantaneous plasticity plus creep, whereas the upper section is only creep; the result of this is the final diameter of the upper section is mostly a function of cladding creep-down during the base irradiation. The final BISON results for upper rod diameter are also over-predicted, though slightly better than pre-bump. Results show approximately 32 μm less than the measured results. This comparison was made at approximately 600 mm from the bottom of the fuel rod. Permanent cladding deformation due to instantaneous plasticity plus creep during the bump is observed over roughly the bottom two-thirds of the rod. BISON results for both smeared and discrete simulations predict the shape of this deformation nicely but under-predict the magnitude. The discrete results also show large diameter oscillations for the bottom section of the rod. Speculation is that these are caused because fuel creep and cracking were not included in the simulation, which would relieve internal stress and tighten the oscillation magnitude. Previous BISON results were also included in Figure 4 for reference.

The differences between the work presented here and the prior work are:

- Discrete vs. smeared pellets
- New fission gas release model, which calculates gaseous swelling [4]
- Nonlinear strain calculation algorithm (i.e. creep strain is calculated, stress is checked, then plastic strain is calculated if necessary)
- Added primary thermal creep in the cladding
- More accurate plenum volume calculation
- Different fuel thermal conductivity models (NFIR [10] instead of Fink/Lucuta [8][9])

Future work will include quantifying how each of these changes affects the simulation. Based on [16], we expect that the strongest effect is due to gaseous swelling model

No adjustments to input parameters were made to tune the simulation results to better fit the experimental data. The input parameters used in this study are consistent between each simulation and are based on consensus among the authors.

5. Conclusions

Rod diameter measurements (pre and post power bump) and fission gas release for the Risø3 GE7 experiment were presented and compared to BISON calculations with smeared and discrete pellets.

In terms of overall PCMI behaviour, BISON compares well to the experiment measurements. For the base irradiation, BISON predicted a smaller diameter than the measurement. This indicates that too much creep strain was calculated in BISON. Final, or post-bump, diameter comparisons between BISON results and measurements are closer in magnitude, especially for the discrete case. However, the amplitude of the pellet-mid to pellet-end (ridging) BISON calculations are much larger than measurements. We speculate that the larger mid to end pellet amplitude is due to modelling the fuel as linear elastic and ignoring creep and fuel cracking.

Measurement of cladding oxide thickness is also worth some discussion. Experiment measurements of outer cladding oxide thickness were a continuous 4 μm along the length of the pin and varied from 0 to 11 μm on the cladding inner diameter. Of course, ignoring the effects of cladding oxidation would lead to an underestimate of final cladding diameter and may also affect the ridging behaviour.

6. Acknowledgements

The submitted manuscript has been authored by a contractor of the U.S. Government under Contract DE-AC07-05ID14517. Accordingly, the U.S. Government retains a non-exclusive, royalty free license to publish or reproduce the published form of this contribution, or allow others to do so, for U.S. Government purposes.

7. References

[1] R. L. Williamson, J. D. Hales, S. R. Novascone, M. R. Tonks, D. R. Gaston, C. J. Permann, D. Andrs, and R. C. Martineau, “Multidimensional multiphysics simulation of nuclear fuel behavior,” *J. Nucl. Mater.*, vol. 423, pp. 149–163, 2012. http://dx.doi.org/10.1016/j.jnucmat.2012.01.012

[2] S. R. Novascone, J. D. Hales, B. W. Spencer, and R. L. Williamson, “Assessment of

PCMI Simulation Using the Multidimensional Multiphysics BISON Fuel Performance Code," in Proceedings of Top Fuel 2012, Manchester, United Kingdom, September 2-6, 2012.

[3] G. Pastore, L. Luzzi, V. Di Marcello, P. Van Uffelen. Physics-based modelling of fission gas swelling and release in UO2 applied to integral fuel rod analysis. Nucl. Engrg. Design 256 (2013) 75–86.

[4] G. Pastore, L.P. Swiler, J.D. Hales, S.R. Novascone, D.M. Perez, B.W. Spencer, L. Luzzi, P. Van Uffelen, R.L. Williamson, Uncertainty and sensitivity analysis of fission gas behavior in engineering-scale fuel modeling, J. Nucl. Mater. 456 (2015) 398-408.

[5] D. Gaston, C. Newman, G. Hansen, D. Lebrun-Grandi., MOOSE: A parallel computational framework for coupled systems of nonlinear equations. Nuc. Eng. Des. 239 (2009) 1768–1778.

[6] J. Killeen, E. Sartori, T. Tverberg, "FUMEX-III: A New IAEA Coordinated Research Project on Fuel Modelling at Extended Burnup", Proceedings of Top Fuel 2009, Paper 2176, Paris, France, September 6-10, 2009.

[7] The Third Risø Fission Gas Project Bump Test GE7 (ZX115), Technical Report RISØ-FGP3-GE7, September 1990.

[8] J. K. Fink. Thermophysical properties of uranium dioxide. J. Nucl Materials, 279(1):1–18, 2000.

[9] P. G. Lucuta, H. J. Matzke, and I. J. Hastings. A pragmatic approach to modelling thermal conductivity of irradiated UO2 fuel: review and recommendations. J. Nucl. Mater., 232:166–180, 1996.

[10] A. Marion (NEI) letter dated June 13, 2006 to H. N. Berkow (USNRC/NRR). Safety Evaluation by the Office of Nuclear Reactor Regulation of Electric Power Research Institute (EPRI) Topical Report TR-1002865, Topical Report on Reactivity Initiated Accidents: Bases for RIA Fuel rod Failures and Core Coolability Criteria. http://pbadupws.nrc.gov/docs/ML0616/ML061650107.pdf, 2006.

[11] D. M. Perez, R. L. Williamson, S. R. Novascone, T. K. Larson, J. D. Hales, B. W. Spencer, and G. Pastore, "An evaluation of the nuclear fuel performance code BISON," in Proceedings of the International Conference on Mathematics and Computational Methods Applied to Nuclear Science and Engineering, Sun Valley, Idaho, May 5-9, 2013.

[12] C. M. Allison, G. A. Berna, R. Chambers, E. W. Coryell, K. L. Davis, D. L. Hagrman, D. T. Hagrman, N. L. Hampton, J. K. Hohorst, R. E. Mason, M. L. McComas, K. A. McNeil, R. L. Miller, C. S. Olsen, G. A. Reymann, and L. J. Siefken. SCDAP/RELAP5/MOD3.1 code manual, volume IV: MATPRO–A library of materials properties for light-water-reactor accident analysis. Technical Report NUREG/CR-6150, EGG-2720, Idaho National Engineering Laboratory, 1993.

[13] Y. Rashid, R. Dunham, R. Montgomery, Fuel analysis and licensing code: FALCON MOD01, Technical Report EPRI 1011308, Electric Power Research Institute, December 2004.

[14] M. Limbäck and T. Andersson. A model for analysis of the effect of final annealing on the in- and out-of-reactor creep behavior of zircaloy cladding. In Zirconium in the Nuclear Industry: Eleventh International Symposium, ASTM STP 1295, pages 448–468, 1996.

[15] Y. Matsuo. Thermal creep of zircaloy-4 cladding under internal pressure. Journal of Nuclear Science and Technology, 24(2):111–119, February 1987.

[16] G. Khvostov, K. Mikityuk, M. A. Zimmerman. A model for fission gas release and gaseous swelling of the uranium dioxide fuel coupled with FALCON code. Nuclear Engineering and Design 241 (2011) 2983-3007.

European Nuclear Society
Avenue des Arts 56
1000 Brussels, Belgium
Telephone: +32 2 505 30 50 - FAX: +32 2 502 39 02
topfuel2015@euronuclear.org
www.topfuel2015.org